

ECIO 2012

European Conference on Integrated Optics

Sitges, Spain

Collected Manuscripts

(c) Copyright 2012 The ECIO Board. All rights reserved.

Contents

ID	Author	Title
WeC1	Sergey I. Bozhevolnyi	Plasmonic Waveguides: Fundamentals and Applications
WeC2	Jens H. Schmid, Przemek J. Bock,	Subwavelength nanophotonic structures in silicon waveguides
WeC4	G. Roelkens, S. Keyvaninia, S. S	III-V-on-silicon membrane photonics for nearinfrared and mid-infrared applications
WeE1	Mark G. Thompson, Damien Bonneau	Advances in Integrated Quantum Photonics
WeE4	Jordi Martorell	Generation of Second Harmonic Light from a Low Number of Molecules in the Whispering Gallery Modes
WeF1	A. J. Seeds, E. Rouvalis, M. Nat	High efficiency THz photodetectors
WeF4	Masahiro Uemukai and Toshiaki Su	Integrated Two-Wavelength DBR Lasers for Tunable Photomixing THz-Wave Generation
WeG1	Jean-Marc Fedeli, Badhise Ben Ba	Technology achievements for silicon photonic devices
WeG5	Alexander L. Gaeta	Integrated Nonlinear Nanophotonics in Silicon
ThA1	Wolfgang Sohler	Status and Prospects of Lithium Niobate Integrated Optics
ThB1	Andrea C. Ferrari	Graphene Photonics and Optoelectronics
ThB3	Shinji Yamashita	Carbon nanotube and graphene photonics for ultrafast pulse generation and signal processing
ThC1	Dr. Pierre Viktorovitch	Photonic Crystals: an unprecedented nanoscale enabler of light
ThD1	Gerasimos Konstantatos	Colloidal Quantum Dot Photodetectors
ThE1	Xavier Muñoz-Berbel, Rosalía Rod	Photonic Lab on a Chip. Prospectives for Multiparametric Real-Time Cell Screening
ThF1	David A. B. Miller	Optical Interconnects to Chips
ThF5	Pascual Muñoz	Towards fabless photonic integration
ThG1	Atsushi Sugitatsu	Semiconductor Wavelength Converter with Wide Dynamic Range
ThH1	Stefano Balsamo, Michele Belmont	Integrated optical modulators for high spectral efficiency
ThI1	Niels Gregersen, Yuntian Chen, J	Controlling light emission from single-photon sources using photonic nanowires
ThI4	Andrea Fiore, Sartoon Fattahpoor	Photonic Integrated Circuits operating at the SinglePhoton Level
FrA1	Michael J. Wale	PICs: A Commercial Future
FrA2	N. F. Borrelli	Nano-Structured Optical Glasses
XxA1	D. Costantini, A. Bousseksou, R.	Towards surface-plasmon generation by electrical injection at telecom wavelengths with a semiconductor device
YyA1	F. Koppens	Graphene: a novel platform for capturing and manipulating light at the nanoscale
024	Nadège Courjal, Clément Guyot, G	High aspect ratio LiNbO3 photonic crystals
028	Chris Lee, Sai T Chu and Edwin Y	Portable Micro-Ring Resonator Based Frequency Combs for Optical Frequency Metrology
031	N. Keil, C. Zawadzki, D. de Feli	Polymer Based Platform for Hybrid Photonic Integration
037	Masahide Okazaki, Takao Chichibu	EO Spatial UV-Light Modulator Using PeriodicallyPoled Deep-Proton-Exchaged s-LiTaO3 Waveguide
038	Y. Ikku, M. Yokoyama, M. Takenak	Propagation-Loss Reduction in InGaAsP Photonicwire Waveguides by InP and Al2O3 Passivation Layers

046	B.I. Akca, L. Chang, G. Sengo, K	Integrated AWG Spectrometer for On-chip Optical Coherence Tomography
056	Tong Chen, Hansuek Lee, Jiang Li	27-Meter-Long Ultra-Low-Loss Optical Delay Lines
057	Hansuek Lee, Tong Chen, Jiang Li	Ultra-high-Q wedge resonator on a silicon chip
058	Jiang Li, Hansuek Lee, Tong Chen	High Coherent Microcavity Brillouin Laser
059	Jiang Li, Hansuek Lee, Tong Chen	Microwave Repetition Rate Frequency Comb on a chip
063	N. Huby, J. Bigeon, B. Bêche, J.	Polymer nanotubes and nanowires for integrated photonics
065	Y. Jiao, B.W. Tilma, J. Kotani,	InAs/InP(100) QD waveguide photodetectors for a monolithically integrated optical coherence tomography system around 1.7 μm
067	Aitor V. Velasco, María L. Calvo	Spatial Heterodyne Fourier-Transform Spectrometer Implemented With Silicon Wire Spiral Waveguides
072	Efthymios Rouvalis, Mourad Chtio	High-Speed Uni-Travelling Carrier Photodiodes for InP Photonic Integrated Circuits
074	A.M.Gutiérrez, A.Brimont, A.Aame	A slow light silicon-based Mach-Zehnder Interferometer for frequency mixing applications
075	N. Ismail, K. Wörhoff, A. Driess	Arrayed Waveguide Grating for Polarized Raman Spectroscopy of Human Teeth
090	P. Orlandi, P. Bassi, C. Ferrari	Tunable bandwidth optical filter in SOI
096	A. Corradi, G. Carpintero, B.W.	Integrated dual-wavelength AWG-lasers for millimeter wave generation
100	A. Canciamilla, C. Ferrari, M. M	A variable delay integrated receiver for differential phase-shift keying optical transmission systems
104	S. Stopiński, M. Malinowski, R.	Integrated optical serializer designed and fabricated in a generic InP-based technology
107	C. Holmes, L.G. Carpenter, P.A.	Micro-mechanical Integrated Optical Structures Fabricated through physical micromachining and direct UV writting
108	Jiří Čtyroký, Pavel Kwiecien and	Fourier Series Based 3D Bi-directional Propagation Algorithm for Integrated Photonics
109	D. Geskus, S. Aravazhi, E. H. Be	Ultra-high, broadband gain in a lattice-engineered, Yb-doped double tungstate channel waveguide
115	Twan Korthorst and Remco Stoffer	Photonics Design Automation workflow
116	L. Zhuang, D.A.I. Marpaung, M. B	On-chip Microwave Photonic Signal Processors in Low-Loss, High-Index-Contrast Si3N4/SiO2 Waveguides
117	A. Leinse, R.G. Heideman, W. P.	TriPleX photonic platform technology – Low-loss waveguide platform for applications from UV to IR
122	M.S. Tahvili, X.J.M. Leijtens, P	Design and Fabrication of a Monolithically Integrated AWG-based Optical Pulse Shaper
123	N. Andriolli, S. Faralli, G. Con	All-Optical InP Monolithically Integrated WDM Regenerator for PolSK Signals
124	D. de Felipe. Z. Zhang, F. Soare	Widely-Tunable Polymer Waveguide Grating Laser
127	Papichaya Chaisakul, Delphine Ma	High performance Ge/SiGe quantum well electro-absorption modulator
129	Demis D. John, Renan Moreira, Jo	Demonstration of Etch-less Core Definition Process for Low-Loss Glass Waveguide Fabrication
138	Mohamed-Saïd Rouifed, Papichaya	Quantum-confined Stark effect at 1.3 μm in Ge/SiGe quantum-well structures
145	Mathew George, Raimund Ricken, V	In-band pumped low threshold Ti:Tm:LiNbO3 waveguide laser
153	E. Kleijn, M.K. Smit, M.J. Wale,	New two-port multimode interference reflectors
157	K. Ławniczuk, M.K. Smit, X.J.M.	Photonic integrated multiwavelength transmitters for Fiber-To-The-Home networks – Multi-project wafer run and generic integration concept

158	J. Lloret, F. Ramos, S. Sales an	Fully tunable microwave photonic phase shifter for broadband signals based on a single heterogeneously integrated III-V-on-Silicon microdisk resonator
159	J. C. F. Matthews, M. Lobino, D.	Integrated Optics and Microfluidics for QuantumEnhanced Sensing
165	X. Guo, V. F. Olle, A. H. Quarte	Monolithically integrated variable repetition rate mode-locked laser diode
168	B. Charlet, L. Bastard, J.-E. Br	Supercontinuum source based on ion-exchanged Neodymium doped Q-switched laser
170	K. Poulios, D. Fry, M. Lobino, J	Multi-particle Quantum Walks with 2D & 3D Arrayed Waveguides
172	N. Bamiedakis, A. Hashim, J. Bea	PCB-Integrated Polymer Photonic Devices
176	Jing Zhao, Klaas Dijkstra, Micha	Monolithically integrated filtered-feedback multiwavelength laser with Mach-Zehnder modulators
177	F. M. Soares, K. Janiak, N. Grot	Generic InP-Based Monolithic Photonic Integration Platforms
178	Wouter J. Westerveld, Suzanne M.	Experimental confirmation of universal relations for microring resonators in SOI technology
182	A.Z Subramanian, S. Selvaraja, P	Grating couplers for Si3N4 waveguides at 900 nm
189	Mirko Lobino, Damien Bonneau, Pi	Manipulation of telecom photon path and polarisation in lithium niobate devices
192	Fredrik Laurell, Carlota Canalia	Laser written waveguides in KTP for broadband Type II frequency doubling
201	Abdul Rahim, Jürgen Bruns, Klaus	C-band Performance of a Novel Tunable Integrated Filter for Dispersion Compensation
204	R. E. Simpson, J. Renger, M. Rud	Active plasmonics based on phase change materials
206	Hui Hu, Li Gui, Raimund Ricken a	Wafer-Scale Lithium Niobate on Insulator (LNOI): A New Platform for Integrated Optics
208	J. Pello, J. J. G. M. van der To	Demonstration of an ultra-short polarization converter in InGaAsP/InP membrane
WeP009	Masahiro Oya, Hiroki Kishikawa,	Waveguide-Type All Optical Switch Using Saturable Absorption of Graphene
WeP015	Kirankumar R. Hiremath , Lin Zsc	Nonlocal hydrodynamic Drude resonances of nano-plasmonic scatterers: Modeling and simulations
WeP021	L. J. McKnight, S. Calvez	Reconfigurable Integrated Optics Diode-Laser induced waveguides for visible wavelengths in KYb(WO4)2
WeP022	J.R.Pugh, Y-L.D.Ho, E.Engin, J.G	Photonic Crystal Defect Cavity Q-Factor Optimization Using Slab Thickness
WeP026	F. De Leonardis, V. M. N. Passar	Optical Dispersion Management in Silicon Nanocrystal Slot Waveguides for Soliton Control
WeP027	I. Cestier, V. Eckhouse, G. Eise	Wavelength Conversion Using Kerr Nonlinearity in a GaInP Photonic Crystal Fabry-Perot Resonator
WeP029	S. Dante, D. Duval, L.M. Lechuga	Solving the interferometric readout in sensor devices by an all-optical phase modulation technique
WeP034	Michael Waldow, Andreas Prinzen,	Non-blocking Optical Banyan Switch on SOI
WeP039	Lewis G. Carpenter, Paolo L. Men	Integrated corner mirrors as a platform for miniaturized planar strain sensing
WeP042	L. J. Orbe-Nava, A. Jiménez-Gali	Monolithic Mode-Locked Ring Lasers: Model and Characterization Multi-wafer Project Run
WeP044	S. Malaguti, G. Bellanca, S. Tri	Experiments and modeling of ultra-fast all-optical switching in a GaAs Photonic-Crystal membrane
WeP045	Antonio Pérez-Serrano, Julien Ja	Wavelength multistability in lasers
WeP048	Olivier Gauthier-Lafaye, Antoine	Tailoring reflection of self-collimating multilayer structures
WeP051	P.I.Kuindersma, X.J.M.Leijtens,	Integrated ‘all-optical’ Transmodulator Circuits with non-linear Gain elements and tunable Optical Filters with design, realization & testing in generic InP

		technology
WeP055	Adrián Fdez Gavela, Silvino José	Determination of thickness and refractive index of step-index optical waveguides using LSM and LSE formulation
WeP069	E. H. Bernhardi, H. A. G. M van	Dual-Wavelength Al2O3:Yb3+ Distributed Feedback Waveguide Laser for Microwave Signal Generation
WeP071	Diego Pérez-Galacho, Robert Hali	Adiabatic transitions for sub-wavelength grating waveguides
WeP076	Juan A. Vallés, Ramona Gălătuş	Highly Yb3+/Er3+-codoped microring resonator performance in migration-assisted upconversion regime
WeP077	J. S. Fandiño, P. Muñoz and J. C	Tolerance analysis of a 4×4 MMI-based 90◦ optical hybrid for 100G coherent receivers
WeP083	J.D. Doménech, I. Artundo, P. Mu	Design, fabrication and characterization of a narrow band microwave photonics beamformer in Silicon-On-Insulator
WeP088	J. C. Gates, P. L. Mennea, P.G.R	Integrated optical platform for photon-number resolving, telecom-band detectors for photonic information processing
WeP089	Susan Lindecrantz, Olav Gaute He	Analysis of homogeneous sensitivity of ribwaveguides for Mach-Zehnder interferometer
WeP106	Sergei Mingaleev, Eugene Sokolov	Towards system-level modeling of large-scale active photonic integrated circuits – Recent advances and remaining challenges
WeP114	S.V. Pham, M. Dijkstra, A.J.F. H	Grated Waveguide Optical Cavity for Sensing
WeP118	K. van Dalfsen, S. Aravazhi, S.	Thulium channel waveguide laser with 70% slope efficiency in a monoclinic double tungstate
WeP119	G. C. Ballesteros, J. Matres, J.	Backscattering Effects In Silicon Ring Resonators
WeP125	Silvino José Antuña, Adrián Fdez	Micromolds fabrication by laser lithography for biosensing applications
WeP131	C. Berrospe, X. Mateos, W. Bolañ	On the optimization of the 1.8 μm laser generation in 3 at% Tm :KY0.58Gd0.18Lu0.17(WO4)2 layers on KYW crystal
WeP134	G. F. De La Fuente	3D-internal Laser beam machining into polymers F. Rey-García, C. Bao and C.Gómez-Reino
WeP137	Josep Ferré-Borrull, Mohammad Ma	Modeling Photonic Properties of Quasi-random Nanoporous Anodic Alumina for Application in Organic Devices
WeP140	A.I. Gómez-Varela, M.T. Flores-A	Theory and simulation of an active GRIN beam shaper
WeP142	T.Cao, M.J. Cryan	Incident Angle Dependence For Dual Band Double Negative Index Material Using Elliptical Nanohole Arrays
WeP149	Kristján Leósson, Björn Agnarsso	Fluoropolymer-based integrated biophotonics
WeP154	Johannes Beetz, Matthias Lermer,	Enhanced spontaneous emission from single quantum dots inside short photonic crystal waveguides
WeP156	F. Leo, B. Kuyken, N. Hattasan,	Passive SOI devices for the Short-wave-infrared
WeP162	Ruiyong Zhang, H.-G. Bach, R. Ku	A Polarization Beam Splitter based on MZI-Structure
WeP163	J. M. Ramírez, F. Ferrarese Lupi	Silicon-based light sources: En route to the first injected Silicon laser emitting at 1.54 μm
WeP164	Laurent Vivien, Delphine Marris-	40 Gb/s lateral vs vertical Ge-on-Si photodetectors integrated in silicon waveguides
WeP167	C. Kluge, P. Metz, A. Pradana, Y	Influence of waveguide thickness on the angular color impression of nanostructured organic emission layers
WeP169	L. Chang, B.I. Akca, G. Sengo, K	Polarization-Independent Optical Low-Coherence Reflectometry with a Non-Birefringent ArrayedWaveguide Grating

WeP174	A.Rosa, A.M.Gutiérrez, A.Brimont	A silicon-based tunable multimode interferometer using the thermo-optic effect
WeP175	M. Jubera, A. García-Cabañes and	Photorefractive damage in congruent and Mg doped α-phase channeled LiNbO3 waveguide.
WeP186	S. Keyvaninia, M. Muneeb, S. Sta	Multiple die-to-wafer adhesive bonding for heterogeneous integration
WeP193	Jose A. Lazaro, Victor Solé, Adr	InP Wavelength Shifter Designs for Colorless User Terminals in Passive Optical Networks
WeP195	Peter De Heyn, Diedrik Vermeulen	Ultra-high Q and finesse all-pass microring resonators on Silicon-on-Insulator using rib waveguides
WeP202	Florian Kaiser, Lutfi Arif Ngah,	Polarisation entanglement engineering at telecom wavelength using guided-wave optics
WeP205	Gabriella Cincotti	Optical devices for the Discrete Fourier Tranform
WeP215	A. Méndez, J. Ramiro, A. Alcázar	A new method of second harmonic generation based on light tunneling between waveguide channels
ThP010	Kensuke Inoshita, Hiroki Kishika	Proposal of Optical Waveguide Circuits for Recognition of Optical QAM Codes
ThP016	I. Suárez, H. Gordillo, P. Rodrí	Multicolor wave-guiding in polymer/quantum dot nanocomposite waveguides
ThP017	Jeong-Ho Ha, Hong-Sik Jung	Electrooptic Electric Field Sensor utilizing Ti:LiNbO3 Asymmetric Mach-Zehnder Interferometers
ThP023	A. Choudhary, H.M.H. Chong, K.Pr	Waveguide lasers in (Yb,Nb):RbTiOPO4
ThP025	B. Troia, V. M. N. Passaro, F. D	Design of Efficient Photonic Sensors Based on Vernier Effect in near-IR
ThP032	H.L. Rogers, C. Holmes, P.L. Men	Experimental observation of coupling between physically separated planar waveguides utilising tilted Bragg grating structures
ThP036	M. Aamer, A.M. Gutierrez, A. Bri	Experimental demonstration of an ultra compact SOI polarization rotator
ThP041	B. R. Cemlyn , I. D. Henning, M.	Nonlinear effects of four wave mixing in InP optical circuits at 1550 nm
ThP047	J.L. Stokes, N. Ahmad, J. R. Pug	Fano-Like Resonance in Wavelength Scale Patterned Laser Facets
ThP049	O. Parriaux, Y. Jourlin, S. Tonc	Angularly robust resonant reflection from corrugated slab waveguide by mode coalescence
ThP050	Olivier Parriaux, Svetlen Tonche	Recovery of lost photons in plasmon-mediated transmission across undulated metal film
ThP053	N. Sotiropoulos, H. de Waardt, A	Performance of 80 Gb/s MMI-Based DQPSK Demodulator on SOI
ThP060	Yin-Jung Chang, Wei-Lun Li, and	Ultracompact Plasmonic-Mode-Assisted Polarization Splitter with A Large Fabrication Tolerance
ThP061	Baojie Chen, Sai Tak Chu, and Ed	Nd3+-doped ion-exchanged aluminum germanate glass waveguide for O-band amplification
ThP066	D. Duval, S. Dante, L.M. Lechuga	Reliability of grating couplers incorporated on integrated interferometric biosensors
ThP073	M. Aamer, A. Brimont, A.M. Gutie	Optimized 20 Gbps DPSK demodulator in 220nm SOI
ThP078	J. S. Fandiño, P. Muñoz and J. C	Design of a Frequency Modulation – Direct Detection Microwave Photonic Link receiver monolithically integrated in InP generic technology
ThP079	J. S. Fandiño, P. Muñoz and J. C	Design of a Frequency Modulation – Direct Detection Microwave Photonic Link receiver monolithically integrated in InP generic technology
ThP080	A. Ferrer, J. del Hoyo, A. Ruiz	High gain fs-laser written Yb3+/Er3+-codoped phosphate glass waveguide
ThP081	T. Nappez, E. Ghibaudo, J.-E. Br	Development of a single-mode cost-effective pumping scheme
ThP084	L. Agazzi, K. Wörhoff, and M. Po	Fast quenching processes and their impact on 1.5-μm amplifier performance in Al2O3:Er3+ waveguides
ThP085	Johann Toudert, Javier Martin Sá	Design and optical response of a thin film structure enhancing the

		photoluminescence of an embedded single layer of Er3+ ions
ThP091	M. Jubera, A. García-Cabañes and	Photorefractive effect and optical damage thresholds in z-cut swift heavy ion irradiation LiNbO3 waveguides.
ThP092	Erman Engin, Jeremy L. O'Brien a	Gallium Nitride-on-Sapphire Tunable Photonic Crystal Directional Coupler
ThP110	Carina Heisel, Thomas Henning Lo	GaAsSb/GaAs quantum dot lasers with strong indexguiding
ThP111	Ana Belén González-Guerrero, Lau	Simple and compact integrated silicon interferometer device for biosensing platforms devices
ThP126	S.M. Kostritskii, Yu.N. Korkishk	Electro-optic phase modulators utilizing different phases in proton-exchanged LiNbO3- waveguides
ThP128	Timo Aalto, Mikko Harjanne, Mark	Integration and Packaging of Optoelectronic and Silicon Photonic Chips on a µm-scale SOI Platform
ThP130	Miguel Cabezón, Ignacio Garcés,	Silicon-On-Insulator Chip-to-chip coupling via Vertical Grating Couplers
ThP132	J. Cugat, R. Solé, J. Massons, X	Rib waveguides fabricated by surface structuring with a femtosecond laser on (Yb,Nb):RTP/RTP epilayers
ThP139	R. Zhang, J.J.G.M. van der Tol a	Design and Simulation of a Photonic Crystal Cavity in InP-based Membranes On Silicon
ThP141	N. A. Hueting, E. Engin, A. Md Z	A Gallium Nitride Distributed Bragg Reflector Cavity for Integrated Photonics Applications
ThP143	J. Cugat, R. Solé* , J. Massons,	Cs+ ion exchange channel waveguides on RbTiOPO4
ThP147	Y. De Koninck, M. Tassaert, G. R	A novel electrically pumped III-V on silicon micro-laser
ThP150	J. Martínez de Mendíbil, E. Cant	(Er3+, Yb3+) doped K(Y,Gd,Lu)W waveguide fabrication
ThP151	F. Civitci and H.J.W.M. Hoekstra	Design of Spectrometers and Polarization Splitters Using Adiabatically Connected Slab Waveguides
ThP152	F.Civitci, G.Sengo, A. Driessen,	45° Light Turning Mirrors for Hybrid Integration of Silica Optical Waveguides and Photo-detectors
ThP160	M. Felicetti, J.J.G.M. van der T	Polarization converter post-processing for integrated polarization independent SOA
ThP161	Chaotan Sima, J. C. Gates, H. L.	Interferometric integrated planar Bragg filter for alloptical single-sideband suppression
ThP166	R.C. Guzman, L.J Orbe, G. Carpin	Traveling wave model of an AWG-based multiwavelength laser
ThP173	J. Pello, J. J. G. M. van der To	Chalcogenides applied to microring switching
ThP180	G. A. Torchia, D. Biasetti and E	Femtosecond writing Double line appraoch Waveguides in Er-Yb doped Niobium Borate glasses
ThP181	J. Olivares, M. Jubera, A. Garcí	Recent achievements in LiNbO3 waveguides fabricated by swift heavy ion irradiation
ThP183	G. Roelkens, S.P. Bhat, J.J.G.M.	Feasibility study of an InP membrane on silicon laser
ThP184	R. Menchon-Enrich, J. Mompart, a	Adiabatic Passage of Light in CMOS-Compatible Silicon Oxide Integrated Rib Waveguides
ThP185	Ashim Dhakal, Ananth Z. Subraman	The role of index contrast in the efficiency of absorption and emission of a luminescent particle near a slab waveguide.
ThP188	N. Ismail, L. Chang, G. Sengo, R	Polymer microlenses for collimating light from single-mode silicon oxynitride optical waveguides
ThP190	S. Heidmann, G. Martin, N. Courj	Double polarization active Y-junctions in the mid-IR, based on Ti:diffused Lithium Niobate Waveguides
ThP191	D. Tulli, D. Janner	LiNbO3 integrated optical probe for high-voltage electric field sensing

ThP194	Ronald Broeke	Technology-transparent AWG design in photonic ICs
ThP197	S. Keyvaninia, Y. De Koninck, D.	A novel III-V-on-Si distributed feedback laser design
ThP209	Paolo Bardella, Ivo Montrosset	Design and simulation of DBR lasers with extended modulation bandwidth exploiting photon-photon resonance effects
ThP210	S. Mas, J. M Matres, J. Martí, C	Accurate dispersion characterization in nanophotonic integrated waveguides
ThP212	Thijs Spuesens, Yannick De Konin	Efficient vertical coupling between a silicon waveguide and an InP-based microdisk

Plasmonic Waveguides: Fundamentals and Applications

Sergey I. Bozhevolnyi
Institute of Technology and Innovation (ITI), Faculty of Engineering, University of Southern Denmark, Niels Bohrs Allé 1, DK-5230 Odense M, Denmark
e-mail: seib@iti.sdu.dk

Abstract: Recent years have seen an explosion of research into plasmonics instigated by a great promise of enabling energy-effective and highly-integrated optical interconnects that would exploit a special type of electromagnetic waves called surface plasmon-polaritons (SPP) propagating along and being controlled by metal circuitry, while also being strongly confined (beyond the diffraction limit) in the lateral cross section [1,2]. These remarkable characteristics open unique prospects for the design of highly integrated SPP-based photonic signal-processing systems, nano-resolution optical imaging techniques and sensors. This tutorial introduces the main SPP-based waveguide configurations and reviews a number of fundamental issues within the area of sub-wavelength SPP waveguides and circuitry [1-3]. Finally, the possibilities for immediate practical applications of SPP waveguide components for real data traffic management will be discussed along with the most recent achievements in this direction [4].

References

[1] T. Ebbesen, C. Genet, and S. I. Bozhevolnyi, *Surface-plasmon circuitry*, Physics Today **61**, 44 (May 2008).
[2] *Plasmonic Nanoguides and Circuits*, S. I. Bozhevolnyi, ed. (Pan Stanford, 2009).
[3] D. K. Gramotnev and S. I. Bozhevolnyi, *Plasmonics beyond the diffraction limit*, Nature Photonics **4**, 83 (2010).
[4] FP7-ICT-STREP "Merging plasmonic and silicon photonics technology towards Tb/s routing in optical interconnects (PLATON)" (http://www.ict-platon.eu/).

Subwavelength nanophotonic structures in silicon waveguides

Jens H. Schmid, Przemek J. Bock, Jean Lapointe, Siegfried Janz, Dan-Xia Xu
Institute for Microstructural Sciences
National Research Council Canada
Ottawa, Canada
Jens.schmid@nrc-cnrc.gc.ca

M. Ibrahim, Winnie N. Ye
Department of Electronics
Carleton University
Ottawa, Canada

***Abstract*—We review and discuss our recent studies of subwavelength grating (SWG) structures for engineering the refractive index of silicon microphotonic waveguides. Various applications are presented, such as fiber-chip coupling structures, waveguide crossings and athermal waveguides made with a polymer-silicon hybrid core.**

Keywords-Silicon photonics; subwavelength gratings; fiber-chip coupler; waveguide crossings; athermal waveguides;

I. INTRODUCTION

Integrated silicon photonic circuits are expected to have a major impact on optical interconnects and data transport applications in the near future, as well as being used for biosensing and spectroscopy. In the design of silicon waveguide devices the refractive index of the waveguide core is naturally assumed to be fixed, being the material refractive index of silicon. We have recently demonstrated the use of the subwavelength grating (SWG) effect to tune effectively the index of a waveguide core simply by lithographic patterning, thus introducing a new degree of freedom in silicon waveguide design. The use of SWGs with a periodicity smaller than one half of the wavelength of light to suppress any diffraction effects, as effective media with spatially averaged refractive index is already well established in free space optics [1].

II. APPLICATIONS OF THE SUBWAVELENGTH GRATING EFFECT IN SILICON PHOTONICS

An example for the application of the SWG effect to a so-called silicon photonic wire waveguide, i.e. a submicron silicon strip waveguide, is illustrated schematically in Fig. 1a. Here, periodic gaps are etched into a standard silicon photonic wire and an SWG waveguide is formed with an effective core index determined by the SWG duty ratio.

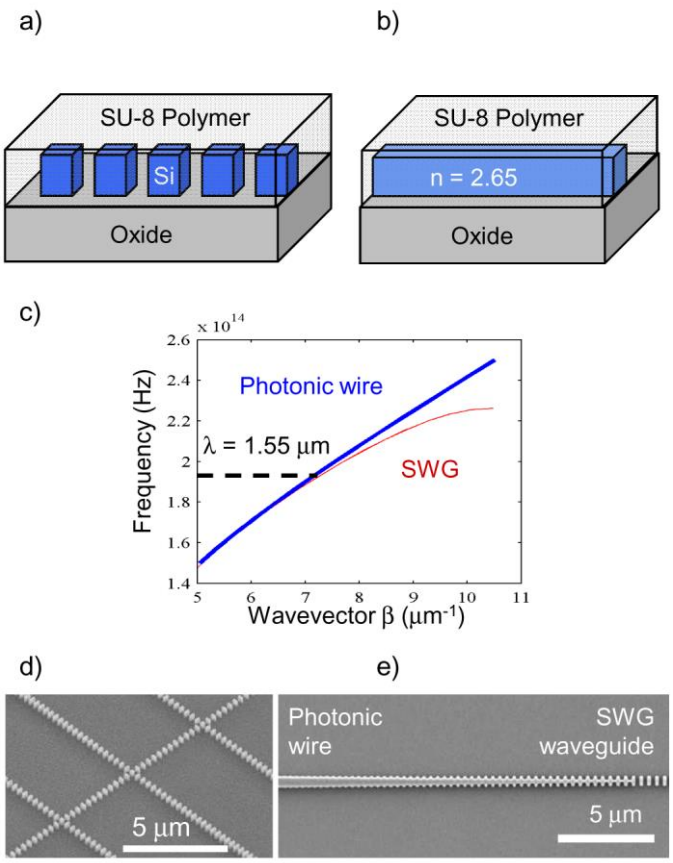


Fig. 1 a) Schematic of a silicon SWG waveguide. b) Equivalent wire waveguide with spatially averaged core index. c) Comparison of the calculated dispersion diagrams of the structures shown in a) and b). d) Scanning electron micrograph (SEM) of SWG waveguide crossings. e) SEM of low-loss SWG fiber-chip coupling structure.

To confirm theoretically the concept of spatial refractive index averaging in an SWG waveguide with period Λ = 0.3 μm and

50% duty ratio we compare its dispersion relation with that of an equivalent photonic wire waveguide with identical cross section and averaged core index of $n = 2.65$, as shown in Fig. 1b. The two dispersion curves are overlaid in Fig. 1c. The SWG waveguide shows the typical behaviour expected for a periodic structure, namely a flattening of the dispersion as the Bragg condition is approached at $\beta \approx 10.5\ \mu m^{-1}$, corresponding to a free space wavelength of $\lambda = 1.33\ \mu m$. For the operating wavelength of 1.55 μm, however, the dispersion curves of the segmented and the equivalent photonic wire waveguide are well matched. Experimentally, we have observed wave guiding in SWG waveguides with a propagation loss as low as 2.1 dB/cm [2].

We have demonstrated several applications of SWG waveguides, for example highly efficient waveguide crossings as shown in Fig. 1d, which enable the design of complex high density photonic circuits [3], and photonic wire fiber-chip couplers with extremely low coupling loss as depicted in Fig. 1e and described in [4]. Refractive index engineering by SWG patterning can also be used in two dimensions for slab waveguides. This has been applied in design of a novel microspectrometer, where an SWG nanostructure fulfills a dual purpose by acting as an effective slab waveguide for diffracted light and as a lateral cladding for a channel waveguide [4]. Surface grating fiber-chip couplers with enhanced performance and reduced fabrication complexity due to the incorporation of SWG structures have also been reported [5-9].

III. ATHERMAL SILICON SWG WAVEGUIDES

We have recently used SWG waveguides to address another important issue with silicon photonic circuits, which is the temperature dependence of their optical output signals caused by the comparatively high thermo-optic (TO) material coefficient of silicon ($dn_{Si}/dT = 1.8\times10^{-4}\ K^{-1}$). The temperature dependence of silicon wire waveguides can be reduced by using a polymer overcladding with a negative TO coefficient to compensate for the silicon thermo-optic effect [10,11]. Athermal operation of waveguides, i. e. $dn_{eff}/dT = 0$, where n_{eff} is the mode effective index and T is the ambient temperature, is achieved if waveguide dimensions are chosen such that the respective overlaps of the mode with the silicon core and the polymer cladding results in a cancellation of their combined contributions to the waveguide effective TO coefficient. This can be accomplished in narrow silicon wires with a fairly delocalized mode [12], or with slot waveguides, in which a large fraction of the modal field is confined to a narrow gap filled with the low-index polymer [13]. With SWG waveguides the spatial index averaging effect can be exploited for mitigating the silicon thermo-optic effect by filling the gaps with polymer material of negative TO coefficient for an appropriate grating duty ratio.

The effect has been experimentally demonstrated in [14], where athermal waveguide behavior was observed for SWG waveguides with a composite core consisting of interlaced subwavelength segments of silicon and SU-8 polymer, the latter having a thermo-optic material coefficient of $dn_{SU8}/dT = -1.1 \times 10^{-4}\ K^{-1}$. SEM pictures of three SWG waveguides with different duty cycles are shown in Fig. 5a. In Fig. 5b the measured and calculated waveguide effective thermo-optic coefficient are shown as a function of SWG duty ratio. For increasing volume ratio of silicon material in the waveguide core the plots show a sign reversal from negative to positive thermo-optic coefficients. In other words, the thermal behavior of the SWG waveguide is dominated by the polymer material for low duty ratios and by silicon for high duty ratios. Athermal waveguide operation is achieved for an SWG duty cycle of 61%, for TE polarization and 85% for TM polarization. The challenging fabrication of SWG waveguides with high duty cycles can be circumvented by using a subwavelength *sidewall* grating (SWSG) waveguide, as shown in Fig. 2c. Our recent experimental results show that athermal SWSG waveguides can be designed for both TE and TM polarized light with duty cycles of ~50%.

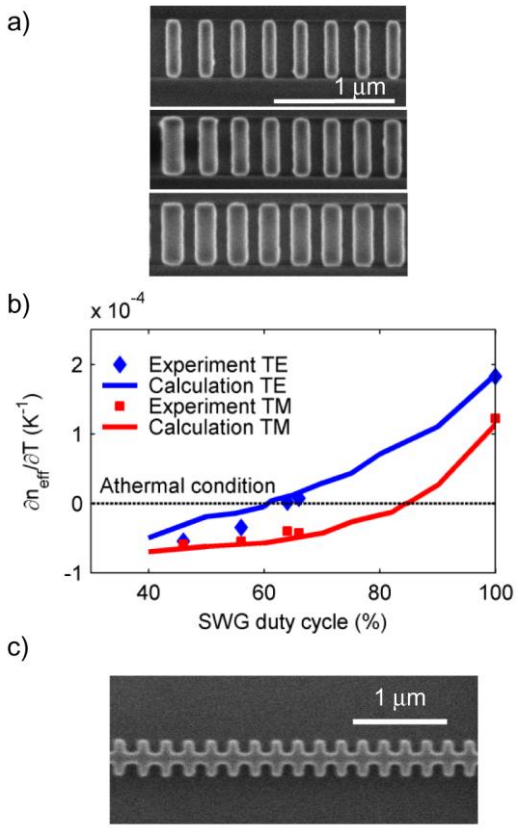


Fig. 2 a) SEM micrographs of SWG waveguides with Si duty ratios of 46%, 56% and 66%. b) Experimental and theoretical results for the effective thermo-optic coefficient of SU-8 clad silicon SWG waveguides as a function of grating duty cycle. c) SEM of a SWSG waveguide.

IV. OUTLOOK AND CONCLUSIONS

We have described a number of practical implementations of SWG structures in silicon waveguides that can improve device performance or enable novel functionalities. Several others have been published recently. Mode profile engineering as

employed for the athermal SWG waveguides can also be used to achieve ultrafast nonlinear all-optical switching [15]. Engineering the refractive index of slab waveguides with SWGs may prove to be a suitable method of adapting to integrated optics conventional components such as lenses [16,17] or transmission gratings, which are common in free space optics. Calculations have shown that SWGs can be used as effective cladding material with optimized refractive index contrast in the design of multi-mode interference couplers with superior performance [18]. The numerous applications of SWGs in silicon photonics demonstrated in the past few years underline the versatility afforded by adapting this method of refractive index engineering to integrated optics.

ACKNOWLEDGMENT

This work is supported in part by the Genome and Health Initiative (GHI) program of the National Research Council Canada (NRC).

REFERENCES

[1] J. N. Mait and W. W. Prather, Eds., "Selected papers on subwavelength diffractive optics," SPIE Milestone Series, V. Ms 166 (2001).
[2] P. J. Bock, P. Cheben, J. H. Schmid, J. Lapointe, A. Delâge, S. Janz, G. C. Aers, D.-X. Xu, A. Densmore, T. J. Hall, " Subwavelength grating periodic structures in silicon-on-insulator: a new type of microphotonic waveguide," Opt. Express **18** (19) 20251-20262 (2010).
[3] P. J. Bock, P. Cheben, J. H. Schmid, J. Lapointe, A. Delâge, D.-X. Xu, S. Janz, A. Densmore, T. J. Hall, "Subwavelength grating crossings for silicon wire waveguides," Opt. Express **18** (15) 16146-16155 (2010).
[4] P. Cheben, P. J. Bock, J. H. Schmid, J. Lapointe, S. Janz, D.-X. Xu, A. Densmore, A. Delâge, B. Lamontagne, T. J. Hall, " Refractive index engineering with subwavelength gratings for efficient microphotonic couplers and planar waveguide multiplexers," Opt. Lett. **35** (15) 2526-2528 (2010).
[5] R. Halir, P. Cheben, S. Janz, D.-X. Xu, I. Molina-Fernández, J. G. Wangüemert-Pérez, "Waveguide grating coupler with subwavelength microstructures," Opt. Lett. **34** (9) 1408-1410 (2008).
[6] R. Halir, P. Cheben, J. H. Schmid, R. Ma, D. Bedard, S. Janz, D.-X. Xu, A. Densmore, J. Lapointe, I. Molina-Fernández, "Continuously apodized fiber-to-chip-surface coupler with refractive index engineered subwavelength structure," Opt. Lett. **35** (19) 3243-3245 (2010).
[7] X. Chen, H. K. Tsang, "Nanoholes grating couplers for coupling between silicon-on-insulator waveguides and optical fibers," IEEE Phot. Journal **1** (3) 183-190 (2009).
[8] L. Liu, M. Pu, K. Yvind, J. M. Hvam, "High-efficiency, large-bandwidth silicon-on-insulator grating coupler based on a fully-etched photonic crystal structure," Appl. Phys. Lett. **96** (5) 051126 (2010).
[9] X. Chen, H. K. Tsang, "Polarizatioin-independent grating couplers for silicon-on-insulator nanophtonic waveguides," Opt. Lett. **36**(6) 796-798 (2011).
[10] J.-M. Lee, D.-J Kim, H. Ahn, S.-H Park, and G. Kim, "Temperature dependence of silicon nanophotonic ring resonator with a polymeric overlayer," J. Lightw. Technol. **25** (8) 2236-2243 (2007).
[11] W. N. Ye, J. Michel, L. C. Kimerling, "Athermal high-index-contrast waveguide design," IEEE Phot. Technol. Lett. **20** (11) 885-887 (2008).
[12] J. Teng, P. Dumon, W. Bogaerts, H. Zhang, X. Jian, X. Han, M. Zhao, G. Morthier, and R. Baets, "Athermal silicon-on-insulator ring resonators by overlaying a polymer cladding on narrowed waveguides," Opt. Express **17** (17) 14627-14633 (2009).
[13] J.-M. Lee, D.-J. Kim, G.-H. Kim, O-K. Kwon, K.-J. Kim, and G. Kim, "Controlling temperature dependence of silicon waveguide using slot structure," Opt. Express **16** (3) 1645-1651 (2008).
[14] J. H.Schmid, M. Ibrahim, P. Cheben, J. Lapointe, S. Janz, P. J. Bock, A. Densmore, B. Lamontagne, R. Ma, W. N. Ye, D.-X. Xu, "Temperature-independent silicon subwavelength grating waveguides," Opt. Lett. **36** (11) 2110-2112 (2011).
[15] I. Glesk, P. J. Bock, P. Cheben, J. H. Schmid, J. Lapointe, S. Janz, "All-optical switching using nonlinear subwavelength Mach-Zehnder on silicon," Opt. Expr. **19**(15) 14031-14039 (2011).
[16] U. Levy, M. Abashin, K. Ikeda, A. Krishnamoorthy, J. Cunningham, Y. Fainman, "Inhomogeneous dielectric metamaterials with space-variant polarizability," Phys. Rev. Lett. **98** 243901 (2007).
[17] D. H. Spadoti, L. H. Gabrielli, C. B. Poitras, M. Lipson, "Focusing light in a curved space," Opt. Express **18** (3) 3181-3186 (2010).
[18] A. Ortega-Moñux, L. Zavargo-Peche, A. Maese-Novo, I. Molina-Fernández, R. Halir, J. G. Wangüemert-Pérez, P. Cheben, J. H. Schmid, "High performance multimode interference coupler in silicon waveguides with subwavelength structures," Phot. Technol. Lett. **23**(19) 1406-1408 (2011).

III-V-on-silicon membrane photonics for near-infrared and mid-infrared applications

G. Roelkens, S. Keyvaninia, S. Stankovic, M. Tassaert, N. Hattasan, A. Gassenq, P. De Heyn, Y. De Koninck, P. Mechet, R. Kumar, M. Muneeb, D. Vermeulen, G. Morthier, R. Baets, D. Van Thourhout

Photonics Research Group - INTEC
Ghent University - imec
Ghent, Belgium

***Abstract*—We give an overview of our work in the field of heterogeneously integrated III-V-on-silicon photonic integrated circuits for communication and sensing applications.**

Keywords: heterogeneous integration; III-V on silicon

I. INTRODUCTION

Silicon-based photonic integrated circuits are gaining considerable importance for a variety of applications, from telecommunications to sensors. The interest in this technology stems mostly from the expectation that the maturity and low cost of CMOS-technology can be applied for advanced photonics products. Other driving forces for silicon photonics include the design richness associated with the high refractive index contrast as well as the potential for integration of photonics with electronics. The lack of silicon light sources and photodetectors for various wavelength ranges requires the integration of III-V semiconductor devices on the silicon platform to complete the toolkit. For these devices thin layers of III-V semiconductors are bonded to silicon. The III-V/silicon laser gets its gain from the III-V layers but couples its output light into a silicon waveguide. For the detectors light is guided in the silicon waveguide layer and is coupled to the absorbing III-V layer stack on top. Besides lasers and detectors, many other types of devices can be realized on this III-V/Silicon platform.

We focus on adhesive die-to-wafer and wafer-to-wafer bonding processes, based on DVS-BCB as a bonding agent, for the integration of III-V semiconductors on silicon. Adhesive bonding is chosen due to the relaxed requirements on the III-V wafer surface quality (contamination, particles, roughness). The technology is described in detail in [1]. Based on this technology, various types of heterogeneously integrated laser sources, photodetectors and other optical functionality were fabricated, which will be outlined in this paper, both for telecom and datacom applications as well as for spectroscopic sensor systems in the short-wave and mid-wave infrared.

II. DATACOM/TELECOM APPLICATIONS

A. mW-level output power III-V/silicon lasers

Two device geometries for milliwatt level output power are considered. In a first approach a hybrid mode laser, analogous to the device structure proposed by UCSB/Intel [2], was developed. In this approach the optical mode is predominantly confined to the silicon waveguide layer. The difference between our design and the UCSB/Intel one is the presence of the low-index DVS-BCB bonding layer (sub 100nm) between the silicon waveguide and the III-V epitaxy. Careful design of the epitaxial layer stack is required to accommodate variations in bonding layer thickness. As a proof-of-principle, hybrid 1310nm Fabry-Perot laser diodes were realized. 4mW laser output power from a single laser facet at room temperature was obtained [3]. By incorporating a grating in the top surface of the silicon waveguide layer, single mode lasers with 40dB side mode suppression ratio can be obtained. Since in these devices the optical mode is predominantly confined in the silicon waveguide layer, the confinement factor in the III-V quantum wells is relatively low. This impacts the threshold current of the device. Therefore, an alternative laser architecture was developed, in which the optical mode is fully confined to the III-V waveguide layer in the gain section, while the mode is pushed into the silicon waveguide layer for the (potentially wavelength selective) feedback [4]. 2mW laser output from a cleaved Fabry-Perot device and operation at 70C was obtained.

B. Micro-lasers

Other communication applications (such as intra-chip optical communication) require rather a compact light emitter with moderate output power (10-100 microwatt) and low power consumption. This can be realized using micro-laser sources such as micro-disk lasers and photonic crystal lasers. Micro-disk lasers with threshold currents below 350uA were demonstrated with about 100uW of power evanescently coupled to a silicon waveguide underneath [5]. These micro-disk devices turn out to be very versatile devices since they have been used as optical flip-flop, all-optical gate, switch and modulator [6]. The ultimate down-scaling in size was obtained using photonic crystal lasers evanescently coupled to a silicon waveguide, which were optically pumped through the silicon waveguide layer [7]. A novel device geometry, combining high gain by strong confinement in the III-V layer and wavelength selective feedback by patterning in the silicon layer is also under investigation [8].

Part of this work was carried out in the framework of FP7-IP-HELIOS, FP7-ERC-MIRACLE and the Dutch smartmix-Memphis project

C. Photodetectors

While Ge-photodetectors allow for monolithic integration on a silicon waveguide circuit, III-V semiconductor photodetectors typically outperform Ge detectors in terms of dark current and flexibility in epitaxial layer structure. Therefore, several types of III-V photodetectors were realized on a silicon waveguide platform. InGaAs photodetectors using evanescent coupling between the silicon waveguide layer and the III-V layer show close to theoretical responsivity [9]. For optical access network applications, an alternative device configuration was realized, which is transparent for 1490nm/1550nm upstream signals, while strongly absorbing for the 1300nm downstream wavelength range [10].

D. Membrane optical gates / switches

Besides lasers and photodetectors, also III-V membrane optical gates were realized. These devices are based on a thin (sub 100nm thick) III-V membrane coupled to a silicon waveguide circuit. The gate is based on the strong change in transmission (>40dB) when pumping the quantum wells in the thin film. This allows fabricating an all-optical broadcast and select switch [11]. Besides switching, the same device was used as an optical amplifier and regenerator.

III. SWIR/MWIR SPECTROSCOPY APPLICATIONS

The short-wave (1.4-3µm) and mid-wave infrared wavelength range (3-8µm) is also attractive for several applications. In particular, the field of spectroscopic sensing exploits the strong gas/liquid/solid absorption features in this wavelength range. Given its transparency window (1-4µm), silicon photonics allows realizing integrated spectroscopic systems by combining active III-V devices on Silicon-On-Insulator (SOI) passive circuits in this wavelength range. The availability of an integration platform for this wavelength range could enable ultra-compact, low-cost sensor solutions that outperform existing solutions by their selectivity and sensitivity. This requires the integration of short-wave/mid-wave infrared light sources and photodetectors on top of the silicon waveguide circuit.

As a first step towards fully integrated spectroscopy systems, the heterogeneous integration of short-wave infrared InGaAsSb photodetectors was demonstrated, operating up to 2.5µm. Two device geometries were considered, one based on evanescent outcoupling, and another based on grating-assisted coupling. While the first approach provides the highest responsivity [12], the latter approach has larger tolerances in fabrication since thicker adhesive bonding layers can be used. Responsivities above 1A/W have been obtained in recent experiments at 2.3µm using the evanescent coupling approach.

IV. CONCLUSIONS

The combination of high precision patterning methods in silicon fabs and high gain and efficient detection provided by III-V semiconductors provides a winning combination for advanced integrated opto-electronic devices. The design space is large and there is ample opportunity for optimization towards specific performance objectives. The critical technological step in hybrid III-V / silicon devices is obviously the die-to-wafer bonding step. While early approaches suffered from low yield the technology has now become more mature.

REFERENCES

[1] G. Roelkens et al., “III-V/silicon photonics for on-chip and inter-chip optical interconnects," LASER & PHOTONICS REVIEWS 4, 751-779 (Nov. 2010)

[2] Fang, A. W., Park, H., Kuo, Y.-h., Jones, R., Cohen, O., Liang, D., Raday, O., Sysak, M. N., Paniccia, M. J., and Bowers, J. E., Hybrid silicon evanescent devices," MATERIALS TODAY 10(7-8), 28-35 (2007).

[3] S. Stankovic, G. Roelkens, D. Van Thourhout, R. Jones, M. Sysak, J. Heck, 1310nm evanescent hybrid III-V/Si laser based on DVS-BCB bonding,Integrated Photonics Research, Silicon and Nano-Photonics (IPR), Canada, p.IWC3 (2011)

[4] M. Lamponi, S. Keyvaninia, F. Pommereau, F. Lelarge, G. de Valicourt, G. Roelkens, D. Van Thourhout, D. Bordelc, S. Messaoudenec, J.-M. Fedelic, G.-H. Duan, Heterogeneously integrated InP/SOI laser using double tapered single-mode waveguides through InP die to SOI wafer bonding,Group IV Photonics , p.WB6 (2010)

[5] G. Roelkens et al., Laser sources on a heterogeneous III-V/silicon platform, IEEE Photonics 2011 p.395-396 (2011)

[6] L. Liu, R. Kumar, K. Huybrechts, T. Spuesens, G. Roelkens, E.-J. Geluk, T. de Vries, P. Regreny, D. Van Thourhout, R. Baets, G. Morthier, An ultra-small, low-power, all-optical flip-flop memory on a silicon chip,Nature Photonics, 4(3), p.182-187 (2010)

[7] Y. Halioua, A. Bazin, P. Monnier, T. J. Karle, G. Roelkens, I. Sagnes, R. Raj, and F. Raineri, "Hybrid III-V semiconductor/silicon nanolaser," Opt. Express 19, 9221-9231 (2011)

[8] Y. De Koninck, G. Roelkens, R. Baets, Cavity Enhanced Reflector Based Hybrid Silicon Laser,23rd Annual Meeting of the IEEE Photonics Society, United States, (2010)

[9] Z. Sheng, L. Liu, J. Brouckaert, Sailing He, D. Van Thourhout, InGaAs PIN photodetectors integrated on silicon-on-insulator waveguides,Optics Express, 18(2), p.1756-1761 (2010)

[10] D. Vermeulen, T. Spuesens, P. De Heyn, P. Mechet, R. Notzel, S. Verstuyft, D. Van Thourhout, G. Roelkens, III-V/SOI photonic integrated circuit for FTTH central office transceivers in a PTP network configuration,ECOC, Italy, p.Tu.5.C.2 (2010)

[11] O. Raz, M. Tassaert, G. Roelkens, D. Van Thourhout, H.J.S. Dorren, Bias-Free, Low Power and Optically Driven InP on SOI Switch for Remotely Configurable Photonic Packet Switches,ECOC 2011, Switzerland, (2011)

[12] N. Hattasan, A. Gassenq, L. Cerutti, J. B. Rodriguez, E. Tournié, G. Roelkens, Heterogeneous integration of GaInAsSb p-i-n photodiodes on a silicon-on-insulator waveguide circuit ,IEEE Photonics Technology Letters, 23(2011), p.1760 (2011)

Advances in Integrated Quantum Photonics

Mark G. Thompson, Damien Bonneau, Erman Engin, Alberto Peruzzo, Konstantinos Poulios, Jasmin Meinecke, Pete Shadbolt, Daniel Fry, Jonathan C. F. Matthews, Anthony Laing, Xiao-Qi Zhou, Pisu Jiang, Alberto Politi , Mirko Lobino, Jeremy L. O'Brien

Centre for Quantum Photonics, H. H. Wills Physics Laboratory & Department of Electronic Engineering, University of Bristol, UK

Mark.Thompson@Bristol.ac.uk

***Abstract*— This paper presents recent advances in integrated quantum photonic waveguide circuits, including fast manipulation of path and polarization encoded qubits, dynamically reconfigurable circuits for on-chip entanglement generation and manipulation, multi-particle quantum walks, and new technologies for photon pair generation and manipulation including Lithium Niobate and Silicon technology platforms. These results represent key steps in the development of practical quantum photonic technologies for applications in quantum communication, metrology, simulation, computation and fundamental science.**

Keywords- single photon source; four wave mixing; silicon ring resonator; reverse bias

I. INTRODUCTION

Quantum information technologies offer completely new approaches to encoding, processing and transmitting information. By harnessing the properties of quantum mechanics, such as superposition and entanglement, it has been shown possible to realise fundamentally new modes of computation [1-2], simulation [3-4] and communication [5], as well as enhanced measurements and sensing [6]. Quantum information processing promises huge computation power, whilst quantum communications offers the ultimate in information security - guaranteed by the laws of physics. Of the many prospective physical systems in which to encode quantum information, photons are a particularly promising approach due to their properties of low noise, easy manipulation and low transmission losses.

Until recently, optical implementations of quantum architectures have been realised using bulk optical elements bolted onto optical tables, with photons propagating in free space. Although many proof-of-principle experiments have been reported, such an approach rapidly becomes impractical as the complexity of the quantum optical circuits increases, thereby making them inherently unscalable and confining them to research laboratory optical tables. However, developments over the past few years have overcome these bottlenecks through implementation of integrated quantum circuits [7] allowing quantum information science experiments to be realised that are inherently stable and orders of magnitude smaller than their equivalent bulk optic implementations. This approach has been used to realise high fidelity operation of key quantum photonics components.

II. ON-CHIP QUANTUM INTERFERENCE AND LOGIC GATES

On-chip quantum interference is a vital requirement of many quantum photonics circuits. To demonstrate quantum operation of integrated beam splitters, single photons were launched into the two input waveguides of a directional coupler with 50:50 coupling ratio. Fig 1a shows a schematic of the directional coupler, which was fabricated in the silica-on-silicon material system, and Fig. 1b shows the variation of coincidences as a function of the separation between the two photons. The curve clearly shows the expected dip around the zero delay, with a high fidelity visibility of V = 100.1% ± 0.4%, demonstrating the excellent quantum interference behaviour of the integrated chip operating at the single photon level [8].

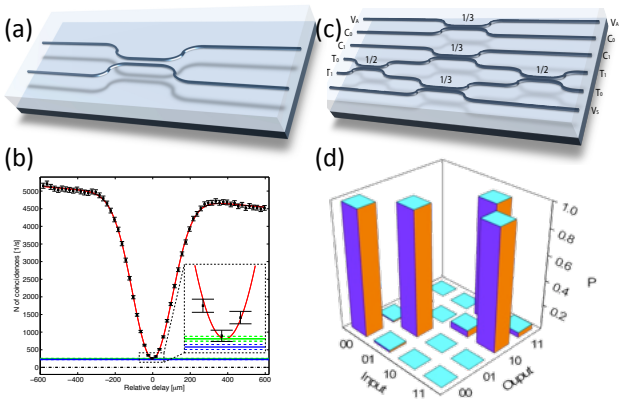


Figure 1. Left column: Schematic diagram of a directional coupler and quantum interference measurement. Right column: Schematic of the integrated CNOT gate, and measured truth table.

Besides single photons operation, quantum information processing requires universal two-qubit gates. The CNOT gate is one such universal two-qubit gates, and its integrated photonic circuit implementation is shown schematically in Fig 1c. To perform measurements on the CNOT gate, output outcomes for each of the input states are measured in the computational basis. The measured truth table is shown in Fig 1c, giving a high logical basis fidelity of F = 96.9% ± 0.2%, highlighting the great advantage of using an integrated optical circuit for highly stable circuits with precisely controlled optical paths lengths and optical split ratios [8].

III. ADVANCED COMPONENTS

Multiport beam splitters are interesting and useful devices for the field of quantum information processing. They have applications including the production of highly entangled photonic states that form the basis of many of the powerful protocols in quantum information processing, and they promise a straightforward implementation of compact and robust multiport circuits. Quantum interference of two- and four-port multi-mode interference (MMI) devices have been investigated using correlated photon pairs, demonstrating that they can operate in the quantum regime with high fidelity [9]. The 2x2 MMI yields a two-photon visibility of V = 95.6 ± 0.9%, whilst operation of the 4×4 port MMI device (show schematically in Fig 2a) exhibits complex quantum

interference behaviour. A new technique to fully characterize such multiport devices has been developed, which removes the need for phase-sensitive measurements and may find applications for a wide range of photonic devices [9].

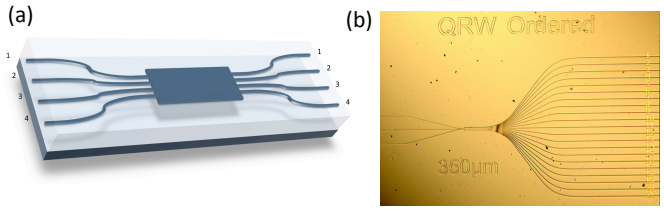


Figure 2. (a): 4x4 multimode interference device. (b): optical micrograph of a 21 waveguide quantum random walk device.

Large waveguide arrays offer another advanced photonic component that yields interesting and useful quantum interference dynamics. Quantum walks of correlated photons offer the possibility of studying large-scale quantum interference; simulating biological, chemical, and physical systems; and providing a route to universal quantum computation. Using SiON waveguide circuits (Fig 2b) the quantum walks of two identical photons in an array of 21 continuously evanescently coupled waveguides has been demonstrated [10]. The observed quantum correlations violate the classical limit by 76 standard deviations, with correlations that depend critically on the input state of the quantum walk. These results present a powerful approach to achieving quantum walks with correlated particles to encode information in an exponentially larger state space.

IV. Reconfigurable Quantum Photonics Circuits

Highly reconfigurable quantum photonic circuits have been demonstrated which can generate two-qubit entangled states with any amount of entanglement and single-qubit states with any amount of mixture, perform two-qubit state tomography and process tomography, and implement the measurements necessary for a Bell violation experiment [11]. The device is a silica-on-silicon waveguide circuit (Fig. 3), and consists of a reconfigurable state preparation stage, which can prepare any separable two-qubit pure state, a postselected two-qubit entangling gate, and a reconfigurable measurement stage, which together with measurement in the logical basis can perform arbitrary qubit measurement on each of the two outputs of the entangling gate. Dynamic reconfigurability is realised using thermal phase shifters.

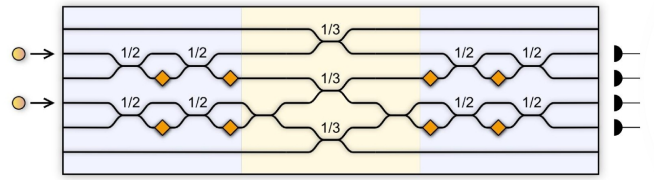


Figure 3. Waveguide architecture of the reconfigurable entangling circuit implemented using voltage-controlled thermal phase shifters, drawn as orange diamonds and directional couplers (marked with its respective splitting ratio).

V. New Quantum Photonics Technology Platforms

To date, quantum photonics integrated circuits have been realised in low index contrast waveguide material systems, such as silica [12] and silicon-oxy-nitride [10], and rely on slow thermo-optic phase shifters. Such technologies offer benefits in terms of low propagation losses, but their associated large bend radii and low speed of operation limits the scalability and usefulness of this technology. As alternative technologies Lithium Nioabte and Silicon-on-Insulator waveguide circuits have been investigated for both fast control and circuit miniaturization. Using Lithium Niobate waveguide circuits, fast polarisation and path control of single photons at 1550 nm has been achieved utilising the electro-optic effect [13]. Heralded single photon state engineering, quantum interference, fast state preparation of two entangled photons and feedback control of quantum interference have all been demonstrated. Using the silicon-on-insulator material system, quantum waveguide circuits have been realised that are two-orders of magnitude smaller than previous implementations, demonstrating quantum interference in MMI devices and the on-chip manipulation of entanglement [14]. In addition, the on-chip generation of correlated photon pairs has been demonstrated in silicon micro-ring waveguide resonators, demonstrating the possibility of on-chip integration of both waveguide circuits and photon pair sources.

VI. Conclusion

The ability to construct complex, interferometrically stable, multi-purpose circuits is crucial for the development of future quantum technologies and the pursuit of fundamental quantum science. Within this work we have developed a toolbox of key integrated quantum photonic components that can be utilised for a wide range of quantum information science experiments.

VII. References

[1] M. A. Nielsen and I. L. Chuang, 1st ed. Cambridge University Press, 2004, p. 675.
[2] D. Deutsch, *Proc of the Royal Society A: Mathematical, Physical and Engineering Sciences*, vol. 400, no. 1818, pp. 97–117, Jul. 1985.
[3] R. Feynman, *Int J Theor Phys*, 1982.
[4] S. Lloyd, *Science*, vol. 273, no. 5278, pp. 1073–1073, 1996.
[5] N. Gisin and R. Thew, *Nature Photon.*, vol. 1, no. 3, pp. 165–171, 2007.
[6] V. Giovannetti, S. Lloyd, and L. Maccone, *Science*, vol. 306, p. 1330, 2004.
[7] M. G. Thompson, A. Politi, J. C. F. Matthews, and J. L. O'Brien, *IET Circuits Devices and Systems*, vol. 5, no. 2, pp. 94–102, 2011.
[8] A. Laing, A. Peruzzo, A. Politi, M. R. Verde, M. Halder, T. C. Ralph, M. G. Thompson, and J. L. O'Brien, *Appl Phys Lett*, vol. 97, no. 21, p. 211109, 2010.
[9] A. Peruzzo, A. Laing, A. Politi, T. Rudolph, and J. L. O'Brien, *Nat Comms*, vol. 2, p. 224, Mar. 2011.
[10] A. Peruzzo, M. Lobino, J. C. F. Matthews, N. Matsuda, A. Politi, K. Poulios, X.-Q. Zhou, Y. Lahini, N. Ismail, K. Worhoff, Y. Bromberg, Y. Silberberg, M. G. Thompson, and J. L. O'Brien, *Science*, vol. 329, no. 5998, pp. 1500–1503, Sep. 2010.
[11] P. J. Shadbolt, M. R. Verde, A. Peruzzo, A. Politi, A. Laing, M. Lobino, J. C. F. Matthews, M. G. Thompson, and J. L. O'Brien, *Nature Photonics*, vol. 6, no. 1, pp. 45–49, Dec. 2012.
[12] A. Politi, M. J. Cryan, J. G. Rarity, S. Yu, and J. L. O'Brien, *Science*, vol. 320, no. 5876, pp. 646–649, May 2008.
[13] D. Bonneau, M. Lobino, P. Jiang, C. M. Natarajan, M. G. Tanner, R. H. Hadfield, S. N. Dorenbos, V. Zwiller, M. G. Thompson, and J. L. O'Brien, *arXiv.org*, vol. quant-ph. 18-Jul.-2011.
[14] D. Bonneau, E. Engin, K. Ohira, N. Suzuki, H. Yoshida, N. Iizuka, M. Ezaki, C. M. Natarajan, M. G. Tanner, R. H. Hadfield, S. N. Dorenbos, V. Zwiller, J. L. O'Brien, and M. G. Thompson, *arXiv*, Jan. 2012.

Generation of Second Harmonic Light from a Low Number of Molecules in the Whispering Gallery Modes

Jordi Martorell

ICFO-Institut de Ciencies Fotoniques, 08860 Castelldefels (Barcelona), Spain
and
Departament de Fisica i Enginyeria Nuclear, Universitat Politecnica de Catalunya, 08222 Terrassa, Spain

Unmarked sensitive detection of molecules is needed in many applications where a hidden substance must be identified. Typically, at least 1 billion molecules would be required to generate detectable light through an optical nonlinear process. By trapping the light in the whispering gallery modes of a high Q spherical micro-resonator we observed second harmonic light from less than 100 molecules. Quasi-phase matched second harmonic on the sphere surface was achieved by a periodic pattering of the molecular surface layer and pulse stretching to compensate temporal walk-off.

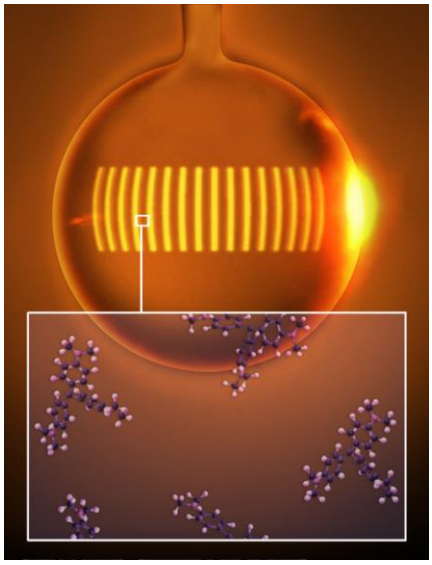


Figure 1 Picture of the microsphere and molecular periodic pattern.

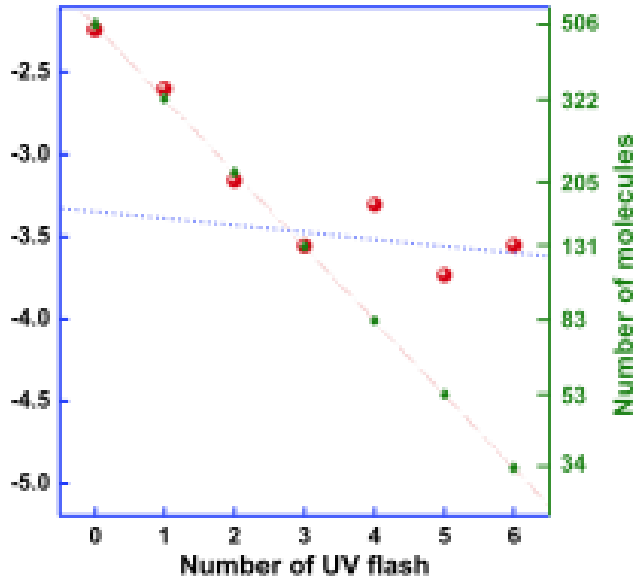


Figure 2 SH signal in a log scale (red spheres) as a function of the UV flash number used to destroy the NL molecules. The corresponding number of molecules (green dots) is estimated taking into account the initial surface concentration.

We report on the design and fabrication of a nonlinear spherical resonator to experimentally measure second harmonic generation (SHG) from molecules deposited on its surface. This generation requires phase matching in the whispering gallery modes, which we achieved by implementing a new procedure to periodically pattern with nanometric precision a molecular surface mono-layer, schematically shown in Figure 1. Temporal walk-off between the fundamental and SH pulses reduced the interacting length down to a very short distance. With radii of approximately 180 μm, pulse overlap at the perimeter of the sphere may be lost well before a single cavity round-trip is completed. To circumvent this problem the pump pulses were stretched using 140 m of an optical fiber loop to ensure permanent overlap. Using such type of walk-off

compensation allowed us to reduce the surface molecule concentration by four orders of magnitude. As shown in Figure 2, approximately between 50 to 100 molecules were needed to measure a change in the SH light [1, 2]. This result confirmed the relevant role played by such high Q micro-spheres. As indicated above, when molecules are deposited on a flat transparent substrate, typically one would need 1 billion molecules to obtain a measurable SHG signal. The possible application of nonlinear spherical micro-resonators in the detection of small molecules will be discussed.

[1] J. L. Dominguez-Juarez, G. Kozyreff, and J. Martorell, Nat. Commun. **2**, 254 (2011).
[2] G. Kozyreff, J. L. Dominguez-Juarez, and J. Martorell, Laser Photonics Rev. **5**, No. 6, 737–749 (2011).

High efficiency THz photodetectors

(invited)

A. J. Seeds[1], E. Rouvalis[1], M. Natrella[1], H. Liu[1], M. Chtioui[2], F. van Dijk[2], G. Carpintero[3], and C. C. Renaud[1]

[1]Department of Electronic and Electrical Engineering, University College London, Torrington Place, London, WC1E 7JE, UK
[2]III-V Lab, a joint Laboratory of "Alcatel Lucent Bell Labs", "Thales Research & Technology" and "CEA-LETI", Campus Polytechnique, 1, Avenue A. Fresnel, 91767, Palaiseau Cedex, France
[3]Universidad Carlos III de Madrid, Av. de la Universidad, 30. Leganés 28911, Madrid, Spain
a.seeds@ee.ucl.ac.uk

***Abstract*—We present a review of our latest work on Uni-Travelling Carrier Photodiodes for high efficiency THz emission. The detectors' waveguide structure allows for both higher responsivity and saturation power thus achieving the highest published THz figure of merit (P_{THz}/P_{opt}^2) up to 1.5 THz for such devices. We also discuss new material development using solid source MBE and the possibility of monolithic integration within a photonic heterodyne source.**

Keywords—Optical Heterodyne Generation (OHG), Terahertz, Traveling Wave Photodiode (TW-PD), Uni-Traveling Carrier Photodiode (UTC-PD).

I. INTRODUCTION

Frequencies in the Terahertz (THz) region are of growing interest for applications in security, biology, medicine and communications [1]. Continuous wave (CW) THz sources have been demonstrated for different parts of the band offering various levels of power and efficiency [2]. One of the most promising techniques for tuneable, CW THz sources is Optical Heterodyne Generation (OHG) in Ultra-Fast Photodetectors [3]. The key element for OHG-based systems is an high-bandwidth photodetector to generate the THz signal. The Uni-Travelling Carrier Photodiode (UTC-PD) has demonstrated a high 3-dB bandwidth together with improved output power capabilities [4]. Nevertheless, as most of the THz frequency span is located well beyond the 3-dB bandwidth of most photodiodes, the importance of the high frequency roll-off becomes critical for efficient THz generation. Travelling-Wave photodiodes (TW-PDs) can offer a substantial enhancement at high frequencies with a roll-off approaching the 20 dB/decade theoretical limit [5]. Here we present the integration of these two independently demonstrated photodetection schemes into a single device, the Travelling-Wave Uni-Travelling Carrier photodiode (TW-UTC-PD). We report record levels of output power and THz figure of merit (P_{THz}/P_{opt}^2 in W^{-1}). Novel materials growth using advanced Molecular Beam Epitaxy (MBE) technology and the development of a platform for monolithic integration of these devices with tuneable lasers towards a fully integrated OHG source are also discussed.

II. THE TW-UTC-PD CONCEPT

To achieve high conversion efficiency in photomixing devices, one should maximise the generated output power and minimise the required optical input power. The concept of UTC-PDs was originally proposed as a means of enhancing the transit-time that in photodetectors with a p-i-n epitaxial structure is limited by the slow hole transport. In the case of a UTC-PD, light is absorbed in the p-doped layer and only faster electrons drift through the depletion layer. To achieve fast speed of operation, absorption layers must generally be kept thinner than p-i-n PDs resulting in a significantly lower responsivity. This limitation can be overcome by using a waveguide-fed, edge-coupled configuration. This is also compatible with a Travelling Wave (TW) design that can offer a substantial improvement in performance at frequencies above the 3-dB bandwidth. To independently design the active mesa structures and the coupling waveguide, the device demonstrated in our work uses tapered mode-conversion waveguides [4], [5]. In such a structure, the TW electrodes can be designed in order to optimize the extrinsic frequency response of the device. For this design the objective was velocity matching and as such this would not be a true travelling wave design. However with such design a roll-off that is substantially less than 40 dB/decade could be achieved making these devices suitable for efficient THz generation.

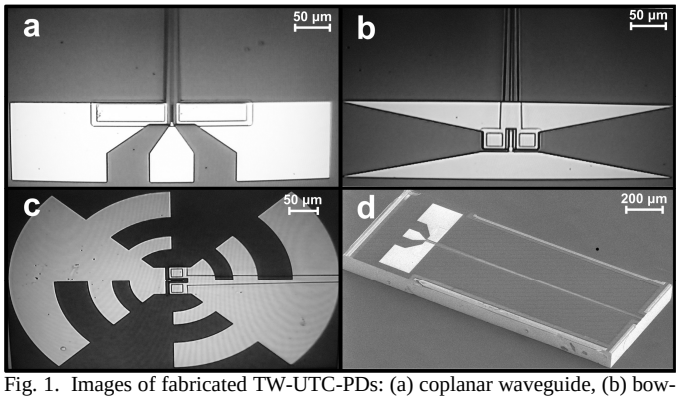


Fig. 1. Images of fabricated TW-UTC-PDs: (a) coplanar waveguide, (b) bow-tie, (c) log-periodic, (d) cleaved chip with coplanar waveguide electrodes [5].

III. THZ EMISSION

Devices with diluted optical input waveguides achieved responsivities up to 0.53 A/W. TW-UTC-PDs integrated with Coplanar Waveguides (Fig. 1(a), 1(d)) have demonstrated a 3-dB bandwidth of up to 108 GHz and record power levels of 2.4 mW at 150 GHz and 1 mW at 200 GHz at a maximum DC

This work was supported by Engineering and Physical Sciences Research Council and the European Commission within the framework of the European projects MITEPHO and iPHOS. Dr. Rouvalis' work is currently supported under the EPSRC Doctoral Prize Fellowship scheme.

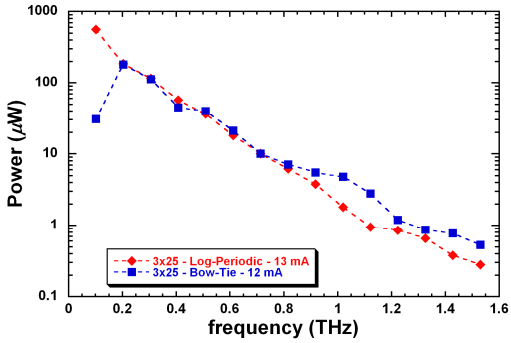


Fig. 2. THz output power from log-periodic (red) and bow-tie (blue) heat sink-mounted antenna-integrated devices measured with a Thomas Keating power meter and a Golay cell [5].

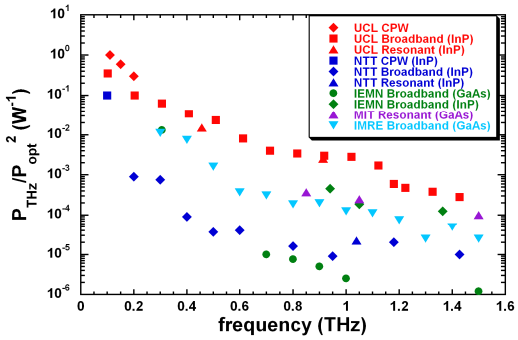


Fig. 3. Comparison between state-of-the-art Terahertz figure of merit from various photomixing sources [5].

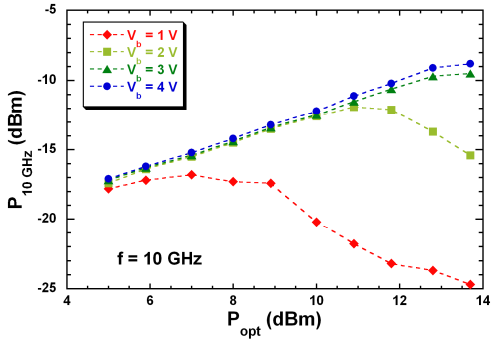


Fig. 4. Total power delivered from MBE-grown InGaAsP UTC-PD as a function of optical input power for various levels of applied reverse bias.

photocurrent of 23 mA [5]. TW-UTC-PDs were also integrated with broadband antennas such as a Bow-Tie antenna (BTA) and a Log-Periodic antenna (LPA) shown in Fig. 1(b) and Fig. 1(c) respectively. Two 3×25 μm^2 TW-UTC-PDs, one with a LPA and one with a BTA showed the highest radiated THz power. Power measurements were taken from 102 GHz up to 1.53 THz using an OHG system based on widely tunable SG-DBR lasers. The results are shown in Fig. 2. Record power levels from a broadband photomixer of up to 5 μW at 1 THz have been achieved with an input optical power of only 40 mW. It is noteworthy that these optical power levels are readily available from Semiconductor Optical Amplifiers (SOAs). To quantify the optical-to-THz conversion efficiency, the THz figure of merit can be used. From Fig. 3, it can be observed that as well as record power in the range of measurements, record THz figures of merit were achieved from the BTA-integrated device with 0.003 W^{-1} at 1.02 THz and 0.00035 W^{-1} at 1.53 THz.

IV. Novel Material Growth Using MBE

Recently, TW-UTC-PD structures were grown using our solid source MBE facility. To investigate the quality of the material, simple vertically-illuminated test UTC-PDs were fabricated with a 20 μm diameter optical window. To the best of our knowledge, these are the first UTC-PDs grown on an InP substrate with a non-Al structure by solid source MBE. The total delivered power from the test structures at 10 GHz, as a function of the optical power, for various levels of applied reverse bias voltage is plotted in Fig. 4.

V. Monolithically Integrated OHG Systems

Apart from the superior THz efficiency, another important aspect of the TW-UTC-PD photomixer technology is the compatibility with integration platforms. Current InP PIC technologies use photodetectors that have limited bandwidth and low saturation currents. Recently, TW-UTC-PD layers were grown on top of MQW epitaxy and were fabricated using technology that will allow monolithic integration with tunable lasers. Despite the increased series resistance caused by 1-μm thick cap layers for waveguiding, the fabricated devices demonstrated a 3-dB bandwidth of 110 GHz and an output power at 120 GHz of more than 1 mW [6]. In addition, PICs with dual photodetectors and MMI couplers were fabricated. The motivation for including a second photodetector on the chip, which will feed an external mixer with a local oscillator, arises from the hybrid integration of phase locking electronics to minimise loop delay. In the passive sections, losses of 2.6 dB/mm were measured. In the final PICs these photodetectors will be integrated with tunable lasers, amplifiers and modulators to form photomixing millimeter-wave transmitter for wireless communications. However, this technology can exhibit a generic approach for monolithic integration of high-saturation current photodetectors with a 3-dB bandwidth of more than 100 GHz in InP PICs used in optical communications receivers.

Acknowledgement

The authors acknowledge the important contribution of the Centre for Integrated Photonics to this work in terms of device fabrication and useful discussions on the design.

References

[1] P. H. Siegel, “Terahertz Technology,” IEEE Transactions on Microwave Theory and Techniques, vol. 50, no. 3, 2002.

[2] M. Tonouchi, “Cutting edge terahertz technology,” Nature Photonics, vol. 1, no. 2, 2007.

[3] M. J. Fice, E. Rouvalis, L. Ponnampalam, C. C. Renaud, and A. J. Seeds, “Telecommunications technology-based THz sources,” Electronics Letters, vol. 46, no. 26, 2010.

[4] E. Rouvalis, C. C. Renaud, D. G. Moodie, M. J. Robertson, and A. J. Seeds, “Travelling-Wave Uni-Travelling Carrier Photodiodes for continuous wave THz generation,” Optics Express, vol. 18, no. 11, 2010.

[5] E. Rouvalis, C. C. Renaud, D. G. Moodie, M. J. Robertson, and A. J. Seeds, “Continuous Wave Terahertz Generation from Ultra-Fast InP-Based Photodiodes,” IEEE Transactions on Microwave Theory and Techniques, vol. 60, no. 3, 2012.

[6] E. Rouvalis, M. Chtioui, M. Tran, F. van Dijk, M. J. Fice, C. C. Renaud, G. Carpintero, and A. J. Seeds, “High-speed Uni-Traveling Carrier Photodiodes for InP Photonic Integrated Circuits,” in *European Conference on Integrated Optics (ECIO) 2012*, accepted for publication.

Integrated Two-Wavelength DBR Lasers for Tunable Photomixing THz-Wave Generation

Masahiro Uemukai and Toshiaki Suhara
Department of Electrical, Electronic and Information Engineering,
Graduate School of Engineering, Osaka University, Osaka, Japan
E-mail: uemukai@eei.eng.osaka-u.ac.jp

***Abstract*— A 780-nm-band integrated tunable two-wavelength AlGaAs DBR laser with PN junction heaters was designed and fabricated. Tunable coherent THz wave generation in 0.8-1.2 THz using GaAs photomixers was demonstrated.**

Keywords-component; DBR lasers; two-wavelength lasers; tunalbe lasers; integrated optoelectoronics; THz-wave generation

I. INTRODUCTION

By mixing optical waves of slightly different wavelengths from two near-infrared semiconductor lasers in a low-temperature-grown (LT) GaAs-based photomixer, coherent THz waves at the beat frequency can be generated [1]. Monolithically integrated two-wavelength DBR lasers for beat signal generation were reported [2-4]. The advantages of using a monolithically integrated laser are the compactness, the good spatial mode matching and the high stability of the wavelength difference. In our previous work, an integrated two-wavelength laser was designed and fabricated, and coherent THz wave generation by photomixing was demonstrated [4].

In many applications of THz wave, frequency tunable coherent THz wave is required. Monolithic dual-mode DFB laser for this purpose was demonstrated [5]. In this work, we design and fabricate a 780-nm-band integrated tunable two-wavelength DBR laser, and demonstrate frequency tunable coherent THz wave generation by photomixing of the integrated two-wavelength laser output.

II. DEVICE DESCRIPTION

The integrated AlGaAs quantum-well tunable two-wavelength DBR laser is constructed with two tunable DBR lasers and a Y-branch waveguide amplifier, as shown in Fig. 1. Each DBR laser consists of a narrow ridge active channel and a surface relief DBR grating with a PN junction heater for wavelength tuning. The DBR lasers with slightly different grating periods of Λ_1 and Λ_2 oscillate at slightly different wavelengths. The optical waves from the two DBR lasers are combined into the single output channel of the Y waveguide amplifier and emitted from the output facet. By current injection to the heaters beside the DBRs, the lasing wavelength can be tuned through the Bragg wavelength change due to temperature rise.

For 0.4-nm difference between Λ_1 and Λ_2, for example, lasing wavelength difference of 2 nm, corresponding to beat frequency of ~1 THz, can be obtained. Preliminary test using DBR lasers fabricated from the same wafer used in this work showed that 1 nm lasing wavelength shift was obtained by 10°C temperature rise of the DBR. In order to design the heater, thermal conduction analysis was performed and temperature rise distributions in the lateral direction were approximately calculated. Then the size and the position of the heater were determined for obtaining 10°C temperature difference between the two DBR gratings. By current injection to the short wavelength side heater, the wavelength difference can be decreased to 1 nm. In contrast, by current injection to the other side heater, the wavelength difference can be increased to 3 nm. By current injection to one of the two heaters, the wavelength difference between 1 and 3 nm (frequency difference between 0.5 and 1.5 THz) can be expected.

III. DEVICE FABRICATION

At first, the slope structures were formed by RIE using shadow masks. The heater regions were covered by conventional SrF_2 masks for the vertical sidewalls. The first-order DBR gratings with different pairs of grating periods were fabricated by EB writing and two-step RIE. The ridge structures were then formed by EB writing and RIE using SrF_2 masks. Pad electrodes for the two DBR lasers, the two heaters and the Y-branch waveguide were formed on a BCB insulator layer, and an n-electrode was evaporated on the backside. After cleaving, HR and AR coatings were deposited on the rear and front facets. The laser was mounted on a Cu heatsink.

IV. EXPERIMENTAL RESULTS

The dependences of the output power from the output channel on the injection current to each DBR laser were measured at an amplifier current of 70 mA under CW operation. The two DBR lasers have slightly different light-current characteristics. The threshold currents were 40 and 47 mA, and the output powers were 12 and 9 mW at an oscillator current of 70 mA. The lasing spectra were measured under simultaneous current injections to the two DBR lasers and the Y waveguide

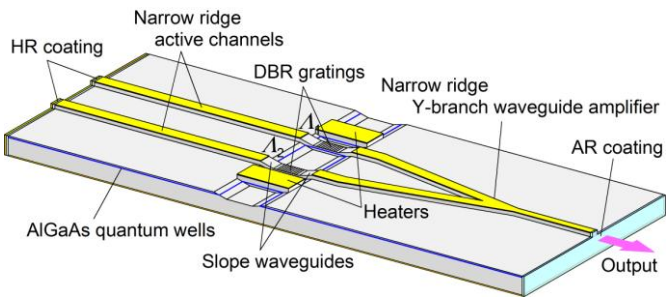


Figure 1. Schematic of integrated tunable two-wavelength DBR laser.

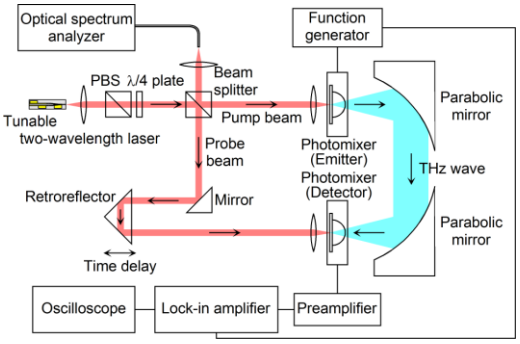


Figure 2. Experimental setup for coherent THz wave generation and detection using tunable two-wavelength laser and two photomixers.

amplifier. The wavelength difference of 2.0 nm (0.99 THz beat frequency) was obtained. By proper adjustment of the injection currents to the two DBR lasers, the same output level of about 8 mW and a side-mode suppression ratio of 25 dB were obtained. Good spatial overlap between the amplified lights from the two DBR lasers on the front facet was confirmed.

An experimental setup for coherent THz wave generation and detection using the tunable two-wavelength laser is shown in Fig. 2. Two LT-GaAs dipole-type photomixers (Hamamatsu Photonics K.K., G10620-11) were used as an emitter and a detector. A polarized beam splitter (PBS) and a λ/4 plate were inserted to reduce optical feedback. The laser beam from the two-wavelength laser was split into the pump and probe beams. The pump beam was focused onto the emitter. The emitter was biased with a rectangular voltage of ±15 V at a frequency of 10 kHz. The generated THz wave was collected and focused on the detector by a pair of off-axis parabolic mirrors. The probe beam was focused on the detector electrode gap, where the THz wave was focused. The detector photocurrent was detected by a lock-in amplifier. Delay time was scanned by moving a retroreflector on a translation stage.

Injection currents for the two DBR lasers and the Y waveguide amplifier were adjusted to obtain two-wavelength oscillation with almost equal powers. The lasing spectrum at oscillator injections of 59.5 and 64.0 mA and an amplifier injection of 80.0 mA is shown in Fig. 3(a) (no heater injection). The wavelength difference of 2.00 nm (0.99 THz beat frequency) was stable, while the optical power of each peak was not so stable. This may be due to insufficient reduction of the optical feedback. A total power before the PBS was measured as about 15 mW. By scanning the delay time, a periodic signal was obtained as shown in Fig. 3(b). This corresponds to the cross-correlation signal between the THz wave electric field and the photoexcited carrier number in the electrode gap [6]. The frequency determined from the period of the signal was 1.02 THz, which was in good agreement with the laser beat frequency.

With a current injection to the short wavelength side heater at 60 mA, a smaller wavelength deference of 1.62 nm (0.80 THz) was obtained, as shown in Fig. 3(a). By scanning the delay time, the periodic signal was also obtained and the frequency was estimated as 0.82 THz (Fig. 3(b)). On the other hand, a wider wavelength difference of 2.46 nm (1.21 THz) was obtained (Fig. 3(a)) with a current injection to the long wavelength side heater at 60 mA. The periodic signal was obtained and the frequency was estimated as 1.22 THz (Fig.

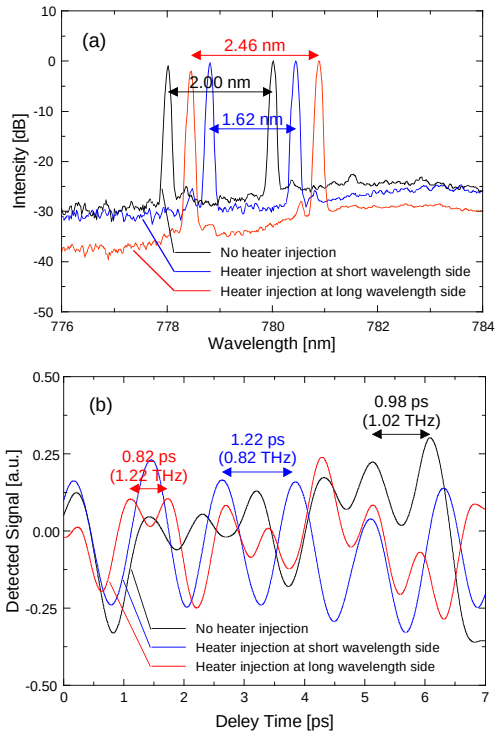


Figure 3. (a) Measured spectra of tunable two-wavelength oscillation, and (b) dependence of detected signals on delay time.

3(b)). The frequency of the generated THz wave was changed as the laser beat frequency was changed. Frequency tunable coherent THz wave generation was achieved by photomixing of the integrated tunable two-wavelength DBR laser.

ACKNOWLEDGMENT

The authors would like to thank Dr. H. Kan, Dr. A. Watanabe, H. Kitajima and A. Higuchi, Hamamatsu Photonics K.K., for valuable discussion.

REFERENCES

[1] K. A. McIntosh, E. R. Brown, K. B. Nichols, O. B. McMahon, W. F. Dinatale, and T. M. Lyszczarz, "Terahertz photomixing with diode lasers in low- temperature-grown GaAs," Appl. Phys. Lett., vol. 67, pp. 3844-3846, Dec. 1995.

[2] M. Maeda, T. Hirata, M. Suehiro, M. Hihara, A. Yamaguchi, and H. Hosomatsu, "Photonic integrated circuit combining two GaAs distributed Bragg laser diodes for generation of the beat signal," Jpn. J. Appl. Phys., vol. 31, pt. 2, pp. L183-L185, Feb. 1992.

[3] R. K. Price, V. B. Verma, K. E. Tobin, V. C. Elarde, and J. J. Coleman, "Y-branch surface-etched distributed Bragg reflector lasers at 850 nm for optical heterodyning," IEEE Photon. Technol. Lett., vol. 19, pp. 1610-1612, Oct. 2007.

[4] M. Uemukai, H. Ishida, A. Ito, T. Suhara, H. Kitajima, A. Watanabe, and H. Kan, "Integrated AlGaAs quantum-well ridge-structure two-wavelength distributed Bragg reflector laser for terahertz wave generation," Jpn. J. Appl. Phys., vol. 51, 020205, Feb. 2012.

[5]N. Kim, J. Shin, E. Sim, C. W. Lee, D.-S. Yee, M. Y. Jeon, Y. Jang, and K. H. Park, "Monolithic dual-mode distributed feedback semiconductor laser for tunable continuous-wave terahertz generation," Opt. Express., vol. 17, pp. 13851-13859, Aug. 2007.

[6] K. Shibuya, M. Tani, M. Hangyo, O. Morikawa, and H. Kan, "Compact and inexpensive continuous-wave sub-terahertz imaging system with a fiber-coupled multimode laser diode," Appl. Phys. Lett., vol. 90, 161127, April 2007.

Technology achievements for silicon photonic devices

Jean-Marc FEDELI, Badhise BEN BAKIR, Antoine DESCOS, Jean Michel HARTMANN,

CEA,LETI, Minatec Campus, 17 rue des Martyrs, F-38054 GRENOBLE cedex 9, FranceA

Contact: jean-marc.fedeli@cea.fr

Laurent VIVIEN, Delphine MARRIS-MORINI, Gilles RASIGADE, Melissa ZIEBELL

Institut d'Electronique Fondamentale, Univ. Paris-Sud, CNRS, Bât. 220, F-91405 ORSAY Cedex – France.

***Abstract*— Silicon Photonic high performance generic building blocks will be reviewed such as few mW sources by III-V/Si heterogeneous integration, 40G Si modulators and Ge detectors for interchip communications.**

Keyword: silicon photonics, hybrid lasers, silicon modulator, germanium photodetector.

I. INTRODUCTION

In the last years, submicron silicon photonics have generated an increasing interest in the recent years, mainly for optical telecommunications or for optical interconnects in microelectronic circuits. The rationale of silicon photonics is the reduction of the cost and energy of communications systems through the integration of photonic components and an electronic integrated circuit (IC) on a common chip (telecommunications applications), or the enhancement of IC performance with the introduction of optics inside a high performance chip (core to core communications), or low cost sensors. By co-integrating optics and electronics on the same chip, high- functionality, high-performance and highly integrated devices can be fabricated with a well-mastered microelectronics fabrication process. In addition, advances in CMOS photonics will move the emphasis from device component to architecture. The FP7 HELIOS project aims to combine a photonic layer with a CMOS circuit by using microelectronics fabrication processes. It will make CMOS photonics accessible to a broad circle of users in a foundry-like, fabless way. The objectives of the project are manifold and one is the development of high performance generic building blocks for a broad range of applications: WDM sources by III-V/Si heterogeneous integration, fast modulators and detectors, passive circuits and packaging.

2. Hybrid InP directly bonded on Si sources

The heterogeneous integration of III-V materials by bonding consists in the transfer an III-V heterostructure from its original growth substrate to a silica surface. The III-V components are then fabricated on 200mm SOI processed wafer using wafer-scale processing. This technique allows a high density of integration, collective processing and the use of high-quality III-V layers. Light can be directly coupled into a silicon waveguide underneath the III-V epitaxy. Most of the laser functions can be moved into the silicon part by designing the III-V layer only as a gain material while the cavity lies in the silicon region. The III-V heterostructure (InP based stack) are placed only at specific location by die-to-wafer bonding. The strong point is that it reduces the cost of the integration process since expensive III-V stacks can be bonded only where they are needed (fig 1).

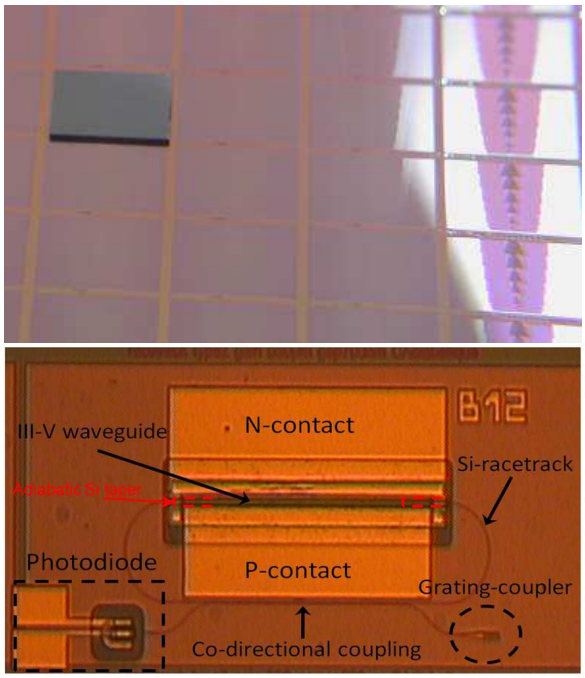


Figure 1: InP die on silicon photonics circuit with SiO_2 molecular bonding and view of fabricated lasers on Si

After molecular bonding, mechanical grinding and InP chemical etching are performed in order to leave the thin heterostructure on the waveguide layer with a controlled SiO2 separation layer. Decontamination steps of the rear side of the wafers are required before the introduction of the wafers in a microlectronics fab at the back-end level. With DeepUV lithography, fine patterns can be defined with high alignment with the waveguide layer. Then etching of InP in 200mm format is performed using reactive ion etching (RIE) with CH4/H2 gases as the thin thickness of the heterostructure requires low etching speed. The defined InP structures for SOA or laser are then cladded with a thick silica before openings for electrodes formation [1].

Despite the lack of engineering of the current flow, the ring laser operates under continuous mode. Derived from the L-I characteristics, the laser threshold is 30 mA with a maximum output power of 6 mW at 15 °C giving about 3mW in the output fiber. For monitoring, a photodiode was defined with

the III-V stack. The dark current is 1nA and without optimization, the sensitivity is 0.3 A/W [2].

3. Si modulators

Modulation in silicon is usually obtained by free carrier concentration variation. Carrier depletion is a high speed effect that has been widely used to achieve fast modulators [3]. Thick modulators (400nm) have been also fabricated based on carrier depletion in a PIPIN diode in the Helios project, demonstrating large 40 Gbit/s-extinction ratio simultaneously with low optical loss. A schematic view of the device cross section is shown in Fig. 2. The silicon rib waveguide width is 420 nm, the rib height is 390 nm and the etching depth is 290 nm, leading to quasi-TE and quasi-TM single mode propagations at a wavelength of 1.55 µm [4].

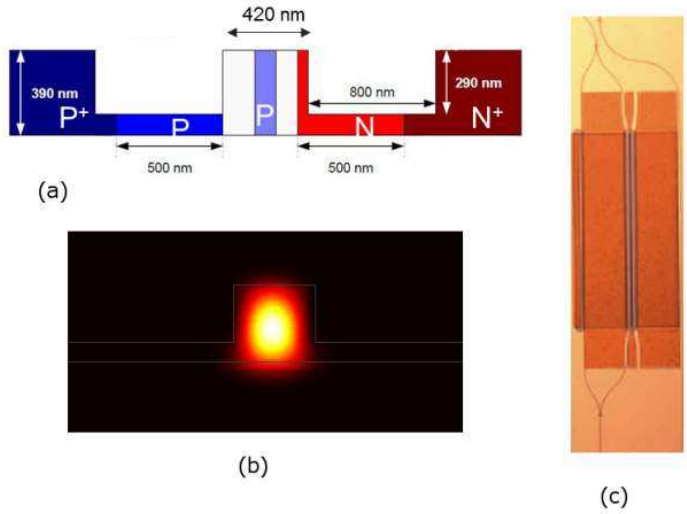


Figure 2: (a) Schematic view of lateral PIPIN phase shifter; (b) Optical mode profile at 1.55 µm; (c) Optical microscope view of the MZI modulator

Compared to a regular PIN diode, a P-doped slit with a nominal doping concentration of 3.10^{17} cm-3 is inserted in the intrinsic region of the lateral PIN diode and acts as a source of holes. Optical loss is then reduced because a large part of the waveguide is not intentionally doped, and the metallic contact regions are far from the light propagation area. At equilibrium, holes are confined in the p-doped slit centered in the rib. When a reverse bias is applied to the diode, holes are swept out of the active region. The optical modulator is fabricated on a 200mm SOI wafer with a 2 µm BOX and a 400 nm silicon film with microelectronic tools such as Deep-UV optical lithography and RIE. A self-alignment technique was used to guarantee the Boron implantation in the middle of the waveguide, to align the left P and right N doped region at the border of the waveguide. This guarantees the repeatability of the results from die to die on a wafer.

A silicon optical modulator based on a reverse biased pipin diode embedded in a Mach-Zehnder interferometer working at 40 Gbit/s was demonstrated. Two phase shifter lengths were presented, one 0.95 mm long with an ER of 3.2 dB, and an optical loss of 4.5 dB, and one 4.7 mm long with an ER of 6.2 dB, and an optical loss of 6 dB. Further improvements can be considered, including the increase of the doping level in the active region and a push-pull operation to increase the ER.

4. Ge photodetectors

High speed and high responsivity germanium photodetectors have been fabricated in the Helios project and exhibited a zero-bias 40Gbit/s pin Ge photodiode integrated at the end of a Si waveguide using the butt coupling approach [5]. A 10µm long silicon recess was etched at the end of the waveguide (220nm thick, 500nm wide) down to a thin silicon layer of about 50nm. Ge was selectively grown by RP-CVD in the Si cavity. A thick silica layer which can block the implantation, was deposited and a self-aligning process was used to perfectly to define the gap between n-type and p-type doped regions of the Ge PD, that were implanted with phosphorous and boron ions, respectively. Changing the width of the gap modify the transit time and thus the bandwidth. Electrodes were then defined withTi/TiN/AlCu metal stack deposition and etching. The photodetectors were connected to a demux composed of a 2D surface grating coupler and two 16 channels AWG (Fig 3) to define a 16 channels receiver.

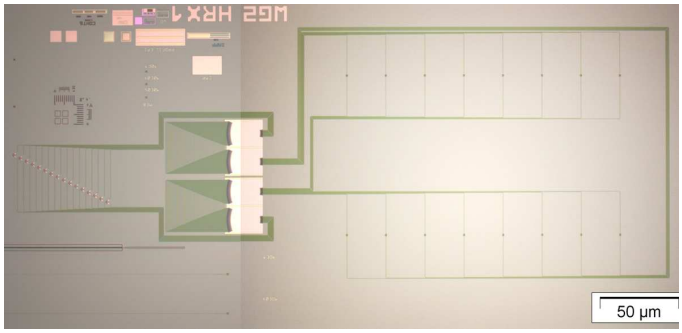


Fig. 3: Top-view Optical Microscopy of the 16 channel receiver with 2D couplers (left) and Ge PD before metallization (right).

ACKNOWLEDGMENT

These results were obtained thanks to many IEF and LETI researchers. The precious help of numerous people of the 200mm LETI fabrication line is gratefully acknowledged. The research leading to these results has partially been funded by the European Community's Seventh Framework Program through the HELIOS project

REFERENCES

[1] B. Ben Bakir & al" *Electrically driven hybrid Si/III-V Fabry-Pérot lasers based on adiabatic mode transformer"* Optics Express, Vol. 19 Issue 11, pp.10317-10325 (2011)

[2] B. Ben Bakir & al " *Hybrid Si/III-V lasers with adiabatic coupling*" IEEE GFP 2011 Conference Invited paper ThB1.

[3] D. J. Thomson & al, "*High contrast 40Gbit/s optical modulation in silicon*," Opt. Express, vol. 19, pp. 11507-11516, 2011.

[4] M.Ziebell &al, *"40 Gbit/s low-loss silicon optical modulator based on a pipin diode"*, to appear in Optics Express in 2012

[5] L.Vivien & al, *"Zero-bias 40gbit/s germanium waveguide photodetector on silicon*," Opt. Express 20, 1096-1101 (2012)

Integrated Nonlinear Nanophotonics in Silicon

Alexander L. Gaeta
School of Applied and Engineering
Cornell University
Ithaca, NY USA
a.gaeta@cornell.edu

***Abstract*—We describe our recent work on the creation of nonlinear optical devices in silicon-based nanowaveguides for a wide variety of applications including ultrafast optical processing and frequency metrology.**

Keywords-component; nonlinear optics; four-wave mixing; frequency combs; all-optical processing.

A highly promising research area that recently has emerged is nonlinear optics using silicon photonics. Since the birth of nonlinear optics, researchers have continually focused on developing efficient nonlinear optical devices that require low optical powers. The strong light confinement in silicon waveguides results in a high effective nonlinearity and enables tuning of the waveguide dispersion, which is essential for phase matching of parametric nonlinear optical processes such as four-wave-mixing (FWM). We have demonstrated FWM-based frequency conversion in Si waveguides using as little as 1 mW of pump power in a ring-resonator geometry and over bandwidths exceeding 800 nm in a straight-waveguide device with 100 mW of power. In addition, by using the concept of time-space duality on a silicon chip we have show temporal stretching, compression, and characterization of optical waveforms which allows for seamless transformation between the GHz and THz regimes. Lastly, we are able to produce broadband frequency combs by using FWM parametric oscillation in ring resonators which offers the possibility of CMOS-compatible multiple-wavelength sources and all-optical clocks.

.

Status and Prospects of Lithium Niobate Integrated Optics

Wolfgang Sohler
Applied Physics
University of Paderborn
Paderborn - 33098, Germany
sohler@physik.uni-paderborn.de

***Abstract*—Status and prospects of $LiNbO_3$ (LN) integrated optics will be reviewed with emphasis on waveguide lasers, nonlinear frequency converters, single photon devices and their respective applications. Moreover, a new platform for LN-based nanophotonics will be introduced.**

Keywords-integrated optics; lithium niobate; waveguide laser; frequency converter; photon pair source; quantum memory.

I. INTRODUCTION

Among the different materials used for integrated optics since a long time, ferroelectric Lithium Niobate ($LiNbO_3$, LN) offers a unique combination of excellent electro-optical, acousto-optical, and nonlinear properties. Moreover, it can be easily doped with laser-active ions and enables a simple fabrication of low-loss optical waveguides by doping with transition metals or by ion-exchange processes. Meanwhile, integrated LN devices find wide commercial applications e.g. as high-bandwidth electro-optical modulators for the optical internet or as phase modulators for signal processing in all-optical gyroscopes.

The status of LN integrated optics will be reviewed emphasizing new waveguide structures, devices and applications in the last years. In particular, the large potential of waveguide lasers, of nonlinear frequency converters and ultra-fast all-optical signal processing devices and of single photon sources and quantum memories will be discussed. Finally, Lithium-Niobate-On-Insulator (LNOI) will be introduced as a promising new platform for LN-based integrated optics and nanophotonics.

II. WAVEGUIDE LASERS

LN can be easily doped with laser-active (rare earth) ions by several methods; in particular, a simple diffusion technique proved to be very successful. Based on this technique, a whole family of Er-doped waveguide lasers of excellent quality has been developed emitting in the wavelength range 1530 nm < λ < 1603 nm. Free running lasers of the Fabry-Pérot type, harmonically mode-locked lasers (5 ps / 10 GHz), Q-switched lasers (4 ns / 1 kHz / 1 kW), Distributed Bragg Reflector- (DBR-) and Distributed Feedback- (DFB-)lasers, self-frequency doubling devices, ring and acousto-optically tuneable lasers have been reported [1]. They all are optically in-band pumped by λ = 1480 nm radiation.

Recently, also Tm-doped waveguide lasers have attracted increased attention [2]. By exploiting the $^3F_4 \rightarrow {}^3H_6$ transition, their emission wavelength is within the band 1650 nm < λ < 1900 nm. Such lasers will find applications in spectroscopy, medicine, remote sensing and material processing. As example, a Ti:Tm:LN waveguide laser of very low threshold and long emission wavelength will be reported [3]. The simple Fabry-Perot type laser - without any wavelength selective component in the cavity - is in-band pumped at 1650 nm and emits near 1890 nm (Fig. 1). This is the longest emission wavelength from a Tm:LN laser reported so far. The strong relaxation oscillations can easily be suppressed by feedback controlled pumping.

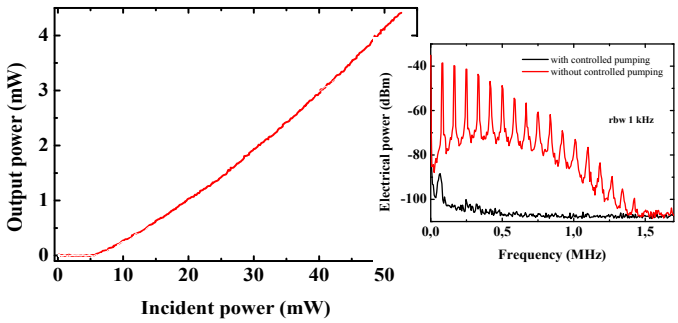


Figure 1. Left: Power characteristics of a Ti:Tm:$LiNbO_3$ waveguide laser: output power (TE) at 1890 nm emission wavelength versus incident pump power (TE) at 1650 nm. Right: Relaxation oscillations, displayed as RF-spectrum of the photodiode current without (red) and with (black) feedback controlled optical pumping (here: 14 mW pump power) [3].

III. SECOND ORDER NONLINEAR DEVICES

It was the quasi phase matching (QPM) concept, realized by periodic poling of LN waveguides with periodicities from ~ 30 µm down to < 1 µm, which enabled an enormous broadening of the wavelength range accessible for nonlinear frequency converters and all-optical signal processing devices. They all rely on three-wave nonlinear interactions, determined by energy conservation and QPM.

As examples, nonlinear wavelength converters in the mid-infrared (MIR), near-infrared (NIR) and visible spectral ranges will be presented with most interesting applications in absorption spectroscopy, optical communications and stellar interferometry. To introduce just one example, special modules with Ti:PPLN waveguides have been developed for nonlinear wavelength conversion from the NIR to the MIR and back again by sum frequency (SFG) and difference frequency generation (DFG) (Fig. 2) [4]. Using these modules, free space

optical communication in an atmospheric window was demonstrated at 3.8 µm wavelength. Using the same approach, also MIR absorption spectroscopy of methane was investigated in the wavelength range 3.26 µm < λ < 3.42 µm.

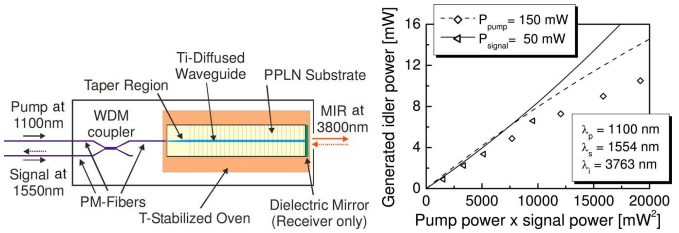


Figure 2. Left: Scheme of the transmitter and receiver modules for MIR generation via DFG. The receiver module has an additional dielectric mirror for the pump to enable copropagating DFG of MIR and pump radiation from right to left. Right: Measured output power of the transmitter module (symbols), depending on pump and signal power levels coupled to the waveguide. The curves represent corresponding calculations [4].

IV. SINGLE PHOTON (PAIR) SOURCES AND QUANTUM MEMORIES

Periodically poled LN (PPLN) waveguides enabled the development of a variety of single photon (pair) sources for applications such as quantum key distribution (QKD) [5]. The principle is to exploit spontaneous parametric down conversion (SPDC) to generate a pair of (entangled) photons. Energy of pump photons and periodicity Λ of the ferroelectric domains determine energy and bandwidth of the two generated photons. As example, special sources are currently developed for quantum repeaters; the wavelength of one photon matches an absorption line of a rare-earth doped crystal or waveguide (e.g. 880 nm for Nd) used as quantum memory, while the wavelength of the other is in a telecom band (e.g. 1345 nm).

Several rare earth-doped waveguides have been developed during the last years not only for laser applications, but also for photon echo-based quantum memories. To be specific, special Er-doped waveguides have been fabricated (Fig. 3, left) to demonstrate e.g. stimulated photon echoes in the ensemble of Er-ions. More recently, Tm-doped channel waveguides have been developed (Fig. 3, right) and used to demonstrate single photon storage and retrieval [6].

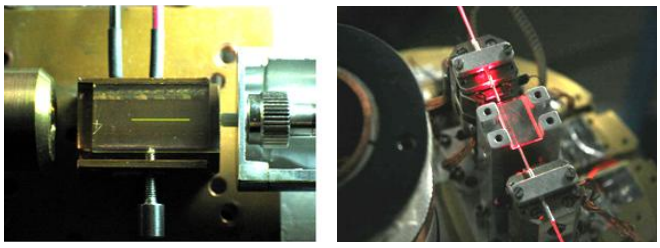


Figure 3. Left: Ti:Er:LN waveguide (λ_{memory} = 1531 nm). Right: Ti:Tm:LN waveguide (λ_{memory} = 795.5 nm) [6].

V. LITHIUM NIOBATE ON INSULATOR (LNOI) PLATFORM, NANOPHOTONIC WAVEGUIDES AND DEVICES

Recently, a novel platform for LN waveguides of high refractive index contrast was demonstrated [7]. Similar to the fabrication of Silicon-On-Insulator (SOI), an ion-implantation based "smart cut" process is used, followed by crystal-bonding, to fabricate a single crystalline LN film on a PECVD-deposited SiO_2-layer on a LN substrate. Therefore, the new wafer-scale platform is called LNOI (Fig. 3). Similar to SOI, it enables the development of "photonic wires", and of ultra-compact integrated devices and circuits [7]. However, - in contrast to SOI – the excellent electro-optic, acousto-optic and nonlinear optical properties of LN can be exploited. Moreover, also LNOI can be doped with rare-earth ions to get a laser active material.

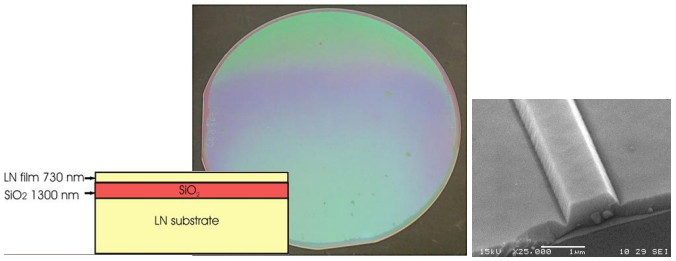


Figure 4. Schematic cross-section (left) and photograph (middle) of a LNOI-wafer of 3`` diameter. Right: SEM micrograph of a LNOI "photonic wire" of 1 µm top width and 730 nm thickness [7].

VI. CONCLUSIONS

Status and prospects of LN integrated optics have been reviewed emphasizing the most promising fields and applications. Though impressive results have been achieved, there are still a large number of laser-active ions with numerous electronic transitions to be investigated as amplifiers, lasers and even quantum memories in LN waveguides. The enormous wavelength flexibility of nonlinear wavelength converters will enable additional attractive applications. And the field of integrated quantum optics just started to grow at an enormous rate. It might be that LNOI serves as an attractive platform to develop nanophotonic devices and to combine them in integrated circuits for a large bunch of applications.

REFERENCES

[1] W. Sohler, B. K. Das, D. Dey, S. Reza, H. Suche, and R. Ricken, "Erbium doped lithium niobate waveguide laser", IEICE Trans. Electron. E, vol.88–C, No..5, pp.990-998, 2005.

[2] E.g.: E. Cantelar, J. A. Sanz-Garcia, G. Lifante, F. Cusso, and P. L. Pernas, " Single polarized Tm^{3+} laser in Zn-diffused $LiNbO_3$ channel waveguides", Appl. Phys. Lett., vol 86, pp.161119-161121, 2005.

[3] M. George, R. Ricken, V. Quiring, and W. Sohler, "In-band pumped low threshold Ti:Tm:$LiNbO_3$ waveguide laser", submitted to ECIO`2012.

[4] K.-D. Büchter, H. Herrmann, C. Langrock, M.M. Fejer, and W. Sohler: "All-optical Ti:PPLN wavelength conversion modules for free-space optical transmission links in the mid-infrared", Optics Letters, vol. 34, no. 4, 470- 472 (2009).

[5] S. Tanzilli, A. Martin, F. Kaiser, M.P. De Micheli, O. Alibart, and D.B. Ostrowsky, "On the genesis and evolution of Integrated Quantum Optics", Laser & Photonics Reviews, vol. 6, no 1, pp. 115–143 (2012)

[6] E. Saglamyurek, N. Sinclair, J. Jin, J. A. Slater, D. Oblak, F. Bussières, M. George, R. Ricken, W. Sohler, and W. Tittel, "Broadband waveguide quantum memory for entangled photons", Nature, vol. 469, pp. 512-515, 2011.

[7] G. Poberaj, H. Hu, W. Sohler and P. Günter, „Lithium niobate on insulator (LNOI) for micro-photonic devices", Laser & Photonics Reviews. doi: 10.1002/lpor.201100035 (published online 2012)

Graphene Photonics and Optoelectronics

Andrea C. Ferrari
University of Cambridge, Engineering Department, Cambridge CB3 OFA, UK

The richness of optical and electronic properties of graphene attracts enormous interest. So far, the main focus has been on fundamental physics and electronic devices. However, it has also great potential in photonics and optoelectronics, where the combination of its unique optical and electronic properties can be fully exploited, the absence of a bandgap can be beneficial, and the linear dispersion of the Dirac electrons enables ultra-wide-band tunability[1]. The rise of graphene in photonics and optoelectronics is shown by several recent results, ranging from solar cells and light emitting devices, to touch screens, photodetectors and ultrafast lasers [1]. Despite being a single atom thick, graphene can be optically visualized [2]. Its transmittance can be expressed in terms of the fine structure constant [3]. The linear dispersion of the Dirac electrons enables broadband applications. Saturable absorption is observed as a consequence of Pauli blocking [4,5]. Chemical and physical treatments enable luminescence [1,6]. Graphene-polymer composites prepared using wet chemistry [4-6] can be integrated in a fiber laser cavity, to generate ultrafast pulses, and enable broadband tunability [4,5]. Graphene's suitability for high-speed photodetection was demonstrated in an optical communication link operating at 10 Gbit s^{-1} [7]. However, the low responsivity of graphene-based photodetectors compared with traditional III-V-based ones is a potential drawback. By combining graphene with plasmonic nanostructures, the efficiency of graphene-based photodetectors can be increased by up to 20 times, because of efficient field concentration in the area of a p-n junction [8]. Additionally, wavelength and polarization selectivity can be achieved by employing nanostructures of different geometries [8]. Light-graphene interaction can be tailored by using microcavities [9]. Photodetection of far-infrared radiation (from hundreds of GHz to a few THz) is important for a variety of potential applications, ranging from medical diagnostics to process control, and homeland security. THz radiation penetrates numerous commonly used dielectric materials, otherwise opaque for visible and mid-IR light. At the same time, it allows spectroscopic identification of hazardous substances and compounds, through their characteristic molecular fingerprints. In this spectral region, due to the unavoidable doping, Pauli blocking does not allow detection exploiting the common photon-induced creation of charge carriers. Efficient THz detection in grapheme can be achieved exploiting the oscillating fields in a graphene field effect transistor [10]. This enables high-sensitivity, room temperature, large-area operation, not limited to a specific region of the THz range [10].

1. F. Bonaccorso et al. Nat. Photon. 4, 611 (2010)
2. C. Casiraghi et al. Nano Lett. 7, 2711 (2007).
3. R. R. Nair et al. Science 320, 1308 (2008).
4. T. Hasan, et al. Adv. Mat. 21,3874 (2009)
5. Z. Sun et al. ACS Nano 4, 803 (2010); Nano Research 3, 653 (2010)
6. T. Gokus et al. ACS Nano 3, 3963 (2009)
7. T. Mueller et al. Nat. Photon. 4, 297 (2010)
8. T.J. Echtermeyer et al. Nat. Commun. 2, 458 (2011)
9. M. Engel et al. arXiv:1112.1380 (2011)
10. L. Vicarelli et al. arXiv:1203.3232v1 (2012)

Carbon nanotube and graphene photonics for ultrafast pulse generation and signal processing

Shinji Yamashita
Department of Electrical Engineering and Information Systems, Graduate School of Engineering
The University of Tokyo
Tokyo, Japan

***Abstract*—We review the nonlinear photonic properties, saturable absorption and third-order nonlinearity, of one and two dimentional forms of nano-carbon, Carbon nanotube (CNT) and graphene, and their applications to mode-locked lasers and nonlinear functional devices.**

Optical pulsed fiber lasers offer a broad-range of applications in various fields, such as optical communications, optical signal processing, fiber sensings, laser surgery etc. Passively mode-locked fiber lasers can generate transform-limited optical very short pulses by introducing a saturable absorber (SA) in the laser cavity. We are developing new types of passively mode-locked fiber lasers for telecom and sensing applications, using carbon nanotube (CNT) or graphene as a SA. We are also investigating the nonlinear functional devices using them. Here we review our recent progress of these mode-locked fiber lasers and nonlinear functional devices [1].

Graphene and semiconducting CNTs absorb photons corresponding to their band structure. This absorption is exicitonic and saturable, and its recovery time is inherently fast, <1ps, which is fit for the laser mode locker for fs-pulse generation [1][2]. Typical saturable absorption (SA) fluence is comparable to that of conventional semiconductor-based saturable absorber (SESAM). It has been known that they also have high third-order nonlinearity (n_2~2×10^{-12} m^2/W). We usually use the thin (~1μm) layer of CNTs on substrates or optical fiber ends as a SA, either by the spray, the CVD, or the optical deposition method [3]. The CNT thin film is normally placed perpendicular to the light path. For the high power applications, however, we have a problem of optical damage. We proposed a new configuration based on the evanescent field interaction of the propagating light with CNTs using overcladding-less waveguide, D-shaped fiber, and so on [1].

We have applied the CNT-based SA in many kinds of passively mode-locked fiber lasers. CNT-based SA can operate in transmission, reflection, and even bi-directional modes. Therefore, it is applicable to any laser configurations, such as a ring- and a linear-cavity lasers. We have demonstrated that these lasers can easily generate high-quality nearly transform-limited pulses with pulsewidths as short as a few hundred femtosecond, regardless of the laser configurations [1]. Compared with other SAs, CNT-based SA is small, low-loss, and compatible to fibers. Thus we can apply it to mode lock very short cavity fiber lasers to generate very stable pulse trains at high repetition rate. By using high-gain Er:Yb fiber together with high finesse fiber cavity and CNT-based SA, we have succeeded in generating pulses at 5GHz repetition rate from a 2cm-long fiber laser [4]. We made a further improvement recently to achieve up to 20GHz repetition rate from down to 5mm-long fiber lasers, and also demonstrated in supercontinuum (SC) generation spanning from 1.4μm to 1.7μm in highly nonlinear fiber (HNLF) using the 10GHz fiber laser as a seed source [5]. We also realized a high-power mode-locked fiber laser by using CNT-coated D-shape fiber as the SA. We achieved the average power as high as 250mW and the pulse energy as high as 6.5 nJ with the repetition rate of 38.9 MHz [6].

Graphene is more attractive than CNT because of its wavelength independence. We demonstrated that the optical deposition is also possible and that the mode locking properties are quite similar to the CNT-based one [7]. We also realized short-cavity (1cm) high-repetition-rate (10GHz) graphene-based mode-locked fiber laser [8].

As for the nonlinear functional devices, we succeeded in wavelength conversion of 10Gb/s NRZ signal through nonlinear polarization rotation (NPR) [9] and four-wave mixing (FWM) [10] in the CNT-coated D-shaped fiber.

REFERENCES

[1] S. Yamashita, "A tutorial on nonlinear photonic applications of Carbon nanotube and graphene (Invited tutorial)," Journal of Lightwave Technology, vol. 30, no. 4, pp.427-447, Feb. 2012.

[2] S. Y. Set, et al., Journal of Lightwave Technology, vol. 22, no. 1, pp.51-56, Jan. 2004.

[3] K. Kashiwagi and S. Yamashita, Japanese Journal of Applied Physics, vol. 46, no. 40, pp.L988-L990, Oct. 2007.

[4] S. Yamashita, et al., Photonics Technology Letters, vol.17, no.4, pp.750-752, Apr. 2005.

[5] A. Martinez, and S. Yamashita, Optics Express, vol.19, no.7, pp.6156-6163, Mar. 2011.

[6] Y. W. Song, S. Yamashita, and S. Maruyama, Applied Physics Letters, vol.92, no.2, pp.021115-1-3, Jan. 2008.

[7] A. Martinez, K. Fuse, B. Xu and S. Yamashita, Optics Express, vol.18, no.22, pp.23054-23061, Oct. 2010.

[8] A. Martinez, and S. Yamashita, in Proceedings of Conference on Lasers and Electro-Optics (CLEO) 2011, no.CMBB4, May 2011.

[9] K. K. Chow, S. Yamashita, and Y. W. Song, Optics Express, vol.17, no.9, pp.7664-7669, Apr. 2009.

[10] K. K. Chow and S. Yamashita, Optics Express, vol.17, no.18, pp.15608-15613, Aug. 2009

Photonic Crystals: an unprecedented nanoscale enabler of light.

Dr. Pierre Viktorovitch
Institut des Nanotechnologies de Lyon (INL)
CNRS-Ecole Centrale de Lyon, France

Extended abstract

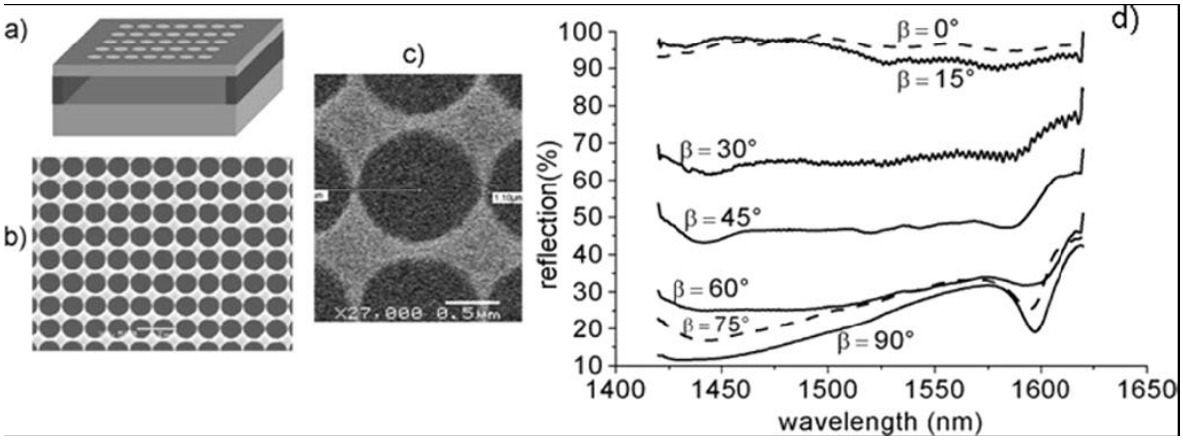
Inside the wide family of periodic photonic structures, dielectric photonic crystals have played a fast growing part during the last 25 years, their specificity inherently lying in the high index contrast of the periodic modulation (generally more than 200%) introduced in the optical medium. The concept of three dimensional photonic crystal (3D PhC) was simultaneously introduced by S. John [1] and E. Yablonovitch [2]: it is currently considered as a must for 3D spatial and temporal confinement of the light. In practice the fabrication of 3D PhCs is very difficult, and most of the developments have concerned the production of 1D and 2D PhCs formed in wave-guiding dielectric slabs. These high-index-contrast periodic structures can indeed be fabricated using planar technological approaches that are familiar to the world of integrated optics and microelectronics. They consist practically in 1D or 2D structuring of a planar dielectric/semiconductor membrane waveguide, where photons are "index guided", that is to say vertically confined by the profile of the optical index. In most of the reported works, 1D-2D PhCs are meant to operate solely in the 2D wave-guiding configuration and, hence, are limited to a 2D control of photon trajectory: in this context, they have been the matter of an innumerable number of reports, publications, conferences and tutorials. In the present tutorial, we will not therefore contribute further to this abundant literature and will not talk about 2D PhCs operation, where control of light is restricted to the sole in plane wave-guiding configuration. We will instead concentrate on more recent developments where use is made of 1D-2D PhC membranes for efficient 3D harnessing of light, along a variety of configurations including both in plane wave-guided and free space radiated regimes.

The history of 1D-2D periodic photonic structures has started with the original discovery of diffraction gratings by James Gregory, a Scottish mathematician and astronomer, by passing sunlight through a bird feather and observing the diffraction pattern produced [3]. Since then, they have been the matter of considerable developments, namely for the manipulation of light in free space with angular and wavelength resolution. The seminal publication of Wood in 1902 [4], where the author reports on the observation of strong intensity variations (so called Wood anomalies) in the spectrum of an optical beam diffracted by a diffraction grating, has triggered the production of considerable amount of investigations throughout the 20th century, beginning with the theoretical treatment proposed by Rayleigh in 1907 [5], inspired by the genius intuition that propagating diffraction order can be converted into an evanescent diffraction order and vice versa. In the nineteen sixties, the emergence of rigorous theories of the diffraction and enough powerful computation tools allowed for the accurate description of Wood anomalies. In 1965, Hessel and Onliner introduce the concept of resonance anomalies, associated with the excitation of surface waves or guided waves, depending upon the structure considered [6]. Surface waves, which will be called, later on in the 20th century, surface plasmons, are observed in metallic gratings; the guided waves are observed in dielectric gratings and will be referred to as guided-mode resonances (GMRs). These authors share the common idea with Rayleigh that, when Wood anomalies are present, the photons experience successive modal conditions, where they propagate (or radiate) in free space and where they are wave-guided within the grating structures, that is to say evanescent in free space at least during the time spent within the gratings. The first experimental demonstration of guided

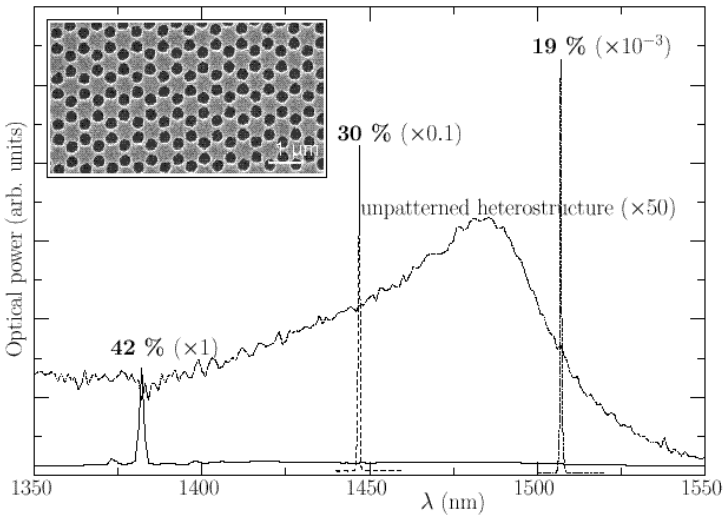
mode resonances in dielectric gratings was reported by Mashev and Popov [7]. The first practical applications based on these resonant periodic structures, proposed by Magnusson *et al.* [8], [9] (tunable filters, polarization resolved reflectors…), have stimulated number of works, made possible by the relentless progress of lithographic and etching techniques.
The observation and analysis of Wood anomalies (or GMRs) have also been reported in 1D and 2D dimension PhC membrane structures [10], the general applied concepts being essentially the same as those used in a conventional dielectric grating. As analysed in detail for the first time by X. Letartre *et al.* in [11], one specific added value of the high index contrast typical of PhC structures, within the general context of resonant gratings, lies in the capability of PhC membrane waveguides to provide an efficient lateral confinement of photons during their wave-guided stage. In particular, if the wave-guided resonances operate around a high symmetry point (e.g., the so-called Γ-point of the first Brillouin zone), where the dispersion characteristics are very flat, the light is efficiently slowed down. This specificity offers the possibility to design and produce very compact surface-addressable devices, endowed with comfortable angular aperture, while retaining excellent characteristics such as, for instance, a high reflectivity yield.

The physical principles of surface-addressable resonant PhC membrane structures will be presented in detail: they build on the numerous works published since the seminal publication of Wood and are based on the resonant coupling of incoming optical beam (radiated mode) with wave-guided Bloch modes in the PC membrane, which may occur whenever wavelength and *k*-vector matching conditions are met. The essential driving forces and controlling parameters will be described and routes for simple design rules, resulting in the production of structures endowed with the desired characteristics in the space-time domain will be given.

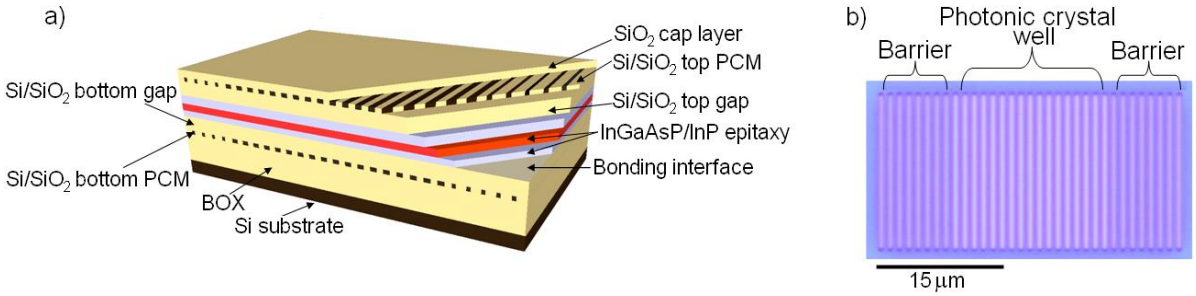
Exemplifying use of surface-addressable resonant PhC membrane structures in a variety of devices will be presented [12]: this will include large bandwidth compact reflectors [13, 14], narrow bandwidth single PhC membrane active resonators for laser emission [15], optical amplification and bi-stability [16], new family of VCSEL devices [17-19], including CMOS-compatible ultra-compact 1.55-µm emitting VCSELs using double photonic crystal mirrors [20, 21]. A few illustrations of these devices are shown below.



(a) Schematic representation of broadband and compact 2-D Photonic Crystal reflector. (b) SEM general view. (c) SEM close-up view of one cell of the lattice. (d) Experimental reflectivity spectra of the square lattice with elliptical holes, for various angles of polarization of the incident wave (see [14]).



Low threshold, room temperature vertical emitting laser based on an InP two-dimensional photonic crystal membrane (graphite lattice): laser emission spectra for various air hole filling factors. A SEM top view of the structures is shown in the inset (see [15]).



CMOS-compatible VCSELs using double photonic crystal mirrors: schematic view (a) and top SEM view (b) (see [21])

Acknowledgements

The research leading to these results has been funded in part by the French National Research Agency (ANR project HEVICAL) and by the European Community's Seventh Framework Programme (FP7/2007-2013) under grant agreement n° 224312 HELIOS. Achievements reported in this tutorial have been made possible by a tight cooperative work between CEA-LETI and INL-CNRS / Ecole Centrale de Lyon.

References

[1] S. John, "Strong localization of photons in certain disordered dielectric superlattices" *Phys. Rev. Lett.*, vol. 58, pp. 2486-2489, 1987.

[2] E. Yablonovitch, "Inhibited Spontaneous Emission in Solid-State Physics and Electronics" *Phys. Rev. Lett.*, vol. 58, pp. 2059-2062, 1987.

[3] Letter from James Gregory to John Collins, dated 13 May 1673. Reprinted in: "*Correspondence of Scientific Men of the Seventeenth Century....*," ed. Stephen Jordan Rigaud, vol. 2, pp. 251–255, Oxford, England, Oxford University Press, 1841. See especially page 254. Available online at: Books.Google.com

[4] R. W. Wood, "On a remarkable case of uneven distribution of light in a diffraction grating spectrum," *Philos. Mag.*, vol. 4, pp. 396-402, 1902.

[5] Lord Rayleigh, "Note on the remarkable case of diffraction spectra described by Prof. Wood," *Philos. Mag.*, vol. 14, pp. 60–65, 1907.
[6] A. Hessel and A. A. Onliner, "A new theory of Wood's anomalies on optical gratings," *Appl. Opt.*, vol. 10, pp. 1275-1297 (1965).
[7] L. Mashev and E. Popov, "Diffraction efficiency anomalies of multicoated dielectric gratings," *Opt. Commun.*, vol. 51, pp. 131-136, 1984.
[8] S. S. Wang, R. Magnusson, J. S. Bagby, and M. G. Moharam, "Guided-mode resonance in planar dielectric-layer diffraction gratings," *J. Opt. Soc. Am. A*, vol. 7, pp. 1470-1474, 1990.
[9] R. Magnusson and S. S.Wang, "New principle for optical filters," *Appl. Phys. Lett.*, vol. 61, pp. 1022-1024, 1992.
[10] See for example : V. N. Astratov *et al.*, "Resonant coupling of near- infrared radiation to photonic band structure waveguides," *J. of Lightw. Technol.*, vol. 17, pp. 2050-2057, 1999.
[11] X. Letartre, J. Mouette, C. Seassal, P. Rojo-Romeo, J.-L. Leclercq, and P. Viktorovitch, "Switching devices with spatial and spectral resolution combining photonic crystal and MOEMS structures," *J. of Lightw. Technol.*, vol. 21, pp. 1691, 2003.
[12] See also the review paper: P. Viktorovitch, B. Ben Bakir, S. Boutami, J.-L. Leclercq, X. Letartre, P. Rojo-Romeo, C. Seassal, M. Zussy, L. Di Cioccio, and J.-M. Fedeli, "3D harnessing of light with 2.5D photonic crystals," *Laser & Photon. Rev.*, vol. 4, no. 3, pp. 401–413, 2010.
[13] C. F. R. Mateus, M. C. Y. Huang, Y. Deng, A. R. Neureuther, and C. J. Chang-Hasnain, "Ultra-broadband mirror using low index cladded subwavelength grating," *IEEE Photon. Technol. Lett.*, vol. 16**,** no**.** 2, pp. 518–520, 2004.
[14] S. Boutami, B. B. Bakir, H. Hattori, X. Letartre, J.-L. Leclercq, P. Rojo-Romeo, M. Garrigues, C. Seassal, and P. Viktorovitch, "Broadband and compact 2-D photonic crystal reflectors with controllable polarization dependence," *IEEE Photon. Technol. Lett.*, vol. 18, pp. 835-838, 2006.
[15] J. Mouette, C. Seassal, X. Letartre, P. Rojo-Romeo, J.-L. Leclercq, P. Regreny, P. Viktorovitch, E. Jalaguier, P. Perreau, H. Moriceau, "Low threshold, room temperature vertical emitting laser based on an InP two-dimensional photonic crystal," *Electron. Lett.*, vol. 39, pp. 526, 2003.
[16] C. Cojocaru, F. Raineri, P. Monnier, C. Seassal, X. Letartre, P. Viktorovitch, A. Levenson, R. Raj, "Ultrafast dynamics of the third-order nonlinear response in a two-dimensional InP-based photonic crystal," *Appl. Phys. Lett.*, vol. 85, pp. 1880, 2004.
[17] H. T. Hattori, X. Letartre, C. Seassal, P. Rojo-Romeo, J.- L. Leclercq, and P. Viktorovitch, "Analysis of hybrid photonic crystal vertical cavity surface emitting lasers" *Opt. Express* vol. 11, 1799, 2003.
[18] M. C. Y. Huang, Y. Zhou, and C. J. Chang-Hasnain, "A surface-emitting laser incorporating a high-index-contrast subwavelength grating," *Nat. Photonics*, vol. 1, pp. 119–122, 2007.
[19] S. Boutami, B. Ben Bakir, J.-L. Leclercq, and P. Viktorovitch, "Compact 1.55-μm room-temperature optically pumped VCSEL using photonic crystal mirror," *Electron. Lett.*, vol. 43, pp. 282–283, 2007.
[20] C. Sciancalepore *et al.*, "Quasi-3D light confinement in double photonic crystal reflectors VCSELs for CMOS-compatible integration," *IEEE J. of Lightw. Technol.*, vol. 29, no. 13, pp. 2015–2024, Jul. 2011.
[21] C. Sciancalepore, B. Ben Bakir, X.Letartre, J. Harduin, N. Olivier, C. Seassal, J.-M. Fedeli, and P.Viktorovitch, "CMOS-compatible ultra-compact 1.55-μm emitting VCSELs using double photonic crystal mirrors," *IEEE Photon. Technol. Lett. (in press).*

Colloidal Quantum Dot Photodetectors

Gerasimos Konstantatos
ICFO-Institut de Ciencies Fotoniques, Mediterranean Technology Park, 08860 Castelldefels, Barcelona, Spain

Abstract. We review recent progress in light sensors based on solution-processed quantum dots. We focus on visible-, near-infrared, and short-wavelength infrared photodetectors based on quantum-confined PbS nanocrystals. These devices have shown room-temperature D* values above 10^{13} Jones, while fully-depleted photodiodes based on these same materials have achieved MHz response combined with 10^{12} Jones D*.

Keywords: Photodetectors, colloidal quantum dots, photoconductive gain, photodiodes, solution-processed

I. Introduction

Materials that absorb light more effectively than silicon or where silicon does not are of great interest in photodetection and imaging. Strategies include top-surface detectors having 100% fill factor; and means of signal amplification within the photodetector itself, utilizing photoconductive gain [1].

These considerations motivate intense research activity in new materials and structures that expand the spectrum of absorption; minimize the thickness of semiconductor needed to absorb light completely; and amplify signal. Ideally, these materials should be integrable with silicon electronics or with flexible substrates, utilizing ink-jet printing, solution-casting, low-temperature evaporation, and layer-by-layer techniques which are very attractive alternatives to high-temperature epitaxial growth.

Here we discuss recent advances in light sensing, with materials compatible with low-temperature processing and large-area integration. We focus on colloidal quantum dots (CQDs)[2] in which nanoscale phenomena such as quantum confinement[3] play a major role in the optical and electronic properties of the semiconductor. Colloidal quantum dots are nanostructured materials synthesized and processed from solution phase which offer bandgap tunability through the quantum size effect. Rapid advances in colloidal quantum dot synthesis and photophysics have led to a high degree of control over nanoparticle size, shape, and composition [2]. We focus on two different types of photodetector (photodiodes and photoconductors); and discuss the device concepts, materials and physical phenomena that have underpinned these improvements in performance.

II. Photodiodes and Photoconductors

In a photodiode the electrons and holes generated by the incoming photons move to opposite electrical contacts, so the quantum efficiency of such devices cannot exceed unity. However, photodiodes can have fast response times determined by the transit time of the photogenerated carriers, and can be less than electron-hole recombination time, which are typically microseconds or less for the direct-gap semiconductors commonly used.

Photoconductors, on the other hand, are capable of high gain [4] because one type of charge carrier (say holes) is able to circulate through an external circuit many times before it recombines with its opposite carrier (say electrons), which remain trapped in the photoconductor bulk in the meantime. CQD photoconductors with responsivities in the range of 100 – 1000 A/W, corresponding to gains of 100 to 1000 have thus been reported [5, 6]. While these high gains increase responsivity and simplify the read-out circuits, they also reduce the bandwidth because of the long circulating carrier lifetimes involved.

The performance of a photodetector can be improved, not only by maximizing its electrical response to light, but also by minimizing the noise in its electrical output, which can obscure real signals. One can thus examine the noise-equivalent power (NEP), which reports the optical power at which the signal to noise ratio (SNR) is 1 (or 0 dB). The normalized detectivity D^* - equal to $(A_dB)^{1/2}R/i_n$ *(expressed in cm* $Hz^{1/2}/W$ *or Jones)* where A_d is the detector's active area, B is the noise measurement bandwidth, R the responsivity, and i_n the noise current - is a figure of merit that seeks to normalize for variations in device geometry and sampling conditions, thus providing a metric that enables comparison among different devices. The best solution-processed detectors have achieved D* values of up to $5x10^{13}$, which is comparable with the best values reported for single-crystal photodiodes.

III. Photodiode mechanisms and performance

Photodiodes rely on the use of two media - at least one of them a semiconductor - in which a significant difference in the materials' work functions produces a built-in potential. An internal field in the semiconductor depletion region near the junction propels electrons and holes in opposite directions. In the simple case of a fully-depleted device, high internal quantum efficiency is achieved if $t_{life} > t_{extract}$, where t_{life} is the lifetime of excess charge carriers, and $t_{extract} = L^2/\mu V_{bi}$ is the time taken to transport them to their respective contacts via the built-in field. In addition, L is the contact separation, μ is the mobility of the slower carrier, and V_{bi} is the built-in potential across the junction[36].

Solution-processed semiconductors exhibit carrier mobility in the range 10^{-5} – 10^{-3} cm^2/Vs and thus, even for a thin depletion region 100 nm thick and a typical built-in voltage of 1 V, drift times are in the range 100 ns – 10 us. Fortunately, some of the most promising semiconductors incorporated into colloidal quantum dots used in solution-processed photodetector realization have unusually long exciton lifetimes – greater than 1 microsecond [7] – that have led to excellent photodiode

quantum efficiencies, with even the first reports well above 50%. The high internal quantum efficiencies these findings entail also indicate that – when their surfaces are well-passivated using suitably-functionalized ligands – colloidal quantum dot solids achieve carrier lifetimes comparable to their exciton lifetimes: thus, well-passivated colloidal quantum dots incorporated into densely-packed solid-state films do not suffer from an excess of nonradiative recombination such as that assisted by midgap recombination centers [8]. Since the absorbance of many materials is in the 10^4-10^5 cm^{-1} range near the absorption onset, only reaching 10^6 cm^{-1} far above the bandgap, it is of interest to make devices that include light-absorption moieties as thick as micrometers. Typically, doping control in colloidal quantum dot solids has led to devices that are fully-depleted only if their thicknesses are 100-200 nm[9]. A majority of micrometer-thick devices will in this case be far from fully-depleted, demanding efficient transport through a quasi-neutral layer. In certain colloidal quantum dots solids, minority diffusion lengths in excess of 100 nm, and reaching as high as 200 nm, have been reported [7, 9] owing to the use of very short organic bidentate linker molecules. Minority electron mobilities of 10^{-3} cm^2/Vs combined with an absence of midgap traps thus extended diffusion lengths into to these very attractive lengthscales for solution-cast direct-gap optoelectronic materials.

A CQD PbS Schottky photodiode was reported in 2009 with excellent sensitivity out to 1.6 um ($D^* = 10^{12}$ Jones) and high bandwidth in the MHz range [9]. High sensitivity was achieved via the joint optimization of electron and hole transport, leading to high quantum efficiencies, as well as control over film morphology and defect passivation, which maximized the shunt resistance and minimized dark current. The MHz temporal response was achieved through the realization of a fully-depleted device, and this bandwidth further confirms that carriers are extracted via drift in these devices on the sub-microsecond timescale.

IV. Photoconductor mechanisms and performance

Photoconductors, unlike photodiodes, rely on a unipolar mode of conduction and the conductance increases upon illumination. The increased conductance state is determined by the carrier lifetime and thus if the lifetime exceeds the transit time of the flowing carrier through the device, many charges worth of current may be integrated for each photon absorbed. A leverage to control the carrier lifetime and thereby the gain is provided by the trap states. These traps serve both to delay band-to-band recombination, and also to impede the extraction of the trapped carrier, a condition necessary to photoconductive gain.

The first solution-cast optoelectronic device to outperform its epitaxial counterparts was a photoconductive photodetector reported in 2006 [5]. A key insight leading to this advance was the realization that excess noise could accumulate along the transport path if the interfaces between the nanoparticles making up the semiconductor film were randomly time-varying due to trapping and de-trapping effects from thermally- or optically-generated carriers [10]. This multiplicative noise, also known as transport noise, was obviated through a processing strategy wherein pure (trap-free) colloidal quantum dot films were first realized; and only once the electrical connections between adjacent nanoparticles were forged were the remaining exposed surfaces of the nanoparticles decorated with sensitizing centers.

Many advances in solution-cast photoconductor performance have since been reported. For example, PbS nanoparticles with a diameter of less than 3 nm can have a bandgap that is three times that of bulk PbS, and the resulting strong quantum confinement can be exploited to achieve high-detectivity visible-wavelength light sensing[6]. The quantum size effect affords wide spectral tunability within a single materials system and processing architecture, enabling multispectral detectors that monolithically integrate pixels sensitive in the visible, near infrared, and short-wavelength infrared.

Building on a long history of studies of bulk PbS photoconduction[1], recent reports have elucidated the chemical origins of traps having different energies, and different lifetimes, as a function of chemical species and nanoparticle size and preparation. This enabled the implementation of a single trap state lifetime and video-frame-rate-compatible photoconductor behavior[11].

V. Conclusions

Solution-processed light sensors offer a wide suite of advantages in imaging and photodetection. The convenient integration of light sensing materials with a variety of substrates enables separate optimization of each function: silicon electronics, ideally suited to volume manufacture, low-noise read-out, and a comprehensive array of analog and digital functions, can be augmented with a 100%-fill-factor, spectrally-tunable, optically dense, low-crosstalk light sensing layer customized for efficient conversion from the optical to the electronic domain. Ever-growing dexterity in manipulating materials at the nanoscale - the engineering matter on the quantum and plasmonic lengthscales - provides for an unheralded degree of customization and optimization in coming generations of light sensing arrays.

REFERENCES

[1] L. Sosnowski, *et al.*, "Lead sulphide photoconductive cells," *Nature* 159 (1947) 818-819.

[2] C. B. Murray, *et al.*, "Synthesis and characterization of nearly monodisperse CdE (E = S, Se, Te) semiconductor nanocrystallites," *Journal of the American Chemical Society* 115 (1993) 8706-8715.

[3] L. Brus, "Electronic wave functions in semiconductor clusters: Experiment and theory," *Journal of Physical Chemistry* 90 (1986) 2555-2560.

[4] R. L. Petritz, "Theory of photoconductivity in semiconductor films," *Physical Review* 104 (1956) 1508-1516.

[5] G. Konstantatos, *et al.*, "Ultrasensitive solution-cast quantum dot photodetectors," *Nature* 442 (2006) 180-183.

[6] G. Konstantatos, *et al.*, "Sensitive solution-processed visible-wavelength photodetectors," *Nature Photonics* 1 (2007) 531-534.

[7] K. W. Johnston, *et al.*, "Efficient Schottky-quantum-dot photovoltaics: The roles of depletion, drift, and diffusion," *Applied Physics Letters* 92 (2008) 122111-3.

[8] D. A. R. Barkhouse, *et al.*, "Thiols passivate recombination centers in colloidal quantum dots leading to enhanced photovoltaic device efficiency," *ACS Nano* 2 (2008) 2356-2362.

[9] J. P. Clifford, *et al.*, "Fast, sensitive and spectrally tuneable colloidal-quantum-dot photodetectors," *Nature Nanotechnology* 4 (2009) 40-44.

[10] A. Carbone, P. MAzzetti, " Grain-boundary effects on photocurrent fluctuations in polycrystalline photoconductors. *Physical Review B* 57 (1998) 2454–2460.

[11] G. Konstantatos, *et al.*, "Engineering the temporal response of photoconductive photodetectors via selective introduction of surface trap states," *Nano Letters* 8 (2008) 1446-1450.

Photonic Lab on a Chip. Prospectives for Multiparametric Real-Time Cell Screening

Xavier Muñoz-Berbel
Centre Nacional de Microelectrònica (IMB-CNM, CSIC)
Campus UAB 08193 Bellaterra, Barcelona, SPAIN

Rosalía Rodriguez-Rodríguez
School of Pharmacy, Department of Pharmacology,
Universidad de Sevilla, Sevilla, SPAIN

Bergoi Ibarlucea
Centre Nacional de Microelectrònica (IMB-CNM, CSIC)
Campus UAB 08193 Bellaterra, Barcelona, SPAIN

Jordi Vila-Planas
Centre Nacional de Microelectrònica (IMB-CNM, CSIC)
Campus UAB 08193 Bellaterra, Barcelona, SPAIN

Stefanie Demming
Institut für Mikrotechnik, Technische Universität
Braunschweig, 38124 Braunschweig, GERMANY.

Stephanus Büttgenbach
Institut für Mikrotechnik, Technische Universität
Braunschweig, 38124 Braunschweig, GERMANY.

Andreu Llobera
Centre Nacional de Microelectrònica (IMB-CNM, CSIC)
Campus UAB 08193 Bellaterra, Barcelona, SPAIN
Andreu.llobera@imb-cnm.csic.es

***Abstract*—A Photonic Lab on a Chip (PhLoC) based on Poly(dimethylsiloxane) (PDMS) suitable to be used for multiparametric screening is presented. By recursive positioning of air mirrors at both sides of the system, light propagates via multiple internal reflection. In addition to its high level of integration, the system here presented only requires a single photolithographic step and the fabrication is based on low cost materials. Experimental results have shown that the proposed PhLoC is able to perform real time scattering or scattering+absorption measurements without any change in its configuration. Stained and non-stained monocytic cells were analyzing using a broadband light source. Limit of detection (LOD) of 54.9±0.7 cells (in scattering regime using unlabelled cells), 53±1 cells (in scattering+ absorption regime using labeled cells) were obtained. Finally, the system has also been used for measuring the dead/live cell ratio, obtaining a LOD of 7.6±0.4%.**

Keywords-component; Photonic lab on a chip, biophotonics, cell screening

I. INTRODUCTION

Photonics has emerged as a unique, extremely powerful technology for contactless real-time analysis in the life sciences and medicine. Using light as an interrogation mechanism in life sciences has major advantages, such as high-sensitive non-invasive analysis. Biophotonics is powerful and mature enough to provide the next generation of diagnosis and prognosis tools. In this context, technology mergers, such as the combination of microfluidics and photonics (obtaining the so-called photonic lab-on-a-chip), will be required to enable the real time measurement of relevant analytes in very small sample volumes. A first step towards spectroscopy on a chip was taken with the lens-less, ultra wide field cell monitoring array platform based on shadow imaging (LUCAS) [1]. Nevertheless, such platform has severe drawbacks for diagnosis, since it cannot perform multi-wavelength measurements (as could be the case of fluorescent labeling) and is not suitable for studies of cell growth or culture. Hence, the use of the LUCAS configuration is restricted to cell counting.

Nowadays, the first steps towards developing photonic lab-on-a-chip have been given. Such systems take advantage of the optical properties of the materials used to define micro-optical components inside or in the vicinity of the interrogation region [2,3]. When related to cell screening, however, it must be taken into account that a full understanding of the inherent process undoubtedly requires both an advanced architecture and protocol, since cells may undergo simultaneous events when affected by a disease. This issue is the current trend where most of the effort is currently being applied. In this context, the optimal configuration would a biophotonic system either able to work in different regimes depending on the cell culture under study or suitable to perform white light spectroscopy on a chip.

In this work, a photonic lab-on-a-chip able to work in two working regimes: LS (scattering), LS+ABS (scattering+ absorption), is presented. The acquisition protocol only requires a single measurement of 30 ms so as to record the spectral response of the cell culture placed at the interrogation region. If the cells are unlabelled or do not have absorption bands in the wavelength range under study, a scattering band (flat absorption band) is obtained. Conversely, when they are labeled, a superimposed absorbance band is observed. In both working regimes, the population can be determined. The applicability of the proposed system, it has been used for simultaneously determining the population of labeled and unlabeled cells, as well as the dead/live ratio.

II. Materials and Methods

Cell culture and labeling human monocytic cell line THP-1 (ECACC No.88081201) was maintained in RPMI 1640 medium (Gibco, 21875-034) with 20% fetal bovine serum (Gibco,10106-169) at 37 ºC in 5% CO2. Before each experiment, cells were rinsed twice in PBS tempered at 37ºC and kept alive in an incubator under controlled temperature and atmosphere. To obtain the dead cell population monocytes were fixed with 4% paraformaldehyde in PBS for 10 minutes. Afterwards, cells were stained with trypan blue (Gibco, 15250-061) in PBS (1:1) for 5 minutes and rinsed twice in PBS. For the dead/live ratio measurement, both populations were diluted to obtain the desired cell proportions.

The optofluidic system is presented in figure 1. It forms a complex system with a high degree of monolithic integration, since they comprise self-alignment systems for adequate positioning of fiber optics, lenses and focusing mirrors. Light propagates in the system following a zig-zag path with the help of integrated air mirrors [4]. In such conditions, the air mirrors meaningfully lengthen the optical path without increasing dramatically the overall size of the reactor. A broadband light source (Ocean Optics HL-2000, Dunedin, FL, USA) is coupled into the input multimode fiber optics with a diameter of 230 µm, which in turn is located in the self-alignment microchannels. At the end of this microchannel, a microlens corrects the numerical aperture of the fiber optics, having then parallel beams. Light enters into the interrogation region and interacts with the media that fills this region. The readout comprises an identical fiber optics, which carries the signal to a spectrometer (Ocean optics HR4000, Dunedin, Fl, USA) with a spectral resolution of 2 nm. The integration time has been fixed to 30 ms.

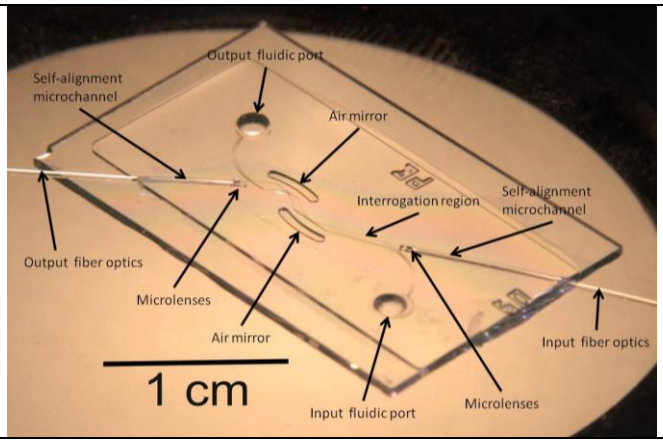


Figure 1: Picture of the PhLoC.

III. Characterization

When measuring unlabelled cells (LS regime), A plateau of maximal sensitivity is obtained at wavelengths between 580 and 700 nm, which simultaneously corresponds to an LOD minima, with values between 86 ± 1 and 54.9 ± 0.7 cells, respectively. Conversely, when using stained monocytes, the maximum sensitivity was obtained at the trypan blue absorption band (580-600 nm). At such range, a minimum LOD between 53±1 and 61±1 cells was obtained. Here, overall spectra is formed both by contributions of biomarkers and scattering.

Once the spectral response for both stained and non-stained monocytes has been achieved, the next step is the determination of the dead/live ratio.

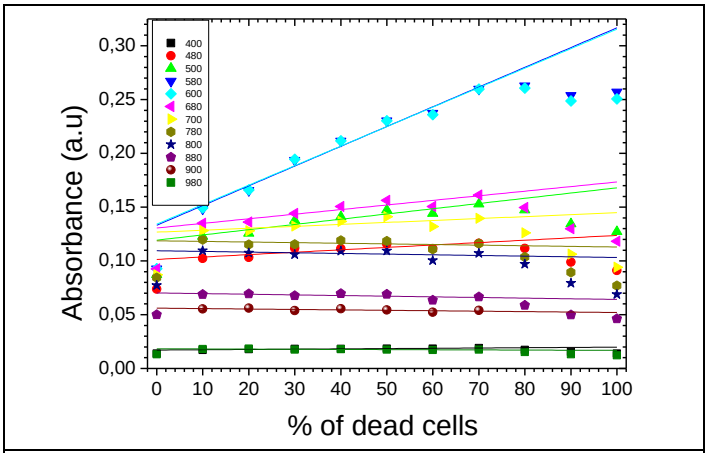


Figure 2: Absorbance vs % of dead cells using the PhLoC

To this effect, prepared samples ranging between 0% and 100% of labeled cells were measured. The spectra showed a transition from a flat scattering band (for 0% dead cells), to the conditions where the trypan absorption peak is very clearly visible (100% dead cells). The absorbance as function of % of dead cells is shown in Figure 2. The highest sensitivity corresponds to the trypan blue region (580-600 nm), with sharp decrease for both longer and shorter wavelengths. From these data, an experimental LOD of 7.6±0.4% is obtained. In other words, the PhLoC here presented has a performance comparable to the Neubauer cell counters, but only requiring 30 ms seconds for its measurements and with the possibility of multiparametric (by detecting different wavelengths) and continuous cell monitoring.

Acknowledgment (Heading 5)

The research leading to these results has received funding from the European Research Council under the European Community's Seventh Framework Programme (FP7/2007-2013) / ERC grant agreement n° 209243. And also from the Explora project TEC2010-10039-E

References

[1] Cui X., Lee L.M., Heng X., Zhong W., Sternberg P.W., Psaltis D., Yang C. *PNAS*, 2008, 105(31).10670-10675.

[2] Llobera A., Demming S., Wilke R., Büttgenbach *Lab Chip* 2007. 7. 1560 -1566.

[3] S.Balslev, A.M.Jorgensen, B.Bilenberg, K.B.Mogensen, D.Snakenborg, O.Geschke, J.P.Kutter, and A.Kristensen. *Lab Chip*. 2006. 6, 213-217.

[4] Llobera A., Wilke R., Büttgenbach S. *Talanta* 2008. 75. 473–479.

Optical Interconnects to Chips

David A. B. Miller
Ginzton Laboratory, Stanford University
348 Via Pueblo Mall
Stanford CA 94305-4088, USA
dabm@ee.stanford.edu

***Abstract*— This tutorial will introduce the requirements on reducing energy and increasing density in future interconnects beyond the capabilities of wires, and discuss resulting requirements on optical and optoelectronic devices and technologies for interconnects to chips.**

Keywords-optical interconnects; modulators; plasmonics

Power now dominates as a major constraint in information processing, and it will remain so for the foreseeable future and beyond. Already we cannot connect all the transistors and processors to one another or to memory or the outside world at the desired bandwidths without generating too much heat. This power dissipation not only constrains performance within the box; it also leads to economic and environmental limits [1]. In addition, topological and bandwidth density limitations of electrical wiring already limit longer interconnections, limitations that optics can readily remove.

Optics can in principle solve the energy problems of interconnects while also allowing higher interconnect densities, especially for longer off-chip distances [1,2]. The underlying physics is that optical interconnects only have to drive the optical transmitter devices and charge the photodetectors, not charge the capacitance of an electrical line to the signal voltage, a benefit of optics that ultimately comes from the quantum nature of light – in particular, the photoelectric effect.

The challenges with optics, however, are to come up with optoelectronic devices that themselves require low enough drive energies that they offer a practical benefit, and to generate technology that can be manufactured in large volumes at low cost. Electrical wires operate at energies of ~ 1 pJ/bit or higher for off-chip interconnects and ~ a few 100 fJ/bit to ~ 1 pJ/bit for global on-chip interconnects. To give sufficient energy benefit, therefore, total system energy of < 100 fJ/bit will be required for optical interconnects to chips, and this in turn means we will require optical output devices (lasers or modulators) that are efficient at ~ 10 fJ/bit transmitter energies, and optical receivers (photodetectors and associated circuitry) that can operate with < 1 fJ/bit of received energy. Large volume manufacture likely requires that we can exploit technologies such as silicon integrated circuit manufacture. We likely also require that the optoelectronics technology is very well integrated with electronics so that the capacitances between devices and electronic drive and receiver circuits can be kept low enough for good enough energy performance.

These energy numbers are aggressive targets for optoelectronic devices, though they are not unphysical. Various device technologies are now being explored as low-energy modulators that could be integrated with silicon manufacture in the growing field of silicon photonics, such as silicon-based modulators [3], for example. Quantum-confined Stark effect (QCSE) quantum well modulators are one possible transmitter approach that could scale to particularly low numbers, including sub-fJ operation in recent Ge devices on Si [4, 5]. Photodetectors with capacitances in the fF range are possible with tightly integrated approaches such as small Ge detectors on Si. Nanophotonic resonators and nanometallic antennas for confining light to very small subwavelength scales [6] might allow devices to operate into the aJ/bit range.

For interconnects it will also be important to make optical devices such as wavelength splitters very small. One important opportunity is to exploit nanophotonic structures for new generations of such components. For example, particularly small wavelength splitters might be possible with non-periodic superprism structures [7] or by innovative nanometallic approaches [8].

In summary, these and other approaches to novel optical and optoelectronic devices exploiting nanophotonics and quantum confinement are very promising for future applications such as optical interconnects, and such interconnects may be the key to enabling future information processing systems to continue to scale in performance.

The author acknowledges the financial support of the Interconnect Focus Center, one of six research centers funded under the Focus Center Research Program, a Semiconductor Research Corporation program.

REFERENCES

[1] D. A. B. Miller, "Device Requirements for Optical Interconnects to Silicon Chips," Proc. IEEE **97**, 1166 - 1185 (2009)

[2] D. A. B. Miller, "Optical interconnects to electronic chips," Appl. Opt. **49**, F59-F70 (2010)

[3] G. T. Reed, G. Mashonovich, F. Y. Gardes and D. J. Thomson, "Silicon optical modulators," Nature Photonics **4**, 518 – 526 (2010)

[4] S. Ren, Y. Rong, S. A. Claussen, R. K. Schaevitz, T. I. Kamins, J. S. Harris, and D. A. B. Miller, "Ge/SiGe Quantum Well Waveguide Modulator Monolithically Integrated with SOI Waveguides, IEEE Photonics Technol. Lett. **24**, 461 – 463 (2012)

[5] D. A. B. Miller, "Energy consumption in optical modulators for interconnects," submitted to Optics Express.

[6] L. Tang, S. E. Kocabas, S. Latif, A. K. Okyay, D.-S. Ly-Gagnon, K. C. Saraswat and D. A. B. Miller, "Nanometre-Scale Germanium Photodetector Enhanced by a Near-Infrared Dipole Antenna," Nature Photonics **2**, 226 – 229 (2008)

[7] M. Gerken and D. A. B. Miller "Multilayer Thin-Film Structures with High Spatial Dispersion," Applied Optics **42**, 1330 – 1345 (2003)

[8] T. Tanemura, K. C. Balram, D.-S. Ly-Gagnon, P. Wahl, J. S. White, M. L. Brongersma, and D. A. B. Miller, "Multiple-Wavelength Focusing of Surface Plasmons with a Nonperiodic Nanoslit Coupler," Nano Lett. **11**, 2693–2698 (2011)

Towards fabless photonic integration

Pascual Muñoz
Universitat Politècnica de València & VLC Photonics, S.L.
www.upv.es & www.vlcphotonics.com
c/ Camino de Vera s/n - 46021 Valencia - Spain
pmunoz@iteam.upv.es / pascual.munoz@vlcphotonics.com

***Abstract*—In this paper, the current state for generic photonic integration is reviewed from a fabless user perspective.**

I. Brief historical perspective

Generic integration for photonics is part of a vertical specialisation through the industry value chain. Restructuring results in different stages being controlled by different firms, compared to vertical integration within the boundaries of individual firms. This was the case for the US semiconductor industry, described in [1]. Large corporations as AT&T and IBM designed and manufactured both their components, and the main equipment and processes required to manufacture them in house. Specialisation in two parts of the food chain, design and manufacturing, lead to manufacture specialists and fabless design firms. For photonic integration, the seed for generic integration appears in 2007 [2], although some work by HHI early in 2000 already contains the spirit of generic photonic circuits [3]. Subsequent technical and organisational developments lead to the current generic foundry processes.

II. Current state of the art

The current state of the art for foundries offering generic photonic integration fab services is summarised in Fig. 1. *Operationally* the foundries can be described as follows. Some foundries are publicly funded research institutions (IMEC [4], CEA-LETI [4], IME [5], HHI [6], COBRA [6] and IMB-CNM [7]), whereas other are privately/publicly held companies (AMO [8], Luxtera [9], Oclaro [6], LioniX [10]). Most of them are located in Europe, except IME (Singapore) and Luxtera (USA). A significant difference exists also on the current state of access to the foundries. Silicon is well settled and access already open. However, access to InP generic technology is yet being developed in research projects which offer brokerage for accessing, but a clear roadmap exists [11]. In most of the cases access is through a Multi-Project Wafer (MPW) run, where the space of a wafer is shared amongst different designers by dividing it into reticules. However, some of the foundries do only perform dedicated runs (AMO, IME and IMB-CNM). Formalisation of the access is done either directly with the foundry, or through a brokering organisation, as ePIXfab, JePPIX and OpSIS. The track record on MPW wafer runs is hold by IMEC/CEA-LETI through their broker service ePIXfab, that at the end of 2012 will account for nearly 30 runs in total since 2007. On the InP side, COBRA has issued 1 MPW run per year since 2007, hence at the fall of 2012 a total of 7 will have been completed. LioniX has recently finished its first MPW on TripleX^{TM} technology.

The photonic integration *technologies* offered can be considered mature and well developed in terms of photonic performance. The colour matrix in Fig. 1 shows the available photonic building blocks within each platform. The most remarkable technical aspects for each technology are now highlighted. For SOI, the trend during 2011 was the inclusion of ring modulators and photodetectors. This is currently being offered, or planned to be in the very short term, by all the SOI platforms. The combination with CMOS electronics is a feature offered to date exclusively through OpSIS using Luxtera technology. For InP, the use of Oclaro's industrial fab (traditionally an InP component manufacturer using a vertical model) to produce generic PICs was certainly a milestone, whereas HHI is the sole generic InP foundry offering a high speed (balanced) photo-detector, that can be combined with other passives. Silicon Nitride generic technology is mature but a bit unexplored, owing to its very recent jump into the generic foundry arena. Fig. 2 shows some examples of designs and PICs authored by Universitat Politècnica de València (UPV) and VLC Photonics S.L., a fabless design house that operates with generic technologies.

Tools for designers, Photonic Design Kits (PDK), are available in most of the platforms. PDK's allow to perform in a seamlessly integrated software environment both the photonic simulation and the mask layout, incorporating photonic process information from the foundries. Whereas PhoeniX Software is becoming the de facto standard in Europe, others as Luxtera have proprietary libraries embedded into EDA software as Cadence. The foundries not having PDK's communicate at a GDS level.

Back-end processes as packaging are one of several open issues, already identified and being addressed by some of the foundry players. The development of generic packages that can be reused amongst very different PIC designs, minimising non-recursive engineering costs, is already in place for InP Oclaro and HHI, whereas it will be developed for SOI by IMEC in the midterm.

III. What's next?

Europe was certainly the cradle of generic photonic integration, both for Silicon and InP photonics. Recently in 2011, US is following the trend with OpSIS and Luxtera for Silicon. While semiconductor industry already *offshored* its production to Asia [12], it is still unclear whether US and EU photonic industry will do as well in the near future. To the date, OpSIS first MPW run was already done at IME in Singapore.

Foundry	IMEC	CEA-LETI	AMO	IME	LUXTERA	HHI	Oclaro	COBRA	LioniX	IMB-CNM
Technology	SOI	SOI	SOI	SOI	SOI	InP	InP	InP	SiNx	SiNx
Location	BEL	FRA	GER	SGP	USA	GER	UK	NL	NL	ESP
Access	MPW	MPW	Dedicated	Dedicated	MPW	MPW	MPW	MPW	MPW	Dedicated
Open	Yes	Yes	Yes	Yes	Yes	Yes	No	No	Yes	Yes
Broker	ePIXfab	ePIXfab	No	No	OpSIS	No	FP7 Project	JePPIX	No	No
Cost per	Area	Area	Project	Project	Area	Area	Area	Area	Area	Project
SHWVG										
DEWVG										
WVGX										
Y-B										
DC										
MMI										
SPGC										
PSGC										
SSC										
EOM										
TOM										
CIM										
RR										
AWG										
DBR										
SOA										
PD										
BPD										
PKG										
SW										
ELECT										

Fig. 1: State of the art in generic foundry processes. (Colour code: Green=Available, Grey=Not Available, Orange=In progress. Abbreviations: SHWVG Shallow waveguide, DEWVG Deeply etched waveguide, WVGX Waveguide crossing, Y-B Y-branch, DC Directional coupler, MMI Multi-Mode Interference coupler, SPGC Single Polarisation Grating Coupler, PSGC Polarisation Splitting GC, SSC Spot-Size Converter, EOM Electro-Optic Modulator, TOM Thermo-Optic Modulator, CIM Carrier-Injection Modulator, RR Ring Resonator, AWG Arrayed Waveguide Grating, DBR Distributed Bragg Reflector, SOA Semiconductor Optical Amplifier, PD Photo-Detector, BPD Balanced PD, PKG Packaging, SW Software, ELECT Electronics).

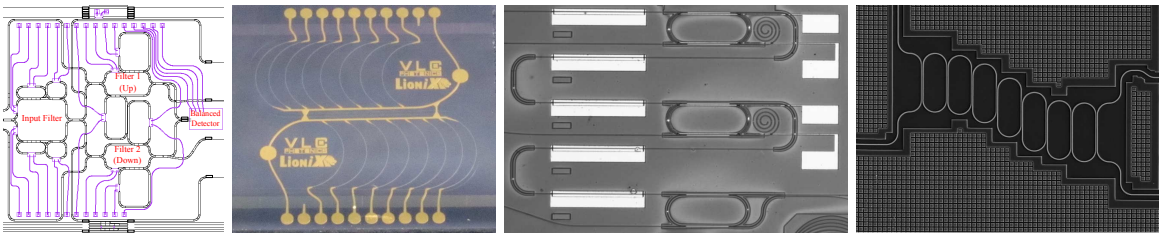


Fig. 2: Designs and PICs produced using generic foundry processes. Starting at the top line, from left to right: a) Microwave Photonics discriminator, FP7 NMP-EuroPIC with HHI InP technology, design by UPV; b) Tap and delay chip in LioniX MPW run#1 TripleX^{TM} technology, design by VLC Photonics S.L.; c) Microwave photonics phase shifter in JePPIX MPW run#3, COBRA InP technology, design by UPV; and d) apodised CROW filter in IMEC MPW run#6 SOI technology, design by UPV.

Currently there is no known initiative to establish an *InP generic foundry* in the US, whereas EU InP generic foundries will be established commercially in approximately 5 years [11]. We might also see a step forward in the short term by other US InP companies, as OpSIS/Luxtera did for Silicon.

The photonic design and prototyping *fabless firm ecosystem*, fostered by generic technologies, started to develop in Europe by 2009. Nowadays, it is made up of half a dozen of SMEs, at a rate of 1-2 companies started-up per year. This number might keep growing in the short term. Conversely in the US, start-ups have a strong linkage to a foundry/technology. US fabless PIC companies based upon generic integration might appear in the short term.

Acknowledgements

This work has been partially supported by the Spanish Plan Nacional de I+D through grants TEC2010-21337 ATOMIC and TEC2008-06145 CROWN.

References

[1] J. T. Macher and D. C. Mowery, "Vertical specialization and industry structure in high technology industries," *Advances in Strategic Management*, vol. 21, pp. 317–355, 2004.

[2] "Towards a foundry model in micro- and nanophotonics: A vision for Europe," tech. rep., EC FP6 NoE ePIXnet Steering Committee, March 2007.

[3] M. Hamacher, R. Kaiser, H. Heidrich, P. Albrecht, B. Borchert, K. Janiak, R. Loffler, S. Malchow, W. Rehbein, and H. Schroeter-Janssen, "Monolithic integration of lasers, photodiodes, waveguides and spot size converters on GaInAsP/InP for photonic IC applications," in *Indium Phosphide and Related Materials, 2000. Conference Proceedings. 2000 International Conference on*, pp. 21–24, IEEE, 2000.

[4] "ePIXfab, the Silicon photonics platform." http://www.epixfab.eu.

[5] "Institute of Microelectronics, Singapore." http://www.ime.a-star.edu.sg.

[6] "Joint European Platform for InP-based Photonic Integrated Components and Circuits (JePPIX)." http://www.jeppix.eu.

[7] "Instituto de Microelectrónica de Barcelona, Centro Nacional de Microelectrónica (IMB-CNM)." http://www.imb-cnm.csic.es.

[8] "Gesellschaft für Angewandte Mikro- und Optoelektronik." http://www.amo.de.

[9] "Optoelectronic System Integration in Silicon." http://depts.washington.edu/uwopsis/.

[10] "LioniX, microfluidics and integrated optics." http://www.lionixbv.nl.

[11] M. Smit, M. Wale, D. Robbins, and H. Ambrosius, "The road to a multi-billion Euro market in InP-based Integrated Photonics: JePPIX ROADMAP 2012," tech. rep., JePPIX, 2012.

[12] C. Brown, G. Linden, and J. T. Macher, "Offshoring in the Semiconductor Industry: A Historical Perspective," *Brookings Trade Forum*, pp. 279–333, 2005.

Semiconductor Wavelength Converter with Wide Dynamic Range

Atsushi Sugitatsu
High Frequency & Optical Devices Work
Mitsubishi Electric Co.
4-1 Itami City, Hyogo, Japan
Sugitatsu.Atsushi@ap.MitsubishiElectric.co.jp

***Abstract*—Semiconductor optical amplifier based wavelength converter in Mach-Zehnder interferometer configuration realizes bit rate transparent and wide dynamic range wavelength conversion up to 43 Gbps employing simple feedback control with monitor PD and gain control SOA.**

Keywords- Mach-Zehnder; Wavelength converter; SOA; PD; Dynamic range

I. INTRODUCTION

Rapid global growth of mobile phone including huge amount of smart phone spreads in addition to the conventional internet so that increasing rapid internet traffic require continuous optical communication network expansion over the world. Sustainable growth of the optical backbone network must be realized simultaneously. Therefore all optical network is one of the plausible candidate to meet the above request and optical wavelength conversion is an key technology for the next generation optical communication network with energy efficiency and flexibility.

Among various wavelength converter technologies, a semiconductor optical amplifier (SOA) is most plausible one due to advantages of its compactness, high conversion efficiency, and possibility of higher order degree integration. Thus, several wavelength converter technologies with SOA have been investigated, such as SOA Mach-Zehnder interferometer (MZI) based on cross-gain modulation (XGM) and cross-phase modulation (XPM) [1-3] or four-wave mixing (FWM).

Monolithic integration is mandatory for the next generation devices, such as 40G MZ TLD [4], 100GbE PD [5], and so on. Since SOA-MZI wavelength converter integrates several optical parts, such as SOAs, PDs, and waveguides, in the same manner.

However, wavelength converter based on SOA has disadvantage of limited dynamic range for an input signal power. To overcome this, we have proposed an SOA-MZI wavelength converter with gain control SOA (G-SOA) and expanded dynamic range by adjusting G-SOA gain manually [6].

This paper presents a wide dynamic range wavelength converter using a simple feedback control with a monitor photo diode (PD) and a G-SOA. We demonstrate wide dynamic range wavelength conversion for 43 Gbps NRZ signal.

II. SOA-MZI BASED WAVELENGTH CONVERTER

A wavelength converter not only covers C-band wavelength range but also accommodates with wide speed range of bit rate and different format of RZ and NRZ in order to support all optical network. Figure 1 shows schematic diagram of SOA-MZI wavelength converter. The basic SOA-MZI consists of two SOAs and phase shifters located on both MZ arms. Port P1, P2 and P3 are a probe light input port, a signal light input port and an output port of wavelength converted signal, respectively. Continuous wave (CW) probe light injected into the P1 passes through SOA1 and SOA2 in the MZI configuration. Signal light launched into the P2 passes through the G-SOA which is located to control signal input power, propagating through SOA2 along with the probe light. As probe light is modulated by signal light through XGM and XPM in SOA2, it is transformed to wavelength converted signal through interference between those probe lights from the SOA1 and the SOA2 and then emitted from the P3.

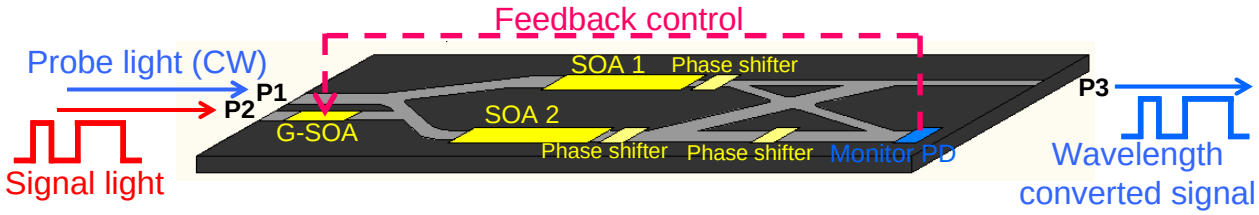


Figure 1. Schematic diagram of SOA-MZI wavelength converter monolithically integrated with a monitor PD and a gain control SOA

It is important to achieve enough fast response to support wide speed range of 2.5 Gbps to 40 Gbps and both RZ and NRZ. To achieve the above, SOA designs in MZI require high gain in small active area [1]. Wavelength converter with such optimized design has accomplished bit rate transparent between 2.5 Gbps and 40 Gbps with both RZ and NRZ format.

III. A SIMPLE FEEDBACK CONTROL METHOD AND WAVELENGTH CONVERTER CONFIGURATION TO ENHANCE DYNAMIC RANGE

This type of wavelength converter needs to be well organized to achieve such a high performance. An important point is the signal input power into the SOA2, which set to be some specific value under various conditions. In the real network, input signal power could vary so that the device needs a function to keep the input power constant. Since the phase modulation of the probe light depends strongly on signal input power into the SOA2, this restricts the superior wavelength conversion for wide signal input power range. One solution is to keep the signal power into the SOA2 constant at optimal signal power level in order to enhance dynamic range of input power for wavelength conversion by adjusting G-SOA.

We introduced a simple feedback control to maintain a constant signal power into SOA2. In particular, it is to keep the monitor PD current at its maximum by controlling the G-SOA bias current. The monitor PD after MZI on the opposite side of the P3 detects the wavelength converted signal level for feedback control. The feedback control is based on relationship between signal power into the SOA2 and wavelength converted power. Figure 2 (a) shows calculated average power of wavelength converted signal as a function of bias current of the G-SOA for 43 Gbps NRZ signal under constant signal input power at the P2. Figure 2 (b), (c) and (d) are calculated eye diagrams at points A, B, and C in Fig.2 (a), respectively. The signal power into the SOA2 depends on bias current of the G-SOA. Clear eye opening is obtained at the maximum average power of wavelength converted signal of the point B. As wavelength converted signal with high extinction ratio and high amplitude is obtained under the condition that phase difference of the probe lights in MZ arms is π radian, the average power of wavelength converted signal becomes the highest. In case of lower bias current at the point A, eye pattern is deteriorated in Fig.2 (b). Phase difference of probe lights is smaller than π radian for lower input signal due to reduction in

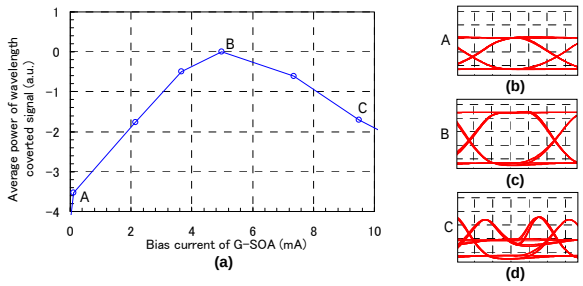


Figure 2. Characteristics of average power of wavelength converted signal and eye diagrams for 43Gbps NRZ signal. (a) Calculated average power of wavelength converted signal as a function of bias current of G-SOA. (b) The eye diagram at the point of A. (c) The eye diagram at the point of B. (d) The eye diagram at th e point of C

gain of the G-SOA and thereby average power of wavelength converted signal becomes small and extinction ratio is also low. Meanwhile, if the bias current of the G-SOA becomes high at the point C, eye pattern is distorted in Fig.2 (d). As the phase difference is larger than π radian for higher input signal due to increase of the G-SOA, overshoot occurs because of overmodulation for interferometer of probe lights and then its average power also decreases and extinction ratio becomes low.

For this reason, waveform with high extinction ratio and amplitude is obtained at the maximum power of wavelength converted signal. Since the monitor PD can detect its average power, signal power into SOA2 is maintained at optimal level and clear eye opening is easily obtained for wide dynamic range of signal input power by keeping the monitor PD current at its maximum by adjusting the G-SOA bias current using feedback control.

IV. EXPERIMENTAL SETUP AND RESULTS

Figure 3 shows schematic diagram of experimental setup. The wavelength and power of the probe light are 1537 nm and +6 dBm, respectively. The signal light of 1535 nm wavelength is modulated at 43 Gbps NRZ 2^{31}-1 pseudo random bit sequence (PRBS). The monitor PD and the G-SOA are connected with a feedback control system which detects the monitor PD current and adjusts the G-SOA bias current to keep the monitor PD current at its maximum. Wavelength converted signal is detected by oscilloscope and optical power meter.

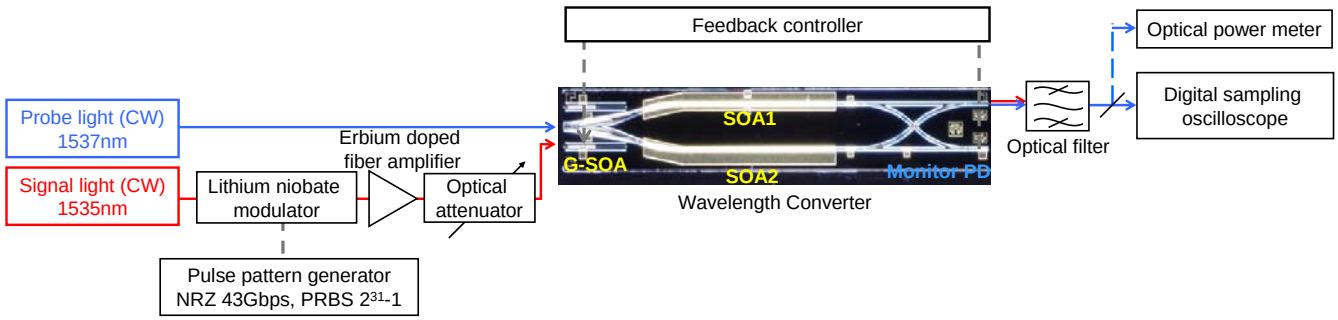


Figure 3. Schematic diagram of experimental setup.

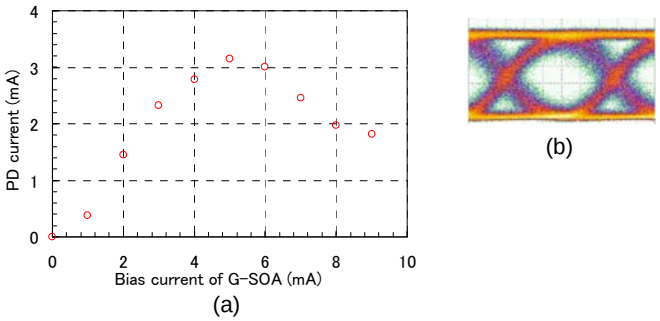


Figure 4. (a) Monitor PD current versus bias current of G-SOA. (b) The eye diagram of converted signal at the maximum monitor PD current.

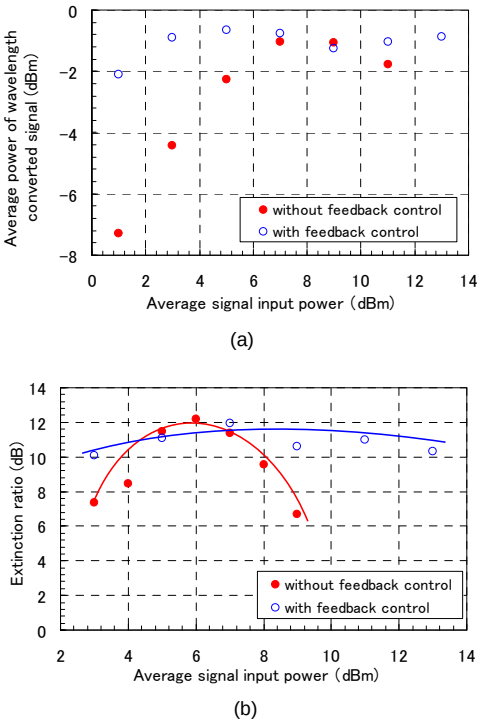


Figure 5. Characteristics of average power of wavelength converted signal and extinction ratio as well as eye diagrams of converted light. (a) Average power of wavelength converted signal as a function of average signal input power. (b) Extinction ratio versus average signal input power. (c) (d) Eye diagrams with feedback control in the power of +13 dBm and +3dBm, respectively.(e) and (f) Eye diagrams without feedback control in the power of +9dBm and +3dBm, respectively.

Figure 4 (a) shows the measured monitor PD current versus bias current of the G-SOA. Figure 4 (b) is an eye diagram at 5mA bias current of the G-SOA which indicates the maximum value of monitor the PD current. Clear eye opening is obtained at the maximum monitor PD current. These results coincide with the simulation results in Fig.2.

Figure 5 (a) shows measured average output power of wavelength converted signal as a function of average input signal power. The open circle is with feedback control and the closed circle is without feedback control and bias current of the G- SOA was fixed at 9.3 mA. Whereas the variation of average power of wavelength converted signal without feedback control is more than 7 dB, one with feedback control is less than 1.65 dB. The variation of its average power was suppressed by feedback control.

Dynamic range is evaluated with the extinction ratio of wavelength converted signal. Figure 5(b) shows measured extinction ratio versus average signal input power. Wavelength converted signal quality depends on signal power into the SOA2 tightly, but variation of extinction ratio is compensated by controlling the G-SOA with feedback control. Here, we set the criteria of extinction ratio to be more than 10 dB. The extinction ratio without feedback control is nearly 2dB range of signal power from +5 dBm to +7 dBm. In contrast, as dynamic range with feedback control is from +3 dBm to +13 dBm, feedback control prolongs dynamic range from 2 dB to 10 dB. Figure 5 (c) and (d) shows obtained eye diagrams with feedback control at the power of +13 dBm and +3 dBm, respectively. Figure 5 (e) and (f) are ones without it at the power of +9 dBm and +3 dBm. In case of no feedback control, eye diagram is distorted (closed) for high (low) signal input. Feedback control adjusted the bias current of the G-SOA to optimal current for each signal power, such as the bias current of 2.5 mA in Fig.5 (c) and 13.5 mA in (d). As a consequence, clear eye opening are obtained during wide dynamic range for input signal power.

V. Conclusion

Wide dynamic range wavelength converter with the monitor PD and the G-SOA using a simple feedback control are presented. The simple feedback control method was experimentally verified and wide dynamic range of 10 dB for 43 Gbps NRZ signal have been successfully demonstrated under the condition of extinction ratio above 10 dB.

References

[1] T. Hatta, et al., “Polarization-Insensitive Monolithic 40Gbps SOA-MZI Wavelength Converter With Narrow Active Waveguides”, IEEE J. Quantum Electron., vol.13, no.1, pp. 32-39, 2007.

[2] Y. Miyazaki, *et al.*, “Polarization – Insensitive SOA-MZI Monolithic All-Optical Wavelength Converter for Full C-band 40Gbps-NRZ Operation”, ECOC 2006, Th3.4.2 (2006).

[3] D. Apostolopoulos, *et al.*, “A New Scheme for Regenerative 40Gb/s NRZ Wavelength Conversion using a Hybrid Integrated SOA-MZI”, OFC 2010, OThS6 (2010).

[4] N. Ohata, *et al.*, “43Gbps Wavelength converter with wide dynamic range of 14dB”, CLEO/Pacific Rim2009, ThG1-3 (2009).

[5] T. Takiguchi, et al., “40G RZ-DQPSK Transmitter Monolithically Integrated with Tunable DFB Laser Array and Mach-Zehnder Modulators”, OFC2011, OMU3 (2011).

[6] Takemura, et al., “25Gbps x 4ch photodiode array with high responsivity for 100Gbps Ethernet”, ECOC2010, P2.11

Integrated optical modulators for high spectral efficiency

Stefano Balsamo, Michele Belmonte
LiNbO3 modulator R&D
OCLARO Corporation
Via Fellini 4, 20097 San Donato Milanese, Italy
Stefano.balsamo@oclaro.com

***Abstract*—Coherent modulation formats have gained considerable importance in high-capacity, high-efficiency optical systems. A key component for achieving good transmission performances are Lithium niobate modulators, which can be designed and optimized to operate with BPSK, QPSK, 16-QAM and OFDM modulation schemes providing excellent results.**

Keywords-$LiNbO_3$; coherent systems; modulators.

I. INTRODUCTION

Since the first introduction of WDM systems in the 1990's, fiber optic networks capacity have continuously increased their capacity in order to respond to the growth of data traffic. The two main pillars of this huge capacity expansion have been WDM (that is, wavelength division multiplexing) and fiber amplifiers (e.g., EDFAs), while the dominant transmission format was IMDD (intensity modulation with direct detection). However, the principle of wavelength multiplexing has been fully exploited and the spectral limit of the optical amplifiers has been reached by packing up to 80 channels with 50 GHz spacing. Increasing the channel data rate up to 40 or 100 Gbps is not practically feasible with 50 GHz channel spacing, since strong crosstalk is present between adjacent channels. Moreover, at these bit rates, dispersion and PMD have a significant impact on transmission performances.

These limitations can be efficiently overcome with new modulation formats based on the phase of optical signals. In this case, the modulation is not simply on-off (intensity based), but based on phase changes as well, and it can be binary, quaternary, or even more complex. Modulation formats such as differential phase shift keying (DPSK), or differential quadrature phase-shift keying (DQPSK), are already present in commercial transmission systems with excellent results [1].

Using higher-level modulation schemes plus coherent detection, electronic DSP are capable of eliminate impairments such as chromatic dispersion (CD) and polarization mode dispersion (PMD), extending the maximum reach of the systems considerably. A further advantage is to multiplex two orthogonal polarizations of the optical signal:. Polarization Division Multiplexing (PDM or simply PM), devices are becoming very useful in recent long-haul coherent systems, in combination with polarization-diversity receivers. The higher level formats allow to "pack" a given data rate into a lower data rate (e.g., in case of 100G, the modulators work at 25 Gbaud, while the aggregate data rate is 100Gbps. Thus, strong increase of the spectral efficiency can be achieved [2], [3]. On the component side, the requirements on laser sources and other components have become more stringent, and all-optical generation of these new formats has justified a strong development effort for new modulators capable of working with complex, multilevel and even polarization-multiplexed signals. [4], [5].

Lithium niobate technology is considered quite "mature" [6], yet it has already supported the introduction of many important breakthroughs in network capacity and spectral efficiency. These devices were first introduced into the first 2.5Gbps systems, passing to 10 Gbps WDM systems and then supporting 40G RZ-DPSK and DQPSK transmission in a well-established class of new commercial systems. Recently, new evolutions of $LiNbO_3$ modulator architectures have opened the way to a innovative, efficient and reliable multilevel coherent transmitter. The high extinction, broad-bandwidth and low driving voltage of $LiNbO_3$ devices allow generation of clean and undistorted signal constellations in QPSK, 16QAM and more complex configurations such as multicarrier and OFDM [7], [8], [9].

In this paper, we review some of the main characteristics of multilevel optical modulators for coherent formats, putting in evidence the limitations, perspectives and challenges of such devices on the Lithium niobate platform.

II. MODULATOR SCHEMES

A. Basic building blocks

The most common Lithium niobate intensity modulators used in practical optical communication systems are based on the Mach-Zehnder Interferometer (MZI). The optical structure consists of a couple of parallel phase modulators plus a splitter and a combiner sections which transforms an RF signal into an intensity modulation of a CW laser signal.

The introduction of four-symbol modulation formats such as (D) QPSK has brought into modulator's product lines the so-called "dual parallel" or I-Q MZI [8]. This device can produce 4 complex signals (module and phase are necessary to characterize each of them), and it becomes in turn the building block for 8-PSK, 16-QAM, 64-QAM [9] and more. Due to the complex signal constellations required in M-PSK and M-QAM formats, there are several options for generating the same configuration. In some cases, the I-Q modulators can be cascaded and combined with a predefined attenuation [8], [9] to achieve the desired amplitude and phase, or they can be cascaded, including in some cases also phase modulators [10]. Among the recently developed coherent formats, the

multicarrier approach has attracted considerable attention: OFDM in particular is widely considered as the most promising technique. This format requires not only complex modulation, but also optical filter functions such as interleavers for separating the optical subcarriers [5].

The basic building blocks required for integration of higher order modulation formats are already available within Lithium niobate technology, and in principle all the passive devices can be allocated on the same substrate. Nevertheless, there are drawbacks due to the shallow contrast of the waveguides, and some hybrid integration solutions provided interesting results.

B. Cascading and integration issues

Despite its simple concept, QPSK devices must be very carefully optimized in order to achieve high extinction ratios and precise 90° phase shift between the 4 symbols. The basic building blocks (splitters, couplers, etc.), even if robust when working in simple configurations, might not be to suitable for the stringent requirements of coherent transmission, thus optimization must be performed on the whole structure to ensure that all optical paths are balanced. Generally speaking, a complex cascade of curves, splitters, couplers and I-Q modulators implies careful design of filtering sections to get rid of any unwanted coupling of radiated waves into adjacent devices. The cascade also brings in more extra losses, which must be kept as low as possible to limit the need for optical amplification in the transmitter. Moreover, the spurious chirp generated inside the amplitude modulators, in particular, is detrimental to the transmission performances, and it must be tightly controlled through electro-optic sections design.

Moreover, in real system design, the devices must have photo-detectors, which must be then integrated with the modulator chip inside its package. These PD's have much more stringent requirements than in simpler devices in order to set the operating bias point and keeping it stable over time and temperature, and in some formats such as DQPSK they can also be required to be broadband up to 1 GHz.

C. Polarization Multiplexing: issues and challenges

Another "modulation dimension" can be added, as it was mentioned before, by using orthogonal polarizations that share the same optical fiber without disturbing each other during propagation. Lithium niobate devices are strongly birefringent and have their maximum electro optic efficiency only on TE or TM polarization (depending on the wafer cut): as a consequence, the two polarization channels must be modulated in the same state and eventually rotated. This step can be done either by a polarization rotator and combiner realized with PLC with a wave plate [9], or by an integrated polarization rotator and combiner directly on $LiNbO_3$, (even if it requires much more space on the chip). The wave plate has been already used successfully in passive PLC components, such as the AWG.

III. SIZE REDUCTION: HYBRID APPROACH

One key point of optical integration is size reduction. Lithium niobate modulators are several cm long, in order to get low driving voltages and low power consumption. Because of the additional optical building blocks, multilevel devices can become exceedingly large due to the shallow curves which can be fabricated on this substrate to keep propagation losses low. Hybrid integration with silica-based PLCs is an enabling technology which reduces the chip size on Lithium niobate substrate, allowing a more efficient utilization of the wafers in production and concentrating the technological effort on some building blocks for high-efficiency, high-speed electro-optic modulation, while leaving the optical splitting and combining functions to a different platform (PLC or similar). This approach is probably a good compromise also for the higher-level modulation schemes (e.g., 16- and 64-QAM).

Taking this approach to the extreme consequences, one could think of putting on the LiNbO3 substrate only phase modulators, while all splitters and combiners sections are cascaded on PLCs. Part of the benefits which come from this approach, are paid in terms of higher insertion loss and more complex alignment processes but, on the other hand, a given nested structure can be coupled with different PLC pairs in order to get different modulation formats [9], [10].

IV. CONCLUSIONS AND DISCUSSION

Lithium niobate technology remains a key building block of coherent transmitters. All the most advanced modulation formats such as multicarrier, OFDM and coherent QAM, benefit from the electro-optical characteristics of $LiNbO_3$ devices, whose performances are still unsurpassed for long-haul transmission. The challenge of new multilevel optical transmission has brought into development and production new hybrid integration techniques, which will allow further evolution and scalability of the networks.

REFERENCES

[1] M. Nakazawa, T. Hirooka, M. Yoshida, K. Kasai, "Ultrafast Coherent Optical Transmission," IEEE J. Select. Topics Quantum Electron., vol. 18, no. 1, pp.363-376, 2002.

[2] P. J. Winzer, "Modulation and Multiplexing in Optical Communications," Proc. of CLEO/IQEC 2009.

[3] R. Ludwig et al., "Ultrafast Transmission Systems using Coherent Technology," Proc. of OECC 2011.

[4] T. Kawanishi, T. Sakamoto, M. Isutzu, "High-Speed Control of Lightwave Amplitude, Phase and Frequency by Use of Electrooptic Effect," IEEE J. Select. Topics Quantum Electron., vol. 13, no. 1, 2007.

[5] H. Yamazaki, T. Yamada, Y. Sakamaki, A. Kaneko, A. Sana. H. Masuda, Y. Miyamoto, "Advanced optical modulators with hybrid configuration of silica-based PLC and LiNbO3 phase-shifter array for ultra-high-speed transport networks," Proc. of First ITU-T Kaleidoscope Academic Conference, 2008

[6] E. L. Wooten, K. M. Kissa, A. Yi-Yan, "A Review of Lithium niobate Modulators for Fiber-Optic Communications Systems," IEEE J. Select. Topics Quantum Electron., vol. 6, no. 2, pp.69-82, 2000.

[7] T. Kawanishi et al., "High-speed dual-parallel Mach-Zehnder modulator using thin Lithium niobate substrate," Proc. of OFC/NFOEC 2008.

[8] G. W. Liu et al., "Monolithically Integrated Quad Mach-Zehnder IQ Modulator for Optical 16-QAM Generation," Proc. of CLEO/QELS 2010.

[9] Y. Doi, T Yamada, "Recent progress on hybrid silica-PLCs/LiNbO3 modulator for advanced transmission formats" OptoeElectronics and Communications Conference (OECC), 2010 pp. 564 - 565

[10] A. Chiba, T. Sakamoto, T. Kawanishi, K. Higuma, M. Sudo, J. Ichikawa, "16-level quadrature amplitude modulation by monolithic quad-parallel Mach-Zehnder optical modulator," Electron. Lett. Vol. 46 No. 3, 2010.

Controlling light emission from single-photon sources using photonic nanowires

Niels Gregersen,* Yuntian Chen and Jesper Mørk
DTU Fotonik, Department of Photonics Engineering
Technical University of Denmark
Building 343, Ørsteds Plads, Kongens Lyngby, Denmark
* ngre@fotonik.dtu.dk

Christophe Sauvan and Philippe Lalanne
Laboratoire Charles Fabry de l'Institut d'Optique
CNRS, Université Paris-Sud, Campus Polytechnique, RD 128, 91127 Palaiseau, France

Mathieu Munsch, Julien Claudon, Joël Bleuse, Nitin S. Malik, Emmanuel Dupuy and Jean-Michel Gérard
CEA-CNRS-UJF group "Nanophysique et Semiconducteurs"
CEA, INAC, SP2M
F-38054 Grenoble, France

***Abstract*—The photonic nanowire has recently emerged as an promising alternative to microcavity-based single-photon source designs. In this simple structure, a geometrical effect ensures a strong coupling between an embedded emitter and the optical mode of interest and a combination of tapers and mirrors are used to tailor the far-field emission pattern. This non-resonant approach relaxes the demands to fabrication perfection, allowing for record-high measured efficiency of fabricated nanowire single-photon sources. We review recent progress in photonic nanowire technology and present next generation designs allowing for electrical contacting, polarization control, improved efficiency and simplified fabrication.**

Keywords-photonic nanowire, single-photon source, single photons, electrical pumping, polarization control

I. INTRODUCTION

A major challenge for the realization of future quantum photonic applications is the development of solid-state light-emitting devices capable of emitting single photons on demand. [1] The semiconductor quantum dot (QD) embedded in a engineered microstructure appears as a promising platform for such a single-photon source (SPS). The self-assembled QD features a high radiative yield without bleaching or blinking. For practical applications, it is desirable to trigger the photon using an electrical pulse, and this can be achieved by integrating the QD into a *p-i-n* structure to realize a single-photon LED.

For the quantum communication and quantum information applications, a near-unity efficiency ε, defined as the number of detected photons by the collection optics per trigger, is desired. The fabrication of self-assembled QDs allowing for a nearly perfect conversion of excitons to emitted photons is well-established, however to obtain a high efficiency the photonic environment must be engineered such that all the emitted light couples to the collection optics.

For an InAs QD embedded in GaAs, the large refractive index of GaAs limits the photon extraction efficiency to a few percent. This extraction efficiency can be improved by placing the emitter inside a high quality (Q) microcavity [2] and taking advantage of cavity quantum electrodynamics. The relevant figures of merit are the β factor describing the spontaneous emission rate into the fundamental cavity mode over the emission total rate and the probability γ describing the ratio of the power collected by the collection optics and that of the fundamental mode. Assuming a perfect radiative yield, the total efficiency ε is then given by the product $\beta\gamma$. In high-Q microcavities, a β close to 100 % is achieved using the Purcell effect, however fabrication-induced imperfections limit the γ leading to efficiencies of microcavity-based SPSs $\leq$ 44 %. [2] Furthermore, these devices feature an autocorrelation function at zero time delay $g^{(2)}(\tau = 0)$ generally much larger than 0, most likely due to cavity-feeding effects, and these resonant systems only operate over the limited bandwidth of the cavity resonance.

As alternative we have explored the photonic nanowire geometry which is better adapted to efficient collection of light. In this geometry, a geometrical effect ensures a β close to unity, [3] and the combination of a top conical tapering [4] and a metal mirror [5] allows for control of the far-field radiation pattern. This has lead to the proposal of optically [6] and electrically [7] pumped designs with predicted efficiencies of ~ 90 % and to the experimental demonstrated of an optically pumped device with an efficiency of 72 %. [8]

II. PHOTONIC NANOWIRE SPS DESIGNS

The photonic nanowire SPS designs considered in this work are illustrated in Fig. 1. The nanowire is simply a GaAs cylinder placed on a substrate. Single photons are emitted by an InAs QD and they couple to the fundamental mode of the nanowire with a probability which can be optimized by choosing the correct nanowire radius. At an emission wavelength of λ = 950 nm, a β of 96 % is obtained for an optimum radius R_{nw} of 120 nm. [3] This high β is the result of a geometrical screening effect dampening the electric field strength of radiation modes inside the nanowire. [9] For even smaller radii, the guided mode is no longer supported and the same screening effect results in strong inhibition of the spontaneous emission [9] realized without the presence of a bandgap.

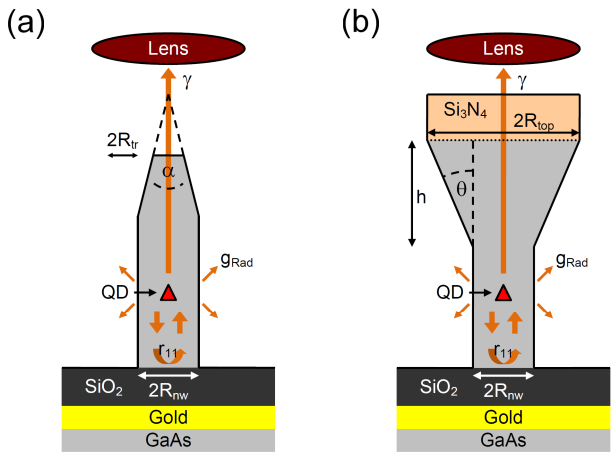


Figure 1. Optically pumped photonic nanowire designs based on a regular tapering (a) and an inverted taper (b).

Due to symmetry, half of the photons in the fundamental mode will be propagating towards the substrate and it is necessary to implement a bottom metal mirror [5] reflecting these photons back towards the top. We include a thin dielectric layer of thickness ~ 10 nm to suppress coupling to surface plasmons resulting in a reflection coefficient $R_{11} = |r_{11}|^2$ of 91 %.

Using the mirror we ensure that the emitted photons in the fundamental mode propagate towards the top of the nanowire, however for a nanowire radius R_{nw} of 120 nm, the fundamental mode waist is narrow leading to a wide far-field radiation pattern and a poor coupling to the objective lens. To improve this coupling it is thus necessary to expand the mode waist such that the resulting output beam divergence is reduced. [4] The two designs presented in Fig. 1. represent two different strategies for achieving this mode expansion.

The design in Fig. 1(a) features a regular conical tapering of opening angle α. As the fundamental mode propagates forward, the radius of the nanowire decreases. For R_{nw} below ~ 100 nm, the nanowire can no longer support a guided mode, and the fundamental mode expands rapidly. For sufficient small values of α, the taper thus allows for an adiabatic expansion of the fundamental mode, [4] resulting in a large mode waist and a narrow far field profile. Furthermore, the mode is adiabatically expanded into the surrounding air leading to a strong reduction of the reflection at the semiconductor-air interface. The adiabatic expansion primarily takes part in the lower part of the taper, and thus a truncated taper with truncation radius of R_{tr} = 60 nm gives the same performance as the perfectly sharp tip.

The top part of the photonic nanowire is engineered to suppress reflection. There is thus no cavity meaning that the emitted photons escape immediately and are thus much less subject to scattering from fabrication imperfections than they are in e.g. the high-Q micropillar cavity. A scanning electron micrograph (SEM) of a full device based on the regular conical tapering is illustrated in Fig. 2(a). Indeed, this device features a measured efficiency 72 % combined with a very clean single photon emission with $g^{(2)}(\tau = 0)$ below 0.8 %. [8]

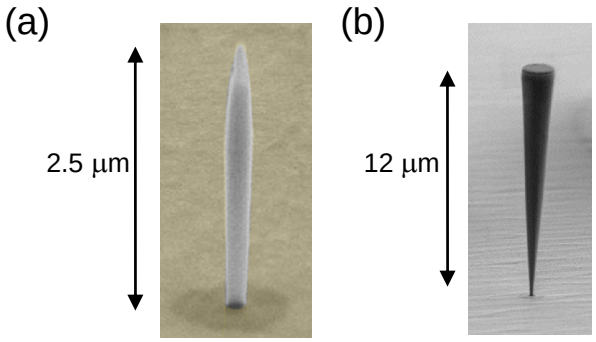


Figure 2. Scanning electron micrographs of nanowires implementing a regular conical tapering (a) and an inverted conical tapering (b).

However, the design in Fig. 1(a) suffers from several weaknesses. The fabrication of the regular conical tapering with opening angles ≤ 5° is quite challenging using our top-down approach. [8] Furthermore, due to the large part of the mode extending into the surrounding air, the implementation of a top metal contact which does not perturb the optical field profile is not immediate. For this reason we have investigated a photonic nanowire design implementing an inverted conical tapering [7] with side angle θ. The design is illustrated in Fig. 1(b). The bottom part of the design is identical to that in Fig. 1(a), however the top part features an inverted conical tapering and an anti-reflection coating. Here, the fundamental mode is adiabatically expanded not outside the nanowire as it is the case for the regular tapering, but inside the photonic nanowire. Since the mode stays inside the nanowire, we introduce an anti-reflection coating to eliminate the reflection occurring at the semiconductor-air interface.

We compute the efficiency of these devices using a single mode model based on an elements-splitting approach. [6] Assuming an emitter placed in an antinode of the field, the efficiency in this model is given by

$$\varepsilon = \beta\gamma \frac{\left(1+|r_{11}|\right)^2}{2\left(1+\beta|r_{11}|\right)}, \qquad (1)$$

where the fraction on the RHS of (1) represents a correction due to the reflection of the downwards propagating light by the metal mirror.

The predicted efficiencies for the two designs are given in Fig. 3 as function of α and θ. For a 0.8 NA objective lens, the regular design features a maximum predicted efficiency of 95 % for $\alpha \leq 2°$, however we note that an efficiency of 85 % requires an opening angle below 5°. In comparison, the maximum efficiency for the inverted taper design is 92 % and a high efficiency above 85 % is maintained for a side wall angle θ up to 10°. Furthermore, the maximum efficiency of 92 % is achievable for a taper height h of only 12 μm. A SEM image of such an inverted taper is shown in Fig. 2(b). While opening angles for regular conical taperings below 2° may be achievable using a bottom-up fabrication method, these results show that the inverted taper approach is less demanding in

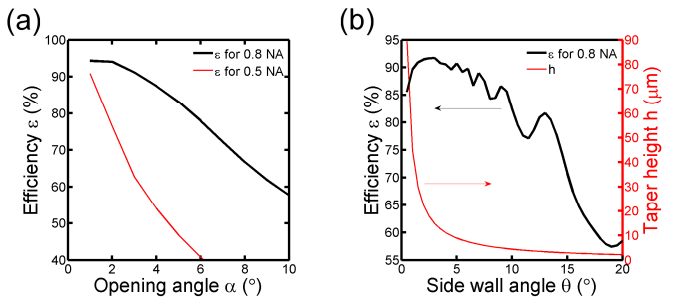


Figure 3. Predicted efficiency ε for the regular taper design (a) as function of opening angle α. Predicted efficiency and taper height for the inverted taper design (b) as function of side wall angle θ for R_{top} = 900 nm.

terms of side wall angle and thus represents an attractive alternative well adapted to our top-down fabrication technique.

III. Polarization Control

The photonic nanowire designs considered so far feature rotational symmetry and thus support two degenerate optical modes with orthogonal polarization states. In standard semiconductor QDs the emitter is not strongly polarized in one direction, and the emitter thus couples to the two modes with equal probability. For such emitters one approach to achieving polarization control is to lift the degeneracy of the optical modes by introducing an elliptical cross-section. [10]

The computed fundamental modes in a photonic nanowire PW_0 featuring an elliptical cross-section with diameters $d_{\parallel}$ = 280 nm and $d_{\perp}$ = 130 nm are shown in Fig. 4. We observe that the moderate degree of anisotropy leads to a dramatic contrast in mode amplitudes. The fundamental mode $M_{\parallel}$ with dominating electric field component aligned parallel to the major semi-axis remains well confined to the elliptical nanowire, while the orthogonal mode $M_{\perp}$ is subject to strong selective deconfinement.

We have fabricated elliptical nanowires with dimensions similar to PW_0 and with various orientations of the major semi-axis with respect to the crystal [110] axis. A SEM image of such a device is shown in Fig. 5(a). To quantify the control of the polarization we have measured the intensities $I_{\parallel}$ and $I_{\perp}$ along the two axes using a polarization filter. For each device we

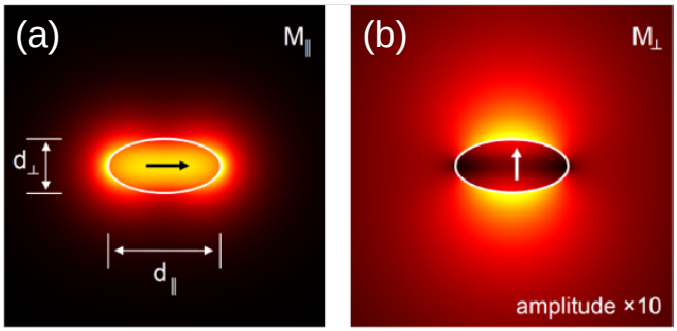


Figure 4. Field amplitude of the fundamental modes $M_{\parallel}$ (a) and $M_{\perp}$ (b) with dominating field component oriented parallel and perpendicular respectively to the large semi-axis. The white line illustrates the nanowire boundary. From [10].

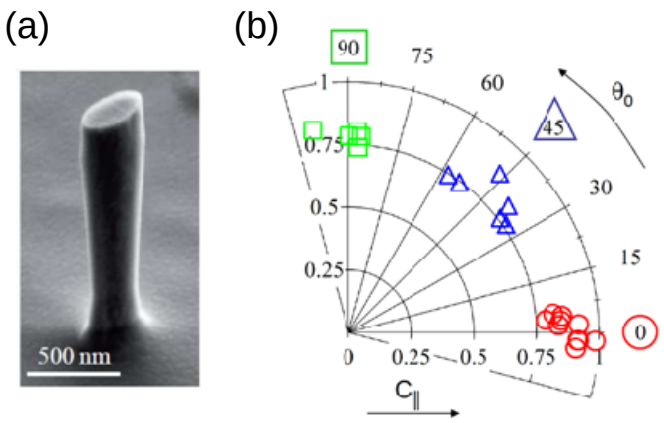


Figure 5. Scanning electron micrograph of the elliptical nanowire (a). Degree of linear polarization (b) as function of polarization angle for various ellipse orientations θ_0 = 0°, 45° and 90°. From [10].

define the degree of linear polarization as $C_{\parallel} = I_{\parallel} / (I_{\parallel} + I_{\perp})$. Polarized emission was collected for a number of devices, and $C_{\parallel}$ and the polarization angle θ_0 are shown in Fig. 5(b). We observe that a high degree of linear polarization $C_{\parallel} \geq 75$ % is reproducibly obtained demonstrating that the orientation of polarized light is indeed imposed by the orientation of the ellipse. [10]

References

[1] A. Shields, "Semiconductor quantum light sources," Nat. Photonics, vol. 1, pp. 215-223, April 2007.

[2] E. Moreau, I. Robert, L. Manin, V. Thierry-Mieg, J. M. Gérard and I. Abram, "A single-mode solid-state source of single photons based on isolated quantum dots in a micropillar," Physica E, vol. 13, pp. 418-422, 2002.

[3] Y.-R. Nowicki-Bringuier, R. Hahner, J. Claudon, G. Lecamp, P. Lalanne and J. M. Gérard, "A novel high-efficiency single-mode single photon source," Ann. Phys. Fr., vol. 32, pp. 151-154, 2007.

[4] N. Gregersen, T. R. Nielsen, J. Claudon, J. M. Gérard and J. Mørk, "Controlling the emission profile of a nanowire with a conical taper," Opt. Lett., vol. 33, pp. 1693-1695, August 2008.

[5] I. Friedler, P. Lalanne, J. P. Hugonin, J. Claudon, J. M. Gérard, A. Beveratos and I. Robert-Philip, "Efficient photonic mirrors for semiconductor nanowires," Opt. Lett. **33**, 2635-2637, November 2008.

[6] I. Friedler, C. Sauvan, J. P. Hugonin, P. Lalanne, J. Claudon and J. M. Gérard, "Solid-state single photon sources: the nanowire antenna," Opt. Express, vol. 17, pp. 2095-2110, February 2009.

[7] N. Gregersen, T. R. Nielsen, J. Mørk, J. Claudon and J. M. Gérard, "Designs for high-efficiency electrically pumped photonic nanowire single-photon sources," Opt. Express, vol. 18, pp. 21204-21218, September 2010.

[8] J. Claudon et al, "A highly efficient single-photon source based on a quantum dot in a photonic nanowire," Nat. Photonics, vol. 4, pp. 174-177, March 2010.

[9] J. Bleuse, J. Claudon, M. Creasey, N. S. Malik and J. M. Gérard, "Inhibition, Enhancement and Control of Spontaneous Emission in Photonic Nanowires," Phys Rev. Lett., vol. 106, pp. 103601, March 2011.

[10] M. Munsch et al, "Single Mode Spontaneous Emission in an Elliptical Photonic Nanowire," accepted for publication in Phys. Rev. Lett.

Photonic Integrated Circuits operating at the Single-Photon Level

Andrea Fiore, Sartoon Fattahpoor, Thang Hoang, Leonardo Midolo, Francesco Pagliano, Dondu Sahin and Arjan Sprengers
COBRA Research Institute
Eindhoven University of Technology
P.O. Box 513, NL-5600MB Eindhoven, The Netherlands
a.fiore@tue.nl

Johannes Beetz, Matthias Lermer, Sven Höfling and Martin Kamp
Technische Physik, Universität Würzburg
Am Hubland, 97074 Würzburg, Germany

Alessandro Gaggero, Francesco Mattioli and Roberto Leoni
Istituto di Fotonica e Nanotecnologie (IFN), CNR, via Cineto Romano 42, 00156 Roma, Italy

We present an approach to the full integration of active and passive single-photon devices on a single chip. Single-photon sources coupled to waveguides are realized by embedding InAs quantum dots (QDs) in photonic crystal (PhC) cavities. In order to control the QD-cavity coupling, devices for the electrical control of both the exciton energy and the cavity resonant wavelength are demonstrated. A waveguide single-photon detector is obtained by patterning superconducting NbN nanowires on top of the ridge waveguides, resulting in high efficiency and low jitter. This set of technologies opens the way to fully integrated quantum photonic circuits for quantum information processing based on photonic qubits.

I. INTRODUCTION

Quantum information processing (QIP) enables new protocols and functionalities in communication and computing. Quantum key distribution, allowing the secure exchange of cryptographic keys, is a first commercial application of QIP, while the tantalizing perspective of computational speed-up for a number of important problems has motivated much research in the direction of quantum computers. Single photons are one of the preferred implementation of quantum bits, since they can be transmitted at long distances with low loss and will form an integral part of any future QIP system. However, the production, processing and detection of single photons is still mostly realized using discrete, free-space or fiber-optic devices, resulting in unacceptable complexity and cost when circuits with several photons need to be built. The development of an integrated quantum photonic circuit is therefore the only possible solution to advance the state-of-the-art of photonic QIP in both science and applications. While passive quantum circuits have been demonstrated before [1], we are working on a concept which enables the full integration of active and passive devices, including sources and detectors of single photons. The main building blocks of this quantum photonic integrated circuit (Fig. 1) will be presented.

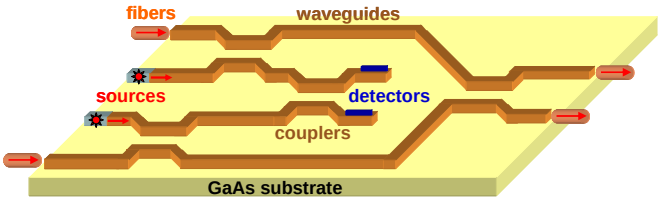


Figure 1 Schematics of a quantum photonic integrated circuit

II. WAVEGUIDE SINGLE-PHOTON SOURCES

Single-photon sources can be realized by using the radiative recombination from the excited state of a single two-level system, whereby one and only one photon is produced. Single QDs, due to their quantized energy structure, represent a good approximation of a two-level system at sufficiently low temperatures (<50 K). We use self-assembled InAs QDs on GaAs substrates, which have shown high radiative efficiency and relatively long coherence times. In order to efficiently funnel the QD emission into a waveguide a PhC cavity is patterned around the QD. This brings the additional advantage of shortening the radiative lifetime through the Purcell effect, which increases the emission rate and helps fighting decoherence. However this also contributes a major challenge: As the exciton/cavity coupling critically depends on their spectral alignment, a tuning method is required for either the cavity or the exciton. Tuning of the exciton energy is possible by applying an electric field to take advantage of the Stark effect. When several QD/cavity systems are needed, for example to produce several single photons in different waveguides, the cavities should all be resonant at the same wavelength, a major technological challenge. We have investigated two approaches to this problem. The first relies on the use of a short PhC waveguide, instead of a small cavity, as a broadband channel for photon emission. Indeed, in a PhC waveguide the suppression of in-plane emission due to the PhC bandgap results in efficient funneling into the guided mode over a large frequency range, making the fine control of the spectral resonance unnecessary [2]. We have demonstrated a spontaneous emission coupling factor β>80% in ≈20 μm-

long waveguides, along with a small enhancement of the spontaneous emission rate[3]. The second approach is based on the electrical control of the PhC cavity wavelength. This is realized by having the PhC mode extend over two closely-spaced membranes, and varying their distance electromechanically. This results in a change of the mode wavelength, which can reach several tens of nm [4]. In a first experimental demonstration [5], we have shown electrical tuning over 10 nm with an applied voltage of only 6V (Fig. 2). This technique, differently from other PhC tuning methods, allows tuning also at low temperatures, as needed for integrated QIP applications.

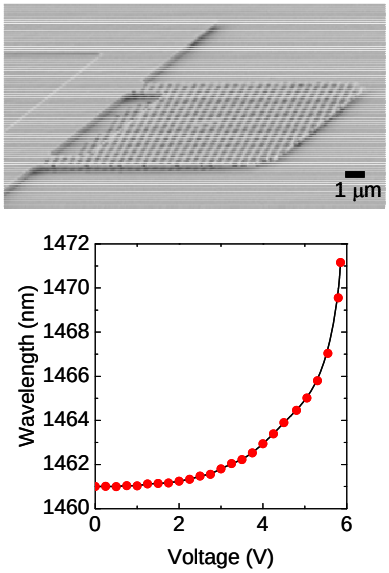


Figure 2 Top: Electron microscope image of a double-membrane tuneable PhC cavity. Bottom: Tuning curve

III. WAVEGUIDE SINGLE-PHOTON DETECTORS

Single-photon detection in GaAs waveguides can be obtained by using the "hot-spot" detection mechanism in superconducting nanowires. Ultrathin NbN films are deposited on top of a GaAs/AlGaAs ridge waveguide by sputtering, and then patterned as narrow wires (100 nm wide, tens of µm long). The evanescent field of the guided mode interacts with the wires, resulting in a modal modal absorption coefficient of several hundreds of cm^{-1}, ensuring nearly 100% absorptance. The device is cooled at 4 K and biased with a current close to the critical current of the superconducting wire. When the photon is absorbed, a region with a large population of electrons in the normal state forms, resulting in a resistance appearing in the wire, which produces a voltage pulse in the external circuit. With this structure we have demonstrated [6] waveguide detectors with quantum efficiency ≈20% and timing jitter ≈60 ps, which are very well suited for application in quantum photonic integrated circuits.

IV. CONCLUSION

We have demonstrated the main building blocks of a scalable quantum photonic integrated circuit. They are all based on the same GaAs/AlGaAs material basis and therefore can be integrated on the same chip. This should open the way to solid-state quantum processing of several tens of qubits.

ACKNOWLEDGEMENTS

This work is supported by the European Commission within the FP7 project QUANTIP and from the Dutch Technology Foundation STW, applied science division of NWO and the Technology Program of the Ministry of Economic Affairs.

REFERENCES

[1] A. Politi, M.J. Cryan, J.G. Rarity, S. Yu and J.L. O'Brien, "Silican-on-Silicon Waveguide Quantum Circuits", Science, vol. 320, pp 646-6649, 2008

[2] T. Lund-Hansen, S. Stobbe, B. Julsgaard, H. Thyrrestrup, T. Sünner, M. Kamp, A. Forchel, and P. Lodahl, "Experimental Realization of Highly Efficient Broadband Coupling of Single Quantum Dots to a Photonic Crystal Waveguide", Phys. Rev. Lett., vol. 101, 113903, 2008.

[3] T. B. Hoang, J. Beetz, L. Midolo, M. Skacel, M. Lermer, M. Kamp, S. Höfling, L. Balet, N. Chauvin, and A. Fiore, "Enhanced spontaneous emission from quantum dots in short photonic crystal waveguides", Appl. Phys. Lett., 100, 061122 (2012)

[4] M. Notomi, H. Taniyama, S. Mitsugi and E. Kuramochi, "Optomechanical wavelength and energy conversion in high-Q double-layer cavities of photonic crystal slabs", Phys. Rev. Lett., vol. 97, p. 023903, 2006.

[5] L. Midolo, P.J. van Veldhoven, M.A. Dundar, R. Notzel and A. Fiore, "Electromechanical tuning of double-membrane photonic crystal cavities", Appl,. Phys. Lett. vol. 98, p. 211120 (2011)

[6] J.P. Sprengers et al., "Waveguide superconducting single-photon detectors for integrated quantum photonic cicuits", Appl. Phys. Lett. vol. 99, p. 181110, 2011

PICs: A Commercial Future

Michael J. Wale
Oclaro Technology Ltd.
Caswell, Towcester, Northamptonshire, NN12 8EQ, UK
Mike.Wale@oclaro.com

***Abstract* — Photonic Integrated Circuit (PIC) technology offers attractive, cost-effective solutions for many applications. This paper reviews the present status of commercial exploitation and suggests new approaches to design and manufacture which could enhance availability and exploitation.**

Keywords - photonic integration, PIC, integrated optics

I. INTRODUCTION

Photonic integrated circuit (PIC) technology has now reached a high level of capability and is being exploited in important applications, particularly in telecommunications. By allowing many of the fundamental building blocks of photonic systems (optical amplifiers, lasers, modulators, couplers, waveguides, etc.) to be combined on a single chip, PICs can provide important benefits in terms of cost, size and manufacturability over solutions based on discrete elements. Such a versatile technology should have many applications across the industry. This paper examines the current status and suggests developments that could facilitate just such a market expansion.

II. CURRENT STATUS

PIC technology was originally developed in response to the needs of the telecommunications industry. In Europe, numerous collaborative R&D projects, supported by the EU, provided an impetus and support for these developments. In this paper, we shall focus particularly on PICs based on III-V semiconductor materials such as InP, which can support active functions (amplifiers, lasers) alongside modulation and passive elements such as wavelength multiplexers. InP-based PICs are now in volume production for several important applications in telecommunications, such as integrated transmitters and receivers for high-speed fibre optic links in the core of the network. Fig. 1 shows a wafer of integrated InP-based tunable laser-modulator devices [1,2] under test at Oclaro's wafer fab at Caswell, UK. These devices provide the photonic core of a tunable 10Gbit/s transceiver using the industry-standard 'XFP' format. Devices with similar functionality are presently being manufactured by at least two other companies in Europe and the USA. The demand for these and similar components is substantial and at an annual level of several hundred thousand components. Monolithically integrated solutions are rapidly displacing bulkier, more costly components based on discrete devices or combinations of less complex PICs.

As network capacity demands continue to escalate, integrated solutions will increasingly become ubiquitous. In order to achieve high spectral efficiency at data rates of 40Gbit/s, 100Gbit/s and above, the use of advanced modulation formats such as dual-polarization QPSK, with differential or coherent detection, is mandatory. Complex modulator circuits with in-phase and quadrature channels are required, as shown for instance in Fig. 2, and in the case of coherent detection, an optical network containing 90° hybrid couplers and multiple balanced photoreceivers is required. Monolithic solutions are attractive in these applications, in terms of cost, size, manufacturability and performance.

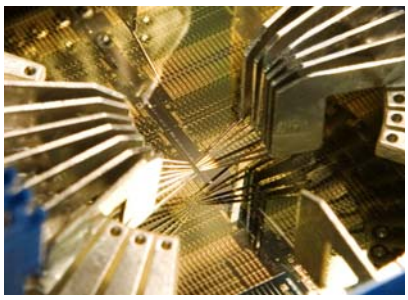


Fig. 1: Integrated InP DSDBR tunable laser-Mach Zehnder modulator devices undergoing on-wafer test

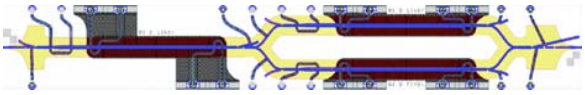


Fig. 2: RZ-DQPSK transmitter component for 40Gbit/s transponder realized in InP [3].

PIC technology is also highly attractive for multi-channel transmitters and receivers based on wavelength-division multiplexing (WDM). Fig. 3 shows a 4x28Gbit/s transmitter device featuring 'grid' tuning, i.e. all of the channels can be tuned en-bloc across the full ~40nm extent of C-band [4].



Fig. 3: Integrated tunable transmitter providing 4x28Gbit/s channels with grid-tuning.

High functionality, multi-channel, fixed-wavelength devices [5] have now been in production for some years, with applications in network nodes in WDM transmission systems.

III. CHALLENGES

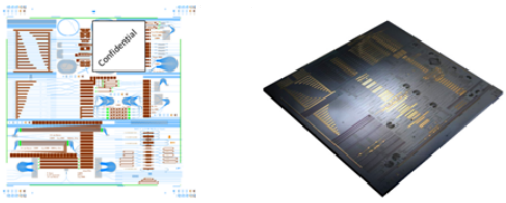
From the foregoing discussion we can readily see the importance of PIC technology within the telecommunications field. Nevertheless there are many challenges, both technical and financial [2], that face any PIC manufacturer. The fabrication processes can be complex (a tunable transmitter PIC such as those described above typically involves 5 or 6 stages of epitaxy) and, although high yields are now achieved, these devices remain demanding in terms of manufacturing expertise. The entry cost is high and the capital investments needed to maintain the necessary manufacturing infrastructure at the state of the art are very substantial. At the same time, volumes in the optical telecommunications market, although significant, are much smaller than those encountered in the silicon IC industry, which shares many of the same economic challenges. We should therefore examine whether new industrial models could be invented which could provide the basis for manufacture in higher volumes, facilitate technology access for a wider range of products and companies and thus provide the stimulus for the virtuous spiral of increased revenues and investment, lower costs and higher profitability.

IV. GENERIC INTEGRATION PLATFORMS

In order to achieve economies of scale, it will be mandatory for a wide range of products, addressing applications in different fields, to employ the same fabrication processes. Furthermore it is highly advantageous to define a generic integration platform [6], in which circuits are constructed from pre-defined building blocks (e.g. waveguides, optical amplifiers, couplers, phase shifters) contained in design libraries, rather than being designed from scratch for each new application. Sophisticated design tools will assist the designer in laying out a complex circuit based on these building blocks and in simulating its performance.

Although this is standard practice in microelectronics, it represents a radically new approach in the photonics industry. The European Network of Excellence project, ePIXnet, defined such a scenario in the early years of the present century [6] and a number of European research projects, notably EuroPIC [7] and PARADIGM [8] for InP and HELIOS for silicon photonics [9], are presently working on the task of validating this new approach.

One very attractive feature of the generic platform approach is that it facilitates the combination of different designs on a single mask set, processed in a multi-project wafer (MPW) run. This methodology is familiar in microelectronics and presently facilitated in that field by organizations such as EuroPractice [10]. An analogous way of working is now being introduced in the photonics field by the JePPIX platform for InP [11] and ePIXfab for silicon [12]. Fig. 4 shows how a set of different designs can be combined on a single mask and wafer, thereby reducing the cost for each circuit. Such an approach could widen access to PIC technology significantly and facilitate its adoption by small companies (SMEs).



Fig, 4: Sample designs in the JePPIX process: mask layout (left) and finished multi-project wafer cell (right). Illustrations c/o TU Eindhoven

Current European projects [7,8] are addressing all aspects of generic platforms in InP, from the design of the platform itself to software and design systems, and are providing experience of releasing such a platform to external designers. This work will provide a sound basis for an assessment of generic platforms as a business concept.

V. CONCLUSIONS

It is clear that PICs will continue to have a bright future for high-performance telecommunications and they show great promise for other fields, provided we can find ways to reduce entry costs, find sufficient volume in adjacent markets and thereby take this technology to higher levels of market penetration and economic viability. Present European projects are playing a vital role in exploring the potential of the generic platform approach, which could achieve just that objective.

ACKNOWLEDGMENT

The author would like to thank the partners of the ePIXnet, EuroPIC and PARADIGM projects, as well as his colleagues at Oclaro, for many valuable discussions.

REFERENCES

[1] M.J. Wale, “Photonic Integration Challenges for Next-Generation Networks”, Symposium on “InP and Si Integrated Photonics: Competition or Symbiosis?” ECOC 2009, Vienna, 21 September 2009.

[2] A. Carter, “Unlocking the value of fab ownership”, Compound Semiconductor, **16** (1), February 2010, pp. 34-37.

[3] C.F. Clarke, R.A. Griffin and T.C. Goodall, “Highly Integrated DQPSK Modules for 40 Gb/s Transmission”, Proc. Conf. Optical Fiber Communication, 2009, paper NWD3.

[4] R. Blum, “Highly Integrated InP Laser Arrays: Closing the Gap Between Datacom & Telecom”, Workshop on *Data and Telecom: Convergence of Hardware*, 37th European Conference on Optical Communication, Geneva, Switzerland, 18 September 2011.

[5] R. Nagarajan et al., “Large-Scale Photonic Integrated Circuits”, IEEE J. Sel. Top. Quant. Electron. JSTQE, **11** (1), Jan/Feb 2005, pp. 50-65.

[6] ePIXnet Steering Committee, “Towards a foundry model in micro- and nano-photonics: a vision for Europe”, available at www.epixnet.org.

[7] http://www.europic.org/

[8] http://paradigm.jeppix.eu/

[9] http://www.helios-project.eu/

[10] http://www.Europractice.org

[11] http://www.jeppix.eu

[12] http://www.epixfab.eu/

Nano-Structured Optical Glasses

N. F. Borrelli
S&T Division, Corning Incorporated
Corning N.Y. USA
Borrellinf@Corning.com

Abstract—A variety of oxide glasses and glass-ceramics that contain thermally or optically developed nanostructures will be described along with the properties that derive from the nano-phase, or structural rearrangement. The derived properties include photosensitive, photochromic, photo-adaptable color, photorefractive (induced refractive index), photo-machinable, and polarizing.

I. Introduction

Oxide glasses provide a wide range of static optical properties, like color, refractive index, dispersion, deep UV transparency to name a few. One can extend the range of properties by adding components to the glass that can be ultimately be phase separated from the matrix glass by an appropriate thermal treatment. The generic term glass-ceramics could be applied. Here for the most part the particle size of the developed phase is on the nanometer scale rendering the glass essentially transparent in spite of relatively large refractive index mismatch. The bulk of what will be discussed here involves the development nano-phases of Ag-halide, LiF, or Li-metasilicate. From these phases and with in most cases an additional optical treatment the following properties can be exhibited; photosensitive, photochromic, photo-adaptable color, photorefractive, photo-machinable, and polarizing to name the most interesting. Although we will not discuss them here, where the separated phase is crystalline then the incorporation of rare-earth or transition metal ions for laser and amplifier applications is possible.

II. List of Glass Systems and Derived Properties

In Table 1 we list the matrix glass system(s), the phase separated component, and the property exhibited. We will proceed to give examples of the properties listed above in the Table with a brief explanation of what physical processes are involved in the process as well as the some of the applications.

A. Photosensitive glasses

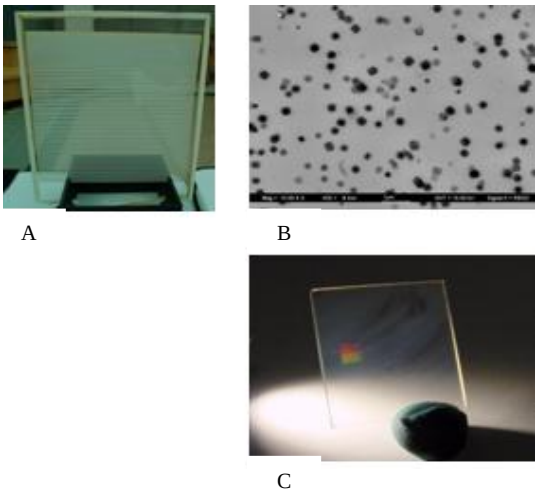
Class of alkali silicate glasses (sufficient non-bridging oxygen) that incorporate Ag^{+1} Au^{+1} or Cu^{+1} at a level of 0.01-0.1% and a photosensitizing agent usually Ce^{+3} at a level of 0.03% into the glass composition. Light exposure into the absorption of the Ce^{+3} (310nm) followed by a thermal treatment produces an image formed by Ag, (Au) nanoparticles as shown in Fig. 1.



Figure 1. Example of Ag-based (top) and Au-based photosensitive glasses

B. Augmented Photosenstive (Photorefractive and Photo-machinable)

The nanoparticles produced in the process described above can in select glasses be nucleation sites to effect phase separation leading to the formation of a nano-crystalline phase. In one case a NaF phase is produced where the particle size of the NaF nanocrystal can be controlled by the thermal treatment rendering the exposed region either opaque or transparent. In the latter case the refractive index of the exposed region is lowered, so that high resolution diffraction grating structures can be made. In Fig. 2 is shown an example of both the photo-written opaque effect and a hologram produced from the transparent effect.



A B C

Figure 2 NaF-based glasses. (A) opaque pattern, (B) fine grain particles leading to transparency, (C) hologram made from B-type samples.

Classification	matrix glass	derived phase	property
Photosensitive[1,2]	Alkali silicate	Ag, or Cu	Photo-induced color patterns
Photochromic[3,4,]	Alkali borosilicates	Ag or Cu-halides	Reversible darkening
Polarizing[5]	Alkali borosilicates	Elongated Ag or Cu-halides +(reduction)	Waveplates polarizers
Photoadaptive[6]	Alkali borosilicates	Ag halides	Change color corresponding to exposure color
Photorefractive[7]	Alkali silicate	NaF	UV-induced refractive index change after HT
Photrefractive[8,]	Ge-silicate	Structural rearrange	Direct deep UV induced index change
Photo-machinable[2]	Li-alumino silicate	$Li_2O.SiO_2$	Preferentially etched And lens arrays

Table I Summary of Phenomena.

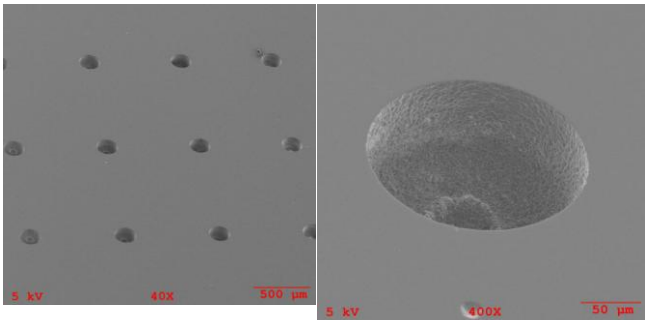


Figure 3 Example of photo-machinable Fotoform ™.

In another example the glass the phase produced that is photo-nucleated is a Li-meta-silicate phase. This phase develops an overlapping dendritic morphology which is 20 times more soluble in acid than that of the unexposed glass leading to a method to photo-machine patterns. An example of making wells using this material is shown in Fig. 3. Another utilization of this material/process as a consequence of the fact that the crystalline phase is denser than the unexposed glass is able to fabricate microlenses [9]. The method involves exposing through a mask where a circular region is blocked. During the thermal treatment to 600C the denser surround squeezes the soft glass out and surface tension produces the spherical surface (Fig. 4).

C. Photocromic

There are a special class of glasses that allow the incorporation of Ag and halogens then when thermally treated form a nano-dispersion of silver-halide particles. Analogous the photographic process, when exposed to UV-blue light the glass darkens from the absorption produced by the photo-reduction of Ag on the Ag-halide particle. This darkening and fading behavior is shown in Fig. 5.

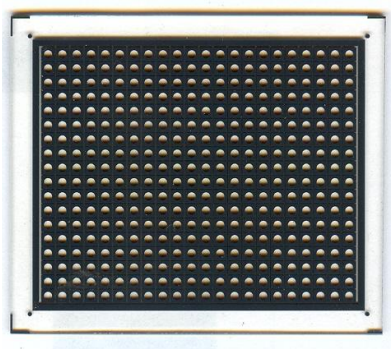


Figure 4 Example of lens array.

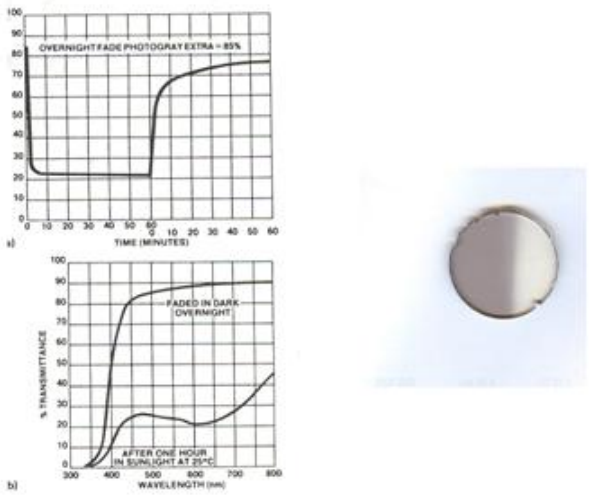


Figure 5 Example of darkening and fading of a photochromic glass.

Unlike the photographic process the absorption in this case is reversible because the hole is not trapped so it can diffuse and ultimately recombine with the reduced Ag.

D. Polarizing Glass

The process described above for the formation of Ag-halide nanoparticle in glass was the basis for another useful optical material, namely a polarizer. After the Ag-halide phase is produced by the thermal development the glass is reheated while being subjected to a load (uniaxial stress) at around the softening temperature. This elongates the glass and in the process applies a shear stress to the then liquid Ag-halide particle causing it to elongate. Upon cooling one the elongated Ag-halide is frozen in as an elliptical shape the extent of elongation (aspect ratio) is dependent on how much stress was applied. The elongated silver halide particle is then chemically reduced to Ag-metal by a thermal treatment in pure H_2. The anisotropy in shape produces two distinct absorption bands corresponding to the two surface plasmon resonances, parallel and perpendicular to the long axis of the particle as shown in Fig. 6. Using this process one is able to make polarizing glass with >50db extinction over the 800-2000nm wavelength range. (Polarcor™)

E. Photorefractive

Photorefractive in this context refers to permanent UV-induced refractive index changes in glass. In Table I we have listed two different glasses and the methods by which the photorefractive effect is achieved. The first is related to the glass mentioned in section B as that where a NaF nano-phase is photo-initiated. By a slight modification of the composition and a different thermal development schedule one can maintain the nanoparticle small enough to render the glass transparent. Because the refractive index of NaF is 1.32, the exposed and thermally developed region will have an overall lower refractive index than the unexposed region; order of 10^{-4} to 10^{-5}. The permits holographic patterns to be made (see Fig. 2C) The other photorefractive glass has an entirely different mechanism from the one described above. It is based on the Fiber Bragg Grating (FBG) phenomenon. The mechanism has been much conjectured, especially the augmented molecular H_2-impregnated version, but it inarguably involves the optical alteration of Ge bonding in the otherwise silica network.[10]We have exhibited the bulk glass version of this phenomenon; that is we made basically a $xGeO_2$-$(1-x)SiO_2$ composition. The exposure uses a spatially filtered KrF 248nm laser through a silica phase mask to produce the grating. The induced refractive index that can be achieved is of the order of 0.001. An example of a grating performance made on the glass is shown in Fig. 7.

F. Photoadaptive

This behavior refers to phenomena whereby the glass color or state of polarization is altered permanently by the exposure to light. In an alkali boro-silicate glass one can initiate a process that is essentially a combination of the photochromic and photosensitive mechanisms described above. The glass after

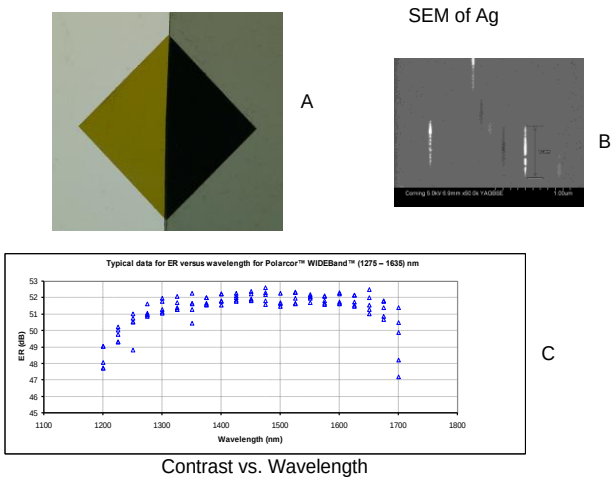


Figure 6 Polarizing glass; (A) visual contrast, (B) SEM of elongated silver particles

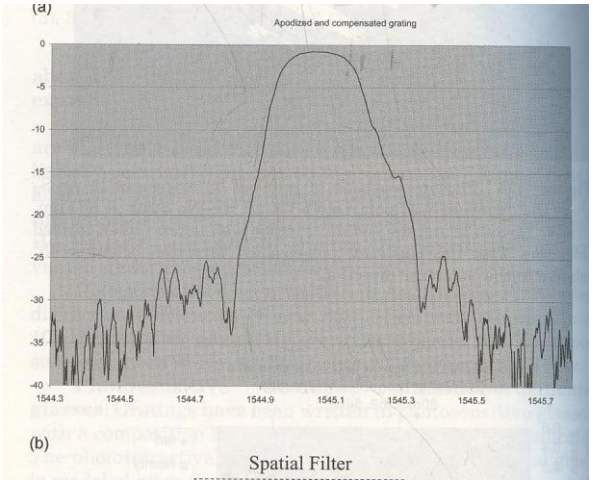


Figure 7 example of the performance (db vs. wavelength) of a grating made in the Ge-silicate glass.

heat treatment develops an Ag-halide phase; (blue curve in Fig. 8B and lowest band of Fig. 8A). The absorption feature is attributed to silver nanoparticles on the Ag-halide particle. Exposure to Hg-lamp (310nm) produces a pink color (middle band of Fig. 8A) which is not reversible (yellow curve of Fig. 8B);.This corresponds to some kind of rearrangement of the Ag on the Ag-halide particle; (note the appearance of two absorption peaks) Exposure to a black light 365nm source produces a reversible photochromic effect (not shown). Further exposure to a pulsed 355nm laser produces yet another altered absorption state (pink curve of Fig. 8B and upper band in Fig. 8A) which is a "bleaching" effect. A dichroic behavior can be produced by an exposure to the polarized Ar-ion 508nm laser (Fig. 8C).

III. DISCUSSION

We have described a wide variety of optical effects in a number of glasses attributable to photo-thermal induced nano-

structures in the respective glass. What is common to all of them derives from the fact that glass presents a multi-component system from which a number of stable and meta-stable phases can be produced either thermally, or by a combination of heat and light. These induced phases often, more than not impart changes in either the optical, chemical, or mechanical properties from the mother glass. A number of the above glasses showing the derived properties have been commercialized under trade names like *Photogray Extra™ Fotoform™ FotaLite™ and Polarcor™*. Clearly because of limited space detailed description of the different phenomena is not possible. In any event the references attached will contain more detail. Ref. [10] below contains material relevant to a number of the effects discussed in more detail.

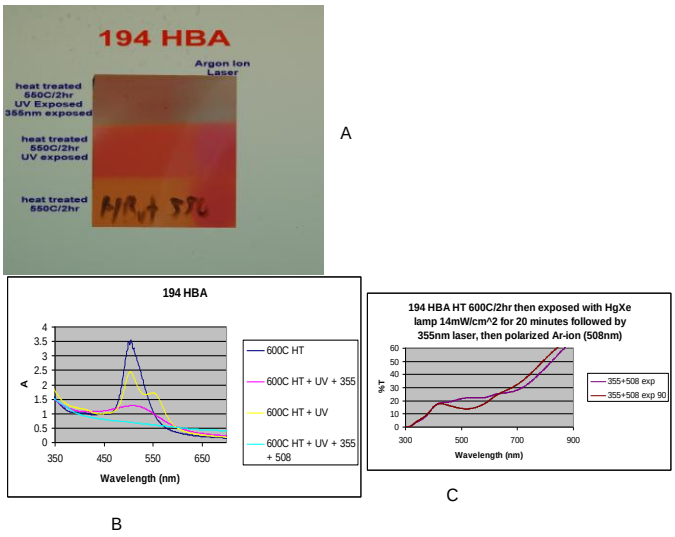


Figure 8 Examples of the photo-adaptive behavior, (A) color change as noted and described in text, (B) corresponding absorption spectra for the conditions noted, (C) evidence of dichotic behavior when bleached.

ACKNOWLEDGMENTS

The author thanks the members of the technical staff of the Corning Incoporated research laboratory, both past and present for their contribution to this paper.

REFERENCES

[1] S.D. Stookey, "Colorization of Glass by Ag, Au, Cu" J. Am Cer. Soc. 32,246, 1949.

[2] N. F. Borrelli and T.P. Seward III, Photosensitive glasses and glass-ceramics".

[3] W.H. Armistead and S. D. Stookey US Patent 3 208 860.

[4] R. J. Araujo, Treatise on Materials Science and Technology, Vol 12 Academic Press, 1977.

[5] N. F. Borrelli and T.P. Seward, "Polarizing Glass" New Glass. 37(1) page 27, 2012.

[6] N. F. Borrelli and T.P Seward, "Photo-induced optical anisotropy and color adaptation in silver-containing glasses," Appl. Phys. Lett. 34(6), 395 , 1979.

[7] Corning Photorefractive Glass, Photonic Materials, Product sheet, March 2003.

[8] N. Borrelli et al. "UV sensitivity in conventionally melted Germanium-silicate Glass", SPIE, San Diego, 2000.

[9] N. F. Borrelli et al. "Photolytic technique for producing microlenses in photosensitive glass" Appl. Opt. 24, 2520. 1985.

[10] N. F. Borrelli, Microoptics Technology, 2nd ed, pgs 286-290, Marcel Dekker 2005.

Towards surface-plasmon generation by electrical injection at telecom wavelengths with a semiconductor device

D. Costantini, A. Bousseksou, **R. Colombelli**
Institut d'Electronique Fondamentale
Univ. Paris Sud et CNRS, UMR8622
91405 Orsay, France

L.Greusard, R. Rungsawang, Y. De Wilde
Institut Langevin
ESPCI ParisTech, CNRS UMR 7587
75231 Paris Cedex 05, France.

A. Accard, J. Decobert, G-H. Duan
Alcatel-Thales III-V Lab,
route de Nozay, 91461 Marcoussis cedex, France.

T. Zhang, S. Callard
Institut des Nanotechnologies de Lyon
Site Ecole Centrale de Lyon
36 Avenue Guy de Collongue, 69134 Ecully, France

***Abstract*— We propose and demonstrate a strategy to electrically generate surface-plasmons (SP) in the telecom range. The core idea is that properly designed semiconductor laser active regions might compensate the large losses that SPs experience in the telecom wavelength range. We show that laser devices based on tensile-strained semiconductor quantum wells - hence emitting transverse magnetic polarized light - are suitable for plasmon generation *via* electrical injection. Experimental evidence is obtained using near-field microscopy measurements.**

Surface Plasmon Polariton, generation, electrical injection

I. INTRODUCTION

Several surface plasmon polariton (SPP) passive components have been demonstrated to date, showing attractive performances for extreme light confinement and high bandwidth modulation [1,2]. On the other hand, the lack of a viable technology to compensate the large optical losses, typical of SPPs, partly limits practical applications. As a matter of fact, efforts have been recently devoted to the development of active SPP devices, for the their generation, amplification [3] and stimulated emission [4,5]

II. A SEMICONDUCTOR-BASED APPROACH

We propose a semiconductor active region which enables plasmonic active devices in the telecom wavelength range. Plasmonic devices based on planar architectures typically require transverse magnetic (TM) polarized light. To satisfy this requirement at λ=1.3-1.55 µm our choice fell on diode lasers based on tensile-strained InGaAlAs semiconductor quantum wells, which operate in TM polarization as demonstrated in Ref. [6]. Furthermore, this semiconductor gain medium is compatible with electrical injection (end-fire coupling architectures can be implemented relatively easily, as Ref. [7] shows for longer, mid-infrared wavelengths). This characteristic represents an advantage for practical uses and for device integration.

In this work, we build on the previous demonstration of mid-infrared (λ=7.5 µm) SPP generation with a compact semiconductor device [8]. Integrated SPPs generation is obtained by coupling a laser source with a plasmonic waveguide *via* a judiciously designed coupler grating section which compensate for the missing momentum. In order to transfer the concept at short telecom wavelengths, we have performed in-depth numerical analysis to study and maximize the coupling efficiency by playing on the device parameters [9] (Fig. 1).

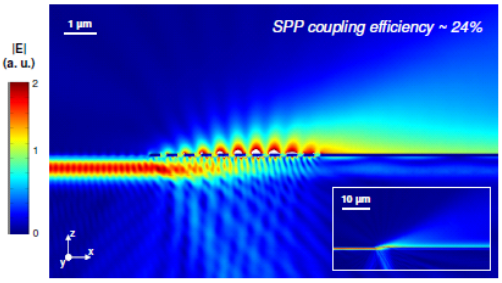


Fig.1. Finite element simulation presenting the absolute value of the electric field in the coupler design. The waveguided mode (injected from the left) is efficiently converted into a plasmonic mode (propagating towards the right).

We have then experimentally elucidated the effect of the proximity of the metallic contacts to the device active region [10]. This is a crucial ingredient: in order to efficiently couple the laser light with the propagating SPPs it is necessary to enhance the interaction between the metal and the waveguided mode. In turn, this enhanced interaction leads to increased waveguide losses. We have identified and experimentally developed a structure which represents an optimal trade off between coupling efficiency and optical loss. As a second step, we have realized 1st-order metallic DFB lasers, which constitute one of the building blocks of the SPP generator. Figure 2 shows the correct device behavior, with a single mode emission that correctly tunes (from λ=1288 to 1322 nm) with the grating period. Note: the laser development allowed us to experimentally measure the differential gains which can be expressed by this active cores. They are in the hundreds of

cm^{-1}/kA. These extremely high values are promising in view of developing loss-compensated metallic meta-structures, or even semiconductor-based spasers.

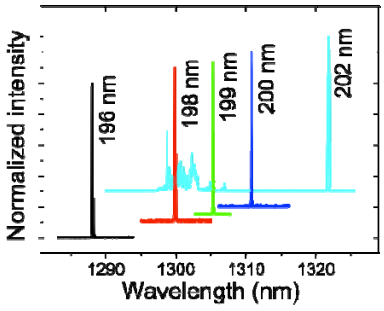


Fig. 2 Single mode emission for five different periods of the DFB grating (from p=196nm to p=202nm).

Finally, we demonstrate SPP generation by providing the *electrically-pumped* version of the slit-doublet experiment [11] in the near-field (Fig. 3). Two coupler gratings and a central passive plasmonic waveguide are placed between two identical DFBs, which act as laser sources. Counter-propagating SPPs are injected by the couplers – as schematized in Fig. 3a - and plasmonic standing waves appear on the central passive section. The SPP generation by electrical injection is demonstrated in Fig 3c, which shows the noteworthy result of transmission SNOM measurements on the surface of the passive waveguide section. In order to detect beyond any doubt the presence of plasmonic waves in the near field, we will present NSOM measurements performed with two additional approaches: aperture less scattering-NSOM, and fiber-based near-field microscopy.

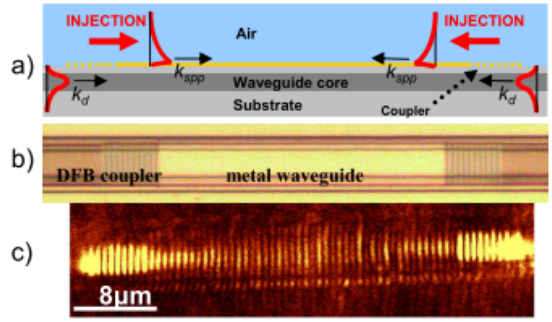


Fig3. a) Schematic (lateral view) of the SPP generator device. Red curves represent the absolute value of the electric field of the laser and the SPP mode. b) Optical image (top view) of the SPP generator device. c) Near field measurement of the passive waveguide surface. Oscillations of the plasmonic standing wave on the passive metallic waveguide are clearly visible.

In the final part of the talk we will discuss a topic which can be of interest for device applications, i.e. the reduction of plasmonic ohmic losses *via* the sole patterning of the top metal layer, and initial results will be presented. We will also discuss the perspective which this integrated approach - based on semiconductor active cores - opens up for the development of electrically pumped semiconductor spasers (Surface Plasmon Amplification by Stimulated Emission of Radiation).

[1] T. W. Ebbesen, C. Genet, and S. I. Bozhevolnyi, "Surface plasmon circuitry," *Phys. Today,* vol. **61**, issue 5, pp. 44, 2008.

[2] D.Gramotnev and S. I. Bozhevolnyi, "Plasmonics beyond the diffraction limit," *Nat. Phot*., vol **4**, pp. 83, 2010.

[3] P. Berini and I. De Leon, "Surface plasmon–polariton amplifiers and lasers" *Nat. Phot*., vol **6**, pp 16–24, 2012.

[4] M. T. Hill, M. Marell, E. S. Leong, B. Smalbrugge, and C.-Z. Ning, "Lasing in metal-insulator-metal sub-wavelength plasmonic waveguides" Opt. Exp., vol 17, no 13, pp.11107, 2009.

[5] S.-H. Kwon, J.-H. Kang, C. Seassal, S.-K. Kim, P. Regreny, Y.-H. Lee, C.M. Lieber, and H.-G. Park, " Subwavelength Plasmonic Lasing from a semiconductor nanodisk with silver nanopan cavity", Nano Lett. 10, 3679 (2010)

[6] J. Decobert, N. Lagay, C. Cuisin, B. Dagens, B. Thedrez, and F. Laruelle, "MOVPE growth of AlGaInAs–InP highly tensile-strained MQWs for 1.3 mm low threshold lasers," Journal of Crystal Growth, vol. **272**, pp. 543, 2004.

[7] J.-P. Tetienne, A. Bousseksou, D. Costantini, R. Colombelli, A. Babuty, I. Moldovan-Doyen, Y. De Wilde, C. Sirtori, G. Beaudoin, L. Largeau, O. Mauguin and I. Sagnes, "Injection of midinfrared surface plasmon polaritons with an integrated device," *App. Phys. Lett*., vol **97**, pp. 211110, 2010.

[8] A.Babuty, A. Bousseksou, J.-P. Tetienne, I. Moldovan Doyen, C. Sirtori, G. Beaudoin, I. Sagnes, Y. De Wilde, and R. Colombelli, "Semiconductor Surface Plasmon Sources," *Phys. Rev. Lett*., vol. **104**, pp. 226806, 2010.

[9] J.-P. Tetienne, A. Bousseksou, D. Costantini, Y. De Wilde, and R. Colombelli, " Design of an integrated coupler for the electrical generation of surface plasmon polaritons", Opt Exp., vol. **19**, no. 19, pp. 18155-18163, 2011.

[10] D. Costantini, A. Bousseksou, M. Fevrier, B. Dagens, R. Colombelli, "Loss and gain measurements of tensile-strained quantum well diode lasers for plasmonic devices at telecom wavelengths", IEEE, Journal of Quantum Electronics, vol **48**, pp. 73. 2012.

[11] L Aigouy, P. Lalanne and J. P. Hugonin, G. Julie and V. Mathet, M. Mortier " Near-Field Analysis of SurfaceWaves Launched at Nanoslit Apertures", *Phys. Rev. Lett,*vol **98**, 153902, 2007.

Graphene: a novel platform for capturing and manipulating light at the nanoscale

Graphene, a two-dimensional sheet of carbon atoms, has recently emerged as a novel material with unique electrical and optical properties. Graphene has zero band gap, high-mobility charge carriers with an effective mass of zero and - despite its thickness of a single atomic layer - it still absorbs significant (~2.3%) light in the visible and near infrared region. Because these unique characteristics are all present in one material, graphene has great potential for opto-electronic applications, such as ultrafast photo-detection and optical switches.

In this talk, I will review recent experimental work on exploiting graphene as a host for guiding, switching and manipulating light and electrons at the nanoscale [1,2]. This is achieved by exploiting surface plasmons: surface waves coupled to the charge carrier excitations of the conducting sheet. Due to the unique characteristics of graphene, light can be squeezed into extremely small volumes and thus facilitate strongly enhanced light-matter interactions. I will discuss recent observations of propagating and localized optical plasmons in graphene nano-structures. The plasmon wavelength can be tuned and plasmon propagation can even be switched on and off in-situ, simply by tuning the carrier density by electrostatic gates. These results pave the way towards ultrafast modulation of nanoscale optical fields, resonantly confined in graphene nano-structures or propagating along graphene ribbons.

The second part of the talk is devoted to a novel hybrid graphene-quantum dot photodetector [3] which exhibits a gain mechanism that can generate multiple charge carriers from one incident photon. Strong and tunable light absorption in the quantum-dot layer creates electric charges that are transferred to the graphene, where they recirculate many times due to graphene's high charge mobility and long trapped-charge lifetimes in the quantum-dot layer. We demonstrate a gain of 10^8 electrons per photon and a record-high responsivity of 10^7 A/W. Our devices also benefits from gate-tunable sensitivity and speed, spectral selectivity from the short-wavelength infrared to the visible, and compatibility with current circuit technologies.

References

[1] J. Chen, M. Badioli, P. Alonso-González, S Thongrattanasiri, F Huth, J Osmond, M. Spasenović, A. Centeno, A. Pesquera, P. Godignon, A. Zurutuza, N. Camara, J. Garcia de Abajo, R. Hillenbrand, F. Koppens, “Optical nano- imaging of gate-tuneable graphene plasmons”, arXiv 1202.4996 (2012)
[2] F. Koppens, D. Chang, J. García de Abajo, “Graphene Plasmonics: A Platform for Strong Light–Matter Interactions”, Nano Letters 11, 3370–3377 (2011).
[3] G. Konstantatos, M. Badioli, L. Gaudreau, J. Osmond, M. Bernechea, P. Garcia de Arquer, F. Gatti, F. Koppens, “Hybrid graphene-quantum dot phototransistors with ultrahigh gain”, Nature Nanotechnology (in print). See also arXiv 1112.4730 (2011).

High aspect ratio $LiNbO_3$ photonic crystals

Toward 3D $LiNbO_3$ micro and nano structures

Nadège Courjal, Clément Guyot, Gwenn Ulliac, Hui-Hui Lu, Benattou Sadani, Fadi Baida, Maria-Pilar Bernal
FEMTO-ST Institute, University of Franche-Comté
Besançon, France
Nadege.bodin@univ-fcomte.fr

***Abstract*—We report easy to implement techniques for the fabrication of high aspect ratio $LiNbO_3$ photonic crystals. The methods rely on optical grade dicing followed by focused ion beam (FIB) milling. A 2D photonic crystal with an extinction ratio of -14dB is demonstrated. We show how the techniques can be combined for the development of 3D photonic crystals.**

$LiNbO_3$, ridge waveguides; photonic crystals,

I. INTRODUCTION

Writing photonic crystals (PhCs) in $LiNbO_3$ waveguides appears as a very attractive way of developing ultra-compact optical processing devices [1-2]. All the reported dynamic $LiNbO_3$ PhCs are integrated on annealed proton exchange (APE) waveguides. The photonic bandgaps that are experimentally observed in these PhCs exhibit rough spectral edges, whereas sharp bandgap edges would enable reduced driving power. This practical problem results from the conical shape of the holes and from the weak confinement of the optical guided mode [3].

To circumvent this issue, thin films of $LiNbO_3$ have been recently developed [4]. These films allow a tight confinement of the optical mode. An improvement of the photonic bandgap edge sharpness is consequently expected. But the fabrication of thin layers of $LiNbO_3$ is a difficult task that implies in particular ion implantation. In this work we propose easy-to-implement alternative methods that improve the extinction ratio of $LiNbO_3$ based PhCs. These methods open the way toward 3D $LiNbO_3$ micro and nanostructures.

II. DESCRIPTION OF THE PROCESS

The fabrication process can be used indifferently with X-cut, Z-cut $LiNbO_3$ substrates, and slice-cut samples. A first step consists in fabricating a planar waveguide either by Ti-indiffusion, by Annealed Proton Exchange (APE) or by Ti-APE which is a combination of both techniques. The ridge structure is realized in a second step by "optical grade dicing" with a circular precision saw (DISCO DAD 321) as described in [5]. The use of a dicing saw for the development of ridges had already been mentioned notably in [6], but the reported aspect ratios (width/depth) were not as high as what can be seen in Fig. 1(a). Indeed, we have managed to fabricate ridges with a width of 1µm and a depth of 526µm. Fig. 1(b) shows that the light can be guided through such extreme structures.

Even if this performance is not needed for the implementation of optical waveguides with low losses, it provides nevertheless an idea of the enormous capability of the method, notably for the development of thin $LiNbO_3$ layers. We have shown in [5] that propagation losses as low as 0.5dB/cm may be obtained through Ti-diffused ridge waveguide with a top width of 6µm and a depth higher than 20µm.

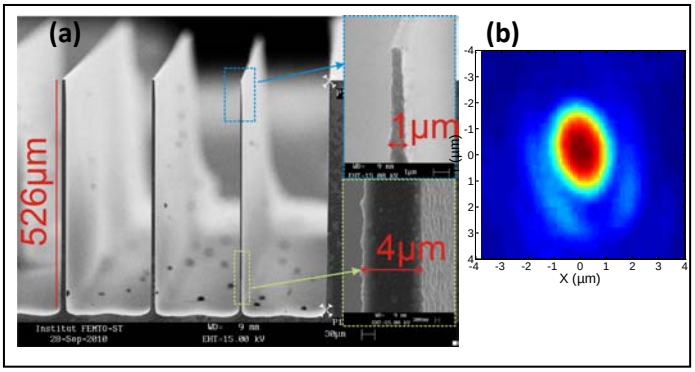


Figure 1. (a) SEM view of the ridge structures with a depth of 526 µm. The insets show zoom views of the thinnest ridge of the serie. (b) Output mode of a 526µm deep 6µm large ridge waveguide made by Ti-indiffusion followed by proton exchange.

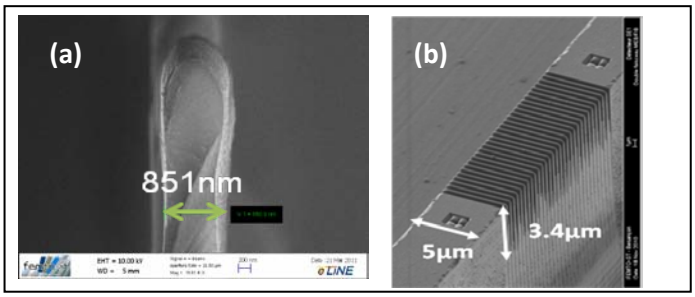


Figure 2. SEM views of ridge structures with a depth of 35 µm. (a) Ridge obtained by optical grade dicing followed by Ti-indiffusion. (b) Bragg gratings fabricated by FIB milling the top of the ridge.

In Fig. 2(a), we show that the top corner of the ridge can be smoothed if the Ti-indiffusion step is done after dicing the ridge. The process also helps reducing the roughness of the walls to 20nm. In what follows we propose to integrate PhCs into ridge waveguides by FIB writing

III. HIGH ASPECT RATIO AND 3D $LiNbO_3$ PHCS

Firstly, the ridge is diced in a Ti-indiffused planar waveguide. The PhC is then written on the top of the ridge by FIB milling. If applied to the fabrication of 1D-PhCs, the method can lead to 3.4µm deep gratings with a period of 1.1µm, as illustrated in Fig. 2(b). But from the resulting transmission response, we can conclude that this aspect ratio is not sufficient enough for obtaining large extinction ratios. This is due to the weak vertical confinement of light within the Ti indiffused waveguide. Similar results have been observed in 2D-PhCs written in Ti-indiffused ridge waveguides [7]. In what follows, the 2D-PhC is written on a Ti-APE ridge waveguide.

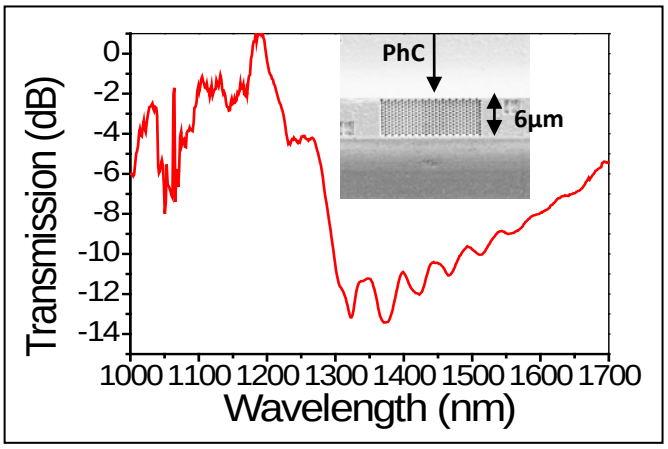


Figure 3. Normalised transmission spectrum through the PhC (TE wave). Inset : SEM view of the PhC structure.

The PhC is made of a triangular lattice of 12x15 holes. It is designed to have a spectral gap between 1300 nm and 1800 nm for TE-polarized waves. The diameter of the holes is D=312 nm, and the periodicity of the lattice is a=520 nm. The normalized transmission response through the PhC is measured by means of a LEUKOS® supercontinuum source and a Q8381 Advantest® Optical Spectrum Analyzer (OSA) as described in [7]. In Fig. 3, the transmission shows a photonic gap over the wavelength range [1300 nm-1700 nm[, which is in good agreement with numerical predictions. The extinction ratio is measured to be -14dB, which represents a significant improvement in comparison with the -2.2dB previously reported [7]. This improvement is due to a larger interaction length and to a stronger light confinement within the Ti-APE ridge waveguide.

IV. HIGH ASPECT RATIO AND 3D $LiNbO_3$ PHC

The method can advantageously be applied to the fabrication of 3D-PhCs if the ridge is tilted with an angle of 90° during the FIB milling step. A PhC can indeed be engraved on the edge of the ridge. Preliminary tests dedicated to the fabrication of Bragg gratings show that a large improvement of the aspect ratio can be reached in comparison with what is achieved by FIB milling the top of the waveguides. Indeed, the conical shape of the holes results from the redeposition of $LiNbO_3$ on sidewalls during the FIB milling process. This redeposition is partially avoided when the beam goes through the entire thickness of the ridge, because a part of the milled material is evacuated at the opposite side of the ridge.

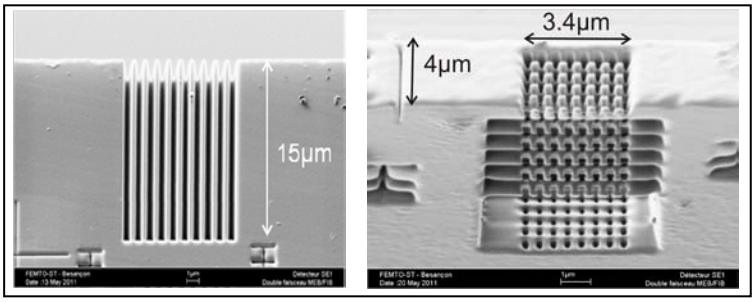


Figure 4. SEM views of $LiNbO_3$ PhCs made by FIB milling the edge of the ridge. (a) Deep gratings. (b) 3D $LiNbO_3$ PhC

This is illustrated in Fig. 4(a), where we can see gratings with a depth of 15µm and a period of 1.1µm. Moreover, this approach gives promising perspectives toward the fabrication of $LiNbO_3$ 3D-PhCs as can be seen in Fig. 4(b).

As a conclusion, we have shown that complex micro and nanostructures can be integrated in $LiNbO_3$ optical waveguides by combining optical grade dicing and FIB milling. In the presentation, we will show detailed optical characterization of the transmitted and reflected spectra through the 2D-PhCs. Alternative methods based on reactive ionic etching will also be presented.

ACKNOWLEDGMENT

The authors would like to acknowledge E. Lantz, L. Froehly, and T. Sylvestre for fruitful discussions. This work was supported by the Conseil general de Franche Comté under the grant 2011C-07322.

REFERENCES

[1] M. Roussey, M.-P. Bernal, N. Courjal, D.V. Labeke, F.I. Baida, and R. Salut, “Electro-optic effect exaltation on lithium niobate photonic crystals due to slow photons,” Appl. Phys. Lett., vol. 89, pp. 241110, 2006

[2] N. Courjal, S. Benchabane, J. Dahdah, G. Ulliac, Y. Gruson, and V. Laude, “Acousto-optically tunable lithium niobate photonic crystal,” Appl. Phys. Lett., vol. 96, pp. 131103, 2010

[3] G.W. Burr, S. Diziain, and M.-P. Bernal, "The impact of finite-depth cylindrical and conical holes in lithium niobate photonic crystals," Opt. Express , Vol. 16, pp. 6302-6316, 2008

[4] R. Geiss, S. Diziain, R.Iliew, C. Etrich, H. Hartung, et al., “Light propagation in a free-standing lithium niobate photonic crystal waveguide,” Appl. Phys. Lett., Vol. 97, pp. 131109, 2010

[5] N. Courjal, B. Guichardaz, G. Ulliac, J.-Y. Rauch, B. Sadani, H.-H. Lu, and M.-P. Bernal, “High aspect ratio lithium niobate ridge waveguides fabricated by optical grade dicing,” J. Phys. D: Appl. Phys., Vol. 44, pp. 305101, 2011

[6] Kiminori Mizuuchi, Tomoya Sugita, Kazuhisa Yamamoto, Tatsuo Kawaguchi, Takeshi Yoshino, and Minoru Imaeda, "Efficient 340-nm light generation by a ridge-type waveguide in a first-order periodically poled MgO:$LiNbO_3$," Opt. Lett., Vol. 28, pp. 1344-1346, 2003

[7] N. Courjal, J. Dahdah, G. Ulliac, P. Sevillano, B. Guichardaz and F. Baida, “Optimization of $LiNbO_3$ photonic crystals: toward 3D $LiNbO_3$ microcomponents,” Optics Express, Vol. 19, pp. 23008, 2011

Portable Micro-Ring Resonator Based Frequency Combs for Optical Frequency Metrology

Chris Lee[1], Sai T Chu[1] and Edwin Y.B. Pun[2]
[1] Dept. Physics and Mat. Sci; [2] Dept Elect. Engr.
City University of Hong Kong
Tat Chee Avenue, Kowloon Tong
Hong Kong, China SAR
saitchu@cityu.edu.hk

Joss Bland-Hawthorn and Sergio Leon-Saval
Institute of Photonics and Optical Science
School of Physics A28
The University of Sydney, NSW 2006
Australia

***Abstract*— A temperature stabilized CMOS-compatible frequency comb based on an integrated optical micro-ring resonator is demonstrated. The instrument operates in the wavelength interval 1520-1600 nm with a wide free spectral range of 577 GHz. By embedding a highly sensitive "resistive thermal device" (RTD) on the surface of the chip to provide temperature feedback to the thermal electric cooler, the bench top unit achieves temperature stability of ~ 5:10^7 over a 24 hour period with good power stability. Our approach reduces the cost and complexity of existing high precision frequency combs currently used in the fields of metrology, remote sensing and stellar spectroscopy where high stability is required for prolonged periods of time.**

Keywords-component; Integrated optics; micro-ring resonator; Frequency comb; metrology

I. INTRODUCTION

With the emergence of frequency combs used for precision metrology over the past decade, there has been a pressing need to improve on the already present techniques that are available from optical clocks to high precision spectroscopy [1]. Of particular interest are the measurement of radial velocities that would be indicative of stellar phenomena, and the existence of exoplanets [2]. These measurements would require a comb that has a free spectral range (FSR) that is large enough to be able to be resolved accurately and calculated for easily, but would also need a long-term stability in order to eliminate drift and to be able to allow for precise measurements over an extended period of time [2-4]. In this paper we will investigate the compact micro-ring resonator as turnkey frequency comb source that is capable of generating a large FSR while maintaining a thermal stability for an extended period of time. Our results show that through the use of a thermoelectric cooling (TEC) device mounted in series with a resistive thermal device (RTD) has been able to not only maintain thermal stability, but also to rectify thermal imbalances, when they exist.

II. DEVICE CONCEPT AND FABRICATION

Figure 1A shows the schematic of the new device where the generation of the optical frequency comb signal arises from a combination of a wide band amplified spontaneous source (ASE) covering both C and L band between 1520 nm to 1620 nm and a micro-ring resonator. The PBS is used to linearize the ASE output and allow the polarization to be tuned for more versatility in measurement [8].

The integrated resonator device is mounted on the TEC, and is controlled and relayed with the RTD. The light source could easily be replaced with a fiber laser or filtered high power source, which would allow for a broader comb bandwidth, and could allow the comb spectrum produced to span an octave [5, 7]. The temperature dependence of the RTD-TEC combination can be directly measured without knowledge of the stability of the source. The electronic circuitry and power supply, along with all the optical components are fitted inside a standard high 19" rack mount. A photograph of the fabricated device is shown in Figure 1B.

The resonator used has a 47 μm radius and was fabricated with Hydex® high index core material (n=1.7), produced from chemical vapor deposition (CVD) onto a silica substrate similar to those reported in [5].

III. MEASUREMENT RESULTS

Figure 2 shows the output spectrum of the frequency comb with FSR of 577 GHz (4.6 nm) and Q factor of ~ 1x10^5, an acceptable spacing in order to achieve well-spaced peaks for astrophysical observations. To investigate the stability of the frequency comb, the output of the comb generator is monitored by a wavelength meter (HP 86120C). From the stability that is present within the device, measurements taken over a 24-hour period indicate that the device maintain its stability this period. Figure 3 show the ambient temperature and wavelength stability over a 24-hour monitoring period. From these data, it is apparent that the temperature can be stabilized within the TEC-RTD feedback component, and that the operational stability resulted in a wavelength fluctuation that was within 5 pm (min to max) with a standard deviation of less than 1 pm. These results show that this device's performance can produce a comb that is capable to measure to within 100 m/s for radial velocities. Furthermore, the longer-term stability shows that the device can operate in the range of hours to days, where other devices have only been able to maintain for much shorter time scales [6].

Although the current stability result needs to be improved by approximately 100 times for it to satisfy the detection

requirement of radial velocities of exoplanets [2-4], stability can be improved by an increase of the number of resonant peaks, which has a correction factor of sqrt(# of peaks), and by improving the TEC design. With the device as operated within this experiment, it can be expected that by increasing the TEC-RTD feedback array to a two-stage TEC-RTD feedback, one can effectively increase the stability to a higher degree for a longer period of time. With the single stage, there was a sufficient lag within the response to the temperature reduction, which could and did have a pronounced effect on the wavelength stability (Figure 3). By increasing the TEC to a dual stage TEC, this lag could be reduced, as the temperature spikes would be greatly managed and reduced as well. This should result in less of an extreme for thermal stabilization at a given temperature.

IV. Conclusion

We have shown that a frequency comb created from an ASE light source pumping a micro-ring resonator is capable of maintaining both a good FSR spacing and a high temperature stability. Furthermore, due to the dual pumping nature of this comb to achieve C and L band emission, the comb can be tuned in order to further flatten the profile of the comb output [9]. By having good FSR, small linewidth, flattened profiling and good temperature stability, this device should perform well in attaining measurements of radial velocities within astronomical fields. Additionally, with the reduced size and cost of this device, its versatility can be capitalized upon and can be made part of smaller observational stations, increasing the adaptability of taking these measurements in optical metrology.

Acknowledgment

This work is funded by the City University of Hong Kong Applied Research Grant, Project Number 9667039. STC thanks Amonics Ltd for their help in the assembly of the instrument.

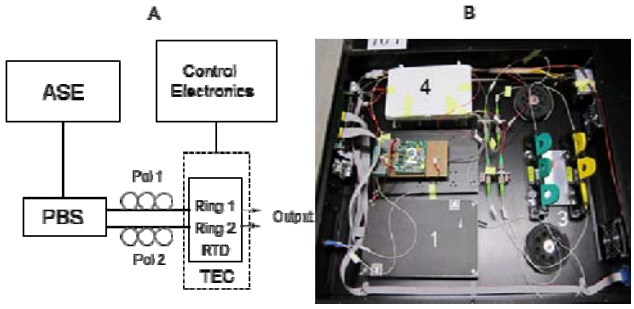


Figure 1 Fabricated portable frequency comb device. A) Schematic of the device where the frequency comb is generated from the micro-ring resonator response by the ASE excitation. B) A photograph of the frequency comb where 1 – ASE source, 2 – micro-ring resonator device, TEC and control electronic, 3 – polarization controller, 4 – PBS and fiber management.

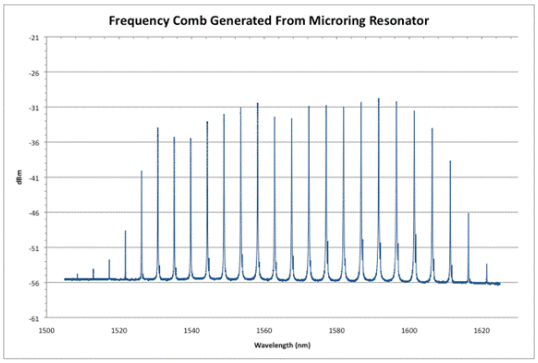


Figure 1 Frequency Comb signal from the resonator-based Er-doped ASE device. The comb effectively spans both the C and L band, and can be tuned for increased flatness via two LD pump diodes.

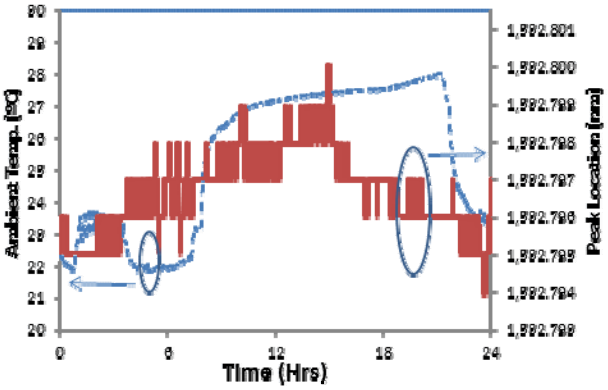


Figure 3 Stability of the frequency comb location drift over the monitoring period plot along with the ambient temperature. The min to max drift of the measured data is within 5 pm with one sigma at 1 pm.

References

[1] Th. Udem, R. Holzwarth, T. W. Hänsch. Nature 416, 233–237 (2002).

[2] Tilo Steinmetz et al, Science 321, 1335-1337 (2008).

[3] Sebastian Lopez. Science 321, 1301-1302 (2008).

[4] C. H. Li et al. Nature 452, 610 (2008).

[5] L. Razzari et al.,Nature Photonics 4, 41-45 (2010).

[6] T. M. Fortier, A. Bartels, S. A. Diddams. Octave-spanning, Optics Letters 31 (7), 1011-1013 (2006).

[7] P. Del'Haye, T. Herr, E. Gavartin, M. L. Gorodetsky, R. Holzwarth, T. J. Kippenberg. Physical Review Letters 107 (6), 063901-1 – 063901-4 (2011).

[8] H. Lin. Applied Optics 49 (14), 2653-2657 (2010).

[9] A. Gusarov, F. Liegeois Optics Communications 234, 391-397 (2004).

Polymer Based Platform for Hybrid Photonic Integration

N. Keil, C. Zawadzki, D. de Felipe, Z. Zhang, N. Grote
Photonic Components Department
Fraunhofer Institute for Telecommunications, HHI
Einsteinufer 37, 10587 Berlin, Germany
norbert.grote@hhi.fraunhofer.de

***Abstract*—*Integration Platform Session*: The paper presents on overview of a polymer based hybrid integration platform developed at HHI. The crucial building blocks involved are described, and examples of recently developed components are given.**

Keywords- polymer waveguides; passive fiber coupling; ultra-thin film elements; multiplexer; transceiver; PSK receivers; tunable laser

I. INTRODUCTION

For implementing photonic integrated circuits (PIC) various platform technologies are being investigated and applied. Besides monolithic solutions on III-V (mainly InP) and silicon semiconductors, hybrid integration has attracted a great deal of attention. With more and more increasing complexity of photonic integration it is foreseeable that both monolithic and hybrid technologies will eventually be merged with each other in a complementary manner to establish a photonic multi-PIC integration process. As hybrid integration platform planar lightwave circuit (PLC) boards relying on silica (SiO_2) are traditionally used. Another more recent approach, which basically represents a refinement of the silica process, employs SiN_4/SiO_2 waveguides (TriPlex^{TM}). At HHI we have been developing an alternative PLC platform (referred to as PolyBoard) that is based on polymer waveguide material. Despite the evident strengths of the silica technology, use of polymers provides distinct features that allow for added design and processing opportunities for performance enhancement and potentially achieving lower fabrication costs, including: simple layer deposition by spinning; micro-machinability with optical grade surfaces/facets; fairly large thermo-optical (TO) coefficient for efficient TO tuning/switching; easy-to- integrate ultra-thin film elements (UTFE) for implementing very compact and temperature-independent passive optical functionalities; possibility of combining polymer material with a wide range of other materials; and refractive index contrast >1.5% feasible to further reduce chip-size. The present paper gives an outline of the PolyBoard technology and presents recent implementations of respective optical components.

II. POLYBOARD CONCEPT AND ELEMENTS

The concept of the PolyBoard technology is schematically illustrated in Fig. 1. It utilizes a PLC board with buried monomode waveguides which are formed in a layer stack of commercially available polymer material spun onto a Si substrate (4-6 inch diam.). The crucial technological features of this hybrid - and thereby modular and flexible - integration platform are:

- Buried waveguides with adjustable index contrast $\Delta n = 0.005$ -0.030 to serve as on-chip optical interconnects and basis for optical waveguide device structures (e. g. AWG); lateral and vertical (under investigation) tapering feasible
- Efficient thermo-optical tuning exploiting fairly large TO coefficient ($> 10^{-4}K^{-1}$) and inherently low thermal conductivity of polymers
- Passive alignment and attachment of single-mode fibers using etched, laterally self-aligned U-shaped grooves; mean optical SMF/waveguide coupling loss ~ 0.25 dB (for $\Delta n = 0.011$)
- Vertical coupling out of light accomplished by means of 45° turning mirrors formed into the wavguides, in the simplest way by micro-machining (dicing saw)
- Integration of photodetectors by surface-mounting of back-side illuminated pin diodes (up to 25 GHz bandwidth)
- End-facet coupling of edge-emitting laser devices using active alignment and gluing (coupling loss: ~ 2 – 4 dB)

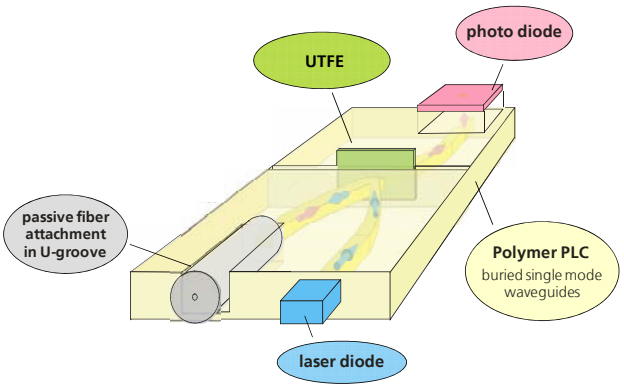


Figure 1. Schematic illustration of HHI's PolyBoard technology

- Implementation of passive-optical functions by integrating ultra-thin film elements (UTFE) with temperature-independent performance; UTFE's comprised of dielectric layers on polymer substrate film with total thickness ranging from ~ 10 µm to ~ 25 µm; functions realized: various optical filters; polarization beam splitter (Fig. 2) and rotator; optical reflector

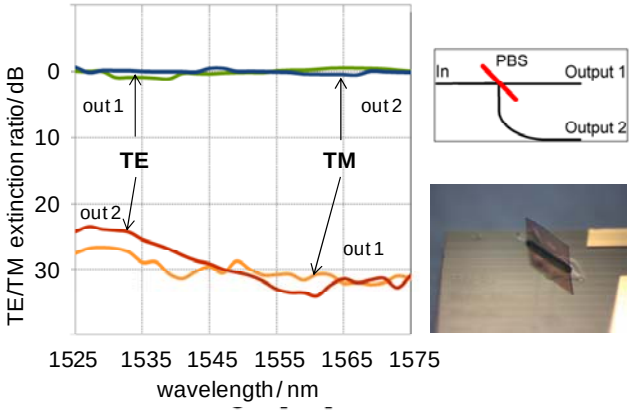


Figure 2. Performance of UTFE based polarization beam splitter (PBS)

III. POLYBOARD BASED PHOTONIC INTEGRATED COMPONENTS

On the basis of the PolyBoard process various integrated components have been realized recently. These include:

Using UTFE based band-pass filters 1300/1550 nm 1x2 multiplexers/demultiplexers were realized with fiber-to-fiber insertion loss down to 1 dB. More complex spectral functionalities (CWDM, triplex) and extension of channels are under development, with the main challenge being the achievement of the very low insertion loss figuress required. Furthermore optical reflector chips were fabricated for OTDM network monitoring to reflect wavelengths > 1630/1650 nm.

Optical transceivers for 2.5 GHz operation were realized incorporating a 1310/1550 nm UTBE filter as wavelength splitter, HHI's proprietary CSDFB laser as 1310 nm transmitter and two photodiodes, surface-mounted as outlined above, to form the signal detector and a tapped monitor diode, respectively. Such chips are readily extendable to form extremely compact transceiver arrays for point-to-point PON systems.

Different variants of photodetector components have been developed. For WDM-PON applications photodiode arrays were integrated with an arrayed waveguide grating (AWG) in which a UTFE polarization rotator is used for TE/TM compensation to reach polarization independence. Related devices have also been fabricated to accomplish a compact read-out chip for Fiber Bragg-Grating strain sensors.

The detection of phase-shift keyed (PSK) transmission signals requires dedicated receivers that are used either in a direct interferometric or coherent detection mode. For both concepts PSK receiver chips were developed. A direct PSK receiver with 25 GBd symbol rate was demonstrated that was designed with a delay interferometer containing a UTFE polarization rotator and a patented arrangement of thermo-optic heaters for fine phase adjustment. In this way the crucial residual polarization dependent frequency shift could be kept at a level as low as +/- 125 MHz [1].

Regarding coherent phase demodulation a fully integrated 28 GBd dual-polarization QPSK receiver chip was developed that is comprised of two 2x2 MMI based 90° hybrid mixers for the TE and the TM signal, each of them vertically coupled with an 4-array of 25 GHz bandwidth photodiodes. To separate the two polarization states an UTFE-PBS has been inserted into the input waveguides as sketched in Fig. 3 [2]. Packaged in a CCRx compliant housing the receiver exhibits a responsivity of about 0.02 A/W, a phase error < +/- 3, and a common mode rejection ratio of < 20 dB. The unit was successfully tested in 28 GBd QPSK and 10 GBd 16 QAM systems experiments.

Finally, wavelength-tunable lasers were fabricated and investigated relying on a thermally tunable Bragg grating formed in a polymer waveguide which again was butt-coupled to a reflective InP based gain element [3]. Very recently a tuning range of >50 nm could be reached in the extreme case at only 170 mW of electrical heater power consumption(Fig. 4).

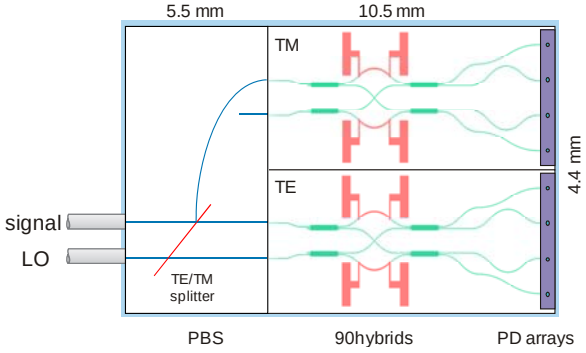


Figure 3. Schematic of developed PolyBoard based 25 GBd DP-QPSK receiver chip

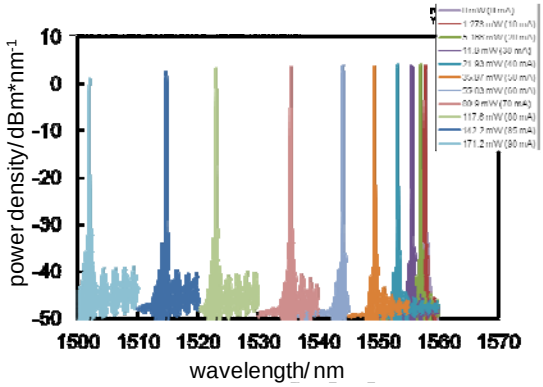


Figure 4. Wavelength tuning behavior of polymer waveguide grating laser with > 50 nm tuning range

[1] J. Wang, C. Zawadzki et al., „Polarization insensitive 25-Gbaud direct D(Q)PSK receiver based on polymer planar lightwave hybrid integration platform", Opt. Express 19, 12197-12207, 2011

[2] J. Wang, M. Kroh et al., „Integrated polarization diverse coherent receiver based on polymer PLC with high polarization extinction ratio for 100 G Ethernet applications", OFC 2012, paper OM2J4

[3] F. M. Soares et al., „Hybrid Photonic Integration of InP-Based Laser Diodes and Polymer PLCs", Proc. IPRM 2011, pp. 423-427, 2011

EO Spatial UV-Light Modulator Using Periodically-Poled Deep-Proton-Exchaged s-$LiTaO_3$ Waveguide

Masahide Okazaki, Takao Chichibu,
Syuhei Yoshimoto, Hirofumi Mizuno
Research and Development Center
Dainippon Screen Mfg. Co., Ltd.
Kyoto, Japan

Toshiaki Suhara
Graduate School of Engineering
Osaka University
Osaka, Japan

***Abstract*— We propose and demonstrate an electro-optic spatial light modulator using a deep-proton-exchanged waveguide in periodically poled MgO:s-$LiTaO_3$ thin crystal for UV laser light. The fine pixel profile, the good contrast and low driving voltage were accomplished at 355nm wavelength.**

Keywords-component; proton-exchage; domain inversion; lithium tantalate; spatial light modulator; ultraviolet (UV) laser

I. INTRODUCTION

A few approaches for electro-optic (EO) laser light modulation using ferroelectric domain inverted grating structures were demonstrated [1, 2]. We are developing EO Bragg deflection spatial light modulators aiming at applications to mask-less microlithography apparatuses and laser display systems [3]. For application to lithography systems, in particular, high-speed modulation of high-power UV laser light is an essential requirement. Therefore, crystals having a high optical damage threshold, e.g., MgO doped stoichiometric lithium tantalite (MgO:SLT) [4] should be adopted to avoid the optical damage problem [2]. Use of a waveguide structure allows implementation of compact and stable devices of low driving voltage and small pixel size. However, conventional shallow waveguides, such as annealed proton-exchanged waveguides [5], having a shallow mode depth of several microns are not suitable for implementation of modulations for high power laser light. Waveguides of lager mode size are required to avoid the optical damage by reducing the light power density, and reduce propagation losses caused by scattering. In this report, we propose a new device structure using a deep-proton-exchanged (DPE) waveguide. We developed a DPE waveguide in MgO:SLT of a mode size as large as 20μm. We accomplished successful spatial light modulation at 355nm UV wavelength in the modulator constructed by the DPE waveguide in a periodically poled crystal. The fine pixel profile and the good contrast were obtained.

II. DEVICE DESCRIPTION AND DESIGN

The EO Bragg deflection modulator as a building block of the spatial light modulator is shown in Fig.1. Let Λ, L, λ, n_e be the grating period, the grating thickness, the optical wavelength and the extraordinary refractive index, respectively. An

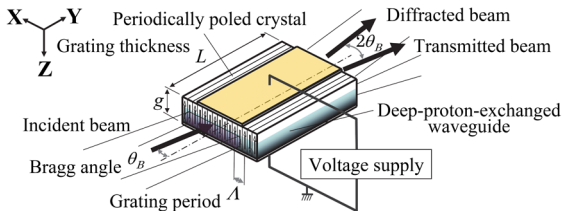


Figure 1. Configuration of the electrooptic Bragg deflection modulator.

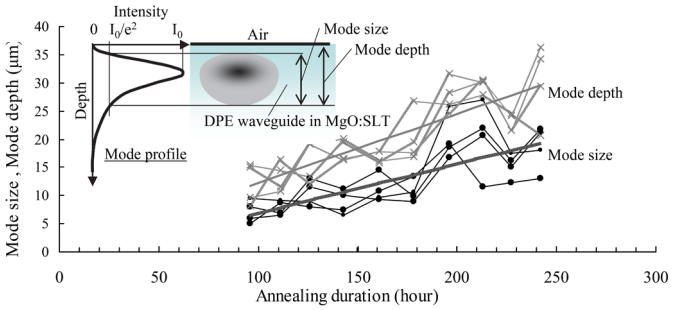


Figure 2. Measured result of the mode size and the mode depth.

incident beam with a polarization parallel to the Z axis enters the waveguide in a Z-cut MgO:SLT crystal at the Bragg angle $\theta_B = \sin^{-1}(\lambda/2\Lambda)$. When the driving voltage is applied between the electrodes, the light is diffracted. The efficiency η for the fundamental order Bragg diffraction is given by

$$\eta = \sin^2(\kappa L), \quad \kappa = \pi \Delta n_e/\lambda, \quad \Delta n_e = -2n_e^3 r_{33} V/\pi g, \quad (1)$$

where κ and Δn_e are the coupling coefficient and the Fourier amplitude of the periodic modulation in extraordinary refractive index, V is the voltage applied between electrodes, g the distance between electrodes, and r_{33} the Pockels constant [6]. We adopted the DPE waveguide to avoid the optical damage, reduce the propagation loss, and improve the pixel profile. In order to reduce the driving voltage, the distance between electrodes and the crystal thickness should be small. To obtain the high resolution (small pixel size), the electrode width, the distance between adjacent electrode segments and the domain period should be short. In addition, the crosstalk should be minimized. To satisfy these requirements, we

This work was supported by the Innovation Promotion Program, New Energy and Industrial Technology Development Organization (NEDO) (FY21-No,0427003).

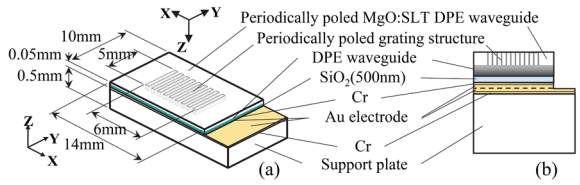


Figure 3. Fabricated modulator. (a) Perspective view. (b) Cross section.

adopted Λ=7.5μm, g=50μm and L=5mm. For λ=355nm, r_{33}=36.0pm/V and n_e=2.34 (MgO:SLT), the voltage for the maximum diffraction efficiency was calculated as 6V from (1).

III. Fabrication

As a preliminary experiment to establish the DPE waveguide fabrication technology, waveguides in 1 mol% MgO:SLT were fabricated by proton exchange in pyrophosphoric acid at 230 deg for 20 min and annealing at 400 deg with various annealing duration. A laser beam at 355nm wavelength with a diameter of 23μm was fed into the fabricated waveguides, and the guided mode profiles were measured on the output facet. The measured mode size and depth, defined in the inset of Fig.2, are plotted in Fig.2 against the annealing duration. It turned out that an annealing duration of 200 hours or longer was necessary to obtain a mode size with a diameter of 20μm.

Fig.3 shows the fabricated modulator. This modulator consists of two elements. One of the elements is a DPE waveguide in a Z-cut MgO:SLT crystal with a thickness of 50μm. A periodically poled grating structure with a period of 7.5μm and an interaction length of 5mm was formed in the central area. Another one is a SLT crystal with a thickness of 500μm as a robust support plate. Then, a planner waveguide was formed in the crystal by proton exchange in pyrophosphoric acid at 230 deg for 20 min and annealing at 400 deg for 238 hours. A SiO_2 buffer layer was deposited by RF sputtering. Cr/Au thin films were deposited over each crystal. The DPE waveguide was direct bonded to the support plate with Au layers in-between. The DPE waveguide substrate was polished to reduce the thickness to ~50μm.

IV. Experimental Result

Fig.4(a) shows the experimental setup for spatial light modulation with multiple pixels. A mode-locked neodymium 3rd harmonic laser of 355nm wavelength was used. Electrodes of 50 segments with a period of 7.5μm were formed on a separate glass substrate. These electrode segments were put in contact with the waveguide crystal with orientation parallel to the diffracted beam as shown in Fig.4(b), and were driven by parallel signals. Fig.5(a) and (b) show 2 examples of spatial light modulation patterns obtained at 10V driving voltage. In this demonstration, adjacent 5 electrodes were connected together to compose one pixel of 37.5μm width. Fig.5(a) shows a pattern where 5 pixels of odd serial numbers were diffracted, and Fig.5(b) shows a pattern where 5 pixels of even serial numbers were diffracted. The fine pixel profile and the good contrast suitable for mask-less microlithography apparatuses were accomplished.

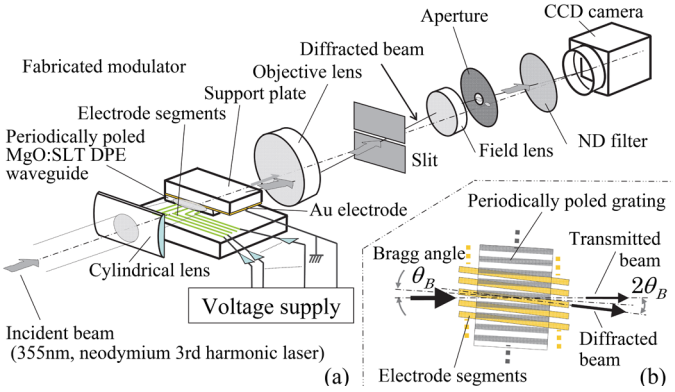


Figure 4. Experimental setup for spatial light modulation. (a)Perspective view. (b)Orientation of electrodes.

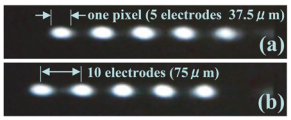


Figure 5. Photograph of the spatial light modulation output.

V. Conclusions

We have successfully demonstrated the EO spatial UV-light modulator using periodically-poled deep-proton-exchanged MgO:SLT waveguide. We are developing the spatial light modulator of higher resolution and larger number of pixels.

Acknowledgment

The authors thank Dr. M. Fujimura, Osaka University, for helpful discussions, and Dr. M. Arita, Dainippon Screen Mfg. Co., Ltd., for supervising the project progress.

References

[1] H. Gnewuch, C. N. Pannell, G. W. Ross, P. G. R. Smith, and H.Geiger, "Nanosecond response of Bragg deflectors in periodically poled $LiNbO_3$," IEEE Photon. Technol. Lett., vol. 10, no. 12, pp. 1730–1732, Dec. 1998.

[2] M. Yamada, "Electrically induced Bragg-diffraction grating composed of periodically inverted domains in lithium niobate crystals and its application devices," Rev. Sci. Instrum., vol. 71, no. 11, pp. 4010–4016, 2000.

[3] M. Okazaki, T. Chichibu, S. Yoshimoto, T. Inoue, and T. Suhara, "Electrooptic Bragg Deflection Modulator for UV Laser Light Using Periodically Poled MgO:s-$LiTaO_3$," IEEE Photon. Technol. Lett., vol. 23, no. 22, pp. 1709-1711, Nov. 2011.

[4] Y. Furukawa, M. Nakamura, S. Takekawa, K. Kitamura, T. Hatanaka, K. Nakamura, H. Ito, A. Alexandrovski, and M. M. Fejer, "Nearly stoichiometric $LiTaO_3$ for bulk quasi-phase matched devices," in Advanced Solid-State Lasers, C. Marshall, Ed. Washington, DC: Optical Society of America, 2001, vol. 15, OSA Trends Optics and Photonics, Paper PD5.

[5] M. Lobino, M. Marangoni, R. Ramponi, E. Cianci, V. Foglietti, S. Takekawa, M. Nakamura, and K. Kitamura, "Optical-damage-free guided second-harmonic generation in 1% MgO-doped stoichiometric lithium tantalate," Optics Letters, vol. 31, no. 1, pp. 83-85, 2006.

[6] H. Nishihara, M. Haruna, and T. Suhara, Optical Integrated Circuits. McGraw-Hill, pp. 77-83, 1989.

Propagation-Loss Reduction in InGaAsP Photonic-wire Waveguides by InP and Al_2O_3 Passivation Layers

Y. Ikku, M. Yokoyama, M. Takenaka and S. Takagi
Department of Electrical Engineering and Information Systems, University of Tokyo
Tokyo, Japan
ikku@mosfet.t.u-tokyo.ac.jp

O. Ichikawa, M. Hata
Sumitomo Chemical Company Ltd.
Tsukuba, Japan

***Abstract*—Scattering loss in InGaAsP photonic-wire waveguides fabricated on III-V-OI on Si wafer was effectively reduced by InP and Al_2O_3 passivation layers. Thus the propagation loss was improved from 1.7 dB/mm to 0.4 dB/mm.**

Keywords-InGaAsP photonic wire waveguide; scattering loss; III-V CMOS photonics

I. INTRODUCTION

III-V CMOS photonics [1] has been an attractive platform which can integrate high-performance III-V semiconductor based CMOS transistors [2, 3] and InP-based photonic-wire waveguide devices [4] on III-V on insulator (III-V-OI) on Si wafer. The strong optical confinement of the III-V-OI wafer enables drastic reduction of the sizes of III-V photonic devices as like silicon photonics. Using this platform, a sharp bend waveguide with 5-μm bend radius and an ultra-small arrayed waveguide grating multiplexer have been demonstrated [5]. In addition, the loss reduction of the InGaAsP photonic-wire waveguides has been demonstrated by atomic layer deposited (ALD) Al_2O_3 activated direct wafer bonding [6]. However, the propagation loss of the InGaAsP photonic-wire waveguide was still 1.7 dB/mm, higher than that of Si photonic-wire waveguides. Thus, the propagation-loss reduction in the InGaAsP photonic wire waveguide is mandatory for achieving large scale photonic integrated circuits.

In this paper, we have investigated scattering loss in the InGaAsP photonic-wire waveguides. The loss mainly comes from scattering at the (1) top, bottom and (2) sidewall of the waveguide as shown in Fig. 1. To suppress scattering at the waveguide surfaces, we have introduced the InP and Al_2O_3 passivation layers that effectively reduced the propagation loss from 1.7 dB/mm to 0.4 dB/mm.

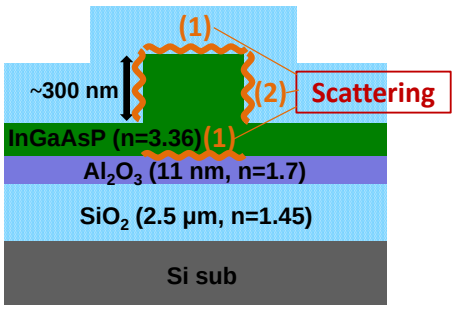


Fig. 1 Scattering of InGaAsP photonic-wire waveguide.

II. FABRICATION

To investigate scattering loss in the InGaAsP photonic-wire waveguide, we have prepared three types of waveguide: (a), (b), and (c) as shown in Fig. 2. Figure 2(a) shows the conventional waveguide structure, in which the InGaAsP (λ_g=1.25μm)/Al_2O_3 layer is directly bonded on the SiO_2 buried oxide (BOX) layer with SiO_2 passivation. The Al_2O_3 layer enables the large surface energy of the bonded interface without any plasma treatments [6]; however, the InGaAsP/Al_2O_3 interface is still rough, increasing the scattering loss. To improve the scattering loss at the bottom interface of the waveguide, we have put 25-nm-thick InP layers on the top and bottom of the InGaAsP layer as shown in Fig. 2(b). We expect that the surface roughness of the InP/Al_2O_3 interface is much improved as compared with the InGaAsP/Al_2O_3 interface. The InP layer is also expected to reduce scattering at the InP/Al_2O_3 interface because the index contrast between InP (n=3.17) and Al_2O_3 (n=1.7) is smaller than that of between InGaAsP (n=3.36) and Al_2O_3. We have also examined an 11-nm-thick Al_2O_3 passivation layer deposited on the waveguide by atomic layer deposition (ALD) before SiO_2 passivation as show in Fig. 2(c). The scattering at the sidewall of the waveguide is expected to be reduced by Al_2O_3 passivation because the index of Al_2O_3 is higher than that of SiO_2 [7].

The fabrication procedure is as follows. Firstly, 5.5-nm-thick Al_2O_3 layer is deposited on a 2-inch III-V wafer and a SiO_2/Si wafer by ALD.

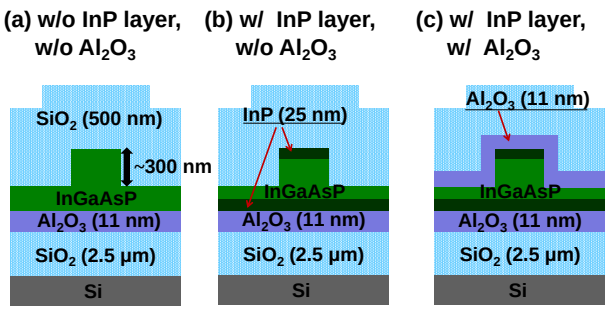


Fig. 2 Schematics of three types of fabricated waveguides.

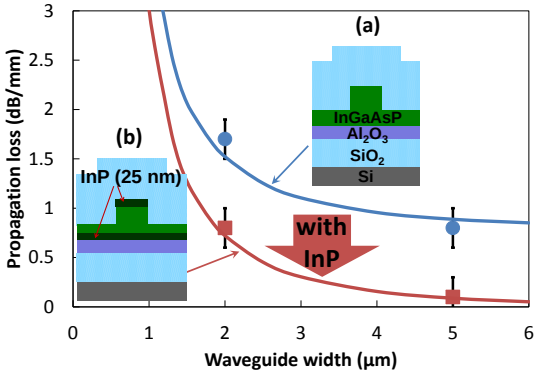


Fig. 3 Propagation losses of the waveguides (a) without InP passivation and the waveguide (b) with InP passivation.

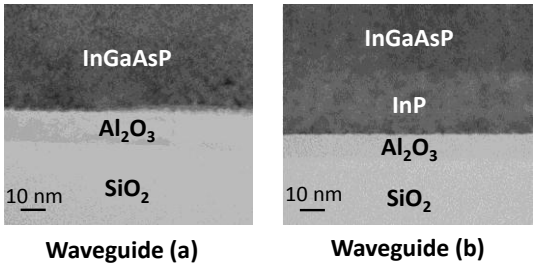


Fig. 4 TEM images of the bonded interfaces of the waveguide (a) and (b).

After bonding, the wafer was annealed at 350 °C for 1 hour. Then, the InP substrate was selectively etched by HCl. After patterning by photolithography, the waveguide mesa was formed by reactive ion etching (RIE). Finally the SiO_2 or Al_2O_3/SiO_2 passivation layer was deposited.

III. Measurement

To investigate the scattering loss, the propagation loss was measured by the cut-back method. Figure 3 shows the propagation losses of the waveguides (a) and (b) as a function of the waveguide width. The solid lines show the simulated propagation losses based on the scattering model by Payne and Lacey [8], which explain well the experimental results. By introducing the InP layers at the bottom and top of the waveguides, the propagation loss in the 2-μm-wide waveguides was reduced from 1.7 dB/mm to 0.8 dB/mm and the loss in the 5-μm-wide waveguides was also reduced from 0.8 dB/mm to 0.1 dB/mm. Figure 4 shows the transmission electron microscopy (TEM) images of the bonded interfaces of the waveguide (a) and (b). It is clearly observed that the interface between InP and Al_2O_3 is more flat than that between InGaAsP and Al_2O_3. Thus, the propagation-loss reduction of approximately 0.7 – 0.9 dB/mm was obtained by the smooth InP/Al_2O_3 interface in conjunction with the less index contrast between InP and Al_2O_3.

The scattering at the sidewall of the waveguide was also examined by comparing the propagation losses between the waveguides (b) and (c) as shown in Fig. 5. The propagation loss of the 2-μm-wide waveguide was reduced from 0.8 dB/mm to 0.4 dB/mm by Al_2O_3 passivation due to the less index contrast between InGaAsP and Al_2O_3 as compared with

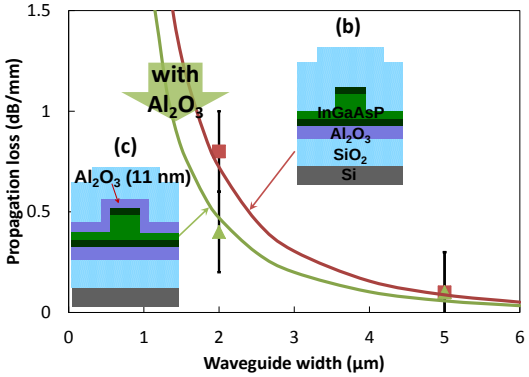


Fig. 5 Propagation losses of the waveguides (b) without Al_2O_3 passivation and the waveguide (c) with Al_2O_3 passivation

that between InGaAsP and SiO_2. The propagation loss of the waveguide (c) increases from 0.1 dB/mm to 0.4 dB/mm when the waveguide width decreases from 5 μm to 2 μm, indicating that the sidewall roughness is still not negligible even with Al_2O_3 passivation. Therefore, the propagation loss is expected to be reduced to less than 0.4 dB/mm by the optimizing dry etching of InGaAsP and lithography.

IV. Conclusions

We have investigated the scattering loss in the InGaAsP photonic-wire waveguide. The propagation loss was reduced from 1.7 dB/mm to 0.4 dB/mm by the InP and Al_2O_3 passivation layers owing to the reduction in scattering at the bottom, top and sidewall of the waveguide. Since the propagation loss of the 5-μm-wide waveguides, in which the sidewall scattering is not significant, is approximately 0.1 dB/mm, the propagation loss of the InGaAsP photonic-wire waveguide is expected to be lowered as that of the Si photonic-wire waveguide by improving sidewall roughness.

Acknowledgment

This work was supported by Grant-in-Aid for Young Scientists (A) from MEXT.

References

[1] M. Takenaka, M. Yokoyama, M. Sugiyama, Y. Nakano and S. Takagi., OFC, OThS5, 2010.

[2] M. Yokoyama, T. Yasuda, H. Takagi, H. Yamada, N. Fukuhara, M. Hata, M. Sugiyama, Y. Nakano, M. Takenaka and S. Takagi., *Appl. Phys. Express.*, Vol. 2, 124501, 2009.

[3] M. Yokoyama, R. Iida, S. H. Kim, N. Taoka, Y. Urabe, T. Yasuda, H. Takagi, H. Yamada, N. Fukuhara, M. Hata, M. Sugiyama, Y. Nakano, M. Takenaka and S. Takagi., IEDM, 3.1, 2010.

[4] M. Takenaka and Y. Nakano., *Optics Express Letters*, Vol. 15, no. 13, pp. 8422-8427, 2007.

[5] M. Takenaka, M. Yokoyama, M. Sugiyama, Y. Nakano and S. Takagi., *Appl. Phys. Express.*, Vol. 2, 122201, 2009.

[6] Y. Ikku, M. Yokoyama, R. Iida, M. Sugiyama, Y. Nakano, M. Takenaka and S. Takagi., IPRM, Mo-2.2.2, 2011.

[7] T. Alasaarela, D. Korn, L. Alloatti, A. Säynätjoki, A. Tervonen, R. Palmer, J. Leuthold, W. Freude, and S. Honkanen., Opt. Express 19, 11529-11538, 2011.

[8] F. P. Payne and J. P. R. Lacey., Opt. Quantum Electron. 26, 977–986, 1994.

Integrated AWG Spectrometer for On-chip Optical Coherence Tomography

B.I. Akca, L. Chang, G. Sengo, K. Wörhoff,
M. Pollnau, and R.M. de Ridder
Integrated Optical Microsystems Group,
MESA+ Institute for Nanotechnology, University of Twente
Enschede, The Netherlands
B.I.Akca@utwente.nl

V. Duc Nguyen, J. Kalkman, and T.G. van Leeuwen
Biomedical Engineering & Physics
Academic Medical Center,
University of Amsterdam
Amsterdam, The Netherlands

Abstract— **We present experimental results of spectral-domain optical coherence tomography systems using arrayed-waveguide gratings (AWG) for the 800-nm and 1300-nm spectral ranges. A phantom is imaged by using the 1300-nm AWG.**

Keywords-arrayed waveguide grating; optical coherence tomography; integrated optics

I. INTRODUCTION

Optical coherence tomography (OCT) [1] is an interferometric imaging technique which has been developed in the last 20 years. It generates high resolution cross-sectional images up to a few millimeters deep. Nowadays OCT is gaining widespread use in the clinic, particularly in ophthalmology. However, current OCT systems generally are bulky and expensive. Integrated optics is expected to make OCT system significantly smaller and more cost efficient [2-4]. In spectral-domain OCT (SD-OCT), one of the key components is the spectrometer where light is diffracted and dispersed via diffraction gratings. In integrated optics, the arrayed waveguide grating (AWG), first proposed by Smit [5], was designed and used as a dispersive element in telecommunications for wavelength division multiplexing. With their high resolution and compactness, AWG spectrometers can provide excellent performance in SD-OCT.

In this work, silicon-oxynitride (SiON) based AWG spectrometers were designed to be used in SD-OCT imaging of retina and skin. We perform OCT characterization and imaging with the 1300-nm AWG spectrometer. In addition, a new method to enhance the depth range of the OCT system using an AWG was introduced. By omitting the output channels from an AWG operating around 800-nm, the depth range has been improved from 1 mm to 3.3 mm.

II. AWG SPECTROMETERS

In this work, the free spectral range (FSR) values of our AWG spectrometers are chosen to be 20 nm and 78 nm for λ_c = 800 nm and 1300 nm, respectively, by considering the design limitations. The bandwidths of the light sources that we used in the OCT measurements are much smaller than the bandwidths of the AWG spectrometers: $\Delta\lambda_{FWHM}$ = 13 nm and 40 nm, respectively. In this way, the axial resolution is mainly determined by the bandwidth of the light source. The bandwidths of the chosen light sources limit the theoretical axial resolution (for air, n = 1) to Δz = 23 μm and 18.5 μm for λ_c = 800 nm and 1300 nm, respectively.

For both spectral ranges, we aim at a maximum depth range of z_{max} = 1 mm, which requires a wavelength spacing of $\delta\lambda$ = 0.16 nm and 0.4 nm for the 800-nm and 1300-nm AWG, respectively. Both spectrometers were fabricated with single-mode SiON channel waveguides.

III. OCT MEASUREMENTS

A schematic of the fiber-based SD-OCT system with AWG spectrometer is shown in Fig. 1(a). The Michelson interferometer was illuminated with a superluminescent diode having a partially-polarized 40-nm-bandwidth Gaussian-like spectrum centered at 1300-nm. Via a circulator the light was coupled into a 90/10 beam splitter. Polarization controllers were placed into both, sample and reference arm. The back reflected light was redirected through an optical circulator to the spectrometer. The diffraction grating, which is commonly used in this SD-OCT system, was replaced by the integrated AWG. The beam coming from the AWG output waveguides was focused onto a 46 kHz CCD linescan camera using a high numerical aperture (NA) camera lens. A moveable mirror was placed in the sample arm for testing the depth range and resolution. The acquired spectra are processed by first subtracting the reference arm spectrum, then compensating the dispersion, and finally re-sampling to k-space. The obtained spectra were Fourier transformed to obtain the OCT signal. As a demonstration of OCT cross-sectional imaging using the AWG spectrometer, an image of a three-layered scattering phantom is obtained by using part of a fiber-based OCT set-up with the 1300-nm AWG as spectrometer, see Fig. 1(b).

IV. ENHANCED DEPTH RANGE

For obtaining a large depth range, the AWG spectrometer must have a high wavelength resolution, while a high axial resolution requires a wide FSR. As the output spectrum of a usual AWG is discretized in a number of output waveguides, the combination of large depth range and high axial resolution requires a large number of output channels, up to a point where space limitations inhibit further improvement. One possible

This work is supported by the Smart Mix Program of the Netherlands Ministry of Economic Affairs and the Netherlands Ministry of Education, Culture and Science.

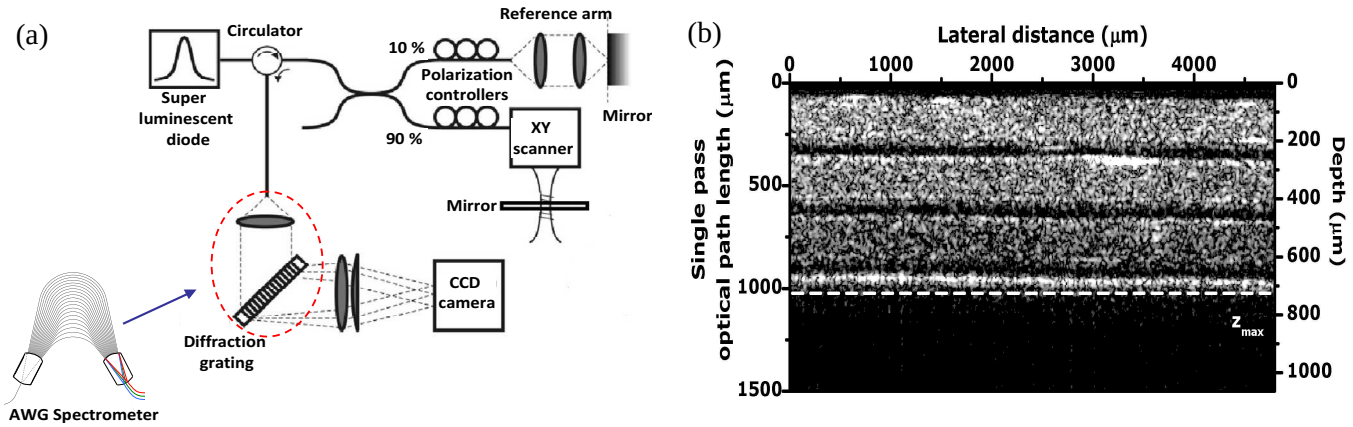


Figure 1. **(a)** Optical measurement set-up of fiber-based Michelson interferometer with integrated arrayed waveguide grating (AWG) spectrometer. **(b)** An OCT image of the three-layered scattering phantom measured with the AWG as spectrometer in SD-OCT.

solution is omitting the output channels (or removing them from a conventional AWG by dicing [6]). In this way, the wavelength discretization will be determined by the number of pixels on the camera, which can be much larger than the number of output channels, thus enhancing the depth range significantly. The designed depth range of 1 mm was achieved experimentally. The dashed line in Fig. 2(a) shows a fit of the roll-off function to the measured data. For enhancing the maximum depth range, the output channels of the AWG were removed by dicing the chip near the output facet of the second free propagation region.

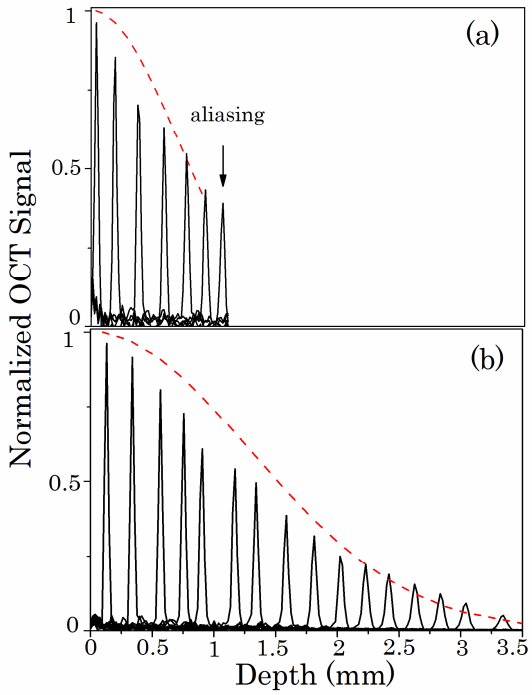


Figure 2. Measured OCT signal versus depth and fit of the roll-off (dashed line) for the 800-nm AWG, **(a)** with, and **(b)** without output channels.

The high-NA lens, shown in Fig. 1(a), is replaced by an objective lens, arranged to provide 10× magnification, thus addressing 450 CCD pixels, which increased the number of sampling points from 125 (number of output waveguides) to 450. The overall spectral resolution which is given by the combination of these two resolutions, i.e. the convolution of the diffraction pattern of the AWG for a single frequency, and the finite size of the CCD pixel, was calculated as 0.0465 nm. Theoretically, this resolution results in an improved depth range of 3.45 mm. Experimentally, the maximum depth range was enhanced from 1 mm to 3.3 mm, as shown in Fig. 2(b). The dashed line in Fig. 2(b) is the fit of the OCT roll-off in depth.

V. CONCLUSIONS

SiON-based AWG spectrometers have been designed and fabricated for on-chip spectral-domain OCT systems. A phantom image was taken by using a fiber-based SD-OCT set-up with the 1300-nm AWG spectrometer. In addition, the depth range of the SD-OCT system using 800-nm AWG has been improved to the level of existing bulk commercial systems by removing the output waveguides of the AWG. By integrating one of the most challenging parts of the SD-OCT system onto a chip, we have moved a significant step forward toward on-chip SD-OCT systems.

VI. REFERENCES

[1] D. Huang et al., “Optical coherence tomography,” Science, vol. 254, pp. 1178-1181, 1991.

[2] D. Culemann, A. Knuettel, and E. Voges, “Integrated optical sensor in glass for optical coherence tomography”, IEEE J. Select. Topics Quantum Electron. vol. 5, pp. 730-734, 2000.

[3] E. Margallo-Balbas, M. Geljon, G. Pandraud, and P. J. French, “Miniature 10 kHz thermo-optic delay line in silicon,” Opt. Lett., vol. 35, no 23, pp. 4027-4029, Dec. 2010.

[4] G. Yurtsever, P. Dumon, W. Bogaerts, and R. Baets, “Integrated photonic circuit in silicon on insulator for Fourier domain optical coherence tomography,” Proc. SPIE, Optical Coherence Tomography and Coherence Domain Optical Methods in Biomedicine XIV, vol. 7554, San Francisco, CA, USA, 2010, pp. 1-5.

[5] M. K. Smit and C. van Dam, “PHASAR-based WDM-devices: principles, design and applications,” IEEE J. Select. Topics Quantum Electron., vol. 2, pp. 236–250, 1996.

[6] N. Cvetojevic, J. S. Lawrence, S. C. Ellis, J. Bland-Hawthorn, R. Haynes, and A. Horton, “Characterization and on-sky demonstration of integrated photonic spectrograph for astronomy,” Opt. Express, vol. 17, pp.18643, 2009.

27-Meter-Long Ultra-Low-Loss Optical Delay Lines

Tong Chen, Hansuek Lee, Jiang Li, Oskar Painter, and Kerry Vahala
Thomas J. Watson, Sr. Laboratory of Applied Physics,
California Institute of Technology,
Pasadena, California, U.S.A.
vahala@caltech.edu

***Abstract*—Using a wet etch process, 27 meter long waveguides having optical loss of less than 0.1dB/m are demonstrated. These are the longest, to date, ultra-low loss waveguide fabricated.**

Keywords-optical waveguide;ultra-low loss.

I. INTRODUCTION

A large gap exists between the loss of optical fiber and chip-based photonic waveguides. For silica waveguides, the difference in loss is not fundamental and instead is caused by process-induced surface roughness. Partially closing this gap could benefit applications in sensing, radio-frequency photonics and signal processing. The question of reducing optical loss in photonic circuits has been considered for some time [1] and there has been considerable progress [2, 3]. In this work, a process previously used to fabricate high-Q resonators in silica [4], has been modified to create 27 meter long delay lines with a loss of 0.1dB/m as measured by optical backscatter reflectometry. These are the longest ultra-low-loss waveguides ever fabricated. Additionally, losses as low as 0.037 dB/m are inferred from resonator optical Q measurements.

II. RESULTS

In cross section the silica waveguides have a wedge profile that is air-clad with the mode guided in the wedge region and mechanical support provided by a silicon pillar at the interior [4]. Figure 1A shows a single spiral with a path length of approximately 7 meters. Backscatter measurements using a Luna OBR 4400 are presented in Fig. 2B and a linear decrease is observed (on the log scale) over nearly the full 7 meters of the spiral path. The inferred loss rate from this data is 0.05dB/m and provides a lower bound on the waveguide attenuation rate. To refine the estimate, the impact of the varying backscatter signal with variation of the spiral radius can be calibrated using a model. A corrected value of 0.08dB/m for the loss of the device in Fig. 1A is then obtained.

Fig. 2A shows four spirals cascaded on a single wafer to create a 27m (physical length) waveguide. Each spiral is approximately 4cm in diameter and features inward and outward, interlaced Archimedean-shaped waveguides that are connected at the spiral center by an adiabatic coupler. The adiabatic coupler features a completely undercut silica guide that is designed so as to maintain propagation in the fundamental transverse mode through the clockwise to counter-clockwise turn. Analysis of waveguide attenuation in spirals 3 and 4 gives approximately 0.1dB/m for the waveguide loss and insertion loss of less than 0.1dB for the adiabatic coupler. Spirals 1 and 2 show an apparent

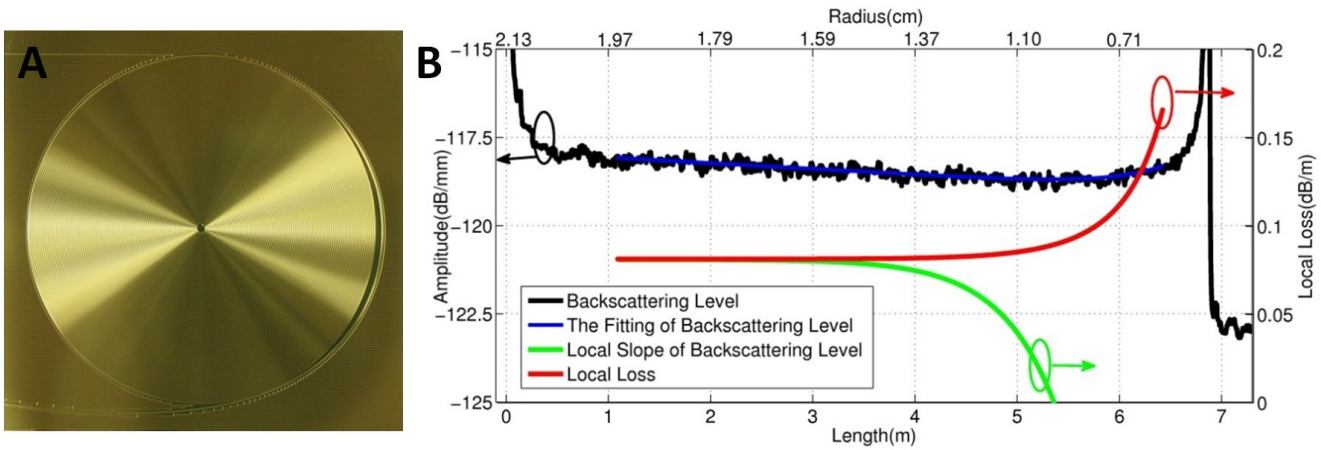


Figure 1. **(A)** An optical micrograph of a 7 meter physical path length, one-way spiral with a diameter of 4.3 cm. (B) Optical backscatter reflectometer measurement of the spiral waveguide shown in panel A. On account of the return path, the backscatter decay rate is twice as large as the actual waveguide loss rate. The blue curve is a fit to the backscatter level, while the green curve gives a fit to the local backscatter decay rate and the red curve uses a model to infer the actual local waveguide attenuation, which is approximately 0.08 dB/m over most of the spiral. The upper axis gives the radius from center while the lower axis gives the physical path length.

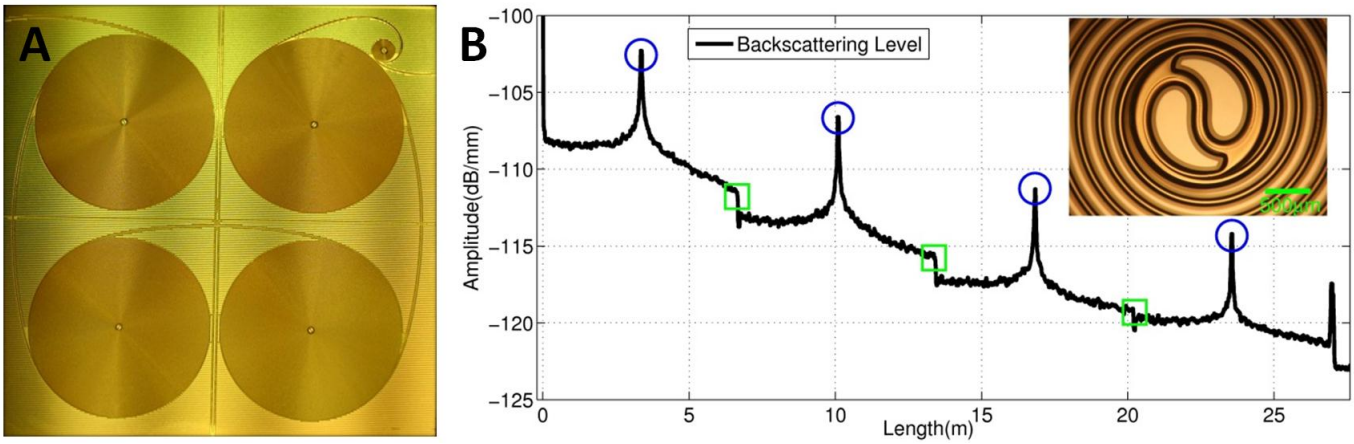


Figure 2 **(A)** Optical micrograph of a cascaded, four-spiral waveguide having a physical path length of 27 meters. The input port is in the upper left of the image, and the waveguides connecting neighboring spiral delays are visible. The entire chip is 9.5 cm ×9.5 cm. **(B)** Optical backscatter reflectometer measurement of the spiral waveguide shown in panel A. The periodic singularities (blue circles) in the backscatter signal correspond to the optical wave transiting the inner adiabatic coupling region of each spiral. Other discontinuities (green squares) in back scatter occur when the optical wave transfers between the spirals and result from higher order transverse modes being mode filtered. The inset is a magnified view of the adiabatic coupling section, which is approximately 1mm in diameter.

waveguide loss of 0.2dB/m, which is attributed to the presence of higher order radial modes. These modes mask the fundamental mode in the observed backscatter signal until they are filtered through their higher level of attenuation. The slight difference in optical loss (0.08dB/m vs. 0.1dB/m) for the spirals of Fig. 1A and 2A might reflect some slight process variation in the fabrication of these devices.

To obtain the dependence of attenuation on waveguide bending, the Q factor of disk resonators of varying diameters is measured. Data in Fig. 3 show that optical attenuation as low is 0.037dB/m can be obtained in these structures, corresponding to an optical Q factor of 670 million. AFM measurements of the upper, wedge and lower surfaces have also been performed on these resonators giving corresponding

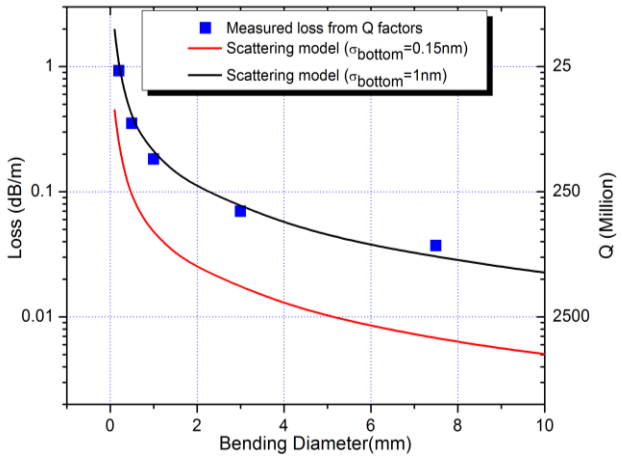


Figure 3. Bending loss data obtained from resonator Q measurements plotted versus the bending diameter. The black curve is a fit to the data using roughness data provided in the text and obtained using an AFM. The principle source of roughness is the lower dielectric interface and an estimate of the bending loss in case this surface can be smoothed to the level of the upper surface is provided as the red curve.

rms roughness variances of 0.15 nm and 0.48 nm with correlation length of approximately 200nm for the upper and wedge surfaces, respectively. The roughness of the lower surface is as large as 1-2 nm in amplitude and has been used as a fitting parameter to model the loss versus diameter in Fig. 3. Also, a projection of the predicted loss is given assuming that the lower surface roughness could be reduced to that of the upper oxide surface. In the current design, loss levels lower than 0.01dB/m could be realized.

ACKNOWLEDGMENT

We gratefully acknowledge the Defense Advanced Research Projects Agency under the iPhod program and the Kavli Nanoscience Institute at Caltech. H. L. thanks the Center for the Physics of Information and the help from Kiyoul Yang and Seokmin Jeon.

REFERENCES

[1] R. Adar, M. Serbin, and V. Mizrahi, "Less than 1 dB per meter propagation loss of silica waveguides measured using a ring resonator," J. of Light. Tech. **12**, 1369-1372 (1994).

[2] T. Kominato, Y. Hida, M. Itoh, H. Takahashi, S. Sohma, T. Kitoh, and Y. Hibino, "Extremely low-loss (0.3 dB/m) and long silica-based waveguides with large width and clothoid curve connection," in Proceedings of ECOC (Stockholm, Sweden, 2004).

[3] J. F. Bauters, M. J. R. Heck, D. John, D. Dai, J. S. Barton, C. M. Bruinink, A. Leinse, R. G. Heideman, D. J. Blumenthal, and J. E. Bowers, "Planar waveguides with less than 0.1 dB/m propagation loss fabricated with wafer bonding," Optics Express, **19**, 24090-24101 (2011)..

[4] T. J. Kippenberg, J. Kalkman, A. Polman, and K. J. Vahala, "Demonstration of an erbium-doped microdisk laser on a silicon chip," Physical Review A, **74**, 051802 (2006).

Ultra-high-Q wedge resonator on a silicon chip

Hansuek Lee, Tong Chen, Jiang Li, Ki Youl Yang, Oskar Painter, and Kerry Vahala
Thomas J. Watson, Sr., Laboratory of Applied Physics, California Institute of Technology,
Pasadena, CA 91125, USA
vahala@caltech.edu

***Abstract*— A new optical resonator featuring nearly 1 billion Q factor, the highest for any chip-based device, is reported. Fabrication uses only standard semiconductor processes, enabling precise size control and access to microwave-rate free-spectral-range operation.**

Keywords-Resonator; Silicon Photnoics;

I. INTRODUCTION

High optical Q performance in microcavities depends upon use of low absorption dielectrics and fabrication of very smooth (low scattering) interfaces. For chip-compatible devices, silica has the lowest intrinsic material loss [1]. Microtoroid resonators combine this low material loss with a reflow technique in which surface tension is used to smooth lithographic and etch-related blemishes [2]. At the same time, reflow smoothing makes it very challenging to fabricate larger diameter UHQ resonators and likewise to leverage the full range of integration tools and devices available on silicon. The devices reported here attain ultra-high-Q performance using only conventional semiconductor processing methods on a silicon wafer. Moreover, the best Q performance occurs for diameters greater than 500 microns, a size range that is difficult to access using microtoroids on account of the limitations of the reflow process. Microcombs will benefit from such a combination of UHQ and larger diameter resonators (microwave-rate free-spectral-range) to create combs that are both efficient in turn-on power and that can be self-referenced [3]. Moreover, integrated reference cavities and ring gyroscopes are two other applications that can benefit from larger (1 − 50mm diameter) UHQ resonators. Fabrication control of the free-spectral range (FSR) to 1 : 20,000 is also demonstrated here, opening the possibility of precision repetition rate control in microcombs or precision spectral placement of modes in certain nonlinear oscillators [4, 5].

II. RESONATOR DESIGN AND FABRICATION

The resonator described here is motivated by earlier work in which a resonator having a distinctive wedge-shaped cross section was described [6]. In that work, the mode was isolated from the lithographic blemishes near the outer rim of the resonator by using a shallow wedge angle, resulting in Q factors as high as 50 million. In the current work, we have boosted the optical Q by about 20X beyond these earlier results through a combination of process improvements. The fabrication process begins with thermal oxide on silicon, followed by photo-lithography and oxide etching with buffered hydrofluoric acid. The oxide disk structures function as an etch mask for an isotropic XeF_2 dry etch of the silicon. The final device is shown in figure 1. The wedge angle can be controlled

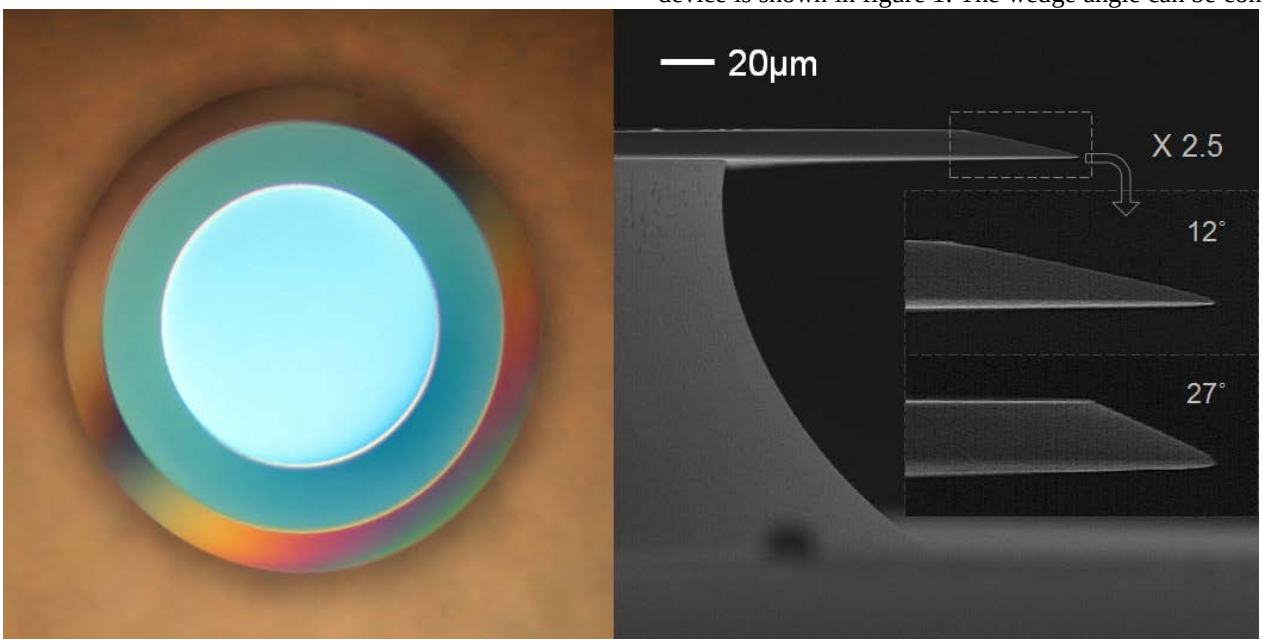


Figure 1. (Left) Optical micrograph shows a top view of a 1mm diameter wedge resonator. (Right) A scanning electron micrograph shows the side-view of a resonator. The insets give slightly magnified micrographs of resonators in which the wedge angle is 12 degrees (upper inset) and 27 degrees (lower inset).

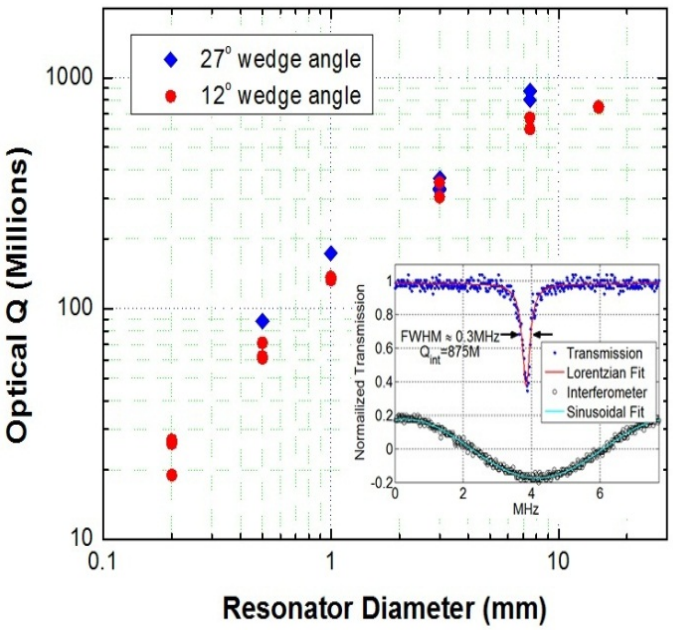


Figure 2. The measured Q factor plotted versus resonator diameter. 10μm oxide thickness is used for both of the wedge angles shown (12 ˚, 27˚). The inset shows a spectral scan for the case of a record Q factor of 875 million. The sinusoidal curve accompanying the spectrum is a calibration scan performed using a fiber interferometer.

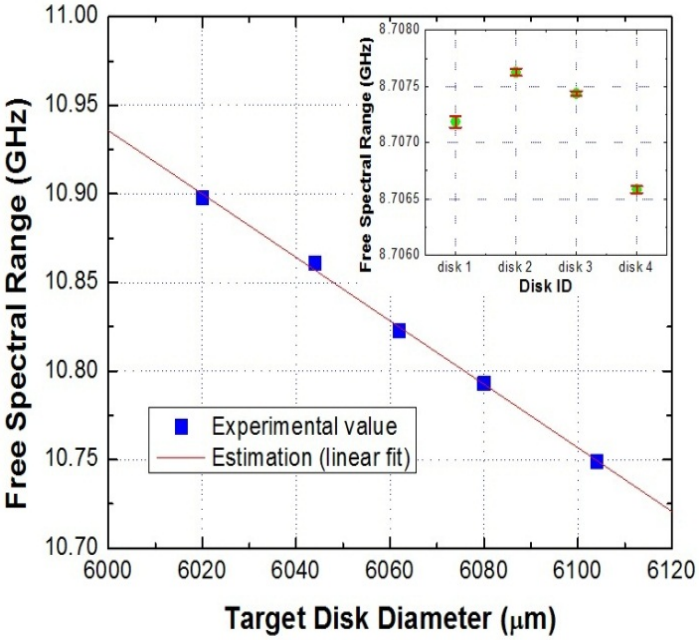


Figure 3. The measured free spectral range (FSR) versus the target design-value resonator diameter on a lithographic mask. The plot shows one device at each size and five different sizes. The rms variance is 2.4MHz. The inset shows the FSR data measured on four devices having the same target FSR. An improved variance of 0.45MHz is obtained.

in the range from 10˚ to 30˚ as shown in the inset of the figure through adjustment of the photoresist adhesion using commercially available adhesion promoters.

III. Quality Factor and Control of FSR

Intrinsic Q factor was obtained by measuring spectral line shapes using a tunable external cavity semiconductor laser. Coupling to the resonators relied upon an optical taper [7, 8]. For accurate calibration of the laser scan, a portion of the laser output was also monitored using a calibrated Mach-Zehnder interferometer having a free spectral range of 7.75 MHz. Figure 2 shows Q factor measurements for various resonator sizes and for two different wedge angles, 12˚ and 27 ˚. The inset in figure 2 shows a spectral scan obtained on a device having a record Q factor of 875 million. The Q factor for these new resonators is not only higher in an absolute sense than microtoroids, but it also accesses an important regime of resonator FSR that has not been possible using microtoroids. This range has become increasingly significant in applications like microcombs where self-referencing is important [3]. Beyond accessing this microwave rate FSR, the fabrication process allows for precision control of the FSR value as illustrated in figure 3. This allows for a high-level of repetition rate control in microcombs, and also access to stimulated Brillouin oscillation, where exact matching of the FSR to the Brillouin shift is necessary.

Acknowledgment

We gratefully acknowledge the Defense Advanced Research Projects Agency under the iPhod and Orchid programs and also the Kavli Nanoscience Institute at Caltech. H. L. thanks the Center for the Physics of Information.

References

[1] K. J. Vahala, “Optical Microcavities,” Nature 424, 839-846 (2003).

[2] D. K. Armani, T. J. Kippenberg, S. M. Spillane & K. J. Vahala, “Ultra-high-Q toroid microcavity on a chip.” Nature 421, 925–929 (2003).

[3] T. J. Kippenberg, R. Holzwarth & S. A. Diddams, “Microresonator-based optical frequency combs.” Science 332, 555–559 (2011).

[4] M. Tomes, & T. Carmon, “Photonic micro-electromechanical systems vibrating at X-band (11-GHz) rates.” Phys. Rev. Lett. 102, 113601 (2009).

[5] I. S. Grudinin, N. Yu & L. Maleki, “Brillouin lasing with a CaF2 whispering gallery mode resonator.” Phys. Rev. Lett. 102, 043902 (2009).

[6] T. J. Kippenberg, J. Kalkman, A. Polman & K. J. Vahala, “Demonstration of an erbium-doped microdisk laser on a silicon chip.” Phys. Rev. A 74, 051802 (2006).

[7] M. Cai, O. J. Painter & K. J. Vahala, “Observation of critical coupling in a fiber taper to silica-microsphere whispering gallery mode system. Phys. Rev. Lett. 74, 051802 (2006).

[8] S. M. Spillane, T. J. Kippenberg, O. J. Painter & K. J. Vahala, “Ideality in a fiber-taper-coupled microresonator system for application to cavity quantum electrodynamics.,” Phys. Rev. Lett. 91, 043902 (2003).

High Coherent Microcavity Brillouin Laser

Jiang Li, Hansuek Lee, Tong Chen, Oskar Painter and Kerry Vahala
Thomas J. Watson, Sr., Laboratory of Applied Physics
California Institute of Technology
1200 E. California Boulevard, Pasadena, CA 91125, USA
vahala@caltech.edu

***Abstract*—The first chip-based stimulated Brillouin laser (SBL) is demonstrated. The efficiency is 90% and it exhibits record coherence for an on-chip device: Schawlow-Townes frequency noise of 60 milliHz^2/Hz and low technical noise.**

Keywords-stimulated Brillouin; high coherence; Laser;

I. INTRODUCTION

High coherence lasers are important for high-performance microwave oscillators [1]; coherent fiber-optic communications [2]; remote sensing [3]; and in atomic physics [4]. In these applications, the twin goals of miniaturization and attainment of high coherence prove challenging, because quantum noise and technical noise contributions to laser coherence typically increase as laser-cavity form factor is decreased [5]. We demonstrate a stimulated Brillouin laser (SBL) that attains the highest level of coherence reported for a chip-based device. Schawlow-Townes noise of 60 milliHz^2/Hz is measured at an output power of approximately 400μW, and low-frequency technical noise is comparable to commercial fiber lasers. The devices are also the first chip-based SBLs and leverage a new ultra-high-Q wedge cavity that enables precise matching of the Brillouin gain shift to the free-spectral-range (FSR), thereby guaranteeing oscillation. More than 90% conversion of lower-coherence pump to high-coherence output is possible, and threshold powers around 60 microWatts are measured.

II. MATCHING OF FSR TO BRILLOUIN SHIFT

While stimulated Brillouin scattering is a well-known effect, its application in microcavities for laser sources has only recently been documented [6,7]. The principle challenge is to create sufficiently high-Q devices with the requisite mode spacing so as to precisely frequency match the narrow-band Brillouin gain spectrum. So far, this matching process has been somewhat statistical in nature, relying upon variation in resonator size and shape to create accidental matches. In this work, we apply a new process for fabricating resonators of precisely controlled diameter with Q factors as high as 870 million [8]. Using only lithography and a buffered hydrofluoric etch, wedge-shaped resonators are created as shown in the top left inset of Fig. 1. The diameter of these devices can be controlled to sub micron precision making possible an exact frequency match to the Brillouin process. In the measurement, the resonator is pumped on resonance through a fiber taper coupler [9] and Brillouin oscillation occurs in the opposite direction. The threshold for the process is typically in the range

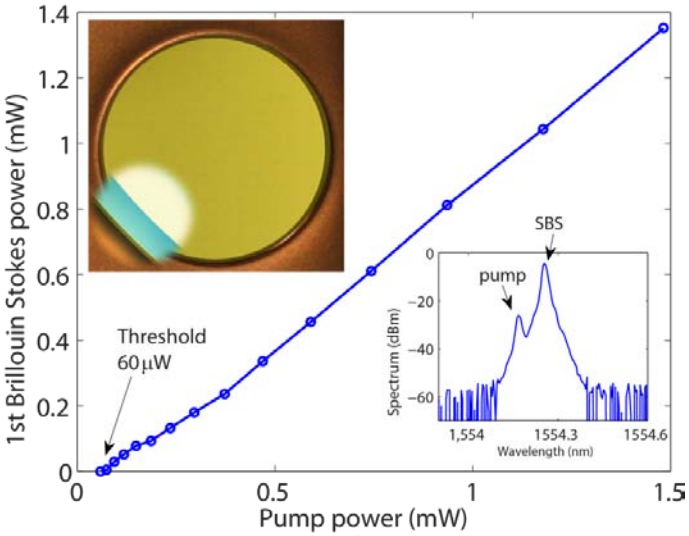


Fig. 1. Main panel: Output power of the first Brillouin Stokes laser line versus coupled optical pump power. Insets: (lower) Optical spectrum showing the Stokes line and the pump wave. Pump is suppressed since laser output power propagates opposite to the direction of pumping. (upper) Micrograph of disk resonator.

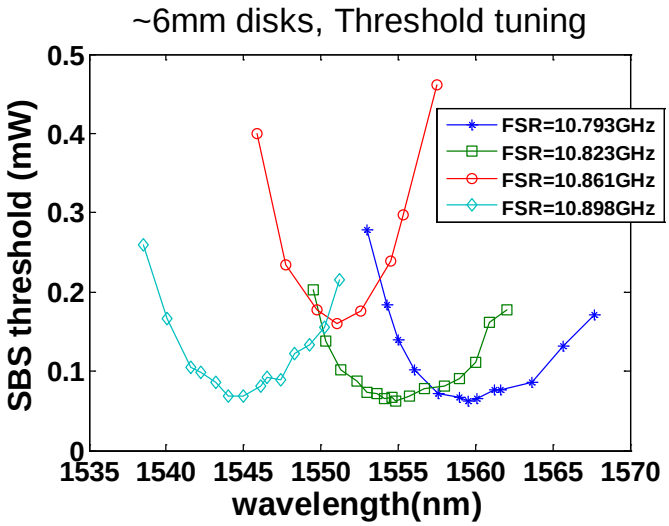


Fig. 2. Measured threshold versus pump detuning on four resonators, each of slightly different diameter (and hence FSR). The minima correspond to matching of the FSR with the Brillouin gain maximum. Tuning of the pump wave away from the maximum causes mismatch and hence an increase in threshold.

of 60-100 microWatts. By adjusting the cavity loading so as to critically couple the pump at the desired laser output power,

This work is sponsored by DARPA ORCHID program.

95% differential efficiency is achieved with output power more than 1mW, as shown in Fig. 1.

The precise control of microcavity diameter to achieve a frequency match with the Brillouin process is illustrated in Fig. 2 where four resonator diameters (lithography mask sizes: 6020, 6044, 6062 and 6080 microns) were tested at a series of pump wavelengths in the 1550 nm band. In each device, the pump wavelength was sequentially tuned along resonances belonging to the same azimuthal mode family. The minimum threshold corresponds to excitation at the Brillouin gain maximum. The rise in threshold away from the minimum (for a given resonator diameter) reflects slight tuning of the Brillouin gain-peak frequency shift Ω_B with pump wavelength change due to photon-phonon momentum conservation.

III. Phase Noise Characterization of High Coherence Laser

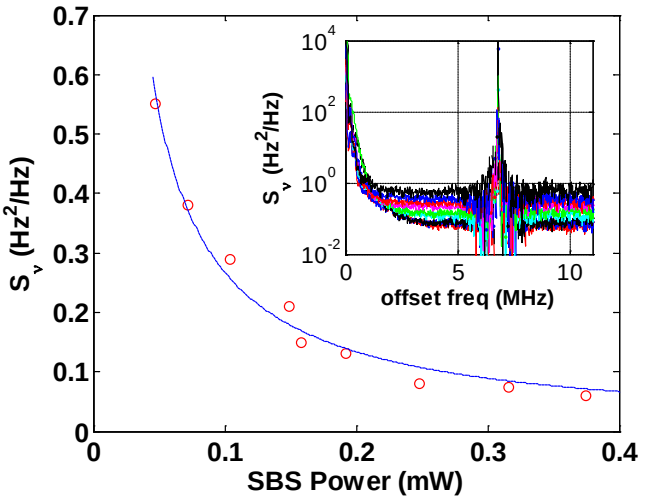


Fig. 3. Main panel: Measured Schawlow-Townes noise versus laser output power. A minimum noise level of 60 milliHz^2/Hz is obtained at 375 microWatts. Inset: Frequency fluctuation spectrum Sv at different output powers. The peak at 6.7MHz is due to the data conversion from the sinc like transfer function of Mach-Zehnder interferometer.

The phase noise of these devices has been characterized in several ways. A Mach-Zehnder interferometer is used to measure the SBL frequency noise from around 0.1 MHz to 10MHz. Above 1 MHz frequency offset, the device is quantum limited. The measured Schawlow-Townes noise is plotted in Fig. 3 and features a characteristic inverse-power dependence. At 375 micoWatts of output power, the measured Schawlow-Townes frequency noise is 60 milliHz^2/Hz, which is the lowest level ever reported for a chip-based device. The use of fiber-based SBLs to generate coherent microwaves has also been reported [10]. By operating the current device in cascade we can generate a coherent microwave signal by photomixing the Stokes lines together on a high-speed photodetector. The Fig. 4 inset shows that a narrow beat note is observed between the second and third order SBS stokes lines at 10.889GHz. The phase noise of the microwave beat note is measured on a phase noise analyzer and is plotted in Fig. 4. This phase noise spectrum permits analysis of residual technical noise contributions to the SBL and will be discussed.

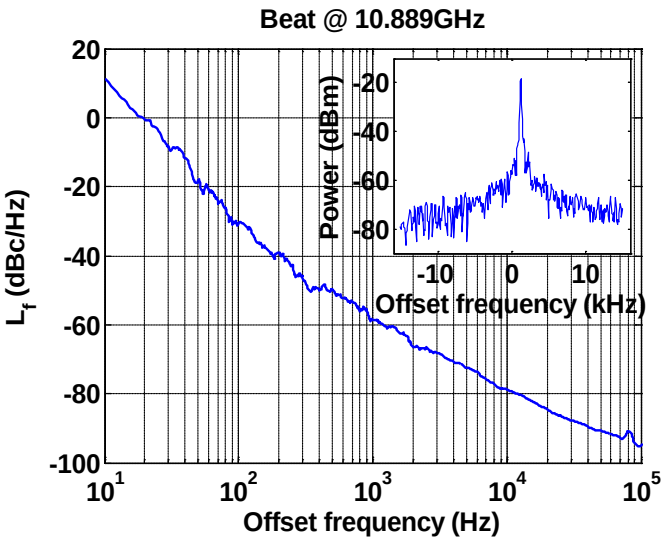


Fig. 4. Main panel: Phase noise of the microwave beat note at 10.889GHz produced by mixing the 2nd and 3rd order Stokes lines on a fast photodetector. Inset: Electrical spectrum of the beat note.

References

[1] T. Fortier, M. Kirchner, F. Quinlan, J. Taylor, J. Berquist, T. Rosenband, N. Lemke, A. Ludlow, Y. Jiang, C. Oates and S. Diddams, "Generation of ultrastable microwaves via optical frequency division", Nature Photonics 5, 425-429 (2011)

[2] E. IP, A. Lau, D. Barros and J. Kahn, "Coherent detection in optical fiber systems", Opt. Exp. 16, 753-791 (2008)

[3] C. Karlsson, F. Olsson, D. Letalick, and M. Harris, "All-fiber multifunction CW coherent laser radar at 1.55μm for range, speed, vibration, and wind measurements, " Appl. Opt. 39, 3716-3726 (2000)

[4] H.S. Margolis, G.P. Barwood, G. Huang, H.A. Klein, S.N. Lea, K. Szymaniec and P. Gill, "Hertz-level measurement of the optical clock frequency in a single $^{88}Sr^+$ ion", Science 306, 1355-1358 (2004).

[5] K. Vahala and A. Yariv, "Semiclassical theory of noise in semiconductor lasers-Part I, " IEEE J. Quantum Electron. 19, 1096-1101 (1983)

[6] M. Tomes and T. Carmon, "Photonic Micro-Electromechanical Systems Vibrating at X-band (11-GHz) Rates, " Phys. Rev. Lett. 102, 113601 (2009)

[7] I. Grudinin, A. Matsko and L. Maleki, "Brillouin Lasing with a CaF_2 Whispering Gallery Mode Resonator, " Phys. Rev. Lett. 102, 043902 (2009)

[8] H. Lee, T. Chen, J. Li, K. Yang, S. Jeon, O. Painter and K. Vahala, "Ultra-High-Q wedge-resonator on a silicon chip," arXiv:1112.2196 (2011)

[9] S. Spillane, T. Kippenberg, O. Painter and K. Vahala, "Ideality in a Fiber-Taper-Coupled Microresonator System for Application to Cavity Quantum Electrodynamics," Phys. Rev. Lett. 91, 043902 (2003)

[10] M.L. Dennis, R.M. Sova and T.R. Clark, "Dual-wavelength Brillouin fiber laser for microwave frequency generation," Optical Fiber Communications Conference, OWJ6 (2007)

Microwave Repetition Rate Frequency Comb on a chip

Jiang Li, Hansuek Lee, Tong Chen and Kerry Vahala
Thomas J. Watson, Sr., Laboratory of Applied Physics
California Institute of Technology
1200 E. California Boulevard, Pasadena, CA 91125, USA
vahala@caltech.edu

***Abstract*—A silicon-chip microcomb accessing the important microwave-rate FSR range is reported. The microcombs feature a few mW threshold level and comb heterodyne beat of several 100 Hertz. Microcombs with repetition rates ranging from 2.6GHz to 132GHz are demonstrated.**

Keywords-Frequency comb; Four-wave mixing; Integrated Optics; microcavities;

I. INTRODUCTION

There is currently intense interest in microcombs and there have been demonstrations using silica micro-toroids [1], CaF_2 diamond-milled rods [2,3], silicon-nitride rings on silicon [4], high-index silica rings on silicon [5], and in fiber Fabry-Perots [6]. One priority in this subject is the attainment of microwave-rate free-spectral-range (FSR) in a chip-based platform so as to enable self-referencing [7]. However, there are presently no on-chip micro-combs having repetition rate less than 80 GHz. Moreover, the following scaling of threshold power with FSR makes it challenging to reduce FSR without increasing threshold power.

$$P_{th} = \frac{(1+K)^3}{8K}\frac{n}{n_2}\frac{\omega}{\Delta\omega}\frac{A}{Q^2} \qquad (1)$$

where K is the normalized external coupling rate, n_2 (n) is the nonlinear index (refractive index), $\Delta\omega\,(\omega)$ is the free-spectral-range (optical frequency), A is the mode area, and Q is the resonator optical Q factor. In this work, we report a silicon-chip-based microcomb that accesses the important microwave-rate FSR range. At the same time, the device also achieves a low threshold turn-on power typically in the range of a few mW.

II. EXPERIMETNAL RESULTS

Improving the optical Q factor is an extremely effective way to offset the impact of reduced FSR ($\Delta\omega$) on threshold, as indicated in (1). Higher Q creates larger resonant build-up so that a given coupled power creates a greater Kerr-induced four-wave-mixing (FWM) of signal and idler waves. It also reduces oscillation threshold since optical loss is reduced. The microcomb of this work uses a new chip-based resonator that provides Q factors as high as 870 million [8,9]. Significantly, these devices do not require silica reflow [10], which becomes problematic at diameters approaching 1mm. Rather, only conventional semiconductor processing methods are necessary (lithography and wet etch) so that ultra-high-Q devices featuring FSR's of a few GHz to hundreds of GHz are possible.

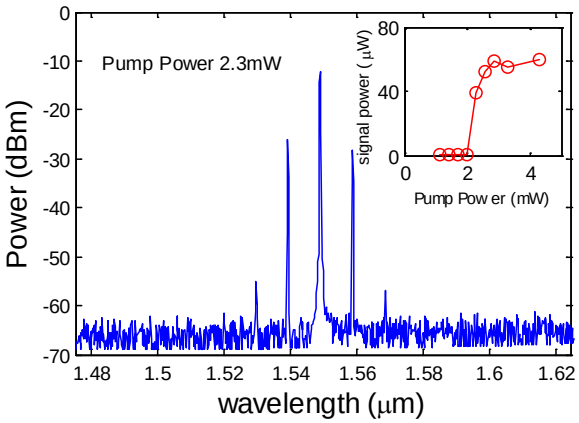


Fig. 1. Optical spectrum of the first generated lines just above threshold using a 2mm wedge disk. Inset: Power of first generated lines vs. coupled pump power.

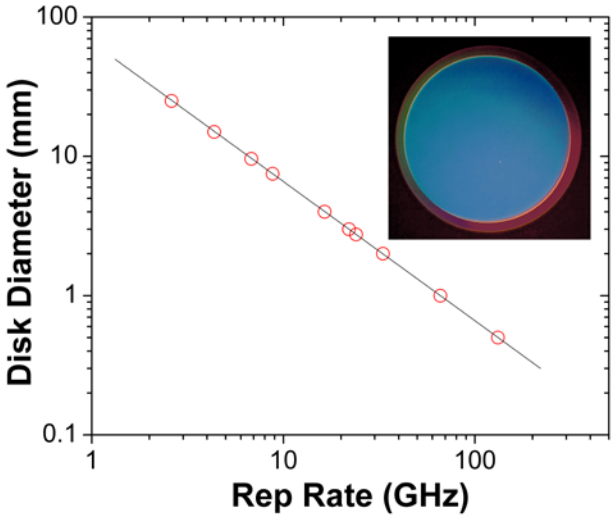


Fig. 2. Demonstrated microcomb rep rates from 2.6GHz to 132GHz plotted versus resonator diameter. Inset: A photomicrograph image of a 2mm disk.

This work is sponsored by the DARPA QUASAR program.

In a typical experimental setup, the amplified pump laser is coupled to the disk resonator using a tapered fiber [11] and is thermally locked within the cavity resonance [12]. When the coupled, pump power exceeds threshold, FWM lines turn-on very abruptly (see Fig. 1. inset). A threshold less than 2.3mW is measured for a 2mm, wedge disk having an intrinsic Q of 300 million. An optical micrograph of this disk resonator is provided in Fig. 2. Fig. 1 shows that the first generated FWM lines are typically multiple cavity FSR away from the pump, where the dispersion is compensated by nonlinear phase shift and the parametric gain is maximized. Interestingly, only modest pumping above threshold is required to generate densely-spaced, comb lines with repetition rate equal to one cavity FSR. Fig. 3 shows about 200 comb lines with 33.2GHz spacing generated with coupled pump power of only 7.5mW. At even higher power levels, a comb bandwidth of 68THz for 33.2 GHz rep rate (>2000 comb lines) is observed. Using these devices, chip-based microcombs with repetition rates covering the entire microwave spectrum have been demonstrated (see Fig. 2 main panel). The 2.6GHz repetition rate is the smallest demonstrated so far for any microcomb.

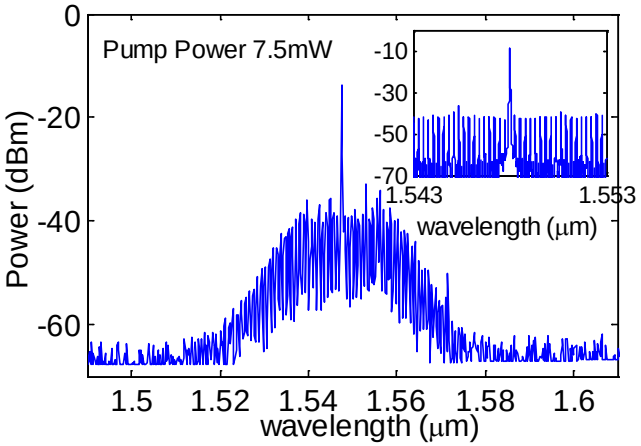


Fig. 3. Optical spectrum of the Kerr comb with 200 comb lines and with comb spacing 33.2GHz at pump power 7.5mW. Inset: zoom-in measurement of the Kerr comb with 10nm span and RBW 20pm.

In order to characterize the coherence of this microwave rate Kerr-comb, we directly demodulate the optical comb by detection on a fast photo-receiver with bandwidth 25GHz. The detected electrical spectrum using a 3mm disk (FSR=21.9 GHz) is shown in Fig. 4. Without any external locking, the free-running, mode-locked Kerr comb features a 3dB repetition rate linewidth in the 100s Hertz level, which illustrates the high coherence of the Kerr comb.

In conclusion, a chip-based microcomb at microwave rates from 132GHz to 2.6GHz has been demonstrated for the first time. The Kerr comb beat note is easily detected and is highly coherent with a typical free-running beat linewidth at the 100s of Hertz level. The devices also feature milliWatt level threshold.

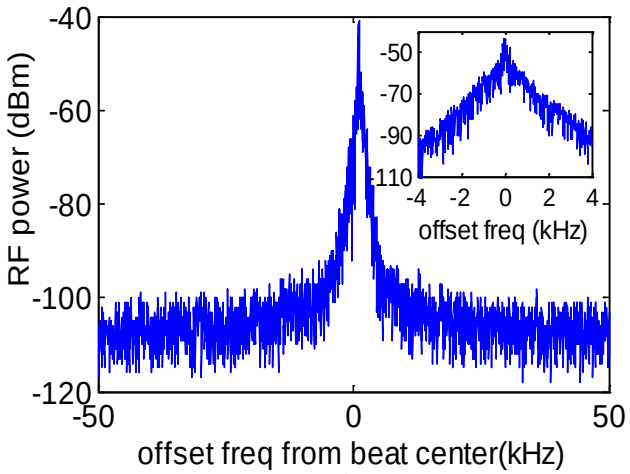


Fig. 4. Microwave beat note spectrum of the 21.9GHz repetition rate Kerr comb (RBW 300Hz, span 100kHz). Inset: zoom in measurement of the beat note, span 8kHz, RBW100Hz.

REFERENCES

[1] P. Del'Haye, A. Schliesser, O. Arcizet, T. Wilken, R. Holzwarth and T. J. Kippenberg, "Optical frequency comb generation from a monolithic microresonator," Nature 450, 1214 (2007)

[2] A. A. Savchenkov, A. B. Matsko, V. S. Ilchenko, I.Solomatine, D. Seidel, and L. Maleki, "Tunable Optical Frequency Comb with a Crystalline Whispering Gallery Mode Resonator," Physical Review Letter 101, 093902 (2008)

[3] I. S. Grudinin, N. Yu, and L. Maleki, "Generation of optical frequency combs with a CaF_2 resonator," Opt. Lett. 45, 878-880 (2009).

[4] J. S. Levy, A. Gondarenko, M. A. Foster, A. C. Turner-Foster, A. L. Gaeta, and M. Lipson, "CMOS-compatible multiple-wavelength oscillator for on-chip optical interconnects," Nature Photon. 4, 37-40 (2010)

[5] L. Razzari, D. Duchesne, M. Ferrera, R. Morandotti, S. Chu, B. E. Little, and D. J. Moss, "CMOS-compatible integrated optical hyperparametric oscillator," Nature Photon. 4, 41-45 (2010)

[6] D. Braje, L. Hollberg, and S. Diddams, "Brillouin-enhanced hyperparametric generation of an optical frequency comb in a monolithic highly nonlinear fiber cavity pumped by a cw laser," Phys. Rev. Lett. 102, 193902 (2009)

[7] T. J. Kippenberg, R. Holzwarth, and S. A. Diddams, "Microresonator-Based Optical Frequency Combs," Science 332, 555-559 (2011)

[8] H. Lee, T. Chen, J. Li, O. Painter and K. Vahala, "Ultra-High-Q Micro-Cavity on a Silicon Chip", FIO (2011)

[9] H. Lee, T. Chen, J. Li, K. Yang, S. Jeon, O. Painter and K. Vahala, "Ultra-High-Q wedge-resonator on a silicon chip," arXiv:1112.2196 (2011)

[10] D. K. Armani, T. J. Kippenberg, S. M. Spillane and K. J. Vahala, "Ultra-high-Q toroid microcavity on a chip," Nature, 421, 925-929 (2003)

[11] S. M. Spillane, T. J. Kippenberg, O. J. Painter, and K. J. Vahala, "Ideality in a Fiber-Taper-Coupled Microresonator System for Application to Cavity Quantum Electrodynamics," Phys. Rev. Lett. 91, 043902, (2003)

[12] T. Carmon, L. Yang, and K.J. Vahala, "Dynamical thermal behavior and thermal self-stability of microcavities," Optics Express 12, 4742 (2004)

Polymer nanotubes and nanowires for integrated photonics

N. Huby, J. Bigeon, B. Bêche
Institut de Physique de Rennes UMR CNRS 6251,
263 avenue Général Leclerc
Rennes, France

J.-L. Duvail
Institut des Matériaux, UMR CNRS 6502
2 rue de la Houssinière
Nantes, France

D. Duval
Nanobiosensors and Bioanalytical Applications Group
CIN2 (CSIC) and CIBER-BBN
Campus UAB, Barcelona, Spain

Organic 1D-nanostructures are elaborated and characterized for applications in integrated photonics. The wetting template method enables the control of aspect ratio (length and diameter) of hollow or filled individual 1D-nanostructure. Organic nanotubes and nanowires are integrated on photonic chips. An optical coupling occurs with integrated organic micro-structures (disk-reservoir) and allows propagation in 1D-nanostructures with losses about hundred db/mm. Nanotubes are here particularly interesting since they are easy to produce and they present a lack of investigation in nanophotonics.

keywords-nanotubes, polymer, interconnections, integrated optical circuit, wetting template, UV-lithography

I. INTRODUCTION

Integrated photonics offers great opportunities for components and devices with increasing requirements in terms of higher performances, wider applicability, lower energy consumption, high speed data transport and highly sensitive sensors. The comprehension of optical properties at the nanometer scale and the design of densely packed photonic devices are two essential fields of investigation. High aspect ratio nanostructures (nanowires and nanotubes) are particularly attractive for controlling and modulating light. Sub-wavelength structures are based on spatial optical confinement at nanoscale which modifies light propagation and light-matter interaction. This near field feature can interlink and process optical signals more efficiently, which makes it very attractive for on-chip data transport. The second major application directly concerned is related to highly sensitive sensors. Within the evanescent field, small changes at, or near, the surface can be probed. This makes 1D-nanostructures based devices much more sensitive than other evanescent-based sensors fabricated by planar lithography technique.

A large number of studies have been reported on dielectric nanowires based photonic devices (inorganic and organic) while nanotubes (other than carbon nanotubes) present a real lack of investigation for photonics applications. Due to the technological rupture in material processes, organic 1D-nanostructures emerged as a new class of building blocks in nanophotonics [1,2,3,4]. Indeed strategies based on organic materials (small molecules and polymers) are of great interest since they are flexible, biocompatible, multifunctional, energy friendly and cheap. Behind these advantages the main attractive aspect is their liquid-phase processability enabling innovative fabrication methods.

II. FABRICATION OF 1D-NANOSTRUCTURES

The nanotubes and nanowires fabrication has been performed by the wetting template strategy [5] described in Figure 1. Commercially available 60-µm thick alumina porous membranes (anodized aluminium oxide, AAO) are impregnated with SU8 photoresist. This chemically amplified polymer is sensitive to near UV radiation, presents thermal stability and is available in a wide range of formulations covering a large variety of viscosities. Two resins have been used in this work: the SU8-2002 and the SU8-2025 with viscosity of 2.49 Pa.s and 4500 Pa.s respectively. First, the AAO membrane is placed onto a resist film at room temperature (Figure 1a). For the most viscous SU8, the temperature is then increased up to 60°C in order to lower the viscosity and so to favour the impregnation. After diffusion of the SU8 in the 200 nm-diameter pores of the membrane, the whole sample was exposed to UV light (λ=365 nm) for polymerisation (Figure 1b).

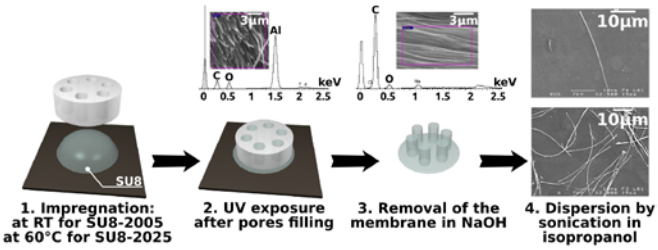


Figure 1: Wetting template method for 1D-nanostrutures elaboration. The filled or hollow aspect is related to the viscosity of the SU8 protoresist.

After the full conversion of the resin (200 mJ/cm^2), the sample is immerged in a selective NaOH (1.5 M) solution for 12 hours leading to the full dissolution of the membrane (Figure 1c). The solution was centrifuged in order to replace NaOH with isopropanol. EDS (energy dispersive X-ray spectroscopy) measurements have been performed before and after the NaOH treatment in order to control the efficient removal of the membrane. Finally, the dispersion of nanotubes or nanowires into isopropanol (chosen for its

low surface tension γ=21.8 N/m) is improved by a ultrasonication (Figure 1d).
The resulting nano-objects exhibit different morphology according to the resist viscosity. The more viscous polymer SU8-2025 leads to nanowires while the less viscous one SU8-2002 forms tubular objects. The reason is related to impregnation mechanism. Indeed the diffusion into the whole thickness of the membrane is significantly faster for the less viscous resin (few minutes compared with half an hour for the more viscous).

III. THEORETICAL WAVEGUIDING BEHAVIOUR

Theoretical study of the modal waveguiding behaviour in such nanostructures is presented. The eigenvalue equation deduced from Maxwell's equations has been solved by implementing it in Matlab software. Regarding the nanowire geometry, propagation characteristics are obtained by solving the well-known eigenvalues equations of the single clad fiber. The effective index n_{eff} for each of the four first modes is plotted as a function of the NW diameter ϕ normalized by the wavelength λ in Figure 2a. The grey zone is related to the NWs fabricated in this work. As the only existing mode is HE_{11}, single mode propagation is anticipated.
The theoretical investigation of optical propagation in nanotubes geometry is based on an analytical formalism developed recently [6]. The modal cut-off thicknesses of the NTs are obtained by resolving numerically the eigenvalue equations. These cut-off values (outer ϕ_{out} and inner ϕ_{in} diameter) govern the presence or not of a mode in the structure. An exception arrives for the hybrid mode HE_{11} which is always present in cylinder structures.

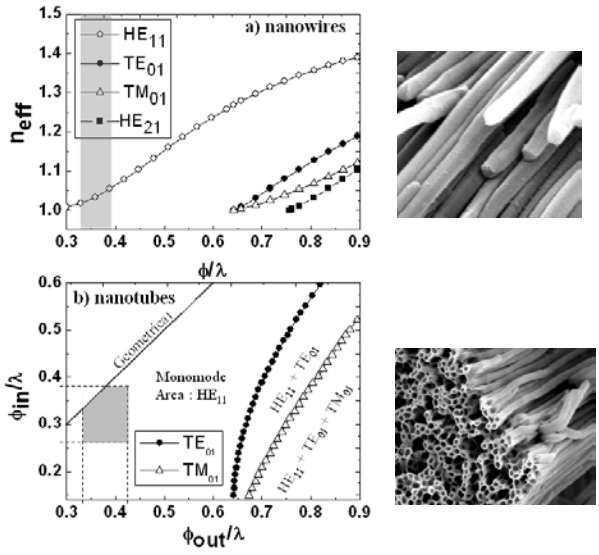


Figure 2 Theoretical investigations. a) Effective refractive index n_{eff} versus the normalized diameter of the NWs. b) Map of mode areas for SU8 nanotubes as a function of inner ϕ_{in} and outer ϕ_{out} diameters. The grey zones highlight the area related to the nanostructures fabricated here.

Cut-off values are plotted for the TE_{01} (transverse electric) and TM_{01} (transverse magnetic) modes as the normalized inner diameter ϕ_{in}/λ versus normalized outer diameter ϕ_{out}/λ.

As a result a map of monomode and multimode areas for tubular structures is depicted in Figure 2b. The geometrical limit corresponds to the fact that ϕ_{in} cannot exceed ϕ_{out}. The grey zone highlights the area related to NTs fabricated as described afterward. It clearly proves that only a single mode feature exists in these SU8 nanotubes.

IV. INTEGRATION ON PHOTONIC CHIP

SU8 NTs and NWs have been integrated along organic SU8 microstructures designed on a photonic chip in order to evaluate their optical waveguiding properties. The SU8 microstructures were previously patterned on a Si/SiO_2 substrate by a one-step UV-lithography process. The chip consists of microstructures such as ridge waveguides (6 μm width) and photons disk-reservoirs (200 μm-radius disk) where the light is confined at the edges of the curved structures. These disk-reservoirs are particularly interesting for coupling with sub-wavelength object since the evanescent tail is displaced in the low-index medium (air) due to the curvature radius.
Top-view field intensity map have been recorded during light propagation in single nanostructure. The strong confinement of the field in a coupling zone between a disk-reservoir and a single NT or a single NW is shown on Figure 4a and 4b respectively. In both cases, the light is confined at the edge of the disk and throughout the NT and NW. Experimental data analysis leads to scattering losses about hundred dB/mm [7] for red and infrared light.

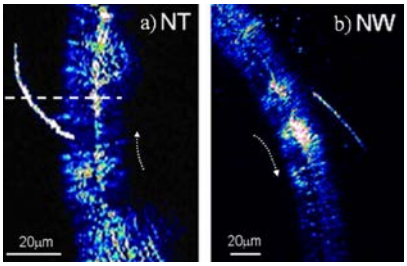


Figure 4: Schematic illustration of the photonic chip Light is injected into the core of the waveguide on the right side andpropagates to the disk reservoir where whispering gallery modes (WGM) are excited.

ACKNOWLEDGMENTS

The authors thank A. Carré, Cyril Hamel and Ludovic Frein for technical support as well as J. Le Lannic for SEM images. These works were supported by Region Bretagne and Pays de la Loire.

REFERENCES

[1] W. T. Hammond, and J. Xue, Appl. Phys. Lett. **97**, 073302 (2010)
[2] Xing X.; Zhu H., Wang Y.; Li B. *Nanolett.* **2008**, 8, 2839.
[3] J. J. Ju, S. K. Park, S. Park, J. Kim, M.-S. Kim, M.-H. Lee, and J. Y. Do, Appl. Phys. Lett. **88**, 241106 (2006).
[4] O'Carroll D.; Lieberwirth I.; Redmond G. *Nat. Nanotech*. **2007**, 2, 180.
[5] Steinhart M.; Wendorff J.H.; Greiner A.; Wehrspohn R.B.; Nielsch K.; Schilling J.; Choi J.; Gösele U. *Science* **2002**, 296, 1997.
[6] Duval D.; Bêche B. *J. Opt.* **2010**, 12, 075501.
[7] N. Huby, J.-L. Duvail, D. Duval, D. Pluchon and B. Bêche Appl. Phys. Lett. 99, 113302 (2011)

InAs/InP(100) QD waveguide photodetectors for a monolithically integrated optical coherence tomography system around 1.7 μm

Y. Jiao, B.W. Tilma, J. Kotani, R. Nötzel, M.K. Smit, E.A.J.M. Bente
COBRA Research Institute, Eindhoven University of Technology
Eindhoven, The Netherlands
y.jiao@tue.nl

***Abstract*—InAs/InP(100) quantum dot (QD) waveguide photodetectors are presented in this paper. The devices are fabricated using the layer stack of semiconductor optical amplifiers (SOAs) and are compatible with the active-passive integration technology. The characterization and simulation on the devices have shown good potential to be used in a monolithically integrated swept-source optical coherence tomography (SS-OCT) system in 1.6 to 1.8 μm wavelength range.**

Keywords-quantum dot; photodetector; optical coherence tomography; integrated optoelectronics

I. INTRODUCTION

The swept-source optical coherence tomography (SS-OCT) in 1.6 to 1.8 μm wavelength range is of great interest in medical imaging. The swept-source scheme provides higher sensitivity [1] while the long wavelength offers deeper imaging depth [2]. Two main components are required to open up OCT imaging in an SS-OCT system in this long wavelength range. The first is a swept laser source. In previous work [3], we have developed an experimental monolithically integrated tunable laser around the 1.7 μm wavelength region using InAs/InP(100) quantum dots (QDs) as its optical amplifiers. The feasibility of this laser had been demonstrated in a free-space Michelson interferometer setup. A suitable photodetector is thus the second main component that is essential to realize the potential for OCT imaging in the 1.6 to 1.8 μm range. Such detectors are not readily available commercially. In this paper we present InAs/InP(100) QD waveguide photodetectors which meet all the requirements for application in an SS-OCT system in the 1.6 to 1.8 μm wavelength range. The main advantage is that the presented photodetectors can be monolithically integrated with our swept laser and other components.

II. DEVICES AND MEASUREMENTS

The QD waveguide photodetectors are realized by applying a reverse-bias voltage on a shallowly etched ridge waveguide QD semiconductor optical amplifier (QD-SOA). The QD-SOA structure is fabricated using a technology that is fully compatible with the active-passive optical integration scheme at our research institute [4]. As can be seen in Fig. 1, the layer stack of the QD photodetector is identical to that of the QD-SOAs which were used in our swept laser. This opens up a way of further integration of all active and passive components in a SS-OCT system. The fabricated two chips (with different total lengths) consist of 26 devices each with different device lengths.

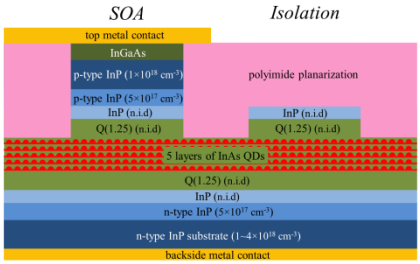


Figure 1. The cross-section structure of the QD-SOA section and isolation section.

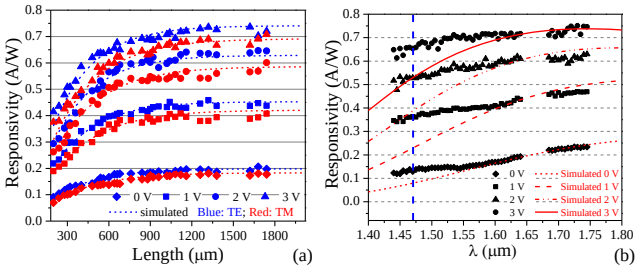


Figure 2. (a) The responsivities of 32 devices with different lengths at a wavelength of 1640 nm. (b) The spectral responses of a 960 μm-long device under different reverse-bias voltages for TE polarization.

Several properties of the photodetectors have been measured to demonstrate the feasibility of their use in the monolithically integrated SS-OCT system in 1.6 to 1.8 μm wavelength range. The measurements on the dark current lead to a conclusion that a sufficiently low dark current (< 30 nA) can be achieved by choosing the appropriate device length (< 1000 μm) and bias voltage (< 3 V). The responsivities as a function of length of the waveguide and bias voltages have also been measured as shown in Fig. 2(a). It is clear from the figure that the responsivity increases with the device length and after reaching a certain length (around 950 μm), almost all the photons are absorbed. It also can be seen that the responsivity of the QD photodetector can reach as high as 0.7 A/W which is more than sufficient for the SS-OCT application. The measured

spectral response of a device with a 960 μm length is shown in Fig. 2(b). It is clear in Fig. 2(a) and (b) that the responsivity of the photodetector increases dramatically with the reverse-bias voltage. The device shows a flat response over a whole 300 nm wavelength range which well satisfies the requirement for the SS-OCT application in 1.6 to 1.8 μm wavelength range.

The electrical signal bandwidth of the photodetectors is determined by measuring the photocurrents under a modulated optical input. The measurement is performed on several devices with different lengths and under several bias voltages. For a device with a length of 200 μm and a bias voltage of 2 V, the 3 dB bandwidth can reach 83 MHz, which is adequate for the OCT application.

III. Simulations

A modified rate equation model based of a QD-SOA model [4] is applied for the simulation of photodetection with current extraction. An equivalent circuit model is used to analyze the factors that limit the bandwidth of the devices.

Since we used identical QD active material and layer stack for the photodetector as for QD-SOA, the QD rate equation model and several of the parameters used in [4] were slightly modified to simulate the behavior of the photo-absorption of the QDs. The major modification from [4] is the change from current injection to current extraction. Another modification is that the multiple photon groups used for representing different wavelength components in the gain spectra is reduced to only one photon group which represents a single wavelength as in the measurements. The advantage of this modified model is that only one major parameter (carrier extraction rate from wetting layer to SCH layer) is adjusted to match the simulation with the measured data for one particular value of the reverse-bias voltage while all the other parameters for QD-SOA keep unchanged.

Simulations on the length-dependent responsivities are shown in Fig. 2(a) in dashed curves. As can be seen in the figure, the simulation results match very well with the measured data. Simulations for the spectral behavior of the photodetectors are also performed as shown in Fig. 2(b) in red curves. It can be seen in the figure that for wavelengths longer than 1.6 μm, the simulation matches well with the measured spectrum. But for the shorter wavelengths below 1.6 μm, there is a clear deviation between simulation and measurement. The absorption coefficient of the QDs in the shorter wavelength region is underestimated. One of the reasons can be the exclusion of contributions from higher-order excited states in the QDs. Such states would not show up in the ASE spectra in forward bias, but can play a role in absorption. Another reason which is more probable is the exclusion of contribution from the wetting layer. The energy level of the WL corresponds to a wavelength of 1.47 μm [4] and is indicated as a blue line in Fig. 2(b). This wavelength locates in the wavelength region where a clear deviation occurs.

The QD waveguide photodetectors can also be modeled using an equivalent circuit method [5]. The theoretical 3 dB bandwidth can be calculated by translating the photodetectors and connecting electronics into the equivalent circuit. By matching the simulated 3 dB bandwidth with the measured one, the value of probe pad capacitance C_p and the voltage dependency of junction capacitance C_{pd} of the diode can be determined as shown in Fig. 3. As C_p does not change as voltage, it keeps a relatively high value (as high as 46 pF). This is mainly due to the large area of the metal contact used in our devices. It can also be seen that there is a significant improvement on C_{pd} as the bias voltage increases. It is mainly due to the expansion of the depletion region as the voltage increases.

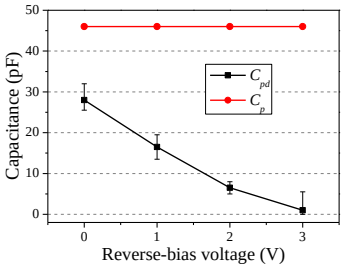


Figure 3. The determined values of C_{pd} and C_p under different reverse-bias voltages. The error bars indicate the variability of C_{pd} when the ±5 % relative deviation of the bandwidth values used in the calculation is considered.

IV. Conclusion

In this paper we have presented the QD waveguide photodetectors and have shown them to meet all requirements for application in SS-OCT in the 1.6 to 1.8 μm wavelength range. Both rate equation model and equivalent circuit model have well explained the behaviors of the photodetectors. The devices have shown good potential to be used in a monolithically integrated long-wavelength SS-OCT system.

Acknowledgment

The authors thank the support from the BrainBridge project, China Scholarship Council (CSC) and the NRC Photonics grant.

References

[1] M. Choma, M. Sarunic, C. Yang, and J. Izatt, "Sensitivity advantage of swept source and Fourier domain optical coherence tomography," *Opt. Express*, vol. 11, pp. 2183-2189, 2003.

[2] V. M. Kodach, J. Kalkman, D. J. Faber, and T. G. van Leeuwen, "Quantitative comparison of the OCT imaging depth at 1300 nm and 1600 nm," Biomed. Opt. Express, vol. 1, pp. 176-185, 2010.

[3] B. W. Tilma, Y. Jiao, J. Kotani, B. Smalbrugge, H. P. M. M. Ambrosius, P. J. Thijs, X. J. M. Leijtens, R. Notzel, M. K. Smit, and E. A. J. M. Bente, "Integrated Tunable Quantum-Dot Laser for Optical Coherence Tomography in the 1.7 μm Wavelength Region," IEEE J. Quant. Electron., vol. 48, pp. 87-98, 2012.

[4] B. W. Tilma, M. S. Tahvili, J. Kotani, R. Notzel, M. K. Smit, and E. A. J. M. Bente, "Measurement and analysis of optical gain spectra in 1.6 to 1.8 μm InAs/InP (100) quantum-dot amplifiers," Opt. Quant. Electron., vol. 41, pp. 735-749, 2009.

[5] H. Jiang and P. K. L. Yu, "Equivalent circuit analysis of harmonic distortions in photodiode," IEEE Photon. Technol. Lett., vol. 10, pp. 1608-1610, 1998.

Spatial Heterodyne Fourier-Transform Spectrometer Implemented With Silicon Wire Spiral Waveguides

Aitor V. Velasco, María L. Calvo
Faculty of Physical Sciences
Universidad Complutense de Madrid
Madrid (Spain)
avillafr@pdi.ucm.es

Pavel Cheben, Prezemek Bock, Jens H. Schmid,
Jean Lapointe, André Delâge, Siegfried Janz,
Dan-Xia Xu, Mirosław Florjańczyk
Institute for Microstructural Science
National Research Council
Ottawa (Canada)
Pavel.Cheben@nrc-cnrc.gc.ca

***Abstract*—The design, fabrication and characterization of a Fourier-transform planar waveguide microspectrometer are presented. The device comprises an array of 32 Mach-Zehnder interferometers with increasing optical path differences between arms across the array, achieving a wavelength resolution of 0.1 nm within a free spectral range of 1.6 nm. Spiral Si-wire waveguides are used in the arms of the interferometers in order to reduce the footprint of the device to less than 12 mm^2.**

Keywords- spatial heterodyne spectroscopy; silicon-on-insulator waveguides; Fourier-transform spectrometer

I. INTRODUCTION

Compact high-resolution spectrometers and multiplexers are required for a wide range of applications such as optical communication networks, health diagnosis, environmental sensing and space instrumentation, to name a few [1]. Arrayed waveguide gratings (AWGs) can achieve sub-nanometer resolution [2], but require a single mode input waveguide, which largely limits their optical throughput (*étendue*), which is critical when spatially extended and incoherent sources are analyzed. Planar waveguide Fourier-Transform spectrometers based on the principle of Spatial Heterodyne Spectroscopy (SHS) have been recently propose to overcome this *étendue* limitation [3,4]. SHS is an interferometric technique based on the Michelson interferometer [5], and in which moving mirrors are replaced by diffraction gratings [6]. The SHS concept can be implemented by a waveguide array of Mach-Zehnder interferometers (MZI) with increasing path differences [3,7]. Full spectrum analysis within the free spectral range of the device is performed in a single measurement, by Fourier analysis of the output stationary interference pattern.

In this work, we present a SHS-FT spectrometer with enhanced resolution in a small footprint by implementing tightly coiled spiral waveguide structures in a MZI array.

II. PRINCIPLE OF OPERATION

Our Fourier-transform spectrometer comprises an array of N silicon wire waveguide MZIs with an increasing path length difference ΔL_i, which is achieved by combining in each MZI an arm with a straight waveguide and another arm with a spiral waveguide. Thanks to the high contrast index of the silicon-on-insulator (SOI) platform, spirals with high path lengths can be implemented in a reduced diameter of a few hundred micrometers. For a given input spectral distribution, the dispersive nature of the MZIs produces a wavelength-dependent oscillatory pattern (interferogram $F(x_i)$) at the outputs of the array, allowing to retrieve the full input spectrum p_{in} by discrete Fourier cosine transform of the interferogram:

$$p_{in}(\bar{\sigma}) = \frac{\Delta x_{\max}}{N} P_{in} + 2\frac{\Delta x_{\max}}{N}\sum_{i=1}^{N} F(x_i)\cos 2\pi\bar{\sigma}x_i \qquad (1)$$

where x_i is the path delay of the i-th MZI, Δx_{max} is the maximum optical path difference, P_{in} is the input power, and $\bar{\sigma} = \sigma - \sigma_L$ is the shifted wavenumber, relative to the Littrow wavenumber σ_L. The resolution $\delta\lambda$ and free spectral range $\Delta\lambda$ of the spectrometer are determined by $\delta\lambda = \lambda_0^2/(\Delta L_{max} \times n_{eff}) = 2\Delta\lambda/N$, where λ_0 is the spectrometer central wavelength and n_{eff} is the effective index of the waveguide mode.

The distortion of the interferogram, produced by different propagation losses across the MZI array and phase errors arising from fabrication imperfections, need to be calibrated and corrected in the spectral retrieval algorithm.

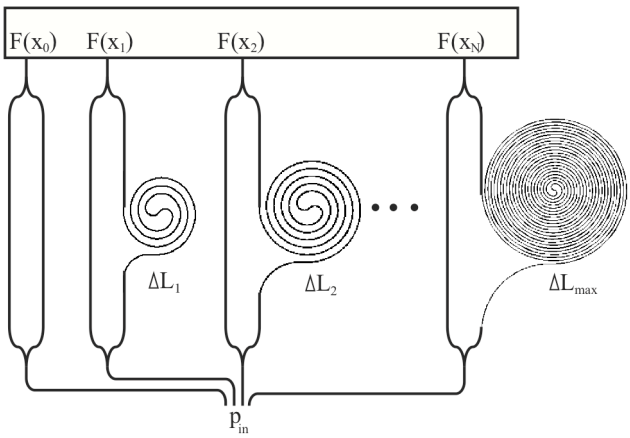


Figure 1. Schematic of the Fourier-transfrom spectrometer.

III. Design and Fabrication

The SHS-FT spectrometer comprises 32 MZIs with a maximal physical length difference ΔL_{max} = 1.13 cm. With an estimated effective index of $n_{eff,}$ = 2.12 for TM polarization at a central wavelength of 1.55 μm, the device is designed for a resolution of 0.1 nm and a free spectral range of 1.6 nm. To simplify optical measurements, a single input was used, followed by cascaded 1:2 *y*-splitters. Efficient subwavelength grating couplers [7] were included both at the input and the outputs of the chip.

Samples were fabricated on SOI substrates with a 0.26 μm thick silicon and a 2 μm thick buried oxide (box) layers. All structures were defined in a single patterning step by electron beam lithography with high contrast hydrogen silsequioxane (HSQ) resist, and transferred into the silicon layer by inductively coupled plasma reactive ion etching (ICP-RIE).

IV. Experimental Results

The fabricated device was thermally stabilized using a Peltier stage and the output interferogram was characterized using a high-resolution tunable semiconductor laser over the range 1549 nm - 1551 nm, with a wavelength step of 1 pm (Fig. 2). A polarization controller was used to select TM input field. Phase errors and propagation loss were characterized by fitting the output wavelength-dependent signal at each MZI to a sinusoidal function, and corrected in the spectral retrieval algorithm. Experimental results show an average effective index of 2.18 with variations under 1% among the MZI array.

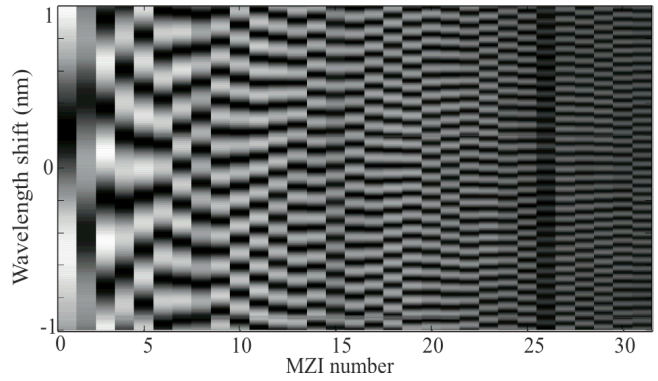


Figure 2. Output power distribution of the 32 MZI for a 2 nm wavelength scan centered at 1.55 μm.

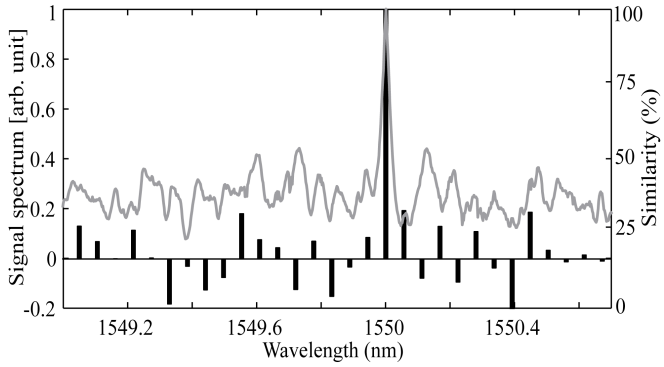


Figure 3. Measured spectral search similarity of a narrowband source centered at 1550 nm (gray), and Fourier-based retrieved spectrum (black).

The device was tested with two different types of numerical analysis of the output pattern (Fig. 3). First, a spectral search technique was used, comparing the measured interferogram with patterns obtained for different wavelengths during the calibration step [9]. Second, a Fourier-based spectral retrieval was used. The oscillations at the output of each MZI from the calibration step were used to define a $N \times N$ transformation matrix T such that $F(x)=p_{in} \times T$, taking into account the measured phase and amplitude errors. The discrete input spectrum of the actual measurement was obtained by multiplying the output pattern by a pseudoinverse T^{+} of the transformation matrix.

V. Conclusions

A planar waveguide Fourier-transform spatial heterodyne spectrometer has been demonstrated for the first time in silicon wire waveguides. The spectrometer comprises an array of unbalanced Mach-Zehnder interferometers with spiral waveguide delays. Phase errors and propagation losses of the MZI array were characterized and compensated. The use of tightly coiled spiral waveguides allows a high spectral resolution of 0.1 nm for a device footprint of only 12 mm^2. The potential applications include disposable biological and environmental sensing, hand-held spectroscopic instrumentation, and sensing from microsatellite platforms.

Acknowledgments

Financial support from the Spanish Ministry of Science and Innovation is acknowledged under grant TEC2008-04105.

References

[1] P. Cheben, "Wavelength dispersive planar waveguide devices: Echelle gratings and arrayed waveguide gratings," in Optical Waveguides: From Theory to Applied Technologies, Eds. M. L. Calvo and V. Laksminarayanan, Chapter 5, CRC Press, London, 2007

[2] P. Cheben, J. H. Schmid, A. Delâge, A. Densmore, S. Janz, et al., "A high-resolution silicon-on-insulator arrayed waveguide grating microspectrometer with submicrometer aperture waveguides," Opt. Express, vol. 15, pp. 2299-2306, 2007.

[3] P. Cheben, I. Powell, S. Janz, and D.-X. Xu, "Wavelength-dispersive device based on a Fourier-transform Michelson-type arrayed waveguide grating," Opt. Lett., vol. 30, pp. 1824-1826, 2005.

[4] M. Florjańczyk, P. Cheben, S. Janz, A. Scott, B. Solheim, and D. X. Xu, "Multiaperture planar waveguide spectrometer formed by arrayed Mach-Zehnder interferometers," Opt. Express, vol. 15, pp. 18176-18178, 2007.

[5] P. Jacquinot, "The luminosity of spectrometers with prisms, gratings, or Fabry-Perot etalons," J. Opt. Soc. Am., vol. 44, pp. 761-765, 1954.

[6] J. M. Harlander, F. L. Roesler, J. G. Cardon, C. R. Englert, and R. R. Conway, "A Spatial Heterodyne Spectrometer for Remote Sensing of Earth Middle Atmosphere" Appl. Opt., vol. 41, pp. 1343-1345, 2002.

[7] K. Okamoto, H. Aoyagi, and K. Takada, "Fabrication of Fourier-transform, integrated-optic spatial heterodyne spectrometer on silica-based planar waveguide," Opt. Lett., vol. 35, pp. 2103-2105, 2010.

[8] P. Cheben, P. J. Bock, J. H. Schmid, J. Lapointe, S. Janz, et al., "Refractive index engineering with subwavelength gratings for efficient microphotonic couplers and planar waveguide multiplexers" Opt. Lett., vol. 35, pp. 2526-2528, 2010.

[9] P. R. Griffiths and J. A. de Haseth, Fourier Transform Infrared Spectrometry, 2nd ed., New York: John Wiley & Sons, 2007, pp. 246-249.

High-Speed Uni-Travelling Carrier Photodiodes for InP Photonic Integrated Circuits

Efthymios Rouvalis[1*], Mourad Chtioui[2], Michael Tran[2], Frédéric van Dijk[2], Martyn J. Fice[1], Cyril C. Renaud[1], Guillermo Carpintero[3], and Alwyn J. Seeds[1]

[1]Department of Electronic and Electrical Engineering, University College London, Torrington Place, London, WC1E 7JE, UK
[2]III-V Lab, a joint Laboratory of "Alcatel Lucent Bell Labs", "Thales Research & Technology" and "CEA-LETI", Campus Polytechnique, 1, Avenue A. Fresnel, 91767, Palaiseau Cedex, France
[3]Universidad Carlos III de Madrid, Av. de la Universidad, 30. Leganés 28911, Madrid, Spain
*e.rouvalis@ee.ucl.ac.uk

***Abstract*—We report on the design, growth and fabrication, and experimental assessment of Ultra-Fast InGaAsP/InP Uni-Travelling Carrier Photodiodes (UTC-PDs) suitable for active-passive monolithic integration with various Multiple Quantum Well (MQW) devices. The final Photonic Integrated Circuits (PICs) are expected to enable high bit rate (>10 Gbps) wireless transmission at a carrier frequency of 120 GHz. The proposed devices achieved a high 3-dB bandwidth of up to 110 GHz and a generated output power of more than 0 dBm (1 mW) at 120 GHz.**

Keywords*—*Uni-Travelling Carrier Photodiode (UTC-PD), Wireless Transmission, Monolithic Integration, Microwave Photonics, Millimeter-waves.

I. INTRODUCTION

The field of high speed wireless communications has seen a tremendous evolution recently driven by the demand for wireless bit rates over 1 Gbps [1]. The bandwidth being limited in the traditional bands, carrier frequencies in the millimetre-wave range have to be utilised, especially those above 60 GHz, where the bandwidth allocated would enable the required data rates. Recent work has shown the advantages of photonic techniques and components for that frequency range [2]. For the photonic solution, photomixing in a fast photodetector is the key technique to generate the carrier frequency.

Despite their great potential, most optoelectronic photomixing systems suffer from high power consumption that is the result of poor fibre-to-chip coupling and polarization dependent loss. Monolithic passive-active integration of Distributed Feedback (DFB) lasers with tunable sections [3], Electro-Absorption Modulators (EAMs), Semiconductor Optical Amplifiers (SOAs) and Multimode Interference (MMI) couplers in a single photonic integrated circuit (PIC) can offer a solution for efficient generation of an optical heterodyne signal that can be used as an input to a high bandwidth photodiode. Nevertheless, fast photodiodes are usually fabricated in a waveguide configuration with a thin absorber layer. Uni-Travelling Carrier Photodiodes (UTC-PDs) have been demonstrated as efficient Terahertz photomixers in [4] and [5]. In this paper we demonstrate high speed (f_{3dB} > 100 GHz) UTC-PDs based on epitaxial regrowth in a Multiple Quantum Well platform with generated output power of 1 mW at 120 GHz. Losses in passive sections and MMI couplers were also assessed. We expect this technology to lead to photomixing PICs suitable for 10 Gbps wireless transmission at 120 GHz.

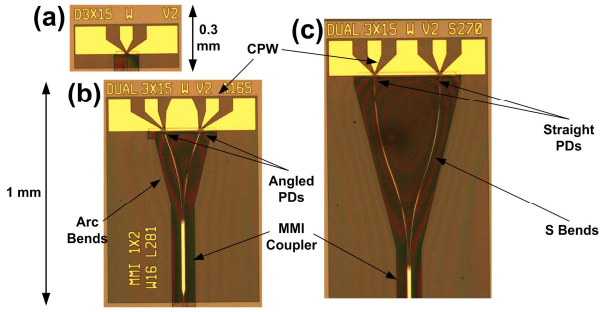


Figure 1: Images of chips with (a) Single UTC-PDs, (b) Dual angled UTC-PDs with Arc-Type bends and (c) Dual straight UTC-PDs with S-type bends.

II. UTC-PD DESIGN CHALLENGES

One of the main challenges is to design fast photodetectors despite the high series resistance that is introduced from the thick top cladding layer. This thicker layer is introduced to allow for both a strong passive waveguide section and to enable integration with laser structure where the InP contact layer is usually thick to avoid coupling of the optical mode into the strongly guiding layer just under the metal contact, also used as the p-contact layer for the photodiode. Light from passive waveguide sections is evanescently coupled into the photodiode absorber. An optimisation process based on a semi-analytical model [5], showed that the active area dimensions for maximum power generation at the target frequency of 120 GHz was 3×15 μm^2. In this simulation a constant level of optical power was considered at the input of the UTC-PD to account for the length-dependent responsivity.

III. GROWTH AND FABRICATION

The developed UTC-PDs are made on semi-insulating InP substrate using gas source molecular beam epitaxy. For the fabrication of these devices we implemented monolithic integration of passive waveguides and optical couplers, and photodiode (PD) active sections. This was done with two epitaxial growth steps. The process flow of our integrated UTC-PDs fabrication is then mainly based on dry and wet

This work was supported by the European Commission within the framework of the European project iPHOS (grant agreement no: 257539). Dr. Rouvalis' work was supported by the Engineering and Physical Sciences Research Council under the EPSRC Doctoral Prize Fellowship scheme.

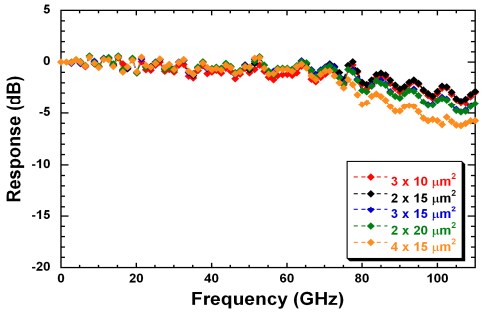


Figure 2: Frequency response up to 110 GHz from UTC-PDs with various active area dimensions.

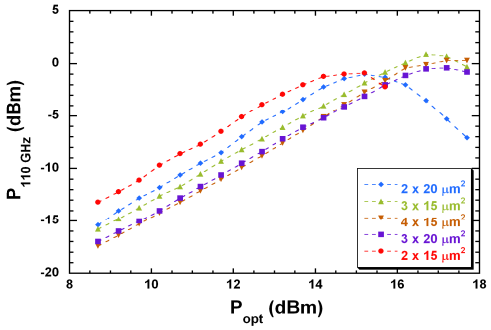


Figure 3: Power saturation at 110 GHz for various UTC-PDs with different active area dimensions. The reverse bias voltage was 3 V.

etchings for the realisation of shallow ridge waveguides, PD mesa, and PD isolation. Finally, a BCB planarization step is performed, followed by a metallisation step for electrodes interconnection. This process flow uses fabrication steps that are compatible with the integration of MQW active sections and the realisation of shallow ridge laser and SOA waveguides.

IV. Single Photodiodes

The mask that was designed for these devices included various types of UTC-PDs with different passive sections. The performance of the UTC-PDs was first measured on chips with single devices (Fig 1(a)). The responsivity at 1.55 μm of devices with a short waveguide (70 μm) was found to be 0.35 A/W despite the fact that the waveguide was not designed for coupling from a fiber and the absence of an anti-reflection coating. The frequency response from the single UTC-PDs was assessed using two external cavity lasers, coplanar probes and a microwave power meter. The frequency response for devices with various dimensions can be seen in Fig. 2. A 3-dB bandwidth between 80 and 110 GHz was measured depending on the device active area dimensions. The generated RF power at 110 GHz as a function of the optical input power was measured to investigate saturation effects. The results are shown in Fig. 3. The maximum output power was generated by a device with an active area of 3×15 μm^2. Devices with smaller active area dimensions suffer from stronger saturation while the larger devices have a limited frequency response due to a higher capacitance.

V. Dual Photodiodes

Chips with dual photodiodes and 1×2 MMI couplers were also assessed (Fig. 1(b), 1(c)). Single photodiodes with the same chip length were also included in the mask in order to evaluate the propagation loss independently from the insertion loss introduced from the MMI coupler and the S-type and Arc-type waveguide bends. The responsivity at 1.55 μm of devices with chip lengths varying from 770 μm to 1170 μm was compared to the one found from single devices with a short input waveguide (70 μm). An average propagation loss of 2.6 dB/mm was found from these measurements.

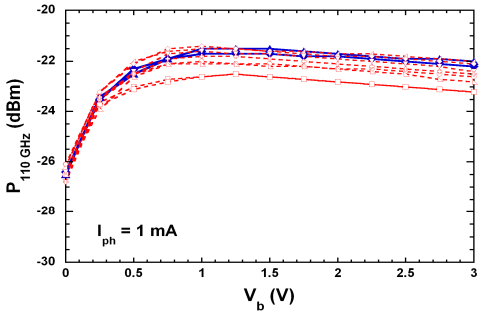


Figure 4: Generated power at 110 GHz for straight (blue) and angled (red) UTC-PDs.

Three types of dual 3×15 μm^2 photodiode chips were assessed. The first one included Arc-type bends and angled photodiodes to minimize the chip area and the other two included S-type bends and angled and straight photodiodes respectively. The total insertion loss (MMI + bends) was found to be 3.2 dB, 3.6 dB and 4.3 dB respectively by comparing the measured responsivity with the one from single devices with the same chip length.

In order to investigate the effect of the angled photodiodes and coplanar waveguides on the frequency response of the UTC-PDs, the generated output power at 110 GHz (Fig. 4) was measured from straight and angled photodiodes at the same photocurrent level (1 mA). An additional average loss of only 0.5 dB at 110 GHz was measured from the angled photodiodes, proving that they are a viable solution for the demonstration of a monolithically integrated heterodyne source.

Acknowledgement

The authors thank François Lelarge for his contribution through epitaxial growth and Genevieve Glastre for useful discussions.

References

[1] H.-J. Song, and T. Nagatsuma, “Present and Future of Terahertz Communications,” IEEE Transactions on Terahertz Science and Technology, vol. 1, no. 1, pp. 256–263, 2011.

[2] A. Stöhr et al., “Millimeter-Wave Photonic Components for Broadband Wireless Systems,” IEEE Transactions on Microwave Theory and Techniques, vol. 58, no. 11, pp. 3071–3082, 2010.

[3] F. van Dijk et al., “Monolithic dual wavelength DFB for narrow linewidth heterodyne beat-note generation,” Proc. IEEE Intl. Topical Meeting Microw. Photon. (MWP), 2011, pp. 73–76.

[4] E. Rouvalis, C. C. Renaud, D. G. Moodie, M. J. Robertson, and A. J. Seeds, “Travelling-Wave Uni-Travelling Carrier Photodiodes for continuous wave THz generation,” Optics Express, vol. 18, no. 11, pp. 11105–11110, 2010.

[5] E. Rouvalis, C. C. Renaud, D. G. Moodie, M. J. Robertson, and A. J. Seeds, “Continuous Wave Terahertz Generation From Ultra-Fast InP-Based Photodiodes,” IEEE Transactions on Microwave Theory and Techniques, vol. 60, no. 3, 2012.

A slow light silicon-based Mach-Zehnder Interferometer for frequency mixing applications

A.M.Gutiérrez, A.Brimont, A.Aamer, J.Martí, P.Sanchis
Nanophotonics Technology Center
Universitat Politecnica Valencia
Valencia, Spain
angucam@ntc.upv.es

D.J.Thomson, F.Y.Gardes, G.T.Reed
School of Electronics and Computer Science
University of Southampton
Southampton, UK*
*Some work performed whilst at the University of Surrey

J-M.Fedeli
CEA-LETI
Campus Minatec
Grenoble, France

***Abstract*—A silicon photonic-mixer Mach-Zehnder modulator enhanced via slow-light has been demonstrated. An input frequency signal from 1GHz to 10.25GHz is successfully up-converted with low conversion losses ~7dB and excellent quality of the received signal showing an optimum EVM ~8%.**

Keywords-Integrated; Mixing; Up-conversion; Modulator

I. INTRODUCTION

Radio-frequency (RF) analog data processing in Analog Photonic Links (APL) encompasses numerous potentially applications such as Radio-over-Fiber (RoF), antenna remoting, subcarrier transmission or photonic analog-to-digital conversion. The use of silicon photonic devices to generate analog RF signals may lead to chip-size reduction and power-efficiency improvements. In addition, the Silicon-On-Insulator (SOI) platform offers the possibility of mass-manufacturing as well as cost-effective integration with CMOS electronics. In APLs, RF signals are converted into the optical domain by an electro-optic modulator for which the most important achievements have been demonstrated during recent years by means of the plasma dispersion effect, although mostly for digital communications. However, very little attention has been given to analog applications [1,2]. Besides the transport of RF signals over fiber, nowadays, signal mixing is an interesting and necessary technique. In contrast to conventional electrical mixing schemes, photonic mixing techniques for RoF communications feature superior characteristics such as ultra-wide bandwidth and immunity to electromagnetic interference. Several works have reported photonic mixers [3,4] using commercial $LiNbO_3$ modulators due to their highly linear characteristic when operated at quadrature. However, to our knowledge, no work on silicon photonic mixers has been demonstrated so far.

In this work, a silicon-based Mach-Zehnder modulator enhanced via slow-light propagation is used as photonic mixer for frequency up-conversion. Performance of our APL is measured in terms of Spurious Free Dynamic Range (SFDR) and conversion losses. EVM is also measured for the mixed received signal under a QPSK format modulation. Furthermore, comparisons between the slow and fast light regions and optimization of the operating bias point have been carried out.

II. DEVICE STRUCTURE

Silicon-based electro-optic Mach-Zehnder modulator used as photonic mixer is shown in Fig. 1.

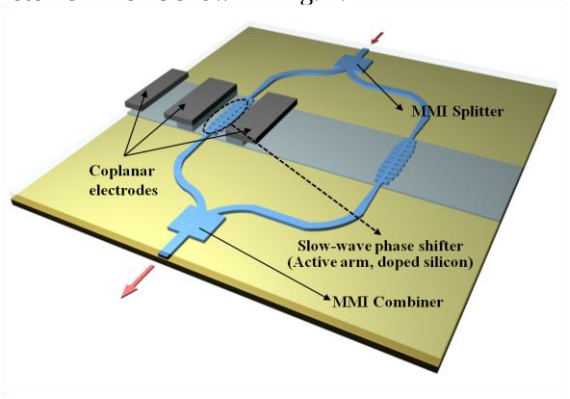


Figure 1. Schematic of the slow-wave modulator used for mixing.

Slow light propagation is achieved through the use of a 1D periodic structure consisting of a laterally corrugated waveguide with a reverse biased *pn* junction embedded. Optical phase modulation in the slow wave waveguide is converted into amplitude modulation via the use of an asymmetric MZI structure. As was demonstrated in [5] from digital measurements, the slow-light effect enhanced the modulation efficiency, allowing modulation data rates up to 40 Gb/s over an interaction length of only 500µm at a group index of only ~11.

III. EXPERIMENTAL RESULTS

For the study of the mixing efficiency, a two-tone test has been carried out. The IF and OL frequencies are set to 1GHz and 9.25GHz respectively. Nonlinearity depends on the operating bias point of the MZI transfer function but also on the nonlinear response intrinsic to the material in the active region. In the case of $LiNbO_3$ modulators, the former is the dominant contribution to the nonlinear performance. Therefore, the

quadrature bias (QB) point, is usually exploited to convert the IF frequency to the third-order intermodulation distortion (IMD3) products ($2f_{IF}\pm f_{OL}$). However, in our case, the nonlinear response of the free-carrier dispersion in silicon together with the slow-light propagation also plays a prominent role in the mixing performance. To evaluate the intermodulation distortion performance of our silicon modulator, we have defined and measured the conversion losses, as in [3], as the ratio between the photo-detected electrical power at f_{IF} and the photo-detected electrical power of the considered intermodulation term at $f_{IF}+f_{OL}$=10.25GHz for IMD2 and $2f_{IF}+f_{OL}$=11.25GHz for IMD3. So, when a given intermodulation product power is maximized with the bias point, the conversion losses of the product should be minimized. Initially, we investigated the nonlinear performance and conversion losses at QB. Conversely to $LiNbO_3$ modulators, we obtained large conversion losses (55dB for 15dBm IF input power) for the IMD3. Furthermore, lower conversion losses were measured (35dB for 15dBm IF input power) for the IMD2. Based on these results, the modulator was biased at minimum transmission (MITB), where usually the IMD2 products are maximized and dominate over the third-order and the fundamental terms [6].

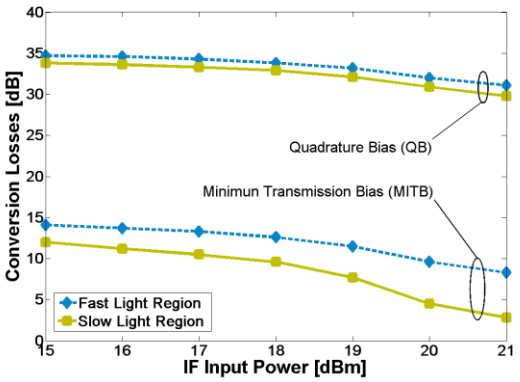


Figure 2. Conversion losses at QB and MITB bias points for both slow and fast-light regions at IMD2 intermodulation frequency. OL input power was set to be 20dBm.

In this case, conversion losses for IMD2, shown in Fig. 2, were reduced by more than half (around 13dB for 15dBm IF input power) and therefore a significant improvement results in conversion losses (~30dB) between biasing the modulator at QB or MITB. On the other hand, lower conversion losses were also obtained in the slow light region when compared to the fast light region (~2-4dB more at MITB and ~1dB at QB). As a result, the IMD2 frequency (10.25GHz) and MITB operation point was chosen to up-convert a vector modulated signal. For our SFDR, defined as the output power difference between the intersection of the IMD3 power signal at 11.25GHz with the noise floor and the IMD2 power signal at 10.25GHz, $62.8dB.Hz^{2/3}$ and $60.2dB.Hz^{2/3}$ for the slow and fast light regimes have been measured respectively. These results confirm again the enhanced performance brought by the slow-light regime. In both cases, a third order intercept point around ~25dBm has been measured.

For the EVM measurements, a I/Q modulated signal at the f_{IF}=1GHz under a digital modulation scheme of QPSK with 20Mbps is up-converted to $f_{IF}+f_{OL}$=10.25GHz frequency with the electro-optic modulator biased at MITB point. It is clear from the Fig. 3 that enhanced performance in terms of EVM is obtained in the slow light regime over the entire range of IF input powers. Outstanding results have been obtained with a very low optimum EVM of 8% and 12% for both slow and fast light regimes, respectively, allowing a very clean constellation. This confirms that the received signal is of acceptable quality.

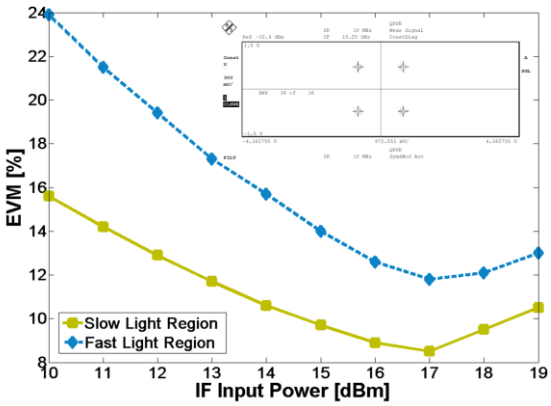


Figure 3. EVM as a function of IF Input Power for both fast and slow light propagation. Inset shows received constellation in the slow light region case at the optimum point of IF input power (17dBm).

IV. Conclussions

We have shown an efficient method of generating mixing products in a silicon modulator exploiting the nonlinearity produced by both the MZI transfer function and the plasma dispersion effect in silicon. The conversion efficiency has been enhanced via slow-light propagation in the active region of the modulator. Optimum performance has been achieved at MITB with low conversion losses around 7dB and large SFDR of $62.8dB.Hz^{2/3}$. Finally a 20Mbps QPSK signal at 1GHz has been successfully up-converted to 10.25GHz. A minimum EVM of about 8% has been achieved, meeting well enough the EVM requirements for an acceptable quality of the received constellation.

Acknowledgment

Financial support from HELIOS (Photonics Electronics Functional Integration on CMOS) FP7-224312 and Generalitat Valenciana under PROMETEO-2010-087 R&D Excellency Program (NANOMET) are acknowledged. The authors thank the Dr. J. Herrera for its useful help.

References

[1] F. Vacondio, M. Mirshafiei, J. Basak, L. Ansheng, L. Ling, M. Paniccia, and L. A. Rusch, IEEE J. Sel. Top. Quant., 16, 141 (2010)

[2] S. Muping, Z. Lin, R. G. Beausoleil, and A. E. Willner, IEEE J. Sel. Top. Quant. 16, 185 (2010).

[3] J. Marti, V. Polo, F. Ramos, and J. M. Fuster, Wireless Personal Communications 15, 31 (2000).

[4] B. Cabon, Trans. Comp. Scie. & Eng. and Elect. 17, 13 (2010).

[5] A. Brimont, D. J. Thomson, P. Sanchis, J. Herrera, F. Y. Gardes, J. M. Fedeli, G. T. Reed, and J. Martí, Opt. Exp. 19, 20876 (2011)

[6] Thesis D. Marpaung, University of Twente, Netherlands (2009).

Arrayed Waveguide Grating for Polarized Raman Spectroscopy of Human Teeth

N. Ismail, K. Wörhoff, A. Driessen, R. M. de Ridder, and M. Pollnau
Integrated Optical Micro Systems Group,
MESA+ Institute for Nanotechnology,University of Twente,
P.O. Box 217, 7500 AE Enschede, The Netherlands
n.ismail@ewi.utwente.nl

L.-P. Choo-Smith,[1] A. C. Baclig,[2] P. J. Caspers,[2] G. J. Puppels,[2]
[1]IBD - National Research Council Canada,
Winnipeg, Manitoba, Canada
[2]Center for Optical Diagnostics and Therapy, Department of Dermatology, Erasmus-University Medical Center
Rotterdam, The Netherlands

***Abstract*— We designed an arrayed-waveguide grating spectrometer for the detection of early dental caries in teeth through polarized Raman spectroscopy. Measurement results on extracted human teeth demonstrate the feasibility of the approach. (Abstract)**

Keywords-component; Raman spectroscopy; integrated optics;

I. INTRODUCTION

The use of Raman spectroscopy, and in particular polarized Raman spectroscopy (PRS) has been shown to be applicable for the detection of dental caries [1, 2] and gives complementary information to that which can be obtained using conventional techniques such as visual inspection and OCT. Furthermore, PRS can be used reliably for detecting dental caries even at an early stage [2]. In our work we aim at realizing low-cost, hand-held devices for polarized Raman spectroscopy of teeth. Here, the speed of the device is a very important aspect since both the operator who is holding the device and the subject under examination will inevitably move during the measurement. For *in-vivo* measurements the device must be able to acquire a Raman signal over the entire spectral region of interest in a matter of a few seconds [3]. We choose as the core element of our device the arrayed-waveguide grating (AWG) [3], which enables simultaneous access to all spectral components of the input signal, leading to a fast measurement irrespective of the required spectral range and resolution. The working principle of the AWG can be described as follows: light from an input channel waveguide is guided to a free-propagation region (FPR) where it diffracts in the horizontal direction and is coupled to an array of channel waveguides which are arranged on a circle of radius R equal to the length of the FPR. On this circle the arrayed waveguides are spaced by a center-to-center distance $d << R$. The arrayed waveguides have a linearly increasing length with step $\Delta L = m\lambda_c/n_{eff}$, where m is an integer, λ_c is the central wavelength of the AWG, and n_{eff} is the effective refractive index of the arrayed waveguides at λ_c. Light exiting from the array enters a second FPR where the output terminations of the arrayed waveguides are again arranged on a circle with radius R. The center of this circle coincides with the entrance facet of the central output channel of the AWG. In this arrangement, when light at wavelength λ_c is sent through the input channel, a circular wave front is generated at the output of the array, and the light is focused into the central output channel. At a different wavelength ($\lambda \neq \lambda_c$) the circular wave front at the output tilts with respect to the one for λ_c and the focal spot is located at a different spatial position. Waveguides can be placed at different positions at the output of the second FPR to collect individual spectral components of the input signal. A potential disadvantage, the limited free spectral range (FSR) achievable for a given device size, can be overcome by a technology platform providing larger refractive index contrast, or by accepting spectrally folded, yet non-overlapping peaks, as discussed in [5].

II. POLARIZED RAMAN SPECTROSCOPY OF TEETH

The method relies on measuring the Raman signal from tooth enamel in the spectral region from 375 cm^{-1} to 1175 cm^{-1}. In this region the strongest band is the symmetric P-O stretching vibration of the phosphate ions $(PO_4)^{3-}$ located near 959 cm^{-1}, which arises from hydroxyapatite crystals of tooth enamel. Information on the state of the disease is provided by the ratio of the intensities of two orthogonal polarization states (perpendicular and parallel to the polarization of the excitation laser) of the 959 cm^{-1} hydroxyapatite peak. Their intensity ratio is referred to as the depolarization ratio, $\rho_{959} = I_{959}(\perp) / I_{959}(\parallel)$. In sound enamel the hydroxyapatite signal is highly polarized in the direction parallel to that of the excitation laser, and the value of the depolarization ratio is approximately $\rho_{959} = 0.10 \pm 0.04$ [2]. As the carious lesion develops, the depolarization ratio increases to $\sim 0.4 \pm 0.12$ due to a structural modification of the tooth enamel [2].

III. AWG DESIGN AND CHARACTERIZATION

The device is designed for an excitation wavelength of 830 nm because it induces less fluorescence background in tissue than shorter wavelengths. With this excitation wavelength the hydroxyapatite peak is positioned at ~901 nm. To resolve the peak the AWG is designed to have a central wavelength of 901 nm, a FSR of ~22 nm between 890 and 912 nm, and a resolution of 0.2 nm. The AWG is fabricated using single-mode silicon oxynitride [6] channel waveguides with with 2.2 µm width and 0.52 µm height. The waveguide core and cladding refractive indices are 1.509 and 1.445 at 830 nm, respectively. The AWG has a working order of $m = 41$ to avoid

This work was supported in the Innovative Research Program (IOP) Photonic Devices funded by the Dutch Ministry of Economic Affairs.

overlap (at higher imaging orders) between the excitation wavelength and the hydroxyapatite peak. In Fig. 1 we show the measured spectral response of the central AWG channels compared to the simulation results. The characterized device has a central wavelength of 900.78 nm (for TE polarization), a resolution of 0.2 nm and a FSR of ~22 nm (as designed). Furthermore, the characterized AWG exhibits a polarization-dependent response in which the wavelength shift between the TE and the TM polarizations is 0.5 nm.

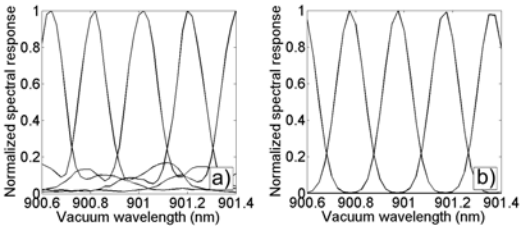


Figure 1. Normalized spectral response of the central channels of the AWG for the transverse-electric (TE) polarization. (a) measured; (b) simulated.

IV. EXPERIMENTAL RESULTS

The setup used to perform polarized Raman measurements with the AWG is shown in Fig. 2.

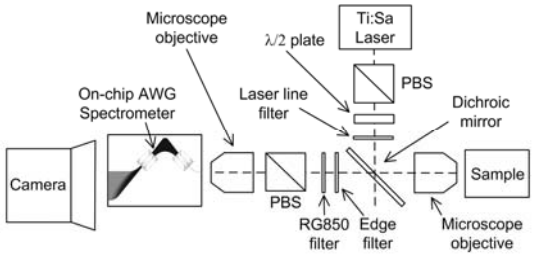


Figure 2. Schematic diagram of the setup used for the polarized Raman experiments.

Light from a linearly polarized Ti:Sapphire laser at 830 nm is sent through a polarization beam splitter (PBS) oriented parallel to the laser polarization. A half-wave plate, initially with one of its optical axes parallel to the laser polarization, is placed after the PBS. The laser light exiting the λ/2 plate, after passing through a laser-line filter (Semrock LL01-830-12.5), is reflected from a dichroic mirror (Semrock LPD01-830RS-25) and focused onto the sample (extracted human tooth) with a ×40 microscope objective having numerical aperture NA = 0.65. The light backscattered from the sample is then collected by the same optics. The Rayleigh-scattered component is again reflected (rejected) by the dichroic mirror while the Raman-scattered wavelengths are transmitted. An edge filter (Semrock LP02-830RS-25) and an additional red-glass filter (RG 850) are used to further suppress residual reflected and Rayleigh-scattered light at the laser wavelength. At this point we position a second PBS with the same orientation as the first, and a ×50 (NA = 0.85) microscope objective to focused the light onto the input channel of the AWG spectrometer. The spectroscopic measurement is performed by imaging the output channels of the AWG onto an electron-multiplying charge-coupled device (Andor iXonEM DV887ECS-BV, EMCCD) through a camera lens (JML f0.95 50 mm). In order to perform the measurements for perpendicular polarization, the λ/2 plate is rotated by 45°, to rotate the laser polarization by 90°.The measurements were performed on extracted human tooth samples presenting clinical white spot lesions as early dental caries. We used 200 mW of incident power on the tooth surface. The Raman signal was strong and clearly visible with integration times as short as 10 s. In Fig. 3 we show representative spectra measured with 80 s integration time and 10 accumulations.

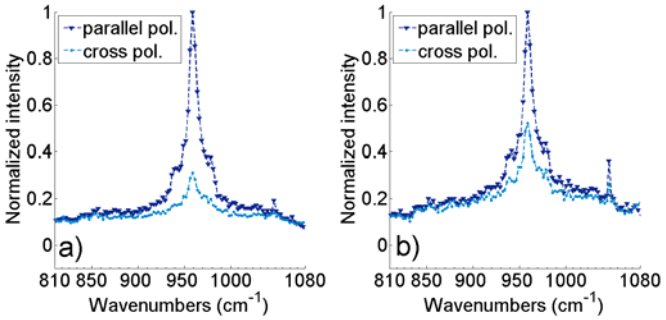


Figure 3. Raman spectra of (a) sound and (b) carious tooth enamel for both, parallel (triangles) and cross (dots) polarizations acquired with the AWG.

We calculate depolarization ratios of $\rho_{959} = 0.16 \pm 0.047$ for the sound regions and $\rho_{959} = 0.41 \pm 0.01$ for the carious regions, which are close to the values reported in the literature [2].

V. CONCLUSIONS

We have designed and fabricated an AWG spectrometer to be used in polarized Raman spectroscopy of human teeth. Our measurement results, which are comparable with the ones found in the literature for both, sound and carious regions of tooth enamel, demonstrate the feasibility of our approach.

REFERENCES

[1] W. Hill and V. Petrou, "Caries Detection by Diode Laser Raman Spectroscopy," Applied Spectroscopy, vol. 54, pp. 795-799, 2000.

[2] A. C.-T. Ko, L.-P. i. Choo-Smith, M. Hewko, M. G. Sowa, C. C. S. Dong, and B. Cleghorn, "Detection of early dental caries using polarized Raman spectroscopy," Optics Express, vol. 14, pp. 203-215, 2006.

[3] E. B. Hanlon, R. Manoharan, T.-W. Koo, K. E. Shafer, J. T. Motz, M. Fitzmaurice, J. R. Kramer, I. Itzkan, R. R. Dasari, and M. S. Feld, "Prospects for in vivo Raman spectroscopy," Physics in medicine and biology, vol. 45, pp. R1-R59, 2000.

[4] M. K. Smit, "New focusing and dispersive planar component based on an optical phased array," Electronics Letters, vol. 24, pp. 87-88, 1988.

[5] N. Ismail, L.-P. Choo-Smith, K. Wörhoff, A. Driessen, A. C. Baclig, P. J. Caspers, G. J. Puppels, R. M. de Ridder, and M. Pollnau, "Raman spectroscopy with an integrated arrayed-waveguide grating," Optics Letters, 2011.

[6] K. Wörhoff, C. G. H. Roeloffzen, R. M. d. Ridder, A. Driessen, and P. V. Lambeck, "Design and application of compact and highly tolerant polarization independent waveguides," Journal of Lightwave Technology, vol. 25, pp. 1276-1283, 2007.

Tunable bandwidth optical filter in SOI

P. Orlandi, P. Bassi
Dipartimento di Elettronica, Informatica e Sistemistica,
Università di Bologna,
Bologna, Italy,
piero.orlandi@unibo.it

C. Ferrari, A. Canciamilla, F. Morichetti, A. Melloni
Dipartimento di Elettronica e Informazione,
Politecnico di Milano,
Milano, Italy

M. J. Strain, M. Sorel
School of Engineering,
University of Glasgow,
Glasgow, United Kingdom

***Abstract*—Compact tunable silicon-on-insulator bandpass filters are fabricated. The novel proposed geometry provides filter bandwidth tunability from 10% to 90% of the free spectral range, preserving high off-band rejection (>16 dB).**

Keywords- Optical filter; Mach-Zehnder interferometer; ring resonator; silicon-on-insulator;

I. INTRODUCTION

Dynamically reconfigurable and adaptive photonic integrated circuits are key components of the next generation telecom systems. Among them, filters tunable in both central wavelength and bandwidth are highly desirable to implement flexible and adaptive system functionalities. Tuning the bandwidth of integrated optical filters is not an easy task and only a few geometries have been demonstrated so far. A single ring resonator (RR) with tunable coupling sections [1,2] offer poor design flexibility, limited bandwidth and reduced off-band rejection. Filters combining a Mach-Zehnder Interferometer (MZI) with RRs [3] provide high off band rejection but exhibit a severely limited bandwidth tuning range due to in-band ripples and insertion loss. Design flexibility, bandwidth tunability, high off-band rejection and simple control can all be obtained using a single unbalanced MZI with all-pass RRs [4]. Here we demonstrate a simpler design, where the phase response of only one arm of the MZI is shaped with two RRs cascaded in all-pass configuration. This simplified approach, that requires only the tuning of the RRs and of the MZI unloaded arm phases, provides a wider bandwidth reconfiguration range, an easier management with reduced power consumption and central wavelength tunability over the full Free Spectral Range (FSR), trading off a modest decrease in the off-band rejection. This geometry has been tested by realizing devices with three different FSRs (200, 100, 25 GHz) on a silicon-on-insulator (SOI) platform.

II. FILTER DESIGN AND FABRICATION

The device topology and the relevant design parameters are shown in Fig. 1. L_r is the RR cavity length. The length difference ΔL between the arms of the MZI is set equal to L_r to match the FSR of the RRs. Bandwidth tunability is achieved controlling φ_r, the absolute value of the phase shift that is antisymmetrically applied to the two RRs. The coupler splitting ratio K_c at the input and output sections of the MZI has been set to 50% to get a symmetric behavior of the Through (P_T) and the Cross (P_C) port spectral characteristics when the additional

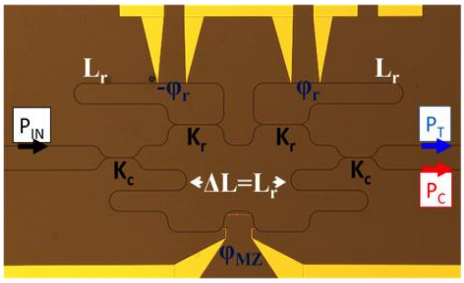


Figure 1. Optical microscope photograph of the 100GHz FSR device with the design parameters.

phase shift φ_{MZ} is changed by π. The phase change φ_{MZ}, together with φ_r, allows to tune also the filter central wavelength. The RRs power coupling coefficient K_r is critical for the design of this structure. It has been optimized to obtain the maximum bandwidth tunability range, keeping acceptable minimum off-band rejection for practical applications. An optimum value around the 75% has been found through extensive circuit simulations performed with Aspic™ (www.aspicdesign.com).

In order to test our proposed design, a 220nm-thick silicon core layer on a 1μm buried oxide sample of SOI from SOITEC was patterned as described in [5]. Deposition of a metallic bilayer of NiCr/Au onto the waveguides allows control of both φ_r and φ_{MZ} via the thermo-optic effect.

III. FILTER FUNCTIONALITY

The device behavior as a function of the differential phase shift $\Delta\varphi=2\varphi_r$ between the two RRs is shown in Fig. 2 for a filter with FSR=100 GHz. When $\Delta\varphi=0$ the RRs resonate at the same wavelength, being the RRs and the MZI FSRs equal, the maximum bandwidth condition is achieved at the Through port. The Cross port spectral behavior shows the minimum achievable bandwidth and minimum off-band rejection (blue line in Fig. 2). The differential phase shift can be easily varied by heating up one of the ring resonators and cooling down the other in a push-pull configuration. This operation allows to continuously tune the bandwidth at the two ports of the device until $\Delta\varphi=2\pi$ is reached and the spectral characteristics are swapped with respect to the initial situation (red lines in Fig 2). When $\Delta\varphi=\pi$ the device acts as a symmetric interleaver (green line of Fig. 2), similar to the device analyzed in [6]. The off-band rejection under this condition is larger than 20 dB. Similar behavior is obtained for the other fabricated devices.

Part of this work has been founded by the italian PRIN 2009 Shared Access Platform to PHotonic Integrated REsources (SAPPHIRE) project (http://sapphire.dei.polimi.it/)

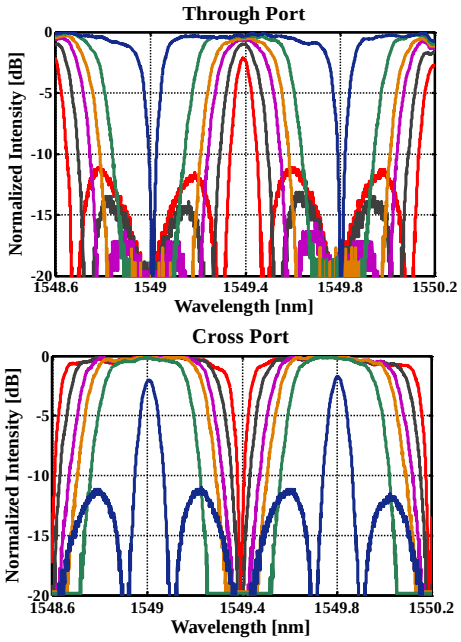


Figure 2. Experimental bandwidth tuning at the two output ports of the filter. The differential phase shift between the RRs is varied from $\Delta\varphi=0$ (blue lines) to $\Delta\varphi=2\pi$ (red lines)

Their overall performances are summarized in Table 1. Note that the lower the minimum achievable bandwidth, the lower the minimum off-band rejection. The experimental results show a wide bandwidth tunability range for all the tested devices with a maximum range for the 100 GHz one (from 90% to 10% of the FSR) and a minimum range for the 25 GHz one (from 83% to 14% of the FSR). The off-band rejection is larger than 16 dB for all the possible bandwidths of the 200 GHz device while it is larger than 10 dB for the 25 GHz filter. As it can be expected, the best performances are achieved by the device with the smaller cavity length (e.g. 200 GHz ring cavity length) since this guarantees smaller losses. Nonetheless, even the largest device fits in a footprint of roughly 0.5 mm^2 enabling dense on chip integration. The realized devices also show a maximum deviation of about 1% between fabricated and desired FSR.

The power consumption for thermal tuning is the same for all the devices, independently of the FSR. Moreover, the push pull configuration guarantees that power consumption does not even depend on the bandwidth condition. For the device whose performance is illustrated in Fig. 2, power consumption is roughly equal to 29.7 mW for the whole tuning range. However, this value can be offset if central wavelength tuning is required, since it is realized varying the total power dissipated over the RRs and the MZI to allow a rigid shift of the whole filter characteristic. The filter central wavelength of the filter spans the entire FSR by varying the total dissipated power by ~60 mW from a minimum of 4.7 mW to a maximum of 64.9 mW.

Finally, the functionality of the filter has also been tested on a 10 Gbit/s OOK modulated signal always achieving the error free condition with a small power penalty at the receiver.

IV. Conclusions

A novel single stage filter in Mach-Zehnder configuration, realized with Silicon on Insulator technology, with only one arm loaded by ring resonators has been demonstrated. It guarantees wide tunability range, easy management and acceptable off-band rejection keeping a low foot print. The generality of the design has been successfully demonstrated testing devices with three different FSRs. Furthermore, system experiments have successfully demonstrated that the designed filter can be an ideal tool for modern telecom systems based on the gridless and colorless paradigm.

Acknowledgment

We thank the JWNC staff at Glasgow University for support in fabrication of the devices and Antonio Samarelli for helpful discussions.

References

[1] J. Yao and M.C. Wu, "Bandwidth-tunable add–drop filters based on micro-electro-mechanical-system actuated silicon microtoroidal resonators," Opt. Lett. vol. 34, pp. 2557-2559, September 2009.

[2] L. Chen, N. Sherwood-Droz and M. Lipson, "Compact bandwidth-tunable microring resonator," Opt. Lett., vol 32, pp. 3361-3363, November 2007.

[3] Y. Ding et al., "Bandwidth and wavelength-tunable optical bandpass filter based on silicon microring-MZI structure," Op. Express, vol. 19, pp. 6462-6470, March 2011.

[4] M.S. Rasras et al., "Demonstration of a fourth-order pole-zero optical filter integrated using CMOS processes," J. Lightwave Technol., vol. 25, pp. 87-92, January 2007.

[5] A. Canciamilla et al., "Silicon coupled-ring resonator structures for slow light applications: potential, imapirments and ultimate limits," J. Opt., vol 2, 104008 (7 pp.), September 2010.

[6] C.K. Madsen and J.H. Zaho, Optical Filter Design and Analysis: A Signal Processing Approach. New York, NY. Jhon Wiley & Sons, inc., 1999.

TABLE I. Measured Filter Parameters of the Fabricated Devices

Designed FSR [GHz]	**Filter performance**				**Filter geometry**	
	Bandwidth tunability Range [GHz]	***Minimum off band rejection [dB]***	***Central wavelength tunability***	***Experimental FSR [GHz]***	***L_r [μm], r***	***Footprint size [μm^2]***
200	23 – 173	16	Entire FSR	197.8	305.2	557.2x307.8
100	9 – 88.5	10	Entire FSR	99.4	710.4	662.4x288.3
25	3.7 – 20.8	10	Entire FSR	25.1	2841.6	817.3x708.3

Integrated dual-wavelength AWG-lasers for millimeter wave generation

A. Corradi, G. Carpintero*, B.W. Tilma, P. J. Thijs, M.K. Smit, E.A.J.M. Bente
COBRA Research Institute, Eindhoven University of Technology
Eindhoven, the Netherlands
a.corradi@tue.nl

Abstract— **We have designed integrated dual-wavelength lasers in which an array waveguide grating is used as intra-cavity filter to allow lasing on two wavelengths within a common arm of the device. The devices have been designed with the purpose to exploit the beating of the two wavelengths on a photodiode in order to generate a 70GHz carrier wave. Both linear and ring laser configurations have been designed.**

Keywords- millimeter waves; sub-terahertz; dual-wavelength;

I. INTRODUCTION

Millimeter wave frequencies (30 GHz - 300 GHz) are of great interest in the development of broadband wireless communication systems because they can provide short range communications with data rates above 1 Gbp/s [1, 2]. Furthermore, millimeter waves can be exploited for surveillance aims [3] and for microcrack detection in concrete structures [4].

In the European Union FP7 iPHOS project, the goal is to use optical techniques to generate a 70 GHz or 120 GHz carrier wave through mixing of two low noise optical data modulated carrier frequencies on a fast photodiode coupled to an antenna. The work described in this paper concerns the development of a single semiconductor chip containing a laser source and a data modulator system.

II. DUAL WAVELENGTH AWG-BASED LASER

The source has to provide two wavelengths separated by a frequency that can be tuned around 70 GHz (68-74 GHz, E-band). Power in both wavelengths should be equal with a total output power of 10mW. The phase noise in the frequency difference signal of < 90 dBc/Hz at 100 kHz would be suitable for a communication speed filling the whole band. This can be realised by using lasers with a free running laser linewidth of several hundreds of kilohertz and then stabilizing them actively to e.g. a reference etalon with a feedback loop time of approximately 5 ns.

The aim of our work is to design and fabricate an integrated dual wavelength laser in which an intracavity Arrayed-Waveguide Grating (AWG) is used to select two cavity modes. An AWG-based laser (AWGL) has several advantages over other multi-wavelength lasers and discrete tunable lasers (e.g. DFB lasers). Firstly, it has the ability to deliver light at the available wavelengths simultaneously into the same output waveguide. Secondly, the fine tuning of the wavelength can be done through a electro-optic phase modulator (PHM) which is voltage controlled. Since the current passing through this type of PHM is typically in the nA to μA range, low power (in the order of μW) is needed to control it. As a consequence, the heat dissipation in the PHM is negligible and only a minor effect occurs on the amplification required in the cavity. Thirdly, the coarse tuning of the two wavelengths is determined by the same filter (AWG). When the temperature of the AWG filter changes, the frequency difference between its transmission channels will not change in first order. In fourth place, the layout of the laser can be made such that both wavelengths are amplified by the same semiconductor optical amplifier (SOA). In this way many sources of the frequency noise of the laser output are shared. Consequently, the noise level of the difference frequency between the two wavelengths supported will be considerably lower than that one which would result from the beating between two wavelengths amplified by two independent SOAs.

III. DESIGN CHOICES

Active-passive technology allows the integration of SOAs, PHMs and monitoring photodiodes (PDs) on the same chip. Three different type of wafers have been used for fabrication. These wafers differ in the gain material structure: 4-Quantum-Well, 2-QW and single-QW. 4-QW active-layer devices will provide higher power whereas single-QW devices are expected to perform with a lower noise level due to the lower amplified spontaneous emission (ASE) intensity (at the same length).

A. Linear dual-wavelength laser

The schematic of the linear AWGL configuration is depicted in Figure 1. The cavity contains, from right to left, an SOA which amplifies both wavelengths and an AWG with 70 GHz channel spacing. Two of the AWG channels are connected, through a waveguide, to a balanced Michelson interferometer (MI) containing a PHM in each arm. PDs are connected to a higher order output of the AWG: they monitor the power in each of the two wavelengths.

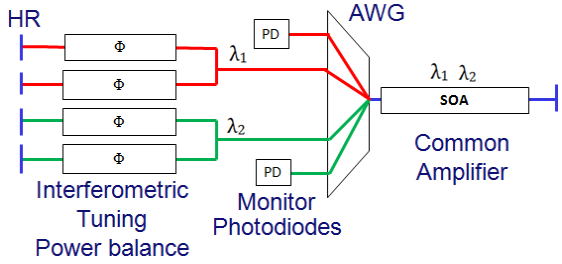


Fig.1. Schematic of the linear AWG-based laser.

This work is supported by the iPHOS project (European Union FP7).
* G. Carpintero, UC3M, Universidad Carlos III de Madrid, Spain.

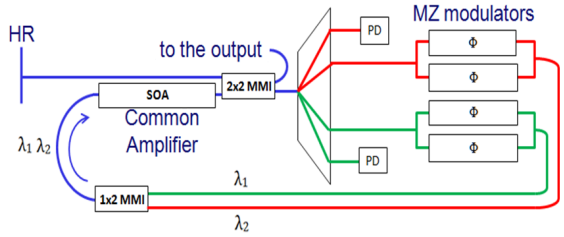


Fig.2. Schematic of the ring AWG-based laser.

The wavelength selection results from the combination between the transmission of the AWG and the cavity modes. The fact that we have two wavelengths being amplified in the same SOA means that we have to equalise the power in the two wavelengths actively. This is achieved using the MI configuration which allows to set a transmission loss for each wavelength channel. The MIs will be actively controlled by signals derived from the monitor photodiodes. Each MI can also be used to tune the optical length of the cavity by applying an offset voltage to both PHMs. This tuning is limited by the side-mode suppression required in the output of each channel. Although this stabilisation technique results in a more complex design, using the same amplifier for two wavelengths gives the advantage to have the same carrier densities and the same variations in ASE for both wavelengths (the wavelengths separation is so small that they can be considered to be inside a homogeneous gain region).

B. Ring dual-wavelength laser

Several versions of ring AWG-based lasers with slightly different design characteristics have been included in the mask-set. The ring devices will be used to investigate and to exploit the predisposition for single-mode lasing of ring cavities. The schematic of one of these lasers is depicted in Figure 2. An AWG is used as intra-cavity filter. Two of the AWG channels are connected to a balanced Mach-Zehnder interferometer (MZ) containing a PHM in each arm. This MZ construction is used for the fine tuning and to balance the power in the two arms. The MZs are connected, through a waveguide, to a "2 by 1" Multi-Mode Interferometer (2x1 MMI). An SOA connected to the common arm of the AWG amplifies both wavelengths. A 2x2 MMI is inserted between the common SOA and the AWG in order to extract the signal from the ring cavity. One of the output waveguides is connected to a high-reflective coated facet that acts as a mirror. The feedback signal from the facet forces the ring cavity to work in the clockwise direction. This is required in order to have light onto the photodiodes which are connected to higher order outputs of the AWG and that are monitoring the power at the two wavelengths.

IV. DEVICE LAYOUT

A picture of the linear laser during fabrication is presented in figure 3. Two extensions can be noticed in this layout. The first is that in total four independent wavelength channels are available each at 70 GHz distance (0.56 nm). This allows to choose the wavelengths nearest the gain maximum or to choose two wavelengths 140 GHz apart. The unwanted channels can be excluded using the MI settings. The second extension is that this design allows to connect four waveguides with optical amplifiers to one end of the AWG. In this way four independent device configurations are available. By activating

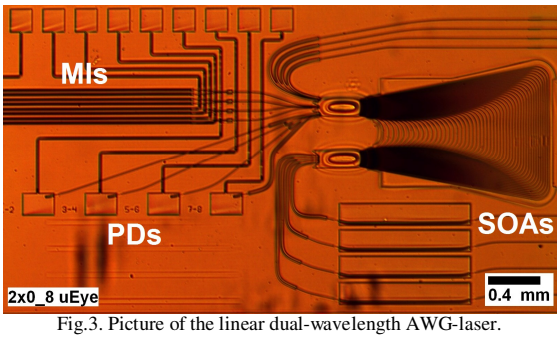


Fig.3. Picture of the linear dual-wavelength AWG-laser.

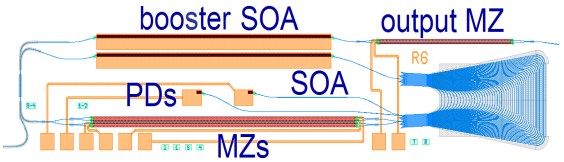


Fig.4. Mask layout of the linear AWG-based laser.

only one of these amplifiers, the optimal wavelength with respect to the gain peak in the amplifier can be selected.

The mask layout of the ring laser is depicted in figure 4. Also in this case an extension can be noticed. The actual output waveguide is connected to a booster SOA in order to amplify the signal and then to a MZ that will be used as data modulator.

In both configurations the free spectral range (FSR) of the AWG has been designed equal to 1120 GHz (8.96 nm) which is sufficiently large to avoid lasing effects at higher orders of the AWG. The cavity length of the linear (ring) AWGLs is 9-10 mm (13-14 mm) thus, for these devices a mode spacing of approximately 4 GHz (5.5 GHz) is predicted. The channel width (Full-Width Half-Maximum, FWHM) of the AWG is designed to be 36 GHz. Only small loss differences (~0.1 dB) are needed to suppress other modes. Laser simulations show that such a channel width provides sufficient suppression of the longitudinal side modes of the cavity. These simulations are also used to demonstrate the tuning and loss control using the MIs (MZs). The length of the PHMs has been chosen equal to 2 mm for the linear device and equal to 3.3 mm for the ring laser in order to make sure that a 2π phase shift can be obtained with reverse voltage lower than 6 V (a linear phase shift efficiency around 0.33rad/V·mm single path is expected). Since both wavelengths are tunable over at least half the cavity-FSR, the frequency difference between the two wavelengths generated can be tuned over a significant portion of the relevant mm-wave frequency band and probably over the full band. Furthermore, the switching speed of the PHMs in reverse bias can be up to several tens of GHz [5].

REFERENCES

[1] G.Fettweis, "WIGWAM: System concept for 1Gbit/s and beyond", IEEE 802 plenary meeting, November 2005.

[2] European Union FP7 iPHOS project website www.iphos-project.eu .

[3] R. Appleby and C. Cameron, "Seeing hidden objects with millimeter waves", Physics World, pp. 35-39, January 2012.

[4] S.Oka *et al.*, "Inspection of concrete structures using millimetre-wave imaging technology" NTT Technical review, 7(3) pp. 1-6 (2009).

[5] L. Xu, "Monolithic integrated reflective transceiver in Indium Phosphide". PhD thesis, Eindhoven University of Technology, Eindhoven, The Netherlands, 2009. ISBN 978-90-386-1891-3.

A variable delay integrated receiver for differential phase-shift keying optical transmission systems

A. Canciamilla, C. Ferrari, M. Mattarei,
F. Morichetti, S. Grillanda, A. Melloni
Dipartimento di Elettronica e Informazione
Politecnico di Milano, Milano, Italy
canciamilla@elet.polimi.it

M. J. Strain, M. Sorel
School of Engineering
University of Glasgow
Glasgow G12 8LP, United Kingdom

P. Orlandi, P. Bassi
Dipartimento di Elettronica, Informatica, Sistemistica
Università di Bologna
Bologna, Italy

***Abstract*— An integrated variable delay receiver for DPSK optical transmission systems is presented. The device is realized in silicon-on-insulator technology and can be used to detect DPSK signals at any bit-rates between 10 and 15 Gbit/s.**

Keywords- differential phase-shift keying, interferometer, optical receiver, tunable delay-lines, silicon photonics

I. INTRODUCTION

Differential phase-shift keying (DPSK) optical transmission systems offer several advantages over traditional on-off keying (OOK) systems in terms of tolerance to fiber chromatic dispersion and nonlinearities. Direct-detection of DPSK signals requires the conversion of phase modulation to intensity modulation, which is usually performed by means of a delay interferometer with a fixed delay equal to the inverse of the signal bit rate (e.g. 100 ps delay at 10 Gbit/s). However, it has been demonstrated that the detection of signals affected by bandwidth-narrowing due to concatenated filters [2] or by chromatic dispersion [3] may be improved if the delay at the receiver deviates from the one-symbol delay. Furthermore, receivers capable of demodulating signals at variable bit-rates would better fulfill the requirements of optical communication systems, which are evolving towards higher flexibility and dynamic bandwidth allocation.

For these reasons, in the last years variable delay DPSK receivers have been attracting an increasing interest. Several solutions have been recently proposed in free-space [4] and optical fiber [5] technology. While offering large delay tunability and good optical performance, these devices are bulky and expensive. An integrated solution for an interferometer with adaptive delay has been realized by using cascaded Mach-Zehnder interferometers (MZI) [6], yet this device only provides a discrete switching between three delays.

In this contribution we introduce and experimentally demonstrate an integrated variable delay receiver for DPSK optical communication systems. The variable delay is attained by means of a coupled resonator optical waveguide (CROW) coupled to one arm of a conventional asymmetric MZI. The device is realized in silicon-on-insulator technology and can be used to detect DPSK signals at any bit rates between 10 and 15 Gbit/s.

II. DESIGN

According to the schematic of Fig. 1(a), the proposed device consists of an integrated unbalanced MZI with a continuously tunable delay line coupled to the delay arm. The delay line is realized by using a CROW in a reflective configuration [7] and is used to modify the mutual delay between the two arms of the MZI, and hence the FSR of the receiver. The maximum attainable free spectral range $FSR_{max} = c/(n_g \Delta L_{MZI})$, where c is the vacuum light speed and n_g the waveguide group index, is given by the MZI delay ΔL_{MZI} when the CROW is out of resonance. The FSR of the device can be reduced by setting to resonance an increasing number of resonators, each resonator providing a delay comprised between 0 (off-resonance condition) and $T_{max} = 2/(\pi B)$, where B is the CROW bandwidth [7]. In Fig. 1 the case of a 2-ring structure is considered, but more resonators can be cascaded to increase the delay tunability. Partial detuning of the last ring is exploited to produce any intermediate delay between 0 and

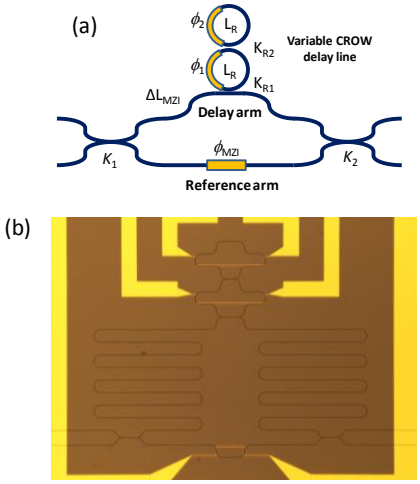


Figure 1. (a) Schematic of the integrated variable bit-rate DPSK receiver and (b) optical microscope photograph of the fabricated device.

Part of this work has been funded by the Italian National Research Project SAPPHIRE (Shared Access Platform to PHotonic Integrated REsources) (http://sapphire.dei.polimi.it/).

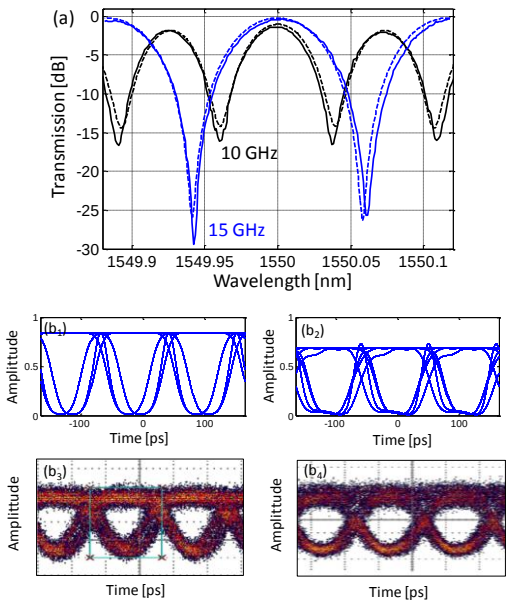


Figure 2. (a) Simulated (dashed) and measured (solid) transmission of the tunable delay MZI for FSR = 15 GHz (blue) and 10 GHz (black). (b) Simulated (b_1, b_2) and measured (b_3, b_4) eye-diagram of a 10 Gbit/s binary DPSK signal detected by the variable delay MZI with a FSR of (b_1, b_3) 15 GHz and (b_2, b_4)10 GHz.

T_{max} [7]. No significant signal distortion occurs at any delay provided that the CROW group delay is constant versus wavelength across the signal spectrum. This condition is achieved if B is at least twice as large as the desired FSR of the receiver. Moreover the coupling coefficients K_{Ri} of the resonators are optimized to achieve a ripple-free amplitude and delay response of the CROW [8].

III. Fabrication and Experimental Results

The proposed device was fabricated on a silicon on insulator (SOI) platform [9]. The optical waveguide core is 220 nm thick, 480 nm wide and is covered with 1 µm-thick oxide layer (n_g = 4.2 for TE polarization). As shown in the photograph of Fig. 1(b), metallic heaters were deposited onto the waveguides to thermally adjust the round trip phase ϕ_1 and ϕ_2 of the rings and the phase ϕ_{MZI} of the reference arm. The MZI unbalance is ΔL_{MZI} = 4736 μm. The rings of the CROW have length L_r = 473 μm, and the coupling coefficient K_{R1} and K_{R2} are 0.64 and 0.2, respectively. The resulting CROW bandwidth is B = 37 GHz, corresponding to T_{max} = 17 ps.

The simulated (dashed lines) and measured (solid lines) frequency domain response of the device is shown in Fig. 2(a) for a TE polarized input light. When both rings are set off-resonance (blue curves), the device exhibits the maximum FSR_{max} = 15 GHz, corresponding to a time delay of 66 ps between the two MZI arms, and an extinction ratio ER > 25 dB. By setting both rings to resonance, a 34 ps delay is added and the FSR reduces to 10 GHz (black curves). Note that the device insertion loss increases by only 1 dB between the maximum and the minimum FSR condition. Optimized power coupling coefficients, K_1 = 0.6 and K_2 = 0.5, were used to compensate for the delay-dependent loss in the CROW and to guarantee ER > 15 dB at any intermediate FSR. The maximum electric power consumption required to feed the heaters is about 30 mW even in the worst case (phase shift of π for each ring and for the MZI's reference arm).

The variable delay MZI was employed to receive a 10 Gbit/s binary DPSK signal transmitted at a wavelength of 1550 nm. Fig. 2(b) shows the simulated (b_1, b_2) and measured (b_3, b_4) eye-diagrams of the intensity modulated signal at the output of the variable delay MZI when the FSR of the receiver is set to 15 GHz (b_1, b_3) and 10 GHz (b_2, b_4), respectively. When the symbol rate does not match the FSR of the receiver, the eye-diagram is triangularly shaped because of strong intersymbol interference (ISI), causing an evident splitting of the signal transitions. The optimum 100-ps delay achieved by setting both rings on resonance improves the quality of the received signal, widening the eye aperture and narrowing the signal transitions. This result demonstrates the suitability of a MZI loaded with a reflective CROW delay line to detect DPSK signals with no evident signal distortions. A deeper investigation on the system performance of the device with signals at higher bit-rates and high power is currently being performed.

IV. Conclusion

To summarize, we have presented the first integrated DPSK receiver with a continuously tunable delay. The functionality of the device, which has been realized on an SOI platform, has been demonstrated on a 10 Gbit/s binary DPSK signal, but can be extended to generic DPSK systems with more complex data symbol constellations. A variable delay between 66 ps and 100 ps has been achieved, enabling the use of the receiver to demodulate signals at bit-rates between 10 and 15 Gbit/s.

Acknowledgment

We thank the JWNC staff at Glasgow University for support in fabrication of the devices.

References

[1] G. Bosco and P. Poggiolini, "On the joint effect of receiver impairments on direct-detection DQPSK systems," J. Lightwave Technol., vol. 24, pp. 1323-1333, 2006.

[2] B. Mikkelsen, C. Rasmussen, P. Mamyshev, and F. Liu, "Partial DPSK with excellent filter tolerance and OSNR sensitivity," Electron. Lett., vol. 42, pp. 1363-1364, 2006.

[3] Y. K. Lizé et al., "Free spectral range optimization of return-to-zero differential phase shift keyed demodulation in the presence of chromatic dispersion," Opt. Express, vol. 15, pp. 6817-6822, 2007.

[4] J. Li, K. Worms, R. Maestle, D. Hillerkuss, W. Freude, and J. Leuthold, "Free-space optical delay interferometer with tunable delay and phase," Opt. Express, vol. 19, pp. 11654-11666, Jun. 2011.

[5] Y. Dai and C. Shu, "Bit-rate variable DPSK demodulation based on cascaded four-wave mixing," Opt. Express, vol. 19, pp. 2952-2958,2011.

[6] Y. Nasu, K. Hattori, T. Saida, Y. Hashizume, and Y. Sakamaki, "Silica-based adaptive-delay DPSK demodulator with a cascaded Mach-Zehnder interferometer configuration," European Conference on Optical Communications (ECOC), We.8.E.5, Torino, Italy, 2010.

[7] F. Morichetti, A. Melloni, C. Ferrari, and M. Martinelli, "Error-free continuously-tunable delay at 10 Gbit/s in a reconfigurable on-chip delay-line," Opt. Express, vol. 16, pp. 8395-8405, May 2008.

[8] A. Melloni and M. Martinelli, "Synthesis of Direct-Coupled-Resonators Bandpass Filters for WDM Systems," J. Lightwave Technol., vol. 20, pp. 296, 2002.

[9] A. Canciamilla et al., "Silicon coupled-ring resonator structures for slow light applications: potential, impairments and ultimate limits," Journal of Optics, vol. 12, pp. 104008, 2010.

Integrated optical serializer designed and fabricated in a generic InP-based technology

S. Stopiński[1,2], M. Malinowski[2], R. Piramidowicz[2], M. K. Smit[1], X. J. M. Leijtens[1]
1) COBRA Research Institute, Technische Universiteit Eindhoven, Eindhoven, the Netherlands,
2) Institute of Microelectronics and Optoelectronics of Warsaw University of Technology, Warsaw, Poland
S.Stopinski@tue.nl

***Abstract*—This work presents design and characterization results of an optical pulse serializer, realized as an Application Specific Photonic Integrated Circuit (ASPIC) in a novel, generic InP-based technology and fabricated in a multi-project wafer run. The measurement results show high-speed (32 Gbit/s) output signal as a result of optical time domain multiplexing of parallel input signals. The on-off modulation of independent data channels is provided by means of electro-optical amplitude modulators with extinction ratio better than 20 dB.**

Keywords- photonic integrated circuit, indium phosphide (InP), generic integration technology, serialization, OTDM, data read-out

I. INTRODUCTION

Generic photonic integration technology will cause a breakthrough in the field of design, fabrication and application of photonic integrated circuits (PICs). During the last years a major research effort has been conducted in order to develop and establish generic integration technology platforms both for Si and InP-based PICs [1].

The EU NMP EuroPIC project, a collaboration of European key players in InP-based photonics, aims to establish a standard production chain based on the generic technology approach [2]. One of the objectives is to prove that the same process can be used to fabricate photonic devices for various fields of application and covering a wide range of functionalities. In order to achieve this, ten pilot application specific photonic integrated circuits (ASPICs) have been designed in a novel way and fabricated in multi-project wafer runs [3-5].

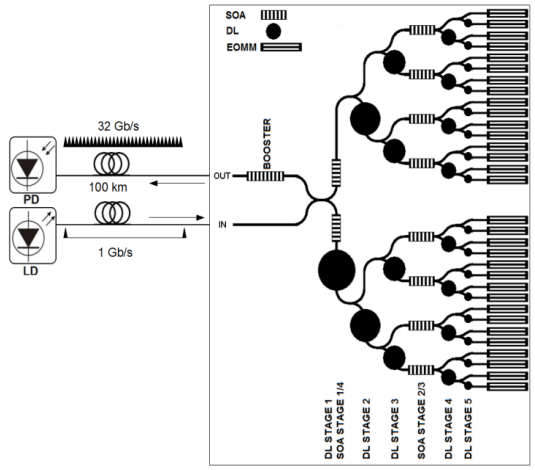


Figure 1. Schematic of the read-out system

II. SYSTEM SPECIFICATIONS AND ASPIC DESIGN

One of the pilot applications of the EuroPIC project is a read-out unit for the KM3NeT project [6]. KM3NeT (an acronym for Cubic Kilometer Size Neutrino Telescope) is a European project aiming to develop a large volume neutrino detector, consisting of thousands of photomultipliers deployed at the bottom of the Mediterranean Sea. The basic module of the telescope is a glass sphere with 31 photomultipliers assembled inside. A 3D array of such spheres will form the detector. The read-out system has to transmit the digitized output data of the photomultipliers to the central analysis station. The required sampling frequency is 1 GHz, the BER coefficient 10^{-9}, and the total power consumption inside a single module should be kept below 7W.

The schematic of the proposed read-out system is shown in Fig. 1. It makes use of a fiber link between the central station and an application specific photonic integrated circuit (ASPIC) mounted inside the glass sphere. The operation principle is based on time-domain multiplexing of optical signals by means of optical delay lines [7]. The input signal, a 1 GHz optical pulse-train with very narrow pulses is distributed among 32 waveguides by five stages of 3dB MMI (multi-mode interference) power splitters, after which the 32 different signals are modulated by a reflective Michelson Interferometer array and coupled through the five stages back to the input port. The pulses are on-off modulated. In the five-stage network a number of delay lines has been included as indicated by the black circles in Fig. 1. The delay lines have been designed such that after being coupled back to the input port each pulse has got a delay such that the 32 pulses are serialized, what results in a 32 Gb/s optical signal. The SOAs (semiconductor optical amplifiers) are used to compensate the losses introduced by the circuit components.

As a proof-of-concept an 8:1 serializer has been designed using the Oclaro Ltd. (UK) foundry platform. Fig. 2 shows the mask layout of the photonic circuit with dimensions 2x6 mm^2. The circuit is built with using three basic structures – deeply-etched waveguides, phase modulator sections (utilizing

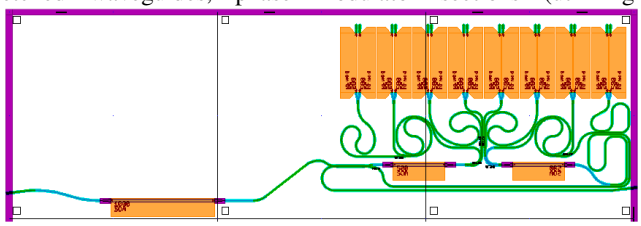


Figure 2. Mask layout of the 8:1 integrated optical serializer

quantum-confined Stark effect for enhanced electro-optic effect) and shallowly-etched SOAs. By combining the abovementioned building blocks more complex components can be formed, such as spiral delay lines, 1x2 and 2x2 MMI power splitters/couplers and MMI reflectors. Coupling between deeply- and shallowly etched structures is provided by low-loss transition elements. The whole circuit operates in a reflecting regime, so that the total area required is two times smaller as compared to a transmission configuration.

Michelson modulators are built by using a 1x2 MMI power splitter at the input, phase modulator sections and MMI reflectors. Biasing of one of the phase modulator sections with a proper voltage introduces a phase shift, which results in destructive interference at the output of the modulator. For this type of modulator the measured driving voltage is $V_\pi = 3$ V and the extinction ratio exceeds 20 dB [8].

III. MEASUREMENT RESULTS

The chip has been fabricated, together with other EuroPIC ASPICs, in a multi-project wafer run at Oclaro Ltd in the UK. The characterization took place at the Optical Measurement Laboratory of the COBRA Research Institute.

Fig. 3 shows the time-domain response of the 8:1 serializer circuit. It has been measured by launching a pulse laser signal ($\lambda_c = 1550$ nm, 150 ps time duration of a pulse, 80 MHz repetition rate) into the chip and measuring the output signal with a digital communication analyzer (DCA). During the measurement all three SOAs have been biased so that all of the channels are activated. As a result, 8 serialized pulses are observed at the output of the chip. The measured delay between adjacent channels, 32-33 ps (accurate determination is limited by the broadening of the pulses due to the 30 GHz bandwidth of the DCA) is slightly larger than the design value of 31.25 ps.

The SOA gain has been optimized by tuning the injection current so that the pulses of the first and fifth channels have the same power. However, the power of the pulses depends as well on the transmission of the Michelson modulators, so that the determination of the propagation losses in the delay lines is not possible. There is a slight asymmetry in the transmission characteristics of the modulators [8]. The asymmetry is most likely the effect of unwanted excitation of higher order waveguide modes, which results in an asymmetric power splitting by the MMI power splitter.

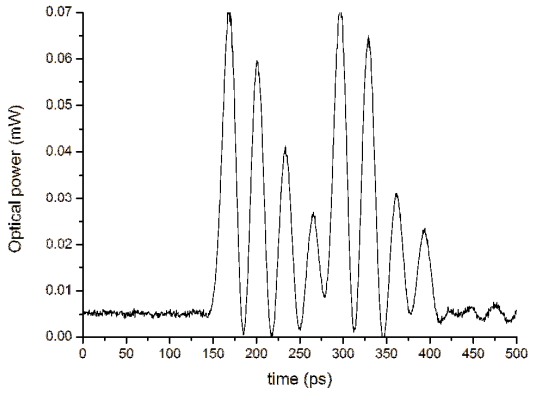


Figure 3. Pulse response of the 8:1 serializer circuit

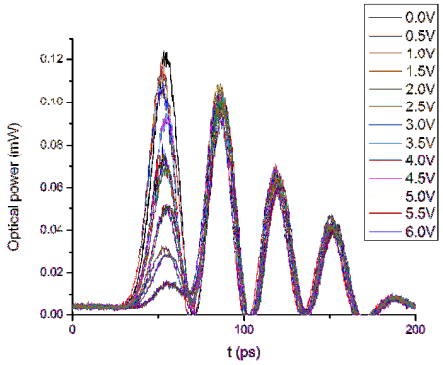


Figure 4. Independent modulation of the first channel

To observe the performance of the circuit when one of the channels is modulated, light from the pulse laser has been launched to the circuit and one of the modulator arms has been driven. Fig. 4 shows the result, when only the booster and one of the inline amplifiers are activated and the second inline amplifier is off. The measurement has been performed for a reverse bias voltage applied to the modulators ranging from 0 V up to 6 V with a 0.5 V step. The figure presents the output signal when the first channel is modulated. The results prove that it is possible to modulate one of the channels while not affecting the others. The extinction of the pulses is not complete, due to the broad wavelength spectrum of the input femtosecond laser signal. The value of the phase shift in the electro-optical modulators is wavelength dependent so it is different for each wavelength component. This results in non-complete destructive interference at the output of the modulator.

IV. SUMMARY AND CONCLUSIONS

An 8:1 integrated optical serializer has been designed and fabricated in a generic InP-based technology. The device works as intended and time domain multiplexing of the optical signals has been observed. Possibility of modulation of independent data channels has been shown as well. The circuit makes use of modulators with good optical properties, i.e. extinction ratio exceeding 20 dB and low driving voltage (3 V). First characterization results demonstrate the potential of the novel generic way of production.

ACKNOWLEDGMENT – The research leading to these results has received funding from the European Community's Seventh Framework Programme FP7/2007-2013 under grant Agreement NMP 228839 EuroPIC.

REFERENCES

[1] M.K. Smit et al., IET Optoelectron., Vol. **5**(5), pp. 187–194, 2011
[2] EuroPIC – www.jeppix.europic.eu
[3] K. Ławniczuk et al., Proceedings of the 2011 Annual Symposium of the IEEE Photonics Benelux Chapter, 173-176, 2011
[4] M.S. Tahvili et al., Proceedings of the 2011 Annual Symposium of the IEEE Photonics Benelux Chapter, 57-60, 2011
[5] J.J.G.M. v. d. Tol et al., Proceedings of the 2010 Annual Symposium of the IEEE Photonics Benelux Chapter, 221-224, 2010
[6] KM3NeT – www.km3net.org
[7] A. Aboketaf et al., Optics Express, vol. 18, 13529-13535, 2010
[8] S. Stopinski et al., Proceedings of the 2011 Annual Symposium of the IEEE Photonics Benelux Chapter, pp. 161-164, 2011

Micro-mechanical Integrated Optical Structures

Fabricated through physical micromachining and direct UV writting

C. Holmes, L.G. Carpenter, P.A. Cooper, H.L. Rogers, J.C.Gates, P.G.R.Smith
Optoelectronics Research Centre, University of Southampton
Southampton, UK, SO17 1BJ
chh@orc.soton.ac.uk

***Abstract*—The work presented, reports recent developments in the fabrication of micro-mechanical integrated optical components. Combining physical micromachining and direct UV-writing, micro-membranes micro-cantilevers and micro-bridge structures are fabricated.**

Keywords-component; UV-writing; physical micromachining; micro-cantilevers; micro-membranes; micro-bridges

I. INTRODUCTION

Microelectromechanical Systems (MEMS) have revolutionized today's technology, with applications ranging from triggering mechanisms in automotive airbags to motion detectors in the latest smart phones. Analogous to these electronic components, similar constructions using optical means of detection are also finding increased niches of application. Such optical components carry the distinct advantage over electronic components in that they can operate in extreme environments (e.g. highly flammable environments and in areas of strong EM-interference). In addition to this environmental operation advantage, under certain detection modes these components can also have optical-multiplexing advantages and form part of distributed remote sensing networks via optical fiber connections.

The majority of micro-mechanical structures operate by exploiting the mechanics of certain architectures. These are typically low-mass structures that include membranes, cantilevers and bridge forms. These fundamental low-mass structures have all been exploited in the fabrication of optical micro-mechanical structures, for both planar and optical fiber based platforms [1-6].

Unlike previous developments of planar-integrated optical micro-mechanical structures, the components developed by this group have the unique advantages of not being limited to variations in source power, are more rugged than free-space alignment approaches and have the capability to spectrally multiplex signals. The reported components are fabricated from a silica-on-silicon platform, which is conducive to standard optical fiber connections, thereby allowing simple integration of devices into a distributed sensing network via standard fiber communication components.

The fabrication approach of these components is uniquely achieved through a combination of direct UV writing [7] and physical micromachining [5, 6]. Direct UV writing is used to write single mode waveguides and Bragg gratings whilst physical micromachining is used to construct the low-mass structures. Using this combination of fabrication methods, micro-membrane, micro-cantilever and micro-bridge components have been fabricated, as illustrated in Figure 1. Detection of physical changes to these microstructures is monitored through interpreting optical responses of a Fabry-Perot cavity. In order to permit multi-parameter multiplexing, Bragg gratings are used to form the Fabry-Perot cavity, either side of the structure, as illustrated in Figure 1. As these Bragg gratings are designed with equal period the cavity formed is spectrally selective, allowing multiplexed operations.

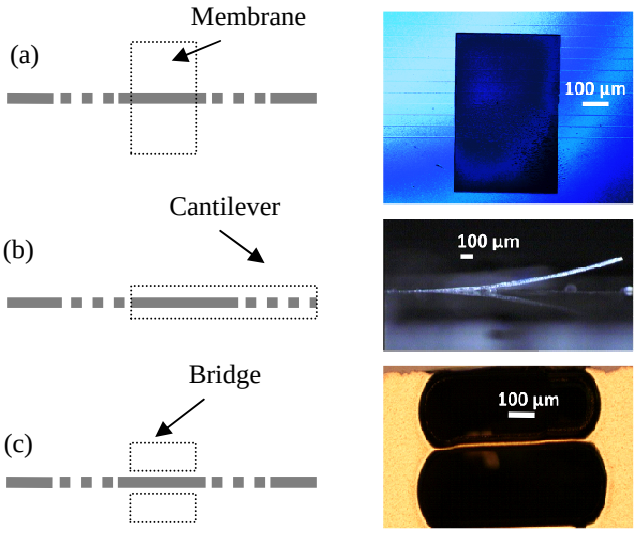


Figure 1 Images of the three micromechanical integrated optical components developed, indicating waveguide (thick grey) Bragg grating (dashed grey) and micro-mechanical component (thin black dashed line), for (a) micro-membrane (b) micro-cantilever (c) micro-bridge.

Deflection of the microstructures are monitored through changes in Fabry-Perot Bragg grating (FPBG) signatures. As the micro-structure mechanically deforms stress induced optical responses occur, altering the Free Spectral Range (FSR) of the Fabry-Perot fringes. Assuming the central Bragg wavelength of the FPBG is negligibly affected by the component's actuation, it can be used to compensate for thermal variations [6].

The method of fabrication permits such devices to be made as it indiscriminately removes both silica and silicon material and can create deep vertical structures. Another advantage of the fabrication techniques is that they do not require cleanroom processing or hazardous chemical etchants, such as HF acid.

II. FABRICATION

The reported devices are fabricated on a silica-on-silicon platform, achieved using flame hydrolysis deposition (FHD). Wafer construction begins with a silicon wafer with a thick thermally grown oxide (~15 µm). FHD core and underclad layers are subsequently deposited and consolidated. The core layer is doped with germanium and boron such to make it photosensitive to UV light, which is enhanced through hydrogenation of the wafer. Using a direct UV writing technique both waveguides and Bragg gratings are written into the core layer [7], with a frequency doubled argon-ion laser. The UV writing process uses a patented dual beam writing technology [7] to define waveguides and Bragg gratings in a single processing step. After UV writing physical micromachining is performed. This step physically removes silica and silicon material (depending upon the component to be fabricated) from the chip. A subsequent potassium hydroxide (KOH) etch is made to remove excess silicon material. After fabrication the chip is packaged by fiber pigtailing, as illustrated in figure 2. The pigtail is secured with UV-curing epoxy and is robust enough to survive mechanical testing.

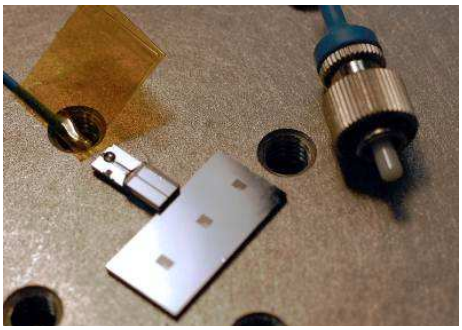


Figure 2 Photograph of three micro-membrane structures integrated into a single optical chip.

III. RESULTS AND DISCUSSION

Due to the high consolidation temperatures associated with FHD fabrication and the different expansion coefficients of silica and silicon, the thin (~50 µm) silica layers are under significant compressive stress. This stress results in buckling of the microstructure under particular conditions. Effects that result from this static buckling include:

- Spectral chirp in Bragg signatures
- Mechanical nonlinear responses
- An asymmetric response to physical actuation

Through considering these effects design optimization can be made. Furthermore these effects can be exploited to actually enhance the performance of the sensing component. For example, the pre-buckling of a membrane can be used to distinguish between positive and negative pressure differentials [6].

A typical FPBG signature, for a 5 mm long cantilever structure, is illustrated in Figure 3. This spectrum can be monitored with either a broadband source and Optical Spectrum Analyzer (OSA) or a tunable laser source and photodiode. It is understood that for slowly varying responses a broadband source and OSA, is best suited as the central Bragg peak can be used as a thermal reference the microstructure [6]. However, component sensitivity can be enhanced through monitoring the mechanical resonance, measured using the laser configuration and a lock-in-amplifier [8].

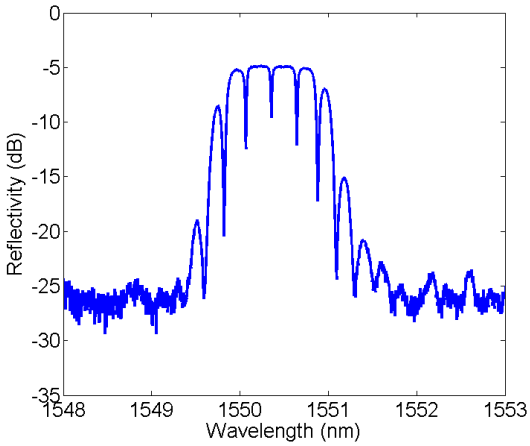


Figure 3 The Fabry-Perot Bragg grating signature of a 5mm cantilever device.

IV. SUMMARY

The latest developments in micro-mechanical integrated optical structures, fabricated using direct UV writing and physical micromachining have been reported. We shall summarize the latest results including design considerations and mechanically nonlinear phenomena arising from the large compressive stresses associated with fabrication. We shall report on the limitations to device footprint and sensitivity of detection.

REFERENCES

[1] H. Bae, X.M. Zhang, H. Liu and M. Yu, "Miniture surface-mountable Fabry-Perot pressure sensor constructed with a 45° angled fiber", Optics Lett., vol. 35, pp.1701-1703, 2010 .

[2] S.R. Manalis, S.C. Minne, A. Atalar and C.F. Quate, "Interdigital cantilevers for atomic force microscopy", Appl. Phys. Lett. vol 69, pp.3944-3946, 1996.

[3] H. Bezzaoui and E. Vogues, "Integrated optics combined with micromechanics on silicon", Sens.Act. A, vol. 29, pp.219-223, 1991.

[4] W. Fang and J.A.Wickert, "Determining mean and gradient residual stresses in thin films using micromachined cantilevers", J. Micromech. Microeng., vol. 6, pp301-309, 1996.

[5] C.Holmes, L.G.Carpenter, H.L.Rogers, J.C.Gates and P.G.R.Smith, "Quantifying the optical sensitivity of planar Bragg gratings in glass micro-cantilevers to physical deflection", J. Micromech. Microeng. vol. 21, 2011.

[6] C. Holmes, L.G. Carpenter, J.C.Gates, P.G.R.Smith, "Miniturisation of Bragg-multiplexed membrane trnsducers", J. Micromech. Microengin. vol. 22, 2012.

[7] S. Watts, "Bragg gratings: optical microchip sensors", Nature Photonics, vol. 4, pp. 433-434, 2010.

[8] L.G.Carpenter, C.Holmes, H.Rogers, P.G.R.Smith, J.C.Gates, "Integrated optic glass microcantilevers with Bragg grating interrogation", Opt. Ex., vol. 18, pp.23296-23301, 2010.

Fourier Series Based 3D Bi-directional Propagation Algorithm for Integrated Photonics

Jiří Čtyroký
Department of Guided-Wave Photonics
Institute of Photonics and Electronics AS CR, v.v.i.
Prague 8, Czech Republic
ctyroky@ufe.cz

Pavel Kwiecien and Ivan Richter
Department of Physical Electronics,
Faculty of Nuclear Sciences and Physical Engineering
Czech Technical University in Prague, Czech Republic
pavel.kwiecien@fjfi.cvut.cz, ivan.richter@fjfi.cvut.cz

***Abstract* — A 3D bi-directional mode expansion propagation algorithm based on Fourier series using trigonometric functions is briefly described. Nonlinear complex coordinate transformations are used as boundary conditions in transversal coordinates. In vertical direction, the adaptive spatial resolution algorithm can be alternatively applied, too. Mirror symmetries can be fully utilized to reduce numerical effort. Applications to a subwavelength-grating waveguide SOI mode transformer and a novel planar metal-dielectric slot waveguide are shown.**

Keywords-numerical modeling; bi-directional mode expansion; Fourier modal methods; plasmonic slot waveguide; subwavelength-grating waveguide

I. INTRODUCTION

Numerical modelling is an ever more important part of analysis and design of novel integrated photonic structures and devices. Despite the tremendous progress in computing power and memory of modern computers, realistic 3D modelling still remains rather challenging. Perhaps the most frequently used method for modelling 3D structures is the well-known finite-difference time domain (FDTD) method. Modelling of structures larger than just a few wavelengths in each direction is, however, still rather demanding. Frequency-domain modal methods are generally less flexible but bring deeper physical insight into the wave effects in photonic structures, and are especially well suited for modelling structures consisting of longitudinally uniform segments. In this contribution, a fully vectorial 3D bi-directional mode expansion propagation algorithm based on trigonometric Fourier series is presented. It represents an extension of a 2D method [1] into 3D. Similar as in [1], nonlinear complex coordination transformations [2] are used in both transversal coordinates as efficient perfectly matched layers (PML). The application of trigonometric (sin and cos) expansion functions instead of complex exponentials typically used in Fourier modal methods enables to fully utilize mirror symmetries of the problem to reduce the problem size without any additional effort. It is known that adaptive spatial resolution algorithm (ASR) [3, 4] helps significantly reduce the numerical effort, but it makes modelling of complex devices difficult. For this reason it can be alternatively applied only to one – vertical – direction. Fourier factorization rules [4,5] are correctly applied in both transversal directions using the approach described in [6]. The full-vector mode solver is based on transversal components of magnetic field intensity.

II. THE ALGORITHM

The structure to be modelled is considered as a concatenation of a finite number of longitudinally uniform sections. In each section, the piecewise-constant transversal permitivity distribution is supposed. Infinite transversal cross-section of a real structure is mapped into a finite calculation window (shown in Fig. 1) using nonlinear complex coordination transformations $x \rightarrow x'$, $y \rightarrow y'$ described in [2]. Coloured (shadowed) part of the cross-section represents the transformed (PML) region, the white central part of the cross-section is not modified by the transformation.

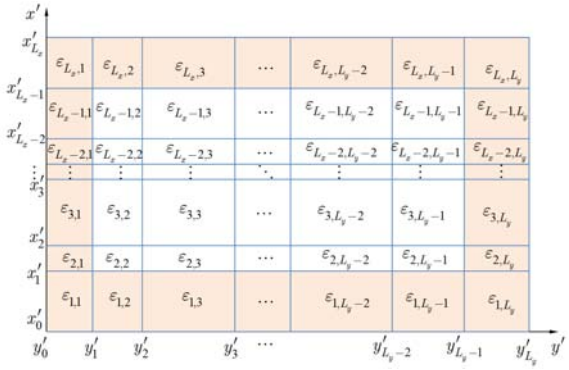


Figure 1. Transversal computation window with schematic representation of a piecewise-constant permittivity distribution after the complex nonlinear transformation.

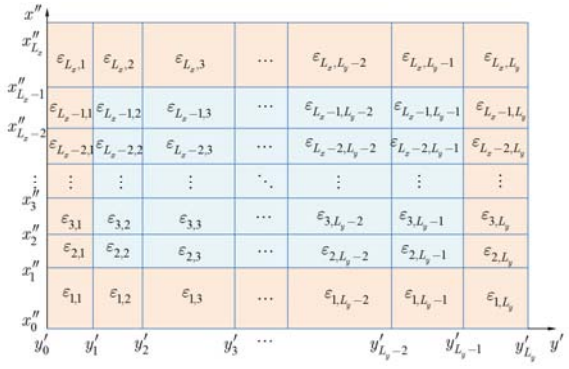


Figure 2. Transversal computation window after the application of the ASR transformation in vertical (x) direction.

Another transformation – the ASR transformation [3, 4] – can be alternatively applied to the vertical (x) coordinate at the inner part of the cross-section. After the transformation, the thicknesses of all inner horizontal layers become identical (see Fig. 2), the transformed vertical permittivity distribution becomes almost smooth, and thus the number of Fourier expansion terms required for sufficient accuracy is significantly reduced. This algorithm is thus well suited not only for modelling integrated photonic components fabricated by 2D patterning of a layered planar structure as SOI, InP, silica-on-silicon and similar devices, but also for 3D structures with metallic (plasmonic) components.

III. EXAMPLES

As a convergence test of the basic algorithm, the effective refractive index of the quasi-TE_{00} mode of a silicon nanowire embedded in SiO_2 versus the number of expansion terms is shown in Fig. 1. The results of the film mode matching method [10] were used as a reference.

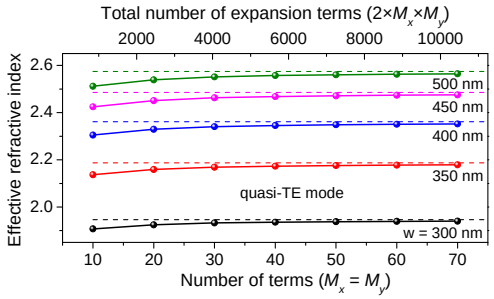


Figure 3. Effective refractive index of the fundamental quasi-TE mode of a silicon nanowire embedded in SiO_2 versus the number of Fourier expansion terms. The wire height is 260 nm, the width varies from 300 to 500 nm. The wavelength is 1550 nm.

As a next example, calculated optical field distribution in the SOI subwavelength grating waveguide mode transformer [8] embedded in SU8 resist with 60 subwavelength sections is shown in Fig. 4. The calculated coupling losses at the wavelength of 1550 nm are 0.61 dB and 0.45 dB for TE_{00} and TM_{00} mode, respectively. 60×70 Fourier terms were used in the calculation.

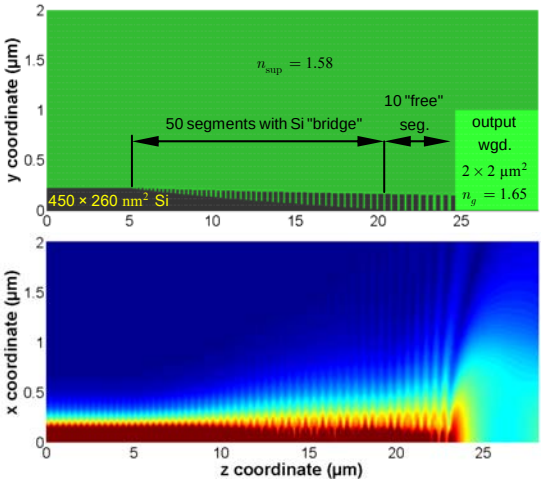


Figure 4. a) Top view of the mode transformer; because of symmetry, only one half of the structure is considered.
b) calculated optical field distribution, TE_{00} excitation. Perfectly conducting magnetic wall was placed at the symmetry plane.

In Fig. 5, the cross-section and the calculated mode field distribution of a metal-dielectric slot waveguide [9] is plotted. The waveguide is formed by a very thin Si nanowire embedded in SiO_2 and separated from an Au layer by a 30 nm slot. 80×60 Fourier terms were used. Fig. 6 shows the geometry and the field distribution of a very sharp S-bend in this waveguide. All these results have been, in fact, checked with another our modal method, namely aperiodic rigorous coupled wave analysis (aRCWA) technique, their comparison will be shown.

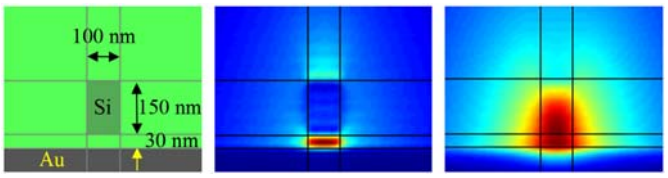


Figure 5. a) Cross-section of the metal-dielectric slot waveguide, b) vertical electric field component, c) horizontal magnetic field component of the plasmonic mode.

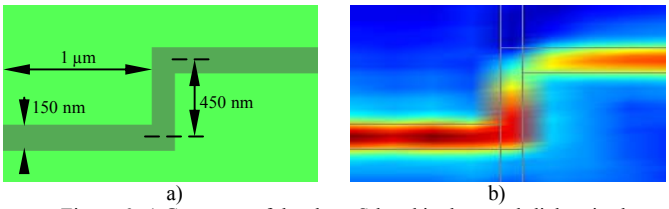


Figure 6. a) Geometry of the sharp S-bend in the metal-dielectric slot waveguide, b) distribution of a vertical electric field component.

IV. ACKNOWLEDGMENTS

This work was financially supported by the Czech Science Foundation and the Ministry of Education, Youth and Sports of the Czech Republic (projects P205/10/0046, P205/12/G118, OC09061 and OC09038).

[1] J. Čtyroký, "Improved bidirectional-mode expansion propagation algorithm based on Fourier series," J. Lightwave Technol., Vol. 25, pp. 2321-2330, 2007.

[2] J. P. Hugonin and P. Lalanne, "Perfectly matched layers as nonlinear coordinate transforms: a generalized formalization," J. Opt. Soc. Amer. A, Vol. 22, pp. 1844-1849, 2005.

[3] T. Vallius and M. Honkanen, "Reformulation of the Fourier modal method with adaptive spatial resolution: application to multilevel profiles," Optics Express, Vol. 10, pp. 24-34, 2002.

[4] J. Čtyroký, P. Kwiecien, and I. Richter, "Fourier Series-Based Bidirectional Propagation Algorithm with Adaptive Spatial Resolution," J. Lightwave Technol. Vol. 28, pp. 2969-2976, 2010.

[5] P. Lalanne and G. M. Morris, "Highly improved convergence of the coupled-wave method for TM polarization," J. Opt. Soc. Amer. A, Vol. 13, pp. 779-784, 1996.

[6] L. Li, "Use of Fourier series in the analysis of discontinuous periodic structures," J. Opt. Soc. Amer. A, Vol. 13, pp. 1870-1876, 1996.

[7] L. Li, "Fourier modal method for crossed anisotropic gratings with arbitrary permittivity and permeability tensors," J. of Optics A: Pure and Applied Optics, Vol. 5, pp. 345-355, 2003.

[8] P. Cheben, P. J. Bock, J. H. Schmid, et al., "Refractive index engineering with subwavelength gratings for efficient microphotonic couplers and planar waveguide multiplexers," Optics Letters, vol. 35, pp. 2526-2528, 2010.

[9] M. Fujii, J. Leuthold, and W. Freude, "Dispersion Relation and Loss of Subwavelength Confined Mode of Metal-Dielectric-Gap Optical Waveguides," IEEE Phot. Technol. Letters, vol. 21, pp. 362-364, 2009.

[10] L. Prkna, M. Hubálek, and J. Čtyroký, "Field modeling of circular microresonators by film mode matching," IEEE Journal of Selected Topics in Quantum Electronics, vol. 11, pp. 217-223, 2005.

Ultra-high, broadband gain in a lattice-engineered, Yb-doped double tungstate channel waveguide

D. Geskus, S. Aravazhi, E. H. Bernhardi, L. Agazzi, S. M. García-Blanco, and M. Pollnau
Integrated Optical MicroSystems Group,
MESA+ Institute for Nanotechnology, University of Twente,
Enschede, The Netherlands
m. pollnau@utwente.nl

***Abstract*—150 dB/cm gain over 55 nm wavelength range between 977-1032 nm is obtained in a 47.5% Yb-doped potassium double tungstate waveguide amplifier. The dependence of luminescence lifetime and gain on Yb concentration is investigated.**

Keywords-Double tungstate; optical amplifier; rare-earth ions; integrated optics

I. INTRODUCTION

On-chip photonic integration requires the regeneration of optical signals at very high rates. Semiconductor optical amplifiers operate in the saturated regime, hence their gain recovery time limits the maximum achievable data rates. Rare-earth-ion-doped fiber amplifiers provide superior characteristics for high-speed amplification, but their gain of ~30-50 dB requires employing several meters of fiber length, making this solution unsuitable for on-chip integration. Recently, we have demonstrated that Yb^{3+}-doped potassium double tungstate can provide a modal gain up to ~1000 dB/cm in channel-waveguide and thin-film geometry [1], making this material highly suitable for amplification and lasing in micro- and nano-structured optical devices. Here we investigate the Yb^{3+}-concentration and wavelength dependence of modal gain around 1 µm in microstructured $KGd_xLu_yYb_{1-x-y}(WO_4)_2$ channel waveguides.

II. SAMPLE FABRICATION

Yb^{3+}-doped $KY(WO_4)_2$ layers were grown by liquid-phase epitaxy onto undoped, (010)-oriented, laser-grade-polished, 1-cm^2-sized $KY(WO_4)_2$ substrates in a $K_2W_2O_7$ solvent at temperatures of 920–923°C [2]. Co-doping the layers with appropriate percentages of optically inert Gd^{3+} and Lu^{3+} ions enables the growth of lattice-matched layers with enhanced refractive-index difference between layer and substrate, allowing for thinner active layers [3]. Partial replacement of Lu^{3+} by Yb^{3+} ions of similar ionic radius resulted in up to 47.5at.% Yb^{3+}-doped $KGd_xLu_yYb_{1-x-y}(WO_4)_2$ layers with a refractive-index contrast between layer and substrate of up to ~2×10^{-2} (Fig. 1). The samples were between 180–320 µm long and the layer surface was polished down to 2.2–3.5 µm thickness. Microstructuring by Ar-beam etching [4] provided 1.4-µm-deep, 6-µm-wide ridge waveguides along the N_g optical axis (Fig. 2). The microstructured samples were overgrown by a layer of undoped $KY(WO_4)_2$.

This work was supported by The Netherlands Organisation for Scientific Research through VICI Grant no. 07207 “Photonic integrated structures”.

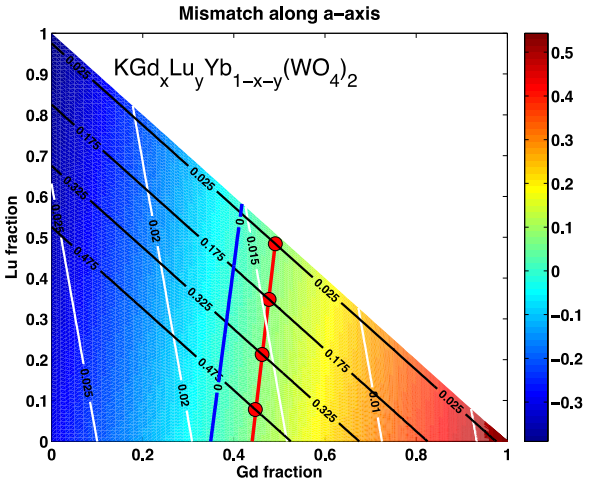


Figure 1. Lattice mismatch (color bar), refractive index contrast (white lines), and doped Yb^{3+} fraction (black lines) of $KGd_xLu_yYb_{1-x-y}(WO_4)_2$ thin layers with the undoped $KY(WO_4)_2$ substrate versus Gd^{3+} and Lu^{3+} fractions, calculated along the crystal *a*-axis. The blue line indicates the compositions for which lattice matching is achieved along this crystal axis, while the red line indicates the compositions for which minimum mismatch is obtained when considering both, the *a*- and *c*-axes.

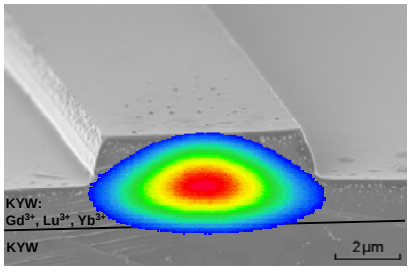


Figure 2. Cross-section of a channel waveguide prior to $KY(WO_4)_2$ overgrowth.

III. AMPLIFIER PERFORMAMCE

Lifetime-quenching processes induced by increased energy migration among Yb^{3+} ions and subsequent energy transfer to impurities or cooperative upconversion can diminish the achievable excitation density. Luminescence-decay

measurements show an increasing lifetime with increasing Yb^{3+} concentration, see the measured data and fit in Fig. 3, which is an effect of radiation reabsorption. Using the formalism presented in Ref. [5], we corrected the measured lifetime for this effect (blue line), resulting in a lifetime quenching from ~270 µs to slightly less than 200 µs at 47.5at.% Yb^{3+} concentration. Apparently this small amount of quenching does not affect the achievable gain significantly.

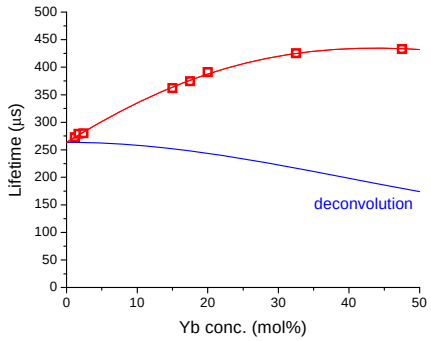


Figure 3. $^2F_{5/2}$ lifetime as a function of Yb^{3+} concentration. The red line is the fit with the equation given in [5], while the blue line is the deconvolution of the fit that shows the self-quenching contribution.

We performed small-signal-gain measurements using a pump-probe-beam set-up with a Ti:Sapphire pump laser operating at 932 nm, a broadband probe-beam source polarized parallel to the N_m optical axis, mechanically modulated with a frequency of 142 Hz, and a monochromator selecting the signal wavelength λ_S. Pump and signal light were combined and coupled into the channel waveguide by an objective lens. Light emitted from the opposite waveguide end was collimated by an objective lens and residual pump light was suppressed by a dichroic filter and a spectrometer set to 980.6 nm. The amplified signal was detected by an InGaAs detector and discriminated from luminescence at this wavelength by lock-in amplification. Using a spatially resolved rate-equation model, we determined the pump power establishing transparency at λ_S. Relative to this 0-dB transmitted signal intensity, transmitted signal intensities at other pump powers were investigated and the modal gain was determined [1]. Results for different Yb^{3+} concentrations of 15at.%, 20at.%, and 47.5at.% versus launched pump power are displayed in Fig. 4. With increasing dopant concentration the gain increases because of an accordingly increasing absorbed pump power density and Yb^{3+} excitation density.

For the 47.5at.% sample we investigated the gain at different signal wavelengths experimentally and theoretically, exploiting the transition cross-sections determined for this mixed compound. While the measured peak gain amounted to 935 dB/cm at the zero-phonon line of 980.6 nm, we could achieve gain exceeding 150 dB/cm at several other wavelengths spanning a large wavelength range, indicated by the symbols in Fig. 5. Comparison with the calculated data (lines) shows that this gain level of > 150 dB/cm can be achieved continuously over a wavelength range of 55 nm, between 977 nm and 1032 nm.

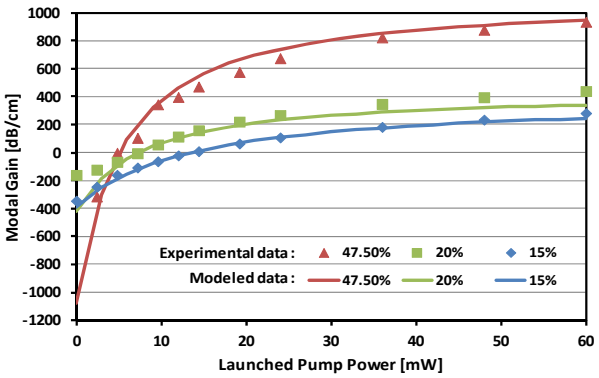


Figure 4. Waveguide modal gain at 981 nm versus launched pump power for different Yb^{3+} concentrations.

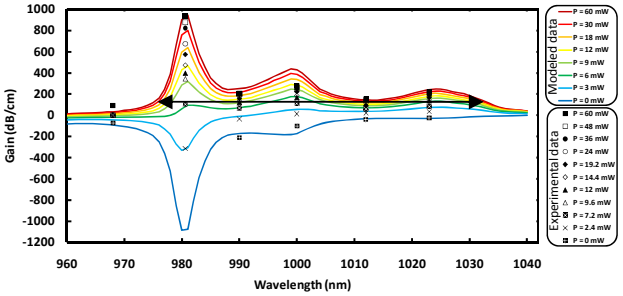


Figure 5. Waveguide modal gain for an Yb^{3+} concentration of 47.5% and different launched pump powers, calculated (lines) and measured (symbols); indication (arrow) of the spectral range of 55 nm with g_{mod} > 150 dB/cm.

V. CONCLUSIONS

Ultra-high gain has been demonstrated in $KGd_xLu_yYb_{1-x-y}(WO_4)_2$ channel waveguides over a wide wavelength range around 1 µm wavelength. Further improvement seems feasible with higher dopant concentrations. These results suggest that Yb^{3+}-doped waveguides may set a new wavelength standard at 1 µm for on-chip signal amplification.

REFERENCES

[1] D. Geskus, S. Aravazhi, S. M. García-Blanco, and M. Pollnau, "Giant optical gain in a rare-earth-ion-doped microstructure," Adv. Mater., vol. 24, in press, 2012.

[2] Y. E. Romanyuk, C. N. Borca, M. Pollnau, S. Rivier, V. Petrov, and U. Griebner, "Yb-doped $KY(WO_4)_2$ planar waveguide laser," Opt. Lett., vol. 31, pp. 53-55, January 2006.

[3] F. Gardillou, Y. E. Romanyuk, C. N. Borca, R. P. Salathé, and M. Pollnau, "Lu, Gd codoped $KY(WO_4)_2$:Yb epitaxial layers: towards integrated optics based on $KY(WO_4)_2$," Opt. Lett., vol. 32, pp. 488-490, March 2007.

[4] D. Geskus, S. Aravazhi, C. Grivas, K. Wörhoff, and M. Pollnau, "Microstructured $KY(WO_4)_2$:Gd^{3+}, Lu^{3+}, Yb^{3+} channel waveguide laser," Opt. Express, vol. 18, pp. 8853-8858, April 2010.

[5] F. Auzel, G. Baldacchini, L. Laversenne, and G. Boulon, "Radiation trapping and self-quenching analysis in Yb^{3+}, Er^{3+}, and Ho^{3+} doped Y_2O_3," Opt. Mater., vol. 24, pp. 103-109, October 2003.

.

Photonics Design Automation workflow

Twan Korthorst and Remco Stoffer
PhoeniX Software
Enschede, The Netherlands
info@phoenixbv.com
www.phoenixbv.com

Andrea Melloni and Davide Roncelli
Filarete srl
Milan, Italy
info@aspicdesign.com
www.aspicdesign.com

Abstract—**A Photonics Design Automation workflow is discussed, in which the whole chain from initial idea to final reticle composition is supported by an integrated software tool chain.**

Keywords: Photonics Integration Platforms; Generic Manufacturing; Photonics Design Flow Automation; Design Rule Checking; Generic Integration Software

I. INTRODUCTION

In the electronics industry, the use of 'Electronics Design Automation' (EDA) is wide-spread. A foundry offers a set of building blocks (BBs), which a designer can use to create a complex device. The BBs and their combination are guaranteed to work as expected if the given design rules are respected. Software takes care of any step of the design process, from physical analysis to layout and flags any design rule violation before the final design is shipped to the foundry. Furthermore, simulation tools are integrated in or link directly into the EDA environment and assist the designer in his work.

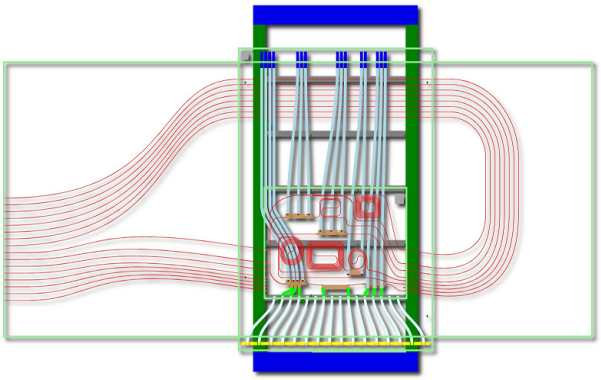


Figure 1: *Example of an InP chip mounted on a silica motherboard [11] with electrical connections as it appears in the developed photonics design automation environment.*

In photonics, such design kits have not been available until recently. In the European FP7 projects 'Europic' [1], 'Paradigm' [2] and 'Helios' [3] a number of European software companies have worked together to set up a Photonics Design Automation (PDA) tool set. Just like in EDA, photonic foundries define a number of building blocks, which are implemented in software ranging from mask layout through physical and circuit simulators. The circuit simulator is able to call the physical simulation software, or query a building block directly, in order to quickly simulate the response of a device. Furthermore, it can call the mask layout software to export the circuit design into a physical mask layout.

Since most building blocks of one foundry have equivalent BBs in other foundries, many designs will be transferable from one foundry to another with only minor changes to the layout (due to differences in BB sizes and port locations), but significant changes to mask layers (due to differences in technologies and process flows). This is regularly used in practice by Design Houses such as VLC Photonics [8] and Effect Photonics [16].

This paper describes the process that any design for a fabrication run goes through, from the designer's mind to a final, realized, and packaged chip.

II. DESIGN FLOW

A designer of a PIC (Photonic Integrated Circuit), who wants to have his design realized by a foundry, typically starts his design by modeling it in a circuit simulator. In a circuit simulator, one designs an optical circuit by placing building blocks from the foundry library with their properties into the circuit layout. The designer does not care how exactly a building block is implemented; the foundry just specifies the input / output ports and, possibly in conjunction with physical layer simulators, the wavelength-dependent scattering matrix (S-matrix) of the block. By clicking together a circuit and specifying its input and outputs, the designer can very quickly calculate the spectral response of the complete device. He can then optimize it for better functionality or for better robustness with respect to fabrication technology tolerances.

Once a satisfactory design has been created in the circuit design tool, it can be transferred, via the PDA framework, to a mask layout environment. The user specifies a die type available in the foundry and (if packaging options are available) a package. Such a combination of die type and package defines the locations of optical and electrical input and output ports. In this environment, the designer can adjust the exact layout of his design to optimize for space constraints and to make sure all connections (both optical and RF or DC electrical connections) are correct.

In the mask layout software, the designer might only be allowed to see the outline of the foundry-defined building blocks. A foundry can protect its IP by just exposing a bounding box and the locations and dimensions of access waveguides and connections for electrical signals, as shown by the private building blocks in Figure 2.

The research leading to these results has received funding from the European Community's Seventh Framework Programme FP7/2007-2013 under grant agreement n° 228839 EuroPIC

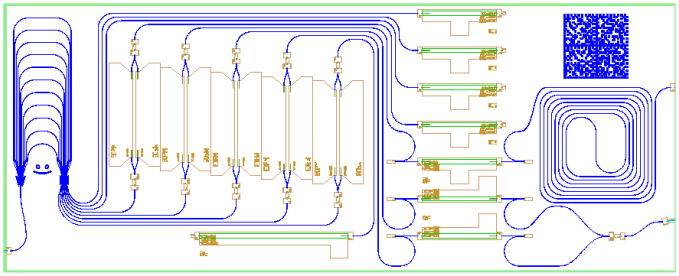


Figure 2: Mask design with bounding boxes for IP licensed building blocks.The AWG is developed by BrightPhotonics [7]

When the designer is satisfied with his mask layout, he exports it to a mask file. This process involves post processing on the mask layers that are defined by the foundry; for example, a waveguide on the final mask might have to be a little wider than designed to correct for under etch, or a final mask layer might have to be a local inversion of the designed waveguide. During the automatic mask export, the software performs design rule checks (DRC) on both the logical and mask layer levels; an example of a logical check is the radius of curvature of a waveguide, while an example of a mask layer check is whether a metallization layer and a waveguide layer overlap – or are closer than a given distance to each other.

Since the designer has no knowledge of the inner workings of a private building block, the mask files that are produced will be incomplete as the IP-protected building blocks are left open. The export process also generates a list of used building blocks and their locations. When the foundry receives designs created with the developed design environment, for example for a Multi Project Wafer run, it assembles all the mask files from the users into one reticle mask set. Furthermore, it uses the building block information supplied by the users to fill in the private building blocks in all designs with its own proprietary mask data. After this final mask assembly, the reticles can be created.

III. Future Outlook

A set of re-usable building blocks that are available in foundry processes will lead to huge cost reductions. This will open up the application of photonics integration technologies to a much larger public. Instead of optimizing the fabrication technology for every specific application, the product design will be adapted to the capabilities of available, mature, high performance fabrication processes. The presented PDA environment plays a central role (see Figure 3) in the whole product and value chain from concept application to material, through design to manufacturing.

The developed PDA framework is not restricted to the software vendors setting it up and the involved foundries. Other parties can create their own plug-ins and building blocks. For example, two different Arrayed Waveguide Grating plug-ins have been created by third parties [7, 15] and are actively being used in the MPW runs designs.

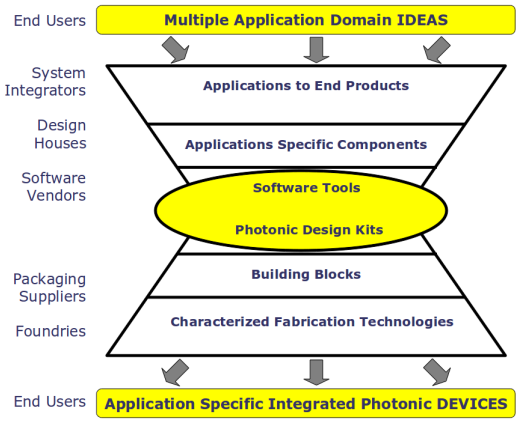


Figure 3: Photonics Design Automation as central pivot point in the 'food chain' [6].

IV. Conclusions

The design flow as described in this paper has been applied successfully within a number of projects. MPW runs in InP [1, 2, 5], TriPleX™ [5] and SOI [4] have been run on the platform, and more than 50 designs have been successfully implemented in the past six months, for six different foundries and two packaging providers.

Acknowledgment

The authors wish to thank all partners in the EuroPIC, Paradigm-JePPIX, Memphis and Helios projects for making Photonics Design Automation a success. Special thanks go to M. Hoekman of LioniX [9], D. Szymanski of Oclaro [10], M. Robertson of CIP Photonics [11], F. Soares of FhG/HHI [12], P. Dumon of IMEC [13], M. Fournier of CEA-Leti [14], E. Kleijn of TU/e COBRA PhI [15], R. Broeke of Bright Photonics [7] and P. Muñoz of VLC Photonics [8].

Part of this work has been made possible by the European Commission through Framework Programme 7 and the Dutch Ministry of Economic Affairs by the SmartMix programme.

References

[1] http://europic.jeppix.eu
[2] http://paradigm.jeppix.eu
[3] http://www.helios-project.eu
[4] http://www.epixfab.eu
[5] http://www.smartmix-memphis.nl
[6] http://www.tdk4pe.eu
[7] http://www.brightphotonics.eu
[8] http://vlcphotonics.com
[9] http://www.lionixbv.com
[10] http://www.oclaro.com
[11] http://www.ciphotonics.com
[12] http://www.hhi.fraunhofer.de
[13] http://www.imec.be
[14] http://www.leti.fr
[15] http://w3.ele.tue.nl/nl/oed
[16] http://effectphotonics.nl/

On-chip Microwave Photonic Signal Processors in Low-Loss, High-Index-Contrast Si_3N_4/SiO_2 Waveguides

L. Zhuang, D.A.I. Marpaung, M. Burla,
M.R.H. Khan, and C.G.H. Roeloffzen
Chair of Telecommunication Engineering, EEMCS
University of Twente
Enschede, The Netherlands
L.Zhuang@ewi.utwente.nl

W.P. Beeker, A. Leinse, and R.G. Heideman
LioniX B.V.
Enschede, The Netherlands
W.P.Beeker@lionixbv.nl

***Abstract*—This paper gives a brief review of several world-first on-chip microwave photonic (MWP) signal processing functionalities which have been enabled by Si_3N_4/SiO_2 TriPleX™ planar waveguide technology. The realized devices demonstrate that the on-chip solution for MWP signal processing has the capability of providing various functionalities in compact form and low manufacturing cost. This promises the future prevailingness of its implementation for practical MWP applications.**

Keywords-microwave photonic signal processing, on-chip, low-loss, high-index-contrast, Si_3N_4/SiO_2, photonic integrated circuit

I. INTRODUCTION

Microwave photonic signal processing leverages the small size, weight and power consumption, low propagation loss, and large instantaneous bandwidth of optics to realize high-frequency (microwave/millimeter wave) RF systems. Therefore, MWP signal processing systems have the potential to feature functionality and performance better or in excess to the capability of conventional electrical RF systems. Motivated by this promise, many dedicated investigations have been conducted in the past few decades to realize functionalities such as RF filtering, amplitude and phase manipulation, and beamforming [1]. Despite these appealing functionalities, conventional MWP signal processing systems constructed using discrete optical components usually suffer from the lack of robustness and cost efficiency that hinder their wide deployment for practical applications. Evident from the recent efforts [2], on-chip MWP signal processor will be the key to solve this problem. This requires photonic integrated circuits (PICs) implementation of the desired functionalities and a waveguide technology that provides low propagation loss, low chip-interface coupling loss, small bend radius and CMOS-comparable fabrication cost efficiency. We believe that the TriPleX™ waveguide technology is well suited for the on-chip MWP processing. In this paper, we give a brief review of several on-chip MWP signal processing functionalities which have been realized in this CMOS-process-equipment compatible, low-loss, high-index-contrast Si_3N_4/SiO_2 planar waveguide technology. The advantageous feature of this waveguide technology is the very low propagation loss of 0.1 dB/cm at a small bend radius of 70 μm [3]. The waveguide technology is described in Section II. In Section III some examples of the on-chip MWP signal processing using TriPleX™ technology are presented.

II. WAVEGUIDE TECHNOLOGY

The optical waveguide consists of two stripes of Si_3N_4 with a thickness of 140 nm stacked on top of each other with SiO_2 as an intermediate layer of 500 nm thickness and cladding material. A scanning electron microscope (SEM) image of the waveguide cross section is shown in Fig. 1a. The use of this double-stripe geometry increases the effective index of the optical mode as compared to the single-stripe geometry, thus increasing the confinement of the mode and thereby reducing the bend loss. The widths of the stripes have been optimized to result in a well confined mode and the waveguide only supports a single (TE) mode at a wavelength of 1550 nm. The propagation loss characterization of this waveguide is shown in Fig. 1b. A very low propagation loss of 0.1 dB/cm is achieved simultaneously with a small bend radius of 70 μm, which are the key factors to enable on-chip MWP signal processing and compact form for practical applications. Moreover, good fabrication uniformity is also evident from the measurement results.

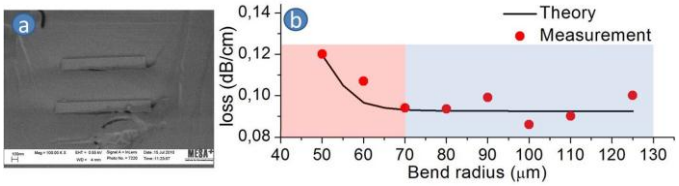


Fig.1. Measured waveguide propagation loss for various bend radii (inset: a SEM image of the double-stripe waveguide)

III. ON-CHIP IMPLEMENTATION OF MWP FUNCTIONALITY

A. Optical beamformer

As the most complex on-chip MWP signal processor to date, an optical ring resonator (ORR)-based 16 × 1 true-time-delay beamformer chip has been realized in TriPleX™ technology. The beamformer chip is used to steer the beam direction of a phased array antenna system for mobile satellite communication applications [4]. For such an application, the photonic chip should be capable of delaying a wideband RF signal (with a bandwidth in excess of 4 GHz) in a programmable manner. The required maximum delay in this

The realizations of the devices described in this paper are financially supported by Dutch Point One R&D project PNE101008, SANDRA project within European FP7 program, and MEMPHIS project supported by Agentschap NL of The Netherlands.

case is 290 ps. Since the delay is implemented using cascaded resonators, larger delay means higher losses for the signals. For this reason the propagation loss in the optical waveguides should be minimized. The maximum tolerable on-chip propagation loss in this case is 0.2 dB/cm [4]. The beamformer chip that fulfills these requirements is shown in Fig. 2. It consists of a 16 × 1 binary-tree combing circuit inserted symmetrically with a total of 40 ORRs delay elements, an optical sideband filter (OSBF) consisting of an asymmetric MZI with an ORR in each arm (for filter-based single-sideband suppressed-carrier modulation), and a dedicated coupling section for optical carrier-reinsertion operation. Thanks to the small bend radius of the waveguide, the complete footprint of the chip measures 0.7 × 2.2 cm. The chip is programmable using thermo-optical tuning scheme. The first successful antenna pattern demonstration of broadband squint-free beam steering using such an optical beamformer chip has been reported in [5].

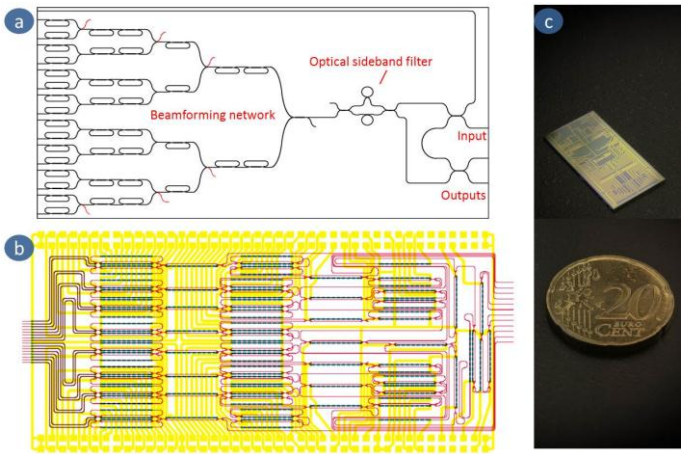


Fig.2. (a) beamformer architecture, (b) chip mask layout, and (c) a photo of fabricated beamformer chip.

B. Separate optical carrier phase tuning

In addition to the use as true-time delay lines, the ORRs of the beamformer can also perform separate carrier tuning (SCT). Hence, a single delay line using a cascade of multiple ORRs can separately and independently control the group delay over the sideband and the carrier phase shift of an optical single-sideband full-carrier (OSSB-FC) modulated signal. This is an essential functionality in several MWP signal processing systems which require true time delay and SCT. As a result, this ORR-based solution allows the realization of on-chip MWP signal processing such as multi-tap microwave photonic filters and beamformers using OSSB-FC modulation. The first demonstration of this on-chip functionality has been reported in [6]. The demonstrator circuit uses the same building blocks as in the beamformer chip, which consists of a cascade of a 2-ORR delay line, a 2-ORR carrier tuner, and an OSBF.

C. Photonic chip frequency discriminator

Another enabling MWP functionality that has been realized using TriPleX^{TM} technology is PM/IM conversion. By properly arranging multiple stages of add-drop ORRs, the world-first on-chip MWP frequency discriminator has been realized [7], as shown in Fig. 3. This discriminator enables various functionalities like high performance microwave photonic link and ultrawideband pulse shaping. Using this chip, a high performance phase-modulated microwave photonic link has been demonstrated [7], which exhibits a high spurious-free dynamic range (SFDR) of 113 dB·Hz$^{2/3}$. Furthermore, the chip has also been implemented for the world's first on-chip impulse-radio ultrawide-band (IR-UWB) pulse shaper [8]. With full programmability, the chip is capable of generating wideband RF pulses with high complexities. This opens up the path to the realization of low cost and compact UWB transmitters.

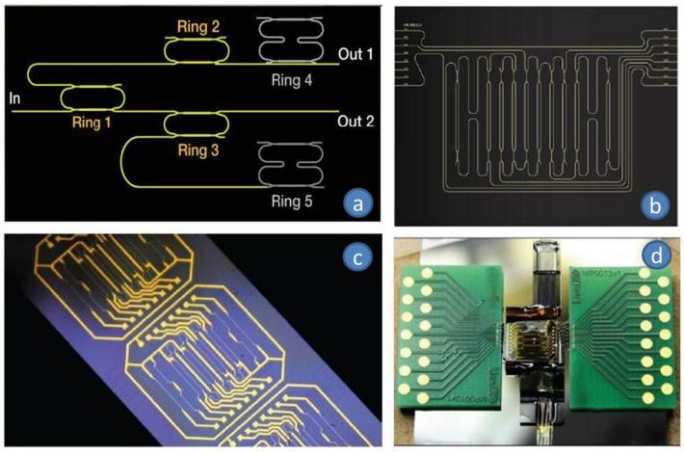


Fig.3. (a) architecture, (b) chip mask layout, (c) bare chip, and (b) packaged chip of frequency discriminator.

IV. CONCLUSION

Several integrated MWP signal processing devices enabled by a low-loss, high-index-contrast Si_3N_4/SiO_2 waveguide technology has been presented. These demonstrations emphasize the important role of PICs for the future of microwave photonics.

[1] J. Capmany and D. Novak, "Microwave photonics combines two worlds," *Nat. Photonics* **1**(6), 319-330 (2007).

[2] I. Gasulla, J. Lloret, J. Sancho, S. Sales, J. Capmany, "Recent breakthroughs in microwave photonics," *IEEE photonics Journal* **3**(2), 311-315 (2011).

[3] L. Zhuang et al., "Low-loss, high-index-contrast Si_3N_4/SiO_2 optical waveguides for optical delay lines in microwave photonics signal processing," *Opt. Express* **19**(23), 23162-23170 (2011).

[4] D. Marpaung et al., "Towards a broadband and squint-free K_u-band satellite terminal," *Proc. of the Fourth European Conference on Antennas and Propagation (EuCAP 2011)*, 2774-2778 (2011).

[5] M. Burla et al., "System integration and radiation pattern measurements of a phased array antenna employing an integrated photonic beamformer for radio astronomy applications," *Applied Optics*, in press.

[6] M. Burla et al., "On-chip CMOS compatible reconfigurable optical delay line with separate carrier tuning for microwave photonic signal processing," *Opt. Express* **19**(22), 21475-21484 (2011).

[7] D. Marpaung,et al, "A photonic chip based frequency discriminator for a high performance microwave photonic link, " *Opt. Express* **18**(26), 27359-27370 (2010).

[8] D. Marpaung et al., "Impulse radio ultrawideband pulse shaper based on a programmable photonic chip frequency discriminator," *Opt. Express* **19**(25) 24838-24848 (2011)

TriPleX™ photonic platform technology

Low-loss waveguide platform for applications from UV to IR

A. Leinse, R.G. Heideman, W. P. Beeker, M. Hoekman, C.M. Bruinink
LioniX BV
Enschede, The Netherlands
a.leinse@lionixbv.nl

C. G. H. Roeloffzen, L. Zhuang, D. A. I. Marpaung, M. Burla
Chair of Telecommunication Engineering, EEMCS
University of Twente
Enschede, The Netherlands

***Abstract*—The CMOS compatible fabrication equipment, the transparency from UV to IR and the capability of batch processing make the TriPleX™ waveguide platform very suitable for a large variety of applications. In this paper a description of the technology and examples of applications in different wavelength ranges are given. These applications exploit the low loss properties at relatively high index contrasts in the TriPleX™ technology**

Keyword: TriPleX™, integrated optics, opto-fluidics, low-loss

I. INTRODUCTION

In the last years the proprietary TriPleX™ waveguide technology [1] of LioniX has been further developed and has become one of the three main integrated optical platforms (next to InP and SOI) in the Netherlands. TriPleX™ structures are realized with CMOS compatible fabrication equipment and the materials used are based on chemical end products of LPCVD processes, resulting in very reproducible material properties, allowing design by geometry. TriPleX™ is also offered as Multi Project Wafer (MPW) services together with PhoeniX BV [9]. The basic concept of a TriPleX™ waveguide consists of a multilayer stack of stoichiometric silicon nitride and silicon oxide. These materials have an opposite stress when deposited on a silicon wafer (nitride is tensile and oxide is compressive) and stacking them in a multilayer results in a macroscopically low stress layer stack. A typical cross section of the TriPleX™ waveguide is shown (in box geometry) in figure 1.

II. FABRICATION

The TriPleX™ waveguide technology can be used to create several different waveguide geometries, which are all based on the same fabrication process. The standardized geometries all require a single lithography step only. The only difference is in the exact details of the process (waveguide width, layer thickness, etch depth). In addition the TriPleX™ technology also allows fabricating low loss spot size converters which can be incorporated in the same chip. A more detailed description of the fabrication process is also given in [2].

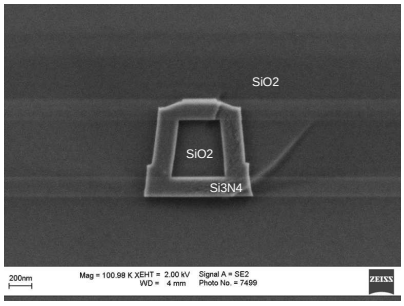


Figure 1: SEM cross section TriPleX waveguide

III. RESULTS

Waveguides were realized with different geometries varying from single stripes to complete high contrast box shape waveguides (figure 1). Characteristic for TriPleX™ is its low loss behavior at relatively high index contrast. On waveguide structures that allow bend radii of 70 micron waveguide propagation losses in ring resonators of 0.1 dB/cm were measured (figure 2) [7] allowing small footprint optical devices with low loss, which are extremely suitable for Microwave Photonics applications. In a recent publication [3] the TriPleX™ technology was further optimized and measurements were performed on its low loss performance at lower index contrast. Record low propagation losses of **<0.1dB/m** were reported on these devices. In figure 3 the measured los as a function of wavelength is shown in which losses of < 0.1 dB/m are seen for wavelengths of 1580-1610 nm.

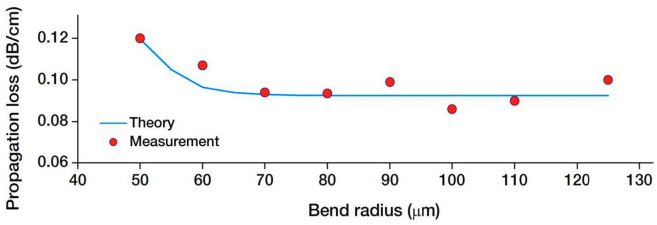


Figure 2: Measured propagation lossfor various bendradii (figure coming from [7])

IV. APPLICATIONS

With the current status of the fabrication process different applications, ranging from visible light to IR can be realized. The technology is also offered via MPWs allowing an easy access to the technology for designers. In the following section

two of the application areas will be discussed.

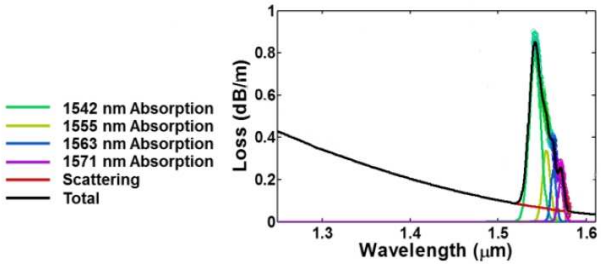


Figure 3: Propagation loss vs wavelength (40 nm thick nitride stripe [3])

A. Application 1: Microwave Photonics: Optical beam forming networks

An application in which the low loss properties of the TriPleX™ waveguides are essential is *optical beam forming*. In this application the antenna signals of a phased array antenna are delayed in the optical domain (with optical ring resonators operating at 1550 nm) and combined coherently on the same chip to achieve a squint free, broadband, steerable phased array antenna. Schematic the system of such an optical beamformer is shown in figure 4. The OBFN chip itself is build up from ring resonators that are combined in a binary tree configuration. An example of a realized device is shown in figure 4. With the high contrast TriPleX™ waveguides the optical beamforming was demonstrated and a more detailed analysis of this application is given is several publications [4][5]. This product is currently being commercialized by Satrax BV (www.satrax.nl)

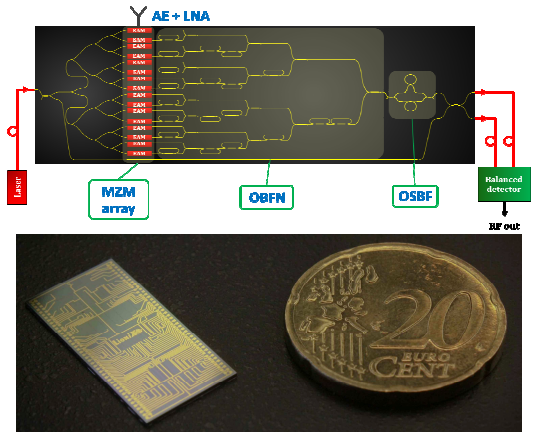


Figure 4: (top) Ring resonator-based optical beamformer scheme (AE=antenna element, LNA=low-noise amplifier, MZM= Mach–Zehnder modulator, OBFN=optical beamforming network, OSBF=optical sideband filter). (bottom) Realized optical chip

B. Application 2: Optofluidics

Another advantage of the TriPleX™ technology is the ability to combine the waveguide technology with fluidic channels (optofluidics) opening a whole new range of possible applications. A variety of measurements can be done probing the fluids in the fluidic channel. By applying the right chemical on top of the waveguides in the defined sensing windows the devices can be realized for a specific application. Two examples of applications based on this technology are

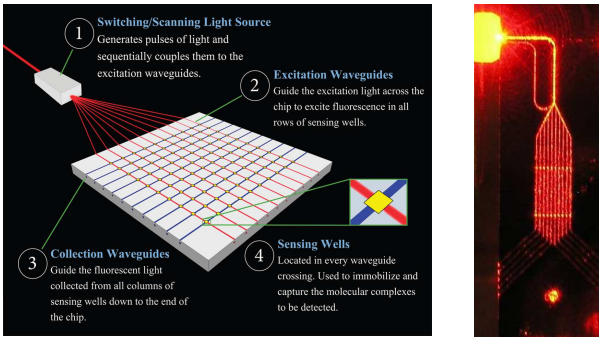


Figure 5: (left) Schematic overview of microarray application, (right) Picture of the optical LMCchip in 633 nm excitation

described in [8] and [6]. In both applications the sensing in the fluidic channel is based on fluorescence of biomarkers on top of the waveguides. The evanescent field of the optical mode in the waveguide excites the biomarker and the fluorescence of this biomarker is detected. The applications are described in more detail in the two publications. In figure 5 two pictures of the applications are shown. The optofluidic TriPleX™ technology was offered in 2011 on a MPW basis by CMC Microsystems in Canada. Currently the further optimization of the MPW design kit is under development.

V. CONCLUSIONS

The TriPleX™ waveguide technology is a stable waveguide platform technology with which design by geometry in MPW runs is possible. With the same fabrication technology applications ranging from UV to IR are possible and the technology can also be combined with microfluidics, opening a whole range of optofluidic applications.

REFERENCES

[1] F. Morichetti, et al (2007) “Box-Shaped Dielectric Waveguides: A New Concept in Integrated Optics?”, Journal of Lightwave Technology, 28 (7). pp. 2579-2589. ISSN 0733-8724

[2] R.G. Heideman et al, “Large-scale integrated optics using TriPleX™ waveguide technology: from UV to IR”, SPIE Photonics West, 24-29 Jan 2009, San Jose, California, U.S.A.

[3] J. Bauters, et al. (2011), “"Planar waveguides with less than 0.1 dB/m propagation loss fabricated with wafer bonding," Optics Express, Vol. 19 Issue 24, pp.24090-24101 November 10, (2011))

[4] A. Meijerink et al.(2010) “Novel ring resonator-based integrated photonic beamformer for broadband phased array receive antennas - part I: design and performance analysis”, Journal of Lightwave Technology, 28 (1). pp. 3-18. ISSN *0733-8724*

[5] L. Zhuang, et al. (2010) “Novel ring resonator-based integrated photonic beamformer for broadband phased array receive antennas - part II: experimental prototype”. Journal of Lightwave Technology, 28 (1). pp. 19-31. ISSN 0733-8724

[6] A. Prak et al. (2011) “Integration of optical waveguides and microfluidics in a miniaturized antibody micro-array system for life detection in the NASA/ESA ExoMars mission”, Proc. SPIE 7928, 79280L

[7] L. Zhuang, et al.(2011) “Low-loss, high-index-contrast Si3N4SiO2 optical waveguides for optical delay lines in microwave photonics signal processing” Optics express, 19 (23). pp. 23162-23170. ISSN 1094-4087

[8] R Duer, et al. (2010), “In-Plane Parallel Scanning: A Microarray Technology for Point-of-Care Testing“, Anal. Chem., 2010, 82 (21), pp 8856–8865

[9] http://www.phoenixbv.com/flyers/MPWTriPleXTM.pdf

Design and Fabrication of a Monolithically Integrated AWG-based Optical Pulse Shaper

M.S. Tahvili[1], X.J.M. Leijtens[1], P.J. Williams[2], M.J. Wale[1,2], M.K. Smit[1], and E.A.J.M. Bente[1]
[1]COBRA Research Institute, Eindhoven University of Technology, Eindhoven, the Netherlands
[2]Oclaro Technology Ltd., Caswell, Towcester, Northamptonshire, NN12 8EQ, United Kingdom
s.tahvili@tue.nl

Abstract— **We present design, fabrication and first characterization results of an InP-based integrated optical pulse-shaper. An AWG with 50GHz channel spacing is designed to split the input signal from a mode-locked laser. The AWG has 20 output channels and covers 8nm bandwidth. The phase and amplitude in each channel is controlled using electro-optic phase modulators and SOAs. The light reflects back on a facet end with an HR-coating, is recombined in the AWG and returns through the input waveguide. The double-pass design makes the chip size compact, i.e. 6×6mm^2.**

Keywords- Photonic Integration; Optical pulse-shaping; Multi-project wafer run.

I. INTRODUCTION

An optical pulse train is composed of a series of equally spaced spectral components in the frequency domain. For many applications it is necessary to control the relative spectral phase and amplitude of optical pulses. Dispersion compensation in high-speed optical communications and optical waveform synthesis for bio-imaging systems are two examples. In general, it is possible to (almost) arbitrarily shape the optical pulses by controlling the phase and amplitude of each and every spectral component [1]. In the so-called line-by-line shaping approach, the incident optical pulse is decomposed into its constituent spectral components by a spectral disperser element which is usually a grating. The phase and amplitude of the spatially dispersed spectral components are then modulated according to a required pattern. A shaped output pulse is obtained after the spectral components are recombined by a second lens and grating.

Programmable liquid-crystal modulator arrays are most commonly used to allow independent, simultaneous control of spectral phase/amplitude pattern of optical pulses. To explore the possibilities to bring the many advantages of photonic integration to this field, we have designed a monolithically integrated AWG-based optical pulse-shaper. An instance of a previously demonstrated tunable integrated semiconductor optical pulse shaper is presented in [2]. The chip presented in this paper is fabricated on an InP-based manufacturing platform which is available in the framework of EuroPIC multi-project wafer runs.

The current design includes a total number of 20 SOAs as well as 20 phase modulators. In the following sections, we discuss the chip design and present characterization of the 50GHz AWG element and phase modulators. Characterization of the chip is ongoing at the time of publication.

This work is supported by the IOP Photonic Devices program managed by STW and Agentschap NL. The research leading to these results has received funding from European Community's Seventh Framework Programme FP7/2007-2013 under grant agreement NMP 228839 EuroPIC.

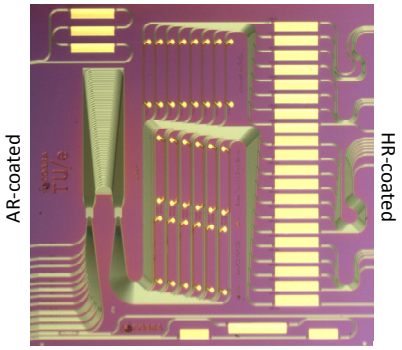


Fig.1. Microscope image of the realized 6×6mm^2 pulse shaper chip.

II. CHIP DESIGN AND CHARACTERIZATION

The pulse shaper device is to be combined with our (quantum dot) mode-locked lasers which have a spectral bandwidth of up to 8nm. The purpose of the chip is to compensate the chirp profile over optical pulses and any dispersion in the optics after the device. The light from the mode-locked laser is injected to the pulse shaper chip on an AR-coated facet. The light passes through an AWG which decomposes the spectral components. Filtered spectral components pass through electro-optic (EO) phase modulators (PMs) and SOAs and then reflect back on a facet end with an HR-coating. Frequency components are then recombined in the AWG and return through the input waveguide. The reflection geometry is used to make the system more compact. The two directions are separated in a circulator outside the chip.

A microscope image of the realized chip is presented in Fig.1. To equalize path lengths in the AWG arms as much as possible, optical path length differences in different channels are calculated and extra sections of waveguides are added to each channel. Some specifications of basic building blocks used to design the current photonic chip are listed in Table 1. Total on-chip loss (double-pass, excluding gain of SOAs) is in the order of 20dB.

Table 1. Building blocks in design of the pulse shaper

Required elements	Specification
Passive straight/ curved waveguide	Width=1.5µm, min radius=150µm, deeply etched, 5-6dB/cm loss, total length~ 9.2mm
AWG	Size 1×3.5 mm^2, 8nm (~1THz) FSR, 20 channels, 50GHz spacing
EO phase modulator	Width=1.2µm, length=1mm
SOA	Width=1.9µm, length=750µm, shallowly-etched
Transition element	Shallow-deep taper, active passive transition

A. AWG: Spectral filter

To achieve detailed phase control, the input signal from the mode-locked laser will be split using a 50GHz channel spacing AWG; this is the minimum number which is currently practically manageable. The AWG has 20 output channels and a free spectral range (FSR) of 8nm. Each channel includes a PM and an SOA. The designed AWG is cyclic and is designed for 0.4nm 3dB channel width. To characterize the AWG, SOA components may be used as on-chip broadband sources. We bias the SOA in channel 11 at I_{SOA}=30mA and record the optical spectra at the input waveguides at the AR-coated facet. Fig.2 shows recorded optical spectra at each of the input/output waveguides. The single pass on-chip loss is around 10dB. FSR is 8nm and the AWG passband is flat within 3dB.

The spectral shape of AWG channels is not as expected. Each channel seems to consist of two lobes which have 50GHz 3dB bandwidth and are separated by 0.4nm. Therefore, the channel width is effectively doubled. There is less than 1dB difference in height of each peak. Regarding the relative height of the two lobes, it is not possible that the shape of AWG channels is due to polarization. Measurements on a 750µm-long SOA shows that the ratio of generated TE/TM amplified spontaneous emission (ASE) light is over 15dB. Nevertheless, the curved waveguides and, most importantly, the AWG contribute to polarization conversion. We have investigated the effect of polarization dispersion of the AWF in [3].

B. PhaseModulators

The PMs on the pulse shaper chip are used to apply a certain phase mask on the frequency components of the input pulse. To increase the phase shifting efficiency, the PMs are oriented parallel to the wafer major flat. Therefore, the linear EO effect adds to the quantum-confined Stark effect (QCSE) shift which is generally regarded as quadratic in nature resulting in a nonlinear phase tuning characteristic.

The 1mm-long PMs are operated by applying a reverse bias voltage. The dark current is measured to be 2.5nA to 4nA for reverse bias V_{PM}=0 to V_{PM}=–5V. Fig.3 (right axis) shows the I-V curve of a PM in presence of the ASE light generated by the SOA which is biased at I_{SOA}=30mA. The current through the PM is I_{PM}=2µA at V_{PM}=0V and increases to I_{PM}=21µA at V_{PM}=–5V. The increased reverse current is caused by higher light absorption in presence of the external electric field due to QCSE. To quantify the amount of induced excess losses, we have measured the optical power at the AR-coated facet for several values of V_{PM}. The result is shown in Fig.3 (left axis). Up to a reverse bias of V_{PM}=–4V, the excess loss is lower than 1dB which is tolerable.

In order to characterize the phase tuning performance of phase shifters, we have made use of the spectral filtering behavior of the AWG. The neighboring channels of the AWG are designed to have 3dB overlap at FWHM. Therefore, if an external light signal with a wavelength in between the central wavelengths of two adjacent channels is injected to the chip, the power is effectively split between the two channels. In each arm, the light will pass through the PM and SOA, reflect back on the HR-coated facet and then recombine by the AWG to return to the input waveguide. This structure forms an interferometer which is used to characterize the phase shifters.

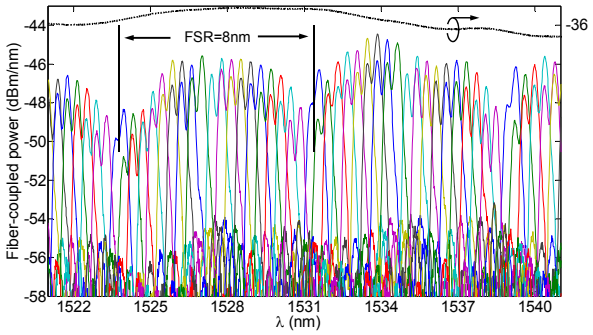


Fig.2. Fiber-coupled optical spectral power measured at input/output waveguides. The SOA in channel 11 is biased at 30mA; generated ASE is shown (dotted curve, right axis).

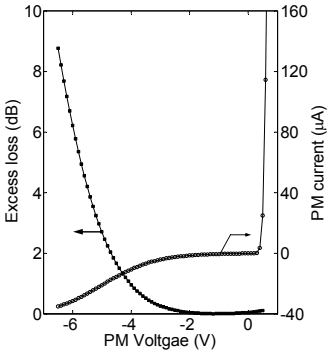


Fig.3. Induced excess loss (dB, left axis) and current through the phase shifter (µA, right axis) vs. applied voltage on a 1mm-long phase shifter.

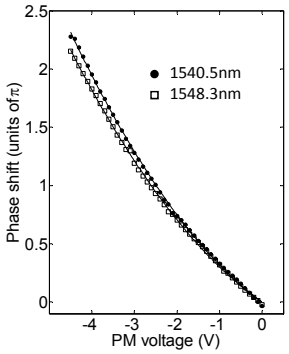


Fig.4. Measured phase shift (circles at λ=1540.5nm, open squares at λ=1548.3nm) and quadratic polynomial fitted curve (solid line).

Changing the bias voltage on a phase shifter in one arm induces a phase difference and thus changes the return optical power due to interference. In order to increase the signal to noise ratio, we have used the lock-in technique by modulating the SOA in one arm. The measured values of induced phase shift (circles at λ=1540.5 and squares at λ=1548.3) vs. the applied voltage are shown in Fig.4. The quadratic polynomial fitted curve is shown as a solid line. The required voltage for a 2π phase change (double-pass) is approximately 2.5V.

III. CONCLUSIONS

We have presented characterization of the AWG spectral filter and phase modulators on an integrated pulse shaper chip. The chip will be employed in combination with our quantum-dot mode-locked laser source to compensate the spectral chirp of the generated optical pulses. The settings of the phase modulators for pulse compression can be derived from the known spectral phase of the optical pulses from the quantum dot laser source. Measured phase tuning behavior of phase modulators is required for calculation of control signals.

REFERENCES

[1] S.T. Cundiff and A.M. Weiner, "Optical Arbitrary Waveform Generation" Nature Photonics, vol. 4, pp. 760–766, Nov. 2010.

[2] M.J.R. Heck, et.al., "Design, fabrication, and characterization of an InP-based tunable integrated optical pulse shaper," IEEE J. Quant. Electron. Vol. 44, pp. 370–377, 2008.

[3] M.S. Tahvili, et.al., "Design and Fabrication of a Monolithically Integrated AWG-based Optical Pulse Shaper," in Proc. IEEE Photonics Society Benelux Chapter, pp. 57-60, Gent, Belgium, Dec. 2011.

All-Optical InP Monolithically Integrated WDM Regenerator for PolSK Signals

N. Andriolli, S. Faralli, G. Contestabile
Scuola Superiore Sant'Anna
Pisa, Italy

J. Bolk, X.J.M. Leijtens
COBRA Research Institute
Technical University of Eindhoven
Eindhoven, The Netherlands

***Abstract*—A monolithically integrated Indium Phosphide optical circuit performing WDM regeneration of Polarization Shift Keying signals is presented. The scheme is based on hard-limiting amplification in a saturated Semiconductor Optical Amplifier. A Q-factor improvement of around 2 is reported on two different wavelengths.**

***Keywords*—All-optical regeneration, polarization shift keying.**

All-optical regeneration has been widely investigated with the aim of improving the quality of the optical signals without recurring to expensive and power-hungry optoelectronic regenerators. Studies mainly focused on conventional non-return-to-zero (NRZ) or return-to-zero (RZ) on-off-keying (OOK) modulation formats [1]. Recently, the research on all-optical regenerators also included the application to alternative modulation formats and multi-wavelength operation [2]. Indeed, the simultaneous regeneration of many optical signals at different wavelengths could represent a significant step toward the commercial viability of all-optical regeneration solutions, since a number of optoelectronic regenerators can be replaced in a single shot.

In this work we present an Indium Phosphide-based photonic integrated circuit (PIC) performing all-optical regeneration of wavelength division multiplexed (WDM) Polarization Shift Keying (PolSK) signals. The device has been fabricated exploiting JePPIX [3], the European platform for the manufacturing of Indium Phosphide-based PICs. Such platform pushes a generic integration technology, where standardized building blocks and foundry process are enforced, without technologies specifically developed or optimized for a given application. The actual PIC is here demonstrated performing all-optical regeneration of 10 Gb/s PolSK signals at different wavelengths, achieving a Q-factor improvement of around 2.

The realized device implements the scheme sketched in Fig. 1(a), presented in [2] to realize simultaneous all-optical regeneration of constant-envelope (CE) WDM signals. For these signals the regenerator should be placed in a WDM amplification site, preceded by an Erbium-doped fiber amplifier (EDFA) to pre-amplify the signals and by a dispersion compensating fiber (DCF) to recover the CE property. Then the WDM comb enters the regeneration block, where the component signals are demultiplexed by means of an arrayed waveguide grating (AWG). Each signal travels in and saturates a Semiconductor Optical Amplifier (SOA) so that it is regenerated thanks to the hard-limiting effect on the noise. Moreover, there is no pattern effect since the signals are all CE. Before the second AWG multiplexes all channels, an optical attenuator can be used on each path to provide power equalization. Finally a second EDFA can be used as a booster. The functions in the highlighted box of Fig. 1(a) have been implemented on a Indium Phosphide PIC fabricated in a multi-project wafer run of JePPIX Indium Phosphide platform [3] at the COBRA research institute of the Eindhoven University of Technology. This platform enables a generic foundry model, where the process is application blind and a small set of building blocks are used as basic elements for more complex photonic circuits. The layout and a picture of the realized PIC are shown in Fig. 1(b) and (c), respectively. Differently from the scheme in Fig. 1(a), the same AWG has been used both as a mux and a demux, in order to ensure consistent pass-band characteristics. The AWG has been designed to have a central frequency of 1534 nm and a free spectral range (FSR) of 19.5 nm. The ASE spectrum of one of the SOAs in the PIC measured at OUT1 is shown in Fig. 2(a). Each of the four AWG paths, destined to a specific wavelength channel, connects two different SOAs: the currents can be properly tuned to saturate the first SOA, and set the second SOA to

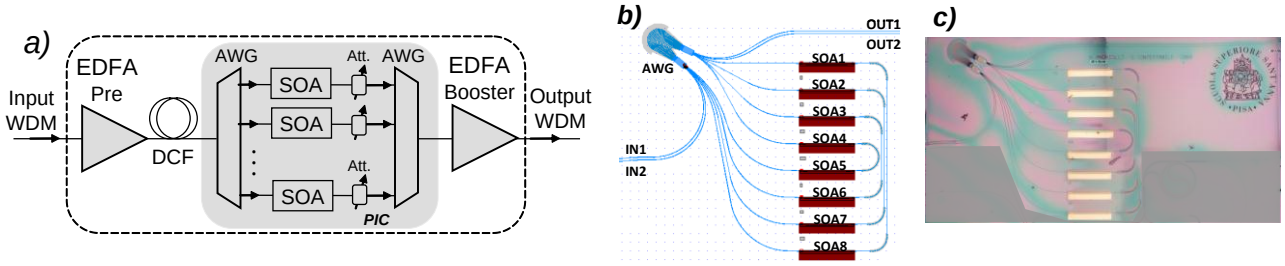


Fig. 1. (a): Scheme of the WDM regenerator of constant-envelope signals; (b): layout of the designed PIC; (c): picture of the fabricated PIC.

The work described in this paper was partially supported in by the Italian Ministry of Foreign Affairs, through the project RODIN.

transparency. Input and output waveguides have been duplicated, to ensure proper operation even in case of device realization problems. All the SOAs in the PIC have a fixed length of 500 μm, the same gain (a small signal gain of 10 dB has been measured) and saturation current (around 70 mA) [4]. To determine the proper input optical power to ensure SOA saturation, an input/output power characteristic has been measured on a test SOA identical to the previous ones fed with a current of 80 mA: the results, measured fiber-to-fiber are presented in Fig. 2(b), showing that a fiber input power of 15-to-20 dBm is required to have strong SOA saturation.

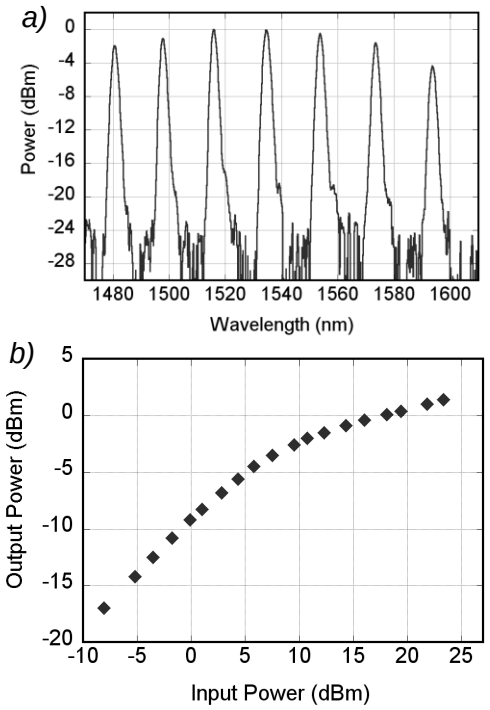


Fig. 2. (a) SOA8 ASE spectrum measured at OUT1; (b) optical input/output power characteristics of a test SOA at 80 mA on the same chip.

The experimental setup is sketched in Fig. 3(a). A 10 Gb/s PolSK signal is generated by using a tunable laser (at 1534 and 1553.5 nm, corresponding to two AWG pass bandwidth peaks) whose output lightwave is rotated and injected at $\pi/4$ in respect of the axes of a $LiNbO_3$ phase modulator driven by a 2^{31}-1 long Pseudo Random Bit Sequence (PRBS). This PolSK signal is combined with ASE noise from an EDFA source, after crossing a tunable optical bandpass filter (TBPF) centered at the signal wavelength. To properly set the optical power and the polarization into the PIC, an EDFA, another TBPF, a variable optical attenuator (VOA), and a polarization controller (PC) are utilized. Tapered fibers are used to couple light to and from the PIC. For each experiment the two SOAs on the optical path are fed with a current of 80mA and 20mA, respectively, to obtain the maximum available gain from the first one and to set to transparency the second one. PolSK demodulation is obtained by using a PC and a polarization beam splitter (PBS). The signal is thus detected by means of a pre-amplified receiver, composed of an EDFA, a TBPF, and a 10 dB optical attenuator (OA) connected to a sampling oscilloscope equipped with a 30 GHz optical head used for eye diagram acquisition and Q-factor measurement.

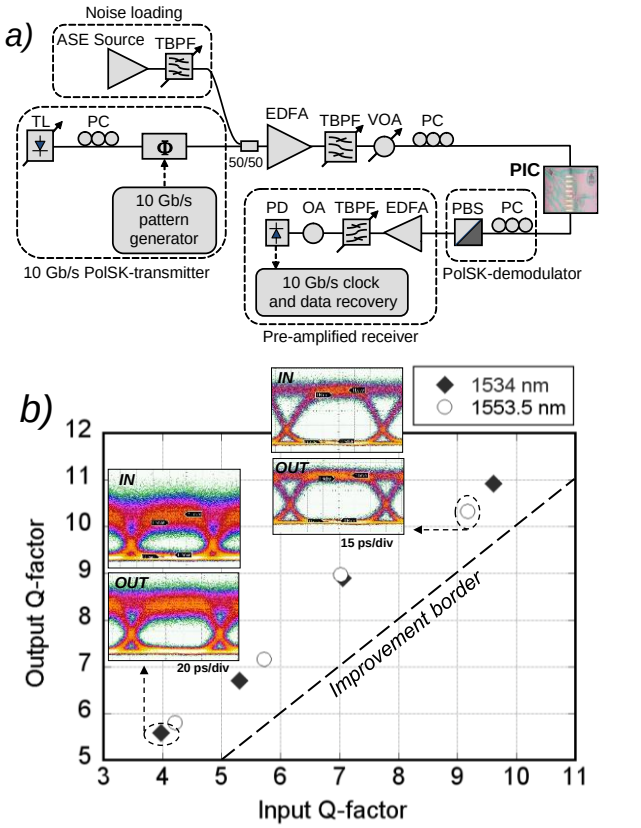


Fig. 3. (a) Experimental setup; (b) Input-output Q-factor evolution and example of input-output eye diagrams.

Fig. 3(b) shows the output Q-factor as a function of the input Q-factor for two tested wavelengths, as well as two examples of input and output eye diagrams. Thanks to the limiting amplification in the PIC, a Q-factor improvement up to 2 can be observed for every signal. This is slightly larger at 1534 nm compared to 1553.5 nm, since the former wavelength is closer to the SOA gain peak. A clear eye opening confirms the Q-factor results showing a significant noise compression. The PBS demodulator actually selects one polarization state so that the "ones" level is clearly compressed while the "zeros" level is mainly determined by the PBS contrast ratio.

In this paper an Indium Phosphide PIC realized through JePPIX platform is shown to perform WDM regeneration of 10 Gb/s PolSK signals. A Q-factor improvement of around 2 and a clear eye-opening are reported on two different channels.

REFERENCES

[1] M. Rochette et al., "2R optical regeneration: an all-optical solution for BER improvement," *IEEE J. Sel. Topics Quantum Electron.*, vol. 12, no. 4, pp. 736–744, Jul./Aug. 2006.

[2] G. Contestabile, M. Presi, and E. Ciaramella, "All-Optical Regeneration of 40 Gb/s Constant Envelope Alternative Modulation Formats," *IEEE J. Quantum Electron.*, vol. 46, no. 3, pp. 340–346, Mar. 2010.

[3] X. Leijtens, "JePPIX: the platform for Indium Phosphide-based photonics," *IET Optoelectron.*, vol. 5, no. 5, pp. 202–206, Oct. 2011.

[4] F. Bontempi, S. Pinna, N. Andriolli, C. Porzi, G. Berrettini; X. Leijtens, J. Bolk, A. Bogoni, and G. Contestabile; "All-optical monolithically integrated differential XOR," in *OFC/NFOEC2012 Tech. Dig.*

Widely-Tunable Polymer Waveguide Grating Laser

D. de Felipe. Z. Zhang, F. Soares, W. Rehbein, W. Brinker, H. N. Klein, C. Zawadzki, M. Moehrle, N.Keil and N. Grote
Photonic Components Department
Fraunhofer Institute for Telecommunications, HHI
Berlin, Germany
david.felipe@hhi.fraunhofer.de

P. Groumas
Photonics Communications Research Laboratory
School of Electrical and Computing Engineering, NTUA
Athens, Greece

***Abstract*—A tunable laser structure integrated in a hybrid polymer waveguiding platform consisting of a InP-based curved-stripe gain chip and a thermo-optically tunable waveguide grating is presented. A sophisticated heater design allows tuning ranges above 50 nm with a peak power degradation lower than 2 dB. Lasing linewidths of 500 KHz have been achieved and 2.5 Gb/s back-to-back transmission experiments have also been successfully proven showing clean and open eye diagrams.**

Keywords-polymer waveguide platform; tunable polymer waveguide grating laser.

I. INTRODUCTION

In recent years, wavelength-division-multiplexing passive optical networks (WDM-PON) as well as coherent detection schemes have attracted a great deal of attention. These applications demand cost-effective and yet high-performance tunable laser sources to be used in colorless transceivers and as tunable local oscillator, respectively. To this end, hybrid-integrated tunable waveguide grating lasers comprised of an active gain element and a thermo-optically (TO) tuned polymer Bragg reflector have been proposed [1-3]. With such structures, wavelength tuning over 26 nm has been achieved [1].

In the present work, a tunable polymer waveguide grating laser (PWGL) consisting of a curved-stripe (CS) InP-based gain chip and an integrated thermo-optically tunable polymer waveguide Bragg grating has been developed using HHI's PolyBoard hybrid integration platform [4]. A tuning range of more than 50 nm has been achieved by using a sophisticated heating structure. Laser linewidths of even below 500 KHz have been obtained for some devices. Direct modulation at 2.5 Gb/s has been also successfully performed.

II. PRINCIPLE OF OPERATION AND STRUCTURE

A schematic of the structure of the proposed PWGL is shown in Fig.1. A curved-stripe gain chip with a high-reflection (HR) coating at the rear facet acts as the optical gain medium while the waveguide grating in the PolyBoard platform is used as a wavelength selective feedback mirror. Wavelength tuning is accomplished by using a heater electrode in the vicinity of the polymer grating, which induces a change in the effective refractive index of the waveguide due to the TO effect, which again produces a shift in the Bragg wavelength of the grating. The buried-heterostructure-type InP based CS gain chip comprises a MOVPE grown InGaAsP multi-quantum well active region with a PL wavelength of 1570 nm. The gain chip is butt-coupled to the polymer waveguiding platform using a 9° angled facet to avoid undesired back-reflections. In order to obtain high mode overlap between the gain chip and the polymer waveguide, the gain chip waveguide has been laterally tapered from 2.4 µm to 0.9 µm in width. Further information on the coupling technique of the InP active device to the PolyBoard can be found in [4].

The PolyBoard waveguide platform consists of a buried waveguide structure with an index contrast of $\Delta n=0.02$ made of commercially available polymer material. For such an index contrast, a waveguide cross-section of 3.5 µm x 3.5 µm has been used to ensure monomode behavior. For implementing the selective mirror, 3rd- or 5th-order sidewall-corrugated Bragg gratings are formed in the waveguide core layer without the need for an extra lithographic and etching step. The reflectivity and bandwidth can be well-controlled by modifying the amplitude of the corrugation and the length of the grating, respectively [2]. For the tuning feature, a metal heater has been deposited in the surroundings of the corrugated waveguide. Along the waveguide grating, air trenches have been etched on both sides in order to achieve higher heat confinement. The fairly high TO coefficient ($dn/dT \sim 10^{-4}$/°K) of the polymer material, together with its low thermal conductivity and the proposed heating structure, provided an appreciably large tuning range at low heating power. An additional phase control heater has been added for fine wavelength tuning and adjustment of the side-mode suppression ratio (SMSR).

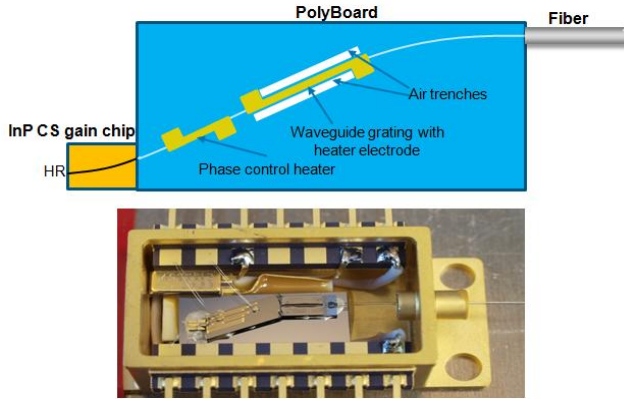


Figure 1. Schematic structure of the tunable PWGL based on HHI´s PolyBoard (up) and a picture of an assembled device (bottom).

III. DEVICE PERFORMANCE

The output power of a tunable PWGL at different heating powers has been measured on a device containing a waveguide grating with a length of 700 µm. The drive current of the gain chip was chosen to amount to 50 mA. The phase control heater was not used with these measurements. Results are shown in Fig. 2, where it can be seen that a tuning range in excess of 50 nm across the C-band has been obtained using less than 170 mW of heating power. The decay of the peak power degradation of the laser over this wide tuning range was found to be lower than 2 dB, while the SMSR could be maintained at values well below -26 dB. By using the phase heater, however, to optimally adjust the phase inside the laser cavity, will further reduce the SMSR values significantly.

Linewidth measurements have been performed using a self-homodyne method. For this investigation, a device with a 2500 µm long grating and a distance between the back-facet of the gain chip and the polymer grating of 1220 µm was used. Obtained values are shown in Fig. 3, where the lineshapes and the 3-dB linewidth values for different heating currents are depicted. Linewidths below 750 KHz have been obtained for the heater powers indicated, and in some cases values even below 500 KHz were measured.

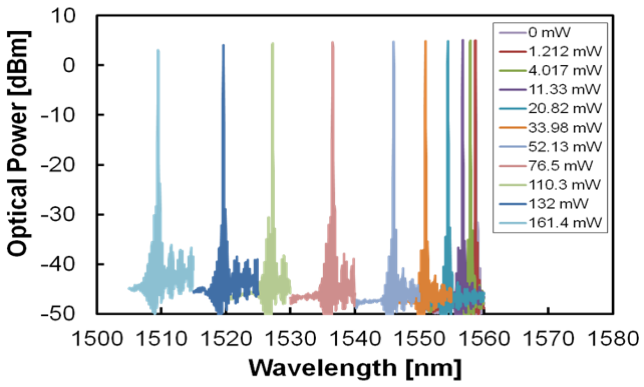


Figure 2. Optical spectrum for different electrical powers applied to the heater electrode.

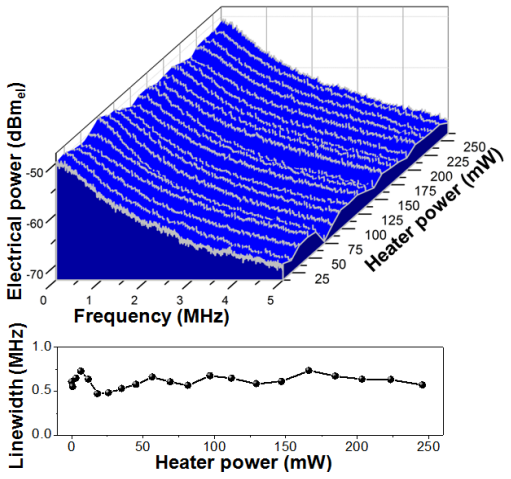


Figure 3 Lineshapes measured using a self-homodyne method (top) and 3-dB linewidth values (bottom) obtained for different heating powers.

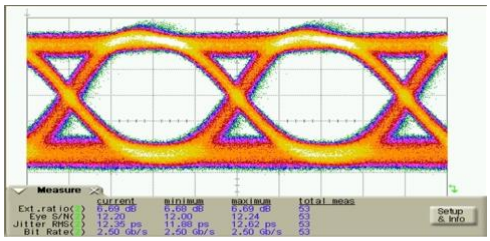


Figure 4. Back-to-back eye diagram of the NRZ modulation at 2.5 Gb/s.

Furthermore, a back-to-back transmission test was carried out by directly modulating the gain chip using pseudo-random non-return-to-zero (NRZ) data (2^{31}-1) at a rate of 2.5 Gb/s. The laser structure used in this experiment exhibited the same dimensions as the one used for the linewidth evaluation. A result is shown in Fig. 4 proving the achievement of open and clear eye diagrams with extinction ratios of 6.7 dB.

As a further development, this tunable PWGL structure can be modified aiming at higher speed modulation by reducing the total cavity length. It shall also be mentioned that - in the framework of the EC funded project POLYSYS - the investigated tunable laser structure has also been implemented on the basis of an electro-optically (EO) active polymer to eventually form the feed laser of polymer EO modulators. First results will be presented at the conference.

IV. CONCLUSIONS

In this paper a tunable PWGL based on HHI's PolyBoard hybrid integration platform has been presented. Due to an optimized electrode design for efficient heat confinement and thus low power consumption, a tuning range higher than 50 nm with a heating power of less than 170 mW has been achieved. Peak power degradation in this tuning range is lower than 2 dB, and linewidths below 500 KHz have been measured. Direct modulation capability of at least 2.5 Gb/s was successfully proven.

ACKNOWLEDGMENTS

The reported work has been mainly funded by the German Federal Ministry of Education and Research (projects: ADVantagePON and CONDOR). Related activities using EO polymers are funded by the EC in the framework of the STREP POLYSYS (IST FP-7, grant # 258846)

REFERENCES

[1] G. Jeong. M. Y. Park. C. Y. Kim, S.-H. Cho, W. Lee, G. Jeong, and B. W. Kim, "Over 26 nm Wavelength Tunable External Cavity Laser Based on Polymer Waveguide Platforms for WDM Access Network", Photon Techn. Lett., vol. 18 no. 20, pp 2102-2104, 2006.

[2] K.-H. Yoon, S.H. Oh, K. S. Kim, O-K. Kwon, and D. K. Oh, "2.5-Gb/s hybridly-integrated tunable external cavity laser using a superluminiscent diode and a polymer Bragg reflector", Optics Express, vol. 18 no. 6, pp 5556-5561, March 2010.

[3] F. M. Soares, Z. Zhang, G. Pzyrembel, M. Lauermann, M. Moehrle, C. Zawadzki, B. Zittermann, N. Keil and N. Grote, "Hybrid Photonic Integration of InP-Based Laser Diodes and Polymer PLCs", Proc. IPRM 2011, pp. 423-427, 2011.

[4] N. Keil, C. Zawadzki, Z. Zhang, J. Wang, N. Mettbach, N. Grote, and M. Schell, "Polymer PLC as an Optical Integration Bench," in Proc. OFC'11 (Los Angeles, CA, USA), paper OWM1, 2011.

High performance Ge/SiGe quantum well electro-absorption modulator

Papichaya Chaisakul, Delphine Marris-Morini, Mohamed-Saïd Rouifed, Xavier Le Roux, Samson Edmond, Jean-René Coudevylle, and Laurent Vivien
Institut d'Electronique Fondamentale, Univ. Paris-Sud
CNRS UMR 8622, Orsay, FRANCE
E-mail: Papichaya.chaisakul@u-psud.fr

Giovanni Isella, Daniel Chrastina, Jacopo Frigerio
Laboratory for Epitaxial Nanostructures on Silicon and Spintronics, Dipartimento di Fisica
Politecnico di Milano
Como, ITALY

***Abstract*— A 23 GHz Ge/SiGe multiple quantum well electro-absorption waveguide modulator is demonstrated with 10 dB extinction ratio (ER). 9 dB ER is achieved with 1V swing with energy consumption limited to 108 fJ per bit.**

Keywords-component; Quantum-confined Stark effect, Ge/SiGe, multiple quantum well modulators

I. INTRODUCTION

To be a viable replacement of copper wires at the chip scale, optical interconnects have to meet aggressive requirements in terms of power consumption, data density, and preferably monolithic integration with silicon. The devices should operate over a wide spectral range with an energy consumption of less than 100 fJ/bit [1]. Such low power consumption and wideband devices are unlikely with conventional silicon modulators based on a Mach–Zehnder interferometer (MZI) or a resonator [1, 2]. In this aspect, the electro-absorption (EA) modulator is one of the best approaches to obtain low energy consumption and high speed modulation due to its small footprint and sub-picosecond operation time for a wide spectral range [3]. Ge, a group IV material like Si, has been successfully monolithically integrated into CMOS fabrication processes by semiconductor companies [4, 5]. Interestingly, Ge quantum wells (QWs) [6, 7] have demonstrated a QCSE as strong as that of III-V semiconductor QWs. So far, high speed modulation using Ge/SiGe MQWs has been demonstrated up to 3.5 GHz using a surface illuminated p-i-n diode structure [8] and a transmission at 7 Gbps has also been demonstrated in waveguide configuration based on butt-coupling between the MQW structure and a Silicon-on-Insulator (SOI) waveguide [9]. In this paper, we demonstrate a modulator with a modulation bandwidth of 23 GHz obtained from a Ge/SiGe MQW waveguide. The modulator also exhibits high extinction ratio over a wide spectral range with an estimated energy consumption of as low as 108 fJ per bit. The schematic view of the fabricated device is shown in Fig. 1.

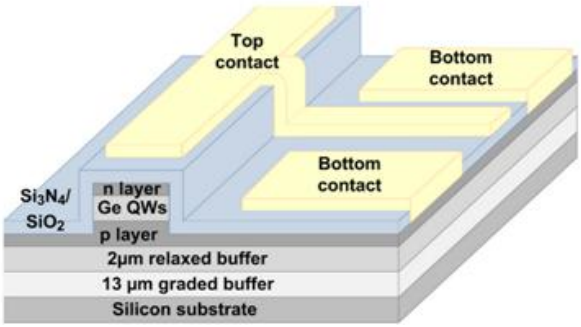


Figure 1. Schematic view of the 3 μm × 90 μm Ge/SiGe MQW modulator; Ge/SiGe MQWs were grown by low-energy plasma-enhanced chemical vapor deposition [10] and detailed epitaxial layers can be found in Ref 7.

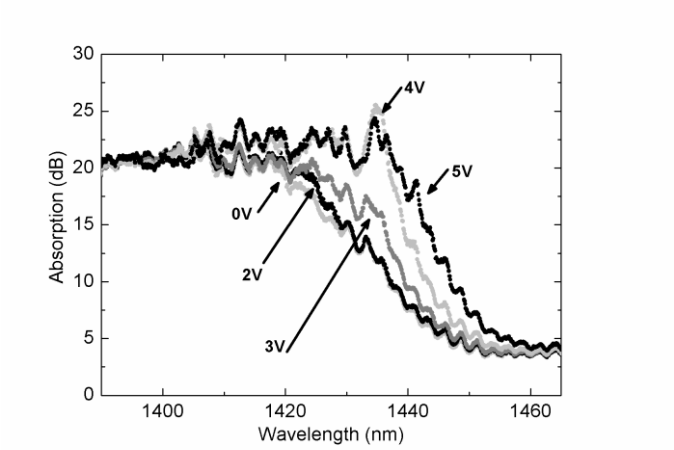


Figure 2. Absorption spectra of the 3 μm wide 90 μm long Ge/SiGe MQW waveguide as a function of wavelength and photon energy for reverse bias voltages of 0, 1, 2, 3, 4, and 5 V.

II. EXPERIMENTAL RESULTS

Transmission spectra of the Ge/SiGe MQW waveguides at several reverse bias voltages are shown in Fig 2. By increasing the reverse bias voltages, the red shift of the absorption spectra, which is a characteristic of the QCSE, is observed. Extinction ratio achieved using different bias can be deduced by substracting transmission spectra, and are reported in Fig 3 and 4. From Fig 3. an extinction ratio (ER) higher than 6 dB for a wide spectral range between 1425 and 1446 nm is obtained, with a maximal ER value of around 10 dB achieved between 1433 and 1442 nm for a reverse bias of 5 V and between 1433 and 1437 nm for a reverse bias of 4 V. From Fig 4. with a voltage swing of only 1 V between 3 and 4 V and of only 2 V between 3 and 5 V, ER higher than 6 dB is obtained from 1433 to 1437 nm and from 1433 to 1444 nm respectively. As seen in Fig 2., the absorption loss at 0 V of the Ge/SiGe waveguide used in this work is around 5.5 – 12 dB at the wavelength region between 1433 and 1444 nm. This absorption loss could be decreased by optimizing the light confinement in the MQW region. Indeed the overlap of the first optical mode with the MQW region is only 12 % and part of the optical loss also comes from the overlap between the optical mode and the 2 µm thick $Si_{0.1}Ge_{0.9}$ relaxed buffer and the doped regions. The frequency response of the modulator was evaluated at 1448 nm using an opto-RF vector network analyzer (Agilent 86030A). The normalized optical response at the dc reverse bias of - 4.5 V as a function of frequency is given in Fig. 5. The 3 dB cut-off frequency of 23 GHz was experimentally obtained. For energy consumption, the junction capacitance of the waveguide device with a size of 3 µm × 90 µm and 20 Ge QWs is calculated to be 62 fF, which is also consistent with the values extracted from S_{11} parameter measurement. From energy/bit = 1/4 (CV_{off}^2-CV_{on}^2), the energy consumption per bit of the EA modulator in this paper can estimated to be 108 fJ/bit for a voltage swing of 1 V between 3 and 4 V biases.

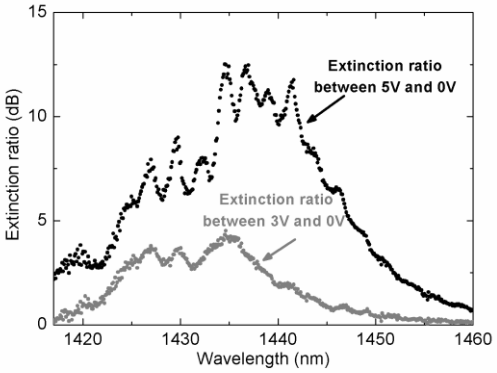


Figure 3. Extinction ratio of the waveguide between 0 and 3, 5 V

The research has received funding from the French ANR under project GOSPEL (Direct Gap related Optical Properties of Ge/SiGe Multiple Quantum Wells). Financial support for the epitaxial growth was provided by the Cariplo foundation through NANOGAP project.

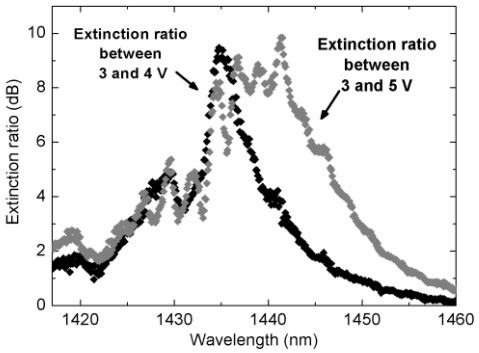


Figure 4. Extinction ratio of the waveguide for a voltage swing of 1 V between 3 and 4 V and of 2 V between 3 and 5 V

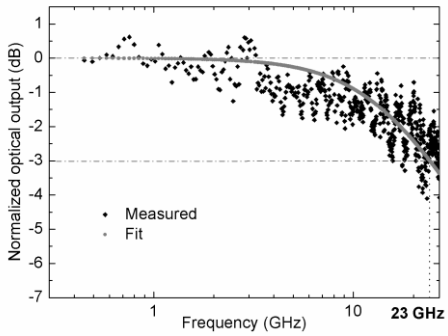


Figure 5. Normalized optical response at the dc reverse bias of - 4.5 V.

REFERENCES

[1] D. A. B. Miller, "Device requirements for optical interconnects to silicon chips," Proc. IEEE 97, 1166–1185 (2009).

[2] D. Marris-Morini et al., "Recent progress in high speed silicon-based optical modulators," Proceedings of the IEEE 97 (7), 1199-1215 (2009).

[3] S. Schmitt-Rink et al., "How fast is excitonic electroabsorption?," Opt. Lett. **15**, 60–-62 (1990).

[4] Luxtera, Inc. (March 14, 2007), "Integrated Photodetector on Mainstream SOI-CMOS Wafer"

[5] S. Assefa ET AL., "CMOS-integrated high-speed MSM germanium waveguide photodetector," Opt. Express **18**, 4986-4999 (2010).

[6] Y.-H. Kuo et al., "Strong quantum-confined stark effect in germanium quantum-well structures on silicon," Nature **437**, 1334–1336 (2005).

[7] P. Chaisakul et al., "Polarization dependence of quantum-confined Stark effect inGe/SiGe quantum well planar waveguides," Opt. Lett. **36**, 1794–1796 (2011).

[8] Y. Rong et al., "Quantum-confined Stark effect in Ge/SiGe qunatum wells on Si," IEEE J. Selected Topics Quant. Electron. **16**, 85–92 (2010).

[9] S. Ren et al., "Ge/SiGe quantum well waveguide modulator monolithically integrated with SOI waveguides," IEEE Photon. Tech. Lett. (to be published).

[10] G. Isella et al., "Low-energy plasma-enhanced chemical vapor deposition for strained Si and Ge heterostructures and devices," Solid State Electron. **48**, 1317-1323 (2004).

Demonstration of Etch-less Core Definition Process for Low-Loss Glass Waveguide Fabrication

Demis D. John, Renan Moreira, Jonathon S. Barton, Jared F. Bauters,
Martijn J. R. Heck, John E. Bowers and Daniel J. Blumenthal
Electrical & Computer Engineering Department
University of California Santa Barbara, Santa Barbara, California, U.S.A.
demis@engineering.ucsb.edu

Abstract*— We demonstrate for the first time the selective oxidation of Silicon Oxynitride and use it to create a novel process for etchless waveguide definition. The oxidation process is characterized for SiO_xN_y and Si_3N_4 films, and the sidewall smoothing mechanism is simulated. Fabricated waveguides exhibited losses of 0.103 dB/cm at 1610 nm and 0.177 dB/cm at 1550 nm, where C-band loss were limited by molecular vibrational resonances.

Keywords: Waveguides, Thermal Oxidation, Silicon Oxynitride

I. Introduction

The large disparity between the propagation losses of optical fibers and planar waveguides is often attributed to the sidewall roughness of integrated waveguides, created by the etching process. In the silicon-on-insulator platform, numerous groups have addressed this problem with the local oxidation of silicon (LOCOS) [1-4] process, which reduces propagation loss by about an order of magnitude.

The Silicon Oxynitride (SiO_xN_y) / Silicon Dioxide (SiO_2) planar lightwave circuit (PLC) platform is a mature technology for various applications, in which the oxynitride mole ratio can be varied to tailor the core refractive index. SiO_xN_y can also be thermally oxidized [5,6], and it stands to reason that a similar sidewall smoothing technique can be applied to the ubiquitous SiO_xN_y/SiO_2 glass waveguide platform to define waveguides with reduced sidewall roughness.

In this work we present a characterization of the thermal oxidation of SiO_xN_y using spectroscopic ellipsometry, with relation to the chemical processes involved. Additionally, a model for the mechanism of sidewall smoothing is proposed using a 1-dimensional approximation of the diffusion of oxidant species. This is then applied to the fabrication of SiO_xN_y waveguides of varying widths, which are subsequently measured with optical frequency domain reflectometry (OFDR) to obtain wavelength-dependent losses [7]. Lastly, the loss spectrum is used to infer the presence of various molecular absorption resonances.

II. Selective Oxidation of Silicon Oxynitride

In a standard LOCOS process, a material with low oxidation rate is used to block the diffusion of oxidant in lithographically defined areas, allowing exposed silicon to oxidize. In the case of SiO_xN_y waveguides with SiO_2 cladding, we can use a layer of SiO_xN_y as the core layer, and block oxidant diffusion in the waveguide core area with Si_3N_4, which is essentially SiO_xN_y with zero oxygen content. Thus the exposed SiO_xN_y is converted into cladding oxide.

This research was supported by the Defense Advanced Research Projects Agency, Microsystems Technology Office, Program: Integrated Photonic Delay (iPhoD), Issued by DARPA/CMO under Contract No. HR0011-09-C-0123. *The views and conclusions contained in this document are those of the authors only.*

Fig. 1 shows a schematic of the core definition process, including the use of thermally oxidized silicon substrates for lower claddings. Deposited SiO_2 is used for upper claddings after removal of the Si_3N_4 oxidation mask.

III. Thermal Oxidation of Silicon Oxynitride

Kuiper et al. proposed in [6] that Silicon Nitride undergoes thermal oxidation with the following reaction:

$$Si_3N_4(s) + 6\,H_2O(g) = 3\,SiO_2(s) + 4\,NH_3(g) \quad (1)$$

where the gaseous oxidant, water vapor, replaces nitrogen within a solid silicon nitride molecule, creating solid silica and gaseous ammonia as a byproduct. The rate of oxidation is limited by out-diffusion of the ammonia molecule, which inhibits the reaction rate at the oxidizing interface. Due to the dependence on diffusion, the rate follows an exponential temperature-dependence. Since each nitrogen atom generates a rate-limiting ammonia molecule, the oxidation rate should be highly dependent on the amount of nitrogen in the SiO_xN_y film. This is exhibited in Fig. 2, where the SiO_xN_y refractive index increases with increasing nitrogen content, and thus shows a lower oxidation rate.

Additionally, water vapor and ammonia will be left in the film at the completion of the thermal oxidation. This fact manifests in two effects impacting waveguide characteristics. First, since NH_3 is larger and has a lower diffusion coefficient than H_2O, the generated thermal oxide tends to have higher indices (and N_2 concentration) at low temperatures. This is likely due to the trapping of NH_3 which allows the thermal oxide to undergo thermal nitridation [8]. Secondly, both of these molecules exhibit molecular vibrational resonances in the C-band, via O-H and N-H overtones, so wavelength dependent loss analysis should be able to detect the residual solute gases.

The effect this technique has on sidewall roughness has been investigated by modeling the diffusion of oxidant as spherical point sources along the line-edge of the etched oxidation mask.

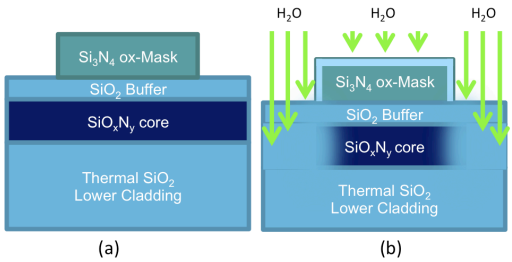


Figure 1. (a) Schematic of waveguide definition via local oxidation of SiO_xN_y showing deposited films & etched oxidation mask. (b) Shows conversion of SiO_xN_y to cladding oxide via thermal steam oxidation.

In Fig. 3a, we propagate the diffusion front away from the line-edge (as measured with atomic force microscopy), and calculate the resultant root-mean-square (RMS) roughness and correlation length (L_c), shown in Fig. 3b. As diffusion radius increases, RMS roughness decreases and L_c increases. Both of these trends reduce scattering losses [9].

IV. Waveguide Fabrication & Measurement

A 1 mm thick silicon substrate with 15 µm of thermal oxide was used for the lower cladding. Plasma Enhanced Chemical Vapor Deposition (PECVD) was used to deposit 970 nm of SiO_xN_y waveguide core layer, with the O_2/N_2 gas flow ratio chosen to produce a refractive index of 1.58 at 1550 nm. 1 µm of SiO_2 was subsequently deposited as an oxidation buffer, and 50 nm of sputtered Si_3N_4 for the oxidation mask. Sputtered nitride exhibits a lower oxidation rate than PECVD films, and thus requires less physical etching to pattern. Standard lithographic and dry-etching techniques were used to pattern the oxidation mask with an Archimedean spiral configuration of 26 interleaved waveguides, ranging from 2.5 µm to 15.0 µm in width. Core definition proceeded by subjecting the wafer to steam oxidation for 3 hours at 950°C with a 200 sccm flow of water vapor. The nitride oxidation mask was then removed via dry etch, and 10 µm of PECVD SiO_2 upper cladding was deposited in batches, with 1050°C, 3hr anneals performed after every 4 µm of deposition. The spiral facets were diced (shown in Fig. 4), and light was coupled from cleaved optical fibers to the waveguides with index matching gel to lower reflections.

OFDR was used to measure the backscattered power versus distance into each waveguide, as described in [7]. Analysis of the power vs. distance slopes of full-range OFDR scans (1525 nm – 1610 nm) yielded the losses shown in Fig. 5a, with a lowest loss of 14.7 dB/m for the widest, 15 µm waveguide. These values are average losses over the OFDR scan range, so narrow-band analysis was performed with a 10 nm range, as shown in Fig. 5b, revealing a 20 dB/m range of propagation losses for the 13.0 µm width. This loss spectrum shows a minimum loss of 11.2 ± 0.4 dB/m from 1585 nm to 1610 nm, and the 15 µm width exhibits 10.3 ± 0.8 dB/m from 1590 nm to 1610 nm. The loss peak near 1510 nm is explained by the presence of N-H vibrational overtones. Losses around 1610 nm could be limited by either scatter or SiO-H & Si-H bonds. This will be determined in the future by fitting the loss vs. width data to scattering loss models.

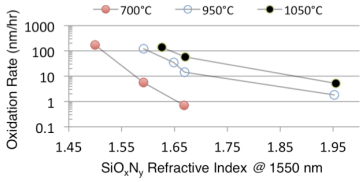


Figure 2. Oxidation rates for a range of temperatures and refractive indices.

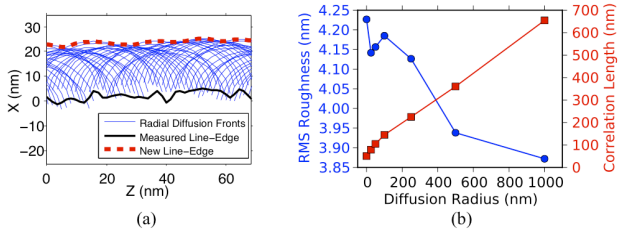


Figure 3. The 1-D simulation is shown in (a), and (b) shows the resulting sidewall roughness RMS (circles) and L_c (squares) for varying diffusion radii.

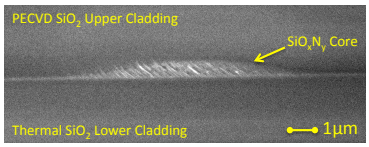


Figure 4. A cross-section image of a 9.5 µm x 0.96 µm waveguide core.

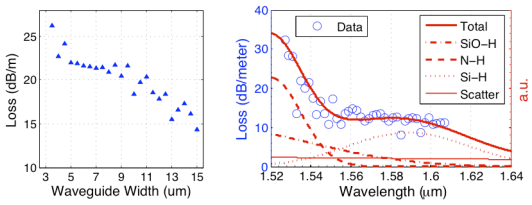


Figure 5. (a) Shows losses averaged over the full OFDR spectral range for each waveguide width, while (b) shows a narrow-wavelength OFDR loss spectrum for the 13.0 µm width, with approximate bond resonances.

V. Conclusion

We have developed and demonstrated a process for the local oxidation of SiO_xN_y, applied to silica-based waveguides. We modeled the sidewall smoothing mechanism and characterized the oxidation process with regards to the residual nitrogen, temperature and index dependence. Lastly we fabricated and measured the wavelength-dependent losses of SiO_xN_y waveguides showing a minimum loss of 10.3 ± 0.4 dB/m, and revealed the bond resonances dominating losses.

Acknowledgment

The authors would like to thank Scott Rodgers, Brandon Knott and Jonathan Doylend for support and helpful discussions.

References

[1] L. Rowe, M. Elsey, N. Tarr, A. P. Knights, and E. Post, "CMOS-compatible optical rib waveguides defined by local oxidation of silicon," *Electronics Letters*, vol. 43, no. 7, pp. 392–393, Mar. 2007.

[2] R. Pafchek, R. Tummidi, J. Li, M. A. Webster, E. Chen, and T. L. Koch, "Low-loss silicon-on-insulator shallow-ridge TE and TM waveguides formed using thermal oxidation," *Applied Optics*, vol. 48, no. 5, pp. 958–963, 2009.

[3] J. Cardenas, C. B. Poitras, J. T. Robinson, K. Preston, L. Chen, and M. Lipson, "Low loss etchless silicon photonic waveguides," *Optics Express*, vol. 17, no. 6, pp. 4752–4757, Mar. 2009.

[4] M. P. Nezhad, O. Bondarenko, M. Khajavikhan, A. Simic, and Y. Fainman, "Etch-free low loss silicon waveguides using hydrogen silsesquioxane oxidation masks," *Optics Express*, vol. 19, no. 20, pp. 18827–18827, 2011.

[5] D. Choi, D. B. Fischbach, and W. D. Scott, "Oxidation of Chemically-Vapor-Deposited Silicon Nitride and Single-Crystal Silicon," *Journal of the American Ceramics Society*, vol. 72, no. 7, pp. 1118–1123, 1989.

[6] A. Kuiper, M. F. C. Willemsen, J. M. L. Mulder, JB Oude Elferink, F. H. P. M. Habraken, and W.F. van der Weg, "Thermal oxidation of silicon nitride and silicon oxynitride films," *J. Vac. Sci. Technol. B*, vol. 7, no. 3, pp. 455–465, May 1989.

[7] J. F. Bauters, M. J. R. Heck, D. D. John, J. S. Barton, C. M. Bruinink, A. Leinse, R. G. Heideman, D. J. Blumenthal, J. E. Bowers, "Planar waveguides with less than 0.1 dB/m propagation loss fabricated with wafer bonding," *Optics Express*, vol. 19, no. 24, pp. 24090, Nov. 2011.

[8] Y. Hayafuji and K. Kajiwara, "Nitridation of Silicon and Oxidized-Silicon," *Journal of The Electrochemical Society*, vol. 129, no. 9, pp. 2102–2108, Sep. 1982.

[9] K. K. Lee, D. R. Lim, H.-C. Luan, A. Agarwal, J. Foresi, and L. C. Kimerling, "Effect of size and roughness on light transmission in a Si/SiO2 waveguide: Experiments and model," *Applied Physics Letters*, vol. 77, no. 11, pp. 1617–1619, Sep. 2000.

Quantum-confined Stark effect at 1.3 µm in Ge/SiGe quantum-well structures

Mohamed-Saïd Rouifed, Papichaya Chaisakul, Delphine Marris-Morini, Xavier Le Roux, Samson Edmond, Jean-René Coudevylle, and Laurent Vivien
Institut d'Electronique Fondamentale, Univ. Paris-Sud
CNRS UMR 8622, Orsay, FRANCE
E-mail: mohamed-said.rouifed@u-psud.fr

Jacopo Frigerio, Giovanni Isella, Daniel Chrastina
Laboratory for Epitaxial Nanostructures on Silicon and Spintronics, Dipartimento di Fisica
Politecnico di Milano
Como, ITALY

***Abstract*—We demonstrate a room-temperature strong quantum confinement Stark effect (QCSE) in Ge/SiGe multiple quantum wells (MQW) heterostructures, embedded in PIN diode. The device is designed to operate at 1.3µm, and QCSE is shown by photocurrent measurement in a surface illuminated device.**

Keywords : electroabsorption; Quantum Confined Stark Effect, Ge/SiGe MQW; optical interconnects.

I. INTRODUCTION

Optical interconnects in chip-scale distance have been considered as an efficient alternative to electrical interconnects [1]. To integrate both electrical and optical devices on the same chips, the fabrication of the latter with processes compatible with Silicon CMOS (Complementary Metal-Oxide Semiconductor) is highly desirable [1]. Ge-based photonics has shown recently impressive results with demonstrations of light source [2], modulator [3], waveguides [4] and photodetectors [5-6]. Electroabsorption modulator based on Quantum Confined Stark Effet (QCSE) was formerly demonstrated with group III-V material [7], and recently in group IV material like Ge/SiGe multiple quantum well structures (MQW) [8-9]. Among the advantages of MQW structures in comparison to bulk materials, MQW structures can be engineered to shift the operating wavelength of QCSE. In this work we demonstrate room-temperature QCSE in Ge/SiGe MQWs working at 1.3µm.

II. DEVICE DESIGN AND FABRICATION

To work at 1.3µm, a blue shift of the absorption edge from 0.8eV for bulk Ge to 0.95eV is needed. Different methods can be used to achieve this wavelength shift, among them are the increase of the confinement in the quantum wells by, for example, using very narrow quantum well, or the use of SiGe material as the quantum well or the use of strain engineering to increase the band gap energy in Ge quantum well [10].

We designed Ge/SiGe QW structure by strain engineering in order to work at 1.3 µm. In comparison with our first demonstration [9] working at 1.4 µm Ge concentration is now decreased in the barriers and in the relaxed buffer (a strain compensated structure is used). Therefore, Ge well is more compressively strained relative to the relaxed buffer and its band gap energy is increased. In the fabricated device, 21% of Si is used in the relaxed buffer and 35 % in SiGe barriers while the wells are made of pure Ge.

The $Ge/Si_{0.35}Ge_{0.65}$ MQW structure is embedded in a PIN diode, allowing large electrical field to be applied across the active region. The structure is grown by low energy plasma-enhanced chemical vapor deposition (LEPECVD) [11]. On a 100mm Si(001) substrate, a 11µm $Si_{1-y}Ge_y$ graded buffer was linearly grown from y=0 to y=0.79 of germanium concentration with rate of 7%/µm. This graded buffer allows achieving very high quality QW structures despite the large lattice mismatch between Si and Ge, which is very useful to study material properties. After this graded buffer, 2µm of $Si_{0.21}Ge_{0.79}$ is added forming a fully relaxed virtual substrate (VS) on where PIN diode can be grow. P region was then deposed, which consists a 500nm boron-doped $Si_{0.21}Ge_{0.79}$ layer, followed by 50nm $Si_{0.21}Ge_{0.79}$ spacer. The MQW region is formed by 10 nm of Ge (well) and 15nm $Si_{0.35}Ge_{0.65}$ (barrier) which are repeated 20 times to achieve 20 QW's. This thick structure is possible thanks to the average Ge concentration in Ge/SiGe MQW layers equal that of the buffer layer. Finally, a 50nm $Si_{0.21}Ge_{0.79}$ cap layer and 100nm phosphorus-doped $Si_{0.21}Ge_{0.79}$ n-type layer are added to form the top contact.

A square surface 100µmx114µm illuminated PIN diode was fabricated for the photocurrent measurement. UV lithography and dry etching were used to pattern the mesa. For metallic contacts, 20nm of Ti and 300nm of Au are evaporated and lifted-off for both n and p contacts. The schematic view and optical microscope image of the fabricated device are show in figure (1).

III. EXPERIMENTAL RESULTS

Photocurrent measurements of the Ge/SiGe MQWs at several reverse bias voltages were performed at room temperature. The incident light, normal to the surface of diode, was randomly polarized from tunable laser from 1245nm to 1350nm with step of 1nm. A chopper was used to modulate the input light at 0.5 kHz and a lock-in amplifier permits to measure precisely the photocurrent spectra, provided that a reference photocurrent measurement at a given wavelength is used for normalization.

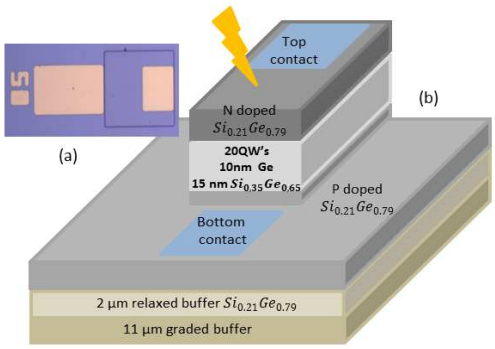


Figure 1. (a). Optical microscopic top view of device. (b), Cross section showing the differents layers.

To estimate the strength of band-to-band absorption for light incident perpendicular to QW structures, the fraction of light absorbed per well γ_{well}, can be calculated by the following equation in case of $\gamma_{well} << 1$ [12]:

$$N \times \gamma_{well} = \frac{\Delta P}{P_0} \quad (1)$$

Where ΔP the optical power absorbed in the MQW's and P_0 is the incident power. N is the number of wells in the intrinsic region. To calculate the fraction of light absorbed per well from the photocurrent measurements, the following relation is used [9]:

$$I_{ph} = \frac{eP_0 N \gamma_{well}(\lambda)\lambda}{hc} \quad (2)$$

Where P_0 is the incident optical power, taking into account the reflection at the surface of device, h is Planck constant, e is electron charge, c is the speed of light and λ is wavelength.

The absorption spectra obtained from this method is reported in figure (2). As a consequence of the confinement effect in the MQW and the strain between Ge in QW and the VS, a shift of absorption edge from 0.8eV for bulk Ge to 0.96eV is clearly observed. At low reverse bias (-1V is used in order to have electric field applied across the entire PIN diode, in order to collect all photogenerated carriers), clear exciton peak is seen in the spectra at 1.277 µm which can be attributed to the transition between heavy hole level and electronic state at Γ point. It can be noted that at higher wavelength (1.34µm), the residual fraction of light absorbed, attributed to the indirect absorption in the quantum wells is rather small in comparison with direct gap absorption.

When the reverse bias is increased, the two mean characteristics of QCSE are observed in the measured spectra: the absorption edge is shifted toward larger wavelength, and the excitonic peak absorption is decreased. From those two effects, absorption per well at 1.3 µm goes from 1.5×10^{-3} to 3.5×10^{-3} when bias varies from 1 to 5V.

IV. Conclusion

In this work, we demonstrate the possibility to engineer Ge/SiGe MQW structures. Strong quantum confined Stark effect was demonstrated at 1.3 µm, which will enable reliable

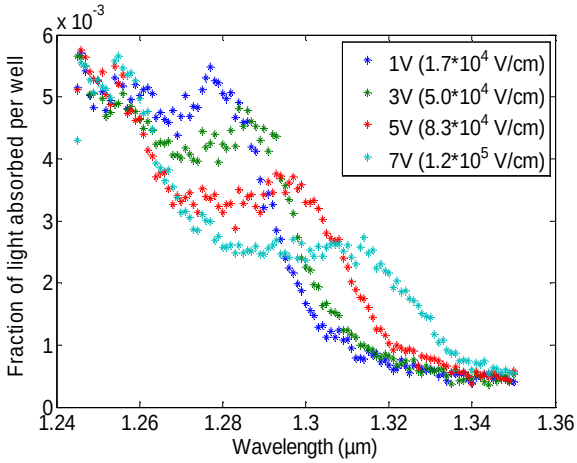


Figure 2. Absorption spectra for different applied electrical field from photocurrent measurement.

design of integrated photonic devices based on Ge/SiGe MQW structures.

Acknowledgment

The research has received funding from the French ANR under project GOSPEL (Direct Gap related Optical Properties of Ge/SiGe Multiple Quantum Wells). The fabrication of the device was performed at the nano-center CTU-IEF-Minerve, partially funded by the "Conseil Général de l'Essonne". Financial support for the epitaxial growth was provided by the Cariplo foundation through NANOGAP project

References

[1] D. A. B. Miller, "rationale and challenges for optical inteconnects to electronic chips," IEEE Proceedings, 88 (6), 728-749 June 2000.

[2] X. Sun, et al "Toward a Germanium Laser for Integrated Silicon Photonics", IEEE Journal of Selected Topics in Quantum Electronics, 16 (1), 124-131, January/Febrary 2010.

[3] P. Chaisakul, et al "23 GHz Ge/SiGe multiple quantum well electro-absorption modulator" Optics Express, 20 (3), 3219-3225, (2012).

[4] O. Fidaner, et al "Optical Link on Silicon Employing Ge/SiGe Quantum Well Structures", LEOS Meeting, 852-853 (2007).

[5] P. Chaisakul, et al "Ge/SiGe multiple quantum well photodiode with 30 GHz bandwidth", Applied Physics Letters, 98, 131112 , 2011.

[6] O. Fidaner, et al "Ge–SiGe Quantum-Well Waveguide Photodetectors on Silicon for the Near-Infrared", IEEE Photonics Technology Letters, 19 (20), 1631-1633, 2007.

[7] D. A. B Miller, et al, "Band-edge electroabsorption in quantum well structures: The quantum-confined stark effect", Phys. Rev. Let., 53 (22), 1984

[8] Y-H. Kuo, et al, "Strong quantum-confined Stark effect in germanium quantum-well structures on silicon", Nature, 437, 1334-1336 2005.

[9] P. Chaisakul, et al "Quantum-confined Stark effect measurements in Ge/SiGe quantum-well structures", Opt. Let. , 35(17), 2913-2915, 2010.

[10] L. Lever, et al "Design of Ge–SiGe Quantum-Confined Stark Effect Electroabsorption Heterostructures for CMOS Compatible Photonics", Journal of Lightwave Technology, 28 (22) 3273-3281, November 2010.

[11] G. Isella, et al "Low-energy plasma-enhanced chemical vapor deposition for strained Si and Ge heterostructures and devices," Solid State Electron. 48, 1317-1323 (2004).

[12] P. Blood, "On the dimensionality of optical absorption, gain, and recombination in Quantum-Confined structures", Journal of Quantum Electronics, 36 (3), (2000).

In-band pumped low threshold Ti:Tm:$LiNbO_3$ waveguide laser

Mathew George, Raimund Ricken, Viktor Quiring and Wolfgang Sohler
Applied Physics
University of Paderborn
Paderborn - 33098, Germany
mathew.george@uni-paderborn.de

***Abstract*—The first in-band pumped Ti:Tm:$LiNbO_3$ waveguide laser emitting at 1890nm is reported. A special cavity enables pumping at 1650nm with a threshold of 4mW, a slope efficiency of 11% and up to 4.5mW output power.**

Keywords-integrated optics; waveguide; laser; lithium niobate; thulium.

I. INTRODUCTION

Thulium (Tm) based lasers utilizing the $^3F_4 \rightarrow {}^3H_6$ radiative transition find applications in spectroscopy, medicine, remote sensing and material processing. Lasing action from a variety of Tm doped crystals has been reported in the literature [1]. Tm:$LiNbO_3$ (LN) lasers pumped at 795 nm ($^3H_6 \rightarrow {}^3H_4$ transition) were already demonstrated both in bulk [2] and waveguide geometries [3, 4]. Here we report the first demonstration of a Fabry-Pérot type Ti:Tm:LN waveguide laser in-band pumped at 1650 nm and operating near 1890 nm emission wavelength. This is the longest emission wavelength from a Tm:LN laser reported so far. The Tm-doped waveguide structure is similar to that successfully employed as waveguide quantum memory recently [5].

II. LASER FABRICATION

A. Tm Diffusion Doping and Waveguide Fabrication

0.5 mm thick Z-cut wafers of undoped optical grade congruent lithium niobate were Tm-doped near the +Z-surface before waveguide fabrication. A vacuum deposited Tm layer of 32 nm thickness was in-diffused at 1130 ^{0}C during 150 hours in an argon-atmosphere followed by a post treatment in oxygen (1 hour). The diffusion profile was determined by secondary neutral mass spectroscopy. The maximum Tm concentration (at the surface) is 1.25 x 10^{20} cm^{-3}; the Tm penetration depth ($d_{1/e}$) is 9 µm. Afterwards, photolithographically defined, 6.5 µm wide, 104 nm thick Ti stripes were deposited on the Tm-doped sample and in-diffused at 1060 ^{0}C for 9.6 hours. In this way optical channel guides were formed in the 30 mm long sample; they are single mode structures for wavelengths > 1500 nm.

B. Cavity Formation

The laser cavity was formed by two special dielectric multilayer mirrors, vacuum-deposited on the end faces of the Ti:Tm:LN waveguide. The pump coupler (PC) mirror has a high reflectivity (R > 90 %) at wavelengths > 1800 nm, but a high transmission (T > 90 %) at the 1650 nm (pump) wavelength. The output coupler (OC) mirror has a high reflectivity (R > 95%) at both, pump and laser wavelengths, enabling in this way double pass pumping. The calculated finesse of the cavity at 1890 nm is 32, assuming 0.1 dB/cm propagation losses (see discussion below).

III. EXPERIMENTAL RESULTS

A. Waveguide Characterization

The waveguide propagation losses due to scattering are 0.3 dB/cm measured for TE polarization at 1505 nm [6]. They decrease at longer wavelengths to ~ 0.1 dB/cm at 1900 nm. The mode distributions were measured as well. For example, the full width at half maximum of the TE mode at 1650 nm is 7.8 µm x 5.8 µm.

The absorption and fluorescence characteristics of Ti:Tm:$LiNbO_3$ channel guides, fabricated in the same way as described above, are presented in Fig.1 together with the energy level scheme exploited. The strong absorption band around 1650 nm enables efficient in-band pumping (see also inset of Fig.1). Several maxima in the fluorescence spectrum indicate a potential laser emission at ~1760 nm, ~1800 nm and ~1850 nm for free running devices as already demonstrated in the past by pumping at ~795 nm [3, 4]. Emission at longer wavelengths is reported for the first time in this contribution.

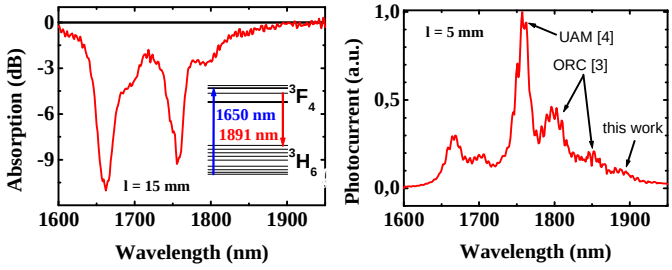


Figure 1. Measured TE absorption (left; l = 15 mm) and fluorescence (right; l = 5 mm) spectra of Ti:Tm:$LiNbO_3$ channel guides of length l for 1600 nm < λ < 1900 nm together with the corresponding energy level scheme of Tm-ions.

B. Laser Power Characteristics

Using a 1650 nm pump, laser emission was only found around 1890 nm in TE polarization independent on the pump

polarization. Fig. 2 presents the recorded power characteristics. Lasing was found to set in at 6 mW of incident pump power corresponding to ~ 4 mW of coupled pump power only. With increasing pump power the spectrum of the pump laser shifts to somewhat longer emission wavelengths resulting in an even better pump absorption (see also Fig. 1). The result is a slightly increasing slope efficiency up to 11% at ~50 mW incident pump power. The output power of up to 4.5 mW (limited by the available pump power) was stable over time. Both, maximum output power and slope efficiency surpass the results reported so far for Tm:LN waveguide lasers [3, 4] by a factor of 7 and 11, respectively. Moreover, the laser threshold is lower by more than an order of magnitude.

The power characteristics have also been modeled using the commercial software RP Fiber Power. As input parameters the measured data discussed above and absorption and emission cross sections from the literature [7] were used.

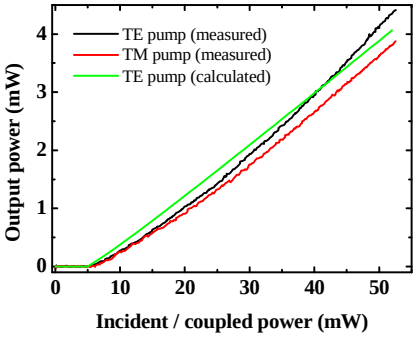


Figure 2. Power characteristics of the Ti:Tm:$LiNbO_3$ waveguide laser for TE polarized emission: output power at 1890 nm emission wavelength versus incident (experiment) and coupled (simulation) pump power at 1650 nm.

C. *Relaxation Oscillations*

When investigating the time dependence of the laser output, nearly undamped relaxation oscillations were observed as pulses of 84 kHz repetition frequency (pump power dependent) with a duty cycle of a few percent. An example – presented as RF-spectrum of the electrical photodiode output – is shown in Fig. 3. The relaxation oscillations could be suppressed by feedback controlled pumping as described in [8].

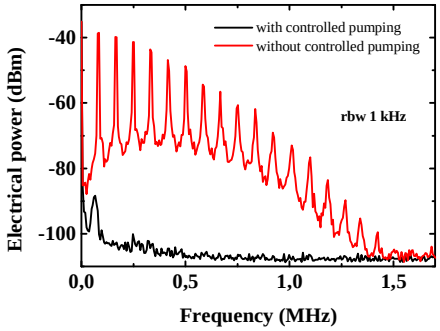


Figure 3. Relaxation oscillations of the laser output, displayed as RF-spectrum of the electrical output of the photodiode without (red) and with (black) feedback controlled optical pumping (here: 14 mW pump power).

D. *Laser Emission Spectra*

Laser emission spectra were measured with a spectrometer of 0.25 nm resolution. Irrespective of the pump polarization, the emission was found to be near 1890 nm and TE polarized with a spectral envelope of a few nanometers (see Fig. 4). However, the fine structure of the laser spectra changed from scan to scan and was also found to be pump power dependent.

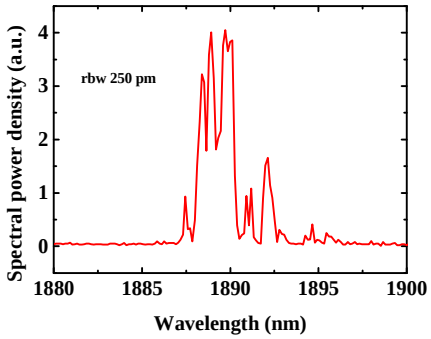


Figure 4. TE polarized laser emission spectrum for operation with 32 mW of incident pump power (1650 nm; TE polarised).

IV. Conclusions

The first in-band pumped Ti:Tm:$LiNbO_3$ waveguide laser was developed. The laser is pumped at 1650 nm and has a remarkably low threshold of ~ 4 mW coupled pump power only. Its emission wavelength is 1890 nm with a spectral width of a few nanometers. The laser output is TE polarized for both pump polarizations. We expect that appropriate spectral filtering yields stable single mode emission. If the filtering is tunable, the broad wavelength range 1750 nm < λ < 1920 nm might be accessible. Moreover, simulation results indicate several possibilities for a further optimization of the device with respect to threshold, slope efficiency and output power.

References

[1] K. Schoelle, S. Lamrini, P. Koopmann and P. Fuhrberg, “2 micron laser sources and their possible applications”, in Frontiers in Guided Wave Optics and Optoelectronics, B. Pal, Editor, Croatia: Intech, 2010, pp. 471-500.

[2] L. F. Johnson, A. A. Ballman, “Coherent emission from rare earth ions in electrooptic crystals”, J. Appl. Phys., Vol. 40, pp. 297- 302, 1969.

[3] J. P. de Sandro, J. K. Jones, D. P. Shepherd, M. Hempstead, J. Wang and A. C. Tropper, “Non-photorefractive CW Tm-indiffused Ti:$LiNbO_3$ waveguide laser operating at room temperature”, IEEE Phot. Tech. Lett., Vol.8 pp. 209-211, 1996.

[4] E. Cantelar, J. A. Sanz-Garcia, G. Lifante, F. Cusso, and P . L. Prernas, “Single polarized Tm^{3+} laser in Zn-diffused $LiNbO_3$ channel waveguides”, Appl. Phys. Lett., Vol 86, pp.161119-161121, 2005.

[5] E. Saglamyurek, N. Sinclair, J. Jin, J. A. Slater, D. Oblak, F. Bussières, M. George, R. Ricken, W. Sohler, and W. Tittel, “Broadband waveguide quantum memory for entangled photons”, Nature, Vol. 469, pp. 512-515, 2011.

[6] R. Regener and W. Sohler, “Loss in low-finesse Ti:$LiNbO_3$ optical waveguide resonators”, Appl. Phys. B, Vol. 36, pp. 143-147, 1985.

[7] E. Cantelar, M. Quintanilla, P.L. Pernas, G.A. Torchia, G. Lifante, F. Cussó “Polarized emission and absorption cross-section calculation in $LiNbO_3$:Tm^{3+} ”, J. Lumin. Vol. 128, pp. 998-991, 2008.

[8] M. George, S. Reza, H. Suche, R. Ricken, V. Quiring and W. Sohler, “Self-pulsing Ti:Er:$LiNbO_3$ waveguide laser”, Proc. CLEO Europe 2009, paper cj.p.32-thu.

New two-port multimode interference reflectors

E. Kleijn[1], M.K. Smit[1], M.J. Wale[2], X.J.M. Leijtens[1]
1: Cobra Research Institute, Eindhoven University of Technology, Eindhoven, the Netherlands
2:Oclaro Technology Ltd, Caswell, Towcester, Northamptonshire NN12 8EQ, United Kingdom

Multi-mode interference reflectors (MIRs) are versatile components. Two new MIR designs with a fixed 50/50 reflection to transmission ratio are introduced. Measurements on these new devices and on devices similar to those in [1] are presented and compared to the design values. Measured losses are between 0.4 and 4.6dB. The measured power split ratio is in excellent agreement with the predicted split ratio of reflection and transmission.

integrated mirror; MIR; multimode interference; reflector

I. INTRODUCTION

An integrated reflector that keeps transmitted light available on chip can be used to create an on-chip laser. This laser could then be used as light source in larger photonic integrated circuits.

In [1] we introduced two-port MMI reflectors (MIRs) that can provide both reflection and transmission on chip. They are fabrication tolerant and can be made in the same fabrication steps as deep-etched waveguides. The ease of fabrication is the main advantage of MIRs, when compared to distributed Bragg reflectors (DBRs). Measurements of the first two-port MIRs in [1] showed that they were working as expected, but still had relatively high losses. Here we present new measurements on similar devices, plus measurements on two new MIR types.

First we introduce the basic concept of the MIR. Then section III discusses the design of the measured devices. We then briefly describe the characterization methods. Section V presents the measurement results, before we conclude in section VI.

II. CONCEPT

Multimode interference reflectors (MIRs) are based on the same principles as multimode interference couplers (MMIs) [2]. The main difference between MIRs and MMIs is that the output waveguides have been replaced by mirrors. This is shown schematically in Figure 1. The mirrors can be low loss, as long as the critical angle for total internal reflection is sufficiently below 45 degrees. By tapering the multimode section of the MIR, the ratio between reflection and transmission can be set freely. This is similar to the effect in MMIs as first mentioned by Besse et al. in [3].

III. DEVICE DESIGN

The devices were designed for an indium phosphide waveguide layer stack of Oclaro ltd (UK). The core consists of multiple quantum wells, leading to an equivalent slab refractive index of 3.25. The lateral cladding was air, with index 1.0. As part of the European project PARADIGM, Oclaro provided foundry services to us.

Four different types of MIRs were designed. They are labeled type A, C, D and E. Type A is based upon a 2x2 MMI using paired interference. Type E is based on a 2x2 MMI using general interference. These two types are new kinds of MIRs. Both types have a fixed 50/50 R/T ratio. Figure 1a. shows the shape of these MIRs. Type C (Figure 1b.) and D have symmetric and asymmetric butterfly MMIs as underlying types respectively. For the last two types the transmission to reflection ratio can be chosen by tapering the MIR. The amount of tapering is indicated by the width deviation dW. The value of dW can be normalized by dividing by the base width W. A negative dW means the device is narrower in the middle.

Table I presents the design values for all the devices. To be able to compare the new results to those in [1], the width and normalized width deviation dW/W are the same. The lengths are slightly different to compensate for the difference in layer stacks. Improvements to the device model allowed for more accurate predictions of the split ratio as a function of dW/W, than presented in [1]. This resulted in reflection to transmission ratios ranging from 22%/78% to 92%/18%. The designs were optimized for TM. All devices had input waveguide widths Wwg of 2 um.

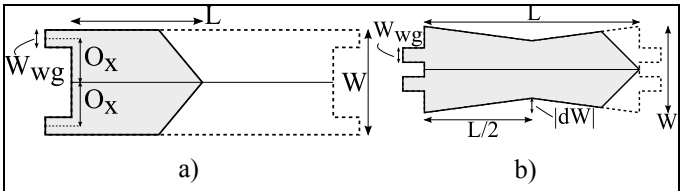


Figure 1. a) Schematic of an A/E type MIR (filled shape). The underlying MMI is dashed. For type A, Ox=W/6. For type E, Ox=(W-Wwg)/2. b) Schematic of a C type MIR (filled shape) based upon a butterfly MMI (dashed). Length L, width W, input waveguide width Wwg and width deviation dW.

IV. CHARACTERIZATION STRUCTURES

Two separate characterization structures were used for measuring the transmission and reflection of the devices. The first structure forms a Fabry-Pérot cavity out of two MIRs. The cavity has a fringed wavelength response. The reflectivity of the devices can be calculated from the ratio of the maximum and minimum of these fringes, provided cavity propagation losses are know or negligible.

TABLE I. MIR DESIGN VALUES AND MEASUREMENT RESULTS

ID *	W [um]	L [um]	dW/W	Rdesign [%]	*R* TE [%]	*T* TE [%]	*R* TM [%]	*T* TM [%]	Loss TE [dB]	Loss TM [dB]	Loss sim [dB]
A1	9.0	57.0	0.0000	50	30.9	41.7	34.3	41.9	1.4	1.2	0.7
C1	6.0	252.7	1.1869	22	5.5	51.4	3.1	54.2	2.5	2.4	1.0
C2	6.0	51.0	-0.1792	23	18.2	29.8	19.1	45.4	3.2	1.9	1.3
C3	6.0	65.4	-0.0849	36	20.0	29.7	29.2	44.5	3.0	1.3	1.1
C4	6.0	78.4	0.0000	50	28.6	29.4	38.9	32.7	2.4	1.5	1.0
C5	6.0	90.7	0.0849	63	36.4	24.6	44.6	30.3	2.2	1.3	0.9
C6	6.0	105.1	0.1792	77	43.7	9.1	42.9	22.0	2.8	1.9	0.9
C7	6.0	124.6	0.3119	92	40.8	4.7	30.1	5.0	3.4	4.6	0.9
D1	7.5	48.2	-0.2500	28	18.6	27.4	22.0	29.3	3.4	2.9	3.6
D2	7.5	67.8	-0.1500	50	20.3	20.5	37.3	32.8	3.9	1.5	1.5
D3	7.5	80.8	-0.0830	64	27.7	12.2	48.4	26.2	4.0	1.3	1.0
D4	7.5	96.8	0.0000	80	41.8	9.2	58.4	15.2	2.9	1.3	1.0
D5	7.5	110.3	0.0700	90	35.0	5.0	61.3	9.4	4.0	1.5	0.9
E1	5.0	54.4	0.0000	50	25.8	34.6	36.2	54.4	2.2	0.4	0.6

* input waveguide width is 2.0 um for all devices.

The second characterization structure uses a 1x2 MMI coupler to split the input power over a reference waveguide and a waveguide containing an MIR. The device transmission is then given by the difference in transmission between the reference and the device waveguide.

V. MEASUREMENT RESULTS

Using the characterization structures, described in the previous section, the power reflection *R* and power transmission *T* of the MIRs were measured for TE and TM polarization. Table I. lists the measurement results for all the devices. Device losses were calculated as:

$$\text{Loss}=-10\log(R+T)\ [\text{dB}]$$

When looking at Table I. it is clear that a large number of devices have less than 2 dB loss for TM. The devices were optimized for TM, which is why the losses for this polarization also match quite well with the values obtained from simulations. These predicted losses include the effect of a 3deg angle deviation of the mirror from perfectly vertical and imaging losses in the devices. Mirror roughness is not taken into account.

For TE polarization the device performs worse, with up to 3 dB polarization dependent loss. A more thorough inspection reveals that devices C1, C7 and D1 show relatively large losses. These devices also have the largest normalized width deviation dW/W. We assume that for these high taper angles mode conversion takes place and the imaging properties of the MIR start to break down.

Figure 2. shows that the normalized reflection coefficient of the fabricated devices match well with the design values. Notable exceptions are device C1 and D1. It is possible that mode conversion also plays a role here.

The losses presented in [1], corresponding to devices C2 through D7, ranged from 4.7 to 7.9 dB. Similar designs presented here have losses ranging from 1.2 to 4.6 dB. The two new MIR types show losses of 1.2 dB and 0.4 dB for types A and E respectively.

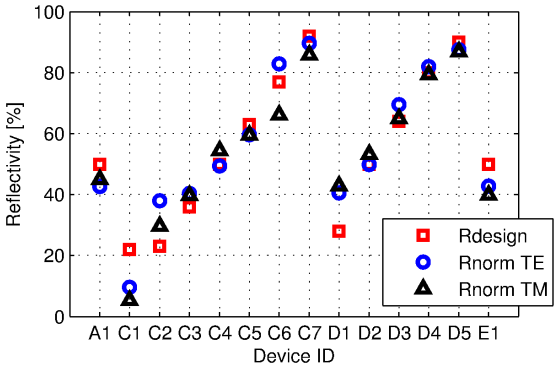


Figure 2. Normalized reflection coefficients (Rnorm = R/(R+T)) and design coefficients for TE and TM versus device ID.

TABLE II. BEST DEVICE CHOICE

Split ratio R/(R+T)	Criterion	Best device choice
< 20	Loss	C*
20 – 30	Loss	C
30 – 65	Loss	C or D
50,	Pol. Dependence	A
50	Loss	E
>65	Loss	D

*Does not agree well with simulation. When designing for ratios <20%, characterization is necessary.

VI. CONCLUSION

Two new MIR types were presented that show the lowest losses measured so far. The other measured devices show considerably lower losses than reported before. Furthermore, for type C and D, the ratio between reflection and transmission can be well controlled by tapering the MIR. Which device type to use depends on the requirements of the application, as shown in Table II.

MIRs can be fabricated in processes supporting deep-etched waveguides without making any changes to the process. Together with the measured low loss operation this leads us to conclude that MIRs are a valuable addition to existing components in photonic integrated circuits.

ACKNOWLEDGMENT

The research leading to these results has received funding from the European Community's Seventh Framework Programme FP7/2007-2013 under grant agreement ICT 257210 PARADIGM.

REFERENCES

[1] E. Kleijn, T. de Vries, H. Ambrosius, M. Smit, X. Leijtens, "MMI reflectors with free selection of reflection to transmission ratio," in Proceedings of the 15th Annual Symposium of the IEEE Photonics Benelux Chapter, 18-19 November, 2010, Delft, The Netherlands, nov. 2010, pp. 189-192.

[2] L. Xu, X. Leijtens, B. Docter, T. de Vries, E. Smalbrugge, F. Karouta, M. Smit, "MMI-reflector: A novel on-chip reflector for photonic integrated circuits," Optical Communication, 2009, ECOC '09. 35th European Conference on, sep 2009, pp. 1-2.

[3] P. Besse, E. Gini, M. Bachmann, H. Melchior, "New 2x2 and 1x3 multimode interference couplers with free selection of power splitting ratios," Journal of Lightwave Technology, vol. 14, no. 10, pp. 2286-2293, oct. 1996.

Photonic integrated multiwavelength transmitters for Fiber-To-The-Home networks

Multi-project wafer run and generic integration concept

K. Ławniczuk, M.K. Smit, X.J.M. Leijtens
COBRA Research Institute
Eindhoven University of Technology
Eindhoven, the Netherlands
e-mail: k.lawniczuk@tue.nl

M.J. Wale
Oclaro Technology Ltd.
Caswell, Towcester, Northamptonshire
NN12 8EQ, United Kingdom

R. Piramidowicz, P. Szczepański
Faculty of Electronics and Information Technology,
Warsaw University of Technology
Warsaw, Poland

***Abstract*— In this paper we present measurement results of monolithically integrated photonic transmitters for application in the next generation Fiber-to-the-Home (FTTH) networks. 4- and 8-channel transmitters were integrated onto a single chip, using multiple lasers with distributed Bragg reflector (DBR) resonators and electro-optical modulators in Mach-Zehnder configuration. Optical signals are multiplexed into a single output port using an arrayed-waveguide grating (AWG).**

Keywords-component; photonic integration, multiwavelength transmitters, InP, multi-project wafer run

I. INTRODUCTION

Nowadays photonic integration is the most promising technology for realization functionally advanced and compact optical circuits. Additionally, by offering high-speed elements that operate at a data rate of at least 10 Gbps, this technology may satisfy the requirements for photonic devices to be used in the next generation optical communication systems. In such networks, like future-proof FTTH systems, the key components (transceivers) are typically localized in the central office (CO) [1]. It means that in the CO the detection of upstream signals and the transmission of downstream signals take place. By combining passive and active optical components into a monolithically integrated photonic circuit, a multi-wavelength transmitter for the CO can be made. We have chosen indium phosphide (InP) and related ternary and quaternary compounds as an attractive material for the integration, mainly because of the direct-bandgap properties suitable for light generation and detection, light guiding, and fast phase modulation.

II. DESIGN AND FABRICATION

The photonic integrated transmitters presented in this paper were realized on an InP-based platform following the generic integration concept [2]. This approach enables design and fabrication of a wide variety of different photonic devices using the same technological processes and a limited set of basic building blocks [3]. Additionally, by participating in multi-project wafer (MPW) runs a significant reduction in fabrication and packaging costs of photonic chips should be possible in the near future. Within the EU programme EuroPIC [4] we explore such generic processes and develop photonic building blocks in cooperation with foundry fab partners: Oclaro in the United Kingdom and Fraunhofer Heinrich Hertz Institute in Germany. Our devices were realized in an industrial fab according to these generic concepts as one of the first multiwavelength transmitters of this kind.

One of the methods to realize photonic multiwavelength transmitters is through integration of an array of DBR-based lasers with an AWG. In our photonic circuit, the downstream modulated (DS) signals, as well as the upstream data (CW), are generated by a single device. To generate the DS data, modulation is required. This has been done by introducing electro-optical modulators in a Mach-Zehnder configuration, as schematically presented in Fig. 1 (*left*). The AWG acts here as multiplexer of all generated CW and modulated DS signals and directs the signals into a common output waveguide.

The photograph of the fabricated chip is shown in Fig. 1 (*right*). It contains a 4-channel and an 8-channel transmitter as well as a number of test structures of DBR laser. The transmitters integrate DBR-based lasers with 1-mm-long Mach-Zehnder modulators (MZMs). Each DBR laser consists of 4 sections: (1) a front grating (FDBR) providing partial reflection (50 µm long), (2) a rear grating (RDBR) giving near 100% reflection (500 µm long), (3) a phase control section (PH) to fine tune the phase of the generated signal (130 µm long), and (4) a semiconductor optical amplifier (SOA) that provides the gain within the structure (500 µm long). The wavelength selection is done by proper design of the grating period of the DBR sections and this can be additionally fine-tuned by current injection into each of the gratings and to the phase elements as well. The tuning range of the DBR-based lasers is sufficient to tune each of the sources to the peak of the

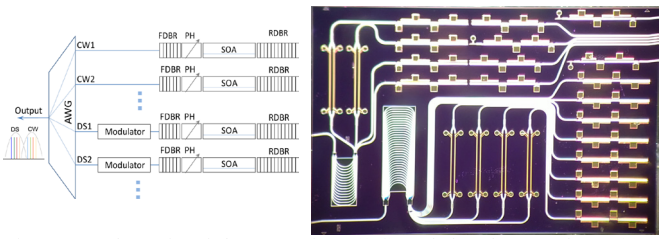


Figure 1. Schematic of the transmitter (*left*) and the photograph (*right*) of the fabricated devices. The size of the chip is only 4 mm x 6 mm.

proper AWG passband. The AWGs were designed for a central wavelength of 1550 nm, and a channel spacing of 100 GHz (8-channel device) and 200 GHz (4-channel device).

III. MEASUREMENTS RESULTS

The measurements were done at room temperature using a lensed fiber-tip to couple the light out from the chip. A high resolution (0.16 pm) Optical Spectrum Analyzer, APEX P2041A, was used to record the spectral characteristics of the transmitters. To obtain static characteristics, we used needle probes to bias the SOAs, DBRs, PHs and modulators. To measure the dynamic RF response of the MZMs, a submount and wire bonding to DC and RF pads was required.

The measured emission spectra of the 4-channel transmitter, with a channel spacing of 200 GHz, are presented in Fig. 2. The conditions set to the DBR laser were chosen to optimize the device for the generated wavelength and the output power. The SOAs were biased around 100 mA and the DBRs between 0.6 mA and 12.5 mA. The obtained threshold currents of the DBR lasers are less than 18 mA. The measured out-coupled output power is above 1 mW. The fine tuning of the lasers (of 1.5 nm within the AWG passband) can be done by applying the current to the phase section and this experiment is shown in Fig. 3 for one of the DBR lasers from the 4-channel transmitter. The measured tuning range of a single DBR is 9 nm.

The static extinction ratios of one of the modulators integrated into 8-channel transmitter and wire-bonded device is presented in Fig. 4. The obtained V_π is 4.6 V (reverse biased) with the static extinction ratio up to 25 dB. The signal directed to the modulator originated in the DBR laser integrated within the circuit. We performed the measurements for different

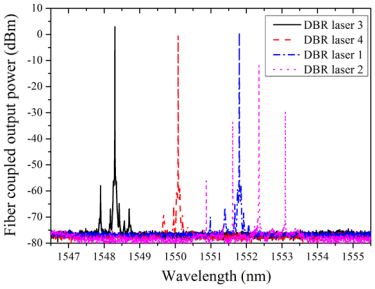


Fig. 2. Emission spectra measured for the 4-channel transmitter. The wavelength generated by the DBR laser no 2 was not properly tuned to the center of the AWG passband, which can be noticed on the spectrum.

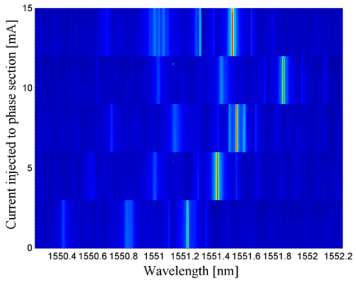


Fig. 3. The fine tuning of the DBR laser no 1 while biasing the SOA with 60 mA and changing the current injected to the PH. The source can be adjusted to the required wavelength, within the AWG passband by proper bias of the PH element. DBR mirrors remain unbiased for the experiment.

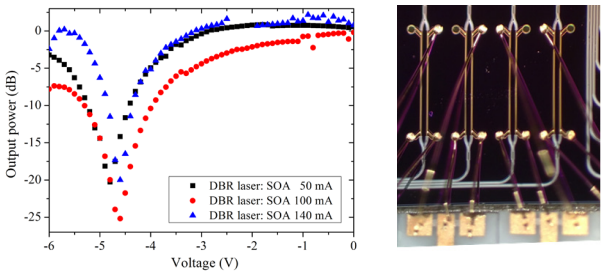


Fig. 4. Measured extinction ratio of 1 mm long MZM while changing the current injected to the SOA of the DBR laser (*left*). The photograph of wire-bonded modulators (*right*).

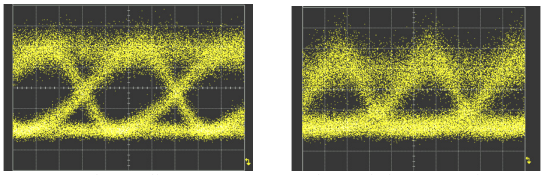


Fig. 5. Detected eye-diagrams at 12.5 Gbps of the MZM in B2B (*left*) and after transmission through 20 km long SMF (*right*).

currents injected to the SOA to evaluate that the V_π is not significantly dependant on the injected optical power. The dynamic RF experiments showed that this kind of MZM can operate with the data rates up to 12.5 Gbps, which is shown in Fig. 5. For the RF dynamics we performed measurements in back-to-back (B2B) configuration (without a fiber) and after introducing 20 km long single-mode fiber (SMF) into transmission setup.

IV. SUMMARY

We demonstrated the operation of monolithically integrated photonic transmitters based on DBR lasers and Mach-Zehnder modulators. The results show that complex photonic integrated circuits can be effectively realized using a generic approach and fabricated through participating in the standardized MPW runs offered by the foundry's platform. First characterization results of the devices show very promising performance of this type of photonic circuit to be used in next generation optical networks.

ACKNOWLEDGMENT

The research leading to these results has received funding from European Community's Seventh Framework Programme FP7/2007-2013 under grant agreement NMP 228839 EuroPIC.

The authors would like to acknowledge the help of Christophe Kazmierski from the III-V Lab (Marcoussis, France) in testing the photonic transmitters.

REFERENCES

[1] M.M.de Laat, R.L.Duijn, E.G.C.Pluk, G.N.van den Hoven, P.J.Urban, H.de Waardt, "FlexPON: a Hybrid TDM/WDM Network enabling Dynamic Bandwidth Reconfiguration using Wavelength Routing," in Proceeding of the ECOC, 20-24.09.2009, Vienna, Austria, p.1.6.3, 2009.

[2] M.Smit, X.Leijtens, E.Bente, J.Van der Tol, H.Ambrosius, D.Robbins, M.Wale, N.Grote, M.Schell, "Generic foundry model for InP-based photonics," IET Optoelectron., vol.5, iss.5, pp. 187-194, 2011.

[3] X.J.M. Leijtens, "JePPIX: the platform for InP-based photonics," IET Optoelectronics, vol.5, no. 5, pp. 202—206, 2011.

[4] EuroPIC, "European manufacturing platform for Photonic Integrated Circuits," http://www.europic.org/.

Fully tunable microwave photonic phase shifter for broadband signals based on a single heterogeneously integrated III-V-on-Silicon microdisk resonator

J. Lloret, F. Ramos, S. Sales and J. Capmany
Optical Communications Group, ITEAM Research Institute
Universitat Politècnica de València
Camí de Vera s/n, 46022 Valencia (Spain)
E-mail: jualloso@iteam.upv.es

G. Morthier, D. Van Thourhout and T. Spuesens
Photonics Research Group, INTEC Department
Universiteit Gent - IMEC
St. Pietersnieuwstraat, 41, 9000 Gent (Belgium)

N. Olivier and F.-M. Fédéli
CEA-LETI
MINATEC Campus
17 Rue des Martyrs, 38054 Grenoble (France)

***Abstract*—We present a novel broadband microwave photonic phase shifter based on a single III-V microdisk resonator heterogeneously integrated on a silicon-on-insulator waveguide. Fully 2π phase shift tunability is accomplished by free-carrier-induced effective index modulation.**

I. INTRODUCTION

The past years have witnessed an increasing interest in the development of generation, transport and processing tasks of radio frequency (RF), microwave and millimeter-wave signals directly in the optical domain [1]. This field of activity is known as microwave photonics (MWP) [2]. One of the applications that have focused significant efforts within the MWP field consists of the implementation of flexible filters free from bandwidth constraints [1]. To this end, the efficient design of broadband tunable microwave phase shifters is of key importance [1]. The state-of-the-art tends towards integrated CMOS-compatible approaches, especially those based on silicon-on-insulator (SOI), which lead to high-density integration [3]. However, the slow dynamics of silicon can hamper the assembly of SOI-based circuits in practice [4]. To overcome this limitation hybrid approaches based on the integration of silicon with a direct band gap compound, especially those belonging to the III-V group, stand out as a promising solution for high-speed signal processing [5]. In this paper, we present a novel broadband microwave photonic phase shifter based on an InP microdisk resonator (MDR) heterogeneously integrated on a SOI waveguide.

II. PRINCIPLE OF OPERATION

The propagation in the MDR is based on the whispering-gallery modes, which are confined to the edges of the cavity resulting in a resonant-type transfer function. The principle of operation relies on the exploitation of the phase transfer function of the MDR operated in over-coupled regime in combination with using optical single sideband (OSSB) modulation. The OSSB, composed of the optical carrier and the modulation sideband, must be accurately placed in the vicinity of a resonance. In this way, the optical carrier and the sideband experience different phase change in accordance with the MDR phase transfer function. The phase induced on the optical carrier can be controlled by altering the notch spectral position through effective index modulation enabled by carrier injection in the cavity. As a result, this fact allows for controllable phase shift tunability of the microwave signal.

III. EXPERIMENTAL SETUP

Fig. 1(a) sketches the experimental setup of the InP/SOI MDR based MWP phase shifter. A weak spectral line centered at 1562 nm was generated by a tunable laser in continuous wave (CW). The input RF signal, $s_{in}(t)$, was imprinted on the optical carrier by means of an intensity modulator (IM) operated in dual-drive configuration, giving as a result OSSB modulation. The signal at the output of the IM was sent into the 9-μm-diameter MDR, which is molecularly bonded on top of a SOI circuit containing a 750-nm-wide and 220-nm-high Si strip waveguide. The disk-to-waveguide gap determines the coupling factor (k), which was found to be ~ 6 %. The total area, including both the input and output vertical grating couplers is ~ 0.1 mm^2 (see inset Fig. 2). More details on the fabrication of such a device are given in [5]. Both optical waves are then weighted and phase-shifted accordingly to the MDR transfer function, which can be spectrally shifted by modifying the effective index through carrier injection. To this end, a tunable voltage source was connected to the metal contacts of the MDR. Polarization controllers were inserted at both the modulator and the MDR input to avoid power penalty derived from polarization mismatching. Finally, the optical signal exiting the MDR output was detected using a high-bandwidth photodetector (HBW PD), amplified by means of a high-gain electrical amplifier (EA) and acquired by a vectorial

network analyzer (VNA). In the inset of Fig. 2 a footprint image of fabricated MDRs is illustrated.

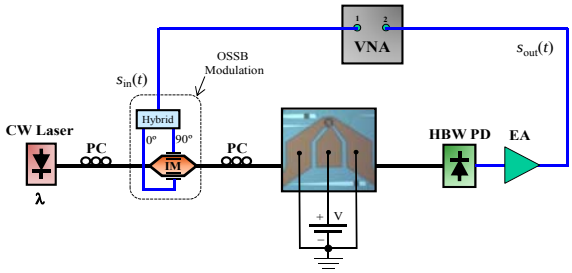


Fig. 1. Sketch showing the experimental setup.

IV. Results

The gain and phase transfer functions of the device as a function of the injected current are shown in Fig. 2. The total optical power inserted at the input vertical grating coupler was 1 dBm. The frequency of the modulating signal was adjusted from 5 to 20 GHz. The notch-type transfer function can be progressively tuned by applying different currents. It is important to notice that the notch depth depends on the current as well. By increasing the current, the roundtrip loss in the cavity decreases due to a higher gain in the III-V layer. To develop phase-shifting functionalities the over-coupled operating regime is desired since a lower power penalty compared to the critical case is featured and still 2π phase transitions in each notch are obtained. In the inset of Fig. 2, the spectral position for both the optical carrier and modulation sideband within the phase transfer function are also depicted. By sweeping the current from 1.5 to 1.725 mA, the carrier experiences a phase change of nearly 360º.

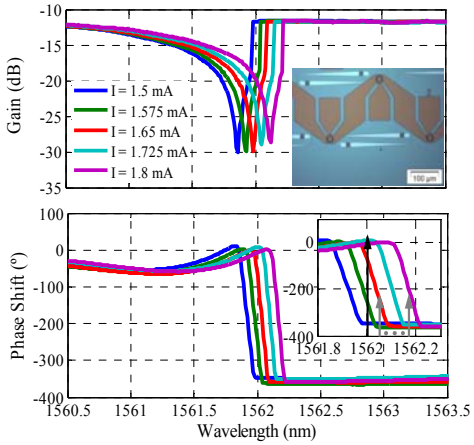


Fig. 2. Gain and phase transfer functions with the injection current.

Fig. 3 shows the results for both the phase shift and power of the detected microwave signal as a function of the injection current. It can be seen that quasi-linear and continuously tunable phase shifts are obtained. The maximum achievable phase shift at a certain frequency is limited by the abruptness of the phase slopes of the transfer function. In particular, a minimum modulating frequency of 18 GHz is required to reach a phase shift of ~ 2π radians. The functionality as a phase shifter is also demonstrated for lower frequencies, however, full 360º shifts are not obtained. According to the gain transfer function, a phase change is accompanied by a power penalty. A power variation of ~ 12 dB within the tunability range comprising from 1.5 to 1.725 mA is obtained when the modulating frequency, Ω, is 18 GHz.

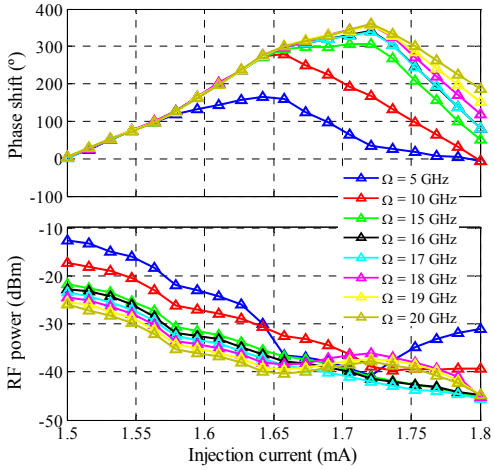


Fig. 3. RF phase shift and power as a function of the injection current for different modulating frequencies.

V. Conclusions

A novel broadband MWP phase shifter based on a single III-V/SOI MDR has been proposed and demonstrated. Quasi-linear and continuously tunable ~ 360º phase shifts have been obtained when considering radiofrequencies greater than 18 GHz. Phase shift tunability has been accomplished by modifying the effective index through carrier injection in the III-V compound. As a consequence, the tunability speed is limited by the carrier dynamics in the semiconductor, which is in the scale of hundreds of *ps*. This fact greatly improves the performance compared to other similar SOI-based approaches, in which the thermo-optic effect is used as tunable mechanism. To the best of our knowledge, it represents the smallest approach for photonic phase shifting of microwave signals reported so far.

Acknowledgment

The authors acknowledges the financial support given by the EU FP 7 through the projects GOSPEL, WADIMOS and HISTORIC; GVA PROMETEO 2008/092 and also the I + D TEC2011-29120-C05-05 and TEC2008-06145.

References

[1] J. Capmany, B. Ortega, D. Pastor and S. Sales, "Discrete-time optical processing of microwave signals," IEEE J. of Ligthwave Technol., vol. 27, no. 2, pp. 702–723, 2005.

[2] J. Capmany and D. Novak, "Microwave photonics combines two worlds," Nat. Photonics, vol. 1, no. 6, pp. 319–330, 2007.

[3] R. Soref, "The past, present and future of silicon photonics," IEEE J. Sel. Tops. Quantum Electron., vol 12, no. 6, pp. 1678−1687, 2006.

[4] R. L. Espinola, M.-C. Tsai, J. T. Yardley, R. M. Osgood, "Fast and low-power thermooptic switch on thin film silicon-on-insulator," IEEE Photon. Technol. Lett., vol. 15, no. 10, pp. 1366−1368, 2003.

[5] D. Van Thourhout, T. Spuesens, S. Kumar, L. Liu, G. Roelkens, R. Kumar, G. Morthier, P. Rojo-Romeo, F. Mandorlo, P. Regreny, O. Raz, C. Kopp and L. Grenouillet, "Nanophotonic devices for optical interconnect," IEEE J. Quantum Electron., vol. 16, no. 5, pp. 1363−1375, 2010.

Integrated Optics and Microfluidics for Quantum-Enhanced Sensing

J. C. F. Matthews, M. Lobino, D. Bonneau & J. L. O'Brien
Centre for Quantum Photonics, University of Bristol, Bristol, UK

A. Crespi, R. Ramponi, R. Osellame
Istituto di Fotonica e Nanotecnologie – CNR and Physics Department - Politecnico di Milano, Milan, Italy

A. Politi
Now at: Center for Spintronics and Quantum Computation, University of California, Santa Barbara, USA

C. R. Neal
Microvascular Research Labs, University of Bristol, Bristol, UK

***Abstract*—We report entangled multi-photon quantum metrology states of light that are manipulated and generated within a Silica-on-Silicon chip. We report use of such states in conjunction with optofluidics to sense concentration of room temperature protein.**

Keywords-component; Sensing; microfluidics; quantum photonics

I. INTRODUCTION

Measurement lies at the heart of all science and technology. Currently, the most accurate and commonly deployed method for sensing optical path length (e.g. physical distance, sample concentration or birefringence) is to use interferometry with classical coherent light. In this setting, precision in measurement of an optical phase change $\Delta\phi$ is limited by shot noise, according to $\Delta\phi \sim 1/\sqrt{N}$, where N equates to the total number of photons that pass through the sensing apparatus. Quantum states of light, however, offer an approach for enhancing precision in measurement beyond the shot noise limit and achieve *Heisenberg limited* precision in measurement — $\Delta\phi \sim 1/N$ [1].

The prospect of quantum enhanced sensing promises practical applications that notably include measuring light sensitive samples and experiments where the measurement apparatus itself is altered by light, such as photon pressure on optics in gravity wave detection. Underlying principles of quantum enhanced sensing have been investigated with large scale bulk optical architectures [2,3], allowing observation of super-sensitivity of up to four entangled photons [4] and super-resoluton of up to five entangled photons [5]. The advent of integrated quantum photonics [6,7] has provided a new platform for developing more advanced quantum metrology schemes requiring complex optical networks and as a practical miniaturized sensing tool. Here we describe how multi-photon entangled states of light can, in lithographic waveguide architecture, be manipulated [8] and generated [9] in a heralded manner [10,11]. We also report the first step in developing a quantum enhanced sensing tool for biological applications, by using an opto-fluidic chip fabricated with laser inscription [14] in conjunction with two-photon entanglement to measure protein concentration [15].

This work was supported by: EPSRC, ERC, IARPA, the Leverhulme Trust, PHORBITECH, QAP, Q-ESSENCE, QIP IRC, QUANTIP and NSQI. J.L.O'B acknowledges support through a Royal Society Wolfson Merit Award.

II. HERALDED GENERATION OF PHOTONIC ENTANGLED STATES ON CHIP

Previous demonstrations of four or more photon quantum metrology states have used post-selection to ignore unwanted components of the overall quantum state. While this is ideal to verify the underlying quantum mechanics, it does lower the overall efficiency of a quantum enhanced sensing device, in some cases below the shot noise limit. This is due to the fact that post-selection does not prevent excess photons, that are not part of an optimal quantum metrology state, from passing through the sensing apparatus and the measured sample. The ability to herald (or signal) the generation an optimal quantum metrology state—in our case via detecting auxiliary photons—circumvents the problems posed by post-selection by exposing the measured sample to only optimal photons, when heralding is used with fast optical switching.

A. Method

The typical state of interest in quantum metrology is the multi-photon "NOON" state of N photons, entangled across two modes a and b that allows Heisenberg limited precision beyond the shot noise limit, and taking the form

$$|N :: 0\rangle = \frac{1}{\sqrt{2}} \left(|N\rangle_a |0\rangle_b + |0\rangle_a |N\rangle_b \right) \qquad (1)$$

where $|n\rangle_j$ represents the Fock state of n photons occupying mode j. NOON states are heralded [9-11] for N=2 and N=4 using the circuit given in figure 1(a), at outputs j and k by respectively launching $N+2 = 4$ and $N+2 = 6$ photons respectively into modes b and c and detecting one auxiliary photon at each of the heralding outputs i and l.

The waveguide circuit is lithographically patterned with thermal resister to control the internal phase (ϕ as shown in figure 1a) which is used to control quantum interference in the heralding scheme—on applying a voltage across the thermal resister, the relative optical phase of quantum states guided through the interferometer is varied in a stable, controlled manner [8]. The 3.5μm core waveguides are lithographically patterned from doped Silica fabricated on a Silicon substrate

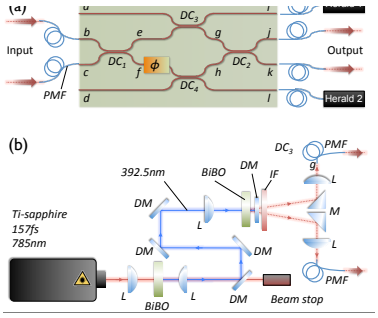


Figure 2. Setup for heralding N=2- and N=4-photon entangled states for quantum metrology. (a) The circuit realised in a monolithic chip that generates heralded entanglement. (b) The spontanoues parametric down conversion source used to generate multi-photon states that are then launched into the chip.

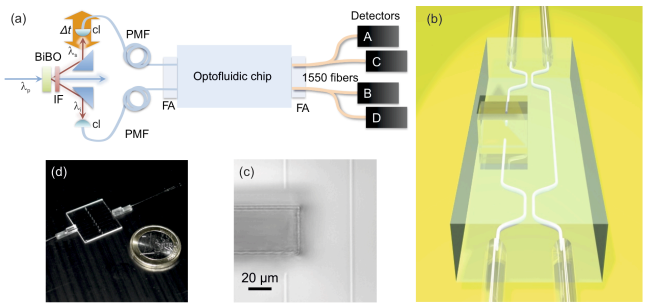


Figure 1. The opto-fluidic chip used for measuring protein concentration with entangled light. (a) The experimental setup, including external photon source. (b-c) The opto-fluidic chip that consists of mach-zehnder interferometers and rectangular micro-channels.

using standard methods and are designed for single mode operation in the 780nm region.

Multi photon states of four- and six-photons are produced by pumping spontaneous parametric down conversion (SPDC) as shown in figure 1(b). A Ti:sapphire pulsed laser (157fs) laser is upconverted to 390nm and focused onto a BiBO crystal cut for non-collinear down-conversion to produce pairs of photons with wavelength 780nm, filtered spectrally using high transmission interference filters and spatially into two modes by focusing onto polarization maintaining fibres (PMF). The photons are injected into the chip using butt-coupled arrays of PMF pitched to match those of the waveguide. Coincidental events are then detected using commercially available silicon avalanche photo diode single photon counting modules (SPCM).

III. Sensing Protein Concentration In Optofluidics With Entangled Light

Optofluidics offers an accurate means to deliver small volumes of fluid into integrated optics for biological and chemical sensing with interferometry [12-14]. A leading approach to rapidly fabricate both waveguides and micro-fluidics in a single device laser inscription [14], which provides an attractive platform with which to realize practical, miniaturized quantum enhanced sensing devices.

A. Method

Our integrated optofluidic device is fabricated in a pure silica chip (figure 2) using a focused 300 fs pulsed laser at a wavelength of 1030 nm (1 MHz repetition rate)—laser irradiation for the waveguide circuit (figure 4) and the microchannels is performed in the same run. The microchannel is realized by irradiating a helicoidal path in order to obtain double- pyramidal structure followed by selective etching using HF acid.

A range of concentrations of Bovine Serum Albumin in aqueous buffer solution is injected into the microfluidic channel. Two indistinguishable photons are generated externally to the chip via SPDC and launched into the chip. The resulting quantum interference pattern is dependent upon protein concentration, which is therefore determined via accumulated photon statistics with an increase frequency interference pattern.

IV. Concluding Remarks

We report integrated optics as a promising architecture to realize practical quantum metrology. The inherent stability and near-perfect mode overlap of waveguide architecture is ideal for the application to quantum metrology. The results presented here of heralding quantum metrology states [9] and using them to measure a biological sample delivered within the device via microfluidics [15] support the promise of integrated optics for realizing practical quantum enhanced sensing tools.

Acknowledgment

We thank J. P. Hadden, A. Laing, A. Lynch, G J. Pryde, J. G. Rarity, F. Sciarrino, A. Stefanov and X. Q. Zhou for helpful discussion.

References

[1] V. Gioveannetti, S. Lloyd, L. Maccone, *Science* **306**, 1330-1336 (2004).

[2] J. G. Rarity, P. R. Tapster, E. Jakeman, T. Larchuk, R. A. Campos, M. C. Teich, B. E. A. Saleh, *Phys. Rev. Lett.* **65**, 1348 (1990).

[3] M. W. Mitchell, J. S. Lundeen, A. M. Steinberg *Nature* **429**, 161-164 (2004).

[4] T. Nagata, R. Okamoto, J. L. O'Brien, K. Sasaki, S. Takeuichi, *Science* **316**, 726-729 (2007).

[5] I. Afek, O. Ambar, Y. Silberberg *Science* **328**, 879 (2010).

[6] A. Politi, M. J. Cryan, J. G. Rarity S. Yu, J. L. O'Brien *Science*, **320**, 646-649 (2008).

[7] A. Politi, J. C. F. Matthews, M. G. Thompson, J. L. O'Brien, *IEEE Journal of Selected Topics in Quantum Electronics*, **15**, 6, 1673-1684 (2009).

[8] J. C. F. Matthews, A. Politi, A. Stefanov, J. L. O'Brien, *Nature Photon.* **3** 346 (2009).

[9] J. C. F. Matthews, A. Politi, D. Bonneau, J. L. O'Brien, *Phys. Rev. Lett.* **107**, 163602 (2011).

[10] H. Lee, P. Kok, N. J. Cerf, J. P. Dowling *Phys. Rev. A* **65** 030101 (2002).

[11] P. Kok, H. Lee, J. P. Dowling, *Phys. Rev. A* **65** 052104 (2002).

[12] C. Monat, P. Domachuk, B. J. Eggleton, *Nat. Photon.* **1**, 106 (2007).

[13] R. R. Gattass, E. Mazur, *Nat. Photon.* **2**, 219, (2008).

[14] R. Osellame, V. Maselli, R. M. Vazquez, R. Ramponi , G. Cerullo, *Appl. Phys. Lett.* **90**, 231118 (2009).

[15] A. Crespi, M. Lobino, J. C. F. Matthews, A. Politi, C. R. Neal, R. Ramponi, R. Osellame, J. L. O'Brien, Unpublished, Pre-print: *arxiv:1109.3128 [quant-ph]*

Monolithically integrated variable repetition rate mode-locked laser diode

X. Guo, V. F. Olle, A. H. Quarterman, A. Wonfor, R. V. Penty and I. H. White.
Centre for Photonic Systems, Electrical Engineering Division, Engineering Department
University of Cambridge, Cambridge, CB3 0FA, UK

***Abstract*—A monolithically integrated mode-locked laser diode system is presented. Pairs of 7.6 ps pulses are generated at 1550 nm. An integrated Mach-Zehnder modulator pulse-picker allows electronically tunable repetition rates from 14 GHz to 219 MHz.**

Keywords – mode-locked lasers; tunable repetition rate; monolithic integration; foundry approach

I. INTRODUCTION

Thanks to their advantageous combination of versatility, cost and size, continuous wave diode lasers have come to replace the more traditional solid-state and gas lasers for a wide range of both commercial and scientific applications. Mode-locked laser diodes (MLLDs), however, are yet to meet with the same level of widespread success despite sharing many of their advantages. While MLLDs are not expected to compete with mode-locked solid state or fibre lasers in terms of pulse duration or average power, their simplicity, compactness and low cost does make them highly desirable as a potential source for applications in areas such as biophotonics [1] and optical sampling [2].

One disadvantage of MLLDs for these applications is that due to their inherently short cavities it is difficult to achieve repetition rates below 10 GHz, with 1 GHz being the record to date [3]. This in turn places a limit on pulse energy for a given average power, and thus limits their use for nonlinear applications. It also means that it is difficult to use these pulse trains to probe biological processes when using markers with characteristic lifetimes of 100s of picoseconds or longer. External cavity semiconductor lasers can bypass this problem, but only at the cost of increased complexity [4].

The solution proposed in this paper is the monolithic integration of a MLLD with a Mach-Zehnder modulator (MZM), which is used as a pulse picker. In addition to the achievement of sub-GHz repetition rates, this approach also allows the repetition rate to be tuned electronically over a wide range, a property which may itself have interesting applications, for example in asynchronous optical sampling (ASOPS) [2]. This approach allows us to demonstrate 7.6 ps pulse trains at 1550 nm over a range of repetition rates from 14 GHz to 219 MHz. The fabrication of this device makes use of the advantages offered by a foundry approach in a manner analogous to CMOS electronics [5]. Thus the device is assembled purely from generic building blocks, reducing development costs and further simplifying the device design.

The research leading to these results has received funding from the European Community's Seventh Framework Programme FP7/2007-2013 under grant agreement NMP 228839 EuroPIC and from the UK EPSRC via the MUSIC project.

II. DEVICE DESCRIPTION

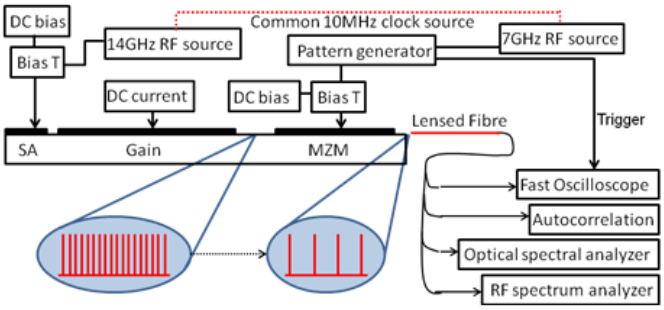


Figure 1. A schematic diagram of the integrated device and of the drive electronics used for hybrid modelocking and modulation of the pulse train, along with the associated characterization equipment.

Fig. 1 shows a schematic of the device and the associated electronics. The active components of the laser diode are a 2.1 mm long gain section and a 50 μm long saturable absorber section. A length of passive waveguide brings the total cavity length to 3.0 mm, resulting in a fundamental repetition rate of 14 GHz. The laser output passes through a MZM with arms containing two 1090 μm long electro-optic phase shifter sections. The output facet is AR coated and angled at 7 degrees to prevent feedback. Pulses are collected by a lensed fibre and then passed into instruments used to measure the laser performance. The whole device is mounted on a copper heaksink whose temperature is maintained at 20°C.

The master oscillator is hybrid mode-locked by applying a DC current of 129.6 mA to the gain section, and a DC reverse bias of 1.67 V with an RF modulation of 18 dBm at a frequency close to the fundamental repetition rate to the absorber section via a bias tee. Modulation of the pulse train is achieved by applying a square wave between 4.15 V and 2.15 V at the desired frequency to one arm of the MZM. A programmable pattern generator, synchronized to the hybrid modelocking frequency, is used to prepare the desired drive waveform. By varying the frequency and duty cycle of the waveform pulse trains with variable repetition rates can be prepared, with the achievable repetition rates only limited by the fundamental repetition rate of the laser at the upper limit, and by the maximum data length of the pattern generator at the lower limit.

III. RESULTS AND DISCUSSION

Fig. 2 shows oscilloscope traces of pulse trains at repetition rates of 14 GHz and 219 MHz. At 219 MHz two pulses are

seen to be transmitted by the MZM rather than a single pulse. This is because the maximum frequency of the pattern generator used here was 12.5 GHz, which corresponds to a minimum bit length of 80 ps, slightly longer than the spacing between pulses. A higher bandwidth pattern generator would allow single pulses to be selected. Colinear second harmonic autocorrelations of the pulse train allows a pulse duration of 7.6 ps to be measured, assuming a sech-squared fit.

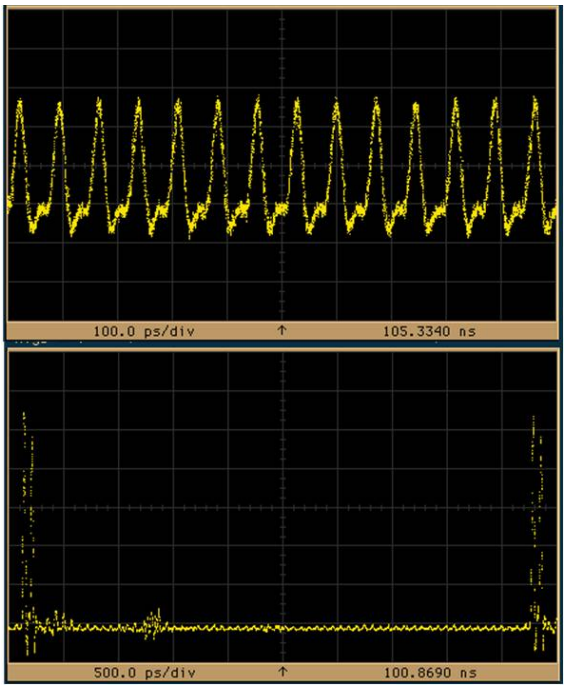


Figure 2. Sampling oscilloscope traces of modulated pulse trains at repetition rates of 14 GHz and 219 MHz. The double pulses at 219 MHz result from the limited bandwidth of the pattern generator.

It is clear that an architecture integrating a MLLD with an MZM can be used to demonstrate a very compact device that is able to achieve repetition rates usually associated with much larger sources. However, a potentially more significant advantage of this device concept is that the MZM allows the repetition rate to be switched electronically in discrete steps, while fine continuous tuning of the repetition rate can be achieved by varying the hybrid modelocking frequency, giving the device a very large degree of repetition rate flexibility.

Figure 3 demonstrates that continuous tuning of the fundamental repetition rate over an 8 MHz range is possible without loss of hybrid modelocking stability, while figure 2 shows switching of the repetition rate by a factor of 64. While lacking the flexibility of a continuously tunable laser [6], the combination of coarse discrete control and fine continuous control of the repetition rate is attractive, both in terms of the simplicity of the device, in terms of the electronic control of the repetition rate, and in term of the very large dynamic range that can be achieved. In fluorescence sampling, for example, the ideal repetition rate is one close to the fluorescence lifetime of the dye used, so as to maximize the data acquisition rate while still allowing the sample to recover between pulses. This device can be tuned simply to achieve optimal conditions for a given dye.

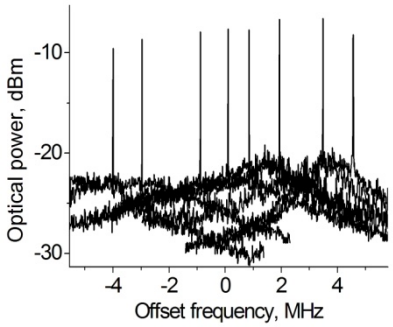


Figure 3. RF spectra of the fundamentally mode-locked laser at eight different hybrid modelocking frequencies, showing a continuous tuning range greater than 8 MHz.

A switchable repetition rate also makes this device potentially suitable as a low cost source for applications such as ASOPS [2], which uses two lasers with slightly different repetition rates to perform delay line free pump-probe experiments. When compared to a classical pump-probe system, ASOPS can provide superior data acquisition times and reduced complexity thanks to the elimination of a mechanical delay stage. Key laser parameters in an ASOPS system are the repetition rate and the frequency offset between the two lasers, which control the effective delay length and the time resolution. In the device presented here both of these parameters are electronically controllable over a large range, enabling much greater freedom than a system based on solid-state or fibre sources. A further advantage of this device is its low cost compared to these sources, particularly in the context of foundry-based design and manufacture.

IV. CONCLUSIONS

We demonstrate a monolithically integrated source consisting of a MLLD and a MZM. For simplicity and low cost the device is designed and fabricated under a foundry approach. The source emits 7.6 ps pulses at 1550 nm, and at repetition rates which can be tuned electronically over a very large range. This cheap and flexible source is expected to be suitable for applications in biophotonics and optical sampling.

REFERENCES

[1] M.Kuramoto et al "Two-photon fluorescence bioimaging with an all-semiconductor laser picosecond pulse source," Opt. Lett. **32**,2726 (2007).

[2] P.E. Elzinga et al. "Pump/probe method for fast analysis of visible spectral signatures utilizing asynchronous optical sampling," Appl. Opt. **26**, 4303-4309 (1987).

[3] S. Cheung et al. "1-GHz Monolithically Integrated Hybrid Mode-Locked InP Laser," IEEE Phot. Tech. Lett. **22**, 1793 (2010).

[4] K. Kim et al. "1.4kW high peak power generation from an all semiconductor mode-locked master oscillator power amplifier system based on eXtreme Chirped Pulse Amplification (X-CPA)," Opt. Exp. **13**, 4600 (2005).

[5] M. Smit et al. "Generic foundry model for InP-based photonics," IET Optoelectron. **5**, 187 (2011).

[6] K.G. Wilcox et al. "Repetition-frequency tunable mode-locked surface emitting semiconductor laser between 2.78 and 7.87 GHz," Opt. Exp. **19**, 23453 (2011).

Supercontinuum source based on ion-exchanged Neodymium doped Q-switched laser

B. Charlet, L. Bastard, J.-E. Broquin, D. Bucci,
E. Ghibaudo
IMEP-LAHC - 3, parvis L. Néel
BP 257, 38016 Grenoble, FRANCE
lionel.bastard@minatec.grenoble-inp.fr

***Abstract*— Supercontinuum generation consists in launching a high peak power pulsed laser in a nonlinear medium, usually a photonic crystal fiber (PCF). It allows obtaining an ultra-wide band spectrum source. In this article, we present a glass integrated optics Q-switched laser, which can be used to directly pump the PCF, without bulk coupling optics. This laser is made by ion-exchange in a Neodymium-doped phosphate glass. The laser emits 2.4 kW peak power pulses with 0.6 ns duration. The laser output is directly coupled to a PCF. A supercontinuum spectrum spanning from 400 nm to 1600 nm is thus generated.**

Glass integrated optics, ion-exchange, Q-switched laser, supercontinuum, photonic crystal fiber.

I. INTRODUCTION

Supercontinuum sources have raised a great deal of interest since their first realization by Alfano et al. in 1970[1]. Indeed, sources with a broadband spectrum and high brilliance are useful for numerous applications like spectroscopy, metrology or optical coherent tomography (OCT). Supercontinuum sources using photonic crystal fiber (PCF) as the non-linear medium have enabled huge performances improvements in the past ten years[2]. These fibers have allowed supercontinuum generation with spectra ranging from the UV to the IR when pumped with either mode-locked or Q-switched lasers around 1 µm. However, a special care is required in order to devise an efficient coupling scheme between the pulsed laser and the PCF. The most common solution is to use some bulk optics to couple the pump laser in the PCF. Fiber lasers can be used to avoid this coupling optics. However, the saturable absorber is not integrated in these devices[3], so that bulk optics is needed inside the laser cavity.

An alternative technology that could avoid the need for bulk coupling optics is glass integrated optics. This technology is indeed compatible with optical fibers and allows producing both passive[4] and active devices such as amplifiers[5] and lasers[6]. Moreover, a Q-switched laser realized by ion-exchange has been demonstrated by R. Salas-Montiel et al.[7] and an optimized structure has been recently published, allowing a 1 kW peak power emission[8]. This value of peak power is compatible with supercontinuum generation in PCF.

In this paper, we present a supercontinuum generated using a fully integrated Q-switched laser directly coupled to a PCF. We first present the realization of the laser cavity, designed to allow a direct coupling with the PCF. In the second part, we present the hybridization of the saturable absorber, leading to a pulsed laser operation. The supercontinuum source realized with this laser is then characterized.

II. DEVICE REALIZATION AND CHARACTERIZATION

The laser cavity consists of an amplifying waveguide and two reflectors stuck on the waveguide facets. The waveguides are made by ion-exchange in a commercially available phosphate glass substrate (Schott™ IOG1) doped with 4.7 wt% Neodymium oxide. It is realized by silver/sodium ion-exchange in a (20% mol $AgNO_3$ - 80% mol $NaNO_3$) salt bath. Amplification using the Neodymium system in our glass requires a pump at the wavelength of 800 nm and a signal at the wavelength of 1054 nm. In order to obtain an efficient amplification, the waveguides have been designed in order to provide single-mode operation at those two wavelengths.

After realization, their single-mode behavior was assessed by near field intensity distribution measurement. The propagation losses were also measured and were found to be 0.1±0.1 dB/cm. The mode intensity distribution were used to compute the coupling efficiency of these modes with that of the PCF at the signal wavelength. A value of 70% was found.

Numerical simulations were carried out to compute the output power of Fabry-Perot lasers using the measured waveguide mode field distributions with a 100% reflection coefficient mirror on one side and a variable one on the other side. It appears that a 4% reflection coefficient (corresponding to the reflection on the bare glass facet) leads to an output power value close to the maximum. Since the dielectric mirrors we use are deposited on a 100 µm thick microscope slide, it is not possible to approach the optical fibre close enough to obtain a good coupling with the waveguide. Removing the mirror and using instead the 4% reflection of the facet is thus a very attractive solution which allows a direct coupling with an optical fibre.

The Fabry-Perot structure containing a 100% reflector on one side and 4% reflector on the other side has thus been implemented on a 4 cm long waveguide. 440 mW pump power has been launched inside the structure using two lenses as presented on Fig.1. An output power of 160 mW has been obtained with the maximum pump power.

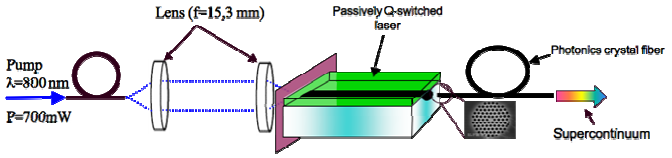


Figure 1. Schematic view of the supercontinuum source.

III. Q-SWITCHED OPERATION AND SUPERCONTINUUM GENERATION

The element used as a saturable absorber is a dye termed BDN for bis(4-dimethylaminodithiiobenzil)nickel[9]. This dye is included in a cellulose acetate matrix so that it can be shaped as a 100 µm thick film which is cast on the glass wafer containing the waveguides. In this configuration, the saturable absorber is distributed all along the laser cavity. However, only the evanescent top part of the transverse photon flux interacts with the saturable absorber, since the refractive index of the cellulose acetate cladding is lower than that of the glass wafer.

An experiment was then conducted using polymer films with different BDN concentrations. The structure of these pulsed lasers is presented on Fig. 1. The pulse duration τ, repetition rate T, and average output power P_{avg} have been measured. The peak power P_{peak} of the pulses could then be inferred using (1).

$$P_{peak} = T.P_{moy}/\tau. \quad (1)$$

For the optimal BDN concentration of $6x10^{23}\,m^{-3}$, pulses with an average power of (37 ± 1) mW, a pulse duration of (0.65 ± 0.1) ns and a repetition rate of (50 ± 2) µs were measured. This corresponds to a pulse energy of (1.86 ± 0.2) µJ and a peak power of (2,8 ± 0.6) kW. The polymer cladding of devices with BDN concentrations above $6x10^{23}\,m^{-3}$ have been irreversibly damaged due to the too high value of the intra-cavity peak power. Taking into account the 70% coupling coefficient of the device with the PCF, a peak power of (2.0 ± 0.5) kW is available in the PCF, which is adequate for supercontinuum generation.

The supercontinuum source has been realized by directly coupling the Q-switched laser output to an 8 m long PCF as shown on Fig. 1. A quantitative measurement of the spectrum emitted by the supercontinuum source has been carried out in three steps. First, the visible wavelengths were measured using 10 nm wide optical filters centered on 450, 500, 550 and 600 nm and a calibrated photodetector. The first part of the IR spectrum was measured directly through an OSA. The second part was measured through the same OSA. However, a low-pass optical filter has been inserted to prevent the second order of the 1054 nm or 800 nm signal to interfere with the measurement. The complete spectrum is represented on Fig. 2.

The spectrum presented on Fig. 2 shows that a supercontinuum was indeed generated. It spans from 450 to 1600 nm and is comparable with the state of the art[10]. This work thus proves the feasibility of an integrated supercontinuum source which does not require any coupling optics between the pump laser and the PCF.

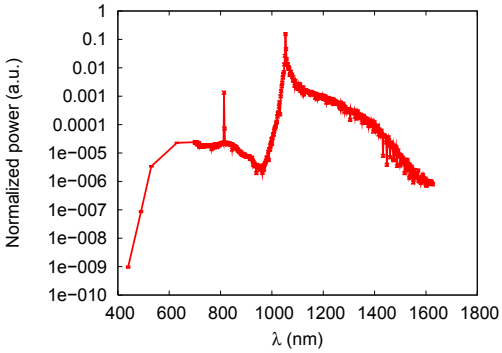


Figure 2. Spectrum emitted by the supercontinuum source.

IV. CONCLUSION

The realization of a supercontinuum source based on a glass integrated optics laser is presented in this paper. The Q-switched laser is based on an ion-exchanged waveguide designed to let one bare facet that can be used for direct coupling with the PCF. This device is then free of coupling optics and is thus more efficient while less subject to vibrations. A BDN-doped cellulose acetate film deposited on the glass wafer acts as the saturable absorber and allows a Q-switched operation. With this structure, pulses of 2.8 kW peak power and 0.6 ns duration have been obtained. Once coupled in the 8 m long PCF, these pulses have produced a large spectral output ranging from 450 to 1600 nm.

[1] R. R. Alfano and S. L. Shapiro, "Emission in the Region 4000 to 7000 Å Via Four-Photon Coupling in Glass," Physical Review Letters, vol. 24, pp. 584-587, 1970.

[2] J. M. Dudley, L. Provino, N. Grossard, H. Maillotte, R. S. Windeler, B. J. Eggleton, and S. Coen, "Supercontinuum generation in air–silica microstructured fibers with nanosecond and femtosecond pulse pumping," JOSA B, vol. 19, pp. 765-771, 2002.

[3] J. Alvarez-Chavez, H. Offerhaus, J. Nilsson, P. Turner, W. Clarkson, and D. Richardson, "High-energy, high-power ytterbium-doped Q-switched fiber laser," Optics Letters, vol. 25, pp. 37-39, 2000.

[4] J. E. Broquin, "Ion-exchanged integrated devices," 2001, p. 105.

[5] J. M. P. Delavaux, S. Granlund, O. Mizuhara, L. Tzeng, D. Barbier, M. Rattay, F. S. Andre, and A. Kevorkian, "Integrated optics erbium-ytterbium amplifier system in 10-Gb/s fiber transmission experiment," Photonics Technology Letters, IEEE, vol. 9, pp. 247-249, 1997.

[6] S. Blaize, L. Bastard, C. Cassagnètes, and J. Broquin, "Multiwavelengths DFB waveguide laser arrays in Yb-Er codoped phosphate glass substrate," Photonics Technology Letters, IEEE, vol. 15, pp. 516-518, 2003.

[7] R. Salas-Montiel, L. Bastard, G. Grosa, and J. E. Broquin, "Hybrid Neodymium-doped passively Q-switched waveguide laser," Materials Science and Engineering: B, vol. 149, pp. 181-184, 2008.

[8] B. Charlet, L. Bastard, and J. E. Broquin, "1 kW peak power passively Q-switched Nd3+-doped glass integrated waveguide laser," Opt. Lett., vol. 36, pp. 1987-1989, 2011.

[9] Z. Zhu and E. Garmire, "Optical bistability in BDN dye," Quantum Electronics, IEEE Journal of, vol. 19, pp. 1495-1498, 1983.

[10] J. M. Dudley, G. Genty, and S. Coen, "Supercontinuum generation in photonic crystal fiber," Reviews of Modern Physics, vol. 78, p. 1135, 2006.

Multi-particle Quantum Walks with 2D & 3D Arrayed Waveguides

K. Poulios, D. Fry, M. Lobino, J. C. F. Matthews, J. D. A. Meinecke, A. Peruzzo, X. Zhou, M. G. Thompson & J. L. O'Brien
Centre for Quantum Photonics
University of Bristol, Bristol, UK

A. Politi
Now at: Center for Spintronics and Quantum Computation
University of California Santa Barbara, USA

N. Ismail & K. Wörhoff
Integrated Optical Microsystems Group, MESA+ Institute for Nanotechnology
University of Twente, Enschede, The Netherlands

R. Keil & A. Szameit
Institute of Applied Physics
Friedrich-Schiller-Universität, Jena, Germany

N. Matsuda
NTT Basic Research Laboratories, NTT Corporation
Atsugi, Japan

***Abstract*—Multi-photon quantum walks on integrated circuits are demonstrated, showing non-classical correlations, in one and two dimensional networks. Time evolution of quantum walks and a scheme for simulating fermionic quantum walks using entanglement are demonstrated.**

Keywords-quantum walk; direct write; integrated waveguides;

I. INTRODUCTION

Quantum walks [1] are the direct quantum-mechanical analogue of classical random walks. They offer the possibility of exploring processes in physical and biological systems, studying large scale quantum interference and provide a route to universal quantum computing.

Continuous-Time Quantum Walks (CTQW) have been realized in different platforms, with single and multiple quantum particles. Single particle CTQW can be described in the context of classical wave theory. Conversely, multi-particle CTQW [2] exhibit truly non-classical behavior and pave the way to new applications in quantum information science.

Integrated circuits provide the ideal platform for implementing large networks of CTQW, due to their inherent interferometric stability and small size. Non-classical interference of single photons has been demonstrated on integrated platforms [3] and is at the heart of emerging quantum technologies [4].

Lithographic fabrication of waveguides is restricted to one dimensional waveguide arrays. The direct-write laser technique for inscribing waveguides in a substrate [5] allows the creation of arrays in three dimensions; hence more complex networks can be fabricated. Coupling between adjacent waveguides can individually be controlled during fabrication and, due to the ability of writing structures in three dimensions, second order coupling for non-adjacent waveguides is present. Here we demonstrate large scale, on chip, non-classical interference and quantum correlations of pairs of indistinguishable photons in the context of CTQW in 1-dimensional and 2-dimensional graph structures.

II. INTEGRATED CONTINUOUS TIME QUANTUM WALKS

A. Method

Photons propagating through a 1-dimensional coupled waveguide array (Fig. 1) are modeled assuming nearest-neighbor coupling with the Hamiltonian for coupled oscillators, setting $\hbar = 1$:

$$\hat{H} = \sum_{j=1}^{N}[\beta_j \alpha_j^{\dagger}\alpha_j + C_{j,j-1}\alpha_{j-1}^{\dagger}\alpha_j + C_{j,j+1}\alpha_{j+1}^{\dagger}\alpha_j] \quad (1)$$

where the creation and annihilation operators $\alpha_j^{\dagger}$ and α_j acting on waveguide j obey Bose-Einstein statistics, β is the propagation constant of the waveguides and C the coupling between neighbouring waveguides.

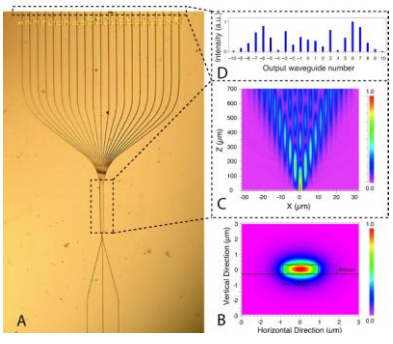


Figure 1. (A) An optical micrograph of a 21 waveguide quantum walk device. (B) Simulation of the transverse profile of the guided mode in the waveguide. (C) Single photon propagation in the array. (D) Output pattern of laser light propagating trough the waveguide array.

This work was supported by ERC, EPSRC, QIP IRC, the Leverhulme Trust, the Japan Society for the Promotion of Science, IARPA, QUANTIP, PHORBITECH and the Centre for Nanoscience and Quantum Information.

Time evolution is governed by the unitary operator $U(t) = exp(-iHt)$. The probability of a coincidental detection of the two indistinguishable input photons at output waveguides q and r, is given by the correlation function:

$$\Gamma_{q,r}(z) = \frac{1}{1+\delta_{q,r}} \left| U_{q,q'} U_{r,r'} + U_{q,r'} U_{r,q'} \right|^2 \quad (2)$$

For classical light, including random phase fluctuations that mimic certain properties of quantum light, diagonal correlations $\Gamma_{q,q}$ are related to correlations in the off-diagonal lobes $\Gamma_{q,r}$, $q \neq r$ according to the inequality [6]:

$$V_{q,r} = \frac{2}{3}\sqrt{\Gamma_{q,q}^{(Cl)} \Gamma_{r,r}^{(Cl)}} - \Gamma_{q,r}^{(Cl)} < 0 \quad (3).$$

This can be violated in the presence of quantum interference.

B. *Results [2]*

The 1-dimensional CTQW network consists of an array of 21 evanescently coupled silicon-oxy-nitride (SiO_xN_y) waveguides. The measured correlation matrices for adjacent waveguides input photons show the distinct differences between distinguishable and indistinguishable input photons (Fig. 2), demonstrating the non-classical correlations between indistinguishable photons. The vanishing of the off-diagonal lobes indicates a generalised Hong-Ou-Mandel type interference [7] over a large network of 21 modes.

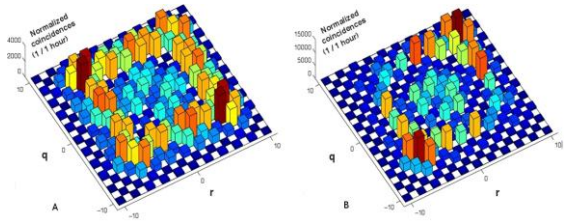


Figure 2. Measured correlation matrices for inputting the photons in adjacent waveguides, when photons are (A) distinguishable and (B) indistinguishable.

The true quantum-mechanical nature of the correlations observed is corroborated by the violations of the inequality Eq. 3 (Fig. 3).

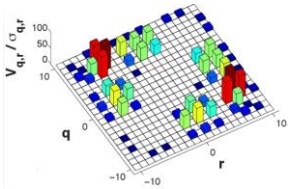


Figure 3. Violations of the inequality Eq. 3, measured for indistinguishable photons, expressed in standard deviations, showing uniquely non-classical behaviour.

III. TIME EVOLUTION

Since the length of the coupling region in the devices measured directly relates to the time of the evolution of the CTQW, by measuring the correlations between indistinguishable photons for different lengths, the coherent evolution of CTQW [8] can be investigated. We experimentally measure three different time steps and confirm the coherent evolution of the input state. The network here has a finite number of waveguides, allowing us to study boundary conditions when photons reach the outermost waveguides.

IV. SIMULATING FERMION CTQW USING ENTANGLEMENT

We show that by using bipartite, two-level entanglement for photon pairs injected in two identical CTQW networks (defined here by the TE and TM modes of the waveguides) and detecting the two-fold coincidences between these two networks, we can simulate the statistics of two non-interacting fermions undergoing a CTQW using photons [9]. Pauli's exclusion principal is observed across many modes, depicted by the vanishing of the diagonal elements of the correlation matrix.

V. 2-DIMENSIONAL QUANTUM WALKS

Three-dimensional waveguide array structures inscribed in a fused silica substrate by the use of a tightly focused femto-second laser have been proposed as a potential convenient platform for manipulating quantum states of light [10]. We experimentally demonstrate the first 2-dimensional CTQW of correlated photons [11] and observe non-classical correlations beyond the classical limit.

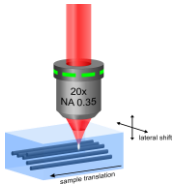


Figure 4. Schematic depicting the direct-write laser technique.

Non-classical interference of photons propagating in orthogonal planes is present, with the output statistics depending on the input state of the photons. Violations are observed across the network showing behavior that cannot be simulated with classical light across a 2-dimensional lattice.

VI. CONCLUDING REMARKS

The inherent stability and small footprint of integrated quantum photonic circuits defines them as an ideal test bed for implementing large, complex networks of CTQW. The direct-write technique opens new, exciting ways for implementing more complex networks, enabling non-trivial coupling between modes of the network.

REFERENCES

[1] Y. Aharonov, L. Davidovich and N. Zagury, "Quantum random walks", Phys. Rev. A, 48, 1687, 1993.

[2] A. Peruzzo, M. Lobino, J. C. F. Matthews, N. Matsuda, A. Politi, K. Poulios et al., "Quantum walks of correlated photons", Science, 329, 1500, 2010.

[3] A. Politi, M. J. Cryan, J. G. Rarity, S. Yu and J. L. O'Brien, "Silica-on-silicon waveguide quantum circuits", Science, 320, 646, 2008.

[4] J. L. O'Brien, A. Furusawa and J. Vuckovic, "Photonic quantum technologies", Nature Photonics, 3, 687, 2009.

[5] A. Szameit and S. Nolte, "Discrete optics in femtosecond-laser-written photonic structures", J. Phys. B: At. Mol. Opt. Phys., 43, 163001, 2010.

[6] Y. Bromberg, Y. Lahini, R. Morandotti and Y. Silberberg, "Quantum and classical correlations in waveguide lattices", Phys. Rev. Lett., 102, 253904, 2009.

[7] C. K. Hong, Z. Y. Ou and L. Mandel, "Measurement of subpicosecond time intervals between two photons by interference", Phys. Rev. Lett., 59, 2044, 1987.

[8] J. D. A. Meinecke, K. Poulios et al., unpublished.

[9] J. C. F. Matthews, K. Poulios , J. D. A. Meinecke, A. Politi et al., "Simulating quantum statistics with entangled photons: a continuous transition from bosons to fermions", arXiv:1106.1166v1, 2011.

[10] R. Keil, A. Szameit, F. Dreisow, M. Heinrich, S. Nolte and A. Tünnermann, "Photon correlations in two-dimensional waveguide arrays and their classical estimate", Phys. Rev. A, 81, 023834, 2010.

[11] K. Poulios, D. Fry, J. D. A. Meinecke, A. Politi, J. C. F. Matthews, R. Keil et al., unpublished.

PCB-Integrated Polymer Photonic Devices

N. Bamiedakis, A. Hashim, J. Beals IV,
R. V. Penty, I. H. White
Electrical Engineering Division, Department of Engineering
University of Cambridge, 9 JJ Thomson Av.
Cambridge, CB3 0FA, UK
nb301@cam.ac.uk

T. Hutter, S. R. Elliott
Department of Chemistry
University of Cambridge, Lensfield Road
Cambridge, CB2 1EW, UK

Abstract— **This paper describes recent achievements in the integration of polymer waveguides onto low-cost PCBs and their further functionalisation with active materials for the formation of hybrid photonic devices suitable for use in various application areas.**

Keywords- optical interconnects; opto-electronic printed circuit boards; polymer waveguides;

I. INTRODUCTION

The deployment of optics in board-level communications has received particular interest in recent years due to the increasing demand for interconnection bandwidth in servers, data centres and supercomputers [1, 2]. The limited bandwidth of electrical interconnects as well as their inherent disadvantages, such as susceptibility to electromagnetic interference, size and density issues and increased requirements in terms of power consumption and thermal management when operating at high data rates (> 5 Gb/s), have led to the consideration of the use of optics for short-reach on-board and on-chip communication links. While for on-chip communications silicon photonics is the leading candidate, owing to its compatibility with CMOS technologies, for board-level communications (card-to-card and module-to-module, i.e. link lengths in the range 0.1-1 m), polymer-based waveguide technologies appear to be the most promising solution owing to their potential to be cost-effectively integrated onto conventional printed circuit boards (PCBs). Firstly, a new range of polymer materials has been recently developed possessing the essential mechanical and optical properties to be directly integrated with electronics onto PCBs and the environmental stability to withstand the operating conditions of standard electronic systems [3, 4]. Secondly, multimode waveguides are developed for use as they offer relaxed alignment tolerances and therefore, reduced assembly and packaging costs in the formation of optoelectronic (OE) PCBs. Numerous different integration approaches have been proposed for the formation of such hybrid systems and various demonstrators have been reported in recent years differing in system design, fabrication and assembly methods. Significant work has been carried out in this area by our research group, resulting in novel PCB-integrated polymeric photonic components and the demonstration of complex board-level polymeric architectures.

The potential to cost-effectively form optical waveguides on PCBs can be further enhanced by providing additional functionality in the optical layer, thus enabling the use of OE PCBs in other applications areas than optical interconnects, such as sensing and display. Towards this goal, collaborative research has been carried out looking into the functionalisation of the polymer waveguides with different materials such as liquid crystals, active glasses and chemical dyes and has resulted in the demonstration of novel photonic structures. In this paper therefore, we review our recent work on the integration of polymer multimode waveguides on PCBs and present various demonstrated hybrid polymeric photonic devices. Specifically, we present optoelectronic units and functionalised polymeric devices formed on low-cost PCBs such as (i) a 10 Gb/s optical transceiver, (ii) a PCB-integrated liquid-crystal optical gate, and (iii) a PCB-integrated ammonia optical sensor. The work reported here highlights the versatility of such hybrid polymeric photonic devices and demonstrates their suitability for use in a wide range of applications areas.

II. POLYMER MATERIALS AND OE PCBS

The work reported here is based on the use of siloxane polymer materials developed by Dow Corning Corp. (OE-4140 and OE-4141). These polymer materials have been appropriately engineered to possess the essential properties for integration onto PCBs: they can withstand the high temperature environments (in excess of 250°C) required for solder reflow and PCB lamination processes, exhibit low optical losses below 0.05 dB/cm at 850 nm, and the essential environmental stability for a long-life operation [5]. While the materials also allow patterning with processes suitable for large-scale manufacturing such as stamping and embossing, the waveguide components presented here are fabricated with standard photolithographic techniques.

The basic design of the OE PCBs is based on low-cost FR4 substrates and assumes that the electronic and photonic components reside on different sides of the board. The top side of the board accommodates all electronic components and signal tracks, whilst the optical waveguides are formed on the board underside (Fig. 1a). The interface between the optical and electrical layers of the board is achieved with simple electro-optic connectors that accommodate the active optoelectronic devices (laser and photodiode) and which can be mounted onto the board with conventional pick-and-place assembly tools. The use of such connectors eliminates the need to form any beam-turning elements in the optical layer thereby simplifying the fabrication of the OE PCBs. To allow integration with the different active materials, selected waveguide regions are left exposed to the air. Details of this board-level integration method can be found in [6].

This work is funded by the UK Engineering and Physical Science Research Council via the Cambridge Integrated Knowledge Centre (CIKC).

III. HYBRID POLYMERIC PHOTONIC DEVICES

A. *10 Gb/s PCB-integrated optical transceiver*

As a proof-of-principle of the proposed on-board integration method, a 10 Gb/s optical transceiver is formed on low-cost FR4 substrates with conventional methods of PCB manufacturing (Fig. 1). This optoelectronic unit integrates the electronic driving circuits of the transmitter and receiver modules with a polymer 1×2 Y-splitter enabling bidirectional 10 Gb/s optical communication [6]. The unit can be deployed as a front-end optical unit interfacing with standard MMF.

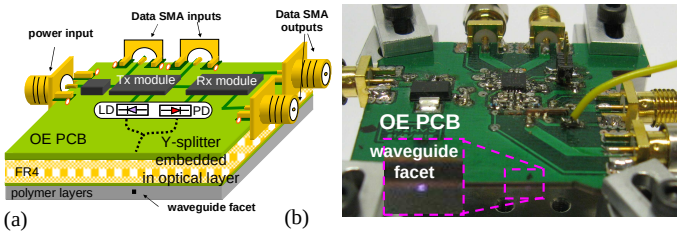


Figure 1. (a) Schematic of realised optical transceiver and (b) photograph of the actual unit with inset picture of illuminated output waveguide facet.

B. *PCB-integrated liquid-crystal optical gate*

Polymer multimode waveguides are integrated with liquid-crystal (LC) materials on standard FR4 substrates forming an active optical cladding switch (Fig. 2). The copper layer of the PCB is used to apply an electrical field across the LC-waveguide interaction region and control the orientation of the LC molecules and therefore, the optical absorption along the waveguide structure. Low ON-state losses of 0.5 dB are demonstrated while a 15 dB extinction ratio between the ON and OFF state is achieved over a wide wavelength range [7].

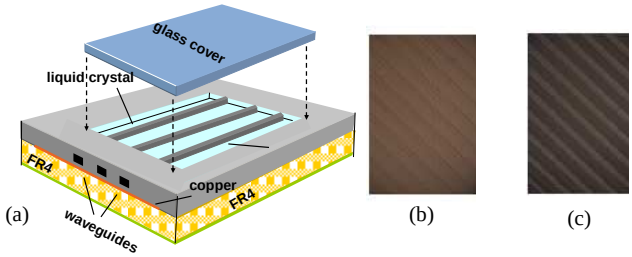


Figure 2. (a) Schematic of the liquid-crystal optical switch and images of the optical waveguides in the (b) ON and (c) OFF state.

C. *PCB-integrated ammonia gas sensor*

A platform for the formation of low-cost PCB-integrated optical gas sensors has been developed. Regions of polymer waveguides integrated onto PCBs are left exposed to the air and are coated with chemical dyes that are sensitive to the presence of specific analytes (Fig. 3a). The sensor operation relies on the change in optical absorption of the dye-coated waveguide region as a function of the concentration of the analyte's molecules in the air. The use of waveguide arrays coated with different dyes can further enable detection of multiple gases from a single chip and the generation of a "behaviour fingerprint" for each analyte of interest. As a proof-of-principle, polymer multimode waveguides are fabricated on FR4 substrates and functionalised with chemical dyes that are sensitive to the presence of ammonia (NH_3) (Fig. 3) [8]. Linear sensor operation is achieved with both good reversibility and repeatability and with sensitivities of approximately 30 ppm. The potential to detect multiple analytes from a single device is also demonstrated using principal components analysis (PCA).

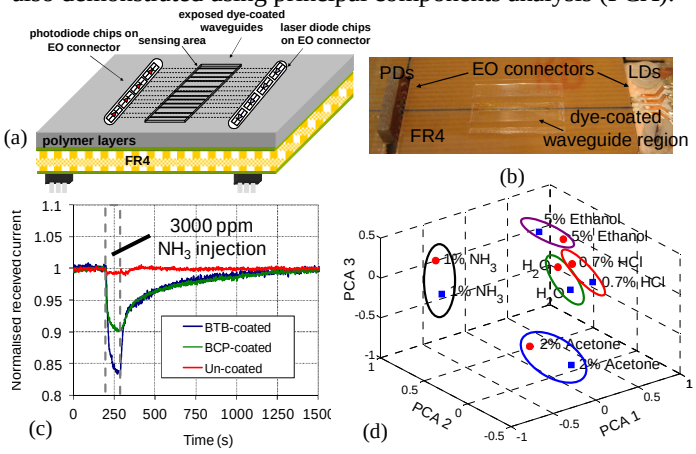


Figure 3. (a) Schematic of PCB-integrated optical sensor, (b) image of realised proof-of-principle demonstrator, (c) typical response to NH_3 presence and (d) results of PCA analysis on the sensor response to different analytes .

IV. CONCLUSION

Multimode polymer waveguides constitute a promising candidate for use in board-level optical interconnections as they can be cost-effectively integrated onto standard PCBs. The further functionalisation of the optical waveguides with active materials can result in hybrid polymeric photonic devices suitable for use in other application areas. Recent achievements in this field demonstrate the potential of the technology and provide promising incentive for further development.

ACKNOWLEDGMENTS

The authors would like to thank Dow Corning Co. for the provision of the polymer materials and the Electronics Development Workshop at the University of Cambridge for the production of the PCBs.

REFERENCES

[1] J. Bautista, "The potential benefits of photonics in the computing platform," in *Optoelectronic Integrated Circuits VII*, pp. 1-8, 2005.

[2] P. Pepeljugoski, et al., "Data center and high performance computing interconnects for 100 Gb/s and beyond," in *OFC/NFOEC*, pp. 1-3, 2007.

[3] H. Ma, et al., "Polymer-based optical waveguides: Materials, processing, and devices," *Advanced Materials*, vol. 14, pp. 1339-1365, 2002.

[4] M. P. Immonen, et al., "Investigation of environmental reliability of optical polymer waveguides embedded on printed circuit boards," *Microelectronics Reliability*, vol. 47, pp. 363-371, 2007.

[5] J. V. DeGroot Jr., "Cost-effective optical waveguide components for printed circuit applications," in *Passive Components and Fiber-based Devices IV*, pp. 678116-12, 2007.

[6] N. Bamiedakis, et al., "Optical transceiver integrated on PCB using electro-optic connectors compatible with pick-and-place assembly technology," in *Optoelectronic Interconnects and Component Integration IX*, pp. 76070O-11, 2010.

[7] J. Beals IV, et al., "Electro-optic integration of liquid crystal cladding switch with multimode passive polymer waveguides on PCB," in *CLEO/QELS*, pp. 1-2, 2009.

[8] N. Bamiedakis, et al., "Low-cost PCB-integrated polymer waveguide sensor for gas detection," in *CLEO/QELS*, pp. 1-2, 2011.

Monolithically integrated filtered-feedback multi-wavelength laser with Mach-Zehnder modulators

Jing Zhao[1], Klaas Dijkstra[2], Michael J. Wale[3], Peter Maat[2], Meint K. Smit[1], Xaveer J.M. Leijtens[1]

[1] Eindhoven University of Technology, COBRA, Photonic Integration Group
P.O. Box 513, 5600MB Eindhoven, the Netherlands
[2]Astron Netherlands Institute for Radio Astronomy, Oude Hoogeveensedijk 4, 7991 PD Dwingeloo, the Netherlands
[3] Oclaro, Caswell, Towcester, Northamptonshire, NN12 8EQ, U.K.

***Abstract* - A novel multi-wavelength transmitter monolithically integrated on InP is presented. The device consists of four-channel filtered-feedback multi-wavelength laser and four Mach-Zehnder modulators. The design of the circuit and experimental results will be discussed.**

***Keywords* - Photonic Integrated Circuits; multi-wavelength; transmitter.**

I. INTRODUCTION

Progress in wavelength-division-multiplexing (WDM) technologies for broadband telecommunication systems has raised the demands for integrated laser-modulator transmitters, especially multi-wavelength transmitters, due to their efficiency in increasing the flexibility and reducing the cost of WDM systems. Different integrated transmitters have been reported, such as multi-section hybrid silicon DBR lasers integrated with electro-absorption modulators [1], tunable distributed feedback (DFB) lasers with Mach-Zehnder modulators on InP [2], and tunable distributed Bragg reflector (DBR) laser arrays with electro-absorption modulators (EAMs) on InP [3].

Here we present a novel monolithically integrated multi-wavelength transmitter based on filtered optical feedback and using Mach-Zehnder modulators on InP material. This transmitter is designed in the mature and stable surface ridge active/passive InP-based integration technology of Oclaro Ltd. (UK) [4], and fabricated through a generic multi-project wafer (MPW) run on the JePPIX platform [5].

This paper describes the design and characterization of the transmitter chip as well as the characterization of the analog photonic link formed by one channel of the integrated laser and modulator.

II. INTEGRATED LASER-MODULATOR DESIGN

The circuit design is divided into two parts: the design of a filtered-feedback multi-wavelength laser (FFMWL) [6], and the design of the four identical Mach-Zehnder modulators that are connected to the laser. Fig.1a shows the schematic layout of the transmitter. The FFMWL part consists of four Fabry–Pérot (FP) lasers each formed by a SOA with two multimode interference reflectors (MIRs) [7]. And the FP lasers are wavelength locked through a feedback section with an arrayed waveguide grating (AWG) and a common MIR. The FFMWL can thus emit simultaneously at four channels, of which the lasing wavelength is determined by the AWG. At the left side of each FP laser, the light is routed to a Mach-Zehnder (MZ) modulator for each wavelength channel. Fig. 1b is the microscope photograph of the fabricated multi-wavelength transmitter. This device uses an AWG with 3 inputs and 5 outputs with wavelength channels spaced at 200 GHz (1.6 nm@ λ=1550 nm), and a central wavelength of 1550 nm. The central channel of the 3 inputs ends in the common 1-port MIR to produce the feedback; the other two channels are for characterization only. On the other side, 4 outputs are connected to 4 channels of the FP lasers while phase shifters (PHS) are included to adjust the phase of the feedback. Each FP laser has a 320-μm-long gain section in a 750-μm-long cavity, which produces a 50-GHz FP mode spacing [6]. With curved waveguides the outputs of the FP lasers are coupled to the MZ modulators and each of the modulated signals is guided to the 7° angled anti-reflective coated facet. Two 1×2 multimode interference (MMI) couplers are used as power splitter and combiner for the MZ modulator. The phase shift function in the modulator arm is achieved with a 1-mm-long lumped-element electrode on a 1.2-μm-wide deeply-etched ridge waveguide, through p-i-n doped epitaxial layers which contain the InGaAsP MQW core. The metallization and the waveguide cross-section of the phase shifters are according to the Oclaro design. The two modulator arms can be independently driven. The footprint of the transmitter chip is 2×4 mm^2.

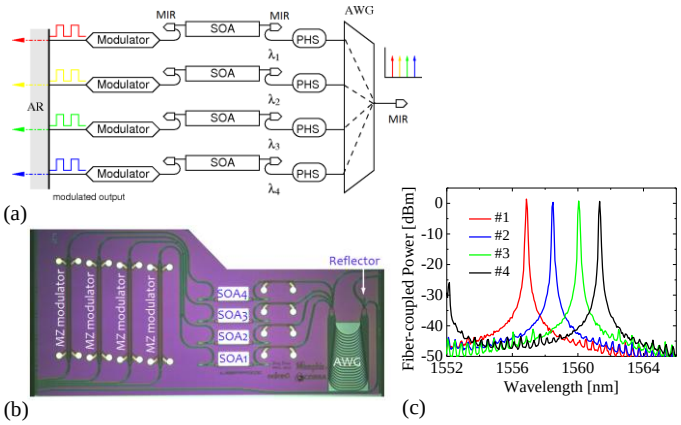


Figure 1 (a) Schematic of the 4-channel transmitter device and (b) Microscope photograph of the realized device. The chip dimension is 2×4 mm^2. (c) Superimposed lasing spectra of the four lasers channels.

III. CHARACTERIZATION

The device is mounted on a copper cold finger platform which in turn is mounted on a thermo-electric cooler (TEC), as shown in Fig. 2a. The TEC and a thermistor are mounted on the same cold finger to stabilize the chip at 20ºC during all the measurements. The chip is 23º tilted in order to allow the lensed fiber coming straight from the bottom in the photograph to couple the light properly from the waveguide with 7º facet angle.

All the electrodes on the transmitter chip have been wire bonded to their corresponding tracks on a custom designed PCB board which is surrounding the copper platform (Fig. 2a). Lasers and phase shifters are connected to laser current driver and voltage control, respectively. For the modulators, the electrodes on input side are bonded to the coplanar waveguide (CPW) on the PCB, where the GSG RF probe can be placed for high frequency measurement, and the electrodes on the output side are bonded to 50 Ω impedance terminations arranged on the PCB, as Fig. 2b indicates.

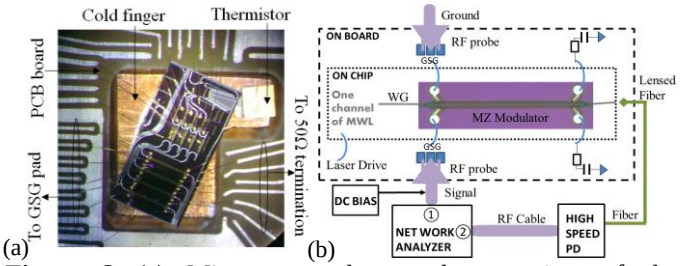


Figure 2 (a) Microscope photograph top view of the transmitter wire bonded with testing board; (b) Schematic for one channel transmitter connection in the photonic link measurement setup.

Firstly four channels of the multi-wavelength laser are measured consecutively with all the modulator electrodes open. Fig. 1c shows the measured lasing spectra with the laser injection current in the range of 75mA to 85mA. A similar measurement on such a FFMWL has been discussed in detail in [6]. Here we concentrate on the measurement with modulators.

The four laser channels operate on wavelengths spaced 200GHz, with slightly different output power. Here we take channel 1 as an example. When the injection current is 85mA, the laser has a CW single wavelength output at 1556.8 nm, with 1.36 dBm optical power in the fiber as measured by an HP 81618A power meter. With this laser as input, the MZ modulator light versus voltage (LV) transfer function is measured for each arm of the modulator, while the other arm is grounded, and the result is plotted in Fig. 3a. The modulator imbalance V_{IMB}, DC extinction ratio ER_{DC}, and voltage for π phase shift, V_π, are labeled in the figure. ER_{DC}≈21 dB, and V_π≈4 V, are similar for all 4 channels of the transmitter, whereas the V_{IMB} varies from 0.3 V to 2 V, due to the imperfect symmetry of the two arms of the modulators.

The small-signal RF EO measurement setup is shown in Fig. 2b. A CW single wavelength output from the FFMWL is fed into the MZ modulator. One arm of the modulator is grounded, and the other arm is connected to the port 1 RF output of the electrical network analyzer (ENA), through

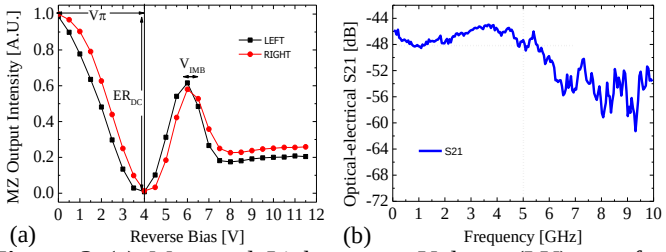


Figure 3 (a) Measured Light versus Voltage (LV) transfer function (alternate arm at 0V); (b) Small signal optical-electrical S21 for the integrated laser-modulator formed photonic link.

GSG RF probe. The modulated optical output coupled from the fiber is routed to a high-speed photodiode (R2560A). The detected signal is sent back to port 2 of the ENA. Thus a microwave photonic link is built [8]. The bias voltage is set to the quadrature point of the modulator, and the input RF signal frequency is swept from 50 MHz to 10 GHz, with -10 dBm power. With the modulator output power at -2 dBm in the fiber, which was the maximum value at the quadrature point, an intrinsic analog photonic link gain is measured around -45 dB up to 5 GHz as shown in Fig. 3b. Although the link gain is largely limited by the output power of the integrated laser, it can be improved by introducing a push-pull drive configuration, optimizing the PCB and using more accurate calibration. This will also help to increase the bandwidth, as the bond wires in this first-version PCB are rather long.

IV. SUMMARY AND ACKNOWLEDGEMENT

The monolithic integration of an FFMWL with MZ modulators on InP is reported for the first time. Characterization of the laser-modulator transmitter mounted on a PCB board was carried out. The modulators have a V_π around 4V and DC extinction ratio of 21 dB. The photonic link formed by this transmitter has an intrinsic gain around -45 dB with 5 GHz bandwidth.

The authors acknowledge the support of the Smart Mix Program of the Netherlands Ministry of Economic Affairs and the Netherlands Ministry of Education, Culture and Science.

REFERENCES

[1] M. Sysak, *et al.*, "Integration of hybrid silicon lasers and electro-absorption modulators," *Opt. Exp., vol. 16, pp. 12478–12486, 2008*

[2] Y. Shibata, "Integration of semiconductor Mach-Zehnder modulator with tunable-wavelength laser diode" *Proc. conference on Lasers and Electro-Optics (CLEO2011)*, May 1-6 2011, Maryland, US

[3] R. Nagarajan, *et al.*, "400 Gbit/s (10 channel ×40 Gbit/s) DWDM photonic integrated circuit", *Electron. Lett.*, vol.41, pp. 347-349, 2005

[4] A. J. Ward, *et al.*, "Widely Tunable DS-DBR Laser With Monolithically Integrated SOA: Design and Performance", *IEEE J. Quantum Electronics* vol. 11, no. 1, Jan./Feb. 2005

[5] X. Leijtens, "JePPIX: the platform for InP-based photonics," *IET Optoelectronics*, vol. 5, pp. 202—206, 2011.

[6] J. Zhao, *et al.*, "Monolithic Integrated Filtered-feedback Multi-wavelength Laser" *Proc. Optical Fiber Communication Conference (OFC 2012)*, March 4-8, 2012, Los Angeles, California, US.

[7] E. Kleijn, *et al.*, "MMI reflectors with free selection of reflection to transmission ratio," *Proc. the 15th Annual Symposium of the IEEE Photonics Benelux Chapter*, Nov.18-19, 2010, Delft, The Netherlands.

[8] C.H. Cox, "Analog Optical Links Theory and Practice", 2004, Cambrighe University Press.

Generic InP-Based Monolithic Photonic Integration Platforms

F. M. Soares, K. Janiak, N. Grote
Photonic Components department
Fraunhofer Institute for Telecommunications, HHI
10567 Berlin, Germany
norbert.grote@hhi.fraunhofer.de

D. Szymanski, M. J. Wale
Oclaro Technology Ltd, Caswell, Towcester Northampton-shire, NN12 8EQ, UK

Mike.Wale@oclaro.com

***Abstract*—The capability of two InP-based, generic platforms for the fabrication of Photonic Integrated Circuits (PICs) is described. Examples of several different complex PICs, fabricated using industrial process facilities will be given.**

I. INTRODUCTION

In the photonic components arena photonic integration, both hybrid and monolithic, has regained enormous momentum since the past decade in order to cope with the steadily increasing demand for more and more complex devices (e.g. for phase-modulation transmission), lower-footprint, reduction of assembly effort and lower power consumption. So far, however, this field is characterized by a wide range of proprietary, application-specific integration technologies and, owing to the limited production volumes for each one, the entry cost for new users and products is often high. To mitigate this fragmentation, the introduction of standardized photonic integration technology relying on well defined building blocks is considered an attractive solution, eventually facilitating a generic foundry operation for photonic integrated circuits (PIC), including Multi-Project Wafer runs [1, 2]. In pursuit of such a revolutionary approach, which rendered silicon microelectronics so extremely successful, two major European projects, EuroPIC [3] and PARADIGM [4], have recently been launched. Across the two projects, a total of more than 20 partners are collaborating to join their complementary skills in design, software development, InP based epitaxy and processing technologies, characterization, packaging and, last but not least, applications. The present paper focuses on the InP integration platforms for which the "foundry" partners, Oclaro and Fraunhofer-HHI, are mainly responsible.

II. PLATFORM CAPABILITIES

The InP platforms currently provided by these project partners are targeting C-band applications. HHI's platform uses a semi-insulating substrate to essentially enable high-speed receiver type PIC structures. Oclaro's PIC process, on the other hand, is being developed from the "transmitter side" relying on N^+-substrate technology. In PARADIGM both platforms will be mutually extended to incorporate transmitter and receiver functionalities, respectively. Table I provides an overview of (composite) buildings blocks currently available at each partner. All of the building blocks are described in a comprehensive Design Manual that has been compiled by the EuroPIC consortium and made available to EuroPIC users to generate their own PIC designs. The list of building blocks designed for C-band operation will be steadily extended, particularly through the PARADIGM project, where partner TU Eindhoven/COBRA will also be developing a platform for extended-wavelength (up to ~ 2 µm) applications.

TABLE I. OCLARO's AND HHI's CURRENT INP PLATFORMS

(Composite) building blocks	Oclaro	HHI
Substrate	N^+-InP	InP:Fe
Waveguide, ridge type, weak and strong guiding	X	X
Waveguide transition elements	X	X
Waveguide crossing	X	X
Isolation slots	X	X
Curved waveguides, S-bend	X	
Circular arc		X
Y-coupler		X
Waveguide spot-size converter	X "3 µm" spot	X "10 µm" spot
Phase shifter	X carrier injection	X thermo-optic
Electro-optic phase modulator	X reverse bias	
pin PD	X dc, low band-width (10 GHz)	X high band-width (40 GHz)
Balanced pin PD		X 40 GHz
MMI coupler	X 1x2, 2x2	X 1x2, 2x2, 1x4
SOA	X	
Tunable DBR grating	X	

Key element of HHI's receiver platform is a waveguide integrated pin photodiode that has already been under development and optimization for many years. The p-i-n structure is located on top of a semi-insulating waveguide comprised of a stack of quaternary and InP layers, which again are formed on an InP:Fe substrate to facilitate very high-speed operation. 40 GHz bandwidth is guaranteed. Three rib waveguides with different index contrasts are offered. Optical transitions between those waveguides are defined as separate building blocks. On the basis of such waveguides a variety of passive optical building blocks are available, such as Y-junctions, crossings, bends and also thermo-optic phase shifters. Furthermore, the waveguides can be designed with spot-size converters ("tapers") providing "10 µm" mode expansion for optimal fiber coupling. With regard to composite building blocks, the platform contains Multimode Interference (MMI) couplers as well as balanced PDs (40 GHz).

Oclaro's platform is based on the integration process developed over many years and used commercially for devices such as tunable laser-Mach Zehnder PICs employed in tunable XFP-format transceivers [6]. Again, it provides a generic monolithic integration process that supports integration of basic blocks and their application in a number of composite building blocks, as listed in Table I. A library-based, building-block approach allows complex optical sub systems to be designed and realized, including semiconductor laser- and modulator based PICs operating up to >10GHz or 10Gb/s.

III. PIC IMPLEMENTATIONS

A broad range of PICs have been designed covering both optical communication and sensors applications. Respective chips were fabricated on 3-inch wafers utilizing the aforementioned generic building blocks and a Multi-Project Wafer (MPW) run approach.

Figure 1 displays a chip that was made on HHI's platform and which is to form the core of a read-out unit for Fiber-Bragg-Grating (FBG) sensors. It incorporates an AWG, an array of 4 Mach-Zehnder Interferometer delay line structures and a 5-array waveguide-integrated balanced photodetectors (BPD). Figure 2 shows a detector chip for the demodulation of 28 Gbaud quadrature phase-shift keying (QPSK) signals. It is comprised of a 2x4 MMI 90° hybrid with tapered input waveguides and two balanced PD pairs [5]. Though not specifically developed in EuroPIC the same fabrication process was used for this PIC which is already exploited in commercial products proving the relative maturity of the technology.

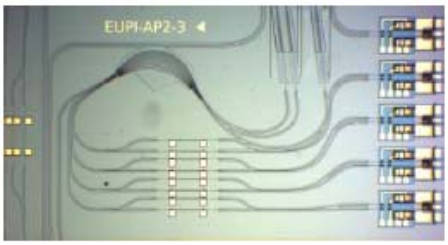


Figure 1. FBG read-out chip (HHI platform; proposal/design: FiberSensing/Bright Photonics)



Figure 2. 28GBaud QPSK receiver chip (HHI)

Two representative PICs made on the Oclaro N+-platform are shown in Figure 3, illustrating how a common foundry process may serve completely different applications. An AWG-based optical pulse shaper for bio-imaging (Fig. 3 left) comprises passive waveguide elements integrated with electro-optical phase modulators and Semiconductor Optical Amplifiers (SOAs). Fig. 3 (right) shows a multi-wavelength transmitter for application in a Fibre-to-the-Home (FTTH) network. It integrates eight Distributed Bragg Reflector (DBR) lasers with four Mach-Zehnder modulators. The light from eight channels is multiplexed and coupled to a single output channel by an AWG. The transmitter exhibits a wide open eye with extinction ratio >24 dB at 12.5 Gb/s after transmission through 20 km of fibre.

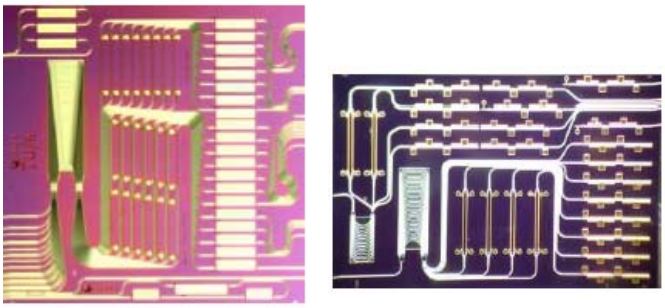


Figure 3. Pulse shaper for a bio-imaging microscope (left), and hybrid TDM-WDM transmitter PIC (right). Designs: TU Eindhoven, PIC fabrication: Oclaro

IV. CONCLUSIONS AND ACKNOWLEDGEMENTS

Funded by the European Commission a joint development is being undertaken to establish generic foundry services for the fabrication of InP based application-specific PICs in Europe. MPW runs were successfully conducted at Oclaro and Fraunhofer-HHI demonstrating the viability of this approach.

Funding from the European Community's 7th Framework Programme FP7/2007-2013 under grant agreement NMP 228839 (EuroPIC) and ICT 257210 (PARADIGM) is gratefully acknowledged.

[1] JePPIX Roadmap 2012: The road to a multi-billion Euro market in InP-based Integrated Photonics (to be found e.g. via [3], [4])

[2] M. Smit et al., "A Generic Foundry Model for InP-based Photonic ICs", OFC 2012 (Los Angeles, March 2012), category 8, invited paper (to be published)

[3] http:// europic.jeppix.eu

[4] http://paradigm.jeppix.eu

[5] H.G. Bach et al., "100 Gb/s Photoreceivers for Coherent and Direct Detection", OFC 2011 (Los Angeles, March 2011), paper OML1 (invited paper).

[6] A. Carter, "Unlocking the value of fab ownership", Compound Semiconductor, **16** (1), February 2010, pp. 34-37.

Experimental confirmation of universal relations for microring resonators in SOI technology

Wouter J. Westerveld, Suzanne M. Leinders,
Koen W.A. van Dongen, H. Paul Urbach
Department of Imaging Science and Technology
Delft University of Technology, Fac. of Applied Sciences
Lorentzweg 1, 2628 CJ Delft, The Netherlands

Jose Pozo, Remco A. Nieuwland
Technical Sciences Expertise Centre, TNO
PO Box 155, 2600AD, Delft, The Netherlands

Mirvais Yousefi
Photonic Sensing Solutions
P.O. Box 146003, 1001LC, Amsterdam, The Netherlands

***Abstract*— We present a detailed characterization of a set of microring resonators with bent radii of 1.5 µm, fabricated in silicon-on-insulator technology. Results are in good agreement with the universal relations for coupling between microresonators and dielectric waveguides.**

Optical ring resonators, silicon on insulator (SOI)

I. INTRODUCTION

Photonic microring resonators in silicon-on-insulator (SOI) technology have gained substantial academic as well as industrial interest over the last decade, for example in the fields of sensing and telecommunications [1]. The high index contrast allows for a small device footprint, and industrial CMOS lines offer the possibility of cost-effective mass-production. In 2000, Amnon Yariv published [2] elegant universal relations for coupling between microresonators and dielectric waveguides, and we demonstrate the validity of this model for extremely small resonators in this work.

We designed a set of racetrack-shaped ring resonators (Fig. 1) with a straight section of 10 µm and a very small bend radius of 1.5 µm (circumference l = 30 µm). Such a shape is required for specific applications such as local and directional sensing of mechanical strain [3], but also comes with severe losses. The track consists of Si-in-SiO_2 waveguides with a cross-section of 450 nm by 220 nm, which are fabricated at IMEC via ePIXfab. Light is evanescently coupled from a connecting waveguide to the racetrack by separating the two guides only 200 nm apart over a length L. The transmission spectrum of the connecting waveguide shows dips at the resonance wavelengths of the track, and the shape of these dips strongly depends on the amount of light coupled to the track with respect to the loss of light in the resonator round-trip.

II. THEORY

The resonator is depicted in Fig. 1, to which light is evanescently coupled from the single-mode input waveguide. We describe this coupling with the matrix notation for a lossless coupler [2]

$$\begin{pmatrix} b_1 \\ b_2 \end{pmatrix} = \begin{pmatrix} te^{i\phi_t} & \kappa e^{i\phi_\kappa} \\ -\kappa e^{-i\phi_\kappa} & te^{-i\phi_t} \end{pmatrix} \cdot \begin{pmatrix} a_1 \\ a_2 \end{pmatrix}, \qquad (1)$$

where (a_1,a_2), and (b_1,b_2) represent the modal amplitudes in the waveguides as depicted in Fig. 1. The coupling amplitudes of

This work was supported by TNO and by the IOP Photonic Devices programme of NL Agency of the ministry of EconomicAffairs. We also gratefully acknowledge the EU-funded ePIXfab for wafer-scale fabrication of the devices.

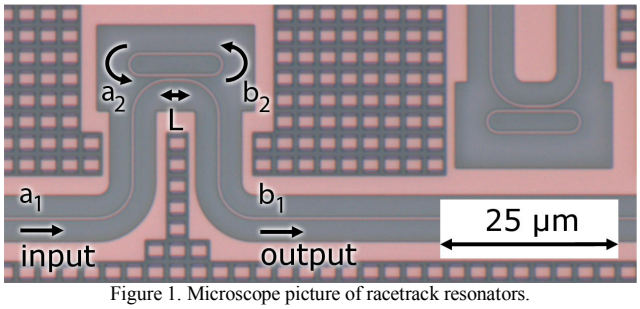


Figure 1. Microscope picture of racetrack resonators.

the light that goes straight through the coupler, t, and the light that is coupled to the racetrack, κ, obey the relation for power conservation: $\kappa^2 + t^2 = 1$. The light that is coupled to the racetrack makes a round-trip described by $a_2 = \alpha\, e^{-i\theta} b_2$, where α is the amplitude transmission, and θ is the phase delay. We express the total phase delay of the monochromatic light (vacuum wavelength λ) traveling a round-trip through the racetrack waveguide in terms of its effective index n_{eff}

$$\theta + \phi_t = n_{\text{eff}}(\lambda)\ 2\pi/\lambda \cdot l \qquad (2)$$

where it is assumed that the effective index in the coupler region is equal to the effective index of the waveguide. The strong modal dispersion of silicon waveguides is assumed linear around λ_c = 1550 nm, so that we can write the wavelength dependent effective index as

$$n_{\text{eff}} = n_{\text{eff}}(\lambda_c) + \frac{\partial n_{\text{eff}}}{\partial \lambda}(\lambda - \lambda_c). \qquad (3)$$

The effective group index, $n_g \equiv n_{\text{eff}} - \lambda \cdot \partial n_{\text{eff}}/\partial\lambda$, is introduced to describe this relation. The power in the output waveguide, $|b_1|^2$ is calculated from Eq. (1)

$$|b_1|^2 = \frac{\alpha^2 + |t|^2 - 2\alpha|t|\cos(\theta+\phi_t)}{1+\alpha^2|t|^2\cos(\theta+\phi_t)}|a_1|^2 \qquad (4)$$

Light at the output waveguide b_1 is minimal at the resonance

$$n_{\text{eff}}/\lambda_m \cdot l = m \qquad (5)$$

Where Eq. (4) reads

$$|b_1|^2 = \frac{(\alpha - t)^2}{(1-\alpha t)^2}|a_1|^2 \qquad (6)$$

Transmission dips to zero, or critical coupling, occurs when the straight-through power t^2 in the coupler is equal to the round-trip power transmission α^2 in the resonator.

The light is coupled to the racetrack by means of a directional evanescent field coupler, as depicted in Fig. 2. The

coupling between the incoming wave a_1 and the outgoing wave $b_1 = t\, a_1$, is given by [5]

$$|b_1|^2 = \cos^2(K(L + L_0))|a_1|^2 \qquad (7)$$

where K is the coupling coefficient that depends on the overlap between the fields of the two modes, i.e. the waveguide dimensions and separation. The coupling that already occurs in the bends of the directional coupler waveguide is accounted by introducing the effective coupler length $L+L_0$.

III. Results and Conclusions

Separate devices are fabricated to characterize the directional couplers, see Fig. 2 (right). The straight-through transmission t of the directional couplers is characterized by measuring the power from a_1 to b_1 and from a_3 to b_3 for couplers with various lengths L. Light is coupled from optical fibers to the waveguides via an out-of-plane grating coupler [4], and the alignment is automated to provide high repeatability of the power coupled in-and-out of the circuit. The parameters of the coupler K and L_0, as well as in-coupling $|a_1|^2$, as described in Eq. (7), are fitted to the measured spectra. The characterization of the coupler is presented in Fig. 2 (left).

For the characterization of the microracetrack resonators, the parameters in Eq. (4) are fitted to the measured spectra. The track length l and coupling κ (from Fig. 2) are fixed and all other parameters are fitted. The resolution bandwidth of the optical spectrum analyzer is incorporated in this fitting by convoluting the spectrum as calculated with Eq. (4) with a Gaussian curve with a full-width-half-max of 20 pm. An accurate initial guess of n_{eff} and n_g (the positions of the dips) in Eq. (4) is necessary for the Levenberg-Marquardt fitting algorithm. The mode number m is estimated from Eq. (5) where the effective index n_{eff} was calculated using a mode solver (film mode matching method in FimmWave, PhotonDesign). The resonance dips where found using *findpeaks* [6] and from this n_{eff} and n_g are estimated via Eq. (5).

The resonance dip closest to a vacuum wavelength of 1550 nm is presented in Fig. 3, for a set of racetracks with a varying length of the directional coupler. It is clearly seen that under-coupling (small lengths) or over-coupling (long lengths) lead to shallow resonance dips, while the close-to critical coupled racetracks shows an extinction of -25 dB.

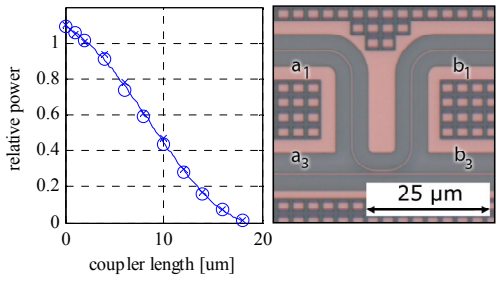


Figure 2.(right) Microscope picture of an individual directional coupler. (left) Transmitted power as function of the coupler length. o is $a_1 \rightarrow b_1$, x is $a_3 \rightarrow b_3$, and the solid line is fitted.

In conclusion, the measured transmission spectra of our microracetrack resonators are in good agreement with the universal relations for coupling between microresonators and dielectric waveguides as presented by Yariv.

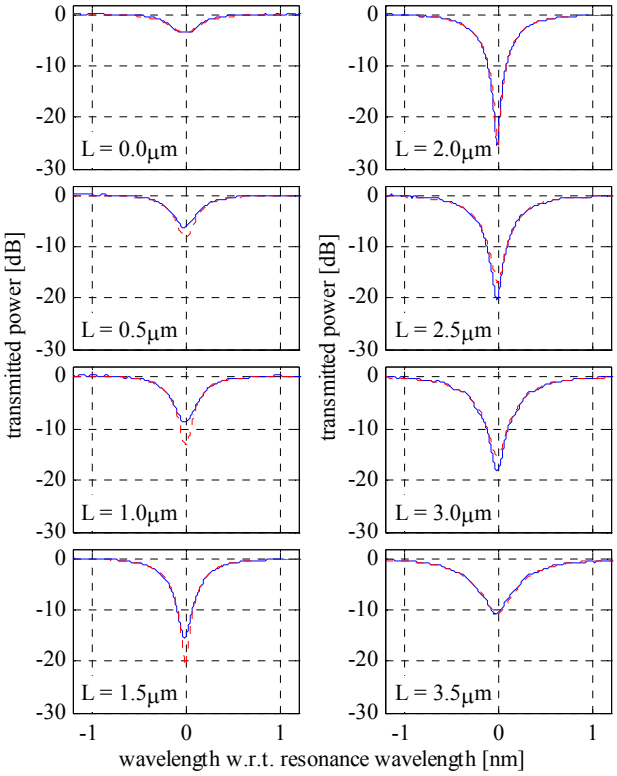


Figure 3. Measured spectra of the racetrack resonators with incrasing length L of the evanescent coupler section. Dashed lines indicate the fitted spectra.

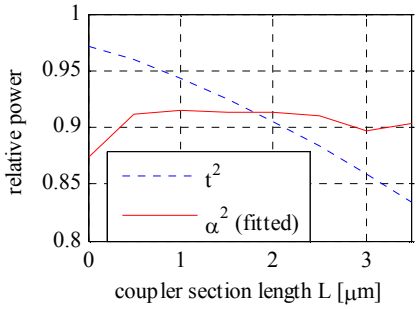


Figure 4. Fitted ring transmission (-0.4 dB) versus coupler length (solid), also coupling through power (dashed). Critical coupling occurs at the crossing.

References

[1] W. Bogaerts *et al*, Laser and Photonic Reviews **6**, 47 (2012)

[2] A. Yariv, Electronic Letters **36**, 321 (2000).

[3] W.J. Westerveld *et al*, Optics Letters **37**, 479 (2012).

[4] W.J. Westerveld *et al*, IEEE J. of Quantum Electronics **47**, 561 (2011).

[5] C. Pollock and M.Lipson, Integrated Photonics (Kluwer, 2003).

[6] *findpeaks* by Tom O'Haver (www.wam.umd.edu/~toh/, 2012)

Grating couplers for Si_3N_4 waveguides at 900 nm

A.Z Subramanian[1], S. Selvaraja[1], P. Verheyen[2], A. Dhakal[1], K. Komorowska[1], and R.Baets[1]
[1]Photonics Research Group, INTEC department
Centre for Nano and Biophotonics, Ghent University
9000, Ghent, Belgium
[2]imec, Kapeldreef 75, 3001 Leuven, Belgium

***Abstract*— We demonstrate a 1-D grating coupler for silicon nitride wires with an average efficiency of 7 dB in the 890-910 nm wavelength range. The effect of etch depth on the grating efficiency is presented and compared with the theoretical results.**

Keywords-Grating coupler, Silicon nitride ,Silicon photonics, Integrated optics, Fiber coupler

I. INTRODUCTION

Grating couplers (GCs) enable efficient coupling from optical fibres to photonic integrated components (PICs) without the need of using lenses or inverted tapers [1]. They avoid expensive methods such as end-polishing and the use of lens fibre to couple light into the waveguides, and also allows wafer level testing of PICs. GCs with high efficiency have been successfully demonstrated for telecom wavelengths and have become a standard practice for coupling light in and out of PICs in silicon photonics [2-3]. However, GCs for a high index contrast (HIC) platform at visible or near-visible IR wavelengths have not been investigated in detail. The visible and near-visible IR bands are important for several applications such as sensing and spectroscopy [4], especially in a biological context given the high penetration depth of light in tissue in these bands. Visible wavelengths also avoid water absorption band which helps in preventing cell damage at high powers. GC-based PICs will help in realizing efficient and easy-to-use integrated spectrometers and sensors. Silicon nitride (Si_3N_4) is a versatile HIC platform for its transparency in both visible and infrared spectrum. Besides it is compatible with the well established CMOS process technology therefore enabling low-cost photonic devices much like in silicon photonics.

In this paper, we present the design, fabrication and theoretical calculations for the GC for Si_3N_4 based PICs in the 890-910 nm band. Finally we report the experimental results on the coupling efficiency and its dependence on the wavelength, coupling angle, and etch depth of the grating.

II. GRATING COUPLER DESIGN

Design and fabrication of silicon based PICs for telecommunication is well established and standardized. However, silicon cannot be used for visible wavelengths owing to strong absorption below 1.1 µm. Si_3N_4 (n~2.0) is transparent in the visible region and at 900 nm the effective wavelength inside the medium is approximately equal to that of silicon (n~3.5) at 1550 nm. This equivalence makes available the existing standard silicon PIC design and masks (at 1550 nm) to be used for Si_3N_4 applications at 900 nm.

For designing GCs, a cross-section of 220 nm × 450 nm was used to define the core of Si_3N_4 waveguide. For this dimension, Si_3N_4 waveguide was single mode at 900 nm. The two GCs were connected together by 4 mm long waveguide 10 µm wide (at the start and end) and tapered down to 450 nm. The GC period and fill factor (pitch/period) was fixed at 630 nm and 0.55 respectively. The etch depth of GCs (65-220 nm), coupling angle (8°-12°) and the wavelength (890-910 nm) were left as free parameters to maximize the coupling efficiency. The gratings were designed for TE polarisation, using CAMFR, an eigenmode expansion tool [5]. The underlying oxide thickness has a major influence on the coupling efficiency. Its value is chosen in such a way that the downward radiated light which gets reflected at the oxide/substrate interface interferes constructively with the direct upward radiated light. This effect is depicted in Fig. 1 for the central wavelength (900 nm) of the coupler. Based on this result the oxide thickness was fixed at 2.5 µm.

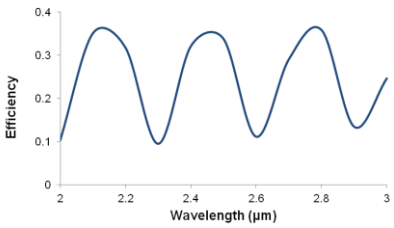


Figure 1. Effect of buried oxide thickness on the coupler efficiency

III. FABRICATION AND CHARACTERISATION

A. *Si_3N_4 deposition and grating fabrication*

For the fabrication, 200 mm bare Si wafer is used as the substrate. Plasma enhanced chemical vapor deposition is used to first deposit 2.5 µm of silicon dioxide (SiO_2) followed by 220 nm of Si_3N_4. The SiH_4, N_2 and NH_3 gas flow was optimized for Si_3N_4 deposition at 400^oC, which ensured CMOS back-end compatibility. After layer deposition, the waveguide and the GCs were patterned by using 193 nm optical lithography and reactive ion etch process. The waveguide was 220 nm deep etched, and GCs were patterned with different etch depths by controlling the etch duration. Photoresist is used as an etch mask for both the etch processes. After dry etching, the wafers were cleaned by using oxygen plasma and a wet chemical process. Finally, after pattering wafers some of the wafers were covered with 1.5 µm of SiO_2.

This work is supported by the ERC grant InSpectra

Lastly, the dies were cleaved from the wafer for optical characterization.

B. Optical characterisation of waveguide and GCs

All measurements were performed by coupling light from a tunable laser source (890-910 nm) using single mode fibre into the Si_3N_4 waveguides. Another similar fibre is positioned above the output GC to collect the light and connected to the power meter. Both the fibres were mounted on a goniometer controlled stage to change the tilt angle. The coupling efficiency is determined from the fibre-to-fibre transmission for the TE polarisation. The position of the fibre is optimized for the maximum transmission. The waveguide loss was measured by measuring the change in fibre-to-fibre transmission through spirals of different length (1-7 cm, with bend radius 10 μm).

IV. Results and Discussion

The average propagation loss in the uncladded and cladded Si_3N_4 wire was measured to be 3.75 dB/cm and 1.9 dB/cm over the wavelength range of 890-910 nm. The GC efficiency was extracted by subtracting the waveguide loss contribution from the total fiber-to-fiber transmission loss. The efficiency was measured for uncladded samples for four different GC etch depths- 65 nm, 95 nm, 145 nm, and 220 nm and each of those was measured at different tilt angles- 8°, 10° and 12°. Fig. 2 shows the GC efficiency variation with respect to the grating etch depth at 909 nm for 10° tilt angle. There is good correspondence between the theory and experimental results except for the 220 nm etched GC. This discrepancy can be attributed to the high reflection loss for fully etched structures as shown by the calculated reflection loss in fig.2 below.

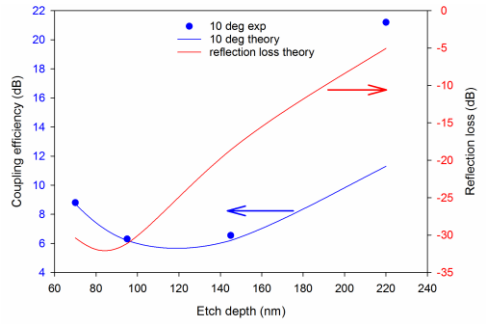


Figure 2. Experimental (blue circle) and theoretical (blue line) coupler efficiency, and reflection loss (red line) vs. etch depth at 909 nm at 10° angle

The best efficiency was recorded for 100 and 145 nm etch GCs at 12° and 8° tilt angle. Fig. 3 shows the GC bandwidth over a 80 nm wavelength span and compares it with the experimental results (890-910 nm) for the variation of GC efficiency at different tilt angles for 100 nm and 145 nm etch depths. Theoretically the best efficiency (4-5 dB) is observed at longer wavelengths (920-930 nm) than used in the experiments. The period of the grating can be optimised to shift the efficiency peak to the desired wavelength range as for the current work the standard SOI GC design was used for the Si_3N_4 GCs as well.The discrepancy between the theory and the experiment (890-910 nm) is attributed to the variation (~250 nm) in the absolute value of the buried oxide thickness leading to reduced efficiency than predicted by the theoretical model. It is equally important to mention here that these experiments were performed without using index matching fluid (IMF) and it is expected that using IMF would reduce the reflection losses and further improve the efficiency. Nevertheless, an efficiency in the range of of 6-8 dB was achieved in the 890-910 nm wavelength range with 145 nm etched GC at 8° launch angle. It is worthwhile to mention here that Si_3N_4 is a deposited material therefore it is possible to further boost the efficiency to <1.5 dB by depositing a mirror underneath the grating to 100% reflect the downward radiated light [4-5].

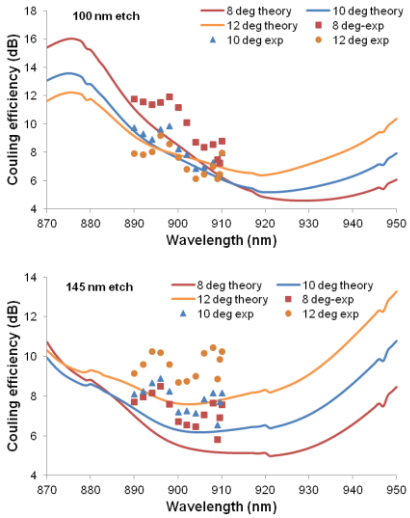


Figure 3. Coupler efficiency vs. wavelength at different tilt angles for 100 nm (top) and 145 nm etched (bottom) GC.

In conclusion, to our knowledge a GC at near-visible wavelengths has been demonstrated for the first time using Si_3N_4 waveguide with an average coupling efficiency of 7 dB.

References

[1] T. Shoji, T. Tsuchizawa, T. Watanabe, K. Yamada, and H. Morita, "Low loss mode size converter from 0.3 μm square Si wire waveguides to singlemode fibres," Electron. Lett., vol. 38, pp. 1669–1670, 2002.

[2] F. Van Laere, et al., "Compact and highly efficient grating couplers between optical fiber and nanophotonic waveguides," J.Lightw. Technol., vol. 25, pp. 151–156, 2007.

[3] D. Taillaert, W. Bogaerts, P. Dumon, D. Van Thourhout, and R. Baets, "Bridging the gap between nanophotonic waveguide circuits and single mode optical fibers using diffractive grating structures," J. Nanosci. Nanotechnol.,vol. 10, pp. 1551–1562, 2010.

[4] D. Taillaert, P. Bienstman, and R. Baets, "Compact efficient broadband grating coupler for silicon-on-insulator waveguides," Opt. Lett., vol. 29, pp. 2749-2751, 2004.

[5] S. Selvaraja et al, Highly Efficient Grating Coupler between Optical Fiber and Silicon Photonic Circuit,Conference on Lasers and Electro-Optics (CLEO) 2009 , United States, p.CTuC6 (2009)

[6] I. M. White, J. Gohring, and X. Fan, "SERS-based detection in an optofluidic ring resonator platform," Opt. Exp., vol. 15, pp. 17433-17442, 2007.

[7] P. Bienstman and R. Baets, "Optical modelling of photonic crystals and VCSELs using eigenmode expansion and perfectly matched layers," Opt.Quantum Electron., vol. 33, pp. 327–341, 2001.

Manipulation of telecom photon path and polarisation in lithium niobate devices

Mirko Lobino, Damien Bonneau, Pisu Jiang,
Mark G. Thompson, and Jeremy L. O'Brien
Centre for Quantum Photonics, H. H. Wills Physics Laboratory & Department of Electrical and Electronic Engineering
University of Bristol
Bristol, United Kingdom

Chandra M. Natarajan, Michael G. Tanner, and Robert H. Hadfield
Scottish Universities Physics Alliance and School of Engineering and Physical Sciences
Heriot-Watt University
Edinburgh, United Kingdom

Sanders N. Dorenbos and Val Zwiller
Kavli Institute of Nanoscience,
Technische Universiteit Delft
Delft, The Netherlands

Abstract— **We demonstrate fast polarisation and path control of photons at 1550 nm in lithium niobate waveguide devices using the electro-optic effect. A common technological platform is used to show heralded single photon state engineering, fast two photon state preparation and feedback control of quantum interference. These results point the way to a single platform that will enable the integration of nonlinear single photon sources and fast reconfigurable circuits for future photonic quantum information science and technology.**

Keywords-component; **quantum information, quantum photonics, quantum interference.**

I. INTRODUCTION

Integrated optical circuits are a promising approach for the implementation of optical quantum information protocols [1]. Manipulation of single photons in optical waveguide have been recently demonstrated in reconfigurable circuit that work at visible wavelength and use slow thermo optical phase shifters [2].

Fast operation of reconfigurable waveguide circuits at telecom wavelengths is crucial for their integration with the existing optical telecom networks as well as to benefit from the technologies developed in that area.

A fast electro-optic effect and a consolidated technology for the fabrication of low loss waveguides at telecom wavelengths using either proton exchange or titanium indiffusion (Ti:LN) makes lithium niobate (LN) an appealing platform for fast reconfigurable quantum photonic devices. Lithium niobate is used in telecommunications networks where 40 GHz modulators are standard and polarization manipulation based on the electro-optic effect have also been demonstrated for bright light [3,4]. Furthermore lithium niobate is particularly appealing for the prospect of directly integrating periodically poled waveguide photon sources [5] on a single substrate.

This work was supported by Nokia, EPSRC, ERC, PHORBITECH, QUANTIP, NSQI, FOM, and NWO (Vidi grant). M. L. acknowledges a Marie Curie IIF. R.H.H. acknowledges a Royal Society University Research Fellowship. J. L. O'B. acknowledges a Royal Society Wolfson Merit Award.

Here we demonstrate fast polarization and path control of photons at 1550 nm using a common technology based on lithium niobate electro-optical devices [6].

II. EXPERIMENTAL SET-UP

A. Photon generation and detection

Photon pairs at 1550 nm wavelength were generated by spontaneous parametric down-conversion (SPDC) in a bismuth borate (BiBO) crystal and collected into two polarization maintaining optical fibers [see Fig. 1(a)]. Superconducting single photon detectors (SSPDs) [7] provide telecom wavelength single photon sensitivity with low dark counts and high timing resolution in the experiments presented here.

B. Single photon path manipulation

Figure 1(b) shows the experimental setup used for heralded single photon state preparation. One photon from a pair is measured directly by an SSPD providing the trigger signal for the pulse generator that controls a Mach-Zehnder interferometer (MZI).

For every trigger event, a voltage pulse was sent to the MZI with a controllable delay. This pulse induced a relative phase shift which prepares the single photon in a superposition of being in the two possible output of the MZI. We drove the MZI with a voltage pulse of 20 ns duration and 4 ns rise time that switched between a π, corresponding to the identity transformation, to a 0 phase shift, for the swap transformation, which routed the photon to the second SSPD.

By measuring the number of heralded counts as a function of the delay applied to the driving pulse we reconstructed the time response of the interferometer and measured a switching efficiency of 97.9±0.1%.

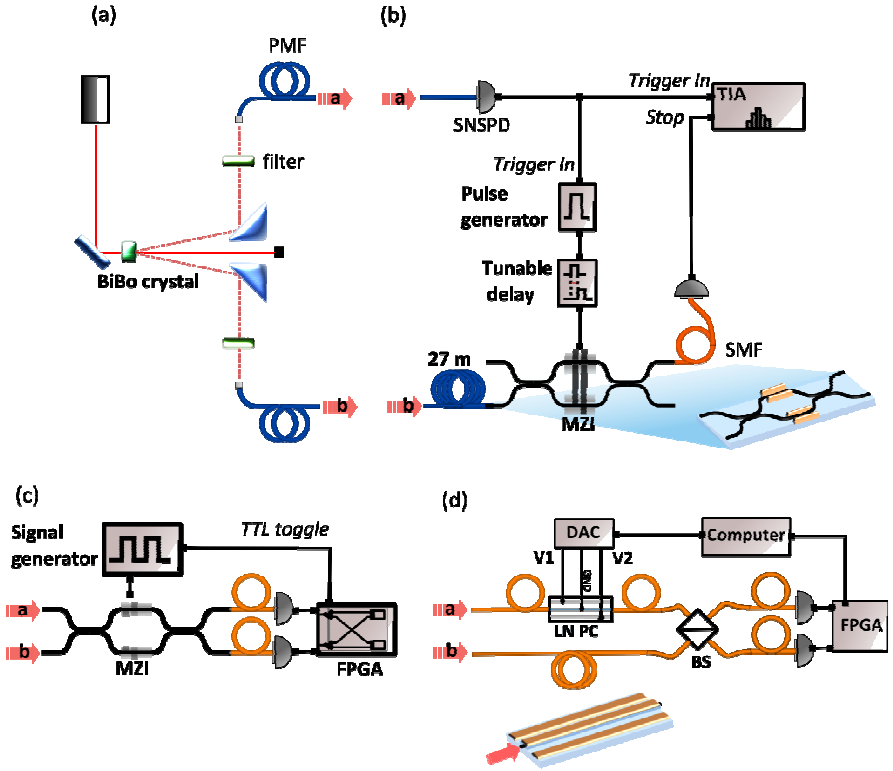


Figure 1: Fast path and polarisation control of single photons in lithium niobate waveguides.

C. *Two photon state preparation*

Figure 1(c) shows the scheme for the fast switching of a two-photon entangled state. Two photons from the same pair are injected in the two inputs of the MZI. A signal generator drives the MZI with square waves alternating between two voltages V(0) and V(π/2) at 4 MHz. These voltages correspond to a crosser and a balanced beam splitter configuration respectively.

Coincidental events for the two voltages are recorded in separate counters embedded in a field programmable gate array (FPGA) board. In the case where the MZI acts as a balanced beam-splitter, quantum interference occurs and the two photon NOON state is prepared. By delaying the arrival of one photon with respect to the other we were able to show the NOON state preparation in a Hong-Ou-Mandel dip measurement [8]. On the contrary when the MZI acted as a crosser, the number of coincidence counts was independent on their relative delay.

D. *Polatization manipulation*

Using a lithium niobate polarization controller driven by two voltages, we manipulate the polarization of single photons to implement a feedback loop for robust quantum interference between two paths which interfere on a beam splitter [Fig 1 (d)].

We demonstrate a bidimensional quantum interference pattern in the number of coincidental events recorded after the beam splitter as a function of the two driving voltages. Starting from random overlap in polarization between the two photons, we then use a gradient descent algorithm to iteratively choose the two applied voltages and demonstrate recovery of the quantum interference.

III. CONCLUSIONS

Rapid manipulation of the polarization and path degrees of freedom of single photons will be essential for future quantum technologies as well as fundamental quantum science. The ability to perform both path and polarization manipulation in a single platform is particularly appealing. Furthermore, lithium niobate promises the ability to directly integrate periodically poled LN single photon sources. Ultimately it should also be possible to integrate SSPDs into the waveguide circuit via growth of NbTiN directly onto LN substrates [9].

REFERENCES

[1] J. L. O'Brien, A. Furusawa, J. Vučković, *Nat. Photon.* **3**, 687 (2009).

[2] P. Shadbolt *et. al.*, *Nat. Photon.* **6**, 45 (2012).

[3] A. J. P. van Haasteren, J. J. G. M. van der Tol, M. O. van Deventer, and H. J. Frankena, *J. Lightwave Technol.* **11**, 1151 (1993).

[4] N. G. Walker and G. R. Walker, *J. Lightwave Technol.* **8**, 438 (1990).

[5] A. Martin *et al.*, *New J. Phys.* **12**, 103005 (2010).

[6] D. Bonneau *et. al.*, *Phys. Rev. Lett.* **108**, 053601 (2012).

[7] R. H. Hadfield, *Nat. Photon.* **3**, 696 (2009).

[8] C. K. Hong, Z.Y. Ou, and L. Mandel, *Phys. Rev. Lett.* **59**, 2044 (1987).

[9] S. N. Dorenbos *et al.*, *Appl. Phys. Lett.* **93**, 131101 (2008).

Laser written waveguides in KTP for broadband Type II frequency doubling

Fredrik Laurell, Carlota Canalias
Department of Applied Physics, KTH,
Albanova, Roslagstullsbacken 21,
106 91 Stockholm, Sweden
fl@laserphysics.kth.se

Thomas Calmano, Sebastian Müller, Günter Huber
Universität Hamburg, Institut für Laser-Physik, Luruper Chaussee 149, 22761 Hamburg, Germany
tcalmano@physnet.uni-hamburg.de

***Abstract*— Femto-second laser writing was used to fabricate waveguides in KTP with losses below 0.8 dB/cm. They were used for efficient broad bandwidth, Type II frequency doubling of cw Ti-sapphire laser radiation at 1080.4 nm.**

Keywords; laser written waveguides, low loss, broad bandwidth, KTP, type II frequency doubling

I. INTRODUCTION

$KTiOPO_4$ (KTP) is widely used in nonlinear optics thanks to its large nonlinear optical coefficients, good mechanical properties and strong optical damage resistance. Its extraordinary wide phasematching bandwidth for noncritical Type II frequency doubling with fundamental wavelengths around 1 μm has made it the material of choice for green laser [1]. High quality waveguides has been fabricated in KTP by Rb ion-exchange [2] and spontaneous domain reversal of the ion-exchanged region can be obtained, which has been utilized for fabrication of segmented waveguides for very efficient quasi-phase matching (QPM) [3]. However, these waveguides have reproducibility and stability problems [4]. Recently laser written waveguides were made in periodically poled KTP and used for frequency doubling [5],[6]. These were stable with circular mode-fields and used for fs-laser frequency doubling. However, the losses were much higher than for ion-exchanged waveguides, the phasematching bandwidth was narrower and the normalized conversion efficiency was far from ideal.

Three dimensional micro-structures can be fabricated in several dielectrics utilizing nonlinear absorption processes with focused femtosecond lasers [7]. Channel waveguides are made by focusing the laser radiation inside the sample, while the sample is translated. Simple straight waveguides as well as more complex passive structures as splitters and couplers have been made this way [8],[9]. Active devices like lasers and amplifiers have been obtained in rare-earth doped glasses, and crystalline hosts like Nd:YAG and Yb:YAG. The low loss has made it possible to obtain lasing with high slope efficiency (75%) and an output power of nearly 0.8W [10].
In this paper we present a modified laser waveguide writing procedure, which provide low loss, single-mode waveguides in KTP. These were used for Type II frequency doubling and provided broadband phasematching with close to ideal efficiency.

II. WAVEGUIDE FABRICATION

A set of x-propagating channel waveguides were produced in a z-cut flux grown KTP crystal ($10\times5\times1$ mm^3). Laser pulses at 775 nm with a pulse duration of 150 fs, and a repetition rate of 1 kHz were focused 150 μm below the polished surface of the crystals using an aspheric lens (N.A.=0.55). The crystal was translated transversally in the focused beam (spot size, 2 μm ($1/e^2$)) with a motorized translation stage at a velocity of 25 μm/s. The threshold for material modification was about 0.6 μJ and a pulse energy of 2.5 μJ was used to form the tracks/waveguides described below. Several different pairs of parallel tracks were inscribed in the sample and the distance between two adjacent tracks was changed between 16 μm and 25 μm to obtain waveguides with different width. After polishing the final length of the sample was 9.5 mm.

III. WAVEGUIDE CHARACTERISATION

The characteristic of laser written waveguides is the guiding next to the damaged region caused by a stress induced refractive index change [8]. When two tracks of damage are written into the crystal, see Fig. 1, guiding can be obtained in six positions around the tracks where the strongest confinements are in position a and b. The damaged regions were in

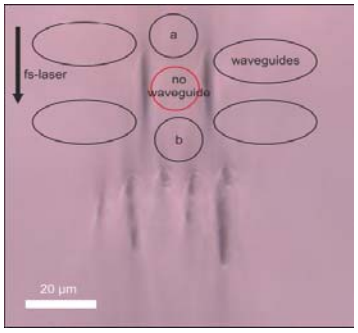


Figure 1 Bright-field microscope image of the end facet of the crystal where a pair of tracks with a distance of 18 μm was written.

this case approx. 21 μm in height and 3 μm in width. The modal properties depend on the track separation and the index modification. With a separation of 20 μm or less fundamental TE and TM modes could be guided, and when the tracks were placed further apart higher order transverse modes were guided. In Fig. 2 the TE near field for the two positions a and b can be seen when light from a HeNe laser was launched through the waveguide. In this case the track separation was 18 μm and the numerical aperture, N.A. =0.06.

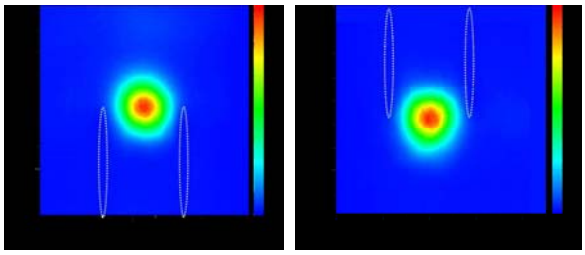


Figure 2.Near field intensity distribution at 633 nm for the two waveguides, a and b, in Fig 1. The tracks are indicated by white dotted lines.

The waveguide losses were quite low for all the waveguides written this way. A conservative upper limit for the single mode waveguides in Fig. 2 were estimated by coupling the HeNe laser through the waveguide and comparing launched and transmitted power. Taking the Fresnel reflections under consideration, but not the coupling losses gave a loss below 0.8 dB/cm for both the TE and the TM mode. A more accurate number must be determined with the interferometric technique developed by Regener and Sohler [12].

IV. Frequency Doubling Experiments

The waveguide was evaluated in a Type II frequency doubling experiment using a continuous wave Ti-Sapphire laser as the fundamental source. The condition for birefringent phasematching is obtained as,

$$\frac{1}{2}\left[n_z(\lambda_F) + n_y(\lambda_F)\right] = n_y(\lambda_F/2)$$

where the refractive indices are given by the Sellmeier's equations for KTP and d_{24} = 7.6 pm/V is the appropriate nonlinear coefficient [1]. This gives a bulk phasematching wavelength, λ_F, of just above 1080 nm at room temperature. As the index increase for these stress-induced waveguides is below 10^{-3} this means that the waveguide phasematching also should be obtained around this wavelength. Unfortunately this is in a wavelength region where the laser power has dropped to quite a low level. The Ti-sapphire radiation was rotated 45 degrees to simultaneously excite the TE_{00} and the TM_{00} mode and coupled into the waveguide with a 10x objective. The radiation at the output was collected with a 20x objective and imaged on a calibrated power meter. 7.3 μW of green light in the TE_{00} mode was generated with 8.0 mW at 1080.4 nm. It corresponds to a normalized efficiency of 11.5%/W, which is higher than what has been obtained previously using laser written waveguides in KTP, despite that those were done with QPM utilizing substantially higher nonlinear coefficients [5],[6].

Noncritical Type II phasematching for bulk KTP has a temperature bandwidth of 175°/cm [1]. A preliminary measurement of the bandwidth for our waveguides, when the sample was heated from room temperature to 80°, was in good agreement with this number. It should be compared to the temperature bandwidth for QPM frequency doubling, which is below 1°/cm in the same wavelength range.

V. Conclusions and Outlook

Femto-second laser writing was used to fabricate waveguides in KTP with losses below 0.8 dB/cm at 633 nm. Type II frequency doubling generated 7.3 μW of green light for 8.0 mW of input radiation at 1080.4 nm from a cw Ti-sapphire laser. This corresponds to a normalized conversion efficiency of 11.5%/W. The bandwidth for this process is so wide that no temperature control was required.

Further work, to be presented at the conference, will include frequency doubling using a high power, narrow linewidth, polarized, tunable, CW Yb- fiber laser as the source.

Acknowledgments

We acknowledge support from the Linneus Center ADOPT financed by the Swedish Research Council, the Deutsche Forschungsgemeinschaft and the Joachim Herz Stiftung.

References

[1] J. D. Bierlein and H. Vanherzeele, "Potassium titanyl phosphate: properties and new applications", J. Opt.Soc. Am. B., **6**, 622 (1989).

[2] M. G. Roelofs, P. A. Morris, and J. D. Bierlein, "Ion exchange of Rb, Ba, and Sr in $KTiOPO_4$", J. Appl. Phys. **70**, 720 (1991).

[3] F. Laurell, J. B. Brown, and J. D. Bierlein, "Sum-frequency generation in segmented KTP waveguides", Appl. Phys. Lett. **60**, 1064 (1992).

[4] F. Laurell, "Periodically poled materials for miniature light sources," Opt. Maters. **11,** 235 (1999).

[5] S. Campbell, R. R. Thomson, D. P. Hand, A. K. Kar, D. T. Reid, C. Canalias, V. Pasiskevicius, and F. Laurell, "Frequency-doubling in femtosecond laser inscribed periodically-poled potassium titanyl phosphate waveguides", Opt. Express, **15**, 17146 (2007).

[6] C. Tu, Z. Huang, K. Lou, H. Liu, Y. Wang, Y. Li, F. Lu, H.T. Wang, "Efficient green-light generation frequency doubling of a picosecond all-fiber ytterbium-doped fiber amplifier in PPKTP waveguide inscribed by femtosecond laser direct writing", Opt. Expr., **18**, 25183 (2010).

[7] B. C. Stuart, M. D. Feit, S. Herman, A. M. Rubenchik, B. W. Shore, and M. D. Perry, "Nanosecond-to-femtosecond laser-induced breakdown in dielectrics", Physical Review B **53** (4), 1749 (1996)

[8] S. Nolte, M. Will, J. Burghoff, A. Tuennermann, "Femtosecond waveguide writing: a new avenue to three-dimensional integrated optics" Applied Physics A: Materials Science & Processing, **77**, 1 (2003)

[9] K. Suzuki, V. Sharma, J. Fujimoto, E. Ippen, and Y. Nasu, "Characterization of symmetric [3 x 3] directional couplers fabricated by direct writing with a femtosecond laser oscillator," Opt. Express **14**, 2335 (2006).

[10] T. Calmano, J. Siebenmorgen, , O. Hellmig, K. Petermann, G. Huber, "Nd:YAG waveguide laser with 1.3 W output power, fabricated by direct femtosecond laser writing", Applied Physics B, **100**, 1 (2010).

[11] T. Calmano, J. Siebenmorgen, A. Paschke, C. Fiebig, K. Paschke, G. Erbert, K. Petermann, and G. Huber, "Diode pumped high power operation of a femtosecond laser inscribed Yb:YAG waveguide laser [Invited]," Opt. Mater. Express **1**, 428 (2011).

[12] R. Regener and W. Sohler , "Loss in Low-Finesse Ti $LiNbO_3$ Optical Waveguide Resonators", Appl. Phys. B **36**, 143 (1985).

C-band Performance of a Novel Tunable Integrated Filter for Dispersion Compensation

Abdul Rahim, Jürgen Bruns, Klaus Petermann
Fachgebiet Hochfrequenztechnik,
Technische Universität Berlin, Einsteinufer 25,
10587,Berlin, Germany
Email: abdul.rahim@tu-berlin.de

Stefan Schwarz, Christian G. Schäffer
Fakultät für Elektrotechnik,
Lehrstuhl für Hochfrequenztechnik,
Helmut-Schmidt-Universität, Holstenhofweg 85
22043 Hamburg Germany

***Abstract*—A novel dispersion compensating filter comprising higher order MMI couplers is fabricated in SOI platform. Characterization of the filter has shown that it can compensate residual dispersion for WDM channels over the entire C-band.**

***Index Terms*—Dispersion Compensation, Multimode Interference Coupler, Silicon-on-Insulator**

I. Introduction

In integrated optics, various basic and advance filtering operations have been realized. Mostly they involve 2-port couplers. Realization of future filter applications using 2-port couplers will lead to complex filter architectures. [1] and [2] have proposed filters for signal processing applications using higher order couplers but they have not been experimentally demonstrated. Filters involving higher order couplers will require smaller number of couplers and smaller waveguide lengths. This will result in compact filters with smaller loss.

Silicon photonics provides higher order Multimode Interference (MMI) couplers with low imbalance and small phase errors over the entire C-band [3]. Such higher order couplers are imperative for the realization of advance filtering applications. We have experimentally demonstrated a filter for fiber chromatic dispersion compensation using 4-port MMI couplers in silicon photonics. Chromatic dispersion is the major cause of Inter Symbol Interference (ISI) at high data rates in Standard Single Mode Fiber (SSMF). ISI can be eradicated by pre or post compensation of dispersion using dispersion compensating filter.

II. Filter Description and Design

A generalized waveguide layout of an N stage filter for dispersion compensation using symmetric M-port MMI couplers is shown in Fig. 1. Each stage is composed of an M-port Mach-Zehnder Interferometer (MZI) as shown by the dotted section in Fig. 1. The first MMI coupler splits the input signal distorted by chromatic dispersion into M equal components. They are time delayed, recombined and split by each stage of the filter. The dispersion compensated signal is received at one of the output ports of the last MMI coupler. Remaining output ports of the last MMI couplers are used for monitoring purpose. By adjusting the phase of the time-delayed signals on the delay lines, the filter produces different linear group delay slopes for a certain fraction of the filter Free Spectral Range (FSR) making the filter tunable [4].

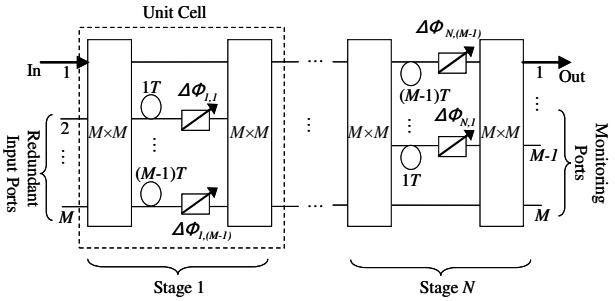


Fig. 1. Waveguide layout of a generalized filter comprising M-port MMI couplers. A single stage is shown in the dotted section. Ports with arrows are for input and output. Other ports are either redundant or used for monitoring purpose.

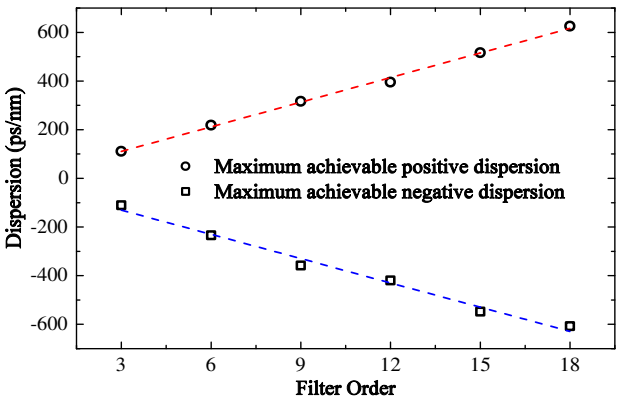


Fig. 2. Relation of attainable dispersion from a filter comprising M-port MMI couplers vs the filter order.

The maximum achievable dispersion from the filter depends on the order R of the filter. For a given group delay ripple and fraction of filter FSR with linear group delay slope, the attainable dispersion increases with an increase in the order R of the filter. In order to have a linear group delay for at least 40 % of the filter FSR and a group delay ripple of less than ± 3 ps, fig. 2 shows the relationship of the maximum achievable filter dispersion and the order R of the filter. The filter order

R, defined as $N(M-1)$ for the filter shown in fig. 1, can be increased by either increasing the order *M* of the MMI coupler or the number of stages *N*. The two approaches lead to a compromise between the performance and loss of the device. Former approach degrades the filter performance due to more susceptibility to fabrication tolerance and bandwidth limitation of the higher order MMI coupler, which is related inversely with the order of the MMI coupler. Latter approach leads to filter with large loss resulting from the large overall waveguide length for the filter.

We have realized a filter which is composed of three 4-port MMI couplers, which are connected by delay lines. It is a 6th order filter. The filter is designed to have an *FSR* of 100 GHz. 4-port MMI couplers provide a good compromise between the performance and loss of the filter. Phase shifting elements are embedded on the delay lines by using thermo-optic effect in metallic heaters. The filter is fabricated in 4 μm Silicon on Insulator with 1 μm buried oxide.

III. Results and Discussion

The fabricated device is characterized for transmission and group delay. A laser signal swept with a wavelength increment of 3 pm is in and out coupled by using lensed fibers. Modulation Phase Shift (MPS) method is used for the measurement of group delay. The polarization of the input signal is adjusted at the tip of the in-coupling fiber. Polished facets and lensed fibers limit the coupling loss to 0.5 dB per facet. The insertion loss originating from the waveguide loss and excess loss of the MMI couplers is 6 dB.

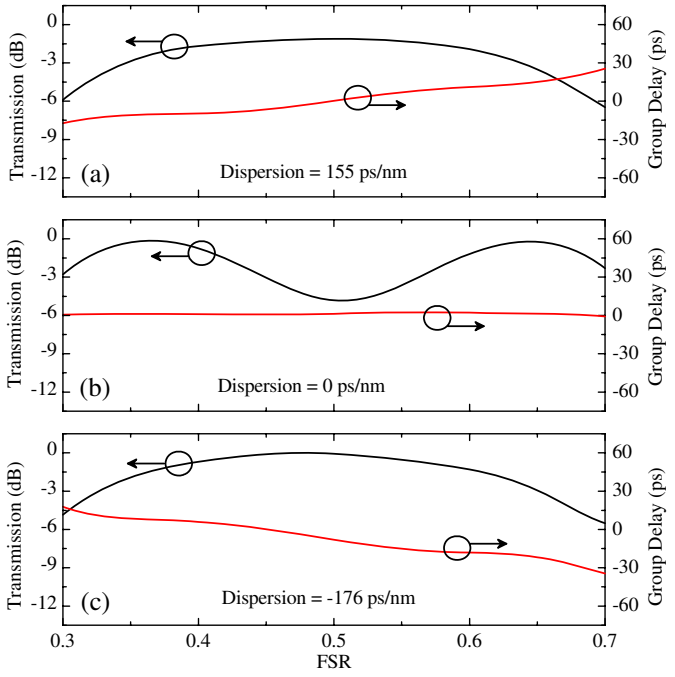


Fig. 3. Measured transmission (solid, black) and group delay slope (solid, red). Fraction of the filter *FSR* with positive (a), zero (b) and negative (c) dispersion for the fabricated filter.

Measurement results for only TE polarization are presented here because the fabricated device is not subjected to birefringence tuning. Fig. 3 is a measurement result, which shows the fraction of the filter *FSR* that has a linear group delay slope. The filter is tuned to compensate positive, no and negative residual dispersion as shown in fig. 3 (a), (b) and (c) respectively. In each FSR, the group delay is linear for atleast 0.32 nm (40 % of the filter *FSR*), which is sufficient to compensate residual dispersion for 40 Gbps WDM systems. The group delay ripple for the tuned filter stays below $\pm$ 5 ps.

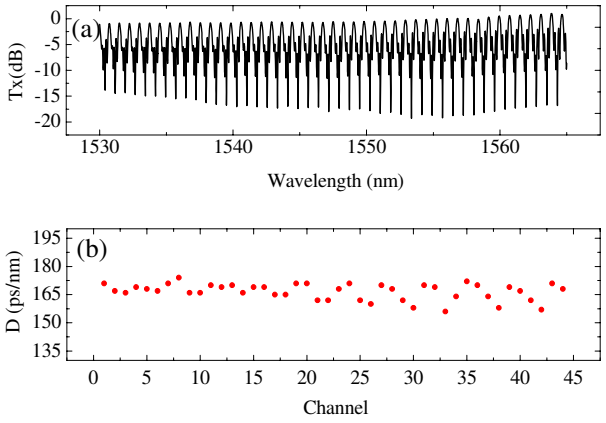


Fig. 4. (a) Measured transmission over a bandwidth of 35 nm (44 WDM channels) in the C-band, (b) Variation in filter dispersion for group delay ripple of less than $\pm$ 5 ps with more than 40 % of filter *FSR* with linear group delay.

To characterize the filter in C-band, measurement result in fig. 3 (c) is performed from 1530 nm to 1565 nm (44 WDM channels). Fig. 4 (a) shows the measured transmission for the filter. The variation in insertion loss is around 1.5 dB. Fig. 4 (b) shows the variation in filter dispersion for 44 WDM channels in the C-band. For a group delay ripple of less than $\pm$ 5 ps with more than 40 % of filter *FSR* with linear group delay, the maximum variation in filter dispersion is only 18 ps/nm.

IV. Conclusion

We have demonstrated the performance of a novel dispersion compensating filter over the entire C-band. 40 % of the filter *FSR* has a linear group delay with less than $\pm$ 5 ps of group delay ripple. The variation in dispersion for multiple WDM channels is only 18 ps/nm.

Acknowledgment

The authors would like to thank the financial support of German Research Foundation (DFG).

References

[1] C. Doerr et al., IEEE Photon. Technol. Lett., Vol. 17, No. 12, 2005.
[2] G.Cincotti, Opt. Lett, Vol. 36, No. 12, 2010.
[3] K. Voigt et al., Group IV Photon. 2008, pp. 209-211.
[4] A.Rahim et al., OFC 2012, OTh4D.4.

Active plasmonics based on phase change materials

R. E. Simpson, J. Renger, M. Rude, R. Quidant, V. Pruneri
ICFO-Institut de Ciencies Fotoniques,
Mediterranean Technology Park,
Castelldefels (Barcelona), Spain
robert.simpson@icfo.es

***Abstract*- Phase change materials are suggested as a means to attenuate surface plasmon polariton waves. In particular, the transmitted power was attenuated by 7 dB using the prototypical phase change material Ge2Sb2Te5.**

Keywords- Phase Change; plasmonics; Modulation; Nanophotonics

I. INTRODUCTION

The surface plasmon resonance is the collective oscillation of charge at the interface between two materials with dielectric constants of opposite sign. Usually, the resonant frequency of this interfacial charge occurs at visible or near infra-red frequencies. The surface plasmon polariton (SPP), is a guided wave of the electronic charge that is able to propagate at the interface between the two materials. The propagation constant of the surface plasmon at the boundary of a semi-infinite dielectric and a metal is given by expression (1).

$$\beta = k\sqrt{\frac{\epsilon_m n_s^2}{\epsilon_m + n_s^2}} \qquad (1)$$

where k is the wavenumber of the metal, ε_m the dielectric constant of the metal ($\varepsilon_m = \varepsilon'_m + i\varepsilon''_m$) and n_s is the refractive index of the dielectric. The SPP wave is guided when $\varepsilon_m < -n^2_s$ [1]. It follows that modulation of the SPP is possible by changing the refractive index of the dielectric such that in one state the $\varepsilon_m < -n^2_s$ and in the other state $\varepsilon_m \approx -n^2_s$.

Phase chase data storage materials, which are usually based on chalcogenide materials, exhibit large changes in refractive index when switched between their covalent and resonant bonding states [2-3]. The prototypical phase change material $Ge_2Sb_2Te_5$ (GST), for instance, can be switched with a 20 fs laser pulse [4] from a refractive of $n \approx 6.5 + i1.4$ to $n \approx 4.0 + i0.1$ [6]. Furthermore, for this particular type of material the structural phase can be switched back and forth 10^9 times [6] yet is stable at stable at temperatures below 85 °C for periods of years [5]. The most recent phase change material research, however, has concentrated on its use in electrical phase change random access memory (PCRAM)- a technology which due to the phase change material's short switching time [5], cycleability [5] and scalability [7] is a strong candidate to replace FLASH memory. Individual bits are written to the phase change memory cell using electrical Joule heating to induce the phase change. The electrical resistivity changes by several orders of magnitude and can thus be read electrically.

In the case of GST, the large change in optical properties is attributed to a change in the local atomic coordination of the Ge atoms. In one state the Ge atoms are predominantly octahedrally coordinated by Sb and Te atoms [9] with p-orbital bonds aligned with adjacent molecular units [3]. The p-orbital electrons are effectively delocalized between atoms leading to a high polarisability and consequently, a large refractive index. In the other state, the p-orbital alignment is lost and a substantially lower refractive index is observed [2,3,9]. The energy necessary to change the bonding state of all the atoms in the phase change material (PCM) scales with its volume thus PCMs are well suited to nano scale switching applications such as nanophotonic modulators and memories.

Generally, the losses of SPP waves restrict their useful transmission range to just a few hundred microns [10]. However, even with these high losses SPP waves do hold some promise for novel memory and processing concepts where a high density of phase change memory cells are located within the useful range of the SPP wave. Research in this field is still in its early stages with most of the most prominent work employing the different solid-solid phase transitions of Gallium [11]. However, basing the plasmonic phase change technologies around chalcogenide materials has the added advantage of allowing the phase change to be detected using the change in optical and electrical properties thus allowing hybrid photo-electronic devices, which might find use in future computing technologies. Herein, the potential of plasmonic modulation via a thermally induced phase transition in GST is discussed.

II. EXPERIMENTS

The samples were prepared on silica glass substrates (200 um) with the following structure: a Ti seed layer (30 nm), a gold layer (60 nm), a silica layer (190 nm) and finally the GST layer. The Ti and gold layers were deposited by thermal evaporation whilst the silica layer was deposited from an SiO_2 target in an Argon atmosphere of 0.25 Pa. The GST layer was formed by sequentially depositing 0.5 nm thick GeTe and Sb2Te3 layers in an argon atmosphere or 0.5 Pa. The input and output gratings were fabricated in the resultant structure by focussed ion beam milling. The grating line width was 0.2 µm whilst the pitch was 1.025 µm. Output gratings, of the same structure, were milled at distances varying from between 200 µm and 40 µm from the input grating. A schematic of the resultant structure is given in figure 1. The GST was deposited in a covalently bonded state but focussing 800 nm laser light through a 0.4 NA compound objective, with a optical power of ~40 mW at the sample surface, changed the material to its resonantly bonded state. Finally, prior to measurement, a thin

Poly(methyl methacrylate) film was deposited on the sample surface.

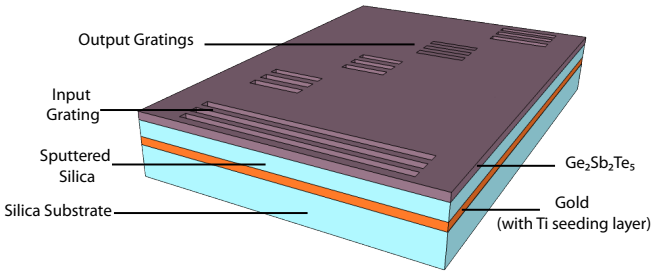


Figure 1: Schematic of the sample used to measure the transmission of surface plasmons polaritons dependence on the bonding state of Ge2Sb2Te5.

SPP waves were excited at the sputtered silica - gold interface by illuminating the input grating with focussed 1550 nm laser light. The light scattered from the output grating was collected in transmission mode using a plasmon leakage microscope. A full description of the set-up can be found in [12]. A CCD camera was used to collect images of the scattered light with 16 bit resolution. Measurement of the scattered light was performed by integrating the intensity measured by the camera across the area of each output grating. A typical image is shown in figure 2.

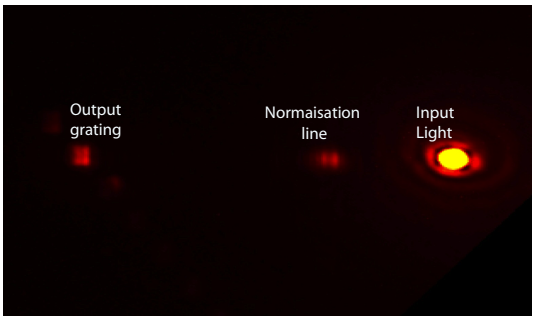


Figure 2: A typical image collected for the transmission of a surface plasmon through using a covalently bonded $Ge_2Sb_2Te_5$ layer.

III. Conslusions

The linear attenuation coefficient, α, of the SPP wave significantly increased from 0.01 μm^{-1} for covalently bonded GST to 0.04 μm^{-1} for resonantly bonded GST; the difference in transmitted intensity of the SPP was approximately 7 dB. Although 7 dB is quite a small change in transmitted power, it is believed that the combination of new phase change materials and a novel sample design will yield useful switchable plasmonic modulators and memory devices that will find new applications in hybrid electro-photonic computing.

Acknowledgment

R. E. Simpson is grateful for his NEST-COFUND fellowship.

References

[1] J. Homola, S. S. Yee, and G. Gauglitz. Surface plasmon resonance sensors: review. *Sensor Actuat B-Chem*, 54:3–15, 1999.

[2] K. Shportko, S. Kremers, M. Woda, D. Lencer, J. Robertson, and M. Wuttig. Resonant bonding in crystalline phase-change materials. *Nature Mater.*, 7 (7):653–658, 2008.

[3] B. Huang and J. Robertson. Bonding origin of optical contrast in phase-change memory materials. *Phys. Rev. B*, 81(2):081204R, 2010.

[4] K. Makino, J. Tominaga, and M. Hase. Ultrafast optical manipulation of atomic arrangements in chalcogenide alloy memory materials. *Opt. Express*, 19(2):1260–1270, 2011.

[5] S. Raoux and M. Wuttig, editors. Phase Change Materials: Science and Applications. *Springer Verlag*, 2008.

[6] R. E. Simpson, P. Fons, A. V. Kolobov, T. Fukaya, M. Krbal, T. Yagi, and J. Tominga. Interfacial Phase-Change Memory. *Nature Nanotech. July*, 6:501 – 505, 2011.

[7] R. E. Simpson, M. Krbal, P. Fons, A. V. Kolobov, J. Tominaga, T. Uruga, and H. Tanida. Toward the ultimate limit of phase change in . *Nano. Lett.*, 10(2): 414–419, 2010.

[8] A. Kolobov, P. Fons, A. Frenkel, A. Ankudinov, J. Tominaga, and T. Uruga. Understanding the phase-change mechanism of rewritable optical media. *Nature Mater.*, 3(9):703–708, 2004.

[9] A. V. Kolobov, M. Krbal, P. Fons, J. Tominaga, and T. Uruga. Distortion-triggered loss of long-range order in solids with bonding energy hierarchy. *Nature Chem.*, 3(4):311–316, 2011.

[10] H. Raether. Surface Plasmons. Springer Verlag, 1988.

[11] K. F. MacDonald, Z. L. Samson, M. I. Stockman, and N. I. Zheludev. Ultrafast active plasmonics. *Nat Photon*, 3(1):55–58, 2009.

[12] J. Grandidier, S. Massenot, G. C. des Francs, A. Bouhelier, J.-C. Weeber, L. Markey, A. Dereux, J. Renger, M. U. Gonzalez, and R. Quidant. Dielectric-loaded surface plasmon polariton waveguides: Figures of merit and mode characterization by image and fourier plane leakage microscopy. *Phys. Rev. B*, 78:245419, Dec 2008.

Wafer-Scale Lithium Niobate on Insulator (LNOI): A New Platform for Integrated Optics

Hui Hu*, Li Gui, Raimund Ricken and Wolfgang Sohler
Applied Physics
University of Paderborn
Paderborn - 33098, Germany
hhu@sdu.edu.cn

***Abstract*—The development of wafer-scale single crystalline thin lithium niobate films on a SiO_2/LN substrate (LNOI) is reviewed. They can serve as a new platform for ultra-compact active integrated photonic devices and circuits.**

Keywords-integrated optics; lithium niobate; photonic wires; periodical poling; second harmonic generation.

I. INTRODUCTION

Optical waveguides of high refractive index contrast – such as the well-developed Silicon-On-Insulator (SOI) "photonic wires" - can have a very small cross section (< 1 μm^2) and bending radius (~ 10 µm), enabling the development of ultra-compact photonic integrated devices and circuits. A corresponding technology for Lithium Niobate-On-Insulator (LNOI) is still in its infancy, though LNOI offers – in contrast to SOI - excellent electro-optic, acousto-optic, and nonlinear optical properties. Moreover, it can be easily doped with rare-earth ions to get a laser active material.

In this contribution, the fabrication of wafer-scale LNOI as a new platform for high-density integrated optics with active devices of high efficiency is reported. Moreover, fabrication and properties of (periodically poled (PP)) LNOI photonic wires are reviewed with the demonstration of Second Harmonic Generation (SHG) as a specific example.

II. FULL WAFER FABRICATION OF LNOI

In analogy to the fabrication of SOI [1], a "smart cut" process was used for the fabrication of single crystalline LN films on SiO_2 on a LN substrate. The full wafer fabrication process is schematically sketched in Fig. 1.

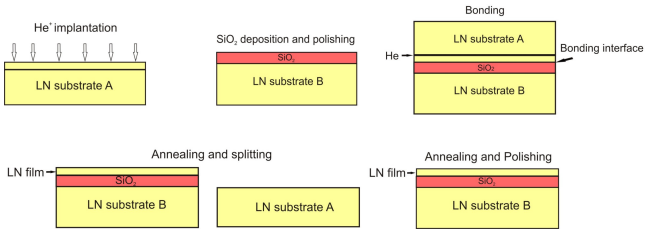


Figure 1. Fabrication scheme of LNOI: a "smart cut" single crystalline LN-film of sub-micrometer thickness is directly bonded to a SiO_2/LN substrate.

At first, a Z-cut LN wafer (A) of 3`` diameter is implanted by 250 keV He-ions with a dose of 4×10^{16} ions/cm^2, forming a thin amorphous layer at ~ 760 nm depth. Another Z-cut LN handle sample (B) is coated by a SiO_2-layer of 1.3 µm thickness by plasma enhanced chemical vapor deposition (PECVD) and then annealed at 450 ^oC for 8 hours. With a chemical mechanical polishing (CMP) process, the surface roughness is reduced from about 6 nm to 0.35 nm enabling direct wafer bonding. The bonded pair of samples is then annealed to improve the bonding strength; by a further increase of the temperature to 228 ^oC for 2 hrs the sample splits along the He implanted layer. Afterwards, it is annealed at 450 ^oC for 8 hours. Fig. 2 presents a LNOI wafer of 3 inch diameter fabricated by the process sketched above. The good homogeneity of the interference colors shows the homogeneity of the fabrication process.

Different sandwich structures with a thin metal electrode either underneath the SiO_2 layer or underneath the $LiNbO_3$ film have also been fabricated. Such structures should enable electric field induced poling and electro-optic control of light propagation. Even LNOI with a MgO:$LiNbO_3$ film has been demonstrated [2].

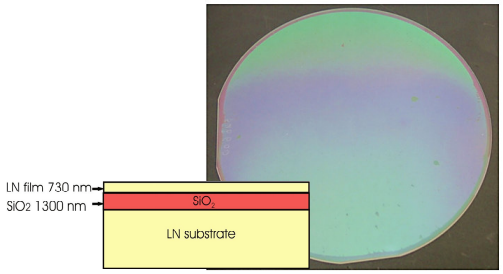


Figure 2. Schematic cross-section (left) and photograph (right) of a LNOI-wafer of 3`` diameter.

III. LNOI PHOTONIC WIRES

A. *Fabrication*

LNOI photonic wires have been fabricated by Ar-milling Fig. 3, left). Photoresist stripes of 1-7 µm width and 1.7 µm thickness were used as etching mask (The etching ratio of LN and photoresist is about 1). Using an Oxford Plasmalab System 100 etching system, photonic wires were defined by

Ar-milling for 60 min with 100 W inductively coupled plasma power and 70 W RF power coupled to the sample table; the result was an etching depth of 460 nm. Fig. 3 (middle) shows a scanning electron micrograph (SEM) of a photonic wire of 1 µm top width. The SiO_2 layer can be seen underneath the LN layer. On both sides of the ridge, etched trenches can be observed resulting from etching by ions reflected by the angled walls of the ridge [3].

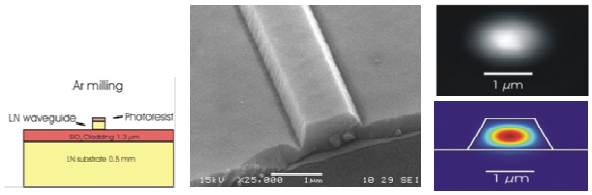


Figure 3. Fabrication scheme of a LNOI photonic wire (left). SEM micrograph of a fabricated structure of 1 µm top width (middle). Measured and simulated qTM-polarized mode distributions (λ = 1550 nm) (right).

B. *Mode Distributions, Dispersion Properties and Losses*

A tunable laser diode was used to investigate the photonic wires around 1550 nm wavelength. Fig. 3 (upper and lower right) shows the measured and calculated mode distribution for quasi TM-polarization of a photonic wire of 1 µm top width, respectively. The waveguide mode dispersion is determined by the material dispersion of core and cladding materials and also by the waveguide dimensions. Some results are displayed in Fig. 4 together with the dispersion of bulk LN and SiO_2. Also the group index has been calculated; it agrees well with the measured one [3]. The measured propagation losses are 9.9 dB/cm for qTM-polarization [3].

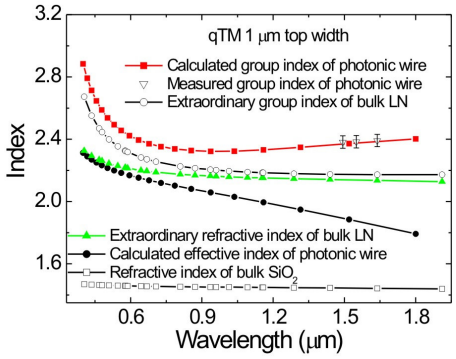


Figure 4. Calculated effective and group indices for the fundamental qTM mode in a photonic wire of 1 µm top width and 730 nm thickness versus wavelength. Measured group indices, calculated group indices of bulk LN, and refractive indices of bulk LN and SiO_2 are shown as well for comparison.

IV. Periodically Poled LNOI (PPLNOI)

A. *Fabrication*

Periodically poled (PP) bulk LN samples (A) (see Fig. 1) of 3.2 and 9 µm periodicity were processed in the same way as described above to fabricate PPLNOI. To get periodically poled photonic wires, Ar-milling was used again. Fig. 5 shows an optical micrograph of a photonic wire with 3.2 µm periodicity.

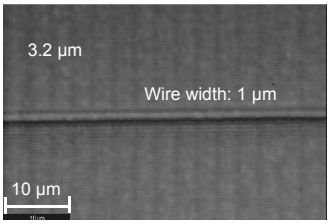


Figure 5. Optical micrograph of a PPLNOI photonic wire and substrate of 3.2 µm periodicity.

B. *SHG in in PPLNOI Photonic Wires*

A 1064-nm narrow-band laser diode of up to 40 mW output power was used to demonstrate quasi phase matched (QPM) second harmonic generation (SHG) in a PPLNOI photonic wire of 9 µm periodicity. The calculations showed that third order QPM type I SHG should be possible in a wire of 1 µm top width and 730 nm thickness. Fig. 6 shows calculated and measured results [4].

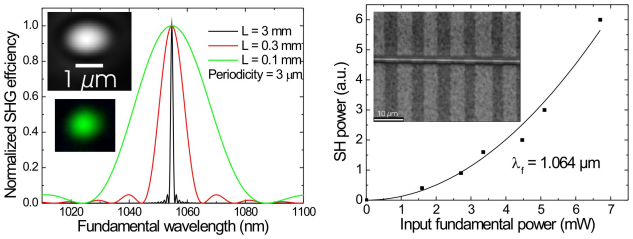


Figure 6. Left: Calculated QPM SHG efficiency for different interaction lengths L. Insets: measured fundamental (1064 nm) and SH (532 nm) mode distributions (qTM). Right: measured (dots) and simulated (solid line) SH power versus fundamental input power. Inset: optical micrograph of a PPLNOI photonic wire of 1 µm top width and 9 µm domain periodicity.

V. Conclusions

The recent development of LNOI has been described. It might become a new platform for ultra-compact integrated photonic devices and circuits [5]. The great potential of LNOI based devices will lead to novel concepts and architectures for high-density integrated optics with highly efficient electro-optical, nonlinear-optical, and laser/amplifier devices.

References

[1] Bruel, M., "Silicon on insulator material technology", Electron. Lett., 31, 1201-1202 (1995)

[2] H. Hu, L. Gui, R. Ricken, W. Sohler,"Towards nonlinear photonic wires in lithium niobate", Proc. of SPIE, Vol. 7064, 7064R, San Francisco, USA, SPIE Photonic West, 2010

[3] Hu, H., Ricken, R. and Sohler, W., "Lithium niobate photonic wires," Opt. Express 17(26), 24261-24268 (2009)

[4] H. Hu, D. Buechter, R. Ricken, and W. Sohler, "Periodically poled LNOI photonic wires", Proc. 15th European Conference on Integrated Optics (ECIO 10), paper FrPD3, Cambridge, UK, 2010

[5] G. Poberaj, H. Hu, W. Sohler, and P. Günter, "Lithium niobate on insulator (LNOI) for micro-photonic devices", Laser Photonics Rev., in press

Demonstration of an ultra-short polarization converter in InGaAsP/InP membrane

J. Pello, J. J. G. M. van der Tol, H. P. M. M. Ambrosius, P. J. van Veldhoven and M. K. Smit
COBRA Research Institute,
Eindhoven University of Technology (TU/e)
Eindhoven, The Netherlands
j.pello@tue.nl

S. Keyvaninia, G. Roelkens
Photonic Research group, INTEC,
Ghent University–IMEC,
Ghent, Belgium

***Abstract*—An ultra-short (< 10 µm length) polarization converter is demonstrated in an indium phosphide based membrane. Measurements show very high polarization conversion efficiency (97 %) with low excess losses (~ 1 dB).**

Keywords: Indium phosphide; integrated optics; polarization converter; triangular waveguide.

I. INTRODUCTION

Membrane photonics platforms have been developed in the past few years to lower the power consumption of photonic chips and increase the density of components they can integrate [1]. However, the typical high-index contrast realized in these platforms results in a strong difference between the propagation properties of the TE and TM polarized modes. In order to avoid problems due to, among others, polarization-dependent dispersion and losses, it is essential to supply these platforms with polarization handling capabilities.

The basic component to control the polarization in photonic integrated circuits is the polarization converter, which enables the conversion of TE polarized light into TM, and vice versa. Recently, several interesting membrane polarization rotators have been demonstrated on the SOI platform. However, they are either relatively long [2], or rely on very tight fabrication accuracy [3].

In this paper, we not only demonstrate the first polarization converter in an InP membrane (a material of special interest since gain materials can be integrated inside to fabricate active devices [1]), we also show that it can be made as short and show performances similar to the best converters made on SOI [2-3], while being potentially more tolerant.

II. THEORY

The design of the polarization converter presented here has been described in detail elsewhere [4]. The device relies on the beating between the two eigenmodes of chemically etched triangular waveguides (see Fig.1). The input polarization state is projected on these eigenmodes and after propagating over the designed distance in two oppositely-loaded triangular waveguides, the new polarization state obtained is rotated by 90° with respect to the input state.

As compared to the design of [4], a rectangular waveguide of length *x* is added between the two triangular waveguides for characterization purposes (cf. section IV).

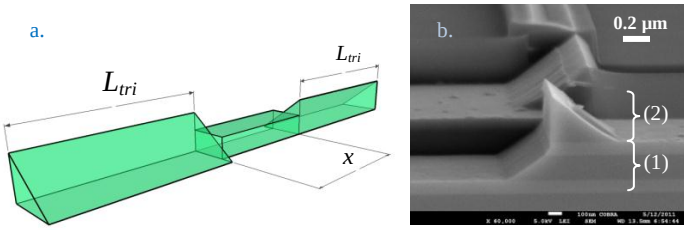


Figure 1. (a.) Schematic and (b.) SEM picture (before bonding) of the presented polarization converter

III. FABRICATION

Like other devices realized previously on the IMOS (Indium phosphide membrane on silicon) platform, the polarization converter presented here is first fabricated using standard lithography, dry-etching and wet-etching steps on a III-V epitaxial layer-stack, before being bonded on a carrier wafer and released from the initial substrate [1].

As shown in Fig. 1b, the layers grown on the InP substrate before the fabrication starts can be separated into a stack (1) (InGaAs-100 nm / InP-200 nm / InGaAs-100 nm), which will be used to protect the membrane during substrate removal, and a stack (2) (InP-250 nm / InGaAsP-20 nm / InP-130 nm), which forms the membrane itself and will contain the devices.

As mentioned in the fabrication plan of [4], the 20 nm-thin InGaAsP layer of the membrane is used to define very accurately two different membrane thicknesses, without damaging the material. After depositing a 50 nm-thick SiN_x layer on the sample by plasma-enhanced chemical vapor deposition (PECVD), an e-beam lithography step, with ZEP520 resist, is used to open this layer in the areas where the membrane should be only 250 nm-thick (e.g. for the input and output rectangular waveguides of the polarization converter). The sample is then etched chemically first in solution (A) 1HCl: $4H_3PO_4$ and subsequently in solution (B) $1H_2SO_4$: $1H_2O_2$: $10H_2O$, to selectively remove the (InP-130 nm / InGaAsP-20 nm) layers from the areas open in the SiN_x layer.

In the following step, the rectangular waveguides and the straight sidewalls of the triangular waveguides of the future polarization converter are defined simultaneously. The previous SiN_x layer is removed using buffered hydrofluoric acid (BHF) and a new 50 nm-thick SiN_x layer is deposited. A second e-beam lithography is carried out to open trenches in the SiN_x layer around all the future devices. These trenches are then etched into the III-V membrane layers using the SiN_x

layer as a mask in a reactive ion etching (RIE) CH_4–H_2 process. In order to create the slopes of the triangular waveguides at the end of the fabrication, it is important to align the future polarization converters along the right crystallographic direction (i.e. parallel to the primary flat if working with a (100) InP substrate).

The last part of the polarization converters' patterning consists in the fabrication of the sloped sidewalls of the triangular waveguides. Once again, the previous SiN_x layer is removed and a new SiN_x layer is deposited. A final e-beam lithography is used to open locally the areas of the future triangular waveguides in the SiN_x layer. This time the dry-etching time of the SiN_x layer has to be controlled so that the SiN_x is removed from the horizontal areas but not from the vertical sidewalls defined previously (this is rendered possible by the relatively good conformality of the SiN_x PECVD deposition and the strong verticality of the SiN_x RIE process used). Finally, the stack (2) is etched chemically in the regions open in the SiN_x layer, using the solutions (A) and (B) mentioned previously. Since the etching produced by these solution stops on the (112) plane of InP, a 35° slope running from the top of the SiN_x covered sidewall to the first InGaAs etch-stop layer below is obtained (see the background of the SEM picture in Fig.1b).

After the triangular waveguides have been defined, the SiN_x layer is removed, and a 300 nm-thick SiO_2 cladding layer is deposited on top of the whole chip. Meanwhile, a 1.5 µm-thick layer of SiO_2 is deposited on a silicon carrier wafer. The InP chip is then bonded upside-down on the silicon carrier wafer using a 100 nm-thick BCB (Benzo-cyclo-butene) layer as a glue. In the final step, the substrate and the stack (1) are removed by selective wet-etching, using solution (A) and (B).

IV. Measurements

The most efficient way to couple light into and out of membrane photonics chips is through the use of grating couplers [1]. However, these diffractive structures are optimized for exciting the TE-polarized mode in the chip, and due to their highly polarization-dependent behavior, in practice they act as TM-filters with 50-dB extinction ratio… This means that when grating couplers are used, polarization converters cannot be characterized by rotating the input polarization and measuring the polarization state of the output light. In order to verify the polarization conversion behavior of the presented device, an alternative technique, relying on the variation of the length parameter x (see Fig.1a), is used.

The rectangular waveguide of length x introduced between the two triangular waveguides of the polarization converter can sustain the standard TE and TM modes. As described in [4], for a TE-polarized input light, the polarization state after propagating through the first triangular section is a complex superposition of the TE and TM modes that we can call $\boldsymbol{P}_{intermediate}$. Since the TE and TM modes propagate at different speed in the rectangular waveguide, a phase-shift is created between them that linearly increases with x. This in turn will modify the designed behavior of the polarization converter and cause the polarization state of the light leaving the device after propagating through the second triangular waveguide to contain some TE component instead of the fully TM polarized state predicted by design when $x = 0$. However, when x is a multiple of $L_{2\pi} = 2\pi / (\beta_{TE} - \beta_{TM})$, (where $\beta_{TE,TM}$ are the propagation constants of the standard TE and TM modes) the phase-shift created by the propagation through the rectangular waveguide is a multiple of 2π, which means that the polarization state at the input of the second triangular waveguide is exactly $\boldsymbol{P}_{intermediate}$. For these values of x, the device functions as a polarization converter.

A set of 16 devices was printed, where each device consists of two oppositely-loaded triangular waveguides of length L_{tri} = 2.3 µm with a rectangular section of length x in between (x was varied from 4 to 11.5 µm). The TE-TE transmission of each device at $\lambda = 1.55$ µm was measured separately and plotted as a function of the length x of the rectangular section (see Fig. 2). As expected from the wave nature of light, the linear relation between the phase-shift created in the rectangular section and its length x is translated into a *cosine*^{2} variation of the TE-TE transmission versus x. The curve obtained is used to determine that the polarization conversion efficiency (PCE) of this family of devices is close to 97 %, while the excess losses (as shown by the devices x = 4 µm and 10 µm) can be as low as 1 dB.

Another set of devices identical to the previous one but with L_{tri} = 2.6 µm is analyzed in the same way and shows a polarization conversion efficiency of 92 %, with equally low excess losses, which shows that the tolerance on the triangular waveguide length is rather relaxed.

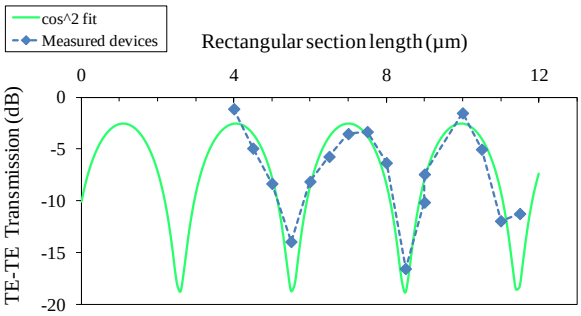


Figure 2. Demonstration of the device's polarization conversion behavior

V. Conclusion

An ultra-short polarization converter in InGaAsP/InP membrane is fabricated and characterized. Measurements show very high polarization conversion efficiency (97 %) with low excess losses (~ 1 dB). Further experiments are needed to estimate the spectral behavior of the device.

References

[1] J.J.G.M. van der Tol, R. Zhang, J. Pello, F. Bordas, G. Roelkens, et al., "Photonic integration in indium-phosphide membranes on silicon," IET Optoelectron., vol. 5, no. 5, pp.218–225, 2011

[2] L. Liu, Y. Ding, K. Yvind, and J. M. Hvam, "Efficient and compact TE–TM polarization converter built on silicon-on-insulator platform with a simple fabrication process," Opt. Lett., vol. 36, no. 7, pp. 1059–1061, 2011

[3] A. V. Velasco, M. L. Calvo, et al., "Ultracompact polarization converter with a dual subwavelength trench built in a silicon-on-insulator waveguide," Opt. Lett., vol. 37, no. 3, pp.365–367, 2012

[4] J. Pello, J. J. G. M van der Tol, G. Roelkens, H. P. M. M. Ambrosius, and M. K. Smit, "Design of a new ultra-small polarization converter in InGaAsP/InP membrane," presented at the 15th European Conference on Integrated Optics, Cambridge, UK, April 2010, paper WeB2.

Waveguide-Type All Optical Switch Using Saturable Absorption of Graphene

Masahiro Oya, Hiroki Kishikawa, Nobuo Goto, and Shin-ichiro Yanagiya
Department of Optical Science and Technology
The University of Tokushima
2-1 Minamijosanjima-cho, Tokushima 770-8506, Japan
Email: {m.ohya, h.kishikawa, goto, giya}@opt.tokushima-u.ac.jp

Abstract— **In photonic routing nodes, pico-second switching will be a key function. We propose an all optical switch consisting of two-stage Mach-Zehnder interferometers, whose arms contain graphene saturable absorber films. The switching characteristics are theoretically analyzed and numerically simulated by FD-BPM.**

Keywords-component; optical switch; saturable absorption; graphene; asymmetric X-junction coupler

I. INTRODUCTION

Pico-second optical switching devices are required in photonic switching nodes. The authors have studied on all-optical wavelength-selective switches, where switching is controlled by amplifying the optical guided wave with Raman amplifiers placed in the waveguides of the switch.[1,2] The switch, however, requires waveguide-type efficient crystalline Raman amplifiers. In this report, we propose introducing graphene films for controlling the optical amplitudes with the similar switch architecture. We discuss the switching characteristics using a reported experimental result on saturable absorption by Bao et al.[3] Complete switching can be achieved by controlling the optical wave using nonlinear saturable absorption. The switching characteristics are verified by FD-BPM simulation.

II. MODELING OF GRAPHENE ABSORPTION

In the proposed switch, the amplitude of an optical signal is controlled by a control light. First, we consider a model of optical nonlinearity of a monolayer graphene as illustrated in Fig.1.[3] Although this saturable absorption is observed for an optical input by changing the incident intensity, we consider the incident light is sum of a weak signal light and an intense control light, where the polarization or wavelength of these two lights are assumed to be different.

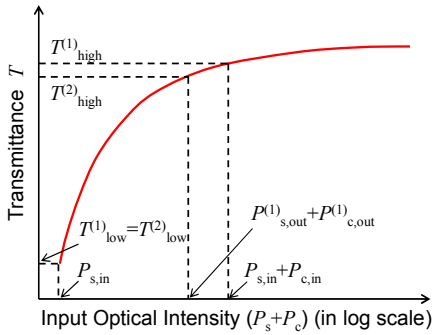
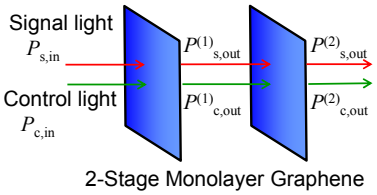


Fig.1 Saturable absorption in graphene

This work was supported in part by JSPS KAKENHI (23656243).



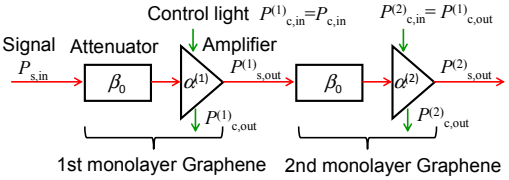


Fig.2 Modeling of two-stage graphene

A model for two-stage monolayer graphene is shown in Fig.2. Although absorption is increased for the signal light more than that for a single graphene, the amplitude of the optical signal can be controlled with a wider range. When the incident light is weak $P_{s,in}$ and without control light, the transmittance of the first graphene is low $T^{(1)}_{low}$. The transmission coefficient for the optical amplitude is given by $t^{(1)}_{low}=(T^{(1)}_{low})^{1/2}=\beta_0$. By increasing the incident light intensity $P_{s,in}+P_{c,in}$ including control light, the transmittance increases to $T^{(1)}_{high}$. The transmission coefficient is given by $t^{(1)}_{high}=(T^{(1)}_{high})^{1/2}=\beta_0\alpha^{(1)}$. For the second grapheme, the control light is attenuated to $P^{(1)}_{c,out}=\beta_0\alpha^{(1)}P_{c,in}$ through the first graphene. The transmittance of the second graphene is decreased to $T^{(2)}_{high}$. Then, the transmission coefficient of the second graphene is $t^{(2)}_{high}=(T^{(2)}_{high})^{1/2}=\beta_0\alpha^{(2)}$.

From the experimental result [3], we find $\beta_0=0.556$ $(=0.309^{1/2})$. for $P_{s,in}<3\text{mW}/\mu\text{m}^2$, and $\beta_0\alpha^{(1)}=0.894$ $(=0.8^{1/2})$ for $P_{s,in}+P_{c,in}=10\text{mW}/\mu\text{m}^2$. Then, $\alpha^{(1)}=1.608$ is obtained. For the second graphene, we find $\beta_0\alpha^{(2)}=0.866$ $(=0.75^{1/2})$ for $P^{(1)}_{s,out}+P^{(1)}_{c,out}=8\text{mW}/\mu\text{m}^2$. Then $\alpha^{(2)}=1.558$ is obtained.

III. OPTICAL SWITCH ARCHITECTURE

A proposed optical switch is illustrated in Fig.3. The device consists of two cascaded interferometers whose couplers are asymmetric X-junction couplers. Two-stage graphene films are inserted in the two waveguides of the first interferometer. The graphene films in arm A or B is modeled by an attenuator having amplitude attenuation coefficient β_0^2 and an amplifier having amplitude amplification coefficient of $\alpha_i=\alpha_i^{(1)}\alpha_i^{(2)}$, i=A or B. A fixed attenuator β_{fix} is employed in one arm of the second interferometer.

The output fields through the switch are related to the input fields as

$$\begin{aligned}\begin{pmatrix}A_{out}\\B_{out}\end{pmatrix}&=\left(\frac{1}{\sqrt{2}}\right)^3\begin{pmatrix}1&1\\-1&1\end{pmatrix}\begin{pmatrix}1&0\\0&\beta_{fix}\end{pmatrix}\begin{pmatrix}1&1\\-1&1\end{pmatrix}\\&\times\begin{pmatrix}\beta_0^2\alpha_B&0\\0&\beta_0^2\alpha_A\end{pmatrix}\begin{pmatrix}1&1\\-1&1\end{pmatrix}\begin{pmatrix}A_{in}\\B_{in}\end{pmatrix}\\&=\frac{\beta_0^2}{2\sqrt{2}}\begin{pmatrix}a_{11}&a_{12}\\a_{21}&a_{22}\end{pmatrix}\begin{pmatrix}A_{in}\\B_{in}\end{pmatrix}\end{aligned}\quad(1)$$

where

$$\begin{cases}a_{11}=\alpha_A-\alpha_B-\beta_{fix}(\alpha_A+\alpha_B)\\a_{12}=\alpha_A+\alpha_B+\beta_{fix}(-\alpha_A+\alpha_B)\\a_{21}=-(\alpha_A-\alpha_B)-\beta_{fix}(\alpha_A+\alpha_B)\\a_{22}=-(\alpha_A+\alpha_B)+\beta_{fix}(-\alpha_A+\alpha_B)\end{cases}.\quad(2)$$

When optical signal is incident only at one input port as $A_{\text{in}}=E_{\text{in}}$ and $B_{\text{in}}=0$, (1) becomes

$$\begin{pmatrix}A_{out}\\B_{out}\end{pmatrix}=\frac{\beta_0^2E_{in}}{2\sqrt{2}}\begin{pmatrix}a_{11}\\a_{21}\end{pmatrix}.\quad(3)$$

From this equation, we find the conditions for switching as follows:

(i) When $\alpha_{\text{A}}=1$, $\alpha_{\text{B}}=1+2^{1/2}$ and $\beta_{\text{fix}}=1/(1+2^{1/2})$,
$A_{\text{out}}=-\beta_0^2E_{\text{in}}$, $B_{\text{out}}=0$,

(ii) When $\alpha_{\text{A}}=1+2^{1/2}$, $\alpha_{\text{B}}=1$ and $\beta_{\text{fix}}=1/(1+2^{1/2})$,
$A_{\text{out}}=0$, $B_{\text{out}}=-\beta_0^2E_{\text{in}}$.

Therefore, amplification of the amplitude coefficient of 2.414 is required for switching. The two-stage graphene films can provide $\alpha_i=\alpha_i^{(1)}\alpha_i^{(2)}=2.505$ from Section III. A control power of 10mW/μm^2 is considered to be a little too large for switching. Although the switching is accompanied by an insertion loss of β_0^2, complete switching can be achieved.

IV. FD-BPM SIMULATION

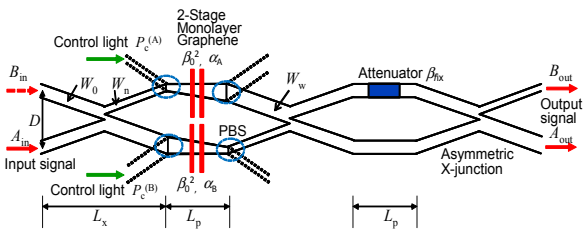


Fig.3 Switch architecture containing graphene films.

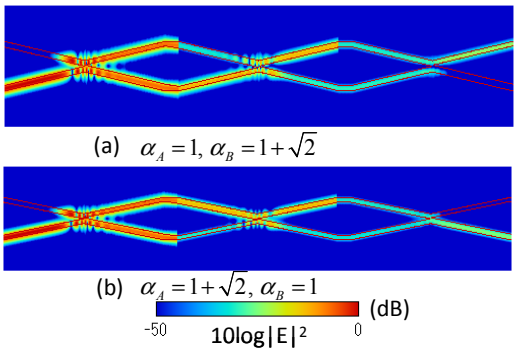


Fig.4 Simulation results of switching.

The switching operation is numerically simulated by FD-BPM. We consider two-dimensional slab waveguide model. The core and cladding regions have refractive indices of n_{c} = 1.461 and n_{s} = 1.45, respectively. The waveguide widths of the fundamental, narrow and wide waveguides of the asymmetric X-junctions are W_1 = 3.0μm, W_{n} = 2.6μm and W_{w} = 3.4μm, respectively. Optical waves are assumed to be TE mode. The lengths of the X-junction coupler and the parallel waveguides are L_{x} = 16mm and L_{p} = 1mm, respectively. The total length is 50mm. The distance of the input ports is D= 23μm.

Table I Switched output intensities.

Control Arm	Theory		Simulation	
	$\lvert A_{\text{out}}\rvert^2$	$\lvert B_{\text{out}}\rvert^2$	$\lvert A_{\text{out}}\rvert^2$	$\lvert B_{\text{out}}\rvert^2$
B	0	9.55×10^{-2}	3.36×10^{-4}	9.83×10^{-2}
A	9.55×10^{-2}	0	8.74×10^{-2}	3.05×10^{-4}

The switching operation at λ = 1550nm is confirmed as shown in Fig. 4, where squared electric fields $|E|^2$ are plotted. In the simulation, amplification is equivalently simulated just by increasing the electric field by multiplying the gain coefficient α at a plane located at the end of the waveguide region for the amplifier. In a similar manner, the attenuator is modeled by multiplying the electric field by β_0 or β_{fix} at the beginning of the attenuator. The normalized output intensities are summarized in Table I.

V. CONCLUSION

An all-optical switch using saturable absorption of graphene was proposed. Since only attenuation is used in controlling the guided wave, an insertion loss of 10.2dB (β_0^2=3.09) is inevitable. However, complete switching between the two output ports can be achieved.

REFERENCES

[1] H. Kishikawa and N. Goto, J. Lightwave Technol., vol.23, no.4, pp.1631–1636, Apr. 2005.
[2] H. Kishikawa, K. Kimiya, N. Goto, and S. Yanagiya, J. Lightwave Technol., vol.28, no.1, pp.172–180, Jan. 2010.
[3] Q. Bao, H. Zhang, Z. Ni, Y. Wang, L. Polavarapu, Z. Shen, Q. H. Xu, D. Tang, and K. P. Loh, Nano Res., nol.4, no.3, pp.297–307, Mar. 2011.

Nonlocal hydrodynamic Drude resonances of nano-plasmonic scatterers: Modeling and simulations

Kirankumar R. Hiremath[1], Lin Zschiedrich[2], Sven Burger[1,2], Frank Schmidt[1]
[1]Computational Nanooptics Group, Konrad-Zuse-Zentrum für Informationstechnik Berlin, Germany
[2]JCMwave GmbH, Berlin, Germany
hiremath@zib.de

***Abstract*—As the plasmonic scatterers get much smaller than the wavelength of the incident light, local material models like the Drude model and the Lorentz model become inadequate to describe accurately the light-matter interactions. To overcome this, a sophisticated nonlocal hydrodynamic Drude model is investigated. In practice, it is further simplified and simulated with the curl-free approximation, which generates spurious resonances. In this work we discuss a weak formulation based rigorous numerical investigations of the nonlocal hydrodynamic Drude model. This approach does not use the curl-free approximation, and thus avoids spurious resonances. The simulated results agree good with Mie results, and the method is capable of handling arbitrarily shaped scatterers.**

I. Introduction

The dispersive material properties of plasmonic structures are usually described by the Drude model and the Lorentz model. These material models take into account spatially *purely local* interactions between electrons and the light. Recent investigations have shown that these local models are inadequate as the size of the plasmonic scatterers become much smaller than the wavelength of the incident light [1], [2]. To overcome this, a sophisticated *nonlocal* material model is required, such as the hydrodynamic model of the electron gas [3].

The hydrodynamic model is formulated by coupling macroscopic Maxwell's equations with the equations of motion of the electron gas. This gives rise to a hydrodynamic polarization current. Considering only the kinetic energy of the free electrons, it yields the nonlocal hydrodynamic Drude model, which is given in frequency domain by a coupled system of equations

$$\nabla\times\mu_0^{-1}(\nabla\times\vec{E})-\omega^2\varepsilon_0\varepsilon_{\mathrm{loc}}\vec{E} = i\omega\vec{J}_{\mathrm{HD}}, \quad (1)$$
$$\beta^2\nabla(\nabla\cdot\vec{J}_{\mathrm{HD}})+\omega(\omega+i\gamma)\vec{J}_{\mathrm{HD}} = i\omega\omega_{\mathrm{p}}^2\varepsilon_0\vec{E}, \quad (2)$$

where $\vec{E}$ is the electric field, $\vec{J}_{\mathrm{HD}}$ is the hydrodynamic current, $\varepsilon_{\mathrm{loc}}$ is the relative permittivity due to the local-response, β^2 is a term proportional to the Fermi velocity, γ is the damping constant, and $\omega_{\mathrm{p}}^2=\frac{e^2 n_0}{\varepsilon_0 m_{\mathrm{e}}}$ is the plasma frequency of the free electron gas.

II. Curl-free approximation: Spurious resonances

Recently the nonlocal hydrodynamic Drude model has been simulated with the finite difference time domain (FDTD) method, but with the curl-free approximation $\nabla\times\vec{J}_{\mathrm{HD}}=0$ [4]. As a consequence of this approximation, the tensorial grad-div operator $(\nabla(\nabla\cdot\vec{J}_{\mathrm{HD}}))$ appearing in the governing equation for the hydrodynamic current simplifies to vectorial linear Laplacian operator $(\nabla^2\vec{J}_{\mathrm{HD}})$. This was needed to render the system into a form suitable for the standard FDTD framework. However the comparison with the analytical Mie theory [1] showed that this approach produces spurious plasmonic resonances below the plasma frequency $(\omega/\omega_p<1)$ [5].

III. Weak formulation

Here we outline a weak formulation based rigorous numerical approach for simulation of the nonlocal hydrodynamic Drude model. Details can be found in [6]. We start with (1) for the electric field. An appropriate ansatz space for the electric field is the Sobolev space $H(\mathrm{curl},\Omega)=\{\vec{E}\in(L^2(\Omega))^3\,|\,\nabla\times\vec{E}\in(L^2(\Omega))^3\}$, which contains fields with weakly defined curl-operator defined on the domain Ω [7, Sec. 3.5].

Multiply (1) with a trial function $\varphi\in H(\mathrm{curl},\Omega)$, and integrate over Ω. Then partial integration yields

$$\int_\Omega\left((\nabla\times\varphi)\cdot(\mu_0^{-1}\nabla\times\vec{E})-\omega^2\varphi\cdot\varepsilon_{\mathrm{loc}}\vec{E}\right)dV \quad + \int_{\partial\Omega}\varphi\cdot(\vec{n}\times(\mu_0^{-1}\nabla\times\vec{E}))\,dA = i\omega\int_\Omega\varphi\cdot\vec{J}_{\mathrm{HD}}\,dV, \quad (3)$$

with the outer normal $\vec{n}$. Here we need to define boundary conditions of the electric field on $\partial\Omega$, which is formulated by the Dirichlet to Neumann (DtN) operator. Using total-field/scattered-field formulation, one gets

$$\int_\Omega((\nabla\times\varphi)\cdot(\mu_0^{-1}\nabla\times\vec{E})-\omega^2\varphi\cdot\varepsilon_{\mathrm{loc}}\vec{E}-i\omega\varphi\cdot\vec{J}_{\mathrm{HD}})\,dV+ \int_{\partial\Omega}\varphi\cdot\mathrm{DtN}(\vec{E})\,dA=-\int_{\partial\Omega}\varphi\cdot(\vec{n}\times(\mu_0^{-1}\nabla\times\vec{E}_{\mathrm{inc}}))\,dA+ \int_{\partial\Omega}\varphi\cdot\mathrm{DtN}(\vec{E}_{\mathrm{inc}})\,dA,\ \forall\ \varphi\in H(\mathrm{curl},\Omega), \quad (4)$$

where $\vec{E}_{\mathrm{inc}}$ is the exciting field.

For (2) an appropriate ansatz space is the Sobolev space $H_0(\mathrm{div},\Omega_{\mathrm{s}})=\{\vec{J}_{\mathrm{HD}}\in(L^2(\Omega_{\mathrm{s}}))^3\,|\,\nabla\cdot\vec{J}_{\mathrm{HD}}\in(L^2(\Omega_{\mathrm{s}}))^3,\ \vec{n}\cdot\vec{J}_{\mathrm{HD}}=$

0 on $\partial\Omega_s\}$. This restricts the hydrodynamic current to the plasmonic scatterer, and imposes zero normal component on the boundary of the scatterer.

Then the variational form of (2) reads as

$$-\int_{\Omega_s} \beta^2(\nabla\cdot\psi)(\nabla\cdot\vec{J}_{\rm HD})\,dV + \omega(\omega+i\gamma)\int_{\Omega_s}\psi\cdot\vec{J}_{\rm HD}\,dV \\ -i\omega\omega_p^2\int_{\Omega_s}\psi\cdot\varepsilon_0\vec{E}\,dV = 0, \forall\ \psi\in H_0(\mathrm{div},\Omega_s). \quad (5)$$

After the problem is formulated in the Sobolev space $H(\mathrm{curl},\Omega)\times H_0(\mathrm{div},\Omega_s)$ for $(\vec{E},\vec{J}_{\rm HD})$, one can use Nédélec finite element spaces, which lead to a consistent discretization of the problem, fulfilling the required boundary and material interface conditions [7, Ch. 5]. We solving the resultant discrete coupled system of with a sparse LU decomposition.

IV. Numerical examples

A. Cylindrical plasmonic nanowires

We validate the present approach by simulating a test case of cylindrical nanowire in [1], for which analytical solution based on Mie theory is available. When this setting was simulated with the curl-free hydrodynamic current approximation as in [4], spurious (model induced) resonances were produced, which has been discussed in detail in [5].

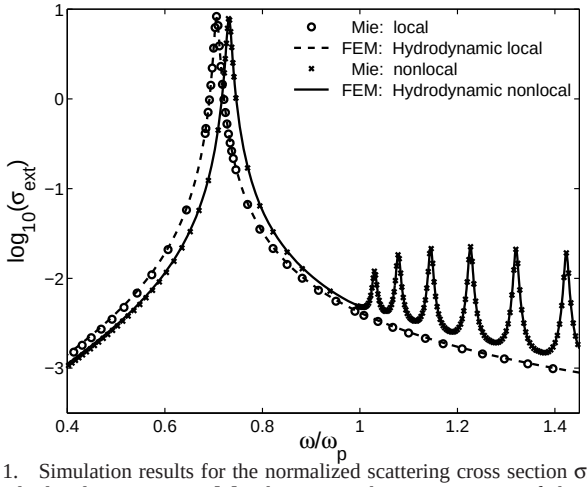


Fig. 1. Simulation results for the normalized scattering cross section $\sigma_{\rm ext}$ of the cylindrical nanowire in [1]. The curves show comparison of the finite element numerical solutions for the nonlocal and the local hydrodynamic model with the corresponding analytical solutions based on the Mie theory.

Consistent with the observations in [1], peaks due to nonlocal interactions are present *only* beyond the bulk plasma frequency. The positions of the surface plasmon resonance and the nonlocal hydrodynamic Drude resonances agree very good with the analytical Mie results.

B. V groove channel plasmon-polariton waveguides

To demonstrate capability of the method to handle an arbitrary shaped geometry, we simulate a channel plasmon-polariton (CPP) waveguide with a V groove.

We consider a V groove configuration as shown in clip of Fig. 2. First we simulated it for the local Drude model. As seen from the dashed curve in Fig. 2, several resonance modes

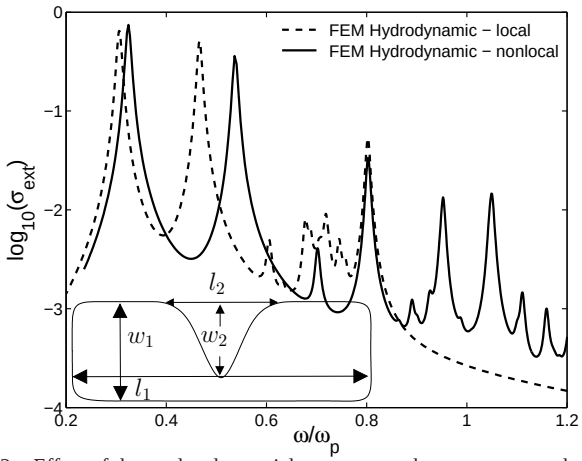


Fig. 2. Effect of the nonlocal material response on the resonance modes of V groove CPP waveguide. The waveguide parameters are as: $l_1 = 7$ nm, $w_1 = 1$ nm, a groove of length $l_2 = 0.7$ nm, width $w_2 = 0.7$ nm is placed in the center. The material and the hydrodynamic parameters are taken as in the case of cylindrical nanowires in [1]. The sharp corners of the waveguide are rounded with corner radius of 0.1 nm. Resonances are excited by a unit amplitude, *x*-polarized plane wave propagating in the direction of minus *y*-axis.

are excited. When this setting is simulated for the nonlocal Drude model, the mode spectrum changes significantly (the solid-line curve). Some of the local Drude model modes such as at $\omega/\omega_p = 0.306332$ and $\omega/\omega_p = 0.80262$ experience small shifts towards high frequency, whereas the others like at $\omega/\omega_p = 0.466485$ and $\omega/\omega_p = 0.605087$ undergo noticeable shifts towards high frequency. As in the case of the cylindrical nanowires, also for the V groove waveguide a completely new set of resonances appear at the frequencies beyond the plasma frequency. For the present simulation setting, some of these hydrodynamic resonance modes are more prominent than the higher order waveguide resonance modes. It gives the indication with the inclusion of nonlocal effect, the modal properties of the CPP waveguides change significantly.

Acknowledgments

This work is partially funded by the DFG (German Research Foundation) priority program 1391 “Ultrafast Nanooptics”.

References

[1] R. Ruppin. Extinction properties of thin metallic nanowires. *Optics Communications*, 190(1-6):205–209, 2001.

[2] S. Palomba, L. Novotnyb, and R. E. Palmer. Blue-shifted plasmon resonance of individual size-selected gold nanoparticles. *Optics Communications*, 281(3):480–483, 2008.

[3] A. D. Boardman. *Electromagnetic surface modes*, chapter Hydrodynamic theory of plasmon-polaritons on plane surfaces, pages 1–76. John Wiley and Sons Ltd., 1982.

[4] J. M. McMahon, S. K. Gray, and G. C. Schatz. Calculating nonlocal optical properties of structures with arbitrary shape. *Physical Review B*, 82:035423, 2010.

[5] S. Raza, G. Toscano, A. P. Jauho, M. Wubs, and N. A. Mortensen. Unusual resonances in nanoplasmonic structures due to nonlocal response. *Physical Review B*, 84:121412, 2011.

[6] K. R. Hiremath, L. Zschiedrich, and F. Schmidt. Numerical solution of nonlocal hydrodynamic Drude model for arbitrary shaped nano-plasmonic structures using Nédélec finite elements. arXiv:1201.1527v2 (submitted to J. Comp. Phys.), 2012.

[7] P. Monk. *Finite Element Methods for Maxwell's equations*. Oxford Science Publications, 2003.

Reconfigurable Integrated Optics

Diode-Laser induced waveguides for visible wavelengths in $KYb(WO_4)_2$

L. J. McKnight, S. Calvez
Institute of Photonics, University of Strathclyde,
Glasgow, United Kingdom,
loyd.mcknight@strath.ac.uk

***Abstract*— We demonstrate the formation of quasi-stable transient fabrication-free waveguides in $KYb(WO_4)_2$ using the electronic index change induced by diode-laser pumping which could lead to reconfigurable integrated optics. Mode profiles and index changes have been measured.**

Fabrication; Waveguide Characterization; Double Tungstates; Diode-Pumping;

I. INTRODUCTION

Optical waveguides typically require complex, time consuming and expensive fabrication techniques including ion-implantation, dry-etching, laser writing and optical or e-beam lithography to define circuits [1]. It is therefore desirable to produce waveguides and devices with a fabrication-free technique to remove the costs and complexities of fabrication. It would also be possible to define and optimize integrated devices during use, in situ. Such a technology would allow for a range of novel reconfigurable devices, circuits with small footprint and the possibility for extended functionality.

The stoichiometric crystal $KYb(WO_4)_2$, referred to as KYbW, differs significantly from typical laser crystals in that the crystal is doped to 100% [2]. KYbW has high active Yb^{3+} density of $6.4x10^{21}$ cm^{-3}, one of the highest of any available material and as a consequence offers a peak absorption length at 981nm of 13.3µm, one of the shortest of any material [2].

Intense laser pumping of crystals doped with optically active ions causes a refractive index change due to both thermal and athermal causes [3-5]. The cause of athermal index change is due to the linear polarizability of excited ions being different to that of unexcited ions. This athermal index change is known as the electronic index change as it relates to the electronic state of the ion rather than the local crystal temperature.

It has been shown that this electronic refractive index change is not only of significance for wavelengths near the absorption and emission peaks but is also of significant magnitude for wavelengths for which the crystal is transparent [4]. Index changes in Yb^{3+} doped materials for wavelengths far away from the peak 980nm absorption are shown to be due to the existence of strong charge transfer absorption bands in the range from 200-300nm [4].

The electronic refractive index change has been shown to dominate over thermal index changes in a range of materials including Nd^{3+} and Yb^{3+} systems [5]. This index change can create significant guiding effects in laser systems [6,7]. ΔN_e, the electronic refractive index change, depends on the linear polarizability, Δp, of the material and the density of inverted ions ΔN with the following equation [5]:

$$\Delta N_e = 2\pi \frac{n_0^2 + 2}{3} \Delta p \frac{\Delta N}{n_0} \quad (1)$$

where n_0 is the initial refractive index of the material.

From previous work [4] it is possible to estimate the maximum possible electronic refractive index change by assuming that 50% of the Yb^{3+} ions are excited into the $^2F_{7/2}$ energy level and this is shown in Figure 1. These values of refractive index change are significantly larger than that usually achieved by ion-implantation and laser writing fabrication techniques [1].

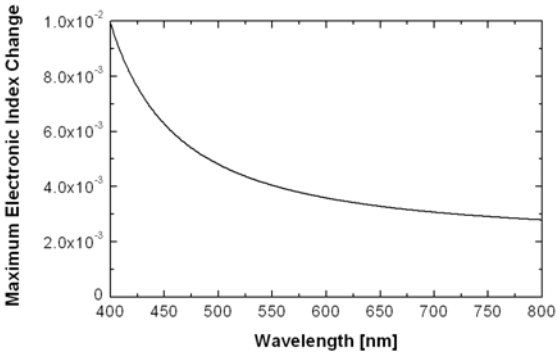


Figure 1. Maximum electronic refractive index change in KYbW assuming 50% of Yb^{3+} ions are excited into the $^2F_{7/2}$ energy level for a range of wavelengths for which the crystal is transparent.

II. EXPERIMENTAL

We orientated a 4 × 4.5 × 5 mm KYbW crystal to allow diode-laser pumping along the a-axis and allow maximum absorption for light polarized parallel to Nm. Pumping was achieved with a diode-laser offering 16W at 980nm. Fast-axis diode-laser light was collimated and focused to a strip with full width half maximum of 23µm on the crystal surface. The slow-axis diode-laser light was focused and apertured to produce a 4.5mm long top-hat strip on the crystal surface. This pumping region defined the refractive index profile and thus the guided mode area of the waveguide.

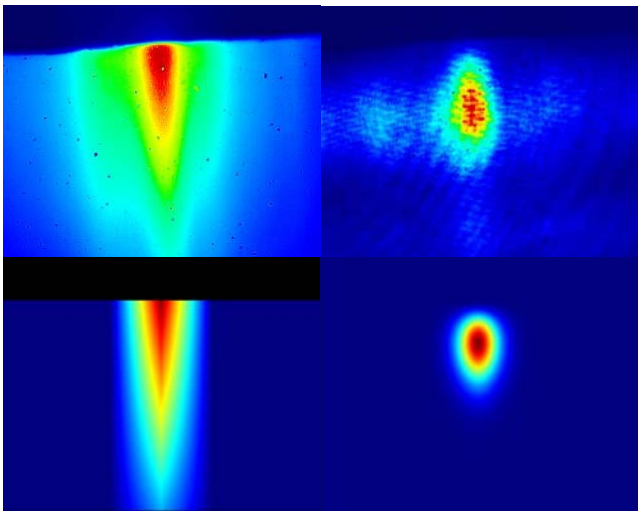


Figure 2. (a) Measured 1000nm+ luminescence due to pumping. (b) Measured guided He-Ne mode profile. (c) Reconstructed refractive index profile chosen to match luminescence. (d) Reconstructed mode profile by optimising the magnitude of refractive index change in c. Individual images sizes are width=153µm, height =123µm.

The diode-laser was operated quasi-CW with a pulse length of 1ms and variable repetition rate in order to reduce and monitor significant thermal refractive index changes.

The normalized refractive index change profile of the cross-section of the waveguide could be determined by measuring the 1000nm+ luminescence from the crystal surface when pumped with the diode-laser. The crystal surface was imaged with a CCD camera and is shown in Figure 2a). This luminescence is proportional to the number of excited ions and is thus proportional to the electronic index change.

He-Ne probe light was coupled into the waveguide with microscope objectives. Probe light was chopped with a mechanical rotating chopper with a duty cycle of 1% to ensure that the probe pulse arrived at the crystal for a fraction of the pump pulse. The He-Ne chopper was temporally locked to the diode-laser to ensure that the probe pulse arrived after the creation of the waveguide and before removal of the waveguide.

The guided mode of the waveguide is shown in Figure 2b). The measured mode profile has a FWHM width of 20µm and a FWHM height of 31µm. Unguided He-Ne light was measured to diffract to a width of 100µm after 4mm propagation in the crystal making it easy to distinguish between guided and unguided light.

Using finite element analysis software (COMSOL) it was possible to reconstruct the refractive index profile of the waveguide in order to estimate the refractive index change created by diode-laser pumping. Figures 2c) and 2d) show the normalized reconstruction of the refractive index profile and guided mode respectively. Using this technique a peak refractive index change of 1×10^{-4} was calculated. This value is significantly lower than the theoretical maximum due to the low pump absorption of 1.2W used in this experiment.

To confirm that the waveguide is formed by the electronic index change, and not some other mechanism, the temporal

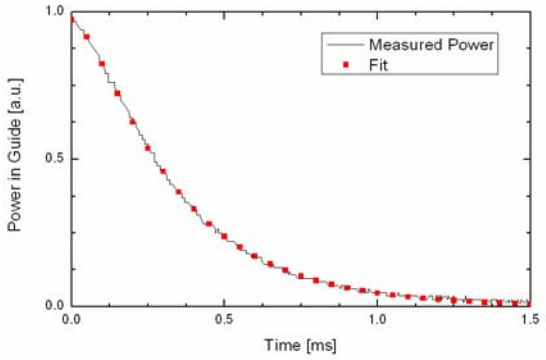


Figure 3. He-Ne power in waveguide after switch off of the diode-laser pump. This power has been shown to be proportional to the refractive index change of the waveguide due to the small index change and large coupling angle. Overlaid is a fit using equation 2.

characteristics of the waveguide were examined. The He-Ne chopper was removed and constant probe light was injected into the waveguide during its creation and removal. Waveguide output light was focused onto a detector to monitor the power in the waveguide as the pump was removed and thus the waveguide was removed.

It was found that the decay is comprised of a small negative thermal component with a lifetime of 75µs and a large positive electronic component with a lifetime of 300µs. This electronic lifetime agrees well with the value available in literature for KYbW (350µs [2]) and the thermal lifetime is similar to that for transient gratings. The negative sign of the thermal component is consistent with the pumping direction as the dN/dT is negative across the waveguide. The orientation of the crystal could be chosen to minimize this thermal component [3].

We propose the formation of a variable directional coupler using the same waveguide formation technique. Suitable design parameters will be presented at the conference.

REFERENCES

[1] J. MacKenzie “Dielectric Solid-State Planar Waveguide Lasers: A Review,” IEEE Journal Selected Topics in Quantum Electroncs, vol. 13, no. 3, pp.626-637, 2007.

[2] M. C. Pujol, M. A. Bursukova, F. Guell, X. Mateos, R. Sole, J. Gavalda, et al., "Growth, optical characterization, and laser operation of a stoichiometric crystal KYb(WO4)(2)," Physical Review B, vol. 65, no. 16, pp., 2002.

[3] E. V. Ivakin, A. V. Sukhadolau, O. L. Antipov, and N. V. Kuleshov, "Transient grating measurements of refractive-index changes in intensively pumped Yb-doped laser crystals," Applied Physics B-Lasers and Optics, vol. 86, no. 2, pp. 315-318, 2007.

[4] R. Moncorge, O. N. Eremeykin, J. L. Doualan, and O. L. Antipov, "Origin of athermal refractive index changes observed in Yb3+ doped YAG and KGW," Optics Communications, vol. 281, no. 9, pp. 2526-2530, 2008.

[5] R. C. Powell, S. A. Payne, L. L. Chase, and G. D. Wilke, "Index-of-Refraction Change in Optically Pumped Solid-State Laser Materials," Optics Letters, vol. 14, no. 21, pp. 1204-1206, 1989.

[6] A. M. Prokhorov, V. I. Zhekov, M. I. Studenikin, and V. P. Danilov, "An induced-waveguide YAG : Er3+ laser (lambda=2.9 mu m) using Y1.5Er1.5Al5O12 crystals," Laser Physics, vol. 10, no. 2, pp. 526-531, 2000.

[7] L. J. McKnight, S. Calvez, “Gain-guided KYb(WO4)2 Laser,” Europhoton 2010, Hamburg, 29th Aug 2010.

Photonic Crystal Defect Cavity Q-Factor Optimization Using Slab Thickness

J.R.Pugh, Y-L.D.Ho, E.Engin, J.G.Rarity, M.J.Cryan
Dept. of Electronic and Electrical Engineering
University of Bristol
Bristol, BS8 1UB, UK
Jon.pugh@bristol.ac.uk, m.cryan@bristol.ac.uk

G.R.Nash
College of Engineering, Mathematics and Physical Sciences
University of Exeter
Exeter, EX4 4QF, UK

***Abstract*— Three mechanisms are studied which give rise to a high-Q L3 cavity mode in a 2D photonic crystal slab where the in-plane photonic bandgap is closed due to increased slab thickness.**

Keywords-component; Photonic Crystals; Quality-factor; 2D Photonic Crystal Slab Cavities

I. INTRODUCTION

There has been much interest in the design of high Quality (*Q*) factor, low mode volume (*V*) photonic crystal (PhC) defect cavities in many different wavelength ranges and material systems. In our work, optical resonators are constructed by removing three holes from a 2D PhC composed of a hexagonal lattice of air holes in a slab of AlGaInSb, which is a promising candidate for the realization of room temperature lasers emitting in the 3-4μm region [1]. Such structures are typically designed so that the slab thickness is chosen so that only the lowest-order optical mode in the vertical direction is supported [2]. However, in the case of *Q* factor, a number of studies have shown that thicker slabs can lead to stronger confinement [3,5]. Here, the 3D Finite-Difference Time-Domain (FDTD) and frequency-domain Plane Wave Expansion (PWE) methods have been used to study of the effect of slab thicknesses which exceed that for single vertical mode propagation. A new structure design is suggested which allows high-*Q* PhC cavity modes to exist where there is no bandgap by choosing slab thicknesses equal to a multiple of half the guided mode wavelength [3]. In this case we believe the three confinement mechanisms of (i) "Gentle" in-plane confinement, (ii) Minimisation of overlap to in-plane Bloch modes and (iii) Vertical cavity resonance coincide to give rise to very high *Q*-factors.

II. PHOTONIC BANDGAP & L3 CAVITY DESIGN

Light can be localized in all three dimensions using the combination of a 2D photonic crystal and a slab with a lower refractive index medium, such as air, above and below [4]. To create a photonic bandgap as a function of the in-plane Bloch wave vectors, as seen in figure 1(a), a uniform 2D pattern of holes in a slab of thickness, d=1μm and refractive index, n=3.826, is designed using RSoft BandSOLVE (BS) PWE simulations to forbid the transmission of light at the desired wavelength. The structure is not periodic in the y-direction but it does have a symmetry plane through the centre of the slab, therefore we can apply parity to the simulations and view only those Bloch modes that are even with respect to the y-parity – i.e. the E-field is perpendicular to the hole axis. Band diagrams at this thickness show there is no photonic bandgap due to the 2nd-guided band dropping below the lowest-order band edge in terms of frequency. The figure also shows the position for the two resonant modes in an unmodified L3 cavity. Figure 1(b) shows results from 3D band solving with superimposed 3D FDTD results (uniform mesh cell size 50nm), showing the position of resonant modes relative to the upper and lower band edges. These results show that at a thickness of 1μm a PBG no longer exists.

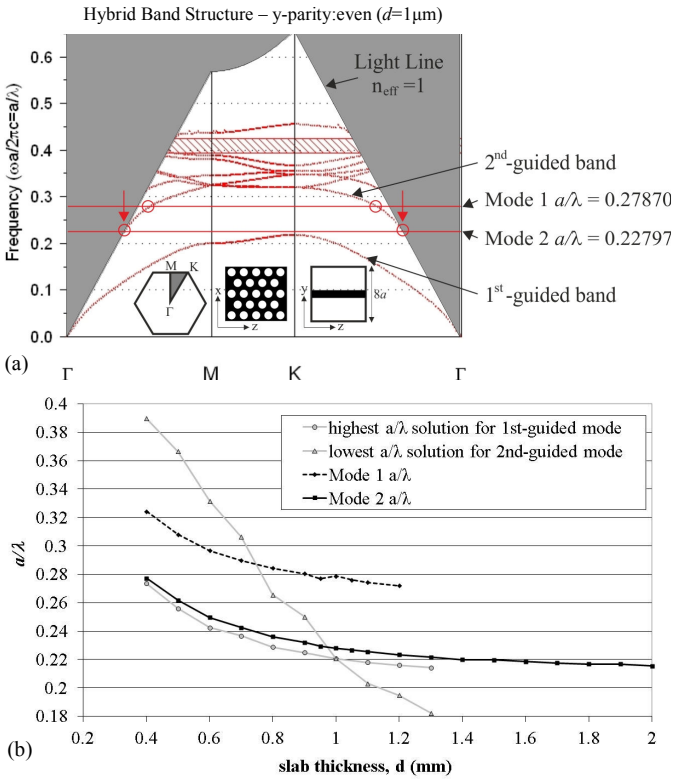


Figure 1. (a) 3D Dispersion diagram for modes with even y-parity of a 2D PhC slab composed of a hexagonal lattice of air holes, slab thickness, d=1μm, r/a=0.35, a=0.884μm, n=3.826. Insets show *k*-space lattice along with irreducible Brillouin Zone (shaded grey) and real-space representations of the slab in the y- and x-planes. (b) 3D PhC band diagram solutions for the even y-parity bandgap at varying d.

Whilst the effect of slab thickness exceeding that for single vertical mode propagation has been studied for single defect

cases, our work [5] is the only example for L3 defects that can result in very high-Q factors due to gentle confinement of the mode [6]. The cavity geometry is elongated in the z-direction as shown in figure 2(a) and in Pugh *et al* [5], where three thicknesses of slab were investigated in detail: 400nm, 800nm and 1μm. The interesting result is seen for d=1μm and the effect of displacing the outer holes of the L3 cavity at this thickness.

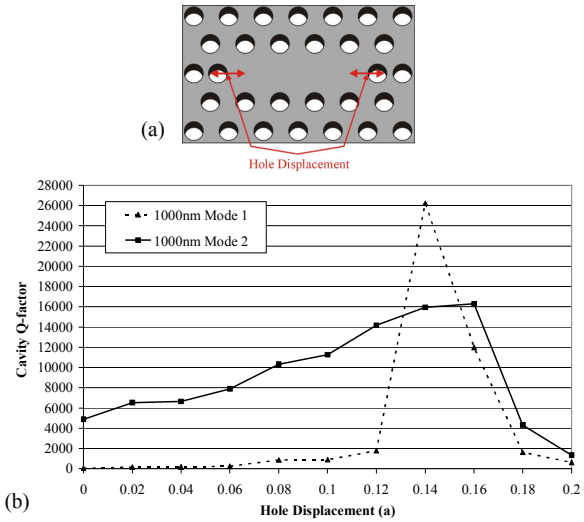


Figure 2. (a) Outer-hole displacement of an L3 defect cavity in a 2D hexagonal PhC [5]. (b) The effect of displacing the outer holes of the L3 cavity along z for the 1μm thick slab.

is shown in figure 2(b) – two modes are strongly confined at 0.14a displacement, mode 1 at λ=3.375μm with a Q~2.7x10^3 and mode 2 at λ=3.914μm with a Q~1.6x10^3. The position of these two modes in relation to the 3D bandgap is shown in figure 1(b). Displacing the holes plays two roles – Firstly, the E-field profile across the cavity in real space becomes more closely Gaussian in shape for the high Q cases, minimizing the E-field within the light-cone in k-space [6]. Secondly, the resonance wavelength shifts aligning it with the vertical cavity resonance for a particular slab thickness – an effect which gives the otherwise low-Q mode 1 a dramatic increase in Q at particular hole displacements. Figures 3(a) and (c) show real space representations of the $|E_x|$-field amplitude of mode 1 through the centre of the cavity in the y- and x-planes respectively. A further representation of mode 1, which is important for explaining the origin of the high-Q is the abs(E_x(re))-field through the centre of the cavity plotted in k-space shown in figure 3(b). First suggested by Srinivasan *et al* [7], this representation of the mode can quantify its losses through propagation into the light cone (solid line). Importantly in this paper, it also allows the losses into the 2nd-guided band of the PhC to be quantified by overlapping its k-path length onto figure 3(b) (dashed line) – the abs(E_x(re))-field here is very small. Therefore, increasing the slab thickness beyond the maximum thickness for only lowest-order optical mode in the vertical direction to propagate (d~460nm) and beyond the thickness for a full 3D even mode bandgap nevertheless allows for a high-Q PhC cavity mode to propagate.

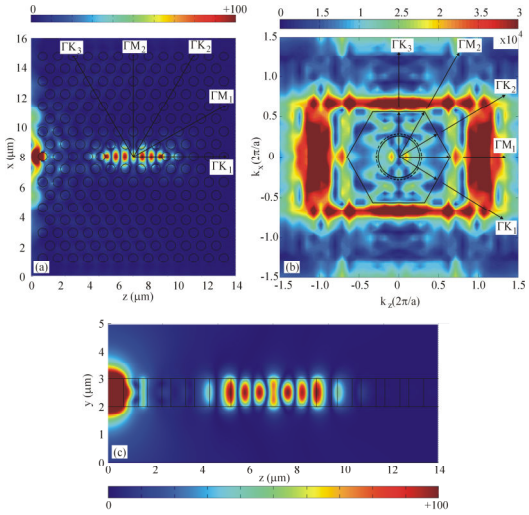


Figure 3. FDTD frequency snapshot representation of the behaviour of mode 1 at 0.14a hole displacement through the centre of the cavity in the (a) y- and (c) x-planes. (b) shows the abs(E_x(re)) k-space plot of (a).

III. CONCLUSIONS

This paper presents a study of two resonances in a modified L3 PhC slab cavity in a slab of thickness 1μm – mode 1 at λ=3.375μm with a Q~2.7x10^3 and mode 2 at λ=3.914μm with a Q~1.6x10^3. It is the behaviour of mode 1 that makes this study especially unique – a sudden rise in cavity-Q (beyond that of mode 2) is observed where no bandgap exists for the mode; this was found when changing the cavity geometry to a point where three confinement effects are believed to coincide: (i) There were small $|E_x|$-field components within the light-cone – a consequence of a nearest-Gaussian $|E_x|$-field distribution along the cavity of hole displacement cases, (ii) Small amounts of overlap between the cavity mode and the 2nd-guided band when viewed in k-space and (iii) Good vertical cavity resonance, where the guided wavelength approximately equalled the slab thickness. This high-Q is extremely sensitive to any change in cavity or slab properties which could be a useful property in switching or sensing applications. It is also an important result in terms of the fabrication of slab devices, since thin slabs can be very fragile and having high-Q cavity modes available in thicker slabs will make them more robust.

REFERENCES

[1] GR Nash *et al*, "Midinfrared GaInSb/AlGaInSb quantum well laser diodes operating above 200K", *App. Phys. Lett.* **94**, 091111 (2009).

[2] UK Khankhoje *et al*, "Modelling and fabrication of GaAs photonic-crystal cavities for cavity quantum electrodynamics", *Nanotech.* **21**, 065202 (2010).

[3] A Tandaechanurat *et al*, "Increase of Q-factor in photonic crystal H1-defect nanocavities after closing of photonic bandgap with optimal slab thickness," Optics Express, **16**, 1, 448-455 (2008).

[4] O Painter *et al*, "Defect modes of a two-dimensional photonic crystal in an optically thin dielectric slab" *J. Opt. Soc. Am. B* **16** 2 (1999).

[5] JR Pugh *et al*, "Design and fabrication of a midinfrared photonic crystal defect cavity in indium antimonide" *J. Opt. A: Pure Appl. Opt.* **11** 054006 (2009).

[6] Y Akahane *et al*, "High-Q photonic nanocavity in a two-dimensional photonic crystal" *Nature* **425** 944-947 (2003).

[7] K Srinivasan *et al*, "Momentum space design of high-Q photonic crystal optical cavities" *Opt. Exp.* **10** 5 670-684 (2002).

Optical Dispersion Management in Silicon Nanocrystal Slot Waveguides for Soliton Control

F. De Leonardis, V. M. N. Passaro, B. Troia *
Photonics Research Group, * CNIT UdR Bari
Dipartimento di Elettrotecnica ed Elettronica
Politecnico di Bari
Via Edoardo Orabona n. 4, 70125 Bari – Italy
E-mail: passaro@deemail.poliba.it
URL: http://dee.poliba.it/photonicsgroup

A. V. Tsarev
Laboratory of Optical Materials and Structures
A.V. Rzhanov Institute of Semiconductor Physics
Siberian Branch of Russian Academy of Sciences
Novosibirsk, 630090, Russia
E-mail: tsarev@isp.nsc.ru

***Abstract*— An investigation of group velocity dispersion for silicon nanocrystals-based sandwiched slot waveguides is proposed in this paper. Main guidelines to manage the group-velocity dispersion for controlling optical solitons in optical processing applications are found. Comparisons between single and double slot nanocrystal structures show intriguing properties.**

Keywords-Nanoscrystals; Nonlinear optics; Group Velocity Dispersion; Optical Soliton.

I. INTRODUCTION

In the last few years, a number of research study has been performed in order to exploit the third-order nonlinear effects in silicon for ultrafast signal processing [1-2]. However, the enhancement of non-linear effects in silicon based photonic components is still a key point in order to achieve active and more complex guiding structures. Non-linear materials, such as silicon nanocrystals (Si-nc), can be developed by using conventional CMOS fabrication processes [3]. In this paper, formation and control of optical solitons are theoretically demonstrated in dispersion-engineered silicon nanocrystal slot waveguides.

II. WAVEGUIDE OPTICAL DISPERSION

In this Section, a full parametric analysis is presented in order to design the Si-nc slot waveguides with a desired group velocity dispersion (GVD) coefficient. Then, design guidelines for excitation and control of optical soliton in Si-nc slot waveguides are found. The GVD-induced pulse broadening is known to scale with the dispersion length $L_D = T_0^2 / |\beta_2|$, being β_2 the GVD coefficient and T_0 the pulse width, while SPM-induced chirp scales with the nonlinear length $L_{NL} = (\gamma P_0)^{-1}$, with $\gamma = 2\pi n_2 / (\lambda A_{eff})$ the nonlinear parameter, n_2 the Kerr coefficient and P_0 the peak power of pulses launched at wavelength λ into the fundamental mode with effective mode area A_{eff}. The formation of fundamental soliton ideally requires $L_{NL} = L_D \ll L$ for a waveguide of length L. The previous relationship indicates that both $|\beta_2|$ and γ should be large enough to induce the formation of solitons in short waveguides, with lengths $L \leq 1$ cm. In this sense, the horizontal slot waveguide based on Si-nc should guarantee an optimization in the soliton formation with respect to standard SOI rib waveguides. Two Si-nc slot waveguides, named WG1 and WG2, have been investigated, as in Fig. 1(a) and (b). The rib width is W, the slot region filled with Si-nc has thickness G for WG1 and G_1, G_2 for WG2. The bottom and top silicon layers have thickness H_1 and H_2, respectively. Finally, the silicon layer between two slot regions in WG2 has thickness h. These geometrical parameters can be selected in order to control the values of $|\beta_2|$.

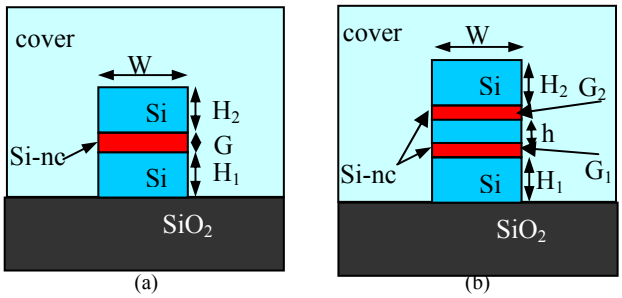


Figure 1. Cross section of SOI horizontal slot waveguide based on Si-nc: a) single slot, b) double slot.

In order to investigate the influence of geometrical parameters of Si-nc slot waveguide and the cover medium on the optical dispersion properties, a number of parametric simulations have been carried out. In Fig. 2 GVD coefficient spectra for quasi-TM modes are shown as a function of different values of cover refractive index n_c (air, water solution, silicon oxide), assuming H_{rib} = 430 nm for both structures WG1 and WG2. Each curve has been achieved by full vectorial Finite Element Method (FEM) [4] in the wavelength range 1250 ÷ 1750 nm, taking into account the Sellmeier equation for refractive index dispersion. In Fig. 2 we have assumed $H_1 = H_2$ = 200 nm, W = 200 nm and G = 30 nm for WG1, while $H_1 = H_2$ = 135 nm, W = 200 nm, $G_1 = G_2$ = 30 nm and h = 100 nm for WG2. Waveguide WG1 can clearly guarantee both normal and anomalous regime. On the contrary, structure WG2 only

moves its GVD spectra in the normal region. In addition, the increase of cover refractive index induces either $|\beta_2|$ increasing or decreasing for WG1 and WG2, respectively. In its turn, this effect induces a shift of zero GVD point (ZGVD) towards higher wavelengths, confirming the superiority of WG1 over WG2 regarding GVD dispersion.

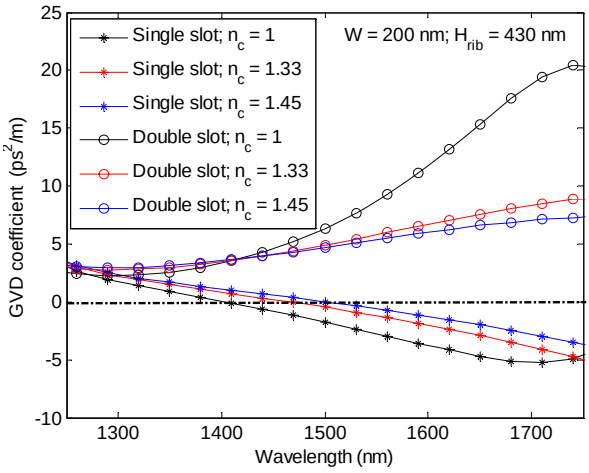


Figure 2. GVD coefficient spectra for various cover refractive indices.

GVD spectra for different values of W and slot thickness are shown in Fig. 3. The curve peak increases with increasing the structure width and decreasing the slot thickness. Thus, Figs 2-3 leads to conclude that WG2 structure is not suitable for soliton formation.

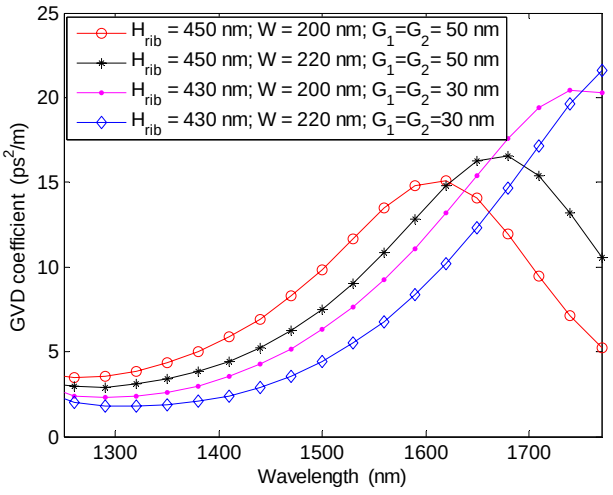


Figure 3. GVD coefficient spectra of WG2 structure for various widths and slot thicknesses.

Fig. 4 show the GVD coefficient at λ =1550 nm versus the total rib height for both structures considered and for different cover refractive index. The curves of Fig. 4 can be considered an useful tool to design the Si-nc slot waveguide with a desired GVD coefficient. Third order dispersion (TOD) coefficient has been also evaluated as a function of total rib height and different cover refractive index, showing moderate values, always less than 0.03 ps^3/m for WG1.

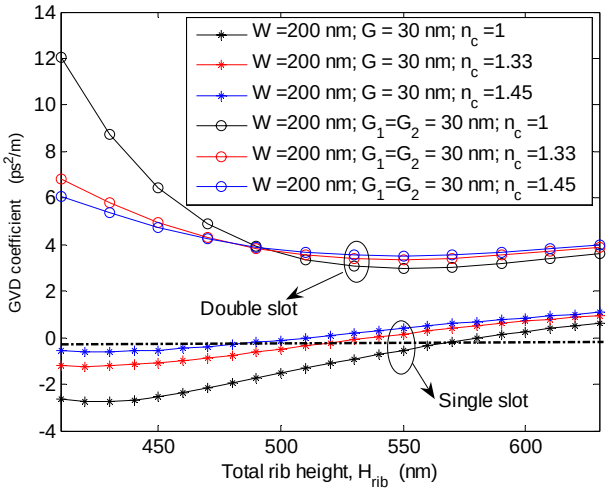


Figure 4. GVD coefficient versus rib total height for various cover refractive indices (λ =1550 nm).

III. Soliton Theory

Space-time evolution of optical solitons is described by the pulse propagation equation written for the slowly-varying amplitude $A(z,t)$ of the modal electric field $E(\mathbf{r},t)$ traveling along the propagation direction z [1]. We have considered the Si-nc slot waveguide WG1 (W = 200 nm, G = 30 nm, n_c= 1, and H_{rib} = 378 nm) excited by a Gaussian optical pulse with T_{FWHM} = 100 fs, and peak power selected to satisfy a specific condition, $N = (L_D/L_{NL})^{1/2} = 1.9$. Kerr coefficient in silicon nanocrystals, n_2 = 4×10^{-17} m^2/W, α_{Si} = 1 dB/cm, α_{Si-nc} = 15 dB/cm , β_{Si}^{TPA} = 0.5 cm/GW and β_{Si-nc}^{TPA} = 5 cm/GW for silicon and Si-nc layers, respectively, are assumed. After travelling over length less than 1.5 mm, the optical pulse is affected by a temporal broadening and distortion but, at around 3 mm, the pulse recovers and converts itself in a compressed hyperbolic-secant shape. Optical losses, TPA and FCA have an initial influence but, however, a stable soliton is expected to be achieved for lengths larger than 4 mm.

References

[1] F. De Leonardis and V. M. N. Passaro, "Ultrafast Raman Pulses in SOI Waveguides for Nonlinear Signal Processing," *IEEE J. Sel. Top. in Quantum Electron.*, vol. 14**,** pp. 739-751 (2008).

[2] Y.-H. Kuo, H. Rong, V. Sih, S. Xu, M. Paniccia and O. Cohen, "Demonstration of wavelength conversion at 40Gb/s data rate in silicon waveguides," *Opt. Express*, vol. 14**,** n. 24, pp. 11721–11726 (2006).

[3] A. Martınez, J. Blasco, P. Sanchis, J. V. Galan, J. Garcıa-Ruperez, E. Jordana, P. Gautier, Y. Lebour, S. Hernandez, R. Spano, R. Guider, N. Daldosso, B. Garrido, J. M. Fedeli, L. Pavesi, and J. Martı, "Ultrafast All-Optical Switching in a Silicon-Nanocrystal-Based Silicon Slot Waveguide at Telecom Wavelengths," *Nano Lett.***,** vol. 10, pp. 1506–1511 (2010).

[4] Comsol Multiphysics by COMSOL, Stockholm, single license (2005).

Wavelength Conversion Using Kerr Nonlinearity in a GaInP Photonic Crystal Fabry-Perot Resonator

I. Cestier, V. Eckhouse, G. Eisenstein
Electrical Engineering Dept.
Technion
Haifa, Israel

S. Combrié, A. De Rossi
Thales Research and Development
Thales
Palaiseau, France

***Abstract*—We report GaInP photonic crystal Fabry-Perot resonators containing integrated reflectors. Efficient wavelength conversion of 30 ps pulses was demonstrated where the Kerr effect dominates and the device speed is limited by the resonator structure.**

Photonic crystals; Kerr effect; Optical switching devices

I. INTRODUCTION

Photonic crystals (PhC) hold the promise of complex functional photonic components for future photonic devices and circuits. Nonlinear PhC resonators are key components for ultrafast, ultra-compact and low energy consuming all-optical switches and logic devices [1-2]. Most reported PhC resonators are small volume cavities with high Q values in which the switching speed is limited by the long cavity life time. A different type of resonator based on a 1.3 mm long PhC waveguide with cleaved end facets serving as reflectors was introduced in [3]. Wavelength conversion of a 10Gbit/s signal was demonstrated in that device.

In this paper we describe all-optical switching based on the instantaneous Kerr effect in a new type of nonlinear GaInP PhC Fabry-Perot (FP) resonator. GaInP is particulary advantageous for this and other nonlinear applications since its large bandgap (1.9 eV) prevents losses due to two photon absorption in the 1550 nm wavelength range. Any fast nonlinearity exhibited by the device is therefore exclusively due to the Kerr effect. The FP resonator we report is a low loss PhC waveguide containing integrated reflectors which have a complex wavelength dependent transfer function. This results in a series of transmission resonances with various spectral widths and offers some degree of freedom when choosing the control (pump) and signal (probe) wavelengths, in switching and wavelength conversion experiments. Efficient wavelength conversion of 30 ps wide pulses as well as an extremely large static and low frequency (below 500 kHz) response due to thermal effect were demonstrated. At high frequencies, the switching process is strictly due to the instantaneous Kerr effect and the device speed is determined by the resonator life time.

II. RESULTS

The device consists of a W1 type PhC waveguide that contains mode converters which enhance the coupling efficiency and eliminate the end facet reflectivities. The 250 µm long FP resonator is created by placing identical reflectors, composed of two holes, within the waveguide [4]. The resonator is shown schematically in the inset of Fig. 1(a). The finesse spectrum was extracted from linear transmission spectroscopy and is presented is Fig. 1(a). Due to the reflector complex transfer function, the finesse shows a periodic modulation which is superimposed on a general increase for long wavelength. This wavelength dependent finesse induces a series of transmission resonances with various spectral widths, ranging from 4 GHz to 37 GHz.

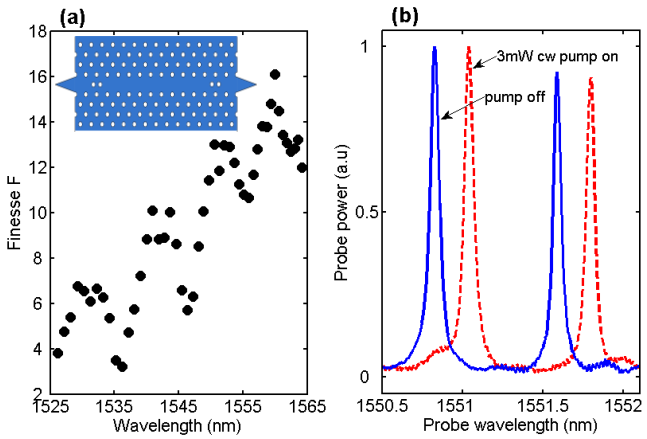


Figure 1. (a) Finesse spectrum of the resonator. Inset: Structure of the resonator. (b) Static transmission spectrum: pump off (blue) and on (red).

The static nonlinear response was measured first and is presented is Fig. 1(b). The blue line corresponds to the linear transmission of FP fringes over a 2 nm range obtained with a weak broad band source (ASE of an EDFA). The influence of a CW pump on the fringes was measured by combining a signal to the EDFA source. The obtained transmission is described by the red line, which clearly shows a red shift of the FP fringes. In this probe wavelength range the 3 mW CW pump induced a phase shift $\delta\varphi$ of $\pi/3$. The static nonlinearity was quantified by the phenomenological parameter γ according to $\gamma=\delta\varphi/4PL$ with P and L being the circulating pump power and the resonator length, respectively. γ takes on the large value of $\gamma=2.2 \times 10^5$ $m^{-1}W^{-1}$ for the mode at $\lambda=1551$ nm. The γ values were extracted for each fringe shift across the transmission spectrum and have a linear dependence on the group index at the probe

wavelength. These values are about two orders of magnitude larger that the corresponding values obtained from self-phase modulation (SPM) [5] and four wave mixing (FWM) [6] experiments in similar waveguides.

The dynamic nonlinear response of the device was tested by modulating a CW tunable laser and using a low power (≈1 mW) tunable CW probe. The response of the resonator depends on two factors, the fundamental response of the nonlinearity and the structural limitations imposed by the life time of the cavity. All-optical switching was performed with the control and signal optical signals aligned to two distinct FP resonances. Fig. 2(a) shows the dependence on resonance width of small-signal modulation responses for frequency range of 50 MHz to 20 GHz. The modulated pump was aligned with a fringe having a large spectral width of 35 GHz while the probe was tuned to fringe peaks of different widths (labeled in the legend). The modulation bandwidths correspond to the resonance spectral widths, indicating that the wavelength conversion is induced by an instantaneous process and is structurally limited. Since the pump causes an increase in the modal index (confirmed by the large signal modulation results), we conclude that the nonlinearity is due to the Kerr effect. The response a very low frequencies, 50 kHz to 500 kHz, was more than two orders of magnitude larger than that in the low frequency range of Fig. 2(a) but dropped off fast beyond 500 kHz. This indicates that the very large static response shown is Fig. 1(b) is due to a thermal effect. Wavelength converted results for large signal are illustrated in Fig. 2(b) and (c) for 92 ps and 30 ps wide pump pulse, respectively. Fig. 2(b) shows the 200 mW peak power input pump (black) and converted probe waveforms for a probe aligned to a fringe with spectral width of 20 GHz (blue) and 5.5 GHz (red). The probe wavelengths with no pump were tuned to the valley on the long wavelength side of the fringe. The converted probes follow the sense of the pump modulation, consistent with an index increase induced by the pump. The converted probe aligned with the narrower resonance shows a higher contrast. The converted pulse is obtained from the shifting fringe crossing the CW probe; therefore a narrower fringe causes a larger change in probe transmission yielding a pulse with higher contrast. Fig. 2(c) shows the probe transmission dynamics for 30 ps wide pump pulses and a probe which was tuned to the peak of a fringe with a spectral width of 5.5 GHz. The converted signal exhibits the complementary modulation of the pump. The converted probe outputs are shown for different coupled pump pulse energies. For contrasts of 20% to 60% the required switching energies are in the range of 5 pJ to 18 pJ.

III. CONCLUSION

To conclude, we have demonstrated efficient and fast all-optical switching in a GaInP PhC FP resonator based on the instantaneous Kerr effect. Structural parameters determine the speed at which the device can be operated in wavelength conversion experiments. 30 ps wide pulses were converted using pulse energies of a few pJ.

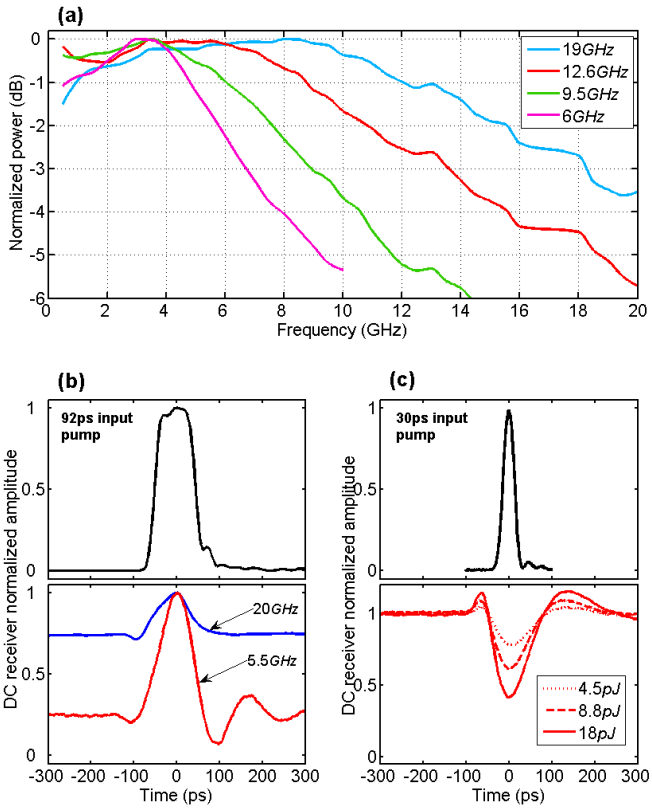


Figure 2. (a) Small-signal modulation response of converted probe for various probe fringes. (b) and (c) Pump and probes transmission dynamics of a single 92 ps and 30 ps wide pulse, respectively.

ACKNOWLEDGMENT

This research was supported by the project GOSPEL within the seventh framework of the European Commission.

REFERENCES

[1] K. Nozaki, T. Tanabe, A. Shinya, S. Matsuo, T. Sato, H. Taniyama, and M. Notomi, "Sub-femtojoule all-optical switching using a photonic-crystal nanocavity," Appl. Phys. Lett. **87**, 151112 (2005)

[2] T. Tanabe, M. Notomi, S. Mitsugi, A. Shinya, and E. Kuramochi, "All-optical switches on a silicon chip realized using photonic crystal nanocavities," Nat.Photonics **4**, pp. 477–483 (2010)

[3] I. Cestier, V. Eckhouse, G. Eisenstein, S. Combrie, P. Colman, and A. De Rossi, "Resonance enhanced large third order nonlinear optical response in slow light GaInP photonic-crystal waveguides," Opt. Express **18**, pp. 5746–5753 (2010)

[4] M. Mulot, M. Swillo, M. Qui, M. Strassner, M. Hede,and S. Anand, "Fabry-Perot cavities based on two-dimensional photonic crystals fabricated in InP membranes," J. Appl. Phys. **95**, pp. 5928–5930 (2004)

[5] S. Combrie, Q. Vy Tran, C. Husko, P. Colman, and A. De Rossi, "High quality GaInP nonlinear photonic crystals with minimized nonlinear absorption," Appl. Phys. Lett. **95**, 221108 (2009)

[6] V. Eckhouse, I. Cestier, G. Eisenstein, S. Combrie, P. Colman, A. De Rossi, M. Santagiustina, C. G. Someda, and G. Vadala, "Highly efficient four wave mixing in GaInP photonic crystal waveguides," Opt. Lett. **35**, pp. 1440–1442 (2010)

Solving the interferometric readout in sensor devices by an all-optical phase modulation technique

S. Dante, D. Duval, L.M. Lechuga
Nanobiosensors and Bioanalytical Applications Group
CIN2(CSIC) and CIBER-BBN
Campus UAB, 08193, Cerdanyola del Valles, Barcelona, Spain
stefania.dante@cin2.es

C. Dominguez
Micro and Nanosystem Department
Instituto de Microelectronica de Barcelona, CNM (CSIC)
Campus UAB, 08193, Cerdanyola del Valles, Barcelona, Spain

***Abstract*—A novel phase modulation system based on an all-optical approach for integrated interferometric devices is presented. This method provides real-time linear phase read-out for highly sensitive, label-free and user-friendly biosensing applications oriented to a Lab-on-Chip final implementation.**

Keywords – Mach-Zehnder interferometer, Bimodal interferometer, biosensor, integrated optics, phase modulation.

I. INTRODUCTION

Current needs for highly sensitive, real-time and fast detections of biological/chemical targets in extremely reduced amount of samples, have motivated the seek for Lab-on-Chip (LOC) sensing platforms. These compact devices include a highly sensitive transducer, properly functionalized for the application of interest, a microfluidic network for sample preparation and delivery and electronics for signal acquisition and processing. The transducer is one of the key elements for suitable LOC operation: it must be enough sensitive, reliable and stable in time. Integrated optical sensors, based on evanescent wave interaction, are the most suitable candidates as they have demonstrated their capability for real-time and label-free applications. In particular interferometric transducers are one of the most sensitive configurations [1], allowing limits of detection (LOD) in the range of 10^{-7} refractive index units (RIU), which corresponds to pM analyte concentrations. Different configurations have been suggested in the last decades, as Mach-Zehnder (MZI), Young (YI), Hartman (HI) or Back-scattering (BSI) Interferometers. More recently a simpler configuration, the so-called Bimodal Waveguide Interferometer (BiMW), based on a two-mode interference scheme, has been demonstrated [2] as a valid alternative to more complex MZI or YI devices. In the BiMW device an interference pattern is created at the output of a single channel waveguide supporting two transversal modes: the fundamental and the first order ones of a same polarization. In this configuration, beams separation and recombination through Y junctions is unnecessary, reducing fabrication tolerances influence and consequently increasing device performance. The detection limit obtained with BiMW device is comparable with the one from MZI sensor.

But despite their high sensitivity, interferometric devices suffer an important limitation due to their intrinsic periodic nature. Since output intensity is a periodic function of the phase change to be detected, clear output interpretation is prevented by signal ambiguity and sensitivity fading. Furthermore input fluctuations can give rise to false positive responses, inadmissible for real clinical practice. For these reasons, commercial interferometric biosensors are scarce.

All the drawbacks arising from the periodic interferometric output can be solved with a phase modulation system able to provide a linear signal read-out. Moreover it is immune to sensitivity variations and input fluctuations. Common methods for phase tuning in integrated optical devices rely on electro-optic, acousto-optic, thermo-optic or magneto-optic working principles. Their validity has been demonstrated, but they are not suitable for a complete LOC integration, since they require further and not conventional fabrication processes/materials, often incompatible with microfluidics, and they need expensive and bulky electronic equipment, unserviceable for LOC implementation.

We present here the implementation of an all-optical phase modulation system for MZI and BiMW devices, requiring only a standard Fabry-Perot commercial laser diode as light source to induce the phase modulation. Interferometric devices are fabricated using standard CMOS compatible processes at clean-room facilities. The sensors are constituted by $Si/SiO_2/Si_3N_4$ rib waveguides, optimized for visible light operation.

II. PHASE MODULATION WORKING PRINCIPLE

In standard interferometric measurements, output signal is described by $I(t) \propto \cos(\Delta\varphi_S(t))$, where $\Delta\varphi_S(t)$ is the phase change induced by a biological interaction, which depends on the difference of effective refractive index between the two interfering modes.

In our approach, a phase variation between the modes propagating in the device (MZI or BiMW) is induced by changing the wavelength of the input light beam (a few nms). In both devices, a change of propagating wavelength will differently modify the effective refractive indexes of the two propagating modes, resulting in a variation of their phase difference. According to our previous numerical simulations, the wavelength change necessary to induce a 2π phase variation between the two modes is less than 2 nm for both MZI and BiMW devices. This value depends on geometric

parameters, materials (i.e. refractive index) and central operating wavelength (in our case λ_0=660 nm). Such wavelength variation can be obtained by taking advantage of a drawback of common semiconductor laser diodes: the power dependence of their wavelength emission. The use of a sinusoidally varying driving current for the laser source allows an output analysis by Fourier Transform method.

When introducing a phase modulation function, the interferometer output is transformed in:

$$I(t) \propto \cos[\Delta\varphi_S(t)+\mu_M \sin(\omega_M t)] \quad (1)$$

being μ_M and ω_M the modulation amplitude and frequency respectively. By choosing the proper modulation amplitude, μ_M, it can be demonstrated that the phase change induced by a biological reaction occurring in the device sensing area can be directly and real-time evaluated from the inverse tangent of two consecutive signal harmonics [3]. Fig.1 summarizes this detection technique: a laser beam with varying wavelength is used to excite mode propagation in the interferometer and its output is deconvoluted with Fourier analysis in order to get a linear response. A Labview application gives the real-time phase extraction and its unwrapping: the signal obtained in this way is linear and shows a theoretically infinite working range.

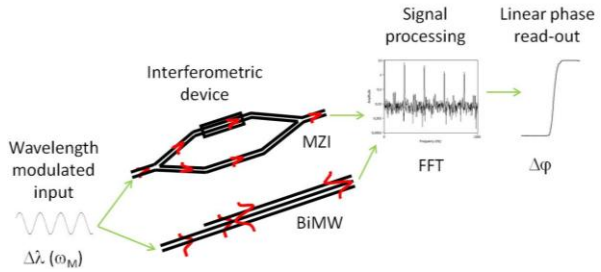


Figure 1. Scheme of the all-optical phase modulation approach for integrated interferometric devices (MZI or BiMW).

III. EXPERIMENTAL

For our experiments, a laser diode ML101J27 (Thorlabs) with nominal wavelength of 660 nm has been employed as light source. Light propagation inside the interferometer is obtained by end-fire method, by focusing the input beam with a 40x objective at the entrance of a polished waveguide. In the case of MZI the single mode output light is collected by a Si photodiode (Thorlabs, DET36A), while in the case of BiMW the bimodal output is measured with a two sections photodiode (Hamamatsu, S4349). Temperature stabilization is required for both the laser diode mount and the BiMW holder, as in the BiMW device there is no reference arm to compensate for temperature variations.

Fig. 2 shows the comparison between the standard interferometric pattern (i.e. DC component in this modulation scheme, in Fig.2a)) and the linear phase signal (Fig.2b)) corresponding to the detection of an index change of $\Delta n = 1.8 \cdot 10^{-3}$ RIU. Measurements have been done in TE polarization, with a BiMW device operated with a driving current of (143±36) mA and a modulation frequency of f_M=215 Hz. The index change is induced in the device sensing area by injecting a solution of HCl while milli-Q grade water is used as buffer. Refractive index of the solution is measured prior to injection with a commercial Abbe refractometer. A calibration curve obtained in these conditions shown a detection limit for index changes of $\Delta n_{min} = 4 \cdot 10^{-7}$ RIU, comparable with standard interferometric schemes.

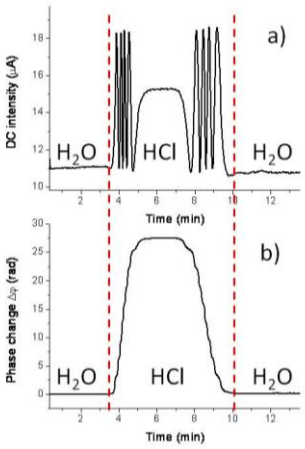


Figure 2. Detection of an index change $\Delta n = 1.8 \cdot 10^{-3}$ RIU, for TE polarization on a BiMW device. a) standard intensity interferometric pattern and b) linear phase read-out.

With this simple and cost-effective modulation approach, phase information is not deduced anymore from the variations of the intensity interference pattern (as shown in Fig.2a), but is directly evaluated (Fig.2b). All the issues arising from the periodic nature of interferometric signals are therefore solved. Furthermore the sensitivity to index changes is the same as reported with the standard configuration employing a bulky He-Ne laser, but an easily integrated laser diode is employed in this case, allowing portable sensing platforms implementation.

Biosensing evaluations are currently being performed in order to study the device sensitivity for immunosensing detections.

ACKNOWLEDGMENT

Authors acknowledge financial support from M. Botin foundation. S. Dante acknowledges the "Programa de Formación de Profesorado Universitario (FPU)" of the "Ministerio de Educación" of Spain.

REFERENCES

[1] M.C. Estevez, M. Alvarez, and L.M. Lechuga, "Integrated Optical Devices for Lab-on-a-chip Biosensing Applications", Laser Photonics Rev., DOI 10.1002/lpor.201100025.

[2] K. E. Zinoviev, A. B. González-Guerrero, C. Domínguez and L. M. Lechuga, "Integrated Bimodal Waveguide Interferometric Biosensor for Label-Free Analysis", J. Lightwave Technol., 2011, vol. 29(13), pp. 1926-1930.

[3] S. Dante, D. Duval, B. Sepulveda, A.B. Gonzalez-Guerrero, J.R. Sendra and L.M. Lechuga, "All-optical phase modulation for integrated interferometric biosensors", Opt. Express, in Press.

Non-blocking Optical Banyan Switch on SOI

Michael Waldow, Andreas Prinzen, Jens Bolten, Thorsten Wahlbrink, Heinrich Kurz
AMO GmbH, Otto-Blumenthal-Straße 25, 52074 Aachen, Germany
waldow@amo.de

***Abstract*— An integrated spatially non-blocking 2x2 Banyan switch on silicon on insulator (SOI) is demonstrated. The device relying on thermally switched microring resonators has a footprint of less than 0.02 mm² and shows negligible channel crosstalk. The presented novel switch topology features a high scalability for application in many-core interconnections for network on-chip architectures.**

Keywords-component: Integrated optics, optical switches, ring resonator, Silicon on insulator technology

I. INTRODUCTION

Optical communication systems are dominating data communication on long distances today. Recently optical communication systems have steadily gained interest also on very short distances like on-chip optical interconnection. Silicon builds the ideal material platform for these so-called network-on-chip (NoC) architectures due to its well established technology of the CMOS industry and the possibility to integrate electronic and optical devices monolithically.

Crucial elements in NoCs are optical routing and switching structures. Particular switch topologies relying on silicon microring resonators are highly beneficial in terms of power consumption and device footprint [1]. Microresonator based optical switches on silicon rely in general on a change of the index of refraction by an external control signal. Therefore different physical effects can be applied, like the prominent plasma-dispersion effect, the thermo-optical effect or the linear electro optic effect in strained silicon [2]-[3].

The standard topology for a non-blocking switch, i.e. a switch which allows anytime establishing a connection from any free input port to any free output port, is the crossbar switch (s. Fig 1(a)). In a crossbar switch input and output ports are connected via a grid of switching elements. Several microresonator based photonic crossbar switches have been presented [4]-[5]. A major drawback of this switch topology is its limited scalability as the number of switching elements N_{SWITCH} scales quadratically with the number of input ports ($N_{SWITCH}=N_{PORTS}^2$). Furthermore, the number of necessary waveguide crossings, which impose additional losses and channel crosstalk, also scales with the square of the number of input ports. Recently published topologies of 4x4 non-blocking silicon routers rely on 8 microrings, 10 waveguide crossings with a footprint of 0.07 mm² [6] or rely on 6 Mach-Zehnder interferometers, 6 waveguide crossings with a footprint of 0.48 mm² [7].

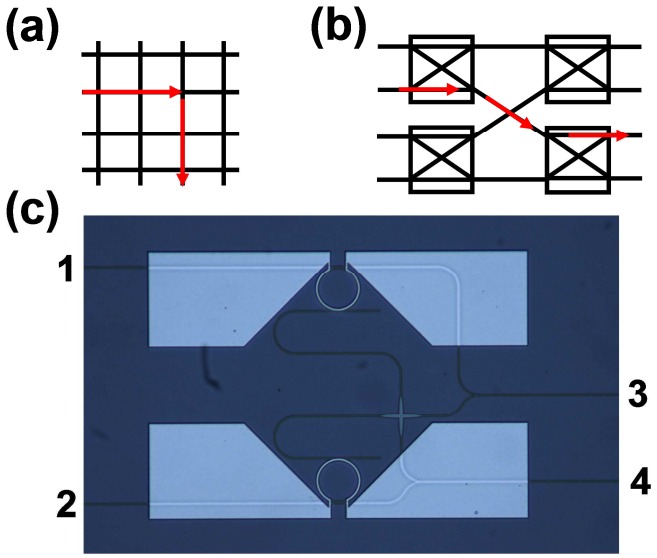


Fig. 1. Schematic drawing of the topology of a (a) 4x4 crossbar switch and a (b) 4x4 Banyan-Switch. Exemplarily an established connection between input 2 and output3 is highlighted (red arrows). (c) Microscope image of the realized 2x2 Banyan switch on SOI.

The Banyan switch represents a highly modular topology as it is built out of several identical 2x2 switching elements arranged in multiple stages making it an easy and highly scalable topology (s. Fig. 1(b)). In a Banyan network the number of switching elements is reduced to $N_{SWITCH}=N_{PORTS}*\log_2 N_{PORTS}$, simultaneously the number of waveguide crossings is decreased drastically. As an example, the topology of a 4x4 crossbar switch and a 4x4 Banyan-switch is shown in Fig. 1(a) and Fig. 1(b). A previously realized integrated optical 4x4 Banyan switch structure on SOI is based on Mach-Zehnder interferometers and relies on several centimeter long waveguides as well as micrometer-sized waveguide cross-sections [8].

In this work for the first time a silicon nanophotonic Banyan-switch relying on microring resonators is demonstrated. The presented device topology is highly scalable, requires a minimum number of waveguide crossing and switching elements and features a low device footprint of less than 0.02 mm².

II. DEVICE FABRICATION AND CHARACTERISATION

The 2x2 Banyan switch is fabricated on SOI substrate consisting of a 2 µm thick buried oxide layer and a 220 nm thick device layer. Definition of the structures is carried out by

electron-beam lithography (EBL) using hydrogen silsesquioxane (HSQ) as an EBL resist. Pattern transfer into the silicon is achieved by HBr-chemistry based inductive coupled reactive ion etching. Switching elements consist of symmetrically coupled microring resonators with a ring radius of 10 µm and a coupling gap of 150 nm. Silicon waveguide widths and heights are 350 nm and 220 nm, respectively. Waveguide crossing are based on elliptical tapered silicon waveguides to a maximum width of 2 µm. As a cladding material a spin-on glass is used, resulting in a cladding height of 850 nm. On top of the cladding material Aluminium micro-heaters with a thickness of 100 nm and a minimum width of 1 µm and centered to the silicon ring resonators are defined via optical lithography and a subsequent lift-off step. In Fig. 1(c) a microscope image of the realized 2x2 Banyan switch on SOI is shown. The switch features two input and two output ports and consists of two thermo-optic switching elements based on ring resonators, two signal combiners and a single waveguide crossing.

Characterization of the integrated nanophotonic 2x2 Banyan switch is carried out using a conventional optical end-fire setup. A switching operation, i.e. a change in the resonance wavelength of a ring resonator, is initiated by altering the applied voltage at the contact pads of the micro-heater. Resulting switching characteristic for an operation wavelength of λ=1334.54nm are depicted in Figure 2(a). Shown is the normalized change in optical transmission for $|S_{31}|^2$ (black) and $|S_{41}|^2$ (grey) as a function of applied voltage to the contact pads of the upper micro-heater. From Figure 2(a) an electrical controlled increase in optical transmission $|S_{31}|^2$ of 11dB and a decrease in optical transmission $|S_{41}|^2$ of 4dB for an increase of the electrical control voltage can be identified. Accordingly in Figure 2(b) the switching characteristics for $|S_{32}|^2$ (black) and $|S_{42}|^2$ (grey) as function of applied voltage to the contact pad of the lower micro-heater are shown. From both graphs of Figure 2 it becomes clear, that with the presented device optical signals can be routed from any input port to any desired optical output port by using electrical control signals. Additional to the switching operation of the 2x2 Banyan switch the interaction of the two utilized switching elements has been characterized. In an extensive study a negligible channel crosstalk of less than 0.01 dB for all switching channels has been detected.

III. Conclusion

In summary, we have presented a Banyan switch as a new switch topology for silicon nanophotonic routers relying on microring resonators. The presented switch topology is highly scalable, modular and can be easily scaled up to larger numbers of input and output channels. The realized device features a low footprint of 0.02 mm², has a maximum change in optical transmission of 12 dB, shows negligible crosstalk and provides a switching time of about 10 µs. Switching in the presented device is based on the thermo-optic effect, but the presented concept can be easily expanded to faster switching mechanisms like depletion of charge carriers or electro-optic effects in strained silicon structures.

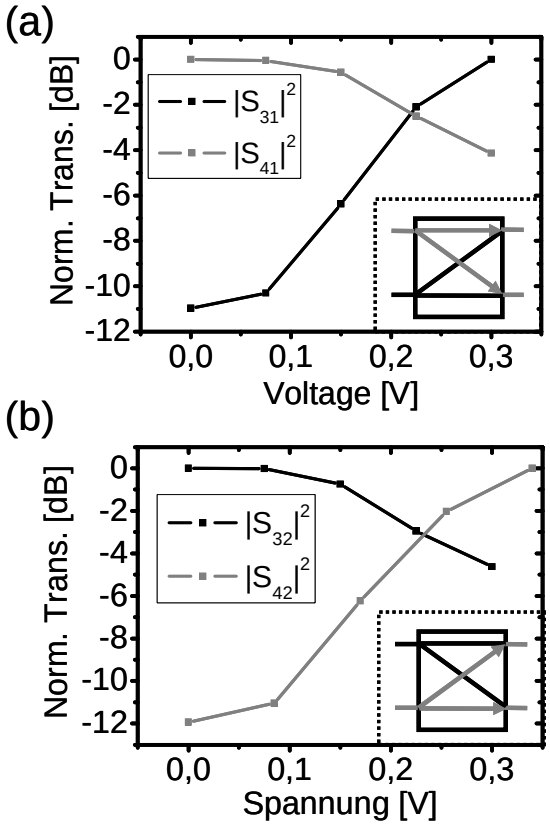


Fig. 2. (a) Normalized optical transmission from input 1 to output 3 and output 4 as function of applied voltage to the heater of ring 1 and (b) from input 2 to output 3 and output 4 as function of applied voltage to the heater of ring 2

References

[1] W. Poon, X. Luo, F. Xu, and H. Chen, "Cascaded microresonator-based matrix switch for silicon on-chip optical interconnection", Proc. of the IEEE, vol. 97, pp. 1216-1238, Jul. 2009.

[2] Q. F. Xu, B. Schmidt, S. Pradhan, and M. Lipson, "Micrometre-scale silicon electro-optic modulator," Nature **435**, 325–327 (2005).

[3] B. Chmielak, M. Waldow, C. Matheisen, C. Ripperda, J. Bolten, T. Wahlbrink, M. Nagel, F. Merget, and H. Kurz, "Pockels effect based fully integrated, strained silicon electro-optic modulator", Opt. Express, vol. 19, no.18, pp. 17212-17219, Aug. 2009.

[4] Shih-Jung Chang, Chi-Yu Ni, Zhipeng Wang, and Yung-Jui Chen, "A Compact and Low Power Consumption Optical Switch Based on Microrings", IEEE Phot. Tech. Lett., Vol. 20, No. 12, pp. 1021-1023, 2008.

[5] B. E. Little, S. T. Chu, W. Pan, and Y. Kokubun, "Microring resonator arrays for VLSI photonics", IEEE Photon. Technol. Lett., vol. 12, pp. 323–325, Mar. 2000.

[6] N. Sherwood-Droz, H. Wang, L. Chen, B. G. Lee, A. Biberman, K. Bergman, and M. Lipson, "Optical 4x4 hitless silicon router for optical Networks-on-Chip (NoC)", Opt. Express, vol. 16, no. 20, pp. 15915-15922, Sept. 2008.

[7] M. Yang,1, W. M. J. Green, S. Assefa, J. Van Campenhout, B., G. Lee, C. V. Jahnes, F. E. Doany, C. L. Schow, J. A. Kash,1 and Y. A. Vlasov, "Non-Blocking 4x4 Electro-Optic Silicon Switch for On-Chip Photonic Networks", Opt. Express, vol. 19, no. 1, pp. 48-54 Jan. 2011.

[8] Y. Li, J. Yu, and S. Chen, "Rearrangeable nonblocking SOI waveguide thermooptic 4x4 switch matrix with low insertion loss and fast response", Phot. Tech. Lett., vol. 17, no. 8, pp. 1641-1643, Aug. 2005.

Integrated corner mirrors as a platform for miniaturized planar strain sensing

Lewis G. Carpenter, Paolo L. Mennea, Helen L. Rogers, Christopher Holmes, James C. Gates and Peter G.R. Smith
Optoelectronics Research Centre
University of Southampton
Southampton, UK
lc906@orc.soton.ac.uk

***Abstract*—Corner mirrors provide a route to create more compact two dimensional strain rosettes. Based on silica-on-silicon, our device fabrication utilizes physical micromachining and direct UV writing. A grating based loss technique has shown our corner mirrors to have excess losses of 1.15dB for TM polarization.**

Keywords-component; Strain sensor; Planar Integrated Optics; Bragg Gratings;

I. INTRODUCTION

Corner mirrors can be used to provide a route to achieve higher density optical components on an integrated chip. However the ability to redirected light and expose evanescent fields at the point of turning, provides an alternative geometry for a range of integrated devices. These include: optofludic switches, plasmon couplers and strain sensors. In our work we create a device utilizing Bragg gratings and a corner mirror to allow interrogation of strain in two axes in a compact integrated package. Bragg grating based strain rosettes have been demonstrated in fibers, however these devices can be bulky in order to accommodate the fiber bend radius (~1mm) [1]. Correctly placing the fiber Bragg gratings can also be difficult due to their cylindrical shape and usually employs the need for separate packaging to ensure the correct angle between the gratings is obtained (e.g. the Delta rosette) [1]. Our device combines the waveguides, several Bragg gratings and a corner mirror in a 2x2cm footprint, allowing strain to be sensed in confined space with a single optical connection. Previously integrated corner mirrors have been demonstrated in Si_3N_4/SiO_2 multilayer hollow waveguides with losses of TE 1.0dB and TM 0.8dB [2] and in SiO_2 TE 1.48dB and TM 1.08dB [3] all losses are measured at 1550nm. In previous work we have reported a device containing a pair of corner mirrors with average individual insertion loss of ~0.96dB for TM [4]. A schematic of the corner mirror device is shown in Fig. 1. The strain can be sensed in both direction x and y, see Fig.1, through the strain-optic effect tuning the Bragg grating central wavelength preferentially for the grating parallel to the applied strain. In other work, by our group, we have shown that three point bending achieves 280pmN^{-1} Bragg grating wavelength tuning for the TM polarization at 1550nm [5].

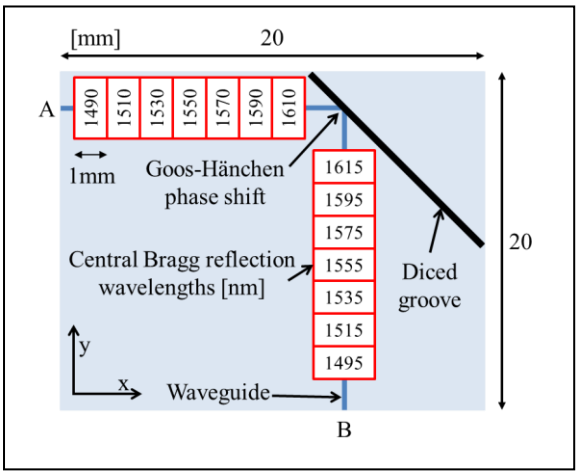


Figure 1. Schematic of corner mirror device, showing the order of the Bragg grating central wavelengths.

II. DEVICE FABRICATION AND CHARACTERIZATION

Our fabrication technique for silica corner mirrors utilizes physical micromachining using a commercially available precision dicing saw. Waveguides and Bragg grating are inscribed into silica-on-silicon substrates by direct UV writing (DUVW). DUVW creates single mode integrated channel waveguides, with low loss waveguides propagation (typically around 0.24dBcm^{-1}) [6] and allows us to produce Bragg gratings within the telecommunications C-band (1525-1565nm). These complementary techniques are suited to rapid prototyping and small batch production of silica integrated optic devices without the need for cleanroom processing. The corner mirror demonstrated in this work, as shown in Fig. 2, was fabricated by dicing a groove through the silica into the silicon. The groove was formed using a diamond impregnated nickel bonded blade (55mm diameter) at 20krpm with a translation speed of 0.1mms^{-1}. Investigation of grooves diced with these parameters have been measured to a give surface roughness (S_a) of around 19nm. Channel waveguides and Bragg gratings are then directly inscribed into the planar core layer, the groove location is detected precisely by monitoring the reflected UV laser light from the sample.

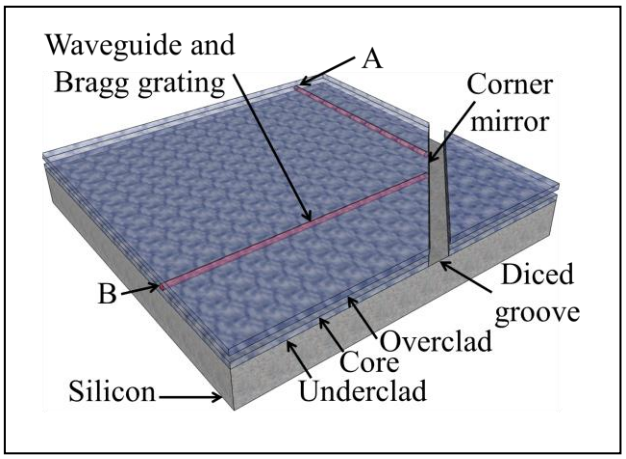


Figure 2. Schematic of corner mirror showing the silica planar layers and silicon substrate.

Once the groove has been detected the sample is rotated by 90° and the Goos-Hänchen phase shift is accounted for [7] by an appropriate offset.

$$S_{TE} = \left(\frac{\lambda}{\pi n_{eff}}\right)\frac{\tan\alpha_c}{(\sin^2\alpha - \sin^2\alpha_c)^{1/2}}, \qquad S_{TM} = \frac{S_{TE}}{(\sin^2\alpha_c)}. \quad (1)$$

Where S_{TE} is the Goos-Hänchen phase shift for the TE polarization, S_{TM} is the Goos-Hänchen phase shift for the TM polarization, λ is the wavelength of interest, n_{eff} is effective refractive index, α_c is the critical angle and α is the angle at which the waveguide intersects the mirror. For a wavelength of 1550nm, an effective refractive index of 1.448, a critical angle of 43.7° and at 45° waveguide / mirror intersection, the Goos-Hänchen phase shift is calculated to be 2.1µm and 4.5µm for TE and TM respectively. As the sample is offset from the center of the rotation stage, Eulerian angles along with an offset (the stage center) are utilized to ensure the point at which the waveguide must start (after the Goos-Hänchen phase shift) is returned to. Bragg gratings are inscribed before and after the corner mirror, as shown in Fig. 1.

The wide spectral range (1490-1615 nm) of Bragg gratings gives a non-destructive, ratiometric route for measuring the loss of the corner mirror [6]. The device was characterized using a broadband SLED source (1480-1630nm), an optical spectrum analyzer, 50/50 coupler and a polarizer where TE and TM polarizations can be independently interrogated. Reflection spectra, see Fig. 3, were collected sequentially from facets A and B (see Fig. 1). The Bragg gratings are fitted using a Gaussian fitting algorithm by which the ratio of their amplitudes are taken and from which the insertion loss of the mirror can be calculated, as shown in Fig. 4. By using the technique described in [6], an insertion loss of the corner mirror can be calculated. For wavelengths between 1490nm and 1615nm the insertion loss of the corner mirror is 1.15dB for the TM mode and 1.63dB for the TE mode. These results are comparable to those previously obtained and to those achieved in silica [3]. We shall present our latest results in the application of this corner mirror to applied two dimensional strain.

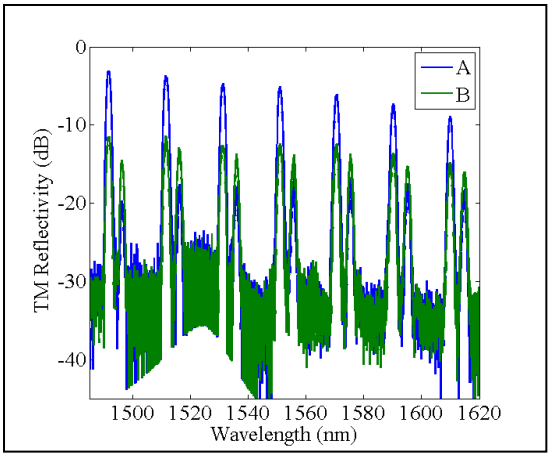


Figure 3. TM Reflection spectra collected from facet A and B of the corner mirror device.

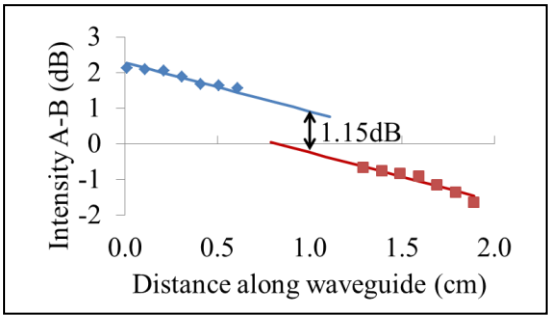


Figure 4. Ratio of reflected power of each Bragg grating relative to its chip position. The corresponding central Bragg wavelengths from left to right follow the order from facet A to B as shown in Fig. 1.

[1] D. C. Betz, G. Thursby, B. Culshaw, and W. J. Staszewski, "Advanced layout of a fiber Bragg grating strain gauge rosette," Journal of Lightwave Technology, vol. 24, no. 2, pp. 1019-1026, 2006.

[2] H.-K. Chiu, F.-L. Hsiao, C.-H. Chan, and C.-C. Chen, "Compact and low-loss bent hollow waveguides with distributed Bragg reflector," Optics express, vol. 16, no. 19, pp. 15069-15073, Oct. 2008.

[3] S. Wiechmann, H. J. Heider, and J. Müller, "Analysis and design of integrated optical mirrors in planar waveguide technology," Journal of Lightwave Technology, vol. 21, no. 6, p. 1584, 2003.

[4] L. G. Carpenter, H. L. Rogers, C. Holmes, J. C. Gates, and P. G. R. Smith, "Physically micromachined silica-on-silicon integrated corner mirrors," Lasers and Electro-Optics Europe (CLEO EUROPE/EQEC), 2011 Conference on and 12th European Quantum Electronics Conference, 2010.

[5] C. Holmes, J. C. Gates, C. B. E. Gawith, and P. G. R. Smith, "Strain tuning of a composite silica-on-silicon direct ultraviolet written planar Bragg grating," Optical Engineering, vol. 49, no. 4, p. 044601, 2010.

[6] H. L. Rogers, S. Ambran, C. Holmes, P. G. R. Smith, and J. C. Gates, "In situ loss measurement of direct UV-written waveguides using integrated Bragg gratings," Optics Letters, vol. 35, no. 17, pp. 2849-2851, 2010.

[7] A. W. Snyder and J. D. Love, "Goos-Hänchen shift," Applied optics, vol. 15, no. 1, pp. 236-8, Jan. 1976.

Monolithic Mode-Locked Ring Lasers: Model and Characterization Multi-wafer Project Run

L. J. Orbe-Nava, A. Jiménez-Galindo, G. Carpintero del Barrio
Department of Electronics Technology
Universidad Carlos III de Madrid
Leganes, Madrid, Spain
lorbe@ing.uc3m.es, ajgalind@pa.uc3m.es

***Abstract*—We present a traveling wave numerical model for a 15 GHz monolithically integrated symmetrical mode-locked ring laser, for which the results have been compared against experimental data from devices fabricated within a JePPIX platform run. On both, experimental and numerical, we show the relation that exists between the losses in the saturable absorber and the resultant pulse width when the device operates in a stable modelocking regime. Simulation results show good agreement with experiments for a given set of bias conditions which allows us to analyze the saturable absorber model.**

Mode-locked lasers, optical pulse generation, semiconductor ring lasers.

I. INTRODUCTION

Semiconductor lasers are suitable light sources for high rate optical fibre communications as well as for signal processing systems due to a range of unique characteristics such as small size, high efficiency, low cost and integration potential. This integration potential can only be realized if the requirement of cleaved facets to realize the optical resonator of a laser diode is avoided. Semiconductor ring lasers possess the attractive characteristic that the optical resonator is implemented through a circular waveguide, having as an added advantage the precise control by lithography of the cavity length. Due to this interest, research on these devices has already demonstrated continuous-wave (CW) [1] and single-mode operation [2] two decades ago. Moreover, ring lasers have been shown to operate in two counter-propagating directions (clockwise, CW and the counter-clockwise, CCW) [3].

Ring laser structures have been also used to implement integrated mode-locked sources, where it was shown that the counter-propagating modes actually allow the device to operate in a colliding pulse mode-locked (CPM) regime [4]. Extremely high pulse repetition rates up to 860 GHz have been shown [5]. It is not usual to find such high repetition rates in integrated devices due to the lengths of the ring resonators, due to bending loss limits on the curve waveguide radius, and they were attributed to intracavity back reflections in the ring resonator. Thus, the development of suitable models for the description of the ring laser devices is required.

In the present analysis, we present a travelling-wave model description of a 15 GHz monolithically integrated symmetrical mode-locked semiconductor ring laser. This model allows the inclusion of active and passive sections, in order to describe devices produced within an active-passive InP-based integration technology such as it is offered within the Joint European Platform for Photonic Integration of InP-based Components and Circuits, JePPIX [6]. The devices were designed, fabricated and tested, and we compare the experimental results against the model.

II. NUMERICAL MODEL OF A MODE-LOCKED SEMICONDUCTOR RING LASER

For the ring laser description, we have chosen the forward-difference time-domain travelling wave (FDTD-TW) modelling technique [7], which allows describing laser structures where the longitudinal dimension needs to be taken into account [8], such as in distributed feedback lasers (DFB). In our case, the FDTD-TW description of the device naturally originates the two counter-propagating modes, and allows including in the description the back reflection effects within the cavity. The most common form of implementation of this model is through a Transfer-matrix technique in which the entire structure is divided into several elemental sections. This establishes a time-domain technique which also incorporates the multimode nature of each propagation direction on the ring as well as spectral mixing effects.

The simulated device structure, shown in Fig. 1, is a symmetrical mode-locked ring laser composed by two optical amplifiers of 200 μm length each (SOA1 and SOA2), separated by a 30 μm saturable absorber (SA) and a passive section of 4970 μm, with a total cavity length of 5400 μm (15GHz modal frequency spacing) as seen in Fig. 1. The model also includes a 50/50 Multi-Mode Interference Coupler (MMI). We have used for the models the laser parameters as in reference , with the additional consideration that the carrier lifetime in the saturable absorber depends of the applied reverse bias voltage [9], modeled through varying the loss coefficient α [10].

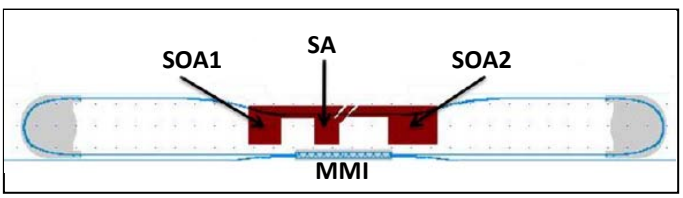


Figure 1. Simulated Semiconductor ring laser structure

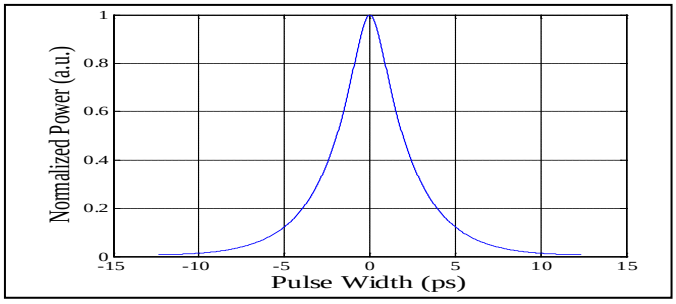


Figure 2. Spectral response of the numerical model

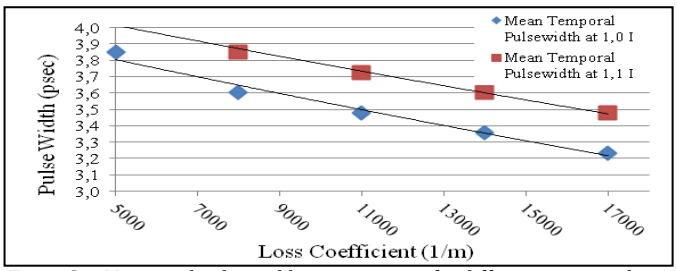


Figure 3. Numerical pulse width measurements for different current values. The inset shown the autocorrelation of the resulting pulses in the model for the conditions on Figure 2.

Selecting a bias level in which mode locking is observed, with I = 1.1I and α = 5000 m^{-1}, where I represents the initial current in which mode-locking is obtained, the simulation results show optical pulses in the output. Fig. 2 shows the result of autocorrelating the numerical output for one such pulse, obtaining a pulse width of 4.034 psec, which adjusts to a Lorentzian profile and a temporal pulse width of 2.06 psec. In the optical spectrum we find modes spaced by 0.125 nm, providing the expected repetition rate of 15 GHz. From the autocorrelation data, we are able to investigate the dependence of their pulse width against the reverse bias voltage (i.e. the loss coefficient α), much in the same way as in the experiment. Fig. 3 shows the pulsewidth decreasing exponential trend when the loss coefficient in the saturable absorber is increased, equivalent to an increase on the reverse bias of the saturable absorber.

III. Device Characterization

An optical chip was fabricated within the JePPIX platform following the ring structure on Fig. 1, with 7º angled output waveguides to avoid reflections. When the two gain sections are short-circuited, we have measured the optical output from the counter-clockwise direction. The optical pulses were measured on an APE Pulse-Check optical. Fig. 4 shows the experimentally observed autocorrelation for the bias conditions I = 110 mA and V_{SA} = -2.6 V, offering a Gaussian profile for the measured autocorrelation and a temporal pulse width of 2.50 psec. For two different bias levels, 105 and 110 mA, we have measured the pulse width dependence on the reverse voltage on the absorber averaging three consecutive measurements at each voltage level. The experimental results offer a decreasing trend, as seen in Fig 5, which agrees with the numerical result for the highest values of the reverse bias.

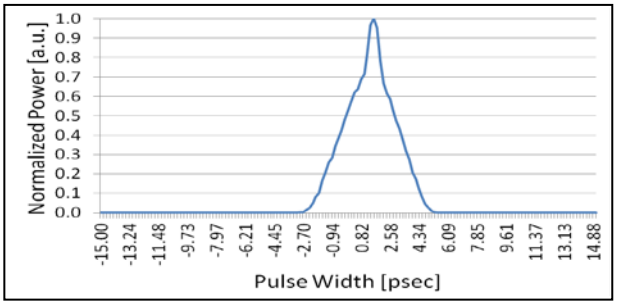


Figure 4. Experimental autocorrelation trace.

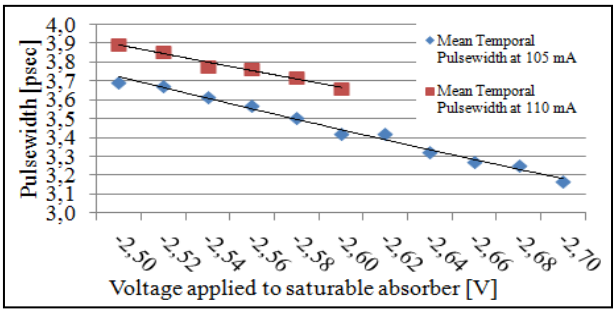


Figure 5. Experimental pulse width measurements for the ring laser's CCW output for two different current values.

However, the limited range of reverse bias over which we achieved mode locking requires further investigation.

References

[1] Krauss, T., P.J.R. Laybourn, and J. Roberts, *CW operation of semiconductor ring lasers.* Electronics Letters, 1990. **26**(25): p. 2095-2097.

[2] Hohimer, J.P., et al., *Single-frequency continuous-wave operation of ring resonator diode lasers.* Applied Physics Letters, 1991. **59**(26): p. 3360-3362.

[3] de Dios, C., *Generación de Pulsos Cortos mediante Diodos Láser Gain Switching. Estudio de Técnicas de Compresión Experimental basadas en Lazos Ópticos no Lineales NOLM*, in *Electronic Technology*. 2010, Universidad Carlos III de Madrid: Madrid. p. 261.

[4] Hansen, P.B., et al., *A 1.54 µm monolithic semiconductor ring laser: CW and mode-locked operation.* Photonics Technology Letters, IEEE, 1992. **4**(5): p. 411-413.

[5] T. Shimizu, I. Ogura and H. Yokoyama, *"860 GHz rate asymmetric colliding pulse modelocked diode lasers,"* Electronics Letters, vol. 33, no. 22, pp. 1868-1869, 1997.

[6] *Joint European Platform for Photonic Integration of InP-based Components and Circuits* [Online] http://www.jeppix.eu

[7] Orbe-Nava L.J., Guzmán-Martínez R.C. and Carpintero-de-Barrio G., Traveling wave model of a twin ridge semiconductor laser, Proceedings of the 2010 Annual Symposium of the IEEE Photonics Benelux Chapter, pp. 281-284, 2010.

[8] Orbe-Nava L.J., Guzmán-Martínez R.C. and Carpintero-del-Barrio G., *Modelo de propagación de un láser semiconductor en anillo*, in *Simposio Anual de la Unión Científica Internacional de Radio 2011*, Leganés, Madrid. p. 53.

[9] Bente. E., Barbarin Y., Heck M. and Smit M., *Modeling of integrated extended cavity InP/InGaAsP semiconductor modelocked ring lasers.* Opt. Quant Electron. 2008. Vol. 40: p.131-148.

[10] Tsang C.F., Marcenac D.D., Carroll J.E., Zhang L.M., Comparison between power matrix model and time domain model in modelling large signal responses of DFB lasers, IEE Proceedings-Optoelectronics, vol. 141, pp. 89-96, 1994.

Experiments and modeling of ultra-fast all-optical switching in a GaAs Photonic-Crystal membrane

S. Malaguti[1], G. Bellanca[1], S. Trillo[1]
[1] Department of Engineering, University of Ferrara,
Via Saragat 1, 44122 Ferrara, Italy
stefania.malaguti@unife.it

S. Combrié[2], A. De Rossi[2]
[2] Thales Research and Technology,
Route Departementale 128, 91767, Palaiseau, France

***Abstract*— We investigate ultra-fast all-optical switching relying on two-photon-absorption as ruling nonlinear effect in a GaAs Photonic-Crystal membrane. Experiments as well as FDTD modeling provide an unabridged description of such an intriguing nonlinear dynamics.**

Keywords-switch; all-optical switching; photonic crystal; two phton absorption.

I. INTRODUCTION

Over the past years, high-bandwidth (10-100 Gb/s) low-power consumption (few pJ per bit) all-optical signal processing has attracted considerable attention, especially because of its applications within the future ICTs. Meanwhile, 2D photonic crystals (PhCs) are being one of the most promising technologies able to fulfill such high-performance requirements. In fact, by embedding high index material membranes in air, PhCs allow tight confinement and excellent control of the flow of light. Moreover, by exploiting the strong light-matter interaction, PhCs can exacerbate the inherent nonlinear effects of III-V compound semiconductors. This latter feature, in particular, is being an appealing field of study, with remarkable applications in the design of ultra-fast all-optical switching devices [1,2]. From the standpoint of topology, a simple switch could be thought as a resonator coupled to an input and an output waveguide (see inset of Fig. 1 (left)). Such a trivial structure, once driven by means of a high intensity pump, is able to carry a probe signal from the bus to the drop waveguide. The pump signal, by triggering the nonlinear effects inside the cavity, tunes the resonance toward the out-of-resonance probe frequency. This process makes the probe see a sort of bus to drop bridge mediated by the excited cavity, then performing an all-optical switch in (so-called) pump-probe operations. Clearly, performances in switching functionalities are closely related to the structure characteristics. In particular, the pump power required to excite the nonlinear effects inside the cavity has been demonstrated to scale as the V/Q ratio, being Q the quality factor and V the modal volume of the cavity. High Q, small volume PhC nano-cavities supply unmatched values of the Q/V ratio allowing high-performance switching operations [3]. In this work we aim to provide further insights into PhCs switching capabilities both, via experimental demonstration and modeling investigation. In order to address these issues, we first experimentally demonstrate the superiority of PhCs technology in switching difference time domain (FDTD) method that, by including the main nonlinear effects of semiconductors, demonstrates capability for predicting the experimental data.

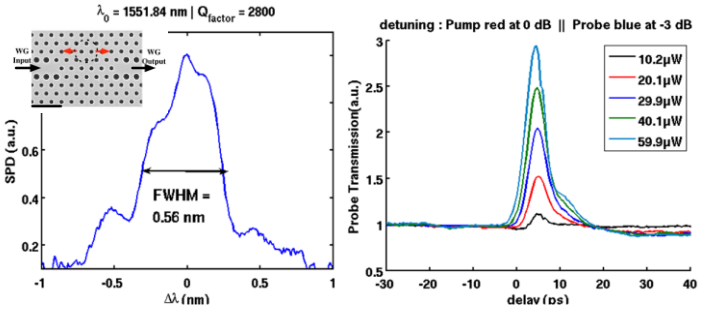


Fig. 1: Spectral response of the GaAs H0 nano-cavity (left) and time-resolved dynamics of the probe transmission (right). Switching is obtained in pump-probe configuration with the pump on resonance and the probe blue-shifted at -3 dB point of the spectral response.

II. EXPERIMENTAL RESULTS

Experiments are performed over a PhC membrane, being the PhC composed by a triangular lattice of air-holes in a GaAs bulk. The topology consists of a H0 cavity coupled to two (input and output) sections of a waveguide, in a in-line configuration [4]. As shown in Fig. 1 (left), the cavity spectral response exhibits a resonance at 1551.84 nm, with a line-width (evaluated as the spectral FWHM) of almost $\Delta\lambda$ = 0.56 nm (Q ~ 2800). Measurements are carried out in non-degenerate pump-probe operations, where the sample is excited via a strong pump signal with carrier frequency at the cavity resonance, and a probe signal blue-detuned by 0.5 nm away from the resonance. The laser emits pump pulses at average power of 100μW and at 36.6 MHz repetition-rate, corresponding to a peak power of 280mW (or average power of 10μW) in the waveguide. To provide the switching efficiency, we use the switching contrast (SC) per required pump power as a figure of merit. The SC is defined as the ratio of the probe power measured at the output waveguide with the pump ON to that with the pump OFF. Fig. 1 (right) shows typical dynamics (in terms of SC vs different input power) as it is expected when the driving nonlinear effect is the two-photon-absorption (TPA), while Kerr nonlinearity and parasitic losses remain negligible. A good SC (1:3) is achieved with relatively low pump power (~60μW), when the probe

temporally overlaps (delay equal to zero) the pump while the fast dynamics governed by the carriers relaxation time guarantees high bit-rate transmission.

III. 2D-FDTD NONLINEAR MODELING

In order to model the experiments, we set up a full-vectorial time-domain Maxwell's equations solver. The membrane allows for a reasonable description in 2D by using the effective index in the vertical direction and perfect matched layer (PML) absorbing boundary conditions in the plane of PhC. Furthermore, we include in the simulator the master equations accounting for the major nonlinear effects in semiconductors. To provide a best suited model of the nonlinear dynamics, we incorporate the equations accounting for TPA nonlinearity and its related effects. In particular, photon absorption is written as an intensity depletion according to the relation $\partial I/\partial t = -\beta_{TPA} I^2$, where β_{TPA} is the TPA coefficient and I the optical intensity. TPA induced free-carrier-absorption (FCA) is ruled by the equation $\partial I/\partial t = -\sigma_{FCA} NI$, where σ_{FCA} is the cross sections for free-electron and N the free-carrier density. The rate of free carriers generated by photon absorption obeys the following relationship:

$$\frac{\partial N}{\partial t} = \frac{c^2 \varepsilon_0^2 n^2 \beta_{TPA}}{8\hbar\omega_0} I^2 - \frac{N}{\tau} + D\nabla^2 N^2, \qquad (1)$$

being c the speed of light in vacuum, n the unperturbed refractive index, $\hbar$ the Planck constant, ω_0 the carrier frequency, τ the carrier relaxation time and D the diffusion coefficient. The latter term in the right-hand side of Eq. (1) describes the carriers diffusion, i.e. the phenomenon according to which the charges spread as the gradient of their concentration. This causes a shortening of the effective carrier life-time that cannot be thoroughly ignored in PhC based components [5]. Furthermore, we account for the change of the refractive index induced by plasma effect by means of a Drude model [6]. Finally, even though the Kerr nonlinearity is not the ruling effect, it is expected to counteract the TPA contribution. For this reason, self- and cross- phase modulation induced by the refractive index perturbation are included according to the relation $\Delta n = n_2 I^2$, being n_2 the Kerr coefficient. In Fig. 2 are shown the outcomes of the simulations in pump-probe regime versus increasing pump powers. The numerical results show to be in good agreement with the experimental data. As an aside, we numerically evaluate the peak power that enters the structure by calculating the Poynting flux in a section of the input waveguide. In order to do it quite accurately, we define an effective membrane thickness as:

$$h_{eff} = \frac{\left[\int n(r)^2 \,|F(y)|^2 \, dy\right]^2}{\int n(r)^4 \,|F(y)|^4 \, dy}, \qquad (2)$$

where F is the slab mode profile, n the refractive index and y the vertical (perpendicular to the PhC plane) direction. Furthermore, to account for the tight confinement of the resonator, we use the total quality factor Q_{tot} (with $1/Q_{tot} = 1/Q_l + 1/Q_i$, being Q_l and Q_i the loaded and the intrinsic quality factor, respectively).

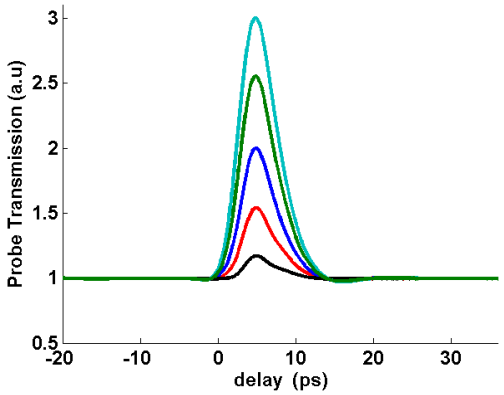


Fig.2: FDTD probe transmission for increasing values of the pump power density in a pump-probe configuration.

The ratio h_{eff}/Q_{tot} give us a reasonable scaling factor for the nonlinear coefficients used in the numerical calculations. In this way, we estimate a threshold power of almost 270mW (black curve in Fig. 2) in excellent agreement with measurements.

IV. CONCLUSION

In conclusion, we have demonstrated that GaAs PhC based devices are promising switching components. Moreover, by implementing a FDTD approach which account for the nonlinear effects, we have obtained good agreement with the experimental results. Our modified FDTD simulator shows an useful design-tool to investigate more sophisticated switching configurations.

ACKNOWLEDGMENT

The authors acknowledge funding from the EC under the project Copernicus.

REFERENCES

[1] K. Nozaki, T. Tanabe, A. Shinya, S. Matsuo, T. Sato, H. Taniyama and M. Notomi, "Sub-femtojoule all-optical switching using a photonic-crystal nanocavity", Nature Photon. vol. 4, 477 - 483 (2010).

[2] T. Tanabe, M. Notomi, S. Mitsugi, A. Shinya, and E. Kuramochi, "Fast bistable all-optical switch and memory on a silicon photonic crystal on-chip", Opt. Lett, vol. 30, 2575 (2005).

[3] K. Nozaki, and T. Baba, "Laser characteristics with ultimate-small modal volume in photonic crystal slab point-shift nanolaser", Appl. Phys. Lett, vol. 88, 211101 (2006).

[4] C. Husko, A. De Rossi, S. combrié, Q. V. Tran, F. Raineri, and C. W. Wong, "Ultrafast all-optical modulation in GaAs photonic crystal cavities", Appl. Phys. Lett, vol. 94, 021111 (2009).

[5] T. Tanabe, H. Taniyama, and M. Notomi,n"Carrier Diffusion and Recombination in Photonic Crystal Nanocavity Optical Switches", J. Lightwave Tech, vol. 26, 1396 (2008).

[6] A. De Rossi,_ M. Lauritano, S. Combrié, Q. V. Tran, and C. Husko, "Interplay of plasma-induced and fast thermal nonlinearities in a GaAs-based photonic crystal nanocavity", Phys. Rev. A, vol. 79, 043818 (2009).

Wavelength multistability in lasers

Antonio Pérez-Serrano
IFISC (UIB-CSIC),
Universitat de les Illes Balears,
E-07122 Palma de Mallorca, Spain.
antonio@ifisc.uib-csic.es

Julien Javaloyes
Departament de Física,
Universitat de les Illes Balears,
E-07122 Palma de Mallorca, Spain.
julien.javaloyes@uib.es

Salvador Balle
IMEDEA (UIB-CSIC),
C/ Miquel Marqués 21,
E-07071 Esporles, Spain.
salvador@imedea.uib-csic.es

***Abstract*—We theoretically discuss the impact of the cavity configuration on the possible longitudinal mode multistability in homogeneously broadened lasers. We present a general method allowing to perform a direct bifurcation diagram and to determine the stability of the solutions of a Travelling wave model. We find, in agreement with recent experimental reports, that multistability is more easily reached in Ring than in Fabry-Pérot cavities which we attribute to the different amount of Spatial-Hole Burning in each configuration.**

Laser Theory, Travelling Wave Model, Ring Lasers.

I. Introduction

Ring Lasers (RLs) present a large variety of dynamical regimes arising from the nonlinear interaction of the counter-propagating waves mediated by the active medium, e.g. bidirectional CW emission, oscillation regimes, mode-locking and chaos. In addition, RLs with low degrees of backscattering present regimes of bistable unidirectional emission [1] which can be exploited for all-optical signal processing and storage [2]. Recently it was experimentally demonstrated [4] that the emission wavelength of bidirectional semiconductor ring lasers (SRLs) can be selected by optical injection at wavelengths corresponding to the modes of the cavity; upon removal of the optical injection, the emission wavelength remains stable at the chosen value. It was found that this multistability can coexist with the directional bistability shown by these devices, therefore it can be of interest for all-optical signal processing applications at higher-logical level [5], as well as to fabricate multi-wavelength sources and fast and widely tunable sources that can generate mm-wave or THz modulated optical carrier. The SRL technology not only can be used to perform the processing, it is also can be used as the direct output of the routing decisions that result from the processing, and can be directly interfaced with the optical networks. On the other hand, this multistability has, to our knowledge, never been explained or reported in Fabry-Pérot (FP) lasers, hence it recalls for an explanation of the different behaviour shown by RLs and FP lasers regarding multistability.

In this contribution, we investigate theoretically the multistability by means of a Travelling Wave Model (TWM) for a homogeneously broadened medium with the appropriate boundary conditions [6] that allow us to model RLs and FP lasers. We take into account that the presence of counter-propagating fields creates a spatial modulation or grating of the population inversion (D_2). We compute the monochromatic steady state solutions of the system via a shooting method and we numerically perform their linear stability analysis by diagonalising the jacobian obtained from the evolution operator of the discretized system.This method allow us to construct direct bifurcation analysis of the TWM.

Performing this analysis, we found that the physical reason for such different behaviour of FP and RLs is the quite different degree of spatial hole burning in the gain. Therefore, high-quality SRLs, with low reflectivity couplers, allow to observe longitudinal mode multistability much more easily than their equivalent FP configurations. FP devices can exhibit multistability if diffusion is strong enough to wash out the grating effectively: in this limit the grating lifetime is much shorter than carrier lifetime, and cross-saturation dominates over self-saturation.

II. Model

For simplicity, we assume the active medium to be composed of two level atoms, although the model and techniques developed can be readily extended to other active medium cases, e.g. semiconductor case.

The presence of the two counter-propagating fields makes that a grating in the carrier density appears which couples in a nonlinear way the two waves; we include this effect by decomposing the carrier density D, in different spatial contributions, and cutting the resulting hierarchy via carrier diffusion. We consider that the electric field is quasi-monochromatic and it is decomposed into forward (+) and backward (-) waves propagating in opposite directions. We also consider a quasi-resonant light matter interaction in the Rotating Wave Approximation (RWA). With these assumptions, the dimensionless equations that defines the TWM read

$$\pm\frac{\partial A_\pm}{\partial s} + \frac{\partial A_\pm}{\partial \tau} = B_\pm - \alpha A_\pm \,, \tag{1}$$

$$\frac{1}{\gamma}\frac{\partial B_\pm}{\partial \tau} = -(1+i\delta)B_\pm + g(D_0 A_\pm + D_{\pm 2}A_\mp) \,, \tag{2}$$

$$\frac{1}{\epsilon}\frac{\partial D_0}{\partial \tau} = J - D_0 + \Delta\frac{\partial^2 D_0}{\partial s^2} - (A_+B_+^* + A_-B_-^* + c.c.), \tag{3}$$

$$\frac{1}{\eta}\frac{\partial D_{\pm 2}}{\partial \tau} = -D_{\pm 2} - \frac{\epsilon}{\eta}(A_\pm B_\mp^* + A_\mp^* B_\pm) \,, \tag{4}$$

where $A_\pm$ are the slowly varying components of the counter-propagating electric fields, $B_\pm$ are their respective polariza-

tions, D_0 is the quasi-homogeneous inversion density and $D_{\pm 2}$ are the spatially-dependent contributions to the grating in the population inversion density, g is a gain coefficient, α are the internal losses, δ is the detuning, Δ is the diffusion coefficient, ϵ and η are the decay times for D_0 and $D_{\pm 2}$ respectively, γ determines the spectral width of the gain spectrum and J is the pump. Equations (1-4) must be completed with the boundary conditions for the electric fields which read

$$\begin{aligned} A_+(0) &= tA_+(1)e^{i\gamma\omega_0} + rA_-(0), \\ A_-(1)e^{-i\gamma\omega_0} &= tA_-(0) + rA_+(1)e^{i\gamma\omega_0}, \end{aligned} \tag{5}$$

where ω_0 is the carrier frequency, r and t represents the reflectivity and transmissivity of the waves at the point coupler, then $|t|^2 + |r|^2 = 1 - \phi$, where ϕ are the losses at the point coupler. In the following we shall take $\gamma\omega_0 = 2\pi m$ where $m = 0, 1, 2...$ then $i\gamma\omega_0 = 1$ without loss of generality: it simply means that we take as the carrier frequency ω_0 that corresponding to one of the modes of the cavity.

III. Numerical analysis and results

The numerical analysis consisted in using a multidimensional shooting algorithm to find the monochromatic solutions [7]. The linear stability analysis of these solutions was performed using a temporal map that advances the solution one time step including the boundary conditions, that allows to find the Floquet matrix that represents the linear operator governing the time evolution for the perturbations around one given monochromatic solution. Finally, the Floquet multipliers that determine the eigenvalues of the system were found. Fig. 1 shows the computed eigenvalues for mode number $m = 2$, (a) $J = 3$ and (b) $J = 4$ for a RL with typical semiconductor parameters. The monochromatic solution for $m = 2$ is unstable (stable) for $J = 3$ ($J = 4$). We reapeat this process to construct bifurcation diagrams like the one shown in Fig. 1 (c). We found that in the regime of stable unidirectional emission, RLs exhibit multistability among several longitudinal modes even when one mode is resonant with the atomic gain line. In this regime the emission wavelength can be selected among that of several cavity modes by injection of external optical pulses, in agreement with experimental reports [4]. However, multistability is not found for an equivalent FP laser (see Fig. 1 (d)), the resonant mode is stable until it reaches a multi-mode instability.

The physical reason for such different behaviour of FP and RLs is the quite different degree of spatial hole burning in the gain. Fig 2 (a) shows the absolute value of D_2 averaged along the cavity. In the ring laser, $\langle |D_2| \rangle$ saturates at a comparatively low value as soon as the pitchfork bifurcation leading to unidirectional emission occurs; for FP configurations, the necessarily higher reflectivity of the facets makes $\langle |D_2| \rangle$ larger than in the equivalent ring, and it increases continuously with the pump level. In order to confirm that the grating term is what destroys multistability in the FP, we consider a system with very high diffusion, which reduce the values of D_2. As shown in Fig. 2 (b), in this case multistability is reached.

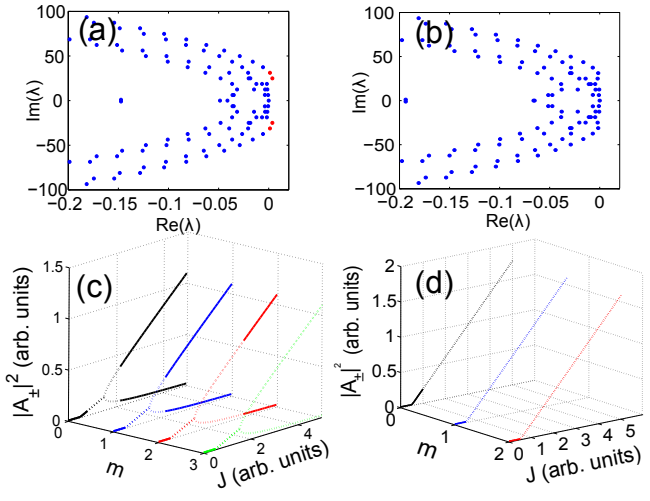


Fig. 1. Real versus imaginary part of the eigenvalues for $m = 2$, (a) $J = 3$ and (b) $J = 4$. Eigenvalues in blue (red) have $Re(\lambda) < 0$ ($Re(\lambda) > 0$). Bifurcation diagram for the first modes of a RL (c) and for an equivalent FP laser (d). Solid (dashed) lines represent the stable (unstable) solutions.

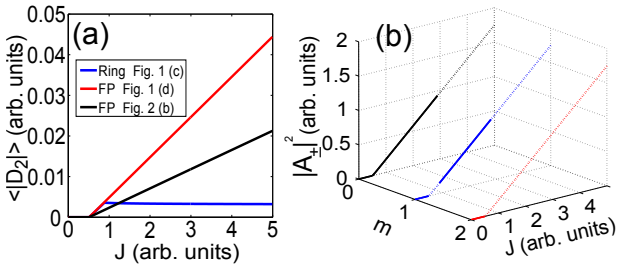


Fig. 2. (a) $\langle |D_2| \rangle$ versus J for the RL in Fig. 1 (c) and FP lasers in Fig. 1 (d) and panel (b). (b) Bifurcation diagram for a FP laser showing multistability after increasing the diffusion.

Acknowledgment

A.P. thanks financial support from the Govern Balear. J.J. thanks financial support from the Ramón y Cajal program by Spanish MICINN. S.B. thanks financial support from project ALAS (TEC2009-14581-C02-01).

References

[1] M. Sorel, G. Giuliani, A. Scire, R. Miglierina, S. Donati, and P. J. R. Laybourn, "Operating regimes of GaAs-AlGaAs semiconductor ring lasers: experiment and model," *Quantum Electronics, IEEE Journal of*, vol. 39, no. 10, pp. 1187–1195, Oct. 2003.

[2] M. T. H. *et al.*, "A fast low-power optical memory based on coupled micro-ring lasers," *Nature*, vol. 432, no. 7014, pp. 206–209, Nov 2004.

[3] Z. Wang, G. Yuan, G. Verschaffelt, J. Danckaert, and S. Yu, "Storing 2 bits of information in a novel single semiconductor microring laser memory cell," *Photonics Technology Letters, IEEE*, vol. 20, no. 14, pp. 1228 –1230, july15 2008.

[4] K. Huybrechts, B. Maes, G. Morthier, and R. Baets, "Tristable all-optical flip-flop using coupled nonlinear cavities," in *2008 IEEE/LEOS Winter Topical Meeting Series*, January 2008, pp. 16–17, IEEE/LEOS Winter Topical Meeting, Sorrento, Italy, Jan 14-16, 2008.

[5] A. Pérez-Serrano, J. Javaloyes, and S. Balle, "Bichromatic emission and multimode dynamics in bidirectional ring lasers," *Phys. Rev. A*, vol. 81, no. 4, p. 043817, Apr 2010.

[6] A. Pérez-Serrano, J. Javaloyes, and S. Balle, "Longitudinal mode multistability in ring and fabry-pérot lasers: the effect of spatial hole burning," *Opt. Express*, vol. 19, no. 4, pp. 3284–3289, Feb 2011. [Online]. Available: http://www.opticsexpress.org/abstract.cfm?URI=oe-19-4-3284

Tailoring reflection of self-collimating multilayer structures

Olivier Gauthier-Lafaye, Antoine Monmayrant, Françoise Lozes-Dupuy
CNRS ; LAAS ; 7 avenue du colonel Roche, F-31077 Toulouse, France
Université de Toulouse ; UPS, INSA, INP, ISAE ; LAAS ; F-31077 Toulouse, France
olivier.gauthier-lafaye@laas.fr

Marco Grande, Giovanna Calò, Vincenzo Petruzzelli
Dipartimento di Elettrotecnica ed Elettronica
Politenico di Bari, Via E. Orabona, 4
70125 Bari, Italy
grande@deemail.poliba.it

Julien Arlandis, Emmanuel Centeno
LASMEA UMR-CNRS 6602 Université Clermont-Ferrand II
Campus des Cézeaux, 24, Avenue des Landais
63177Aubiére Cedex, France
emmanuel.centeno@univ-bpclermont.fr

***Abstract*—In this paper we propose and demonstrate a simple conception scheme for multilayered planar photonic crystals (PhC) offering self-collimated propagation with tailored transmission and reflection. In particular we report on the design of a Distributed Bragg Reflector and anti-reflection structure both composed of 2D PhC layers and unstructured high-index layers. Finally we analyze the propagation of a Gaussian pulse in the periodic structures and we numerically prove the behaviour of the two proposed configurations.**

Keywords: Photonic Crystals, Mesoscopic self-collimation, DBR, antireflection, laser design.

I. INTRODUCTION

Even if Photonic Crystals have been extensively studied in the last decades, they still own exceptional properties that can be investigated and exploited for new kind of optical devices. In particular, self-collimating photonic crystals [1] allow the propagation over long distances of collimated optical beams without requiring any waveguide for the confinement. Self-collimation has also been demonstrated in zero-average-index metamaterial that consist of a 1D structure alternating positive and negative refractive index [2,3]. Recently Arlandis *el al* [4] have demonstrated that mesoscopic self-collimation also arises in photonic crystal superlattices of all-positive index material, proving that zero-average-index is not necessary. Instead, they have shown that the key physical parameter in the PhC slice is a *curvature index* that can be extracted from the iso-frequency curves. The PhC slice is thus designed to provide a negative curvature index that fully compensates the divergence of the beam in the un-patterned slice. Reference [4] also shows how the properties of the superlattice are obtained with accuracy better than 1% by simply inspecting the band diagram of the elementary cell consisting of a single hole. Last, they show how the new degrees of freedom on the phase index and the mesoscopic period can be harnessed to simultaneously provide self-collimation and slow-light.

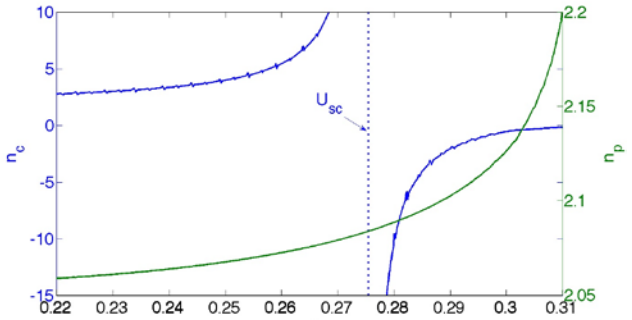


Figure 1. Phase index and curvature index of the first band versus the normalized frequency for the single-hole unit cell of an infinite 2D PhC (a/r=0.28); dashed line corresponds to self-collimation (U_{sc}~0.2754).

In this contribution we extend the concepts introduced in [4] in order to propose and demonstrate a new scheme to design multilayered PhC structures offering simultaneously mesoscopic self-collimation and tailored transmission and reflection. As an example, we design two different structures that realize a Distributed Bragg reflector (DBR) and an anti-reflection stack (AR). Both structures work without resorting to half-hole tapering used in [4] to limit impedance mismatch.

II. DESIGN AND RESULTS

In this work, the design scheme follows the electromagnetic theory proposed in [4]. We first consider an infinite 2D PhC of square lattice with period a and radius r: the effective refractive index of the bulk material is n_b=2.4 (corresponding to a 160 nm-thick GaAs membrane for a wavelength λ=1550 nm). Using Plane Wave Expansion (PWE) method, we compute the first band of this infinite PhC, the unit cell simply consisting of a single hole. Then, we extract from the band diagram, the phase index n_p and curvature index n_c versus the normalized frequency U (a/λ) in the ΓM direction as reported on Figure 1. Self-collimation occurs for a reduced frequency U_{sc} where the curvature index diverges: U_{sc}~0.2754. For reduced frequencies

above U_{sc}, n_c is negative and mesoscopic self-collimation can be obtained when the following relation is satisfied [4]:

$$\frac{l_b}{n_b} + \frac{l_{PhC}}{n_{PhC}^c} = 0 \quad (1)$$

where l_b, n_b are the length and refractive index of the bulk slices and l_{PhC}, n_{PhC}^c are the length and curvature index of the PhC slices. At the same time, the mesoscopic structure can be seen as a 1D multilayer structure where two materials with different refractive index n_b and n_{PhC} are alternated. As Equation (1) does not impose any constraint on the mesoscopic period $l = l_{PhC} + l_b$ (it only sets the ratio l_b / l_{PhC}) and does not involve the phase index n_{PhC}, we can harness these two free parameters to tailor the reflection property like in a standard multilayered structure while preserving self-collimation. For that purpose we introduce a new equation for the optical path *op* in one mesoscopic period:

$$op = n_{PhC} l_{PhC} + n_b l_b = k\frac{\lambda}{4} \quad (2)$$

where k is an integer and $\lambda = a/U$.When this equation is satisfied for k even we obtain a DBR and for k odd an AR stack. There is infinity of solutions that satisfy both equations (1) and (2) for DBR or AR configuration. We arbitrarily set $l_{PhC} = a\sqrt{2}$ (i.e. one period of PhC along ΓM) and choose to search solutions where $l_b > l_{PhC}$ (i.e. more bulk than PhC). With these constraints, the resolution of Equation 2 shows that the lowest values for k are 8 and 9 for a DBR and an AR stack, respectively. The corresponding computed values for a wavelength of λ_0=1550 nm are a_{DBR}=448 nm and $l_b = 1.156a\sqrt{2}$ for the DBR and a_{AR}=452 nm and $l_b = 1.396a\sqrt{2}$ for the AR.

Figure 2 depicts the results of 2D Finite Difference Time Domain (FDTD) simulations for the propagation of a Gaussian beam (unidirectional source to the right, initial waist of 8.5*a*) for a reference raw material (a), the AR stack (b) and the DBR stack (c). Beam is propagated over 50 mesoscopic periods *l* (DBR mesoscopic period is used for the reference). Best selfcollimated AR and DBR are observed for a wavelength equals to $1.02\lambda_0$=1581 nm. This small difference in working wavelength (~2%) confirms that our scheme is accurate enough to guide designing and fabrication well within. Moreover preliminary analysis of the energy distributions confirms that the two proposed schemes follow the abovementioned behaviour (reflection around few % for AR and reflection above 94% for DBR) without requiring half-hole tapering at the interface between PhC and raw slices.

CONCLUSION

In conclusion, the proposed scheme allows simple conception of structures exhibiting both mesoscopic self-collimation and tailored transmission and reflection. In our presentation, we will detail all the key steps of our scheme, the performances and limitations of the structures designed with this scheme. We will also present complementary approaches also exploiting curvature index but allowing more precise prediction at the cost of more complex calculations.

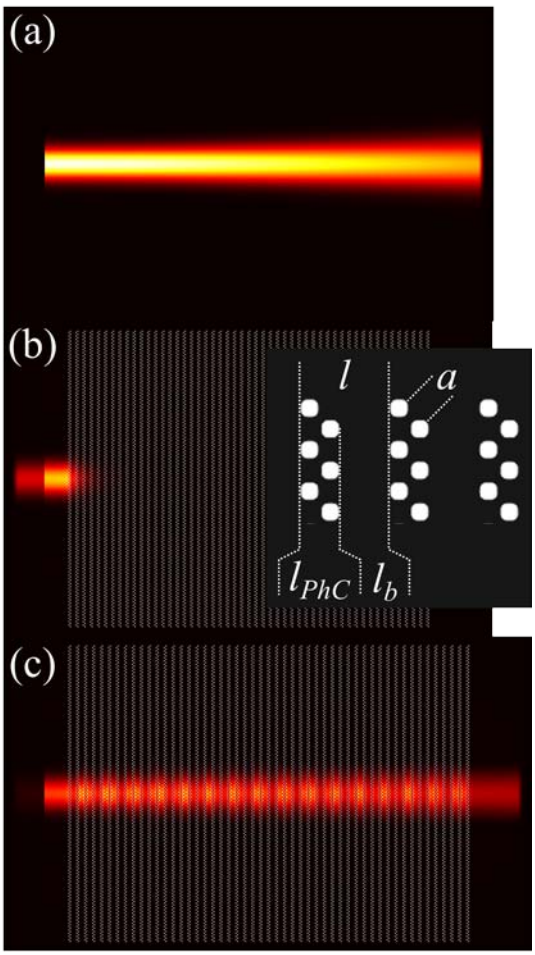


Figure 2. Energy distribution for a) reference raw material, b) DBR (a_{DBR}=448 nm, , l_b=1.156$a\sqrt{2}$) and c) AR (a_{DBR}=452 nm, , l_b=1.396$a\sqrt{2}$) schemes.

ACKNOWLEDGMENT

The authors acknowledge COST Action MP0805 on Novel Gain Materials and Devices Based on III-V-N Compounds. M. G. thanks COST Action MP0805 for the Short Term Scientific Mission and partial financial support from the European Research Office of US Army (contract n. W911NF-11-10284).

REFERENCES

[1] J. Witzens, *et al*, "Self-collimation in planar photonic crystals", IEEE Journal of selected topics in quantum electronics, Vol. 8, n. 6, 2002.

[2] V. Mocella *et al*," Self-Collimation of Light over Millimeter-Scale Distance in a Quasi-Zero-Average-Index Metamaterial", Phys. Rev. Lett. 102, 133902, 2009.

[3] S. Kocaman, *et al*," Zero phase delay in negative-refractive-index photonic crystal superlattices", Nature Photon. 5, 499–505, 2011.

[4] J. Arlandis, E. Centeno, R. Pollès, A Moreau, J. Campos, O. Gauthier-Lafaye and A. Monmayrant, "Mesoscopic Self-Collimation and Slow Light in All-Positive Index Layered Photonic Crystals", Phys. Rev. Lett. 108, 037401, 2012.

Integrated 'all-optical' Transmodulator Circuits with non-linear Gain elements and tunable Optical Filters

with design, realization & testing in generic InP technology

P.I.Kuindersma, X.J.M.Leijtens, J.H.C. van Zantvoort & H. de Waardt
COBRA Research Institute
TU/e Technical University of Eindhoven
Eindhoven, the Netherlands
p.kuindersma@tue.nl

***Abstract*—We characterize integrated InP circuits for high speed 'all-optical' signal processing. Single chip circuits act as optical transistors. Transmodulation is performed by non-linear gain sections. Integrated tunable filters give signal equalization in time domain.**

Keywords: transmodulator; 'all-optical' signal processing; generic InP technology;integrated tunable filters

I. INTRODUCTION

All-optical signal processing, like any other signal processing, can be performed in the time domain as well as in the frequency (wavelength) domain.

Wavelength domain, 'all-optical' signal processing is common practice in today's high speed WDM optical communication systems. The smallest granule in these systems is obviously the individual WDM channel. On the device and component level such WDM system use e.g. multi-wavelength sources, wavelength combiners and splitters, wavelength-selective switches and routers, ROADM's etc. On the component technology level both integrated and free space optics are being used.

The main *time domain 'all optical' signal processing* in today's communication systems is optical amplification, mainly by EDFA's but also with SOA's. Next to the ability to amplify many WDM channels simultaneously, a key advantage of optical amplification is the absence of a high speed roll-off. This is in contrast with electronic amplification, which always rolls off at high frequency. Figures of merit in this respect are f_T (for unity current gain) and f_{MAX} (for unity power gain).

Time domain 'all optical' signal processing also comprises trans modulating data from one wavelength to another. Functionally this is equivalent to optical transistor action. Often this process is called wavelength conversion. Trans modulation of more than one input to a single output is called trans multiplexing. Despite its 'all optical' character, and in contrast with amplification, this process shows a roll off at high signal frequencies, e.g. when cross-gain/cross-phase modulation in SOA's is used. However by differential linear filtering of the trans modulated output (or the input), the output roll off can be equalized optically, up to (very high) frequencies not accessible by electronics or by opto-electronic modulators.

In this paper we describe the design and experimental characterization of InP circuits in which the 'all optical' trans modulator function and the 'all optical' equalization in the time domain are realized in single chips. Since all signal processing is optically only, there are no high speed electrical contacts to the chips. All electrical contacts are dc and provide the necessary control of gain and of phase of the optical waves at various stages in the chip.

InP is chosen as the materials system for the chips, because of its unique ability to combine "actives" (gain sections, but also phase shift sections) with "passives" (waveguides, MMI's)

II. DESIGN, MANUFACTURING AND TESTING OF TRANSMODULATOR CIRCUITS

A. *The operating principle*

The circuits combine three well defined functions

- Transcription of the optical base input data to a new carrier wavelength at the collector output, The collector field strength modulation index is:

$$\Delta E/E_0 = (-1/2)\,(1+j\alpha)\,\Gamma\,(dg/dN)\,(G-1)\,\Delta P_{in,\,base}\,/\,(j\omega+\tau^{-1})$$

  where τ is the gain recovery time.

- Separation of the input wavelength (base → drain) and the output wavelength (emitter → collector), by using a parallel matched pair of gain sections in a phase tunable equal arm length MZ configuration.

- Optical equalization of the slow gain recovery and suppression of the carrier, with tunable unequal arm length MZ filters acting as differential filter and additionally as FM→AM converter. Periodicity, and 360 degree tuning of phase differences, gives proper (and electrically tunable) filter operation, with full C-band (from 1535 to 1565 nm) coverage.

B. *Manufacturing at OCLARO*

The chips were manufactured in a generic InP technology at OCLARO in Caswell/UK while using well established, standard building blocks and process modules. As shown in fig.1, typically 5 or 6 trans modulator circuits (with a total area of 4x4 mm^2) were realized together with very different circuits from other designers on a 12 x 12 mm^2 reticle.

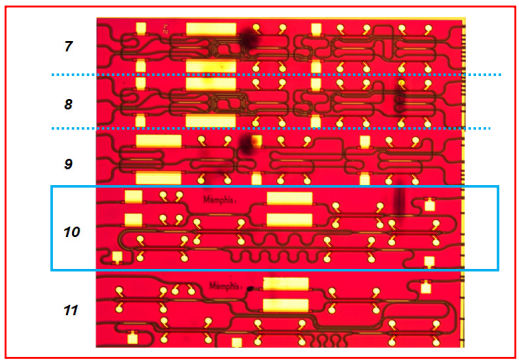


Figure 1. Optical microscope picture of 4x4 mm^2 die, prior to dicing into five transmodulators chips (#7-11). Rectangular bondpads contact gain sections, while small circular bondpads contact deep ridge phase shifters

The "actives" building blocks available and used in the present designs were *a) shallow etched gain sections* and *b) deeply etched phase shifter waveguides* with low capacity electrical contacts, to be used under forward bias. A full description of these modules in terms of "compact models" was not (yet) available at the time of the chip design. In fact some of the properties of the gain- or the phase shift- sections which are of specific interest to the chip designer, could only be determined,(= measured), after realization of the chips.

The "passives" building blocks available and used were *c) straight waveguides* and *d) curved waveguides*, *e) shallow-deep ridge transitions, f) 1x2 MMI's and g) 2x2 MMI's.*

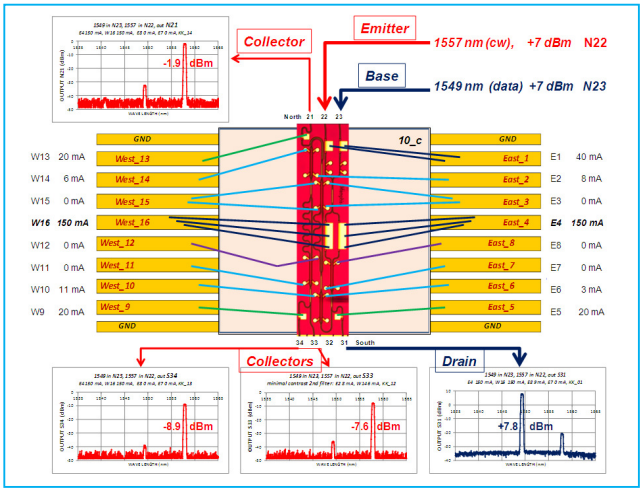


Figure 2. Electrical and optical connections to design #10.
And an experimental demonstration of upto 30 dB spatial filtering efficiency in the collector outputs by using the matched SOA pair

C. *Circuit design, Mask Layout, Mounting, Testing and Characterization of the chips at the TU/e*

Trans modulator circuit design, mask layout, mounting and testing were all carried out at the TU/e in Eindhoven/NL. As illustrated in fig.2, 3 and 4, we developed for the characterization dedicated (but universal) carriers, test fixture, electrical drive/measurement equipment (hard & software) and an optical-mechanical test station. Lensed multi (~4) fiber array are coupled to the North, and simultaneously to the South side of the chip. The electrical connections to the chips are made at the East and West side. On the carriers the (~16) bond contacts from the chip are fed into a standard flexible print connectors.

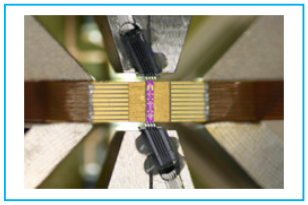


Figure 3. Dedicated carrier with lensed fiber arrays, angled at 24.6 degree

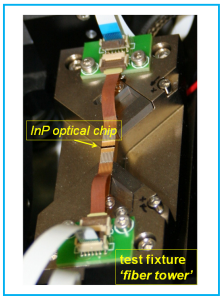
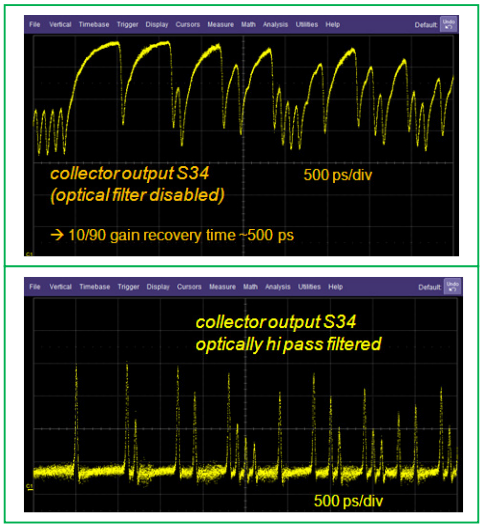


Figure 4. FiberTower test fixture

III. TEST RESULTS, AT 10 GB/SEC BIT RATE

Both testing of the on-chip components and of the fully integrated device (#10) was done. Examples of trans modulated collector outputs at 10Gb/s, before and after differential filtering, are shown below in fig. 5a and fig. 5b.



ACKNOWLEDGMENTS

The cooperation with the R&D team at OCLARO/UK is greatly valued by the authors. For further information on the manufacturing aspects of generic InP technology we refer to: mike.wale@oclaro.com

The Dutch ministry of Economic Affairs financially supported the 'Trans modulator', via the MEMPHIS project.

Determination of thickness and refractive index of step-index optical waveguides using LSM and LSE formulation

Adrián Fdez Gavela[1], Silvino José Antuña Presa[2], Miguel García Granda[3], José Rodríguez García[5]
Physics department
University of Oviedo
Oviedo, Spain
[1]fernandezgadrian@uniovi.es [2]antunasilvino.uo@uniovi.es
[3]mggranda@gmail.com [5]jose@uniovi.es

María Rodríguez Lastra[4]
Energy department
University of Oviedo
Oviedo, Spain
[4]rodriguezlmaria.uo@uniovi.es

***Abstract*— In this work, we demonstrate that the LSM and LSE modes formulation is a good theoretical alternative for determining the thickness and refractive index of planar optical waveguides with step refraction index profile. This wave model only requires the experimental evaluation of the effective indexes of guided modes in the planar optical waveguide. In order to verify the developed formulation, the commercial software Olympios was used for planar optical waveguides simulations. For comparing the theoretical results and simulations with experimental evaluations, several planar optical waveguides, were fabricated and characterized. The prism-film coupler technique and the Metricon equipment were used for effective indexes measurements. A profilometer was used for thickness experimental evaluation. In all cases a good agreement was obtained between theory and experiments.**

Keywords-component; glass, polymers, simulation methods, optical waveguides

I. INTRODUCTION

Recently, polymeric optical waveguides experienced a large growth due to their handling simplicity, potential applications and low cost production. Currently, optical waveguides are being fabricated with different polymers: PVA, PMMA, SAN, etc. [1-3]. Key parameters that have to be known in these waveguides are the thickness and refractive index of the guiding layer. In this paper, the LSE and LSM modes formulation is introduced to theoretically determine thickness and refractive index of monomode and multimode polymeric planar optical waveguides from the modal effective indexes. To execute the calculation of these parameters by this method, we have computed the algorithm in Matlab. The commercial simulation software Olympios was used to verify the results provided by our formulation.

Monomode and multimode polymeric planar optical waveguides were manufactured and characterized. All of them were fabricated using the spin-coating technique [4]. The prism-film coupler method [5] and the Metricon system were used to obtain experimentally the effective indices of the LSE and LSM guided modes. Introducing the experimental effective indexes in our formulation, the thickness and refractive index of the guiding layer are evaluated. In order to verify the accuracy of the algorithm, the thickness and refractive index of several samples were measured with a profilometer. In all cases, the theoretical and experimental results agree very well.

II. THEORY

Generally, optical waveguides propagate hybrid modes, with six electromagnetic field components. When one of the components of the field is negligible compared to the others, the modes can be designated as LSE (Longitudinal Section Electric)-LSM (Longitudinal Section Magnetic), which allows the modeling of electromagnetic propagation in metal guides partially filled with dielectrics [6]. Planar optical waveguides propagate TE-TM modes, which have a fundamental component of electric field. LSE-LSM and TE-TM modes have the same fundamental component of electric field. This characteristic allows analyzing the electromagnetic propagation of planar optical waveguides using the LSE-LSM formulation. In our case, and from the experimental point of view, the electric field dominant component was imposed by laser polarization selection. Furthermore, as our region of interest is free of sources, we can calculate E and H fields from Hertz's potentials [6].

A. LSM Modes

In our case, we focus on planar optical waveguides with step-refraction index profile. We can solve the Helmholtz's equation for these kinds of waveguides using the LSM formulation, and we obtain the following relationship:

$$b = \frac{\tan^{-1}\dfrac{\left(n_s^2\sqrt{n_{effi}^2-1}+\sqrt{n_{effi}^2-n_s^2}\right)n_f^2\sqrt{n_f^2-n_{effi}^2}}{n_s^2\left(n_f^2-n_{effi}^2\right)-n_f^4\sqrt{n_{effi}^2-1}\sqrt{n_{effi}^2-n_s^2}}}{\dfrac{2\pi}{\lambda_0}\sqrt{n_f^2-n_{effi}^2}} \pm \pm \frac{m\pi}{\dfrac{2\pi}{\lambda_0}\sqrt{n_f^2-n_{effi}^2}} \quad (1)$$

being b the thickness, n_s the substrate refractive index, n_{effi} the effective index for each mode, n_f the guiding layer refractive index, λ_0 the wavelength of the laser and m any natural number. Being all parameters known, except n_f, b and m.

Equation (1) can be written in a compact form:

This work has been supported by PhD grant BP09-007 "Severo Ochoa" from FICYT (Principado de Asturias)

$$b = f(n_f, n_s, n_{effi}, \lambda_0, m) \quad (2)$$

B. LSE Modes

We can operate in a similar way for this kind of modes. In this case, the corresponding equation is:

$$b = f(n_f, n_s, n_{effi}, \lambda_0, p) \quad (3)$$

being p any natural number.

In the case of monomode planar optical waveguides, equations (2) and (3) are solved by applying an iterative process. In this way, a set of possible solutions (n_f,b) can be obtained.

The real solution of n_f and b can be detected graphically, being the intersection point of the LSM and LSE solutions.

For multimode planar optical waveguides, the solution for b and n_f is obtained by using the bisection method.

III. SIMULATION

In order to validate the theoretical formulation and for testing the applicability of the LSM and LSE formulation, the Effective Index Method [7,8] was used for comparison by means the simulation software package Olympios.

We have simulated a single-mode waveguide with n_s=1,4700, b=1,2 μm and n_f=1,4900 in Olympios and we obtained n_{eff1}^{LSM}=1,4784 and n_{eff1}^{LSE}=1,4791. Then, these n_{eff1} have been introduced in the algorithm in Matlab and Fig. 1 was obtained.

For multimode waveguide simulations, we have introduced in Olympios: n_s=1,5105, n_f=1,5598 and b=2,9 μm and we obtained for LSM modes: n_{eff1}=1,5566, n_{eff2}=1,5472, n_{eff3}=1,5317 and n_{eff4}=1,5119. Then, these n_{effi} have been introduced in the algorithm in Matlab and we have obtained b=2,9 μm and n_f=1,5599. We have used the same procedure for several samples, and we have achieved satisfactory results.

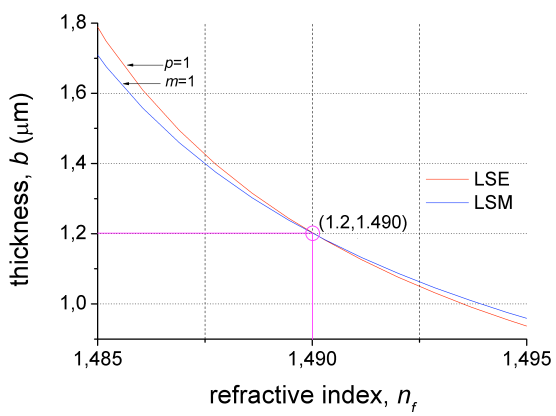


Figure 1. Thickness, b, as a function of refractive index, n_f, for the values m=p=1.

IV. FABRICATION AND EVALUATION

Borofloat glasses substrates (n_s=1.4699 at λ_0=632.8 nm) and the PMMA polymer were used to manufacture single-mode optical waveguides. To made multimode waveguides, we have used soda-lime glasses substrates (n_s=1.5100 at λ_0=632.8 nm) and NOA61 polymer. Different thicknesses of the polymer were deposited on the glass using spin-coating technique.

The next step was the experimental evaluation of the effective index of each guided mode. For this task, the prism-film coupler technique and the Metricon equipment were used.

For the sample PM26, which was manufactured with borofloat and PMMA, we have calculated the effective index for both polarizations, obtaining the following results: n_{eff1}^{LSM}=1.4723 and n_{eff1}^{LSE}=1.4728. Fig. 2 shows the results provided by the algorithm for the sample PM26. The thickness and the refractive index for this sample are: b=1.1 μm and n_f=1.483.

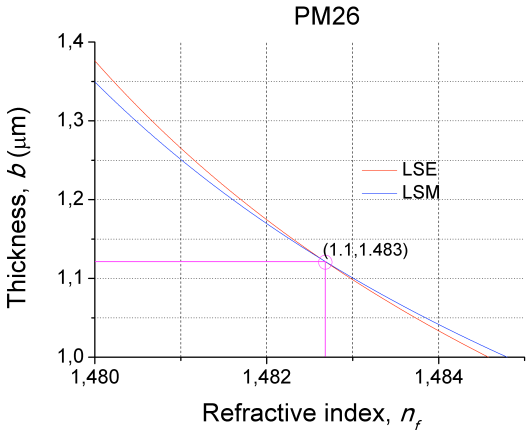


Figure 2. Thickness, b, as a function of refractive index, n_f, for the sample PM26.

Finally, a profilometer was used to verify the thickness results provided by the algorithm. We have used the same procedure for several samples. In all cases, the same agreement between theory and measurements was obtained.

REFERENCES

[1] G. J. Qurechi, V. K. Gupta, A. P. Singh, A. Kapoor, K. N. Tripathi, "Four layer polymeric optical waveguides based on styrene acrylonitrile (SAN)", Proc. SPIE 4679 (2002) 440-444.

[2] R. Kumar, A. P. Singh, A. Kapoor, K. N. Tripathi, "Fabrication and characterization of polyvinyl-alcohol-based thin-film optical waveguides", Opt. Eng. 43 (2004) 2134-2142.

[3] Y. Ren, "Efficiency shifts of prism coupling into polymer waveguides subject to environmental variations", Opt. Mater. 19 (2002) 443-447.

[4] G. A. Luurtsema, "Spin coating for rectangular substrates," M. Sc. thesis, Department of Electrical Engineering and Computer Sciences, University of California, Berkeley, Jul. 1997.

[5] R. Ulrich, "Theory of the prism-film coupler by plane-wave analysis", J. Opt. Soc. Am. 6 (1970) 1337-1350.

[6] T. Itoh, Dielectrics waveguide-type millimeter-wave integrated circuits, in: K. J. Button, J. C. Wiltse (Eds.), Millimeter systems, Vol. 4, in: Infrared and millimeter waves, Academic Press, New York, 1981, pp. 199-271.

[7] E.A.J. Marcatili, "Dielectric rectangular waveguide and directional coupler for integrated optics" Bell Syst, Tech. J., Vol. 48 (Sep. 1969) 2071-2102.

[8] T. Suhara, Y. Handa, J. Nishihara, J. Koyama, "Analysis of optical channel waveguides an directional couplers with graded-index profile", J. Opt. Soc. Am., Vol. 69, Issue 6, (1979) 807-815.

Dual-Wavelength $Al_2O_3:Yb^{3+}$ Distributed Feedback Waveguide Laser for Microwave Signal Generation

E. H. Bernhardi, H. A. G. M van Wolferen, K. Wörhoff, R. M. de Ridder, and M. Pollnau
MESA+ Institute for Nanotechnology, University of Twente, Enschede, The Netherlands

M. R. H. Khan and C. G. H. Roeloffzen
Telecommunication Engineering Group, Faculty of Electrical Engineering, Mathematics & Computer Science, University of Twente, Enschede, The Netherlands

***Abstract*—We report a ytterbium-doped aluminum oxide dual-wavelength distributed feedback channel waveguide laser and its application in the photonic generation of stable microwave signals. A microwave signal at ~15 GHz with a −3 dB width of 9 kHz was created via the heterodyne photodetection of the two laser wavelengths. The long-term (45 minutes) and short-term (10 ms) frequency stability of the microwave signal produced by the free-running laser is better than ±2.5 MHz and ±40 kHz respectively.**

Keywords– Distributed feedback (DFB) laser; dual-wavelength laser; microwave-photonics; Bragg gratings

I. INTRODUCTION

The photonic generation of microwave or millimeter-wave signals has become an essential part of the emerging field of microwave photonics. Microwave signals are usually generated with complex and expensive electronic circuits and propagated along electrical distribution lines, which inherently have high propagation losses. Compared with the electronic solutions, photonic generation of microwaves has many advantages, such as high-frequency operation, low power consumption, low cost, as well as the distribution of the optical carrier signals over large distances via low loss, inexpensive optical fibers [1].

Optical heterodyning is an effective and promising method for photonic generation of microwave signals. One such optical heterodyning technique to generate microwave signals in the optical domain is to make use of a dual-wavelength laser, with the two wavelengths separated by the desired microwave frequency. Due to the fact that the two wavelengths are produced from the same laser cavity, the stability of the generated microwave can be much improved as compared with two individual free-running lasers, since any environmental perturbation will affect both wavelengths in a similar way.

In this work, we report a dual-wavelength distributed feedback (DFB) channel waveguide laser in ytterbium-doped aluminum oxide ($Al_2O_3:Yb^{3+}$). The free-running laser was used to generate a 9 kHz wide microwave beat signal at ~15 GHz with a long-term (45 minutes) frequency- and power stability better than 2.5 MHz and 0.35 dB respectively.

II. FABRICATION

The DFB cavity consisted of a 1-cm-long uniform waveguide Bragg grating, which has been integrated with a 1-μm-thick and 2.5-μm-wide $Al_2O_3:Yb^{3+}$ ridge waveguide [2]. The waveguide layer was deposited on a thermally oxidized standard silicon wafer by means of reactive cosputtering [3]. The sputtering powers applied to the metallic targets were selected such that the resulting Yb^{3+} concentration in the waveguide was approximately 5.8×10^{20} cm^{-3}. The channel waveguides were defined by means of standard lithography and etched ~90 nm deep with a chlorine-based reactive ion etching process [4], after which a silicon dioxide cladding layer was deposited on top of the waveguides. An 80-nm-deep surface relief Bragg grating structure was fabricated in the top surface of the cladding layer by using laser interference lithography and reactive ion etching [2].

When two quarter-wavelength phase-shifts are induced in such a uniform waveguide Bragg grating, two resonance peaks appear in the transmission stop band of the device [5]. These two resonances share a common cavity, which consists of both the phase-shift regions. The wavelength spacing between the resonances depends on the spatial separation and the values of the respective phase-shifts. The required phase-shifts were induced via two sections with 2-mm-long adiabatic sinusoidal widening of the waveguide width [2].

When both phase-shifts are varied symmetrically from a quarter-wavelength phase-shift $\pi/2$, such that one has a value of $\pi/2 - \Delta\theta$ and the other $\pi/2 + \Delta\theta$, the two resonant wavelengths separate symmetrically from each other with respect to the Bragg wavelength. As the value of the phase detuning $\Delta\theta$ increases, the shorter wavelength oscillates more around the $\pi/2 - \Delta\theta$ phase shift, while the longer wavelength concentrates around the $\pi/2 + \Delta\theta$ phase shift, instead of both wavelengths concentrating equally around both phase-shift regions simultaneously, as in the case of $\Delta\theta = 0$. Since each longitudinal mode is being amplified mainly by separate sections of the active medium, the degree of longitudinal mode competition is reduced, which results in less fluctuations in the optical power, and consequently also less frequency fluctuations in the laser generated microwave signal.

III. CHARACTERIZATION

The laser was optically pumped by a 976 nm diode laser of which the light was launched into the waveguide via the 980 nm port of a wavelength-division-multiplexing (WDM) fiber which was butt-coupled to the chip, while the laser emission was collected through the 1030 nm port of the WDM

This work was supported by funding through the Smartmix ‘‘Memphis’’ programme of the Dutch Ministry of Economic Affairs

fiber. The laser emission was sent to a 40 GHz photodetector which was connected to an electrical spectrum analyzer. The measured beat signal at 15.0426 GHz confirmed that the laser was operating on two longitudinal modes (Fig. 1).

The two sidebands which are visible on either side of the main microwave peak are produced by relaxation oscillations from the two respective longitudinal modes. The two relaxation–oscillation frequencies were used to calculate the Lamb's coupling constant, a value that indicates whether there exists weak ($C \approx 0$) or strong ($C \approx 1$) mode competition between the two oscillating wavelengths [6]. The calculated value of $C = 0.23$ indicates that the mode competition was rather weak, since each longitudinal mode was being amplified mostly by separate sections of the active medium.

The long-term frequency stability of the microwave beat signal was measured over a period of 45 minutes with a 100 ms interval. The standard deviation of the microwave frequency during this period was found to be 2.5 MHz, while the power of the microwave signal was stable within 0.35 dB. To investigate the short-term frequency stability, the microwave signal at the output of the photodiode was mixed with a high-purity, stable electrical reference signal with a subhertz linewidth. Since the reference signal was much narrower than the laser beat signal, mixing of the two signals produced a convoluted signal that was nearly identical in shape to the original microwave beat signal produced by the laser, but shifted to the kilohertz range, so that a time trace of this downconverted signal could be measured with an oscilloscope. A short-time Fourier transformation was performed on the time trace of the downconverted signal to obtain a spectrogram over a duration of 10 ms. The short-term frequency stability of the microwave signal during the 10 ms period was 40 kHz.

To determine the linewidth of the laser, a single temporal slice was extracted from a spectrogram with a frequency

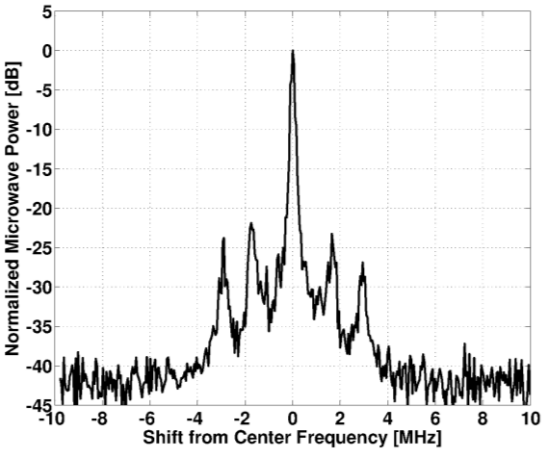


Figure 1. Electrical spectrum of the microwave beat signal centered at 15.0426 GHz, measured with a resolution bandwidth of 50 kHz.

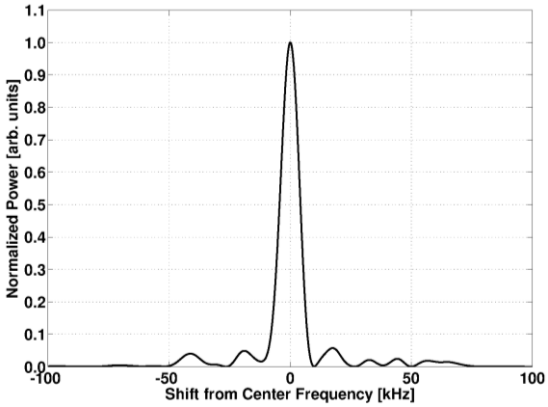


Figure 2. The spectrum which was extracted from a single temporal slice out of a spectrogram with an 8 kHz resolution. The -3 dB width of the microwave signal was below 9.0 kHz.

resolution of 8 kHz. This confirmed that the microwave signal produced by the laser was below 9.0 kHz, which implies an individual laser linewidth below 4.5 kHz (Fig. 2).

IV. Summary

We have demonstrated a continuous wave dual-wavelength $Al_2O_3:Yb^{3+}$ DFB channel waveguide laser for the photonic generation of stable microwave signals. The narrowband microwave beat signal produced by the dual-wavelength laser was centered at ~15 GHz, with a frequency stability of ±2.5 MHz. This result emphasizes the great potential of using rare-earth-ion-doped monolithic waveguide lasers for the photonic generation of stable microwave signals.

References

[1] J. Capmany and D. Novak, "Microwave photonics combines two worlds," Nat. Photonics, vol. 1, pp. 319- 330, June 2007.

[2] E. H. Bernhardi, M. R. H. Khan, C. G. H. Roeloffzen, H. A. G. M. van Wolferen, K. Wörhoff, R. M. de Ridder, and M. Pollnau, "Photonic generation of stable microwave signals from a dual-wavelength $Al_2O_3:Yb^{3+}$ distributed-feedback waveguide laser," Opt. Lett., vol. 37, pp. 181-183, Jan. 2012.

[3] K. Wörhoff, J. D. B. Bradley, F. Ay, D. Geskus, T. P. Blauwendraat, and M. Pollnau, "Reliable low–cost fabrication of low–loss $Al_2O_3:Er^{3+}$ waveguides with 5.4–dB optical gain," IEEE J. Quantum Electron., vol. 45, pp. 454-461, May 2009.

[4] J. D. B. Bradley, F. Ay, K. Wörhoff, and M. Pollnau, "Fabrication of low–loss channel waveguides in Al_2O_3 and Y_2O_3 layers by inductively coupled plasma reactive ion etching," Appl. Phys. B, vol. 89, pp. 311-318, Oct. 2007.

[5] G. E. Villanueva, P. Pérez-Millán, J. Palací, J. L. Cruz, M. V. Andrés, and J. Martí, "Dual-Wavelength DFB Erbium-Doped Fiber Laser With Tunable Wavelength Spacing," IEEE Photon. Technol. Lett., vol. 22, pp. 254-256, Feb. 2010.

[6] M. Brunel, A. Amon, and M. Vallet, "Dual-polarization microchip laser at 1.53 μm," Opt. Lett., vol. 30, pp. 2418-2420, September 2005.

Adiabatic transitions for sub-wavelength grating waveguides

Diego Pérez-Galacho, Robert Halir, Luis Francisco Zavargo-Peche, Juan Gonzalo Wangüemert-Pérez, Alejandro Ortega-Moñux, Íñigo Molina-Fernández
Departamento de Ingeniería de Comunicaciones
Universidad de Málaga, UMA
Málaga, Spain
diego.perez@ic.uma.es

Pavel Cheben
Institute for Microstructural Sciences
National Research Council, NRC
Ottawa, Canada

***Abstract*—Sub-wavelength gratings (SWG) enable refractive index engineering in silicon waveguides, with application spanning from fiber-to-chip grating couplers to wavelength demultiplexers. However, the design of adiabatic tapers between these waveguides is challenging and non-intuitive. In this work, a systematic method for designing adiabatic transitions between SWGs is presented for the first time**

Keywords; taper, silicon-on-insulator, Bragg, SWG.

I. INTRODUCTION

Silicon-on-Insulator is emerging as a major fabrication platform for integrated optics, owing to its high contrast that enables compact and highly integrated devices. Recently a new type of silicon waveguide, the Sub-wavelength Grating (SWG), was presented [1]. SWG waveguides are periodic structures with a pitch smaller than wavelength. Diffraction can thus not take place in these structures. The main advantage of these waveguides is that they allow the designer to engineer the effective refractive index in a wide range [1,2]. The refractive index implemented by SWG waveguides depends on the geometrical parameters of the structure (width (*W*), pitch (*Λ*) and duty cycle (*DC*)), the operation wavelength (*λ*) and light polarization. In order to work in SWG zone, the pitch of the structure must be smaller than the first order Bragg period, given by:

$$\Lambda < \Lambda_{Bragg} = \lambda / (2 \cdot n) \quad (1)$$

Where *n* is the effective index of the Bloch mode propagating through the structure. While working in SWG zone these structures behave like common waveguides, exhibiting no diffraction effects and low losses.

The use of SWGs has been demonstrated in many applications such as efficient fiber-to-chip couplers [3], mode converters [1], crossings between waveguides [4], arrayed waveguide grating multiplexers [5] and high performance MMIs [6]. Extensive use of SWG waveguides in device design requires adiabatic transitions (tapers) between conventional waveguides and SWGs. However, as illustrated in the following sections, the design of such transitions is challenging and non-intuitive, as significant back-reflections that grow with the taper length can occur. Here we present, for the first time, a systematic method for designing adiabatic SWG tapers. The paper is organized in five sections. In section II the proposed taper structure is described. In section III we detail why a conventional, linear taper is not always an appropriate solution, and present and validate our method for designing SWG tapers. Finally, in section IV the main conclusions are drawn.

II. TAPER STRUCTURE

We consider the general taper structure shown in Fig. 1. This structure is a transition between a silicon wire and a SWG waveguide of a different width. Note that a transition between two SWG waveguides of different widths is a particular version of this structure. Here, w_1 and w_4 are the widths of the silicon wire and the SWG waveguide respectively. The pitch of the SWG waveguide (*Λ)* and the duty cycle ($DC = b/a$) have been assumed constant along the structure. The parameters of the taper are w_3 and $CoreDC = w_2/w_1$, which are functions of the propagation direction (*z*). In Fig. 1 w_3 and *CoreDC* vary linearly with *z*. This taper shape avoids small gaps that would result from simple changing the duty cycle of the SWG from 1 to *b*/*a*.

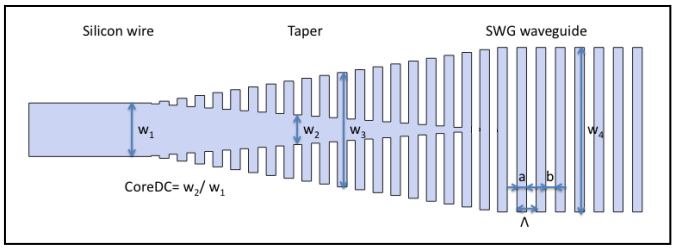


Figure 1. Structure of a taper between a silicon wire and a SWG waveguide.

The analysis has been carried out for TE (in-plane) polarization and using a 2D model obtained through the Effective Index Method. The resulting 2D model has been simulated with the Fourier Eigenmode Expansion Method combined with Bloch mode analysis [7].

III. DESIGN METHODOLOGY

The problem can be formulated as the election of the functions *CoreDC*(*z*) and $w_3(z)$ that maximize power transmission from the silicon wire to the SWG waveguide. The dimensions used in the following design example are w_1 = 0.5μm, w_4 = 3.5μm, Λ = 0.28μm and $a = b$ = 0.14μm. With these values, and a working wavelength of λ = 1.55μm, the SWG waveguide exhibits no diffraction effects.

A. Linear taper

The first approach to the solution is to choose *CoreDC* and w_3 linear functions. Fig. 2 (green line with square markers) shows the taper transmission versus length. Unlike common tapers, transmission reduces as the taper length is increased. This undesirable behavior is caused by the entering of the taper structure in the Bragg zone at some point of its trajectory, causing high-backreflections. In order to avoid this, *CoreDC*(*z*) and $w_3(z)$ must be designed properly.

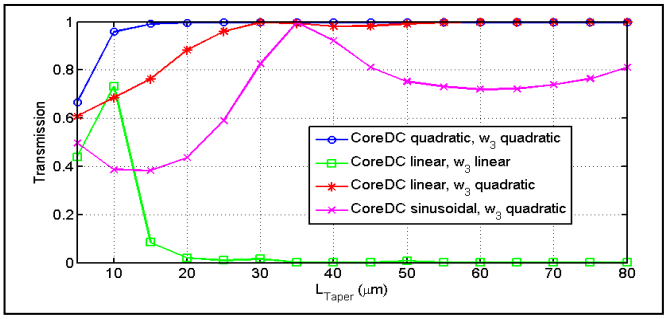


Figure 2. Transmission curves of the designed tapers as a function of length.

B. Choosing adequate shape functions

To minimize back-reflections from the taper, the design method must guarantee an adiabatic transition, while at the same time avoiding the Bragg regime at any point of the taper. Thus, in a first step, a Bloch modal analysis for each combination of *CoreDC* and w_3 is carried out, in order to identify which combinations avoid the Bragg regime. Fig. 3 represents the reflectivity of Bloch mode for each combination of *CoreDC* and w_3. The white area contains the combinations of *CoreDC* and w_3 that yield no reflection, whereas the black area contains the combinations that produce high reflections. The upper-left corner represents the silicon wire waveguide (w_1 = 0.5μm, *CoreDC* = 1), while the lower-right corner represents the SWG waveguide (w_4 = 3.5μm, *CoreDC* = 0). The taper design must connect those points avoiding the high-reflectivity zone. It can be seen how the linear taper goes through the high-reflectivity zone, which explains its spurious behavior.

As an alternative to the linear taper three different tapers are designed, each one avoiding the Bragg zone. The first one varies sinusoidally in *CoreDC* and quadratically in w_3, the second one varies linearly in *CoreDC* and quadratically in w_3, and the third one quadratically in *CoreDC* and in w_3. Their trajectories can be seen in Fig. 3.

To evaluate the performance of the three taper designs, their transmissions are calculated as a function of the length of the taper. In Fig 2 it can be seen that the taper whose trajectory is furthest apart from the Bragg zone (*CoreDC* quadratic, w_3 quadratic) has a better behavior than the other two, obtaining a full transmission with a length of L_{Taper} = 20μm. The proximity to the Bragg zone in the trajectory of the other two tapers (*CoreDC* linear, w_3 quadratic and *CoreDC* sinusoidal, w_3 quadratic) explains their poor behavior.

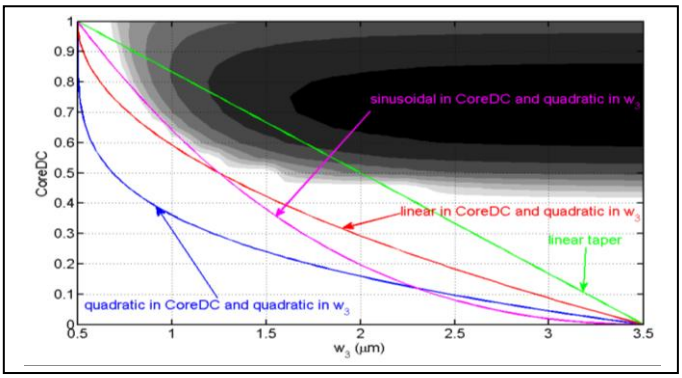


Figure 3. Reflectivity map of a SWG waveguide as a function of CoreDC and w_3 and the trajectories of the designed tapers.

IV. CONCLUSIONS

In this work, a systematic method for the design of adiabatic tapers between SWG waveguides has been presented. Our design example focused on a transition between a Si-wire waveguide and an SWG, but the methodology is general and can be readily applied to any SWG transition.

ACKNOWLEDGMENTS

This work was supported by the Spanish Ministerio de Ciencia (project TEC2009-10152), the Andalusian Regional Ministry of Science, Innovation and Business (project P07-TIC-02946), and the European Mirthe project (FP7-2010-257980).

REFERENCES

[1] P. Cheben, D.-X. Xu, S. Janz, A. Densmore, "Subwavelength waveguide grating for mode conversion and light coupling in integrated optics", Opt. Express, vol. 14, pp. 4695–4702, May 2006.

[2] S. M. Rytov, "The electromagnetic properties of finely layered medium", Sov. Phys, JETP, vol. 2, pp. 466–475, 1956.

[3] R. Halir, P. Cheben, S. Janz, D.-X. Xu, Í. Molina-Fernández, J. G. Wangüemert-Pérez, "Waveguide grating coupler with subwavelength microstructures", Opt. Lett., vol. 34, pp. 1408–1410, April 2009.

[4] P. J. Bock, P. Cheben, J. H. Schmid, J. Lapointe, A. Delâge, D.-X. Xu, S. Janz, A. Densmore, T. J. Hall, "Subwavelength grating crossing for silicon wire waveguides", Opt. Express, vol. 18, pp. 16146–16155, July 2010.

[5] P. Cheben, P. J. Bock, J. H. Schmid, J. Lapointe, S. Janz, D.-X. Xu, A. Densmore, A. Delâge, B. Lamontagne, T. J. Hall, "Refractive index engineering with subwavelength gratings for efficient microphotonic couplers and planar waveguide multiplexers", Opt. Lett., vol. 35, pp. 2526–2528, August 2010.

[6] A. Ortega-Moñux, L. Zavargo-Peche, A. Maese-Novo, Í. Molina-Fernández, R. Halir, J. G. Wangüemert-Pérez, P. Cheben, J. H. Schmid, "High-performance multimode interference coupler in silicon waveguides with subwavelength structures", IEEE Photon. Technol. Lett., vol. 23, pp. 1406–1408, October 2011.

[7] L. Zavargo-Peche, A. Ortega-Moñux, J. G. Wangüemert-Pérez, Í. Molina-Fernández, "Fourier based combined techniques to design novel sub-wavelength optical integrated devices", Progress In Electromagnetic Research, vol. 123, pp. 447–465, January 2012.

Highly Yb^{3+}/Er^{3+}-codoped microring resonator performance in migration-assisted upconversion regime

Juan A. Vallés
Department of Applied Physics and I3A
University of Zaragoza
Zaragoza, Spain
juanval@unizar.es

Ramona Gălăţuş
Faculty of Electronics, Telecommunications and Information Technology
Technical University of Cluj-Napoca
Cluj-Napoca, Romania

***Abstract*—The amplifying and filtering performance of a highly Yb/Er-codoped add-drop filter is analyzed and discussed. The use of the microscopic statistical formalism to describe energy-transfer inter-atomic mechanisms allows determining realistic optimum parameters and working conditions.**

Keywords-optical microring resonator; Yb^{3+}/Er^{3+}-codoping; energy-transfer inter-atomic mechanisms; optimized design.

I. INTRODUCTION

Optical microring resonators are attracting much interest due to their potentiality as fundamental building blocks for a large variety of applications in photonic circuits, including channel dropping filters [1], add/drop (de)multiplexers [2], modulators [3], switches [4], sensors [5] and lasers [6].

The basic structure under analysis (commonly termed an add-drop filter) consists of a microring resonator side-coupled to two straight waveguides for signal input/output. When the structure host material is Yb/Er-codoped the device may exhibit both filtering and amplifying functionalities. However, the required high doping levels enhance efficiency-limiting energy transfer inter-atomic interactions, which have to be considered for an optimized design. Unrealisticly, the optimization studies available have ignored these mechanisms in their models [7]. A precise formalism for the effect of both upconversion and migration is the microscopic statistical formalism (MSF) based on the statistical average of the excitation probability of the Er^{3+} ion in a microscopic level [8]. This formalism was recently adapted to include Yb^{3+}-sensitization and transversally resolved rate equations, which become essential due to the nonlinear character of the energy transfer mechanisms [9].

II. ACTIVE MICRORING RESONATOR TRANSFER FUNCTIONS.

A scheme of the structure is shown in Figure 1. R is the radius of the microring, $2L = 15000\,\mu m$ is the total length of the upper and lower waveguides, L being the length between the waveguide ports and the coupling point. We assume that the microring and the waveguides have the same mode propagation constant, β, amplitude loss coefficient, α, and gain coefficient, g.

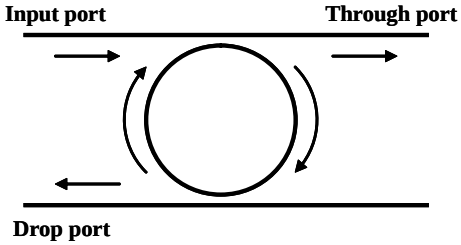


Figure 1. Scheme of the structure: a microring resonator side-coupled to two straight waveguides for signal input/output.

Then, the common complex propagation constant is $\beta - j\alpha + jg$. Let κ_i ($i=1,2$) be the amplitude coupling ratio between the microring and the upper and lower waveguides, t_i be the corresponding transmission ratio, which satisfies $\kappa_i^2 + t_i^2 = 1$. Then, the transfer functions from the input port to the through and drop ports are [7]:

$$|T|^2 = \left| \frac{\left[t_1 - t_2\, exp\left(-j2\varphi\right) \right] exp\left(-j2\psi\right)}{1 - t_1 t_2\, exp\left(-j2\varphi\right)} \right|^2 \qquad (1)$$

$$|D|^2 = \left| \frac{\kappa_1 \kappa_2\, exp\left[-j\left(\varphi + 2\psi\right) \right]}{1 - t_1 t_2\, exp\left(-j2\varphi\right)} \right|^2 , \qquad (2)$$

respectively, where:

$$\varphi = \pi R\left(\beta - j\alpha + jg\right) \quad \text{and} \quad \psi = L\left(\beta - j\alpha + jg\right). \qquad (3)$$

If $g > 0$ in (3) the device is a microring resonator amplifier and the fulfillment of the resonance condition depends also on the gain coefficient g what forces a previous optimizing design based on the expected working conditions.

III. RESULTS AND DISCUSSION

We determine the value of the gain coefficient by calculating it in an Yb/Er-codoped straight waveguide amplifier [7]. We assume the core and cladding indexes and the core dimensions in [10] and the Yb/Er-codoped phosphate glass spectroscopic parameters in [9]. Once the effective

indexes are calculated the radius of the microring, $R = 16.4\,\mu m$, is selected not only to match the resonance condition for pump and signal (the resonant orders of the pump and signal are $m_p = 161$ and $m_s = 102$) but also to keep the radiation loss as low as possible. In our case, the power bend loss coefficient is small enough compared to the assumed power transmission loss coefficient, $2\alpha = 0.5\,dB/cm$, to be neglected. We assume as pump and signal input powers 250 mW and 1 μW, respectively, and their wavelengths are $\lambda_p = 976\,nm$ and $\lambda_s = 1534\,nm$. In order to determine the signal gain coefficient, the transversally-resolved MSF is used to accurately describe the energy-transfer mechanisms contribution in the rate equations. In Fig. 2 the signal gain is plotted as a function of Yb^{3+}-ion concentration for five Er concentrations. The maximum gain, 9.84 dB, is achieved for $N_{Yb} = 1x10^{27}\,m^{-3}$ and $N_{Er} = 4x10^{26}\,m^{-3}$, more realistic values than those reported in [7]. Once g is determined, an optimum coupling ratio $\kappa_1 = \kappa_2 = 0.085$ (and subsequently the central coupling gap [11]) can be calculated.

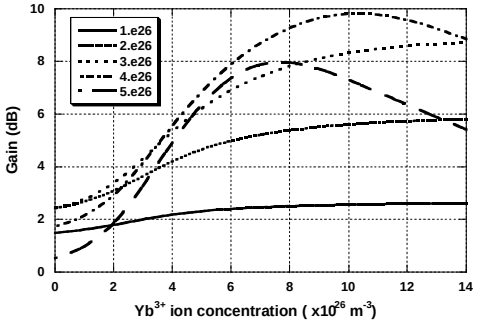


Figure 2. Straight waveguide amplifier gain as a function of Yb^{3+}-ion concentration for five Er concentrations.

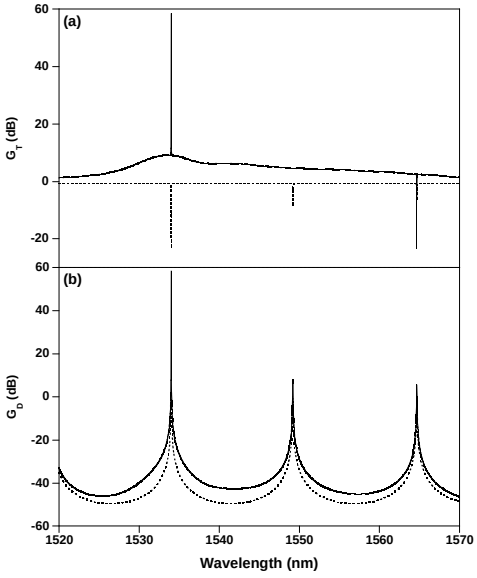


Figure 3. Output spectra of the (a) through and (b) drop ports of the passive (dotted line) and active (solid line) microring structures in the 1.53 nm gain band.

Finally, from the values of through and drop coefficients in (1) and (2) the output power gain spectra are defined as:

$$G_T(dB) = 10\log_{10}\left(|T|^2\right) \text{ and } G_D(dB) = 10\log_{10}\left(|D|^2\right) \quad (4)$$

In the output spectra in Fig. 3 it can be noticed how, if $g = 0$, the device shows a typical filtering behaviour. However, if $g > 0$ in the through port spectrum the device exhibits only the amplifying function whereas in the drop port both functions, amplifying (near the signal resonant wavelength) and filtering (far from the signal resonant wavelength) can be found. The achievable signal power gain reaches 58.3 dB.

ACKNOWLEDGMENT

This work was partially supported by the Spanish Ministry of Economy and Competitiveness under the FIS2010-20821 project, by the Diputación General de Aragón and by the European Social Fund through the Sectoral Operational Programme Human Resources Development 2007-2013, 4D-POSTDOC, contract no. POSDRU/89/1.5/S/52603.

REFERENCES

[1] H. Okamoto, M. Haraguchi and T. Okamoto, "Filtering characteristic of a microring resonator with a gap," Electronics and Communications in Japan Part II-Electronics, vol. 89(5), pp. 25-32, 2006.

[2] B. E. Little, S. T. Chu, P. P. Absil et al., "Very high-order microring resonator filters for WDM applications," IEEE Phot. Technol. Lett, vol. 16(10), pp. 2263-5, 2004.

[3] M. Balakrishnan, M. Faccini, M. B. J. Diemeer et al. "Microring resonator based modulator made by direct photodefinition of an electro-optic polymer," Applied Physics Letters, vol. 92(15), pp.153310, 2008.

[4] M. Foerst, J. Niehusmann, T. Plotzing et al. "High-speed all-optical switching in ion-implanted silicon-on-insulator microring resonators," Optics Letters, vol. 32(14), pp. 2046-8, 2007.

[5] D. X. Dai, S. L. He, "Highly-sensitive sensor with large measurement range realized with two cascaded microring resonators," Optics Communications, vol. 279 (1), pp. 89-93, 2007.

[6] J. Wang, K. Y. Wong, "Polarization characteristics of a light-emmiting polymer microring laser," Applied Physics B-Lasers and Optics, vol. 87(4), pp. 685-91, 2008.

[7] Y. H. Wang, C. S.Ma, X. Yan, D. M. Zhang, "Analysis for amplifying characteristics of Er^{3+}-Yb^{3+}-co-doped microring resonators," Optics & Laser technology, vol. 42, pp. 336-340, 2010.

[8] D. Khoptyar, S. Sergeyev and B. Jaskorzynska, "Homogeneous upconversion in Er-doped fibres under steady state excitation. Analytical model and its Monte-Carlo verification" J. Opt. Soc. Am. B , vol. 22(3), pp. 582-590, 2005.

[9] J. A. Vallés, "Method for accurate gain calculation of a highly Yb^{3+}/Er^{3+}-codoped waveguide amplifier in migration-assisted upconversion regime," *IEEE J. Quantum Electron.*, vol. 47(8), pp. 1151-1158, 2011.

[10] Y. H. Wang, C. S. Ma, D. L. Li and D. M. Zhang, "Formulized analytical technique for gain characteristics of phosphate glass Er^{3+}/Yb^{3+} co-doped waveguide amplifiers," Optica Applicata, vol. 38(2), pp. 329-339, 2008.

[11] C. S. Ma, X. Yan, Y. Z. Xu et al. "Characteristic analysis of bending coupling between two optical waveguides," Optical and Quantum Electronics vol. 37(11), 1055-67, 2005.

Tolerance analysis of a 4x4 MMI-based 90° optical hybrid for 100G coherent receivers

J. S. Fandiño, P. Muñoz and J. Capmany
Optical and Quantum Communications Group.
ITEAM Research Institute.
Universitat Politècnica de València, c/ Camino de Vera s/n, 46020 Valencia (Spain).
E-mail: jasanfan@upvnet.upv.es

***Abstract*—A tolerance analysis of a 4x4-MMI working as a 90° optical hybrid in InP technology is presented. Results predict up to 25 nm bandwidth. 50 nm are expected for width tolerances below ±0.1 μm.**

I. Introduction

Revived interest in coherent optical communications has recently spurred much research in 90° optical hybrids, which have become a fundamental component of coherent receivers. Although several structures have been proposed [1], robustness and tolerance to manufacturing defects make 4x4 MultiMode Interference couplers (4x4 MMI) perfect candidates for fully integrated, high performance 90° optical hybrids. Devices with imbalance below 0.5 dB and phase errors lower than 5° across the whole C band have been already demonstrated using 4 μm SOI technology [2]. Common Mode Rejection Ratios (CMRRs) below 20 dBe for both I and Q channels and phase errors below 7° were also demonstrated in InP over the whole C-band within a temperature range from -5°C to 75°C [3].

However, ever-increasing data traffic will likely require the use of even more complex modulation formats. Tighter restrictions in optical front-end PICs will put a limit to manufacturing tolerances, so as to meet imbalance and phase specifications. In this work, a study on the impact of manufacturing tolerances in the performance of a 4x4 MMI, designed using InP generic integration technology, is presented. Several physical parameters are considered: waveguide's width, core's thickness, core's refractive index, length, and wavelength. Parameters impact is derived in terms of metrics established in the Optical Internetworking Forum (OIF) standard draft for 100G integrated intradyne coherent receivers, such as the CMRR and phase errors for both I & Q channels.

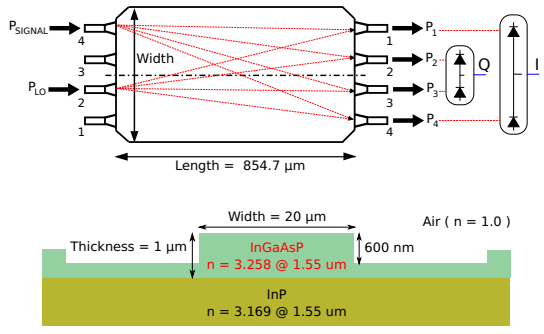


Fig. 1: Top and cross-section view. Nominal device values are shown.

II. Simulation procedure

An overview of the device structure and waveguide cross-section is shown in Fig. 1. Waveguides consists of two layers: InGaAsP as core (n = 3.258 @ λ = 1.55 μm) over an InP substrate (n = 3.169 @ λ = 1.55 μm). They are defined by etching down 600 nm from the top of the core. Firstly, a nominal 90° hybrid was designed using commercial software tools to serve as a reference for the tolerance anaylysis.

Secondly, technology specific manufacturing tolerances were taken into account. These include absolute maximum variations in waveguide's width (±0.1 μm) due to lithography and etching steps, as well as refractive index (±0.004) and thickness (±0.05 μm) due to epitaxial growth. Wavelength was also considered to assess operation bandwidth (±50 nm). Simulation values ([range]@step) are: MMI length=[848,860]@3 μm, n_{core}=[3.250,3.266]@0.004, MMI width=[19.8,20.2]@0.1 μm and core thickness=[0.9,1.1]@0.05 μm. Wavelength interval is [1.5,1.6]@0.25 μm, along with two additional points at 1.5375 and 1.625 μm. Multi-sweep runs were performed, and optical transmission relations between input (2 4) and output (1 2 3 4) ports (Fig. 1) were calculated.

Finally, CMRRs and phases were derived from photodetected currents, and compared with worst-case values given by the OIF standard draft: CMRR Signal to I & Q $\leq$ -20 dBe, CMRR LO to I & Q $\leq$ -12 dBe as well as phase error between I and Q channels $\leq \pm$ 5°. CMRRs are related to cancellation of common mode noise (e.g. RIN), while phase errors result in loss of orthogonality and crosstalk between I and Q channels.

III. Results and discussion

Our tolerance analysis expands in a 5th dimensional space. A versatile visualization technique called *dimensional stacking* was employed to represent results and gain insight into relationships among parameters [4]. This concept is summarized in Fig. 2 (left). For every wavelength, a matrix is plotted

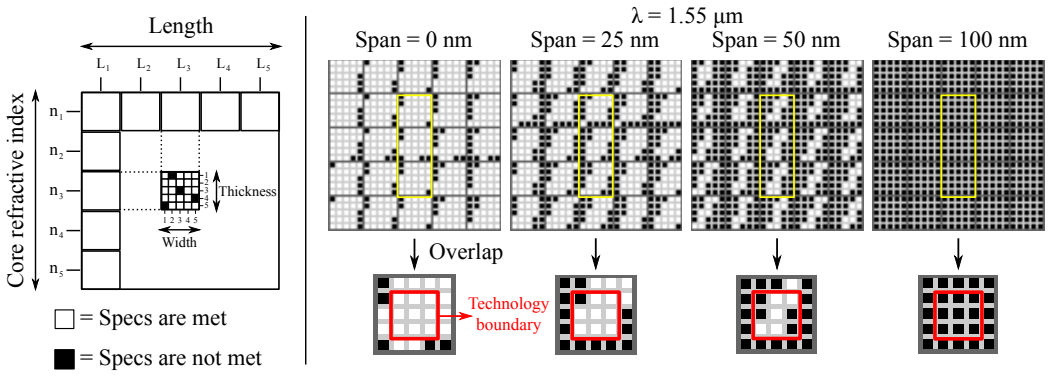


Fig. 2: Left: Dimensional stacking plot diagram, showing distribution of input parameters. Right: Simulation results for different spans.

which contains 5x5 submatrices of 5x5 pixels. Each of these groups contains those simulations where width (horizontal) and thickness (vertical) are varied, while length and refractive index remain fixed. Parameter values increase from left to right and from top to bottom, i.e., pixels in the center of each matrix represent nominal design values. A pixels is coloured white when all specifications are met (both CMRR and phase), and black otherwise.

The final result can be seen also in Fig. 2 (right), where matrices for different wavelength spans are shown. These were formed by overlaping all those matrices whose simulation wavelength falls within a given span around the nominal wavelength (e.g. the 25nm span matrix is formed by overlapping matrices at 1.5375, 1.55 and 1.5625 μm). From these pictures, some interesting conclusions can be drawn. Firstly, it is easily observed that pixel patterns inside each group remain almost unchanged when moving in the vertical direction. This means that waveguide's core refractive index has no significant effect on device performance, which is consistent with basic MMI theory. A change in core refractive index will affect effective indexes of all propagation modes. Since optimum length depends on the difference between them, common changes are cancelled out. Secondly, device is also shown to be highly tolerant to length variations, which span a 15 μm range. This is also consistent with MMI theory and with the fact that CMRRs only measure similarity between output powers, so total insertion losses are not taken into account.

Further processing of this binary data can also be used to estimate operation bandwidth for a given set of manufacturing tolerances. Reversely, it can be employed to define maximum manufacturing deviations to achieve certain design goals (such as bandwidth). In this work, the former approach is considered. We provide values for HHI's InP generic integration technology, but the concept can be applied to any other technology. In general, length manufacturing deviations approach those related to the width ($\pm$ 0.1 μm in this particular case), which are much lower than those required to cause an impact in device performance. Thus, length can be reasonbly assumed to be constant. Afterwards, groups related to technology maximum deviations in n_{core} are overlapped in the vertical direction (Fig. 2, yellow line). The resultant 2D plots shows which combinations of width and thickness match specifications across the given span, assuming that deviations in refractive index can not be controlled. By considering only those contained within the boundary specified by technology (Fig. 2, red line), an approximate 25 nm bandiwdth is expected, which is consistent with previous experimental results [3]. Fig. 2 also shows that an accuracy better than $\pm$ 0.1 μm would be required to achieve operation bandwidth up to 50 nm, regardless of variations in waveguide's thickness.

IV. Conclusions

A tolerance analysis of a 90° optical hybrid based on a 4x4 MMI monolithically integrated in an InP generic integration technology has been performed. CMRRs and phase relations have been analyzed. Simulations show that these specifications can be met, at least, over a 25 nm range for the chosen InP generic integration technology, in good agreement with previous experimental results. Further bandwidth (up to 50 nm) is expected to require accuracy in MMI's width better than $\pm$ 0.1 μm.

Acknowledgements

The authors acknowledge financial support from Spanish MICINN Project TEC2010-21337, acronym ATOMIC. J.S. Fandiño acknowledges financial support through grant FPU-2010 (ref: AP2010-1595). The authors are also grateful to the EuroPIC consortium (FP7 funded programme NMP 228839-2) for access to the design manual and design toolkit of the generic InP fab.

References

[1] M. Seimetz and C.-M. Weinert, "Options, feasibility, and availability of 2x4 90 hybrids for coherent optical systems," *Lightwave Technology, Journal of*, vol. 24, pp. 1317 –1322, march 2006.

[2] L. Zimmermann, K. Voigt, G. Winzer, K. Petermann, and C. Weinert, "C -band optical 90 hybrids based on silicon-on-insulator 4x4 waveguide couplers," *Photonics Technology Letters, IEEE*, vol. 21, pp. 143 –145, feb.1, 2009.

[3] H.-G. Bach, A. Matiss, C. Leonhardt, R. Kunkel, D. Schmidt, M. Schell, and A. Umbach, "Monolithic 90 hybrid with balanced pin photodiodes for 100 gbit/s pm-qpsk receiver applications," in *OFC 2009*, pp. 1 –3, march 2009.

[4] J. LeBlanc, M. Ward, and N. Wittels, "Exploring n-dimensional databases," in *Visualization, 1990. Visualization '90., Proceedings of the First IEEE Conference on*, pp. 230 –237, oct 1990.

Design, fabrication and characterization of a narrow band microwave photonics beamformer in Silicon-On-Insulator

J.D. Doménech, I. Artundo, P. Muñoz and J. Capmany
Optical Communications Group. ITEAM Research Institute
Universitat Politècnica de València,
Camí de Vera s/n, 46020 Valencia (Spain)
E-mail: jodogo@iteam.upv.es

P. Dumon and W. Bogaerts
Interuniversity Microelectronics Center (IMEC),
Department of Information Technology, Ghent University
Sint-Pietersnieuwstraat 41, 9000 Gent, Belgium

***Abstract*—A novel microwave photonics beamformer device concept, for Single Side-Band modulated signals, is presented. The core of the beamformer is a phase-shifter and a channel demultiplexer. Design, fabrication in Silicon-On-Insulator and characterization are reported.**

I. Introduction

Microwave photonics is a well established discipline where the processing of high frequency microwave signals is done completely in the optical domain, with a considerable number of applications[1]. Amongst them, photonic beamforming is of great interest and different implementations exist [2], [3]. Those addressed with integrated optics devices commonly employ ring resonators (RR), due their versatile amplitude and phase response, which in turn can be tuned as reported extensively in the literature (see for instance [4]). In this work we propose an architecture for a beamforming network employing a comb laser [5] as optical source, with Single Side-Band (SSB) modulation scheme, where the central element (the phase shifter) is a tunable all-pass RR (ring side coupled to a waveguide, APRR) and an Arrayed Waveguide Grating (AWG). The fabrication and characterization of a 4x4 AWG with an APRR on each output in Silicon-On-Insulator (SOI) are reported.

II. Beamformer concept

The beamformer concept is depicted in Fig. 1 and consists of a comb laser which is externally modulated by a dual-drive Mach Zender Modulator (MZM), and next demultiplexed by an 1xN channels AWG. Then each channel is filtered with an APRR and finally photodetected, before an antenna element. The phase required for each antenna element in the beamformer can be selected by tuning the corresponding ring in the range allowed by the passband of the AWG. The photodetected phase will be then proportional to the phase difference between the optical carrier and the SSB RF subcarrier, as reported in [6].

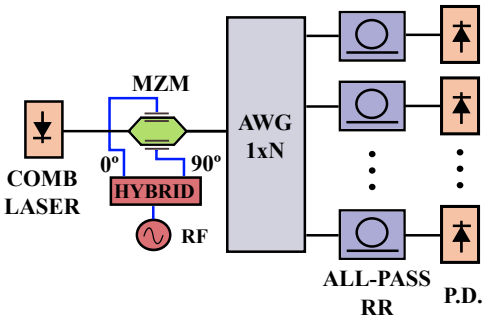


Fig. 1. Schematic of the beamformer device.

III. Design and fabrication

The cross section of the waveguides is height 220nm x width 450nm and the simulated group index for these waveguides is around 4.5. The APRR has been designed to have a free spectral range (FSR) of 0.75nm at a wavelength of $1.55\mu m$ and a coupling constant of $\kappa = 0.5$. The RRs have a perimeter of $711\mu m$ and a straight coupling section of $15\mu m$. The gap between the ring and the access waveguides is 200nm. The coupling constant together with the expected propagation losses (around 3dB/cm) will define the spectral width of the notch in resonance and the $\Delta\lambda_{FWHM}$.

This values have been calculated accordingly to have a $\Delta\lambda_{FWHM}$ and a phase transition that allows to accomplish the maximum phase shift required by design between the optical carrier and the RF subcarrier. At the same time, the on-resonance notch depth has been minimized to avoid extra insertion losses. The beamformer has been designed to introduce a maximum phase shift of 270 degrees for SSB modulated signals up to 40GHz.

The AWG has been designed with 4 input and 4 output channels. The adittional channels at the input side are used for testing purposes. The AWG channel spacing has been set to 3.2nm and with a Gaussian response. The FSR of the AWG has been set to 22.4nm, that is 7 times the channel spacing. This increased FSR will reduce the imbalance between channels in

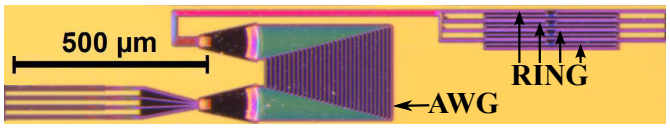


Fig. 2. Micrograph of the fabricated device.

the AWG, at the expense of an increased footprint. With this channel spacing at least 4 resonances of the RR are located within the passband of the AWG.

The devices were fabricated in a 200mm SOI wafer with a Silicon layer thickness of 220nm on top of a $2\mu m$ BOX employing 193nm deep UV lithography. The waveguides, the RRs and the AWG's star couplers have been defined with a deep etch process (220nm). For the input/output grating couplers and for all the waveguide apertures to the slab region of the star couplers in the AWG, an extra shallow etch process (70nm) has been employed to reduce the insertion losses [7]. The AWG footprint is $250\mu m$ x $515\mu m$ using $5\mu m$ waveguides bends. Fig. 2 shows a micrograph of the fabricated device. The inputs and outputs are routed from/to a grating coupler (GC), not shown in the figure, to couple light into/out of the device. The fabrication process did not include thermo-optic heater, hence the APRRs in this device cannot be individually tuned.

IV. Characterization

The chip was tested using standard monomode fibers positioned at 80° angle of the chip surface, aligned to the GCs. The GCs have an efficiency of about 30%. A tunable laser was used to measure the transfer function of the AWG+APRR. All the measurements are normalized to the measurement of a reference straight waveguide on the same chip. Hence the results do not include the GCs losses and represent on-chip figures. Fig. 3 shows the power transfer function for each channel. The on-chip insertion losses are below 3 dB in the four channels and the non-uniformity between channels is 1 dB. The crosstalk in the worst case is 20 dB. In every passband of the AWG, at least four resonances of the APRR can be appreciated.

Fig. 4 shows a single channel characterization with the spectral and phase response. The phase characterization has been carried out with the modulation phase shift method [8]. From Fig. 4-b a 360° phase shift on every resonance of the APRR can be observed. With the current FSR, a maximum SSB RF modulation frequency of 40 GHz can be employed, achieving at most 270° phase shift between the optical carrier and the SSB RF sub-carrier.

V. Conclusions

A beamforming architecture based in a comb laser and all-pass RR has been presented. The AWG-based demultiplexer and the phase shifting sections have been fabricated and characterized. The measurements show a good agreement between design and fabrication. Future work will include integrating more components of the architecture in SOI by means of modulators and photodetectors

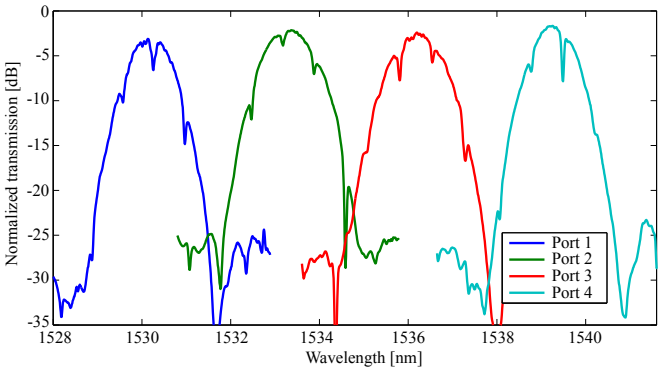


Fig. 3. AWG and all-pass rings combined spectral response

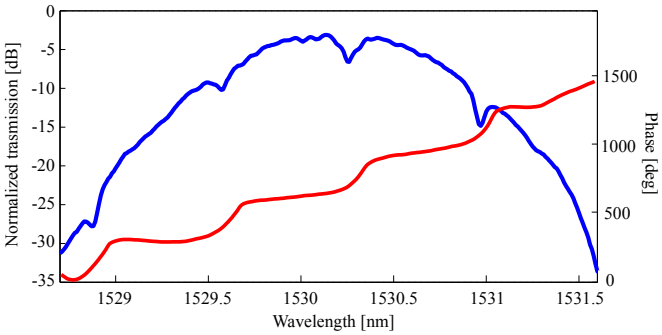


Fig. 4. Amplitude and phase response in a single channel of the device.

Acknowledgment

This work has been funded through the Spanish MICINN project no. TEC2008-06145/TEC and by the GVA through project no. PROMETEO/2008/092. J.D. Doménech acknowledges the FPI research grant no. BES-2009-018381.

References

[1] J. Capmany and D. Novak, "Microwave photonics combines two worlds," *Nature Photonics*, vol. 1, pp. 319–330, 2007.

[2] R. Esman, M. Monsma, J. Dexter, and D. Cooper, "Microwave true time-delay modulator using fibre-optic dispersion," *Electronics Letters*, vol. 28, pp. 1905 –1908, sept. 1992.

[3] N. A. Riza and S. Sumriddetchkajorn, "Micromechanics-based wavelength-sensitive photonic beam control architectures and applications," *Appl. Opt.*, vol. 39, pp. 919–932, Feb 2000.

[4] Q. Chang, Q. Li, Z. Zhang, M. Qiu, T. Ye, and Y. Su, "A tunable broadband photonic RF phase shifter based on a silicon microring resonator," *IEEE Photonics Technology Letters*, vol. 21, no. 1, pp. 60–62, 2009.

[5] M. A. Foster, J. S. Levy, O. Kuzucu, K. Saha, M. Lipson, and A. L. Gaeta, "Silicon-based monolithic optical frequency comb source," *Opt. Express*, vol. 19, pp. 14233–14239, Jul 2011.

[6] J. D. Doménech, P. Munoz, and J. Capmany, "Discretely tunable microwave photonics beamformer based on ring resonators and arrayed waveguide gratings," No. 77191J, Proc. SPIE, 2010.

[7] W. Bogaerts, P. Dumon, D. Van Thourhout, D. Taillaert, P. Jaenen, J. Wouters, S. Beckx, V. Wiaux, and R. Baets, "Compact wavelength-selective functions in silicon-on-insulator photonic wires," *Selected Topics in Quantum Electronics, IEEE Journal of*, vol. 12, pp. 1394 –1401, nov.-dec. 2006.

[8] D. Derickson, *Fiber Optic Test and Measurement*. Prentice Hall PTR, 1998.

Integrated optical platform for photon-number resolving, telecom-band detectors for photonic information processing

J. C. Gates, P. L. Mennea, P.G.R. Smith
Optoelectronics Research Centre
University of Southampton, Southampton, UK
gates@southampton.ac.uk

T. Gerrits, A. E. Lita, B. Calkins, N. A. Tomlin, A. E. Fox, A. Lamas Linares, R. P. Mirin, S. W. Nam
National Institute of Standards and Technology
Boulder, USA

N. Thomas-Peter, B.J. Metcalf, J. B. Spring, N. K. Langford, I. A. Walsmsley
Clarendon Laboratory,
University of Oxford, Oxford, UK

***Abstract*— We report the development of the optical substrates for the demonstration of an integrated photon-number-resolving detector, operating in the telecom band at 1550 nm, employing an evanescently coupled design that allows it to be placed at arbitrary locations within a planar circuit. Up to five photons are resolved in the guided optical mode via absorption from the evanescent field into a tungsten transition-edge sensor. The detection efficiency is 7.2 ± 0.5%. The polarization sensitivity of the detector is also demonstrated.**

Keywords-photon-number resolving detector; telecom-band; integrated

I. INTRODUCTION

Quantum information processing has seen a steady drive towards an integrated format in order to achieve increasingly complex circuit designs. Currently detection of low photon number signals is accomplished off-chip. However there is a drive to add this functionality on-chip to allow scalability, reduce loss and maintain the quantum optical state. Here we present an on-chip integrated photon-number resolving detector using evanescent coupling to a transition edge sensor (TES) [1].

These Evanescently Coupled Photon Counting Detectors (ECPCD's) display the low noise and single-photon sensitivity required to operate in the quantum regime, are compatible with complex, high-density on-chip optical circuits and can be placed at arbitrary locations. In addition the TES is photon-number-resolving, implying the detector can distinguish the energy correlated to the absorption of not only a single photon as in a 'click detector', but energy correlated to discern the absorption of several photons.

TESs are highly sensitive detectors that use the electrical and thermal properties of a superconducting thin film to distinguish the energy of a discrete number of photons. They function across a very broad range of wavelengths and have been used to demonstrate the highest recorded detection efficiencies and photon number resolution. By biasing the material at its superconducting transition temperature via voltage biasing, absorbed photons create a temperature change that can be measured via the resulting change in resistance. To resolve this temperature change, the device's heat capacity must be carefully specified, which in turn limits the volume of superconducting material that may be used. The choice of detector geometry is therefore critical to ensure good energy resolution and high-efficiency absorption. Device operation relies on a number of key factors that can be achieved by use of UV written silica-on-silicon waveguides and will be reported in this work.

II. DEVICE FABRICATION

The photon absorber, in this case a tungsten TES, is placed in the evanescent field of the guided mode of a waveguide passing underneath the detector, as shown in Figure 1. As the mode propagates through the detection region, it is coupled continuously into the detector via absorption. The confinement of the waveguide mode allows potential for extended interaction regions, providing a straightforward way to increase

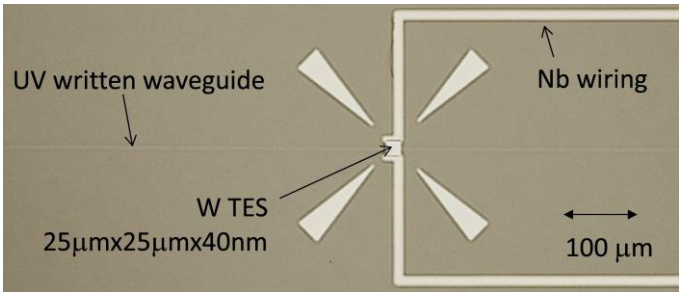


Figure 1. A micrograph of the fabricated TES on top of a UV-written silica waveguide structure.

efficiency without limiting the detector's spectral bandwidth.

The high real and imaginary refractive index of tungsten results in a large polarization dependent absorption while reducing scatter into other modes. The absorption coefficients for the TE and TM modes were measured to be 3 ± 2 cm^{-1} and 55 ± 2.4 cm^{-1} which is in good agreement with our predicted modelled values of 2.3 cm^{-1} and 54.6 cm^{-1}.

The waveguide structure used in this work was fabricated via direct UV writing, where illumination locally increases the refractive index of the silica core layer. The silica core was deposited by flame hydrolysis deposition and contained germanium and boron to induce photosensitivity [2]. The substrate was silicon with a 17 µm thermal oxide layer which acted as the underclad. An over cladding was not fabricated in order to maximize the evanescent coupling to the TES. The planar core/cladding layer refractive index contrast was 0.6% with a core layer thickness of 5.5 µm. The UV written channel was Gaussian in profile with a contrast of 0.3% and a width of ~ 5 µm. A usually minor, but in this case a key feature of the waveguide is the low surface roughness of the planar waveguide structure, which is typically less than 1 nm (R_a). This allows deposition of the TES with only a thin layer of amorphous silicon underneath to relieve the thermal stress at cryogenic temperatures. This deposition process is equivalent to the process used for fibre-coupled TES used in earlier studies [3]. To fabricate the TES detector, a 40 nm thin film of tungsten was DC sputtered onto a thin layer of amorphous silicon. The tungsten layer was patterned and etched such that a 25 µm x 25 µm pad remained directly in contact with the core layer of the silica waveguide. Wiring to the tungsten was established by use of niobium, which was sputtered and lifted off.

III. Characterisation

Optical measurements were performed in a commercial dilution refrigerator at a temperature of 12 mK to test the device and determine its detection efficiency. Pulses of a laser (f_{rep} = 35 kHz, λ = 1550 nm), attenuated to the single-photon level, were delivered to the device via commercial telecom optical fibers (SMF-28). Both ends of the waveguide chip were pigtailed to provide coupling loss information. The detector was voltage biased within its superconducting transition region, and the electrical output was fed into a dc-superconducting quantum interference device (SQUID) circuit. The SQUID output is then amplified at room temperature, and the signal is measured with data acquisition electronics. Full details of the measurement technique can be found elsewhere [1].

Figure 2 shows the experimental results when detecting a coherent state with mean photon number of 0.986. The main plot shows the pulse-peak histogram when light with TM polarization is coupled into the device and illustrates the photon resolving ability of the detector. The TM data shows pulses with up to 5 photons just resolvable. The insert data shows a similar plot for the TE polarization. When measuring along both possible propagation directions we find a total system detection efficiency of 2.9 ± 0.2 % and 3.5 ± 0.2 %. Using this data the TES detection efficiency and insertion loss can be calculated using the known total device transmission and the total system detection efficiency. We found a TES detection efficiency of 7.2 ± 0.5 % and a fiber-pigtail-waveguide transmission of 39.8 ± 4.6 % and 47.9 ± 5.2 % for both propagation directions, respectively. We observe a reduction in the coupling efficiency from the room temperature state and is thought to be a consequence of the thermal contraction of the adhesive used to connect the launch fibre assembly to the chip. The detection efficiency of these devices can be improved by elongating the detector along the waveguide structure to increase the absorption length. In addition, multiplexing several TESs and modifying the waveguide core thickness will further increase the system's performance.

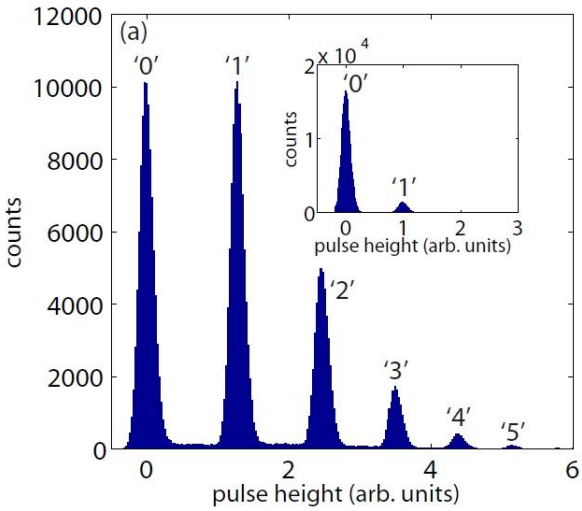


Figure 2. Photon pulse height distribution for a measured coherent state with mean photon number of 0.986. The inset shows the photon pulse height distribution for the anti-optimal TE polarization.

IV. Conclusions

Here we have presented the concept of an evanescently coupled photon-counting detector and demonstrated the first implementation of an on-chip, truly photon number resolving detector. We shall discuss the fabrication and design of the devices in more depth, direct measurement of the absorption of the tungsten layer and considerations when working at extreme cryogenic temperatures.

References

[1] T.Gerrits, N.Thomas-Peter, J.C.Gates, A.E.Lita, B.J.Metcalf, B.Calkins, N.A.Tomlin, A.E.Fox, A.L.Linares, J.B.Spring, N.K.Langford, R.P.Mirin, P.G.R.Smith, I.A.Walmsley, S.Woo Nam "On-chip photon-number-resolving telecommunication-band detectors for scalable photonic information processing" Physical Review A 84(6), 2011, pp.060301

[2] M Svalgaard, C V Poulsen, A Bjarklev, O Poulsen "Direct UV writing of buried singlemode channel waveguides in Ge-doped silica films" Electronics Letters 30 (17) (1994) p. 1401

[3] A. E. Lita, A. J. Miller, and S. W. Nam, "Counting near-infrared single-photons with 95% efficiency," Optics Express 16, 2008, 3032-3040

Analysis of homogeneous sensitivity of rib-waveguides for Mach-Zehnder interferometer

Susan Lindecrantz
Department of Physics and Technology
University of Tromsø
Tromsø, Norway
susan.lindecrantz@uit.no

Olav Gaute Hellesø
Department of Physics and Technology
University of Tromsø
Tromsø, Norway
olav.gaute.helleso@uit.no

***Abstract*— The Mach-Zehnder interferometer has successfully been employed for biosensing with a minimum detectable change of about 10^{-7} in the refractive index. In this paper we use numerical simulations to study the influence of waveguide parameters on the sensitivity. The waveguides considered are rib waveguides made of Si_3N_4, with a sensitive layer of doped PDMS for gas sensing. The sensitivity is found to be strongly dependent on the core thickness relative to the wavelength, and to some extent on the polarization. Maximum sensitivity is obtained for a core thickness of 120 nm for TM-polarized light of wavelength 780 nm and 100 nm for TM-polarized light of wavelength 632.8 nm. The sensitivity does not depend significantly on the height of the ribs or on their width, for the shallow ribs considered (0.5 to 5 nm height).**

Keywords-component; rib waveguide; homogeneous sensitivity; Mach-Zehnder interferomter.

I. INTRODUCTION

We present a study of sensitivity for the development of a waveguide gas sensor. As light propagates in a waveguide, the evanescent field interacts with the cover medium. A change in the refractive index of the cover medium therefore influences the effective refractive index of the guided mode. To make a gas sensor, the refractive index of the cover medium (the sensitive layer) must change when it is exposed to gas. By depositing the sensitive layer on one of the branches of a waveguide Mach-Zehnder interferometer (MZI), changes in the effective index of the mode can be measured and thus indirectly the gas concentration.

The Mach-Zehnder interferometer has previously been used for environmental sensing [1] and biosensing [2]. Two important features are required for the Mach-Zehnder interferometer: single mode behavior and high sensitivity. In this work we present a study of the mode behavior for three different sensitive layers: water (n = 1.33), silica (n = 1.46) and doped PolyDiMethylSiloxane (PDMS, n = 1.412). Doped PDMS will be used as the sensitive layer for gas detection. We will show how the geometrical parameters of a rib waveguide influence the sensitivity of the Mach-Zehnder interferometer. As the sensitive layer will be thicker than the evanescent field, we are restricting the analysis to a homogeneous change in the refractive index of the sensitive layer.

II. MODE BEHAVIOUR

The waveguide considered for this MZI design has a waveguide core of Si_3N_4 (n_c = 2.00) with variable thickness, on top of a silica layer (2 µm thick, n_s = 1.46). The rib height is a few nanometers (see Fig. 1), while the rib width is a few micrometers. For the mode analysis, a 2D simulation is made with the Finite Element Method, using Comsol Multiphysics. Fig. 2 shows the mode behaviors for different rib widths and rib heights, for a core thickness of 150 nm, wavelength of 632.8 nm and TE-polarization.

The simulations show that the waveguide is single mode for rib widths less than 3 µm for rib heights around 5 nm. For even more shallow ribs, the waveguide can be single mode up to 5 µm width. These very shallow ribs will not guide light unless they are several micrometers wide. The effective index of the waveguide changes little with the rib width and the rib height, while it is strongly dependent on the core thickness (not shown).

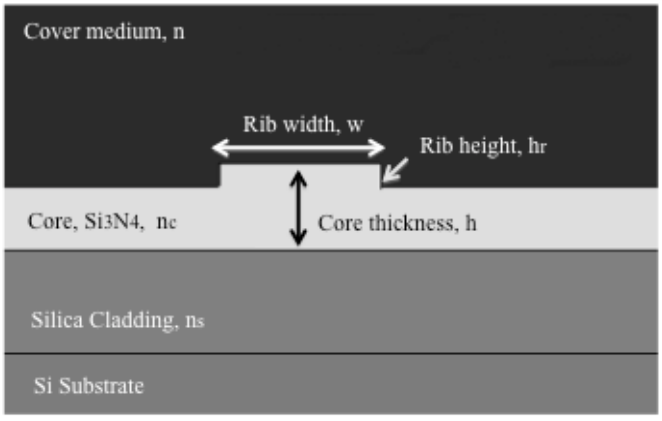


Figure 1. Cross-section of the waveguide, with the different parameters used for the 2D mode analysis.

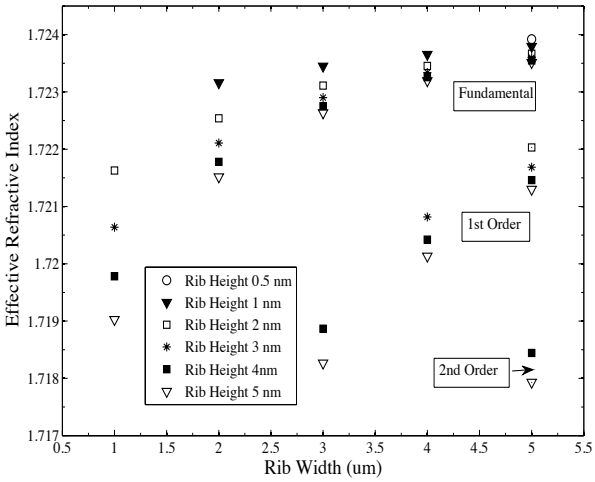


Figure 2. The effective index of the modes of the rib waveguide, versus rib width for six rib heights. The cover medium is doped PDMS (n = 1.412). Core thickness is 150 nm thick, guided by TE-polarized light of wavelength 632.8 nm. The figure shows up to three modes, depening on width and rib height.

III. HOMOGENEOUS SENSITIVITY

The homogeneous sensitivity is defined as the rate of change the effective refractive index of the guided mode, to the rate of change of the refractive index of the cover medium. The homogeneous sensitivity can be expressed as [3,4]:

$$\frac{dN}{dn} = \frac{n}{N}\left[2\left(\frac{N}{n}\right)^2 - 1\right]^{\rho} \cdot \frac{P_o}{P_T} \qquad (1)$$

where n is the cover medium refractive index, N is the effective refractive index of the guided mode in the waveguide, P_o is the power of the guided mode in the cover medium, and P_T is the total power of the guided mode. Here ρ is equal to zero for TE modes and one for TM modes. We have used simulations with the RF module of COMSOL Multiphysics to determine the parameters in (1) for various rib parameters, and used (1) to find the corresponding sensitivity.

Fig. 3 shows the calculated homogeneous sensitivity as function of the core thickness for a waveguide of 1 μm width and 5 nm height and for two wavelengths, 632.8 nm and 780 nm. The analysis shows that the sensitivity is very dependent on the core thickness and to some degree on the polarization of the guided light. The homogeneous sensitivity increases as the core thickness decreases, due to less confinement in the guided core, which implies more power in the cover medium. For even less core thickness, the sensitivity decreases as the mode approaches cut-off. In general, for TE-polarization maximum sensitivity is obtained with a thinner waveguide than for TM-polarization. The maximum sensitivity is highest for TM-polarization. Changing the wavelength merely gives a shift of the curves, as expected.

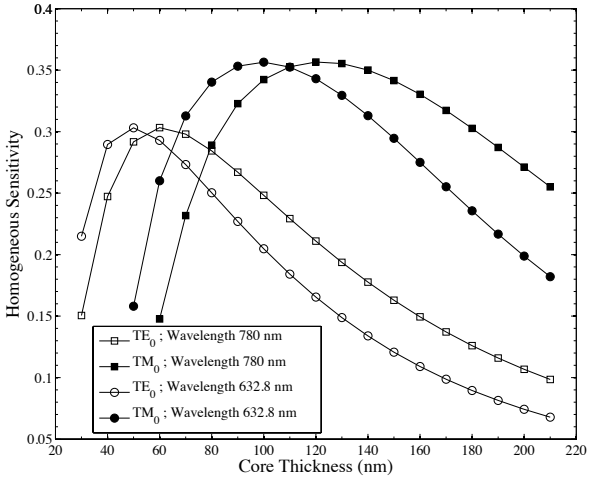


Figure 3. The homogeneous sensitivity as function of core thickness for a cover layer of PDMS (n = 1.412) for a rib waveguide of 1 μm width and 5 nm height. The waveguide were single mode for this rib width.

We have also found that the sensitivity does not vary much as function of the rib width and rib height (not shown). This can be expected from the small change in effective index relative to these parameters in Fig. 1.

In conclusion, the main factors for the sensitivity are the core thickness relative to the wavelength of light, the polarization of the light and the refractive index of the core and cover medium.

IV. FURTHER WORK

We would like to include losses due to sidewall and surface roughness in the numerical simulations.

ACKNOWLEDGMENT

This work is funded by the Research Council of Norway (Nordsatsing).

REFERENCES

[1] Albrecht Brandenburg, Rainer Edelhäuser and Frank Hutter, "Integrated optical gas sensor using organically modified silicates as sensitive films," Sensors Actuators B, vol 11, pp. 361-374, August 2008.

[2] B. Sepúlveda, J. Sánchez del Río, M Moreno, F. J. Blanco, K. Mayora, C. Domínguez and L. M. Lechuga, "Optical biosensor microsystems based on the integration of highly sensitive Mach-Zehnder interferometer devices, " J. Opt. A: Pure Appl. Opt., vol 8, pp. 561-566, June 2006.

[3] K. Tiefenthaler and W. Lujosz, "Sensitivity og grating couplers as integrated-optical chemical sensors," J. Opt. Soc. Amer. B, vol 6, pp. 209-220, October 1989.

[4] F. Prieto, A. Llobera, D. Jiménez, C. Doménguez, A. Calle and L. M. Lechuga, "Design and Analysis of Silicon Antiresonant Refelcting Optical waveguide for Evanescent Field Sensor, " Journal of lightwave technology, vol. 18, no. 7, July 2000.

Towards system-level modeling of large-scale active photonic integrated circuits

Recent advances and remaining challenges

Sergei Mingaleev and Eugene Sokolov
VPI Development Center, Chapaeva str. 5,
220034 Minsk, Belarus
Email: sergei.mingaleev@vpisystems.com

Cristina Arellano, Igor Koltchanov, and André Richter
VPIsystems, Carnotstr. 6,
10587 Berlin, Germany

***Abstract* — Recent advances in the fabrication of large-scale monolithic photonic integrated circuits (PICs) which embed different types of active photonic components require the development of appropriate simulation tools. Specifically, such tools should be fast and accurate in modeling both, passive and active photonic components. This enforces the usage of the system-level simulation approaches, which allow modeling of each individual photonic component with a specific (most suitable) numerical method. Another important requirement is that the simulation speed at the desired simulation accuracy should grow reasonably slowly with the total number of photonic components in the modeled PIC, even when this number is in the order of several thousands (practically achievable in few years). We show that this demand can be satisfied only when the system-level simulation tool mixes within a single simulation both, time-domain and frequency-domain approaches for the description of interconnections between different PIC components. We present our implementation of the suggested time-and-frequency-domain modeling (TFDM) approach in the framework of the simulation tool VPIcomponentMaker™ Photonic Circuits, and discuss its scalability to large-scale active PICs and remaining challenges.**

Large-Scale Photonic Circuits, Integrated Photonics, Time-and-Frequency-Domain Modeling, PIC, TFDM

During the last decade, photonic integrated circuits (PICs) exhibit an exponential increase in complexity, resembling Moore's law in micro-electronics. Specifically, the number of photonic components integrated on a single chip exceeded three hundreds in 2010, and is expected to double every 2.5 years [1]. Note that the current level of integration has been reached by micro-electronics by 1968 – during the infancy of the first electronic circuit analysis programs. Remarkably, now those times are recaptured once again, and we are living in the beginnings of commercially available photonic circuit simulators [2-4].

Importantly, the complexity of simulation techniques that should be used in photonic circuit simulators is greatly superior to those employed in electronic circuit simulators. This complexity is determined by several factors: large diversity of photonic components, broad frequency ranges of optical signals that require usage of advanced signal representations [5], presence of very different time scales, etc. To properly handle such a complexity, modern photonic circuit simulators [2-4] are based on segmentation of the modeled PIC into building blocks ("PIC elements"). Each PIC element is a photonic device that is coupled to other PIC elements only via guided modes of channel optical waveguides – the so-called "ports". Because of this, each PIC element can be considered as "black box" that produces outgoing waves carried by guided modes of the device ports from the corresponding incoming waves. This allows to separate system-level modeling of PICs from device-level modeling of PIC elements.

The device-level modeling can be performed either using traditional photonic simulators, or employing analytical and behavioral models of PIC elements. Importantly, different PIC elements in the same circuit can be modeled by different methods, thus allowing initial rapid prototyping of the circuit and subsequent gradual improving of the simulation accuracy. Development of such a modeling looks sufficiently straightforward and thus shall not be discussed here. In contrast, system-level modeling of PICs presents a real challenge as soon as the modeled PIC includes active or dynamically tunable components, and the total number of PIC elements exceeds several tens.

More specifically, until recently only two approaches to the system-level modeling of PICs have been used. Passive PICs, consisting of linear PIC elements only, could be efficiently modeled in frequency domain [2,4]. In this case, each PIC element is completely described by a frequency-dependent scattering matrix (S-matrix) that relates amplitudes of incoming and outgoing guided modes at all device ports. Employing the S-matrix assembly technique [4], one can calculate S-matrices of any compound passive devices. This approach allows fast and highly precise analysis of passive PICs, and scales nicely with the growing number of linear PIC elements. However, all these advantages fade away as soon as the modeled photonic circuit includes at least one non-passive PIC element.

Within the alternative time-domain modeling (TDM) approach [3,4], all the PIC elements that comprise the modeled PIC are modeled in time domain – including each of the linear PIC elements. Commonly, such a TDM of linear PIC elements is implemented using digital FIR filters designed on the basis of the device S-matrices. And although the accuracy provided

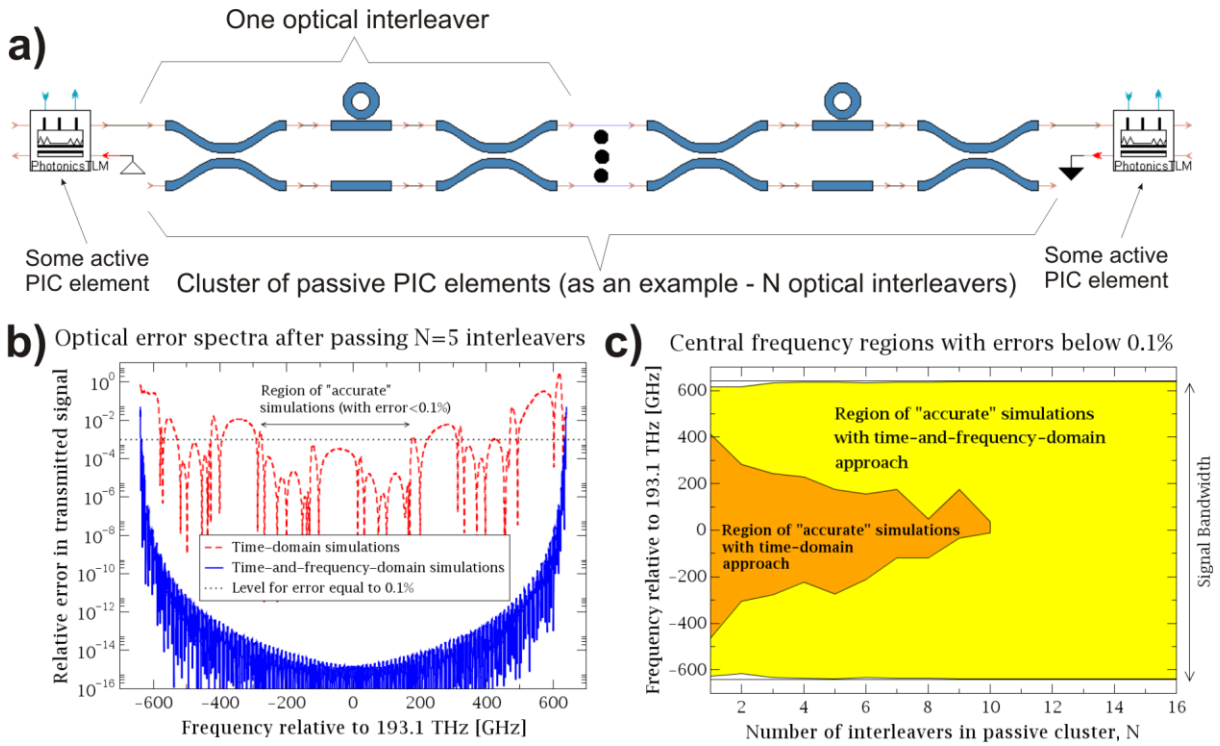


Figure 1. Comparison of the accuracy of pure time-domain modeling (TDM) and time-and-frequency-domain modeling (TFDM) approaches, on the example of modeling cascaded optical interleavers. Important: the time step and overall signal duration remained unchanged in all these simulations.

by FIR filters substantially depends on the quality of the employed FIR design methods, it inherently degrades near the edges of the simulated signal bands (see example in Fig. 1b), even for the best designed FIR filters. In practice, such inaccuracy is not very important for modeling PICs with only several linear PIC elements. However, as we illustrate in Fig. 1c, due to multiplicative effects, the net bandwidth where simulation results remain accurate rapidly decreases and then collapses as the number of PIC elements in the simulated PIC increases. This problem becomes a real toughie in the presence of short-length PIC elements (for example, small micro-rings) since their short impulse responses require smaller time steps for accurate modeling and increased computation effort. Any inaccuracies are further magnified by feedback loops, which are always present in large-scale PICs. For keeping a prerequisite simulation bandwidth, all this enforces to use smaller and smaller time steps as the complexity of the modeled PIC grows, thus precluding scalability of the described TDM approach and making it impractical as the number of PIC elements exceeds several tens.

To overcome aforementioned limitations, we developed [4] a hybrid time-and-frequency-domain modeling (TFDM) technique. Within this approach, the topology of the modeled PIC is first analyzed, and clusters of interconnected passive PIC elements are identified. For each of these clusters, all S-matrices of their individual PIC elements are recursively assembled into a single S-matrix that describes the properties of the cluster as a whole. Finally, FIR filters are designed for each of these clusters, and the usual time-domain approach is employed for modeling properties of the whole PIC including its non-passive components. As we illustrate in Fig. 1 on the example of cascaded optical interleavers surrounded by active PIC elements, such an approach allows to greatly improve accuracy of time-domain simulations keeping the same time step and signal duration. Importantly, the choice of time step in TFDM approach is determined by the needs of modeling active PIC elements, in contrast to TDM approach, where it was rather limited by inaccuracies in modeling passive PIC elements.

We will present further advances in our implementation of the TFDM approach in VPIcomponentMaker™ Photonic Circuits, and shall discuss its scalability and performance in application to large-scale active PICs.

References

[1] M.K. Smit, "Moore's law in photonics", Plenary talk at ECIO, Cambridge, UK, 7-9 April 2010.

[2] A. Melloni et al., "Design Kits and Circuit Simulation in Integrated Optics", in Integrated Photonics Research, Silicon and Nanophotonics, paper JTuB24, July 2010. See also: ASPIC, http://www.aspicdesign.com

[3] D.F.G. Gallagher, "Modelling photonic integrated circuits using TDTW", in Optical Fiber Communication Conference, October 2008. See also: PICWave, http://www.photond.com/products/picwave.htm

[4] S.F. Mingaleev, E. Sokolov, C. Arellano, I. Koltchanov, and A. Richter, "Hybrid time-and-frequency-domain approach for modeling photonic integrated circuits", NUSOD, paper ThA4, September 2011; "Time-and-Frequency-Domain Modeling (TFDM) of hybrid photonic integrated circuits", SPIE Photonics West, paper 8265-19, January 2012; See also: VPIcomponentMaker™ Photonic Circuits, http://vpiphotonics.com/CMPhotonicCircuits.php

[5] A. Lowery et al., "Multiple signal representation simulation of photonic devices, systems and networks", IEEE J. Select. Topics Quantum Electron., vol. 6, pp. 282-296, 2000.

Grated Waveguide Optical Cavity for Sensing

S.V. Pham, M. Dijkstra, A.J.F. Hollink, R.M. de Ridder, G.J.M. Krijnen, P.V. Lambeck, M. Pollnau, and H.J.W.M. Hoekstra

Integrated Optical MicroSystems (IOMS) Group, MESA$^+$ Institute for Nanotechnology, University of Twente
P.O. Box 217, 7500 AE Enschede, The Netherlands

***Abstract*—We demonstrate the versatility of a silicon nitride grated waveguide optical cavity as compact integrated optical sensors for (bulk) concentration detection, label-free protein sensing, and – with an integrated cantilever suspended above it – gas sensing.**

Keywords-integrated optics, sensing, waveguide, grating

I. INTRODUCTION

A grated waveguide (GWG), which is a waveguide with a finite-length grated section, acts as an optical resonator, showing sharp fringes in the transmission spectrum near the stop-band edges of the grating. These oscillations are due to Fabry-Perot resonances of Bloch modes propagating in the cavity defined by the grated section [1]. Any small structural changes in the environment of the GWG, which disturb the evanescent field of the GWG resonant modes, will lead to a shift of its transmission spectrum. Such an effect can be exploited for sensing applications, such as the detection of a bulk refractive index change [2] or nano-displacements of a cantilever suspended above the GWG [3]. Here we present 3 applications: (1) a concentration sensor, based on the bulk index change of the GWG top cladding; (2) label-free protein sensing (PepN enzyme), where the spectral shift of the GWG response is due to the antibody-antigen interaction, leading to growth of an ad-layer on it; and (3) gas sensing, where the GWG detects stress-induced deflections of a doubly-clamped micro-cantilever (micro-bridge) with a 50 nm thick Pd top layer due to H_2 gas absorption by the Pd receptor layer.

II. FABRICATION AND EXPERIMENTS

The Si_3N_4 grated waveguides were fabricated using laser interference lithography. The integrated GWG-cantilever devices have been fabricated successfully using MEMS techniques. Details of the fabrication process were described in [3]. The GWG setup for the (bulk) concentration and label-free protein sensing experiments is shown in Fig. 1a, while the 3D schematic structure of the GWG-cantilever device for gas sensing is shown in Fig. 2a.

To demonstrate (1) concentration sensing, we filled a chamber (cuvette) on the surface of the sensor with a phosphate buffered saline solution of 1 wt% (PBS1x). The evaporation of water from the open cuvette leads to a continuous change of concentration, and hence of the bulk index, which can be deduced from the measured spectral shift of the sensor.

To detect a target biomaterial (2), such as PepN enzyme in this case, its antibody needs to be immobilized on the surface of the GWG device. We followed the standard immobilization process developed by Imenz b.v. [4]. Once the antibody was immobilized on the GWG surface, the cell-free extracted solution, containing the target PepN enzyme and other proteins, was applied and the antibody-antigen interaction was optically monitored through the GWG transmission spectra.

For H_2 gas sensing (3), instead of singly-clamped cantilevers as mentioned in [3], we fabricated devices with a doubly-clamped cantilever and with an aimed gap of g = 200 nm. Initial bending of the cantilever was characterized using a white-light interferometer. The PDMS chamber placed on top of the device was connected with gas bottles (i.e., N_2 and 1% H_2-N_2 mixture) through mass flow controllers. The optical performance of the integrated device was monitored using a tunable laser source with a repeatability of 0.3 pm.

III. RESULTS AND DISCUSSION

A. Bulk concentration sensing

The measured spectral shift of the concentration sensor is shown in Fig. 1b. The results show that changes of the refractive index down to 2×10^{-5} RIU (refractive index unit), and concentration changes down to 0.01 wt% can be resolved.

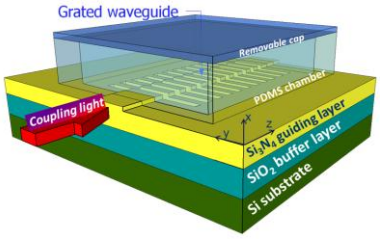
B. Label-free protein sensing

Small changes on the GWG surface, caused by the antibody-enzyme interaction, lead to spectral shifts of the resonant peak, as shown in Fig. 1c. The reaction saturates after ~35 minutes. The total shift was approximately 342 pm, corresponding to the growth of an ad-layer of ~2 nm; the limit of detection for ad-layer growth is around 4 pm.

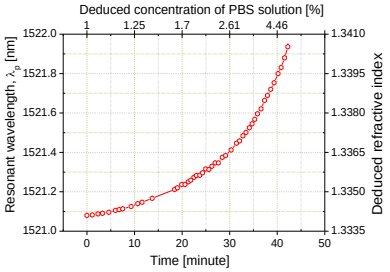
C. Mechano-optical hydrogen gas sensing

Using a white-light interferometer, an initial bending (upwards, i.e., away from the GWG structure) of the micro-bridge of approximately 500 nm was found. This initial bending, which leads to a lower sensitivity at low H_2 concentrations (owing to the relatively large gap of g ~ 700 nm), is due to the difference between residual stresses in the SiO_2 base layer and the Pd receptor film [3].

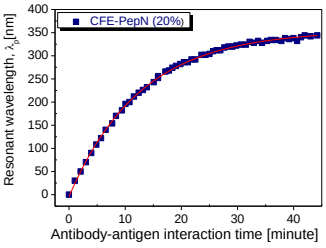
Prior to supplying H_2 gas to the chamber, N_2 gas was flushed in during 15 min with a flow rate of 0.5 sccm and optical transmission curves were captured every minute. The results showed a stable and reproducible resonant peak at



(a)



(b)



(c)

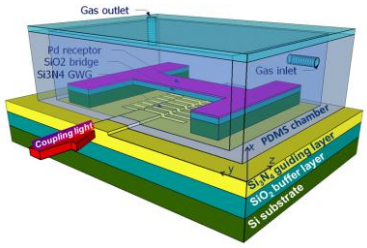
Figure 1. 3D schematic of the Si_3N_4 grated waveguide (GWG) device with a PDMS chamber serving as an open cuvette for bulk concentration sensing and a closed environment for accurate monitoring of the antibody-enzyme interaction **(a)** and performance of devices for **(b)** measurement of PBS concentration, **(c)** label-free protein sensing

λ_p = 1496.631 ± 10^{-3} nm, indicating that such a flow rate did not cause any side effects or mechano-optical vibrations.

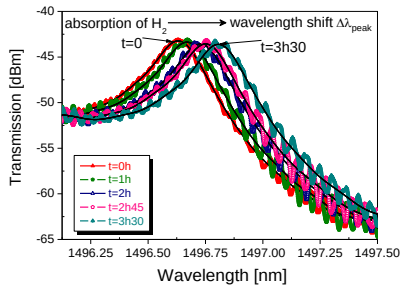
Next we supplied the H_2(1%)-N_2 mixture (flow rate 0.5 sccm) for a longer period of time, during which the transmission spectrum was monitored (see Fig. 2b). The shift $\Delta\lambda_p$ depends almost linearly on time (see Fig. 2c left-hand side), which can be explained partly by noting that the effect of the initially rapid change of the gap size, g, is compensated by lower values of $\partial\lambda_p/\partial g$ at larger gap size. After 3.5 hours the flow of the H_2 (1%)-N_2 mixture was switched off and replaced again by a pure N_2 inflow, leading to desorption. Figure 2c (right-hand side) shows the peak shifts during a four-hour long period of the desorption process.
The result provides a proof of concept of a novel and compact integrated mechano-optical sensor. This result gives us a strong confidence in the feasibility of this type of sensor.

IV. Conclusions

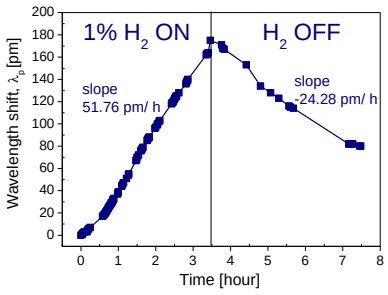
We have demonstrated the great potential of a Si_3N_4 grated waveguide optical cavity as compact integrated optical sensors for concentration detection, label-free protein sensing, and gas sensing. Concentration changes ~0.01 wt%, corresponding to $2x10^{-5}$ RIU, can be resolved. The enzyme is selectively recognized by its corresponding antibody immobilized on the surface of the sensor, and monitored in real-time. Owing to its simple fabrication and effective operation the sensor has potential as an element of a sensitive, on-chip multi-sensing system for label-free detection of a variety of bio-molecules. Hydrogen sensing with a novel and compact integrated optical



(a)



(b)



(c)

Figure 2. 3D schematic of the structure with a PDMS chamber as a reaction environment for H_2 sensing **(a)**, transmission curves of the device in response to the absorption **(b)**, and the wavelength shift versus the reaction time **(c)**.

read-out scheme is demonstrated as a proof of concept for our proposed and successfully fabricated mechano-optical sensor. This new sensor type possesses a great potential as an element for a sensitive and on-chip multi-sensing system, provided that the gap between the GWG and the micro-bridge can be well controlled during fabrication.

Acknowledgments

This research is supported by MEMSland, a project funded by the Dutch Ministry of Economic Affairs and the STW Technology Foundation through project TOE. 6596. We thank the company Imenz b.v. for supplying bio-materials.

References

[1] G.J. Veldhuis, J.H. Berends, R.G. Heideman and P.V. Lambeck, "An integrated optical Bragg-reflector used as a chemo-optical sensor," Pure and Applied Optics, vol. 7: pp. L23-L26, 1998.
[2] W.C.L. Hopman, H.J.W.M. Hoekstra, R. Dekker, L. Zhuang, and R.M. de Ridder, "Far-field scattering microscopy applied to analysis of slow light, power enhancement, and delay times in uniform Bragg waveguide gratings," Opt. Express, **15**(4): pp. 1851-1870, 2007.
[3] S.V. Pham *et al.*, "Read-out of cantilever bending with a grated waveguide optical cavity," Photon. Technol. Lett., IEEE , vol.23, no.4, pp.215-217, 2011
[4] IMEnz Bioengineering BV, LJ Zielstraweg 1 9713 GX Groningen The Netherlands, (http://www.imenz.com/).
[5] L.J. Kauppinen, M. Dijkstra, H.J.W.M. Hoekstra, and R.M. de Ridder, "Label-free Enzyme Sensing with Grated Silicon Photonic Wire," in Proc. Annual Symp. IEEE Photon. Benelux Chapter, (Brussels, 2009), pp. 41-44.

Thulium channel waveguide laser with 70% slope efficiency in a monoclinic double tungstate

K. van Dalfsen, S. Aravazhi, S. M. García-Blanco, and M. Pollnau
Integrated Optics and MicroSystems (IOMS) group
MESA+ Institute for Nanotechnology, University of Twente
Enschede, The Netherlands
k.vandalfsen@utwente.nl

C. Grivas
School of Physics and Astronomy
University of Southampton
Southampton, United Kingdom

***Abstract*—Laser experiments on 1.5at.%, 5at.%, and 8at.% thulium-gadolinium-lutetium-yttrium co-doped, buried, ridge-type channel waveguides in a monoclinic potassium double tungstate demonstrate a maximum slope efficiency of 70% and output powers of 300 mW at ~1.9 µm.**

Keywords-component; thulium; monoclinic double tungstates; channel waveguide; infrared lasers

I. INTRODUCTION

Optical sensors for real-time monitoring of gases for environmental, industrial and medical purposes are being widely investigated. For the detection of CO_2 and NH_3 in human breath, a high-power and compact channel waveguide laser, operating in the 2-µm wavelength region is desirable.

Since the emission spectrum of thulium overlaps with the 2-µm wavelength region, thulium is a suitable candidate for detection of gases in this wavelength region. In addition, the availability of inexpensive diode lasers emitting at 800 nm to optically pump the thulium system facilitates the development of these detectors. When pumped at 800 nm, the efficiency of a thulium laser hinges on the efficiency of a nonlinear cross-relaxation (CR) process, where one ion occupying the $3H_4$ manifold transfers part of its energy to an adjacent ion in the $3H_6$ ground manifold, resulting in both ions occupying the $3F_4$ laser manifold. Since, in this way, a pump photon is converted to a maximum of two laser photons, a maximum quantum efficiency of η_q of up to 2 can be obtained. The theoretical maximum slope efficiency for a thulium laser, calculated by multiplying the Stokes efficiency of λ_P / λ_L = 0.8 µm / 2 µm = 40% by the maximum quantum efficiency of of $\eta_q = 2$, reaches 80%. The CR efficiency is dependent on the relative population densities of the $^3H_4$ and $^3H_6$ manifold, influenced by the pump and laser intensities, as well as the thulium concentration.

The highest efficiencies for thulium lasers reported in the literature are 68% from a planar YAG laser [1], and 69% from germanate fiber and bulk $KLu(WO_4)_2$ monoclinic double tungstate lasers [2,3]. In channel waveguide lasers, the highest reported slope efficiency is 50% in a ZBLAN glass with femtosecond-written channels [4].

In this paper we demonstrate that the inferior slope efficiencies for channel waveguide lasers in monoclinic double tungstates originates in the relatively low dopant concentrations, which consequently negatively influences the CR efficiency. We compare the slope efficiencies for thulium concentrations of 1.5at.% [5], 5at.% and 8at.% and present a compact channel waveguide laser in an Y^{3+}, Gd^{3+}, Lu^{3+} co-doped potassium double tungstate yielding output powers up to 300 mW and a maximum slope efficiency of 70% [6], which is close to the theoretical maximum of 80%.

II. SAMPLE FABRICATION AND EXPERIMENTAL METHODS

Co-doped layers of $KY_xGd_yLu_{1-x-y-z}Tm_z(WO_4)_2$ with x = 40at.%, and z = 1.5at.%, 5at.% and 8at.%, were grown onto pure $KY(WO_4)_2$ substrates by liquid-phase epitaxy at 920−923°C [7]. Ridge-type channel waveguides 10−25 µm wide and 7.7 µm and 14.3 µm high, for the 5at.% and 8at.% concentrations, respectively, were patterned into surface-polished planar waveguides by Ar^+-beam milling [8]. Afterwards, the channels were overgrown with a pure $KY(WO_4)_2$ cladding layer. The 1.5at.%, 5at.% and 8at.%-doped channels were diced and end-face polished to a length of 8.5, 6.7 mm and 4.2 mm, respectively.

The channels waveguides were pumped by a Ti:Sapphire continuous-wave laser at wavelengths of 794 nm in transverse-magnetic (TM, E||N_p), and 802 nm in transverse-electric (TE, E||N_m) polarizations. In-coupling of pump light into the waveguides was optimized using a beam expander and cylindrical lenses with focal lengths of 40 mm and 10 mm, for the horizontal and vertical directions, respectively, thereby obtaining a coupling efficiency of 95%. Commercially obtained dielectric mirrors with a reflectivity of R = 99.9% (HR), 98%, and 92% at 1900–2100 nm and high transmission at the pump wavelength of 790–810 nm (due to an anti-reflection coating at this wavelength) were butt-coupled to the end-facets of the waveguides using index-matching oil (Fluorinert). Round-trip out-coupling efficiencies $T_{out} = 1 - R_1R_2$ of 2%, 8%, 89%, and 99% were tested with mirror combinations of R_1 and R_2 equaling HR and 98%, HR and 92%, HR and 11%, and 2 × 11%, respectively. In the latter two configurations, Fresnel reflection of ~11% at one or both bare

waveguide end-facets provided sufficient feedback for the laser. Losses of 11% for the pump light due to Fresnel reflection at the in-coupling facet were taken into account for the mirror-less laser configuration. The laser power out-coupled from the waveguides was collimated via a 0.25 NA microscope objective and a RG1000 high-pass filter was used to block any residual pump power.

III. Experimental Results

The measured laser output power versus absorbed pump power when pumping the 8at.%-doped sample at 794 nm in TM polarization and 802 nm in TE polarization is shown in Fig. 1a and 1b, respectively. For both pump polarizations an output power as high as ~300 mW was obtained. Slope efficiencies of 70%, 68%, 48%, and 31% were measured when coupling out 99%, 89%, 8%, and 2%, respectively, while pumping at 794 nm in TM polarization (Fig. 1a). When pumping at 802 nm in TE polarization, slope efficiencies of 69%, 70%, 44%, and 33% for out-coupling efficiencies of 99%, 89%, 8%, and 2%, respectively, were also measured (Fig. 1b).

The laser was found to operate at 1842 nm when high out-coupling efficiencies of 89% and 99% were used. The laser shifted via 1950 nm for 8% out-coupling, to a maximum operating wavelength of 2037 nm in case only 2% of the laser was out-coupled. The laser was found to operate on multiple longitudinal modes, but single-transverse mode.

Fig. 2. compares the maximum slope efficiency of the 8at.%-doped sample with the maximum slope efficiencies of 53% obtained in this study in the 5at.%-doped sample with the results previously reported in a 1.5at.%-doped sample [5]. A trend toward higher slope efficiencies is clearly visible with

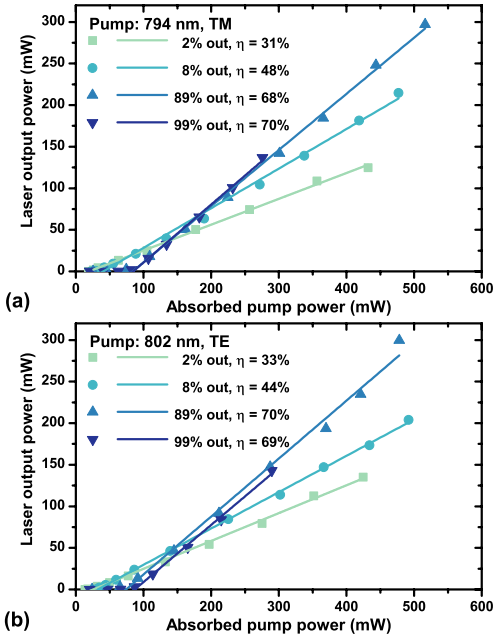


Fig. 1. Output power versus absorbed pump power of a 8at.% thulium-doped channel waveguide laser pumped at (a) 794 nm in TM polarization and (b) 802 nm in TE polarization.

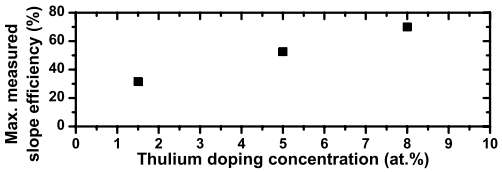


Fig. 2. Maximum measured slope efficiencies for thulium-doped monoclinic double tungstate channel waveguide lasers with different doping levels.

increasing thulium concentrations. Although the result of 70% slope efficiency is close to the theoretical maximum, a slight improvement can be expected when choosing a dopant concentration higher than 8at.%.

Conclusions

Thulium-co-doped monoclinic double tungstate layers have been micro-structured by Ar^{+}-beam milling, yielding ridge-type channels, and overgrown with a pure $KY(WO_4)_2$ cladding. Lasers operating around 2 µm with excellent slope efficiencies of up to 70% and 300 mW of output power have been demonstrated due to efficient CR resulting from the high doping concentration of 8at.%. The highest efficiency was obtained in a mirror-less laser. Operation of the laser was demonstrated between 1842 nm and 2037 nm. The authors believe that the demonstrated laser is the most efficient thulium channel waveguide laser reported to date, and comparable to the best results in other thulium laser configurations.

Acknowledgment

This work was financially supported by the Dutch funcing agencies Senter-Novem and STW through the IOP Photonic Devices project PD-55.

References

[1] A. Rameix, C. Borel, B. Chambaz, B. Ferrand, D. P. Shepherd, T. J. Warburton, D. C. Hanna, and A. C. Tropper, "An efficient, diode-pumped, 2-µm Tm:YAG waveguide laser," Opt. Commun. vol. 142, pp. 239–243, October 1997.

[2] J. Wu, Z. Yao, J. Zong, and S. Jiang, "Highly efficient high-power thulium-doped germanate glass fiber laser," Opt. Lett. vol. 32, pp. 638–640, March 2007.

[3] X. Mateos, V. Petrov, J. Liu, M. C. Pujol, U. Griebner, M. Aguiló, F. Díaz, M. Galan, and G. Viera, "Efficient 2-µm continuous-wave laser oscillation of Tm^{3+}:$KLu(WO_4)_2$," IEEE J. Quantum Electron. vol. 42, pp. 1008–1015, October 2006.

[4] D. G. Lancaster, S. Gross, H. Ebendorff-Heidepriem, K. Kuan, T. M. Monro, M. Ams, A. Fuerbach, and M. J. Withford, "Fifty percent internal slope efficiency femtosecond direct-written Tm^{3+}:ZBLAN waveguide laser," Opt. Lett. vol. 36, pp. 1587–1589, May 2011.

[5] K. van Dalfsen, S. Aravazhi, D. Geskus, K. Wörhoff, and M. Pollnau, "Efficient $KY_{1-x-y}Gd_xLu_y(WO_4)_2$:$Tm^{3+}$ channel waveguide lasers," Opt. Express vol. 19, pp. 5277–5282, March 2011.

[6] K. van Dalfsen, S. Aravazhi, C. Grivas, S. M. García-Blanco, and M. Pollnau, "Thulium channel waveguide laser in a monoclinic double tungstate with 70% slope efficiency," Opt. Lett., in press.

[7] F. Gardillou, Y. E. Romanyuk, C. N. Borca, R. P. Salathé, and M. Pollnau, "Lu, Gd codoped $KY(WO_4)_2$:Yb epitaxial layers: towards integrated optics based on $KY(WO_4)_2$," Opt. Lett. vol. 32, pp. 488–490, March 2007.

[8] D. Geskus, S. Aravazhi, C. Grivas, K. Wörhoff, and M. Pollnau, "Microstructured $KY(WO_4)_2$:Gd^{3+},Lu^{3+},Yb^{3+} channel waveguide laser," Opt. Express vol. 18, pp. 8853–8858, April 2010.

Backscattering Effects In Silicon Ring Resonators

G. C. Ballesteros, J. Matres, J. Martí, and C. J. Oton
Nanophotonics Technology Center,
Universidad Politécnica de Valencia, Camino de Vera s/n, 46022, Valencia, Spain
E-mail: guibalga@ntc.upv.es

***Abstract*—Backscattering can dramatically modify the response of ring resonators and be the limiting parameter of the Q-factor. We present evidence of backscattering, a model, and a fitting procedure that provides a complete characterization of the resonance.**

***Keywords*—resonators; backscattering;**

I. Introduction

Microring resonators are simple to fabricate and used for devices such as optical filters, sensors, modulators etc. A high quality factor is usually the key parameter that determines the performance of the device; however, in this technology what limits its highest possible values is in most cases not the propagation loss, but the backscattering effect due to sidewall roughness [1]. Backscattering in a resonator cannot be accounted for as a loss mechanism because in a cavity it can grow coherently much faster than losses. Backscattering is a well known cause of resonance splitting [2]; but even before splitting occurs, it can dramatically modify the shape of the resonance. If this effect is not taken into account and one extracts the parameters of the ring from a fit, it can produce a good curve agreement but with very wrong results. In this work, we propose a characterization technique and a fitting procedure that allows a complete characterization of all the parameters of the ring including backscattering, without the need of a coherent backscattering measuring system as in [1] and [3].

II. Experiment

The waveguides used are fully-etched 220×450nm channels, covered with a 2μm SiO2 layer. Waveguides were patterned with deep-UV lithography (using EPIXfab facilities). Transverse-electric (TE) polarization was used in all the experiments. The rings had a 20μm radius and two coupling points, providing a *through* and a *drop* port. However, in this experiment we also collect the counter-propagating drop port, which we will call *counter-drop* port. Measuring this port is crucial to fully characterize the ring, as it directly provides the information about the backscattering inside the cavity. The gap of the through and drop couplers was 275nm and 300nm respectively.

Figure 1 shows the measured transmission through all three ports of one microring. It is worth noting that the shape of the resonances is very variable, even though one would expect the loss and the coupling coefficients to be approximately the same in all cases. The reason for this behavior is the backscattering parameter, which is intrinsically noisy, thus producing an apparently random response. It is noisy because reflections are produced by sidewall roughness along the ring, so they are randomly distributed along its length, and the overall reflection coefficient results from the interference of all the components, giving rise to sharp spectral variations. In order to extract the parameters of the ring, one must take into account backreflection, otherwise the estimation of the loss and coupling coefficients would depend on which resonance we select, which is unphysical and would produce wrong results. Therefore, a procedure to extract all the parameters including backreflection is needed in order to understand the behavior of our microring resonator.

III. Theory

Following the guidelines in [4], [5] the following expressions for the signal in the different ports shown in Fig. 1 are easily expressed in terms of quality factors as:

$$T = \left\| 1 - \frac{\frac{2}{Q_{e,1}}(2j(\omega'-1)+\frac{1}{Q})}{(2j(\omega'-1)+\frac{1}{Q})^2+\frac{1}{Q_r^2}} \right\|^2 \quad (1)$$

$$D = \left\| \frac{\frac{2}{\sqrt{Q_{e,1}Q_{e,2}}}(2j(\omega'-1)+\frac{1}{Q})}{(2j(\omega'-1)+\frac{1}{Q})^2+\frac{1}{Q_r^2}} \right\|^2 \quad (2)$$

$$C = \left\| \frac{\frac{2}{Q_r\sqrt{Q_{e,1}Q_{e,2}}}}{(2j(\omega'-1)+\frac{1}{Q})^2+\frac{1}{Q_r^2}} \right\|^2 \quad (3)$$

where ω' is the normalized angular frequency of the resonance under study, and the Q-factors are related to the τ constants of a time-domain analysis through $Q_j = \omega_o \tau_j/2$ and can be expressed as a function of the usual energy coupling and losses constants using the expression in [5] by:

$$K_j = \frac{\omega_o L}{Q_{e,j} v_g} \qquad \alpha = \frac{\omega_o}{Q_i v_g} \qquad \sqrt{R} = \frac{\omega_o L}{2 Q_r v_g} \quad (4)$$

In this expression v_g is the group velocity of the waveguide, K_1 and K_2 are the energy coupling of the input and output waveguides to the ring, α is the intrinsic losses and R is the strenght of the coupling in between the two modes. The Q values $Q_{e,1}$, $Q_{e,2}$, Q_i and Q_r correspond respectively to the extrinsic coupling with the bottom and top waveguides, the intrinsic losses and the coupling constant. Q_r has been related to the total reflectivity in a single-pass, R, that is, the fraction of energy coupled into the counter-propagating mode in one

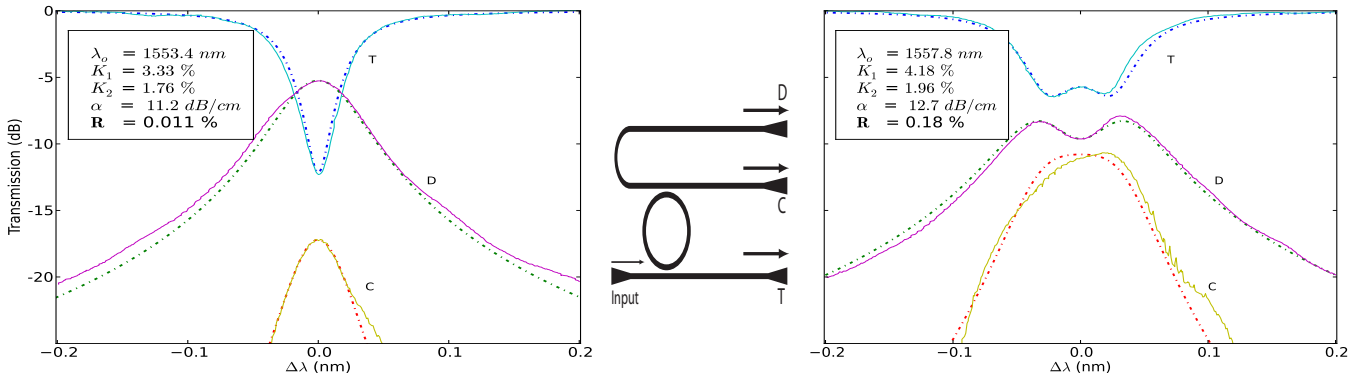


Fig. 1. Detail of 2 consecutive resonances of a ring. Transmission has been normalised. Solid lines are the experimental data and dashed lines are the analytical ones using the parameters extracted from the fitting procedure described in this work. The middle figure shows an schematic of the rings used. The labels in the peaks correspond to: Through (T), Drop (D), Counter-Drop (D).

trip around the ring. It sholud be noted that the total Q-factor is defined as usual, $Q^{-1} = Q_{e,1}^{-1} + Q_{e,2}^{-1} + Q_i^{-1}$. In order to extract the value of the different parameters, a measurement of the through, drop and counter-drop ports is needed. When $\omega' = 1$ (T_o, D_o, C_o) and the full width half maximum $(\Delta\omega')$ of the counter-drop port, the 4 parameters that characterize the ring can be deduced as described in [6]. The expressions that result from particularizing equations 1,2 and 3 for $\omega' = 1$ and measuring the FWHM of the counter-drop port, are given by:

$$Q = \frac{1}{\Delta\omega'}\left(\frac{C_o}{D_o} - 1 + \sqrt{2}\sqrt{\left(\frac{C_o}{D_o}\right)^2 + 1}\right)^{1/2} \tag{5a}$$

$$Q_r = \frac{1}{Q}\sqrt{\frac{D_o}{C_o}} \tag{5b}$$

$$Q_{e,1} = \frac{2}{Q(Q^{-2} + Q_r^{-2})(1 \pm \sqrt{T_o})} \tag{5c}$$

$$Q_{e,2} = \frac{2(1 \pm \sqrt{T_o})}{QD_o(Q^{-2} + Q_r^{-2})} \tag{5d}$$

The sign ambiguity in (5c) and (5d) is a byproduct of the existence of two degenerate operation regimes in the ring with different parameters but the same resonance shape. This ambiguity is well known in cases without any backreflection effect. In our case the ambiguity is not relevant since one of the signs would give rise to a negative loss coefficient, which is unphysical. As the sign has to be the same for all the peaks in a ring, this provides a way to decide the correct sign in the expressions by analyzing more than one peak and looking for non-physical solutions. Although the characteristics of this model imply a uniformly distributed backscattering, reflections really occur at randomly localized points, giving rise to the random nature of the variations of backscattering versus wavelength [7].

IV. Results

From the experimental data we have chosen two consecutive resonances which show quite different behavior in terms of extinction ratio and degree of splitting. The results obtained from the method described in section III for each resonance are shown in the insets of Fig. 1, and the corresponding theoretical curves are superimposed, where a good agreement is observed. It is worth noting that the coupling constants and the loss show small variations among resonances, being R the one showing the strongest variations. This is expected from the nature of backscattering, and demonstrates the validity of our model.

V. Conclusion

We have described an analytical model and a fitting procedure that allows extracting all the key parameters of a ring resonator with two coupling points. We demonstrate that variations of the backscattering parameter are the cause of the strong variations in the shape of different resonances of the same microring. All these parameters can be extracted from simple transmission measurements.

Acknowledgments

The authors acknowledge financial support from the Spanish Ministry of Science and Innovation through contract SINADEC (TEC2008-06333) and Universidad Politécnica de Valencia through PAID-06-10 project 1914.

References

[1] F. Morichetti, A. Canciamilla, M. Martinelli, et al, "Coherent backscattering in optical microring resonators," *Appl. Phys. Lett.,* vol. 96, 2010, p. 081112.

[2] B. E. Little, J. P. Laine, and S. T. Chu, "Surface-roughness-induced contradirectional coupling in ring and disk resonators," *Optics letters,* vol. 22, Jan. 1997, pp. 4-6.

[3] F. Morichetti, A. Canciamilla, C. Ferrari, et al, "Roughness induced backscattering in optical silicon waveguides," *Phys. Rev. Lett.,* vol. 104, 2010, p. 33902.

[4] H. A. Haus, "Waves and fields in optoelectronics," Ch. 7, Prentice-Hall, 1984.

[5] B. E. Little, S. Chu, H. Haus, et al, "Microring resonator channel dropping filters", *J. Lightwave Technol.*, vol. 15, no. 16, 1997, p.998-1005.

[6] G. C. Ballesteros, J. Matres, J. Martí and C. J. Oton, "Characterizing and modelling backscattering in silicon microring resonators," *Opt. Express,* vol. 19, no. 25, 2011, p.24980-24985.

[7] F. Morichetti, A. Canciamilla and, A. Melloni, "Statistics of backscattering in optical waveguides", *Opt. Lett*, vol. 35, no. 11, 2010, p.1777-1779

Micromolds fabrication by laser lithography for biosensing applications

Silvino José Antuña[1], Adrián Fdez Gavela[2], María Rodríguez[3], José Rodríguez[4]
Physics department
University of Oviedo
Oviedo, Spain
[1]antunasilvino.uo@uniovi.es [2]fernandezgadrian@uniovi.es
[3]rodriguezlmaria.uo@uniovi.es [4]jose@uniovi.es

Isabel Álvarez[5], María Teresa Fernández[6], Agustín Costa[7]
Physical chemistry department
University of Oviedo
Oviedo, Spain
[5]alvarezmisabel@uniovi.es [6]mtfernandeza@uniovi.es
[7]costa@uniovi.es

***Abstract*— In this work, we manufacture micromolds by using as materials soda-lime glass and SU-8. In order to copy the scheme that we need in the micromold, an aluminum mask was fabricated by laser lithography containing the scheme. To improve the durability of the micromold, a layer of acrylic conformal coating is deposited over the sample. PDMS polymer was used to manufacture the microchannels by using these micromolds. The confocal microscope was used to characterize all samples.**

Keywords-component; glass, PDMS, SU-8, lithography

I. INTRODUCTION

The fabrication of channels in PDMS is a technique already known [1] as well as their use in electrochemical biosensors as, in this case, capillary electrophoresis microchips. In this work, it has been developed a manufacturing process of micromolds in SU-8 (formulation 50) on a glassy substrate using lithographic processes. The interest in fabricating these micromolds is focused on getting a way of manufacturing PDMS microchannels in a fast, effective and highly repetitive way. In order to achieve that, it is need to focus on increase durability and decrease the degradation.

II. FABRICATION

The micromolds fabrication requires the prior manufacture of a mask containing the pattern of the microchannels to implement. This is done by laser lithography which allows the design of the micromolds with a variety of possibilities. Prototypes we have manufactured so far have been designed with two cross-shaped microchannels. Recently we have begun the manufacturing of prototypes with different shapes. Once the mask has been obtained, its pattern will be transferred by an UV exposure to the SU-8 photoresist.

The manufacture of SU-8 molds is well known [2]. Briefly, in a clean room environment, the first step was cleaning the substrate of soda-lime with piranha, and then on this substrate the SU-8 was coated. The photoresist was prebaked in a hot plate at 95 °C for 15 minutes in contact with the substrate. This step serves to densify the small film deposited during this process since different solvents substances are volatilized. The UV exposure was made with an ultraviolet lamp using the previous made mask in contact with the substrate for 12 minutes. The commercial computational fluid dynamics code Fluent was used in order to optimize the Aluminum mask fabrication. The following steps, due to the characteristics of the mold are the most sensitive for being success in the manufacture process. It should be minimize the tensions existing between glass and SU-8 due to different expansion coefficients they have, allowing the channels to be well attached. Also, the SU-8 at a temperature of 55 ºC improves its internal structure getting better physical properties. A postbake that improves the internal improvement of the SU-8 and the good adhesion to the glass must be done, and this was achieved doing a gradually postbake. First, the sample was placed on a hot plate at 50 °C and gradually the temperature was raised to 95 °C. Once the temperature was achieved, the micromold was postbaked for 15 minutes. After this time, it is absolutely necessary to cool the sample slowly back to 50 °C because the development was carried out with acetone. Acetone has a high capacity for absorbing heat and, if the sample is not cooled, the developed will increase the tensions between the soda-lime and the SU-8 causing it detaching from the substrate. Then, to improve the mechanical properties of SU-8, a cure cycle was done in two steps, for 5 minutes at 150 ºC and 10 minutes at 200 °C. This quickly eliminates acetone by evaporation and the sample was ready for the next step.

To improve the durability of the micromold, a layer of acrylic conformal coating performance was deposited. The product is the 714-462 RS aerosol which allows spray deposition, although this layer was centrifuged to improve the flatness and reduce its thickness. After this last step the micromold is ready to be used.

Finally, the PDMS polymer was deposited over the whole sample and a postbake process was done to 35ºC overnight.

Fig. 1 shows a scheme of the complete manufacture process.

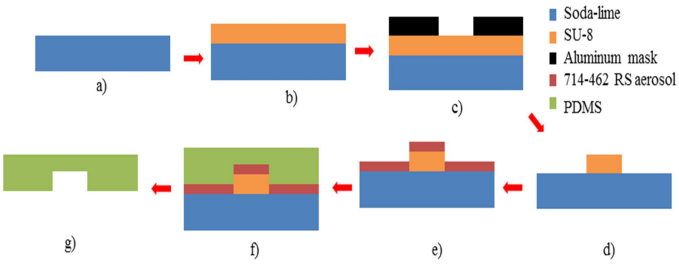


Figure 1. Manufacture process: a) Soda-lime glass was conditioned in a clean room. b) Spin-coating technique was used to deposit SU-8 layer over the glass. c) UV exposure by using an aluminum mask. d) SU-8 developed with acetone. e) A layer of acrylic was centrifuged. f) PDMS was deposited over the sample. g) The mold was retired and the process was finished.

This work has been supported by PhD grant BP09-007 “Severo Ochoa” from FICYT (Principado de Asturias) and by the MICINN (Government of Spain) under project CTQ2011-25814.

III. RESULTS

A confocal microscope was used to characterize the micromolds manufactured and the microchannel obtained.

Fig. 2 shows a 3D profile of a micromold. In Fig. 3 we can observe a 2D profile of the same micromold, as well as the thickness, t_1, and width, w_1. The microchannel characteristics can be measured with the following results: t_1=35 µm and w_1=150 µm.

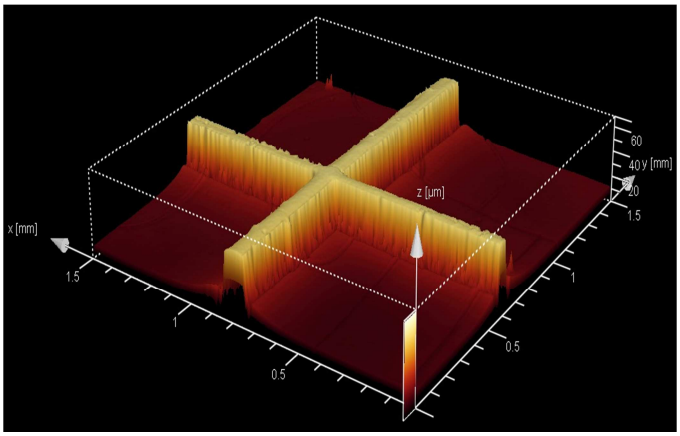


Figure 2. 3D profile of a SU-8 micromold observed with confocal microscope.

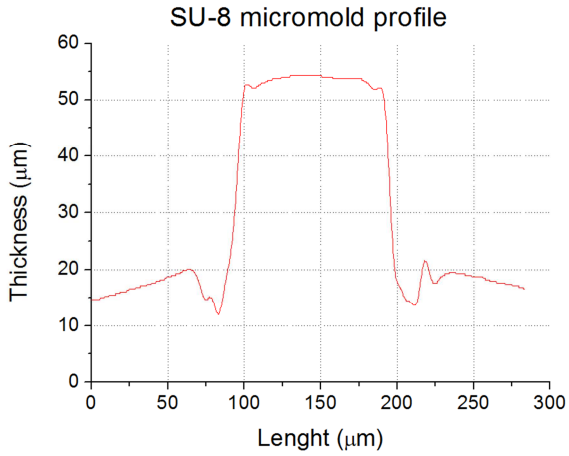


Figure 3. 2D profile of a SU-8 micromold observed with confocal microscope.

Fig. 4 shows a 3D profile of a microchannel manufactured with PDMS by using the micromold in Fig. 2 and Fig. 3. In Fig. 5 we can observe a 2D profile of the same microchannel as in Fig. 4. The thickness, t_2, and width, w_2, of the microchannel can be measured with the following results: t_2=35 µm and w_2=150 µm.

We have manufactured several PDMS microchannel with the same micromold. We have noticed that the micromold has not been modified. If we compare the SU-8 micromold confocal microscopy measurements with the obtained from its inverse replica in PDMS, we obtain a very good agreement in all cases.

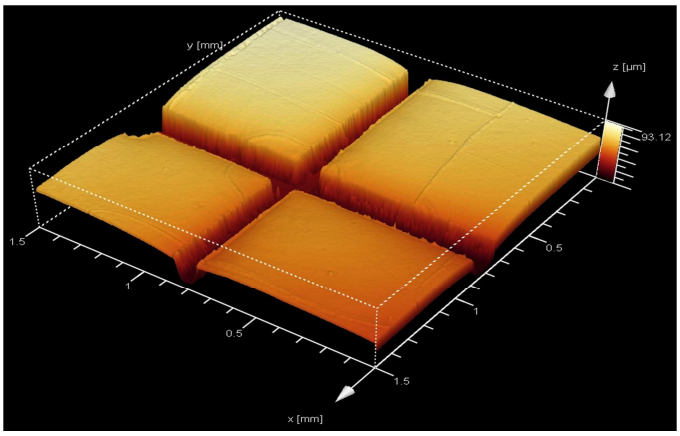


Figure 4. 3D profile of a PDMS microchannel observed with confocal microscope.

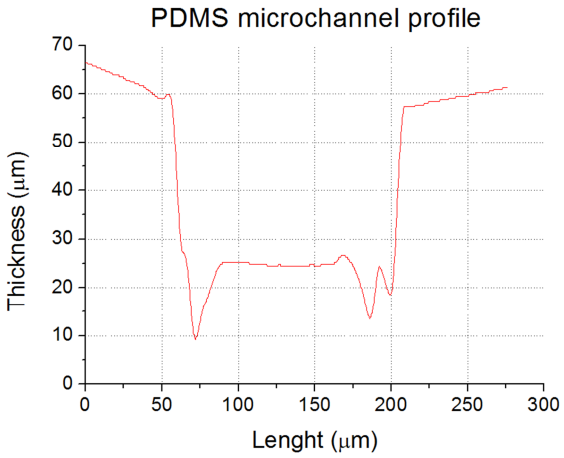


Figure 5. 2D profile of a PDMS microchannel observed with confocal microscope.

REFERENCES

[1] J. C. McDonald, D. C. Duffy, J. R. Anderson, D. T. Chiu, H. Wu, O. J. A. Schueller and G. M. Whitesides, “Fabrication of microfluidic systems in poly(dimethylsiloxane)” Electrophoresis, vol. 21, pp. 27–40, 2000.

[2] M. L. Kovarik, N. J. Torrence, D. M. Spence and R. S. Martin, “Fabrication of carbon microelectrodes with a micromoding technique and their use in microchip-based flow analyses” Analyst, vol. 129, pp. 400-405, 2004.

On the optimization of the 1.8 μm laser generation in 3 at% Tm :$KY_{0.58}Gd_{0.18}Lu_{0.17}(WO_4)_2$ layers on KYW crystal

C. Berrospe, X. Mateos*, W. Bolaños
J. Carvajal, M. C. Pujol, M. Aguiló and F. Díaz
Física i Cristal.lografia de Materials i Nanomaterials
(FiCMA-FiCNA)-EMaS
Universitat Rovira i Virgili, Tarragona, Spain
*xavier.mateos@urv.cat

G. Lifante, J. Martínez and E. Cantelar
Departamento de Física de Materiales C-IV
Universidad Autónoma de Madrid

Abstract

We grew a 3 at% Tm: $KY_{0.58}Gd_{0.18}Lu_{0.17}(WO_4)_2$ active layer on the (010) and (310) faces of a KYW substrate and achieved laser generation in both cases. The comparison reveals a strong thermal dependence on the laser operation in the layer grown on the (010) face. Such comparison under identical experimental conditions demonstrated that the active layer grown on the (310) face shows better laser performance achieving a maximum output power of 28.6 mW in cw regime.

1 Introduction

Research activity on the realization of laser generation in active crystalline composites is growing because of the great challenge of integrating photonic components into smaller and smaller devices. Among all materials studied for such a purpose, the monoclinic rare-earth double tungstates layers doped with an active ion grown on a crystalline substrate of the same family have been a subject of work specially in the recent years for two ions, ytterbium (Yb) and thulium (Tm) operating around 1 μm [1] and 2 μm [2], respectively. Epitaxies with special composition have been extensively studied for optimization of refractive index contrast and lattice matching between the substrate and the guiding layer [3].

Concerning demonstration of Tm laser generation in optimized index contrast and lattice matched 3 at% Tm :$KY_{0.58}Gd_{0.18}Lu_{0.17}(WO_4)_2$ layer also grown on the (010) face of a KYW substrate, a previous work considering planar waveguide [4] demonstrated continuous-wave (cw) operation with a maximum output power of 5 mW at 1844 nm linearly polarized parallel to the N_m (medium refractive index in these monoclinic crystals) optical direction. Also, pulsed Q-switched operation was demonstrated [4].

The motivation of the current work was to improve the efficiency of the laser generation using thulium ions in planar waveguides operating around 1.8 μm. For this purpose, the followed strategy has been study the laser performance of a layer grown on a face where the three thermal conductivity components of these monoclinic crystals are different than those of the layer already studied grown on the (010) face. For this, two planar waveguides grown on the (310) and (010) faces of the KYW substrate were considered and compared.

2 Experimental details

Single crystals of KYW were grown by the Top Seeded Solution Growth (TSSG) method and used as substrate for the growth of a layer with composition 3 at. % Tm :$KY_{0.58}Gd_{0.18}Lu_{0.17}(WO_4)_2$ by the Liquid Phase Epitaxy (LPE) method, on both the (010) and (310) natural faces. The samples were cut and polished in such a way the polarization of the incoming beam was parallel to the N_p (smallest refractive index) principal optical direction in both cases. Laser experiments were carried out pumping the waveguides with a tunable Ti:sapphire laser at 794 nm (maximum of absorption for the N_p polarization). Such a laser is focused onto the samples through a microscope objective with a spot of 64 μm in diameter. Another microscope objective specially designed to work around 2 μm was used to collect the output signal allowing the observation of the confined laser mode. Two mirrors (input and output coupler) were used for laser oscillation, the output coupler had a transmission of 10% at 1.8 μm.

3 Results and discussion

The monoclinic double tungstates show natural faces labelled in figure 1. The growth rate of the two (010) and (310) faces was determined to later grow a layer with a desired thickness. The layers we used for the laser experiments were 10 μm (010) and 11 μm (310) thick with a rms of 24 nm. The optical path in both cases was 5 mm.

For comparison in similar conditions of the two samples, the laser experiments were performed with light parallel to the N_p principal optical direction. The active layer grown on the (310) face operated in cw regime delivering a maximum output power of 28.7 mW at a maximum absorbed power 53 mW operating at 1884 nm linearly polarized parallel to Np. Only, at the highest absorbed power,two polar-

izations (N_p and N_m) coexisted. The corresponding laser wavelengths for the two polarizations were 1880 nm and 1841 nm, respectively. This phenomenon is attributed to the thermal load in the sample as we previously observed in a Tm:KLuW bulk laser [5], so that, thermal load introduces some losses that forces the laser to operate at a higher inversion level resulting in shorter wavelenghts. In addition, at such temperature, it happens that similar gain is reached for another polarization (N_m) in this case, obviously with a different inversion level and at a different wavelength. The laser threshold amounted to an absorbed power of 14 mW. Figure 2 shows the output-input laser characteristics for the layer grown on the (310) face.

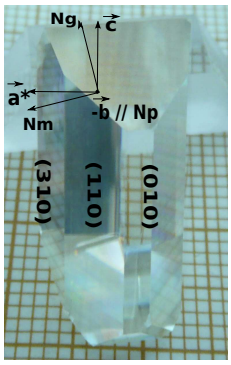


Figure 1: Natural faces and principal optical directions of a KYW single crystal.

The laser experiment with the active layer grown on the (010) face could not operate in cw regime due to thermal problems. The use of a mechanical chopper (50% duty cicle) enabled laser generation with around 1 mW average output power showing simultaneous lasing at 1826 nm (N_m) and at 1832 nm (N_p) from the laser threshold as can be seen in figure 3. Note that the laser threshold is higher in this case than in the case of the layer grown on the (310) face typical for quasi three level lasers with higher electronic occupation in the ground state. The gain curves for each polarization in such crystals [6] explain perfectly the laser wavelengths observed in this work. In a previous work on a similar planar waveguide [4], although a cladding of the same KYW crystal was grown on the active layer, up to 5 mW output power was achieved in cw regime because the pump was parallel to N_m at 802 nm pumping where the absorption is almost half of that at 794 nm for N_p polarization, reducing the thermal load and enabling laser oscillation.

The difference in laser performance shown above could be attributed to the dependence on the thermal conductivity for all directions in each sample. In reference [7], the thermal conductivity tensor of the monoclinic double tungstate crystals was studied and we work to quantify how this could affect to such a difference in laser performance. In addition, the crystalline quality introduced by the defects of the interface between the (310) and the substrate is expected to

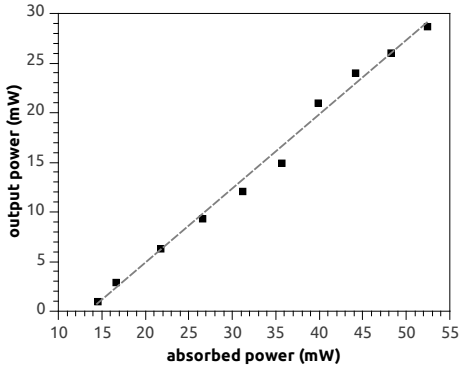


Figure 2: Laser operation of the active layer grown on the (310) face with linear polarization parallel to N_p.

be better than in the (010) face due to the smaller growth rate for the former. The study of it for the two faces resulted in 4 times faster growth rate in the case of the (010) face than that of the (310) face.

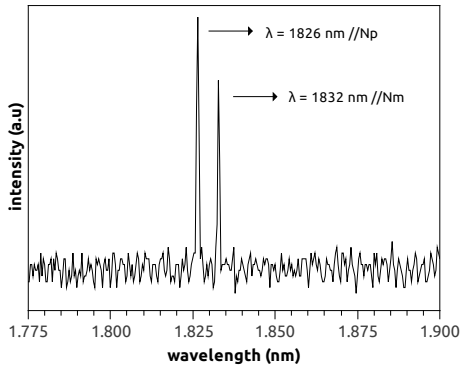


Figure 3: Polarization competition in the laser operation of the layer grown on the (010) face.

4 Conclusion

The growth and laser operation of the active layers grown on the (010) and (310) faces of a KYW substrate have been studied concluding, that that grown on the (310) face performs much better due to the higher dissipation of heat generated in the waveguide. Further work is in progress to study the role of the crystalline defects in the interface of the two layers with the substrate to clarify the influence of the crystalline quality.

5 References

1. H. Kühn, *Opt. Lett.*, **2009**, *34*, 2718.
2. W. Bolaños, *Opt. Mat.*, **2010**, *32*, 469.
3. W. Bolaños, *Cryst. Growth Des.*, **2009**, *9*, 3525.
4. W. Bolaños, *Opt. Express*, **2011**, *19*, 1449.
5. M. Segura, *Laser Phys. Lett.*, **2012**, *9*, 104.
6. X. Mateos, *IEE J. Quant. Electron,* **2006**, *42, 1008.*
7. *S. Vatnik, Appl. Phys. B,* **2009***95, 653.*

3D-internal Laser beam machining into polymers

F. Rey-García, C. Bao and C.Gómez-Reino
UA Microóptica e Óptica GRIN, Dpto Física Aplicada
Universidade de Santiago de Compostela
Campus Vida s/n 15782 Santiago de Compostela, Spain
carmen.bao@usc.es

G. F. De La Fuente
Laboratorio de Aplicaciones del Láser
Instituto de Ciencia de Materiales de Aragón (CSIC)
María de Luna 3, 50018 Zaragoza, Spain
xerman@unizar.es

***Abstract*—Tri-dimensional structures were internally mechanized into polymeric plates of polycarbonate (PC) and polyethyleneterefthalate (PET) by a laser backwriting process performed with plates submerged in water. A Nd:YVO_4 laser emitting at fundamental wavelength (1064 nm) in nanopulsed regime was employed.**

Keywords- polymeric plates; internal laser beam machining; 3D structures; informative panels; LED illumination

I. INTRODUCTION (HEADING 1)

The SURFALUX project is focused on the development of novel and economical materials for safety and general signalization. Another purpose of this research is to obtain economic materials with high resistance to different environmental conditions or to the presence of other external factors as vandalism. Following these principles, plastic materials as polycarbonate (PC) and polyethylene terephthalate (PET) have been successfully applied in safety signalization devices. Moreover, the use of external illumination sources in order to increase the visibility of the signals has been extensively and successfully tested. Thus, informative panels of polymeric materials illuminated by LEDs have been an important researching field within the SURFALUX project.

The laser beam machining of materials has been widely applied during years to a whole range of materials [1-2]. This technique allows the internal engraving of three-dimensional structures. Following this fact, this method could be applied to plastic materials in order to develop panels with determined logos, pictures or other information. However, these kind of materials are fragile to the laser action. The laser machining in air generally provokes defects as recast layers, cracking and heat damages. For this motive, the process was carried out under water. The advantages and processes associated to the use of water in laser processing were extensively reported by Kruusing [3]. The employ of water may provoke a decreasing of the etching rate due to the reduction of the transparency of the liquid as the process progresses [3] and cleaner and more precise profiles for the structures drawn should be obtained.

In this work we present results obtained on the internal engraving of polymeric plates submerged under water by laser beam machining with a Nd:YVO_4 laser operating at the fundamental wavelength on nanopulsed regime. An application to signals and informative panels fabrication with high visibility is proposed.

II. EXPERIMENTAL

Polymeric plates of polyethylene terephthalate (PET), polycarbonate (PC) and poly(methyl methacrylate) (PMMA) with size 10x10 cm submerged in water have been internally mechanized by laser ablation. The laser beam machining was carried out on laser backwriting configuration [4]. The laser beam focuses on an alumina target with an irradiance of $2.8x10^7$ W/cm^2 at a frequency of 2 kHz, reflecting the beam to the polymeric plate placed over there with a distance of 0.65 cm between materials. Thus, the plastic material is mechanized.

A Nd:YVO_4 laser (Powerline E, Rofin) emitting nanopulses at fundamental wavelength (1064 nm) was employed. The laser is fitted with a galvanometer beam steering system and a flat-field lens with a 100 mm focus, to allow scanning the alumina plate within the XY plane. The equipment is provided with a drawn software which allows to obtain letters, logos and other 3D structures into the polymeric plates. An illustrative scheme of the equipment and the method described here is represented in Figure 1.

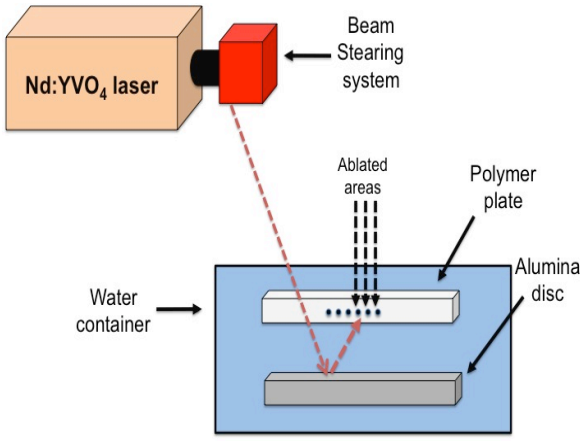


Figure 1: Scheme of laser backwriting of polymeric plates under water.

Once obtained the internal 3D structures, LED sources were coupled to the polymeric plates to illuminate them.

III. RESULTS AND DISCUSSION

Different 3D structures as squares, circles and hexagonal matrices were obtained (Fig. 2). Figure 3 shows the engraving

of a photography, as an instance of the wide range of drawings that can be performed.In this example, the background is clearly visible and defined with high resolution

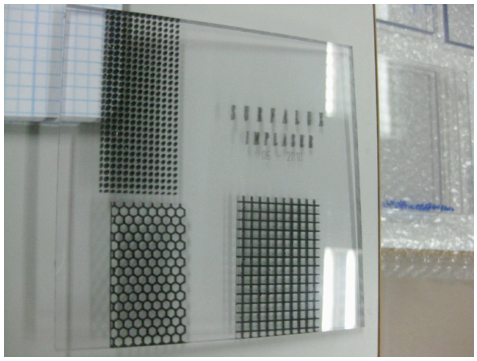


Figure 2: Matrices internally engraved into PC plates.

The internal 3D structures were obtained into PET and PC plates. No successfully results were obtained for PMMA plates. The structures obtained into PC are darker and more defined than those obtained for PET applying the same laser parameters. This difference in color and definition is due to the damage originated to the polymer by the laser action. For the same irradiance and same experimental conditions, the process of ablation is higher in intensity for the PC plates.



Figure 3: 3D internal machinning designs of people into PC plates.

The method developed could be applied to perform informative panels and signals. Moreover, the illumination with LEDs increae the visibility of the panels (Fig. 4). In concordance with the above mentioned for laser damage, the figures obtained into PET plates and illuminated by LEDs are lighter than those obtained into PC plates (Figs. 5).

Moreover, the fact that the information or the pictures were internally drawing is and advantage to their use as informative panels. The atmospheric or human action over the surface of the plates will not damage the tridimensional structure. This fact is an additional advantage to actual devices in which the action of environment over the surface affects the information and it leads to the reposition of the signal. However, if the signal or information is internally engraving, is possible to protect the plate with a protective coating and in the case of damage surface only the external coating must be changed.



Figure 4: Informative panel of PC illuminated by LEDs.



Figure 5: Informative panel of PET with a logo illuminated by LEDs.

IV. Conclussions

Internal tri-dimensional structures were succesfully mechanized into polymeric plates of PC and PET by laser beam machining under water using the laser backwriting configuration. The illumination of the structures by LEDs increase the visibility of the plates an allows their implementation as informative panels. Moreover, the application of a protective coating that could change in future supposes an economical advantage to commercially signals employed nowadays.

Acknowledgments

The authors acknowledge funding from MICINN (TEC2006-10469, CEN 2007-2014, SURFALUX SOL-00030930 and MAT2010-18519), from DGA (T87) and Xunta de Galicia (INCITE08PXIB206013PR).

References

[1] J. Meijer, "Laser Beam Machining (LBM), state of the art and new opportunities", J. Mater. Process. Technol. 149 (2004) 2-17 (references).

[2] A. K. Dubey and V. Yadava, "Laser beam machining - a review", Int. J. Mach. Tools Manuf. 48 (2008) 609-628 (references).

[3] A. Kruusing, "Underwater and water-assisted laser processing: Part 2 - Etching, cutting and rarely used methods", Opt. Laser Eng. 41, 2 (2004) 329-352.

[4] A. Castelo, D. Nieto, C. Bao, M.T. Flores-Arias, M.V. Pérez, C. Gómez-Reino, C. López-Gascón and G.F. De la Fuente, Opt. Commun. 273 (2006)193-199.

Modeling Photonic Properties of Quasi-random Nanoporous Anodic Alumina for Application in Organic Devices

Josep Ferré-Borrull, Mohammad Mahbubur Rahman, Pedro Granero, Lluis F. Marsal, Pilar Formentín, Josep Pallarès
Nano-electronic and Photonic Systems, NePhoS
Universitat Rovira i Virgili
Tarragona, Spain
josep.ferre@urv.cat

***Abstract*—We report the progress on the numerical modeling of the photonic properties of nanostructures based on the nanoporous anodic alumina. With the use of FDTD we show that the quasi-random structure of the material possesses a photonic stop band. We also show the light trapping effect caused by the nanostructuring of organic solar cells using nanoporous anodic alumina as template.**

Nanoporous Anodic Alumina, Modeling,Photonic Stop Band, Organic Photovoltaics

I. INTRODUCTION

Nanoporous anodic alumina (NAA) is a material obtained by the electrochemical etching of aluminum in acid electrolytes with greatly increasing interest in nanotechnology [1,2]. When produced in the adequate conditions NAA shows a porous nanostructure with a self assembly of the pore distribution. The size of the pores and the average interpore distances in such structures can be modulated from a few nanometers to some hundreds of nanometers by combining different anodization conditions, acid electrolytes. Pores in the structures grow perfectly parallel with lengths from shallow pores to several hundreds of microns. Given these possibilities in shaping this nanostructure, NAA has found a great wealth of applications.

Furthermore, the self-assembled nature of NAA is close to that of a Photonic Crystal: it consists of a 2-D triangular lattice of cylindrical parallel pores in an aluminum oxide matrix. However, although the periodicity can be made artificially perfect by using nanoindenting procedures, usually, NAA shows symmetry breaking points that produce domains of random size and orientation. In this sense, we have called such a structure *quasi-random*[3]. In this communication we review the progress achieved in the group NePhoS in the numerical modeling of the photonic properties of NAA. In particular, we use the finite-differences time-domain (FDTD) method to predict the existence of photonic stop bands in the structure in much the same way they are formed in photonic quasicrystals. Then, we use the finite-element method to study the light absorption properties in nanostructured organic solar cells that model those that can be obtained using the NAA as a template.

II. RESULTS

A. *Photonic Stop Bands in Nanoporous Anodic Alumina*

Fig. 1 shows a typical example of the quasi-random distribution of the pores on NAA. It can be seen that this structure is similar to that of a 2D quasicrystals, which exhibit photonic stop bands even with smaller refractive index contrast that its periodic counterparts because of its higher rotational symmetry.

In order to investigate the existence of a photonic stop band we have applied FDTD to simulate the propagation of a wide-band pulse through a given length L of NAA in a direction perpendicular to the pores. The data for the pore distribution was obtained from SEM images of real samples such that in Fig. 1. The simulations permitted to obtain the transmittance spectra but given the random nature of the pore distribution, it was necessary to calculate the ensemble average of the transmittance for a great number of realizations of the nanostructure.

Fig. 2 shows the transmittance spectra for TE polarized light for different pulse path L, expressed in terms of the average interpore distance *a*. The vertical lines indicate the wavelength range of the photonic band gap of a periodic photonic crystal with a triangular lattice with the same refractive indices and lattice constant *a*. It can be seen that transmittance through the NAA shows a clear stop band at the same wavelength range.

B. *Light Ttrapping and Absorption in Organic Solar Cells Nanostructured by NAA*

One of the applications of NAA is as a template to shape at the nanometric scale organic photonic devices such as solar cells. Light interaction with such nanostructures cannot be modeled by the usual methods of the transfer matrix for stratified media given the non-planar geometry and the subwavelength dimensions. We have used the finite-element method to obtain the absorption map on a 2D model of a nanostructured organic solar cell.

The cell model consisted of an interdigitated structure of two organic semiconductors, P3HT and PCBM. We studied the

absorption at P3HT, where excitons are generated that subsequently diffuse to the interface where charge separation occurs. Fig. 3 shows the absorption map on the structure for a wavelength of 450 nm for an inter-digit spacing of 250 nm, 400 nm and 500 nm. It can be seen that for these sizes, which can be obtained with NAA template-assisted nanostructuring, spacing is of the order of wavelength and light forms standing waves in the structure that result in an increase of absorption.

The results for the complete spectrum are shown in Fig. 4, where the total absorption as compared with the absorption of a two-layer planar cell with the same quantity of P3HT is presented. Although for some wavelengths absorption is smaller, for others it is increased because of the light trapping effect observed in Fig. 3.

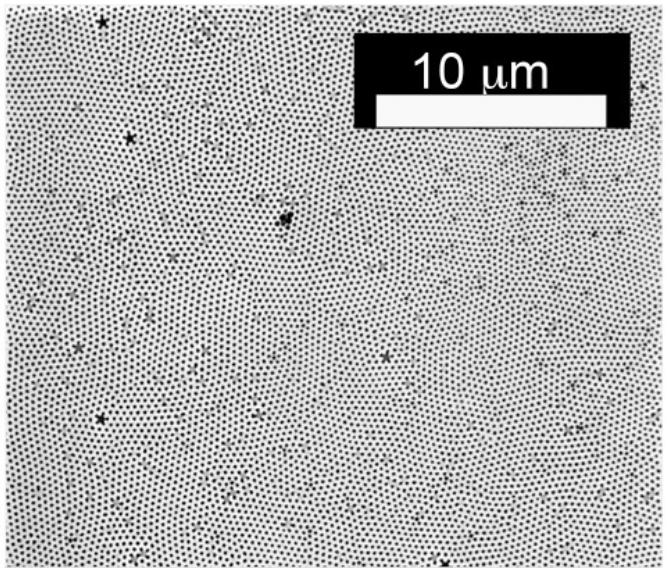


Figure 1. Example of a typical quasi-random nanoporous anodic alumina structure

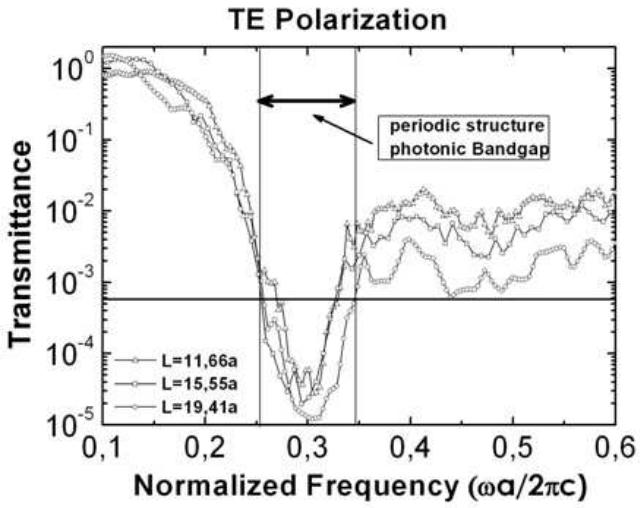


Figure 2. Transmittance in direction normal to the pores of a nanoporous anodic alumina. The minimum in transmittance appears at the same wavelength range than the photonic bandgap in a periodic structure with lattice constant equal to the average interpore distance *a*.

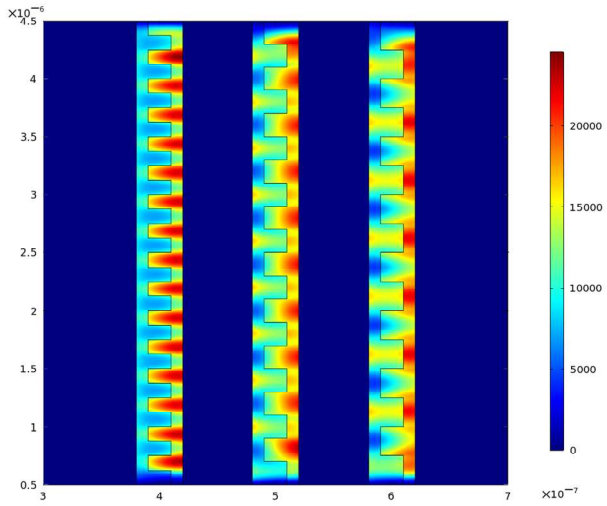


Figure 3. Absorption maps of 2D interdigitated organic solar cells for a wavelength of 450 nm. The inter-digital distances are 250 nm (left), 400 nm (center) and 500 nm (right). The units of the axes are microns.

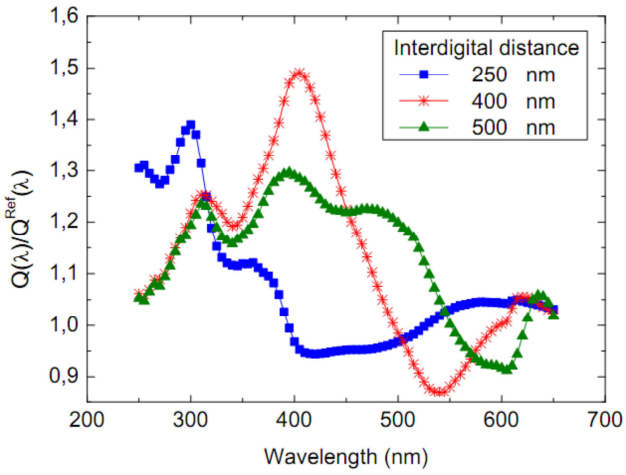


Figure 4. Spectrum of total absorbed energy of the interdigitated organic solar cells with respect to the total absorbed energy by a planar bilayer cell with the same amount of material.

ACKNOWLEDGMENT

This work has been funded by the Spanish Ministry of Science and Innovation (MICINN) under grant no. TEC2009-09551, CONSOLIDER HOPE project CSD2007-00007, 09 and Accion Integrada FR2005-0009 and by the Generalitat de Catalunya under project AGAUR 2009 SGR 549.

REFERENCES

[1] C. J. Ingham, J. ter Maat, W. de Vos, “Where bio meets nano: The many uses for nanoporous aluminum oxide in biotechnology”, Biotechnology Advances, In Press,http://dx.doi.org/10.1016/j.biotechadv.2011.08.005

[2] A. Santos, P. Formentín, J. Pallarés, J. Ferré-Borrull, L. F. Marsal, “Fabrication and characterization of high-density arrays of P3HT nanopillars on ITO/glass substrates”, Solar Energy Materials and Solar Cells, Vol. 94, pp. 1247-1253, 2010 .

[3] M. M. Rahman, J. Ferré-Borrull, J. Pallarès, L. F. Marsal, “Photonic stop bands of two-dimensional quasi-random structures based on macroporous silicon”, Physica Status Solidi C, Vol. 8, pp. 1066-1070, 2011.

Theory and simulation of an active GRIN beam shaper

A.I. Gómez-Varela, M.T. Flores-Arias, C. Bao-Varela and C. Gómez-Reino
"Microóptica y Óptica GRIN" Group, Department of Applied Physics, Facultade de Física e Facultade de Óptica e Optometría, Campus Vida s/n, E15782
Universidade de Santiago de Compostela (USC)
Santiago de Compostela, Spain
anaisabel.gomez@usc.es

***Abstract*—We present theory and simulation of an active GRadient-INdex GRIN device for laser beam shaping by transformation of a Gaussian beam into a uniform beam in a controlled manner.**

Keywords-GRIN material;complex refractive index ;laser beam shaping

I. INTRODUCTION

Beam shaping presented in this work is the process of transforming the irradiance and phase of a non uniform beam into a flat-top distribution [1,2]. This task can be carried out by an active GRIN device consisting in a material with quadratic gain or loss and refractive index profiles in transverse direction to the optical axis. There are two main purposes in the present paper: to present beam shaping condition for active GRIN materials and to simulate beam shapers for irradiance homogenization.

II. THEORY

When an active GRIN material of thickness d is illuminated by a Gaussian beam, the general condition for beam shaping can be written as

$$\mathrm{Im}\left[n_0 \dot{q}(d) q^*(d)\right] = 0 \quad \Rightarrow \quad w(d) \to \infty$$

where n_0 is the complex refractive index along the z axis, $q(d)$ and $\dot{q}(d)$ are position and slope of the complex ray at the output face of the material and Im denotes the imaginary part. Condition says that the beam-half width w of the beam at z = 0 tends to infinite and the input Gaussian distribution becomes flat-top distribution at the output of the active device as shown in Fig. 1. In particular, transformation of a spherical Gaussian beam into uniform spherical wavefront diverging, negative curvature radius, or converging, positive curvature radius, is depicted in Fig. 2.

III. SIMULATIONS

To illustrate the behavior of active GRIN shapers with on-axis gain and loss, a simulation of the transformation of a spherical Gaussian beam into a uniform beam is represented in Fig. 3 and Fig. 4, respectively. The active beam shaper is illuminated by a He-Ne laser operating at 632.8 nm and beam width 0.95 mm. For the on-axis gain beam shaper, the input Gaussian beam is converted to a flat-top beam of 2 mm of aperture at thickness 8.252 mm and in the on-axis loss case the shaper length is 4.936 mm.

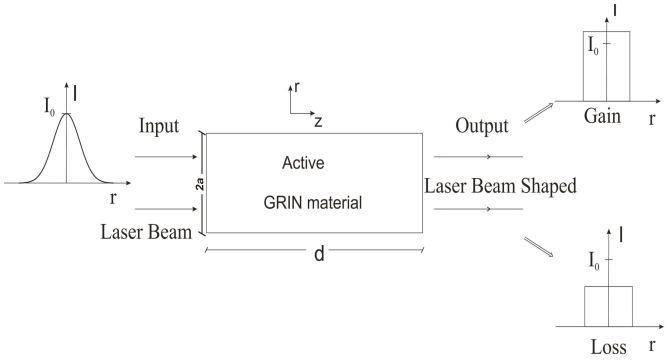


Figure 1. Diagram of beam shaping system by active GRIN material with gain or loss.

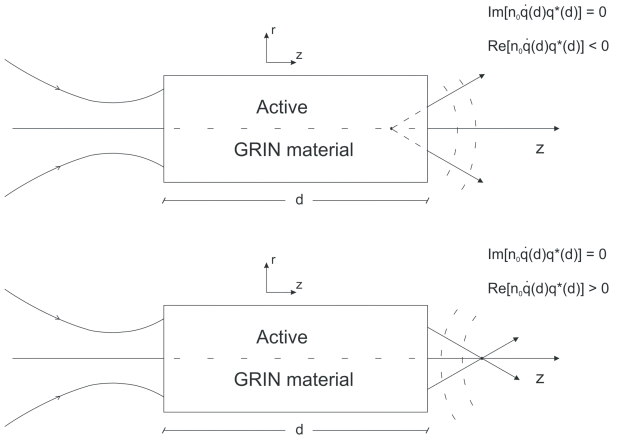


Figure 2. Beam shaping by active GRIN material: transformation of a spherical Gaussian beam into a uniform wavefront a) diverging R(d) < 0 and b) converging R(d) > 0.

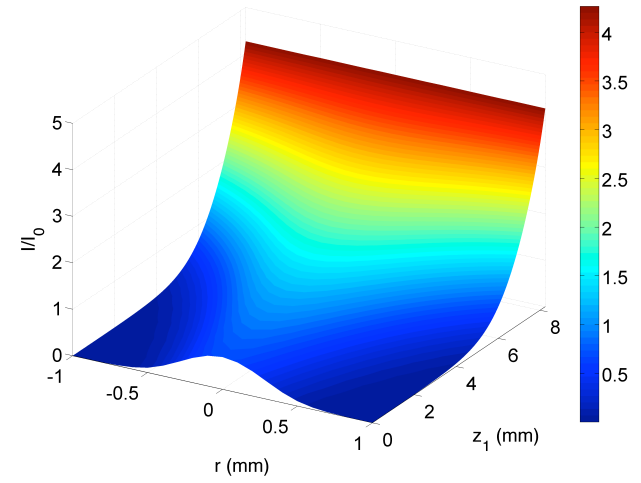


Figure 3. Evolution of the relative irradiance for an on-axis gain beam shaper device. Parameter values: a = 1 mm, $n_{0I} = -10^{-5}$, $n_I(a) = -10^{-4}$, $n_{0R} = 1.62$, $n_R(a) = 1.6$, $g_{0R} = 0.1571352$ mm^{-1}, $g_{0I} = 0.0003540$ mm^{-1}. The beam shaper length is $z_1 = 8.252$ mm.

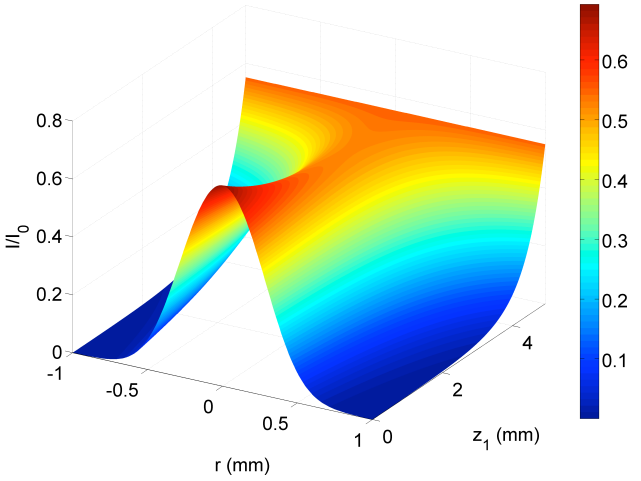


Figure 4. Evolution of the relative irradiance for an on-axis loss beam shaper device. Parameter values: a = 1 mm, $n_{0I} = 10^{-5}$, $n_I(a) = -10^{-4}$, $n_{0R} = 1.62$, $n_R(a) = 1.6$, $g_{0R} = 0.1571354$ mm^{-1}, $g_{0I} = 0.0004316$ mm^{-1}. The beam shaper length is $z_1 = 4.936$ mm.

Simulations have been made for n_{0R} and n_{0I} real and imaginary parts of n_0, $n_R(a)$ and $n_I(a)$ real and imaginary parts of the complex refractive index at r = a and g_{0R} and g_{0I} real and imaginary parts of the complex gradient parameter.

IV. Conclusions

In this paper a novel method for laser beam shaping has been presented. The beam shaper is performed by an active GRIN material with on-axis gain or loss. This fact would provide control on the constant irradiance level of the output laser beam. Light propagation of Gaussian beams in active GRIN materials has been presented and results have been simulated and applied to an active GRIN shaper with on-axis gain and loss to determine beam shaping thicknesses less than 1 cm and to show beam homogenization on 2 mm of aperture.

Acknowledgments

This work has been sponsored by Ministerio de Ciencia e Innovación (MAT2010-18519) and CDTI (SURFALUXSOL-00030930), Spain. Besides, Ana I. Gómez-Varela wants to acknowledge the financial support from the FPU (Formación de Profesorado Universitario) grant 2009 (Ministerio de Educación, Cultura y Deporte, Spain).

References

[1] F. M. Dickey, S. C. Holswade and D. L. Shealy, "Laser beam shaping applications", CRC, Francis and Taylor Group, London, UK, 2006.

[2] C. Gomez-Reino, M. V. Perez and C. Bao, "Gradient-index optics: fundamentals and applications", Springer Verlag, Berlin, 2002.

Incident Angle Dependence For Dual Band Double Negative Index Material Using Elliptical Nanohole Arrays

T.Cao
Faculty of Electronic information and Electrical Engineering, Dalian University of Technology, China(P.R.C) 116024

M.J. Cryan
Photonics Research Group
Department of Electronic and Electrical Engineering
University of Bristol, Bristol, BS8 1UB, UK

***Abstract*— This paper analyzes the scattering coefficients and displacement current of an elliptical nanohole array (ENA) at different angles of plane-wave incidence to show the ENA is double negative(showing both a negative effective permeability μ_{eff} and a negative effective permittivity ε_{eff}) at multiple wavelengths for *p* polarization over a broad range incident angles.**

Keywords-component; formatting; style; styling; insert (key words)

I. INTRODUCTION

Recently, negative index materials(NIMs) have become an exciting prospect because of their extraordinary optical properties such as negative refraction, near-field focusing and subwavelength imaging[1]. It is well known that Metamaterials (MMs) constitute the most promising variant of a negative refractive index material. As such, research on all-angle negative refraction and imaging of MMs has been paid more and more attention: Liu *et al* theoretically demonstrated that all-angle negative refraction could be achieved by metallic nanowires embedded in a dielectric matrix in the visible region, arising from the hyperbolic constant frequency contour of one unique indefinite metamaterial[2]; Purgos *et al* reported a Metal-Insulator-Metal (MIM) composed of Ag/GaP/Ag coupled plasmonic coaxial waveguides which exhibited a wide angle negative refraction at visible wavelengths characterized by the backward phase propagation [3]; Menzel *et al* reported on the effects of arbitrary incidence angles on the anisotropic "Fishnet" structure consisting of three layers made of Ag/MgF_2/Ag [4], however, they have shown that all retrieved parameters strongly depend on the incident angle and can only be applied to the case of normal incidence. In this work, we numerically study the angular dependence of the Displacement current, J_D in a structure composed of 2D aligned elliptical nanohole arrays (ENAs) in the Au-Al_2O_3-Au material system[5]. According to Faraday's law, the magnetic dipolar mode will be excited at the frequencies in which the formation of enclosed current loops can be observed[6]. Thus using this approach we can predict the effects of the incident angle on the double negative index for the ENA structure

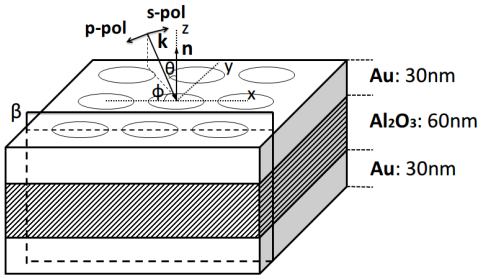


Fig. 1: Schematic of the MIM structure consisting of an Al_2O_3 dielectric layer between two Au films perforated with a square array of elliptical holes suspended in air. The displacement current is shown in the plane β

II. FDTD MODELLING

Figure 1 shows a schematic of the structure which consists of a two-metallic films(30nm thick Au) separated by a dielectric layer (60nm thick Al_2O_3). A two dimensional square lattice ENA(lattice constant: L=687nm, hole diameter: d_1=470nm,d_2=332nm) has been embedded through the entire MIM structure. The unit cell is periodically extended along the x and y directions and the lattice axes coincide with the coordinate axes. The oblique incident angle θ is defined by the angle between wave vector k and the z axis. φ is the angle between the parallel (to the xy plane) component of the wavevector and x axis. The displacement current is shown in the plane β. The layers have a thickness of T_{Au}=30nm and T_{Al2O3}=60nm. A simple Drude model is used for the dielectric constant of the Gold, $\varepsilon(\omega)=1-\frac{\omega_p^2}{[\omega(\omega+i\omega_c)]}$, where ω_p=1.37x10^{16} Hz is the plasma frequency and ω_c=4.08x10^{13} Hz is the scattering frequency for bulk gold. The refractive index of Al_2O_3 is 1.62. The computational domain (687nmx687nmx1000nm) has perfectly match layer(PML) absorbing boundaries in the z direction and periodic boundaries in the x-y plane. The FDTD mesh size is 10nm which was found to be a good tradeoff between accuracy and simulation run time. A plane wave is incident at variable angle on the structure as described in figure 1. Figure 2 shows the simulated transmission spectrum for the *p* polarized plane wave incident at different off-axis angles θ for a fixed $\varphi=0^0$. It can be seen that the transmittance dip/peak tends to reduce when the angle θ increases. However their locations show no obvious deviation,

indicating the negative index can happen at the oblique angle of the incidence.

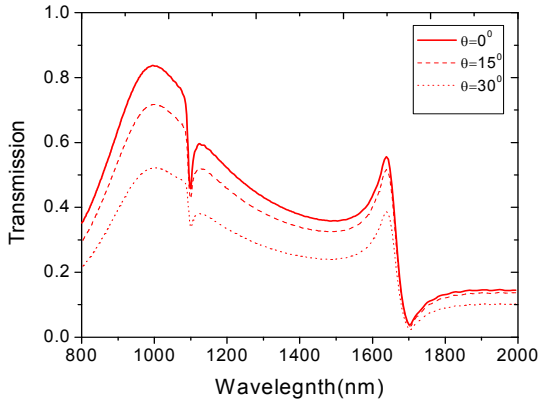


Fig. 2: 3D FDTD simulation of the transmission for the ENA for *p* polarization at different incident angle θ

The longer wavelength resonance at 1680nm is attributed to the L-C circuit resonance, the resonance around 1095nm implies that there is a significant variation in the phase of the light transmitted through the structure because the light going through the different regions interferes destructively. Both of the resonance regions are believed to be connected with the magnetic response. The effective refractive index, effective permeability, μ_{eff} and effective permittivity ε_{eff} for the *p* polarized plane wave at normal incident angle can now be obtained by using the complex coefficients T and R and is shown in figure 3.

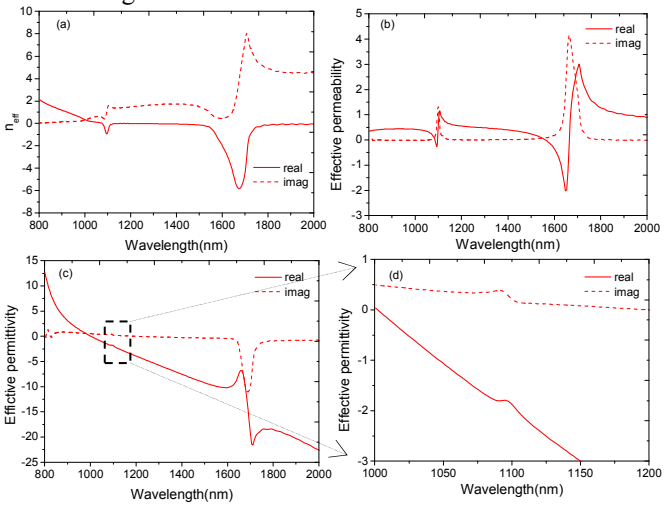


Fig.3 : 3D- FDTD simulation of (a) real and imaginary part of effective refractive index; (b) real and imaginary part of effective permeability μ_{eff} ;(c) real and imaginary part of effective permittivity ε_{eff}; (d) Zoom in picture of the real and imaginary part of effective permittivity ε_{eff} for the elliptical nanohole array;

In order to validate the existence of the magnetic dipoles, we then simulate the J_D at off-normal incident angle θ. The J_D at different θ is shown in Figure 4 showing the expected magnetic dipole.

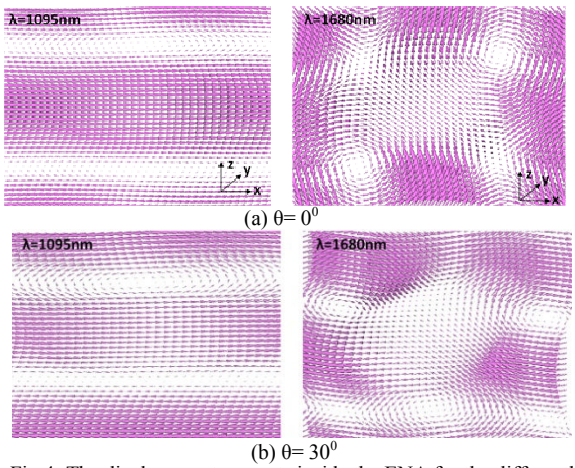


Fig.4: The displacement currents inside the ENA for the differently oblique angle of the incidence at λ =1095nm and λ =1680nm respectively:(a) θ=0⁰ ; (b) θ=30⁰

It can be seen that at rather large angles of incidence (30^0), a loop of the J_D still appears in the structure. This is due to the fact that the orientation of the magnetic dipole is maintained when the incident angle is varied and it can maintain the strength of the magnetic resonance over a wide angle. These results suggest that such a structure can show a negative index over a wide angle of incidence.

III. CONCLUSION

In summary, a broad angle dual band negative index material implemented by an elliptical nanohole array consisting of an Al_2O_3 dielectric layer between two Au films is simulated using the 3D FDTD method. Depending on the polarization of the normally incident light, different spectral behaviour is observed. For *p* polarization, dual band negative index is achieved around 1095nm and 1680nm. We have made a further step in the study of the optical properties of the structure at different incident angle by means of the Displacement current, J_D and transmission spectrum. It can be seen that the formation of closed J_D loops are in a good agreement with the magnetic responses (transmission spectrum) at 1095nm and 1680nm respectively. Such a structure can achieve dual band negative index with broad angle.

[1] J. B. Pendry, "Negative refraction makes a perfect lens," Phys. Rev. Lett. **85**, 3966-3969 (2000).

[2] Y. Liu, G. Bartal, and X. Zhang, "All-angle negative refraction and imaging in a bulk medium made of metallic nanowires in the visible region," Opt. Expr **16**, 15439-15448 (2008).

[3] S. P. Burgos, R. de Waele, A. Polman, and H. A. Atwater, "A single-layer wide-angle negative-index metamaterial at visible frequencies," Nat Mater 9, 407-412 (2010).

[4] C. Menzel, C. Rockstuhl, T. Paul, F. Lederer, and T. Pertsch, "Retrieving effective parameters for metamaterials at oblique incidence," Phys. Rev. B **77**, 195328 (2008)..

[5] Y.G.Ma, L.Zhao, P.Wang, and C.K.Ong, " Fabrication of negative index materials using dielectric and metallic composite route", Appl. Phys. Lett. 93, 184103 (2008)..

[6] T.Cao and M.Cryan, " Study of incident angle dependence for dual band double negative index material using elliptical nanohole arrays," J . Opt. Soc. Am. A, in press

Fluoropolymer-based integrated biophotonics

Kristján Leósson
Dept. of Physics, Science Institute,
University of Iceland, Dunhagi 3, IS107
Reykjavik, Iceland
kleos@hi.is

Björn Agnarsson
Department of Applied Physics,
Chalmers University of Technology, SE-41296
Gothenburg, Sweden
bjorn.agnarsson@chalmers.se

***Abstract* —We describe how an amorphous fluoropolymer, which is well index-matched to aqueous solutions, can be used as a waveguide cladding material, enabling a range of applications in highly integrated biophotonics. Specifically, we report on fluoropolymer waveguide chips integrated with conventional microfluidic circuits, representing a novel lab-on-a-chip platform for evanescent-wave excitation or sensing, with integrated passive and/or thermo-electrically controlled optical circuits for light manipulation. We have also investigated fluorescent conjugated waveguide core polymers as potential on-chip light sources.**

Keywords - Biosensor; Lab-on-a-chip; Polymer waveguides; Integrated biophotonics.

I. INTRODUCTION

Over the last decade there has been rapidly increasing interest in different bio-sensing principles and in new types of biosensors. Among these are optical biosensors which are increasingly being employed for sensing and monitoring applications. Optical sensors are favorable due to their high sensitivity and functional diversity, but also because integrated waveguide circuits can easily be combined with electrical, microfluidic and/or micromechanical components in complex lab-on-a-chip devices for (bio)chemical analysis [1]. Polymers are highly suitable as a material platform, offering a wide range of optical, physical and chemical properties, bio-compatibility, low cost and a large variety of possible processing and patterning techniques.

We have developed an all-polymer waveguide platform that can be used for various types of applications, but is especially suited for excitation and sensing of biological samples and aqueous solutions [2-4]. A special fluorinated polymer, CYTOP (Asahi Glass Co.), with refractive index n=1.34, is used as bottom and (partially) as upper cladding material. An optical polymer of choice can be used as core material. In our studies, we used mainly polymethyl methacrylate (PMMA) or Ormoclear (micro resist technology GmbH), with refractive indices n=1.49 and n=1.54, respectively. Water, buffer solution or a biological solution (refractive index typically in the range 1.33-1.35), containing the specimen to be optically probed or excited, forms a part of the upper cladding layer of the waveguide structure.

CYTOP exhibits high transparency from 200 nm to beyond 2000 nm wavelength and offers strong chemical resistance, non-toxicity and resistance to biodegradation [5]. In spite of its excellent optical characteristics, the use of CYTOP in waveguide fabrication for biophotonics is still not widespread, presumably due to fabrication issues. The untreated CYTOP surface is hydrophobic and securing adhesion in multi-layer photonic structures, such as slab waveguides, has been generally considered to be difficult or even impossible. However, as described below, these difficulties can be overcome, making CYTOP an attractive option as cladding material for a waveguide platform for biophotonics and other dielectric multilayer applications where a low-index optically transparent and chemically stable polymer is needed.

Here, we present the first report of a CYTOP-PMMA-CYTOP waveguide structure fully integrated with a microfluidic circuit, representing a unique lab-on-a-chip platform for biophotonics. Furthermore, we have investigated the use of novel fluorescent polymers as on-chip light sources.

II. FABRICATION

Fig. 1 illustrates a possible fabrication process for a biophotonic chip involving thermo-electric control and integration with microfluidic circuits. Roughly speaking, the process involves the following steps: A suitable substrate is treated with a silane coupling agent to increase adhesion (a). CYTOP is spin-coated and baked at 180°C in an oven. A thin layer of aluminum is deposited on the surface and subsequently removed by wet-etching (b). This treatment is a key factor in making the CYTOP surface hydrophilic and improves adhesion between the CYTOP layer and a subsequently spin-coated polymer layer forming the waveguide core (c). The waveguide core layer can be patterned, e.g., by UV or e-beam exposure (d,e). A photoresist etch stop layer (f) is used to define a sensing region (g). Finally, waveguide channels are encapsulated by spin-coating a CYTOP top cladding layer (h). A layer of photoresist for defining the contact layer is spin-coated on top of a pre-treated CYTOP surface (i), followed by patterning, metallization and liftoff (j). Photoresist is again used to define the sample well (k). Reactive ion etching (RIE) is carried out to selectively etch away the top cladding (l). After RIE, the remaining photoresist is removed using a photoresist remover (m). The surface of the optical chip can now be treated with aminopropyltriethoxysilane (APTES) and bonded to polydimethyl-siloxane (PDMS) for microfluidic applications, following an oxygen plasma treatment (n). Finally, a sample of interest is introduced onto the sensing area in an aqueous solution.

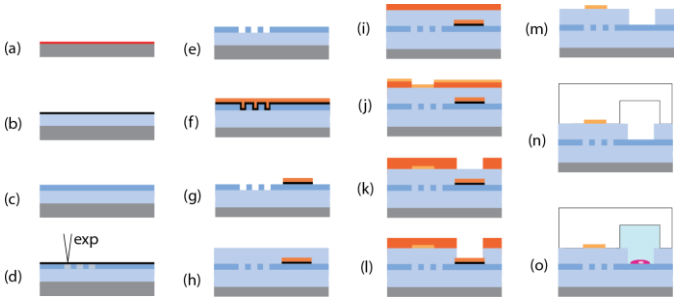


Figure 1. Process flow for fabricating a biophotonic chip with CYTOP waveguide cladding (structures are not to scale). Details are given in the text.

III. PERFORMANCE

Light can be coupled into the high index contrast ($\Delta n \approx 0.25$) waveguides using end-fire coupling from a conventional single-mode optical fiber, or from a tapered lensed fiber to reduce coupling loss. The light can be switched, filtered, modulated, or otherwise manipulated using integrated devices before it is directed to the sensing region(s) were the evanescent part of the guided mode interacts with the sample volume within the penetration depth of the field. The CYTOP bottom cladding plays a crucial role in extending the range of achievable penetration depths of the evanescent part of the mode into the sample, well beyond what is possible with more conventional slab-waveguide systems, such as a high-index oxide on glass, and results in a larger fraction of the excitation power being carried in the evanescent tail on the sample side. For refractive index sensing, this gives improved sensitivity of the guided mode to the cover index [6].

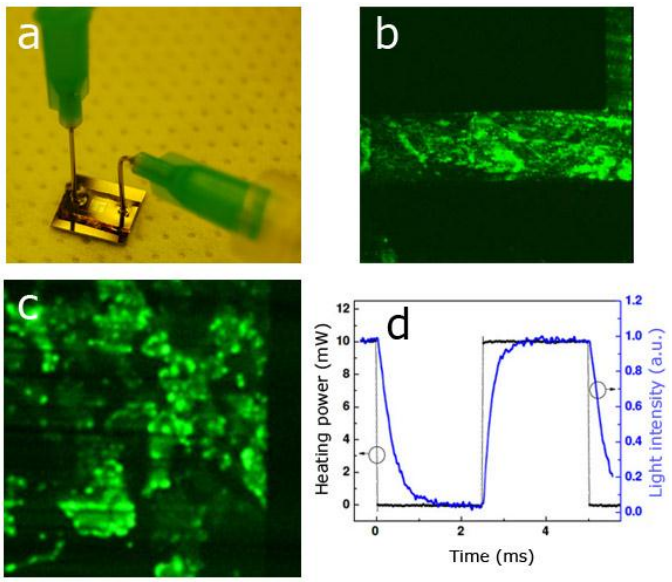


Figure 2. (a) CYTOP-PMMA-CYTOP waveguide chip bonded to a microfluidic circuit. A square-shaped sensing area is visible in the center of the chip. (b) Image of fluorescent beads in water solution passing through a 100-µm wide microfluidic channel above the sensing area. (c) Live dSH2-GFP-expressing cells at the edge of the sensing area. The GFP attaches to focal adhesions in the cells. (d) Example of thermo-optic control; intensity modulation (blue curve) using a Mach-Zehnder interferometer device with a 500 µm x 50 µm footprint, 10 mW driving power and sub-ms response time.

Fig. 2(a) shows a separately patterned PDMS microfluidic circuit with 40-µm deep channels bonded to the waveguide chip. We followed the approach of Ref. [7], using APTES-coating and oxygen plasma treatment to secure a strong polymer-PDMS bond. In Fig. 2(b), fluorescence from polymer beads (Invitrogen FluoSpheres®) in water suspension passing through the microfluidic channel is depicted. Similarly, the near-surface region of live cells expressing a green fluorescent protein (GFP) can be imaged using the evanescent-wave excitation, as shown for transfected pig kidney epithelial (LLC PK1) cells in Fig. 3(c). For applications such as time-lapse imaging of live cells, the excitation can be modulated using on-chip thermo-optic control with a high extinction ratio and sub-ms response time, as illustrated in Fig. 2(d).

End-fire coupling of light from an optical fiber into the waveguides can be highly efficient and wavelength-insensitive. Fiber alignment to high index contrast waveguides, however, imposes a strict tolerance on fiber positioning (10's of nm). This could be partly alleviated using on-chip adiabatic mode conversion, but another interesting option is the incorporation of a light source directly into the waveguide layer. To this end, we have investigated the use of highly efficient fluorescent polymers as waveguide core material, with the potential of realizing optically pumped integrated single-mode laser sources. In particular, we have incorporated an orange-emitting conjugated polymer ADS104RE (American Dye Source) into the CYTOP cladding and tested its performance with respect to external excitation. Fluorescence generated within the waveguide layer was used to monitor scattering from gold nanoparticles in suspension.

ACKNOWLEDGMENT

The project was supported by the Icelandic Science and Technology Policy Council (ISTPC) Framework Programme for Nanotechnology, the ISTPC Graduate Student Fund, the University of Iceland Research Fund, the Reykjavik Energy Environmental and Energy Research Fund and the Icelandic Student Innovation Fund.

REFERENCES

[1] Li, P.C.H., "Microfluidic Lab-on-a-Chip for Chemical and Biological Analysis and Discovery," CRC Press: Boca Raton, FL, USA, 2006

[2] Agnarsson B., Halldorsson J., Arnfinnsdottir N., Ingthorsson S., Gudjonsson T. and Leosson K., "Fabrication of planar polymer waveguides for evanescent-wave sensing in aqueous environments," Microelectronic Engineering 87, 56 (2010)

[3] Halldorsson, J., Arnfinnsdottir, N.B., Jonsdottir, A.B., Agnarsson, B., Leosson, K., "High index contrast polymer waveguide platform for integrated biophotonics," Optics Express 18, 16217 (2010)

[4] Agnarsson, B., Jonsdottir, A.B., Arnfinnsdottir, N.B., Leosson, K., "On-chip modulation of evanescent illumination and live-cell imaging with polymer waveguides," Optics Express 19, 22929 (2011)

[5] Leis, A.P., et al. "Optically Transparent Porous Medium for Nondestructive Studies of Microbial Biofilm Architecture and Transport Dynamics," Appl. Environ. Microbiol. 71, 4801 (2005).

[6] Leosson K. and Agnarsson, B. "Integrated biophotonics with CYTOP," Micromachines, accepted (2012).

[7] Vlachopoulou, M., Tserepi, A., Pavli, P., Argitis, P., Sanopoulou, M., Misiakos, K.., "A low temperature surface modification assisted method for bonding plastic substrates," J. Micromech. Microeng. 19, 015007 (2009).

Enhanced spontaneous emission from single quantum dots inside short photonic crystal waveguides

Johannes Beetz, Matthias Lermer, Sven Höfling and Martin Kamp
Technische Physik, Universität Würzburg
Am Hubland, 97074 Würzburg, Germany
johannes.beetz@physik.uni-wuerzburg.de

Thang Hoang, Leonardo Midolo, Matthias Skacel, Lauren Balet(*), Nicolas Chauvin and Andrea Fiore
Eindhoven University of Technology
COBRA Research Institute
P.O. Box 513, NL-5600MB Eindhoven, The Netherlands
(*) ÉcolePolytechniqueFédérale de Lausanne
CH-1015 Lausanne, Switzerland

We present theoretical and experimental studies of quantum dots (QDs) integrated into short photonic crystal (PhC) waveguides (WGs). Our photoluminescence (PL) data reveals a combined effect of Fabry-Pérot (FP) and slow-light modes, resulting in an increased spontaneous emission rate of the QDs and an improved coupling efficiency to the guided mode. Therewith, our approach has great promise to funnel single photons efficiently (~80%) into PhC WGs and is thus very suitable for integrated quantum photonics applications.

I. INTRODUCTION

Single photon emitters are key building blocks for the implementation of integrated quantum information processing schemes [1]. QDs are perfectly suited for this purpose because they can be easily integrated into semiconductor devices. If embedded into PhC WGs, the QDs benefit from an enhancement of their spontaneous emission by the slow-light effect near the fringe of the WG dispersion. The broad spectral range of the slow-light mode and the large WG mode volume allow for large photon collection efficiencies even in the case of limited spectral and spatial matching.
In contrast to earlier work [2], we investigated short WGs (10-25 µm). WGs with reduced lengths still support slow light modes, but do not suffer under light localization induced by unavoidable fabrication disorder.

II. FABRICATION

The layer structures of our samples are fabricated by molecular beam epitaxy. On top of GaAs substrate a 1.5 µm thick AlGaAs sacrificial layer is grown, followed by a 320 nm GaAs membrane including InAs QDs which emit around 1300 nm. An intermediate SiO_2 etch mask is deposited on the surface before a resist is patterned by electron beam lithography. When the holes of the PhC lattice are defined, one line of holes is omitted in order to form a W1 WG. The pattern is transferred into SiO_2 by CHF_3/Ar reactive ion etching and into the substrate by Cl_2/Ar electron cyclotron resonance etching. Afterwards, the sample is cleaved and both the sacrificial layer and the residual SiO_2 are removed by hydrofluoric acid. Fig. 1 shows the suspended membrane of a fabricated device [3].

III. EXPERIMENTAL RESULTS

For optical characterization the QDs in the center of the WG are excited from the top and the PL is measured either from the top of the device or from the side at the cleaved facet.
In Fig. 2 the obtained spectra of a 17 µm long WG at room temperature are shown next to calculations of the corresponding band diagram [4]. When the PL is collected from above only the first-order guided mode is visible due to its polarization along the defect line of the WG. The fundamental mode on the other hand is polarized perpendicular to the WG and hence detected from the side. The intensity is higher near the cut-off at the low frequency side of the mode where the slow-light regime is prevalent. The FP modes which arise from the two WG end facets and appear only for the propagating fundamental mode, allow for an investigation of the slow-light effect. The spectral distances of the FP peaks is becoming smaller when the band edge is approached, which proves a strong increase in the photon group index. In addition, the Q-factor is increasing, giving evidence that the light is contained in the WG for a longer time owing to the slow-light effect.
Moreover, the expected decrease of the exciton decay time τ is confirmed by time-resolved measurements at low temperature. By comparing emission lines located away from (τ=1.6 ns) and in the slow light regime (τ=0.8 ns), we calculate an enhancement of the spontaneous emission by a factor of 1.7.

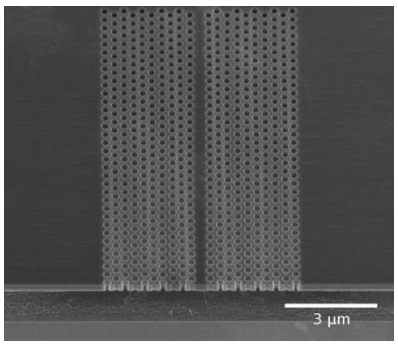


Figure 1.A scanning electron microscope image of a PhC WG.

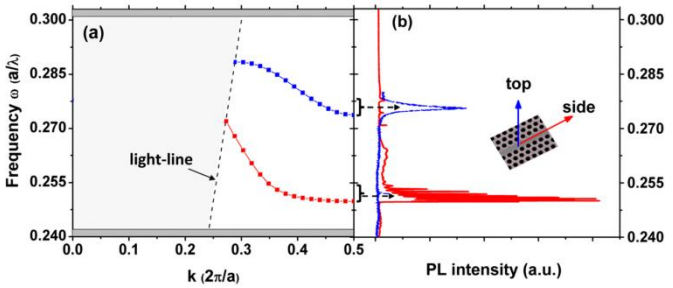


Figure 2.(a) Calculated band diagram and (b) PL data of a W1 PhC WG.

Furthermore, we determined the coupling efficiency into the slow-light mode to be ~80%.

The undoped GaAs membrane used for the devices presented here can also be replaced by a p-i-n diode structure, enabling Stark tuning of the quantum dot. This could be useful for a precise matching of the emission with the slow light mode and for applications where a control of the wavelength is required.

IV. CONCLUSION

We demonstrated that short PhC WGs can enhance the spontaneous emission rate of integrated QDs and the coupling efficiency into the slow-light mode, making this device schema a promising candidate as single photon source for future on-chip photonic circuits.

ACKNOWLEDGMENT

This work is supported by the European Commission within the FP7 project QUANTIP.

REFERENCES

[1] J. L. O'Brien, A. Furusawa and J. Vuckovic, "Photonic quantum technologies", Nature Photon., vol. 3, pp 687-695, 2009

[2] T. Lund-Hansen, S. Stobbe, B. Julsgaard, H. Thyrrestrup, T. Sünner, M. Kamp, A. Forchel, and P. Lodahl, "Experimental Realization of Highly Efficient Broadband Coupling of Single Quantum Dots to a Photonic Crystal Waveguide", Phys. Rev. Lett., vol. 101, 113903, 2008.

[3] T. B. Hoang, J. Beetz, L. Midolo, M. Skacel, M. Lermer, M. Kamp, S. Höfling, L. Balet, N. Chauvin, and A. Fiore, "Enhanced spontaneous emission from quantum dots in short photonic crystal waveguides", Appl. Phys. Lett., in press (arXiv:1201.2874v1).

[4] S. Johnson and J. Joannopoulos, "Block-iterative frequency-domain methods for Maxwell's equations in a planewave basis", Opt. Express, vol. 8, pp. 173-190, 2001.

Passive SOI devices for the Short-wave-infrared

F. Leo, B. Kuyken, N. Hattasan, R. Baets and G. Roelkens
Photonics Research Group, INTEC, Ghent University/imec, B-9000 Ghent, Belgium
Center for nano- and bio-photonics (NB-Photonics), B-9000 Ghent, Belgium
email : francois.leo@intec.ugent.be

***Abstract*—In this paper we report on passive silicon-on-insulator devices for the short-wave-infrared wavelength region. Substantial improvements are achieved for grating couplers, waveguides and ring resonators.**

Keywords – short-wave-infrared; silicon-on-insulator

I. INTRODUCTION

Silicon-on-insulator has attracted a lot of attention in the last decade for photonic applications. At first mainly driven towards telecom applications, the research on SOI optical devices is extending more and more to other applications such as nonlinear optics and gas sensing. In both cases, extending the basic SOI structures to cover the short-wave infrared and Mid-IR region would be highly beneficial. For sensing, the main reason is that many molecules have distinct absorption bands in this region [1]. This allows for unambiguous detection of the presence and concentration of certain molecules. In nonlinear optics, working at longer wavelengths reduces the parasitic nonlinear absorption in silicon, the two-photon absorption (TPA), enormously. Without TPA it is possible to fully benefit from the record nonlinear parameters obtained through the combination of the high linear index leading to high confinement and the high nonlinear index of silicon. This has been recently confirmed by implementations of highly efficient nonlinear optical devices enabling high parametric gain [2] and efficient supercontinuum generation [3]. In this paper we report on highly efficient grating couplers, low loss waveguides and high finesse resonators for the 2.2 μm region.

II. GRATINGS

Grating couplers for the short-wave-infrared have been recently reported by our group [4]. Here we present a more thorough experimental investigation of these gratings. These gratings are fabricated in the 200 mm CMOS pilot line at imec with 193nm DUV lithography. We refer the reader to [4] for more details on the fabrication. The gratings have been measured using standard single mode fibers under an angle of 10 degrees. First the grating period dependence was studied, allowing to reach a record -3.8 dB coupling losses around 2080 nm, with a period of 970 nm (not shown).

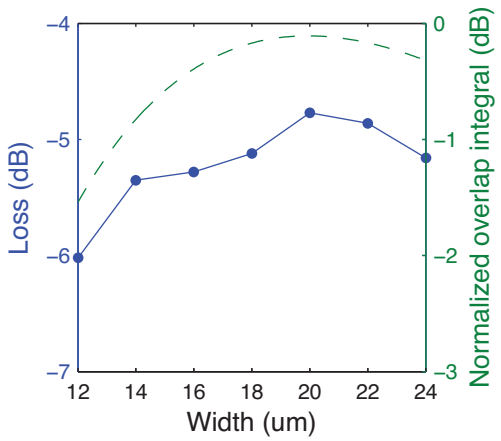


Fig. 1 : Influence of the waveguide width on the attainable fiber-to-chip coupling efficiency

In order to reach such values for longer wavelengths, we then fabricated gratings with different width to study the effect of the transversal overlap between the SOI mode and the fiber mode. The grating under investigation has a period of 1050 nm and a 35% fill factor. The lowest coupling losses are measured at 2240 nm. Fig. 1 shows the evolution of the coupling losses at 2240 nm for different waveguide widths (blue line). It is compared with the theoretical dependence (dashed green line), obtained by calculating the overlap between the mode in the grating and the mode in the fiber. The $1/e^2$-width of the latter was taken to be 13.6 um. We see a good agreement, showing that varying the width has significant impact on the coupling losses. However, it didn't allow reaching such low values than the one measured at 2080 nm with a shorter period. The reason for this is still under investigation.

III. WAVEGUIDES

In this section we report on record low losses of 0.6 dB/cm for single mode waveguides in the short-wave infrared region. The silicon photonic wires used are fabricated in a CMOS pilot line, using 200 mm SOI wafers consisting of a 220 nm silicon waveguide layer on a 2 μm buried oxide layer. The wires are 900 nm wide with no top cladding and are etched through the 220nm silicon waveguide layer. The losses are

measured using a cutback technique. The light is coupled in and out of the waveguides through grating couplers. Fig. 2 shows the measured losses over the grating coupler optical

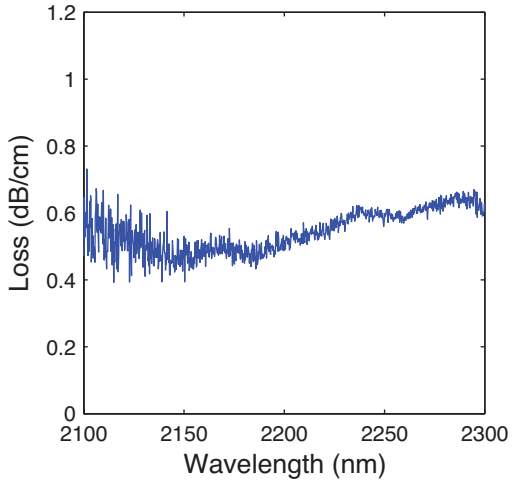


Fig. 2 : Waveguide loss as a function of wavelength for 900nm wide silicon wire waveguides

bandwidth. Let us point out that the strong optical confinement of such waveguides results in a very high effective nonlinearity parameter. It has been estimated to be 150 $(W \cdot m)^{-1}$ [3].

IV. Rings

Fabry-Perot cavities are essential to the fields of nonlinear optics and sensing as they allow increasing both the propagating power and the interaction length (see e.g. [5]). In particular, there is recently a lot of interest in integrated frequency combs [6]. These are equally spaced spectral lines generated from parametric frequency conversion in a high Q microresonator. Integrated combs have been experimentally generated in many different configurations, such as silica toroidal microcavities [7] and Si_3N_4 ring resonators [8], but remain to be observed in silicon. The applications of such a comb lies in precision spectroscopy, atomic clocks and molecular fingerprinting. A silicon microresonator could potentially allow for the integration of such a frequency comb. Here we report on the fabrication of resonators with a finesse of 130, corresponding to a loaded Q of 75000. A microscope picture of the ring is presented on Fig. 3. The ring circumference is 350 µm, the gap is 450 nm and the coupling length is 20 µm. The waveguides are 900nm wide. By injecting the ASE of our laser source through a grating coupler and by looking at the outcoupled spectrum on a SWIR optical spectrum analyzer, a FSR of 3.9 nm can be observed. The changes in depth of the different resonances is due to the limited resolution of our OSA (50 pm). To measure the full width at half maximum we work at one single wavelength and tune the chip's temperature. We measured a finesse of 130, which corresponds to a FWHM of 30 pm. Moreover, we found an on-resonance extinction of more than 13dB showing that our ring is very close to critical coupling.

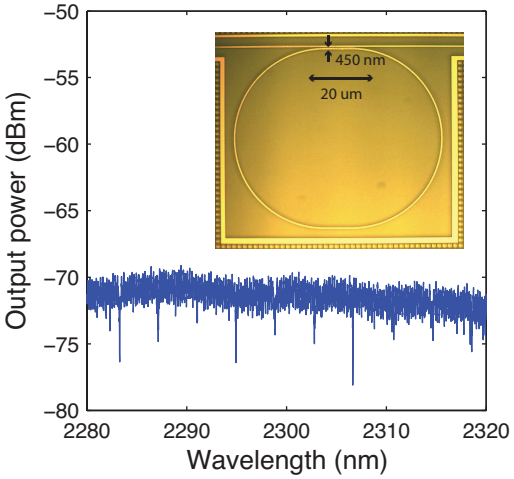


Fig. 3 : Observed transmission spectrum of high-Q ring resonators for the short-wave infrared.

V. Conclusion

While silicon photonics has mostly been used for 1.3µm and 1.5µm applications, we highlight the potential of this platform for longer wavelengths. This observation could lead to the use of SOI waveguide circuits for a new range of applications, including spectroscopic sensing and nonlinear optics.

Acknowledgment

This work was carried out in the framework of the ERC-MIRACLE and the ERC-InSpectra project

References

[1] Crowder *et al*., "Infrared methods for gas detection," in Mid-infrared semiconductor optoelectronics, Springer 2006

[2] B. Kuyken *et al*., "50 dB parametric gain in silicon photonic wires", Optics Letters, 36(21), pp. 20172-20181 (2011)

[3] B. Kuyken *et al*., "Mid-infrared to telecom-band supercontinuum generation in highly nonlinear silicon-on-insulator wire waveguides", Optics Express, 19(22), pp. 4401-4403 (2011)

[4] B. Kuyken *et al*., "Highly efficient broadband silicon-on-insulator grating couplers for the short wave infrared wavelength range," Integrated Photonics Research, Silicon and Nano-Photonics (IPR), Canada, p.IMB6 (2011)

[5] N.A Yebo, P. Lommens, Z. Hens, R. Baets, 'An integrated optic ethanol vapor sensor based on a silicon-on-insulator microring resonator coated with a porous ZnO film', Optics Express, 18(11), pp 11859-11866 (2010)

[6] T.J. Kippenberg, R. Holzwarth and S.A. Diddams, "Microresonator-based opticql frequency combs, Science, 332(6029), pp 555-559 (2011)

[7] P. Del'Haye *et al*., "Optical frequency comb generation from a monolithic microresonator", Nature, 450(7173), p.1214-1217 (2007)

[8] J.S.Levy *et al*., "CMOS-compatible multiple-wavelength oscillator for on-chip optical interconnects," Nat. Photon. 4(1), 37-40 (2010)

A Polarization Beam Splitter based on MZI-Structure

Ruiyong Zhang*, H.-G. Bach, R. Kunkel, K. Janiak, P. Runge, G. Zhou, A. Seeger and S. Schubert
Department of Photonic Components
Fraunhofer Institute for Telecommunications
Heinrich Hertz Institute
Berlin, Germany
*Ruiyong.zhang@hhi.fraunhofer.de

Sebastián Romero García, Alejandro Ortega Moñux, Robert Halir and Iñigo Molina Fernández*
Departamento de Ingeniería de Comunicaciones
Universidad de Málaga
Málaga. Spain
imf@ic.uma.es

***Abstract*—This paper describes a polarization beam splitter (PBS) based on Mach-Zehnder-Interferometer and fabricated in InP technology. The splitting ratio (SR) is better than 16 dB over the optical C-Band.**

Keywords-PBS; InP; Integrated Optics; Optical lithography

I. INTRODUCTION

To extend the data capacity for next generation networks quadrature phase shift keying (QPSK) modulation format and polarization multiplexing is adopted. Therefore PBS becomes a key component in integrated optical receivers. PBSs have already been realized with InP technology with different methods like directional coupler with metal overlay [1], Mach-Zehnder interferometer (MZI) integrated with polarization converter [2], or by modal birefringence of higher order modes [3]. In this paper, we present a PBS based on MZI-structure fabricated with a single optical lithography step. Our design does not require a polarization rotator like in [2], and we use waveguide widths to introduce birefringence rather than metal overlay as in [4].

II. DESIGN AND FABRICATION

The schematic layout of the MZI-PBS is shown in figure 1. It is composed of two identical 2x2 multimode interference couplers (MMI) and two straight waveguides between the MMIs.

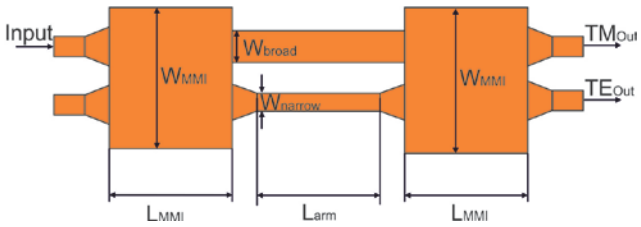


Figure 1. Schematic view of the MZI-PBS

The first MMI equally splits the input light into two straight waveguides with a phase difference of 90° for both polarizations. Subsequently, the arm length and widths are designed to achieve a 180° phase shift between TE and TM polarization.

$$\Delta\varphi_{TE} = k_0 \left(N_{eff,broad,TE} - N_{eff,narrow,TE}\right) L_{arm} = 0 \qquad (1)$$

$$\Delta\varphi_{TM} = k_0 \left(N_{eff,broad,TM} - N_{eff,narrow,TM}\right) L_{arm} = \pi \qquad (2)$$

Here, k_0 is the wave number, N_{eff} is the effective refractive index of the mode, L_{arm} is the length of the straight waveguides. The subscripts broad and narrow refer to the upper and the lower waveguides respectively. After the first MMI and the straight waveguides, the relative phase differences between the upper and the lower path are 90° and 270° for TE and TM, respectively. After the second MMI, TM polarization is eliminated in the lower output of the PBS and TE polarization is eliminated in the upper output.

The PBS is integrated on a semi-insulating waveguide layer stack being composed of three quaternary optical guiding layers embedded within InP and an upper thicker waveguide layer. The deeply etched rib waveguide was patterned using optical lithography and dry etching techniques. A fabricated PBS-chip is depicted in Figure 2.

The two facets of the chip are anti reflection coated against air.

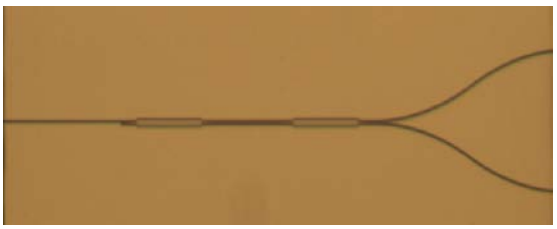


Figure 2. Top view of the fabricated chip

III. MEASUREMENTS

After fabrication and anti reflection coating the PBS was characterized. A tapered single mode fibre was used for coupling the light into the chip. At the output side we used a collimator to couple the light into a measurement photodiode. The polarization of the input light was set to TE and TM separately. The splitting ratio was calculated from the

photocurrent of the photodiode. The splitting ratios for the two polarization states are defined as follows:

$$SR_{TE} = 10 \log (I_{TE\_Out}/I_{TM\_Out}) \quad (3)$$

$$SR_{TM} = 10 \log (I_{TM\_Out}/I_{TE\_Out}) \quad (4)$$

where I_{TE_Out} and I_{TM_Out} are the measured photocurrents for the output TE and the output TM, respectively.

The measurement results (solid lines) for SR are depicted in figure 3 together with the simulated curves (dashed lines).

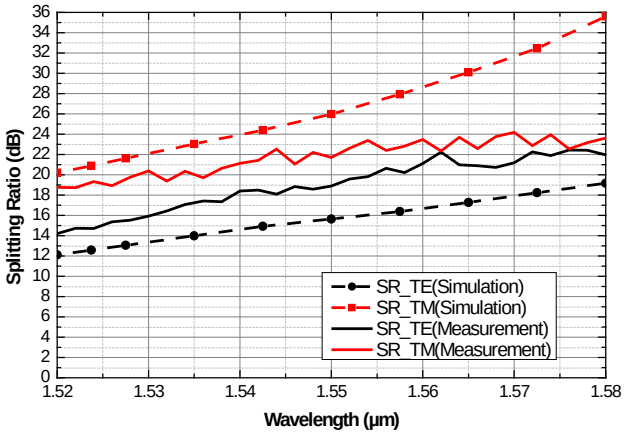


Figure 3. Simulated (dashed lines) and measured SR (solid lines)

Figure 3 shows that the splitting ratio is better than 16 dB over the optical C-Band for both TE and TM. The best value arrives at 22 and 24 dB for TE and TM, respectively. The saturation of the measured SR around 24 dB can be attributed to a limitation of the measurement setup. According to the measured dimension of the PBS using atomic force microscopy (AFM), a simulation was carried out, which indicates a reasonable agreement with the measurements. The measurement errors of the AFM could be attributed to the uncertainty between simulation and measurement.

The measured insertion loss is also calculated and depicted in figure 4. It is defined as follows:

$$IL_{TE} = 10 \log ((I_{TE\_Out}+I_{TM\_Out}) /I_{TE}) \quad (5)$$

$$IL_{TM} = 10 \log ((I_{TE\_Out}+I_{TM\_Out}) /I_{TM}) \quad (6)$$

where I_{TE} and I_{TM} are measured photocurrents as references without the PBS.

The relatively high insertion loss stems from the coupling loss between the tapered fibre and deeply etched straight waveguide. Although required for mode matching, we did not integrate a spot size converter to avoid any unwanted influence on the TE/TM loss difference.

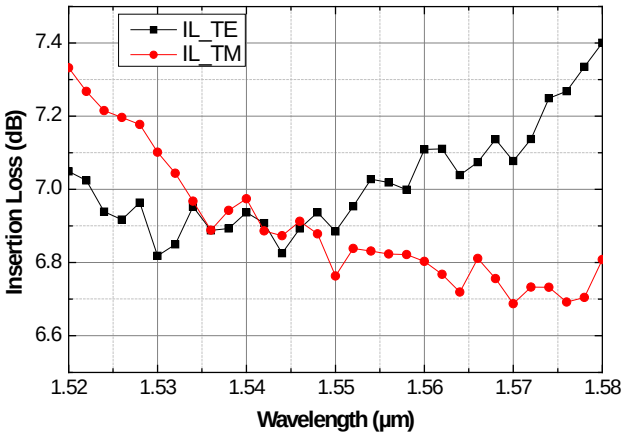


Figure 4. Measured inertion loss as a function of wavelength

CONCLUSION

We designed and fabricated a PBS based on MZI-Structure using different waveguide widths to get the necessary birefringence. The splitting ratio of the PBS achieved more than 16 dB over the optical C-Band.

ACKNOWLEDGMENT

The authors gratefully acknowledge contributions from their colleagues W. Ebert, D. Schmidt, R. Graulich and R. Steingrüber at the FhG Heinrich-Hertz-Institut, Berlin. We thank colleagues A. Steffan and J. Honecker from u2t for giving some helpful ideas. This work was financed partly by the EU project MIRTHE.

REFERENCES

[1] Albrecht et al, “TE-TM mode splitters on InGaAsP-InP,” IEEE Photonics Technology Letters, Vol. 2, No. 2, Feb. 1990.

[2] Augustin et al, “A Compact Integrated Polarization Splitter_Converter in InGaAsP/InP”, IEEE Photonics Technology Letters, Vol. 19, No. 17, September 2007.

[3] J. J. G. M. van der Tol et al, “A short polarization splitter without metal overlays on InGaAsP/InP”, IEEE Photonics Technology Letters, Vol. 9, No. 2, FEBRUARY 1997.

[4] L. B. Soldano et al, “Mach-Zehnder Inteferometer Polarization Splitter in InGaAsP/InP”, IEEE Photonics Technology Letters, Vol. 6, No. 3, March 1994.

Silicon-based light sources: En route to the first injected Silicon laser emitting at 1.54 μm

J. M. Ramírez, F. Ferrarese Lupi, Y. Berencén, D. Navarro-Urrios, O. Jambois, L. López-Conesa, , S. Estradé, F. Peiró, B. Garrido

MIND-In2UB, Department of Electronics
University of Barcelona (UB), Barcelona, Spain

J.M. Rebled
Inst. Cièn. de Mat. de Barcelona (CSIC),Bellaterra, Spain

A. Tengattini, N. Prtljaga, A. Anopchenko, L. Pavesi

Nanoscience Laboratory, Department of Physics
University of Trento, Italy

J.M. Fedeli
CEA, Léti, Minatec campus 17 rue des Martyrs, 38054
Grenoble cedex 9, France.

***Abstract*— Metal-oxide-semiconductor light emitting devices were fabricated by means of a Si-rich silicon oxide layer with Er^{3+} ions implanted. The electroluminescence of different materials was studied. Active ring resonators electrically pumped were fabricated and tested.**

Keywords-silicon nanocomposites; erbium; carrier injection; electroluminescence; power efficiency.

I. INTRODUCTION

In the last years, Silicon-based light sources have been a matter of interest for the scientific community [1]. They provide several improvements and breakthroughs towards the electro-photonic all-silicon implementation by means of the Complementary Metal Oxide Semiconductor (CMOS) technology. Following this idea, some works insisted on the possibilities of exploiting the emission of the first excited level of Er^{3+} ions to achieve reliable and efficient light sources electrically pumped emitting at 1.54 μm. Among a number of materials used as erbium hosts, the SiO_2 with silicon nanoclusters (Si-ncs) has demonstrated to be the most successful because of the optimum environment for Er^{3+} ions, its non-resonant large bandgap (9 eV) and the higher carrier injection provided. Moreover, superior electro-optical performances can be obtained by using a multilayered structure of SiO_2 and non-stoichiometric (SiO_x) layers with Er^{3+} ions [2]. Optical gain under electrical pumping should be possible if an optimized active material is inserted in a high quality resonant cavity. Such a device has never been presented in the literature, because i) the active material has still to be optimized to obtain the inversion population of Er^{3+} by electrical pumping, ii) the SiO_x:Er material is a low refractive index material. Therefore a suitable photonic structure has to be designed in order to confine the light inside. A previous work [3] has managed to get round this difficulty by demonstrating theoretically how to confine the light in this material by using a slot structure. Such a proposal to guide the light is shown as a promising candidate to get a Si-based injection laser. In this paper, we show the work done toward the fabrication of such device and preliminary characterization.

II. EXPERIMENTAL AND RESULTS

A. Fabrication

Multilayered NMOS capacitors were fabricated with a standard CMOS technology, where the control oxide has been replaced by an active multilayer structure. Fig. 1a shows the device structure. Each layer was deposited by Low Pressure Chemical-Vapour Deposition (LPCVD). The silicon excess was introduced either by deposition of SiO_x layers or by Si ion implantation after the deposition of the SiO_2. In particular, two different Si excess were nominally defined for each single layer (20% or 25%). Table I summarizes the composition of the multilayered structures.

TABLE I

MULTILAYERS	
((2 nm 0 % + 3 nm 20 %) x10)+2 nm 0 %	***M1***
((2 nm 0 % + 3 nm 25 %) x10)+2 nm 0 %	***M2***
((2 nm 0 % + 4 nm 20 %) x8)+2 nm 0 %	***M3***
((2 nm 0 % + 4 nm 25 %) x8)+2 nm 0 %	***M4***
((3 nm 0 % + 3 nm 20 %) x8)+3 nm 0 %	***M5***
((3 nm 0 % + 3 nm 25 %) x8)+3 nm 0 %	***M6***
((3 nm 0 % + 4 nm 20 %) x7)+3 nm 0 %	***M7***
((3 nm 0 % + 4 nm 25 %) x7)+3 nm 0 %	***M8***
Dry thermal SiO2	***M9***

Detailed multilayer composition.

Then, a conventional annealing for 1 hour at 900ºC was done in order to obtain the Si-ncs segregation. Finally, an Er^{3+} implantation of about $1x10^{20}$ at/cm^3 was done at 25 keV of energy in all layers. The activation of erbium ions was achieved applying a post-annealing treatment at 800ºC for 6 hours. Notice that there is one device which is not a multilayer structure (M9). This device was fabricated as a Si-ncs free single SiO_2 layer (dry thermal oxide), and used as a reference. A phosphorous-doped polysilicon layer ($1x10^{20}$ at/cm^3) 100 nm thick was deposited on top of the active layers and used as semitransparent electrode. Finally, a new set of devices consisting on optically active ring resonators (μ-cavities) coupled to passive slot waveguides (WG) was designed and fabricated. A slot WG cross-section was required in order to accomplish both the guidance of the light and the effective electrical pumping inside the resonant structure. The new

batch was split in LPCVD multilayers (with the best fabrication parameters obtained from the NMOS capacitors) and Plasma Enhanced Chemical-Vapour Deposition (PECVD) multilayers, for comparison. The total thickness of the multilayer structures was inferred from TEM images (Fig. 1b), showing a good agreement between the nominal (50 nm) and experimental values (53 nm).

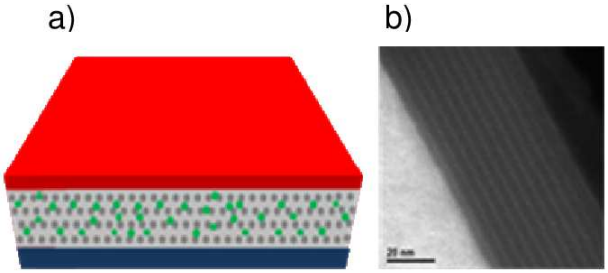


Figure 1: (a) schematic view of the multilayered structure. (b) EFTEM image of a PECVD multilayer obtained by filtering for the c-Si plasmon signal (17 eV).

B. Material optimization

An electro-optical characterization was carried out in all devices. The electroluminescence (EL) spectrum in the infrared was obtained when polarizing under accumulation regime for all devices (see inset of Fig. 2). Essential parameters such as the layer resistivity, the threshold voltage or the optical power at 1.54 µm were obtained. Another interesting feature is the power efficiency (PE), which takes into account the ratio between the injected electrical power and the optical power generated. Fig. 2 shows the averaged PE of devices as a function of the Si excess. Two series of devices have been identified depending on their SiO_2 layer thickness (2nm thick oxides have been marked with black squares and the ones 3nm thick with red circles). A maximum value of the power efficiency is observed in the sample with the lowest Si excess and the thinnest oxide layers, obtaining values around 0.045%. In addition, the PE value for the pure SiO_2 layer has been highlighted with a horizontal blue dashed line.

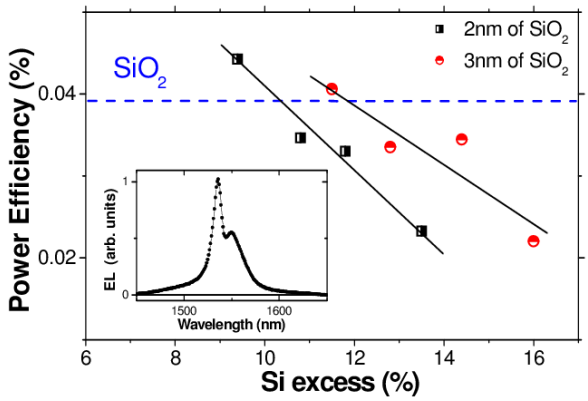


Figure 2: Power efficiency values as a function of the Si excess for the multilayer structures. Two different trends are observed, depending on the SiO_2 layer thickness. Straight lines are guides to the eye. The inset shows a typical EL spectrum at 1.54 µm.

C. Slot structures characterization

Propagation loss measurements have been performed at 1532 nm on the slot WG structures by means of the cut-back technique. It is worth to notice that the cross section of the WG structure in which we performed the losses measurements is the same of that of the resonators. For those set of samples, average losses values of 35 dB/cm have been found.

In order to get more insight on the µ-cavities, transmission measurement have been performed through the ring resonators, using a tuneable laser in a wavelength range around 1535 nm. A maximum Q factor of 2.5 x 10^4 has been found for a resonance at 1546.2 nm (see Fig. 3). These values are comparable with the ones present in literature for similar electrically active slot structures [4].

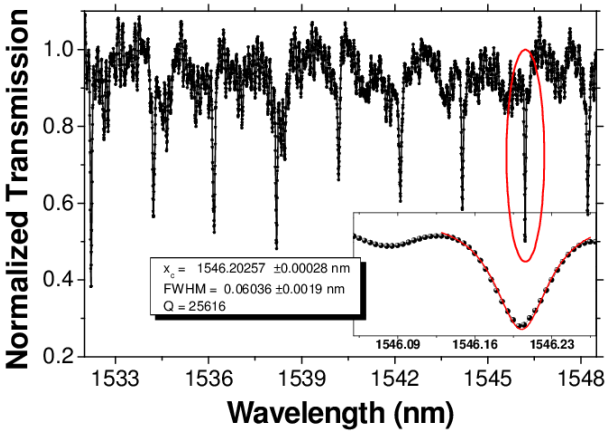


Figure 3: TM polarized transmission spectrum of a 50 µm radius ring, coupled with a 1µm wide waveguide and coupling distance of 220 nm. The inset shows a Lorenzian fit of one particular resonance (red line) at 1546 nm.

III. CONCLUSIONS

Erbium doped multilayer structures were fabricated and embedded in NMOS like capacitors for the electro-optical characterization. An optimization of the material was done in terms of the layer resistivity, voltage threshold, optical power and power efficiency. The best layers were chosen in order to fabricate electrically driven and optically active resonant cavities (slot WG ring resonators). The passive characterization of the structures showed good Q factors and losses comparable with the literature, suggesting a good scenario for the development of the first injected Si laser at 1.54 µm.

ACKNOWLEDGMENT

This work was supported by Spanish Ministry of Science and Innovation and by the EC through the projects TEC 2008-08359 and ICT-FP7-224312 HELIOS and by Italy-Spain integrated actions. FIB facilities at PCB-UB and TEM facilities at CCiT-UB are also acknowledged.

REFERENCES

[1] Y. Berencén, O. Jambois, J. M. Ramírez, J. M. Rebled, S. Estradé, F. Peiró, C. Domínguez, J. A. Rodríguez, and B. Garrido; Optics Letters, vol. 36 (2011) 2617.

[2] A. Marconi, A. Anopchenko, M. Wang, G. Pucker, P. Belluti, and L. Pavesi; *Appl. Phys. Lett.* Vol. 94 (2009) 221110.

[3] V.R. Almeida, Q. Xu, C.A. Barrios, and M. Lipson; Optics Letters, vol. 29 (2004) 1209.

[4] K. Preston and M. Lipson; Optics express, Vol 17 (2009) 1527.

40 Gb/s lateral vs vertical Ge-on-Si photodetectors integrated in silicon waveguides

Laurent Vivien, Delphine Marris-Morini, Paul Crozat, Eric Cassan
Institut d'Electronique Fondamentale, Université Paris-Sud, Orsay - France

Johann Osmond
ICFO, Castelldefels - Spain

Jean Michel Hartmann, Christophe Kopp, Jean Marc Fédéli
Minatec Campus, CEA, LETI, Grenoble - France

Andreas Polzer, Horst Zimmermann
Institute of Electrodynamics, Microwave and Circuit Engineering, Vienna University of Technology, Vienna - Austria

Abstract—**We report and compare results obtained on Ge-on-Si photodetectors in lateral and vertical configurations. A bandwidth of 120GHz was obtained for the lateral photodetector. Both types shown operation up to 40 Gb/s.**

Keywords-Silicon photonics; germanium; photodetector; integrated optics.

I. INTRODUCTION

Very fast optical telecommunications are technologically very challenging. The ever growing demand of faster transmissions and larger volume of information at high bit rates pushes forward research on high speeds and large bandwidths. Among building blocks necessary to achieve an optical circuit with such requirements, as sources [1] or modulators [2], photodetectors are the key component to convert optical signals into electrical ones. Currently, large bandwidth photodetectors are fabricated with III-V materials. III-V materials are however not fully compatible with the mainstream CMOS Si technology and III-V based components require expensive and challenging fabrication technologies. One alternative material is Ge, a Si compatible material which shows a strong absorption in the telecommunication wavelength range, and that allows to fabricate a photodetector monolithically integrated on a Si platform [3]. Such a technology is moreover compatible with CMOS circuitry. We present and compare in this work two different Ge-on-Si photodetectors, both showing large bandwidths and high speed operation.

II. FABRICATION

The two detectors present different p-i-n diode geometries, as schematically shown in Fig. 1. Fig. 1a represents a lateral geometry where the p, i and n doped regions are on the same horizontal plane [4] whereas on the vertical configuration shown in Fig. 1b the p-i-n diode is in a vertical stack [5]. These devices were fabricated on 8 inch SOI wafers with 0.4µm thick Si layer and 1µm thick buried oxide. Passive circuitry was first realized by Deep-UV lithography and reactive ion etching. In particular rib Si waveguides were obtained by etching 110nm of Si. A recess at the end of the waveguide was then defined by etching Si down to a residual thickness of 50nm. In the case of the lateral configuration, the length and the width of the recess were 10µm and 0.5µm, respectively.

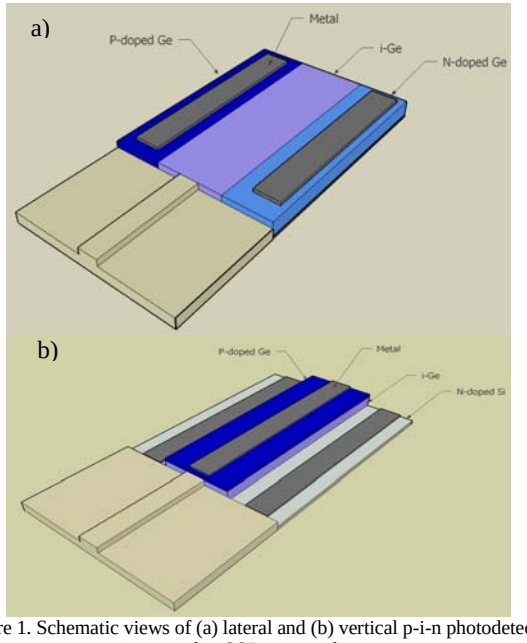


Figure 1. Schematic views of (a) lateral and (b) vertical p-i-n photodetector integrated in SOI waveguides.

Undoped Ge was then epitaxially selectively grown in the recess by Reduced Pressure-Chemical Vapour Deposition (RP-CVD). A photolithographic step was used to defining the first implantation area where boron ions were implanted. A second lithographic step with a phosphorus ion implantation permitted to define the n-doped region of the photodetector. In the case of Ge vertical photodetector, the 50nm thick Si layer at the bottom of the recess was first locally implanted with phosphorus ions to form the N+ ohmic contact. 340 nm of intrinsic Ge capped by 90 nm of in-situ boron-doped Ge are then selectively grown by RP-CVD in the silicon recess. Bottom contacts were defined by UV lithography followed by an etching step down to the N+ silicon region which defines a 3µm wide Ge mesa, whereas its length is 15um.

Ti/TiN/AlCu/Ti/TiN metal stack was then used to form contacts on p and n regions in both cases.

III. RESULTS

The dark current as a function of applied bias was measured at -1V bias for both Ge photodetectors. Dark current values of 4 µA and 18 nA were measured for lateral and vertical configurations, respectively. The relatively high value of the lateral detector dark current was probably due to dopant diffusion during annealing.

The optical responsivity of the Ge photodetectors was measured for a wavelength of 1550nm: 0.8 A/W in the lateral configuration and 0.9 A/W in the vertical configuration. Saturation value was obtained already at 0.1V and 0.3 V, respectively, showing a good collection efficiency of photogenerated carriers.

Normalized optical bandwidths at 1550 nm wavelength are plotted in Fig. 2. In the case of the lateral configuration -3 dB cutoff frequency was estimated to be as high as 120 GHz at -2V bias. The bandwidth was measured with three different techniques and only the one using the beating of two near optical lasers coupled with a 110GHz electrical spectrum analyzer could reach the required frequency range. On the other side the vertical configuration shows a bandwidth of 42 GHz with a reverse bias of 4V. The larger bandwidth of lateral photodetectors compared to vertical photodetectors is likely due to the dopant diffusion during the annealing step, thus reducing the intrinsic region of the diode.

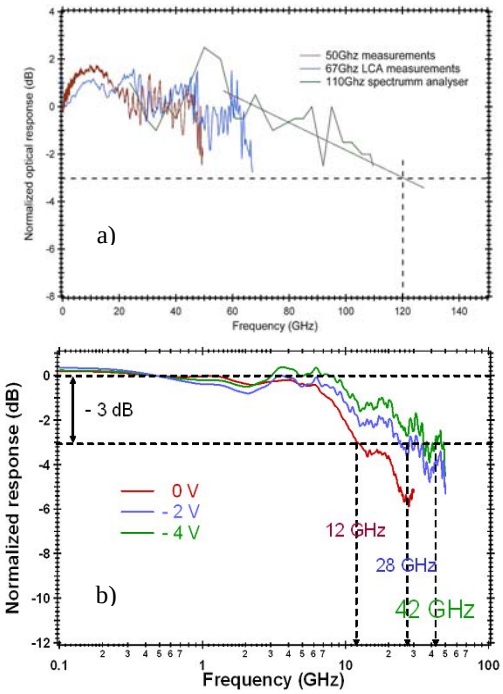


Figure 2. Normalized optical response at 1550 nm wavelength of the (a) lateral and (b) vertical Ge photodetector as a function of frequency for 2V reverse bias voltage and 0, 2 and 4V reverse biases, respectively.

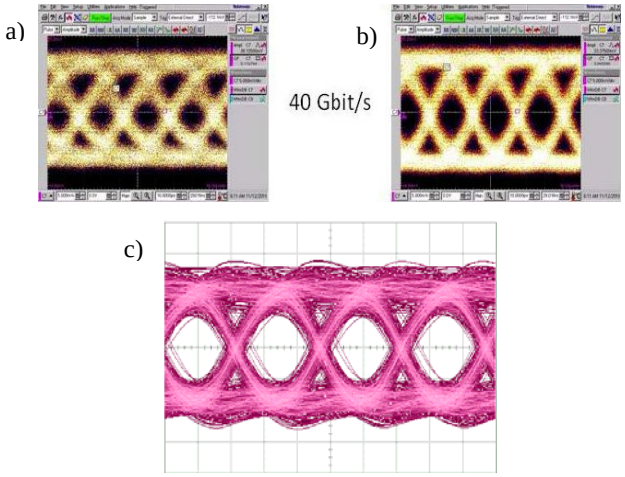


Figure 3. Open eye diagram at 40 GBit/s and at 1550 nm wavelength for lateral photodetector at 0V bias (a) and -1V bias (b) and for vertical photodetector at -4V bias (c).

The data transmission at 40 Gb/s of these Ge waveguide photodetectors were finally checked. Open eye diagrams were obtained for both types of detectors already at zero-bias for lateral configuration (see Fig. 3a and 3b) and at 4V reverse bias for the vertical configuration (see Fig. 3c).

These results demonstrate that very high bandwidths and operation up to 40 Gb/s can be obtained for Ge-on-Si integrated photodetectors. These performances of an important building block in silicon photonics will help in merging integrated optics and electronics for ultra-fast data transmission.

ACKNOWLEDGMENT

The research leading to these results has received funding from the European Community's under grant agreement n° 224312 HELIOS and from the French ANR under project MICROS.

REFERENCES

[1] J. Liu, X. Sun, R. Camacho-Aguilera, L. C. Kimerling, and J. Michel, "Ge-on-Si laser operating at room temperature," Opt. Lett., vol.35 (5), pp. 679–681, 2010.

[2] D. Marris-Morini et al., "Recent Progress in High-Speed Silicon-Based Optical Modulators," Proc. IEEE, vol. 97(7), pp. 1199–1215, 2009.

[3] J. Michel, J. Liu, and L. C. Kimerling, "High-performance Ge-on-Si photodetectors," Nature Photonics, vol. 4, pp. 527–534, July 2010.

[4] L. Vivien et al., "42 GHz p.i.n Germanium photodetector integrated in a silicon-on-insulator waveguide," Opt. Express, vol. 17(8), pp. 6252–6257, 2009.

[5] L. Vivien et al., "Zero-bias 40Gbit/s germanium waveguide photodetector on silicon," Optics Express, vol. 20 (2), pp. 1096-1101, 2012.

Influence of waveguide thickness on the angular color impression of nanostructured organic emission layers

C. Kluge, P. Metz, A. Pradana, Y. Nazirizadeh, M. Rädler, and M. Gerken
Institute of Electrical and Information Engineering
Christian-Albrechts-Universität zu Kiel
D-24143 Kiel, Germany
ckl@tf.uni-kiel.de

***Abstract*— Photoluminescence measurements exhibit an angle-dependent color impression for Alq3 emission layers on a periodically nanostructured substrate. We demonstrate that the color impression is reduced for thick waveguides due to the plurality of outcoupling features.**

OLED; photonic crystal; guided mode extraction; angular dispersion

I. INTRODUCTION

Organic light-emitting diodes (OLEDs) are highly promising as energy and cost efficient light sources. Thin-film guided modes trap about 40% of the generated light in a conventional OLED emission layer [1]. Nanostructuring of the emission layer is one technique to extract the thin film guided modes [2]-[5]. Bragg scattering at the nanostructure causes distinct outcoupling peaks in the emission profile. These lead to angular color impressions [3],[6]. Here, we present a study on the influence of the waveguide thickness on the angular color impression.

II. FABRICATION AND CHARACTERIZATION METHOD

The gratings were fabricated by nanoimprint lithography (UV-NIL). A 200 nm layer of imprint resist was spin-coated onto a glass substrate and structured with a master stamp (grating period Λ=460 nm). The grating depth is 35 nm. By thermal evaporation, a layer of tris(8-hydroxyquinolinato)aluminium (Alq3) was deposited onto the resist and subsequently passivated by a layer of silicon monoxide (SiO). Samples with three different layer thicknesses were fabricated as shown in Fig. 1.

Exciting the samples with a laser diode at 394 nm, an angle-dependent color impression is visually observed in the emission. Fig. 2 shows as an example a series of photographs of sample B taken at different tilts of the sample with respect to the camera. While the emission appears green at 0° and 30°, it shows an orange-red hue at 15°. Such an inhomogeneous illumination is unwanted in many illumination applications. To investigate the origin of this effect in more detail, we measured the photoluminescence (PL) spectra of the samples at different angles θ in a plane perpendicular to the grating grooves. TE and TM polarization were measured separately.

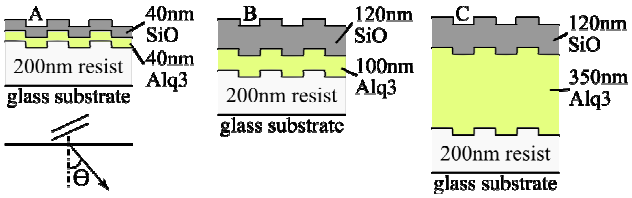


Figure 1. Schematics of fabricated devices A, B, and C with varying layer thicknesses. For all samples the grating period is Λ=460 nm.

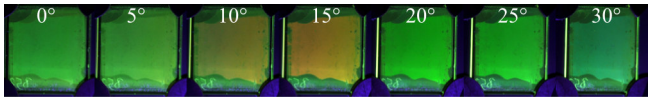


Figure 2. Photographs of the color impression of sample B with the angle θ.

III. RESULTS AND DISCUSSION

A. Emission spectra

Fig. 3 a1), b1), and c1) depict the angle-resolved mixed polarization PL spectra of samples A, B, and C, respectively. The spectra exhibit a modified Alq3 emission with angularly dispersive outcoupling peaks. With the Bragg formula [4], we calculated the effective indices of the modes at λ_0 = 550 nm from the spectra (see Table 1). Each supported mode leads to two outcoupling features in the angular-resolved emission spectrum, one feature per mode propagation direction. Thicker waveguides support more modes and thus lead to more outcoupling features. The TE0 mode of sample A and the TM1 mode of sample C are partially cut-off in the recorded wavelength range, as their effective indices below the substrate refractive index of 1.52 indicate. These cut-off modes show only low intensity outcoupling at longer wavelengths.

TABLE I. EFFECTIVE INDICES OF THE DIFFERENT GUIDED MODES IN SAMPLES A, B, AND C AT A WAVELENGTH OF 550 NM CALCULATED FROM THE EMISSION SPECTRA.

Sample	Effective index (λ_0 = 550nm)			
	TE0	***TM0***	***TE1***	***TM1***
A	1.48[a]	-	-	-
B	1.59	1.56	-	-
C	1.72	1.68	1.55	1.51[a]

The modes denoted with an a are not fully guided.

B. *Angular color-shift*

To quantify the angular color-shifts, the CIE (commission international de l'eclairage) 1931 color coordinates were calculated from the spectra and are shown in Fig. 3 a2), b2), and c2) as xy chromaticity diagrams. We measured the color coordinates of unstructured Alq3 to be (x=0.324, y=0.536), which is close to the 0°-emission of samples A and C. The 0°-emission of sample B is more reddish (x=0.357, y=0.505). With increasing observation angle, the emission color shifts as described by the depicted curves in the chromaticity diagrams. Sample A exhibits a blue shift that is maximum at 28.5° (x=0.289, y=0.448). This blue shift can be attributed to the TE0 outcoupling peak at 470 nm that is about 7 times the unmodified Alq3 intensity at this wavelength. Sample B shows the largest color shifts towards red (x=0.480,y=0.439) at 13.0° and green (x=0.266,y=0.633) at 25.0° degrees. At 25.0° the TE0 and TM0 outcoupling peaks are around 530 nm and approximately 10 times the unmodified Alq3 intensity at this wavelength. Sample C shows the smallest angular color shift. At 25° the outcoupling peaks of TE0 and TM0 are around 580 nm and approximately 2 times intensified, while TE1 and TM1 are around 520 nm and 2.5 times the unmodified Alq3 intensity. The angle-dependent color impression is significantly reduced for sample C due to the large spectral distance of 60 nm between the TE0/TM0- and the TE1/TM1-pair.

In order to compare the color shifts in terms of perceived color, we calculated the average color difference between angles from 0° to 30°, CD_{avg}, that is a figure of merit proposed for the angular color stability of OLEDs [7]. It is defined in the CIE 1976 u'v' color space that is more uniform with respect to the perceived color differences than CIE 1931 xyY. The CDavg values of the samples A, B, and C are 0.0119, 0.0625, and 0.0114, respectively, reflecting the large perceivable color shift of sample B.

IV. Conclusion

By comparing the emission of organic emitters in different nanostructured waveguides, we found that the angle-dependent color impression depends on the waveguide thickness. The number of outcoupling features as well as their position and intensity determine the angle-dependent color impression. If a plurality of modes is present as in sample C, the color impression can be reduced by channeling guided photons into different outcoupling features. Thus, when employing grating structures to increase OLED efficiency, the OLED should be designed such that photons are guided in a plurality of modes with different effective indices.

Acknowledgment

The authors gratefully acknowledge the support from the Bundesministerium für Bildung und Forschung within the project "NanoFutur" (03X5514).

References

[1] A. Chutinan, K. Ishihara, T. Asano, M. Fujita, and S. Noda, "Theoretical analysis on light-extraction efficiency of organic light-emitting diodes using FDTD and mode-expansion methods", *Org. Electron.*, 6, pp. 3-9, 2005.

[2] J. M. Lupton, B. J. Matterson, I. D. W. Samuel, M. J. Jory, and W. L. Barnes, "Bragg scattering from periodically microstructured light emitting diodes", *Appl. Phys. Lett.*, 77, pp. 3340, 2000.

[3] Y. R. Do, Y.-C. Kim, Y.-W. Song, and Y.-H. Lee, "Enhanced light extraction efficiency from organic light emitting diodes by insertion of a two-dimensional photonic crystal structure", *J. Appl. Phys.*, 96, pp. 7629-7636, 2004.

[4] U. Geyer, J. Hauss, B. Riedel, S. Gleiss, U. Lemmer, and M. Gerken, "Large-scale patterning of indium tin oxide electrodes for guided mode extraction from organic light-emitting diodes", *J. Appl. Phys.*, pp. 093111, 2008.

[5] K. Ishihara, M. Fujita, I. Matsubara, T. Asano, S. Noda, H. Ohata, A. Hirasawa, H. Nakada, and N. Shimoji, "Organic light-emitting diodes with photonic crystals on glass substrate fabricated by nanoimprint lithography", *Appl. Phys. Lett.*, 90, pp. 111114, 2007.

[6] L. Tutt and J. F. Revelli, "Distribution of radiation from organic light-emitting diode structures with wavelength-scale gratings as a function of azimuth and polar angles", Opt. Lett., 33, pp. 503-505, 2008.

[7] A. Isphording and M. Pralle, "Quantifying angular color stability of organic light-emitting diodes", *Org. Electron.*, 11, pp. 1916-1919, 2010.

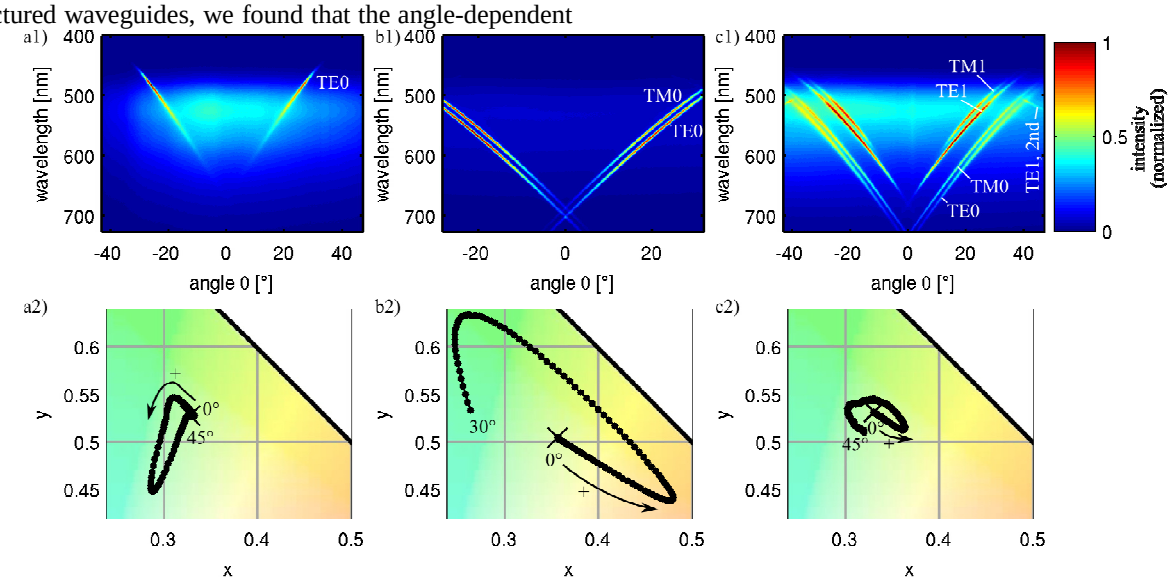


Figure 3. Upper row: Photoluminescence intensity as a function of wavelength and emission angle. Lower row: CIE xy color coordinates for angles from 0° (marked with a cross) up to 45° for samples A and C and up to 30° for sample B. Sample A: a1 and a2. Sample B: b1 and b2. Sample C: c1 and c2.

Polarization-Independent Optical Low-Coherence Reflectometry with a Non-Birefringent Arrayed-Waveguide Grating

L. Chang, B.I. Akca, G. Sengo, K. Wörhoff, R.M. de Ridder, and M. Pollnau
Integrated Optical Microsystems Group, MESA+ Institute for Nanotechnology, University of Twente
Enschede, The Netherlands
l.chang@utwente.nl

***Abstract*—The polarization dependency of an arrayed-waveguide grating (AWG) in an optical low-coherence reflectometry system is investigated. For mixed polarization, signal fading is observed at specific depths. This fading is eliminated by using a non-birefringent AWG.**

Keywords-arrayed waveguide grating; Non-Birefringent waveguides; Optical Low-coherence Reflectometry

I. INTRODUCTION

Optical low-coherence reflectometry (OLCR) is a one-dimensional optical ranging technique where the amplitude and the time delay of backscattered light from different depths in a sample is resolved using multi-wavelength interferometry. It was developed about 20 years ago [1], and has since become a widely-used tool for measuring optical reflectivity as a function of distance. Combining OLCR systems with transverse scanning of the probe beam resulted in optical coherence tomography (OCT) [2]. The size and cost of an OLCR system can be decreased significantly through the use of integrated optics. We demonstrated cross-sectional imaging of a multilayered phantom by use of an arrayed-waveguide grating (AWG) spectrometer in a spectral-domain (SD) OCT system [3], proving that AWG spectrometers [4] are excellent candidates for on-chip SD-OLCR and SD-OCT systems.

The polarization dependency of the spectrometers used in SD-OLCR systems affects the sensitivity roll-off with depth. For controlling the polarization state of the light, extra components are needed which increase the size and cost of the SD-OLCR systems. In this sense, it is more favorable to use a non-birefringent AWG spectrometer in an SD-OLCR system. An AWG spectrometer is polarization independent if its array waveguides are polarization independent, which can be achieved by balancing the material and waveguide birefringence [5]. Although this approach requires a highly fabrication-tolerant design, it makes AWGs advantageous over bulky spectrometers.

In this work, we first discuss the impact of polarization dependency of an AWG on SD-OLCR performance. The modulation effect of polarization on sensitivity roll-off in depth is experimentally verified. Secondly, a polarization-independent AWG is demonstrated as a permanent solution to the polarization-related signal fading problems.

This work is supported by the Smart Mix Program of the Netherlands Ministry of Economic Affairs and the Netherlands Ministry of Education, Culture and Science.

II. BIREFRINGENT AWG SPECTROMETER

An optical waveguide is birefringent, if it exhibits different effective refractive indices for TE and TM polarized light. For a birefringent AWG, the phase delay difference between two adjacent waveguides is different for TE and TM polarized light (for each single wavelength). This phase delay difference leads to a phase front angle difference between TE and TM polarized light at the second free propagation region (FPR). Thus, TE and TM polarized light focus onto different positions at the end of the second FPR.

The spectrum $M(k)$, with k the wavenumber, as measured by a spectrometer is the convolution of the real input spectrum $R(k)$ with the single-wavelength response function (SWRF) $S_{k0}(k)$ of the spectrometer. Preferably, $S_{k0}(k)$ should exhibit a single peak which is as narrow as possible. In case of a birefringent AWG with a mixed polarization input, the SWRF is a double-peak function due to the different focal positions of the TE and TM polarized light. The double-peak SWRF leads to a signal fading problem in the SD-OLCR applications. The SD-OLCR signal $D(z)$ is obtained by taking the Fourier transform (FT) of the measured spectrum, which is equal to the FT of the real spectrum times the FT of the SWRF:

$$D(z) = F_{k\to z}\{M(k)\} = F_{k\to z}\{R(k)\}\cdot F_{k\to z}\{S_{k0}(k)\}. \qquad (1)$$

If each peak of $S_{k0}(k)$ can be approximated as a Gaussian, Fourier transforming the double peak SWRF results in

$$|F_{k\to z}\{S_{k0}(k)\}| = \sqrt{1+2a(a-1)[1-\cos(2\pi\Delta k z)]}\cdot|F(z)|, \qquad (2)$$

where $F(z)$ is a Gaussian, a and $1\text{-}a$ are the percentage of TE and TM intensities respectively, Δk is the wavenumber distance of the two peaks of $S_{k0}(k)$, and z is the depth coordinate. The cosine term in (2) represents a beating effect, of which the spatial frequency is Δk, which depends on the refractive index difference $\Delta n_{\text{TE-TM}}$ of the TE and TM polarized light in the arrayed waveguide region. One way to weaken the beating effect in SD-OLCR signal is reducing $\Delta n_{\text{TE-TM}}$ so far that the beating frequency becomes low enough to push the first beating valley beyond the maximum depth range.

III. EXPERIMENTAL SETUP

A schematic of the SD-OLCR system with an AWG spectrometer is shown in Fig. 1. The free-space Michelson interferometer is illuminated with a broadband light source which is band-pass filtered in order to prevent overlap of

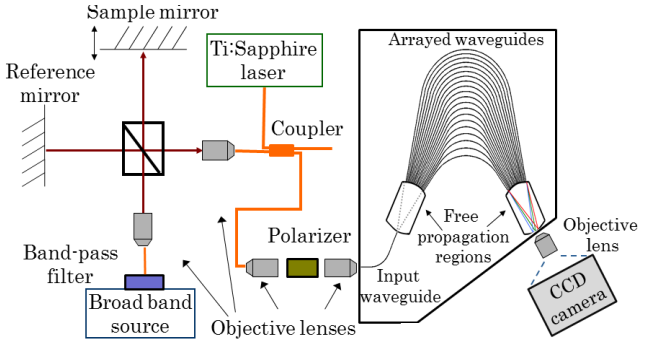


Figure 1. Schematic of the experimental set-up

different spectral orders of the AWG. The light returning from the two arms is combined and focused by an objective lens into a fiber coupler with a 10/90 splitting ratio. A Ti:Sapphire laser is connected to the other input port of the coupler to be used in the AWG SWRF measurements. 90% of the light returning from the two arms is coupled into the AWG by a free-space coupling arrangement, which consists of two objective lenses and an adjustable polarizer. Two AWGs were used in this work, a birefringent AWG centered at 800 nm [6], and a non-birefringent AWG centered at 1300 nm. The output channels of the AWG were removed in order to increase the maximal depth range. The light dispersed in the arrayed waveguides is imaged by a microscope objective lens (NA = 0.12) onto the CCD.

IV. Measurements and Results

The effect of mixed polarization on sensitivity roll-off was investigated for a TE/TM power ratio of 1. The SWRF of the AWG for mixed polarization is given in the inset of Fig. 2 and Fig. 3.

A birefringent AWG (Fig. 2) images a spectral peak at a given wavelength onto different positions for TE and TM polarizations. The depth information is modulated by the FT of the SWRF (dashed line). This modulation leads to signal fading at certain depth and, thus, low SNR at the corresponding position.

As a proof-of-concept, a non-birefringent AWG centered at 1300 nm was designed. Silicon oxynitride channel waveguides

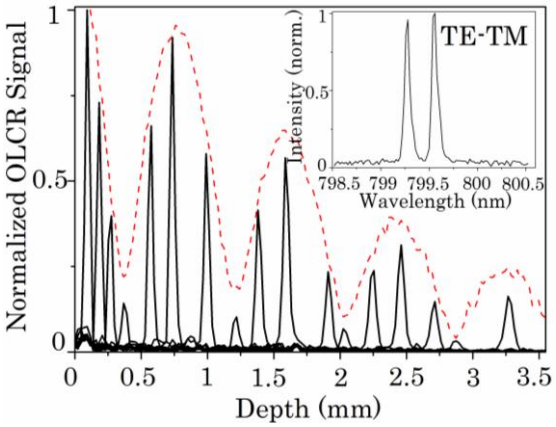


Figure 2. Measured OLCR signal versus depth and roll-off (dashed line) with the 800-nm birefringent AWG for mixed polarized light (TE/TM = 1). The inset is the SWRF of the AWG for TE/TM = 1.

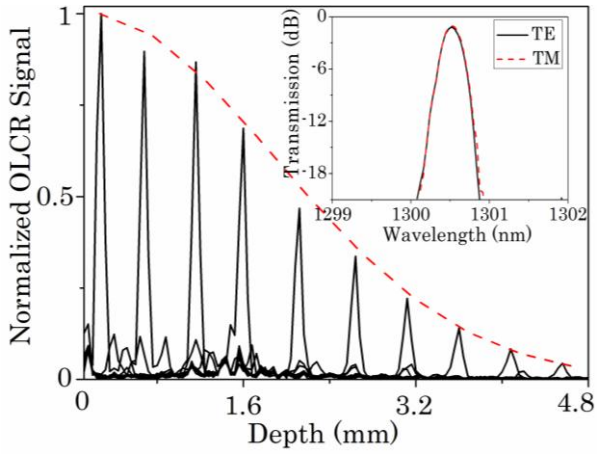


Figure 3. Measured OLCR signal with the 1.3-µm non-birefringent AWG. The inset is the SWRF of the AWG for TE/TM = 1.

with a width of 2.2 µm, height of 1 µm, and core refractive index of 1.52 were fabricated. No significant polarization-dependent shift was observed, as shown in the inset of Fig. 3. The OLCR measurements for mixed polarization (TE/TM = 1) were performed using the set-up shown in Fig. 1 with an infrared camera (320 pixels). No beating effect was observed within the maximum depth range, as shown in Fig. 3.

V. Conclusions

The effect of polarization on sensitivity roll-off has been investigated. For a mixed polarization, signal fading was observed at specific depths. The use of a non-birefringent AWG eliminated this fading completely, as no beating effect for mixed polarization has been observed within the maximum depth range. Such a solution would eliminate the need for polarization control with its associated noise and cost penalties in OCLR systems.

VI. References

[1] R.C. Youngquist, S. Carr, and D.E.N. Davies, "Optical coherence domain reflectometry: a new optical evaluation technique," Opt. Lett. vol. 12, pp.158-160, 1987.

[2] D. Huang, E.A. Swanson, C.P. Lin, J.S. Schuman, W.G. Stinson, W. Chang, M.R. Hee, T. Flotte, K. Gregory, C.A. Puliafito, and J.G. Fujimoto, "Optical Coherence Tomography," Science, vol. 254, pp. 1178-1181, 1991.

[3] V.D. Nguyen, B.I. Akca, K. Wörhoff, R.M. de Ridder, M. Pollnau, T.G. van Leeuwen, and J. Kalkman, Opt. Lett., vol. 36, pp. 1293-1295, 2011.

[4] M.K. Smit and C. van Dam, "PHASAR-based WDM-devices: Principles, design and applications," IEEE J. Sel. Top. Quantum Electron., vol. 2, pp. 236-250, 1996.

[5] K. Wörhoff, C.G.H. Roeloffzen, R.M. de Ridder, A. Driessen, and P.V. Lambeck, "Design and application of compact and highly tolerant polarization-independent waveguides," IEEE J. Lightwave Technol.,vol. 25, pp.1276-1283, 2007.

[6] B.I. Akca, V.D. Nguyen, J. Kalkman, N. Ismail, G. Sengo, F. Sun, T.G. van Leeuwen, A. Driessen, M. Pollnau, K. Wörhoff, and R.M. de Ridder, "Toward spectral-domain optical coherence tomography on a chip", IEEE J. Sel. Top. Quantum Electron., doc. ID 10.1109 (posted 6 October 2011, in press).

A silicon-based tunable multimode interferometer using the thermo-optic effect

A.Rosa, A.M.Gutiérrez, A.Brimont, A.Aamer, P.Sanchis
Nanophotonics Technology Center
Universitat Politecnica Valencia
Valencia, Spain
alroes3@ntc.upv.es

***Abstract*— A silicon-based tunable and compact 2x2 multimode interferometer with 594.5x9µm size has been designed and experimentally demonstrated. The thermo-optic effect is exploited to achieve electro-optical tunability demonstrating above 10dB cross-talk between output ports.**

Keywords-Integrated; Multimode interferometer; silicon photonics; thermo-optic effect

I. INTRODUCTION

Tunable couplers are important devices for optical integrated circuits allowing a high accurate setting of any splitting ratio. In this case, tunable MMI are very attractive due to their intrinsic properties like high theoretical bandwidth and low fabrication tolerances. On the other hand, SOI (Silicon-On-Insulator) platform offers the possibility of mass-manufacturing as well as cost-effective integration with CMOS electronics. Many works in these devices has been reported. In [1], an InGaAsP MMI was demonstrated with 504µm x 18µm dimensions but a poor cross talk (~5.7dB). Also, in [2], a polymer-based photonic MMI (510µm x 10µm) was reported. However, to our knowledge, no work on silicon photonic tunable MMI has been demonstrated so far.

In this work we propose a highly compact silicon-based tunable 2x2 multimode interferometer (MMI). We achieve MMI tunability using the thermo-optic effect, conveniently setting up a titanium heater on the surface. The designed silicon device exhibits a switching crosstalk of 13dB with an MMI structure length of 594.5µm. Such reduce dimensions allow our device to be a promising candidate for on-chip integration.

II. DEVICE STRUCTURE AND THEORETICAL ANALYSIS

The proposed MMI is composed for a multimode waveguide and two outputs and inputs ports provided by tapers. These tapers allow not only minimizing return losses, but also having bigger self-images into the multimode waveguide which benefits the thermo-optic effect to achieve the necessary length for the required phase shift. First of all, the passive MMI was designed as a single photonic cross coupler, as it can be observed in Figure 1. In this passive device, our design parameters are L_{MMI}=594.5 µm and W_{MMI}=9 µm.

The proposed design is based on a π radians phase shift of one of the two folded images at the center of the MMI (at $L_{MMI}/2$). This phase shift results in an interference pattern shifting on the propagation direction, from the original to the new, like a mirrored image. Thermo-optic effect is achieved through an electrode over the waveguide surface in one of two folded images to bring the phase shifting. One can see the self-images distribution in [3].

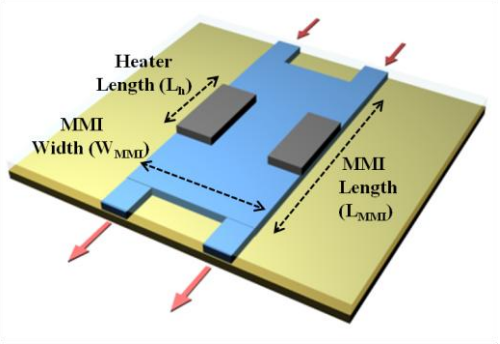


Figure 1. Schematic of the tunable MMI.

The key of this device is that the refractive index must only be changed in a localized place in the device. We can find the relationship between the phase and the index change through next expression:

$$\Delta\varphi = k \cdot \Delta n \cdot L_h \tag{1}$$

where L_h is the heater length over the waveguide to get the optimal phase shift, induced by a localized temperature shift on the waveguide, and $k=2\pi/\lambda$ is the wavelength number[4]. This temperature dependence is given for the thermal coefficient of the material (silicon in our case). Finally, we can define the index change as:

$$\Delta n = \frac{\delta n}{\delta T} \cdot \Delta T \tag{2}$$

In our case, working with silicon, the thermal coefficient is $1.84 \cdot 10^{-4}$ / ºC. We focused on getting the optimal index change for an MMI as small as possible. With our material, a index change with thermo-optic effect around $\Delta n=10^{-2}$ can be obtained. Thus, once known the index change and the desired

phase shift (π radians), we can obtain the necessary length through (1)-(2) equations to finally get the mirrored pattern interference. The theoretical obtained L_h is 77.5 µm.

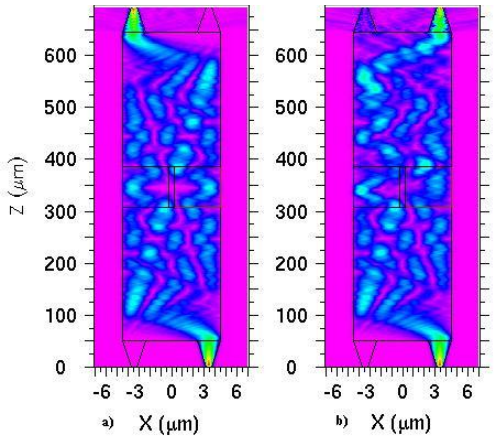


Figure 2. Simulated MMIs: a) Passive MMI b) Active MMI with the phase shift.

On the other hand, L_h has also been optimized via the beam propagation method (BPM) starting from the theoretical value obtained previously. In Figure 2 it can be observed the obtained mirrored pattern interference changing the index in one of the two folded images. In this case, the obtained heater length is L_h=79.5µm. which allow a simulated index change of 0.024. So, good agreement is found between the theoretical and simulations results.

III. Experimental Results

The tunable MMI was fabricated by using e-beam lithography, inductive coupled plasma etching and metal evaporation. A heater over one of the two self-images was placed at the device center. . The MMI tunability was analyzed by measuring the variation of output power for an applied voltage. Figure 3 shows the obtained results for each port and inset shows a SEM image with a detail of MMI ports. From these results, we can determinate the voltage, and therefore the necessary electric current, to get the desired index change. Furthermore, the resistance of the heater can be obtained.

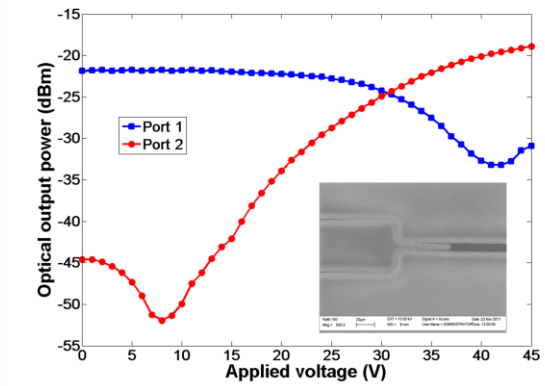


Figure 3. Measured output coupled power for each port as a function of the applied voltage. Coupling losses of 20dB from grattings have been estimated (vertical coupling).

The electrical current is 1.855 mA measured in the desired point in which the voltage reached is 42 V. In this case the device shows a power consumption of around 77mW. Due to this high power consumption, we made a design feedback to optimize the structure allowing a new less electrical power consumption tunable MMI.

One approach to reduce the power consumption is to minimize the required index change. The idea to get a minimum index change is to increment the heater's length (L_h). To make this as efficiently as possible is necessary to increment the two folded images size. We used a taper on the input (and output) achieving a bigger size on the two folded images and then optimizing the size and location heater. In this way, as it shown in Figure 4, the effective index shift was reduced from 0.024 to 0.015. On the other hand, if MMI size is modified (694.5µm x 9.75µm) having optimized heaters, the required index change can be reduced to 0.013, thus decreasing the power consumption.

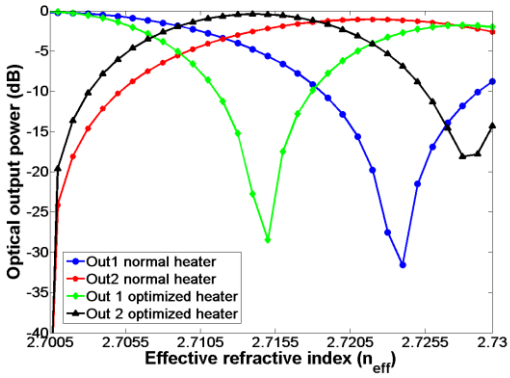


Figure 4. power to output ports for both length of shift index region.

IV. Conclussions

We have demonstrated a very compact (594.5µm x 9µm) silicon-tunable MMI based on thermo-optic effect. Furthermore, we have described an approach to reduce the power consumption through the optimization of the heater size over the self-images, reducing the required index change to make possible the tunable effect. Optimum performance has been achieved with a heater length of 127.5 µm and maximum input port size of 3.5 µm for a minimum power consumption keeping device coupling properties.

Acknowledgment

Financial support from HELIOS (Photonics Electronics Functional Integration on CMOS) FP7-224312 and Generalitat Valenciana under PROMETEO-2010-087 R&D Excellency Program (NANOMET) are acknowledged.

References

[1] D.A. May-Arrioja and P. LiKamWa, IEEE/LEOS Summer Topi. Meet., 2008, pp.39-40, 21-23 July 2008

[2] N. Xie and K. Utaka, Opto-Elect. and Communic. Conf. 2008 and the 2008 Australian Conf. on Opt. Fib. Tech. OECC/ACOFT 2008., , pp.1-2, 7-10 July 2008

[3] L.B. Soldano and E.C.M. Pennings, J. Ligh. Technol., vol.13, no.4, pp.615-627, Apr 1995

[4] J. Leuthold and C. Joyner, J. Light. Technol. 19, 700- (2001).

Photorefractive damage in congruent and Mg doped α-phase channeled $LiNbO_3$ waveguide.

M. Jubera, A. García-Cabañes and M. Carrascosa.
Dpto. de Física de Materiales
Universidad Autónoma de Madrid
Madrid, Spain.
mariano.jubera@uam.es

N. Waasem
Institute of Physics
University of Bonn[2]
Madrid, Spain[1];Bonn, Germany[2]

Abstract: We report on accurate measurements of photorefractive optical damage in congruent and Mg doped α-phase channeled $LiNbO_3$ waveguides. Whereas for undoped waveguides optical damage threshold intensities are about 200 W/cm^2, no optical damage has been found in Mg-doped waveguides up to 1 MW/cm^2. Results are discussed comparing them with data in planar waveguides and with the recent two transport model for the photorefractive effect in undoped $LiNbO_3$

Keywords-component; photorefractive effect, proton exchanged channelled waveguides, optical damag

I. INTRODUCTION

An important issue in many $LiNbO_3$ integrated optics devices is the maximum power that the device is able to safely handle on operation. In most cases the power is limited by the photorefractive (PR) optical damage which, to a greater or a lesser extension, is present in $LiNbO_3$ particularly within the visible region of the spectrum. Thus, a great effort has been devoted to characterize PR damage and to reduce it. Particular attention has been paid to waveguide configurations because the long propagation lengths and the high intensities reached increase optical damage effects. [1].

From the theoretical side, the rough explanation of the beam distortion is very simple: the light induces a refractive index decrease Δn (via charge transport and electrooptic activity in the crystal) which affects mode propagation. However, a more detailed analysis shows the complexity of the subject as it involves the microscopic origin of the charge transport and its interaction with the wavefront change via the index change Δn. In fact, very recently, a new two-center model has been proposed to explain several features that could not been predicted by the previous standard one-center model [2].

The precise control of the proton-exchange (PE) process was found essential for good non linear optical performance of the fabricated waveguides. An important step in the knowledge of the PE guides was put-on by Korkishko and coworkers with their detailed structural studies of layers exchanged under different conditions [3]. These authors revealed the occurrence of seven crystallographic phases depending on the exchange rate x of the resulting compound $H_xLi_{1-x}NbO_3$. One of these phases, the so-called α-phase, can be fabricated alone by using soft proton-exchange recipes with well controlled parameters (see section 2). The corresponding waveguides present very good non linear and electrooptical properties very similar to the $LiNbO_3$ substrates. Unfortunately, they also present moderate photorefractive damage that has been characterized in planar waveguides [4,5]. However, it is still not clear whether the results for planar guides are directly applicable to channeled waveguides which have much higher technological potential.

Hence, the aim of this work is to address accurate measurements of photorefractive optical damage of α-phase $LiNbO_3$ waveguides in channelled configuration. We will consider congruent and Mg-doped waveguides. The results will be compared with those of planar waveguides and discussed to the light of the recent two-center transport model for the photorefractive effect in undoped $LiNbO_3$.

II. EXPERIMENTAL DETAILS.

The α-phase PE waveguides were produced by immersion of the samples in a benzoic acid melt buffered with 3% lithium benzoate at 300 ºC for 48 hours within a sealed ampoule [4]. In order to obtain channelled waveguides, prior to proton-exchange a SiO_2 mask is deposited onto the crystal surface with open channels obtained by standard photolithographic techniques. Thus, we have fabricated "soft proton exchanged" waveguides as opposite to the annealed proton exchanged guides. These wavguides have passed a highly distorting proton exchange phase during fabrication and a single homogeneous structural phase cannot be assured.

A Mach-Zehnder interferometer is used for the quantitative measurement of light-induced index changes [5] in congruent and Mg-doped waveguides. Optical damage is induced by light of 532 nm wavelength and probed with red light of 633 nm wavelength. For Mg doped samples, complementary measurements have been also performed monitoring the

intensity inside the waveguide just at the end of the path length as a function of the incoming light power.

III. RESULTS AND DISCUSSION.

The photorefractive index change versus the light beam intensity I inside the waveguide has been measured for two waveguides of 5 and 10 μm wide. The results are shown in Fig. 1. The values of $|\Delta n|$ are first nearly independent on I (I<100 W/cm^2) as predicted by the standard one-center model of the PR effect. From I >100 W/cm^2 $|\Delta n|$ markedly increases and finally the curve tends to saturate again because of strong optical damage. In fact, the greatest intensity which could reliably be measured (~10^3 W/cm^2 for the sample length used) is limited by this PR damage. The curve follows the typical shape reported for $\Delta n(I)$ data in α-phase congruent planar waveguides although the saturating region appears for higher intensities, (1 KW/cm^2 versus 200 W/cm^2 [5]), i.e. higher light intensities can be propagated in the channelled waveguide. The light intensity dependence is successfully explained through the two-center model [2] where, for the low intensity region, only the Fe impurity plays a role (one-center approach), but as the intensity increases a secondary center (niobium in lithium site) contributes increasing $|\Delta n|$. The final saturating region appears when $|\Delta n|$ is high enough to induce an important distortion of the mode profile and so propagation losses. Then, these data can be considered a further support for the validity of the two-center photorefractive model in undoped $LiNbO_3$ waveguides, either in planar or channel configuration. Similar $\Delta n(I)$ measurements have been carried out for Mg-doped samples and no photorefractive effect has been observed up to 1 MW/cm^2 ($\Delta n << 10^{-5}$). In fact, in this latter case the measurements are much more complicated because of thermal instabilities at the high-intensity range that have been taken into account.

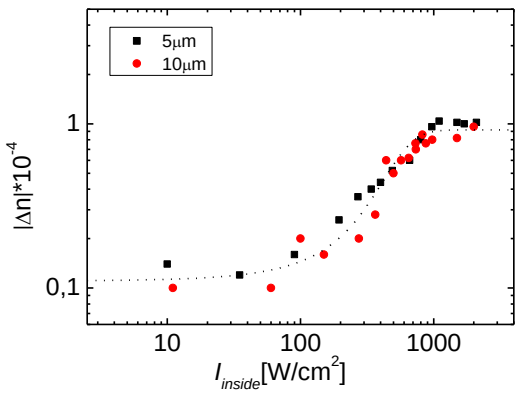


Fig.1 *Logarithmic plot of the photorefractive index change Δn_e versus the light intensity I inside the waveguide. The dotted line is only to guide the eyes.*

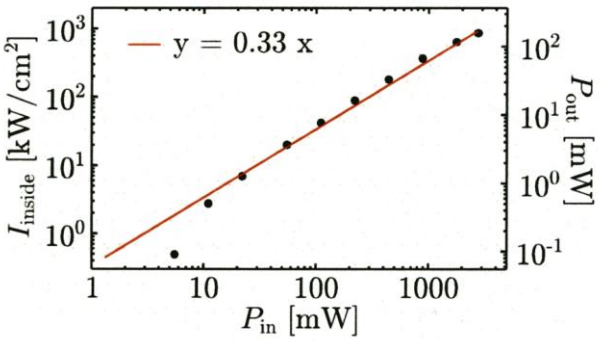


Fig.2 *Logarithmic plot of light intensity inside the waveguide just before emerging from it, I_{inside}, versus de incoming power P_{in} for a Mg-doped sample . The fit is a straight line through the origin.*

A further confirmation of the absence of PR damage has been obtained measuring the light intensity I_{inside} at the end of the waveguide propagation length as a function of the incoming light power P_{in}. A linear dependence up to I_{inside}~1 MW has been obtained demonstrating the absence of PR damage in this intensity range.

In summary photorefractive optical damage of α-phase PE channeled waveguides has been accurately measured finding an intensity response similar in accordance with the recently reported two-center charge transport model [2]. For congruent waveguides the photorefractive effect becomes relevant at light intensities about 400-500 W/ cm^2 slightly higher than in planar guides whereas no optical damage has been found in Mg-doped waveguides up to remarkably higher intensities of 1 MW/cm^2.

ACKNOWLEDGMENT

This work was supported by MICIN, MAT2008-06794-C03 and MAT2011-28379-C03-01. A FPI fellowship is acknowledge by M.J.

REFERENCES

[1] D. Kip and M. Wesner, "Photrefractive waveguides," in Phtorefractive Materials and their applications I: Fundamental phenomena (Springer Berlín, 2006)

[2] J. Villarroel, J. Carnicero, F. Ludtke ,M. Carrascosa, A. García-Cabañes ,J. M. Cabrera, A. Alcazar y B. Ramiro; "Analysis of photorefractive optical damage in lithium niobate: Aplication to planar waveguides"; Opt. Express **18**, 20852-20861 (2010)

[3] Y. N. Korkishko, V. A. Fedorov, "Structural phase diagram of $H_xLi_{1-x}NbO_3$ waveguides: the correlation between optical and structural properties", IEEE J. Selected Topics in Quant. Electr. **2**(2), 187 (1996).

[4] O. Caballero-Calero, A. Alcázar, A. García-Cabañes, J. M. Cabrera and M. Carrascosa, "Optical damage in x-cut proton exchanged $LiNbO_3$ planar waveguides," J. Appl. Phys. **100**, 093103 (2006).

[5] F. Luedtke, J. Villarroel, A. García-Cabañes, K. Buse, and M. Carrascosa, "Correlation between photorefractive index changes and optical damage thresholds in z-cut proton-exchanged-$LiNbO_3$ waveguides," Opt. Express **17**, 658 (2009).

Multiple die-to-wafer adhesive bonding for heterogeneous integration

S. Keyvaninia, M. Muneeb, S. Stankovic, G. Roelkens, D. Van Thourhout
Photonic Research Group, INTEC, Ghent University_IMEC
B-9000 Gent Belgium.
Shahram.keyvaninia@intec.ugent.be

J.-M. Fedeli
CEA-LETI, Minatec Campus, 17 Rue des Martyrs, 38054 Grenoble, France.

***Abstract*— A new process for bonding of III-V dies to processed silicon-on-insulator waveguide circuits using divynilsiloxane-bis-benzocyclobutene (DVS-BCB) was developed using a commercial wafer bonder. High-quality bonding, with ultra-thin bonding layers (< 60 nm) is demonstrated, which is suitable for the fabrication of heterogeneously integrated photonic devices, specifically hybrid III-V/Si lasers.**

Keywords: Adhesive bonding; heterogeneous integration; Silicon-on-Insulator (SOI)

I. INTRODUCTION

Silicon-on-insulator (SOI) is an emerging platform for photonic integrated circuits. It offers the potential for realizing low-cost and compact optical functions, since the standard complementary metal oxide semiconductor (CMOS) massive processing infrastructure can be used to process these optical components. Fabrication of light sources on this platform is still a big problem, due to silicon's indirect bandgap. Heterogeneous integration, achieved through the bonding of III-V semiconductor materials onto SOI, is the most promising approach to address this problem [1]. Commercial silicon and CMOS production is done on wafers with diameters of 200 mm and above, while III-V wafers used in photonics applications have typical diameters of less than 100 mm. Therefore, one-to-one wafer bonding between differently sized wafers is not an effective integration approach. Therefore, a cost-effective approach in heterogeneous integration requires small pieces of III-V material to be bonded on the SOI photonic wafer. We focus on a multiple die-to-wafer adhesive bonding process, where III-V dies are bonded to an SOI wafer using DVS-BCB as the bonding agent. In this paper, we describe a new adhesive wafer bonding process scheme that involves partial curing of the DVS-BCB prior to bonding and attaching the III-V dies to the SOI substrate at room temperature prior to curing in a vacuum atmosphere. An alternative method has been reported earlier, in which adhesive die-to-wafer bonding was demonstrated in a commercial wafer bonder [2]. In that method, spacers are used to keep the III-V die and SOI substrate separate prior to loading the stack in the bonding tool. In this new method no carrier is required to load the top wafer/die into the machine and no vacuum or heating is required prior to contacting the wafers in the bonding chamber. This 'cold bonding' method significantly simplifies the bonding preparation for machine-based multi-die scale bonding and it shows high yield for ultra-thin bonding thicknesses below 60 nm. This process was applied to achieve ultra-thin DVS-BCB bonding layers for the fabrication of several photonic devices, such as III-V/SOI lasers [3].

II. DESCRIPTION OF THE BONDING PROCESS

The bonding process was developed for multiple die-to-wafer bonding, as well as a single die bonding. A MicroTec Süss ELAN CB6L wafer bonder was used for the bonding experiments. The bonding process starts with the cleaning of the SOI substrate and III-V dies. The SOI cleaning is performed by dipping the substrate into a Standard Clean 1 (SC-1) solution heated to 70°C, for 15 min. After this, the DVS-BCB:mesitylene solution is spin-coated onto the SOI substrate. The SOI substrate is then baked for 10 min at 150°C, to let mesitylene evaporate, after which the substrate is slowly cooled down to room temperature. Finally, the SOI is mounted on a carrier wafer made of Pyrex glass. Meanwhile, prior to bonding, two sacrificial layers on the III-V die are removed by selective wet etching, which also removes particles and contaminants from the III-V die surface. The III-V die is then rinsed with DI water, dried and mounted on the SOI die. Since in the presented method the dies are contacted at room temperature, individual dies can easily be pick-and-placed onto the silicon target wafer. They can be aligned manually with an accuracy of 500μm without any extra tools or can be placed more accurately using a flip-chip machine. After that, the SOI substrate on its carrier wafer is mounted on the transport fixture and is loaded into the processing chamber of the wafer bonding tool. The chamber is pumped-down and heated to 150°C with a ramp of 15 °C/min for 10 min, while applying pressure on the III-V/SOI stack. The actual bonding pressure (the applied force per area of the III-V die) is kept in the range of 200 to 400 kPa. After keeping the pressure on the dies for 10 min at 150 °C, the temperature is increased up to 280 °C, with a ramp of 1.5 °C/min. Upon reaching 280 °C, the dies are kept at this temperature for 60 min in a N_2 atmosphere. After the curing, the bonded samples are cooled down (at 6-10 °C/min) and unloaded from the processing chamber. The InP substrate of the III-V die is then removed by selective wet etching, leaving a thin III-V film with the functional layers bonded to the SOI die, ready for further processing.

This work was carried out in the framework of the FP7 HELIOS project

III. DVS-BCB MULTIPLE DIE-TO-DIE BONDING RESULTS

In order to demonstrate the true potential of die-to-wafer bonding, 0.3cm^2 III-V dies were transferred to a quasi-planarized SOI die (fabricated in CEA-LETI), using the ultra-thin bonding recipe. The results are shown in Figure 1.

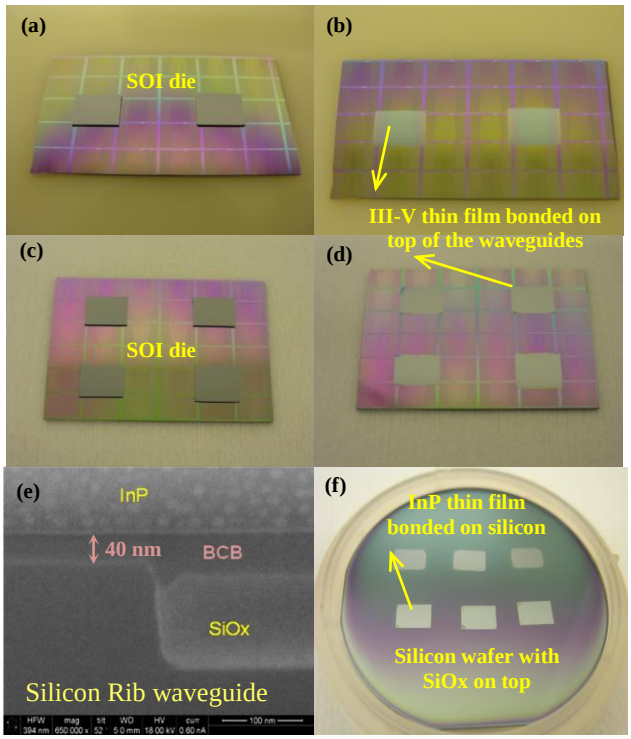


Figure 1. (a-b) two epitaxial 0.3 cm^2 III-V dies bonded on a planarized SOI die before and after the substrate removal process; (c-d) four epitaxial 0.3 cm^2 III-V dies bonded on a planarized SOI die before and after the substrate removal process; (e) SEM image of the bonding interface.(f) 6 InP-membranes (with the individual die area of 0.2 cm^2) bonded on a 50 mm silicon wafer.

The bonding quality was assessed by bonding six III-V dies to a 50 mm silicon wafer with 1.5µm-thick layer of SiO_x on the top. This bonding is usually used for InP-Membrane-on-Silicon applications [4] (see Figure 1f). The InP films were etched away using a wet etching solution to measure the thickness and uniformity of the DVS-BCB bonding layer. The results for the six dies bonding experiment are showing a good uniformity over the whole bonding area and a high reproducibility of the nominal bonding layer thickness. A DVS-BCB: mesithylene dilution of 1:8 (v/v) was used in the experiment, spin coated at 2500 rpm, resulting in an average bonding layer thickness of 60 nm, varying by +/- 5nm over all six dies.

In particular applications, there is a need for bonding different types of III-V dies on a single SOI die or wafer (e.g. a die containing laser epitaxy and a die containing photodetector epitaxy). Here we show that by applying the new bonding recipe, in combination with a graphite foil between the dies and the bonding head, four die bonding using 2 different epitaxial layer stacks (with about 50 µm difference in substrate thickness) can be achieved. This graphite foil is used to compensate for these thickness variations in order to distribute the pressure evenly over all dies during the bonding, as is illustrated in Figure 2. These differences in substrate thickness are difficult to handle using the classical bonding recipes while our new bonding process results in perfectly bonded dies.

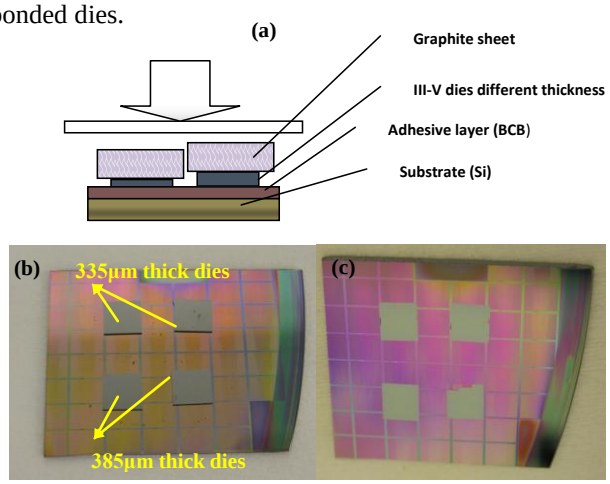


Figure 2. Bonding of four III-V dies, with different substrate thickness, on a planarized SOI die,using a graphite foil to compensate for the die thickness variations: (a) schematic; (b) before substrate removal; (c) after substrate removal.

IV. CONCLUSION

The 'cold bonding' method significantly simplifies the preparation process for machine-based bonding in a multiple die-to-wafer adhesive bonding procedure. The demonstrated DVS-BCB bonding layer thickness is very uniform and ultra-thin DVS-BCB bonding (<60 nm) can be achieved. Additionally, we developed the process for simultaneous bonding of multiple III-V dies with different thickness, suitable for the heterogeneous integration of different types of III-V components on a SOI photonic circuit.

ACKNOWLEDGMENT

This work is supported by EU-funded project Photonics Electronics functional Integration on CMOS (HELIOS). The authors thank Guang-Hua Duan and Francois Lelarge (III-V lab, Paris) for delivering the III-V epitaxial material used in developing this process.

REFERENCES

[1] G. Roelkens, L. Liu, et al., Laser Photonics Rev. P.DOI: 10.1002/lpor.200900033 (2010).

[2] S. Stanković, et al., "Die-to-die adhesive bonding for evanescently-coupled photonic devices," Electrochem. Solid-State Lett., vol. 14, no. 8, pp.H326–H329, May 2011.

[3] M. Lamponi, S. Keyvaninia, et al., "Low-Threshold Heterogeneously Integrated InP/SOI Lasers With a Double Adiabatic Taper Coupler," IEEE Photon. Technol. Lett. 24, 76-78 (2012).

[4] J. Pello et al., "Post-bonding fabrication of photonic devices in an Indium phosphide membrane bonded on glass," in Proc. 16th Ann. Symp. IEEE Photonics Benelux Chapter,Belgium, 2011, pp. 213–216.

InP Wavelength Shifter Designs for Colorless User Terminals in Passive Optical Networks

Jose A. Lazaro, Victor Solé
Dept. of Signal Theory and Communications (TSC)
UPC – Universitat Politècnica de Catalunya
Barcelona, Spain
jose.lazaro@tsc.upc.edu

Adrian Wonfor
Engineering Department
Centre for Photonic Systems, University of Cambridge
Cambridge, United Kingdom

Bernhard Schrenk
Dept. of Electrical and Computer Engineering
National Technical University of Athens
Athens, Greece

***Abstract*—Wavelength shifters (WS) are proposed for Rayleigh backscattering mitigation in bidirectional centralized light passive optical networks (PONs). A dual-arm WS is proposed as it requires simpler driving-signals. InP integration allows compact lossless WS design.**

Keywords: electro-optic modulation; frequency conversion; optical fiber communication; Indium Phosphide (InP)

I. INTRODUCTION

Providing a broadband access connection to final users has been the objective of telecommunication operators during recent years. Nevertheless, fiber deployment closer to the customer was not considered the most cost-effective option until 2005-2007 [1]. Since then, progress in optical technologies, bringing down the component and system cost, coupled with broad-bandwidth demands from triple-play and new services, have been motivating telecommunication companies and cable system operators to deploy a full set of Fiber-To-The-Home architectures (FTTH). Taking into account also energy consumption trends, telecommunication companies are proposing FTTH architectures with minimized consumption, where, Passive Optical Networks (PON) and especially next generation Wavelength De/Multiplexing (WDM) PONs are showing higher power efficiency [2].

User Terminal subsystems are key for the deployment of future access networks, as they have a significant impact on the CapEx, requiring simplicity and cost and energy efficiency for the ONU of the user terminal equipment. In order to fulfill this requirement, wavelength agnostic Optical Network Units (ONU) have been proposed, so that the same device can be used by all the users in the network, providing mass production cost reductions, even for WDM-PONs. One step beyond this is the use of only one fiber per ONU with the same wavelength for upstream and downstream, as preferred by many operators for deployment and installation cost reduction. However, the Rayleigh Backscattering (RB) effect, caused by the intrinsic inhomogeneity of the fiber, introduces a serious limitation in the link performance [3]. Essentially, the RB generated by the upstream (downstream) propagation of the optical signal along the transmission fiber at the upstream (downstream) optical signal interferes with the downstream (upstream) signal if both downstream and upstream are transmitted at the same wavelength.

Several techniques have been proposed for reducing the impact of the RB, based on reducing the overlap between the RB and the signals as in [4], nevertheless, the overlap present between the RB and the signal is reduced but not completely removed. Alternatively, producing a wavelength shift at the ONU over the received downstream carrier to generate a displaced wavelength for upstream data remodulation reduces the RB interference by avoiding the beating between the upstream signal and the scattering at the OLT receiver. In literature, several implementations have been proposed so far, the best using 4-arm $LiNbO_3$ Mach-Zehnder modulator (MZM) structures [5]. To our knowledge no wavelength shifter (WS) has been implemented in InP for providing a compact ONU compatible with cost and energy consumption requirement in PON networks.

II. DESCRIPTION OF THE WAVELENGTH SHIFTER FUNCTIONALITY AND REQUIRED DRIVE SIGNALS

A. General description of the functionality

The targeted functionality of the wavelength shifter involves generating a frequency shift of the incoming wavelength by single side band modulation. The simplest configuration from the point of view of the device structure required for producing a wavelength shifting of the incoming signal is just a device having the capability to generate phase modulation. For example, a simple reflective semiconductor optical amplifier (RSOA) has been used for generating a wavelength shifting of 2.5GHz even using a RSOA with 1GHz bandwidth by applying a sawtooth electrical signal of 2.5GHz, thanks to the chirp-induced phase modulation of the RSOA [6]. Though this has achieved a moderate wavelength shifting of 2.5GHz, this displacement is enough for allowing a Rayleigh Backscattering effect mitigation of 5 dB [6].

This work is supported by the European Commission by FP7 project Network of Excellence, EURO-FOS, ICT 257210 project PARADIGM and Spanish MICINN/FEDER TEC2008-01887.

The main limitation of this approach using the simplest device structure of a single waveguide able to generate a phase modulation is that it requires a very wideband electrical amplifier with enough output power to achieve twice the voltage V_π for the phase modulator [7]. Thus the simplest optical implementation also has the most stringent electrical requirements. This has motivated a further analysis of more complex structures, but mitigating the requirements for the electrical driving signals, as will be described in the next section.

B. Dual-arm modulator based wavelength shifter

The next step in complexity for the wavelength shifter device was considering a dual-arm modulator application-specific optical integrated circuit (ASPIC) as shown in Fig 1.

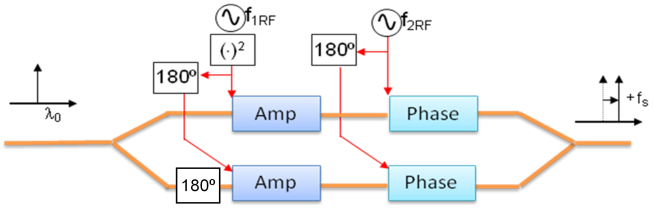


Fig 1: Functional description of the application-specific optical integrated circuit for wavelength shifting based in a Mach-Zehnder modulator, also showing the driving signals for the phase and amplitude (Amp) modulators.

A previous publication [8] analyzes best trade-off considering the performance of the wavelength shifter, measured as spurious free dynamic range (SFDR), and the required electro-optical bandwidth, showing that theoretically a SFDR higher than 35 dB can be obtained by proper synchronization of a tone and its harmonic [8].

C. Triple-arm based wavelength shifter

The requirements for the driving signals can be further

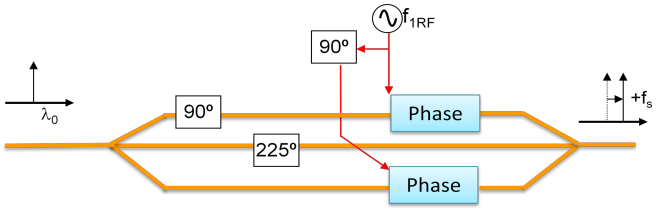


Fig 2: Functional description of the ASPIC for wavelength shifting based in a 3 arms structure, and required driving signals.

reduced by using a slightly more complex ASPIC based on a 3-arm structure as shown in Fig 2. In this case a single tone and appropriate adjustment of electrical and optical phases can also provide a proper wavelength shift of the incoming wavelength.

The triple-arm based wavelength shifter shown in Fig 2 does not include the extra elements that could be required as a variable attenuator driven by a bias current for adjusting the appropriate splitting ratio of the input signal into the 3 arms.

III. ASPIC DESIGN IN INP TECHNOLOGY

The specific ASPIC design depends strongly on the technology platform. We will describe the specific design achieved using the design manual developed by the European project "Photonic Advanced Research And Development for Integrated Generic Manufacturing" (PARADIGM). As described by the title of the project, it aims to provide a generic platform technology for reducing the cost of design, development and manufacturing of ASPICs. In order to do this, a set of basic generic modules are provided. Making use of these building blocks a specific design of the double-arm wavelength shifter is shown in Fig 3, including: strong confinement passive waveguides for input/output and S-bends; SOA weak waveguides; electro-optical phase modulator (φ-mod in Fig 3), several multi-mode interference (MMI) structures as 2:1 and 1:2 power splitters and input/output spot

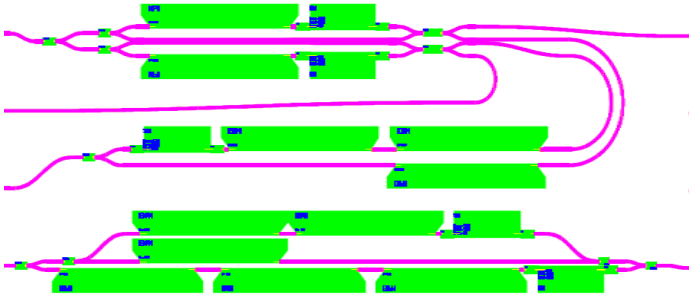


Fig 3: GDS view of the dual-arm (top) and triple-arm (bottom) wavelength shifter corresponding to the functional descriptions of Fig 1 and Fig 2.

size converters for improved coupling.

The layout shown in Fig 3 shows that the implementation of the triple-arm wavelength shifter, though initially more complex, leads finally to a more compact final design.

ACKNOWLEDGMENT

J.A. Lazaro thanks to Prof. Rosa M. Fernandez and Sergio Zarza of the Dept. of Signal Theory and Communications of the UPC for their technical support and fruitful discussions.

REFERENCES

[1] T. S. El-Bawab, "FTTx: The Rise of Broadband Optical Access" Globecom Workshops, 26-30 Nov. Washington, DC, U.S.A., 2007.

[2] A. Lovric et al, "Power Efficiency of SARDANA and Other Long-Reach Optical Access Networks", ONDM'11, S5-2, 2011.

[3] P. Gysel and R. K. Staubli, "Statistical properties of Rayleigh backscattering in single-mode fibers," J. Lightw. Technol., vol. 8, no. 4, pp. 561-567 (1990).

[4] J. A. Lazaro, C. Arellano, V. Polo, and J. Prat, "Rayleigh scattering reduction by means of optical frequency dithering in passive optical networks with remotely seeded ONUs" IEEE Photon. Technol. Lett. vol. 19, no. 2, pp 64-66 (2007)

[5] S. Shimotsu, M. Izutsu, T. Kawanishi, S. Oikawa, and M. Sasaki "Wideband frequency conversion with LiNbO3 optical single-sideband modulator" in Optical Fiber Communication Conference 2001, wk3-2.

[6] M. Omella, P. Chanclou, J. A. Lazaro, J. Prat, "RSOA as a Sawtooth Generator for Rayleigh Backscattering Effect Mitigation", in European Conference in Optical Communication Conference 2010, Mo.1.B.5.

[7] I. Y. Poberezhskiy et al., "Serrodyne frequency translation of continuous optical signals using ultrawide-band electrical sawtooth waveforms," IEEE J. Quantum Electr., vol. 41, no. 12, pp. 1533–1538, Dec. 2005.

[8] M. Omella, J. A. Lazaro, V. Polo, J. Prat, "Driving Requirements for Wavelength Shifting in Colorless ONU With Dual-Arm Modulator", J. Lightw. Technol., vol. 27, no. 17, pp. 3912-3918 (2009)

Ultra-high Q and finesse all-pass microring resonators on Silicon-on-Insulator using rib waveguides

Peter De Heyn, Diedrik Vermeulen, Thomas Van Vaerenbergh, Bart Kuyken and Dries Van Thourhout
Photonics Research Group, Department of Information Technology
Ghent University - *imec*, B-9000
Ghent, Belgium
Peter.DeHeyn@intec.ugent.be

***Abstract*— Low-loss rib waveguides on Silicon-on-Insulator are used to demonstrate ultra high-Q and finesse all-pass microring resonators with record finesse of 1100 and Q of 613000.**

Key words— Microring resonators, Silicon-on-Insulator (SOI)

I. INTRODUCTION

Microring resonators are considered to be key components for integrated photonics, especially in high-index contrast platforms such as Silicon-on-Insulator (SOI). Many promising applications have been demonstrated on this high-yield high-volume platform ranging from data communications, optical interconnects, bio-sensing and non-linear applications [1]. Each application has their own specifications with respect to the coupling between the mircoring and the bus waveguide, but in general one needs a low-loss cavity and thus low-loss waveguides. Although low-loss (~2dB/cm) [1] deep-etched waveguides on SOI using the quasi-TE mode with negligible bending loss for radii up to 5µm [ref] have been demonstrated, the performance of microring resonators is limited by resonance-splitting induced by backscattering [1]. The origin of backscattering can be found in the vertical sidewall roughness of the waveguide. By using the quasi-TM mode which has less overlap with the vertical sidewall roughness the backscattering can be significantly reduced. Another approach to minimize the overlap of the quasi-TE mode with this vertical sidewall roughness is to optimize the waveguide dimensions [2] or use partially etched rib waveguides the waveguides [3]. In this paper, these rib waveguides are optimized and result in lower scattering as well as low bending loss. We demonstrate critically coupled microring resonators with loaded Q factors of 613000 and a finesse of 1100 which is approximately a twofold improvement over previous reported results [4].

II. DESIGN AND FABRICATION

Our design is based on a SOI platform exhibiting a 220nm silicon device layer on a 2µm thick buried oxide layer. We choose a shallow etch step of 70nm. The waveguide width is next to the etch depth, an important design parameter to minimize the bending loss. This loss can be simulated using a 2D mode solver (e.g. Fimmwave Photon Design, UK). As expected a smaller bending loss for a wider waveguide, as a result of the better confinement is found. Simulations reveal that for a radius of 25µm the quasi-TE mode the bending loss of 500nm, 600nm and 700nm wide waveguide is respectively 17.3, 3.1 and 0.81dB/cm. The quasi-TM mode is not supported in these rib waveguides. To compare the bending losses for the different waveguide widths, microring resonators with a radius of 25µm and 50µm were fabricated. Using fiber grating couplers, TE-polarized light is coupled into this all-pass microring resonator.

III. EXPERIMENTS AND RESULTS

The performance of microring resonators is commonly expressed as the intrinsic Q (Q_i) which represents the number of oscillations of the field before the circulating energy is depleted to 1/e of the initial energy and thus represents the losses in the cavity using (1) with n_g the groups index of the mode.

$$\alpha\left[\frac{dB}{cm}\right] = \frac{4.3*2\pi n_g}{\lambda[cm]Q_i} \quad (1)$$

The 3dB bandwidth of a single resonance is then broadened by the coupling towards the ring, expressed in terms of the loaded Q (Q_l) and the Q of the coupling towards the ring (Q_c).

$$\frac{1}{Q_l} = \frac{1}{Q_i} + \frac{1}{Q_c} \quad (2)$$

For large gaps or low coupling towards the microring Q_l evolves into the intrinsic Q_i. This behavior is shown in Fig.1, where the mean Q_l of all resonances in a wavelength range from 1520nm to 1560nm per ring is plotted for varying gap and this for rings with a fixed waveguide width of 500nm, 600nm and 700nm and a radius of 25µm and 50µm respectively. From this figure one can see that for the small waveguide width of 500nm and the smallest radius of 25µm, the Q is converging to a poor Q_i of 50000. For a radius of 50µm, this Q drastically increases to 500000 indicating that the bending loss was indeed the limiting factor for Q which agrees with the trend of the bending loss simulations. The Q of microring resonators with a waveguide width of 600nm with a radius of 50µm is approximately the double than the ones of 25µm which shows that even for this waveguide width the bend loss is not negligible. For a width of 700nm, this difference between the two radii becomes smaller showing that the bend loss is significantly reduced.

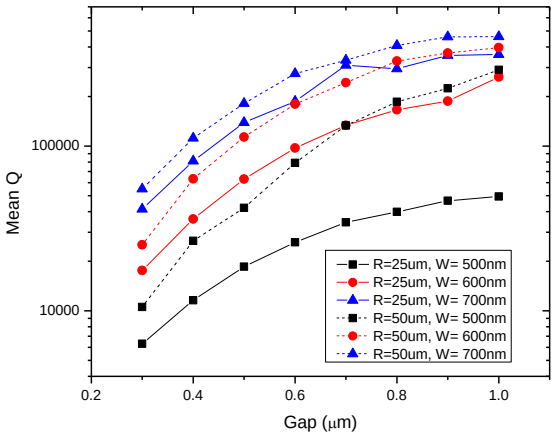


Figure 1: The mean Q_i over all resonances per ring between 1520nm and 1560nm as a function of gap for varying waveguide width (W) and radius (R).

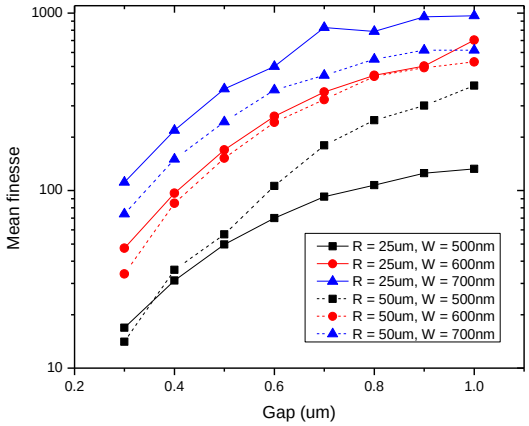


Figure 2: The mean finesse over all resonances per ring between 1520nm and 1560nm in function of gap for varying waveguide width (W) and radius (R).

In a next experiment the finesses of the different rings are compared. The finesse is defined as the Q divided by the free-spectral-range and is a measure for the round trip loss. Its mean value over all resonances per microring is plotted in Fig. 2 for the same varying set of parameters. For a microring with 700nm waveguide width, the finesse for a radius of 50µm is indeed the half of the finesse for a 25µm radius indicating that the waveguide loss is equal for both bending radii or consequently that the bending loss is negligible. For the smaller waveguide widths of 500nm and 600nm, the finesse for the larger bending radius is respectively larger and equal than the smaller bending radius indicating a decreasing bending loss for increasing waveguide width. When the coupling becomes large, such as in the case with waveguide width 500nm and small gaps (<0.5µm) the coupling factor is too large and hiding an effect of Q_i following (2).

Due to the ultra-high Q that reaches easily >100000, any small portion of backscattering results in resonance splitting (±10pm) and degrades the performance. Since this backscattering process is wavelength dependent, some peaks are not affected and show very good performances for either a high Q or finesse in the critically coupled regime such as plotted in Fig. 3. Ring 1 is a microring resonator with waveguide width of 0.7µm, radius of 25µm and gap 0.7µm demonstrating a Q of 417000, an ultra-high finesse of 1100 and an extinction ratio of 17dB. This record finesse enables a whole new set of applications. For example, the enormous finesse, a measure of the Purcell factor, could significantly reduce the threshold in Raman lasers. Other examples include ultra-dense WDM applications, sensing and delay lines.

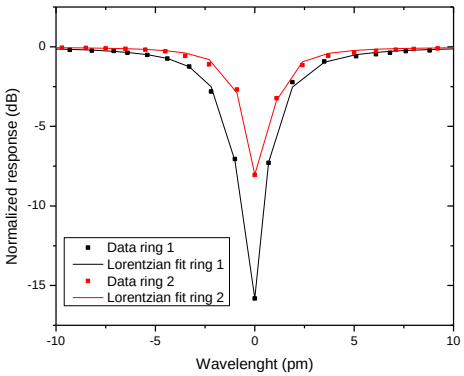


Figure 3: Illustration of two critically coupled microring resonators with a Lorentzian fit. Ring 1: R=25µm, gap=0.7µm, width=0.7µm, around 1550nm. Ring 2: R=50µm, gap=0.7µm, width=0.7µm, around 1530nm.

IV. Conclusions and Outlook

Low-loss rib waveguides on Silicon-on-Insulator are optimized and used to demonstrate all-pass microring resonators with a record finesse of 1100 and Q of 613000. This record finesse could enable a whole new set of applications such as reduced threshold in Raman lasers, ultra-dense WDM applications, sensing and delay lines.

References

[1] Bogaerts, W., De Heyn, P., Van Vaerenbergh, T., De Vos, K., Kumar Selvaraja, S., Claes, T., Dumon, P., et al. "Silicon Microring Resonators". *Laser & Photonics Reviews*, 6(1), 2012

[2] Barwicz, T., Haus, H. "Three-dimensional analysis of scattering losses due to sidewall roughness in microphotonic waveguides". *Journal of Lightwave Technology*, *23*(9), 2719-2732, 2005

[3] Dong, P., Qian, W., Liao, S., Liang, H., Kung, C.-C., Feng, N.-N., Shafiiha, R., et al. "Low loss shallow-ridge silicon waveguides". *Optics express*, *18*(14), 14474-9, 2010

[4] Adams, D., Madejski, G., & Preble, S. "High-Q Shallow Etch Silicon Micro Resonators for Optical Delay". *IEEE Photonics Conference*, p. ThZ2, 2011

Polarisation entanglement engineering at telecom wavelength using guided-wave optics

Florian Kaiser, Lutfi Arif Ngah, Amandine Issautier, Olivier Alibart, Anthony Martin,* and Sébastien Tanzilli†
Laboratoire de Physique de la Matière Condensée, CNRS UMR 7336,
Université de Nice - Sophia Antipolis Parc Valrose 06108 Nice Cedex 2, France.

We report on the association of a guided-wave optics scheme and an integrated optical photon pair generator for obtaining high-quality photonic polarization entangled states at a telecom wavelength, especially suitable for narrow bandwidth photons.

Today's optical telecommunication networks are mostly built using high-reliability fibre and integrated optical components, enabling data rates on the order of several Tbits/s for single fibre lines. Although such high data rates seem currently unreachable with novel quantum information based applications, for which nowadays rates are rather on the order of several Mbits/s and per ITU channel [2], quantum cryptography can offer security levels unattainable with classical means [1].

Quantum networks mainly rely on sources of either single or entangled pairs of photons. The former ones require typically a small experimental apparatus, but the associated security is based on the assumption that the user's locations are not under control of a potential spy. On the contrary, entanglement based quantum applications could offer device-independent security, at the price of justifiable additional expenses.

In this framework, polarisation entanglement is probably the easiest-to-handle observable, thanks to interferometer-free quantum state analysis. Several telecom polarisation entanglement sources have already been reported, mainly relying on type-II non linear spontaneous parametric down-conversion (SPDC), either in bulk or waveguide crystals [3]. However, in order to guarantee high-quality entanglement, perfect indistinguishability of the created photons needs to be ensured for the temporal, spatial, and spectral observables. In addition, the type-II interaction is relatively weak, such that high pump laser powers might be required, especially when ultra-narrow bandwidth photons are to be used for compatibility with optical quantum memory devices (<1 GHz of absorption bandwidth) [4, 5].

In the following, we apply a polarisation entanglement engineering scheme to a type-0 SPDC photon pair generator from which no polarisation entanglement is initially available. The scheme could be further extended to purify entanglement from type-II sources for which perfect control on all parameters is not possible.

EXPERIMENTAL IMPLEMENTATION

The experimental apparatus is shown in FIG. 1. A 780 nm pump laser is actively stabilised against a ^{87}Rb hyperfine transition to achieve a coherence time of about 3 μs. The laser is then coupled via a single mode fibre into a 4.5 cm long periodically poled lithium niobate waveguide (PPLN/W). The channel waveguide was realised

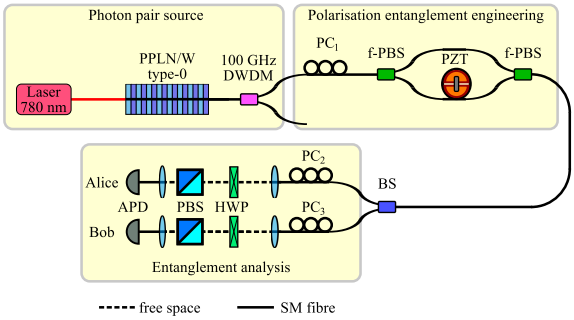


FIG. 1. Experimental setup for polarisation entanglement engineering for photon pairs out of a the type-0 waveguide generator. A 100 GHz DWDM is used for spectral filtering. After the pairs are separated at a beam splitter (BS), the entanglement quality is measured using standard Bell inequality apparatus. Half wave-plate (HWP); polarising beam splitter (PBS); avalanche photodiode (APD).

using the so-called proton exchange technique. This allows exploiting the highest non linear SPDC coefficient (d_{33}) of the crystal, and utilising the type-0 interaction ($V_{\text{pump}} \mapsto V_1 V_2$, the subscripts 1 and 2 describing the two photons). The down-conversion probability of our sample is on the order of 10^{-5} pairs per coupled pump photon. The sample's temperature is stabilised around 387 K so as to reach the desired quasi phase-matching condition, *i.e.* wavelength degenerate paired photons at 1560 nm. In order to make our system compatible with telecom networks at the output of the waveguide, the photons are first collected using a standard single mode fibre, and their natural emission bandwidth ≈ 20 nm $\leftrightarrow$ 2.5 THz) is reduced using a 100 GHz telecom DWDM.

At this stage, the paired photons' polarization state reads $|V\rangle_1|V\rangle_2$, which is clearly a product state although the photons are naturally energy-time entangled. To engineer polarization entanglement on these photons, their states are first rotated diagonal, $|D\rangle_1|D\rangle_2$, using a fibre polarisation controller (PC_1). Then, they are sent to a 7.5 m unbalanced Mach-Zehnder interferometer like birefringent delay line made of two fibre polarising beam splitters (f-PBS) at both its input and output. In this configuration, the $|H\rangle$ component of each photon is delayed by 32 ns compared to the $|V\rangle$ coun-

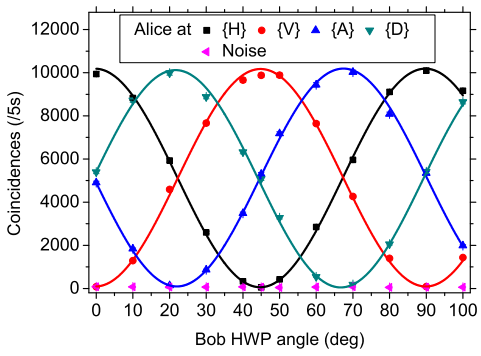


FIG. 2. Two-photon interference patterns for the four standard analysis settings, $\{H; V; A; D\}$, on Alice's side, while Bob's analyser is rotated. Near-unit visibilities underline the high quality entanglement obtained with our setup.

terpart. Polarisation entanglement of the form $|\Phi(\phi)\rangle = \frac{1}{\sqrt{2}}\left(|H\rangle_1|H\rangle_2 + \mathrm{e}^{i\,\phi}|V\rangle_1|V\rangle_2\right)$ is then generated by post selection of photon pairs detected simultaneously. The phase factor ϕ arises from the different path lengths for the two contributions to the entangled state. In order to obtain high-quality entanglement, the photon pair creation time has to be more uncertain than the temporal separation provided by the delay line [6]. This is guaranteed by both the long coherence time of our stabilised laser and the spontaneous character of the photon pair emission. Violating the so-called Bell inequalities further requires ϕ to be constant during the two-photon interference measurement. This is achieved by a home-made stabilisation system comprising a reference laser and a piezo fibre stretcher (PZT) in the delay line (see FIG. 1). The paired photons are then separated using a fibre beam splitter (BS) and sent to standard polarisation analysers at Alice's and Bob's sides. By properly adjusting ϕ with the PZT, we establish the maximally entangled state $|\Phi(0)\rangle$ and proceed to the violation of the Bell inequalities. As shown in FIG. 2, we obtain, for the four standard measurement settings $\{H; V; A; D\}$, raw (net) two-photon interference visibilities exceeding 97±1% (99±1%). This clearly underlines the high quality entanglement achieved with our guided-wave strategy.

CONCLUSION

We have demonstrated a way to engineer polarisation entanglement from initially energy-time entangled paired photon. To do so, a fully fibred birefringent delay line was used and associated with a high-brilliance, wavelength degenerate, type-0 integrated waveguide photon pair generator operating at 1560 nm. We emphasize that this scheme could also be applied in a more general perspective, namely with initial photon pair states that could be subjected to instabilities in the spectral and/or temporal domains. Due to the strong separation of the $|H\rangle$ and $|V\rangle$ components in the delay line (32 ns), this strategy makes it possible to handle single photon bandwidths down to ∼100 MHz [7]. Such narrow bandwidths are of utmost interest for long distance communication protocols based on quantum memories [4, 5].

Moreover, our source delivers near-perfect polarisation entangled pairs of photons at a detected coincidence rate of around 2 kBit/s in a single ITU channel at a pump power of a few tens of μW. Here, the main limitation concerns the rather low maximum detection rates of the employed free-running InGaAs-APDs (IDQuantique id220). This could be circumvented by using high-speed superconducting or frequency up-conversion detectors, with which considerably higher detected coincidence rates should be attainable. In this scope, we calculated that the maximal entangled photon pair rate at the output of this source could reach 1 Mpairs/s, for a pump power of 2 mW, before entanglement quality is degraded by the contribution of double pair emission.

We stress that the association of standard telecom components with a high-brilliance integrated optical biphoton generator, as utilised in this work, is a promising route towards enabling future quantum applications, especially those involving quantum memory devices [4, 5].

ACKNOWLEDGEMENTS

The authors would like to thank V. D'Auria, L. Labonté, M. P. De Micheli, and D. B. Ostrowsky for their help, as well as ID Quantique, and Opton Laser International for technical support. The authors also acknowledge the CNRS, the University of Nice - Sophia Antipolis, l'Agence Nationale de la Recherche for the "e-QUANET" project (grant ANR-09-BLAN-0333-01), the European ICT-2009.8.0 FET open program for the "QUANTIP" project (grant 244026), le Ministère de l'Enseignement Supérieur et de la Recherche (MESR), the Malaysian government (MARA), the Direction Générale de l'Armement (DGA), the Fondation iXCore pour la Recherche, and the Conseil Régional PACA, for financial support.

* Currently with the GAP, University of Geneva
† Florian.Kaiser@unice.fr, Sebastien.Tanzilli@unice.fr

[1] N. Gisin *et al.*, Rev. Mod. Phys. **74**, 145 (2002).
[2] A. R. Dixon *et al.*, Appl. Phys. Lett. **96**, 161102 (2010).
[3] A. Martin *et al.*, New J. Phys. **12**, 103005 (2010), and references therein.
[4] E. Saglamyurek *et al.*, Nature **469**, 512 (2011).
[5] C. Clausen *et al.*, Nature **469**, 508 (2011).
[6] W. Tittel and G. Weihs, Quant. Inf. Comp. **1**, 3 (2001).
[7] F. Kaiser *et al.*, e-print arXiv:1111.5683 (2011).

Optical devices for the Discrete Fourier Tranform

Gabriella Cincotti
Department of Applied Electronics
University Roma Tre
Rome, Italy
cincotti@uniroma3.it

***Abstract*—We review the design guidelines for devices that implements the DFT in the optical domain. We also introduce a novel planar architecture to perform the DFrFT, based on an AWG configuration.**

Fourier transform; waveguide grating router; Mach Zehnder interferometer; orthogonal frequency division multiplexing

I. INTRODUCTION

Orthogonal frequency division multiplexing (OFDM) is the key technology for a large variety of high-speed digital communications over bandwidth-constrained physical media, both wireless and copper wired. The basic idea of multicarrier modulation dates back to 1960s, but it became a practical reality only when the appearance of mass market applications coincided with the availability of efficient electronic digital signal processing (DSP). The two key features for the widespread of OFDM technology are the orthogonality of the subacarriers that enhances the spectral efficiency, and the electronic signal processing to equalize the channel distortion.

OFDM is gaining larger and larger research interest also among the fiber optics community, and at the moment is one of main R&D topic. The modulation/detection combinations for optical OFDM include optical intensity modulation (IM) with direct detection (DD), optical modulation with coherent detection, and all-optical modulation with coherent detection [1]. In the latter case, the discrete Fourier transform (DFT) and the inverse discrete Fourier transform (IDFT) are (analogically) implemented in the optical domain, avoiding high-speed and power consuming DSP, analog to digital converter (ADC) and digital to analog converter (DAC). Recently, the record transmission of a 26 Tb/s transmission has been demonstrated [2].

The implementation of a device that performs the DFT in the optical domain may have different physical implementations, and in the present paper some optical architectures are analyzed. A novel configuration to perform the discrete fractional Fourier transform (DFrFT) is also described, that can be advantageously used in an optical OFDM system.

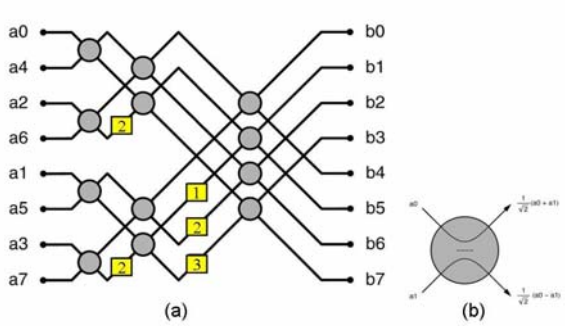


Figure 1. From [4]: (a) meshed fiber network composed of asymmetric couplers and phase shifters that performs the DFT of a parallel input. The phase shifters are represented by the boxes of value -q2π/N (q is the number inside the box). (b) asymmetric coupler.

II. OPTICAL DFT DEVICES

The first architecture to optically implement the DFT was first proposed by M. E. Marhic [3] and later restated by A. E. Siegman [4]. The meshed fiber network of Fig. 1(a) is composed of asymmetric couplers and phase shifters to perform the DFT of a parallel input signal

$$b_m = \sum_{n=0}^{N-1} a_n \exp\left(-j\frac{2\pi mn}{N}\right) \quad (\mathrm{m} = 0,1,2,..,\mathrm{N}-1), \cdot \tag{1}$$

According to the Cooley-Tukey algorithm, the *N*-order DFT of a parallel input signal is evaluated by a chain of log_2N stages, each stage is composed of an asymmetric *2X2 3*dB coupler (Fig. 1(b)), that implements the second-order DFT. However, to be used in optical communications, where data are serially transmitted over a fiber, a serial to parallel (S/P) converter is required. To overcome this limitation, a restatement of the optical DFT approach was formulated for a discrete serial input [5]: the *N*th-order DFT of a sequence of optical bits is obtained by a chain of log_2N stages, each of them composed of a Mach Zehnder Interferometer (MZI) with an output asymmetric coupler, that corresponds to the second-order DFT, as shown in Fig. 2.

A different architecture for the optical *N*th-order DFT has been also proposed with the arrayed waveguide grating (AWG) configuration shown in Fig. 3.

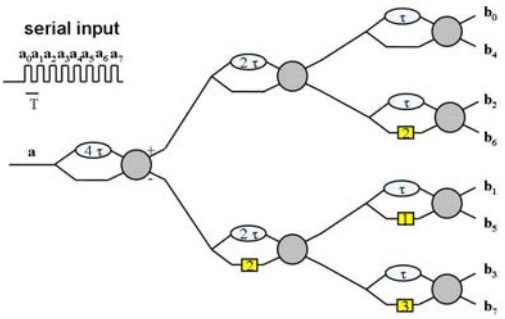


Figure 2. From [6]: tree architecture composed of MZIs with asymmetric couplers and phase shifters that performs the DFT of a serial input. The phase shifters are represented by the boxes of value -q2π/N (q is the number inside the box).

In this case, the array pitches d and d_o have to satisfy the condition

$$d = d_o = \sqrt{\frac{\lambda R}{N}} \qquad l = R \cdot \tag{2}$$

where l and R are the slab length and radius of curvature, respectively. In addition, the delay $\Delta\tau$ introduced by two adjacent waveguides should equate the inverse of the input bit rate.

III. OPTICAL DFRFT DEVICE

It is important to observe that the second slab coupler (Fig. 4(a)) of the AWG performs the spatial DFT of a parallel input signal, and it is equivalent to the two-lens system shown in Fig. 4(b). It is well known that the light distribution in the output plane is the Fourier transform of the input object, and this concept is at the basis of the whole optical information processing. By equally spacing the input and output waveguides, that satisfy Eq. (2), we obtain the DFT. The waveguide grating with delay $\Delta\tau$ is used only to perform the S/P conversion.

If we change the slab length and the curvature radius so that they satisfy the condition

$$d = d_o = \sqrt{\frac{\lambda R}{N}} \qquad R = R_1 \cot\left(p\frac{\pi}{4}\right) \qquad l = R_1 \sin\left(p\frac{\pi}{2}\right) \tag{3}$$

where R_1 is a constant length, we obtain the DFrFT of order $0<p<2$.

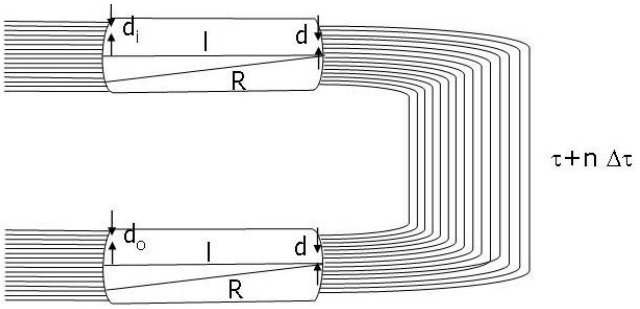


Figure 3. AWG architecture that performs the DFT.

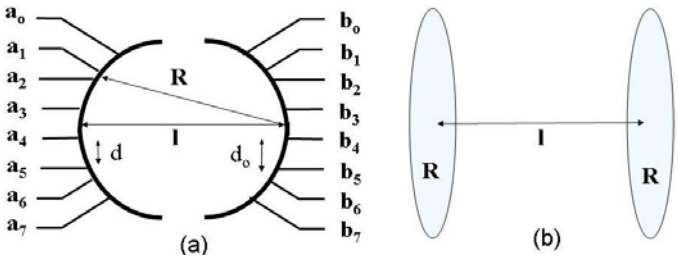


Figure 4. (a) slab coupler configuration. (b) two lenses configuration.

The analog fractional Fourier transform of order p of a signal $x(t)$ is defined as

$$\tilde{x}(u) = F^p\{x(t)\}(u) = \left|\sin\left(p\frac{\pi}{2}\right)\right|^{-\frac{1}{2}} e^{j\frac{\pi}{4}\left\{p-sign\left[\sin\left(p\frac{\pi}{2}\right)\right]\right\}} \cdot \int_{-\infty}^{\infty} x(t) e^{j\pi\left[\left(t^2+u^2\right)\cot\left(p\frac{\pi}{2}\right)-2tu\csc\left(p\frac{\pi}{2}\right)\right]} dt \tag{4}$$

and it is a generalization of the standard Fourier transform, and satisfies the additivity property

$$F^p\left\{F^q\{x(t)\}\right\} = F^{p+q}\{x(t)\} \ . \tag{5}$$

OFDM schemes based on the DFrFT can be advantageously used in high-speed fiber systems, because the corresponding subcarriers satisfy the orthogonality condition; in addition they present a chirped behavior that can be used to compensate chromatic dispersion. Furthermore, the peak-to-average power ratio (PAPR) corresponding for OFDM modulation can be largely reduced if the DFrFT is used.

REFERENCES

[1] [1] W. Shieh and I. Djordjevic, OFDM for optical communications, Elsevier, London 2010.

[2] D. Hillerkuss *et al*., "26 Tbit line-rate super-channel transmission utilizing all-optical fast Fourier transform processing," Nature Photon., vol. 5, pp. 364–371, May 2011.

[3] M. E. Marchic, "Discrete Fourier transforms by single-mode star networks," Opt. Lett., vol. 12, pp. 63-65, 1987.

[4] A. E. Siegman, "Fiber Fourier optics," Opt. Lett., vol. 19, pp. 1215-1217, 2001.

[5] G. Cincotti, "Fiber Wavelet Filters," J. Quantum Electron. 38, 1420-1427, 2002.

[6] D. Hillerkuss, et al, "Simple all-optical FFT scheme enabling Tbit/s real-time signal processing", Opt. Exp. 18, pp. 9324, (2010)

[7] G. Cincotti, "Full optical encoders/decoders for photonic IP routers," J. Lightw. Technol. vol. 22, 337-342 (2004).

[8] G. Cincotti, "Design of optical full encoders/decoders for code-based photonic routers," J. Lightw. Technol. vol. 22, pp. 1642-1650, 2004.

[9] G. Cincotti "Generalized fiber Fourier optics," Opt. Lett., vol. 36, pp. 2321-2323, 2011.

A new method of second harmonic generation based on light tunneling between waveguide channels

A. Méndez, J. Ramiro, A. Alcázar de Velasco
Departamento de Aerotecnia
Universidad Politécnica de Madrid
Madrid, Spain
angel.mendez@upm.es

***Abstract*— A new method for obtaining second harmonic generation is proposed. Tunneling between coupled waveguides provides the required quasi-phase matching. Its simple technological implementation and high conversion efficiency make this novel approach a competitive alternative to existing methods.**

Keywords-component; second harmonic generation; quasi-phase matching; channel waveguides; coupled waveguides

I. INTRODUCTION

Phase matching is key for efficient nonlinear frequency conversion. As material dispersion usually breaks the phase matching condition, different quasi-phase matching (QPM) procedures have been developed, usually based on a periodical or chirped variation of the nonlinear susceptibility [1,2]. An efficient technique to get QPM is by periodically poled structures, although it requires the poling of the crystal, either during its growth or in the device fabrication process [3,4]. Also, periodic poling presents some interferences with waveguides fabrication techniques [5].

In this paper, a different approach is taken for second harmonic generation (SHG). Instead of varying the material parameters, the intensity of the fundamental beam is modulated to avoid the destruction of the generated harmonic, thus providing QPM. This modulation can be obtained thanks to the light intensity transfer between two sufficiently close waveguides.

II. THEORETICAL BACKGROUND

A. Second harmonic generation

When a fundamental wave with frequency ω_1 and wavelength λ_1 interacts with the second-order nonlinear susceptibility of a material a polarization wave at the second-harmonic frequency $\omega_2 = 2\cdot\omega_1$ is produced. Since the polarization wave is forced by the fundamental wave, it travels with the same velocity, determined by n_1, the index of refraction at the fundamental wavelength. The polarization wave generates a second-harmonic wave which travels at a velocity determined by its index of refraction (n_2). In general $n_2 > n_1$ because of dispersion in the material, so that the fundamental and second-harmonic waves travel at different phase velocities [2]. So the field intensities of the fundamental wave and the second harmonic are coupled. The coupling system of equations is obtained from the nonlinear wave equation and is the following:

$$\begin{aligned} \frac{dA_1}{dz} &= \frac{2\mathrm{i}\omega_1^2 d_{eff}}{k_1 c^2} A_2 A_1^* \; e^{-i\Delta kz} \\ \frac{dA_2}{dz} &= \frac{\mathrm{i}\omega_2^2 d_{eff}}{k_2 c^2} A_1^2 e^{i\Delta kz} \\ \Delta k &= 2\mathrm{k}_1 - k_2 \end{aligned} \tag{1}$$

where $A_{1,2}$ are the field amplitude of the fundamental and the second harmonic, respectively, d_{eff} the nonlinear coefficient of the material and k the wave vector. [6].

B. Waveguide tunneling

It is known that when two identical channel waveguides are sufficiently close to each other, the electromagnetic field of the light traveling across one of the channels reaches the other one. Then, energy transfer between the channels takes places resulting in a periodic transfer of light from one channel to the other one. So the field amplitude of the light in one channel as it travels in the z-direction can be expressed as:

$$\frac{dA}{dz} = -\frac{2\pi}{L}\sin\left(2\pi\frac{L}{z}\right) \tag{2}$$

where A is the field amplitude and L the period of the light in one channel. L depends on the characteristics of the waveguides (index profile, index depth, distance between channels, etc.)

C. Quasi-phase matching via channel waveguides coupling (CWG QPM).

The SHG of a waveguide can be improved dramatically by using two channel waveguides to obtain QPM. In this paper we have solved the system of equations shown in (1) but taking

This work was supported by Ministerio de Ciencia e Innovación and Ministerio de Economía y Competitividad of Spain under grants MAT2008-06794-C02 and MAT2011-28379-C03-03, respectively.

into account a change of the field amplitude of the fundamental beam as shown in (2).

With this configuration the fundamental wave is traveling between the two channels periodically. When the spatial frequency of the fundamental wave matches the second harmonic we obtain QPM and the intensity of the second harmonics increases. It is important to notice that both channels produce second harmonic and the second harmonic efficiency at the output is the addition of both channels.

The equations shown here are general and can be used with any nonlinear optical material. However, in the next section the parameters of the lithium niobate are used to show the ratio A_1/A_2 that can be obtained with this new method.

III. RESULTS

For the sake of generality the data will be shown as a function of L. However, the other parameters must be set. In order to obtain some results we have chosen the values of the parameters of $LiNbO_3$.

TABLE I. $LiNbO_3$ parameters

Parameter	***Value***
$d_{eff} = d_{33}$	30x10-6 μm/V
λ_1	1.064 μm
n_1, n_2	2.175, 2.251
I_1	$3 \cdot 10^7$ W/m^2
Propagation length	5 cm

In Fig. 1 the values of the coherence length for the best QPM can be observed. CWG and PPLN QPM for the parameters mentioned above are compared. CWG QPM and first order PPLN QPM occur at the same coherence length, detail of these peaks can be seen in Fig 1b. The maximum SHG is obtained for the PPLN at 6.9 μm but this configuration is very difficult to achieve experimentally [6]. The following maximum is the one obtained with CWG QPM. The next one is obtained with the PPLN at second order.

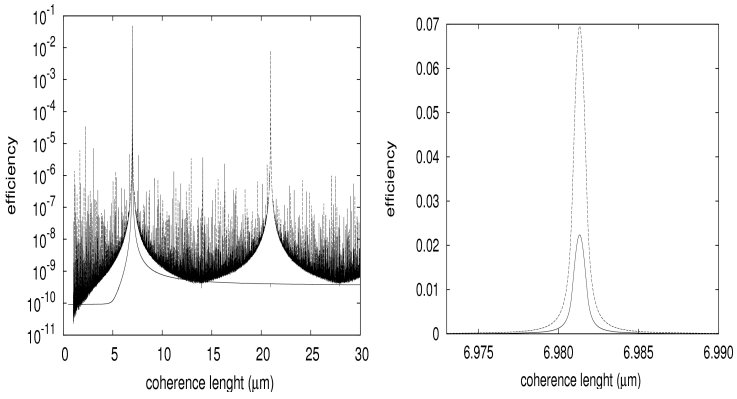


Figure 1. Efficiency of SHG as a function of coherence length in CWG-QPM (continnous line) and first and third order of PPLN-QPM (dashed line).

In Fig 2, the amplitude of SHG is shown as a function of the propagation length (z) for the first-order PPLN, CWG and second-order PPLN, respectively. Fig 2b shows a small range of z to see how the second harmonic grows. The first-order PPLN always increases while the second-order PPLN exhibits a decay at each domain region. It must be noted, however, that obtaining first-order PPLN presents technical challenges that are difficult to overcome [6]. The CWG QPM grows monotonically and offers a second harmonic efficiency remarkably better than second-order PPLN, while being technically more feasible than first-order PPLN.

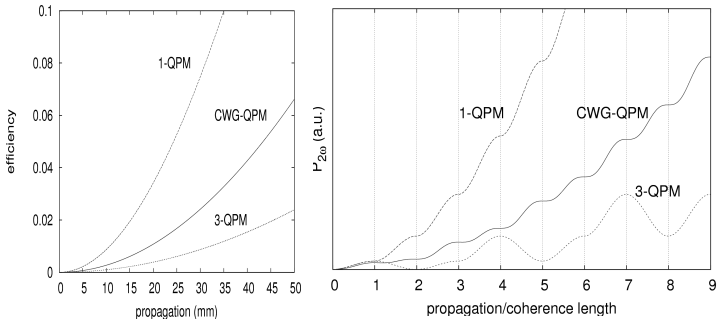


Figure 2. Efficiency for SHG for the first coherence lengths for CWG-QPM and first and third order of PPLN-QPM.

IV. CONCLUSION

We propose a new method for SHG in waveguides, very easy to implement from a technological point of view and with a high conversion efficiency. When compared with PPLN SGH, our novel method shows conversion efficiencies that are lower than those corresponding to first-order PPLN but significantly higher than those of second-order PPLN.

These results and the technical difficulties associated to first-order PPLN, make our proposed method a very competitive alternative for the design of waveguide frequency-doubling devices.

REFERENCES

[1] J. A. Armstrong, N. Bloembergen, J. Ducuing, P. S. Pershan, "Interactions between Light Waves in a Nonlinear Dielectric", PhysRev 127(6) 1918-1939, 1962.

[2] M. M. Fejer, G. A. Magel, D. H. Jundt, R. L. Byer, "Quasi-phase-matched second harmonic generation: tuning and tolerances", Quantum Electronics, IEEE Journal of , vol.28, no.11, pp.2631-2654, 1992.

[3] A. Feisst, P. Koidl., "Current Induced Periodic Ferroelectric Domain Structures In Linbo3 Applied For Efficient Nonlinear Optical Frequency Mixing.", Applied Physics Letters 47.11, 1125-1127, 1985.

[4] L. E. Myers, R. C. Eckardt, M. M. Fejer, R. L. Byer, W. R. Bosenberg, and J. W. Pierce, "Quasi-phase-matched optical parametric oscillators in bulk periodically poled LiNbO3", J. Opt. Soc. Am. B 12, 2102-2116, 1995.

[5] O. Caballero-Calero et al., "Periodic poling of optical waveguides produced by swift-heavy-ion irradiation in LiNbO3", Applied Physics B: Lasers and Optics, 95(3), pp.435-439, 2009.

[6] R.W. Boyd “Non linear optics” 2nd ed. Elsevier Science, pp 95-105, 2003

Proposal of Optical Waveguide Circuits for Recognition of Optical QAM Codes

Kensuke Inoshita, Hiroki Kishikawa, Yoshihiro Makimoto, Nobuo Goto, and Shin-ichiro Yanagiya
Department of Optical Science and Technology
The University of Tokushima
2-1 Minamijosanjima-cho, Tokushima 770-8506, Japan
Email: {k.inoshita, h.kishikawa, y_makimoto, goto, giya}@opt.tokushima-u.ac.jp

Abstract— **Optical processing of optical labels is expected in broadband photonic label routers. We propose optical circuits to recognize optical QAM codes. The circuits are multi-stage connection of previously proposed circuit for QPSK code recognition. The recognition characteristics for 16 and 64 QAM codes are theoretically analyzed.**

Keywords-component; optical QAM code; code recognition; optical waveguide circuit; optical QPSK code

I. INTRODUCTION

Optical processing is expected to be applied in routing nodes for fast processing and reducing power consumption. In broadband networks, optical label routing will be a practical solution because of its simplicity and flexibility. Optical label recognition is one of key functions in label routers. Various label architectures have been investigated, including wavelength multiplexed and multi-level coded pulse trains. The authors have proposed waveguide circuits for recognizing on-off-keying (OOK), binary phase-shift-keying (BPSK), and quadature PSK (QPSK) labels.[1-3]

In recent high-bit rate fiber transmission, optical quadrature amplitude modulation (QAM) has been employed. A 2^M QAM symbol effectively represents 2^M codes. A transmission experiment with 512QAM codes at 64Gbps having bandwidth of 5.4GHz was reported.[4]

In this report, we propose waveguide circuits for recognition of optical QAM codes, by regarding a QAM code as a combination of two QPSK codes whose amplitudes are different. The circuits are based on the previously proposed QPSK recognition circuit. The proposed circuit for 16QAM recognition is theoretically analyzed. A circuit for recognition of 64QAM code is also discussed.

II. RECOGNITION OF 16QAM CODE

A constellation of a 16QAM code set is illustrated in Fig.1. We regard these codes as a combination of two QPSK codes. The optical electric field $E_{16\mathrm{QAM}}$ can be written as

$$E_{16QAM} = E_1 + E_2 , \qquad (1)$$

and

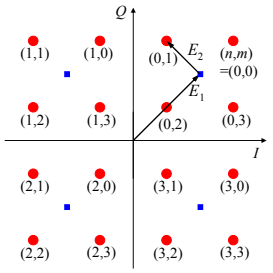


Fig.1 Constellation of 16QAM codes.

$$E_1 = 2E_0 e^{j\pi/4} e^{jn\pi/2}, \quad E_2 = E_0 e^{j\pi/4} e^{jm\pi/2}, \qquad (2)$$

where n, m=0,1,2,3. In Fig.1, sixteen codes corresponding to (n,m) are shown. The fields E_1 and E_2 are regarded as those of QPSK codes of amplitude $2E_0$ and E_0, respectively. Therefore, we consider recognition of the 16QAM code by cascaded connection of two circuits for QPSK code recognition.

Fig.2 shows a waveguide circuit for recognition of a QPSK code, named as QPSK phase recognition circuit (QPRC).[2] This circuit consists of a 3dB directional coupler, two Y-branches, and an asymmetric X-junction coupler. The output fields are related to the input fields as

$$\begin{pmatrix} E_{out}^{(1)} \\ E_{out}^{(2)} \\ E_{out}^{(3)} \\ E_{out}^{(4)} \end{pmatrix} = \frac{1}{2} \begin{pmatrix} 1 & e^{j3\pi/4} \\ e^{j7\pi/4} & e^{j7\pi/4} \\ e^{j5\pi/4} & e^{j\pi/4} \\ e^{j3\pi/4} & 1 \end{pmatrix} \begin{pmatrix} E_{in}^{(1)} \\ E_{in}^{(2)} \end{pmatrix}. \qquad (3)$$

Using two-stage connection of this QPRC, a proposed circuit for recognition of 16QAM codes is formed as shown in Fig.3. In addition to one QPRC and four QPRCs in the first and second stages, respectively, an amplifier having amplitude amplification coefficient of $2^{1/2}$, a 1:2 divider, an attenuator having amplitude attenuation coefficient of 1/2, a 1:4 divider, and a phase shift circuit after the

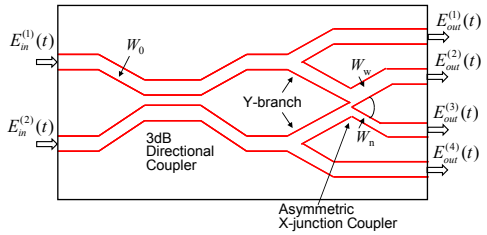


Fig.2 Basic circuit for QPSK code recognition (QPRC).

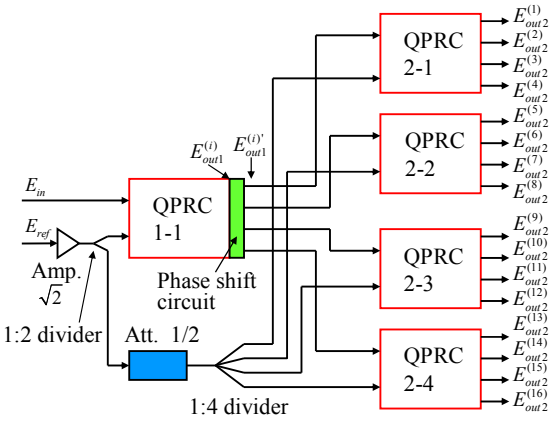


Fig.3 A circuit for recognition of 16QAM codes.

first QPRC. As the inputs E_{in} and E_{ref}, we consider $E_{16\text{QAM}}$ and the following reference signal:

$$E_{ref} = 2E_0 e^{j\pi/4}. \quad (4)$$

The phase shift circuit after the first QPRC is employed to adjust the phases among four outputs. The outputs $E^{(i)'}{}_{\text{out1}}$ are related to the inputs $E^{(i)}{}_{\text{out1}}$ as

$$\begin{pmatrix} E^{(1)'}_{out1} \\ E^{(2)'}_{out1} \\ E^{(3)'}_{out1} \\ E^{(4)'}_{out1} \end{pmatrix} = \begin{pmatrix} 1 & 0 & 0 & 0 \\ 0 & e^{j\pi/4} & 0 & 0 \\ 0 & 0 & e^{j3\pi/4} & 0 \\ 0 & 0 & 0 & e^{j\pi/2} \end{pmatrix} \begin{pmatrix} E^{(1)}_{out1} \\ E^{(2)}_{out1} \\ E^{(3)}_{out1} \\ E^{(4)}_{out1} \end{pmatrix}. \quad (5)$$

When the input given by (1) and (4) are incident, the outputs of the phase shift circuit is given by

$$\begin{pmatrix} E^{(1)'}_{out1} \\ E^{(2)'}_{out1} \\ E^{(3)'}_{out1} \\ E^{(4)'}_{out1} \end{pmatrix} = \frac{E_0 e^{j\pi/4}}{2} \begin{pmatrix} 2e^{jn\pi/2} + e^{jm\pi/2} + 2e^{j3\pi/2} \\ 2e^{jn\pi/2} + e^{jm\pi/2} + 2 \\ 2e^{jn\pi/2} + e^{jm\pi/2} - 2 \\ 2e^{jn\pi/2} + e^{jm\pi/2} + 2e^{j\pi/2} \end{pmatrix}. \quad (6)$$

Therefore, the outputs of QPRC2-k, (k=1,…4) are given by

$$\begin{pmatrix} E^{(1+4(k-1))}_{out2} \\ E^{(2+4(k-1))}_{out2} \\ E^{(3+4(k-1))}_{out2} \\ E^{(4+4(k-1))}_{out2} \end{pmatrix} = \frac{1}{2} \begin{pmatrix} 1 & e^{j3\pi/4} \\ e^{j7\pi/4} & e^{j7\pi/4} \\ e^{j5\pi/4} & e^{j\pi/4} \\ e^{j3\pi/4} & 1 \end{pmatrix} \begin{pmatrix} E^{(k)'}_{out1} \\ E_{ref}/4 \end{pmatrix}. \quad (7)$$

By combining (6) and (7), we find that only one output whose electric field is canceled out for each (n,m) in the electric complex plane. Although the maximum intensity of the outputs for each code depends on the combination of n and m, with the largest value $2.25E_0^2$ for (n,m)=(0,0), (1,1), (2,2), and (3,3), the second minimum intensity is constant 0.125 E_0^2. By using inverters at each output port whose threshold is below 0.125 E_0^2, the output port having null output can be distinguished. Fig.4 shows the output intensities for all codes, where a constant value of 0.01 E_0^2 is added for all outputs as a crosstalk which may occur through the waveguide circuit.

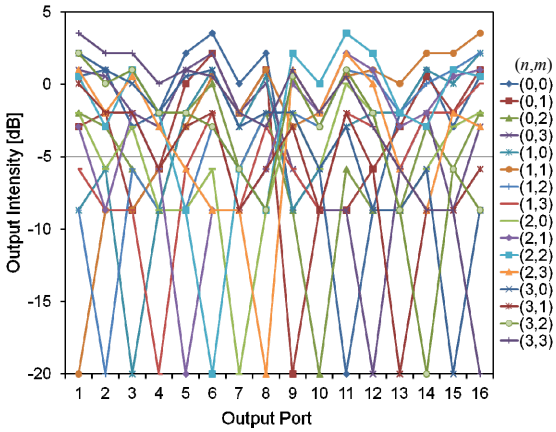


Fig.4 Normalized output intensities from sixteen output ports for all 16QAM codes.

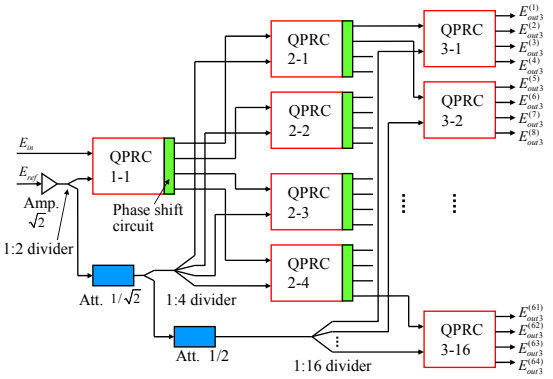


Fig.5 A circuit for recognition of 64QAM codes.

III. RECOGNITION OF 64QAM CODE

We consider a scaled circuit for recognition of 64QAM codes. Electric fields of 64QAM can be composed of three QPSK codes. The circuit can be formed by three-stage QPRCs as shown in Fig.5. The maximum and the second smallest output intensities are $3.0625E_0^2$ and $0.03125E_0^2$, respectively. By using inverters whose threshold is below $0.03125E_0^2$, the output port having null output can be distinguished.

IV. CONCLUSION

Optical waveguide circuits for recognition of 16 and 64QAM codes were proposed. Since the maximum output intensity for each code differs, the code is recognized at the output port whose output is minimum by using inverters. We will further investigate for circuits to recognize multiple symbols.

REFERENCES

[1] H. Hiura, Y. Makimoto, N. Goto, & S. Yanagiya, J. Lightwave Technol., vol.27, no.24, p.5543-5551, 2009.
[2] Y. Makimoto, H. Hiura, N. Goto, and S. Yanagiya, J. Lightwave Technol., vol.27, no.1, pp.60-67, 2009.
[3] A. Ihara, H. Kishikawa, N. Goto, and S. Yanagiya, J. Lightwave Technol., vol.29, no.91, pp.1306-1313, 2011.
[4] S. Okamoto, K. Toyoda, T. Omiya, K. Kasai, M. Yoshida, & M. Nakazawa, ECOC2010, Torino, PD.2.3, pp.19-23, 2010.

Multicolor wave-guiding in polymer/quantum dot nanocomposite waveguides

I. Suárez*, H. Gordillo, P. Rodríguez-Cantó, R. Abargues, S. Albert and J. Martínez-Pastor

UMDO (Unidad Asociada al CSIC-IMM)
Instituto de Ciencia de los Materiales, Universidad de Valencia
PO Box 22085, 46071 Valencia, Spain
*isaac.suarez@uv.es

***Abstract*— Nanocomposites based on colloidal quantum dots incorporated in polymer matrices are proposed. First, CdS, CdTe and CdSe are mixed in PMMA to demonstrate three-color waveguiding. Then, CdSe has embedded in SU8 to implement ridge active waveguides.**

Keywords: colloidal quantum dots, polymer, nanocomposite, organic-inorganic hybrid photonics, waveguides, PMMA, SU8

I. INTRODUCTION

Photonics research is evolving toward the development of novel functional materials able to perform more complex and efficient optical functions. In this way, one of the most promising approaches is the incorporation of nanoparticles into a host matrix to form a nanocomposite [1]. These synthetic multicomponent materials combine the novel properties of semiconducting, metallic or magnetic nanoparticles (e.g., quantum confinement, surface plasmon resonance, superparamagnetism, respectively) with those provided by the matrix. For this purpose the choice of polymers as a host matrix is an attractive approach, because they are cheap, flexible and can be easily processed into films on a great variety of substrates. Moreover, some polymers can be micro and nanopatterned by different lithographic techniques such as imprint, electron beam and ultraviolet lithography [2]. Indeed, polymers are especially suitable materials for integrated optics applications because of its high transparency above 400 nm, low propagation losses and easy fabrication. In this sense, polymer-based nanocomposites can be good candidates for active wave-guiding applications by mixing with semiconducting nanocrystals synthesized by colloidal chemistry [3]. These nanocrystals are usually known as quantum dots (QDs), due to the three dimensional size confinements of carriers. In consequence, its effective bandgap, and hence their photoluminescence (PL) can be tuned by either modifying their radius [4] or the base material, being it possible to cover the whole spectra using CdS, CdSe and CdTe in the visible, and PbS, PbSe, and InAs in the near-infrared. Then, these nanostructures are interesting candidates as active materials [5], and have already been incorporated in sol-gel oxide waveguides to develop optical amplification [6], but also in PMMA to amplify the spontaneous emission [7]. Also recently [8], we have demonstrated the optimum conditions for waveguiding in CdSe-PMMA and CdTe-PMMA nanocomposite films; being it possible to obtain multicolor wave-guiding by dispersing both kinds of QDs into the matrix. In this work, this result is extended to incorporate three families of QDs (CdS, CdSe and CdTe) in a PMMA nanocomposite waveguide; with the intention to show three color wave-guiding as a first step to obtain white light. Also, first results of the dispersion of CdSe QDs in a SU-8 photoresist are presented [9]. As a result, ridge structures able to guide CdSe photoluminescence are implemented.

II. EXPERIMENTAL

Active material used in this work consisted of different sorts of colloidal quantum dots (CdS, CdSe and CdTe) fabricated using the procedure developed by Peng's group [8]. Since each QD family has different chemical nature and size, they will lead to optical transitions at different wavelengths. Exciton absorption peaks are centered at 447, 537 and 580 nm for CdS, CdTe and CdSe, respectively. The PL spectra consist of single Gaussian lines slightly red-shifted with respect to the exciton peak in absorption by about 40 nm.

Nanocomposite solutions have been prepared by mixing colloidal QDs with PMMA or SU8 polymers using a common solvent. The concentration of QDs in the matrix was fixed according to the results found in Ref. 8, where filling factors (ratio of QDs-volume to the total sample volume) between 10^{-4} and 10^{-3} showed optimum waveguiding. The inset of Figs. 1 and 2 depicts the structure of the waveguides. The first one (inset in Fig. 1) consists of QD/PMMA nanocomposite acting as a core of a planar waveguide. The film was processed using the procedure described in [8] and had a thickness of about 0.9 µm. The low refractive index of SiO_2 (1.458 at 600 nm) with respect to the PMMA (1.489 at 600 nm) provides a sufficiently high refractive index contrast to allow waveguiding. In the second structure, SU8 has been chosen as polymer matrix with the intention to implement two-dimensional waveguides with the aid of its photolithographic properties and its high refractive index (1.5108 at 600 nm). The film has a thickness of 2 µm and was patterned into lines of 4, 6, 8, 10 and 20 µm wide using a standard UV lithography procedure [10]. In both cases the SiO_2 was a sol-gel film 650 nm thick processed by the method described in Ref. 8.

III. RESULTS

A. *Multicolor wave-guiding in QD/PMMA films*

QD-PMMA planar waveguides have been characterized by end-fire coupling at 404 nm (GaN diode laser). It has already been demonstrated that for high filling factors (>10^{-3}) of QDs in PMMA, the QDs strongly attenuate the laser beam and waveguiding is not possible [8]. But, if the concentration is low enough, waveguides show small propagation losses and PL can be properly wave-guided. The dispersion of several QD ensembles into the same waveguide enables the observation of guided PL spectra composed by the different "QD colors". Figure 1 shows the guided PL spectra in a waveguide embedding CdS (blue, 452 nm), CdTe (green, 539 nm) and CdSe (red, 601 nm) QDs. It is worth noting that it was critical to adjust the relative amounts of QDs into the matrix in order to avoid (or compensate) reabsorption between QDs families. The PL tail observed at long wavelengths is associated to surface states in CdS QDs. The pictures at the top of Fig. 2 correspond to the three color waveguiding.

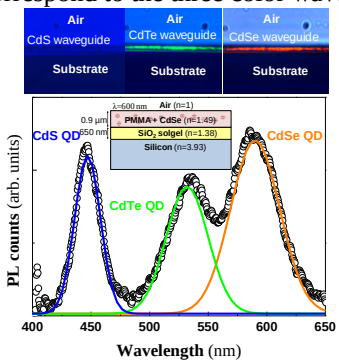


Figure 2. PL waveguided spectra of QD/PMMA thin film with three QD ensembles (CdS, CdTe and CdSe).

B. *Ridge CdSe/SU8 waveguides*

One of the most interesting characteristics of polymers is the possibility to be patterned by different lithographic techniques. Although PMMA is cheap and allows a trouble-free thin film processing, the patterning by lithographic methods is not possible. In this way SU8 was chosen as the resist matrix to embed QDs, because is easily-patterned by using UV photolithography and has a high refractive index (~1.5) [10]. However, the main drawback of SU8 is its chemical incompatibility with as-syntesized QDs. In [10] we proposed the appropriate ligand exchange to disperse QDs in this polymer, making it possible to develop patterns with QD inside. Figure 3 shows a preliminary result of these new patterned structures. The spectra corresponds to the guided-PL of CdSe QDs in an 8 μm SU-8 ridge pumped with a 533 nm DSPP diode laser characterized by end fire coupling. The inset shows a photograph of the guided PL in waveguides with different widths. In all cases the structure is able to confine PL into two dimensions.

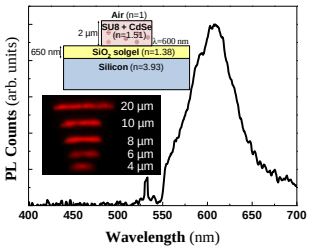


Figure 3. PL waveguided spectra of CdSe QDs into SU8 ridge waveguides.

IV. CONCLUSIONS

The integration of QDs in polymer matrices is an interesting approach for developing active organic photonic devices. In this work, films made by the dispersion of colloidal nanostructures in a PMMA matrix are demonstrated to be a good core for waveguides. Using the appropriate concentrations of QD into the matrix, these films are able to waveguide the PL, and even more than one color when different types of QDs are embedded in the polymer thin film. Finally, these results are extrapolated into a photolithographic polymer (SU8), measuring waveguided PL in ridge structures fabricated by UV lithography.

ACKNOWLEDGMENT

This work was supported through the Spanish MCINN, Generalitat Valenciana and EU-NAVOLCHI Grants Nos. TEC2011-29120-C05-01, PROMETEO/2009/074 and 288869 respectively.

REFERENCES

[1] N. Tomczak, D. Janczeuski, M. Han and G. Julius Vancson, "Designer polymer-quantum dot architectures," Prog. Polym. Sci., vol. 34, pp. 393-430, 2009.

[2] M. A. Uddin and H. P. Chan, "Materials and process optimization in the reliable fabrication of polymer photonic devices," *J. Optoelectron. Adv.Mat.*, vol. 10, pp. 1-17, 2008.

[3] V. I. Klimov, "Nanocrystal quantum dots: from fundamental photophysics to multicolor lasing," *Los Alamos Science*, pp. 214-220, 2003.

[4] P. Alivisatos, " Perspectives on the physical chemistry of semiconductor nanocrystals," *J. Phys. Chem.*, vol. 100, 13226-13239, 1996.

[5] V. I. Klimov, A. A. Mikhailovsky, S. Xu, A. Malko, J. A. Hollingsworth, C. A. Leatherdale, H. J. Eisler and M. G. Bawendi, "Optical gain and stimulated emission in nanocrystal quantum dots," Science, vol. 290, pp. 314-317, 2000.

[6] J. Jasieniak, J. Pacifico, R. Signorini, A. Chiasera, M. Ferrari, A. Martucci and P. Mulvaney, "Luminiscence and amplified stimulated emission in CdSe-ZnS-nanocrystal-doped TiO_2 and ZrO_2 waveguides," Adv. Func. Mater., vol. 17, pp. 1654-1662, 2007.

[7] T. N. Smirnova, O. V. Sakhno, P. V. Yezhov, L. M. Goldenberg and J. Stumpe, "Amplified spontaneous emission in polymer-CdSe/ZnS-nanocrystal-DFB structures produced by the holographi method," *Nanotechnology*, vol. 20, pp. 245707, 2009.

[8] I. Suárez, H. Gordillo, R. Abargues, S. Albert and J. Martínez-Pastor, "Photoluminiscence waveguiding in CdSe and CdTe QDs-PMMA nanocomposite films," *Nanotechnology*, vol. 22, pp. 435202, 2011.

[9] http://www.microchem.com/Prod-SU8_KMPR.htm

[10] to be published

Electrooptic Electric Field Sensor utilizing Ti:$LiNbO_3$ Asymmetric Mach-Zehnder Interferometers

Jeong-Ho Ha, Hong-Sik Jung*
Dept. of Electronic & Computer Engineering
Graduate School, Hongik University
Seoul, Korea
*hsjung@wow.hongik.ac.kr

***Abstract*—The use of a Ti:$LiNbO_3$ asymmetric Mach-zehnder interferometric intensity modulator with a push-pull lumped electrode and a plate-type probe antenna to measure an electric field strength is described. The minimum detectable electric fields are 0.823 and 5.19 V/m at frequencies 500 KHz and 5 MHz respectively.**

Keywords-Optical electric-field sensor; Ti diffused optical waveguide; Mach-Zehnder interferometer; Electro-optical effect

I. INTRODUCTION

Electric field sensors are widely used in electromagnetic compatibility (EMC) technology area and their importance is increasing with the progressing of mobile multimedia communication fields [1]. Even though various kinds of sensors have been developed the all-optical electric-field sensor uniquely has several advantages [2]. In this work, an integrated electro-optic electric field sensor with asymmetric Ti:$LiNbO_3$ Mach-Zehnder interferometer with push-pull lumped electrode structure and a plate-type probe antenna is designed and fabricated.

II. THEORY, FABRICATION AND PROPERTIES OF TI:$LINBO_3$ MACH-ZEHNDER INTERFEROMETRIC MODUALATOR

A configuration of the electro-optic sensing part is shown in Fig. 1. The optical waveguide circuit is an asymmetric Ti:$LiNbO_3$ Mach-Zehnder interferometer with lumped-type push-pull electrode structure.[3] The applied voltage (namely, electric field) produces equal and opposite phase shifts in the light beam propagating in the two parallel channel waveguides (namely, arms), thereby leading to a net phase shift of twice the phase shift per each channel. When the two light beams recombine at the output combiner the phase modulation is converted to an amplitude-modulated signal at the same frequency of the applied signal voltage. Therefore the light signal amplitude is proportional to the applied electric field.

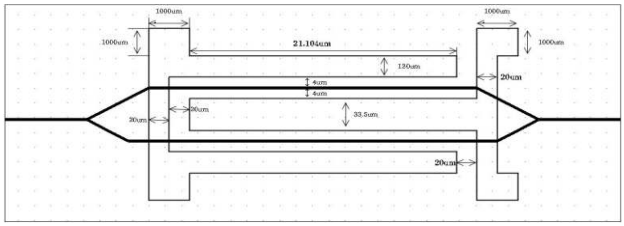


FIG. 1. Schematic diagram of an asymmetric Mach-Zehnder interferometer with metal electrode:

In the electrode structure on the device shown in Fig. 1, the applied signal voltage produces the electric field along the z-axis direction, E_z which cross the channel waveguides in the lithium niobate. This Z-directed electric field interacts with light beam propagating in the channel waveguide to produce electro-optic modulation. The electric field vector of the light wave propagating in the Ti:$LiNbO_3$ channel waveguide should be also oriented in the Z-direction. This electric field generated by the applied voltage modifies the extraordinary refractive index, n_e of the substrate through the linear electro-optic effect which is given by

$$\Delta n_e(E) = -\frac{1}{2} n_e^3 \gamma_{33} E_z \Gamma \qquad (1)$$

where r_{33} is the electro-optic coefficient of lithium niobate (~30 pm/V) and Γ ($0 < \Gamma < 1$) accounts for the numerical degree of the mutual interaction between the applied electric field and the optical field in the channel waveguides. The electrodes are oriented such that the electric field through each arm has opposite polarity and therefore the two phase changes add in determining the net phase difference when the optical signals recombine at the output.

The phase shift produced by the electric field in each arm is converted to amplitude intensity modulation at the combiner of the interferometer. The optical power transfer function of the device can be expressed as follows:

$$P_{out} = P_{in}\cos^2\left(\frac{\Delta\phi}{2}\right) = \frac{P_{in}}{2}\{1 + \cos(\Delta\phi)\} \qquad (2)$$

where $\Delta\phi$ is the net accumulated phase difference between the arms and is composed of two terms $\Delta\phi = \phi_o + \Delta\phi_t(E)$. The inherent phase difference ϕ_o is caused by physical path length and effective refractive index difference between two channel waveguides. The second term $\Delta\phi_t(E)$ is linearly dependent on the electric field. A linear response to the electric field can be obtained by setting the phase bias to $\phi_o = \pi/2$ and operating with a small phase change $\Delta\phi_t(E) \ll 1$.

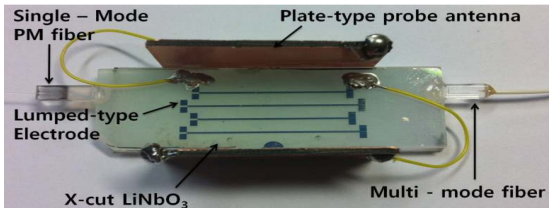


FIG. 2. Photograph of fabricated electric-field sensor with pig-tailed optical fibers and a copper plate-type probe antenna

The Mach-Zehnder interferometer modulators were fabricated on x-cut $LiNbO_3$ substrates using standard photolithographic technique. Channel waveguides were formed

This research was supported by Basic Science Research Program through the national Research Foundation of Korea (NRF) funded by the Ministry of Education, Science and Technology (2010-0021491).

by diffusing a 1050 Å-thick, 7.5 μm-wide stripe of Ti film at 1050 °C in wet ambient. The substrate edges were optically polished to allow butt coupling and pig-tailing. ~3000 Å-thick SiO_2 buffer layer was deposited using e-beam evaporation and 99.99 % pure SiO_2 pellets to prevent the propagation loss caused by the optical absorption of the electrode metal. ~5000 Å-thick aluminum lumped electrodes were fabricated to allow the sensing of electric field. Polarization maintaining single-mode and multi-mode optical fibers were attached to the input and output waveguides, respectively. Finally, a 20 x 10 mm plate-type external probe antenna of copper was attached to the electrode on the substrate. Figure 2 is the microscope photograph of the fabricated device with attached optical fibers and a copper plate-type antenna.

Figure 3 shows the optical output power versus applied voltage measured by the optical power meter. The device has a 23 mm electrode length and a 15.5 μm gap. It exhibited the modulation depth of 80 % and V_π voltage of ~5.0 V at DC, respectively. Even though we actually designed the waveguide such that the operating point was half the value of the maximum intensity of the light power, the operation point was almost quarter the value of the maximum intensity, namely the phase bias of $\phi_o = \sim\pi/4$.

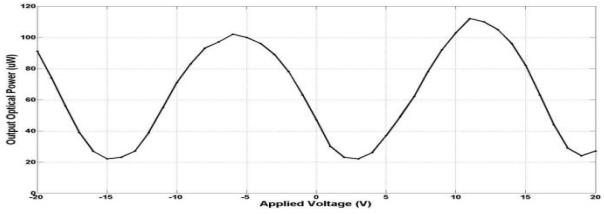


FIG. 3. Electro-optic DC modulation trace on an asymmetric Mach-Zehnder modulator

III. MEASUREMENT AND EXPERIMEMTAL RESULTS

Frequency tests, evaluating the minimum detectable field and frequency response of the fiber coupled sensor were performed using a tunable laser operating at a wavelength of 1.3μm. Incident optical power was of order of ~14 mW. Figure 4 shows a block diagram of the experiment setup. The -20 ~ 20 dBm (10 μW~100mW) RF input to the TEM cell corresponds to the electric field strength from 0.293 m/V to 23.2 m/V. The actual field intensity experienced on the sensor substrate from 23.2 V/m in TEM cell is 0.66 V/m due to the high dielectric constant of $LiNbO_3$ ($\varepsilon \approx 35$).

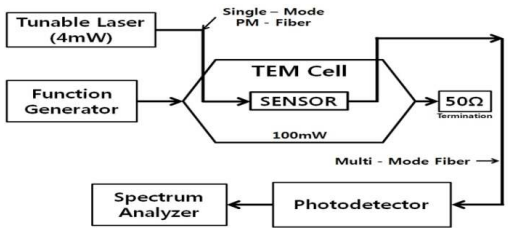
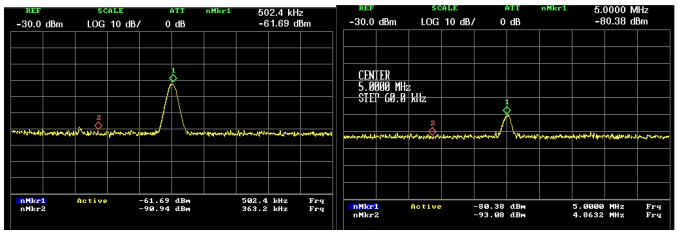


FIG. 4. Block diagram of the test setup for the measurement of electric field sensing and the evaluation of the frequency response

Fig. 5 shows the spectrum analyzer outputs for a 20 dBm input to the TEM cell at frequencies of 500 KHz and 5 MHz. The measured RF power received at the photo-detector was measured to -61.69dBm and -80.38dBm at the applied rf frequencies, respectively.



(a) (b)

FIG. 5. The rf responses of sensor to (a) a 500 KHz and (b) 5 MHz rf input signal into the TEM cell a power level of 100 mW

The noise floor and signal power measured are about -90.94 dBm and -93.08 dBm, and -61.69 dBm and -80.38 dBm at frequencies 500 KHz and 5 MHz, respectively as shown in Fig. 5. Therefore, the internal electric field of 23.2 V/m in TEM cell produces an SNR of ~29 dB and ~13 dB. The minimum detectable electric fields are 0.823 and 5.19 V/m, respectively, based on the $E_{min} = 23.2 \times 10^{(-SNR/20)}$.

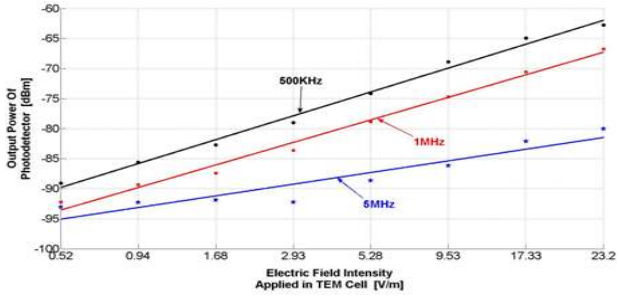


FIG. 6. Graph showing photo-detected signal power versus electric field strength into TEM cell at different frequencies

The figure 6 shows the sensitivity curves at frequencies of 500 KHz, 1 MHz and 5 MHz. As shown in Fig. 6, the sensor exhibits almost linear response for the applied electric field intensity from 0.293 V/m to 23.2 V/m. It has a dynamic range of about 35 dB, 25 dB and 10dB at frequencies of 500 KHz, 1 MHz and 5 MHz, respectively.

IV. CONCLUSION

We have successfully fabricated an electric field sensor which integrated Ti:$LiNbO_3$ Mach-Zehnder interferometer and conventional lumped push-pull electrodes with a plate-type probe antenna, which utilizes the electro-optic effect to modulate the phase of the light propagating in each arm of the device.

REFERENCE

[1] H. Y. Lee, T. H. Lee, W. T. Shay, and C. T. Lee, "Reflective Type Segmented Eelectrooptical Electric Field Sensor," Sensor and Actuators A, 148, 355-358 (2008).

[2] T. H. Lee, P. I. Wu, and C. T. Lee, "Intergraded $LiNbO_3$ Electrooptical Electromagnetic Field Sensor," Microwave and Optical Technol. Lett. 49-9, 2312-2314 (2007).

[3] C. H. Bulmer and W. K. Burns, "Linear Interferometric Modulators in Ti:$LiNbO_3$," J. Lightwave Technol., LT-2, NO. 4, 512-521 (1984).

Waveguide lasers in (Yb,Nb):$RbTiOPO_4$

A. Choudhary, H.M.H. Chong, K.Pradeesh, G.S. Murugan, J. S. Wilkinson and D. P. Shepherd
Optoelectronics Research Centre (ORC) and School of Electronics and Computer Science (ECS)
University of Southampton
Southampton SO171BJ, UK
ac12g10@orc.soton.ac.uk

J. Cugat, R. Solé, F. Díaz and M. Aguiló
Física i Cristal·lografía de Materials i Nanomaterials (FiCMA-FiCNA)
Universitat Rovira i Virgili (URV), Campus Sescelades,
c/Marcel·lí Domingo, s/n
Tarragona 43007, Spain

***Abstract*—In this paper we present lasing results with a planar (Yb,Nb):$RbTiOPO_4$ waveguide device. We also demonstrate channel waveguiding in an ion-beam etched (Yb,Nb):$RbTiOPO_4$ thin film for the first time with a loss of 2.4 dB/cm. To reduce the losses, a study of reactive ion etching of $RbTiOPO_4$ was carried out resulting in structures with a surface roughness of 6.6nm and an etch rate of 13nm/minute.**

Keywords- liquid phase epitaxy, waveguide, laser, $RbTiOPO_4$, ion-beam milling, reactive ion etching

I. INTRODUCTION

Ytterbium (Yb^{3+}) doped materials are very good active media for making power-scalable solid-state lasers operating around 1μm as they have a broad absorption band suitable for diode pumping, a small quantum defect (thus a lower thermal load), a long lifetime and almost no losses due to up-conversion and excited state absorption. Efficient laser operation has been demonstrated in a number of Yb^{3+}-doped crystals [1], and this has recently included Yb^{3+}, Nb^{5+} co-doped bulk RTP [2]. $RbTiOPO_4$ (RTP) belongs to the $KTiOPO_4$ (KTP) family of orthorhombic crystals, which have various applications in non-linear optics. When doped with Yb^{3+}, RTP crystals have a broad emission bandwidth making them very promising candidates for ultrashort pulse generation with pulses as short as 155 fs being demonstrated [3]. Fabrication of these lasers in a waveguide geometry is of interest for making compact ultrafast laser sources with high repetition rates for applications such as metrology [4] or biological imaging [5]. The nonlinear properties of the host crystal also offer the potential for self-frequency-doubling [3]. Towards these goals, liquid phase epitaxy (LPE) has been used to fabricate thin-film planar waveguides exhibiting a loss of 0.7 dB/cm [6]. In this paper, we present the first lasing results with an LPE (Yb,Nb):RTP planar waveguide. We then discuss the fabrication of rib waveguides in an LPE-grown (Yb,Nb):RTP film by ion-beam milling, and finally we describe the etching of RTP substrates by reactive ion etching (RIE).

II. FABRICATION AND RESULTS

A. (Yb,Nb):RTP planar waveguide laser

An 11μm-thick (Yb,Nb):RTP film was grown on an RTP substrate for the planar waveguide laser experiments. The doping concentration for Yb^{3+} ions is $2x10^{20}cm^{-3}$. The measured refractive index contrast is 0.006 and this waveguide supports 3 modes at 1μm. Co-doping with Nb^{5+} allows a higher concentration of Yb^{3+} due to charge compensation [7]. The planar waveguide was pumped by a Ti:sapphire laser operating at 900nm to correspond with the absorption peak for (Yb,Nb):RTP with the electric field polarised parallel to the c-axis. Thin dielectric mirrors were butted directly onto the waveguide end-faces to form the laser cavity. Using an optical chopper to chop the pump source, the characteristic rise and decay of the fluorescence intensity was monitored on a photodiode. On increasing the pump power, a fast and very strong increase in intensity indicated the point at which laser threshold had been achieved. A threshold absorbed power of 276 mW was observed for an HR/HR cavity. Insufficient pump power prevented us from measuring values of slope efficiencies, however, experiments with a high-power laser diode pump are ongoing at the moment and results obtained will be discussed at the conference.

B. Ion- beam milling of Yb:RTP

The laser threshold should be reduced by fabricating channel waveguides within the thin film as long as the waveguide propagation losses are not increased to too high a level. This is especially important in (Yb,Nb):RTP as the Yb^{3+} doping level, and hence maximum gain, is relatively low [2]. As an initial trial, ion-beam milling was used to fabricate rib waveguides in a 5μm-thick (Yb,Nb):RTP film grown on an RTP substrate by LPE. A photoresist layer was spun on the (Yb,Nb):RTP layer, which was then exposed to UV light through a chromium mask. Subsequent development of the resist resulted in the mask pattern being transferred onto the photoresist layer. This was then etched using Ar^+ ion beam milling and after removal of the resist (by plasma ashing), rib waveguides were formed in the active layer. The sample was etched for 2 hours and 20 minutes (min) with a current of 100mA and a voltage of 500V resulting in an etch depth of 3μm. This sample was then edge polished for the waveguiding experiments. The ion-beam milling of the (Yb,Nb):RTP sample resulted in a trapezoidal shaped waveguide with a width of 16μm at the bottom and 6μm at the top.

This work was supported by EPSRC under project EP/H035745/1 and by the Spanish Government under projects TEC2010-21574-C02-02, MAT2011-29255-C02-02, PI09/90527 and by the Catalan government under project 2009SGR235. J. Cugat thanks the Spanish Government for the FPI fellowship BES-2009-024190.

900 nm pump light was launched into the waveguide and the fluorescence output was captured by a CCD camera. A filter was used to remove the pump light and the remaining fluorescence intensity is shown in Fig.1. The mode is asymmetric, as expected, with near-Gaussian profiles with $1/e^2$ beam radii of 8.7μm and 3.3μm in the x and y direction respectively. Numerical modeling carried out using OlympIOs software for the trapezoidal features resulted in $1/e^2$ beam radii of 7.4μm and 2.2μm in the x and y direction respectively for the TM_{00} mode. The difference between the measured and simulated mode profile can be due to higher order modes in the waveguide. The fluorescence spectra was measured and was found to be similar to that observed in bulk (Yb,Nb):RTP [3], as was the measured fluorescence lifetime of 2.2 ms. Losses were measured by the Fabry-Perot method [8] and were found to be 2.4 dB/cm which is higher than the value of 0.7 dB/cm reported in a planar (Yb,Nb):RTP waveguide [6]. The increased losses in the waveguide motivated an attempt to optimise the etching process using RIE.

C. Reactive ion etching of RTP

Optimisation of the RIE process was carried out in RTP substrates (which should give similar results to the etching of Yb^{3+},Nb^{5+} co-doped film). A 300nm thick chromium mask was used to transfer the rib features onto the RTP substrate. Etching was carried out with SF_6 and Ar gases and the gas ratio, gas pressure and RF power were varied in order to optimise the etching process. On varying the ratio of the SF_6:Ar mixture, the etching could be varied between a purely physical process (all Ar) and purely chemical (all SF_6). It was found that the surface quality improved when moving away from the physical etching (similar to the Ar^+ ion beam milling process used previously). After measuring roughness and etch rates versus gas ratio, gas pressure and RF power, optimised RIE parameters were found and used to etch rib features in an RTP substrate. The optimised process resulted in an etch rate for RTP of 13 nm/min and for Cr of 2.3 nm/min giving a selectivity of 5.7. The RMS surface roughness was measured to be 2.4nm in the un-etched region and 6.6nm in the etched region which is a very low value from the point of waveguiding applications. The 3-d profile was measured by a non-contact profiler and is shown in Fig.2. It can be seen that the rib has much steeper sides than found by ion-beam milling, having a side wall angle of 57º compared to the 31º described earlier.

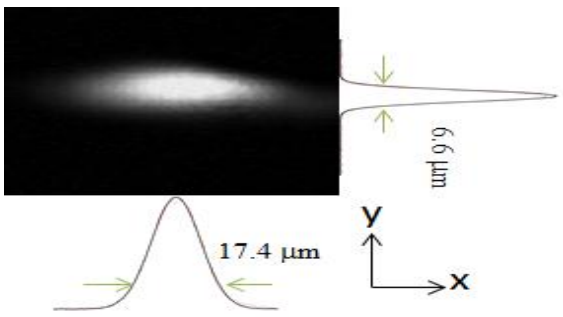


Figure 1. Near field fluorescence intensity for a waveguide etched by ion-beam milling in (Yb,Nb):RTP along with the x and y mode profiles.

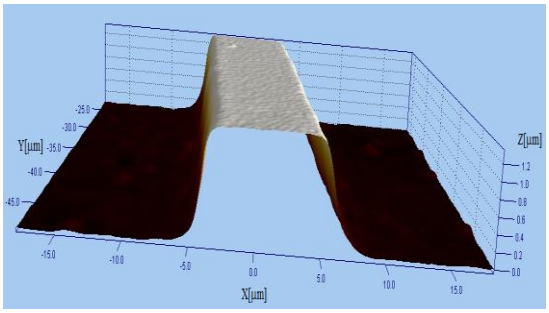


Figure 2. 3-d image of an RIE etched rib feature in RTP

III. CONCLUSIONS AND FUTURE WORK

We have demonstrated lasing in a planar (Yb,Nb):RTP waveguide and will use a higher power diode to pump this waveguide and fully characterise its laser performance. We have also demonstrated rib waveguiding in an ion-beam milled (Yb,Nb):RTP waveguide for the first time but found significantly increased propagation losses. Finally, we have optimised the RIE process in RTP in order to reduce the surface roughness of the etched features and to create steep side walls. Future work will use RIE to produce low-loss rib waveguides in (Yb,Nb):RTP and realise lasers with low threshold powers. Such laser devices could then be the platform for highly compact ultrafast laser sources when combined with integrated passive modelocking elements.

ACKNOWLEDGMENT

We would like to thank Neil Sessions and David Sager for their technical advice and support in the integrated photonics cleanroom at the ORC.

REFERENCES

[1] W.F. Krupke, "Ytterbium solid-state lasers. The first decade," IEEE J. Sel. Topics Quantum Electron., vol.6, pp.1287-1296, 2000.

[2] X. Mateos, V. Petrov, A. Peña, J. Carvajal, M. Aguiló, F. Díaz, P. Segonds, and B. Boulanger, "Laser operation of Yb^{3+} in the acentric $RbTiOPO_4$ codoped with Nb^{5+}," Opt. Lett., vol. 32, pp.1929-1931, 2007.

[3] J. Carvajal, G. Ciatto, X. Mateos, A. Schmidt, U. Griebner, V. Petrov, G. Boulon, A. Brenier, A. Peña, M. Pujol, M. Aguiló, and F. Díaz, "Broad emission band of Yb^{3+} in the nonlinear Nb:$RbTiOPO_4$ crystal: origin and applications," Opt. Express , vol. 18, pp.7228-7242, 2010.

[4] A. Bartels, R. Gebs, M. Kirchner, and S. Diddams, "Spectrally resolved optical frequency comb from a self-referenced 5 GHz femtosecond laser," Opt. Lett., vol. 32, pp.2553-2555, 2007.

[5] S. Chu, T. Liu, C. Sun, C. Lin, and H. Tsai, "Real-time second-harmonic-generation microscopy based on a 2-GHz repetition rate Ti:sapphire laser," Opt. Express , vol. 11, pp.933-938, 2003.

[6] J. Cugat, R. Solé, M.C. Pujol, J.J. Carvajal, X. Mateos, F. Díaz and M. Aguiló, "Waveguiding demonstration on Yb:Nb:$RbTiOPO_4$/$RbTiOPO_4$ (001) epitaxies grown by LPE", Opt. Mat., vol. 32, pp.1648-1651, 2010

[7] J. J. Carvajal, V. Nikolov, R. Solé, Jna. Gavaldà, J. Massons, M. Aguiló, and F. Díaz, "Crystallization region, crystal growth, and characterization of rubidium titanyl phosphate codoped with niobium and lanthanide ions," Chem. Mater., vol. 14, pp.3136-3142, 2002.

[8] R. Regener and W. Sohler. "Loss in low-finesse Ti-$LiNbO_3$ optical wave-guide resonators." Appl. Phys. B, vol. 36, pp.143-147, 1985.

Design of Efficient Photonic Sensors Based on Vernier Effect in near-IR

B. Troia *, V. M. N. Passaro, F. De Leonardis
Photonics Research Group, * CNIT UdR Bari
Dipartimento di Elettrotecnica ed Elettronica
Politecnico di Bari
Via Edoardo Orabona n. 4, 70125 Bari - Italy
E-mail: passaro@deemail.poliba.it
URL: http://dee.poliba.it/photonicsgroup

A. V. Tsarev
Laboratory of Optical Materials and Structures
A.V. Rzhanov Institute of Semiconductor Physics
Siberian Branch of Russian Academy of Sciences
Novosibirsk, 630090, Russia
E-mail: tsarev@isp.nsc.ru

***Abstract*— Integrated architectures based on cascaded ring resonators through the Vernier effect have been theoretically investigated and optimized for sensing applications. Sensitivity higher than 100 µm/RIU allows detection of lead Pb(II) in water (< 50 ppb) and m-xylene gas (< 60 ppm) to be achieved, exhibiting limits of detection as low as 3.5×10^{-6} RIU.**

Keywords-Group IV Photonics; Homogeneous optical sensing; Silicon-on-Insulator; Vernier effect;

I. INTRODUCTION

Photonic sensors have been the subject of intensive research over the last two decades. Interesting applications have been experimentally demonstrated for chemical, biochemical and gas sensing, to name a few. In this paper, photonic sensors based on cascaded ring resonator (RR) configuration and operating in the second regime of Vernier effect [1-2], are theoretically investigated, evaluating design and performance. Modal propagation has been simulated in wire optical waveguides based on CMOS-compatible silicon-on-insulator (SOI) technology. These photonic devices have been already integrated in MZI configurations and fabricated [3] for detection of lead contaminant of water, e.g. BTEX compounds (benzene, toluene, ethylbenzene, xylene) and volatile organic compounds (VOCs) in air. Theoretical results have been compared with experimental measurements in literature [3], demonstrating ultra high performance of cascaded RR photonic sensors based on the Vernier effect.

II. ARCHITECTURES OF PHOTONIC SENSORS BASED ON VERNIER EFFECT

Photonic sensors considered in this investigation are constituted by two cascaded RRs, as sketched in Fig. 1. In particular, the first RR, with perimeter length L_{filter}, acts as a filter, while the second one (perimeter length L_{sensor}) acts as a sensor, being directly exposed to the cover medium. The whole architecture is covered by an insulating thick cladding (e.g., SiO_2, SU-8, teflon), with the only exception of a window opened on the sensing RR, where the test sample to be detected is concentrated. According to MZI configuration [3], the waveguide selected in this investigation is a silicon photonic wire, with height of 260 nm and width of 450 nm.

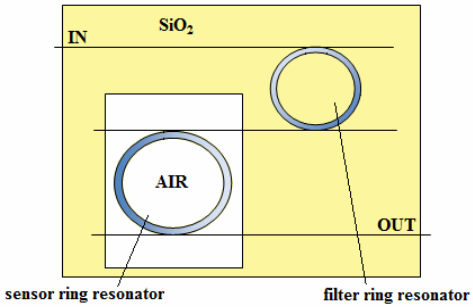


Figure 1. Architectural scheme of an integrated photonic sensor based on Vernier-effect in SOI technology, using a SiO_2 insulating cladding.

Four design configurations have been simulated for m-xylene and lead Pb (II) detection. The first one, named *Sensor 1*, is characterized by SU-8 insulating 2-µm-thick cladding with sensing RR directly exposed to air. The second architecture (*Sensor 2*) is similar to the previous one, with SiO_2 2-µm-thick layer insulating cladding. *Sensor 3* has been assumed by coating the same structure as *Sensor 1* with a micro-extraction polydimethylsiloxane (PDMS) film, 3.5 µm-thick. Finally, the last sensor configuration *Sensor 4* has been assumed by coating the chip *Sensor 2* with a micro-extraction film (400 nm-thick) based on a tetrasulfide-functionalized mesoporous silicate material.

A sophisticated algorithmic procedure has been implemented for design of these sensing architectures based on Vernier effect, by setting the operative wavelength λ_{sensor} = 1529.4 nm and propagation loss coefficient α = 1 dB/cm. Finally, optimal filter and sensing RR perimeter lengths and differences among filter and sensor free spectral ranges (FSRs) have been found, as listed in Table I.

TABLE I. FILTER AND SENSING RR PERIMETER LENGTHS AND ΔFSR CALCULATED FOR VARIOUS SENSOR ARCHITECTURES

Architecture	L_{filter} (µm)	L_{sensor} (µm)	ΔFSR (pm)
Sensor 1	1403.85	1542.90	1.589
Sensor 2	1458.90	1589.25	1.497
Sensor 3	1812.20	1871.75	1.194
Sensor 4	1713.25	1824.10	0.815

Silicon photonic wire modal behavior has been investigated by full-vectorial 2D finite element method (FEM). In FEM mesh generation for effective indices and modal profile calculations, about 50,000 triangular vector-elements have been adopted. Finally, the thickness of the buried oxide is always set to 2 μm, being the top silicon layer 260 nm thick.

III. SENSING PERFORMANCE AND SIMULATIONS

Sensing performance of designed configurations are listed in Table II for each sensing architecture.

TABLE II. PERFORMANCE PARAMETERS OF VARIOUS SENSOR CONFIGURATIONS

Parameters	Sensor 1	Sensor 2	Sensor 3	Sensor 4
$\Delta\lambda_{peak}$* (nm)	1.1573	1.1919	1.4974	1.8236
$\Delta n_{c,min} \times 10^{6}$	6.7423	6.3552	4.0403	3.5373
$\Delta n_{c,max} \times 10^{3}$	3.3	3.2	2.0	2.8
$\Delta n_{eff,min} \times 10^{6}$	2.0227	1.9066	1.6161	1.0612
S_λ μm/RIU	115.73	119.19	149.74	182.36

*induced by $\Delta n_c = 1\times10^{-5}$ RIU (refractive index unit)

Resonance wavelength shifts $\Delta\lambda_{peak}$, wavelength sensitivities S_λ, minimum $\Delta n_{c,min}$, maximum $\Delta n_{c,max}$ detectable cover refractive index (RI) changes and minimum detectable effective RI changes $\Delta n_{eff,min}$, have been considered and calculated in our automatic procedure. In Fig. 2 it is possible to observe dynamic ranges (DRs) for various sensor configurations. Wavelength shifts of Vernier peak $\Delta\lambda_{peak}$ have been simulated as a function of different cover refractive index changes, Δn_c, being the Vernier peak at λ_{sensor} = 1529.4 nm, when sensors operate at rest (absence of test sample from sensible area, $\Delta n_c = 0$). Consequently, when a cover RI change higher than the detectable one $\Delta n_{c,min}$ occurs, a wavelength shift $\Delta\lambda_{peak}$ affects the Vernier overall transmittance. *Sensor 3* and *Sensor 4* have been simulated for m-xylene and lead Pb(II) detection, respectively, considering the PDMS RI change upon xylene ($dn_{PDMS}/dC_{xylene} = 8.7\times10^{-7}$ RIU/ppm) and the mesoporous silica (MS) RI change upon lead Pb(II) ($dn_{MS}/dC_{Pb(II)} = 1.0\text{-}5.0\times10^{-6}$ RIU/ppb).

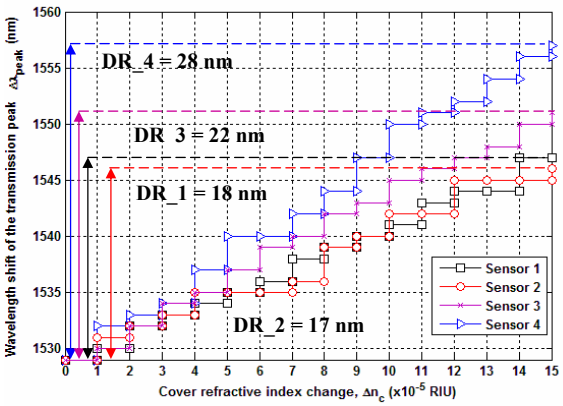


Figure 2. Wavelength shift $\Delta\lambda_{peak}$ versus cover RI change, $\Delta n_c \sim 10^{-5}$ RIU, for various selected sensing architectures.

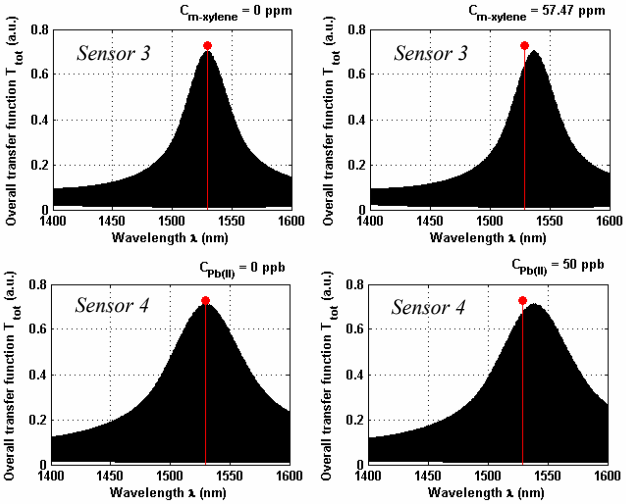


Figure 3. Simulations of *Sensor 3* and *Sensor 4* operation for m-xylene and lead Pb(II) detection. Red line is set at λ_{sensor} = 1529.4 nm.

Our results theoretically confirm *Sensor 3* as the best configuration for m-xylene gas detection using a PDMS cladding film, as in [3]. In fact, in Fig. 3 a m-xylene gas concentration as low as 57.47 ppm can be easily detected, being the relative wavelength shift as long as $\Delta\lambda_{peak}$ = 8 nm. The configuration *Sensor 4* exhibits interesting performance for Pb(II) detection in water. In fact, by considering $dn_{MS}/dC_{Pb(II)} = 1.0\times10^{-6}$ RIU/ppb, a lead concentration as low as 50 ppb generates a wavelength shift $\Delta\lambda_{peak}$ = 11 nm, revealing a ultra high sensing resolution (see Fig. 3). In conclusion, Table III shows a comparison between experimental results [3] through MZI-based sensors and theoretical results calculated in this paper using a Vernier-based approach. The latter shows clear sensing advantages.

TABLE III. COMPARISON BETWEEN VERNIER AND MZI CONFIGURATIONS BASED ON SILICON PHOTONIC WIRE WAVEGUIDES

Performance	Vernier [this paper]	MZI [3]
Sensor 3 – m-xylene detection		
Sensitivity	149.74 μm/RIU	4930 rad/RIU
Resolution	< 60 ppm	< 100 ppm
LOD	4.0403×10^{-6} RIU	0.43 rad
Sensor 4 – Pb(II) detection in water		
Sensitivity	182.36 μm/RIU	2536 rad/RIU
Resolution	< 50 ppb	100 ppb
LOD	3.5373×10^{-6} RIU	0.3 – 1.3 rad

REFERENCES

[1] J. Hu and D. Dai, "Cascaded-Ring Optical Sensor With Enhanced Sensitivity by Using Supended Si-Nanowires," *IEEE Photon. Tech. Lett.*, vol. 23, n. 13, pp. 842-844 (2011).

[2] L. Jin, M. Li, J-J. He, "Highly-sensitive silicon-on-insulator sensor based on two cascade micro-ring resonators with Vernier effect," *Opt. Commun.*, vol. 284, n. 1, pp. 156-159 (2011).

[3] J. Saunders, M. A. Dreher, J. A. Barnes, C. M. Crudden, J. Du, H. Loock, *et al.*, "Detection of lead contamination of water and VOC contamination of air using SOI micro-optical devices," *Conf. Proc. of 7th IEEE Group IV Photon. (GFP)*, pp. 177-179, 1-3 Sept. 2010.

Experimental observation of coupling between physically separated planar waveguides utilising tilted Bragg grating structures

H.L. Rogers, C. Holmes, P.L. Mennea, J. C. Gates, P.G.R. Smith
Optoelectronics Research Centre
University of Southampton
Southampton, UK
hlr1g09@orc.soton.ac.uk

K.R. Daly, G. D'Alessandro
School of Mathematics
University of Southampton
Southampton, UK

***Abstract*— We demonstrate a novel optical device used to couple light from one channel waveguide to another 100 µm away. An investigation into the blaze angle of the tilted gratings used to couple light into the cladding modes is presented.**

Keywords- tilted Bragg gratings; direct UV writing.

I. INTRODUCTION

Tilted Bragg gratings have been implemented in fiber and planar waveguide geometries [1], allowing increased filtering functionality [2], for sensing and wavelength specificity over equivalent non-tilted grating devices. Pairs of Bragg gratings in the same waveguide have also been demonstrated, further increasing the scope of the grating-based sensor for both refractive index and spectral applications [3,4].

We propose a novel geometry of tilted Bragg grating device, taking advantage of the higher index core photosensitive slab waveguide used in the production of direct UV written waveguides and Bragg gratings. The slab waveguide section between a pair of identical channel waveguides with tilted Bragg gratings allows coupling between waveguides separated by 100 µm, a distance much greater than would normally occur for evanescent coupling used in conventional directional couplers. We investigate the effect of the blaze angle of the tilted gratings on the spectral features observed.

II. FABRICATION AND CHARACTERIZATION

The waveguides were fabricated in a silica-on-silicon platform. An under-clad of thick thermal oxide (~15 µm) was grown on a silicon wafer. The core layer, with a refractive index of 1.4551, was deposited via flame hydrolysis deposition (FHD), and doped with germanium for photosensitivity and boron for refractive index control. A cladding layer was deposited post-consolidation, with phosphorus and boron dopants used to achieve a refractive index contrast of 0.010 between core and cladding.

The direct grating writing (DGW) technique [5] was used to inscribe waveguides and tilted Bragg gratings into the photosensitive core layer. The output from a frequency doubled 488 nm argon-ion laser was passed through an acousto-optic modulator before incidence on a 50:50 beam splitter. The photosensitive sample core was placed within the focus of the two interfering UV beams and translated at speed to create waveguiding regions. In order to create grating structures, the sample translation speed and modulation of the UV beam are controlled to create the periodic grating profile. To create tilted Bragg gratings, a rotational stage system was used, and waveguides and gratings written at the appropriate angle. The photosensitive reaction causes an increase in refractive index of around 0.005 in the ~5 µm wide waveguide region.

The fabricated components consist of 2 parallel waveguides separated by 100 µm. The width of each waveguide was ~5 µm. Each pair contains gratings which are 3 mm long, with central wavelength 1550.4 nm and identical blaze angles. The gratings were written with varying degrees of blaze angle, between 5 ° and 45 °. The gratings were written parallel to one another, to observe perpendicular coupling between the waveguides. The region between the two channel waveguides acts as a slab waveguide, vertically confining the propagating light.

Characterization of the sample was performed using the fiberized output of an EDFA ASE source.

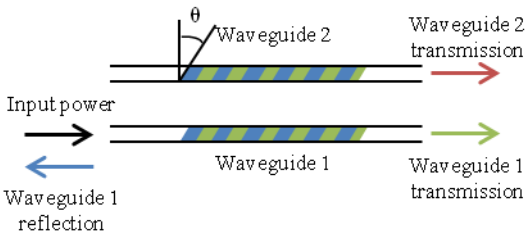


Figure 1. Schematic of fabricated device. Arrows show collection of light: blue is the reflected spectrum from waveguide 1, green is the transmitted spectrum from the waveguide 1, red is the transmitted spectrum from waveguide 2. Light is launched into waveguide along the direction of the black arrow.

This research was funded by EPSRC, UK.

The output passed through a circulator, fiber in-line polarizer and polarization maintaining pigtail to the input at waveguide 1. The reflected spectrum from the gratings was obtained by observing the output of the circulator on an optical spectrum analyzer (OSA). In order to obtain the transmission spectrum, a second PM pigtail was used to collect the output spectrum from the waveguide under observation.

III. Results and Discussion

The measured spectrum from the device is shown in Fig. 2. In this case, we show the device written with a blaze angle of 5 degrees. The purple line shows the reflected spectrum of the tilted Bragg grating. The reflection from the grating is expected to be significant, due to the small blaze angle of the grating. This is corroborated by the large transmission dip (23 dB) observed in the transmission of the same waveguide (black). However, at the output of waveguide 2, we observe a non-zero transmission spectrum (red). A broad transmission is measured, with transmission dips indicative of cladding modes observed.

The presence of the broad transmission (~50 nm) at the output of waveguide 2 indicates that light is being coupled between the two waveguides over the 100 µm slab waveguiding region between. The relatively large distance between the waveguides indicates this is not an evanescent coupling effect; similar waveguides fabricated with normal incidence Bragg gratings stop coupling when separated by a distance of more than 20 µm. The coupling between the waveguides is due to the presence of the tilted Bragg gratings within the waveguide, allowing coupling to the cladding modes in the region between the waveguides, and coupling to the core modes of waveguide 2 to achieve the observed transmission.

Fig. 3 shows the collected spectra from a device with 10° blaze angle. A smaller transmission dip is observed at the

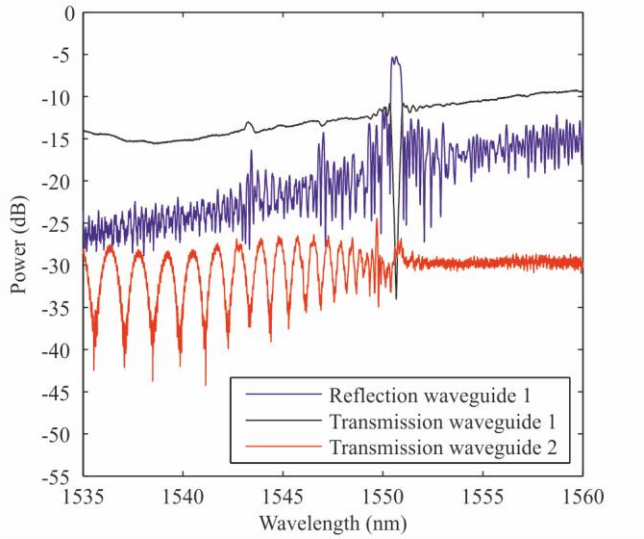


Figure 2. Measured spectrum from the device with 5 ° blaze angle. The reflected spectrum from waveguide 1 is shown in purple, the transmitted spectrum from waveguide 1 is shown in black, and the transmitted spectrum from waveguide 2 in red.

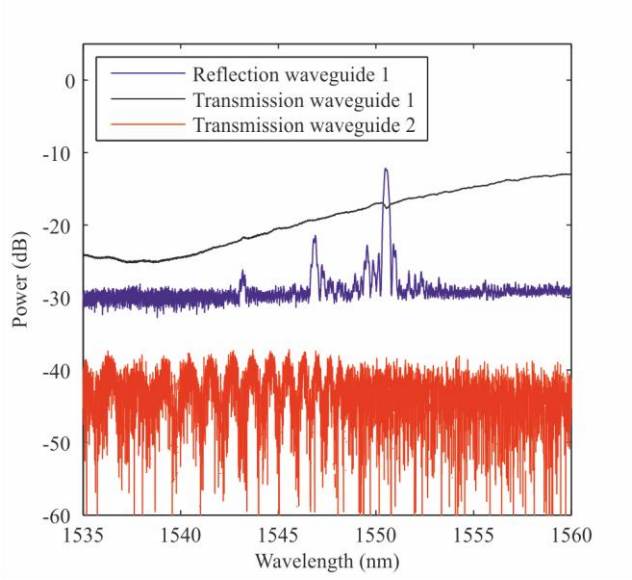


Figure 3. Measured spectrum from the device with 10 ° blaze angle.

output of waveguide 1, and the cladding modes at the output of waveguide 2 are not so well defined. This is due to changes in the coupling mechanism between the core and cladding modes of the waveguides for increased angle [1].

These first non-optimized trial devices have relatively low coupling (0.5 %) and so are not suitable for any type of add-drop function, but offer a potential route for spectral monitoring with the advantage of separated output ports.

IV. Conclusions

We have implemented a waveguide design which allows coupling between two physically separated channel waveguides. Making changes to the blaze angle of the gratings changes the extent to which light propagates through the slab waveguide region between the two defined channel waveguides. The device has potential uses in sensing applications, and further investigation will take place into the limitations of the scheme. We will present theoretical analysis of the coupled mode behavior of the device, using a Cauchy integral method [2], alongside further advances of the experimental design and results.

References

[1] K. R. Daly, C. Holmes, J. C. Gates, P. G. R. Smith, G. D'Alessandro, "Complete mode structure analysis of tilted Bragg grating refractometers in planar waveguides toward absolute index measurement," IEEE Photon. J., vol. 3, pp. 861-871, October 2011.

[2] T. Erdogan, J. E. Sipe, "Tilted fiber phase gratings," J. Opt. Soc. Am. A., vol. 13, pp.296-313, February 1996.

[3] A. C. L. Wong, W. H. Chung, H.-Y. Tam, C. Lu, "Simple tilted Bragg reflector fiber laser for simultaneous sensing of refractive index and temperature," Opt. Express, vol. 19, pp. 409-414, January 2011.

[4] Y. Tissot, H. G. Limberger, R.-P. Salathé, "Ultrawide bandwidth wavelength monitor based on a pair of tilted fiber Bragg gratings," IEEE Photonic. Tech. L., vol. 19, pp. 1702-1704, November 2007.

[5] G.D. Emmerson et al., "Fabrication of directly UV-written channel waveguides with simultaneously defined integral Bragg gratings," *Elec. Lett.*, vol. 38, pp. 1531-1532, November 2002.

Experimental demonstration of an ultra compact SOI polarization rotator

M. Aamer, A.M. Gutierrez, A. Brimont, A. Griol, P. Sanchis
Nanophotonics Technology Center, Universidad Politécnica Valencia, Camino de Vera s/n, 46022
Valencia, Spain
maaa@ntc.upv.es

D. Vermeulen, G. Roelkens
Photonics Research Group, Department of Information Technology, Ghent-University – imec,
B-9000 Ghent, Belgium

***Abstract*— We report the design, fabrication and characterization of a polarization rotator in SOI technology. The device is compact (26µm), and features a measured crosstalk above 10dB, over a 35-nm bandwidth with a polarization conversion efficiency above 90%.**

Keywords- Integrated optics; optical waveguides; polarization rotator; silicon on insulator technology

I. INTRODUCTION

Silicon-on-Insulator (SOI) is being consolidated as the most promising technology to develop photonic devices for telecom applications with an ultra large scale of integration (ULSI) at a low cost [1] due to the high refractive index contrast between silicon (n≈3.45) and silica (n≈1.45) at λ=1.55µm, as well as its compatibility with Complementary Metal Oxide Semiconductor (CMOS) microelectronic tools.

For high index-contrast integrated waveguides, one of the main issues is their strong polarization dependence. To overcome this drawback, a polarization diversity system is required because it enables polarization-insensitivity to arbitrary polarized input light, but may require a polarization rotator as one of the core devices [2]. Several polarization rotators have been suggested but require a complicated fabrication process, due to slanting sidewalls [3], or the use of additional materials [4,5]. An alternative mode evolution approach based on a pair of two different waveguide core layers were proposed in [6] but a non standard 400nm silicon thickness was used in one of the layers and the minimum rotation length was 40µm [7]. Recently, a planar polarization rotator, whose conversion length was also above 40µm, has also been reported [8].

The silicon polarization rotator proposed here is based on a very compact design without slanted side wall, hence requiring less complex fabrication process, being fully compatible for co-integration with standard SOI wafers based on a 220nm thick silicon layer.

II. POLARIZATION ROTATOR THEORY AND DESIGN

The proposed polarization rotator consists of a straight asymmetric structure shallow etched in a strip waveguide configuration as depicted in Fig. 1a, which was also proposed in [9] but only theoretically analyzed and optimized with different parameters. Here, the chosen parameters are h=220nm (silicon thickness in standard SOI wafers), etch depth, ed =70nm, and fill factor of 25%, ff=55nm. The etch depth was chosen to facilitate the integration of the polarization rotator in devices that use conventional gratings to couple light from an external optical fiber [9]. A symmetric-asymmetric waveguide interface allows the excitation of two hybrid modes S1 and S2, depicted in Fig. 1b, with their principal axis tilted by 45 degrees. In order to achieve total polarization conversion, these hybrid modes must be excited equally. This condition is satisfied for a waveguide width of 220 nm, as shown in Fig. 2, taking into account the 25% fill factor.

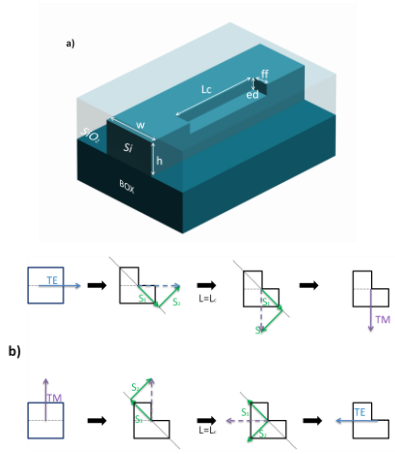


Figure 1. (a) Proposed SOI polarization rotator. (b) Optical axes rotation after propagating along L_c

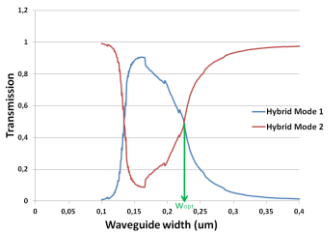


Figure 2.Width for which two hybrid modes are equally excited

Using the equation below, we find that the theoretical length to achieve polarization rotation is around 27 µm.

$$L_c = \frac{\lambda}{2\Delta n_{eff}} \quad (1)$$

where the $\Delta neff$ is the difference between effective indexes of the two hybrid modes. By using a simulation tool (FemSIM), we obtained that $neff_0$=1.5121 and $neff_1$=1.4833, so $L_c \approx 27$ µm at λ=1.55µm. The polarization rotator was then analyzed by means of 3D-FDTD simulations. The figures below show normalized output powers for TE (Fig. 3a) and TM input polarizations (Fig. 3b). Knowing that the length of the input waveguide is about 3 µm, the simulated length to achieve polarization rotation is close to 27 µm, agreeing with the theoretical value.

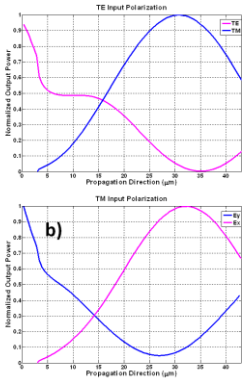


Figure 3. Normalized output power for (a) TE and (b) TM input polarization.

III. FABRICATION AND EXPERIMENTAL RESULTS

The samples were fabricated in two steps. First, the waveguides were fabricated. A direct writing electron beam process was employed. The pattern was transferred into 100nm of HSQ negative resist employing a 30 KeV ebeam exposure. Then, the sample was etched by using an Inductive Coupled Plasma (ICP).

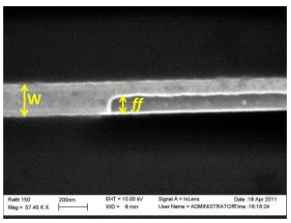


Figure 4. SEM image of fabricated polarization rotator

The second step was to remove the corresponding part of the waveguide to make the asymmetric structure. Once more, a direct e-beam writing process was employed but, in this case, on a patterned sample. So, previously exposed alignment marks were used to align the parts to be removed on the waveguides. This process was carried out by using PMMA positive resist which allows us to protect the rest of the sample during the etching process. The 70nm etching was again carried out by using an ICP system. Figure 4 shows the scanning electron microscope (SEM) image of the fabricated device.

Figure 5 shows experimental measurements. As depicted in Fig. 5a, we measured a 13.7dB crosstalk at λ=1.55µm. Moreover, the measured crosstalk remains above 10dB in a wavelength bandwidth of around 35nm, as shown in figure below. Fig. 5b shows the polarization conversion efficiency, which is larger than 95% at λ=1.55µm

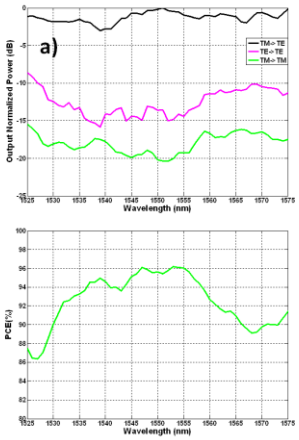


Figure 5. Measured (a) crosstalk and (b) polarization conversion efficiency for 26 µm-long-rotator

IV. CONCLUSION

In conclusion, an ultra compact and broadband polarization rotator in SOI technology has been designed, fabricated and experimentally characterized. The device features a polarization conversion efficiency of 95%, at λ=1.55µm, in a 26 µm-long-device. The next step would be the combination of both the polarization splitter and rotator, in order to demonstrate the performance of polarization diversity schemes.

ACKNOWLEDGMENT

Authors acknowledge funding by the European Commission under project HELIOS (pHotonics Electronics functional Integration on CMOS), FP7-224312, as well as TEC2008-06360 DEMOTEC, TEC2008-06333 SINADEC and PROMETEO-2010-087. Diedrik Vermeulen thanks the Institute for the Promotion of Innovation by Science and Technology in Flanders (IWT) for a grant.

REFERENCES

[1] B. Jalali and S. Fathpour, J. Light. Technol. 24 (2006), pp. 4600-4615.
[2] T. Barwicz, M. R. Watts, M. A. Popovic, P. T. Rakich, L. Socci, F. X. Kartner, E. P. Ippen, and H. I. Smith,Nat. Photonics 1(1), 57–60(2007).
[3] C. Brooks, P. E. Jessop, H. Deng, D. O. Yevick, and G. Tarr, Opt. Eng. 45, 044603 (2006).
[4] H. Fukuda, K. Yamada, T. Tsuchizawa, T.Watanabe, H. Shinojima and S. Itabashi, Opt. Express, 16 (4), 2628-35 (2008).
[5] L. Chen, C. R. Doerr, and Y. Chen, Opt. Lett. **36**, 469-471 (2011).
[6] J. Zhang, M. Yu, G. Lo, and D. Kwong, IEEE J. Selected Topics in Quan. Electron., 16(1), 53-60 (2009).
[7] L.Liu, Y: Ding, K. Yvind, and J. Hvam, Opt. Lett. 36, 1059-1061(2011).
[8] Z. Wang and D. Dai, J. Opt. Soc. Am. B 25, 747-753 (2008).
[9] D. Taillaert, W. Bogaerts, P. Bienstman, T. F. Krauss, P. Van Daele, I. Moerman, S. Verstuyft, K. De Mesel and R. Baets, IEEE J. Quantum Electron. 38, 949-956 (2002).

Nonlinear effects of four wave mixing in InP optical circuits at 1550 nm

B. R. Cemlyn[1†] , I. D. Henning[1], M. J. Adams[1], D. Labukhin[1]
1 School of Computer Science & Electronic Engineering, University of Essex, Colchester CO4 3SQ, UK
brceml@essex.ac.uk

***Abstract*-We demonstrate how side bands arising from four-wave-mixing in semiconductor optical amplifiers affect the generation of nonlinear dynamics in photonic integrated circuits.**

Keywords-component; four-wave-mixing, nonlinear dynamics, photonic integreated circuits, mutual coupling.

I. INTRODUCTION

As demand for transmission capacity continues to grow, closely spaced multicarrier systems combined with advanced modulation and coding techniques offer routes to more fully exploit the available bandwidth of optical fibre. Such systems require integration of key optical components into a single photonic integrated circuit (PIC) [1]. However as system requirements drive PIC complexity higher there arise many more possible mechanisms for mutual coupling between active circuit elements. Moreover semiconductor optical amplifiers (SOAs) are increasingly required in PICs to compensate for optical losses. These SOAs exhibit non-linear behaviour such as four wave mixing (FWM) [2] which has a significant impact on the performance of multicarrier systems. We have shown previously how mutual coupling in a PIC produces nonlinear dynamics (NLD), depending upon the coupling magnitude and the frequency detuning [3,4,5]. In this paper we extend this work to examine the effects on PIC dynamics arising from FWM in on-chip SOAs.

II. OPTICAL CHIP WITH FWM CONTROL

A. Physical Chip and Parameters

Figure 1 shows a diagram of the InP-based PIC studied here. It consists of 2 tuneable (~8 nm) DBR lasers whose fundamental lasing wavelengths are 1561 nm and 1555 nm, the outputs of which are coupled into an SOA via a multimode interference coupler. An aligned fibre acts to collect the chip output, and also provides reflection thereby giving a mutual coupling mechanism between the lasers [3,4,5]. The magnitude of the coupling is controlled both by the SOA gain and the fibre displacement. As the FWM level is dependent only on SOA gain, there is overall control of both the FWM and coupling magnitude. The detuning parameter is controlled via the DBR tuning currents. We characterize the FWM magnitude by the 1st side mode levels (SML), which we have observed as -14 dB to -26 dB for SOA currents between 15 mA and 60 mA.

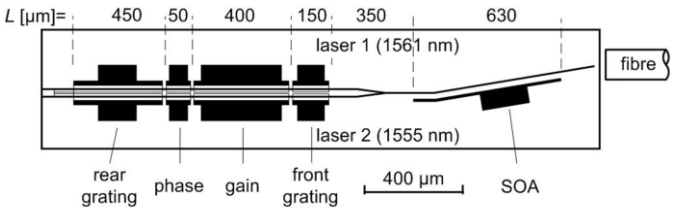


Figure 1: Schematic of the optical chip

B. Travelling Wave Model of Chip

We utilise a travelling wave (TW) model to provide a complete description of the temporal-spatial behaviour of the system [4,5,6]. The model provides for independent control of the FWM and mutual coupling through the SOA current and field transmission magnitudes. The detuning is controlled by adjustment of the phase and group indices of the DBR sections. Our current model provides SMLs of between -39 and -11 dB for SOA currents of between 20 and 160 mA.

III. DETERMINING THE CONRIBUTION OF FWM TO NLD

A. Modelled Relations

To isolate the influence of FWM on chip dynamics we varied the FWM levels and frequency detuning, whilst keeping the total power coupling magnitude constant at -27+/-0.07 dB. For each FWM level, one of the lasers was tuned through the other in 41 detuning steps between approximately -5 GHz and 22 GHz. A transition to NLD was observed at small frequency detunings [3,4,5]. Our results show that the SOA FWM levels have a significant effect on both the frequency boundary of the dynamic transition, and on the general degree of nonlinearity. In figure 2 we show examples of the modelled optical maps for SOA currents of 40 mA (-26 dB SML) and 160 mA (-11 dB SML). The maps are plotted as the detuning between the DBR lasers versus the resulting optical spectrum. It is seen that broadband spectra characteristic of NLD are both prevalent over a greater detuning range and are much broader in the higher SML map. The detuning range of the NLD can be

† B.R. Cemlyn is sponsored by a DTA grant from the UK Engineering and Physical Sciences Research Council (EPSRC).

quantified as a boundary in GHz, and we have done this using 2 different methods, viz. the correlation dimension of the time series [4,5,7] and the repeatability of the time series. The repeatability is calculated as the minimum difference between a signal portion, compared with every other portion of the signal. Figure 3a shows these results, with the boundary clearly increasing with the increasing SML. Additionally, the absolute degree of nonlinearity was found by calculating the mean correlation dimension for all signals of less than 5 GHz detuning. Again this clearly quantifies an increasing degree of nonlinearity as the SML increase (figure 3b).

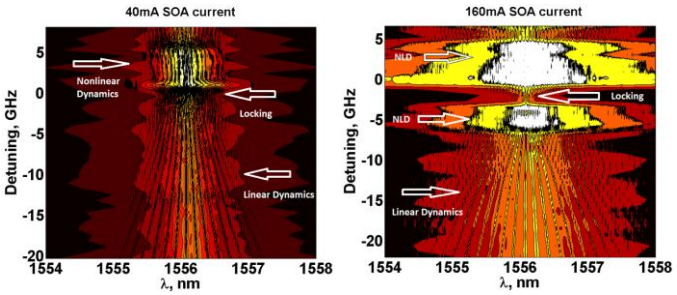


Figure 2: Optical maps for SMLs of -26 dB (lhs) and -11 dB (rhs).

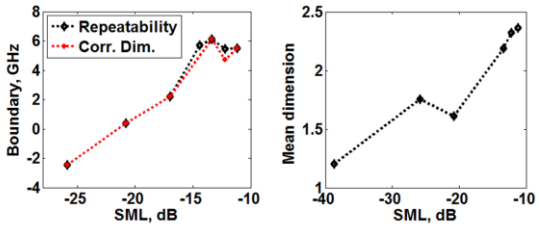


Figure 3: Modelled nonlinear trends as a function of FWM levels: 3a (lhs): frequency boundary linear-nonlinear behavior; 3b (rhs): overall degree of nonlinearity at low detuning (-5 GHz to +5 GHz).

B. Experimental Results

Experimental measurements were made to compare with the modelled data. A constant coupling level was achieved by increasing the SOA current and also displacing the fibre away from the chip, which reduces the degree of coupling between the reflected field and the field at the chip facet. SOA currents of 15 mA, 30 mA and 45 mA were matched with fibre displacements of 390 µm, 320 µm and 200 µm respectively. We calculated that this produced a constant coupling level of -10 dB, and a resultant coupling of approximately -26dB including -14dB fibre reflection and -2dB losses. It was found that the boundary to NLD increases strongly with SML, being 5.4, 7.4 and 8.6 GHz for SML of -26, -19 and -16 dB respectively for the 3 SOA currents. For these, we used the same correlation dimension method as for the simulated results. Figure 4 shows the single-sided spectra as the lasers are tuned across each other at 15 mA (-26 dB) and 45 mA (-16 dB) respectivly.

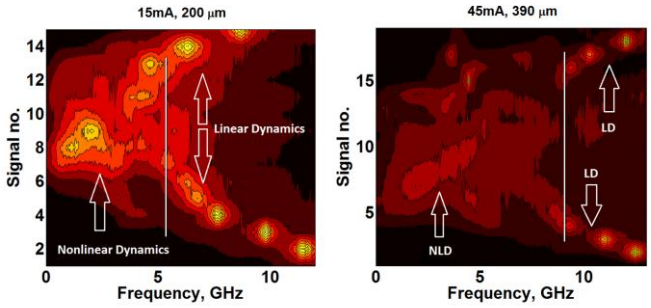


Figure 4: Experimental single-sided spectral maps for SMLs of -26 dB (lhs) and -16 dB (rhs). The vertical white lines show the boundaries between linear dynamics (LD) and NLD that were calculated using the correlation dimension of the time series.

IV. CONCLUSION

We have shown that four wave mixing levels in an SOA in a multi-active component optical system have a significant effect on the boundary to nonlinear dynamics, and the degree of nonlinearity. The increased chances of nonlinear destabilisation of the circuit must therefore be considered when including SOAs to increase PIC power levels. The current analysis uses only coupled CW signals, but will we also show the effect of FWM on coupled modulated (data) signals in such active optical circuits.

ACKNOWLEDGEMENTS

We would like to thank Agilent UK for the loan of the Infinium oscilloscope that was used to collect the experimental time series.

The chip was supplied by CIP, Martlesham, under the PORTRAIT grant, EPSRC number EP/D502225/1.

REFERENCES

[1] F.A. Kish et al., "Current status of large-scale InP photonic integrated circuits," *IEEE Journal of Selected Topics in Quantum Electronics*, vol. 17, no. 6, pp. 1470—1489, Nov. 2011.

[2] S. Diez et al., "Four-wave mixing in semiconductor optical amplifiers for frequency conversion and fast optical switching," vol. 3, no. 5, pp. 1131—1145, Oct. 1997.

[3] M.P. Vaughan, I. Henning, M.J. Adams, L.J. Rivers, P. Cannard and I.F. Lealman, "Mutual optical injection in coupled DBR laser pairs," *Optics Express* vol. 17, no. 3, pp. 2033-2041, Jan. 2009.

[4] B.R. Cemlyn, D.Labukhin, I.D.Henning and M.J.Adams, "Dynamics Transitions in a Photonic Integrated Circuit", *IEEE Journal of Quantum Electronics*, vol. 48, no. 2, pp. 261-268, Jan. 2012.

[5] B. Cemlyn, D Labukhin. M.J. Adams and I.D. Henning,"Dynamical Transitions in a Coupled Integrated Device," presented at the Conference on *Numerical simulation of optoelectronic devices (NUSOD)*, Rome, Italy, September 2011.

[6] D. Labukhin, C.A. Stolz, N. Zakhleniuk, R. Loudon and M.J. Adams, "Nonlinear dynamics of multi-section tunable lasers," *IEEE Journal of Quantum Electronics*, vol. 46, no.5, pp. 689-699, Jun. 2010.

[7] J. P. Toomey, D. M. Kane, S. Valling, and A. M. Lindberg, "Automated correlation dimension analysis of optically injected solid state lasers," *Optics Express*, vol. 17, no. 9, pp. 7592-7608, April 2009.

Fano-Like Resonance in Wavelength Scale Patterned Laser Facets

J.L. Stokes, N. Ahmad, J. R. Pugh, J. G. Rarity and M.J. Cryan
Photonics Research Group, Department of Electrical and Electronic Engineering. Bristol University
Bristol, UK.

G.R. Nash
College of Engineering, Mathematics and Physical Sciences, University of Exeter,
Exeter, UK

Abstract: This paper presents a study of grating structures etched onto the facet of a mid-infrared lasers. It suggests that it is possible to utilise a Fano-type grating resonance to control the emitted laser

Keywords-component; Plasmon; Grating; Fano Resonance

I. INTRODUCTION

There has been much interest in Mid Infrared (3-5μm) lasers in recent years for use in military and gas detection applications [1, 2]. Although room temperature emission has been achieved using Quantum Cascade and Interband Cascade lasers [3, 4], efficient CW emission across the whole wavelength range is challenging. Multi-Quantum well (MQW) ridge waveguide lasers offer an alternative which have much simpler device structures [5]. In order to achieve high output powers wide ridges are normally used, however, this leads to non-ideal, multimoded behaviour.

It has been shown recently that it is possible to suppress multiple modes in these broad-area lasers by the addition of a metallic grating [6]. To understand the physical origin of modal suppression the laser was simulated using the Finite Difference Time Domain (FDTD) method [7], the general simulation can be seen in Fig. 1. The source is placed inside the laser, represented by n=4 for AlGaInSb. This is coated with a dielectric layer of n=2 to prevent short circuiting of the electrically driven laser and a perfect metal grating with 7 slits is added at the surface. We could implement real metal within this FDTD code, but at these wavelengths metal is becoming very ideal. This also allows us to investigate what are known as designer or Spoof plasmons [8], which may play an important role here. We calculated the spectrum reflected back into the laser for a variety of grating parameters and it was found that in certain cases a Fano-like resonance occurs. A Fano resonance is a phenomenon that arises when two resonant processes are allowed to interfere with one another resulting in a spectral response that has a very distinctive lineshape. To see this effect it is imperative that the phase of one resonant process varies rapidly with wavelength whereas the other varies more slowly (fast and slow process respectively) [9]. The typical Fano lineshape and equation is shown and plotted in Fig 2. This general equation gives the interference lineshape, σ, using the energy of the resonant process, E_F, the resonant width, Γ, the photon energy E and the Fano parameter q, where q is the ratio of fast and slow process amplitudes.

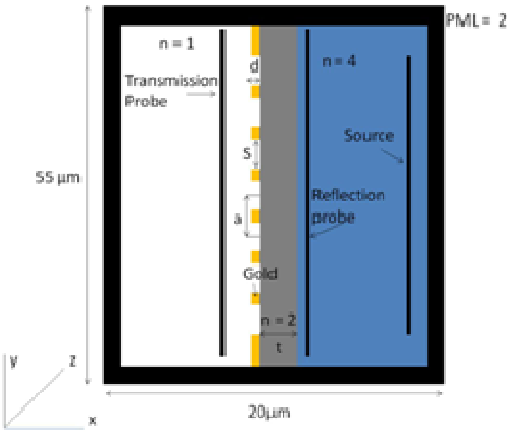


Fig 1: A schematic of the FDTD simulations where *d=70nm,* is the metal thickness, *s* is the slit width, *a* is the slit period, *t* is the dielectric thickness = 700nm. FDTD mesh size = 20nm

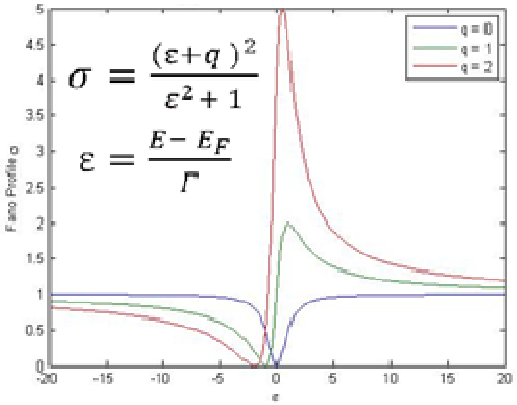


Fig 2: A graph of Fano resonances with different q factors. q=1 is when the fast and slow processes are of equal magnitudes and is the typical Fano lineshape.

It is believed that the Fano resonance that is present in the laser facet occurs between the Fabry-Perot resonance from the 700nm Si_3N_4 dielectric layer and the metallic grating. The grating was initially designed to be a second order grating where the period is equal to the free space laser wavelength, in this case 3.4μm. Thus, normal incidence light will be coupled into the plane of the grating and can be scattered back from the grating. These types of gratings can also support what are termed designer plasmons propagating along the gold surface

[8]. These are surface bound waves that have a dispersion curve very similar to that of a typical plasmon and can arise when a patterned metallic surface has features less the free space wavelength.

II. RESULTS

The reflection from a laser facet can be an important aspect in defining the emission characteristics of the laser. This is because the wavelengths that are more strongly reflected back into the laser are the ones that will undergo the most gain leading them to become the dominant emitted wavelengths. Consequently, if the wavelength of maximum reflection can be tuned then the dominant emitted wavelength can also be tuned. As the typical Fano resonance lineshape has a peak at a given wavelength, especially for the q=2 case, this could be used to select an overall lasing wavelength. Fig. 3 shows two set of results, firstly it shows reflectance for an unstructured 70nm gold layer on the n=2 and n=4 layers as shown in Fig. 1 for a simple Transfer Matrix Method (TMM) calculation and the FDTD method. These results show very good agreement and a shallow resonance associated with the Fabry-Perot resonance can be seen. Fig. 3 also shows a comparison between real gold and the Perfect Electrical Conducting (PEC) metal for the case of an isolated grating in free space and it can be seen that the results are very similar for both cases since gold is tending to a theoretically ideal metal at these wavelengths. The figure also shows the a shallow resonance associated with the grating and it is believed to be the interaction between these two effects that leads to a Fano-like resonance. Fig. 4 now combines the grating with the dielectric layers and shows how the reflectance of the system changes with respect to slit period, a. These curves show that the peak reflected wavelength of the Fano resonance blue shifts with decreasing slit period. This could allow tuning of the lasing wavelength, especially if a sharper Fano resonance could be obtained.

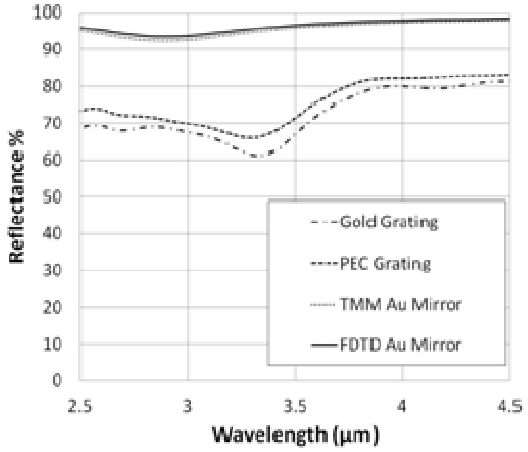


Fig. 3: FDTD simulation showing Gold and PEC reflectance for a slit width, S = 1.7μm, slit period, a = 3.4μm and no dielectric. It also shows FDTD vs TMM for a plane mirror of 70nm on dielectrics as shown in Fig 1.

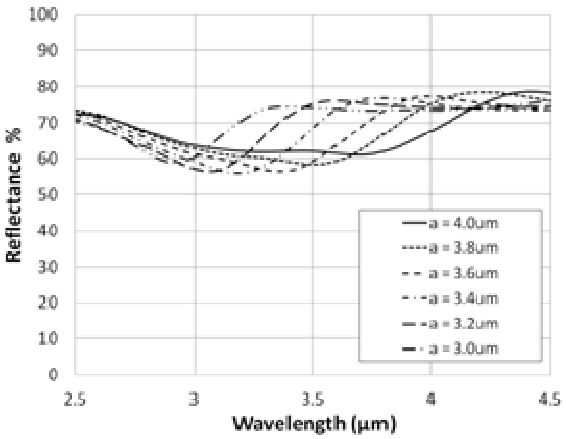


Fig. 4: FDTD simulations showing dependence on slit period, a. Slit width, S = 1.7μm and dielectric thickness, t = 0.7μm

III. CONCLUSIONS

This paper has studied Fano –like resonances in metallic gratings that have been patterned onto the emitting facets of mid infrared lasers. The results suggest that the fast and slow processes that make up the Fano resonance are related to a slow Fabry Perot resonance of the thin insulating dielectric layer, required to prevent shorting out of the laser and a fast resonance associated with the grating. Work is now on going to understand the nature of the grating resonance and the role that designer plasmons may be playing in this. The ultimate aim is to obtain a very narrow Fano lineshape which could be used to control the lasing wavelength of these devices.

After the text edit has been completed, the paper is ready for the template. Duplicate the template file by using the Save As command, and use the naming convention prescribed by your conference for the name of your paper. In this newly created file, highlight all of the contents and import your prepared text file. You are now ready to style your paper; use the scroll down window on the left of the MS Word Formatting toolbar.

REFERENCES

[1] G.Norris *et al*, "Mode behaviour in InAs mid-infrared whispering gallery lasers", App. Phys. Lett. **90**, 011105, (2007).

[2] D.A. Wright *et al.* "Mid-infrared whispering gallery mode ring lasers and LEDs", IEEE Proc.-Optoelectron, Vol. **150**, No. 4, (August 2003).

[3] M. Razeghi."High performance InP based mid-IR quantum cascade lasers", IEEE J. Sel. Top. Quantum Electron**. 15**, 941–951 (2009).

[4] C. S. Kim *et al,* "High-Power Single-Mode Distributed-Feedback Interband Cascade Lasers for the Midwave-Infrared", IEEE Photonic Tech. Lett. Vol. **19**, No. 3, (February 2007).

[5] G. R. Nash *et al*, "Midinfrared GaInSb/AlGaInSb quantum well laser diodes operating above 200 K", Appl. Phys. Lett. **94**, 091111 (2009).

[6] G. R. Nash *et al* "Single Lateral Mode Mid-IR Laser Diode using Sub-Wavelength Modulation of the Facet Reflectivity", arXiv:1108.1382v1.

Angularly robust resonant reflection from corrugated slab waveguide by mode coalescence

O. Parriaux, Y. Jourlin, S. Tonchev[#], A. Tishchenko, F. Lacour[$]

Laboratoire H. Curien UMR CNRS 5516, Lyon University at Saint-Etienne, France
[#] Institute of Solid State Physics, Bulgarian Academy of Sciences, Sofia, Bulgaria
[$]Eurofarad, ZAE du Chêne Saint-Fiacre, 77600 Chanteloup-en-Brie, France
parriaux@univ-st-etienne.fr

***Abstract*—Mode coalescence in a double-sided corrugated high-index dual-mode slab waveguide suppresses the spectral splitting of the normal incidence resonant reflection peak upon an angular offset. The resulting angular robustness enables this polarization- and wavelength-selective reflection effect to be used to optically process free-space light beams emitted by low coherence sources.**

Keywords- *Slab waveguide, Grating, Resonant reflection*

I. INTRODUCTION

Since its discovery in 1985 and the explanation of its mechanism [1], resonant grating reflection has been used with beams of high spatial coherence. The reflection peak width is of the order of one nanometer and the peak position is very sensitive angularly. There have been attempts to broaden the angular spectrum by enhancing the second order intra-guide coupling coefficient by tailoring the duty cycle of a corrugation or by means of a doubly-periodic grating [2]. These designs can however not achieve resonant reflection of a wide bandwidth, wide angular spectrum beam like that of a lensed LED for instance which would be very useful for a number of low-end applications such as coarse WDM.

We report here on a waveguide grating which under normal incidence achieves a polarization selective reflection peak of wide spectrum and moreover exhibits high angular robustness preventing the formation of the reflection dip in the spectrum of rays impinging slightly off-normal which preclude the reflection of a whole light beam of non-zero angular aperture.

II. ANGULARLY ROBUST RESONANT REFLECTION

A remarkable property of double-sided corrugated slab waveguides of very high index propagating a second mode close to its cut-off - here the TE_1 mode - is to exhibit a coalescence of the fundamental TE_0 and TE_1 modes as the corrugation depth increases. This is illustrated in Fig. 1 where an amorphous Silicon (α-Si) slab waveguide of index 3.7 on a glass substrate is given a thickness large enough, t = 130 *nm*, to propagate the TE_1 mode at 850 *nm* wavelength λ. The curves correspond to different sinusoidal undulation amplitudes *d*. The abscissa is the grating period Λ in a numerical experiment at constant wavelength and waveguide thickness *t* under normal TE incidence. The ordinate is the reflection coefficient. As expected, a shallow grating of

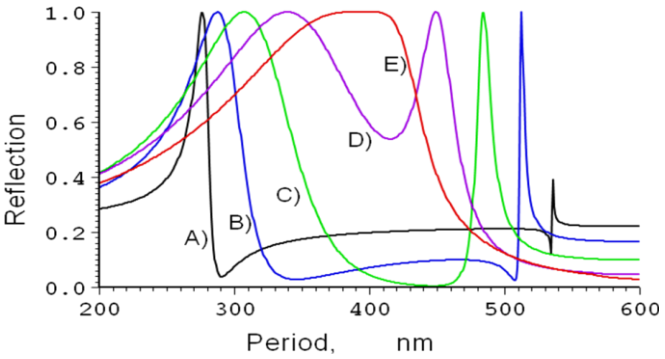


Figure 1. Normal incidence TE reflection spectra of double-sided sinusoidally undulated dual-mode a-Si slab waveguide versus period with grating depth parameter *d = 30, 60, 90, 120, 140 nm* in curves A, B, C, D, E.

increasing period couples the TE_0 mode first, then the TE_1 mode with the resulting narrow reflection peaks. The effective index of the modes is given as $n_e = \lambda/\Lambda$. Increasing the grating depth brings the two effective index closer up to *d = 140 nm* where the two modes have coalesced in a single resonance. As from here, the reflection spectrum is calculated with a grating depth leading to mode coalescence. Spectrum A) of Fig. 2 exhibits a wide reflection plateau of close to 100% reflection. Thus, all spectral components of a relatively wide spectrum light beam experience close to 100% reflection.

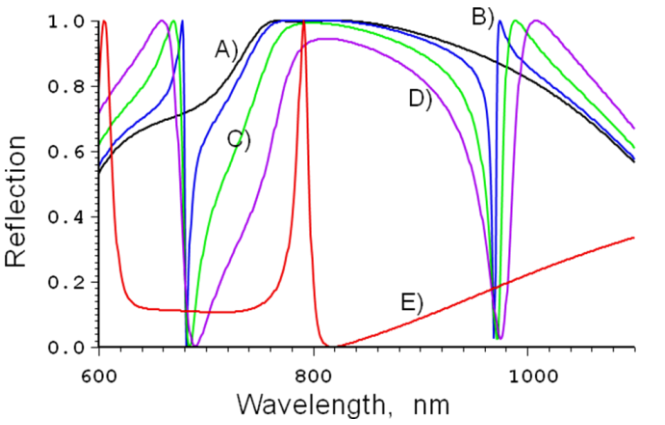


Figure 2. Reflection spectra of 130 nm thick a-Si waveguide with 333 nm period, 120 nm deep double undulation. Curves A, B, C, D are for TE incidence under angles 0, 5, 10, 15 degrees, curve E for TM normal incidence.

The other curves correspond to a tilted incidence in the incidence plane. Remarkably, the wavelength spectrum remains essentially unchanged up to an incidence angle of 15 degrees which roughly corresponds to the angular width of a lensed LED. Consequently, the designed structure represents a high contrast resonant mirror for polarized incoherent light sources of the LED type. Adding to this curve E) representing the TM reflection in the very same element, one has realized an angularly and spectrally robust high contrast polarizer.

A phenomenological vision is given of the coalescence which only takes place if the waveguide/substrate index ratio is larger than about 2. Going back to curve A) of Fig. 1 corresponding to a shallow grating, one realizes that a grating which would couple a normally incident wave to the TE_1 mode of effective index close to the substrate index would also couple the TE_1 mode to the TE_0 mode of effective index close to 3. Furthermore, the intraguide coupling coefficient between TE_0 and TE_1 modes as the overlap integral of the transverse modal electric field in the undulated parts of the slab is very large since the parity of the field of the TE_1 mode and that of the dielectric perturbation which the double-sided undulation represents is odd. The free-space wave and mode coupling condition is thus characterized by a high degree of synchronism and a large coupling coefficient. Going away from this very specific condition, for instance by using a high index oxide waveguide (eg TiO_2, diamond or ZnS), or even by increasing the a-Si waveguide thickness, thus modifying the effective index ratio and the synchronism condition between TE modes, suppresses the coalescence effect. It is therefore a remarkable coincidence that in this spectral range between 700 and 1000 nm are found the cheapest and most efficient LED light sources, high responsivity silicon-based photodetectors, and where the so well controlled a-Si technology of solar cells is for optical purpose a unique very high index and highly transparent material - to the dismay of photovoltaics. This situation is not so unique beyond the Si-gap where a number of transparent high index semiconductors exist, in particular in the far IR where such angularly robust polarization splitter may be very useful.

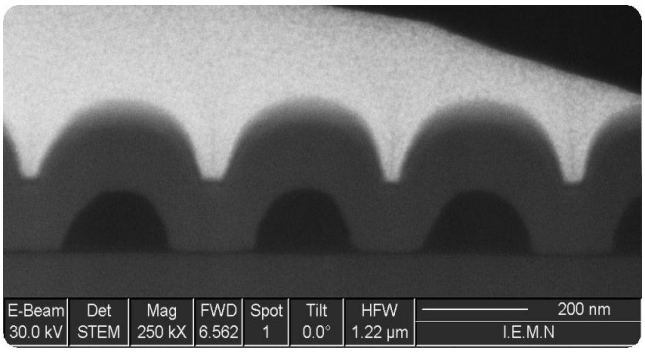


Figure 3. SEM picture of a FIB slice of rounded photoresist lines on glass substrate with 130 nm thick a-Si slab waveguide.

Usual polymer-based polarizers do have a large spectral width and a wide angular aperture with high extinction in the range of -40 dB. They however do not withstand the temperature conditions that prevail in most industrial systems. The functionality demonstration of the above design was made in the form of a binary corrugated photoresist layer on a glass substrate with a conformal a-Si layer on top. The photoresist layer was then post-backed to withstand the a-Si deposition conditions at 150 degree C. Figure 3 is the SEM picture of a FIB slice of the structure showing a very uniform silicon coverage and a perfect resist/silicon interface. The reflection spectrum is close to the modelling expectations as shown in Fig. 4. Accepting a 5% degradation of the TE reflection, the angular acceptance is ±15 degrees.

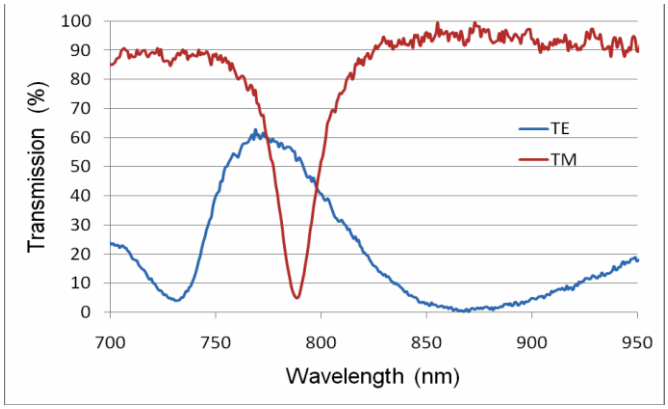


Figure 4. Measured TE and TM reflection spectra under normal incidence on the a-Si grating waveguide of Fig. 3.

III. CONCLUSION

A property of mode coalescence was identified in high index dual-mode waveguides whereby a deep corrugation makes the two modes to coalesce in a single waveguide resonance which is angularly robust and can be at the basis of a family of resonant optical elements processing low temporal and spatial coherence light beams. The demonstrated optical function is a wide band polarizer using the unique properties of an amorphous silicon waveguide fabricated by the highly reliable solar cell technology. This is a breakthrough in that optical waveguide resonances with their inherent selectivity characteristics can act with high contrast on a beam of high NA and large bandwidth.

REFERENCES

[1] G. A. Golubenko, A. S. Svakhin, V. A. Sychugov, and A. V. Tishchenko, "Total reflection of light from a corrugated surface of a dielectric waveguide," Sov. J. Quantum Electron. **15** 886–887 (1985).

[2] F. Lemarchand, A. Sentenac, E. Cambril and H. Giovannini, "Study of the resonant behaviour of waveguide gratings: increasing the angular tolerance of guided-mode filters," J. Opt. A: Pure Appl. Opt. **1** 545-551 (1999).

[3] U. Kroll, J. Meier, and A. Shah, "Hydrogen in amorphous and microcrystalline silicon films prepared by hydrogen dilution", J. Appl. Phys., **80** 4971-4975 (1996)

Recovery of lost photons in plasmon-mediated transmission across undulated metal film

Olivier Parriaux, Svetlen Tonchev[#], Yves Jourlin

Laboratoire H. Curien UMR CNRS 5516, Lyon University at Saint-Etienne, France
[#]Institute of Solid State Physics, Bulgarian Academy of Sciences, 1784 Sofia
parriaux@univ-st-etienne.fr

***Abstract*—Plasmon-mediated transmission across an undulated metal film embedded in a polymer exhibits an application deterring excess loss reducing the resonant transmission to about half of the theoretical 90% expectable with noble metals. Slow dissolution of the polymer surrounding the metal film while measuring the transmission spectrum in floating conditions tends to a near to complete recovery of the missing photons. The loss mechanism is scattering and absorption at crosslinked polymer-metal bridges induced by the first molten clusters of evaporated metal. A solution is given.**

Keywords-*Surface plasmons, Resonant transmission, Scattering*

I. INTRODUCTION

The effect of resonant transmission of an incident free-space wave across an undulated continuous metal film is a known phenomenon resulting from the excitation of the neighboring two TM plasmon modes by means of a periodic undulation [1]. Unlike in the pioneering work on plasmonic integrated optics for the C band [2], the concern here is not to propagate plasmons for their own sake, but to use them as an optical resonator on the path of a free-space wave, trapping the latter by a corrugation grating. If the resonant transmission through a few tens of nanometers thick continuous metal layer would be close to the theoretical predictions based on the bulk metal permittivity (e.g., more than 90% for Gold or Silver), this effect could be implemented with low cost injection and embossing technologies and give rise to a number of polarization-, wavelength-, angle-selective, and spatially resolved light processing functions useful for instance in sensing, information encoding. It was upon the concrete implementation of an encoding function that it became clear that there was a major loss problem: about half the photons were missing [3].

II. EXCESS LOSS IN PLASMONIC RESONANT TRANSMISSION

The experimental simulation of a future monolithic element is sketched in Fig. 1: a glass substrate, a photoresist layer with sinusoidal profile grating conformally coated with a metal film, and a thick resist cover. As curve a) of Fig. 2 shows, the theoretically expectable transmission spectrum of a normally incident wave of TM polarization through a Gold film sinusoidally undulated, embedded in a polymer medium should reach close to 90% when considering the bulk permittivity. The transmission curve a) has a main peak corresponding to the long range plasmon mode and a short range plasmon shoulder.

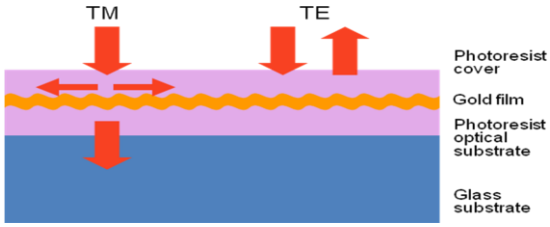


Figure 1. Experimental simulation of a future symmetrical plasmon-mediated resonant transmission element comprising an undulated continuous metal film sandwiched between two thick photoresist layers on a glass substrate.

Curve b) refers to the same structure with two 3 nm thick layers of Chromium showing that using a usual adhesion layer is forbidden. Curve c) is the TE transmission spectrum. Experimentally, a typical TM transmission spectrum through a 30 nm Gold film is represented in Fig. 3: the long range plasmon peak is present and has close to the expected spectral width, but the transmission maximum is about 50% only.

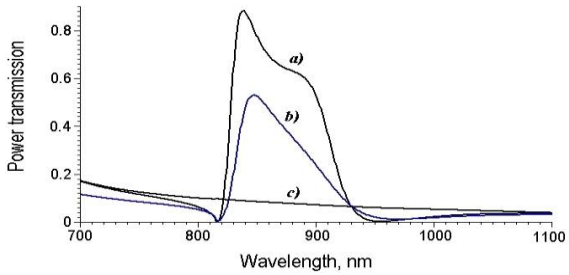


Figure 2. Theoretical TM and TE transmission spectra under normal incidence of a 33 nm thick Gold film with a 60 nm deep sinusoidal grating of 500 nm period embedded in a homogeneous polymer of index 1.63. a): TM transmission. b): TM transmission in the presence of two 3 nm thick Chromium adhesion layers. c): TE transmission

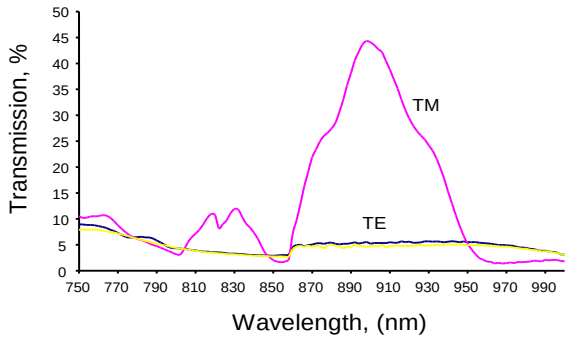


Figure 3. Typical TM and TE experimental transmission spectra across an undulated continuous gold film as depicted in Fig.1

Figure 3 also shows the TE transmission as a base line. The same observation was made with embedded aluminum films of 20 nm thickness: whereas a theoretical maximum of 60% is expectable, hardly 25% transmission was measured.

III. MISSING PHOTONS RECOVERED IN FLOATING GRATING

High magnification microscope observation and SEM scan do not reveal any feature which could explain such high loss: the grating is uniform and smooth. A chemically assisted experiment was therefore made. A model like that of Fig. 1 without the resist cover was made with a 30 nm thick Gold film and a rather ample undulation of 140 nm depth and 600 nm period. The element was installed horizontally in a cuvette in a transmission spectroscopy mount of vertical axis making the acquisition of the transmission spectrum during the experiment. The sample was immersed in acetone which gradually dissolves the photoresist under the metal film. The spectrum is measured at regular time intervals as reported in Fig. 4.

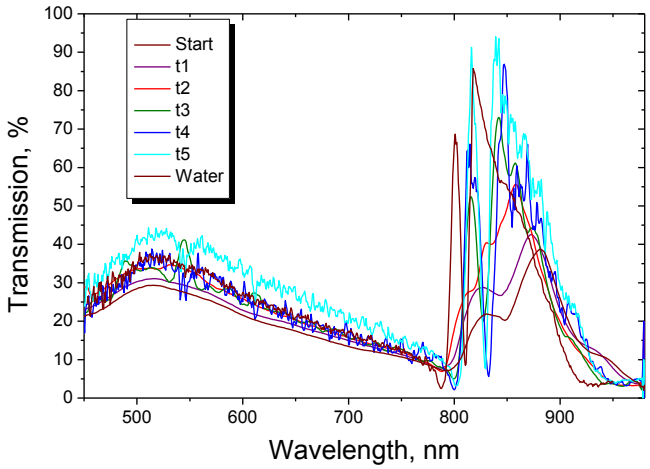


Figure 4. Experimental TM transmission spectra across the structure of Fig. 1 without resist cover under normal incidence during the dissolution of the photoresist. Brown curve: the acetone is replaced by water.

The transmission spectrum is initially smooth and low level since the long range plasmon mode is lossy and leaky at the photoresist side (index of 1.63 against 1.355 for acetone) up to the red curve where the transmission reaches more than about 50%. At that point most of the resist has been dissolved, but there remains a large number of bridging points where the Gold film still sticks on non-dissolved resist clusters as illustrated in the picture of Fig. 5a), and its surface buckles. These bridging points result from the impact of the first molten metal deposits. A close microscope observation through the semi-transparent Gold film reveals as illustrated in picture 5b) a rather regular pattern of dots of different refractivity which a larger magnification permits to attribute to overheated, sometimes carbonized resist spots. The dissolution of these clusters is much slower; the transmission increases slowly and becomes more noisy spectrally as the bridging points give away.

A time of two hours has elapsed between the red and the light blue curve which reaches close to 90% transmission in a quasi free floating condition, i.e., close to the theoretical transmission maximum. Thus, the missing photons have been recovered. The short range plasmon shoulder can even be discerned. There is however still the troublesome presence of a sharp dip within the long range plasmon peak which, together with the noisy aspect of the spectra, sheds doubt on the physical trustworthiness of the measurements. The doubt was dispelled by slowly replacing acetone by water which gives the brown transmission curve spectrally shifted to shorter wavelength by 20 nm under the ca 2% index decrease: the sharp dip has drifted as well. The clue about the dip is revealed by considering curve a) of Fig. 2 again, and simulating a 1 degree incidence offset: the zero at the left of the transmission peak then encroaches onto the latter as an effect of the -1st order coupling of the long range plasmon. Such small angular offset in the described experiment was to be expected with a warped floating grating. Whether the dip amounts to a sharp absorption or/and to the long searched plasmonic resonant reflection peak is still to be determined. The answer is likely to be given at the conference.

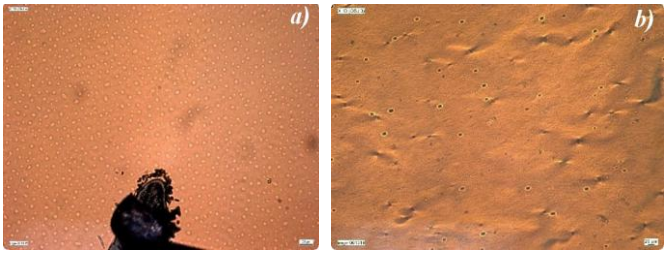


Figure 5. Microscope pictures taken at different steps of the resist dissolution process. a) Before dissolution with refractivity non-uniformities under low magnification. b) Free-floating Gold film with holes and warps.

IV. CONCLUSION

The main outcome of the present search for the missing photons is thus that these have been retrieved. The cause of the excess loss is the non-uniformity of the metal-polymer interface due to chemical crosslinking of the polymer surface by the first evaporated metal drops. How can the missing photons also be retrieved when the metal layer rests on a solid substrate is the next question. It has been shown here that the polymer/metal interface where the plasmon modes have their field maxima must be very uniform without local delamination and complex index variation. If this condition can be satisfied with high T_g polymers like BCB [2], it cannot with moldable polymers of low T_g like PMMA. A solution is found in the field of security features which makes a wide use of the ZnS/metal/ZnS system embedded into moldable polymers. This solution will be demonstrated at the conference.

REFERENCES

[1] I. Avrutsky, Y. Zhao, and V. Kochergin, “Surface-plasmon-assisted resonant tunneling of light through a periodically corrugated thin metal film,” Opt. Lett. 25, (2000) 595–597

[2] T. Nikolajsen, K. Leosson, I. Salakhutdinov, and S. I. Bozhevolnyi, “Polymer-based surface-plasmon-polariton stripe waveguides at telecommunication wavelengths”, Appl. Phys. Lett., 82 (2003), 668-670

[3] Y. Jourlin, S. Tonchev, A.V. Tishchenko, C. Pedri, C. Veillas, O. Parriaux, A. Last, and Y. Lacroute, "Spatially and polarization resolved plasmon mediated transmission through continuous metal films," Opt. Express 17 (2009) 12155-12166

Performance of 80 Gb/s MMI-Based DQPSK Demodulator on SOI

N. Sotiropoulos, H. de Waardt, A.M.J. Koonen
Dept. of Electrical Engineering
Eindhoven University of Technology
Eindhoven, Netherlands
n.sotiropoulos@tue.nl

D. Vermeulen, G. Roelkens
Dept. of Information Technology (INTEC)
Ghent University-IMEC
Gent, Belgium

R. Halir, G. Wangüemert-Pérez
Departamento Ingeniería de Comunicaciones, ETSI Telecomunicación
Universidad de Málaga
Malaga, Spain

***Abstract*—A Silicon-on-Insulator (SOI) Differential Quadrature Phase Shift Keying (DQPSK) demodulator based on a novel Multimode Interference (MMI) design is characterized for a number of operating wavelengths, with results indicating good uniformity and low wavelength dependency.**

Keywords- silicon integrated devices; DQPSK demodulator; MMI; characterization

I. INTRODUCTION

The introduction of multilevel modulation formats in optical communication systems has allowed the efficient scaling of system bit rates, without requiring electronics and photonics operating at very high bandwidths. Of special interest is Differential Quadrature Phase Shift Keying (DQPSK) modulation, which encodes two bits in the phase difference between two consecutive symbols, as it can be very robust against Chromatic Dispersion (CD) and non-linearities [1]. For the demodulation of DQSPK signals, a delay line equal to the symbol duration and phase shifters are required, which means that fiber-based receivers are bulky. On that respect, photonic integration can offer substantial improvement, leading to smaller, more stable and potentially low-cost receivers.

Silicon-based integration platforms are especially suitable for such applications, since they exhibit low losses and photodiodes can be easily accommodated, through hybrid or heterogeneous integration. For that reason, a number of silicon-based demodulators have already been presented [2-4]. The device characterized in this paper uses a MMI design based on a combination of shallowly and deeply etched regions, which results in very low phase errors and maintains compact design [5]. The Continuous Wave (CW) measurements of this 90^0 hybrid have been undertaken and results confirm the very good phase properties of the MMI coupler [5]. In this paper, the integrated demodulator was evaluated in a 40 Gb/s DPSK test bed, in order to determine the system performance of the device.

The work presented in this paper was funded by the Netherlands Ministry of Economical Affairs and the Netherlands Ministry of Eduacation, Culture and Science under Project MEMPHIS and by the Andalusian Ministry of Science, Innovation and Industry under Excellence Research Project P07-TIC-02946

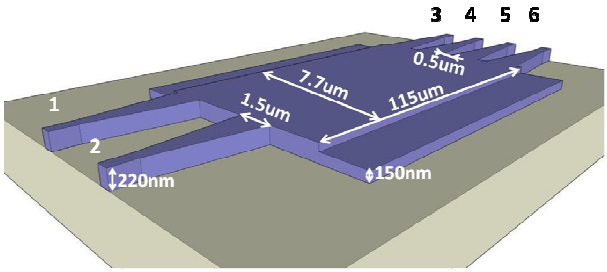


Figure 1 Schematic of the 2x4 MMI

II. DEVICE DESIGN

The device consists of grating couplers for fiber-to-chip coupling, a splitter, a 25 ps delay line (40 GHz Free Spectral Range) and the 90^0 hybrid, implemented in SOI technology. The hybrid is the most critical structure of the design and is based on a 2x4 MMI coupler. The schematic of the MMI is shown in Fig. 1, with the inputs (1 and 2) and outputs (3, 4, 5 and 6) of the structure labeled. The novelty of the MMI is the direct coupling of a shallowly etched multimode region to deeply etched waveguides. The shallowly etched region reduces the index contrast, keeping the phase errors very low. On the other hand, the rest of the waveguides are deeply etched, allowing for small curvature radii. With this approach, good imaging quality and a small footprint for the 90^0 hybrid are achieved.

III. EXPERIMENTAL SET-UP AND RESULTS

The experimental set-up built to test the device is shown in Fig. 2. The demodulator is capable of decoding DQPSK signals at 80 Gb/s, however, the DQPSK transmitter available was limited to 56 Gb/s. For that reason, the device was tested with a binary DPSK signal at 40 Gb/s. A tunable laser source creates the CW signal which enters, after polarization control, the DPSK transmitter subsystem, where it is modulated in order to create the 40 Gb/s Non-Return to Zero (NRZ) DPSK signal.

The output power of the transmitter is fixed at -3 dBm. Then, the signal is inserted to a variable optical attenuator (VOA), where the received power is set. Afterwards, the attenuated signal passes through two amplification stages (EDFAs) and is launched into the chip with a fixed power of +17 dBm. High input power was necessary, in order to compensate for the coupling and on-chip losses, which were around 20-23 dB (approximately 6.5 dB from each of the grating coupler, 6.5 dB insertion loss from the MMI and 1 dB propagation losses). The demodulated signal is coupled out of the device and is amplified by an EDFA to +7 dBm and filtered (to remove the excess ASE noise). The demodulated signal is detected by a balanced photo-detector pair, which lacks an integrated Trans-Impedance Amplifier (TIA). The lack of electrical post-amplification meant that optical amplification after the chip had to be employed, to ensure that the detected electrical signal had a voltage level above the sensitivity of the Error Analyzer (EA).

To verify the performance of the device, BER measurements as a function of the received power for every output of the device, with single-ended detection, for a number

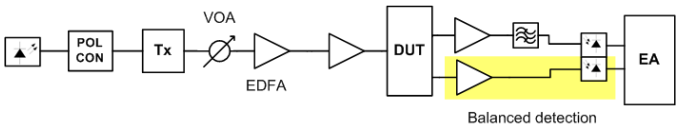


Figure 2 Experimental set-up

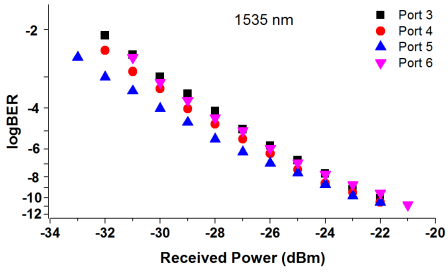


Figure 3a BER vs. received power, λ=1535 nm

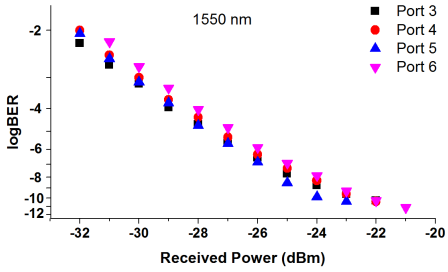


Figure 3b BER vs. received power, λ =1550 nm

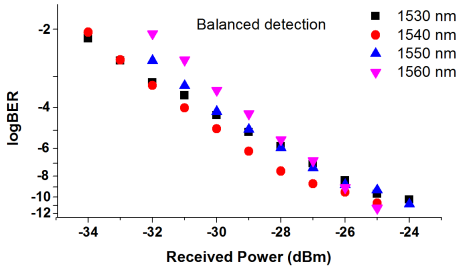


Figure 4 BER vs. received power, balanced detection

of wavelengths were performed. The BER curves for the 1535 and 1550 nm are shown in Figs. 3a-b, obtained using a pattern length of 2^{31}-1 in the experiments. From the results it can be seen that there is good uniformity between all the outputs of the device. As far as wavelength dependency is concerned, optimal performance is observed for the 1535-1550 nm range, with a small penalty for higher wavelengths (not shown here). This is in agreement with the CW measurements, which indicated optimum performance up to a wavelength of 1560 nm [5]. After validating every individual 90^0 hybrid output, experiments involving balanced detection of a pair of outputs were performed. Due to the fact that both outputs needed to be amplified and that the pulse length is quite short, there was a misalignment between the two bit streams that had to be corrected by inserting fiber patch cords and tunable optical delays. That approach required a short pattern length, 2^7-1, to enable the aligning of the bit stream through a scope. The results of balanced detection for outputs 3 and 6 for a number of wavelengths can be seen in Fig. 4. An improvement over the single-ended case, as expected, can be clearly seen. A small wavelength dependency, around 1 dB, can also be observed.

IV. CONCLUSIONS

The system performance of a MMI-based SOI DQPSK demodulator was validated at 40 Gb/s in this paper. The results prove the very good phase error properties of the novel MMI design and demonstrate low wavelength dependency. Combined with integrated photo-detectors, very high-speed, compact and potentially low-cost integrated receivers for advanced modulation formats can be realized.

REFERENCES

[1] D. van den Borne, S.L. Jansen, E. Gottwald, P.M. Krummrich, G.D. Khoe, and H. de Waardt, "1.6-b/s/Hz Spectrally efficient transmission over 1700 km of SSMF using 40 × 85.6-Gb/s POLMUX-RZ-DQPSK," J. of Lightw. Tech., vol.25, no.1, pp.222-232, Jan., 2007

[2] K. Voigt et al., "Performance of 40-Gb/s DPSK demodulator in SOI-technology," IEEE Phot. Tech. Lett., vol.20, no.8, pp.614-616, Apr. 15, 2008.

[3] Y. Sakamaki et al., "One-chip integrated polarisation-multiplexed DQPSK demodulator using silica-based planar lightwave circuit technology," Electr. Lett. , vol.46, no.16, pp.1152-1154, Aug. 5, 2010.

[4] C.R. Doerr, L. Chen , "Monolithic PDM-DQPSK receiver in silicon," 36th European Conf. on Optical Comm. (ECOC), 19-23 Sept., 2010.

[5] R. Halir, G. Roelkens, A. Ortega-Moñux, and J. G. Wangüemert-Pérez, "High-performance 90° hybrid based on a silicon-on-insulator multimode interference coupler," Opt. Lett., vol. 36, no. 2, p.p. 178-180, Jan. 15, 2011.

Ultracompact Plasmonic-Mode-Assisted Polarization Splitter with A Large Fabrication Tolerance

Yin-Jung Chang, Wei-Lun Li, and Hong Chen
Department of Optics and Photonics
National Central University
Jhongli, 32001, Taiwan (R.O.C.)
yjchang@ncu.edu.tw

***Abstract*— An ultra-compact plasmonic-mode-assisted polarization splitter based on directional coupler is proposed and investigated analytically and numerically. A large modal birefringence of > 0.69 is estimated, enabling a clean polarization separation within 5.6 μm.**

Keywords-Polarization splitters; surface plasmons; plasmonic waveguides

I. INTRODUCTION

The advances in nanotechnologies have made the implementation of photonic integrated circuits (ICs) at deep submicron/nanoscale possible in recent years. Featuring strong field confinement in dimensions smaller than the diffraction limit, plasmonic waveguide devices have presented what might be the most promising solution in realizing optical nanocircuitry.

Despite their inherent sub-wavelength guidance capability, plasmonic waveguides suffer from high propagation loss due mainly to the energy dissipation in the conductor (ohmic loss) [1]. This limits their propagation length from a few to hundreds of microns at best, depending on the operating wavelength (~ 30 μm in visible and ~ 300 μm in near infrared). On the other hand, nowdays the silicon (Si) core of a single-mode waveguide operating in optical telecommunication bands can be only a few hundred nanometers. For example, the state-of-the-art strip waveguide with a cross-sectional area of 200×400 nm^2 [2] has been experimentally demonstrated. In view of bringing light from long-haul optical networks into nanoscale photonic ICs, combining the advantages from both dielectric- and plasmonic-based structures, which may be complimentary to each other in nature, could pave the way toward high-performance, ultrahigh-density optical nanocircuitry in the future.

Symmetric metal/multi-insulator/metal and asymmetric metal/multi-insulator (MMI) structures have been explored in the design of low loss, ultracompact plasmonic Bragg gratings [3, 4] and 90° waveguide bends for optical nanocircuitry [5]. In this paper, a new polarization splitter (PS) based on an asymmetric metal/multi-insulator directional coupler (DC) is proposed and investigated. Advantages and performance of this novel PS as well as its fabrication tolerance are revealed and briefly discussed.

This research was support in part by grants NSC-100-2221-E-008-061 from the National Science Council, Taiwan (R.O.C.).

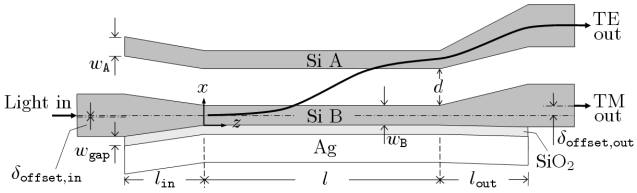


Figure 1. Two-dimensional (2-D) schematic of the proposed polarization splitter in asymmetric metal/multi-insulator configuration.

II. DESIGN PRINCIPLES

The proposed PS is depicted schematically in Fig. 1. It is a DC-based design with one arm (guide B) being in asymmetric silicon/silica/silver configuration and the other a simple Si waveguide (guide A). The respective refractive indices of Si, silica, and silver are $n_{\mathrm{Si}} = 3.5$, $n_{\mathrm{silica}} = 1.46$, and $n_{\mathrm{Ag}} = 0.1441 - j11.2141$ at a free-space wavelength $\lambda_0 = 1550$ nm. The background material is assumed to be air. The silica gap width w_{gap} is set to 100 nm. The guided mode supported by the composite guide B is excited by a 450-nm-wide Si waveguide followed by a linear taper of length l_{in}. The Si core width along the straight section of guide B is 200 nm, whereas the silver region is 300-nm-wide throughout the device. Due to limited computational resources, a 2-D electromagnetic problem was assumed in both analytical calculations and numerical simulations.

The modal birefringence associated with the asymmetric MMI configuration is critical to the PS design as it presents what might be the only enabling mechanism for the polarization splitting in DC-based configuration. In the structure presented above, it is shown that the effective index of the TM mode ($N_{\mathrm{eff,TM}}$) is a strong function of the silica gap width. The largest modal birefringence occurs when the silver region is completely removed but is inevitably accompanied by a minimum TM field confinement. Since $N_{\mathrm{eff,TE}}$ is larger than $N_{\mathrm{eff,TM}}$ by a large margin of more than 0.696 for $w_{\mathrm{gap}} \geq 100$ nm and beyond, the coupling length of the TE polarization is significantly shorter than that of the TM. Consequently, the cross path is intended for the TE propagation while the through path is for the TM. The performance of the present PS may be

strictly described in terms of the splitting ratio (SR) and extinction ratio (ER) defined as follows:

$$\mathrm{SR_{TE}} = 10 \times \log\left(T_{\mathrm{A,TE}}/T_{\mathrm{B,TE}}\right), \quad (1)$$

$$\mathrm{SR_{TM}} = 10 \times \log\left(T_{\mathrm{B,TM}}/T_{\mathrm{A,TM}}\right), \quad (2)$$

$$\mathrm{ER_{cross}} = 1 \times \log\left(T_{\mathrm{A,TE}}/T_{\mathrm{A,TM}}\right), \quad (3)$$

$$\mathrm{ER_{thru}} = 10 \times \log\left(T_{\mathrm{B,TM}}/T_{\mathrm{B,TE}}\right), \quad (4)$$

where $T_{\mathrm{A},i}$ ($T_{\mathrm{B},i}$), $i = \{\mathrm{TE}, \mathrm{TM}\}$, represents the normalized power transmission at the end of guide A (guide B) associated with the TE or TM mode.

III. Results and Discussions

The coupling length and $\mathrm{SR_{TE}}$ of the TE mode with varying separation distance d were first studied using modified coupled-mode equations applicable to a lossy waveguide system [6]. The initial design was then optimized by minimizing the $T_{\mathrm{B,TE}} \times T_{\mathrm{A,TM}}$ product that is a function of d and l through finite-element-based numerical simulations (Fig. 2). This ensures the maximum simultaneous cancellation of the modal power at the undesired output port. The optimized structure parameters are given in [6].

The time-average power flow associated with the respective TE and TM modes in the optimized PS is shown in Fig. 3. The figures of merit defined in (1) – (4) of the device are given in Table I. On the other hand, assume the device length is unchanged, the fabrication tolerance studies reveal that, at a 10-dB criterion for all figures of merit, the proposed PS has a relatively large fabrication tolerance of ± 60 nm ($\pm 30\%$) for the Si core width, which translates to ± 30 nm ($\pm 30\%$) for the silica gap region.

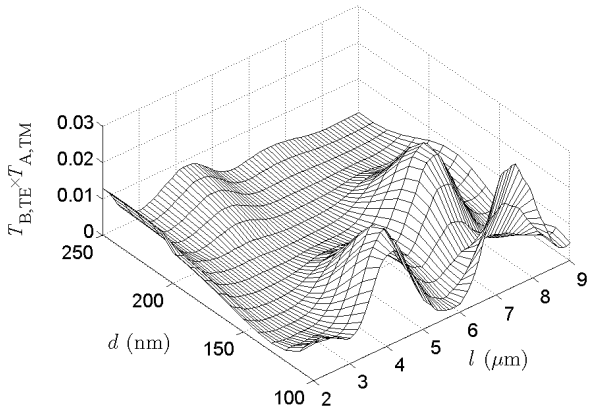


Figure 2. $T_{\mathrm{B,TE}} \times T_{\mathrm{A,TM}}$ product versus separation distance d and straight section length l at $w_{\mathrm{A}} = w_{\mathrm{B}} = 200$ nm.

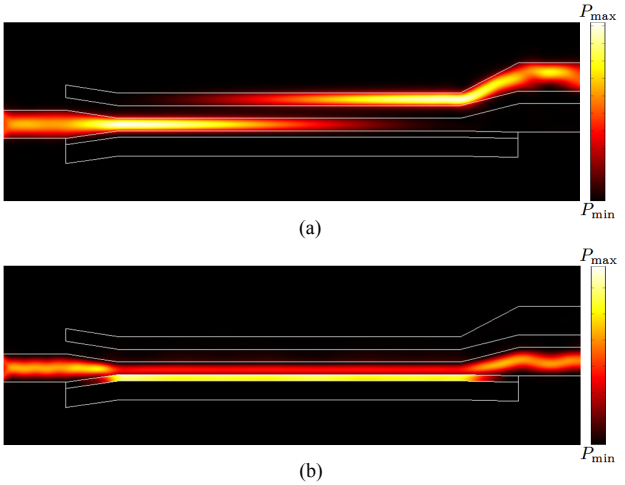


Figure 3. Time-average power flow of the optimized plasmonic-mode-assisted polarization splitter for (a) TE and (b) TM modes at $\lambda_0 = 1550$ nm. The insertion loss is < -0.14 dB for the TE and < -0.32 dB for the TM.

TABLE I
PERFORMANCE OF THE PRESENT POLARIZATION SPLITTER

Figure of Merit	$\mathrm{SR_{TE}}$	$\mathrm{SR_{TM}}$	$\mathrm{ER_{thru}}$	$\mathrm{ER_{cross}}$
$+30\%$ error in width	10.70	18.11	11.13	17.69
Optimized structure	20.73	22.54	20.55	22.71
-30% error in width	12.64	17.55	12.14	18.05

IV. Summary

An ultra-compact DC-based polarization splitter in asymmetric metal/multi-insulator configuration with a critical dimension of 100 nm has been presented. A large modal birefringence of about 0.7 enables a clean separation of TE and TM modes within one TE coupling length. The footprint of the device, including the input/output tapers, is 7.28×1.60 $\mu\mathrm{m}^2$ and the 10-dB fabrication tolerance could be up to $\pm 30\%$ of the targeted widths of Si waveguide and silica gap region.

References

[1] H. Raether, *Surface Plasmons*: Springer, Berlin, 1988.

[2] T. Tsuchizawa, K. Yamada, H. Fukuda, T. Watanabe, J.-I. Takahashi, M. Takahashi, T. Shoji, E. Tamechika, and S.-I. I. a. H. Morita, "Microphotonics devices based on silicon microfabrication technology," *IEEE J. Sel. Top. Quantum Electron.,* vol. 11, pp. 232-240, 2005.

[3] Y.-J. Chang, "Design and analysis of metal/multi-insulator/metal waveguide plasmonic Bragg grating," *Opt. Express,* vol. 18, pp. 13258-13270, Jun. 2010.

[4] Y.-J. Chang and G.-Y. Lo, "A Narrowband Metal–Multi-Insulator–Metal Waveguide Plasmonic Bragg Grating," *IEEE Photon. Technol. Lett.,* vol. 22, pp. 634-636, 2010.

[5] Y.-J. Chang and Y.-C. Liu, "Polarization-insensitive subwavelength sharp bends in asymmetric metal/multi-insulator configuration," *Opt. Express,* vol. 19, pp. 3063-3076, Feb. 2011.

[6] Y.-J. Chang and W.-L. Li, "Directional-coupler-based polarization splitting in asymmetric metal/multi-insulator configuration for optical nanocircuitry," *IEEE Photon. Technol. Lett.,* in press, 2012.

Nd^{3+}-doped ion-exchanged aluminum germanate glass waveguide for O-band amplification

Baojie Chen[1], Sai Tak Chu[2], and Edwin Yun Bun Pun[1]
[1]Department of Electronic Engineering,
[2] Department of Physics and Materials Science,
City University of Hong Kong,
Hong Kong, PR China,
eeeybpun@cityu.edu.hk

Hai Lin
School of Textile and Material Engineering,
Dalian Polytechnic University,
Dalian, PR China,
lhai8686@yahoo.com

***Abstract*—K^+–Na^+ ion-exchanged channel waveguide has been fabricated in Nd^{3+}-doped aluminum germanate (NMAG) glasses. The fabricated waveguide exhibits a loss of ~0.36dB/cm, is single mode at 1.3μm, and the maximum theoretical gain at 1.337μm is 16dB/cm. The ion-exchanged Nd^{3+}-doped NMAG glass waveguide show promises in the development of O-band waveguide amplifier, infrared UV-writing grating waveguide laser, and compact integrated optical device.**

Keywords-Rare earth ion; Germanate glasses; Ion-exchanged waveguide ;Optical Amplifier; Integrated optical devices

I. INTRODUCTION

1.55μm (C-band) optical fiber amplifiers have been extensively used in telecommunication systems, however, it is insufficient for the ever expansion in large-capability and high-speed communication systems [1]. Based on high fidelity and low polarization properties of the second telecommunication window, development on 1.3μm wavelength optical amplifiers becomes important for achieving all-optical amplification. Due to the small energy gaps between the emitting and the next lower energy levels of rare earth ions Pr^{3+}, Dy^{3+} and Ho^{3+}, efficient 1.3μm emission can only be obtained in low phonon energy chloride, sulfide and fluoride glasses. However, these glasses exhibit poor chemical durability and inferior thermal stability. As a result, practical application of 1.3μm emission from these rare earth ions is limited. Fortunately, Nd^{3+} possesses relatively wider energy gap (~5500cm^{-1}) for the $^4F_{3/2}$ emitting level, and even in high phonon energy glass systems it is possible to obtain efficient 1.3μm emission. Thus, practical devices can be obtained using Nd^{3+} ions [2].

In our previous works, high-quality aluminum germanate (NMAG) glasses have been successfully used in making Er^{3+} and Tm^{3+} singly doped ion-exchanged waveguides [3, 4]. In this work Nd^{3+}-doped ion-exchanged NMAG glass waveguide has been prepared and investigated for O-band amplification. Potential combination of the ion-exchanged waveguides and UV-direct writing gratings will give rise to attractive photonic devices such as O-band gain-flatten waveguide amplifiers, 1.3 μm waveguide lasers, and integrated optical waveguide devices and circuits.

II. EXPERIMENTS

Nd_2O_3 doped NMAG glasses were prepared using high-purity chemical powders according to the molar host composition $23Na_2O$-$3MgO$-$22Al_2O_3$-$52GeO_2$-5wt%Nd_2O_3, and the preparation procedure details is described in [3]. Using a Metricon 2010 prism coupler, the refractive indices of the sample were measured to be 1.57758 and 1.56078 at 632.8 and 1536nm wavelengths, respectively. The infrared fluorescence and excitation spectra were recorded using a Jobin Yvon Fluorolog-3 Spectrophotometer with a NIR PMT detector and a commercial CW Xe-lamp source. The emission decay curve was recorded under the same setup with a flash Xe-lamp source. All measurements were carried out at room temperature.

Before preparing ion-exchanged channel waveguides, a 150nm-thick high-quality aluminum film was deposited on the glass surface using an Edwards Auto 306 thermal evaporator, and then 8μm wide windows were opened by wet chemical etching method. The ion-exchange process was performed in pure KNO_3 molten bath at 390 ^oC. After cooling down to room temperature, the aluminum film was removed and the two end-facets of the waveguides were polished for further optical measurements. The near-field mode patterns at 1.3μm were examined using a video camera.

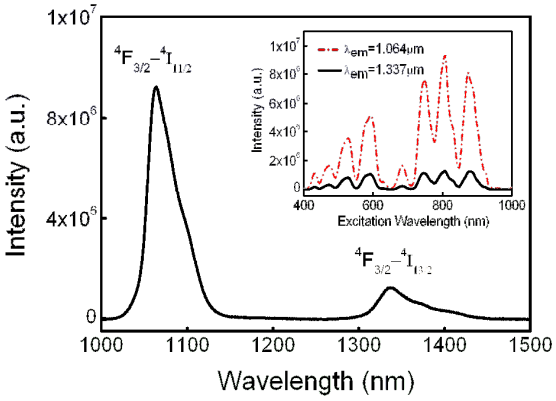


Figure 1. Infrared emission spectra in 5wt% Nd_2O_3 doped NMAG glasses. Inset: Excitation spectra for 1.064 and 1.337 μm emissions

III. DISCUSSION

Figure 1 shows the infrared emissions in the 5wt% Nd_2O_3 doped NMAG glasses under 808nm excitation. The intense 1.064 and 1.337μm emissions can be attributed to the ${}^4F_{3/2} \rightarrow {}^4I_{11/2}$ and ${}^4I_{13/2}$ transitions. The full-width at half-maximum (FWHM) and the lifetime of the 1.337μm emission are ~43nm and 108μs, respectively. The inset shows the excitation spectra of the 1.064 and 1.337μm emissions, and there are eight excitation peaks at 432, 473, 530, 592, 684, 749, 808 and 874nm, respectively.

Thermal K^+–Na^+ ion-exchange process was carried out at 390°C. The refractive index of a slab waveguide as a function of diffusion depth at 632.8nm was derived from the measured mode indices using IWKB method and shown in Figure 2. The surface refractive index is estimated to be 1.5926, and the maximum refractive index change is 0.015. Here, one guided mode at 1536 nm is demonstrated as shown in Figure 2 upper inset, indicating that it is feasible to fabricate single mode waveguide in the wavelength range 1300-1800nm using the ion-exchange process.

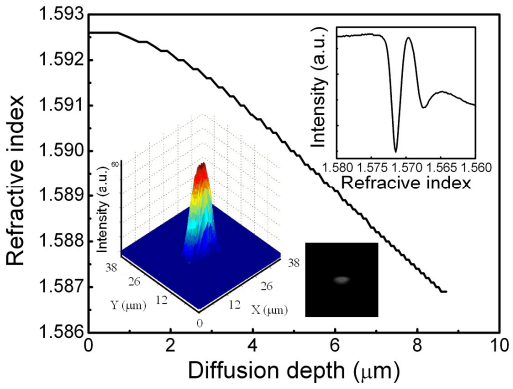


Figure 2. Index profile of a slab waveguide measured at 632.8nm. Upper inset: Prism coupler result measured at 1536nm. Bottom inset: Near-field mode pattern and a 3D representation of the channel waveguide at 1.3μm.

Based on the parameters of slab waveguides, the condition of K^+–Na^+ ion-exchanged process for single mode channel waveguide was selected to be 4h at 390°C. As shown in Figure 2 bottom inset the mode profile confirms that the channel waveguide is single mode at 1.3μm, and the measured mode field diameters were 10.1μm (horizontal, X) and 5.3μm (vertical, Y), respectively, indicating an excellent overlap with those of a standard single-mode fiber. Using cut-back method the loss is ~ 0.36dB/cm at 1.3μm wavelength.

Figure 3 shows the calculated emission cross-sections based upon the Fuchtbauer-Ladenburg formula. The maximum emission cross-sections for the ${}^4F_{3/2} \rightarrow {}^4I_{11/2}$ and ${}^4F_{3/2} \rightarrow {}^4I_{13/2}$ transitions are estimated to be $33.66 \times 10^{-21} cm^2$ and $14.32 \times 10^{-21} cm^2$, respectively. The gain properties of the Nd^{3+} ions can be derived using the emission cross-section parameters. Assuming that the Nd^{3+} ions are partially or totally located at the ${}^4F_{3/2}$ level, the gain $G(\lambda, P)$ can be expressed by the following expression [5]:

$$G(\lambda, P) = 10 \log_{10} \exp(PN\beta\sigma_{em}(\lambda)) \qquad (1)$$

where P is the fractional factor, N is the total dopant concentration, and β is the branching ratio. Figure 3 inset shows the calculated gain spectra of the 1.337 μm emission. The theoretical gain increases as the population density increases. When P reaches 0.8 and 1.0, the signal gains at 1.337μm wavelength are evaluated to be 13dB/cm and 16dB/cm, respectively, indicating that the Nd^{3+}-doped NMAG glass waveguide amplifier is a potential O-band gain medium.

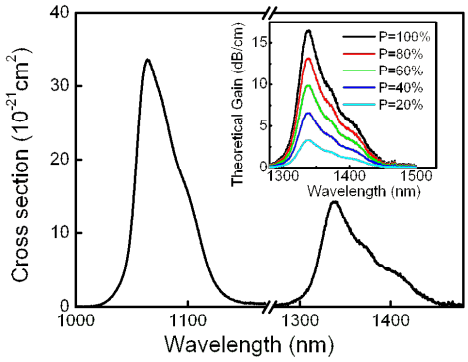


Figure 3. Stimulated emission cross-section profiles for the ${}^4F_{3/2} \rightarrow {}^4I_{11/2}$ and ${}^4F_{3/2} \rightarrow {}^4I_{13/2}$ transitions in 5wt% Nd^{3+} doped NMAG glasses. Inset: Calculated theoretical gain spectra of the ${}^4F_{3/2} \rightarrow {}^4I_{13/2}$ transition.

IV. CONCLUSION

5wt% Nd^{3+} doped NMAG ion-exchanged glass waveguide has been fabricated, and the emission spectra were investigated. Single mode waveguide at 1.3μm was prepared, and the mode field diameters and losses were measured. The maximum theoretical gain at 1.337μm wavelength is calculated to be ~16dB/cm. The results indicate that the Nd^{3+}-doped NMAG glass ion-exchanged waveguide amplifier has potential applications as O-band optical amplifier and laser.

V. ACKNOWLEDGMENT

This work is supported by a City University of Hong Kong Strategic Grant No. 7008099.

VI. REFERENCES

[1] A. Jha, P. Joshi, S. Shen, and L. Huang, "Spectroscopic characterization of signal gain and pump ESA in short-lengths of RE-doped tellurite fibers," J. Non-Cryst. Solids, vol. 353, pp. 1407-1413, March 2007.

[2] B. Karthikeyan, R. Philip, and S. Mohan, "Optical and non-linear optical properties of Nd^{3+}-doped heavy borate glasses," Opt. Commun. vol. 246, pp.153-162, February 2005.

[3] D. L. Yang, E. Y. B. Pun, B. J. Chen, and H. Lin, "Radiative transitions and optical gains in Er^{3+}/Yb^{3+} codoped acid-resistant ion exchanged germanate glass channel waveguides," J. Opt. Soc. Am. B, vol. 26, pp. 357-362, February 2009.

[4] D. L. Yang, E. Y. B. Pun, and H. Lin, "Tm^{3+}-doped ion exchanged germanate glass channel waveguides for *S*-band amplification,"Appl. Phy. Lett., vol 95, pp.151106, October 2009.

[5] Z. Jiang, J. Yang, and S. Dai, "Optical spectroscopy and gian properties of Nd^{3+}-doped oxide glasses," J. Opt. Soc. Am. B, vol. 21, pp. 739-743, Apirl 2004.

Reliability of grating couplers incorporated on integrated interferometric biosensors

D. Duval, S. Dante, L.M. Lechuga
Nanobiosensors and Bioanalytical Applications Group
CIN2 (CSIC) and CIBER-BBN
Campus UAB, Barcelona, Spain
daphne.duval@cin2.es

J. Osmond
Institute of Photonic Sciences
ICFO
Castelldefels, Barcelona, Spain

C. Domínguez
Microelectronics National Center
IMB-CNM (CSIC)
Campus UAB, Barcelona, Spain

***Abstract*—Sub-micronic grating couplers have been integrated on optical waveguides for efficient light in-coupling into interferometric biosensors. Design and fabrication processes are presented as well as the results of the optical characterization and the sensing evaluation.**

Keywords-Grating couplers; interferometers; biosensors; integrated optics.

I. INTRODUCTION

Among the different existing biosensing technologies photonic sensors based on integrated optics (IO) have emerged as one of the most promising candidates for lab-on-a-chip (LOC) platforms due to their high sensitivity, miniaturized size, multiplexed format for array implementation and CMOS compatible fabrication processes. However, the way to couple light into the photonic chip is still a critical aspect for the implementation of a complete LOC platform. Common coupling techniques are based on end-fire method, prism coupling and grating assisted coupling. The two first methods are commonly used in laboratory environment as they are quite versatile and efficient. However, they usually require bulky equipments and critical alignment, making them inconvenient for LOC applications. On the contrary, grating couplers appear to be the most suitable solution as they provide better integration, better alignment tolerance and do not require polishing steps.

Diffraction gratings are fundamental building blocks for integrated optical devices. They have been extensively studied over the last decades and a solid platform for their modeling and fabrication has been built. Nevertheless, up to now very few publications have demonstrated biosensing capabilities of IO sensors incorporating grating couplers.

Taking into account the above considerations, we are seeking to develop highly sensitive IO biosensors incorporating grating couplers with a view to implement a complete LOC platform. Two sensor configurations are employed: the Mach-Zehnder interferometer (MZI) and the bimodal waveguide interferometer (BiMW) which have both demonstrated their capacities for highly sensitive and label-free biosensing [1,2]. In the following, we will show our last results regarding the fabrication and evaluation of the grating couplers for efficient light in-coupling into the interferometric sensors.

II. DEVICE DESIGN AND FABRICATION

In the integrated MZI, a first Y-junction splits the guided light into two arms, the sensing and the reference arms. After a certain distance, the two signals are recombined into an output waveguide via a second Y-junction, producing the interference of both beams. In the BiMW interferometer, two guided modes of the same polarization interfere in a single channel waveguide: TE polarized light is coupled into a waveguide that supports a single transversal mode TE_{00} and, after a certain distance, the guided beam reaches a modal splitter that splits the first guided mode in two transversal modes, the fundamental TE_{00} and the first order TE_{10} modes [2]. Both interferometric devices are formed by Si_3N_4 rib waveguides, enabling precise control of light path and modal behavior. To maximize the sensor sensitivity and to ensure lateral single-mode behavior, the rib height has to be below 2 nm for a waveguide width of 3 μm. For biosensing applications, the protective cladding is removed from a portion of the interferometers, the sensing area, where the evanescent field can probe the external medium.

Due to the dimensions of the interferometers and to the operating wavelength (600-700 nm), the diffractive grating length does not exceed 100 μm with a sub-micronic period. In order to optimize the coupling efficiency, the gratings are designed on wide waveguides (from 20 to 100 μm) which will be then reduced to 3 μm by a width-tapered waveguide. The resonant coupling between the guided mode and the grating is obtained when the following phase matching condition is verified,

$$\sin\theta = n_{eff} + m\frac{\lambda}{\Lambda} \qquad (1)$$

with θ the incidence angle, n_{eff} the effective refractive index of the guided mode, m the diffraction order (here m = -1), λ the wavelength (600-700 nm) and Λ the grating period. The effective index depends on the material and of the dimensions of the waveguide. It has been calculated for each structure under evaluation by the effective index method.

Equation (1) was used to design gratings with incidence angles ranging from 5º to 15º. This range of angles enables an efficient coupling but, above all, it is an important requirement for the implementation of a complete LOC platform where the different units have to be integrated all together in a minimum of space and without disturbing each other. Taking into account

these considerations, the grating period Λ was set to 400 nm for the MZI and to 450 nm for the BiMW. To maximize the coupling, efficiency the grating profile should have a rectangular shape with a duty cycle of 0.5 and depth around 50 nm for both types of devices.

The interferometers were fabricated using standard silicon technologies. The silicon nitride waveguide layer (n_{Si3N4} = 2.00 at 633 nm, thickness between 75 and 350 nm depending on the device) is deposited using LPCVD technique and the rib structure is defined by photolithography and wet etching. The top cladding, a silicon dioxide layer (n_{SiO2} = 1.48 at 633 nm, 2 μm), is then deposited by PECVD. The final wet etching step defines the sensing areas (15 x 0.05 mm^2) and the 2 mm-long grating windows. The gratings are then directly written onto the Si_3N_4 input waveguide by electron beam lithography and reactive ion etching. The gratings have a length of 100 μm and a width equal to the one of the taper (20 to 100 μm).

III. Optical Characterization

To measure the coupling efficiency of the gratings, a light beam from an HeNe laser (λ = 632.8 nm, 5 mW) is coupled into the chip mounted on a rotation stage by focusing the beam on the grating with a lens of 50 mm focal distance. The coupled light propagates in the waveguide until the edge of the chip where it is collected by an objective (x40 and NA=0.65) and monitored by a photodiode connected to a current amplifier. We define the coupling efficiency as $\eta = I_g / I_0$, with I_g the intensity at the output and I_0 the incident intensity. This expression is valid as long as propagation losses are negligible, which is the case with Si_3N_4 rib waveguides. Fig. 1 shows the coupling efficiency measured as a function of the incident angle for a grating with a period of 400 nm written on a MZI device (width taper: 20 μm). The resonant coupling is obtained at 9º35' for the TE_{00} mode (η = 6.4%) and at 1º15' for the TM_{00} mode (η = 2.1%). The coupling efficiency for the TE_{00} mode is quite satisfactory but a more exhaustive development is currently being done to improve it. For example, we have already achieved an efficiency of 12% for the coupling of the TM_0 mode in a planar waveguide.

Moreover, a quite large angle tolerance of about 1º at - 3dB has been measured. This is an important parameter when dealing with portable LOC platform.

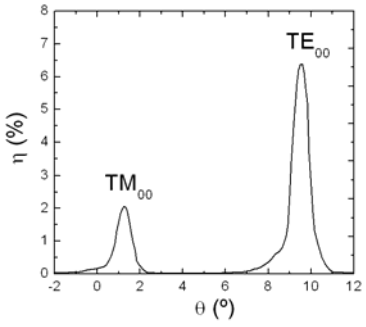


Figure 2. Coupling efficiency at 632.8 nm as a function of the incident angle for a grating (Λ = 400 nm) incorporated on a integrated MZI.

IV. Sensing Evaluation

The sensitivity of the integrated interferometers incorporating grating couplers is evaluated by measuring the phase changes Δφ induced by refractive index variations Δ*n* in the sensing area. A microfluidic header made of PDMS and PMMA is used to control the liquid flow. To achieve truly portable LOC platform, cheap and easily integrated laser diodes are now used. A fiber pigtailed laser diode (λ = 658 nm, 2 mW, TE polarization) is placed above the chip and finely positioned at the excitation angle to reach the coupling.

Fig. 2 shows a calibration curve of a BiMW sensor obtained with a set of solutions of HCl (indices ranging from 1.3332 to 1.3376). Light coupling was achieved via a 450 nm-period grating on (width taper: 20 μm). The inset shows the response of the system to an injection of a solution of HCl 0.2 M with milli-Q water as running buffer ($\Delta n = 1.9 \cdot 10^{-3}$). With these results, a detection limit of $5.9 \cdot 10^{-7}$ in refractive index unit has been achieved.

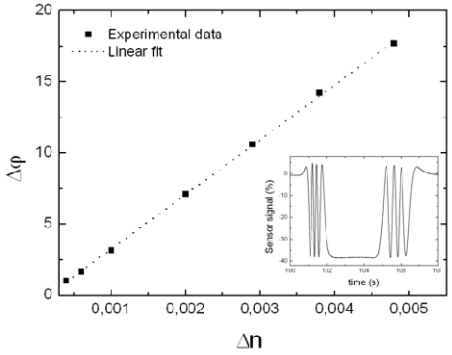


Figure 1. Calibration curve obtained with a BiMW excited via a grating coupler (Λ = 450 nm, TE polarization, 658 nm, θ = 9º50'). Inset: BiMW response to the injection of a solution of HCl 0.2 M.

The detection limit of our system (gratings incorporated in integrated interferometric sensor), obtained with a cheap and easily integrated laser diode, is comparable to the one demonstrated in our previous study using HeNe laser and end-fire method [2]. This strongly supports the adoption of the grating coupler method for the achievement of a truly portable and sensitive LOC platform. Work is in progress to evaluate the surface sensing limit of detection through an immunoassay test.

Acknowledgment

Authors acknowledge financial support from M. Botin foundation. S. Dante acknowledges the "Programa de Formación de Profesorado Universitario (FPU)" of the "Ministerio de Educación" of Spain for financial support.

References

[1] B. Sepulveda *et al.*, "Optical biosensor microsystems based on the integration of highly sensitive Mach-Zehnder interferometer devices", J. Opt. A-Pure Appl. Op., 2006, vol. 8, pp. S561-S566.

[2] K. E. Zinoviev, A. B. González-Guerrero, C. Domínguez and L. M. Lechuga, "Integrated Bimodal Waveguide Interferometric Biosensor for Label-Free Analysis", J. Lightwave Technol., 2011, vol. 29(13), pp. 1926-1930

Optimized 20 Gbps DPSK demodulator in 220nm SOI

M. Aamer, A. Brimont, A.M. Gutierrez, A. Griol, J. Martí, P. Sanchis
Nanophotonics Technology Center, Universitat Politècnica de València, Camino de Vera s/n, 46022
Valencia, Spain
maaa@ntc.upv.es

A. Håkansson
DAS Photonics, Universidad Politécnica Valencia, Camino de Vera s/n, 46022
Valencia, Spain
ahakanson@dasphotonics.com

***Abstract*—We present an optimized 20G-DPSK receiver fabricated in 220nm SOI technology using an unbalanced Mach-Zehnder interferometer in sequence with a Mach-Zehnder delay interferometer. Error-free operation was demonstrated for Duobinary(DB) and Alternating Mark Inversion(AMI) demodulated signals.**

Keywords-Demodulation, differential phase-shift keying (DPSK), silicon-on-insulator (SOI).

I. INTRODUCTION

While PSK requires active coherent detection using a LO, the beauty of DPSK is that it can be directly demodulated using a passive delay-interferometer; Two adjacent bits are superposed and the superposed signal is photo detected. This makes direct photo detection possible, after the demodulator circuit.

Silicon On Insulator (SOI) photonics is an interesting technology for implementing DPSK modulation format [1]. The small bending radius of about 5 microns of the integrated SOI waveguide will allow a very small footprint of the delay-interferometer specifically for lower symbol-rates since the length of the delay line is on the order of cm.

II. DESIGN AND FABRICATION

In order to convert the information in the differential phase change and to recover the binary information a demodulation circuit is implemented using a Mach-Zehnder delay interferometer (MZDI) [2] where one bit is delayed in one arm and then superposed with its adjacent bit at the output.

The proposed structure is depicted in Figure 1 including a MZI switch in series with the 20Gbps MZDI demodulator. The unbalanced MZI works as a switch and by either tuning the wavelength or by heating one of the arms using an integrated micro heater, we can control the input power to the MZDI to reduce the power unbalance between arms of the MZI due to propagation losses and hence, the sensitivity of the receiver can be actively maximized.

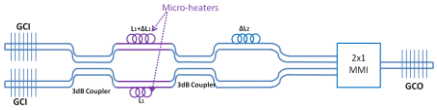


Figure 1: Block Diagram of the proposed DPSK demodulator

Figure 2 shows the simulated spectral response of the whole structure using the transfer matrix method [3]. In the simulation the 1-bit DL was set to fit a 20Gbps symbol rate, the path difference for the MZI switch to 50um and a waveguide propagation loss of 10dB per cm. To reflect the behavior of the MZI switch, the figure includes the input power to each arm of the MZDI, where the green curve is the power penalty at the input of the delay-line arm of the MZDI and the red curve for the opposite arm. It is interesting to note that when the switch is at its extreme (0:1 or 1:0) there is no resonances as expected, and the different total losses correspond to the different losses in the two arms of the MZDI.

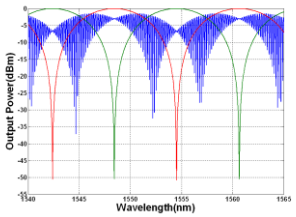


Figure 2 Simulated spectral response at the MZDI inputs (green, red) and at the demodulator output (blue).

The structure was fabricated on SOI wafer with silicon core thickness of 220 nm and buried oxide (BOX) of 2 µm, and covered by a 1µm-thick silica overcladding. The fabrication process was carried out by using electron beam lithography (EBL) and dry etching by using inductively coupled plasma (ICP) system. Plasma enhanced chemical vapor deposition (PECVD) was also used, to grow the overcladding silica layer. The figure below shows scanning electron microscope (SEM) images of the fabricated structure before metal deposition.

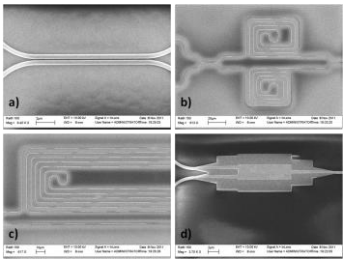


Figure 3: SEM images of a) 3dB Coupler, b) MZI with ΔL1=50µm, c) MZDI, d) 2x1 MMI

III. EXPERIMENTAL RESULTS

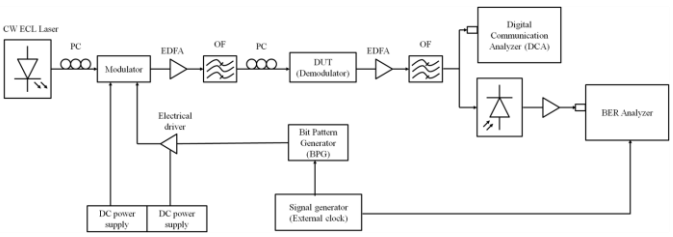


Figure 4: Block diagram of the experimental DPSK demodulation setup

Figure 4 shows the experimental DPSK demodulation setup. Continuous-wave light was generated by an External Cavity Laser (ECL) and was first spanned over the full operational wavelength bandwidth, from 1545nm to 1565nm. Figure 5 shows the obtained experimental spectrum including the optimized performances at 1548.4nm. The optical data stream was generated using a X-cut Lithium Niobate modulator, with the bits generated from a pseudorandom binary sequence pattern generator (PRBS) with a pattern length of 231-1 at 20-Gb/s bit-rate, delivered by a bit pattern generator (SHF BPG 44E) connected to an external clock. The modulated signal is then amplified by an erbium-doped fiber amplifier (EDFA), filtered by 1nm BPF and fiber coupled in and out of our device. The demodulated signal was amplified and filtered again, before being photo-detected by a Digital Communication Analyzer (Infinium DCA-J 86100C), and simultaneously examined on a Bit-Error-Rate Analyzer (SHF EA 44).

The measured spectral response of the 20Gb/s-DPSK demodulator is depicted in Fig 5.

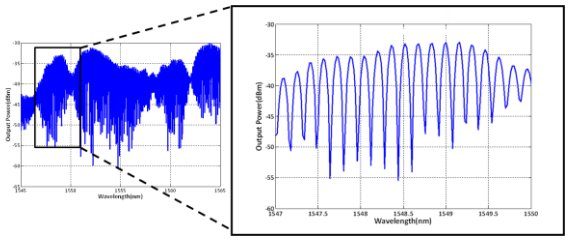


Figure 5: Measured spectral response at the DPSK demodulator. Inset: zoom in resonance of interest.

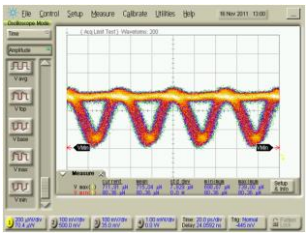


Figure 6: Eye diagram of the 20Gb/s-NRZ-DPSK input signal

Figure 6 shows the eye diagram of the 20Gb/s-NRZ-DPSK input signal while figure 7 shows the obtained eye diagrams of the demodulated AMI (7.a) and DB (7.b) signals.

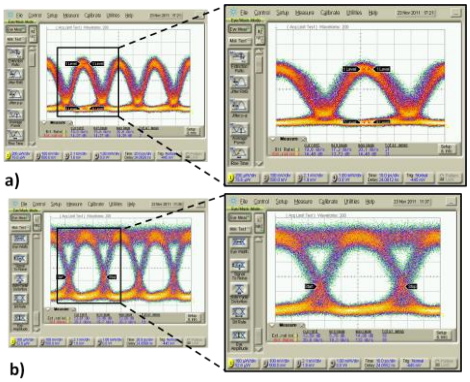


Figure 7: Eye diagram of the 20Gb/s-NRZ-DPSK for a) AMI and b) DB demodulated signals.

The measured extinction ratios, at a bit rate of 20Gb/s, are 14.7dB and 13.59 dB for AMI and DB demodulated signals, respectively. Error-free operation was achieved, and the measured bit-error-rate curves are plotted below.

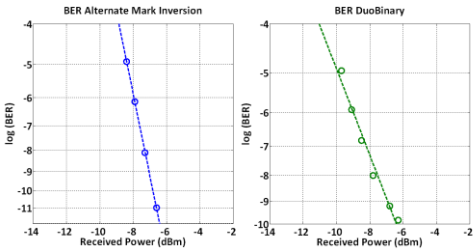


Figure 8: BER curves for based DPSK demodulation at 20 Gb/s operation for a) AMI and b) DB demodulated signals.

IV. CONCLUSION

We demonstrated an optimized design for 20G-DPSK receiver based on a 220 nm SOI unbalanced MZI in series with MZDI. Measured ERs are 14.7dB and 13.59 dB for AMI and DB demodulated signals, respectively and error-free operation was achieved. In the future, active performance will be carried out by heating one of the arms using an integrated micro heater.

ACKNOWLEDGMENT

Financial support from HELIOS (Photonics Electronics Functional Integration on CMOS) FP7-224312 and Generalitat Valenciana under PROMETEO-2010-087 R&D Excellency Program (NANOMET) are acknowledged. We thank J. Herrera for help and support.

REFERENCES

[1] C. Doerr and L. Chen, "Monolithic PDM-DQPSK receiver in silicon," ECOC, pp. 1–3, 2010.

[2] G. Ducournau, M. Grisel, M. Kétata, "Study of DPSK demodulation with all-fiber MZI structure", SCI 2004, Orlando, Florida. SCI 2004 proceedings, ISBN 980-6560-13-2, pp. 87-92.

[3] J.Poon, J.Scheuer, S.Mookherjea, G.Paloczi, Y.Huang, and A.Yariv,"Matrix analysis of microring coupled-resonator optical waveguides", Optics Express, 12, pp90-103 (2004).

Design of a Frequency Modulation - Direct Detection Microwave Photonic Link receiver monolithically integrated in InP generic technology

J. S. Fandiño, P. Muñoz and J. Capmany
Optical and Quantum Communications Group.
ITEAM Research Institute.
Universitat Politècnica de València, Camino de Vera s/n, 46020 Valencia (Spain).
E-mail: jasanfan@upvnet.upv.es

***Abstract*—The steps followed in the design of an InP photonic integrated circuit (PIC) working as a discriminating receiver for Frequency Modulation-Direct Detection (FM-DD) Microwave Photonic links (MPL) are presented, including filter synthesis values.**

I. Introduction

Because of its high bandwidth and long reach, microwave photonic links (MPL) are expected to play an important role in many telecommunication applications, including radio-over-fiber and antenna distribution systems. Even though traditional IM-DD-based MPL have already reached the commercial stage, it is well-known that nonlinearities arising from the modulator transfer function, along with shot and RIN noise produced by the detected optical carrier, put a limit to the maximum attainable spurious-free dynamic range (SFDR) . In order to mitigate these impairments, several techniques have been proposed in recent years, such as adaptative biasing of the modulator and direct optical filtering. More recently, ideal class-B operation has been devised and theoretically shown to allow for significant improvement in dynamic range [1]. Frequency modulation and optical filters acting as frequency discriminators, together with direct detection (FM-DD), have been explored as means to effectively achieve the desired intensity transfer function. Several experimental demonstrations have also been reported so far, including specially designed FBGs [2], ring-assisted fiber Sagnac filters [3], as well as photonic integrated circuits (PIC) using multiple ring resonator [4] and cascaded MZIs [5].

II. Filter synthesis and design

The structure of the device, which includes a tunable optical filter acting as a frequency discriminator and a high speed balanced photodetector integrated in the same chip, can be seen in Fig. 1. A pass-band input filter splits up the spectrum of the FM signal into its upper and lower sidebands, while reducing the power of the optical carrier. Each one of its complementary outputs is fed to another structure (Filter 1 & Filter 2) acting as a frequency discriminator, which modifies the amplitude of sideband harmonics and reduces even more the carrier power. Finally, both signals are detected in a balanced configuration.

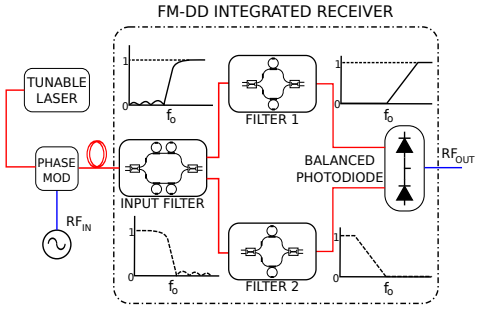


Fig. 1: Block diagram of the device. Optical power transfer functions at the output of each filter are shown.

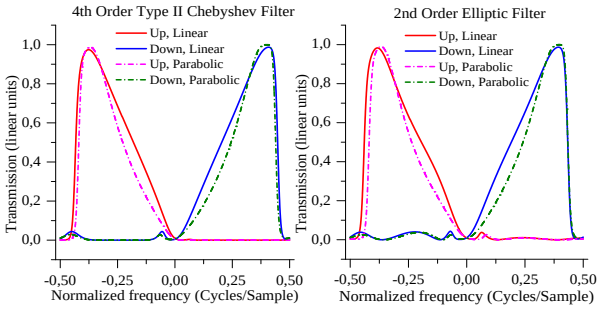


Fig. 2: Simulated transfer function of each input filter (Chebyshev & Elliptic), when combined with two different frequency discriminators (Linear & Parabolic).

All the aforementioned filters were chosen to be implemented by means of integrated ring-loaded Mach-Zehnder interferometers, where the power coupling constants (κ) and relative phases of each ring (ϕ) and each MZI (β) are designed so as to achieve the desired intensity transfer function. Since the response of this structure is intrinsically periodic, powerful digital IIR filter synthesis techniques can be exploited [6]. In principle, any transfer function can be sufficiently approximated if the order is high enough, at the expense of a higher sensitivity to manufacturing defects. Hence, two different designs which differ in the type and order of the

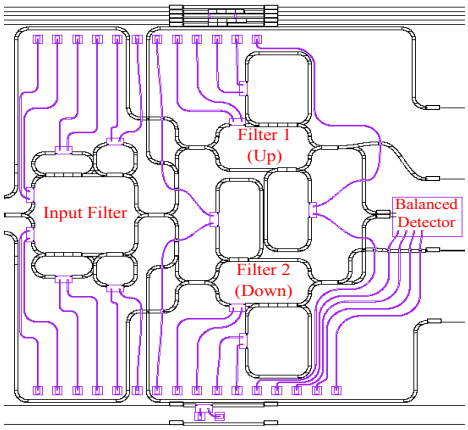


Fig. 3: Chip layout for the Chebyshev design.

input filter were submitted to fabrication: a second-order (N=2) elliptic filter and a fourth-order (N=4) type II Chebyshev filter. Synthesis values $\{(\kappa_i, \phi_i \text{ for } i = 1 \ldots N), (\beta)\}$ are: Chebyshev Type II = {(0.5,1.376)(0.95,-1.351)(0.5,-1.376)(0.95,1.351),(-4.97)}; Elliptic = {(0.72,-1.374)(0.72,1.374),(1.236)}.

In the literature, two main approaches can be found for the design of the discriminator, where variation of the optical intensity response is either linear or parabolic. While the former performs good in terms of harmonic distortion for large modulation index [2], the latter is intrinsically distortion free provided all the sidebands fall within the bandwidth of the filter [7]. In order to achieve both types of response, Filter 1 and Filter 2 were firstly chosen to be second-order (N=2) filters acting as linear frequency discriminators (i.e. they present an optical intensity transmission ramp which scales linearly with frequency). Synthesis values from [6] were employed. These values are: {(0.91,0.009)(0.38,-0.01),(1.589)}. The FSR of the structures is estimated to be around 47 GHz for the elliptic filter design, and 46 GHz for the Chebyshev filter. Combined responses (pass-band plus linear frequency discrimination) are shown in Fig. 2.

Secondly, silicon nitride thermo-optic heaters were laid out, so as to enable fine tuning of the optical phases. This allows to dynamically change the overall response of the device. Assuming fixed coupling constants, an optimization routine was run in order to find those phases which best approximated a parabolic response. Synthesis values are: Parabolic (Up) = {(0.91,0.031)(0.38,-0.366),(0.994)}; Parabolic (Down) = {(0.91,-0.113)(0.38,0.337),(2.177)}. Combined responses (pass-band plus parabolic frequency discrimination) are shown in Fig. 2.

III. Technology and Layout

A section of the layout can be seen in Fig. 3, which shows the device using a Chebyshev type II filter at its input. InP generic process technology developed under EuroPIC EU FP7 project was employed to design and manufacture the chip. Die chip area (6x6 mm^2) limitations lead to the use of deeply etched (1.7 μm) rib waveguides, enabling sharp bends (150 μm), with an InGaAsP core (n = 3.258 @ λ = 1.55 μm, height = 1 μm, width = 2 μm) over an InP substrate (n = 3.169 @ λ = 1.55 μm). Accordingly to design values, a suitable structure to implement 2x2 optical couplers with arbitrary splitting ratios needs to be chosen. Strong confinement of the mode in the deeply etched waveguide does not allow using directional couplers, owing the aforementioned die size limit. Instead, butterfly MMI couplers were used. All couplers were designed using the approximate analytical expressions provided in [8], and then optimized by means of BPM numerical simulations. MMI sections were designed to be 12 μm wide. Tapered transitions to shallow etch (0.2 μm) waveguides were performed in different areas, in order to maximize input/output coupling. Several metal pads (50x100 μm^2) with gold metallization (Fig. 3, magenta lines) allow to supply current to multiple SiN thermo-optic heaters, as well as to the 50 GHz 3dB bandwidth balanced photodiode. Unused inputs/outputs from the MZI 2x2 couplers were routed to left/right chip facets, in order to provide individual characterization and testing of each filter.

IV. Conclusions and Further Work

The steps followed in the design of a photonic integrated circuit acting as a MPL FM-DD receiver have been described. Further work will include a complete experimental characterization of the filters, in order to contrast design targets with real measurements, assessing the quality and reliability of the design and manufacturing process. Experimental work will also be conducted in order to contrast other studies about FM-DD receivers, so as to further understand their performance and practical limitations.

Acknowledgements

The authors acknowledge financial support from Spanish MICINN Project TEC2010-21337, acronym ATOMIC. J.S. Fandiño acknowledges financial support through grant FPU-2010 (ref: AP2010-1595). The authors are also grateful to the EuroPIC consortium (FP7 funded programme NMP 228839-2) for access to the design manual and design toolkit of the generic InP fab.

References

[1] T. E. Darcie and P. F. Driessen, "Class ab techniques for high-dynamic-range microwave-photonic links," vol. 18, no. 8, pp. 929–931, 2006.

[2] T. E. Darcie, J. Zhang, P. F. Driessen, and J.-J. Eun, "Class b microwave-photonic link using optical frequency modulation and linear frequency discriminators," vol. 25, no. 1, pp. 157–164, 2007.

[3] G. Chen, J. U. Kang, and J. B. Khurgin, "Frequency discriminator based on ring-assisted fiber sagnac filter," vol. 17, no. 1, pp. 109–111, 2005.

[4] D. Marpaung, C. Roeloffzen, A. Leinse, and M. Hoekman, "A photonic chip based frequency discriminator for a high performance microwave photonic link," *Opt. Express*, vol. 18, pp. 27359–27370, Dec 2010.

[5] J. M. Wyrwas et al., "Dynamic linearity improvement of phase and frequency modulated microwave photonic links using optical lattice filter discriminators," in *Proc. MWP/APMP, Asia-Pacific*, pp. 41–44, 2011.

[6] C. K. Madsen and J. H. Zhao, *Optical Filter Design and Analysis*. John Wiley & Sons, Inc., 1999.

[7] J. M. Wyrwas and M. C. Wu, "Dynamic range of frequency modulated direct-detection analog fiber optic links," vol. 27, no. 24, pp. 5552–5562, 2009.

[8] P. A. Besse, E. Gini, M. Bachmann, and H. Melchior, "New 2x2 and 1x3 multimode interference couplers with free selection of power splitting ratios," vol. 14, no. 10, pp. 2286–2293, 1996.

Design of a Frequency Modulation - Direct Detection Microwave Photonic Link receiver monolithically integrated in InP generic technology

J. S. Fandiño, P. Muñoz and J. Capmany
Optical and Quantum Communications Group.
ITEAM Research Institute.
Universitat Politècnica de València, Camino de Vera s/n, 46020 Valencia (Spain).
E-mail: jasanfan@upvnet.upv.es

***Abstract*—The steps followed in the design of an InP photonic integrated circuit (PIC) working as a discriminating receiver for Frequency Modulation-Direct Detection (FM-DD) Microwave Photonic links (MPL) are presented, including filter synthesis values.**

I. Introduction

Because of its high bandwidth and long reach, microwave photonic links (MPL) are expected to play an important role in many telecommunication applications, including radio-over-fiber and antenna distribution systems. Even though traditional IM-DD-based MPL have already reached the commercial stage, it is well-known that nonlinearities arising from the modulator transfer function, along with shot and RIN noise produced by the detected optical carrier, put a limit to the maximum attainable spurious-free dynamic range (SFDR) . In order to mitigate these impairments, several techniques have been proposed in recent years, such as adaptative biasing of the modulator and direct optical filtering. More recently, ideal class-B operation has been devised and theoretically shown to allow for significant improvement in dynamic range [1]. Frequency modulation and optical filters acting as frequency discriminators, together with direct detection (FM-DD), have been explored as means to effectively achieve the desired intensity transfer function. Several experimental demonstrations have also been reported so far, including specially designed FBGs [2], ring-assisted fiber Sagnac filters [3], as well as photonic integrated circuits (PIC) using multiple ring resonator [4] and cascaded MZIs [5].

II. Filter synthesis and design

The structure of the device, which includes a tunable optical filter acting as a frequency discriminator and a high speed balanced photodetector integrated in the same chip, can be seen in Fig. 1. A pass-band input filter splits up the spectrum of the FM signal into its upper and lower sidebands, while reducing the power of the optical carrier. Each one of its complementary outputs is fed to another structure (Filter 1 & Filter 2) acting as a frequency discriminator, which modifies the amplitude of sideband harmonics and reduces even more the carrier power. Finally, both signals are detected in a balanced configuration.

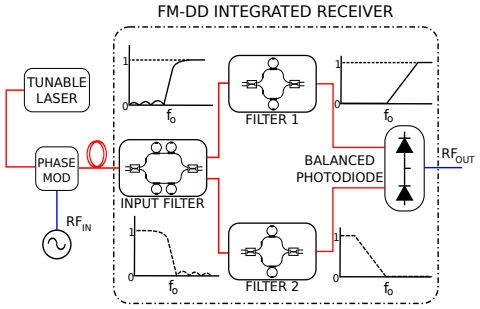


Fig. 1: Block diagram of the device. Optical power transfer functions at the output of each filter are shown.

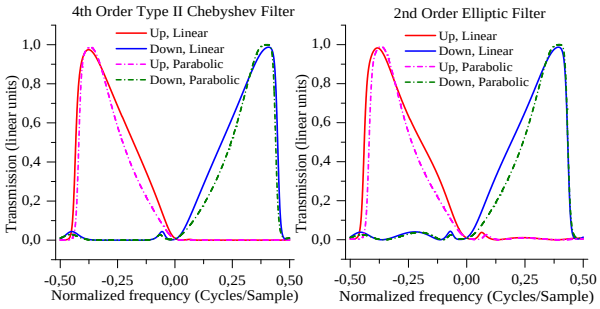


Fig. 2: Simulated transfer function of each input filter (Chebyshev & Elliptic), when combined with two different frequency discriminators (Linear & Parabolic).

All the aforementioned filters were chosen to be implemented by means of integrated ring-loaded Mach-Zehnder interferometers, where the power coupling constants (κ) and relative phases of each ring (ϕ) and each MZI (β) are designed so as to achieve the desired intensity transfer function. Since the response of this structure is intrinsically periodic, powerful digital IIR filter synthesis techniques can be exploited [6]. In principle, any transfer function can be sufficiently approximated if the order is high enough, at the expense of a higher sensitivity to manufacturing defects. Hence, two different designs which differ in the type and order of the

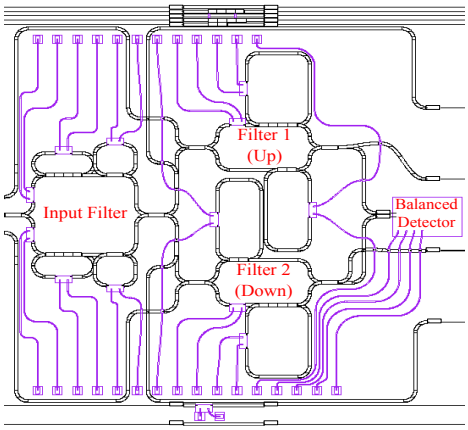


Fig. 3: Chip layout for the Chebyshev design.

input filter were submitted to fabrication: a second-order (N=2) elliptic filter and a fourth-order (N=4) type II Chebyshev filter. Synthesis values $\{(\kappa_i, \phi_i \text{ for } i = 1 \ldots N), (\beta)\}$ are: Chebyshev Type II = {(0.5,1.376)(0.95,-1.351)(0.5,-1.376)(0.95,1.351),(-4.97)}; Elliptic = {(0.72,-1.374)(0.72,1.374),(1.236)}.

In the literature, two main approaches can be found for the design of the discriminator, where variation of the optical intensity response is either linear or parabolic. While the former performs good in terms of harmonic distortion for large modulation index [2], the latter is intrinsically distortion free provided all the sidebands fall within the bandwidth of the filter [7]. In order to achieve both types of response, Filter 1 and Filter 2 were firstly chosen to be second-order (N=2) filters acting as linear frequency discriminators (i.e. they present an optical intensity transmission ramp which scales linearly with frequency). Synthesis values from [6] were employed. These values are: {(0.91,0.009)(0.38,-0.01),(1.589)}. The FSR of the structures is estimated to be around 47 GHz for the elliptic filter design, and 46 GHz for the Chebyshev filter. Combined responses (pass-band plus linear frequency discrimination) are shown in Fig. 2.

Secondly, silicon nitride thermo-optic heaters were laid out, so as to enable fine tuning of the optical phases. This allows to dynamically change the overall response of the device. Assuming fixed coupling constants, an optimization routine was run in order to find those phases which best approximated a parabolic response. Synthesis values are: Parabolic (Up) = {(0.91,0.031)(0.38,-0.366),(0.994)}; Parabolic (Down) = {(0.91,-0.113)(0.38,0.337),(2.177)}. Combined responses (pass-band plus parabolic frequency discrimination) are shown in Fig. 2.

III. Technology and Layout

A section of the layout can be seen in Fig. 3, which shows the device using a Chebyshev type II filter at its input. InP generic process technology developed under EuroPIC EU FP7 project was employed to design and manufacture the chip. Die chip area (6x6 mm^2) limitations lead to the use of deeply etched (1.7 μm) rib waveguides, enabling sharp bends (150 μm), with an InGaAsP core (n = 3.258 @ λ = 1.55 μm, height = 1 μm, width = 2 μm) over an InP substrate (n = 3.169 @ λ = 1.55 μm). Accordingly to design values, a suitable structure to implement 2x2 optical couplers with arbitrary splitting ratios needs to be chosen. Strong confinement of the mode in the deeply etched waveguide does not allow using directional couplers, owing the aforementioned die size limit. Instead, butterfly MMI couplers were used. All couplers were designed using the approximate analytical expressions provided in [8], and then optimized by means of BPM numerical simulations. MMI sections were designed to be 12 μm wide. Tapered transitions to shallow etch (0.2 μm) waveguides were performed in different areas, in order to maximize input/output coupling. Several metal pads (50x100 μm^2) with gold metallization (Fig. 3, magenta lines) allow to supply current to multiple SiN thermo-optic heaters, as well as to the 50 GHz 3dB bandwidth balanced photodiode. Unused inputs/outputs from the MZI 2x2 couplers were routed to left/right chip facets, in order to provide individual characterization and testing of each filter.

IV. Conclusions and Further Work

The steps followed in the design of a photonic integrated circuit acting as a MPL FM-DD receiver have been described. Further work will include a complete experimental characterization of the filters, in order to contrast design targets with real measurements, assessing the quality and reliability of the design and manufacturing process. Experimental work will also be conducted in order to contrast other studies about FM-DD receivers, so as to further understand their performance and practical limitations.

Acknowledgements

The authors acknowledge financial support from Spanish MICINN Project TEC2010-21337, acronym ATOMIC. J.S. Fandiño acknowledges financial support through grant FPU-2010 (ref: AP2010-1595). The authors are also grateful to the EuroPIC consortium (FP7 funded programme NMP 228839-2) for access to the design manual and design toolkit of the generic InP fab.

References

[1] T. E. Darcie and P. F. Driessen, "Class ab techniques for high-dynamic-range microwave-photonic links," vol. 18, no. 8, pp. 929–931, 2006.

[2] T. E. Darcie, J. Zhang, P. F. Driessen, and J.-J. Eun, "Class b microwave-photonic link using optical frequency modulation and linear frequency discriminators," vol. 25, no. 1, pp. 157–164, 2007.

[3] G. Chen, J. U. Kang, and J. B. Khurgin, "Frequency discriminator based on ring-assisted fiber sagnac filter," vol. 17, no. 1, pp. 109–111, 2005.

[4] D. Marpaung, C. Roeloffzen, A. Leinse, and M. Hoekman, "A photonic chip based frequency discriminator for a high performance microwave photonic link," *Opt. Express*, vol. 18, pp. 27359–27370, Dec 2010.

[5] J. M. Wyrwas et al., "Dynamic linearity improvement of phase and frequency modulated microwave photonic links using optical lattice filter discriminators," in *Proc. MWP/APMP, Asia-Pacific*, pp. 41–44, 2011.

[6] C. K. Madsen and J. H. Zhao, *Optical Filter Design and Analysis*. John Wiley & Sons, Inc., 1999.

[7] J. M. Wyrwas and M. C. Wu, "Dynamic range of frequency modulated direct-detection analog fiber optic links," vol. 27, no. 24, pp. 5552–5562, 2009.

[8] P. A. Besse, E. Gini, M. Bachmann, and H. Melchior, "New 2x2 and 1x3 multimode interference couplers with free selection of power splitting ratios," vol. 14, no. 10, pp. 2286–2293, 1996.

High gain fs-laser written Yb^{3+}/Er^{3+}-codoped phosphate glass waveguide

A. Ferrer, J. del Hoyo, A. Ruiz de la Cruz and J. Solis
Laser Processing Group
Instituto de Óptica, CSIC
Madrid, Spain
j.solis@io.cfmac.csic.es

V. Berdejo, J. A. Vallés and M. Á. Rebolledo
Department of Applied Physics and I3A
University of Zaragoza
Zaragoza, Spain
juanval@unizar.es

***Abstract*—In the present work we report a high gain femtosecond-laser directly written waveguide in an Er/Yb co-doped phosphate glass with a maximum internal gain per unit length of 4.1 dB/cm at 1535 nm.**

Keywords- erbium-doped waveguide amplifier; femtosecond laser micromachining; optical waveguides; phosphate glass

I. INTRODUCTION

Femtosecond (fs) laser micromachining of photonic devices inside transparent materials is based on the local structural modification that appears around the focal volume (FV) upon the irradiation. This is a consequence of the nonlinear ionization processes undergoing in this region and the subsequent relaxation mechanisms [1].

The first so fabricated photonic device (waveguide) was demonstrated in 1996, by Davis and coworkers [2]. Since then, several passive devices such as power splitters [3] or directional couplers [4] amongst others have been reported. Active devices such as waveguide based optical amplifiers [5] or lasers [6] have been successfully demonstrated as well. Er:Yb-codoped active devices are of remarkable interest for signal amplification in the C-Band (1530-1565 nm) communications window [7]. In this field of devices, several efforts have been done such as those reported by Della Valle and coworkers [8], where the authors reported a full C-band amplification as well as a peak internal gain per unit length of ~2.5 dB cm^{-1} in a 37 mm-long device. This figure compares well with the 3 dB cm^{-1} value reported previously in state-of-the-art Er:Yb-codoped waveguide amplifiers fabricated by ion exchange in a phosphate glass with similar doping concentrations [9].

The aim of the present work has been to optimize the peak internal gain per unit length, in order to fabricate shorter devices with higher internal gains. In this letter we report a 1.4 cm-long fs-laser directly written waveguide amplifier, fabricated in a custom made phosphate glass in which we have measured a peak internal gain per unit length of 4.1 dB cm^{-1}.

II. EXPERIMENTAL

In order to optimize the Er^{3+} and Yb^{3+} concentrations of the phosphate glass sample, a set of simulations similar to those reported in [10] were performed, using the concentrations as fitting parameters for internal gain per unit length optimization. In this way, the phosphate glass was fabricated following the procedure depicted as well in [10]. During the glass fabrication process, water incorporation in the matrix may occur because of the hygroscopic nature of the reactants used. Because of this phenomenon, the final composition may be slightly different from the calculated on. For this reason, after glass fabrication its composition has been measured by Particle Induced X-Ray spectroscopy. The corresponding measurements are presented in Table I. The optical absorption of the sample was measured with a commercial spectrophotometer, which at 1535 nm reaches a value as high as 1.91 cm^{-1}. Since the sample has a total length of 1.40 cm, this figure corresponds to an absorption loss at 1535 nm of 11.6 dB.

A waveguide has been written in this glass using a setup similar to that presented in [11], using 43 nJ and 370 fs laser pulses at 1036 nm and a repetition rate of 500 kHz. The polarization was set to circular. The irradiation beam was slit-shaped as shown in [12,13] with a 830 µm-width slit, it was focused 100 µm below the surface with a 0.68 NA aspheric lens, and the sample was translated perpendicularly to the incident beam at 60 µm/s. In Fig. 1, the so-written waveguide is presented as seen by a white light transmission microscope (Fig. 1a) as well as its guided mode at 1550 nm (Fig. 1b). The waveguide presents propagation losses of ~0.5 dB/cm and coupling losses of ~0.1 dB/facet with respect to the Hi1060 fiber (used to couple light inside), as measured according to [13]. The guided mode of this coupling fiber is shown in Fig. 1c so as to compare with the waveguide's one (Fig. 1b). The total insertion losses were measured to be 1.27 dB (including

TABLE I. PHOSPHATE GLASS COMPOSITION

Compound	Concentration (molar ± 0.3)	Compound	Concentration (molar ± 0.3)
P_2O_5	68.0	Yb_2O_3	2.6
La_2O_3	12.4	Er_2O_3	1.3
Al_2O_3	10.1	Ce_2O_3	0.9
K_2O	4.8		

Fresnel losses).

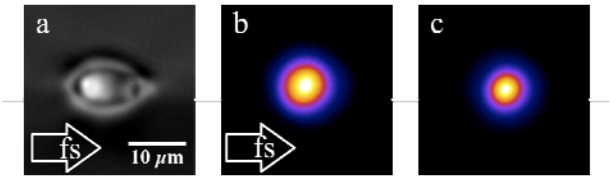


Fig. 1. (a) White light micrograph of the waveguide. (b) 1550 nm guided mode of the waveguide. (c) 1550 nm guided mode of the Hi1060 fiber.

The waveguide was then implemented in an optical amplifier, bi-directionally pumped at 976 nm, as the one described in [10]. The co-propagating pump power was set to its maximum value (366 mW), while the counter-propagating one was systematically increased.

III. Results and Discussion

The curve of the relative gain of the small signal (1535 nm) as a function of the counter-propagating pump power is shown in Fig. 2 (bottom). Before every relative gain measurement, both pumps were set to zero and the signal attenuation was measured as a reference of the stability of the system (red line with circles in Fig. 2).

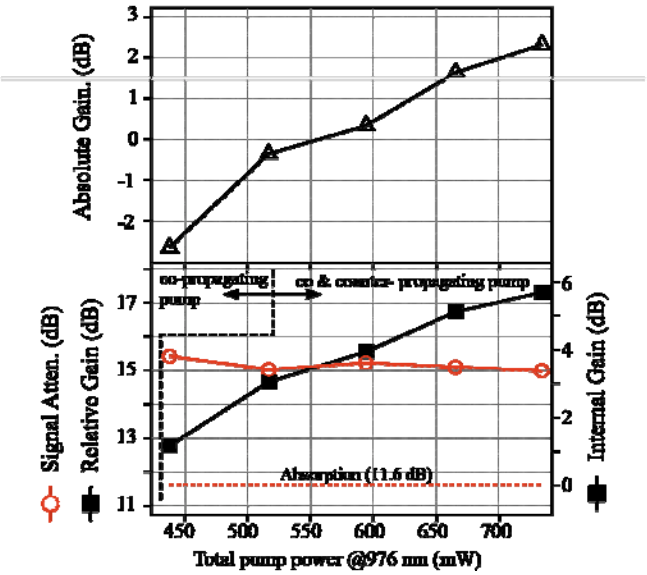


Fig. 2. Signal attenuation (red curve, circles) at 1535 nm, relative gain (black line, squares, left), internal gain (black line, squares, right) and absolute gain (black line, triangles) of the waveguide amplifier fabricated in a Er:Yb-codoped phosphate glass.

The internal gain of the amplifier (Fig. 2) was obtained by subtracting the 11.6 dB of the sample absorption at the signal wavelength, resulting in a maximum value of 5.7 dB. For the 1.4 cm-length amplifier, this figure results in a relative gain per unit length of 4.1 dB/cm, which is one of the highest reported so far. By further subtracting the signal attenuation to the relative gain curve, one may get the absolute gain curve (Fig. 2, top). This amplifier presents a maximum absolute gain of 2.3 dB for a total pump power of 734 mW. These results state the excellent active properties of the glass for the fabrication of compact integrated optical amplifiers in the communications window.

Acknowledgment

This work has been partially supported by the Spanish Ministry of Economy and Competitiveness under FIS2010-20821 and TEC2011-22422 projects and by the D. G. A. A.R. acknowledges a I3P-CSIC postdoctoral contract (co-funded by the ESF). A.F. acknowledges a grant under Project TEC 2006-04538. J. del Hoyo acknowledges a CSIC JAE-Predoc fellowship (co-funded by the EST).

References

[1] S.S. Mao, F. Quéré, S. Guizard, X. Mao, R. E. Russo, G. petite and P. Martin, “Dynamics of femtosecond laser interactions with dielectrics,” *Appl. Phys. A-Mater*, vol. 79, pp. 1695-1709, Jun. 2004.

[2] K. M. Davis, K. Miura, N. Sugimoto and K. Hirao, “Writing waveguides in glass with a femtosecond laser,” *Opt. Lett.*, vol. 21, pp. 1729-1731, Nov. 1996.

[3] D.. Homoelle, S. Wielandy, A. L. Gaeta, N. F. Borrelli and C. Smith, “Infrared photosensitivity in silica glasses exposed to femtosecond laser pulses,” *Opt. Lett.* vol. 24, pp. 1311-1313, Sept. 1999.

[4] A. M. Streltsov and N. F. Borrelli, “Fabrication and analysis of a directional coupler written in glass by nanojoule femtosecond laser pulses,” *Opt. Lett.* vol. 26, pp. 42-43, Jan. 2001.

[5] Y. Sikorski, A. A. Said, P. Bado, R. Maynard, C. Florea and K. A. Winick, “Optical waveguide amplifier in Nd-doped glass written with near-IR femtosecond laser pulses” *Electron. Lett.*, vol. 36, pp. 226-227, Feb. 2000.

[6] S. Taccheo, G. Della Valle, R. Osellame, G. Cerullo, N. Chiodo, P. Laporta, O. Svelto, A. Killi, U. Morgner, M. Lederer and D. Kopf “Er:Yb-doped waveguide laser fabricated by femtosecond laser pulses,” *Opt. Lett.*, vol. 29, pp. 2626-2628, Nov. 2004.

[7] R. Osellame, S. Taccheo, G. Cerullo, M. Marangoni, D. Polli, R. Ramponi, P. Laporta, S.D. Silvestri, “Optical gain in Er-Yb doped waveguides fabricated by femtosecond laser pulses,” *Electron. Lett.*, vol. 38, pp. 964-965, Aug. 2002.

[8] G. Della Valle, R. Osellame, N. Chiodo, S. Taccheo, G. Cerullo, P. Laporta, A. Killi, U. Morgner, M. Lederer and D. Kopf “C-band waveguide amplifier produced by femtosecond laser writing,” *Opt. Express*, vol. 13, pp. 5976-5982, Aug. 2005.

[9] Jaouën, L. du Mouza, D. Barbier, J. Delavaux and P Bruno, “Eight-wavelength Er-Yb doped amplifier: combiner/splitter planar integrated module,” *IEEE Phot. Tech. Lett.*, vol. 11, pp. 1105-1107, Sept. 1999.

[10] J.A. Valles, A Ferrer, J.M. Fernandez-Navarro, V. Berdejo, A.R. de la Cruz, I. Ortega-Feliu, M. Rebolledo and J. Solis, “Performance of ultrafast laser written active waveguides by rigorous modeling of optical gain measurements,” *Opt. Mater. Express*, vol. 1, pp. 564-575, Aug. 2011.

[11] A. Ferrer, V. Diez-Blanco, A. R. de la Cruz, J. Siegel and J. Solis, “Deep subsurface optical waveguides produced by direct writing with femtosecond laser pulses in fused silica and phosphate glass,” *Appl. Surf. Sci.* vol. 254, pp. 1121–1125, Oct. 2007.

[12] Y. Cheng, K. Sugioka, K. Midorikawa, M. Masuda, K. Toyoda, M. Kawachi and K. Shihoyama. “Control of the cross-sectional shape of a hollow microchannel embedded in photostructurable glass by use of a femtosecond laser,” *Opt. Lett.*, vol. 28, pp. 55-57, Jan. 2003.

[13] A. Ferrer, A. Ruiz de la Cruz, D. Puerto, W. Gawelda, J. A. Valles, M. A. Rebolledo, V. Berdejo, J. Siegel and J. Solis. “In situ assessment and minimization of nonlinear propagation effects for femtosecond-laser waveguide writing in dielectrics,” *J. Opt. Soc. Am. B.* vol. 27, pp. 1688-1692, Aug. 2010.

Development of a single-mode cost-effective pumping scheme

T. Nappez, E. Ghibaudo, J.-E. Broquin, D. Bucci, L. Bastard
IMEP-LAHC, 3 parvis L. Néel, Minatec-INPG
BP 257, 38016 Grenoble, FRANCE
elise.ghibaudo@minatec.grenoble-inp.fr

P. Rondeau, J.-P. Schlotterbeck
THALES Avionics
25 rue Jules Védrines, 26027 Valence
FRANCE

***Abstract*—In this article, a new architecture for broad-area laser diode on glass platform is proposed. It is composed of a planar mode converter made by ion-exchange on glass and a Fiber Bragg Grating and provides a single-mode and wavelength selective optical feedback in the multimode pump laser. The spectral locking of the laser diode is experimentally demonstrated with a side mode suppression ratio superior to 25 dB for an injection current inferior to 1 A.**

Integrated optics on glass, wavelength stabilization, single-mode stabilized pumping scheme

I. INTRODUCTION

Ion-exchange on glass is a well-established technology for sensor applications. Its compactness and stability allow schemes of integration that often reduce costs of fabrication and improve performances or security. It has already been used for bio-detection[1], displacement[2] or orientation measurement[3]. Applications in avionics are currently in development since the measurement of an aircraft's True Air Speed (TAS) has been recently demonstrated using a LiDAR containing several ion-exchanged integrated optics elements[4]. This system, supported by the European Community presents modes of failures that are different from the traditional anemo-barometric module. The required features are reliability, compactness, low power consumption and controlled costs. In this work we propose a solution to increase the optical pump power in order to suppress the booster presently required.

Three types of compact pump power are commercially available. The first one consists of a narrow stripe semiconductor laser coupled to a single-mode fiber Bragg grating (FBG) which stabilized the emission wavelength. These sources present a single-mode emission that is well centered at the maximum of the active medium absorption band. Their low-frequency intensity noise is also reduced. However these devices can suffer from catastrophic optical mirror damage (COMD), which limits the maximum achievable output power to 700 mW since the laser facets are damaged under a too high power density[5]. A way to overcome the COMD is to increase the emitter width, decreasing thus the power density. This second type of devices is called broad area laser diodes (BALD) and achieves reliable power emission up to 35W[6]. The pump beam is however multimode and the emission spectrum is a few nanometers wide. A third architecture consists in inserting a taper in the active region. The narrow region acts like a modal filter and ensure a single-mode emission whereas the wide region decreases the power density at the output facet. An output power of 8W has already been demonstrated[7]. However, the price per watt is clearly to the advantage of a BALD structure. Though transverse multimode pumping schemes for single-mode planar operation have already been successfully used for amplification[8] and lasers[9], they were using expensive hybrid glasses and suffered from the low overlap efficiency between pump and signal modes.

We propose in this article a new architecture based on cost-effective multimode pumps. The design, which aims at locking the BALD emission on its fundamental transversal mode, is presented in section II. The realization of the glass device and the optical characterization of the first prototype are then detailed in section III before a conclusion.

II. DESIGN

The aim of the proposed architecture is to lock a BALD emission on its fundamental transversal mode. As schematized in Fig. 1, the multimode pump emission is coupled in a mode converter whose narrow end is single-mode. A butt-coupled FBG provides a wavelength and mode selective feedback in the BALD. The aim of the external cavity is to boost the fundamental mode emission and to stabilize the emission spectrum around the Bragg wavelength.

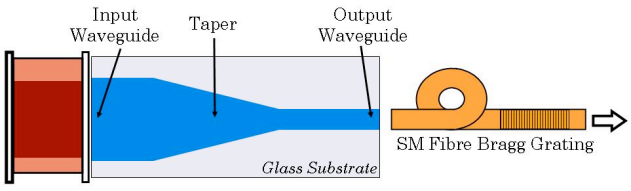


Figure 1. Fundamental mode locking and wavelength stabilization

The output of the mode converter must be designed to ensure single mode operation and minimum coupling losses with optical fibers. It can be achieved with a thermal ion-exchange. This requirement contrasts a priori with the high confinement required at the input waveguide implying a Field Assisted Ion Exchange (FAIE). To overcome this issue, a dielectric mask can be locally deposited on the rear side of the chip, beyond the output waveguide, in order to partially screen

the electric field. This single-step technique has already proven its efficiency and adiabaticity for deep selectively-buried waveguides[10]. Simulations have been carried out in order to fix the ion-exchange processes parameters. The electric field has been fixed at 0.1 V/µm and the exchange time at 7 min. The diffusion aperture of the output waveguide w has thus been chosen in order to optimize the butt-coupling with a standard HI1060 FLEX fiber. The most adapted diffusion aperture appears to be $w = 2.0$ µm with coupling losses around 2 dB. The third part of the design concerns the tapered central zone. The Burns & Milton criterion gives a theoretical condition to design an adiabatic transition[11]. For a taper whose input section is 100 µm wide and assuming an effective index of 1.55, the critical half-angle is 0.18. The length of a linear taper must then be greater than 16 mm. The mode converter chosen is a transition of 20 mm long from the lithography window $w = 100$ µm to $w = 2.0$ µm.

III. Realization and Characterization

A 1.5 mm thick commercial silicate glass substrate is first cleaned with a basic solution. An 80 nm thick alumina mask is deposited by sputtering and the waveguides patterns are inscribed in the mask by photolithography. A polymer film is placed on the rear surface of the glass plate perpendicular to the apertures, in order to screen the electric field on the output waveguide side. A selective FAIE, in a molten salt with a molar concentration of $0.5AgNO_3$-$0.5NaNO_3$, is then realized during 6 min 30 s at a temperature of 270 °C under an applied voltage of 150 V. After removal of the masks, the device is diced and its facets are polished.

The realized glass mode converter is butt coupled to the diode on an optical bench. A commercial FBG, with a reflectivity of (81 ± 3)% collects the light supported by the single-mode output. The FBG output light is then coupled in an optical spectrum analyzer Anritsu MS9710B. Fig. 2 represents the laser diode's direct emission spectrum on the left and the emission spectrum of the device on the right for different injection currents. The BALD emission is stabilized in the spectral band reflected by the grating. Under the threshold of 240 mA, we see the Bragg spectrum in the ASE of the laser. The spectral locking is then obtained by increasing the current. It is characterized by a maximum Side Mode Suppression Ratio (SMSR) of (33.06 ± 0.14) dB at $I = 500$ mA. This ratio is superior to 25 dB for $I < 1$ A. For $I < 2$ A, other laser peaks appear around 981 nm, where the gain of the SC is maximum. The evolution of SMSR can be explained as follows: with the increase of the current, the mode competition in a homogeneous medium allows the preeminent mode to get the energy of the other modes. However, at high power densities the non linear gain suppression leads to a smaller gain discrimination[12]. This effect can be reduced using a smaller detuning between maximum gain peak and Bragg reflectivity. Indeed this value reaches 2 nm at $I = 2$ A in our device.

We also measured the frequency shift with current. We report a shift of -12.0 GHz/100mA, which is five times lower than the BALD's direct emission. The total shift over the 2 A current range is 1.2 nm, which is included in the spectral width of Ytterbium absorption of the seed DFB laser.

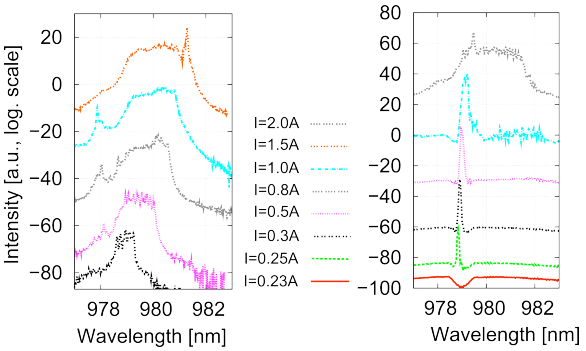


Figure 2. Emission spectrum of the solitary laser diode on the left and of the system on the right for different injection currents.

IV. Conclusion

A new architecture for the integration of broad area laser diode on a glass platform has been reported. Composed of a planar mode converter made by ion-exchange on glass and a FBG, it provides a single-mode and wavelength selective optical feedback in the BALD. It boosts the fundamental emission of the diode and stabilizes its emission spectrum on the Bragg wavelength. We first presented the design of the mode converter. It uses a single-step ion-exchange process whose input and output are respectively adapted to the laser diode and the optical fiber butt-couplings. We demonstrated the spectral locking of the laser diode with a SMSR superior to 25 dB for an injection current inferior to 1 A.

[1] B. Luff et al. "Integrated optical Mach-Zehnder biosensor," J. Lightwave Technol., vol. 16, pp. 583, 1998.

[2] D. Jestel, A. Baus, and E. Voges, "Integrated-optic interferometric microdisplacement sensor in glass with thermo-optic phase modulation," Electronics Letters, vol. 26, pp. 1144-1145,1990.

[3] J. Carriere et al. "An integrated optic gyroscope using ion-exchanged waveguides" IEEE J. Micromech. Microeng., vol. 101, pp. 99-100, 2003.

[4] L. Bastard et al. "Development of a ion-exchanged glass integrated optics DFB laser for a LIDAR application," Proc. SPIE, vol. 7218, pp. 721817, 2009.

[5] A. Moser, "Thermodynamics of facet damage in cleaved AlGaAs lasers," Appl. Phys. Lett., vol. 59, pp. 522-524, 1991.

[6] http://www.axcelphotonics.com/975MM.html

[7] M. Kelemen et al., "Tapered diode lasers at 976nm with 8W nearly diffraction limited output power," Electron. Lett, vol. 41, pp.1011-1013, 2005.

[8] V. Donzella et al. "Ion-exchanged Er^{3+}/Yb^{3+} co-doped waveguide amplifiers longitudinally pumped by broad area lasers," Optics Express vol. 18, pp. 12690-12701, 2010.

[9] P. Madasamy, S. Honkanen, D. Geraghty, and N. Peyghambarian, "Single-mode tapered waveguide laser in Er-doped glass with multimode-diode pumping," Appl. Phys. Lett., vol. 82, pp. 1332, 2003.

[10] L. Onestas, D. Bucci, E. Ghibaudo, and J. Broquin, "Vertically integrated broadband duplexer for erbium-doped waveguide amplifiers made by ion exchange on glass," IEEE Photonics Technol. Lett., vol. 23, (10), pp. 648-650, 2011.

[11] A. Milton, and W. Burns, "Mode coupling in optical waveguide horns," IEEE J. Quantum Electron., vol. 13, pp. 828-835,1977.

[12] J. Wang, and K. Petermann, "Noise analysis of semiconductor lasers within the coherence collapse regime," IEEE J. Quantum Electron., vol. 27, pp. 3-9, 1991.

Fast quenching processes and their impact on 1.5-µm amplifier performance in $Al_2O_3:Er^{3+}$ waveguides

L. Agazzi, K. Wörhoff, and M. Pollnau
Integrated Optical MicroSystems Group,
MESA+ Institute for Nanotechnology, University of Twente,
Enschede, The Netherlands
m. pollnau@utwente.nl

***Abstract*—Spectroscopic investigations reveal the presence of a fast quenching process in erbium-doped aluminum oxide waveguides. We quantify the percentage of quenched ions and make predictions about the amplifier performance.**

Optical amplifiers; integrated optics materials; fast quenching processes; aluminum oxide

I. INTRODUCTION

$Al_2O_3:Er^{3+}$ is an established material for integrated amplifier applications, offering several advantages such as low background losses, a broad emission spectrum, and a relatively high refractive index of 1.65 at 1.5 µm, which enables the fabrication of compact optical waveguide structures [1]. Our growth method allows for straightforward deposition on silicon wafers [2] and monolithic integration with silicon photonic circuits [3]. We have fabricated waveguide amplifiers with a broadband gain over a wavelength range of 80 nm and a peak value of 2.0 dB/cm, which however varies strongly with Er^{3+} concentration [4]. In this paper we report spectroscopic investigations in $Al_2O_3:Er^{3+}$ waveguides that reveal a fast quenching of a fraction of ions – undetected in typical luminescence decay measurements – which increases with concentration: in addition we investigate the effect of the fast quenching on the small-signal gain of $Al_2O_3:Er^{3+}$ integrated channel-waveguide amplifiers.

II. EXPERIMENTAL

$Al_2O_3:Er^{3+}$ layers with a thickness of 1.0 µm were deposited on thermally oxidized silicon substrates by reactive co-sputtering [2]. Ridge waveguides with a width of 4.0 µm were defined using reactive ion etching to an etch depth of ~ 50 nm [1]. The Er^{3+} concentration varied from 1.17 to 3.66×10^{20} cm^{-3}.

Small-signal gain measurements were carried out by launching either 976-nm from a Ti:Sapphire pump source or 1480-nm pump light from a Raman laser source together with 1533-nm signal light from a tunable laser into the channel waveguides using either a lens-coupling or a fiber-coupling setup [4]. The output signal light was separated from the residual pump light by a silicon filter in the 976-nm pumping case and a fiber wavelength division multiplexer in the 1480-nm case, and acquired by a detector and lock-in amplifier.

Funding was provided by the Smartmix Memphis programme of the Dutch Ministry of Economic Affairs.

III. RESULTS AND DISCUSSION

The results of the small-signal gain measurements were fitted with a simple amplifier model described in [4] in order to extract values for the coefficient W_{ETU} of energy-transfer upconversion (ETU) between neighboring Er^{3+} ions, an inter-ionic process which has a detrimental influence on the amplifier performance [5]. The resulting W_{ETU} values show a discrepancy of about one order of magnitude with the results obtained from luminescence decay measurements presented in [6]. The discrepancy is explained by the fact that a certain fraction of Er^{3+} ions undergoes fast quenching which is not resolved in our decay measurements owing to the time response of the set-up. This quenching can be induced by, e.g., active ion pairs and clusters, undesired impurities, or host material defects. Other investigations indicate that such quenching occurs on the ns-µs time scale [7,8]. By modifying the model to account for these fast quenching effects, we derived that the fraction of quenched ions f_q increases from 10% to 33% when the Er^{3+} concentration increases from 1.17 to 3.66×10^{20} cm^{-3}, as shown in Fig. 1, proposing a higher probability of fast quenching with increasing concentration.

These results were afterwards confirmed by nonsaturable absorption experiments, see Fig. 2, in which 1480-nm pump light was launched into the waveguide, and the transmission as a function of launched power was recorded. The transmission is strongly dependent on the amount of quenched ions, and our improved model could fit the results with good accuracy, whereas the former amplifier model could not.

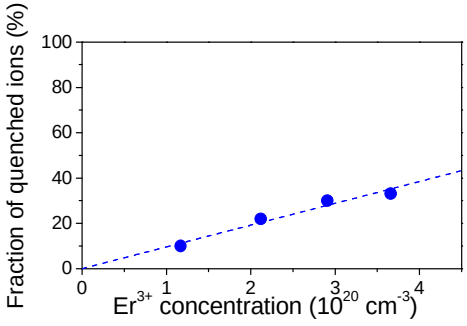


Figure 1. Fraction of quenched ions f_q as a function of Er concentration

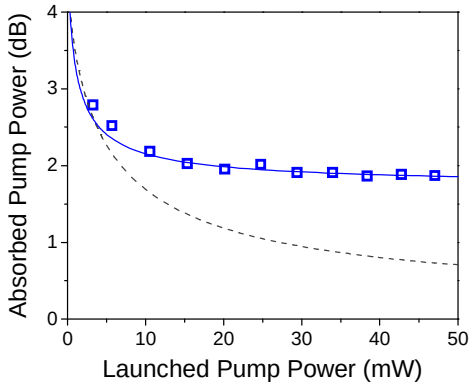


Figure 2. Absorbed versus launched pump power for a waveguide with an Er^{3+} concentration of 3.66×10^{20} cm^{-3} and 1 cm length. The squares are the experimental data, the solid line is a fit with the improved model resulting in f_q = 33%, and the dashed line is a tentative fit with the former amplifier model

The dots in Fig. 3 show the measured internal net gain per unit length for varying Er^{3+} concentration (taken from [4]) for a launched pump power of 100 mW at 976 nm (top graph) and at 1480 nm (bottom graph) and signal power of 1 μW at 1533 nm. The solid lines represent the simulated gain versus Er^{3+} concentration, according to the improved model, under the assumption that f_q keeps on increasing linearly with Er^{3+} concentration even at higher Er^{3+} concentrations than those measured. Since the exact decay time τ_{1q} of the quenched ions is not known, we have performed simulations for three different τ_{1q} values that approximately cover the range found in the literature.

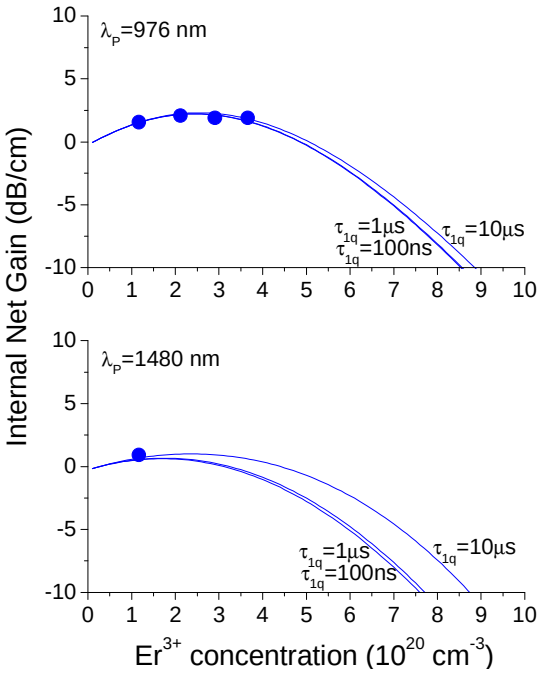


Figure 3. Measured internal net gain per unit length at 1533 nm (dots) versus Er^{3+} concentration. The solid lines represent a gain simulation where fast quenching with three different τ_{1q} values is considered

In the 976-nm case the gain initially grows with Er^{3+} concentration, reaches a maximum value of 2 dB/cm at a concentration of ~ 2×10^{20} cm^{-3}, and then decreases due to the increasingly stronger impact of ETU and fast quenching with Er^{3+} concentration.

In the 1480-nm pump case only one small-signal gain measurement at a concentration of 1.17×10^{20} cm^{-3} was performed [4]. Predictions with the improved model, depending on the different τ_{1q} values, result in a ~ 0.7-1 dB/cm peak at a concentration of ~ $1.5\text{-}2.5\times10^{20}$ cm^{-3}. The gain is lower than in the 976-nm pump case because of the lower population inversion caused by stimulated emission at the pump wavelength from the $^4I_{13/2}$ metastable state.

In both 976-nm and 1480-nm pump cases we observe a difference among the simulations with different τ_{1q} values at high Er^{3+} concentrations for τ_{1q} = 10 μs. This can be attributed to the onset of bleaching of the quenched ions due to the high pump intensity in our channel waveguides. Small-signal gain experiments under 1480-nm pumping are under way to fully investigate the gain behavior at this pump wavelength and further clarify this last point.

V. CONCLUSIONS

A fast quenching mechanism, revealed by spectroscopic investigations, strongly affects the Al_2O_3:Er^{3+}amplifier performance. Simulations that account for the fast quenching predict a higher gain under 976-nm pumping.

REFERENCES

[1] J. D. B. Bradley, F. Ay, K. Wörhoff, and M. Pollnau, "Fabrication of low-loss channel waveguides in Al_2O_3 and Y_2O_3 layers by inductively coupled plasma reactive ion etching", Appl. Phys. B, vol. 89, pp. 311-318, October 2007.

[2] K. Wörhoff, J. D. B. Bradley, F. Ay, D. Geskus, T. P. Blauwendraat, and M. Pollnau, "Reliable low-cost fabrication of low-loss Al_2O_3:Er^{3+} waveguides with 5.4-dB optical gain," IEEE J. Quantum Electron., vol. 45, pp. 454-461, May 2009.

[3] L. Agazzi, J. D. B. Bradley, M. Dijkstra, F. Ay, G. Roelkens, R. Baets, K. Wörhoff, and M. Pollnau, "Monolithic integration of erbium-doped amplifiers with silicon-on-insulator waveguides," Opt. Express, vol. 18, pp. 27703-27711, December 2010.

[4] J. D. B. Bradley, L. Agazzi, D. Geskus, F. Ay, K. Wörhoff, and M. Pollnau, "Gain bandwidth of 80 nm and 2 dB/cm peak gain in Al_2O_3:Er^{3+} optical amplifiers on silicon," J. Opt. Soc. Am. B, vol. 27, pp. 187-196, February 2010.

[5] A. Polman, "Erbium implanted thin film photonic materials," J. Appl. Phys., vol. 82, pp. 1-39, March 1997.

[6] L. Agazzi, K. Wörhoff, and M. Pollnau, "Energy-transfer-upconversion models, their applicability and breakdown in the presence of spectroscopically distinct ion classes," submitted.

[7] P. Myslinski, J. Fraser, and J. Chrostowski, "Nanosecond kinetics of upconversion process in EDF and its effect on EDFA performance," in Optical Amplifiers and Their Applications, vol. 18, paper ThE3, of 1995 OSA Technical Digest Series (Optical Society of America, June 1995).

[8] R. Wyatt, "Spectroscopy of rare earth-doped fibers," in Proc. SPIE 1171-Fiber Laser Sources and Amplifiers, pp. 54-64, February 1990.

Design and optical response of a thin film structure enhancing the photoluminescence of an embedded single layer of Er^{3+} ions

Johann Toudert, Javier Martin Sánchez, Rosalia Serna
Instituto de Óptica, CSIC
Madrid, Spain
johann.toudert@gmail.com

***Abstract*— This paper presents a thin film structure designed for optimizing the excitation efficiency of a single layer of luminescent Er^{3+} ions embedded in a solid host medium. In this structure, the Er^{3+} ions are located on top of a single layer of amorphous Si nanoparticles acting as sensitizers for the rare-earth excitation. This a-Si/Er active layer is sandwiched between two amorphous Al_2O_3 thin layers, the thickness of which is chosen so that the excitation electric field is maximized at the Si nanoparticles. Optical characterization of a thin film with such a structure grown by pulsed laser deposition shows the presence of a bandgap absorption (due to electron confinement in nanostructures a few nm in size), measurable Er^{3+} photoluminescence (in contrast with a single layer of Er^{3+} ions embedded in amorphous Al_2O_3) and evidence of a sensitization mechanism involving the Si nanostructures.**

Keywords: Er, photoluminescence enhancement, a-Si

I. INTRODUCTION

Due to their luminescence properties, Er^{3+} ions are of interest in photonics. For applications in this field, it is generally desirable to embed the rare-earth ions into stable matrices and to maximize their luminescence efficiency (for functional and economical reasons). In such a context, it was shown that the photoluminescence (PL) efficiency of Er^{3+} ions in an amorphous Al_2O_3 (a-Al_2O_3) matrix can be improved if the ions are distributed in separated single layers, rather than randomly in the matrix [1]. Further improvement of the PL efficiency was obtained by depositing the Er on top of a single layer of amorphous Si (a-Si) nanoparticles, acting as sensitizers for the Er excitation [2], thus forming an a-Si/Er active layer. These studies were nevertheless limited to the case of multilayered systems containing several active layers evenly spaced. In this work, we focus on a system based on just a single a-Si/Er active layer embedded in a simple photonic structure designed for maximizing the excitation electric field at the active layer.

II. DESIGN AND PREPARATION OF THE STRUCTURE

A. Definition and optimization of the structure

Figure 1a shows the thin film structures of interest in this paper. A buffer a-Al_2O_3 layer (of thickness t_{buffer}) separates the a-Si/Er active layer (thickness t_{active} of a few nm) from the Si substrate. A second a-Al_2O_3 layer of thickness t_{cap} caps the active layer. For comparison, a similar structure with only a single layer of Er^{3+} ions - called hereafter "Er active layer"- instead of the a-Si/Er active layer will also be considered.

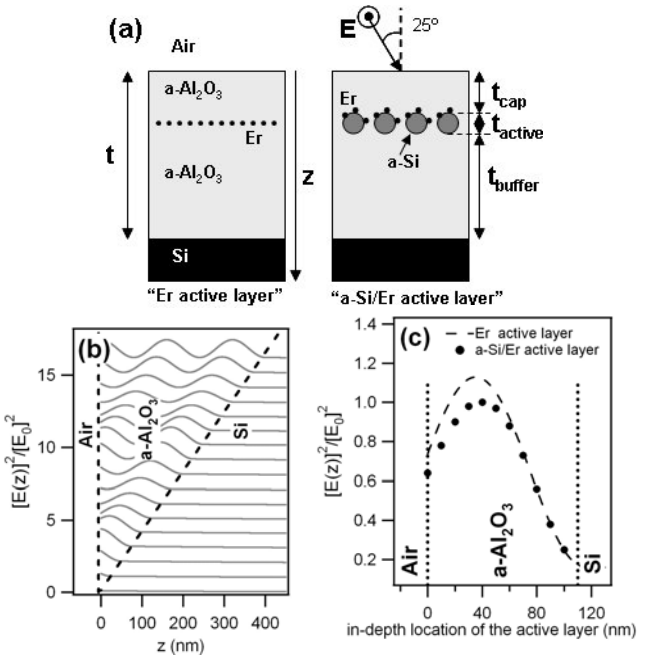


Figure 1: (a) Schematic representation of the film structures studied in this paper, (b) square module of the excitation electric field as a function of the depth **z** in a-Al_2O_3 thin films of various thicknesses (the different curves are displayed with a vertical offset for the sake of clarity, (c) square module of the excitation electric field at an Er or a-Si/Er active layer as a function of its in-depth location inside a 110 nm-thick a-Al_2O_3 film. The incident field incomes from above, with a 25º angle and a S-polarization, as shown in (a) and a 514.5 nm wavelength.

Figure 1b shows a simulation of the square module of the electric field as a function of the depth **z** in a-Al_2O_3 films of different thicknesses t, standing on a bulk Si substrate, assuming a 25º incidence angle, a S-polarization and a 514.5 nm wavelength for the incoming field. The coherent matrix formalism was used for the calculations; the refractive index of a-Al_2O_3 layers was fixed at 1.65. Since a single layer of Er^{3+} ions induces no significant changes to the in-depth complex refractive index of the film, the calculated profiles also hold for thin films of a-Al_2O_3 with an embedded Er active layer (figure 1a, left), located at any depth in the film. It can be seen that

stationary waves develop in the structure with maxima at depths whose value depend on the film thickness t. Thus, an Er active layer should be located at one of these maxima in order to optimize its excitation. Figure 1c presents the evolution of the square module of the excitation electric field at an Er active layer (dashed line; structure depicted on fig. 1a, left) and at an a-Si:Er active layer (dots; structure depicted on fig. 1a, right) as a function of its in-depth location in a 110 nm-thick a-Al_2O_3 film standing on a bulk Si substrate. In the latter case, calculations were performed assuming a trilayer structure for the film, the central layer of thickness t_{active}=5 nm being considered as an effective medium of refractive index and extinction coefficient n_{active}= 2.5 and k_{active}=0.1, respectively. Such values are typical of granular layers of a-Si embedded in a-Al_2O_3. The field profiles are very similar in both cases, with a slight perturbation due to the presence of Si in the a-Si:Er case, and it is seen that the highest values for the excitation field at the active layer are obtained at a depth between 20 and 60 nm.

B. Pulsed laser deposition of the structures

Alternate pulsed laser deposition of Er, Si and Al_2O_3 in vacuum and at room temperature [2] was thus performed to grow a thin film with the structure shown in figure 1a (right), the a-Si:Er active layer consisting of Er^{3+} ions deposited on top of the a-Si material, as required for efficient sensitization of the Er by a-Si nanostructures [2]. Deposition was performed onto transparent fused silica and opaque Si substrates. The Er target was ablated using only one laser pulse, thus depositing a very low amount of material (areal density in the 10^{-13} ions/cm^2 range). Nominal values of 85 nm, 20 nm were used for t_{buffer} and t_{cap}, respectively. The Si amount was chosen so that a-Si nanoparticles a few nm in size form [2]. In these conditions, the active layer is located at a depth of around 20 nm in an almost 110 nm-thick film, thus providing a quasi-maximized excitation field at the active layer in the pumping conditions considered above. A film with the same structure but with only Er doping for the active layer (figure 1a - left), was prepared as reference.

III. OPTICAL RESPONSE

The optical response in the 300-900 nm range of both films was studied by optical transmittance at normal incidence and spectroscopic ellipsometry (65º, 70º and 75º). Room temperature IR PL measurements were performed under visible excitation with an argon laser (25º incidence angle, S-polarization), using standard lock-in techniques. PL was collected at normal incidence through lenses, and detected by a NIR PMT through a single monochromator. The substrates considered for each type of measurements were fused silica and Si, respectively. The transmittance spectrum of the reference film is typical of a transparent dielectric, whereas that of the a-Si/Er active layer-based film presents a bandgap absorption noticeable in the UV and blue regions. This absorption is attributed to electron confinement in Si nanostructures of a few nm in size. A fast analysis of ellipsometry spectra (not shown) confirmed the value of the overall thickness of the films, close to 110 nm. Figure 2b presents the PL spectra of both films: the 1.54 μm PL band characteristic of Er^{3+} ions is observed only for the a-Si/Er active layer-based film. Its excitation spectrum, presented in the right inset of figure 2b, shows a slowly decreasing linear evolution of the 1.54 μm PL as a function of the excitation wavelength, which is typical of a pumping of the Er^{3+} ions through a-Si. The excitation spectrum of directly pumped Er^{3+} ions through direct excitation (measured on a thick and annealed Er-only doped sample) is also shown for comparison.

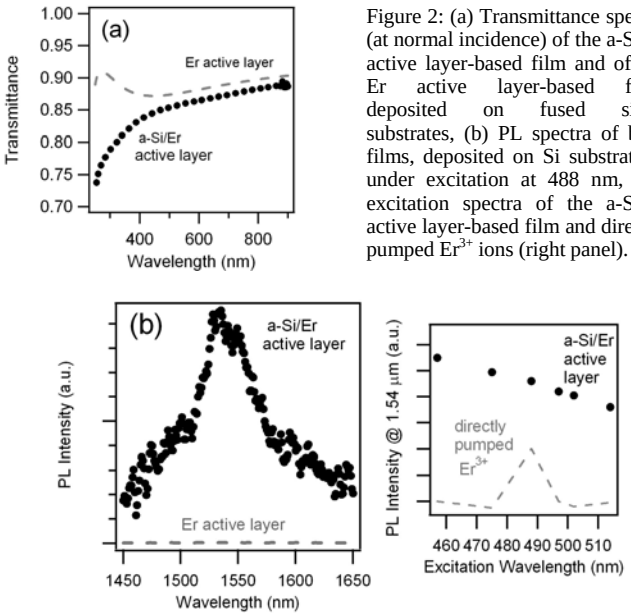


Figure 2: (a) Transmittance spectra (at normal incidence) of the a-Si:Er active layer-based film and of the Er active layer-based film, deposited on fused silica substrates, (b) PL spectra of both films, deposited on Si substrates , under excitation at 488 nm, and excitation spectra of the a-Si:Er active layer-based film and directly pumped Er^{3+} ions (right panel).

IV. CONCLUSIONS

In this paper, we propose a strategy for improving the excitation of a single layer of Er^{3+} ions embedded in a solid host medium. Two aspects are investigated: i) the design and preparation of a 1D photonic structure maximizing the excitation field at the active layer, ii) the contact-sensitization by a-Si nanostructures. The film presenting the pre-defined photonic structure shows a measurable PL at room temperature, in contrast with a film with a comparable structure but without Si nanostructures. Future works should deal with experimental studies to optimize the a-Si nanostructure, the photonic enhancement of the PL excitation, and light extraction.

ACKNOWLEDGEMENTS

The authors thank Pablo Roque and Francisco Valle Brozas for their valuable support during the films elaboration. J.T. acknowledges financial support from the Spanish ministry for Science and Innovation (Juan de la Cierva Grant Nº JCI-2009 – 05098).

REFERENCES

[1] R. Serna, M.J. de Castro, J.A. Chaos, C.N. Afonso and I. Vickridge, "The role of Er^{3+}-Er^{3+} separation on the luminescence of Er-doped Al2O3 films prepared by pulsed laser deposition" Appl. Phys. Lett., vol. 75, pp. 4073-4075, 1999.

[2] S. Núñez-Sánchez, P.M. Roque, R. Serna and A.K. Petford-Long, "Si-nanoparticle Er^{3+} coupling through contact in as-deposited nanostructured thin films", Appl. Phys. Lett., vol 98, pp.151109, 2011.

Photorefractive effect and optical damage thresholds in z-cut swift heavy ion irradiation $LiNbO_3$ waveguides.

M. Jubera, A. García-Cabañes and M. Carrascosa.
Dpto. de Física de Materiales
Universidad Autónoma de Madrid
Madrid, Spain.
mariano.jubera@uam.es

J. Olivares[1] and F. Luedtke[2]
CMAM and Instituto de Óptica[1], Institute of Physics[2]
Universidad Autónoma de Madrid and CSIC[1], University of Bonn[2]
Madrid, Spain[1]; Bonn, Germany[2]

Abstract: We have investigated the photorefractive effect and the corresponding optical damage thresholds of novel $LiNbO_3$ waveguides fabricated by swift-ion irradiation. TE- and TM-mode operation has been characterized and the influence of the beam propagation length analysed. The results are briefly discussed and compared with some data from other type of $LiNbO_3$ waveguides.

I. INTRODUCTION

Photorefractive optical damage is a main drawback for high power photonic devices based on $LiNbO_3$ crystals and waveguides. Thus, a great effort has been devoted to characterize and reduce it. Particular attention has been paid to waveguide configurations because the long propagation lengths and the high intensities reached increase optical damage effects. Most experiments have been performed in Ti-undiffused and PE waveguides whereas the information is scarcer for ion implanted waveguides [1].

Recently, a new method to produce nonlinear $LiNbO_3$ optical waveguides by swift ion irradiation has been reported [2]. It involves irradiation of the substrate with swift-heavy ions (SHI), such as F at 20 MeV, whose electronic stopping power reaches a maximum value inside the crystal instead of on the surface. As a very low fluence ($1\text{-}4\times10^{14}$ cm^{-2}) is sufficient, the fabrication time is reduced by about three orders of magnitude in comparison with similar guides prepared by conventional implantation. The guides, at difference with proton-exchanged (PE) waveguides, support ordinarily and extraordinarily polarized modes showing in both cases step-like, high-jump index profiles (Δn_e=0.1, Δn_o=0.2). Furthermore, good nonlinear and electroptical coefficients have been reported [2,3]. Very recently, using high temperature annealing treatments (350-375 ºC) propagation losses have been reduced under 0.5 dB/cm [4], so that SHI waveguides become very competitive for photonic applications. However, photorefractive optical damage effects have been studied only preliminarily and using non-optimized waveguides with high propagation losses of 1-5 dB/cm [3]. Moreover, those data were taken from a *X*-cut configuration although Z-cut geometries, are usually preferred for efficient non linear applications.

The aim of this work is to address a detailed investigation of photorefractive optical damage of Z-cut $LiNbO_3$ planar waveguides using two complementary approaches: *i)* determination of optical damage thresholds, i.e. maximum light intensity supported by the waveguide without distortion and *ii)* measurements of the corresponding light induced refractive index changes responsible for the beam damage. TE- and TM-mode operation will be characterized and the influence of the propagation length analysed. The results are briefly discussed and compared with some data from other type of $LiNbO_3$ waveguides.

II. EXPERIMENTAL DETAILS.

Planar waveguides have been fabricated by swift ion irradiation (F-20 MeV) on *z*-cut congruent $LiNbO_3$ substrates in the 5 MV Tandem Accelerator at University Autónoma of Madrid. Propagation losses were measured obtaining values below 0.5 dB/cm for both polarizations.

A standard single-beam method using in- and out-coupling rutile prism-couplers, as described in Ref. [5] was used to determine optical damage thresholds (ODT) for two optical different path lengths l of 4 and 16 mm. The optical damage threshold is defined by the in-coupled intensity I_{in} inside the guide at which the out-coupled intensity I_{out} is no longer proportional to I_{in}. In turn, a Mach-Zehnder interferometer is used for the quantitative measurement of light-induced index changes [6]. Optical damage is induced by light of 532 nm wavelength and probed with red light of 633 nm wavelength.

III. RESULTS AND DISCUSSION.

The light-induced refractive index change generated by the TE fundamental mode at λ=532 nm as a function of the light beam intensity inside the waveguide I_{in} has been measured using the Mach-Zehnder technique. Both TE (n_o) and TM (n_e) polarized probe beams at λ=630 nm have been used and the corresponding results are shown in Fig. 1. The obtained curves $\Delta n(I)$ follows the typical shape reported for α-phase proton exchanged waveguides in [6] and successfully explained through a two-centre model in [7]. Then these data can be considered a further confirmation of the validity of that model for the photorefractive effect in $LiNbO_3$ waveguides. At each intensity, Δn for the TM mode is larger than that for TE and, the relation is roughly consistent with the rate $n_e^3 r_{33}/n_o^3 r_{13}=2.8$ (where r_{33} and r_{13} are the corresponding electrooptic coefficients). This indicates that, as expected, these differences arise from the electrooptic effect. The maximum refractive index change is 2.5×10^{-4} and 10^{-4} for TM (n_e) and TE (n_o) modes. Moreover, Δn_e coincides roughly with the values measured for soft proton exchanged waveguides ($2x10^4$) [6]. Finally, when optical damage is induced by TM instead of TE modes, very similar curves to those of Fig. 1 have been obtained reaching the same Δn saturating values.

Optical damage thresholds have been measured for TE and TM modes and two propagation lengths *l*. The results for *l*=16 mm are illustrated in Fig. 2. The ODT values are ~40 and ~100 W/cm^2 for *TM* and *TE* laser beam propagation respectively. The lower intensity threshold for TM modes is consistent with the higher photorefractive index change exhibit in Fig. 1. For *l*=4 mm the intensity threshold shifts to higher light intensities for both polarizations (roughly a factor 6). This result shows the key role played by the propagation length in the ODT although it is rarely considered.

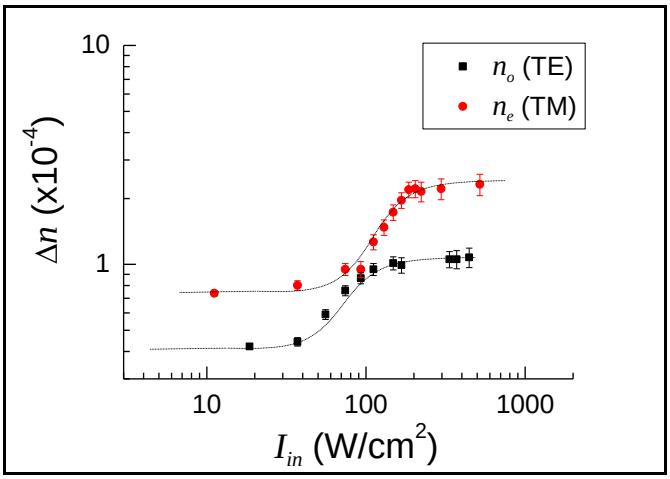


Figure1. Logarithmic plot of the photorefractive index change Δn_e (circles) and Δn_o (squares) versus the light intensity *I* inside the waveguide.

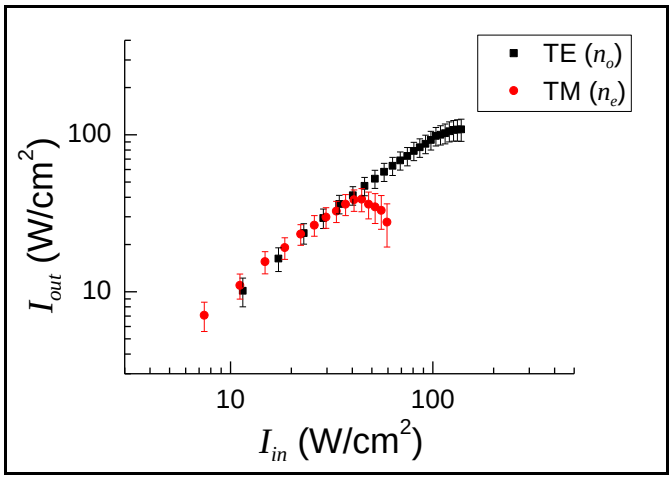


Figure 2. Logarithmic plot of the output intensity I_{out} versus input intensity I_{in} inside the waveguide for TE (squares) and TM propagating fundamental modes (rhombus)

In summary, the photorefractive effect of SHI $LiNbO_3$ waveguides has been characterized finding an intensity response in accordance with the recently reported two-center charge transport model [7]. In addition, the optical damage thresholds for TE and TM polarizations have been determined obtaining values that decrease with the propagation length and that are roughly similar to those of PE waveguides.

ACKNOWLEDGMENT

This work was supported by MICIN, MAT2008-06794-C03 and MAT2011-28379-C03-01.

REFERENCES

[1] D. Kip and M. Wesner, "Photrefractive waveguides," in Phtorefractive Materials and their applications I: Fundamental phenomena (Springer Berlín, 2006)

[2] J. Olivares, G. García, A. García-Navarro, F. Agulló-López, O. Caballero and A. García-Cabañes, "Generation of high-confinement step-like optical waveguides in LiNbO3 by swift heavy ion-beam irradiation," Appl. Phys. Lett. **86**, 183501 (2005).

[3] J.Villarroel, M. Carrascosa, A. García-Cabañes, O. Caballero, M. Crespillo and J. Olivares, "Photorefractive response and optical damage of lithium niobate optical waveguides produced by swift-heavy ion irradiatio", Appl. Phys. B **95**, 429-433 (2009)

[4] M. Jubera, J. Villarroel, A. García-Cabañes, M. Carrascosa, J. Olivares, F. Agullo-López, A. Méndez and J. B. Ramiro, "Analysis and optimization of propagation losses in $LiNbO_3$ optical waveguides produced by swift heavy-ion irradiation", Appl. Phys. B, 10.10007/S00340-012-4897-9, (2012), in press.

[5] O. Caballero-Calero, A. Alcázar, A. García-Cabañes, J. M. Cabrera and M. Carrascosa, "Optical damage in x-cut proton exchanged $LiNbO_3$ planar waveguides," J. Appl. Phys. **100**, 093103 (2006).

[6] F. Luedtke, J. Villarroel, A. García-Cabañes, K. Buse and M. Carrascosa, "Correlation between photorefractive index changes and optical damage thresholds in z-cut proton-exchanged-$LiNbO_3$ waveguides," Opt. Express **17**, 658 (2009).

[7] J. Villarroel, J. Carnicero, F. Ludtke ,M. Carrascosa, A. García-Cabañes, J. M. Cabrera, A. Alcazar and B. Ramiro, "Analysis of photorefractive optical damage in lithium niobate: Aplication to planar waveguides"; Opt. Express **18**, 20852-20861 (2010).

Gallium Nitride-on-Sapphire Tunable Photonic Crystal Directional Coupler

Erman Engin, Jeremy L. O'Brien and Martin J. Cryan
Centre for Quantum Photonics, H. H. Wills Physics Laboratory & Department of Electrical and Electronic Engineering
University of Bristol
Bristol, UK
erman.engin@bristol.ac.uk

***Abstract*—We have designed and simulated a photonic crystal coupler in the GaN-on-Sapphire material system. In this asymmetric layer structure, the losses resulting from above light line operation can be tolerated with devices having short lengths. A 50-50% directional coupler of 5µm length is designed and tuning of the coupling ratio using electro-optic effect is presented.**

Keywords-component; photonic crystal;directional coupler

I. INTRODUCTION

GaN due to its direct bandgap is widely used in light generation devices such as LEDs and lasers in the blue-green spectral regime. Its transparency, which covers the visible and infrared spectrum [1] and electro-optic effect makes it a useful material for integrated photonics applications such as second harmonic generation [2], quantum computation [3], [4] and biosensing [5]. In this study we aim to design a 2D photonic crystal (PhC) coupler [6] in the GaN-on-Sapphire material system which is available with a thin AlN layer for lattice matching. GaN membranes can be achieved with undercutting techniques; however this is relatively more complex. Here we studied a PhC coupler having an asymmetric layer structure, although this increases the losses, with device lengths of the order of few microns these could be tolerable.

II. RESULTS

The layer structure used is 500nm GaN with a 100nm AlN buffer layer on a sapphire substrate. 2D modelling is used initially to simplify the problem and reduce the computational time [7]. We have used the open–source package, MPB [8] to solve band diagrams of PhC structures. In 3D simulations we used MEEP [9], another open source FDTD simulation package.

A. 2D Modelling

The inset in Fig.1(a) shows the simulated structure. Here the material having holes of air has a refractive index of 2.279 which is the effective index of the fundamental TE mode of the slab waveguide. The parameters are r_0, r_1 and r_2, and defined as the radius of the background holes, the radius of the first and second row of holes neighbouring the defects. The lattice constant is represented by a.

In the band diagram of this coupler structure we see that by increasing r_2, the bands shift towards higher frequencies. Here the bands labelled as even and odd bands are defined according to the symmetry of the propagating mode with respect to the symmetry axis of the structure. The coupling occurs due to the beating of these two co-propagating modes. The difference of the wavevectors, Δk of these modes is related to the coupling length, L_{3dB}, which is the length when the input light from the input is split equally between the outputs, and given by the following equation:

$$L_{3dB} = \frac{\pi}{2|\Delta k|} \quad (1)$$

For an increase in r_2, Δk increases for a fixed normalized frequency (the dashed line), resulting in a shorter coupling length as shown in Fig. 1(b).

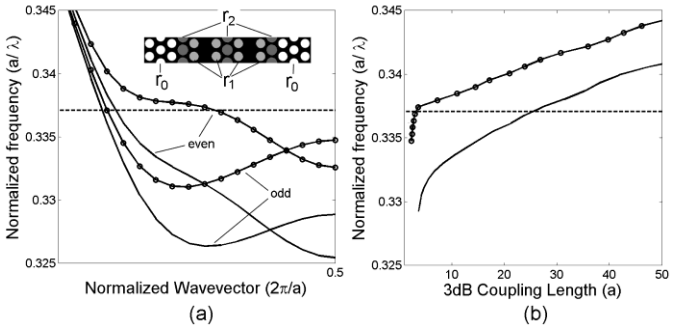


Fig.1: (a) The even-even and even-odd bands of two different coupler geometries. Solid lines are for $[r_0,r_1,r_2]$=[0.32a,0.34a,0.32a] and dotted are for $[r_0,r_1,r_2]$=[0.32a,0.34a,0.38a]. The refractive index of the background is 2.279. (b) The 3dB coupling length versus normalized frequency. The 3dB coupling length is given in terms of a and is the distance where the phase difference between the even-even and even-odd modes is $\pi/2$, that is the input power in one of the waveguides is split equally between the two waveguides.

B. 3D Modelling

In the actual coupler we cascade the two structures having different r_2 values. The structure with smaller r_2 is used for the input and the output regions, whereas the middle part is the coupling region where r_2 is larger. The top view of the simulated 3D structure is shown in Fig.2(a). The coupling region is 8 lattice constants in length and the input output regions are 5 lattice constants long each. The excitation is a Gaussian pulse centered at 800nm wavelength and flux planes

are placed along the waveguide with a lattice constant separation. Fig.2(b) shows the flux along the defect waveguides at 799.3nm wavelength, for two PhC couplers having different hole depths. The solid curves are for infinitely deep holes and the circled ones are for the case where holes stop at AlN-sapphire interface. The second case is more lossy as expected however a shallow etch into the sapphire layer can significantly reduce these losses.

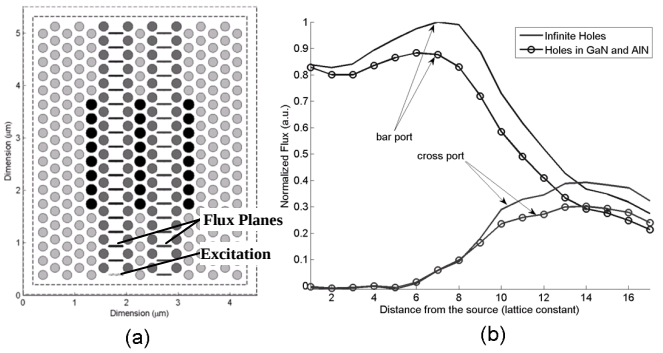


Fig.2: (a) The top view of the simulated 3D structure. (b) The effect of different depth of holes on the behaviour of the coupler. The solid curves show the flux in cross and bar ports in the case when the holes are infinitely deep and the circled ones are when the holes pass through GaN and AlN layer but stop at the sapphire layer.

The device is very sensitive to wavelength such that at 802nm wavelength full switching of input light to the cross port is observed. This requires having tunability of the splitting ratio since due to the fabrication tolerances the actual device could be different from that required. Thermo-optic tuning is possible by changing the temperature of the whole sample however for fast response we can utilize the electro-optic property of GaN. By applying electric field across the material the refractive index can be changed and the desired splitting ratio can be achieved. We have assumed that we could use a transparent upper electrode such as Indium Tin Oxide and a doped AlN layer as a bottom contact. To simulate this we have used a coupler structure similar to the one already described but this time having a longer coupling length of 11 lattice constants to enhance the effect of index change. Fig.3 shows comparison of the unperturbed structure and the one with a 0.1% change in the refractive index of the GaN layer. This change can be achieved by applying 266V across the electrodes. Without any refractive index change 98.5% of the power is in the cross port at 800nm wavelength and when there is a 0.1% refractive index change the power in the cross port drops to 68.5%. The wavelength where the coupler is the most sensitive to changes in the refractive index is around 800.25nm wavelength. At this wavelength it is possible to steer the power in the cross port from 93.6% to 49.2% with the same voltage.

III. CONCLUSION

The results show that while the above the light line operation and the low index contrast of the wafer structure

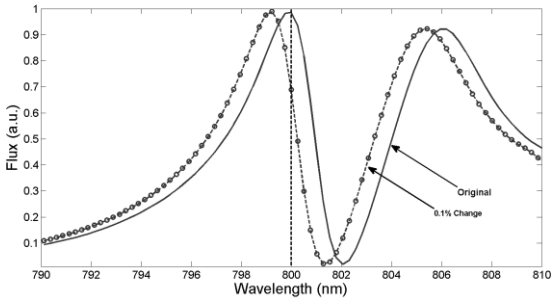


Fig.3: The normalized fluxes, at 5.4μm (20*a*) away from the source, in cross port of the coupler structure with respect to wavelength for the original refractive index value for GaN (no-circles) and the case when the refractive index is changed by 0.1% (circles).

increase losses, it is possible to produce useful integrated devices in a very small device footprint. The advantages of GaN in terms of non-linearity, light emission and tunability combined with the small foot print of PhC devices may counteract the reduced performance.

REFERENCES

[1] Aref Chowdhury, Hock M. Ng, Manish Bhardwaj, and Nils G. Weimann, "Second-harmonic generation in periodically poled GaN," *Applied Physics Letters*, vol. 83, no. 6, p. 1077–1079, 2003.

[2] C. Xiong, W. Pernice, K. K. Ryu, C. Schuck, K. Y. Fong, T. Palacios, and H. X. Tang, "Integrated GaN photonic circuits on silicon (100) for second harmonic generation," *Opt. Express*, vol. 19, no. 11, pp. 10462-10470, 2011.

[3] Yanfeng Zhang, Loyd McKnight, Erman Engin, Ian M. Watson, Martin Cryan, Erdan Gu, Mark G. Thompson, Stephane Calvez, Jeremy L. O'Brien and Martin D. Dawson, "GaN directional couplers for integrated quantum photonics," *Applied Physics Letters*.

[4] A. Politi, M.J. Cryan, J. G. Rarity,S. Yu,and J. L. O'Brien, "Silica-on-Silicon Waveguide Quantum Circuits," *Science*, vol. 320, no. 5876, pp. 646-649, 2008.

[5] J.M. Dawson, R.P. Tompkins, J.R. Nightingale, S. Yeldandi, K. Jo, X.A. Cao, L.A. Hornak, D. Korakakis, T. Myers, and A. Timperman, "Design and Characterization of Optofluidic Photonic Crystal Structures for the Detection of Fluorescent-Labeled Biomolecules," in *213th ECS Meeting*, Phoenix, AZ, May 2008, pp. 18-22.

[6] E. Engin, J. L. O'Brien and M. J. Cryan, "Design and Analysis of a Gallium Nitride-on-Sapphire Tunable Photonic Crystal Directional Coupler," *Journal of the Optical Society of America B, in press.*.

[7] M. Qiu, "Effective index method for heterostructure-slab-waveguide-based two-dimensional photonic crystals," *Applied Physics Letters*, vol. 81, no. 7, pp. 1163-1165,, 2002.

[8] S. G. Johnson and J. D. Joannopoulos, "Block-iterative frequency-domain methods for Maxwell's equations in a planewave basis," *Opt. Express*, vol. 8, no. 3, pp. 173-190, 2001.

[9] A. F. Oskooi, D. Roundy, M. Ibanescu, P. Bermel, J. D. Joannopoulos, and S. G. Johnson, "Meep: A flexible free-software package for electromagnetic simulations by the FDTD method," *Comput. Phys. Commun*, vol. 181, no. 3, pp. 687-702, 2010.

GaAsSb/GaAs quantum dot lasers with strong index-guiding

Carina Heisel, Thomas Henning Loeber, and Henning Fouckhardt
Integrated Optoelectronics and Microoptics Research Group, Physics Department
Kaiserslautern University of Technology, Germany
heisel@physik.uni-kl.de

***Abstract*—Edge-emitting semiconductor lasers with dense lying GaAsSb quantum dots are improved by strong index-guiding. The differential quantum efficiency is increased up to 77% and the threshold current density decreases to 35%.**

Gain-guiding; index-guiding; semiconductor lasers; quantum dot laser; differential quantum efficiency; threshold current density; characteristic temperature

I. INTRODUCTION

Usually gain-guiding is employed in the early stage of semiconductor laser development to get an account of the layer design and epitaxial quality first, before a sophisticated lateral design for index-guiding is added and realized. Especially for quantum dot lasers the way to achieve (lateral) index-guiding is an important issue, since a second epitaxial step (as in the buried heterostructure laser design [1]) for definition of the lateral refractive index profile would be detrimental to the quantum dots due to particle rediffusion. A solution to this problem is strong index-guiding by a deep waveguide rib realized with reactive ion etching. In this contribution experimental results for such laser devices are given – in comparison to the gain-guiding case. The lasers are based on dense lying GaAsSb/GaAs quantum dots (QDs), where results are rarely found in literature so far [2-4].

II. SAMPLE MATERIAL

A. Sample growth with molecular beam epitaxy

All samples are grown in a *DCA R450* molecular beam epitaxy (MBE) machine. The active region of the lasers consists of layer stacks with GaAsSb quantum dots. With precise control of three growth parameters, i.e. growth temperature, Sb/Ga flux ratio, and nominal coverage, we are able to grow very dense lying optoelectronically active quantum dots up to a density of 9.8×10^{10} cm^{-2} [5,6]. The wavelength can be varied in a wide range from 876 nm up to 1035 nm. For the purpose of this paper, samples are selected, which emit at ≈900 nm wavelength.

B. Sample design and fabrication

Our samples are grown on n-doped (001) GaAs wafers, see Fig. 1. The active region consists of 8 GaAsSb quantum dot layers separated by 50 nm undoped GaAs. The 1500 nm thick $Al_{0.5}Ga_{0.5}As$ claddings are p- or n-doped, respectively.

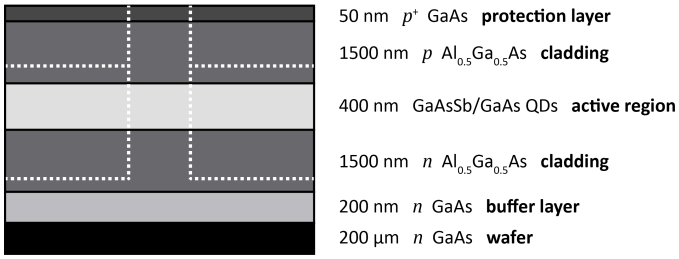


Figure 1. Laser layer design (not to scale). The white dotted lines denote the two etch depths / rib heights

The resonator length of each sample is 1000 µm, the rib width is 100 µm. To compare the laser characteristics gain-guided and index-guided lasers are prepared, the latter with two different etch depths / rib heights. Some of the index-guided samples are etched 1200 nm into the upper cladding, which is 1550 nm thick; the others are etched 3000 nm deep, i.e. through the active region into the lower cladding.

III. MEASUREMENTS

The output characteristics of all samples at different temperatures are measured under pulsed conditions with a pulse width of 1 µs and 0.1% duty cycle. The differential quantum efficiency and the threshold current density are determined. Furthermore, the characteristic temperatures are extracted from the experimental data.

A. Theoretical expectations

The gain-guided lasers have a lateral effective index step of $\Delta n_{eff} \approx 0$ and should show a higher threshold current density j_{th} and a lower differential quantum efficiency η_d than the index-guided devices acc. to [7]. By increasing Δn_{eff} the threshold current density should rapidly decrease and the differential quantum efficiency should increase. After reaching a maximum in η_d a further increase in Δn_{eff} should lead to a decrease in the differential quantum efficiency and the threshold current density should stay constant [7].

In our case Δn_{eff} is varied by definition of a rib waveguide through a standard dry etching process with different etch depths, i.e. rib heights.

B. Differential quantum efficiency

The laser output characteristics of all samples are measured in a temperature range between -180°C and -30°C, controlled

This work has been supported by the 'Deutsche Forschungsgemeinschaft' (German Science/Research Foundation) within the program 'Graduiertenkolleg 792 – Nichtlineare Optik und Ultrakurzzeitphysik' and under contract FO 157/44.

by a thermal resistor heating against LN_2 cooling of the device holder. The differential quantum efficiency η_d is calculated from the slope of the laser characteristics and the emission wavelength of 900 nm [8]. Fig. 2 shows the differential quantum efficiency η_d plotted as a function of sample temperature.

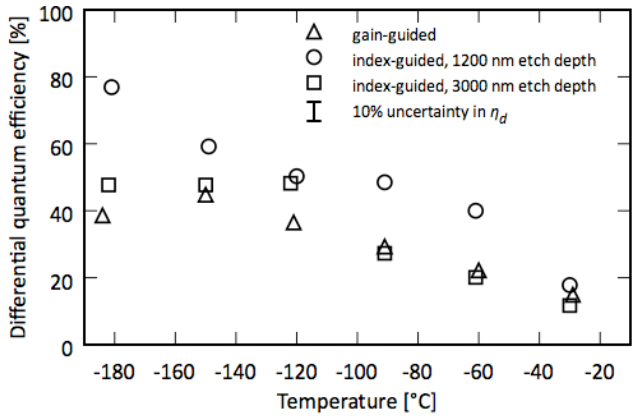


Figure 2. Differential quantum efficiency η_d plotted as a function of sample temperature for lasers with different etch depths, i.e. rib heights

Compared to the gain-guided devices the index-guided ones with 1200 nm etch depth show a higher differential quantum efficiency at all temperatures. It is up to twice as high as in the gain-guided case.

The measured η_d values for the samples etched 3000 nm deep are slightly above the gain-guided ones in the temperature range from -180°C to -120°C. However, above -120°C the differential quantum efficiency is about the same as in the gain-guiding case; obviously etching through the active region into the lower cladding brings no further improvement for η_d as expected acc. to [7] – due to the fact that the lateral mode profile is narrower than the lateral extension of the gain profile in this case.

C. *Threshold current density*

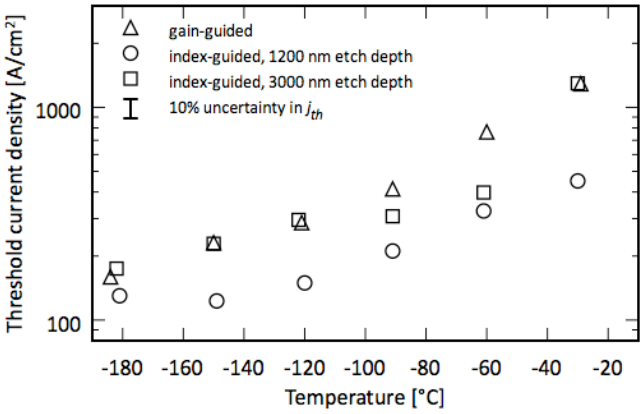


Figure 3. Threshold current density j_{th} plotted as a function of sample temperature for lasers with 1000 µm long and 100 µm wide active regions and different etch depths

The threshold current density j_{th} is determined from the same output characteristics as η_d. Fig. 3 gives the threshold current density j_{th} as a function of sample temperature.

The threshold current densities for the samples etched 3000 nm deep are in the range of those of the gain-guided devices, except for -90°C and -60°C. But very low threshold current densities are achieved for the index-guided devices with 1200 nm etch depth, i.e. only 82% to even only 35% of the value for the gain-guided devices.

D. *Characteristic temperature*

The characteristic temperature T_0 is calculated from the measured data for the temperature ranges -180°C … -120°C and -120°C … -30°C. Table 1 summarizes the results.

TABLE I. CHARACTERISTIC TEMPERATURE T_0

	gain-guided	***index-guided 1200 nm***	***index-guided 3000 nm***
-180°C … -120°C	111 K	415 K	113 K
-120°C … -30°C	56 K	93 K	45 K

Again, the devices with 3000 nm etch depth show no considerable improvement as compared to the gain-guided devices. But the devices with 1200 nm etch depth exhibit considerably higher characteristic temperatures T_0 than the gain-guided devices. Below -120°C it is 3.7-times higher and thus the devices have a much weaker temperature dependence.

IV. DISCUSSION AND CONCLUSIONS

We have reported results on edge-emitting broad area lasers with stacks of GaAsSb quantum dot layers; the dot density is 980 µm^{-2}. We have shown that strong index-guiding due to a deeply dry-etched waveguide rib can improve the output characteristics of the lasers considerably. But further etching down to a level below the active region deteriorates the performance – due to a mismatch of the lateral mode and gain profile widths and possibly due to surface trap states as a result of some rib side wall roughness. Best values achieved for the medium-deep rib and -180°C sample temperature are 77% differential quantum efficiency, 120 A/cm^2 threshold current density, and 415 K characteristic temperature.

REFERENCES

[1] K. J. Ebeling, "Integrated optoelectronics", Springer (1993)

[2] J. Tatebayashi, "Formation and optical characteristics of strain-relieved and densely stacked GaSb/GaAs quantum dots", Appl. Phys. Lett. 89 (2006) 203116

[3] J. Tatebayashi, "Lasing characteristics of GaSb/GaAs self-assembled quantum dots embedded in an InGaAs quantum well", Appl. Phys. Lett. 90 (2007) 261115

[4] K. Gradkowski, "Complex emission dynamics of type-II GaSb/GaAs quantum dots", Appl. Phys. Lett. 95 (2009) 061102

[5] T. H. Loeber, D. Hoffmann, and H. Fouckhardt, "Dense lying GaSb quantum dots on GaAs by Stranski-Krastanov growth", Proc. SPIE Phot. West vol. 7947 – Quantum Dots and Nanostructures, 79470N (2011)

[6] T. H. Loeber, "Ga(As)Sb-Quantenpunkte und -Quantenpunkt-Laser", PhD Thesis Kaiserslautern University of Technology, Verlag Dr. Hut (2011)

[7] G. P. Agrawal, "Lateral analysis of quasi-index-guided injection lasers: Transition from gain to index guiding" in Lightwave Technology, vol. LT-2 (4), pp. 537–543 (1984)

[8] L. A. Coldren, S. W. Corzine, "Diode lasers and photonic integrated circuits", Wiley (1995)

Simple and compact integrated silicon interferometer device for biosensing platforms devices

Ana Belén González-Guerrero and Laura M. Lechuga
Nanobiosensors and Bioanalytical Group
Research Center on Nanoscience and Nanotechnology
(CIN2) CSIC and CIBER
Barcelona, Spain
Anabelen.gonzalez@cin2.es

Carlos Domínguez
Micro and Nanosystem Department
Microelectronics Center (CNM-IMB), CSIC
Barcelona, Spain

***Abstract*—We have recently implemented a new interferometric device based on silicon photonics to be employed as a highly sensitive and label-free biosensor. We show here the working principle, theoretical design, fabrication, and optical and biosensing characterization of the integrated bimodal waveguide interferometer (BiMW), based on two-mode interference.**

Keywords - Bimodal Waveguide Interferometer; biosensor; two-mode-interference; integrated optics.

I. INTRODUCTION

Current diagnostic tests are expensive, require specialized personnel and equipment, and employ indirect detection methods that involve a long analysis time. Integrated optical (IO) biosensors represent an attractive alternative to these devices due to its high sensitivity and the use of a label-free detection scheme. Such devices are the most suitable candidates as transducer elements for its integration in portable lab-on-a-chip platforms (LOC) as they can be miniaturized and mass-produced, obtaining cost-effective devices. Among them, interferometric transducers present the highest sensitivity, achieving detection limits (LOD) around 10^{-7} RIU [1]. Mach-Zehnder (MZI) and Young (YI) Interferometers has been the most usual configurations. In these transducers, the Y divisor is used to split or recombine light, a critical process in order to obtain highly coherent devices. Due to the standard tolerances of current fabrication techniques, the Y-shape splitter is the most complex component of these configurations.

To overcome this limitation, we have developed [2] a simpler configuration using a single waveguide where two modes of the light interfere and we have named this new sensor bimodal waveguide interferometer (BiMW) [3]. In this device, the Y-divisor is replaced by a modal splitter consisting in a jump of the thickness of the waveguide core of several nanometers, a simple process totally compatible with standard fabrication techniques. In this work, the fundamental working principle, design of the structure, fabrication, and optical and biosensing characterization of the BiMW device are discussed.

II. WORKING PRINCIPLE

In a BiMW biosensor (see Fig. 1), the light is coupled into a single-mode rib waveguide. After some distance, the light is coupled into a thicker waveguide which supports two transversal modes. Due to the vertical asymmetry of the junction, fundamental mode of light splits in two, fundamental and first order modes which propagate till the output of the chip. In the bimodal part of the waveguide device, the cladding (cladd) is etched exposing a region of the core to the external medium, the sensor area. An interferometric pattern is obtained at the exit of the waveguide due to the different response of both modes to external changes through the evanescent field.

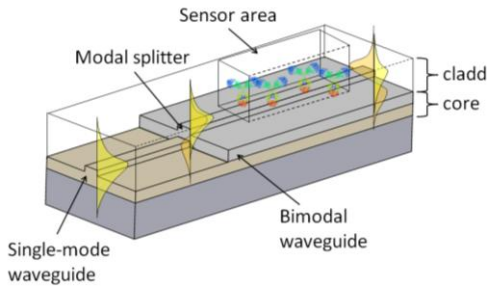


Figure 1. Scheme of a BiMW sensor.

III. SIMULATIONS AND DESIGN

The modal behavior of the light in a waveguide will depend on the thickness of the core, the width and the height of the rib, the refractive index difference between the materials of the cladding and the core, and the wavelength. Using silicon-based materials for the waveguide fabrication and visible wavelengths, our previous modelization indicates that employing SiO_2 as cladding (n=1.46) and Si_3N_4 as core (n=2.00) layers, single-mode behavior will be obtain for a core thickness down to 300 nm, a width of 4 μm, and a rib height down to 4 nm.

Taking account these previous results, we have employed the transfer matrix method to select the thickness of the core of the single and the bimodal mode part of the sensor. This approach was used to represent the profiles of the electric fields of the modes in the bimodal transversal direction (see Fig. 2). By integrating the intensities of the fields at the exit over the

upper and the lower half-planes, the modulation of the output signal as a function of the phase shift between modes can be calculated. The results indicate that in order to obtain more than 70% modulation, the single mode part must have a thickness below 160 nm. The confinement factors for both, the fundamental and first order modes in the bimodal part were calculated as 0.94 and 0.67, respectively.

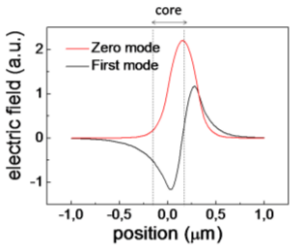


Figure 2. Distribution of the electric field of both modes in the bimodal waveguide.

The losses at the modal splitter junction were studied by two computational electrodynamics modeling algorithms, the beam propagation method (BPM) and the finite-difference time-domain method (FDTD). In BMP, only light dispersed in an angle smaller than 30-40° in the propagation direction is displayed. However, FDTD can show dispersed light for higher angles as well as retrodispersed light. Logarithmic representations of the electromagnetic fields for both algorithms (see Fig. 3) indicate that at the transition junction the quantity of dispersed light is very small, the retrodispersed light is negligible, and that the light is well-confined within the waveguide structure.

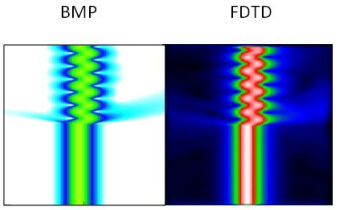


Figure 3. Logarithmic representations of the electromagnetic field in the splitter region of a BiMW device by BMP and FDTD methods.

IV. Fabrication and Characterization

The devices were fabricated using silicon-based standard microelectronics technology at Clean Room facilities. A thermal SiO_2 cladding layer (2 μm) was grown over a silicon wafer. A core layer of 340 nm of Si_3N_4 was deposited by LPCVD technique. The rib channel waveguide was defined by BHF etching using conventional photolithography. Then, the thickness of the single mode part of the waveguide was decreased to 150 nm. The wafer was covered by a protective SiO_2 layer deposited by PECVD technique. A sensing window (15 mm x 50 μm) was opened by wet etching in this layer. The wafer contains 12 chips; the size of each chip was 30 × 10 mm^2 in size and contains 16 BiMW devices.

We have done a structural characterization of the 16 rib waveguides in the same chip by Atomic Force Microscopy (AFM). An average rib width of 4.45 ± 0.02 μm and a height of 1.22 ± 0.03 nm were evaluated. The high reproducibility of the results indicates the quality of the fabrication process. A 3D AFM image of one of the waveguides is shown in Fig. 4a.

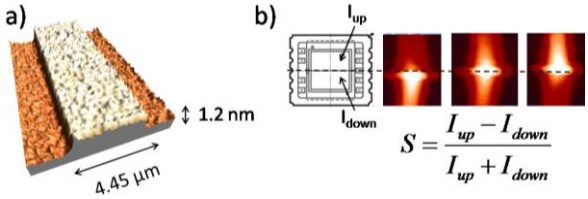


Figure 4. a) 3D AFM image of a rib waveguide and b) output signal.

For the optical characterization of the devices, TE light from a He-Ne laser (15 mW) was coupled into the waveguide using a microscope objective (40×). The interference pattern at the end of the waveguide (see Fig. 4b) was monitored using a two sectional photodiode. The light at the output generates currents I_{up} and I_{down} at the photodetector. The intensity values were used to calculate the normalized output signal (S). The system provided temperature stabilization of the chip with 0.01 degrees accuracy. Using these conditions, the fluctuations of the S parameter did not exceed 1 % during 2 h.

V. Biosensing Evaluation

A 4-channel fluidic cell was fabricated by molding PDMS with a master of PMMA (see Fig. 5a). By using a syringe pump and an injection valve, different solutions were flowed over the sensor surface to functionalize it. In this way, we have immobilized human growth hormone (hGH) by covalent bonding. Then, a 3 nM concentration of the monoclonal antibody against hGH (mAb hGH) was flowed, producing a specific biomolecular interaction which is detected in real-time by the sensor (Fig. 6). The same concentration of a nonspecific antibody (mAb BSA) gives a negligible signal.

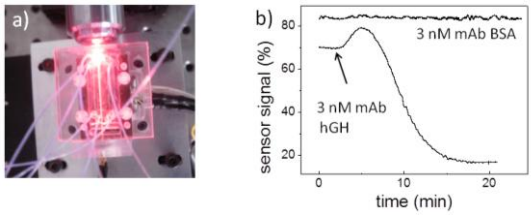


Figure 5. a) 4-channel fluidic cell and b) interferometric detection of a 3 nM of mAb hGH.

Acknowledgment

Authors acknowledge Dr. Ginés Lifante (Autonomous University of Madrid) for performing the simulations with the BMP and FDTD methods and the financial support from M. Botín foundation.

References

[1] M.C. Estevez, M. Alvarez, and L.M. Lechuga, "Integrated Optical Devices for Lab-on-a-chip Biosensing Applications", Laser Photonics Rev., DOI 10.1002/lpor.201100025.

[2] Patent PCT/ES08/070142, 12/669307 (US)

[3] K. E. Zinoviev, A. B. González-Guerrero, C. Domínguez, and L. M. Lechuga, "Integrated Bimodal Waveguide Interferometric Biosensor for Label-Free Analysis", J. Lightwave Technol., 2011, vol. 29(13), pp. 1926-1930.

Electro-optic phase modulators utilizing different phases in proton-exchanged $LiNbO_3$- waveguides

S.M. Kostritskii, Yu.N. Korkishko, V.A. Fedorov,
S.V. Rodnov
RPC Optolink Ltd, Zelenograd STMP
Moscow, Russia
skostritskii@optolink.ru

O.G. Sevostyanov
Physics Department
Kemerovo State University
Kemerovo, Russia
olsevos@yahoo.com

Abstract— ***Electro-optic coefficients of annealed proton-exchanged $LiNbO_3$ waveguides containing different phases were determined. Electro-optic phase modulators, exhibiting improved electro-optic efficiency and low optical losses have been fabricated.***

Keywords - lithium niobate; waveguides; modulators; electro-optics

I. INTRODUCTION

Optical channel waveguides in lithium niobate are a very useful technique for building a variety of integrated optical components such as modulators, splitters and switches. In many of these applications, a low-loss waveguide is essential to achieve a desired device performance. For example, the key element of fiber optical gyroscope (FOG) is the multi-function integrated optics chip (MIOC), that consists the two phase modulators and represents an active necessary part of the Sagnac interferometer [1]. Annealed proton exchange (APE) is now an established technique for fabricating integrated optical devices in $LiNbO_3$ and offers possibility of obtaining low-loss waveguiding material with a good electro-optical performance [2-4]. Even though the APE technique is quite simple technologically, the resulting waveguides exhibit complex structural contents. Our recent research has identified seven different crystallographic phases $H_xLi_{1-x}NbO_3$ (proton exchanged $LiNbO_3$) [5]. However, it was recently reported [1,3,4], that APE process reduces the electro-optical coefficients and provides some marked level of propagation loss related mainly to the guide mode leakage. In this paper, we report characterization of propagation losses and electro-optic efficiency for integrated-optical phase modulators fabricated by APE technique in $LiNbO_3$, since the fabrication conditions, allowing appropriate reduction of propagation losses and recovering electro-optic efficiency, were subjected to our detailed experimental search.

II. FABRICATION AND CHARACTERIZATION TECHNIQUES

A series of power dividers utilizing the different geometries of Y-branching and straight channel guides were delineated in X-cut $LiNbO_3$ substrates, using standard photolithographic technique. The channel width W of waveguides forming an Y-branching was varied in the range from 5.6 to 6.2 μm, where formation of a low-loss single mode channel waveguide, operating within a wavelength region from 1500 to 1580 nm, is expected [2]. To fabricate these waveguide structures with the aid of the annealed proton-exchanged (APE) technique, the substrates were proton exchanged at 175 °C for 60÷90 min in pure benzoic acid and annealed at 360 °C for 6÷8.5 hours. To fabricate the electro-optic phase modulators, the Au-electrodes are deposited around the both straight channels in the after branching section of Y-splitter with an electrode gap G = 10 – 16 μm, that is much larger than the optical mode size (~ 5.5 – 7.0 μm).

Fibre pigtailing was performed with an UV-curing adhesive for two interconnections between channel waveguides and fibre coupling chips at both input and output optical ports. The fiber used in the coupling chips was a standard 5.8-μm-core-diameter, 80 μm-outer-diameter product manufactured by RPC Optolink Ltd. Each pigtailing chips consists of a small piece of lithium niobate, having crystollagraphic orientation same with integrated-optical chip, with a narrow groove for optical fiber mounted inside with the aid of the UV-curried adhesive. Fiber pigtails of coupling chips were spliced with two fibers of an optical fiber cable transmitting cw radiation from 1550-nm laser diode to MIOC and modulated optical signal from MIOC to photodiode.

III. EXPERIMENTAL RESULTS AND DISCUSSION

To study electro-optical efficiency of the phase modulators fabricated at the different technological conditions, we have measured a half wave voltage V_π. In our case of X-cut, Y-propagating geometry of single-mode APE $LiNbO_3$ waveguides V_π is inversely proportional to effective value of electro-optic coefficient r_{33} [3,4]. Thus, if the overlap factor F is known, V_π can be evaluated from a value of r_{33} for actual phase composition, $H_xLi_{1-x}NbO_3$, of waveguide:

$$V_\pi = (\lambda G / n_e^3 r_{33} L F) \qquad (1)$$

where L is interaction length, i.e. length of electrodes in each arm, λ - wavelength of guided light, what was 1534 nm in our experiments, n_e -effective refractive index for TE_0 mode. The overlap factor F depends on the applied field and mode intensity profiles. The main uncertainty in F is due to random variation of mode profile, as the uncertainty of applied field profile can be eliminated entirely by choosing an electrode configuration, which produces an uniform electric field within the waveguides.

It has been found that the highest electro-optic efficiency and, hence, largest value of r_{33} = 30.2 pm/V are observed with modulators utilizing the lowest strained α-phase waveguide. The modulators with higher strained α-phase waveguides show significantly smaller values of r_{33} in the range of 22.5 to 24.3 pm/V, when strain $\varepsilon_{33} \geq 0.8*10^{-3}$ [5]. However, these values are rather interesting for practical application due to good mode confinement in the highly strained α-phase waveguides, that in contrast to the poor mode confinement in the less strained α-phase waveguides. This point is principal at fabrication of the real devices via fiber pigtailing. Application of the longer annealing (for 7.5 – 8.0 hours) has allowed to increase the effective values of electro-optic coefficient r_{33} in the highly strained α-phase waveguides up to 26.4 – 27.2 pm/V. After this annealing, the modulators keep a rather good mode confinement at satisfactory matching with a standard PM-fiber, providing low insertion losses ~2.4 dB, and have improved electro-optical efficiency with V_π = 1.7 ÷ 1.8 V for a MIOC, that utilizes two phase modulators in push-pull operation mode.

IV. OPTIMIZATION OF FABRICATION PROCESS WITH AID OF OPTICAL SPECTROSCOPY DATA

The optical absorption spectroscopy data in visible and near UV ranges were used to evaluate the electro-optical properties of proton-exchanged waveguides in $LiNbO_3$ crystals, as the shift of fundamental absorption edge has been related to the changes of spontaneous polarization P and electro-optical coefficients r_{33} [6]. Interestingly, the electro-optic coefficients estimated from optical spectra for the α, κ and β_i phases are larger than those measured by direct method. The difference may be attributed to the effect of screening (averaging over multiple crystalline phases) in strongly nonuniform layers, which reduces the "effective" value of r_{33} of the low-stress phases, as determined by direct measurements.

The phase composition of the novel waveguide structures formed with APE has been determined by Raman spectroscopy data. Raman spectroscopy study was performed with the aid of a Renishaw Ramascope spectrometer operating at the 632.8 nm and 785 nm excitation wavelengths. In the setup, a linearly polarized laser beam was focused, using a 50× objective, to approximately a 2 μm spot on the optical-grade polished endface of a waveguide under study.

The optimal fabrication conditions for obtaining homogeneous waveguiding layers via the APE techniques can be identified, using this method. It is important to note that even though different-phase waveguides prepared by APE technique have similar refractive indices and strains, there is likely to be a principal difference in some properties (including electro-optic ones [1,5,6]) of these waveguides as formed by this technique at the different fabrication conditions. Indeed, it was reported recently [5] that the dispersion of extraordinary refractive-index increment in the higher strained α-phase and β-phase waveguides formed by APE method was higher compared to that in the low-strained α-phase waveguides. Given these advantages, the control of an exact phase composition of $H_xLi_{1-x}NbO_3$ waveguide is expected to improve the performance of a MIOC device as well. Since no attempts have been reported thus far, an investigation into this possibility is in order and presents an essential task of the proposed effort.

It is worth noting that optical absorption spectroscopy data have suggested a non-monotonic dependence of r_{33} on hydrogen concentration x and strain ε_{33} ($\varepsilon_{33} \sim x$) with a minimum r_{33} reached at intermediate values of x that correspond to the κ and β_1 phases. On the contrary, the direct measurements of electro-optical efficiency of modulators show that the electro-optic effect monotonically decreases as the strain increases. The discrepancy may be ascribed to a significant disordering of crystalline layers and its effect on the r_{33} of a given phase. Our Raman data provide direct evidence of a high degree of such disordering, as a marked broadening of the Raman lines in waveguides with $\varepsilon_{33} \geq 0.7\times10^{-3}$ is clear indicative of the disorder-induced phonon damping. Low-temperature annealing, performed at 85 ^oC to 100 ^oC, is found to be effective to reduce disordering in the higher-strain α-phase waveguides. It is important to note, that compared to the low-strained α-phase, the high-strained phase has a much larger refractive index increment, which enables a better mode confinement and allows sharper waveguide bends, as confirmed by a comparative analysis of the MIOCs utilizing waveguides fabricated with the differently strained α-phase compositions.

V. SUMMARY

The experimental samples of phase modulator fabricated at the optimal technological conditions exhibit the improved electro-optical efficiency with superior propagation and insertion losses compared to the common APE:$LiNbO_3$ modulators. The electro-optical efficiency has been gained by appropriate choice of exchange/annealing ratio.

REFERENCES

[1] S.M. Kostritskii, Yu.N. Korkishko, V.A. Fedorov, A.N. Alkaev, V.S. Kritzak, P. Moretti, S. Tascu, and B. Jacquier, "Leakage of a guided mode caused by static and light-induced inhomogeneities in channel HTPE-$LiNbO_3$ waveguides," Proc. SPIE, vol. 4944, pp. 346-352, 2003.

[2] S.T. Vohra, A.R. Mickelson, and S.E. Asher, "Diffusion characteristics and waveguiding properties of proton-exchanged and annealed $LiNbO_3$ channel waveguides," J. Appl. Phys., vol. 66, pp. 5161-5174, 1989.

[3] Yu. N. Korkishko, and V.A. Fedorov, "Structural phase diagram of $H_xLi_{1-x}NbO_3$ waveguides: The correlation between optical and structural properties," IEEE J. of Selected Topics of Quantum Electron., vol. 2, pp.187-196, 1996.

[4] R. Narayan, "Electrooptic coefficient variation in proton-exchanged and annealed lithium niobate samples," IEEE. J. of Selected Topics in Quantum Electron., vol. 3, pp.796-807, 1997.

[5] Yu. N. Korkishko, V.A. Fedorov, and S.M. Kostritskii, "Optical and X-ray characterization of $H_xLi_{1-x}NbO_3$ phases generated in proton-exchanged $LiNbO_3$ optical waveguides," J. Appl. Phys., vol. 84, pp.2411-2419, 1998.

[6] S.M. Kostritskii, Y.N. Korkishko, V.A. Fedorov, M.V.Proyaeva, and E.A. Baranov "Spontaneous polarization and nolinear susceptipility of various $H_xLi_{1-x}NbO_3$ phases," Technical Physics, vol. 72, pp. 76-82, 2002.

Integration and Packaging of Optoelectronic and Silicon Photonic Chips on a µm-scale SOI Platform

Timo Aalto, Mikko Harjanne, Markku Kapulainen and Sami Ylinen
VTT, Espoo, Finland
firstname.lastname@vtt.fi

***Abstract*—An overview of an integration platform with 1–10 µm thick silicon-on-insulator waveguides is given. It is suitable for the integration and packaging of optoelectronic and silicon photonic (nm-scale) chips. The platform can also contain many passive functions, such as spot-size converters, couplers, wavelength (de)multiplexers/filters and polarization splitters. The footprint of the platform is minimized by using multi-step patterning to realize e.g. mirrors and short MMI couplers.**

Keywords: Silicon-on-insulator; SOI; integration platform; silicon photonics; optoelectronics; hybrid integration; packaging

I. INTRODUCTION

Development of single mode (SM) silicon-on-insulator (SOI) waveguides started in early 1990's and has also been carried out at VTT since 1997. With deep UV lithography the dimensions of SOI waveguides have been reduced from micrometers to <100 nm, and advanced photonic circuits have been realized on nm-scale SOI platforms [1]. At the same time also III-V compound semiconductor optoelectronics has evolved significantly and is now widely used in numerous application areas, such as optical communication, consumer electronics, lighting and sensing. Heterogeneous integration [1–3] has also been developed to combine the complementary benefits of III-V optoelectronics and Si photonics. Increasing the level of integration aims to improve device performance and to reduce cost, power consumption and footprint. To exploit the new technologies in a wide range of applications, and to tackle the thermal and I/O coupling challenges also new packaging methods must be developed [1–3].

This paper first presents a generic platform on 1–10 µm thick SOI that is used to hybrid integrate optoelectronic chips on a passive photonic SOI circuit. A new packaging concept that can be used to integrate also Si (nano)photonic chips, to provide hermetic sealing and to couple light with large fiber arrays is then proposed.

II. PHOTONIC CIRCUITS ON THE SOI PLATFORM

Silicon-on-insulator wafers and chips are here used as a generic integration platform. In general the device layer thickness can be anything from <1 to >10 µm, but here we mainly concentrate on 4 and 10 µm SOI layers where most of the devices reported here have been built. Single mode rib waveguides can be easily realised by dry etching ~50 % of the SOI layer thickness. With an additional ~50% etch step it is possible to gradually convert the rib waveguide into a multi mode strip waveguide without exciting the higher order modes. The same etch step can be used to locally reduce the waveguide thickness, e.g. to achieve better coupling to other optical chips. This multi-step patterning concept is also used to realize and improve many other waveguide components. [1]

The minimum bending radii of rib waveguides are strongly dependent on the SOI thickness, but photonic circuits with small footprint can be realized even on 10 µm SOI using mirrors to turn light horizontally. Also up-reflecting mirrors have been demonstrated to enable optical coupling from/to surface-active optoelectronic components, as well as for wafer-level testing. These wet-etched and metal-coated mirrors are placed behind antireflection (AR) coated waveguide facets. Such facets can also be placed at the edges of the SOI chips to enable reflection-free I/O coupling to e.g. optical fibers.

Passive couplers (1x2, 2x2 etc.) are the basic building blocks of waveguide circuits and they have been demonstrated in various directional, multimode interference (MMI) and adiabatic coupler configurations on SOI. Through-etched MMI 2x2 couplers can be made as short as 285 µm in 4 µm SOI, while adiabatic couplers can have >20 dB extinction ratio (ER) and <1 dB insertion loss at >100 nm bandwidth. Couplers have also been cascaded into Mach-Zehnder interferometers (MZIs) to realize thermo-optic (TO) switches (up to 333 kb/s [5]), wavelength multiplexers and polarization splitters. Also arrayed waveguide gratings (AWGs) have been realized on SOI. By using back-reflecting mirrors and a single star coupler it is possible to realise compact AWGs even on 10 µm SOI. Some SOI waveguide components are illustrated in Fig. 1 and some measured component characteristics are listed in Table I.

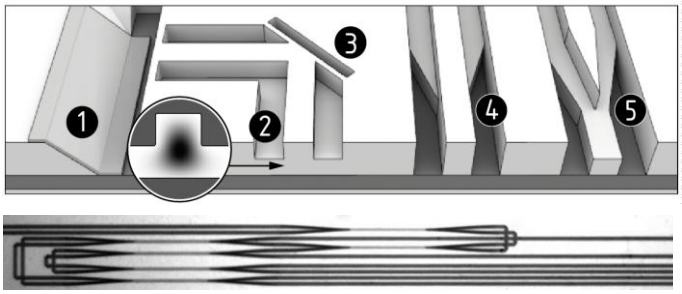


Figure 1. Illustration of some key optical components: 1) Up-reflecting mirror, 2) Single mode rib waveguide, 3) Horizontal mirror, 4) Rib-strip converter, and 5) Vertical taper (above). Microscope image of a compact four-channel MUX built using asymmetric MZIs and horizontal mirrors (below).

This work has been partially funded by Tekes under the FLIPSOI project (Dno. 743/31/09) and by the European Space Agency (ESA) under ESTEC contract No 20174/06/NL/PM (OTUS).

TABLE I. MEASURED PERFORMANCE EXAMPLES ON SOI

Component (SOI thickness)	**Performance**	**Property**
SOI rib waveguide (4/10 µm)	0.1 dB/cm	Propagation loss
Vertical taper (4→2 µm)[a]	0.2 dB	Insertion loss
Rib-strip converter (4/10 µm)	0.05 dB	Insertion loss
Horizontal mirror (4 µm)[a]	0.3 dB/90°	Insertion loss
2x2 coupler (4 µm)[a]	0.3 dB	Insertion loss
TO switching/tuning (4/10 µm)	<1 µs	Response time
Polarisation splitter (4 µm)[a]	>10 dB	Extinction ratio
AWG (4 µm)[a] (depending on number of channels)	2–6 dB 20–30 dB	Insertion loss Extinction ratio

a. Similar values measured/expected for other SOI thicknesses in 4–10 µm range

III. HYBRID INTEGRATION ON THE SOI PLATFORM

There are three main methods to bond optoelectronic chips on the SOI waveguide platform, or on Si in general, namely soldering (e.g. with AuSn), thermo compression (TC) and adhesive bonding. In this paper we concentrate on Au-Au TC bonding and adhesive bonding. Some examples of optoelectronic chips bonded on SOI are illustrated in Fig. 2.

Thermo compression with ~0.5 µm thick Au contact pads has been used to bond laser diodes, mode-locked lasers (MLLs), comb lasers and semiconductor optical amplifiers (SOAs) on 4 µm SOI and Si platforms. By accurately measuring the depth of the flip-chip mounts on SOI and by fine tuning the thickness of the deposited dielectric and metal films the vertical alignment between the optical axes of the SOI waveguides and the optoelectronic chips can be controlled with ±100 nm accuracy. The horizontal alignment accuracy is typically ±1 µm, but in some cases it can be as good as ±500 nm. No performance degradation has been observed in the TC-bonded chips. An example of the measured performance of the optoelectronic assemblies is >10 dB net gain (incl. coupling losses) per SOA in hybrid integrated SOA bars that contain 11 SOAs per chip.

Single photodiodes and 4-ch photodiode arrays have been integrated on SOI using both TC and adhesive bonding. Top-illuminated photodiodes with integrated polymer prisms where TC bonded on SOI so that light from AR-coated SOI waveguide facets was reflected inside the prisms towards the flip-chip bonded photodiodes [6]. These single photodiodes were also able to collect light from 10 SOI waveguides that formed a star-coupler in front of the polymer prism. The inter-waveguide non-uniformity of the responsivity was <0.05 A/W, while the absolute responsivity of >0.7 A/W was almost as high as in the discrete chips. And finally, back-illuminated photodiodes were glued on top of up-reflecting mirrors fabricated on SOI.

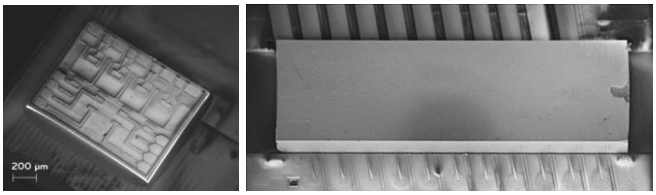


Figure 2. Active devices integrated on the SOI platfrom: Four-channel back-illuminated PD array (left) and 11-channel SOA array (right).

IV. SOI-BASED PACKAGING

Packaging method for an optoelectronic assembly should be selected based on the application-specific needs for mechanical protection, temperature control, electrical and optical I/O coupling, hermetic sealing etc. Conventional concepts use metals, ceramics and polymers as packaging materials [1–3], and these can also be used with the SOI platforms described here. However, in this paper we propose a new packaging concept (see Fig. 3) that combines chip-to-wafer bonding, through-silicon vias (TSVs), wafer-level sealing with a Si cap and passive fiber alignment. Most of these building blocks have already been demonstrated and in future they will be combined to realize advanced optoelectronic modules that provide significant cost and size reductions, improved thermal management and low I/O coupling losses. This Si/SOI-based packaging concept can be used for both optoelectronic and Si (nano)photonic chips. By default the platform will be based on 10 µm SOI equipped with vertical tapers and up-reflecting mirrors to achieve good coupling to standard SM fibers and to all hybrid-integrated devices, with wide bandwidth and low polarization dependency.

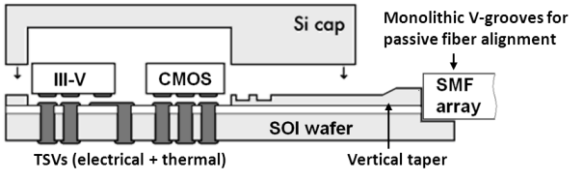


Figure 3. Simplified illustration of the proposed packaging concept.

ACKNOWLEDGMENT

The authors thank Ville Vilokkinen from Modulight Oy, Ludwig Mörl from Heinrich Hertz Institute, Mircea Guina from Tampere University of Technology, Vladimir Mikhrin from Innolume GmbH and Marcel Kroh from u2t Photonics AG for providing the optoelectronic chips for the hybrid integration experiments.

REFERENCES

[1] C. Kopp et al., "Silicon photonic circuits: On-CMOS integration, fiber optical coupling, and packaging," IEEE J. Sel. Top. Quantum. Electron., vol. 17, pp. 498–509, May/June 2011.

[2] L. Zimmermann, G. Preve, T. Tekin, T. Rosin, and K. Landles, "Packaging and Assembly for Integrated Photonics—A Review of the ePIXpack Photonics Packaging Platform," IEEE J. Sel. Top. Quantum. Electron., vol. 17, pp. 645–651, May/June 2011.

[3] T. Tekin, "Review of packaging of optoelectronic, photonic, and MEMS components," IEEE J. Sel. Top. Quantum. Electron., vol. 17, pp. 704–719, May/June 2011.

[4] K. Solehmainen et al., "Development of multi-step processing in silicon-on-insulator for optical waveguide applications," J. Opt. A: Pure Appl. Opt., vol. 8, pp. S455-S460, 2006.

[5] M. Harjanne, M. Kapulainen, T. Aalto, and P. Heimala, "Sub-µs switching time in silicon-on-insulator Mach-Zehnder thermo-optic switch," Photonics Technol. Lett., vol. 16, pp. 2039-2041, 2004.

[6] L. Moerl et al., "Optical coupling of planar III-V pin photodiodes and SOI waveguides using an integrated BCB prism," Proc. IPRM 2010 (Kagawa, Japan, 31 May - 4 June 2010), pp. 1-4, 2010.

Silicon-On-Insulator Chip-to-chip coupling via Vertical Grating Couplers

Miguel Cabezón, Ignacio Garcés, Asier Villafranca
Photonics Technology Group
I3A – University of Zaragoza
Zaragoza, Spain
mcabezon@unizar.es

José Pozo, Pragati Kumar, Andrzej Kaźmierczak
TNO
Delft, Netherlands
jose.pozo@tno.nl

***Abstract*— We present an experimental study on feasibility and tolerance of the interconnection of Silicon-on-Insulator photonic circuits via vertical grating couplers using standard ePIXfab building blocks. Chip to chip coupling efficiency of 2.6dB has been found.**

SOI, Silicon-on-Insulator, Integrated photonics, Vertical Grating Coupler (VGC)

I. INTRODUCTION

During the last years Silicon-on-Insulator (SOI) technology has emerged as one promising platform for integrated optics due to the high refractive index contrast between the core and the cladding of the waveguides. In recent years, the large mismatch in the mode size and mode shape between a SOI waveguide and optical fibers appeared to be one of the main drawbacks of SOI photonics. It has led to extensive research on efficient fiber-to-chip coupling methods. The most accepted solution for this is the employment of Vertical Grating Couplers (VGCs) [1]. They can be placed anywhere on the chip without the necessity of complex back-end process i.e. end-facet polishing. Standard VGCs are already offered as building blocks by foundries, like ePIXfab. [2]. The principle of operation of VGCs, however, is beneficial for other applications too such as vertical stacking of Photonic Integrated Circuits (PICs) [3], as it would help in increasing the integration density.

In this paper such possibilities are discussed by presenting results from the experimental measurements on coupling efficiency between two SOI PICs via standard VGCs. Tolerances to misalignment are also provided in the three spatial dimensions.

II. EXPERIMENTAL SETUP

The experiment envisaged the use of two identical chips containing standard SOI waveguides. The light injection and extraction were carried out by the means of VGCs connected at both ends of high-confinement waveguides by tapers. The same VGCs were used for chip-to-chip and fiber-to-chip coupling. The VGCs are made up of 25 sections of 630 nm period, 70 nm etched gratings on a standard ePIXfab SOI process [1]. Waveguides at this point are 10-um wide and coupled via tapers to 440 nm wide waveguides. The area of the grating is therefore $10 \times 15\ \mu m^2$. A standard SMF was aligned to the grating at an optimum incident angle of 8 degrees. Afterwards, the fiber was attached to the chip with the aid of a polymer cube to increase stability and resistance of the junction, as can be seen in figure 1. Both the fiber and the cube are glued to the chip; the fiber end remains immersed in the glue after drying up, avoiding transitions trough air and reducing the differences between the refractive indices.

The photonics chips were placed horizontally facing each other. This means light has to go through 3 grating interfaces: fiber-to-chip, chip-to-chip and chip-to-fiber. As shown in figure 1, the lower chip was fixed, while the upper one was attached to a six-axis micro-positioning system. Although such system does not allow measurement of the exact position, it was optimized to obtain the maximum coupling efficiency between the chips and tolerances were measured in the correspondent range around it. The light of a tunable laser at 1550 nm was used to excite the chips using a polarization controller, since VGCs have high polarization dependence.

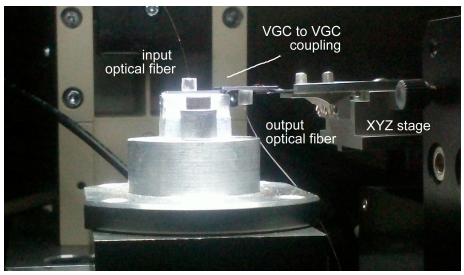


Figure 1. Experimental setup

In order to extract the effect of the chip-to-chip coupling from the whole transmission response, the chips were characterized separately. A multimode fiber (radius of 62.5 μm) was aligned to the output VGC of each chip. The area of the fiber core is much wider than the area of the grating that is about $15\times10\ \mu m^2$, being capable of collecting most of the light coming out of the chip. Losses from the SMF input fiber to the multimode fiber showed 14.3 dB and 10.6 dB insertion losses, respectively. These values are used later as a reference to extract the chip-to-chip coupling efficiency.

III. MEASURED TOLERANCES

The minimum loss achieved for the whole system (from the input to the output fiber) was 27.5 dB; which, according to the

losses measured for each fiber-to-chip interface, leaves a chip-to-chip coupling efficiency of – 2.6 dB. The following measurements are referred to this optimum alignment.

A. *Lateral displacement*

Figure 2 shows the variation of coupling efficiency with respect to the lateral displacement of the upper grating; in other words, when it is horizontally shifted in the direction across the waveguide axis.

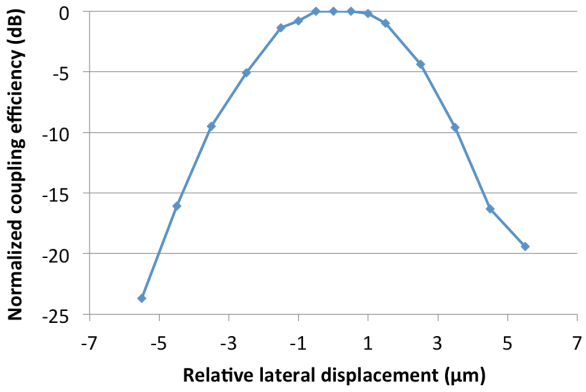


Figure 2. Variation of coupling efficiency with respect to lateral displacement.

As expected, the response is essentially symmetrical and remarkably flat in a range of about 1 micrometer around the maximum. A 3 dB tolerance allows up to 2 µm misalignments in both directions, still symmetrical and gets irregular only for lateral shifts beyond 4 µm.

B. *Longitudinal displacement*

Figure 3 shows the variation of coupling efficiency with respect to displacements of the upper grating along the axis of the waveguide. Negative displacement means increasing the area where the two chips are overlapped. On the other hand, positive displacement means horizontally separating the chips.

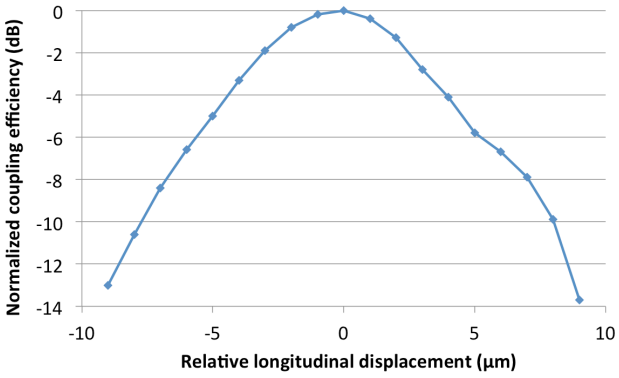


Figure 3. Variation of coupling efficiency with respect to longitudinal displacement

The same displacement implies less overlap reduction between VGCs here than in previous measurement, for this reason, the longitudinal response decays slowly, giving a 3-dB tolerance of ± 4 µm.

It must be noted here that 0 displacement does not mean that the VGCs are completely overlapped; it just refers to the optimum alignment, which may be achieved at a certain longitudinal offset.

C. *Distance between VGCs*

First measurements on vertical displacements did not provide sufficient resolution, since the coupling efficiency showed a periodic response with respect to the separation between the two chips, with a period of about 1 µm. Further investigation was made with the aid of piezoelectric transducers and the result is presented in Figure 4.

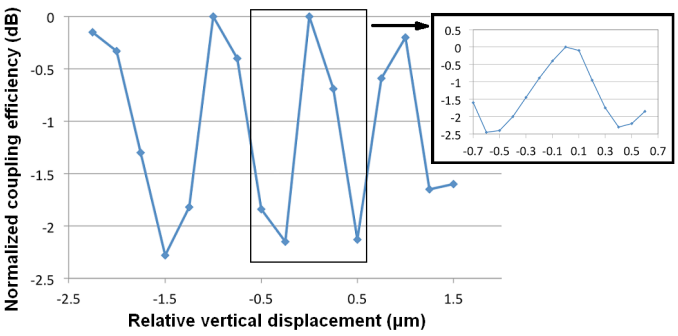


Figure 4. Variation of coupling efficiency with respect to vertical displacement.

The coupling efficiency is clearly sensitive to the displacements in the vertical direction. However, its deviation stays within a range of 2.5 dB, which may be affordable for some applications.

IV. Conclusion

We have measured chip-to-chip coupling efficiency via VGCs on similar waveguides fabricated on standard SOI process. It turns out to be substantially better than the fiber-to-chip coupling since it does not have to deal with mode mismatch between the rectangular waveguides and the circular core of the fiber. We also provide tolerance to misalignments in the 3 dimensions, which will be useful for the future studies of different chip interconnects.

Acknowledgment

This work was partly supported by the Ministerio de Ciencia e Innovación under Grant TEC2010-19418.

References

[1] G. Roelkens, D. Van Thourhout, and R. Baets, "High efficiency grating coupler between silicon-on- insulator waveguides and perfectly vertical optical fibers," Opt. Lett. 32, 1495-1497 (2007)

[2] http://epixfab.eu/

[3] Villalaz, R., Gaylord, T.K. & Meindl, J.D., Quasi-free-space optical coupling between diffraction grating couplers fabricated on independent substrates. *Applied Optics*, 43(29), 5468-5475 (2004)

Rib waveguides fabricated by surface structuring with a femtosecond laser on (Yb,Nb):RTP/RTP epilayers

J. Cugat, R. Solé, J. Massons, X. Mateos, J.J. Carvajal, M.C. Pujol, F. Díaz and M. Aguiló*.
Física i Cristal·lografia de Materials i Nanomaterials (FiCMA-FiCNA)-EMaS. Universitat Rovira i Virgili (URV), Campus Sescelades, c/ Marcel·lí Domingo s/n E43007 Tarragona, Spain. *magdalena.aguilo@urv.cat

A. Ruiz de la Cruz and J. Solis
Instituto de Óptica "Daza de Valdés" (CSIC) Serrano 121, Madrid 28006, Spain

***Abstract*- Channel waveguides in (Yb,Nb):$RbTiOPO_4$/$RbTiOPO_4$ epitaxial layers were fabricated by surface structuring with a femtosecond laser. The channel waveguide modes were successfully excited at 632 nm and simulations of the rib channel at the same wavelength show a high level of light confinement. The output near field pattern of the modes showed a Gaussian shape and the losses obtained were about 2.5 dB/cm. Type II second harmonic generation radiation at 1137 nm has been successfully obtained.**

Keywords: Nonlinear optical crystal, $RbTiOPO_4$, Liquid Phase Epitaxy, waveguides, laser ablation.

I. INTRODUCTION

Rubidium titanyl phosphate, $RbTiOPO_4$ (hereafter RTP) is an interesting nonlinear optical crystal due to its high nonlinear optical and electrooptical coefficients [1]. The doping of RTP with lanthanide ions has attracted the attention because it offers the possibility to merge the nonlinear optical properties of the crystal with the lanthanide emission to obtain a self-doubling material. Among the lanthanide elements, Yb^{3+} has special interest because of its emission at a wavelength close to 1 μm, its simple energy scheme, which consists of only two energy levels, its low quantum defect and high lifetime. The codoping of RTP with Nb^{5+} and Yb^{3+} allows us to obtain an Yb^{3+} concentration in the RTP structure, which is enough for lasing [2]. However, the presence of Nb^{5+} in the crystal structure contributes to decrease the growth rate and increases the stress in the crystal, which often causes defects in the bulk crystal. Due to these bulk crystal defects, as well as the interest to obtain large optical paths, the growth of (Yb,Nb):RTP/RTP epitaxial layers became an alternative [3]. Planar waveguides obtained using this method showed efficient type II Second Harmonic Generation (SHG) [4].

The aim of this work is to study and characterize the microstructuring of (Yb,Nb):RTP/RTP epitaxial layers by femtosecond laser ablation to obtain rib waveguides with high light confinement and low propagation losses.

II. LIQUID PHASE EPITAXIAL GROWTH

Epitaxial layers of (Yb,Nb):RTP were grown on **c** oriented RTP substrates by the Liquid Phase Epitaxy method (LPE), using self-flux solutions. The solution composition was Rb_2O-P_2O_5-TiO_2-Yb_2O_3-Nb_2O_5 = 40.8-27.2-29.76-1.92-0.32, in mol %. After accurately determining the saturation temperature, the substrate, previously cleaned as it is explained in reference [5], was dipped in the solution at a temperature 1 K above the saturation temperature to dissolve the outer part of the substrate. After dissolving for 5 minutes, the solution temperature was decreased up to 2 K below the saturation one to growth the epitaxial layer for several hours. During all the process, the rotation was maintained at about 40 rpm.
The chemical composition of the epitaxial layer was measured by Electron Probe Microanalysis (EPMA) and was $RbTi_{0.971}Yb_{0.015}Nb_{0.014}OPO_4$.

III. FEMTOSECOND LASER SET-UP AND EXPERIMENTAL CONDITIONS

The experimental set-up used to fabricate the channels is shown in Figure 1. A pulsed fs-laser amplification system, with 1 KHz repetition rate and pulse duration of 120 fs was used. The output energy was 1 mJ and the central wavelength was 799 nm. A SLM Hamamatsu X8267 spatial light modulator was used to control the beam wavefront, allowing us to design the intensity of the profile of the focused beam.

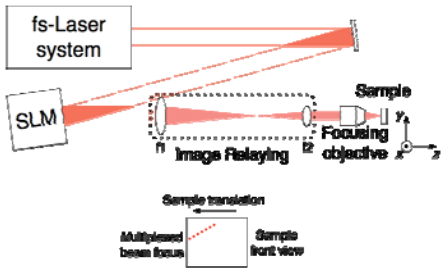


Figure 1. Experimental set-up used to inscribe the superficial channels for the fabrication of waveguides. The focused beam is multiplexed into seven spots, allowing to perform the approximation scanning technique in a single scan.

This work was supported by the Spanish Government under projects TEC2010-21574-C02-02, MAT2011-29255-C02-02, PI09/90527 and by the Catalan Authority under project 2009 SGR235 and partly supported by the EC under the 7th FP, under project Cleanspace, FP7-SPACE-2010-1–GA-263044**.** J. Cugat thanks the Spanish Government for fellowship BES-2009-024190.

To improve the quality of the micromachined channels, we used the approximation scanning method [6]. The SLM was used to multiplex the irradiation beam in seven spots arranged in a diagonal manner, as can be seen in Figure 1. Each spot rewrites the channel written by the previous one, but with a slight lateral displacement.

IV. WAVEGUIDING AND SECOND HARMONIC GENERATION CHARACTERIZATION

A Simulation of the light confinement at a wavelength of 632 nm using the MG Finite Difference method from OlympIOs package software was carried out. We used a trapezoidal channel rib of 13 µm at the top part, a base of 17 µm and 8 µm depth and took into account the refractive indices of the layer and the substrate (1.8956 and 1.8898 at 632 nm, respectively). The confinement obtained in this case was close to 90 %.

Previously to studying the channel waveguides modes and the Type II Phase Matching (PM) Second Harmonic Generation (SHG), the faces perpendicular to the channels direction were polished.

Using the rib waveguide of 13 µm at the top part, the channel waveguide modes were excited at 632 nm and the near field pattern obtained at this wavelength shows a Gaussian profile, as it is shown in Figure 2.

The transmission losses of the rib waveguide were obtained using the expression: Losses=(10/d).log(P_{out}/P_{in}), were d is the waveguide length and P_{out} and P_{in} are the corrected output and input powers. The corrections applied were the Fresnel losses, the objective microscope transmission losses and the mismatch between the spot after the input objective and the rib area. The losses obtained were around 2.5 dB/cm, which is lower than those previously obtained also by fs-laser surface structuring [7] and of the same order than those obtained by ultrafast laser inscription in the crystal bulk [8] in other materials.

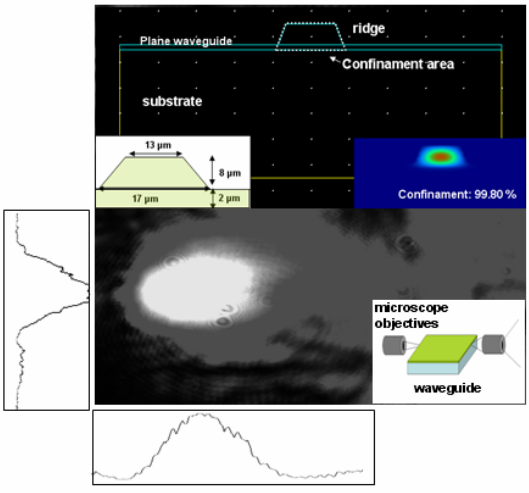


Figure 2. CCD picture of the near field pattern of the mode obtained at a wavelength of 632 nm and the profiles measured at centre of the mode.

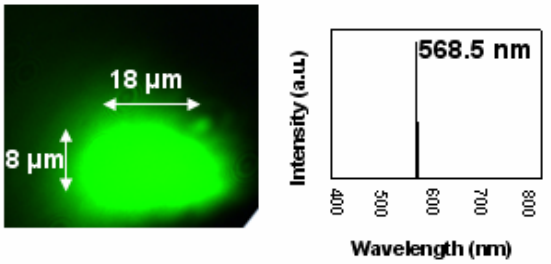


Figure 3. Type II SHG in a (Yb,Nb):RTP rib waveguide from a fundamental radiation of 1137 nm.

A tunable OPO was used to generate radiation with the wavelength required to obtain efficient SHG. The maximum second harmonic efficiency was obtained with a fundamental light of 1137 nm coupled to the channel waveguide parallel to ***a*** with a microscope objective. The second harmonic radiation, with a wavelength of 568.5 nm, was observed with a CCD camera and it is shown in Figure 3.

V. CONCLUSIONS

Femtosecond-laser micromachined rib waveguides were successfully fabricated on (Yb,Nb):RTP epitaxial layers grown on RTP substrates. Numerical simulations of the light confinement in the ribs show confinements close to 90 % at 632 nm. The channel waveguide modes were successfully excited at the same wavelength and the near field pattern obtained showed a Gaussian shape with high symmetry. The transmission losses were around 2.5 dB/cm. Finally, type II PM SHG was obtained from a fundamental radiation of 1137 nm.

REFERENCES

[1] M.E. Hagerman, K. R. Poeppelmeier, “Review of the structure and processing-deffect-property relationships of potassium titanyl phosphate-A strategy for novel thin film photonic devices,” Chem. Mater. , vol7, pp 602-621, 1995.

[2] X. Mateos, V. Petrov, A. Peña, J.J. Carvajal, M. Aguiló, F. Díaz, P. Seconds and B. Boulanger, “Laser operation of Yb^{3+} in the acentric $RbTiOPO_4$ codoped with Nb^{5+},” Optics Leters, vol 32, pp 1929-1931, 2007.

[3] J. Cugat, R. Solé, J.J. Carvajal, M.C. Pujol, X. Mateos, F. Díaz and M. Aguiló, “Crystal growth and characterization of $RbTi_{1-x-y}Yb_xNb_yOPO_4/RbTiOPO_4$ (001) non-linear optical epitaxial layers,” Cryst. Eng. Comm., vol 13, pp 2015-2022, 2011.

[4] J. Cugat, R. Solé, J.J. Carvajal, X. Mateos, M.C. Pujol, J. Massons, F. Díaz and M. Aguiló, “Efficient Type II phase-matching second-harmonic generation in $Ba:Yb:Nb:RbTiOPO_4/RbTiOPO_4$ waveguides,” Optics Letters, vol 36, pp 1881-1883, 2011.

[5] R. Sole, V. Nikolov, a. Vilalta, J.J. Carvajal, J. Massons, Jna. Gavaldà, M. Aguiló and F. Díaz, “Liquid phase epitaxy of $KTiOPO_4$ on $KTi_{1-x}Ge_xOPO_4$ substraes,” J. Cryst. Growth, vol 237-239, 602-607, 2002.

[6] J. Gottmann, G. Schlaghecken, R. Wagner and E.W. Kreutz, “ Fabrication of erbium-doped planar waveguides by pulsed-laser deposition and laser micromachining, “ Onference on Laser Micromachining for Optoelectronic Device Fabrication. Edited by Ostendorf, vol 4941, pp 148 (2003).

[7] D. Wortmann, J. Gottmann, “Fs-laser sttructuring of ridge waveguides,” Appl. Physics A, vol 93, pp 197-201, 2008.

[8] F.M. Bain, W.F. Silva, A.A. Lagatsky, R.R. Thomson, N.D. Psaila, A.K. Kar, W. Sibbett, D. Jaque, C.T.A. Brown, “ Microspectroscopy of ultrafast laser inscribed channel waveguides in Yb:tungstate crystals,” Appl. Physics Letters, vol 98, article nº 141108, 2011

Design and Simulation of a Photonic Crystal Cavity in InP-based Membranes On Silicon

R. Zhang[1], J.J.G.M. van der Tol[1] and M.K. Smit[1]
[1]COBRA Research Institute, Technische Universiteit Eindhoven. Address: P.O. Box 513,5600 MB Eindhoven, The Netherlands

***Abstract*— We aim to make an electrically pumped photonic crystal laser in InP-based membrane on Si. A "W1 like" photonic crystal cavity is designed and simulations show good performance in terms of quality factor and manufacturing tolerance.**

Keywords-photonic crystal laser;electrical pumping; InP_based menbrane bonded on Si; manufacturing tolerance

I. INTRODUCTION

The complexity of photonic integrated circuits (PICs) has been raised significantly these last few years, following Moore's law in Photonics[1]. To satisfy the need for even more complexity, devices and waveguides have to be made smaller and less power consuming. This is especially so for using PICs in combination with Silicon and CMOS chips. InP-based Membrane On Si (IMOS) technology, which has a high vertical index contrast with an ultra-thin (200nm) adhesively bonded membrane layer (see Fig.1), allows the realization of very small devices. A wide range of passive components such as MMIs and ring resonators, have already been realized in this platform with good performances[2]. In COBRA, we are now moving towards making the active devices, such as lasers and amplifiers, in IMOS. Photonic Crystal (PhC) lasers, with its ultra-high Q-factor and low mode volume, has been a hot research topic for more than 30 years. Yet making a directly electrical pumped PhC laser is still quite a challenge, although it has been shown in a few papers[3]. However, the performances of these devices clearly needs improvement. In COBRA, we aim at making a electrical pumped PhC laser in the IMOS platform. Together with the techniques of submicron active-passive integration[4] and AlInAs oxidation[5] developed previously, we expect to make electrically injected PhC lasers with high pumping efficiency and small threshold current as well as low power consumptions.

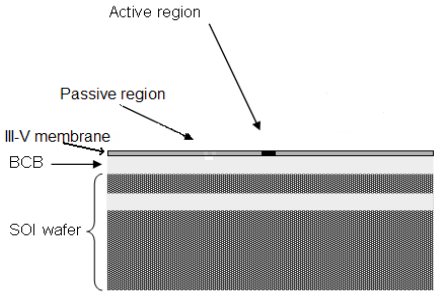
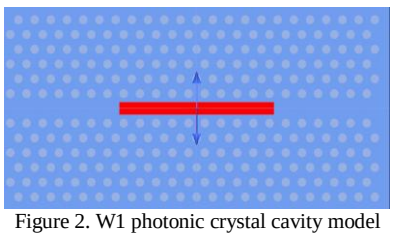


Figure 1. The layer stack of the IMOS platform

In this paper, we describe the design, simulation and tolerance check of a photonic crystal cavity, which we believe could be a promising candidate for the electrical pumped photonic crystal.

II. PHOTONIC CRYSTAL CAVITY MODEL

There is a variety of PhC cavity types. In our case, a "W1 like" cavity (see Fig.2) is chosen. Since this type of cavity has shown to have a high quality factor[6] and meanwhile keeps a good tolerance to manufacturing errors. As shown in Fig.2, light source is in the middle, dark region represents the active material, which are QWs with InGaAsP as the barrier layers. The key feature of this cavity is an extremely small(0.124 um^3) buried active region located in a straight line-defect waveguide in an InP photonic-crystal slab. Optical confinement is realized both by photonic crystal band gap and the refractive index difference between the active region and the passive part.


Figure 2. W1 photonic crystal cavity model

III. SIMULATION RESULTS

A Finite-difference time-domain (FDTD) method is used to perform the 3-D numerical calculations.

A. Simplified and extended models

Firstly, numerical calculation is started with a simplified model. As shown in Fig.3, the main resonant mode shows a high Q factor of 17000 at the wavelength of 1576 nm. The field profile of the cavity mode is shown in Fig.4.

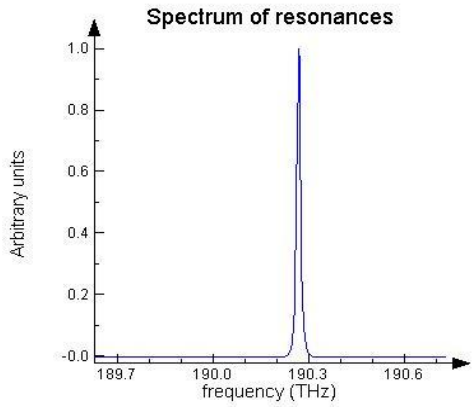


Figure 3. Main resonant mode of simplified model

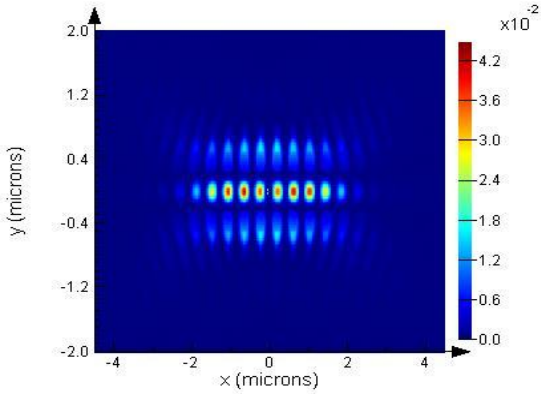


Figure 4. Mode field profile of the main resonant mode

Next, an extended and more complex model is simulated. This model includes more physical factors which could influence the performance of the cavity: doping , AlInAs oxidation and BCB bonding. A reduced quality factor (3507) at the wavelength of 1557 nm is obtained. This decreased value of quality factor is expected. First because doping, especially p-type doping, will increase the optical loss in the cavity and therefore reduce the quality factor. Secondly, oxidation of AlInAs is used to realize the current blocking function. The side-effect of this technique is that there is also a refractive index decrease with the oxidation of AlInAs, which subsequently influence the Q factor negatively. The blue shift of the wavelength is mainly due to the BCB bonding.

B. Tolerance check

Manufacturing imperfections are inevitable during the fabrication process. Therefore it is necessary to check whether this type of cavity is tolerant to the common manufacturing errors. In our simulations, two types of manufacturing errors are mainly considered. The first one is the misalignment of active region with respect to the photonic crystal and the second one is the variation of the hole radius in the PhC arrays.

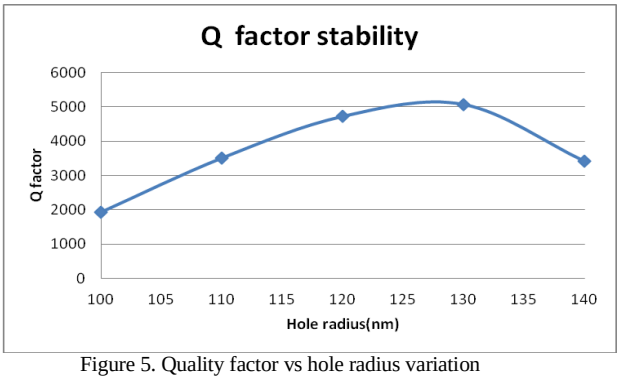


Figure 5. Quality factor vs hole radius variation

In the first case, the active region is "misaligned" by 100nm, which is the maximum alignment error for our Electron Beam Lithography machine. The Q- factor of the cavity decreases to 2623. Fig.5 shows how the Q factor changes with the variation of photonic crystal hole radius. Although there is a slight decrease in the quality factor, both tolerance checks show that this cavity is sufficiently tolerant to the typical manufacturing imperfections.

IV. CONCLUSION AND PERSPECTIVE

In this paper a "W1 like" photonic crystal cavity is designed and simulated. Results show that this cavity gives good performance in terms of quality factor and tolerance to manufacturing imperfections. Calculations also shows that doping and oxidation of AlInAs gives a negative effect on the Q factor, but the negative influence is acceptable and controllable. Together with the techniques of submicron active-passive integration and AlInAs oxidation developed previously, we expect to make electrically injected PhC lasers with high pumping efficiency and small threshold current as well as low power consumptions in the IMOS platform. In cooperation with PHILIPS, manufacturing of the device is currently pursued.

ACKNOWLEDGMENT

The authors thank EU Project HISTORIC for its financial support. Especially, Rui Zhang thanks Dzmitry Dzibrou for his helpful suggestions during the simulation.

REFERENCES

[1] R. P. Nagarajan and M.K. Smit, "Photonic integration", IEEE LEOS Newsletter Vol 21, Nr. 3, pp. 4-10, June, 2007.

[2] J.J.G.M. van der Tol, R. Zhang, J. Pello, F. Bordas, G. Roelkens, H. Ambrosius, P. Thijs, F. Karouta and M.K. Smit, "Photonic Integration in Indium-Phosphide Membranes on Silicon" , IET optoelectronics, June, 2010.

[3] H.G. Park, et al. "Electrically Driven Single-Cell Photonic Crystal Laser", SCIENCE VOL 305, September, 2004.

[4] R. Zhang, et al. "Sub-micron Active-Passive Integration for InP-based Membranes on Silicon" Proc. ECIO 2010, Cambridge, paper ThH1.

[5] R. Zhang, et al, "Oxidation of AlInAs for Current Blocking in a Photonic Crystal Laser", Proc. COMMAD 2010, Canberra (Australia), paper105.

[6] S. Matsuo, et al. "High-speed ultra-compact buried heterostructure photonic-crystal laser with 13 fJ of energy consumed per bit transmitted", NATURE PHOTONICS, VOL4, September, 2010.

A Gallium Nitride Distributed Bragg Reflector Cavity for Integrated Photonics Applications

N. A. Hueting[1], E. Engin[1], A. Md Zain[1], A. Sarua[2], P.J. Heard[2], M.Kuball[2] and M. J. Cryan[1]
[1]Photonics Research Group,
Dept of Electrical and Electronic Engineering
[2]School of Physics,
University of Bristol, Bristol, United Kingdom
N.Hueting@bristol.ac.uk

T.Wang
Dept of Electronic and Electrical Engineering
University of Sheffield
Sheffield, UK

***Abstract*— A deep etched 1D Distributed Bragg Reflector cavity in GaN-AlN-Sapphire has been analytically modeled and simulated using 2D FDTD. A structure fabricated using a hybrid Electron Beam- Focused Ion Beam method was assessed using microphotoluminescence.**

I. INTRODUCTION

Gallium Nitride (GaN) is a promising material system for a number of integrated photonics applications since it is transparent across most of the visible spectrum and can be grown in thin epitaxial layers allowing for integrated photonic component fabrication [1]. Additionally, GaN and its alloys can emit blue/green light and have useful non-linear properties. GaN is widely used in LED and laser applications, but has only recently begun to be assessed as a potential material system for technologies such as Photonic Crystal based circuits and applications [2-4]. A promising area is the use of GaN as a platform for fluorescent and label-free biosensing, where an optical microcavity could enhance the fluorescence from dyes. This paper shows analytic and numerical modelling results for a deep etched 1D DBR cavity and goes on to show a fabricated device using a hybrid E-beam, Focused Ion Beam(FIB) etching process. Finally a micro PhotoLuminescence(PL) study is performed to show that FIB etching has not induced large amounts of excess losses.

II. ANALYTICAL SOLUTION AND MODELING IN FDTD

The Distributed Bragg Reflector shown in Figure 1 was analytically characterized using the Transfer Matrix Method(TMM) with a 1D effective refractive index for the vertical layer structure, the resulting wide stopband is shown in Figure 2. To enable a more accurate model of the structure a 2D Finite Difference Time Domain model was also used [5], with the full cavity structure shown in Figure 1. This will allow for effects such as finite hole depth and non-ideal hole shape to be studied in detail. Figure 2 shows that good agreement is obtained with the simple TMM model, with the slightly lower transmission outside the stopband being caused by diffraction losses that will be accounted for by the FDTD model. Figure 2 also shows the results when a cavity is formed by bringing two DBRs together. Here a resonant wavelength of 676nm is obtained with a Q factor of 356.

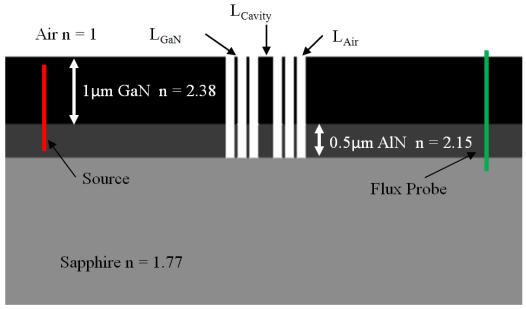


Figure 1. FDTD simulation, LGaN = 67nm, LAir = 159nm, LCavity = 586 nm, FDTD mesh=17nm

It can be seen that the Q factor is unaffected by changing from an etching depth through all layers to etching just to the AlN / Sapphire interface. This is due to the strong confinement of light in the upper GaN layer. The cavity simulated here will need to be modified slightly in order to make it more amenable to nanofabrication by using longer GaN sections in the Air/GaN DBRs. The grating shown is a simple first order case, moving to 3rd order GaN sections will allow easier fabrication, with the penalty of slightly higher diffraction losses and reduced stopband width.

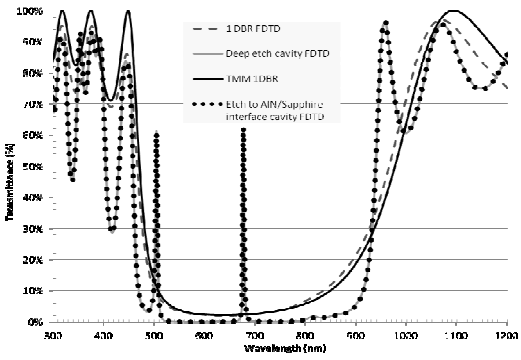


Figure 2. FDTD and analytical transmission plot of Cavity and single 3 period grating

III. FABRICATION AND QUALITY ASSESSMENT

A device based on the above modeling was then fabricated. In order to give lateral as well as vertical confinement to the modes a ridge waveguide was fabricated using Electron Beam lithography and Hydrogen Silsesquioxane (HSQ) resist and BCl3 Inductively Coupled Plasma etching. A typical ridge structure can be seen in Figure 3. The pitting observed in the FIB image is believed to be due to preferential etching of small defects within the GaN and AlN layers and as such we believe these should not be present in the unetched ridge. FIB etching was then used to define the deep etch grating [6] and a current of 70pA was used, the resulting device can be seen in Figure 3. In this initial case a depth of approximately 1µm was achieved. The use of hard metal masks and gas assisted etching will allow much deeper etches to be achieved in future device iterations.

In order to assess quality of the GaN that has been exposed to FIB etching, micro-Photoluminescence(PL) analysis was carried out and results are shown in Figure 4. HeCd 325 nm pumping was used and the results show that there is a small reduction in PL emission from the etched regions and these results suggest that the amount of FIB induced damage could be acceptable here.

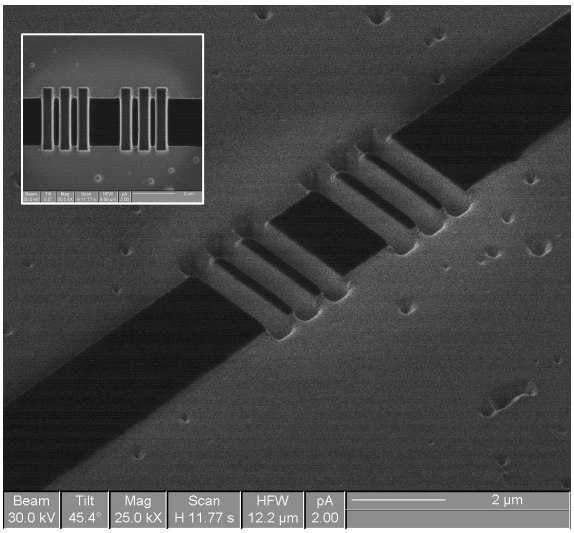


Figure 3. FIB image of grating in ridge waveguide, top view (inset) and tilted sideview

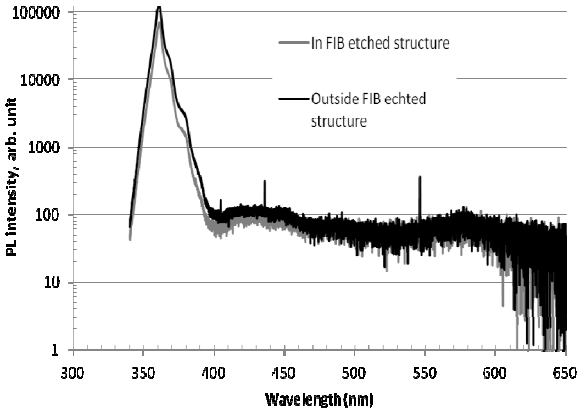


Figure 4. micro-PL analysis of etched and unetched structure

IV. CONCLUSIONS

This paper has presented modeling, fabrication and micro-PL assessment of a deep etched 1D DBR cavity structure. 2D FDTD modeling gives an estimated Q factor of 356 and future work will assess 2D photonic crystal structures which are predicted to allow much higher Q factors. In terms of fabrication, the paper shows a hybrid approach combining E-beam and FIB which allows rapid prototyping of structures embedded in predefined ridge waveguides. FIB induced damage can be an issue and full E-beam based fabrication of devices is being pursued in parallel with this work. These structures will find application in lab-on-a-chip Laser Induced Fluorescence analysis and integrated quantum photonics allowing for the potential integration of blue/green light sources directly on-chip.

REFERENCES

[1] [1] Y. F. Zhang, L. McKnight, E. Engin, I. M. Watson, M. J. Cryan, E. D. Gu, M. G. Thompson, S. Calvez, J. L. O'Brien, and M. D. Dawson, "GaN directional couplers for integrated quantum photonics," Appl. Phys. Lett. 99(2011).

[2] [2] J. Caro, E. M. Roeling, B. Rong, H. M. Nguyen, E. W. J. M. van der Drift, S. Rogge, F. Karouta, R. W. van der Heijden, and H. W. M. Salemink, "Transmission measurement of the photonic band gap of GaN photonic crystal slabs," Appl. Phys. Lett. 93, - (2008).

[3] [3] B. Rong, H. W. M. Salemink, E. M. Roeling, R. van der Heijden, F. Karouta, and E. van der Drift, "Fabrication of two dimensional GaN nanophotonic crystals (31)," Journal of Vacuum Science & Technology B: Microelectronics and Nanometer Structures 25, 2632-2636 (2007).

[4] [4] S. Lis, R. Dylewicz, K. Ptasinski, and S. Patela, "Photonic crystal micro-cavity in GaN-on-sapphire slab waveguide for sensor applications," in Photonic Crystal Materials and Devices Ix, H. R. Miguez, S. G. Romanov, L. C. Andreani, and C. Seassal, eds. (Spie-Int Soc Optical Engineering, Bellingham, 2010).

[5] [5] A. F. Oskooi, D. Roundy, M. Ibanescu, P. Bermel, J. D. Joannopoulos, and S. G. Johnson, "Meep: A flexible free-software package for electromagnetic simulations by the FDTD method," Computer Physics Communications 181, 687-702 (2010).

[6] [6] M. J. Cryan, M. Hill, D. C. Sanz, P. S. Ivanov, P. J. Heard, L. Tian, S. Y. Yu, and J. M. Rorison, "Focused ion beam-based fabrication of nanostructured photonic devices," Ieee J Sel Top Quant 11, 1266-1277 (2005)

Cs^+ ion exchange channel waveguides on $RbTiOPO_4$

J. Cugat, R. Solé* , J. Massons, J.J. Carvajal,
X. Mateos, F. Díaz and M. Aguiló
Física i Cristal·lografía de Materials i Nanomaterials
(FiCMA-FiCNA)
Universitat Rovira i Virgili (URV), Campus Sescelades,
c/Marcel·lí Domingo, s/n
Tarragona 43007, Spain. *rosam.sole@urv.cat

G. Lifante,
Departamento de Física de Materiales C-IV,
Universidad Autónoma de Madrid,
28049 Madrid, Spain.

***Abstract*—In this paper, RTP channel waveguides fabricated by the Cs^+ exchange method are presented for the first time. The losses were estimated being around 1.5 dB/cm. The Second Harmonic Generation was also demonstrated obtaining green conversion at 1133 nm.**

Keywords- $RbTiOPO_4$, Laser lithography, Cs^+exchange waveguides, Near Field Pattern, Second Harmonic Generation.

I. INTRODUCTION

The crystals of the $KTiOPO_4$ (KTP) family have an advantageous set of material properties that make them attractive as nonlinear optical elements in optical frequency conversion devices. Their high nonlinearity, high laser damage threshold, low photorefractive damage susceptibility and wide wavelength, angular and temperature acceptance bandwidth, make them particularly useful for short wavelength generation [1-5].

$RbTiOPO_4$ (RTP) is a crystal of the KTP family that presents an extra advantage in front of KTP. It can be doped with laser active ions with higher coefficient of distribution than KTP, with the possibility to obtain a self-frequency doubling (SFD) material.

In addition to the advantages mentioned above, recently, electric-field poling at room temperature of RTP was demonstrated [6]. Initial studies indicate that the effective nonlinearity in Periodical Poling RTP (PPRTP) crystals is comparable to that of PPKTP crystals.

For all of this, the study of the possibilities of Cs^+ ion exchange on RTP for creating waveguide channels is interesting. This study can be considered as the first step to optimize the Cs^+ ion exchange in RTP for future applications in integrated photonics.

II. CREATION OF CHANNELS

A. Ti channel pattern on the RTP substrate

The RTP crystals used for obtaining substrates were grown by the Top Seeded Solution Growth (TSSG) method. These crystals were cut in plate-shape substrates perpendicular to the ***c*** crystallographic direction.

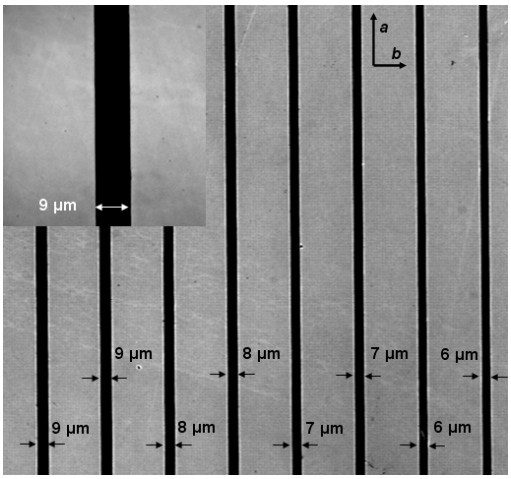


Figure 1. Ti channel patterns on a RTP substrate.

The Ti-mask pattern on the substrate was created in two steps. First, a glass mask was fabricated using a Heilderberg Instruments DWL 66 fs laser lithography equipment. After that, the fabricated mask was applied on the substrate using a MG 1410 mask aligner of conventional lithography.

For both steps the procedure was the same. First, a Ti RF-sputtering at 200 W was used, obtaining a film of 100 nm thickness. Then, a photoresist AZ 1505® (Microchemicals) was spin coated (thickness of 1 µm). After depositing the resist, the sample was UV exposed using one of both techniques mentioned above. Then, the resist was developed and etched using a selective mixture for Ti (H_2O_2 and NH_4OH). The Ti pattern obtained from lithography was formed by straight channels on the RTP substrate (see figure 1) in the range of 6 – 11 ± 0.2 µm of width.

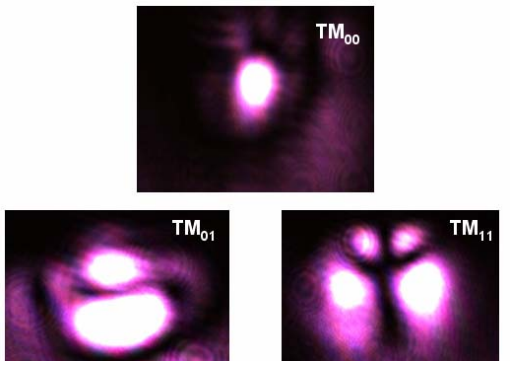


Figure 2. Near Field Pattern of the channel waveguide modes.

B. *Cs+ exchange*

The RTP substrates with Ti channel patterns were used for Cs^+ exchange. The orientation of the substrates was perpendicular to the ***c*** crystallographic direction, because this plane (***a-b***) is interesting since contains the non-critical phase matching type-II SHG directions for ytterbium laser emission wavelength range (from 985 to 1118 nm).

The Cs^+ diffusion was carried out in a crucible filled with 25 g of $CsNO_3$ at 425 ºC. The sample was immersed 6 mm below the surface of the melt in a horizontal way, stirred at 40 rpm and maintained in these conditions during 2 h.

III. CHARACTERIZATION

A. *Near Field Pattern and Transmission Losses*

A CCD camera was used to obtain the near field pattern of the channel waveguides. The modes were exited using objective microscopes and a He-Ne laser emitting at a wavelength of 632 nm and a Ti:Saphire emitting at a wavelength of 972 nm. As an example, figure 2 shows the near field pattern of the TM_{01}, TM_{11} and TM_{00} modes at a wavelength of 972 nm.

To estimate the scattered losses, a modified simple transmission method was used. Modified means that we took into account some corrections, such as Fresnel losses, the mismatch between the spot of the laser and the area of the channel and finally the losses due to the transmission of the microscope objectives. The upper limit of the transmission losses was 1.5 dB/cm.

B. *Second Harmonic Generation experiments*

In order to check the Second Harmonic Generation (SHG) inside the channel waveguides, a pulsed laser beam from an OPO was coupled into the channel waveguides. In this case, an achromatic half-plate was placed between the laser source and the sample at an angle of 22.5 º to ensure the type II SHG. The guided green light obtained exclusively inside the channel

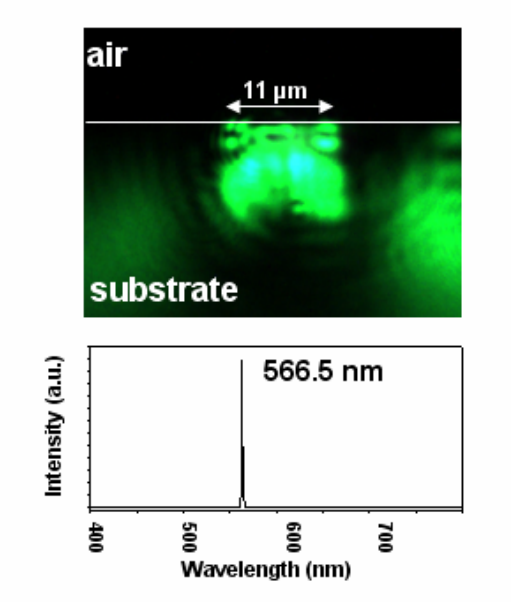


Figure 3. Type II SHG obtained in a 11 µm width Cs^+ ion exchanged channel waveguide.

was collected with a CCD camera, and it is shown in figure 3. This figure shows the type II SHG obtained using the 11 µm width channel. The pumping wavelength was 1133 nm, and the green light obtained had a wavelength of 566.5 nm.

ACKNOWLEDGMENTS

This work was supported by the Spanish Government under projects TEC2010-21574-C02-01/02, MAT2011-29255-C02-02, PI09/90527, and the Catalan Government under project 2009SGR235. J. Cugat thanks the Spanish Government for the FPI fellowship BES-2009-024190

REFERENCES

[1] J.D. Bierlein; H. Vanherzele, "Potassium titanyl phosphate: properties and new applications" J. Opt. Am. B, vol. 6, pp. 622 – 633, 1989.

[2] L.T. Chen; L.K. Cheng; R. L. Harlow; J.D. Bierlein, "Blue light generation using bulk single crystals of niobium-doped $KTiOPO_4$" Appl. Phys. Lett., Vol. 64, 155 – 158, 1994.

[3] F. Laurell; L.K. Cheng; J.D. Berlein, *Compact Blue-Green Lasers*, OSA, 10-11 February 1994, PD9.

[4] L.K. Cheng; L.T. Cheng; J.D. Bierlein; J. Parise, "Phase-matching property optimization using birefringence tuning in solid solutions of $KTiOPO_4$ isomorphs", Appl. Phys. Lett., Vol. 64, 1321 – 1324, 1994.

[5] T. Suhara; M. Fujimura, *Waveguide Nonlinear-Optic devices*, Springer (2003).

[6] H. Karlsson; F. Laurell; L.K. Cheng, "Periodic poling of $RbTiOPO_4$ for quasi-phase matched blue light generation ", Appl. Phys. Lett., Vol. 74, 1519 – 1522, 1999.

A novel electrically pumped III-V on silicon micro-laser

Y. De Koninck, M. Tassaert, G. Roelkens and R. Baets
Photonics Research Group – Ghent University / imec
Center for Nano- and Biophotonics
Ghent - Belgium
yannick.dekoninck@intec.ugent.be

A. Bazin and F. Raineri
Laboratoire de Photonique et de Nanostructures
CNRS-UPR20
Marcoussis - France

***Abstract*—In this article we present a numerical study of a new electrically pumped heterogeneously integrated III-V on silicon micro-laser. The novelty in our design lies in the fact that we use resonant silicon grating cavities to serve as reflectors. The proposed structure is simulated using a 3D FDTD simulator and we provide some preliminary experimental results.**

Keywords: lasers; heterogeneous integration; silicon photonics; III-V; FDTD; gratings

I. INTRODUCTION

In the last decade, Silicon on Insulator (SOI) has proven to be the one of the most important material systems available for integrated photonics because it builds on the maturity of CMOS technology. Its high refractive index contrast allows for high optical confinement and enables sub-micrometer scale photonic components and unprecedented integration of complex optical functionality. Unfortunately, silicon has an indirect bandgap, making it a very inefficient light emitter, hence it is virtually impossible to use it as a gain material for a laser. Over the years, research groups around the world have proposed a number of solutions such as epitaxial growth of an active material on top of the SOI stack or exploiting non-linear optical effects in the silicon itself to generate new frequencies. But probably the most established approach is the heterogeneous integration of a III-V epitaxial stack onto the SOI platform. A III-V substrate containing an epitaxial layer stack on top is bonded upside-down onto the already patterned SOI circuit. After removing the III-V substrate, a series of lithography and etching steps are performed to create the necessary topography that, combined with the underlying silicon structures, forms a laser. Using this technology, a number of devices have been demonstrated, ranging from linear DFB lasers to micro-disk lasers [1]. Unfortunately, these devices are either very large (consuming a lot of silicon real-estate and power) or it is difficult to control the operating wavelength (e.g. in micro-disks tiny variations in disk radius, caused during fabrication or due to heating, can shift the operating wavelength dramatically).

II. RESONANT MIRRORS

Because the operating wavelength of micro-disk/ring lasers has an inherent sensitivity to small disk radius variations, it is sensible to look into the direction of linear, grating based laser cavities, where the operating wavelength can be determined precisely by the grating period and the waveguide's effective index. Here we face a trade-off that is seemingly intrinsic to heterogeneous integration: to optimize the optical gain, the laser mode should be confined to the III-V waveguide. On the other hand, to assure strong reflection over a short distance, the laser mode should be confined to the silicon layer, where the mature CMOS fabrication technology can provide the nanometer scale features that are required to fabricate first order Bragg gratings in the telecom wavelength range.

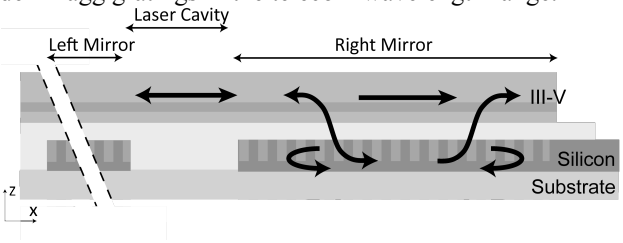


Figure 1: schematic view of resonant mirror

We propose an approach that can potentially provide high reflectivity over a short distance in a clearly defined, narrow, wavelength range and offers an elegant way to couple the generated laser light into a silicon waveguide [2]. The laser consists of a III-V wire with silicon grating structures underneath both ends (see Figure 1). In the center of the laser cavity, the laser mode is completely confined to the III-V cavity, to maximize modal gain. The novelty of this device is in the mirror design: underneath both ends of the III-V waveguide lies a silicon waveguide with a grating corrugation. Both sides are identical, so the following discussion holds for both. Near the edge of the III-V waveguide, a small part of the light couples to the silicon waveguide. The III-V mesa and the underlying silicon grating waveguide are phase-matched at a wavelength that corresponds to one of the two edges of the silicon grating's stop-band. At these edges, the silicon grating waveguide supports so-called resonant band-edge modes. This means that the light coupling from the III-V waveguide into the silicon grating waveguide will start to resonate. After power has built up in that silicon grating cavity, light will start to couple back into the III-V waveguide. The light coupling

Y. De Koninck acknowledges the Research Foundation – Flanders (FWO) for a research grant and IWT-SBO GlucoSens for additional funding

back co-directionally to the incoming light will interfere destructively with the latter and cancel all transmitted light. The light coupling back in the reverse direction is fed back into the laser cavity and provides the required optical feedback, hence the entire structure works as a mirror. Because of the resonant nature of this mechanism, it will only work in a narrow wavelength range, providing good control over the lasing wavelength. Finally, the silicon cavity can be tweaked to leak a small amount of the optical power into an external silicon waveguide to output the generated laser light.

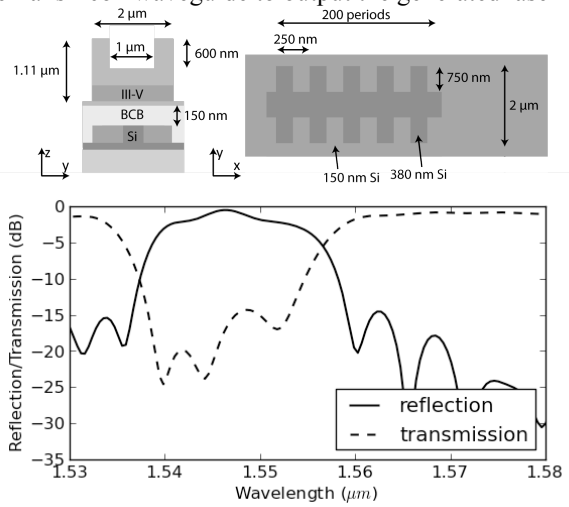


Figure 2: Reflection and transmission spectrum of proposed resonant mirror

The most difficult aspect of this approach is to make sure that the III-V waveguide and silicon grating waveguide are phase matched at the edge of the silicon grating's stop-band. To be able to put electrical contacts for current injection on top, the III-V mesa has to be sufficiently thick such that the metal does not absorb the optical mode inside the mesa. This inevitably leads to a high effective index, which cannot be matched with our silicon platform that offers silicon waveguides up to only 380nm thick. The solution we propose is to etch a slit into the III-V waveguide that pushes the optical mode down and lowers its effective index while still providing a path for the electrical current to flow. In the following sections we provide both optical and electrical simulations to prove that this concept can work.

III. SIMULATIONS

Using a full-vectorial 3D FDTD solver [3] we calculated the reflection and transmission spectrum of the mirror by launching the zeroth order eigenmode of the III-V waveguide and retrieving the reflected and transmitted power fluxes in the III-V mesa. Figure 2 shows the result of these calculations and a detailed description of the structure we simulated. The III-V stack consists of 150 nm n-InP, 4 InGaAs QW's + barriers (120 nm total) and 840nm p-InP. We consider a bonding thickness of 150 nm, which is very feasible [4].

In this particular case, the reflection spectrum is relatively broad (almost 20 nm) because it is the superposition of 3 band-edge resonances in the silicon waveguide (3 distinct dips in the transmission curve). By using a defect mode instead of a band-edge mode, the reflection bandwidth can be narrowed to below 5 nm [2]. The peak reflectivity is 89.2% at λ = 1546 nm. Outside the reflection band the reflectivity of the structure is below 14.5 dB everywhere. Using Silvaco Atlas [5] we verified that the etched slit does not jeopardize the current injection.

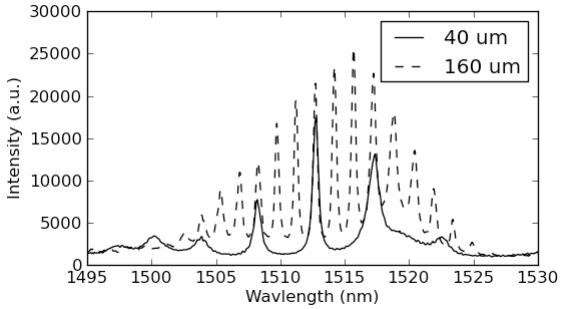


Figure 3: Measured spectrum of ASE in optically pumped sample for 2 different laser cavity lengths (40 µm and 160 µm)

IV. PRELIMINARY EXPERIMENTAL RESULTS

To test the concept of resonant mirrors, a first prototype was fabricated using a thin slab of III-V material that can be pumped optically (similar to [2]) instead of the more advanced etched-slit approach proposed here. The peak of the active material's gain curve we used was centered on 1450 nm while these particular mirrors were designed for wavelengths ranging from 1510 nm to 1580 nm. Nevertheless, we were able to measure amplified spontaneous emission (ASE) in clearly distinguishable longitudinal modes with an FSR consistent with the corresponding device lengths (see Figure 3). Moreover, for different grating periods, the spectral position of the longitudinal resonances shifts accordingly. These observations are strong indications that the proposed concept indeed works.

V. CONCLUSION

We have introduced a novel concept for electrically pumped heterogeneously integrated III-V on silicon lasers based on resonant mirrors. We provide a solution for solving the phase-matching problem and show by means of 3D FDTD simulations that this approach yields high reflection. Finally we offer preliminary experimental results that give a strong indication that our concept works.

[1] G. Roelkens, L. Liu, D. Liang, R. Jones, A.Fang, B. Koch and J. Bowers "III-V/silicon photonics for on-chip and inter-chip optical interconnects" Laser & Photonics reviews, Rev 4. No. 6, pp. 751–779, October 2010.

[2] Y. De Koninck, G. Roelkens and R. Baets "Cavity enhanced reflector based hybrid silicon laser" proceedings of the 23rd annual meeting of the IEEE Photonics society

[3] Ab Initio MEEP (http://ab-initio.mit.edu/wiki/index.php/Meep)

[4] S. Stankovic, Jones, Richard, Heck, John, Sysak, Matthew, D. Van Thourhout, G. Roelkens "Die-to-Die Adhesive Bonding Procedure for Evanescently-Coupled Photonic Devices" Electrochemical and Solid-State Letters, Vol 14(8), pp H326-H329, May 2011.

[5] Silvaco Atlas (http://www.silvaco.com)

(Er^{3+}, Yb^{3+}) doped K(Y,Gd,Lu)W waveguide fabrication

J. Martínez de Mendíbil*, E. Cantelar, G. Lifante
Dept. Física de Materiales, Facultad de Ciencias
Universidad Autónoma de Madrid
Madrid, Spain

G.S. Murugan and J.S. Wilkinson
Optoelectronics Research Centre, University of Southampton. Highfield, Southampton SO17 1BJ. UK

C. Berrospe, X. Mateos, W. Bolaños, J. J. Carvajal, M. Aguiló and F. Díaz
Física i Cristal·lografia de Materials i Nanomaterials (FiCMA-FiCNA)
Universitat Rovira i Virgili (URV), Campus Sescelades, c/Marcel·lí Domingo, s/n
Tarragona, Spain

*jon.martinez@uam.es

***Abstract*—In this work the fabrication and characterization of (Er^{3+},Yb^{3+}) doped K(Y,Gd,Lu)W waveguides are presented. The KYW substrate is obtained by the Top-Seeded Solution Growth technique, and the active guiding layer is grown by Liquid Phase Epitaxy. While this process gives rise to planar waveguides, an ion milling structuring technique has been additionally used to provide lateral confinement to fabricate channel waveguides. The waveguide characterization includes refractive index measurements of the substrate and core regions, geometry of the ridge waveguides, and spectroscopy of the active ions around 1.55 μm. BPM has been used to obtain the modal intensity profiles to estimate the optical confinement of the guided modes.**

Keywords- KYW; Liquid Phase Epitaxy; channel waveguides; rare earth ions; integrated lasers

I. INTRODUCTION

KREW's are monoclinic crystals with three orthogonal optical directions N_g, N_m and N_p, where N_g and N_m are placed in the *a-c* crystallographic plane, and N_p is parallel to the *b* crystallographic axis. Each optical direction has a different refractive index n_g, n_m and n_p, where $n_g > n_m$ and $n_m > n_p$. The high refractive indices of KYW make this material a good candidate for developing integrated optical devices. Furthermore, the large absorption and emission cross sections for rare earth ions (~10^{-20} cm^2) offer low threshold laser operation, and the large ion separation enables high doping levels without quenching of luminescence. It has been demonstrated that it is possible to induce relevant refractive index modification by modifying the Y, Gd and Lu concentrations [1], and by adding active ions such as Er^{3+} Yb^{3+} or Tm^{3+} [1, 2]. As this work is focused on the 1.5 μm wavelength for communications applications, Er^{3+} ions have been chosen as active centers, and Yb^{3+} has also been added due to its efficient energy transfer to the $^4I_{3/2}$ multiplet of the Er^{3+} ion.

In this paper the fabrication and characterization of planar and channel waveguides of (Er^{3+},Yb^{3+}) doped K(Y,Gd,Lu)W on KYW substrates are presented. Details of the optical and spectroscopic properties of the guiding layers are given, with emphasis in the 1.5 μm spectral region. Modal characteristics of the channel waveguides has been also studied by numerical modeling using BPM techniques.

II. EXPERIMENTAL DETAILS

A. Planar waveguide fabrication

KYW crystals have been grown by the Top-Seeded Solution Growth slow-cooling method (TSSG). The fabrication is carried out in a vertical tubular furnace following the experimental setup described elsewhere [2].

Substrates are obtained from the KYW crystals, where they are polished These substrates are then used for the deposition of the active-guiding layer by Liquid Phase Epitaxy (LPE). (Er^{3+},Yb^{3+})doped K(Y,Gd,Lu)W layers were grown on the *-b* direction oriented substrates, as this direction allows polarizations parallel to N_m and N_p, where the absorption cross section at 980 nm is higher. LPE solution was prepared by a 7% mol solute on 93% KYW solvent, in order to control the supersaturation process [3]. Once T_s is achieved, the temperature of the solution is cooled 3 K to achieve the supersaturation of the solution, and the sample is immersed for 3 h in the solution. Finally the sample is removed from the solution, while the furnace is cooled at 15 K/h to prevent thermal shock cracking.

The guiding layer is grown to a thickness of 70 μm and polished to a roughness below 0.3 μm. The final layer is 12 μm thick with a length of 3.8 mm. The guiding layer stoichiometry is found to be $KY_{0.74}Gd_{0.18}Lu_{0.07}Er_{0.005}Yb_{0.005}(WO_4)_2$, which offers a theoretical lattice mismatch of 0.55×10^{-3}. This low value allows epitaxial growth free of internal cracks.

For a more symmetric distribution of the optical mode, a 50 μm thick KYW-cladding was added by LPE. This overcladding also serves to decrease propagation losses.

B. Channel waveguide fabrication

The growth of the substrate and the epilayer for channel waveguides were done following the same procedure as explained in the previous section. In addition to that, the

This work was supported by the Spanish Government under projects DISFOTINT TEC2010-21574-C02-01 and TEC2010-21574-C02-02, MAT2011-29255-C02-02, PI09/90527 and by the Catalan Authority under project 2009 SGR235 and partly supported by the EC under the 7th FP, project Cleanspace, FP7-SPACE-2010-1–GA-263044 and MICROSERES (P2009/TIC-1476) Comunidad de Madrid

substrate is micro-structured by ion milling in order to obtain ridge structures, where the guiding layer is grown.

Channels are structured by ion milling, and a 3% Er^{3+} doped K(Y,Gd,Lu)W epilayer is grown on the structured face of the substrate and then polished down to a 2 µm thickness over the non-structured surface. In this case the grown epilayer composition is found to be $KY_{0.58}Gd_{0.19}Lu_{0.20}Er_{0.03}(WO_4)_2$. This stoichiometry offers a negative lattice mismatch of -0.53×10^{-3} respect to the KYW substrate, which means low internal tension and hence fewer internal cracks. Finally a KYW cladding is deposited by LPE to improve the modal distribution.

The geometry of the fabricated channels is shown in figure 1. Type-I (Fig. 1a) has a triangular geometry, while type-II (Fig. 1b) has a trapezoidal shape. In both cases, a residual planar waveguide of 2 µm depth is left.

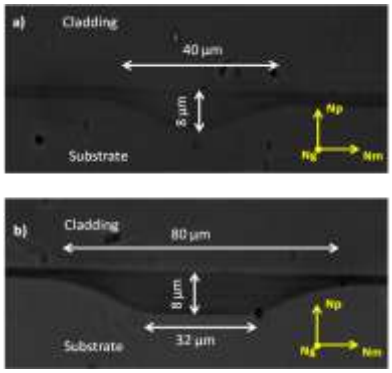


Figure 1. Type-I (a) and Type-II (b) channel waveguides.

III. Results and Discussion

A. Planar waveguide

The refractive indices of the planar waveguide were measured by the prism-coupler method. The fabricated waveguide shows increment in the refractive index of the guiding layer for all polarizations, from 2.1×10^{-3} for N_g polarization and up to 5.4×10^{-3} for N_p polarization, measured at 633 nm. Similar increments are obtained at 1.5 µm wavelength.

B. Channel waveguides

With a $KY_{0.58}Gd_{0.19}Lu_{0.20}Er_{0.03}(WO_4)_2$ guiding layer a higher refractive index increase has been measured for N_m and N_p polarizations. At 633 nm wavelength n_m increases 4.5×10^{-3}, while n_p increases 8.7×10^{-3}. As seen in the simulations (Fig. 2), this refractive index variation is enough for guiding at both pump and emission wavelengths. In Type I channel waveguides, BPM simulations give confinement factors of 0.914 for quasi TE polarization (parallel to N_m) at 1.55 µm wavelength, and 0.970 for a wavelength of 980 nm. For quasi TM polarization (parallel to N_p), the confinement factor increases to 0.930 at 1.55 µm wavelength and to 0.976 for a wavelength of 980 nm.

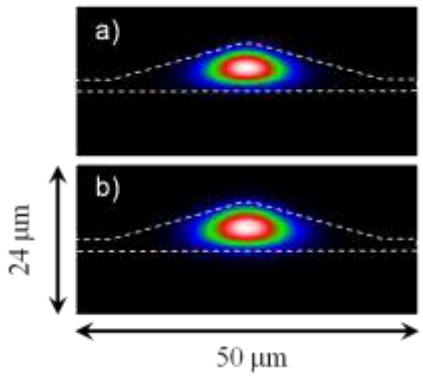


Figure 2. Fundamental quasi TE modes in Type I channel guides at 0.98 µm (a) and 1.55µm (b).

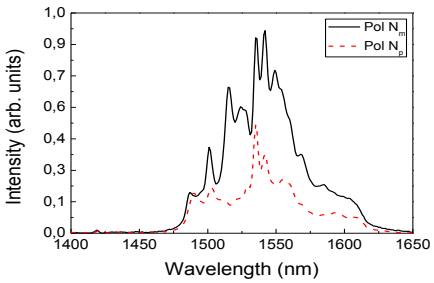


Figure 3. 1.55µm emission of $KY_{0.58}Gd_{0.19}Lu_{0.20}Er_{0.03}W$ / KYW Type II channel waveguide

The guided emission in the 1.55 µm range, due to pumping at 980 nm, was also studied, and is presented in figure 3. These emission spectra correspond to the $^4I_{13/2} \rightarrow {}^4I_{15/2}$ transition of the Er^{3+} ions for N_m and N_p polarizations, with the emission for N_m polarization being more intense than that for the N_p polarization. Identical results are obtained in the planar waveguide and in type I channel waveguides.

IV. Conclusions

Er^{3+} and Yb^{3+} doped K(Y,Gd,Lu)W planar and channel waveguides were successfully fabricated on KYW substrates with low lattice mismatch using the LPE technique. The measured refractive index increments in the guiding layer and the spectroscopic properties of the Er ions in the active region, indicate that these waveguides are promising optical elements for the development of lasers and amplifiers in a guided configuration operating in the 1.5 µm region.

V. References

[1] F. Gardillou, U.E. Romayuk ,C.N. Borca, R.P. Salathé and M. Pollnau. Lu,Gd codoped, "$KY(WO_4)_2$:Yb epitaxial layers: Towards integrated optics based on $KY(WO_4)_2$", Optics Letters **32**,488-490 (2007).

[2] W. Bolaños, J.J. Carvajal, M.C. Pujol, X. Mateos, G. Lifante, M. Aguiló and F. Díaz. "Epitaxial growth of lattice matched $KY_{1-x-y}Gd_xLu_y(WO_4)_2$ thin films on $KY(WO_4)_2$ substrates for waveguiding applications". Crystal Growth & Design **9**, 3525-3531 (2009).

[3] O. Silvestre, M.C. Pujol, R. Solé, W. Bolaños, J. Massons, M. Aguiló and F. Díaz. "Ln^{3+}:$KLu(WO_4)_2$/$KLu(WO_4)_2$ epitaxial layers: Crystal growth and physical characterization". Materials Science and Engineering B **146**, 59-65 (2008).

Design of Spectrometers and Polarization Splitters Using Adiabatically Connected Slab Waveguides

F. Civitci and H.J.W.M. Hoekstra
Integrated Optical MicroSystems Group, MESA+ Institute for Nanotechnology,
University of Twente, Enschede, The Netherlands
f.civitci@utwente.nl

***Abstract*— The design of fully integrated prism spectrometers and polarization splitters in adiabatically connected slab waveguides with two different thicknesses, using principles of geometrical optics, is presented. In addition, the design of mirrors to connect these devices to input and output waveguides is discussed. The proposed structures will be fabricated, using two wet-etching steps, in a Si3N4 layer in-between a buffer and cladding SiO2 layer.**

Keywords- prism spectrometers; polarization splitters; adiabatically connected slab waveguides; waveguide mirrors

I. INTRODUCTION

In the early years (70's) of Integrated Optics (IO), slab waveguide (WG) based devices, such as thin film lenses, prisms, reflectors and polarization splitters were extensively investigated [1]. The design of these components is extremely easy since the propagation of light waves in these slabs can be described by geometrical optics in 2D, using the effective refractive index (*N*) of the fundamental slab modes [2]. Furthermore, slab WG fabrication is not a complicated process. In spite of these advantages, only a small number of integrated devices, which combines more than one of these components to have an IO device, have been implemented [3-5].

In this paper, we describe the design of fully integrated prism spectrometers and polarization splitters in adiabatically connected slab WGs (having two different thicknesses), using principles of geometrical optics. For light transport ridge WGs will be used. The operating wavelength will be around λ = 850 nm. Both the slab and ridge WGs will be implemented in a LPCVD Si_3N_4 layer which is deposited on a buffer SiO_2 layer (grown on a Si substrate) and covered with a cladding SiO_2 layer. The fabrication process that will produce these devices consists of two wet etching step. One is for defining the ridge WGs (20 nm ridge height) and one is for defining the thin slab WG regions (etching down to 40 nm) in the Si_3N_4 layer. The interfaces between the thin and thick slab regions are chosen to be adiabatic in order to decrease conversion to scattering modes and reflection losses at the prism interfaces and the interfaces of the trench used for the polarization splitter [1].

The rest of this paper is organized as follows. First, we will introduce the prism spectrometer and followed by an explanation of the design of this device, in section II. In section III we will consider the design of a fully integrated polarization splitter device. The paper ends with conclusions (section IV).

II. PRISM SPECTROMETER

A schematic picture of the considered prism spectrometer device is shown in figure 1. It is composed of an input WG, a collimation mirror, a prism slab, a focusing mirror and output WGs corresponding to different wavelengths.

The working principle of the proposed spectrometer, to be operated with TE polarized light, can be described as follows. The single-mode input WG is carrying the multi wavelength light, which diverges in the thick slab and is collimated after reflection from the collimation mirror, which is a total internal reflection (TIR) mirror for slab modes defined at the interface between thick (high *N*) and thin (low *N*) slab WGs. After that, the collimated light beam enters the prism slab where it is angularly dispersed with respect to the wavelength. The output beams are coupled into different output waveguides, which correspond to different wavelengths, by the focusing mirror.

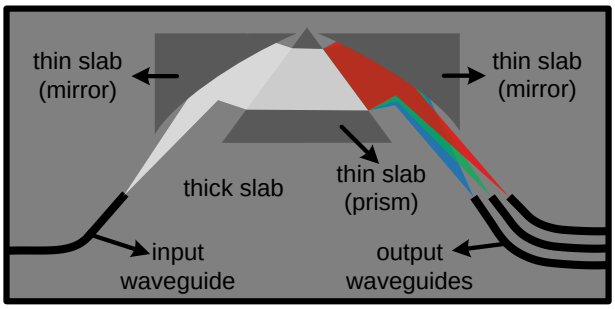


Figure 1. Schematic of the considered prism spectrometer. The light and dark grey area correspond to thick (160 nm) and thin (40 nm) Si_3N_4 slabs, respectively. Ridge waveguides are indicated by black lines.

A. Prism Design

The geometrical structure of a generic slab waveguide based prism spectrometer is shown in figure 2-a. In this figure, η is the prism angle, σ_1 is incidence angle, b is the prism base length and w_i is the input beam width. The effective indices of the thin and thick slabs are denoted by N_1 and N_2, respectively, and we define $D = N_2 / N_1$. Assuming an approximate flat intensity profile at the input of the prism, the resolving power ($\mathcal{R}$) of this spectrometer can be written as

This research is financially supported by the STW Technology Foundation through project 10051.

$$\mathcal{R} = bD' \qquad (1)$$

with $D' = \partial D/\partial\lambda$. Unlike in conventional bulk prism spectrometers, the refractive index dispersion, which generates the angular dispersion, is here mainly provided by the thick slab surrounding the prism. For given materials D' depends only on the two thicknesses of the two slabs. Varying these, in order to optimize D' we arrive at a thickness of 40 nm for the thinner slab, as a safe lower limit to prevent leakage to the Si substrate. Next D' is maximized to a value of 1.21 x 10^{-4} /nm by choosing a thickness of 160 nm for the thicker layer, for which that layer still supports one TE mode.

For the layout of the spectrometer it is of particular importance to take into account mirror aberrations owing to the fact that the output mirror is designed for the central wavelength (850 nm) and introduces extra focal spot broadening for wavelengths nearby. It turns out that these aberrations are at minimum if the prism is operated at minimum deviation. More design aspects for the layout of the spectrometer will be presented during the conference.

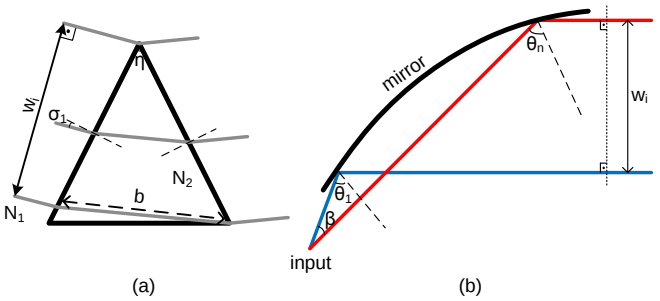


Figure 2. Schematic of (a) a generic prism spectrometer and (b) parabolic collimation mirror.

B. Mirror Design

Both of the mirrors used in the spectrometer device are parabolic mirrors that can be designed by using Fermat's Principle. Figure 2-b shows the schematic of a parabolic collimation/focusing mirror. The mirror geometry can be extracted by choosing the following parameters; the largest angle of incidence (θ_1), input beam width (w_i) and input divergence angle (β). Usually w_i is defined by given $\mathcal{R}$; β should be chosen such that it is compatible with the numerical aperture of the WG modes and it gives an acceptable geometrical aberration (broadening of the focal spot should be smaller than the diffraction limited spot size) in the focusing mirror. Meanwhile θ_1 should be chosen such that it is above the critical angle for TIR. The phase shifts induced on TIR depend on the angle of incidence, which should be taken into account on designing. We calculated the phase shifts for different angles of incidence by assuming an imaginary ridge waveguide with tapered edges, as used for the mirrors. In order to find the phase shift resulting from TIR, we first calculated the modal index of the ridge WGs and then we used these values in the transverse resonance condition equation defined for an equivalent 1-D WG to deduce the (angle dependent) phase shift on reflection (of the fundamental slab modes) at the slanted side walls. The computational results show, among others, that the extra aberrations can be minimized by increasing θ_1.

We generated a sample layout for a prism spectrometer which has a theoretical resolution of 5 nm at 850 nm wavelength. In this sample device, which has a total size of 15 mm x 5 mm, η, w_i, β and θ_1 are given by 130°, 470 µm, 5° and 72.5° respectively.

III. Polarization Splitter

A schematic of the considered polarization splitter device is shown in figure 3. In this device, there is an elliptical focusing mirror which focuses un-polarized light that is launched from the input WG to two output WGs which are corresponding to different polarizations. The polarization splitter slab shown in the figure is similar to the thin film polarizer described in [1], but here we use a trench with non-parallel sidewalls in order to minimize geometrical aberrations in the output. The size of the complete device, which is designed to work at 850 nm wavelength, is 10 mm x 2 mm.

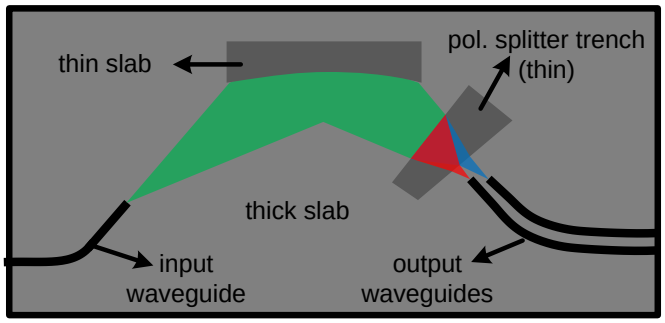


Figure 3. Schematic of the considered polarization splitter.

IV. Conclusions

We described the design of fully integrated prism spectrometers and polarization splitters which are considered to be fabricated in Si3N4 slab waveguides connected adiabatically. As a follow-up, we will fabricate the devices and measure their performances.

References

[1] P.K. Tien, "Integrated optics and new wave phenomena in optical waveguides," Reviews of Modern Physics, vol . 49, pp. 361-420, 1977.

[2] R. Ulrich and R.J. Martin, "Geometrical optics in thin film light guides," Applied Optics, vol. 10, pp. 2077-2085, 1971.

[3] C.C. Tseng, W.T. Tsang and Shyh Wang, "A thin-film prism as a beam seperator for multimode guided waves in integrated optics," Optics Communications, vol. 13, pp. 342-346, 1975.

[4] M. Gibbon, G.H.B. Thompson, S.J. Clements, D.J. Moule, C.B. Rogers, C.G. Cureton, "Optical performance of integrated 1.5 µm grating wavelength-demultiplexer on InP-based waveguide," Electronics Letters, vol. 25, pp. 1441-1442, 1989.

[5] C.H. Jang and R.T. Chen, "Polymer-based 1 x 6 thermooptic switch incorporating an elliptic TIR waveguide mirror," Journal of Lightwave Technology, vol. 21, pp. 1053-1058, 2003.

45° Light Turning Mirrors for Hybrid Integration of Silica Optical Waveguides and Photo-detectors

F.Civitci, G.Sengo, A. Driessen, M. Pollnau, and H.J.W.M. Hoekstra
Integrated Optical MicroSystems Group (MESA+)
University of Twente, Enschede, The Netherlands

A.J. Annema
Integrated Circuit Design Group (CTIT)
University of Twente, Enschede, The Netherlands

***Abstract*—For hybrid integration of an optical chip with an electronic chip with photo diodes and electronic processing, light must be coupled from the optical chip to the electronic chip. This paper presents a method to fabricate metal-free 45° quasi-total internal reflecting mirrors in optical chips that enable 90° out-of-plane light coupling between flip-chip bonded chips. This method is fully compatible with fabrication of conventional optical chips. The mirrors are created using anisotropic etching of 45° facets in a Si substrate followed by fabrication of optical structures. After removal of the mirror-defining Si structures by isotropic etching, the obtained air-optical structure interface directs the output of the waveguides to out-of-plane photo detectors that are mounted flip-chip on the optical chip. Simulations show a reflection efficiency of 72.3 %, while experimentally 47% was measured on a not fully optimized first batch.**

Keywords- light turning mirrors; hybrid integration; silica waveguides; photo-detector arrays; integrated optics

I. INTRODUCTION

In recent years, waveguide (WG) based integrated optic devices have been used in many applications such as tele-communication, optical spectroscopy, biological sensing and signal processing in medical imaging. Usually the WG outputs are measured using photo-diodes (PDs), which are dedicated to certain applications, such as time gating in spectroscopic research or in diagnostics. In particular for (high resolution) spectroscopy a large number of different channel outputs are measured, which can be done most conveniently with 2D arrays of PDs. Monolithic integration of the latter into the Si substrate of an optical chip has several disadvantages: (i) if the PDs and their electronic processing circuitry are fabricated first, the temperature budget to fabricate the optical structures (such as LPCVD and reflow of deposited layers) is severely limited, to about 400 °C, and (ii) fabrication of PDs and their electronic processing circuitry on each optical chip would be far more expensive than processing a CMOS chip that includes PDs and electronics to be flip-chip mounted on an optical die. To enable efficient optical coupling between an optical die and a flip-chip mounted electronics die, low cost high efficiency 45° out-of-plane mirrors in optical chips are favorable. This is the subject of this paper.

A number of techniques have been reported to provide a connection between WGs and PDs of two flip-chip mounted chips. One of these uses a focusing grating coupler on top of a WG to focus the light onto the PD that is placed above the WG [1]. However, this device can only work for a limited wavelength range which is defined by the grating period. In addition, high volume production of such a grating would be very expensive, owing to its relatively small period. Another technique uses focused ion beam (FIB) milling for fabricating total internal reflection (TIR) mirrors at the end of silica WGs [2]. However, this technique is not suitable for high volume production due to the relatively low speed of FIB and the associated high cost. The third technique is based on a metal mirror, at which the desired mirror angle is fabricated by using a superficial layer in the wet etching process of the buffer layer [3]. Although the efficiency of these mirrors is very high (up to 95 %), the thermal budget of the fabrication process is low because the melting temperature of the metal layer used in the mirror is around 650 °C.

In this paper, we propose a new method to fabricate 45° mirrors in optical chips that enable high efficiency 90° out-of-plane light coupling to a flip-chip mounted electronic chip holding 2D PD arrays with their processing electronics. The fabrication process for these mirrors is suitable for batch production and has a thermal budget of 900 °C. The mirror is defined by anisotropic etching of 45° facets in the Si substrate. After optical WG fabrication the mirror is formed, by locally removing the Si facets, at the interface between the optical WG and air.

The paper is organized as follows. Section II reviews the fabrication process steps for realizing the mirror. Section II shows simulation results for estimating the mirror performance; section IV presents some measurement results.

II. FABRICATION PROCESS

The wafer cross-sections corresponding to different steps in the fabrication process flow are shown in figure 1(a)-1(j). The fabrication process starts with 200 nm thermal oxide growth to be used as a mask for the anisotropic Si etching. After that the oxide is patterned by using buffered HF (BHF) etching (1-a). This is followed by 5 µm deep anisotropic etching of Si (1-b). This depth is defined by the required thickness of the buffer layer, which should be 3.5 µm to prevent substrate losses, and by the thickness of the oxide layer above the SiON WG (~1.5 µm) for proper overlap between the diverging WG output and the mirror surface. A TMAH and Triton mixture is used as etchant to form the 45° angled walls [4]. The fabrication process continues with removal of thermal oxide in BHF.

This research is financially supported by the STW Technology Foundation through project 10051.

Then, a 100 nm thick SiN layer is deposited (1-c) just before deposition of the buffer layer in order to prevent molecular diffusion between the latter and the Si substrate. After that a thick Boron Phosphorous Doped Silica Glass (BPSG; index: 1.45) film is grown to form the buffer layer (1-d). BPSG is used in order to get rid of the voids in the as deposited layer by post- deposition annealing [5]. The thickness of the BPSG buffer layer should be at least 5 µm, which is equal to the etch depth defined in the anisotropic Si etching step, in order to be able to obtain a flat surface after the following chemical mechanical polishing (CMP) step. The BPSG layer is annealed just after deposition at 900 °C for 16 hours. The annealing step is followed by CMP step (1-e). Subsequently, the BPSG is thinned in a BHF solution such that a 3.5 µm thick buffer layer will remain between the guiding SiON layer and Si substrate (1-f). This is followed by the deposition and patterning of the core SiON (index: 1.585) layer (1-g). After that the cladding BPSG layer is deposited, annealed and polished (CMP), while using the same process conditions as applied for the buffer BPSG (1-h). Then the isotropic Si etching holes are introduced on top of the elevated Si structures (1-i). Finally, the isotropic Si etching is done through these holes (1-j). In this step XeF2 gas phase etching is used to selectively remove Si. By removing the elevated Si structures, 45° mirrors are created.

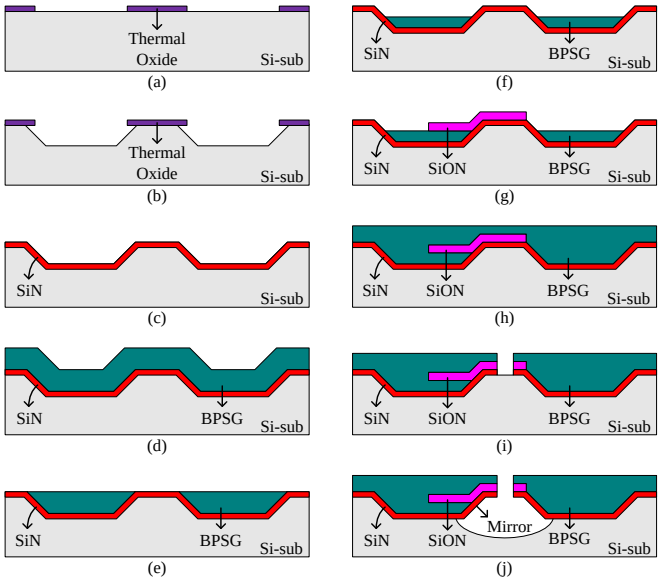


Figure 1. Wafer cross-sections corresponding to different steps in the fabrication process flow.

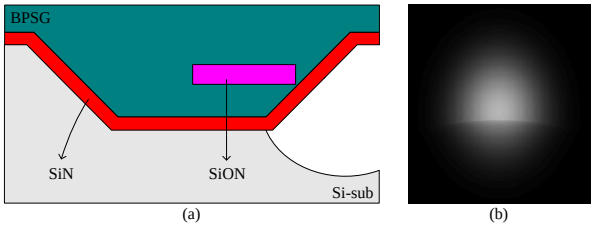


Figure 2. (a) Cross-section of the simplified mirror structure used in the simulation and (b) calculated far field intensity profile.

III. SIMULATIONS

The performance of the proposed mirrors is estimated using a Fourier decomposition of the modal field. The mirror structure used in this simulation is simplified by ignoring the residual SiON layer on the 45° angled wall since the index contrast between BPSG and SiON is very low. Figure 2-(a) shows the cross-section of this (slightly idealized) structure. Figure 2-(b) shows the far field intensity profile. It can be seen from the figure that the intensity profile is not symmetric, which is due to the fact that a part of the Fourier components of the modal field has an angle of incidence on the silica-air interface below the critical angle. For this reason the efficiency of the mirror is calculated to be somewhat below unity, 72.3%.

IV. MEASUREMENTS

The fabricated devices are first characterized by taking the far field intensity patterns of the light reflected from the mirrors. The light of a laser source at 833 nm wavelength is coupled into a single mode optical fiber to excite the WG that is terminated by such a mirror. The light in the WG is reflected from the mirror, hits a diffusive screen 1.5 cm away from the mirror and its image is captured by a camera. The simulated and measured intensity profiles match in size and shape.

The efficiency of the mirror is measured by comparing the mirror output with that of a WG directed to a side facet. Here, differences in the excitation efficiencies of the two corresponding WGs are accounted for by monitoring the light in the WGs with a camera and using the thus measured intensities as a measure for the power in the two WGs. This process is repeated a number of times, to correct for statistical fluctuations. The results show that the efficiency of the fabricated mirror is 47%, which is somewhat lower than the anticipated value (72.3%) due to imperfections in this first batch.

V. CONCLUSIONS

Quasi-TIR based 90° out-of-plane high efficiency light turning mirrors for hybrid flip-chip integration of SiON WGs and CMOS based photodiodes are fabricated. Measurements show an efficiency of 47% while the calculated efficiency is 72.3%; this difference is due to imperfections in fabricating this first batch.

REFERENCES

[1] T. Suhara and H. Nishihara, “Integrated optics components and devices using periodic structures,” IEEE Journal of Quantum Electronics, vol. 22, pp. 845-867, 1986.

[2] K. Watanabe, J. Schrauwen, A. Leinse, D.V. Thourhout, R. Heideman, and R. Baets, “Total reflection mirrors fabricated on silica waveguides with focused ion beam,” Electronics Letters, vol. 45, pp. 883-884, 2009.

[3] M.V. Bazylenko, M. Gross, E. Gauja, and Pak L. Chu, “Fabrication of light-turning mirrors in buried-channel silica waveguides for monolithic and hybrid integration,” Journal of Lightwave Technology, vol. 15, pp. 148-153, 1997.

[4] D. Resnik, D. Vrtacnik, U. Aljancic, and M. Mozek, “The role of triton surfactant in anisotropic etching of {110} reflective planes on (100) Silicon,” Journal of Micromechanics and Microengineering, vol. 15, pp. 1174-1183, 2005.

[5] F. Sun, M.G. Hussein, K. Worhoff, G. Sengo and A. Driessen, “B/P Doping in application of silicon oxynitride based integrated optics,” in Proceedings of CLEO Europe – EQEC, 2009.

Polarization converter post-processing for integrated polarization independent SOA

M. Felicetti, J.J.G.M. van der Tol, E.J. Geluk and M.K. Smit
COBRA Research Institute
Eindhoven University of Technology
Eindhoven, the Netherlands

N. Whitbread and P. Williams[1]
Oclaro Technology Ldt.

***Abstract*— Post-processing of a polarization converter (PC) in an experimental industrial generic foundry process is demonstrated. Insertion of the PC halfway an SOA reduced its polarization dependence from 14 dB to 3 dB.**

Keywords: post-processing, polarization converter, InP, photonic integration.

I. INTRODUCTION

In the European FP7 project EuroPIC, generic photonic foundry processes are being developed based on the integration technologies of Oclaro and the Fraunhofer HHI. In a generic approach the most frequently used photonic building blocks (BBs) can be integrated using a standardized process [1]. However, a polarization converter (PC) is not yet included in the current foundry processes. In this paper we report the post-processing of a passive PC in a PIC fabricated in the experimental foundry process of Oclaro. The existing structures in the chip allow us to test the PC in a polarization independent SOA (PI-SOA) configuration; the connection between the post-processed PC device and pre-processed test structures is obtained using tapered waveguides. First, we will briefly explain the PC working principle and its role in a PI-SOA circuit. Next, we will describe the simulations performed to optimize the tapered waveguides connections. Then we will go through the post-processing steps. The last section shows the measurement results.

II. POLARIZATION-INDEPENDENT SOAS

A single section passive PC is an optical waveguide with a sloped cladding (Fig. 1) connected to straight input-output waveguides. The geometry should be such that the PC can support the two modes M_1 and M_2, +45° and -45° rotated with respect to the TE vector. The two modes recombine into the TM mode in the straight output waveguide, after equal excitation of the two modes by an input TE mode, and propagation along a half beat length $L_{PC} = \pi/(\beta_1 - \beta_2)$ [2]. Here β_n is the propagation constant of the mode M_n. The PC shape has been optimized for the Oclaro layer-stack. Details about the performance and tolerance analysis will be presented in a future paper [3]. A PI-SOA consists of a passive PC placed between two identical SOAs. Fig. 2 shows the circuit working principle with a PC that gives a full conversion from TE to TM and vice versa ($C = P_{out}^{converted}/P_{out}^{total} = 1$). Such a PC works as a half-wave plate. The output power in the case of a TE and TM polarized mode is shown as well, with $G(TE)$ and $G(TM)$ the gain of the SOA in the TE and TM case. Thus, by using a full conversion PC, this circuit gives a signal amplification independent of the input polarization (i.e., assuming that the SOAs are not in saturation. In the case of $C \neq 1$, the output power is $P_{out} = CP_{in}G(TE)G(TM) + (1-C)G(TE)^2$ for a TE input mode and $P_{out} = CP_{in}G(TE)G(TM) + (1-C)G(TM)^2$ for a TM input mode. Thus, the output power depends on the input polarization. We use this circuit as test structure for our PC.

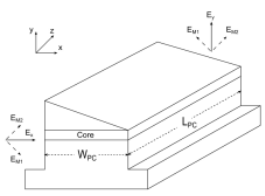


Fig. 1: single section passive PC with sloped cladding.

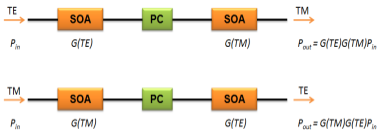


Fig. 2: PI- SOA working principle.

III. TAPER CONNECTIONS

In a PI-SOA test structures (Fig. 3) the SOAs are defined in a direction perpendicular to the major flat, whilst the PC is defined in a direction parallel to the major flat, to etch a sloped top cladding. Tapers allow the connection between the PC (post-processed at COBRA) and the rest of the circuit (pre-processed by Oclaro). A 5 µm distance between the tapers is kept to provide some tolerance for the PC post-processing with tapered input-output waveguides. A tradeoff between device performances and dimensions leads to the choice of the taper length L_T and width W_T. The performance is evaluated in terms of coupling coefficient $k = P_{out}/P_{in}$. A pair of tapers, both 5 µm wide and 100 µm long, give a $k = 0.95$. Since in the PI-SOA test structure the PC is connected by two pairs of coupled tapers, $k = 0.90$; thus, the device has 0.5 dB extra losses due to the taper connections. A 500 µm space is left in between the Oclaro tapers for post-processing of the PC together with input-output tapered waveguides.

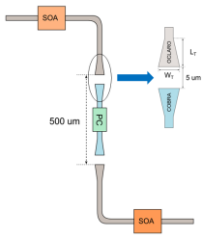


Fig.3: PI-SOA test structure and OCLARO-COBRA taper connection.

[1] Formerly at Oclaro Technology Ldt.

IV. POST-PROCESSING

The PC post-processing consists of two sequential processes: the protection of the pre-processed circuit and the PC post-processing. The pre-processed chip is protected with 400 nm of silicon nitride and with photo-resist. The photo-resist AZ 4533 is spun for 30 sec at 2500 RPM and soft baked for 20 min at 95°C; the spinning time and speed define the thickness of the photo-resist. A photolithography mask is used to open the areas for the PC processing. After the exposure, the photo-resist is developed using AZ-developer diluted 1:1 ratio in H_2O for 2 min and 30 sec. The last step is the photo-resist hard baking. The temperature is ramped from room temperature to avoid strain in the photo-resist, which causes cracks. At 200°C the photo-resist is baked for 20 min. The chip is then ready for the PC processing. First, O_2-hhplasma is applied to promote the adhesion between the EBL resist (ZEP) layer and the silicon nitride layer, which is already underneath the photo-resist; afterwards, the ZEP is spun on the chip. The ZEP layer remains quite uniform from the middle of the opened areas (around 350 nm thick) to 5 µm away from the Oclaro tapers (400 nm); so the structures can be exposed everywhere with the same EBL dose. The PC is processed in two EBL exposures: 1) definition of a rectangular area used to etch the slope in the cladding with HCl; 2) definition of the PC waveguide together with input and output tapered waveguides. The straight sidewalls are etched in the ICP. However, in our first experiments, the post-processed structures show a guiding layer undercut. One of the reasons is that during the wet etching (HCl etching or cleaning steps) the presence of light influences the etch rate. This is known as the photo-electrochemical effect (PEC) and it can be enhanced by the presence of the back metal contact. A cleaning with phosphoric acid has been performed with and without light to verify this hypothesis. The sample cleaned in the dark shows a smaller undercut. Fig. 4 shows the protected Oclaro taper and the COBRA taper with the guiding layer undercut on the real chip, and the post-processed PC on a dummy sample.

V. MEASUREMENTS

In the measurement setup the output fiber of a tunable laser, working at $\lambda = 1550\,\text{nm}$, is connected to a polarization controller. The polarization controller is used sub-sequentially to minimize and maximize the PI-SOA output power to obtain P_{out}^{min} and P_{out}^{max}. We calculate $P_{diff} = P_{out}^{max} - P_{out}^{min}$ for two test structures: one with the PC (SOAs_PC) and one without PC (SOAs_noPC). In SOAs_noPC the PC is replaced with a deep etched passive waveguide 1.5 µm wide. The measurement results (TABLE I) show that P_{diff} is significantly smaller if the PC is present.

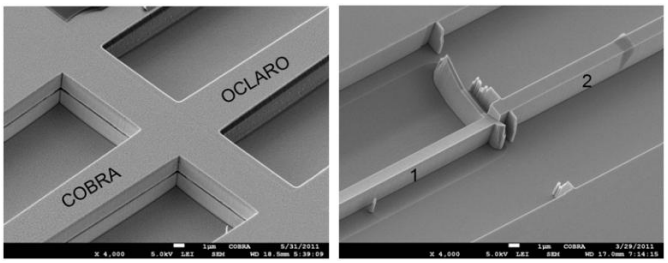


Fig. 4: Oclaro taper and COBRA taper with guiding layer undercut (left); PC (1) with input waveguide (2) on a dummy sample (right).

TABLE I. MEASUREMENTS RESULTS FOR THE POLARIZATION INDEPENDENT SOA

	SOAs length	Drive current I	P_{in}	P_{out}^{max}	P_{out}^{min}	P_{diff}
SOAs_PC	500 µm	35 mA	5 dBm	-16 dBm	-19 dBm	3 dB
SOAs_noPC	300 µm	25 mA	0 dBm	-2 dBm	-16 dBm	14 dB

The losses are high due to the guiding layer undercut. We also measured the losses in an Oclaro passive test structure without taper connections (Bends _Oclaro) and then we compared the result with two passive test structures with taper connections. The first one is made by Oclaro (Bends_tapers_Oclaro); in the second one the central tapered waveguide has been post-processed at COBRA (Bends_tapers_COBRA). The comparison between Bends _Oclaro and Bends_tapers_Oclaro shows that the taper connections introduce 0.5 dB losses (TABLE II) which matches the simulations. Bends_tapers_COBRA has another 0.5 dB extra losses most likely introduced by the guiding layer undercut.

TABLE II. MEASUREMENTS RESULTS FOR TAPER CONNECTION LOSSES

	P_{in}	P_{out}
Bends_Oclaro	0 dBm	-5.3 dBm
Bends_tapers_Oclaro	0 dBm	-5.8 dBm
Bends_tapers_COBRA	0 dBm	-6.3 dBm

VI. CONCLUSIONS

A PC has been post-processed on an Oclaro chip containing test structures for PI-SOAs. The connection between the devices processed by Oclaro and COBRA is realized through tapers which give 0.5 dB extra losses. During the post-processing the Oclaro structures are completely protected. However, a guiding layer undercut of the post-processed structures occurred due to the photo-electrochemical effect. Further tests will verify if the undercut starts to take place during the ICP etching. Measurement results show that the polarization dependence of two SOA's in series reduced from 14 dB to 3 dB with the PC in-between, indicating the presence of a significant polarization conversion.

ACKNOWLEDGMENT

The research leading to these results has received funding from the European FP7 project EuroPIC under grant agreement NMP 228839.

REFERENCES

[1] M. Smit, X. Leijtens, E. Bente, J. Van der Tol, H. Ambrosius, D. Robbins, M. Wale, N. Grote and M. Schell, "Generic foundry model for InP-based photonics," IET Optoelectronics, vol. 5, no. 5, pp. 187-194, 2011.

[2] L. Augustin, "Polarization handling in photonic integrated circuits", PhD thesis, Technische Universiteit Eindhoven, Eindhoven, The Netherlands, 2008. ISBN 978-90-386-1854-8.

[3] M. Felicetti, to be published.

Interferometric integrated planar Bragg filter for all-optical single-sideband suppression

Chaotan Sima, J. C. Gates, H. L. Rogers, P. Mennea, C. Holmes, M .N. Zervas, P. G. R. Smith
Optoelectronics Research Centre
University of Southampton
Southampton, United Kingdom
cs4g09@orc.soton.ac.uk

***Abstract*—An integrated planar Bragg filter is proposed and experimentally demonstrated. X-couplers and Bragg gratings, operating as photonic Hilbert transformer and flat-top band gap reflectors, are incorporated. Optical signals reflected from these two gratings interference with each other are suitable for single sideband suppression. The device is fabricated by Direct UV grating writing technology in silica-on-silicon.**

Keywords-planar Bragg grating; photonic Hilbert transformer; single sideband suppression; direct UV writing

I. INTRODUCTION

In the all-optical communication systems, optical bandwidth is currently limited so frequency efficiency is important to improve the bandwidth performance. One significant approach is to use optical single-sideband (SSB) modulation [1]. Various methods have been proposed and demonstrated [2]-[4]. Bragg-grating-based photonic Hilbert transformers (PHTs) were implemented in the fiber-based optical SSB system [3]. Here we present initial efforts to fabricate an integrated SSB modulation device, based on silica-on-silicon planar geometry which provides a route to realize compact optical modules for applications.

In this work, we practically demonstrate an integrated photonic device, composed of an X-coupler, PHT and flat top reflector, shown in Figure 1. The photonic Hilbert transformer was implemented using an appropriate apodized planar Bragg grating with a π-phase shift in the grating length. Sinc-apodized Bragg grating was utilized as flat top reflector in wavelength region. All structures are located in a single chip and fabricated by direct UV grating writing technology [5].

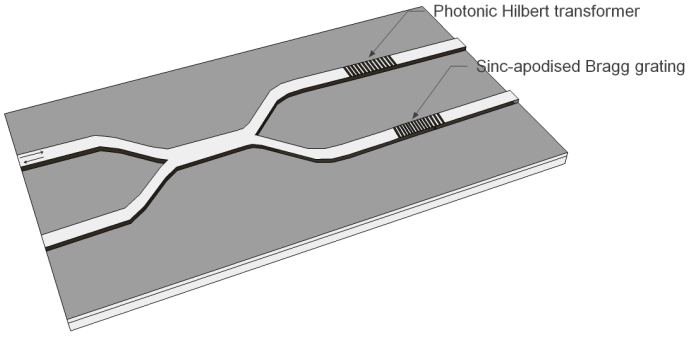


Figure 1 Proposed 3D structure of an integrated all-optical SSB modulator.

II. OPERATION PRINCIPLE

The Hilbert transform in frequency domain is given as [1]:

$$\hat{H}(\omega) = -j\,\mathrm{sgn}(\omega) \tag{1}$$

Where sgn(ω) is the sign function (which is +1 for ω > 0 and -1 otherwise), and ω is the baseband frequency. Thus, the frequency response of the Hilbert transformer has a π-phase shift at ω=0, whereas the amplitude remains constant. To physically realize the PHT, the grating apodization profile is given by [2]:

$$\Delta n(z) \propto \frac{\sin^2(\pi n_{av}\Delta f\,(z-z_0)/c)}{(z-z_0)} \tag{2}$$

For 0≤ z≤ L, where nav is the average refractive index of the planar Bragg grating, c is the speed of light in a vacuum, L is the total grating length, z0 is the zero-crossing point in the apodization function, and Δf is the operative bandwidth. z0 is set to the centre of the grating length for simplicity. The grating period is $\Lambda=\lambda_B/2n_{eff}$.

Sinc-apodized Bragg gratings are applied as flat top reflectors in the other arm. The grating apodization profile is given as:

$$\Delta n(z) \propto \frac{\sin[\pi(z-z_0)]}{(z-z_0)} \tag{3}$$

The sinc-apodized grating is designed to obtain identical reflectivity amplitude response as Hilbert transformer, in order to enhance the suppression effect. Gratings are 12mm long and central wavelength is 1550nm. The grating refractive index modulation depth is Δn = 0.0008. A transfer matrix method is employed to model the grating spectrum. Reflectivity, optical phase, group delay and apodization profile of the Hilbert transform grating (line) and sinc-apodized grating (dot) are illustrated in Figure 2. As anticipated, the sinc-apodized grating responses are similar to the Hilbert transform gating, except the π phase-shift in the central wavelength.

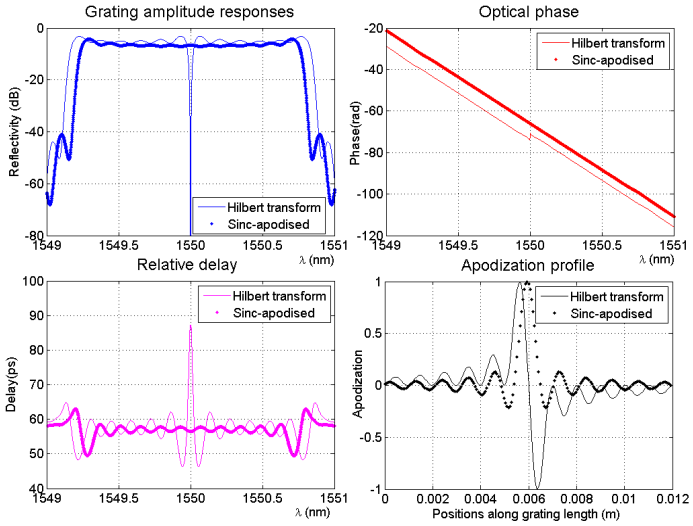


Figure 2 Simulation of Hilbert transform (*line*) and sinc-apodized grating (*dot*) responses in wavelength region.

III. FABRICATION AND MEASUREMENT

The preliminary effort is to fabricate an X-coupler with designed Bragg gratings in each arm, shown in Figure 1. The proposed planar Bragg grating was fabricated using direct UV grating writing (DGW) technology. This method involves focusing two crossed laser beams (λ=244nm) into a photosensitive core of a planar sample. Precise translation of the sample and modulation of the interference pattern creates grating structures and simultaneously define the channel waveguide [5]. This spot size is approximately 6μm in diameter, providing the unique ability over traditional FBG to manipulate the grating's structure at the micron level. This ability allows precise engineering of the amplitude and phase response of the gratings with complex structures.

The effective refractive index of the mode within the gratings was neff =1.4472, the two gratings were both 12mm long and the crossing angle of the X-coupler is 2.5 rad. The experimental data is shown in Figure 3. The grating responses in reflection were directly measured using the optical spectrum analyzer with an erbium fibre based ASE broadband source.

Figure 3(a) shows the reflectivity spectral of Hilbert transform (green) and sinc-apodised (red) gratings. The data is normalized by comparison with the 4% reflection from the cleaved far end of the fiber to calibrate the actual reflection from the grating. In Figure 3(b) the SSB suppression ratio of X-coupler1 is ~7dB, whereas in X-coupler2 in Figure 3(c), an additional phase-shift in one arm of the device results in a suppression of the opposite side band of ~7dB. Greater suppression will be achieved by phase trimming, optimization of the X-coupler parameters and the grating responses.

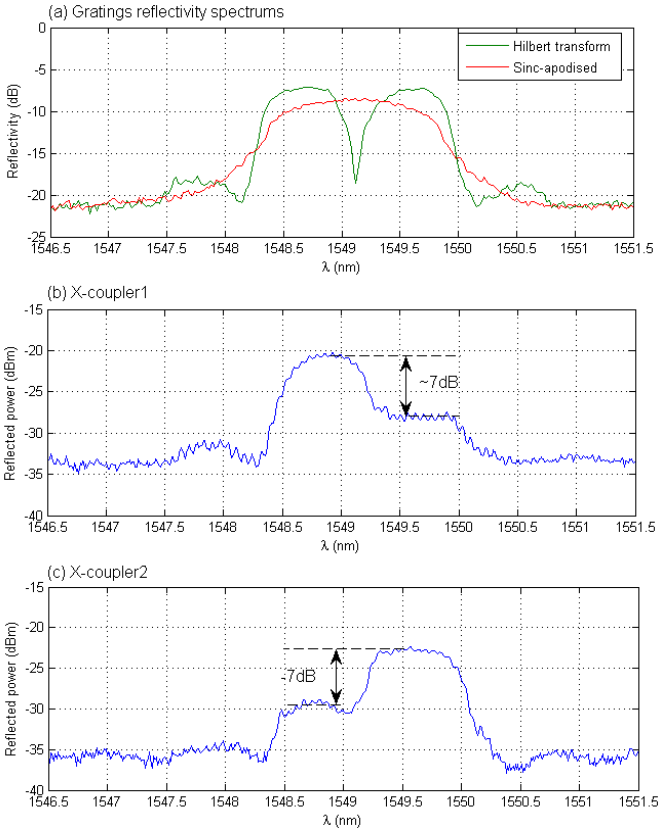


Figure 3 Experimental data: (a) gratings reflectivity spectral with Hilbert transform (*green*) and sinc-apodisation (*red*); (b) reflected power from X-coupler1, with ~7dB suppression ratio; (c) extra phase shift was applied to the X-coupler2, with the suppression ratio around -7dB.

IV. CONCLUSIONS

We have presented preliminarily data demonstrating an interferometric integrated SSB suppression filter. The suppression ratio will be enhanced by tuning the optical phase. In the future, the integrated nature of planar geometry will allow these devices to be combined with other functions, such as thermal tuning elements and liquid crystals to generate reconfigurable devices.

REFERENCES

[1] S. L. Hahn, The Transforms and Applications Handbook, 2nd ed., A. D. Poularikas, ed. CRC Press, 2000, pp. 551.

[2] M. H. Asghari and J. Azaña, "All-optical Hilbert transformer based on a single phase-shifted fiber Bragg grating: Design and analysis," Opt. Lett., vol. 34, pp. 334–336, February 2009.

[3] Z. Li, W. Li, H. Chi, X. Zhang, and J. P. Yao, "Optical single-sideband modulation using a fiber-Bragg-grating-based optical Hilbert transformer," IEEE Photon. Technol. Lett., vol. 23, no. 9, pp. 558-560, May 2011.

[4] C.Sima, J.C.Gates, H.L.Rogers, C.Holmes, M.N.Zervas, P.G.R.Smith, "Integrated all-optical SSB modulator using photonic Hilbert transformer with planar Bragg gratings", CLEO/Europe-EQEC 2011 Munich 22-26 May 2011 CI4.5

[5] G. D. Emmerson, S. P. Watts, C. B. E. Gawith, V. Albanis, M. Ibsen, R. B. Williams, and P. G. R. Smith. "Fabrication of directly UV-written channel waveguides with simultaneously defined integral Bragg gratings". Electronics Letters, vol. 38, pp. 1531–1532, November 2002

Traveling wave model of an AWG-based multiwavelength laser

R.C. Guzman, L.J Orbe, G. Carpintero
Department of Electronic Technology
Universidad Carlos III de Madrid
Leganés, Madrid, Spain, 28911
rcguzman@ing.uc3m.es

A. Corradi, E.A.J.M. Bente,
COBRA Research Institute
Eindhoven University of Technology
Eindhoven, The Netherlands

***Abstract*— This work presents a traveling wave model description of an arrayed waveguide grating (AWG) based multiwavelength laser. The purpose is to design a device with frequency spacing of 70 GHz between channels at 1550 nm central wavelength, aiming to dimension the required channel bandwidth to achieve a target side mode suppression ratio (SMSR) among longitudinal modes.**

I. INTRODUCTION

An Arrayed Waveguide Grating (AWG) is a complex passive component that is commonly used to build multiwavelength lasers. As shown on Fig. 1, the cavity of such a laser is defined between two cleaved facet mirrors (M) of the chip. The AWG acts as an intra-cavity filter, selecting the lasing wavelengths [1], which depend on the passband location of each channel of the AWG. Within each channel, the cavity losses are minimal for the specific wavelength corresponding to its particular passband. As shown on Fig. 1, every single channel is activated by biasing a separate SOA, and biasing more than one SOA simultaneously results lasing at the corresponding channel wavelengths.

Due to the size of the AWG, the cavity defined between the two mirrors (M) is usually in the order of several millimeters and therefore a longitudinal mode spacing in the order of tenths of GHz. This is an important issue, since within each individual wavelength channel, several longitudinal modes compete for gain over the AWG channel bandwidth, which should be as sufficiently narrow in order to have just one lasing wavelength. Narrowing this channel imposes design restrictions, as in this passive device, all of its functional parameters are linked to the physical dimensions in the AWG [2].

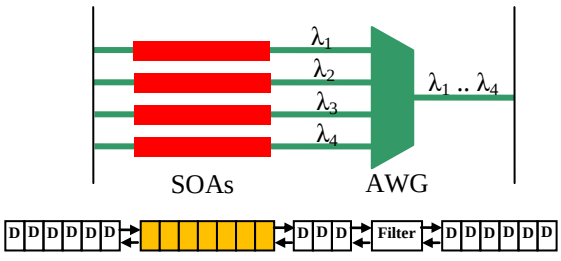


Figure. 1. Schematic of an AWGL and equivalent model.

II. AWG MODEL

An AWG is usually specified by functional characteristics such as number of channels, central frequency and channel spacing, -3 dB channel bandwidth, free spectral range, maximum insertion loss of the central channel or maximum non-uniformity. The AWG has many degrees of design freedom and a specific approach has to be followed for its design to provide the physical dimensions of the device (such as the number and length increment of the array waveguides) that achieve the specifications. We have used the method proposed in [2] to obtain the frequency response of the AWG. The initial specifications are a central wavelength λ_c = 1550 nm, channel spacing $\Delta\lambda$ = 0.56 nm (70 GHz) and a free spectral range FSR = 8.96 nm (1.12 THz), and the transfer function response of the AWG is presented in Fig. 2.

In order to develop a traveling wave model (TWM), we have developed an equivalent description using a multistage digital filter on Matlab©. This filter captures the filtering effect of the AWG channel selection, with the condition of having a linear phase (acts as a time delay). A FIR's filters bank were used in this design to adjust the filter parameters (filter order, stop-band and pass-band attenuation, filter bandwidth, etc.) and match the AWG's response. The digital filter response is depicted in Fig. 3, in which the origin in the x-axis represents the center frequency of the traveling wave simulation (193 THz), and the maximum normalized frequency represents half of the simulated bandwidth (16.216 THz). A spacing frequency of 70 GHz corresponds to a normalized frequency of 0.0043167 and, a FSR = 1.1187 THz corresponds to a normalized frequency of 0.069.

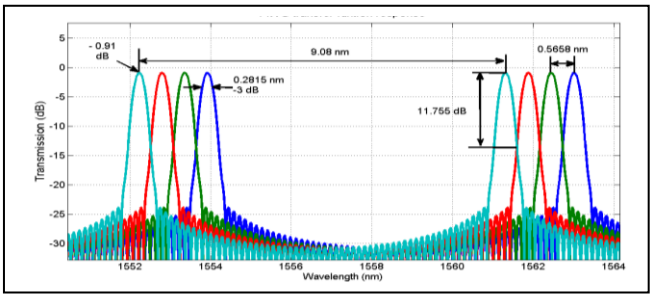


Figure. 2. AWG's transfer function on Matlab with design rules based on [1].

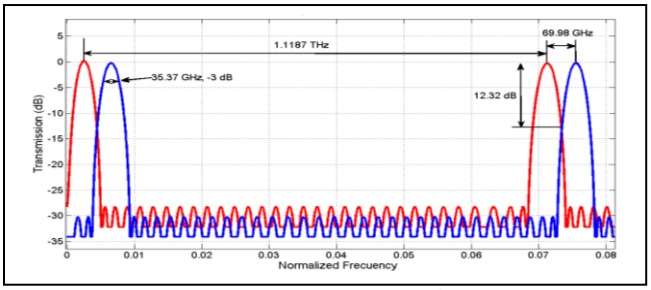


Figure. 3. Matlab AWG equivalent digital filter response.

III. MULTIWAVELENGTH LASER MODEL

We have developed a traveling wave model to describe an AWG-based multi-wavelength laser (or AWGL). The traveling wave model as described in [4] has been used to describe two elementary building blocks: the passive waveguide and the SOAs. As shown on Fig. 1, each channel has an SOA, simulated using 256 sections. This has determined the step size (Δz = 2.26 μm) for the passive waveguides, in which the light is propagated introducing the corresponding delay and sets the total cavity length. The -3 dB gain bandwidth of the SOA is set about 170 GHz. Other important parameters that were used in the simulation are: group index = 3.7, Γ = 0.35, $N_o = 1.5x10^{18}$ cm^{-1}, α = 2800 m^{-1} and ε = 0.05, following the model structure described in [4]. The spontaneous emission has been modeled as a random noise with linear distribution. The AWG is included through the equivalent digital filter determined on the previous section to effectively introduce the intra-cavity filter effect selecting the lasing wavelengths [5]. Biasing one SOA at 2 I_{th}, we observe the single channel on the common output as shown in Fig. 4, having single mode operation with a side-mode suppression ratio (SMSR) better than 30 dB and a FSR = 1.11784 THz. The figure shows also the result of biasing the adjacent channel. When both SOAs are biased simultaneously, we observe the two wavelengths as shown in Fig. 5 with the target channel spacing between them of ΔF_{ch} = 70.15 GHz. This model allows us to analyze the SMSR factor among the longitudinal modes in a single channel depending on the channel bandwidth. This is shown on Fig. 6 for different SOA bias current levels.

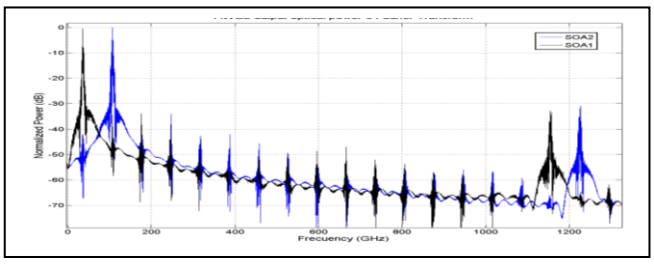


Figure. 4. Simulated optical output spectrum biasing a single channel of the AWGL. The side mode suppression ratio is better than 30 dB.

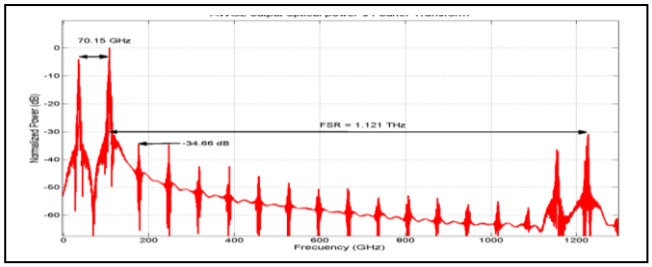


Figure. 5. Simulated optical output spectrum when biasing two adjacent channels of the AWGL.

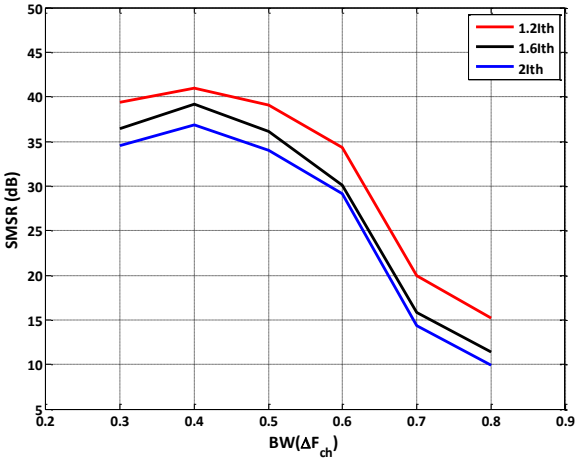


Figure. 6. SMSR among longitudinal modes in the AWGL. The channel bandwidth (BW) is scaled to the channel spacing on the AWG.

ACKNOWLEDGMENT

Part of this work is developed for the project FP7 iPHOS (Integrated photonic transceivers at sub-terahertz wave range for ultra-wideband wireless communications) ICT-2010-257539.

REFERENCES

[1] M. Zirngibl, C. H. Broeke, C. R. Doerr, L. W. Stulz and H. M. Presby, "An 18 Channel multifrequency laser", IEEE photon. Technol. Lett., Vol, No 7, 1996, pp. 870-872.

[2] M.K. Smit, C. van Dam, "PHASAR-Based WDM-Devices: Principles, Design and Applications" IEEE J. Sel. Top. Quant. Electron. vol. 2, no. 236-250, pp. 22–31, 1996.

[3] D. Welch et al., "Large scale InP photonic integrated circuits: Enabling efficient scaling of optical transport networks," IEEE J. Sel. Topics Quantum Electron., vol. 13, no. 1, pp. 22–31, Jan.-feb. 2007.

[4] Tsang C.F., Marcenac D.D., Carroll J.E., Zhang L.M., "Comparison between power matrix model and time domain model in modelling large signal responses of DFB lasers", IEE Proceedings-Optoelectronics, vol. 141, pp. 89-96, 1994.

[5] P. Muñoz, R. García-Olcina, C. Habib, L.R. Chen, X.J.M. Leijtens, J. D. Doménech, M. Rius, J. Campany, T. de Vries, M.J.R. Heck, L. Augustin, R. Notzel, D. Robbins, "Multiwavelength laser based on an Arrayed Waveguide Grating and Sagnac loop reflectors monolithically integrated on InP" IET Optoelectronics, vol. 5, no. 5, pp. 207–210, 2011.

Chalcogenides applied to microring switching

J. Pello, J. J. G. M. van der Tol, M. K. Smit
COBRA Research Institute,
Eindhoven University of Technology (TU/e)
Eindhoven, The Netherlands
j.pello@tue.nl

M. Rude, R. E. Simpson, V. Pruneri
ICFO-Institut de Ciencies Fotoniques
Castelldefels (Barcelona), Spain

S. Keyvaninia, G. Roelkens
Photonic Research group, INTEC, Ghent University-IMEC,
Ghent, Belgium

***Abstract*—We show that switching a phase-change material between its two bonding states can be used to shift the resonant wavelength of a ring resonator and change its Q-factor and extinction ratio, in a reversible and non-volatile way.**

Phase-change material; integrated optics; microring resonator.

I. INTRODUCTION

Optical fiber networks have become the backbone of our telecommunication system. These networks rely on, among others, the modulation, switching and multiplexing of optical signals, all of which can be carried out by ring resonators [1]. In this paper, we explore the use of phase-change materials (PCM) as a means of controlling the resonance of a ring resonator, in a way that is both non-volatile and reversible.

PCMs can exist under two stable solid phases (a covalent bonding phase and a resonant one), which exhibit very different absorptions and refractive indices [2]. It is possible to switch such materials between these two phases reversibly in nanosecond, picosecond and femtosecond time scales using light or current pulses [3], with energies typically on the order of 1 nJ/μm^2. These unique properties have been applied to rewritable DVDs [2], and more recently to electrical phase-change RAM [3]. Here, we show that switching a rectangle of PCM deposited on top of a ring resonator between its two bonding phases can also be used to modify the behavior of the ring, a concept that has the potential both to improve the knowledge of the properties of PCMs, and to demonstrate new applications for PCMs in photonics (e.g. switching, tuning, or use in optical memories).

II. SIMULATION RESULTS

In order to design a device sensitive to the switching of a PCM between its two bonding phases, the behavior of the structure depicted in Fig.1 is simulated, using a ring resonator model and a mode solver [4].

A. Ring resonator model

As described elsewhere [5], the power transmission $|S_{21}|^2$ from port 1 (input) to port 2 (throughput) of a ring resonator (see Fig.1) can be expressed analytically as:

$$|S_{21}|^2 = \frac{t_a^2 + t_b^2\tau^2 - 2t_a t_b \tau\cos\phi}{1 + t_a^2 t_b^2\tau^2 - 2t_a t_b \tau\cos\phi}, \qquad (1)$$

where $t_{a,b}$ are the amplitude transmission coefficients in the two coupling regions (related to the amplitude coupling coefficients $\xi_{a,b}$ through $t_{a,b} = (1 - \xi_{a,b}^2)^{1/2}$), and ϕ and τ are respectively the phase difference and the amplitude attenuation induced by one round-trip in the ring. Considering a ring of perimeter L, of which a section of length x has been covered with PCM (see Fig.1b), ϕ and τ can be expressed as follows:

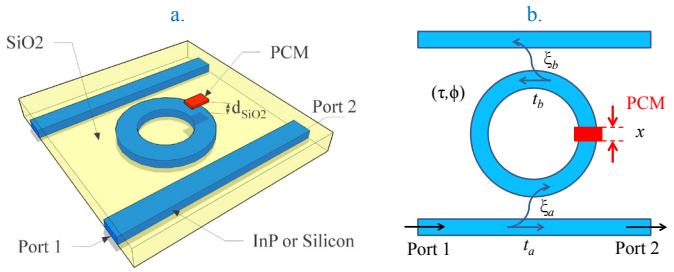


Figure 1. (a.) Aerial and (b.) top view of the proposed microring structure

$$\phi = k_0 n_{eff}(L - x) + k_0 n_{eff_{PCM}} x \ , \qquad (2)$$

$$\tau = e^{-(\alpha(L-x) + \alpha_{PCM} x)/2} \ , \qquad (3)$$

where $k_0 = 2\pi/\lambda_0$ is the propagation constant of the field in vacuum, and n_{eff} and α (n_{effPCM} and α_{PCM}) are the effective index and the attenuation coefficient of the mode propagating in the section of the ring without PCM (with PCM).

B. Mode Solving

Using the dependency of k_0 with wavelength, (1), (2) and (3) allow the theoretical transmission spectrum of the proposed ring structure to be determined. However, in order to do so, t_a, t_b, n_{eff}, α, n_{effPCM} and α_{PCM} need to be determined. The first four of these parameters can be extracted from measurements carried out on fabricated devices [1,6]. But for the parameters of the mode guided in the ring section covered with PCM, there is no experimental data available. Therefore, a mode solving tool is used to calculate these parameters.

The cross-section of the modeled waveguide is shown in Fig.2a. It is a typical monomode InP wire used in previous works [6]. All simulations are carried out at 1.5 μm wavelength, considering only the fundamental TE mode and neglecting dispersion effects. Furthermore, the (complex) refractive index of the PCM layer is set to that of $Ge_2Sb_2Te_5$ (GST), a prototypical PCM [3]: $n_{covalent} = 4.0 + i\ 0.1$ for the

covalent bonding phase or $n_{resonant}$ = 6.5 + i 1.4 for the resonant bonding phase.

One can already observe that, in the infrared, the real part of the refractive index of GST, for both phases, is higher than the refractive index of the material composing the waveguide (n_{InP} = 3.17). This means that in order to minimize the losses due to mode mismatch at the junction between the ring section without PCM and the ring section with PCM, the PCM thickness t_{PCM} has to be kept small with respect to the waveguide thickness.

Another point requiring attention is the strong imaginary part (equivalent to high optical losses) of the refractive index of GST's resonant bonding phase. During measurements on a real device, it is desirable to be able to obtain parameters such as α_{PCM} and n_{effPCM} from the recorded data. In practice, this means that the resonance dip which is characteristic of this type of resonator's transmission spectrum has to be deep enough to be detected and analyzed (fitted) using (1). Since the depth of this resonance dip decreases sharply when the round-trip losses increase (light needs to do many round-trips in the ring in order to exhibit a strong resonating behavior), it is necessary to keep these losses within a reasonable range (e.g. $\tau > 0.8$). Considering that most losses in the ring come from the absorbing nature of the PCM considered, limiting the round-trip losses can be done in two ways: either by reducing the length x of the ring section covered with PCM, or by increasing the buffer distance d_{SiO2} and reducing the PCM layer thickness t_{PCM} in order to limit the overlap of the mode (mostly confined in the InP) with the lossy PCM layer.

After setting the PCM layer thickness to t_{PCM} = 0.02 µm, a set of calculated values of n_{effPCM} and α_{PCM} as a function of d_{SiO2} is obtained for each bonding phase (covalent and resonant) of the PCM layer deposited on top of the waveguide. It is found that switching the PCM from the covalent to the resonant bonding phase only increases the effective index (n_{effPCM}) of the fundamental TE mode by less than 3 %, while making its absorption coefficient (α_{PCM}) shoot up by more than 3000 %.

C. Modelled transmission

In order to observe the effect that switching the PCM between its two phases has on the transmission of the device of Fig.1, the values of n_{effPCM} and α_{PCM} just obtained are input in (1), (2) and (3), together with the parameters of a fabricated device. A typical set of output curves (obtained for t_{PCM} = 0.02 µm, d_{SiO2} = 0.2 µm and x = 2 µm) is plotted in Fig.2c. The dotted curve is the fitted transmission of a fabricated ring of perimeter L = 43.5 µm without any PCM on it. The plain (green) curve shows how this ring's spectrum would be modified if covalent GST were to be deposited on a section of length x = 2 µm of the ring. Finally, the bold (red) curve shows the transmission of the same device after switching the GST layer from the covalent to the resonant bonding phase.

As expected from the small relative change in effective index n_{effPCM} upon PCM switching reported in the previous

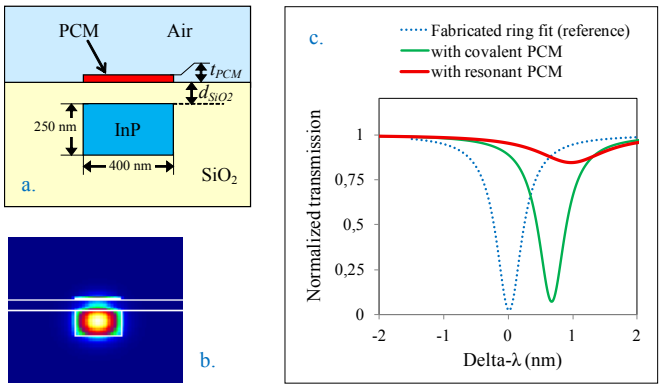


Figure 2. (a.) Schematic and (b.) typical mode profile of an InP wire with PCM on top; (c.) Simulated transmission spectra of the structure of Fig.1 (L = 43.5 µm, $t_{a,b}$ = 0.998, t_{PCM} = 0.02 µm, d_{SiO2} = 0.2 µm, x = 2 µm)

section, the resonance wavelength of the structure with PCM in its resonant bonding phase (bold curve) differs by only 0.28nm from that of the structure with PCM in its covalent bonding phase (plain curve). However, due to the large relative change in the absorption coefficient α_{PCM}, the transmission spectrum exhibits a dramatic change in shape (width and depth of the resonance) when switching the PCM from one phase to the other. In this case, the structure's Q-factor drops from 3000 to 1000, and its extinction ratio from 11.3 dB to 0.7 dB. This behavior could very well be applied to novel phase-change switches. For tuning applications, where one wishes to change the resonance wavelength of the ring without decreasing its Q-factor, an optimized design of the coupling constants $\xi_{a,b}$, or other PCMs exhibiting lower absorption values, should be considered.

III. Conclusion

The design of a structure which enables switching a microring resonator using the phase transition of PCMs has been considered. Simulations run with the parameters of GST, a prototypical PCM, show that both a shift of the resonant wavelength of the ring and a dramatic modification of its Q-factor and extinction ratio can be obtained when switching the PCM between its covalent and resonant bonding phases. Experiments are currently being conducted to verify this behavior.

References

[1] W. Bogaerts, P. De Heyn, T. Van Vaerenbergh, K. De Vos, S. Kumar Selvaraja, et al., "Silicon microring resonators," Laser Photonics Rev., vol. 6, pp. 47–73, 2012

[2] M. Wuttig and Noboru Yamada, "Phase-change materials for rewriteable data storage," Nat. Mater., vol. 6, pp. 824–832, 2007

[3] R. E. Simpson, P. Fons, A. V. Kolobov, T. Fukaya, M. Krbal, T. Yagi, et al., "Interfacial phase-change memory," Nat. Nanotechnol., vol. 6, no. 8, pp. 501–505, 2011.

[4] FIMMWAVE v.5.1, Photon Design, 2008

[5] A. Vörckel, M. Monster, W. Henschel, P.H. Bolivar, H. Kurz, "Asymmetrically coupled silicon-on-insulator microring resonators for compact add-drop multiplexers," IEEE Photonics Tech. L., vol. 15, no. 7, pp. 921–923, 2003

[6] J.J.G.M. van der Tol, R. Zhang, J. Pello, F. Bordas, G. Roelkens, et al., "Photonic integration in indium-phosphide membranes on silicon," IET Optoelectron., vol. 5, no. 5, pp.218–225, 2011.

Femtosecond writing Double line appraoch Waveguides in Er-Yb doped Niobium Borate glasses

G. A. Torchia, D. Biasetti and E. Neyra
Centro de Investigaciones Ópticas CONICET La Plata -CIC BA
CC nº 3 M.B. Gonnet, La Plata, Bs As, Argentina
gustavot@ciop.unlp.edu.ar

R. Haize, V. Jubera and T. Cardinal
ICMB University of Bordeaux
ICMB-UB
Bordeaux, France
veronique.jubera@u-bordeaux1.fr

Abstract— **In this paper we present waveguides made in Niobium Borate glasses doped with Er^{3+} and Yb^{3+} ions. These buried waveguides were fabricated by using femtosecond laser writing under double line approach. Propagation performance and index refractive profiles were studied in this work. Finally, simulated guiding structures by using commercial software RSOft were performed in order to test these guiding structures as potential amplifiers systems for optical communication purpose.**

Keywords-component; waveguides, femtosecond laser writing, Optics communication, niobium borate glasses, Er-Yb

I. INTRODUCTION

Nowadays, femtosecond (fs) laser writing represents a well established technique to achieve optical circuits in a large number of materials either by using passive or active samples. This fast, low cost, and easy method can be applied on a large number of materials such as crystals and glasses. This is possible by adjusting the experimental parameters (writing speed and pulse energy), and also performing different writing strategies [1,2]. In this work we have fabricated the buried waveguides by the so called method "double line approach" this means the laser-matter interaction region is achieved at intensities above the optical breakdown threshold inside the materials by several non linear processes so after that the interaction regions keep a residual stress surrounding the optical breakdown tracks (OBT). Besides at the OBT larger expansion takes places therefore a lower density walls also support the confined light in these guiding structures [3,4].

In this sense, this type of optical waveguides guarantee high power confinement as well as the possibility to tailor several closed region to guide the light but the most advantages is 3D fabrication optical circuits. A variety of good performance photonic applications generated with this technology have been reported as: emitters, lasers, sensors, modulators, etc. [5, 6].

In this paper we explore the possibility to achieve this kind of guiding structures in Niobium Borate Glasses doped with Er^{3+} and Yb^{3+} optically active ions. With respect to the host, as it is well known that the borate glasses enriched with Niobium ions has higher optical transparency from UV to Visible spectral range. Also, the Er^{3+} ions doping this glass improve the luminescence features since the quenching effect is reduced [7]. The Yb^{3+} added in optical materials as it is well known, acts as sensitizer for Er^{3+} ions through energy transfer mechanism that allows increasing the Erbium content in the material [8]. This goal is motivated for optical communication purpose such as integrated optical amplifier based in Er-Yb co-doped samples.

In this work, we will show the propagation characteristics and perform guiding simulations by using RSoft commercial software for optical waveguides obtained.

II. EXPERIMENTAL PROCEDURE

The waveguides were conducted following the well-established technique of laser direct writing under double line approach [2], this means these guiding structures were made by focusing a CPA Ti:Sapphire (Spectra Physics Mai Tai-Spitfire) laser beam lasing at 800 nm into a rectangular piece of 10x 12 mm2 and 2 mm thickness. The CPA system has a repetition rate of 1 KHz with about 120 fs pulse width. The laser beam was focusing 250 µm below sample surface by using a microscope objective 10 X. The waveguides were fabricated by setting the energies per pulse, by using a polarizer and a half plate , at 30 µJ and the writing velocity at 25 µm/s by using a motorized translation stage in a micromachining station which is detailed in [4]. For generate the double tracks structure we have fabricated the waveguides between consecutive straight lines separated 20 µm.

III. RESULTS AND DISCUSSION

A. *Waveguides optical performance*

To explore the light propagation into the resulted buried waveguides, we have used a standard end-fire coupling system as it is described in reference [4]. By means of this system, it is launched laser light coming from 532 nm compact solid state system. Under this procedure, we focus the laser with a 10x objective in one of the polished faces of the sample. At the output, a similar 10X microscope objective was used to collect the near field which is directly focusing onto a beam profile analyzer (BPA). From these pictures and by taking into account the CCD size and the optical magnification, the real size of modal distribution can be determined. The propagation losses were estimated by means of measurement the scattered light

from the top of the waveguides; by averaging registered pictures for the same waveguide we obtain a value of 2dB/cm.

B. Simulations: refractive index profile

By using commercial simulation software RSoft, it was able to simulate a double track waveguide fabricated inside Niobium Borate glasses. To do that, we have to build a function that can describe the refractive index profile after laser interaction. To perform the overall profile, we have considered this function as a sum of Gaussians functions. For each of them, the variation of the modified refractive index profile consists of a central Gaussian, located on the OBT, which spans from a decreasing of 1.35 x 10^{-2} up to an increment of $1x10^{-3}$ with respect to unmodified material. The distance between the lateral Gaussian functions was set at 20 µm, similar to those used for the fabricated the waveguides.

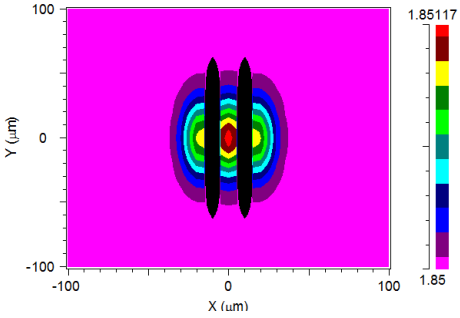


Figure 1. Refractive index profile obtained from RSoft after matching modal distribution.

To find the resultant refractive index profile, we have compared the propagated modes with those simulated by using the above function in the RSoft software. By means of an iterative procedure the simulated modes found coincide with the experimental mode taken by the BPA.

The adjusted refractive index profile by running the above method is shown in Figure 1. A wavelength of 532 nm was used to perform the simulation, this wavelength is the same used for the optical experiments. Figure 2 (top) shows two modes, one corresponding to the experiments (a) and simulations (b), respectively. Finally, in order to know the waveguide's characteristic for optical communication purpose we also performed a simulation for a wavelength of 1550 nm. The propagated mode at this wavelength is also shown in the Figure 2 (c) (bottom). As it can be seen, the mode is almost confined within the waveguide region which is delimited by an open black box. This result suggests that these integrated systems could have good performance for optical communications applications.

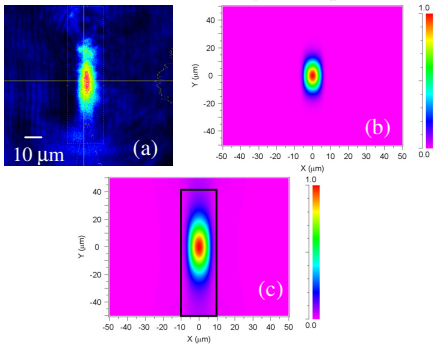


Figure 2. (a) Experimental and (b) simulated mode propagated at 532 nm in the waveguides presented in this paper. (c) Simulated mode at 1550 nm.

IV. CONCLUSIONS

In this paper we present buried waveguides obtained by femtosecond laser writing in Niobium Borate Glasses co-doped with Er-Yb ions for potential application in optics communication. The double tracks approach have shown a refractive index increment between the OBT of 1 x 10 $^{-3}$ and a decreasing of refractive index on OBT of 1.35 x 10^{-2}. These values were retrieved by using commercial software RSoft and are similar to those reported for waveguides fabricated by using this experimental procedure. These waveguides can be good candidates to perform optical amplifiers for optical communications systems.

ACKNOWLEDGMENT

This work was partially supported by Agencia Nacional de Promoción Científica y Tecnológica (PICT 2575) and CONICET (PIP 0394), Argentina. DB wishes to thank to Comisión de Investigaciones Científicas (Bs. As., Argentina) for his student fellowship.

REFERENCES

[1] C. Florea and K. A. Winick, Fabrication and Characterization of Photonic Devices Directly Written in Glass Using Femtosecond Laser PulsesJournal of Lightwave Technology, vol. 21, pp 246-251 , 2003.

[2] J. Burghoff, H. Hartung, S. Nolte and A. Tunnermann, "Structural properties of femtosecond laser-induced modifications in $LiNbO_3$"Appl. Phys. A vol. 86, pp 165-170, 2006.

[3] A. G. Okhrimchuk, A. V. Shestakov, I. Khrushchev, and J. Mitchell, Depressed cladding, buried waveguide laser formed in a YAG: Nd^{3+} cristal by femtosecond laser writing,Opt. Letters, vol. 30, pp. 2248-2250, 2005.

[4] C. Méndez, J.R. Vázquez de Aldana, G.A. Torchia and L. Roso. Optical waveguide arrays induced in fused silica by void-like defects using femtosecond, Applied Phys. B, Lasers and Optics vol. 86, pp 434-346, 2007.

[5] G. Della Valle, S. Taccheo, R. Osellame, A. Festa, G. Cerullo, and P. Laporta, 1.5 µm single longitudinal mode waveguide laser fabricated by femtosecond laser writing, Optics Express, Vol. 15, pp. 3190-3194, 2007.

[6] G.A. Torchia, A. Ródenas, A. Benayas, L. Roso and D. Jaque "Highly efficient laser action, in femtosecond-written Nd:yttrium aluminum crystals", Applied Physics Letters, vol 92, pp 111103, 2008.

[7] L. Petit, T. Cardinal, J.J. Videau, Y. Guyot, G. Boulon, M. Couzi, T. Buffeteau,Erbium luminescence properties of niobium-rich oxide glasses, Journal of Non-Crystalline Solids vol. 35, pp 2076–2084, 2005.

[8] E Cantelar and F Cussó, Analytical solution of the transfer rate equations in $LiNbO3:Er^{3+}/Yb^{3+}$, J. Phys.: Condens. Matter 12 521, 2000.

Recent achievements in $LiNbO_3$ waveguides fabricated by swift heavy ion irradiation

J. Olivares
Instituto de Optica
Consejo Superior de Investigaciones Científicas
Madrid, Spain
j.olivares@io.cfmac.csic.es

M. Jubera, A. García-Cabañes, M. Carrascosa
Dpto. Física de Materiales
Universidad Autónoma de Madrid
Madrid, Spain

F. Agulló-López
Centro de Microanálisis de Materiales (CMAM)
Universidad Autónoma de Madrid
Madrid, Spain

***Abstract*— Optical waveguides having some unique characteritics can be fabricated in Lithium niobate using high energy heavy ions. High optical confinement or very thick optical waveguides can be obtained using moderate (10^{14} cm^{-2}) or even ultralow (10^{11} cm^{-2}) fluences. The method has also been applied to other crystals of photonic interest. We present a review of the recent achievements obtained.**

Lithium niobate, nonlinear optical waveguides, ion irradiation, nanostructures, nanotracks

I. INTRODUCTION

Recently, novel methods for waveguide fabrication have been proposed and tested [1-3] for $LiNbO_3$ substrates, that use heavy-mass ions at energies in the range 5-50 MeV, that require much shorter irradiation fluences (10^{12} - 10^{15} cm^{-2}) than in standard ion implantation. In these methods the crystal amorphization is produced by electronic excitation processes and not elastic collision mechanisms and/or implantation of foreign atoms. The involved physical mechanisms are not yet sufficiently known and intense activity is now devoted to their clarification [4-7]. At variance with light ion implantation these methods rely on the electronic energy deposition (stopping power) and the subsequent relaxation of the excitation into structural defects. The fabricated waveguides present several relevant advantages over those fabricated by conventional low energy light ion implantation [8-9]. For example, they have step-like and high-jump index profiles (~0.2 and ~0.1 for ordinary and extraordinary refractive indexes respectively) and thick easily controllable amorphous layers that allow for supporting highly confined propagation modes. Since a low irradiation fluence is sufficient ($\approx 10^{14}$ cm^{-2}) to produce the waveguides, the fabrication time may be reduced up to two orders of magnitude in comparison with the implantation case. Moreover, good nonlinear optical and photorefractive properties have been already reported [1,3]. In fact, novel microring optical resonators have been recently achieved [10].

The purpose of this paper is to report on our new recent achievements and results concerning the potential and promising properties of those novel waveguides.

II. CONTROL AND OPTIMIZATION OF PROPAGATION LOSSES

Preliminary reported values for propagation losses (PL) yielded values ranging between 1-10 dB/cm [1], which was still high for many applications. In order to reduce PL a systematic study has been carried out for the SHI waveguides looking for an optimized response. Suitable post-irradiation annealing treatments reaching higher temperatures than those previously used, i.e. T~300 ºC, were implemented. We have demonstrated the feasibility of markedly reducing optical losses when annealing treatments in the range (300-375 ºC) are applied. Values under 0.5 dB/cm for both polarizations have been achieved as listed in Table I

Table I: Values of the propagation losses (PL) measured in a planar waveguide fabricated by fluorine ions at 20 MeV and a fluence of $4x10^{14}$ cm^{-2}, after two annealing treatments indicated in the Table. n_o and n_e indicate ordinary and extraordinary polarizations, respectively.

T **(ºC)**	***Time*** **(h)**	***PL-n_o*** **(dB/cm)**	***PL-n_e*** **(dB/cm)**
350	1	0.3	1.5
375	0.25	<0.3	0.5

Good quality planar waveguides have been obtained in congruent LiNbO3 substrates as well as on those doped with Mg. This doping is shown to enhance the optical damage resistivity of the material and it may be particularly useful for high power NLO applications

III. CHANNELLED WAVEGUIDES

In addition to planar waveguides channeled waveguides have also been produced. A two step procedure has been followed. First, planar waveguides were fabricated by soft proton exchange. Then, SiO_2 or aluminium stripped masks were photo-litographically made on top of the waveguide. Finally, in order to obtain the channel waveguides the samples were irradiated with Br ions at 12 MeV. The masks stop the ions and preserve the waveguide previously recorded structure in the protected region. In the areas free of masks, the ion irradiation produces an amorphous layer of 2-3 μm thick with an isotropic refractive index around 2.10 (for λ = 633 nm) lower than the refractive index of the previous waveguide. In Fig.1 a microphotograph of the $LiNbO_3$ surface is shown where two channel waveguides of 12 μm and 20 μm wide can be distinguished.

IV. THICK WAVEGUIDES FOR IR APPLICATIONS

Using higher energy ions, thicker waveguides can be achieved with potential application in the medium infrared. Heavy mass ions, Kr and Xe, having energies of 809 MeV and 1.43 GeV, respectively, were used to produce planar optical waveguides, using fluences as low as $2x10^{11}$ at/cm^2. The irradiations were performed [11] on Z-cut samples at GANIL (Caen, France) and GSI (Darmstadt, Germany). The waveguides had a thickness of 40-50 μm, a refractve index jump of up to 0.04 and propagate both TE and TM polarizations.

ACKNOWLEDGMENT

This work was supported by MICIN, projects MAT2008-06794-C03 and MAT2011-28379-C03.

[1] J. OLIVARES, G. GARCIA, A. GARCIA-NAVARRO, F. AGULLO-LOPEZ, O. CABALLERO, A. GARCIA-CABAÑES, *"Generation of high-confinement step-like optical waveguides in $LiNbO_3$ by swift heavy ion-beam irradiation"*, Appl. Phys. Lett., 86, 183501, 2005

[2] J. OLIVARES, A. GARCIA-NAVARRO, G. GARCIA, A. MENDEZ, F. AGULLÓ-LOPEZ, A. GARCIA-CABAÑES, O. CABALLERO, *"Nonlinear optical waveguides generated in lithium niobate by swift-ion irradiation at ultralow fluences"*, Opt. Lett., 32, 2587, 2007.

[3] J. OLIVARES, A. GARCIA-NAVARRO, A. MENDEZ, F. AGULLO-LOPEZ, G. GARCIA, A. GARCIA-CABAÑES, M. CARRASCOSA, *"Novel optical waveguides by in-depth controlled electronic damage with swift ions"*, Nucl. Instrum. Meth. B, 257, 765, 2007.

[4] J. OLIVARES, A. GARCIA-NAVARRO, G. GARCIA, F. AGULLO-LOPEZ, F. AGULLO-RUEDA, A. GARCIA-CABAÑES, M. CARRASCOSA, *"Buried amorphous layers by electronic excitation in ion-beam irradiated luthium niobate: Structure and kinetics"*, J. Appl. Phys., 101, 33512, 2007].

[5] M. TOULEMONDE, W. ASSMAN, C. DUFOUR, A. MEFTAH, F. STUDER, C. TRAUTMANN, in *"Ion Beam Science: Solved and Unsolved Problems"*, ed. P. Sigmund, (The royal Danish Academy of Sciences and Letters, Copenhagen, 1996), p. 263.

[6] F. AGULLÓ-LÓPEZ, G. GARCÍA, J. OLIVARES, *"Theoretical modeling of swift-ion-beam amorphization: Application to $LiNbO_3$"*, Nucl. Instrum. Meth. B, 249, 118, 2006.

[7] A. RIVERA, A. MENDEZ, G. GARCIA, J. OLIVARES, J. M. CABRERA, F. AGULLO-LOPEZ, *"Ion-beam damage and non-radiative exciton decay in LiNbO3"*, J. Lumin., 128, 703, 2008.

[8] P. D. Townsend, P. J. Chandler and L. Zhang: *"Optical effects of ion implatation"*. (Cambridge University Press, Cambridge, 1994).

[9] F. Cheng. J. Appl. Phys. **106**, 081101 (2009)

[10] A. Majkic, M. Koechlin, G. Poberaj and P. Günter. *"Optical microring resonators in fluorine implanted lithium niobate*," Opt. Express **16**, 8769 (2008).

[11] J. Olivares, M.L. Crespillo, O. Caballero-Calero, M.D. Ynsa, A. García-Cabañes, M. Toulemonde, C. Trautman, F. Agulló-López, "Thick optical waveguides in lithium niobate by swift-heavy ions at ultralow fluences" Opt. Express 17, 24175 (2009).

Feasibility study of an InP membrane on silicon laser

S.P. Bhat, J.J.G.M. van der Tol, and M.K. Smit
PhI group, COBRA Research Institute
Eindhoven University of Technology
Eindhoven, the Netherlands

G. Roelkens
Photonics Research Group
Ghent University/imec
Ghent, Belgium

***Abstract* — Realizing an electrically pumped membrane laser with acceptable performance has been a major challenge so far. In this paper the possibility for such a device is investigated by simulating its optical and thermal properties.**

Keywords-InP; membrane; photonic integration; laser; electrically pumped; simulation; optical; thermal;

I. INTRODUCTION

Recently, high index contrast photonic integrated circuits have become important due to their promise to reduce the footprint and hence their cost. As explained in [1], one of the approaches taken uses an InP-membrane that contains both passive and active regions. To exploit the potential of the compact passive devices already fabricated it is essential to have an on-chip laser.

The idea here is to make the laser by selectively removing the gain material from regions where it is not required and retaining it in regions only where it will be made use of. The controlled partial oxidization of an InAlAs layer, based on [2], will act as a current blocking layer preventing leakage paths and allowing the current only to flow through the core of the active region. This will enhance the efficiency of the laser.

To check for the feasibility, capability and limitations of such a device in an InP membrane adhesively bonded to silicon, optical simulations are performed for confining and guiding light at 1550nm with minimal losses. Along with this, thermal simulations are also carried out to check the power dissipating capability of such a membrane structure

II. OPTICAL SIMULATIONS

The first step towards making any device based on III-V membranes is to make a choice of the layer-stack. This involves selecting the order of the materials in the stack, the thickness, doping type and doping level for each layer. The layers are grown on an n-type InP substrate in the following order: n-InP, n-InAlAs, an active layer consisting of three InGaAs quantum wells separated by Q1.25, p-InP and p-InGaAs. Other parameters for the layer stack are based on simulations [3]. A further choice that has to be made is the geometry of the laser. To avoid complications a simple Fabry-Perot type geometry is chosen.

A. Mode Confinement

The gain layer and the n-InP layer, in which we intend to fabricate the passive waveguides, are vertically separated. So, the mode has to be present in both the layers to a significant extent. This is determined by the thickness of individual layers. Width determination is based on gain considerations and the position of the metal contacts. These contacts have to be far from the active region to avoid high losses and yet have a sufficiently large contact area with the InGaAs layer to minimize electrical resistance. These requirements resulted in the configuration shown in Fig.1.

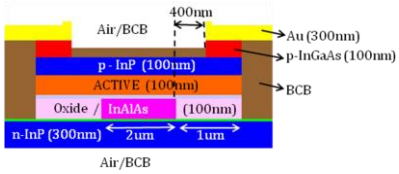


Fig. 1: Laser geometry showing the layer stack and the considered dimensions

B. Doping Effects

A high doping in the different layers decreases the electrical resistance for the current flow. On the other hand, an increase in doping level also increases the optical loss. So, a compromise between the two effects has to be reached. Various doping levels for p- and n-type in the relevant layers are simulated [3]. The optical absorption coefficients are calculated based on [4]. As can be seen from Fig.2, an increase in p-doping has a more significant effect on the loss than the n-doping. Doping levels of $1x10^{18}$ cm^{-3} for both p- and n- type are chosen as the points of compromise as the resistance value for this doping was acceptable (~ 35Ω). This point will become more apparent later.

C. Metal Absorption Loss

Apart from the losses due to doping and a high loss in the InGaAs layer, metal contacts are also an important source of optical loss. To gauge their contribution and to reduce them,

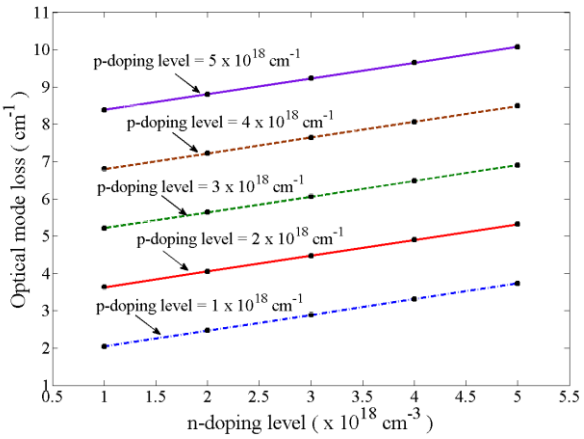


Fig. 2: Optical loss as a function of p-type and n-type doping

The authors thank STW-IMOS project for financial support

more simulations are done [3]. As is apparent from Fig.3, larger distances from the active region reduce the optical loss but increase the electrical resistance. A distance of 400 nm from the interface between InAlAs and its oxide was found to be optimal (see Fig.1).

III. Thermal Simulations

The device fabricated in the InP membrane is to be adhesively bonded to a silicon substrate using BCB. The InP substrate is then etched away completely [5]. This leaves the device sandwiched between air on one side and BCB on the other – both being very good thermal insulators. Two main sources of heat in the laser are identified, the heat produced due to non-radiative recombination and ohmic heating in the resistive path. As there is no good conductive path for this generated heat to flow out, this has the effect of increasing the device temperature. This is confirmed by thermal simulations which show drastic increase in the temperature near the active region [6]. Since the stability of a laser oscillation critically depends on the temperature, a strategy had to be developed to overcome this problem.

A. Power Dissipating Capability

The best way to remove the generated heat is to transfer it to the silicon substrate. Moreover, a Peltier cooling element can be used to maintain the substrate at room temperature.

It is assumed that the laser will be operational upto 70°C. So, simulations are aimed at finding the maximum allowable power dissipation in the active region which raises the temperature of the device from room temperature (20°C) to 70°C [6].

Two strategies worked well in solving the problem. The first is increasing the areas of the metal pads and the second is decreasing the thickness of the BCB layer. Both had the effect of providing a better heat sinking path into the silicon substrate which is maintained at room temperature in all the simulations.

As can be seen from Fig.4, for a 100 µm device length, a power dissipation of 25 mW (through a 400 nm BCB adhesive layer) increased the temperature near the active region to 67°C (340 K). From the estimated voltage drop and resistance calculations, this power corresponds to a current of ~ 5 mA. From the data presented in [7], this is four times the threshold current required for such a laser to function. From a thermal point of view, it is thus feasible to implement such a structure.

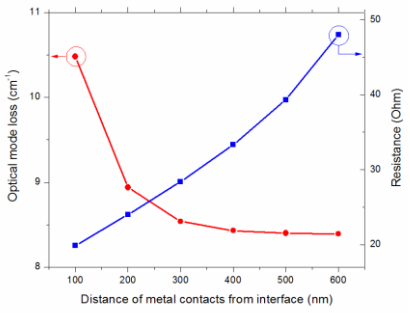


Fig. 3: Variation of the optical mode loss and electrical resistance with metal contact position

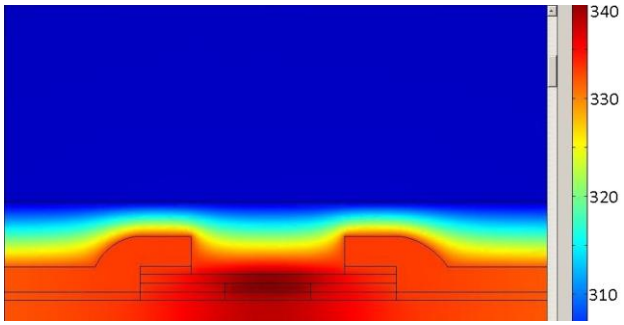


Fig. 4: Temperature contours due to self-heating

B. Device Spacing

Another important criterion which needs to be considered is how close two similar, power dissipating devices can be placed in order not to influence each other thermally. To simulate this, the side walls of the simulation window are modeled to be thermally insulating. This means that no heat enters or exits via these boundaries. The width of the window is expanded till the temperature at these points remains at room temperature; in other words, there is no heat flow into these regions. This results in a device spacing of 140 µm between the devices to thermally isolate them.

Discussion And Conclusions

Parameters for the layer stack and the dimensions of a membrane laser are determined using optical simulations. From a thermal point of view, it is feasible to work with such a structure. A device spacing of 140 µm determined from thermal simulations leads to a device density of 51 per mm^2 which is quite large. Together, these results indicate that an InP membrane laser is feasible.

Acknowledgment

S.P Bhat thanks J. Pello for his help with optical simulations, T. Spuesens and M. Tassaert for discussions on thermal simulations.

References

[1] J.J.G.M. van der Tol, R. Zhang, J. Pello, F. Bordas, G. Roelkens, H. Ambrosius, P. Thijs, F. Karouta and M.K. Smit, "Photonic Integration in Indium-Phosphide Membranes on Silicon", IET optoelectronics, June, 2010.

[2] R. Zhang, J.J.G.M. van der Tol , H. Ambrosius, P. Thijs, B. Smalbrugge, T. de Vries, G. Roelkens, F. Bordas, and M.K. Smit, "Oxidation of AlInAs for Current Blocking in a Photonic Crystal Laser", Proc. COMMAD 2010, Canberra (Australia), paper105.

[3] Photon Design, Fimmwave v.5.1.1, http://www.photond.com.

[4] U. Khalique "Polarization based integration scheme" Phd. Thesis ISBN 978-90-386-1424-3, 2008, p. 16.

[5] Roelkens, G., Brouckaert, J., Van Thourhout, D., Baets, R., No¨ tzel, R., Smit, M.: 'Adhesive bonding of InP/InGaAsP dies to processed siliconon-insulator wafers using DVS-bis-benzocyclobutene', J. Electrochem. Soc., 2006, 153, pp. G1015–G1019.

[6] Comsol Multiphysics 3.0a, Heat transfer module, http://www.comsol.com.

[7] P.J.A. Thijs, L.F. Tiemeijer, P.I. Kuindersma, J.J.M. Binsma and T. van Dongen, "High-Performance 1.5 µm Wavelength InGaAs-InGaAsP Strained Quantum Well Lasers and Amplifiers", IEEE J. Quantum Elect., vol. 21, no. 6. June 1991, p. 1429.

Adiabatic Passage of Light in CMOS-Compatible Silicon Oxide Integrated Rib Waveguides

R. Menchon-Enrich, J. Mompart, and V. Ahufinger
Grup d'Òptica, Departament de Física
Universitat Autònoma de Barcelona (UAB)
E-08193 Bellaterra, Spain
ricard.menchon@uab.cat

A. Llobera
Institut de Microelectrònica de Barcelona (IMB-CNM, CSIC)
E-08193 Barcelona, Spain

V. J. Cadarso
Microsystems Laboratory (LMIS1)
Ecole Polytechnique Fédérale de Lausanne (EPFL)
CH-1015 Lausanne, Switzerland.

***Abstract*— We experimentally demonstrate that a system of three CMOS-compatible total internal reflection waveguides allows a highly efficient and robust transfer of visible light between the outermost waveguides by adiabatically following one eigenmode of the system.**

Adiabatic passage of light; Integrated optical circuits; Silicon technology; total internal reflection (TIR) waveguides

I. INTRODUCTION

During recent years, photonics based on silicon has gained a lot of attention because it offers the possibility to revolutionize computing platforms by manufacturing optical devices using traditional and low-cost complementary metal-oxide-semiconductor (CMOS) technology [1, 2]. Nevertheless, there is still a long way to go in order to implement photonic integrated circuits able to replace and improve the traditional electronic integrated circuits. Thus, new techniques allowing full control of light propagation in silicon based optical devices are very desirable.

Recently, it has been shown that it is possible to transfer a light beam between the outermost waveguides of a system of three identical coupled waveguides in a very efficient way by adiabatically following one eigenmode of the system [3, 4]. In this paper, we present for the first time the implementation of the adiabatic passage technique for visible light in total internal reflection (TIR) waveguides [5] using a fully CMOS-compatible technology [6]. This represents an important technological step forward compared to previous works [3, 4] since it allows a massive and low-cost fabrication of these devices and their incorporation to realistic photonic integrated circuits.

II. ADIABATIC PASSAGE MECHANISM

The adiabatic passage of light in systems of three identical single-mode coupled optical waveguides (as the one schematically depicted in Fig. 1(a)) resembles the well known stimulated Raman adiabatic passage (STIRAP) technique [7]. Light can be efficiently transferred from the right to the left waveguide with almost null intensity in the central waveguide for the whole propagation by following one of the eigenmodes of the system that only involves the external waveguides [6]. To this aim, light is initially injected into the right waveguide and the evanescent couplings are adiabatically modified along the propagation direction by approaching first left and central waveguides and, later on and with a certain overlap, right and central waveguides. Furthermore, it is important to remark that the adiabatic passage in waveguides is a robust process, i.e., insensitive to small variations in the parameter values of the waveguides, a property that previously published directional couplers do not exhibit [5].

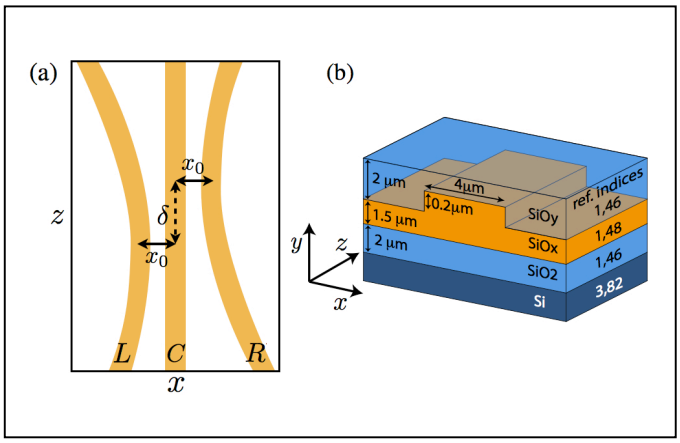


Figure 1. (a) Schematic top view of the geometry of the system of three waveguides consisting of two circularly bent outermost waveguides, left (L) and right (R), and one straight central waveguide (C). The minimum distance between waveguides is given by x_0, and the z distance between the centers of the curved waveguides is defined by δ. (b) Schematic representation of the geometry, specifying the materials and refractive indices, of one of the three TIR waveguides that form the system.

III. Design and Fabrication

The geometry of the adiabatic passage in a system of three coupled waveguides has been optimized by numerical simulations using the software Fimmprop and Fimmwave (Photon Design).

The fabrication process starts thermally growing a layer of 2 μm of silica SiO_2 on a (100) silicon wafer. Then, a layer of non-stoichiometric silicon oxide SiO_x with a refractive index of 1.48 [8] and a height of 1.7 μm is deposited over the silica layer by plasma enhanced chemical vapor deposition (PECVD). At this point, the ribs defining the waveguides are obtained by using the appropriate mask and dry etching in the SiO_x layer. They have a thickness of 0.2 μm and width of 4 μm. Finally, another layer of non-stoichiometric silicon oxide SiO_y of 2 μm with index 1.46, acting as a passivation layer, is deposited on the top of the device using PECVD. Fig. 1(b) depicts the transverse profile of one of the waveguides of the system including the values of the refractive indices and the sizes of the different layers.

IV. Experimental Results

The experimental setup consists of a 635 nm diode laser (Thorlabs S1FC635) connected to one end of a single-mode optical fiber. The other end of this fiber is located on a piezoelectric 3D positioning system (piezosystem jena NV40/3), which allows accurate fiber optics-waveguide alignment. Light propagating inside the waveguides is collected by an infrared single-mode optical fiber placed on another piezoelectric positioning system (piezosystem jena d-Drive) and transferred to a power meter (Newport 1930F-SL).

Insertion and attenuation losses were measured using identical waveguides of different lengths, with values of 3.6±0.3 dB and 0.36±0.01 dB/mm, respectively. We have also characterized the coupling coefficients $\Omega_{R,L}$ as a function of the separation of two waveguides d [6]. The experimental values may be fitted by the decaying exponential curve $\Omega(d)=\Omega_0\exp(-d/l)$ with $\Omega_0=14.9\pm1.5$ mm^{-1} and $l=2.72\pm0.09$ μm. This dependence has been used to check that the coupling coefficients $\Omega_{R,L}$ along the z propagation direction fulfill the adiabaticity requirements of the adiabatic passage of light [3].

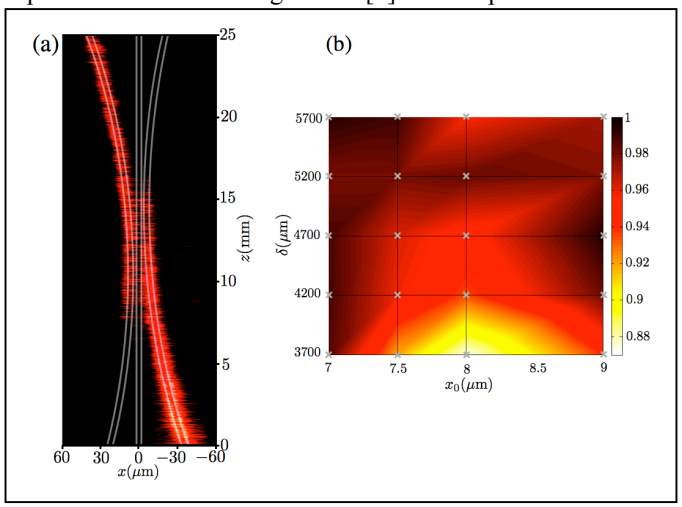


Figure 2. (a) Top view image of one of the fabricated devices in which light losses allow us to observe the adiabatic transfer of light. The radius of curvature of the outermost waveguides is 3.5m, the spatial delay is δ=4200 μm and the minimum separation between waveguides is x_0=7 μm. (b) Relative fraction of light intensity at the output of the left waveguide of the system as a function of δ and x_0. Crosses indicate the experimental measurements.

By taking several images with a CCD camera connected to an optical microscope, a top view picture of the path followed by the light beam across one of the fabricated systems of waveguides has been obtained, see Fig. 2(a). The image confirms the adiabatic transfer of light. We have also demonstrated the robustness of the adiabatic passage of light by measuring the intensity at the outputs of the three waveguides (I_L, I_C and I_R) for several devices with slightly different parameter values. Fig. 2(b) gives the relative fraction of light intensity at the left output, $I_L/(I_L+I_C+I_R)$, for different devices with δ and x_0 parameters varying from 3700 μm to 5700 μm and from 7 μm to 9 μm, respectively. The radius of the outermost waveguides is 3.5 m for all the measured devices. The lowest measured relative fraction value of light at the output of the left waveguide is higher than 0.87 whereas the highest measured relative fraction values are above 0.99, demonstrating the low sensitivity of the adiabatic passage to fluctuations of the parameters.

V. Conclusions

Using CMOS-compatible technology, we have experimentally shown that it is possible to achieve a highly efficient transfer of light between the outermost waveguides of a system of three coupled identical waveguides by adiabatically following one of the eigenmodes of the system. We have also experimentally checked the robustness of the passage against variations of the parameter values of the system. In particular, the measured relative fraction of intensity at the left waveguide output of several systems of waveguides ranges from 0.87 to values above 0.99, for variations of the geometry parameter values between 20% and 35%.

References

[1] R. Baets, et al., "Silicon photonics," in Proc. Int. Symp. VLSI Technol. Syst. Applicat., 2007, pp. 1–3.

[2] W. Bogaerts, P. Dumon, B. Luyssaert, and P. Bienstman, "Nanophotonic waveguides in silicon-on-insulator fabricated with CMOS technology," J. Lightw. Technol., vol. 23, no. 1, pp. 401–412, Jan. 2005.

[3] S. Longhi, G. Della Valle, M. Ornigotti, and P. Laporta, "Coherent tunneling by adiabatic passage in an optical waveguide system," Phys. Rev. B, vol. 76, no. 20, pp. 201101-1–201101-4, 2007.

[4] Y. Lahini, et al., "Effect of nonlinearity on adiabatic evolution of light," Phys. Rev. Lett., vol. 101, no. 19, pp. 193901-1–193901-4, 2008.

[5] K. Okamoto, Fundamentals of Optical Waveguides, 2nd ed. Burlington, MA: Elsevier, 2006.

[6] R. Menchon-Enrich, A. Llobera, V. J. Cadarso, J. Mompart, and V. Ahufinger, " Adiabatic Passage of Light in CMOS-Compatible Silicon Oxide Integrated Rib Waveguides," IEEE Photon. Technol. Lett., preprint, 20 Dec. 2011, doi: 10.1109/LPT.2011.2180519.

[7] K. Bergmann, H. Theuer, and B.W. Shore, "Coherent population transfer among quantum states of atoms and molecules," Rev. Mod. Phys., vol. 70, no. 3, pp. 1003–1025, 1998.

[8] C. Domínguez, J. A. Rodríguez, M. Riera, A. Llobera, and B. Díaz, "Effect of hydrogen-related impurities on the thermal behavior of mechanical stress in silicon oxides suitable for integrated optics," J. Appl. Phys., vol. 93, no. 9, pp. 5125–5130, 2003.

The role of index contrast in the efficiency of absorption and emission of a luminescent particle near a slab waveguide.

Ashim Dhakal, Ananth Z. Subramanian, Roel Baets
Photonics Research Group, INTEC-department
Center for Nano- and Biophotonics
Ghent University
B-9000 Ghent, Belgium

Nicolas Le Thomas
Nanophotonics and Metrology Laboratory
Swiss Federal Institute of Technology Lausanne (EPFL)
CH-1015 Lausanne, Switzerland

***Abstract*—The effect of waveguide index contrast on the absorption of the guided field by a luminescent particle near the core of a slab waveguide is analyzed, together with the Purcell-enhancement of the spontaneous luminescence and it's coupling back into the guided mode. The overall conversion efficiency is strongest for excitation by a TM-pump and coupling of fluorescent light to the TM-mode and depends approximately quadratically on the index contrast.**

Keywords- photonic sensors, nanoparticles, slab waveguide, Green function, spontaneous emission, Purcell effect

I. INTRODUCTION

In the past years, sensors based on photonic integrated circuits have been developed as the backbone for the lab-on-a-chip integration platform [1]. Many of such sensors, such as fluorescence sensors, rely on the coupling of the fluorescence signal from molecules or fluorescent nanoparticles to the underlying guiding structures. Investigation for the optimum waveguide parameters for the best efficiency of such structures has been rarely done, although there is a rich literature on light emission by particles lying close to layered dielectric structures [2-4]. These articles mainly focused on the power radiated in the farfield, keeping in mind applications such as near-field microscopy and light extraction from LEDs. In [4], the enhancement of emission and total power coupled to waveguide has been investigated. Unfortunately, the methods to calculate power coupled to the individual modes, and how that power behaves as a function of various waveguide parameters have attracted little attention. The objective of this work is to analyse how the efficiency of conversion from a guided pump to spontaneous emission coupling to a guided mode depends on the index contrast (Δn) of the waveguide and to derive the optimum thickness. Emphasis is on two very popular waveguide systems: with silicon (Si) and silicon-nitride (Si_3N_4) core materials.

II. METHODOLOGY

Our goal is to investigate the overall efficiency of absorption of a guided mode by a luminescent particle at the core-cladding interface and the subsequent emission into one of the fundamental TE or TM guided modes, taking Purcell enhancement into account. Our methodology is applied to a common slab waveguide with a lower cladding of silica (n_s=1.45), an upper cladding of air (n_1=1), and variable core index n_c and core thickness d.

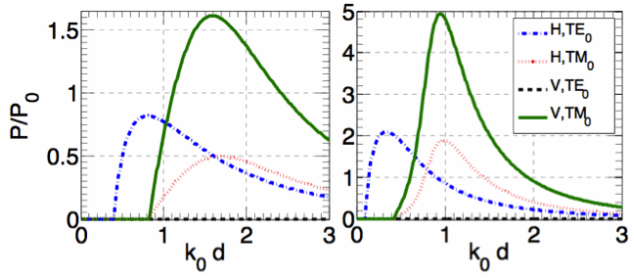


Figure 1: Power coupled to the fundamental modes, for dipoles oriented horizontal (H) and vertical (V) to the waveguide surfaces. The values are normalized to the total power that the dipole would radiate in free space. Left: Si_3N_4; Right: Si core.

The emission problem is modeled as a classical dipole emission problem in a layered medium. The total field at the location of the dipole can be calculated by expanding the dipole field into plane wave components, and applying generalized Fresnel reflectivity formulas [2-5]. The spontaneous decay rate, normalized to the free-space decay rate can then be calculated from the field at the dipole location. The total rate, normalized to free-space rate, P/P_0 turns out to be [4]:

$$\frac{P}{P_0} = 1 + \mathrm{Re}\left\{ \int_0^\infty dk_\rho \frac{\mu_\rho^2}{\mu^2} \frac{3}{4} \frac{k_\rho}{k_1^3 k_{1z}} [k_1^2 r_{TE} - k_{1z}^2 r_{TM}] + \frac{\mu_z^2}{\mu^2} \frac{3}{2} \frac{k_\rho^3}{k_1^3 k_{1z}} r_{TM} \right\} \quad (1)$$

whereby, r_{TE} and r_{TM} are the reflectivity of the whole structure for TE and TM polarizations; μ and k_1 are the wave number in the upper cladding and the total dipole moment, μ_ρ, k_ρ, are the corresponding horizontal components and μ_z, k_{1z} are the corresponding vertical components. We note that each guided mode corresponds to a pole of the reflectivity r_{TE} and r_{TM} . An unappreciated fact is that the power coupled to a mode

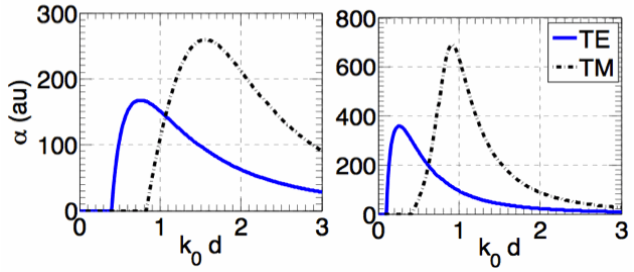


Figure 2: Absorption of the particle for fundamental TE and TM mode excitation as a function of k_0d of the slab waveguide. Left: Si_3N_4 core; Right: Si core

This work has been partially supported by the ERC grant INSPECTRA.

can be determined by calculating only the integral in the real axis around the corresponding pole. We use the Gauss-Kronrod quadrature algorithm [6] to calculate the integral around the poles. Fig. 1 shows the power P/P_0 coupled to the two fundamental modes for Si and Si_3N_4 cores respectively for the two distinct dipole orientations.

The absorption of the guided mode by a particle is directly proportional to the total photon density at the location of the particle, which is further proportional to $|E|^2$ of the considered mode. Alternatively the absorption can be derived from the imaginary part of the effective index of the guided mode in a slab with a thin uniform layer of absorbing particles. Both methods yield the same results, at least in relative terms. Fig. 2 shows the absorption (in arbitrary units) of a particle for Si and Si_3N_4 cores for the two fundamental modes.

The overall efficiency of absorption and subsequent re-emission can be calculated, in arbitrary units, by multiplying absorption and emission rate of the corresponding modes. We assume a random orientation for the radiating dipole, implying that one third of the emitted power is due to vertical dipoles and two thirds due to horizontal ones. The Stokes shift between the pump light and the luminescence can be easily taken into account by shifting the k_0d as required. For simplicity, we ignore the Stokes shift here since it only has a weak impact on the results. The overall efficiencies for all the four pumping and coupling combinations (TE-TE, TE-TM, TM-TE and TM-TM) are plotted as a function of k_0d for Si and Si_3N_4 core in Fig. 3.

III. Results And Discussion

Fig. 1 shows that as much as 1.6 and 5 times the power radiated by the particle in free space (in all possible directions) can be coupled into the waveguide modes, for Si_3N_4 and Si core respectively. The increase in emission rate can be attributed to the Purcell effect in the vicinity of the waveguide. The power coupled to a given mode is evidently dependent on dipole orientation, the cut-off and field confinement conditions of the waveguide. Dipoles oriented normal to the waveguide do not contribute to the TE mode, while dipoles oriented parallel to the waveguide contribute to both the TE and the TM mode. At k_0d values below cutoff, there is no power coupled to the waveguide mode and as k_0d is increased above the cutoff, the coupled power increases abruptly. However, as k_0d is increased further, increased confinement of the field in the core reduces the local field density at the dipole location, thus reducing the emission rate contribution from the mode and consequently the total power coupled to the mode. Keeping aside the obvious difference owing to dipole orientation, the power coupled to the waveguide roughly follows the trend of the field intensity at the dipole location and hence that of the absorption.

The trend that higher index contrast ($\Delta n = (n_c - n_s)$) enhances the emission and absorption efficiencies is evident in Fig. 2 - 4. It is apparent that among several pumping–coupling possibilities, TM pumping and the subsequent coupling to the TM mode has the highest overall efficiency. It is about 2 times stronger than the other polarization combinations in the case of nitride waveguides and about 4 times for silicon. Furthermore the best TM-TM efficiency for silicon is about 10 times stronger than for Si_3N_4.

In Fig. 4 we plot the optimal normalized slab thickness values k_0dn_c corresponding to the maximal efficiency as function of Δn. The corresponding optimal efficiency values are also plotted in Fig. 4, demonstrating that the TM-TM efficiency scales approximately quadratically with Δn. It is also interesting to note that the optimum k_0dn_c-values for higher index contrast for all the curves involving TM modes converges approximately to π (implying that $d=\lambda_0/2n_c$).

In conclusion, the overall efficiency of absorption and subsequent re-emission by a luminescent particle at the core cladding interface of a slab waveguide is most efficient for TM-pumping and subsequent coupling of the Stokes light into the TM-mode of the waveguide. This efficiency scales approximately quadratically with index contrast and is optimal for a slab thickness equal to half the wavelength in the core material. The present analysis can be extended to also describe spontaneous Raman scattering.

References

[1] X. Fan, I. M. White et.al., "Sensitive optical biosensors for unlabeled targets: A review," Anal. Chim. Acta, vol. 620, pp. 8-26 (2008).

[2] W. Lukosz and R. E. Kunz, "Light emission by magnetic and electric dipoles close to plane interfaces", J. Opt. Soc. Am, vol. 67 , pp.1607-1619 (1977).

[3] R. R. Chance, A. Prock, and R. Silbey, ''Molecular fluorescence and energy transfer near interfaces,'' in Advances in Chemical Physics, I. Prigogine and S. A. Rice, eds., vol. 37, pp. 1–65, Wiley, New York, (1978),

[4] L. Novotny, ''Allowed and forbidden light in near-field optics. I. A single diplar light source,'' J. Opt. Soc. Am. A, vol. 14, pp. 91–104 (1997).

[5] M. Paulus, P. Gay-Balmaz, O. J. F. Martin., "Accurate and efficient computation of Green's tensor for stratified media", Phys Rev E, Vol 62, pp. 5797-5807 (2000)

[6] Calvetti, D.; Golub, G. H.; Gragg, W. B. and Reichel, L. "Computation of Gauss-Kronrod Quadrature Rules." *Math. Comput.* vol. 69, pp. 1035-1052 (2000).

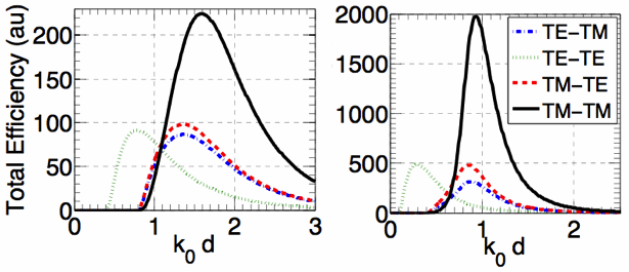


Figure 3: Overall efficiency for several mode excitation and coupling possibilities. (e.g. TE-TM means excited by fundamental TE mode and the emission coupled to fundamental TM mode) Left: Si_3N_4 core; Right: Si core

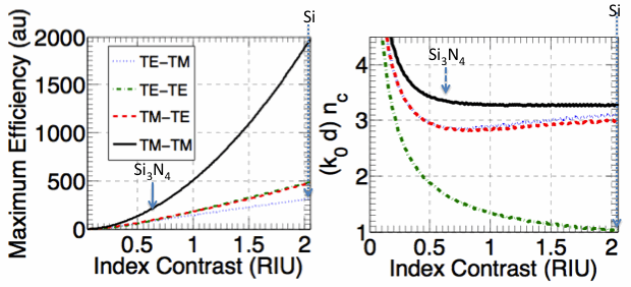


Figure 4: Left: Maximal overall efficiency as function of index contrast. Right: k_0d n_c values corresponding to the maximum overall efficiency.

Polymer microlenses for collimating light from single-mode silicon oxynitride optical waveguides

N. Ismail, L. Chang, G. Sengo, R.M. de Ridder, M. Pollnau, and K. Wörhoff
Integrated Optical Microsystems Group, MESA+ Institute for Nanotechnology, University of Twente
Enschede, The Netherlands
n.ismail@ewi.utwente.nl

Abstract—**We propose a novel technique for microlens fabrication which is compatible with silicon oxynitride technology, and enables the collimation of light exiting the waveguides into beams with divergence angles of ~0.52°.**

Keywords-arrayed microlenses; integrated optics; waveguides

I. INTRODUCTION

Numerous studies have addressed microlens fabrication for different material platforms, and using different techniques [1-6]. Most of these studies aim at using the microlenses in array configurations in which the incident light is directed orthogonally to the plane of the microlenses. Example applications are, but not limited to, free-space optical interconnection networks [1], concentrator photovoltaic systems [2], adaptive optics wave-front detection [3]. On the other hand, microlenses intended for waveguide platforms have been limited to in-plane focusing of light in one lateral direction [4-6], while requiring light to be guided in the vertical direction. Therefore, these lenses present low efficiencies when used to direct light on samples that are placed at large distances from the chip. This functionality is needed, for example, in medical applications that involve Raman spectroscopy or optical coherence tomography (OCT), where large efforts are being made towards the realization of low-cost integrated devices [7, 8]. In this work we propose a novel fabrication technique for the realization of microlenses that enable out-of-chip collimation (as well as focusing) of light from silicon oxynitride (SiON) waveguides. The lenses are realized by low temperature reflow of positive photoresist, and the fabrication steps, presented in the next Section, are compatible with SiON technology. In the last Section we present our simulation results which show that very small beam diameters are achievable with low divergence angles.

II. DESIGN AND PROCESS FLOW

The lenses are designed to collimate light from SiON waveguide structures embedded in a boron-phosphorus doped silica glass (BPSG) cladding. The choice for SiON as the waveguide core is motivated by the large flexibility given by this material in the design phase in terms of tunability of the refractive index, which can be varied continuously from 1.46 to 2.0 by changing the ratio between the oxygen and nitrogen content in the material [9]. The choice of BPSG as a cladding material is mainly motivated by the possibility of depositing thick layers (> 10 µm) with reasonably short deposition times [10]. Thick layers are, in fact, necessary to host the microlenses as explained later in this Section.

In Fig. 1, we show a schematic of a microlens with radius *R*, positioned at a distance *d* from the waveguide facet. The lens is asymmetric, as it is embedded between two different media (BPSG and air). The purpose of having BPSG between the waveguide and the lens, instead of air, is twofold. Firstly, it reduces back reflections from the waveguide end-facet. Secondly, it reduces the angular aperture of the waveguide, which enables positioning the lens at its focal distance without excessive losses due to overfilling the lens aperture. In the design phase the refractive index of SiON, as well as the waveguide geometry and lens radius can be fine tuned to reduce these losses to a minimum (compatibly with the waveguide properties required for the application). In the current design there is a vertical displacement of the lens with respect to the waveguide which is equal to the thickness *a* of the upper cladding. The displacement causes a vertical tilt of the beam of a few degrees as will be discussed in the next Section. The thickness *a* must be chosen in a way to avoid light exiting the waveguide to reach the upper BPSG-to-air interface, since this would cause unwanted reflections leading to a distorted output beam.

The lens, made from photoresist, is located in front of the waveguide, partially embedded in the BPSG layer. For this to be possible a semi-spherical hole is first etched into the BPSG by isotropic etching using buffered hydrofluoric acid (BHF) in which the etch rate is ~450 nm/min [10]. The hole is then filled with the lens polymer (photoresist AZ 9260). As shown in Fig. 2, the fabrication steps involve the use of two masks: a first mask is used for defining a hole of around 2 µm in diameter from which the isotropic etch is initiated; a second low resolution mask is used for defining the lens.

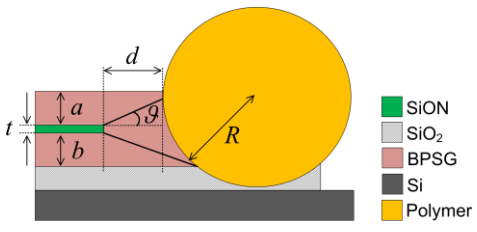


Figure 1. Schematic of microlens, where *t* is the thickness of the SiON layer, *a* and *b* are the thicknesses of the upper and lower BPSG claddings, *d* is the distance of the micro-lens from the waveguide facet, *R* is the lens radius, and ϑ is the angular apertue of the waveguide inside the BPSG.

Financial support from the Dutch IOP Photonic Devices (Senter-Novem and STW) is acknowledged.

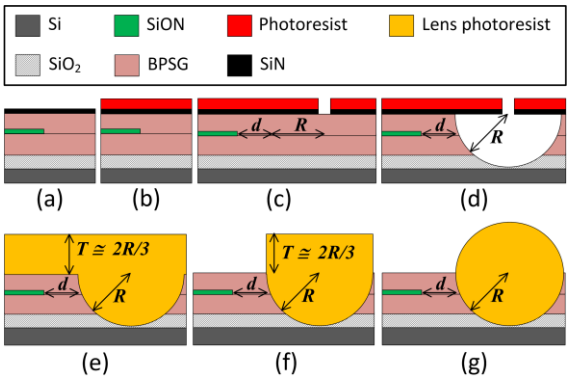


Figure 2. Process flow of microlens fabrication on pre-existing waveguide structure. (a) SiN deposition, (b) Spinning of photoresist and mask exposure, (c) development of photoresist and etching of SiN, (d) Isotropic etch of BPSG through buffered hydrofluoric acid (BHF) to achieve a semi-sphere with radius R, (e) Spinning of lens photoresist with height $T \cong 2R/3$, (f) Exposure and development of resist using the lens mask, (g) reflow of resist at ~130 °C.

For the isotropic etch (see Fig. 2(a-d)) we use SiN as a masking material due to its low etching rate (< 1.3 nm/min) in BHF [11]. In order to obtain a spherical lens we spin photoresist (AZ 9260) with thickness T approximately equal to $2R/3$ (see Fig. 2(e)). The thickness of the photoresist layer must be chosen in a way that after lithography and resist reflow (see Fig. 2 (f-g)), the volume of the photoresist above the surface of the chip is equal to that of the photoresist embedded in the BPSG. For this reason we must take into account the loss of material due to evaporation during the pre-exposure softbake and the successive reflow phase. It is important that, since half of the sphere is hosted in the BPSG and thermal oxide layers, the total thickness of these layers is in the order of the lens radius R. Smaller thicknesses are acceptable in case the light does not reach the silicon substrate, i.e. the angular aperture of the waveguide is small.

III. Simulation Results

We present our simulation results on a microlens structure with the following parameters (refer to Fig. 1): a = 6 µm, b = 15 µm, R = 45 µm, d = 19 µm. The waveguide is designed to be single-mode in the wavelength range 800-900 nm, with core index of 1.552, cladding index of 1.453, and cross-section of 2 µm × 0.3 µm. We considered the thickness of the thermal oxide (on silicon) to be 8 µm. To simulate the structure we make use of the beam propagation method (BPM) [12]. In particular we use 2D BPM with Pade order 3 implemented by Phoenix BV [http://www.phoenixbv.com]. We launch light at a wavelength λ = 850 nm into the waveguide and compute the intensity profile at distances of 2.5 mm and 3 mm from the lens center. For the 2D simulation the waveguide structure is first reduced to an equivalent planar structure via the effective index method. The vertical displacement of the lens with respect to the waveguide by the distance a causes a vertical tilt of the beam of 5.7°. In Fig. 3 we show the obtained intensity profiles at 2.5 mm and 3 mm from the lens center. As can be seen from Fig. 3, the lens produces a beam with an almost circular profile, having FWHM of ~45.5 µm in the vertical direction and ~46.1 µm in the horizontal direction, with divergence angles of 0.80° and 0.52°, respectively in the two directions. The beam profile can be made perfectly circular, in principle, by tapering the waveguide in the horizontal direction. However, at this stage we did not perform this optimization. We observe that without the lens the FWHM of the beam in the horizontal direction, at 2.5 mm from the waveguide facet, is ~1350 µm (30 times larger), and the divergence angle ~15.50° (30 times larger), while in the vertical direction we have a FWHM of ~1930 µm with divergence of 22.14°.

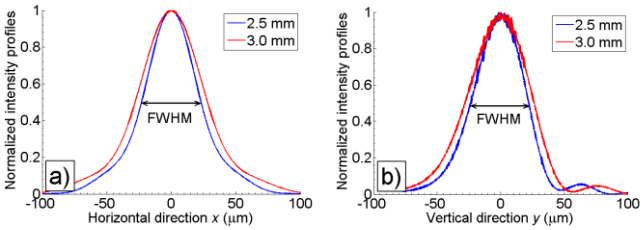


Figure 3. Beam profiles in the horizontal (a), and vertical (b) directions computed at a distances of 2.5 mm and 3.0 mm from the lens center.

IV. Conclusions

We presented a novel technique for the integration of spherical waveguide lenses in SiON technology. The proposed lenses enable collimation of light in both horizontal and vertical directions with small divergence angles. Our method opens new possibilities for the realization of low-cost on-chip devices for different applications such as spectroscopy and OCT. The fabrication of the devices is currently under way.

V. References

[1] S. Kawai "Free-space multistage optical interconnection networks using micro lens arrays," J. Lightwave Technol., vol. 9, pp. 1774 -1779, 1991.

[2] J. Karp, E. Tremblay, and J. Ford "Micro-optic solar concentration and next-generation prototypes," IEEE PVSC, pp. 493 -497, 2010.

[3] V. Lin, H.-C. Wei, H.-T. Hsieh, J.-L. Hsieh, and G.-D. Su "Design and fabrication of long-focal-length microlens arrays for Shack-Hartmann wavefront sensors," Micro Nano Lett., vol. 6, pp. 523 -526, 2011.

[4] D. W. Hewak, and J. W. Y. Lit, "Solution deposited optical waveguide lens," Appl. Opt., vol. 28, pp. 4190-4198, 1989.

[5] J. Ohara, K. Kano, and Y. Takeuchi, "A new fabrication process for micro optical elements using drie and oxidation," IEEE MEMS digest, pp. 279 -282, 2007.

[6] J. Godin, and Y.-H. Lo, "Advances in on-chip polymer optics for optofluidics," CLEO/QELS proc., pp. 1-2, 2009.

[7] N. Ismail, L.-P. Choo-Smith, K. Wörhoff, A. Driessen, A. C. Baclig, P. J. Caspers, G. J. Puppels, R. M. de Ridder, and M. Pollnau, "Raman spectroscopy with an integrated arrayed-waveguide grating," Opt. Lett. vol. 36, pp. 4629-4631, 2011.

[8] B. I. Akca, V. D. Nguyen, J. Kalkman, N. Ismail, G. Sengo, F. Sun, T. G. van Leeuwen, A. Driessen, M. Pollnau, K. Wörhoff, and R. M. de Ridder, "Toward spectral-domain optical coherence tomography on a chip", IEEE J. Sel. Topics Quantum Electron., doc. ID 10.1109 (posted 6 October 2011, in press).

[9] D. Peters, K. Fischer, and J. Müller, "Integrated optics based on silicon oxynitride thin films deposited on silicon substrates for sensor applications," Sensor. Actuat. A: Phy., vol. 26, pp. 425-431, 1991.

[10] S. Lee, G. Ditmer, N. Singh, C. Hodson, A. Goodyear, and M. Cooke, "Thick-film doped-oxide deposition processes for applications in planar lightwave circuit fabrication," IEEE COMMAD proc., pp. 441 - 445, 1990.

[11] K. Williams, K. Gupta, and M. Wasilik, "Etch rates for micromachining processing-Part II," J. Microelectromech. Syst., vol. 12, pp. 761–778, 2003.

[12] A. Ishikawa, M. Izutsu, and T. Sueta, "Beam propagation method analysis of optical waveguide lenses," Appl. Opt., vol. 29, pp. 5064-5068, 1990.

Double polarization active Y-junctions in the mid-IR, based on Ti:diffused Lithium Niobate Waveguides

S. Heidmann, G. Martin
Institut de Planétologie et d'Astrophysique de Grenoble (IPAG)
UJF-Grenoble 1 / CNRS-INSU, UMR 5274
Grenoble, F-38041, France
guillermo.martin@obs.ujf-grenoble.fr

N. Courjal
Université de Franche-Comté.
FEMTO-ST
Besançon. F-25030, France

***Abstract*—Double polarization active beam combiners have been developed for mid-infrared applications, in particular, in the field of high contrast interferometry in astronomy. As the objective of these beam combiners is to achieve high rejection ratios based on proper recombination of the fundamental modes guided by each arm (better than 40dB at the desired wavelength), we will focus our discussion on the fringe contrast obtained, using a monochromatic source and scanning the dark fringe, by internal modulation. In a second time, white light interferograms will be presented, in order to address the spectral dispersion (chromaticity of the combiners), and the efficiency of the modulator in the wideband regime. We will also show our prototypes for improving the effective electro-optic coefficient, based on the fabrication of photonic crystals inside the waveguides.**

Keywords-electro-optics, interferometry, beam combiners, lithium niobate, mid-infrared, modal filtering

I. INTRODUCTION

The context of this work is the development of integrated optic beam combiners devoted to stellar interferometry [1]. In the run for exoplanet detection, the 2.5-5μm observation window has been identified as an adequate band for planet search science [2]. Besides, for spatial applications, the use of compact and light optical beam combiners ensuring robustness and stability of the interferometric signal is mostly welcome. Thus, the development of materials allowing light confinement in both polarizations, together with a good transparency in the mid-IR and able to achieve electro-optic modulation, in order to finely tune the relative phase of the interacting fields, is knowing a rapid development. Indeed, there are recent publications in active materials like lithium niobate beam combiners centered in K-band (2.2μm) [3] and L-band (3.7μm) [4].

Aside from spectral considerations, several issues are requested from an efficient optical beam combiner: First, the ability to filter out high order modes in the waveguides, thus achieving modal filtering and optimizing the contrast of the interference fringes obtained. As the astronomical models are very sensitive to fringe contrast, modal filtering is compulsory in order to improve the quality of the interference data. Second, active control of the phase in the integrated optic device is needed, in order to limit the signal fluctuations and eventually achieve on-chip fringe scan. This can be done using well known electro-optic materials, as long as they exhibit good transparency in the mid-IR. Another important issue is to ensure that both polarizations are guided, since polarization studies are essential to understood astrophysical phenomena, and most of the astrophysical instruments are not polarisation sensitive, giving only information about the intensity and not the vector direction of the electromagnetic field. Finally, it is important to reduce or at least characterize the spectral dispersion of the combiner over the whole observation band (here, 3.4-4.1μm), which means that special geometries have to be designed (achromatic couplers, low dispersion waveguides).

Thus, we have selected LiNbO3 in order to develop new integrated beam combiners, not only due to its transparency up to 5.2μm, but also for its excellent electro-optic properties, that will allow active control of phases. Focusing on double polarization waveguides like Ti-indiffusion, Sohler group demonstrated a first realization in the mid-IR devoted to Difference Frequency Generation [5] and more recently other groups have been working on mid-IR LiNbO3 interferometers [4, 6].

In this paper, we present our results on active Y junctions working in the L-band (monochromatic and wide-band). We will show how the modal filtering allows to obtain high rejection ratios; we analyze the wide band spectra to recover the dispersion characteristics of the combiner and, finally, will present mono- and poly-chromatic modulation in the L-band obtained in both polarizations (TE and TM) using the electro-optic effect.

II. SAMPLE FABRICAION AND EXPERIMENTAL SET-UP

The junctions were fabricated in X-cut Lithium Niobate substrates by Ti:diffusion for 20h at 1020ºC. The width of the channel waveguides ranged from 12-26μm, allowing to obtain single mode behavior at higher wavelengths with the increasing width. The passive behavior of the channel and Y-junctions, including propagation losses, was discussed in a previous paper [6]. In the present work, we present the electro-optic response

of the junctions for the atmospheric window under study, i.e., L-Band. The experimental set-up is shown below:

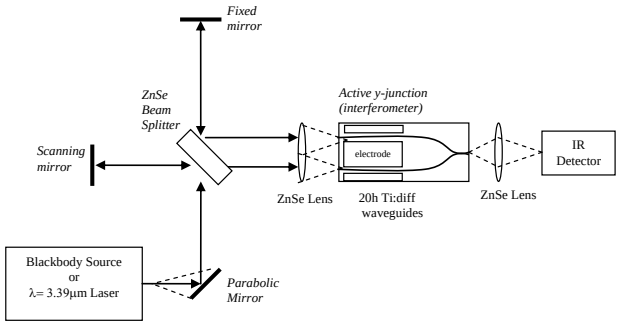


Figure 1. Schematics of the experimental set-up allowing intensity modulation in the mid-IR.

A mid-IR source (either He:Ne λ=3.39µm laser or a Blackbody) is focused on a 20um diameter hole to ensure spatial resolution. Then, the aperture is placed at the focal length (25.4mm) of an off-axis parabola to achieve collimation. The beam passes through a classical Michelson interferometer, using a thick ZnSe plate as beam splitter, allowing lateral separation of two beams to be injected in the waveguide. Injection is ensured by a 25.4mm lens, so that optical power is one, and the numerical aperture matches that of the waveguides. The output field is imaged by a ZnSe lens on the FLIR infrared camera. Modulation is achieved, in this preliminary sample, by electrodes in a push configuration (only one arm under electric field).

III. RESULTS

A. *Monochromatic Fringes*

Light coming from a He-Ne laser at λ=3.39µm was injected at 45° from the vertical X-axis of the waveguide, in order to ensure excitation of both TE and TM polarizations. In the figure shown below, we were able to achieve almost one period scan (OPD 2.96um) while applying a triangle function on the electrodes, obtaining a half-wave voltage of Vπ=22V (or VπLπ= 55 V•cm).

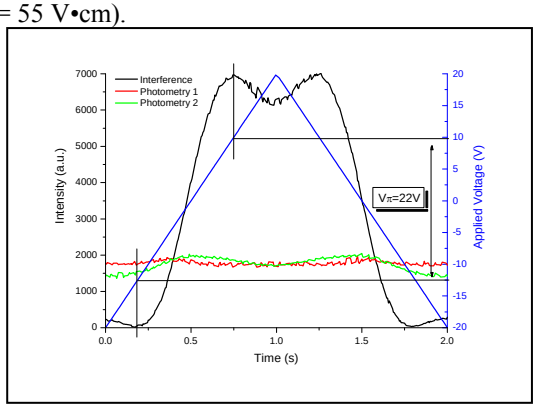


Figure 2. Modulation achieved in the combiner, using monochromatic laser light and a 40Vpp triangular ramp.

Using external modulation, i.e. translating the scanning mirror, we obtained high contrast fringes, showing the filtering capabilities of the system. The average rejection ratio was 300 (25dB), with a best value of 1110 (30.4dB) in a single stage, push type modulator (monochromatic). This is a promising result, but work has still to be done in order to match the 40dB requirements for nulling interferometry.

B. *Polychromatic Fringes*

Injecting light from a Blackbody source, wide band fringes were obtained for TE and TM polarization. We observe that the interference fringes have good contrast (66.8% for a wide band source) and that the waveguide effectively act as a filter since the optical bench (without the waveguide) presents a contrast of 48.0%.

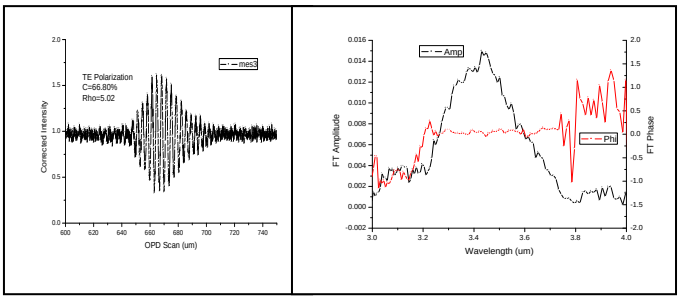


Figure 3. Left: TE wide band fringes. Right: Amplitude and Phase of the Fourier Transform of the wide band fringes.

We notice that the fringes are quite symmetric, which suggests that the combiner is weakly dispersive, as seen in the flat phase spectrum obtained.

Modulation of the central fringe was achieved using the electro-optic effect, and although the modulation amplitude was weaker than in the monochromatic case, we were able to observe it in both polarizations (see figure 4 below, where only TM is shown).

Some polarization issues have to be improved, since we don't find the expected ratio of 3 between extraordinary and ordinary modulation amplitudes, probably due to a poor extinction of the perpendicular contribution. We are currently working on improving the quality of the polarization selectivity.

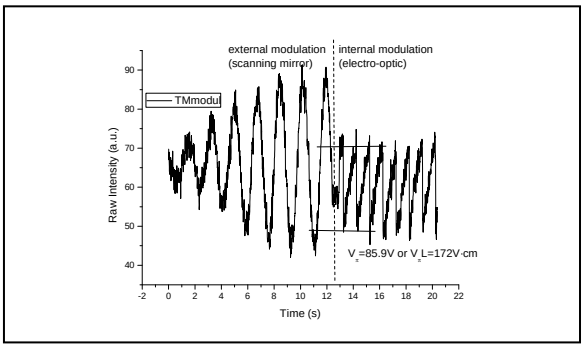


Figure 4. Electro-optic modulation of the wide band fringes in TM polarization. Note that below 13s the fringes are scanned externally.

ANR JEUNES CHERCHEURS 2009, Projet ANR- JC09-507107

IV. CONCLUSION

Active Y-junctions in the mid-IR were obtained and showed filtering and modulation capabilities in both TE and TM polarization. High rejection ratio devices were obtained, showing weak dispersion over the entire L-band. The future devices will include photonic crystals in order to improve the electro-optic response, as well as double stage Mach-Zehnder modulators in order to achieve deeper rejection ratio.

[1] G. Li, T. Eckhause, K.A. Winick, J.D. Monnier and J.-P. Berger, "Integrated optic beam combiner in lithium niobate for stellar interferometer" Proc. Of SPIE, 6268 (2006).

[2] D. Sudarsky, A. Burrows and I. Hubeny, "Theoretical Spectra and Atmospheres of Extrasolar Giant Planets" Astrophysics J. vol. 588 (2), 1121-1148 (2003).

[3] O. Caballero-Calero, R. Burla, T. Moulin, A. Delboulbé, L. Jocou, J-P Berger and G. Martin, "Low voltage, moderate rejection ratio electro-optic modulator at 2.2μm obtained by proton exchange in lithium niobate" Proc. SPIE 7719, 77191D (2010).

[4] H.-K. Hsiao, K. A. Winick, J. D. Monnier and J.-P. Berger, "An infrared integrated optic astronomical beam combiner for stellar interferometry at 3-4 μm" Optics Express, Vol. 17 Issue 21, pp.18489-18500 (2009).

[5] Herrmann, H. and Sohler, W., (1998) "Difference Frequency Generation of tunable, coherent, mir-infrared radiation in Ti:LiNbO3 channel waveguides" J.O.S.A. B, Vol. 5, No. 2, pp. 278-284

[6] G. Martin, P. Kern, E. Le Coarer, K. Perraut, J.-P. Berger and F. Malbet, "Integrated Optics, Interferometry and Active Devices for Astronomy", proceedings of the AMARIS'10 Conference, to be published in Non Linear Optics, Quantum Optics (2010).

$LiNbO_3$ integrated optical probe for high-voltage electric field sensing

D. Tulli, D. Janner
ICFO-Institut de Ciencies Fotoniques, Mediterranean Technology Park
08860 Castelldefels (Barcelona), Spain

V. Pruneri
ICFO-Institut de Ciencies Fotoniques, Mediterranean Technology Park
08860 Castelldefels (Barcelona), Spain
ICREA - Barcelona, Spain

***Abstract*— We present a novel high-voltage optical probe in $LiNbO_3$. A near-cutoff waveguide is centered on a domain inverted region covered with a thin sheet of $LiNbO_3$. DC electric fields up to 20MV/m can be measured.**

Keywords-component; high-voltage optical sensors; ferroelectrics

I. INTRODUCTION

Lithium Niobate ($LiNbO_3$) is one of the most popular materials used in integrated optics because of its electro-optic, nonlinear optical, photorefractive, acoustic and acousto-optic properties [1]. For example, it is used in high speed electro-optic modulators for broadband communication systems [2], wavelength converters [3], and frequency doublers [4]. In addition to telecom applications, thanks to its high dielectric strength and electro-optic properties, $LiNbO_3$ is also used for electric field sensing [5-7]. In the last years, the need for intense electromagnetic field sensing technology has widely increased playing a critical role in various scientific and technical areas, especially in the power industry and in the electromagnetic compatibility (EMC) measurements. So far, several configurations of EO sensors have been proposed, mostly based on waveguide interferometers. In this context, Mach-Zehnder interferometers are employed for their sensitivity. However, they require a tightly controlled biasing to work properly and are very difficult to be operated in very intense electric field.

Recently, new designs for integrated modulators, have been proposed [8] leveraging the micro- and nano-structuring of thin sheets of $LiNbO_3$. Thin sheets are usually directly bonded to a different material or to another $LiNbO_3$ substrate. The use of waveguides at cut-off was proposed for modulation in the field of optical communications [9] and sensing [10]. In this work, we propose an integrated optical probe for high voltage DC fields that can measure electric fields up to 20 MV/m. The novel design leverages a combination of an optical waveguide near cutoff, domain inversion and bonding of thin sheet of $LiNbO_3$ to increase the sensitivity of the device.

II. DEVICE PRINCIPLE AND EXPERIMENTAL RESULTS

The device is sketched in Fig.1. An annealed proton exchange (APE) waveguide near cut-off is fabricated in Z-cut $LiNbO_3$ and centered in a domain inverted region. Another z-cut $LiNbO_3$ substrate is then bonded at room temperature on top of the waveguide, having opposite orientation of the ferroelectric domain. The application of an external electric field parallel to the z axis of the device produces a refractive index change $\Delta n_{\pm}$ between positive and negative domains given by

$$\Delta_{n_{\pm}} = 2 \cdot \frac{n_e^3}{2} r_{33} E$$

where E is the intensity of the external electric field along the z-axis, n_e=2.14 and r_{33}=30.8 pm/V are the refractive index and the electro-optic coefficient along the z-axis, respectively. As a consequence the optical mode will broaden so that, after a sufficient propagation length, a loss is produced due to a mode-profile mismatch of the guided modes in the transition from the active (poled waveguide area) to the passive (unpoled waveguide) region.

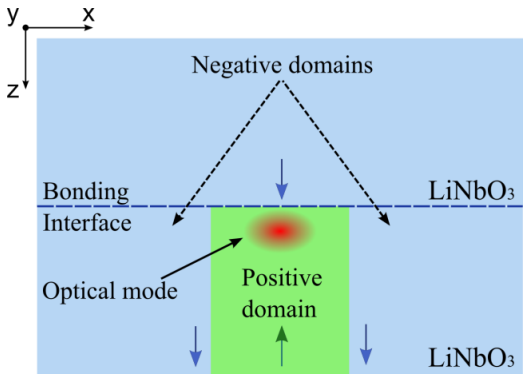


Fig. 1 Cross-section schematic of the optical probe.

The presence of the top layer, apart from enhancing the mode broadening, also contributes to avoid surface depolarization effects that reduce the sensitivity in this type of sensors and can become particularly significative for strong electric fields. Moreover, being made of the same material it avoids discontinuity in the dielectric constant of the sensor and also allow for a very strong and robust bonding.
Taking into account that the electric field across the electro-optic crystal is given by

$$E=V/d$$

where V is the voltage applied to the sensor and d the crystal thickness; it is possible to increase the voltage sensing range

by thinning down the substrate. For this reason, to reduce the total thickness, after bonding two 500 μm substrates, we thinned down the top $LiNbO_3$ to 15 μm achieving a total thickness of 520 μm (Fig. 2).

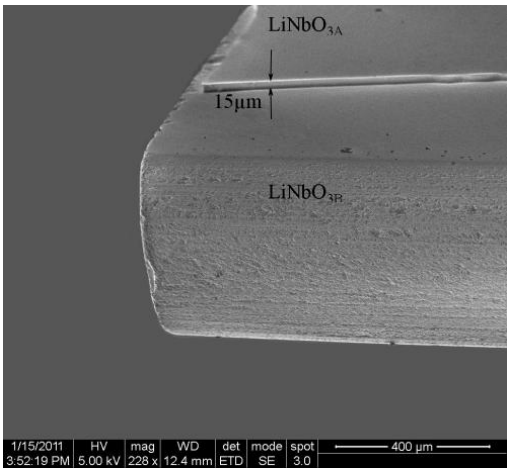


Fig. 2 SEM image of thin plate $LiNbO_3$ bonded on another $LiNbO_3$ substrate

We tested the device as sketched in the schematics of Fig. 3 and the transmission values against different electric fields are plotted in Fig. 4. DC fields up to 2kV/mm, corresponding to an applied voltage of 1040V, were measured. The minimum detectable field is extrapolated to be 14V/mm (7.3 V). The maximum measurable field is limited to the lithium niobate coercive field (20 kV/mm).

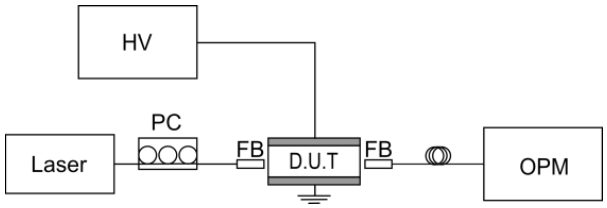


Fig. 3 Block diagram of the dc test setup. HV: high voltage power supply. PC: polarization controller. FB: fiber block. D.U.T.: device under test. OPM: optical power meter.

To improve the sensitivity at lower intensities of the electric field, experiments employing lock-in amplifier techniques are ongoing and will be presented at the conference.

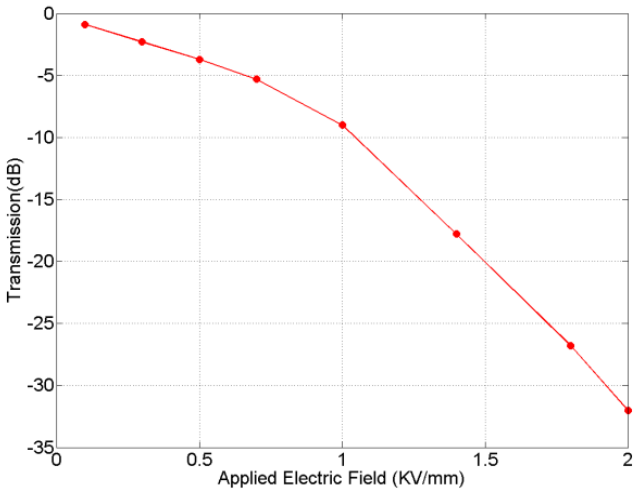


Fig. 4 Experimental results of dc—measurement for a waveguide of 3.5 μm width. The active (poled) length is 10 mm.

REFERENCES

[1] Wong K K 2002 Properties of Lithium Niobate *INSPEC*, London

[2] Ichikawa J 2009 $LiNbO_3$ based optical devices for fiber communication *The Journal of China Universities of Posts and Telecommunications* 16 12-15

[3] Sun J 2005 Wavelength conversion between picosecond pulses in periodically poled $LiNbO_3$ waveguides using pulsed pumping *Microwave and Optical Technology Letters* 46 464–466

[4] Amin J, Pruneri V, Webjorn J, Russell P, Hanna D and Wilkinson J 1997 Blue light generation in a periodically poled Ti:$LiNbO_3$ channel waveguide *Opt. Comm.* 135 41-44

[5] Berini P, Mattiussi G, Lahoud N and Charbonneau R 2007 Wafer-bonded surface Plasmon waveguides *Applied Physics Letters*,90, 061108

[6] T.H. Lee, et al., ''Electromagnetic field sensor using Mach-Zehnder waveguide modulator,'' Microwave and optical technology letters, **48**, .9 (2006)

[7] G. Gaborit, L. Duvilaret, ''Electro-optic sensor: towards vectorial electric field characterization,'' ECIO '05, Grenoble, 2005

[8] Fujimura M, Beniya K and Suhara T 2008 Buried annealed/proton-exchanged $LiNbO_3$ waveguides fabricated by direct bonding *Elec. Lett.* 44 14.

[9] N.H.Zhu, et al, ''Proposal for high extinction ratio $LiNbO_3$ optical waveguide cutoff modulator'' IEEE Proc-Optoelectron **142**, 248-250 (1995) A. Neyer and W.Sohler, ''High-speed cutoff modulator using Ti-diffused $LiNbO_3$ channel waveguide,'' Appl.Phys.Lett **35**, 256-258 (1979)

[10] D. Tulli, D. Janner, M. Garcia-Granda, R. Ricken, V. Pruneri, "Electrode-free optical sensor for high voltage using a domain-inverted lithium niobate waveguide near cut-off", Appl. Phys. B 103, 399-403 (2011)

[11] S.S. Lee et al., ''Integrated optical high voltage sensor using a z-cut $LiNbO_3$ modulator'' Phot. Tech. Lett., **5**, 9 (1993)

Technology-transparent AWG design in photonic ICs

Ronald Broeke
Bright Photonics BV
Maarssen, the Netherlands
ronald.broeke@brightphotonics.eu
www.brightphotonics.eu

***Abstract*—Photonic IC manufacturing moves towards a generic-foundry model in technologies such as InP, SOI and Silicon. This paper discusses an AWG module as part of a Photonics Design Automation workflow, which provides AWG design across technology platforms.**

***Keywords-component*—AWG; photonic integration platform; PIC; Photonics Design Automation; Multi-Project Wafer**

I. Introduction

Photonic Integrated Circuits (PICs) are realized in a wide variety of technology platforms, such as InP[1,2,3], SOI[4,5], Silicon[6], and Triplex[7]. Over the last years there has been a strong trend in photonic circuit development to move towards a generic-foundry based business model[8]. Full commercial deployment is expected in the next five years. The trend is carried, at present, by several projects and initiatives that develop and organize Multi-Project Wafer (MPW) runs, such as EuroPIC[9], Paradigm[10], ePIXfab[11], and JePPIX[12]. A supply chain is established that brings an application idea to a packaged PIC. Cost sharing and standardization in MPW runs result in a shorter time to market and an overall much lower threshold to access Photonic ICs.

The generic-foundry model requires a supply chain without gaps. This includes a software design toolkit with all the building blocks (BBs) that designers need to create a functional PIC design. Foundries, which are responsible for manufacturing, offer a set of basic BBs on their platform to designers via the toolkit. A significant amount of PICs, well over 50% in projects such as EuroPIC and Paradigm, require Arrayed-Waveguide Gratings (AWGs) for advanced features like spectral filtering and (de)multiplexing. However, AWG BBs are not offered by foundries. PIC design efficiency would greatly benefit from AWG design capability across different platforms. Reuse of AWG designs across technologies, or the simultaneous design for multiple platforms is beneficial in, for example, 3D and hybrid photonic integration platforms. In this paper we report on an advanced module, released in September 2011, which provides the desired AWG design capability. The module is compatible with the Oclaro, HHI, and COBRA platforms (all InP), the IMEC and LETI platforms (both SOI), and is extensible to new platforms. It is compatible with the Photonics Design Automation (PDA) as (partly) being developed in the before mentioned projects. The module allows for a fast comparison of AWG performance and size between different technologies, and essentially offers platform transparent AWG design.

The research leading to these results has received funding from the European Community's Seventh Framework Programme FP7/2007-2013 under grant agreement 228839 EuroPIC and under grant agreement ICT 257210 PARADIGM.

II. Design Methodology

Top-down PIC design starts with an application and its specifications. The designer generates a schematic circuit design and performs circuit simulations, all based on available BBs. The next step in the design flow translates the circuit into a mask layout, which is exported to a foundry compatible GDS file for fabrication of the reticle. The reticle on its turn is used in the actual PIC fabrication. The foundry offering a MPW run provides a set of performance-guaranteed BBs and a corresponding design manual to designers. The BBs are embedded in the PDA toolkit developed by Phoenix[13], Filarete and Photon Design[14]. MPW runs all offer BBs such as passive straight waveguides, curved waveguides, and power splitter/combiner building blocks (BB). Depending on the technology there may also be photo-detectors, amplifiers, and/or DBR gratings, among others. BBs are either parametrized or static and they hide the underlying technology (foundry intellectual property). BBs have a geometry, optical and electrical ports, and a performance specification from theory, simulation and/or measurements. BBs have a different representation depending on where in the design flow they are used, i.e. in circuit simulation, layout, components simulation, or GDS generation. The performance of these BBs is guaranteed by the foundry as long as the design rules (DRs) are obeyed.

The AWG is a composite BB (CBB). It is contructed from the basic set of BBs from the foundry, but it was not readily available integrated at circuit level and layout level. The AWG module, however, offers designers a robust way to add an AWG into the design flow. The module shields designers from low level design considerations and has an internal library, which describes the parametrized material and waveguiding properties, such as effective and group indices of refraction. The designer creates the AWG CBB at a functional level for a specific application and applies the CBB in the circuit level design and mask layout as any other BB.

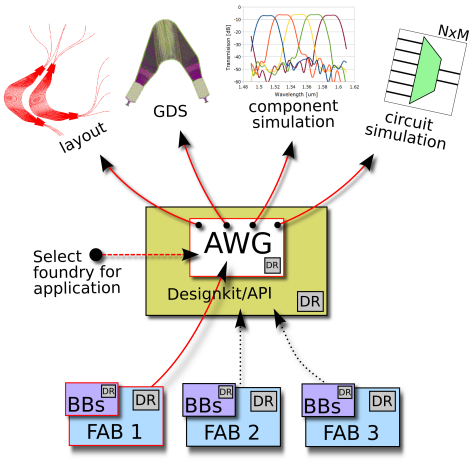


Figure 1. Schematic of the AWG-module design flow. The module provides component simulation, export to circuit simulators, layout, and GDS generation. Red lines indicate foundry FAB-1 has been activated.

III. Toolkit Functionality

Figure 1 shows a schematic of the design flow around the AWG module. When a designer activates a specific foundry, the correct set of foundry BBs and DRs become available. The AWG module initializes a foundry-compatible default AWG, for both geometry and simulation set-up. The AWG CBB has its own set of geometry DRs. The layout can be simulated utilizing a Beam Propagation Method (BPM) from the designkit[13]. All required optical input and output fields and simulation settings are preset, but relevant parameters, for example the simulation grid, can be adapted by expert designers. The AWG layout is exported to GDS using the underlying designkit, which performs additional DR checking at the foundry level. An S-matrix AWG representation, having NxM ports can be exported to PDA flow compatible circuit simulators, such as Aspic[15] (frequency domain) and PICWave[14] (time domain, via a FIR transformation).

An example utilizing the AWG module is shown in Figure 2. Functional specifications of the AWG are fed into the module, which generates a layout for the selected platform. The figure shows AWGs with high-contrast waveguides in the Oclaro and HHI MPW-run technology, respectively, in scale. Each AWG uses a different geometry template, as an example. Several geometry templates are available, which are particularly useful if an AWG has a large Free Spectral Range (FSR) or if the platform has wider waveguides or large radii of curvature. Simulations in the figure have been performed with a 20 degree random phase error with a Gaussian distribution (2σ) added to the array arms to represent fabrication tolerance. It gives rise to the noise floor in the transmitted spectra. Measurement feedback will provide more specific noise values over time and more realistic comparisons between platforms. The result of the foundry-compatible GDS export of the AWGs is shown on the bottom of the figure. The AWG module is actively tested in the Paradigm and EuroPIC projects on the HHI and Oclaro platforms.

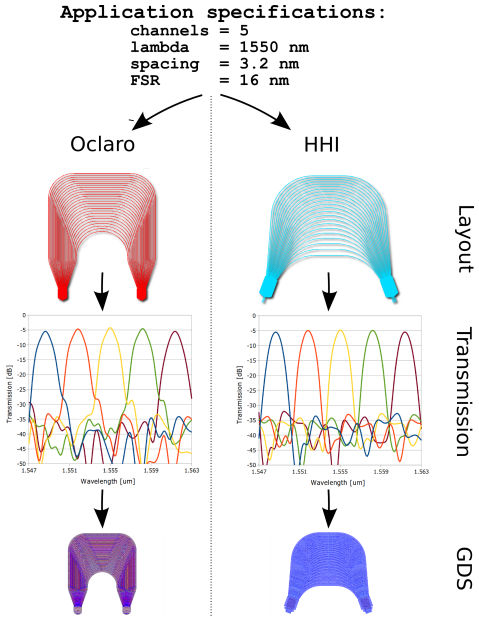


Figure 2. Example of the application-based AWG design flow showing layout, simulation and GDS generation results in two foundries.

IV. Conclusions

The technology-transparent AWG module reported on in this paper adds a missing key building block to the supply chain for photonic integrated circuits across the multi-project wafer runs that are being developed across Europe in several projects. The kit allows novice and expert designers to design, simulate and export AWGs designs, or to compare AWG performance and footprint across technologies to select the best technology for their specific application. This AWG module has been applied in more then 20 MPW designs in two MPW runs in different foundries since its initial release in September 2011.

Acknowledgments

The author wishes to thank Phoenix BV for support on implementing the AWG module in the PDA environment.

References

[1] Oclaro, http://www.oclaro.com
[2] Frauenhofer Heinrich Hertz Institute, www.hhi.frauenhofer.de
[3] COBRA, http://w3.ele.tue.nl/en/cobra/home
[4] IMEC, http://www.imec.be
[5] CEA-LETI, http://www.leti.fr
[6] OPSIS, http://depts.washington.edu/uwopsis
[7] Lionix BV, http://www.lionixbv.com
[8] M. Smit et al., "A Generic Foundry Model for InP-based Photonic ICs", OFC 2012 (Los Angeles, March 2012), category 8, invited paper, unpublished
[9] European manufacturing platform for Photonic Integrated Circuits, http://europic.jeppix.eu
[10] Photonic Advanced Research And Development for Integrated Generic Manufacturing , http://paradigm.jeppix.eu
[11] ePIXfab, http://www.epixfab.eu
[12] Joint European Platform for InP-based Photonic Integrated Components and Circuits, http://www.jeppix.eu
[13] Phoenix BV, http://www.phoenixbv.com
[14] Photon Design, http://www.photondesign.com
[15] Aspic, http://www.aspicdesign.com/

A novel III-V-on-Si distributed feedback laser design

S. Keyvaninia, Y. De Koninck, D. Van Thourhout, R. Baets, G. Roelkens
Photonics Research Group – Ghent University/imec, Ghent-Belgium
Center for nano- and biophotonics (NB-Photonics), Ghent-Belgium
Shahram.keyvaninia@intec.ugent.be

***Abstract*- In this paper we present a new design for III-V-on-silicon distributed feedback lasers. One of the main advantages of the design is that all structures defining the laser cavity are defined in the silicon, resulting in an easier manufacturing and more accurately controlled laser wavelength. Such a hybrid laser design offers much simpler device fabrication, since light coupling elements, like spot-size converters, are not needed. This also reduces the device footprint.**

Keywords: III-V-on-silicon laser; heterogeneous integration; DFB

I. INTRODUCTION

Silicon-On-Insulator (SOI) is gaining interest as a novel platform for integrated optical circuits, since its large refractive index contrast allows for ultra-compact devices. The interest in this technology stems however mostly from the expectation that the maturity and low cost of CMOS-technology can be applied for advanced photonics products. However, the integration of a silicon laser is hampered by silicon's indirect bandgap. Building light sources, and in particular laser sources, on integrated silicon circuits is a big challenge. In that sense the heterogeneous integration of III-V/silicon lasers combines the best of two worlds. In spite of the rapid progress in this technology since about 2006, the design and fabrication of hybrid silicon lasers present specific challenges and trade-offs. There are many choices to be made, both in terms of the cavity structure, the optical coupling between the silicon waveguide and the III-V waveguide and the technological approach. A relatively large variety of device approaches have been reported in the past years [1]. Two main technologies are used to heterogeneously integrate III-V epitaxial layer stacks on a silicon waveguide circuit: molecular bonding and adhesive bonding. We focus on an adhesive die-to-wafer and wafer-to-wafer bonding process, based on DVS-BCB as a bonding agent, given more relaxed requirements on the III-V wafer surface quality (contamination, particles, roughness). This principle has proven to work in several different configurations [1][2]. A promising reported method to achieve a high performance laser cavity is to use an intra-cavity double taper structure, using taper-based mode transformers in both the III-V and silicon waveguides [2]. However, the fabrication of taper-based mode converters is not straightforward because of the narrow tips required and the strong dependence of the performance on alignment accuracy. In this paper we propose a new approach to obtain a compact, efficient and single mode hybrid silicon laser, based on an active DBR grating which requires no complex coupling structures such as narrow-tip tapers in the III-V process.

II. LASER CAVITY DESIGN

The hybrid platform consists of an SOI substrate with a slab of III-V material bonded on top and a thin DVS-BCB bonding layer in between. An optimal laser cavity design should consist of a section where the optical mode is completely confined to the III-V waveguide layer, while the wavelength selective feedback is provided by structures defined in the silicon, thereby taking advantage of the resolution and accuracy of lithography tools in CMOS fabs. Of course, the laser emission should also be coupled efficiently into the silicon waveguide layer.

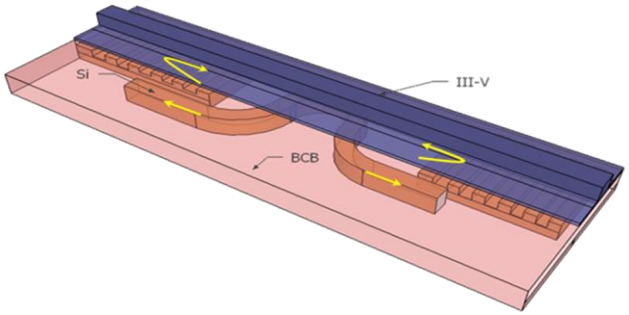


Figure 1: Schematic of the active DBR with the evanescent coupling waveguide in the center of the laser cavity

It would thus be beneficial to think of cavities that do not use an adiabatic taper to couple light between the III-V layer and the silicon waveguides. Besides using resonant cavities in the silicon [3], this can be realized in a DBR-based cavity by using two active DBR gratings with nearly 100% reflection to define the laser cavity and where an evanescent coupling interface is positioned within the laser cavity as the laser output as shown in Figure 1. This hybrid laser design offers much simpler device fabrication and helps to reduce the device footprint.

III. SIMULATION RESULTS

We have simulated the use of DBR reflectors extensively in the context of these hybrid silicon lasers. In a cross-sectional view of the structure, two waveguides can be identified: one in the silicon DBR grating and one in the active layer with a DVS-BCB intermediate layer, as shown in Fig 2. The III-V region used in the simulation has a multiple quantum well (QW) double heterostructure, which consists of a p-InGaAs contact layer, a p-InP clad, 6 InGaAsP QWs surrounded by two

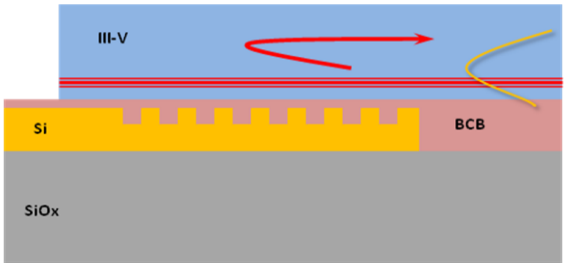


Figure 2: Schematic view of a hybrid DBR reflector in a hybrid silicon laser.

InGaAsP separate confinement heterostructure (SCH) layers, and an n-InP layer. The simulated QW region consists of six 8nm thick InGaAsP (1.55um bandgap wavelength) well layers separated by 10nm thick InGaAsP (Eg=1.17um bandgap wavelength) barrier layers. The thickness of both SCH layers is 100nm and the thickness of the n-InP and p-InP layers are 200nm and 1500nm respectively. The SOI is composed of a mono-crystalline silicon layer (thickness of 400nm) on top of a 2µm thick buried oxide layer on a silicon substrate. The silicon rib grating has a height of 400nm, an etch depth of 180nm and a width of 3µm for the DBR parts. Simulations were performed for the cavity reflectors and the coupling section. A 2D simulation based on the open-source eigenmode solver CAMFR [4] to calculate the first-order to first-order mode reflection of the active waveguide is shown in Figure 3, showing the power reflection as a function of the number of periods and the DVS-BCB thickness, for a grating period of 240nm (for Bragg reflection at 1.55µm), 50% duty cycle and an etch depth of 180nm. The coupling constant κ for two different silicon waveguide heights and two different grating etch depths versus DVS-BCB thickness is plotted in Figure 4.

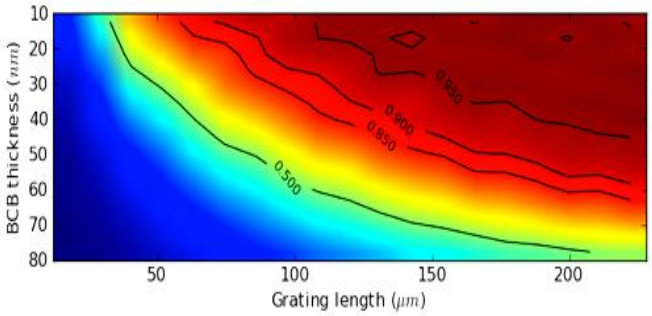


Figure 3: Grating reflection as a function of the number of grating periods and DVS-BCB thickness

For the coupling section a 3D FDTD simulation [5] was performed, to study coupling in the bent waveguide structures and to study the parasitic reflections due to this perturbation in the middle of the cavity. We used the same III-V waveguide with the same epi layers and 2.5µm waveguide width. A 400nm high silicon waveguide, 1.5µm wide, bending radius of 30µm and different coupling length (L) are considered for the simulations. These simulations show that the power fraction reflected into the III-V waveguide because of the coupling section is very low (<-30dB, for a DVS-BCB thickness of 60nm). Figure 5 shows the power coupled to the silicon waveguide underneath versus length for a DVS-BCB thickness of 60nm. The coupling efficiency decreases with increasing coupling length due to the fact that the coupler is a strongly asynchronous directional coupler. In turns out that the coupling is at its maximum when the length of the straight coupling section is of zero length due to the coupling that occurs in the bending parts of the coupler section.

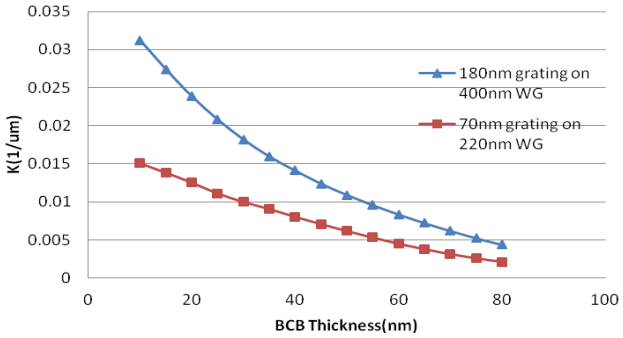


Figure 4: Coupling constant κ for a hybrid grating simulated for different grating cross-sections versus DVS-BCB thickness

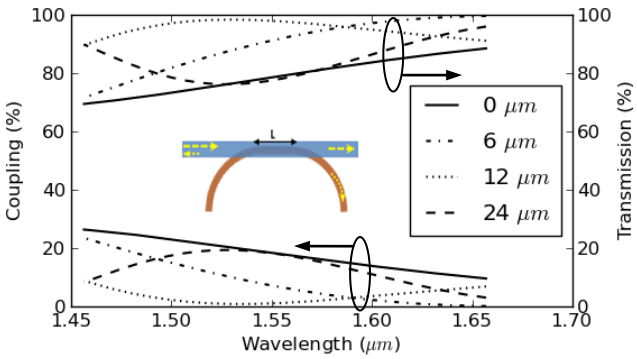


Figure 5: 3D-FDTD simulation results on the evanescent coupling for different coupling lengths *L*

IV. Conclusions

A new concept was proposed for the realization of III-V on silicon hybrid lasers, providing high optical confinement in the III-V waveguide layer, while the wavelength selective feedback elements are implemented in the silicon. This opens up a route towards the large volume realization of single mode lasers with precisely defined emission wavelength on a silicon waveguide platform.

References

[1] G. Roelkens, L. Liu, et al., Laser Photonics Rev. P.DOI: 10.1002/lpor.200900033 (2010).

[2] M. Lamponi, S. Keyvaninia, et al., "Low-Threshold Heterogeneously Integrated InP/SOI Lasers With a Double Adiabatic Taper Coupler," IEEE Photon. Technol. Lett. 24, 76-78 (2012).

[3] Y. De Koninck, G. Roelkens and R. Baets "Cavity enhanced reflector based hybrid silicon laser" proceedings of the 23rd annual meeting of the IEEE Photonics society

[4] CAMFR (http://camfr.sourceforge.net)

[5] Ab Initio MEEP (http://ab-initio.mit.edu/wiki/index.php/Meep)

Design and simulation of DBR lasers with extended modulation bandwidth exploiting photon-photon resonance effects

Paolo Bardella, Ivo Montrosset
Dipartimento di Elettronica e Telecomunicazioni
Politecnico di Torino, Torino, Italy
ivo.montrosset@polito.it

***Abstract*— In high–speed laser devices the occurrence of a photon–photon resonance increases the modulation bandwidth substantially. In this paper our attention is focused on the design of DBR lasers in which this effect is exploited.**

Keywords - DBR lasers, photon-photon resonance, detuned loading, extended modulation, time–domain simulation

I. INTRODUCTION

In conventional high-speed laser devices the modulation response is largely determined by the carrier–photon resonance (CPR). However, the occurrence of a photon–photon resonance (PPR) can increase the –3dB modulation bandwidth substantially. In this paper our attention is focused on the design of a DBR cavity in which the PPR frequency is fixed by the design procedure. The PPR has been observed in distributed Bragg reflector (DBR) laser diodes [1,2], in coupled-cavity-injection-grating (CCIG) lasers [3,5], and in passive-feedback lasers [6,7], but a thorough explanation to achieve this operation condition also in simple DBR lasers has not been presented [8,9]. The design procedure for DBR cavity laser is here identified; the small and large signal modulation results presented support the correctness and accuracy of the proposed design procedure.

II. DESIGN PROCEDURE

In this paper we present a design procedure for a simple DBR cavity that allows obtaining with a good accuracy a PPR effect at the desired frequency. This is very important in practical applications because the gap between the traditional CPR and the PPR in the small signal intensity modulation (IM) response should be filled by the contribution of the two effects in order to avoid unwanted reduction of the device modulation response (Fig.1).

For this reason the CPR response should be as wide as possible respect to the PPR frequency; this can obtained e.g. by operating the laser in the so called detuned loading condition [8]. When the laser is operating in this condition a particular attention must be paid to avoid mode competition between the lasing mode (at longer wavelength respect to the Bragg peak) and the cavity mode on the other side of the stop band. Therefore the cavity should be designed in such a way that the Free Spectral Range of the cavity inside the grating stop band is comparable to the separation between the first two minima of the grating reflectivity function around the Bragg wavelength.

The work reported in this paper has been carried out within the EU FP7 project "Development of low-cost technologies for the fabrication of high-performance telecommunication lasers" (DeLight) under grant agreement n° 224366.

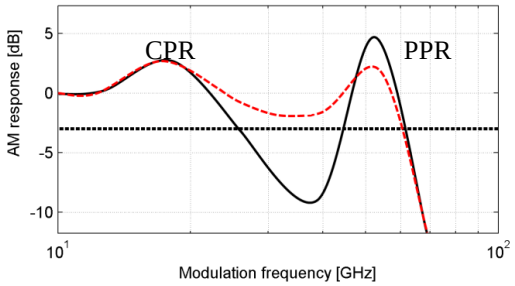


Figure 1. Example of IM responses. The PPR peak is not sufficient to obtain an efficient extension of the modulation bandwidth if a strong gap is present between CPR and PPR (black continuous line): the CPR should be wide enough to flatten the IM response (red dashed line).

Once this condition is fulfilled, and enhanced CPR modulation bandwidth can be obtained without the risk of mode competition, we can then enforce the second condition on the PPR frequency, which corresponds to the separation between the lasing mode and the side mode (PPR mode): we impose this side mode to be on the first side lobe of the reflectivity function as shown in the example of the Round Trip gain and phase function reported in Fig.2.

Using the simple resonance equation condition for the detuned lasing mode and the corresponding side mode generating the PPR one can relate the following cavity parameters: active

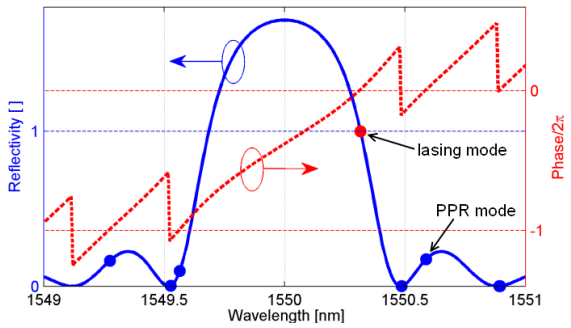


Figure 2. Round Trip Gain (RTG, blue curve) and phase (red curve) function at threshold for a DBR cavity.. The squared red point represents the lasing mode; the blue markers indicate cavity modes below threshold.

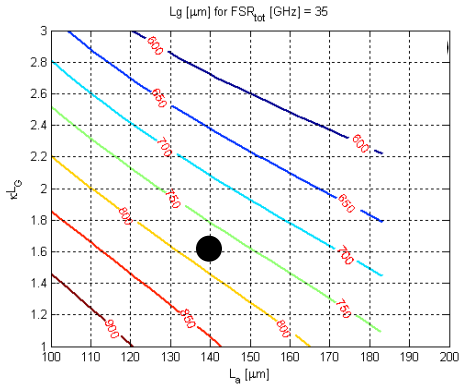


Figure 3. Values of L_G (in μm) required to obtain a 35GHz PPR, as a function of L_A and κL_G. The circular black marker highlights the structure considered in the Time–Domain analysis.

and grating section lengths (L_A, L_G), grating coupling coefficient (κ) and PPR frequency.

The results are reported in the map in Fig. 3, obtained for a chosen PPR frequency of 35GHz between the lasing mode operating at the maximum detuned loading condition and the PPR mode located in the first side mode of the reflectivity function: in the plane (L_A - κL_G) we present the values of L_G satisfying the requested PPR frequency.

III. SIMULATION RESULTS

For the device indicated by the marker in Fig. 3, whose characteristic parameters are illustrated in Table I, we computed the small and the wide digital signal modulation response using our Finite–Difference Travelling–Wave program [10].

In Fig. 4 a color map of the normalized small signal modulation response [11] is presented; the modulation frequency is reported in the abscissa while in the ordinates the lasing mode position respect to the Bragg frequency is varied changing the phase φ_A of the cleaved facet mirror reflectivity at the active region side. A similar tuning effect can be obtained changing the current injected in the Bragg grating.

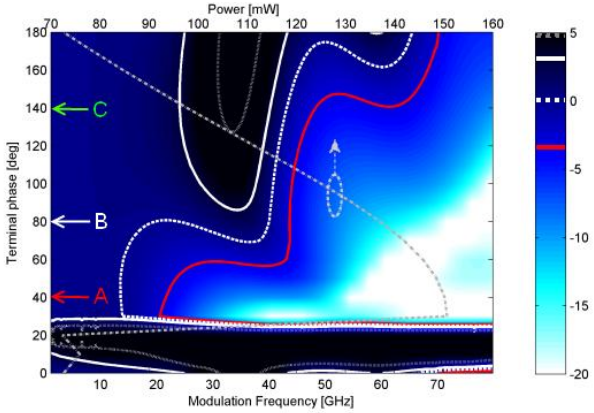


Figure 4. Modulation map of the considered device, obtained at the bias current of 200mA, as a function of φ_A. The red continuous line indicates the -3dB modulation response level, while the white dashed, continuous and dotted lines represent the 0dB, +3dB and +5dB modulation response levels respectively; the gray dash-dotted line refers to the output power whose values are reported on the axis in the upper border of the figure.The 3 values of the φ_A parameter considered for the large signal analysis are indicated with arrows

TABLE I. PARAMETERS USED IN THE TIME–DOMAIN ANALYSIS

Parameters description and symbols [11]	Values
Active region length, L_A	140μm
Bragg grating region length, L_G	780 μm
Grating coupling coefficient, κ	21cm^{-1}
Transversal optical confinement factor, Γ_{xy}	0.15
Differential gain, a	10 10^{-16}cm^2
Transparent carrier density, N_{tr}	10^{18}cm^{-3}
Active region intrinsic losses, $\alpha_{i,A}$	10cm^{-1}
Bragg grating region intrinsic losses, $\alpha_{i,G}$	5cm^{-1}
Linewidth enhancement factor, α	3
Gain compression factor, ε	5 10^{-17} cm^3

Evidence of PPR around 35GHz is quite clear from this modulation map. The dark strip the IM color map in the range 0°–30° corresponds to a self pulsation condition [10].

Large signal modulations were calculated for the three values of terminal phase indicated in Fig 4 using a NRZ PRBS signal at different modulation bit rates. The choice was done to compare the cases without (case A) and with (case B) PPR effect and to see the limitations to the maximum achievable large signal modulation introduced by a too pronounced modulation response peak in the small signal response (case C).

The corresponding eye diagrams are presented in Fig. 5. As shown from the 40Gb/s signal modulation the response with a high resonance peak (case C) is strongly reducing the eye opening and the small signal modulation bandwidth represents in this case an upper limit for the achievable large signal modulation. In the other two cases (A, B) the large signal modulation bandwidth can be extended significantly beyond the –3dB modulation band (up to 40Gb/s and 60Gb/s, respectively).

IV. CONCLUSIONS

A novel procedure to design DBR lasers with extended modulation bandwidth has been presented and validated by large signal digital modulation simulations. The results show that in some conditions it is possible to extend significantly the –3dB modulation bandwidth and also the transmission bit rate.

REFERENCES

[1] O. Kjebon et al., Electron. Lett., 33, pp. 488–489, 1997.
[2] L. Bach et al., IEEE Photon. Technol. Lett., 16, pp. 18–20, 2004.
[3] W. Kaiser et al., IEEE Photon. Technol. Lett., 16, pp. 1997–1999, 2004.
[4] F. Gerschütz et al., Opt. Express, 16, pp. 5596–5601, 2008.
[5] M. Vallone et al., IEEE J. Quantum. Electron., 47, pp. 1269–1276, 2011.
[6] M. Radziunas et al., IEEE J. Sel. Top. Quantum Electron., 13, pp. 136–142, 2007.
[7] U. Troppenz et al., ECOC 2009, 20-24 September, Vienna, 2009.
[8] U. Feiste, IEEE J. Quantum Electron., 34, pp. 2371–2379, 1998.
[9] G. Morthier et al. IEEE J. Quantum Electron., 36, pp. 1468–1475, 2000.
[10] L.A. Coldren, S.W. Corzine, Diode Lasers and Photonic Integrated Circuits, Wiley, New York, 1995.
[11] P. Bardella, I. Montrosset, IEEE J. Sel. Top. Quantum Electron., 11, pp. 361–366, 2005.

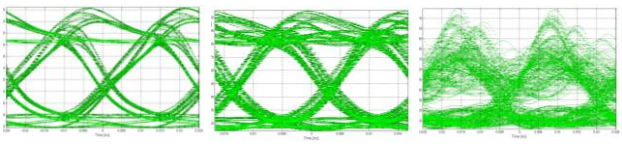


Figure 5. (left) 40Gb/s eye diagram computed for case A; extintion ratio (ER) = 6dB. (center) 60Gb/s eye diagram computed for case B; ER = 4.5dB. (right) 40Gb/s eye diagram computed for case C.

Accurate dispersion characterization in nanophotonic integrated waveguides

S. Mas, J. Matres, J. Martí, C.J. Oton
Nanophotonics Technology Center
Universidad Politécnica de Valencia, Camino de Vera s/n, 46022
Valencia, Spain
smasg@ntc.upv.es

***Abstract*—We report a method for characterizing chromatic dispersion consisting on a heterodyne fiber-based Mach-Zehnder interferometer which is immune to thermal fluctuations of fringes. The method is ideally suited to integrated waveguides, as it allows measuring dispersion and its slope versus wavelength even in short waveguides with considerable loss. We report dispersion measurements of different silicon waveguide geometries together with theoretical simulations which show good agreement with the experimental results.**

Keywords-integrated optics; silicon photonics; dispersion

I. INTRODUCTION

Transporting and processing high bitrate signals require a precise management of chromatic dispersion. Nonlinear effects are also very sensitive to, not only dispersion, but its exact dependence with wavelength, i.e. its higher order derivatives. Most of the dispersion characterization techniques were originally conceived for optical fibers, where propagation distance can be made very long in order to provide large delays. Examples of these are techniques like time-of-flight [1] or phase-shift methods [2]. A short waveguide usually is a few millimeters long, so more precise interferometric techniques are needed like the ones reported in [3-5]. These techniques employ a Mach-Zehnder or Michaelson interferometer; however, in fiber-based interferometers thermal fluctuations in each branch can cause high instability of fringe positions. If signals are low due to high insertion loss of the system, a spectrum can take several seconds or minutes, so the fringe instability can give rise to very noisy phase measurements, which can prevent an accurate characterization. In this work, we show how to compensate for thermal fluctuations using a reference counter-propagating laser beam, and we measure the dispersion of different waveguide geometries together with theoretical calculations.

II. TECHNIQUE

Fig. 1 shows the measurement apparatus. It is a fiber-based Mach-Zehnder interferometer, where one of the branches has an optical delay line (ODL), and the other has the sample. Acoustooptic modulators are also present in both branches, and they are tuned to frequencies differing 40kHz for heterodyne phase detection through a lock-in amplifier. The lock-in amplifier is referenced to the beatings produced by a counter-propagating beam at a fixed wavelength. Therefore, when sweeping the wavelength of the tunable laser, the thermal fluctuations of the optical path equally affect both beams, thus compensating the fringe instability.

To compensate for the response of the system, two measurements with different lengths are necessary, the shortest one to be used as a reference. The purpose of the ODL is to maintain the interferometer balanced in both sweeps, so the linear dependence of the phase versus frequency is removed. As the path variations in the ODL are in air, the phase difference between both measurements is given by:

$$\Delta\phi_{sample}(\Delta\omega)-\Delta\phi_{air}(\Delta\omega)=\left(L_s\beta_1-\frac{L_a}{c}\right)\Delta\omega+L_s\left(\frac{1}{2}\beta_2\Delta\omega^2+\frac{1}{6}\beta_3\Delta\omega^3\right) \quad (1)$$

where the ODL extra path is L_a and the device length is L_s, both lengths with respect to the reference measurement. β_i is the ith derivative of the wavenumber k versus frequency ω. The interferometer is balanced when the first term in $\Delta\omega$ is zero, which provides the value of the group index. And the other terms in $\Delta\omega^2$ and $\Delta\omega^3$ are obtained from a polynomial fit.

III. EXPERIMENT AND RESULTS

Measured samples are silicon channel waveguides embedded in silica, as shown in Fig. 2(a)-(b), which have 2µm oxide buffer, 214.7nm height and 25mm long. Sample A corresponds to a TE polarization channel waveguide with 430nm width. Sample B, used as TM polarization channel waveguide, has 487.2nm width. The sidewall angle introduced in the manufacturing process is 8° and 6° for Sample A and Sample B respectively. Total insertion losses were around 24dB for TE and 15dB for TM.

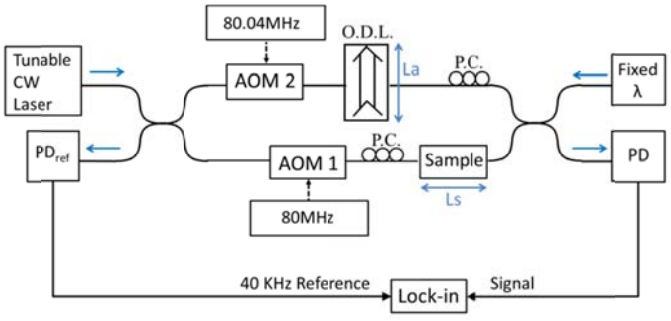


Figure 1. Experimental setup. PC: polarization controller, PD: Photo-detector, AOM: Acousto-optic modulator, ODL: Optical delay line.

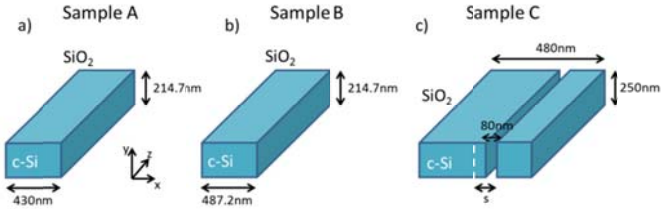


Figure 2. (a) TE polarization, (b) TM polarization, (c) vertical asymmetric slot. Waveguide parameters were extracted from SEM micrographs and were fine-tuned within the measurement error range to optimize the fitting.

Sample C is a 50% asymmetric slot waveguide which has a vertical silica slot between two silicon layers. In asymmetric slot waveguides, the slot location is different than the geometrical center of the waveguide. We define the asymmetry degree as $2s/w$, where s is the distance from the center of the waveguide to the center of the slot, in absolute value, and $w/2$ is half of the total width of the waveguide, see Fig. 2(c). The waveguide parameters are: 14mm long, 250nm height, 80nm slot width, 480nm total width and 5.5° sidewall angle. Total insertion losses were 54dB.

Fig. 3 shows the phase experimental measurement and its polynomial fit. In Fig. 4 we show the dispersion profiles obtained from the fit for each of the three different samples, where numerical simulations performed by using commercial software based on finite element method are also presented for comparison. It can be seen that dispersion values and their slopes reasonably agree with the calculations. Group indices obtained from the ODL are 4.36, 3.21 and 4.17 for Samples A, B and C respectively, while calculated values are 4.35, 3.46 and 4.15, showing a good agreement too.

IV. CONCLUSIONS

A novel method for characterization of dispersion, its dependence with wavelength, and group index, which is immune to thermal fluctuations of the interferometer has been reported. With this method, we have performed an accurate dispersion characterization of conventional silicon strip waveguides for both TE and TM polarizations and for a vertical slot waveguide. Experimental results show a close agreement with theoretical results obtained from simulation.

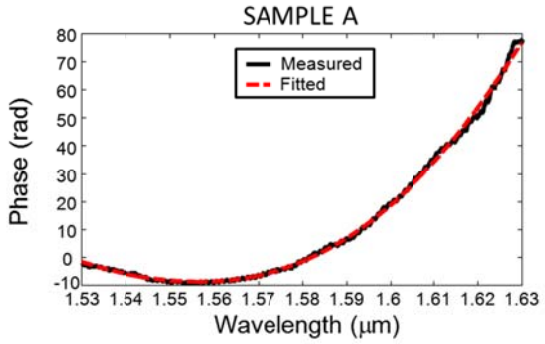


Figure 3. Phase evolution for TE polarization strip waveguide.

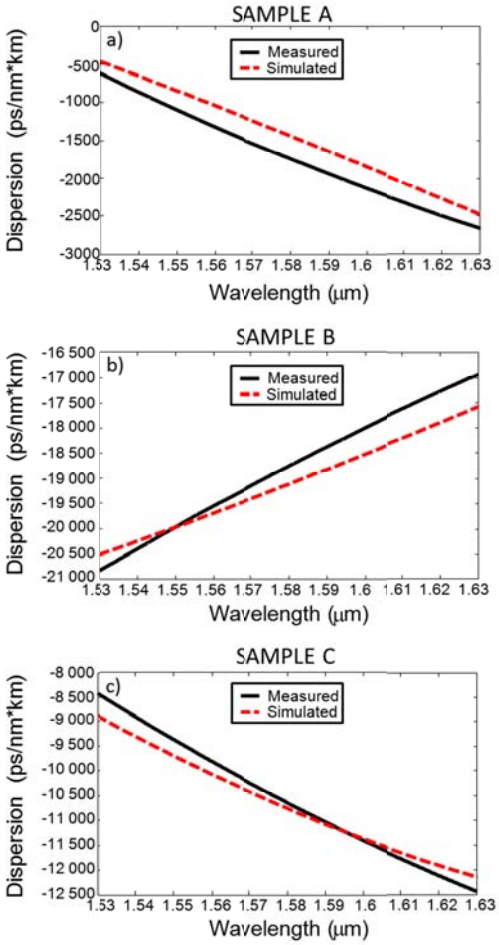


Figure 4. Chromatic dispersion profiles for (a) TE polarization, (b) TM polarization, (c) vertical asymmetric slot.

ACKNOWLEDGMENT

We acknowledge financial support from the Spanish Ministry of Science and Innovation through contracts SINADEC (TEC2008- 06333) and DEMOTEC (TEC2008-06360) and from Generalitat Valenciana through PROMETEO-2010-087 RD Excellence Program (NANOMET).

REFERENCES

[1] L. Cohen and C. Lin, "A universal fiber-optic (UFO) measurement system based on a near-IR Raman laser", IEEE J. Quantum Electron., vol. QE-14,pp.855-859, November 1978.

[2] J. Hult, R.S. Watt and C.F. Kaminski, 'Dispersion measurement in optical fibers using supercontinuum pulses', J. Lightwave Technol., vol. 25,pp. 820-824, March 2007.

[3] L. Thevenaz, J.P. Pellaux and J.P. Von Der Weid, 'All-fiber interferometer for chromatic dispersion measurements', J. Lightwave Technol., vol. 6, pp. 1-7, January 1988.

[4] H.T. Shang, 'Chromatic dispersion measurement by white-light interferometry on metre-length single-mode optical fibres', Elect. Letters, vol. 17,pp. 603-605, August 1981.

[5] J.Y. Lee and D.Y. Kim,'Versatile chromatic dispersion measurement of a single mode fiber using spectral white light interferometry', Opt. Express, vol. 14, pp. 11608-11615, November 2006.

Efficient vertical coupling between a silicon waveguide and an InP-based microdisk

Thijs Spuesens, Yannick De Koninck and Dries Van Thourhout
Photonics Research Group, Department of Information Technology (INTEC)
Ghent University - imec
Ghent, Belgium
thijs.spuesens@intec.ugent.be

***Abstract*—Vertical coupling between a silicon waveguide and an InP-based microdisk structure is investigated and optimized using 3D coupled mode theory simulations. The results are verified with 3D FDTD simulations.**

Keywords-microdisk; vertical coupling; silicon-on-insulator; CMT; FDTD

I. INTRODUCTION

Microdisks have been proven to be useful as ultra-compact high Q passive filters [1], but also several active devices have been successfully demonstrated [2]. One of the most important design parameters in these structures is the coupling between the access waveguide and the microdisk. However, optimization of the coupling efficiency is not trivial as microdisks are inherently multimode in the radial direction. In active microdisk structures this can become even worse when additional vertical modes come into play due to the increased thickness resulting from the extra layers for electrical injection. Especially in more complex configurations when multiple disks are coupled to the same waveguide, such as e.g. a microdisk based multiwavelength laser [3], it is important that the coupling is mainly into the desired mode as otherwise the performance might severely degrade. Here, we investigate the coupling between a silicon waveguide and a heterogeneously integrated InP-based microdisk laser, using both 3D CMT and 3D FDTD methods and present optimum coupling conditions.

II. THEORY AND DESIGN

The results discussed here are for 7.5 µm diameter microdisks with a height of 580 nm and a 100 nm thin slab as shown in Fig.1(a). The gap between the waveguide and the disk is 100 nm. More details about this structure can be found in [2]. Microdisks support the so-called whispering gallery modes (WGM) which propagate at the periphery of the disk cavity. The different WGMs modes can be distinguished by the number of nodes in the azimuthal, radial and vertical direction. The modes with only 1 node in both the radial and vertical direction have the highest Q factor and are therefore the modes of interest and denoted here as fundamental modes. The azimuthal mode number depends on the frequency range of interest and the diameter of the disk. Fig. 1(b-d) shows the mode profiles of a fundamental, first order radial and first order vertical mode respectively. Although, a quite high coupling efficiency can be reached for this microdisk laser structure when using standard 450 nm wide silicon waveguides and a thin bonding layer, it was experimentally found that under these conditions there will also be significant coupling to higher order disk modes. Furthermore, when the waveguide is very close to the disk, the modes in the disk might be perturbed which can result in undesired coupling between higher order disk modes. Therefore, a detailed analysis of the coupling conditions is required.

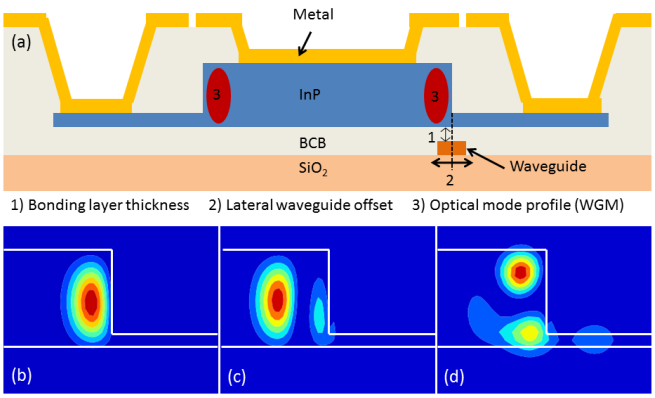


Figure 1. (a) Schematic representation of the cross-section of a microdisk laser. Modeprofile of (b) the fundamental, (c) the first order radial and (d) the first order vertical disk mode.

III. SIMULATION

Typically when simulating vertical coupling conditions between a straight and a bend structure one needs to use 3D FDTD simulations which are very intensive in terms of computational power and time. To investigate the coupling between the microdisk structure and the waveguide we made use of the 3D ring resonator module from Phoenix software [4]. This module is an add-on of their FieldDesigner mode solver and uses a 3D CMT algorithm for the analysis of coupling efficiency. An initial guess for optimal waveguide width can be made by comparing the effective indices of the fundamental mode of both the microdisk and the waveguide. Starting from this initial guess CMT simulation runs are performed where in every run the lateral offset is varied. Over the various runs, which only take up to a few minutes, waveguide dimensions and gap are swept.

The work of T. Spuesens is supported by the Institute for the Promotion of Innovation through Science and Technology (IWT) under a specialization grant Yannick De Koninck acknowledges the Research Foundation-Flanders (FWO-Vlaanderen) for a research grant.

A. *Simulation results using 3D CMT method*

Fig. 2(a) shows the coupling efficiency for a 500 nm wide waveguide versus lateral offset for both the fundamental and the first order radial disk mode. It can be seen that the coupling is maximum for a negative offset of 200 nm. However, for this waveguide width the coupling to the fundamental and first order radial disk mode is in the same order, which is not desirable. In Fig. 2(b) the waveguide width is 750 nm and maximum coupling occurs at a negative offset of 300 nm. One can see that this situation is more desirable as practically all the light couples directly in the fundamental waveguide mode. However, because a 750 nm wide waveguide is already multimode, one needs to be careful that there is no significant coupling between the fundamental disk mode and the first order waveguide mode. It was found that in the case of a 750 nm wide waveguide the coupling to the first order waveguide mode is still sufficiently low. When the waveguide width is increased further the coupling to the first order waveguide mode starts to increase, while the coupling to the fundamental waveguide mode remains the same. Therefore a waveguide width of 750 nm with a 300 nm negative offset seems to be optimal in this situation.

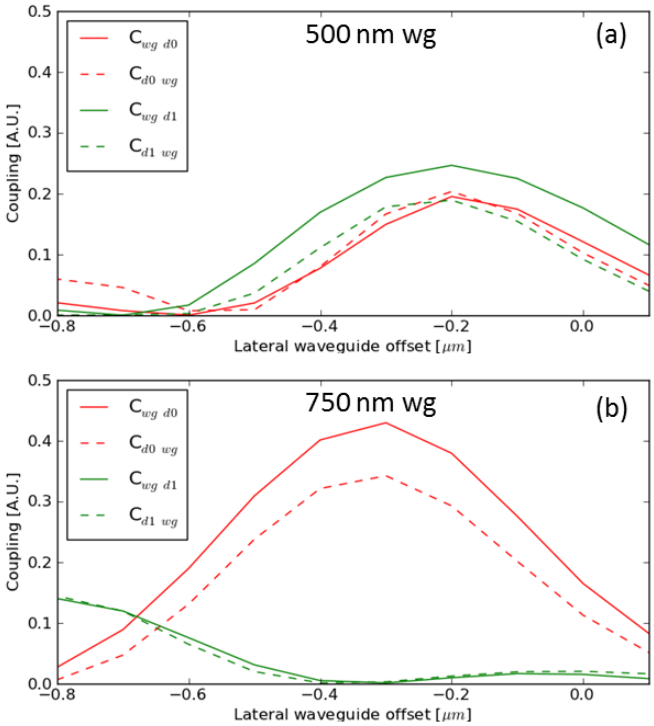


Figure 2. Coupling efficiency between fundamental waveguide mode and fundamental and first order radial disk mode for a (a) 500 nm and (b) 750 nm wide access waveguide. The solid lines represent the coupling from disk to waveguide and the dashed lines the reciprocal.

B. *Simulation results using 3D FDTD*

The bending radii considered here are very small, and results from the CMT simulations were not always perfectly reciprocal as can be seen in Fig. 2. Therefore, the results obtained with the 3D CMT simulations were verified with 3D FDTD using Meep. Fig. 3 shows the field profile of the disk when a CW source is excited in a 500 nm (a) or 750 nm (b) wide waveguide. From this figure it can already be seen that indeed for a waveguide width of 750 nm the coupling is mainly to the fundamental disk mode, while in the case of a 500 nm wide waveguide there is clearly a beating between different modes. To find out what modes are beating, the overlap of the field with the disk mode profiles was calculated. To be able to do this, the time window in the FDTD simulation was kept short such that the light that is coupled from the waveguide into the disk will not make a full roundtrip. The fields were sampled over one period at a cross-section in the waveguide before the disk and a cross-section in the disk as indicated by the red lines in Fig. 3. A Fourier transform was performed on these fields in order to get the frequency dependent field components. From these field components the Poynting vector was calculated for the fields in the waveguide and in the disk. The total amount of power coupled from the waveguide to the disk was calculated and finally, the overlap of mode profiles simulated with FieldDesigner and the field profile simulated with Meep was calculated. For the 500 nm wide waveguide it was found that 22% coupled to the fundamental disk mode and 12% coupled to the first order radial mode, while coupling to other higher order disk modes was negligible. For the 750 nm wide waveguide it was found that 36% was coupled to the fundamental disk mode, while coupling to other higher order modes was negligible. The results obtained with the 3D CMT simulations are thus in good agreement with the 3D FDTD results although the coupling to the first order mode is slightly overestimated in the case of a 500 nm wide waveguide.

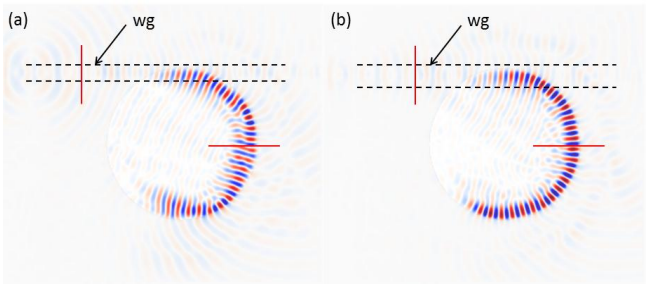


Figure 3. Field profiles of the microdisk for (a) a 500 nm access waveguide with -200 nm offset and (b) a 750 nm access waveguide with -300 nm offset.

ACKNOWLEDGMENT

The authors would like to thank Peter Bienstman for the valuable discussions.

REFERENCES

[1] M. Soltani, Q. Li, S. Yegnanarayanan, and A. Adibi, "Toward ultimate miniaturization of high Q silicon traveling-wave microresonators.," Optics express, vol. 18, no. 19, pp. 19541-57, Sep. 2010.

[2] D. Van Thourhout, T. Spuesens, S. K. Selvaraja, L. Liu, G. Roelkens, R. Kumar, G. Morthier, P. Rojo-Romeo, F. Mandorlo, P. Regreny, and others, "Nanophotonic devices for optical interconnect," Selected Topics in Quantum Electronics, IEEE Journal of, vol. 16, no. 5, pp. 1363–1375, 2010.

[3] J. Van Campenhout, L. Liu, P. Rojo Romeo, D. Van Thourhout, C. Seassal, P. Regreny, L. D. Cioccio, J.-M. Fedeli, and R. Baets, "A Compact SOI-Integrated Multiwavelength Laser Source Based on Cascaded InP Microdisks," IEEE Photonics Technology Letters, vol. 20, no. 16, pp. 1345-1347, Aug. 2008.

[4] Phoenix BV, "3D ring resonator module, FieldDesigner." www.phoenixbv.com, 2011 .